

Fifteenth Symposium

# NAVAL HYDRODYNAMICS

Seakeeping Problems  
Hull-Propeller Interactions  
Nonlinear Free-Surface Problems  
Frontier Problems in Hydrodynamics

sponsored jointly by

OFFICE OF NAVAL RESEARCH

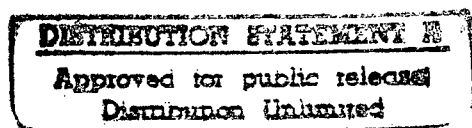
HAMBURGISCHE SCHIFFBAUVERSUCHSANSTALT

NAVAL STUDIES BOARD

COMMISSION ON PHYSICAL SCIENCES, MATHEMATICS,  
AND RESOURCES

NATIONAL RESEARCH COUNCIL

DTIC QUALITY INSPECTED 2



NATIONAL ACADEMY PRESS  
Washington, D.C. 1985

19971124 060

NOTICE: The project that is the subject of this report was approved by the Governing Board of the National Research Council, whose members are drawn from the Councils of the National Academy of Sciences, the National Academy of Engineering, and the Institute of Medicine. The members of the committee responsible for the report were chosen for their special competences and with regard for appropriate balance.

This report has been reviewed by a group other than the authors according to procedures approved by a Report Review Committee consisting of members of the National Academy of Sciences, the National Academy of Engineering, and the Institute of Medicine.

The National Research Council was established by the National Academy of Sciences in 1916 to associate the broad community of science and technology with the Academy's purposes of furthering knowledge and of advising the federal government. The Council operates in accordance with general policies determined by the Academy under the authority of its congressional charter of 1863, which establishes the Academy as a private, nonprofit, self-governing membership corporation. The Council has become the principal operating agency of both the National Academy of Sciences and the National Academy of Engineering in the conduct of their services to the government, the public, and the scientific and engineering communities. It is administered jointly by both academies and the Institute of Medicine. The National Academy of Engineering and the Institute of Medicine were established in 1964 and 1970, respectively, under the charter of the National Academy of Sciences.

This work related to Department of Navy Contract N00014-80-C-0160 issued by the Office of Naval Research under contract authority NR 201-124. However, the content does not necessarily reflect the position or the policy of the Department of the Navy or the government, and no official endorsement should be inferred.

The United States Government has at least a royalty-free, nonexclusive and irrevocable license throughout the world for government purposes to publish, translate, reproduce, deliver, perform, dispose of, and to authorize others so to do, all or any of this work.

Available from:

Naval Studies Board  
National Research Council  
2101 Constitution Avenue  
Washington, D.C. 20418

Printed in the United States of America



## PAPERS COMMITTEE

Odo Krappinger  
Hamburgische Schiffbau-Versuchsanstalt

Ralph D. Cooper  
Flow Research Inc.

Harald G.G. Keil  
Technical University Hamburg-Harburg

Choung M. Lee  
Office of Naval Research

William B. Morgan  
David W. Taylor Naval Ship Research and Development Center

J. Nicholas Newman  
Massachusetts Institute of Technology

Horst Nowacki  
Technical University Berlin

Virendra C. Patel  
University of Iowa

Michael Schmiechen  
Versuchsanstalt für Wasserbau und Schiffbau Berlin

Heinrich Söding  
Institut für Schiffbau Hamburg

## ORGANIZING COMMITTEE

Harald G.G. Keil  
Technical University Hamburg-Harburg

Jürgen Friesch  
Hamburgische Schiffbau-Versuchsanstalt

Odo Krappinger  
Hamburgische Schiffbau-Versuchsanstalt

Som D. Sharma  
Institut für Schiffbau Hamburg

## SYMPOSIUM AIDES

Astrid Wischhusen  
Hamburgische Schiffbau-Versuchsanstalt

Jutta Hamer  
Institut für Schiffbau Hamburg

Naval Studies Board Members

Robert A. Frosch (Chairman)  
General Motors Corporation

Bernard F. Burke  
Massachusetts Institute of  
Technology

David E. Mann  
Physical Dynamics, Inc.

George F. Carrier  
Harvard University

Vincent V. McRae  
IBM - Federal Systems  
Division

Seymour J. Deitchman  
Institute for Defense  
Analyses

William J. Moran  
Lockheed Missiles and Space  
Co., Inc.

Philip M. Diamond  
The Aerospace Corporation

Thomas O. Paine  
Thomas Paine Associates

Edward A. Frieman  
Science Applications  
International Corporation

David S. Potter  
General Motors Corporation

Ivan A. Getting  
Los Angeles, California

Robert M. Powell  
Lockheed Missiles and Space  
Co., Inc.

Willis M. Hawkins  
Lockheed Corporation

Allan R. Robinson  
Harvard University

Robert J. Hermann  
United Technologies

John W. Rouse, Jr.  
University of Texas

John C. Hopkins  
Los Alamos National  
Laboratory

George S. Sebestyen  
Defense Systems, Inc.

Benjamin Huberman  
Consultants International  
Group, Inc.

Peter Swerling  
Peter Swerling Corporation

David W. Hyde  
Texas Instruments

Lee M. Hunt  
Executive Director

Peter J. Mantle  
Office of the Chief of Naval Operations

James G. Wilson  
Consultant

Commission on Physical Sciences,  
Mathematics, and Resources Members

Herbert Friedman (Chairman)  
National Research Council

Edward A. Frieman  
Science Applications Inter-  
national Corporation

Thomas Barrow  
Standard Oil Company

Edward D. Goldberg  
Scripps Institution of  
Oceanography

Elkan R. Blout  
Harvard Medical School

Mary L. Good  
UOP, Incorporated

Bernard F. Burke  
Massachusetts Institute of  
Technology

Thomas F. Malone  
Saint Joseph College

George F. Carrier  
Harvard University

Charles J. Mankin  
Oklahoma Geological Survey

Herman Chernoff  
Massachusetts Institute of  
Technology

Walter H. Munk  
Scripps Institution of  
Oceanography

Charles L. Drake  
Dartmouth College

George E. Pake  
Xerox Research Center

Mildred S. Dresselhaus  
Massachusetts Institute of  
Technology

Robert E. Sievers  
University of Colorado

Joseph L. Fisher  
Office of the Governor  
Commonwealth of Virginia

Howard E. Simmons, Jr.  
E.I. du Pont de Nemours &  
Co., Inc.

James C. Fletcher  
University of Pittsburgh

Isadore M. Singer  
Massachusetts Institute of  
Technology

William A. Fowler  
W.K. Kellogg Radiation  
Laboratory

John D. Spengler  
Harvard School of Public  
Health

Gerhart Friedlander  
Brookhaven National  
Laboratory

Hatten S. Yoder, Jr.  
Carnegie Institution of  
Washington

Raphael G. Kasper  
Executive Director

Lawrence E. McCray  
Associate Executive Director

## FOREWORD

The Fifteenth Symposium on Naval Hydrodynamics was held in Hamburg, Federal Republic of Germany, on September 2-7, 1984, under the joint sponsorship of the Office of Naval Research, the National Research Council, and the Hamburgische Schiffbau-Versuchsanstalt (HSVA) with the support of Institut für Schiffbau, the Deutsche Forschungsgemeinschaft, and the Freie und Hansestadt Hamburg. The symposium was the culmination of several years of intense and careful preparation, and its success is a result of the dedication of many people involved in that work.

The traditional policy of featuring current research results in important problem areas in ship hydrodynamics was reflected in the selection of the major themes of the symposium. The four major themes were Seakeeping Problems; Hull-Propeller Interactions; Non-linear Free-Surface Problems; and Frontier Problems in Hydrodynamics. Two sessions were allocated for each theme, except for the last theme, which had only one session. Thirty-three papers of excellent technical quality were presented. Participants came from as many as twenty-four countries.

A highlight of the symposium was the Seventh Georg Weinblum Memorial Lecture, given as an opening technical session. The lecture given by Professor Marshall P. Tulin of the University of California at Santa Barbara on "Surface Waves from the Ray Point of View" was an inspiring example of challenging ship hydrodynamics research.

There is no way to properly acknowledge all the contributions made by many people to the success of the Fifteenth Symposium on Naval Hydrodynamics. Only a few contributions can be mentioned here. Among those contributors, first and foremost is Professor Dr.-Ing. Odo Krappinger of the HSVA, who served as co-chairman of the Program Committee and was the central coordinator in Germany for all activities involved in the organization and manage-

ment of the symposium. He was ably assisted by Professor H. Keil of Technical University Hamburg-Harburg, Professor S.D. Sharma of Institut für Schiffbau Hamburg, and Dipl.-Ing. J. Friesch of HSVA. Professor Keil, of all the Organizing Committee members, deserves a special acknowledgment for his untiring efforts in ensuring a pleasant and constructive scientific and social atmosphere for the symposium. The acknowledgment would not serve its full purpose if the gracious and dedicated service of Frau Astrid Wischhusen of HSVA were not mentioned. She has perhaps been the major worker behind the scene in carrying out all the many administrative tasks. The Deutsche Forschungsgemeinschaft is also gratefully acknowledged for providing encouragement and financial support for the symposium, as is the Freie und Hansestadt Hamburg for providing the elegant and functional Congress Center for the symposium site. A similar expression of appreciation is extended to the following three individuals for their inspiring addresses during the opening ceremonies: Herr Pawelczyk, Bürgermeister Hamburg; Professor Pfarr, Vice President of the University of Hamburg; and Dr. Frank Press, President of National Academy of Sciences (whose address was read by Mr. Ralph Cooper of the National Research Council). A successful symposium would not have been possible without the able assistance and coordination of Mr. Lee M. Hunt, Executive Director of the Naval Studies Board of the National Research Council, and Ms. Elizabeth Lucks of his staff. They carried out the tremendous task of publishing this proceedings.

Finally, a special and personal expression of gratitude is extended to Dr. Robert E. Whitehead, Dr. Albert D. Wood, and Dr. Arthur M. Diness, of the Office of Naval Research, and Mr. Ralph D. Cooper, of the National Research Council, for their invaluable counsel and encouragement throughout the entire period of the symposium.

Choung M. Lee  
Fluid Mechanics Program  
Office of Naval Research

## CONTENTS

	Page
<u>OPENING CEREMONY</u>	
O. Krappinger, Hamburgische Schiffbau-Versuchsanstalt	3
A. Pawelczyk, Second Mayor of Hamburg	3
H.M. Pfarr, Vice-President of the University of Hamburg	4
F. Press, National Academy of Sciences	5
<u>7TH GEORG-WEINBLUM-MEMORIAL-LECTURE</u>	
SURFACE WAVES FROM THE RAY POINT OF VIEW	9
M.P. Tulin, University of California, Santa Barbara, USA	
<u>SESSION I</u>	
<u>SEAKEEPING PROBLEMS</u>	
NONLINEAR FORCED MOTIONS OF FLOATING BODIES	33
W.-M. Lin, J.N. Newman and D.K. Yue, Massachusetts Institute of Technology, Cambridge, USA	
DISCUSSION	
R.W. Yeung, University of California, Berkeley, USA	48
E.O. Tuck, University of Adelaide, Australia	48
A.T. Chwang, University of Iowa, USA	48
AUTHORS' REPLY	48
SHIP MOTIONS IN SHALLOW WATER BY UNIFIED THEORY	
R. Børresen and O.M. Faltinsen, Norwegian Institute of Technology, Trondheim, Norway	
<u>SESSION II</u>	
<u>SEAKEEPING PROBLEMS</u>	
UNSTEADY WAKE VELOCITIES DUE TO WAVES AND MOTIONS MEASURED ON A SHIP MODEL IN HEAD WAVES	69
A.B. Aalbers and W. van Gent, Maritime Research Institute Netherlands (MARIN), Wageningen, The Netherlands	
SIMULATION OF COMBINED ENGINE AND RUDDER MANEUVERS USING AN IMPROVED MODEL OF HULL-PROPELLER- RUDDER INTERACTIONS	83
P. Oltmann, Hamburgische Schiffbau-Versuchsanstalt, Hamburg, Germany	
S.D. Sharma, Institut für Schiffbau, Hamburg, Germany	
DISCUSSION	
J. Matusiak, Technical Research Center of Finland, Espoo, Finland	106
V. Ankudinov, Tracor Hydraulics Inc., Laurel, USA	106
AUTHORS' REPLY	108
ON THE SHIP MOTION REDUCTION BY ANTI-PITCHING FINS IN HEAD SEAS	109
M. Bessho and Y. Kozuka, National Defense Academy, Yokosuka, Japan	
DISCUSSION	
H. Isshiki, Technical Research Institute Hitachi Zosen Corp., Osaka, Japan	117
R. McGregor, University of Glasgow, United Kingdom	117
J.-Y. Wu, University of Glasgow, United Kingdom	118
AUTHORS' REPLY	118
MULTIPLE SCATTERING OF SURFACE WATER WAVES AND THE NULL-FIELD METHOD	119
P.A. Martin, University of Manchester, United Kingdom	
<u>SESSION III</u>	
<u>SEAKEEPING PROBLEMS</u>	
ADDED RESISTANCE IN WAVES OF HULL FORMS WITH BLUNT BOW	135
M. Ohkusu, Kyushu University, Kasuga, Japan	
DISCUSSION	
S. Bindel, Ecole Nationale Supérieure de Techniques Avancées, Paris, France	148
AUTHOR'S REPLY	148

NONLINEAR DEVELOPMENT OF HEAD SEAS ALONG A LARGE SLENDER BODY	149
C.C. Mei and E. Lo, Massachusetts Institute of Technology, Cambridge, USA	
THE EFFECT OF BOW FLARE AND NONLINEARITIES ON THE PREDICTION OF LARGE AMPLITUDE MOTIONS AND DECK WETNESS	163
J.F. O'Dea and D.A. Walden, David W. Taylor Naval Ship Research and Development Center, Bethesda, USA	
DISCUSSION	
T. Fukasawa, University of Tokyo, Japan	174
W.C. Webster, University of California, Berkeley, USA	174
T. Loukakis, National Technical University, Athens, Greece	174
S. Bindel, Ecole Nationale Supérieure de Techniques Avancées, Paris, France	175
R. McGregor, University of Glasgow, United Kingdom	175
AUTHORS' REPLY	175
THE UNIFIED SLENDER-BODY THEORY: SHIP MOTIONS IN WAVES	177
P.D. Sclavounos, Massachusetts Institute of Technology, Cambridge, USA	
DISCUSSION	
J.S. Pawlowski, National Research Council, Ottawa, Canada	193
AUTHOR'S REPLY	193
A NEW DEVELOPMENT IN THE THEORY OF OSCILLATING AND TRANSLATING SLENDER SHIPS	195
R.W. Yeung and S.H. Kim, University of California, Berkeley, USA	
DISCUSSION	
P.D. Kaklis, National Technical University, Athens, Greece	213
J.S. Pawlowski, National Research Council, Ottawa, Canada	215
AUTHORS' REPLY	216

#### SESSION IV

##### PROPELLER-HULL INTERACTIONS

LOCAL PROPELLER BLADE FLOWS IN UNIFORM AND SHEARED ONSET FLOWS USING LDV TECHNIQUES	221
S.D. Jessup, C. Schott, M. Jeffers and S. Kobayashi, David W. Taylor Naval Ship Research and Development Center, Bethesda, USA	
DISCUSSION	
J. Blaurock, Hamburgische Schiffbau-Versuchsanstalt, Hamburg, Germany	236
W.E. Ball, Admiralty Research Establishment, Haslar, United Kingdom	236
M.S. Chang and N.C. Groves, David W. Taylor Naval Ship Research and Development Center, Bethesda, USA	236
AUTHORS' REPLY	236
CORRELATION OF WAKE MEASUREMENTS AT MODEL AND FULL SCALE SHIP	239
J. Kux, Institut für Schiffbau, Hamburg, Germany	
J. Laudan, Hamburgische Schiffbau-Versuchsanstalt, Hamburg, Germany	
DISCUSSION	
E. Baba and T. Nagamatsu, Mitsubishi Heavy Industries Ltd., Nagasaki, Japan	258
K.-H. Mori, Hiroshima University, Higashi-Hiroshima, Japan	258
D. Fry, David W. Taylor Naval Ship Research and Development Center, Bethesda, USA	259
T.T. Huang, David W. Taylor Naval Ship Research and Development Center, Bethesda, USA	259
E.-A. Weitendorf, Hamburgische Schiffbau-Versuchsanstalt, Hamburg, Germany	259
AUTHORS' REPLY	259
THEORETICAL PREDICTION OF UNSTEADY PROPELLER CHARACTERISTICS IN THE NON-UNIFORM WAKE FIELD	261
H. Maruo, M. Ikehata, Yokohama National University, Yokohama, Japan	
M. Ando, Hitachi Shipbuilding Comp. Ltd., Osaka, Japan	
DISCUSSION	
J.C. Breslin, Stevens Institute of Technology, Hoboken, USA	276
S. Jessup, David W. Taylor Naval Ship Research and Development Center, Bethesda, USA	276
H. Schwanecke, Berlin Ship Model Basin (VWS), Berlin, Germany	276
AUTHORS' REPLY	276
CALCULATION OF THE TURBULENT FLOW AROUND THE STERN AND IN THE WAKE OF A BODY OF REVOLUTION WITH THE PROPELLER IN OPERATION	279
L.-D. Zhou and J.-L. Yuan, China Ship Scientific Research Centre, Wuxi, PR China	
DISCUSSION	
M.S. Chang and T.T. Huang, David W. Taylor Naval Ship Research and Development Center, Bethesda, USA	288
M. Schmiechen, Berlin Ship Model Basin (VWS), Berlin, Germany	289

L. Larsson, SSPA, Maritime Consulting AB, Gothenburg, Sweden	289
G. Dyne, SSPA, Maritime Consulting AB, Gothenburg, Sweden	289
AUTHORS' REPLY	290

#### SESSION V

##### NONLINEAR FREE-SURFACE INTERACTIONS

SPLASHLESS BOW FLOWS IN TWO DIMENSIONS?	293
E.O. Tuck, University of Adelaide, Australia	
J.M. Vanden-Broeck, University of Wisconsin, Madison, USA	
DISCUSSION	
C.-S. Yih, University of Michigan, Ann Arbor, USA	300
R.F. Halliday, University of Sydney, Sydney, Australia	300
S.D. Sharma, Institut für Schiffbau, Hamburg, Germany	301
AUTHORS' REPLY	301
NECKLACE VORTEX AND BOW WAVE AROUND BLUNT BODIES	303
K.-H. Mori, Hiroshima University, Higashi-Hiroshima, Japan	
DISCUSSION	
M. Abe, Mitsui Eng. & Shipbuilding Comp., Akishima Lab., Tokyo, Japan	315
S. Bindel, Ecole Nationale Supérieure de Techniques Avancées, Paris, France	315
A. Kracht, Berlin Ship Model Basin (VWS), Berlin, Germany	315
V.C. Patel, Iowa Institute of Hydraulic Research, Iowa, USA	315
E. Baba, MHI Nagasaki Technical Institute, Nagasaki, Japan	315
H. Miyata, University of Tokyo, Tokyo, Japan	315
AUTHORS' REPLY	316
BOW FLOW FIELD OF SURFACE SHIPS	319
D.J. Fry and Y.H. Kim, David W. Taylor Naval Ship Research and Development Center, Bethesda, USA	
DISCUSSION	
A.J. Musker, Admiralty Research Establishment, Haslar, United Kingdom	346
S.D. Sharma, Institut für Schiffbau, Hamburg, Germany	346
AUTHORS' REPLY	346
SHIP-GENERATED SOLITONS	347
R.C. Ertekin, W.C. Webster and J.V. Wehausen, University of California, Berkeley, USA	
DISCUSSION	
H. Isshiki, Technical Research Institute, Hitachi Zosen Corp., Osaka, Japan	361
A.J. Musker, Admiralty Research Establishment, Haslar, United Kingdom	361
S.J. Lee, G.T. Yates and T.Y. Wu, California Institute of Technology, Pasadena, USA	361
AUTHORS' REPLY	363

#### SESSION VI

##### NONLINEAR FREE-SURFACE INTERACTIONS

EDGE WAVES CREATED BY A LONGSHORE CURRENT AND A RIDGE IN THE SEA-BED	367
C.S. Yih, University of Michigan, Ann Arbor, USA	
A STUDY OF NONLINEAR WAVE RESISTANCE BY A ZAKHAROV-TYPE INTEGRAL EQUATION	373
G. Dagan and T. Miloh, Tel-Aviv University, Ramat-Aviv, Israel	
DISCUSSION	
G. Jensen, Institut für Schiffbau, Hamburg, Germany	385
K. Eggers, Institut für Schiffbau, Hamburg, Germany	385
AUTHORS' REPLY	385
EFFECT OF BOW SHAPE ON FREE-SURFACE SHEAR FLOW	387
K. Takekuma, MHI Nagasaki Experimental Tank, Nagasaki, Japan	
K. Eggers, Institut für Schiffbau, Hamburg, Germany	
DISCUSSION	
H. Miyata, University of Tokyo, Tokyo, Japan	401
K.-H. Mori, Hiroshima University, Higashi-Hiroshima, Japan	402
A. Kracht, Berlin Ship Model Basin (VWS), Berlin, Germany	403
C.P. Thomsen, Fachhochschule Hamburg, Hamburg, Germany	403
V.C. Patel, University of Iowa, Iowa City, USA	404
S. Ogiwara and A. Masuko, Ishikawajima-Harima Heavy Industries Co. Ltd., Yokohama, Japan	404
AUTHORS' REPLY	405

WAVE-TRAPPING DUE TO A POROUS PLATE	407
A.T. Chwang, Institute of Hydraulic Research, University of Iowa, Iowa City, USA	
Z. Dong, Tsinghua University, Beijing, PR China	
DISCUSSION	
H. Isshiki, Technical Research Institute, Hitachi Zosen Corp., Osaka, Japan	417
AUTHORS' REPLY	417
ON THE INFLUENCE OF NONLINEARITY OF BOUNDARY CONDITIONS AT THE HULL AND WATER SURFACE	419
IN THE PROBLEM OF A SHIP'S WAVE RESISTANCE	
E.L. Amromin, A.N. Ivanov, I.O. Mizin and Y.S. Timoshin, Krilov Shipbuilding Research	
Institute, Leningrad, USSR	
DISCUSSION	
E. Baba, Mitsubishi Heavy Industries Ltd., Nagasaki, Japan	425
R.F. Halliday, University of Sydney, Sydney, Australia	425
A.J. Musker, Admiralty Research Establishment, Haslar, United Kingdom	425

## SESSION VII

### PROPELLER-HULL INTERACTIONS

A DIFFERENTIAL PREDICTION METHOD FOR THREE-DIMENSIONAL LAMINAR AND TURBULENT BOUNDARY	429
LAYERS OF ROTATING PROPELLER BLADES	
N.C. Groves and M.S. Chang, David W. Taylor Naval Ship Research and Development Center,	
Bethesda, USA	
DISCUSSION	
J.P. Breslin, Stevens Institute of Technology, Hoboken, USA	444
AUTHORS' REPLY	444
A PERFORMANCE PREDICTION THEORY FOR PARTIALLY SUBMERGED VENTILATED PROPELLERS	445
O. Furuya, Tetra Techn. Inc., Pasadena, USA	
DISCUSSION	
W.B. Morgan, David W. Taylor Naval Ship Research and Development Center,	461
Bethesda, USA	
E.A. Weitendorf, Hamburgische Schiffbau-Versuchsanstalt, Hamburg, Germany	461
AUTHOR'S REPLY	461
FREE-SURFACE EFFECT ON THE HULL-PROPELLER INTERACTIONS	463
R. Yamazaki and K. Nakatake, Kyushu University, Fukuoka, Japan	
DISCUSSION	
J. Blaurock, Hamburgische Schiffbau-Versuchsanstalt, Hamburg, Germany	477
H. Nowacki, Technical University of Berlin, Berlin, Germany	477
S.D. Sharma, Institut für Schiffbau, Hamburg, Germany	477
E. Baba, Mitsubishi Heavy Industries Ltd., Nagasaki, Japan	477
M. Schmiechen, Berlin Model Basin (VWS), Berlin, Germany	478
AUTHORS' REPLY	478
ON WAKE AND THRUST DEDUCTION FROM PROPULSION TESTS ALONE - A RATIONAL THEORY OF SHIP	481
HULL-PROPELLER INTERACTION	
M. Schmiechen, Berlin Model Basin (VWS), Berlin, Germany	
DISCUSSION	
L.-D. Zhou, China Ship Scientific Research Center, Wuxi, PR China	499
G. Dyne, SSPA Maritime Consulting AB, Gothenburg, Sweden	499
M. Abe, Mitsui Eng. & Shipbuilding Comp. Akishima Lab., Tokyo, Japan	499
K. Nakatake, Kyushu University, Fukuoka, Japan	500
AUTHOR'S REPLY	500

## SESSION VIII

### FRONTIER PROBLEMS

CALCULATION OF STERN FLOWS BY A TIME-MARCHING SOLUTION OF THE PARTIALLY-PARABOLIC EQUATIONS	505
H.C. Chen and V.C. Patel, University of Iowa, Iowa City, USA	
DISCUSSION	
Y.-T. Lee and T.T. Huang, David W. Taylor Naval Ship Research and Development	521
Center, Bethesda, USA	
T. Loukakis, National Technical University, Athens, Greece	521
K.-A. Mori, Hiroshima University, Higashi-Hiroshima, Japan	521
AUTHORS' REPLY	522



A CALCULATION METHOD FOR SHIP STERN FLOWS USING AN ANALYTICAL BODY-FITTED COORDINATE SYSTEM	525
L. Broberg, Chalmers University of Technology, Gothenburg, Sweden	
L. Larsson, SSPA and Chalmers University of Technology, Gothenburg, Sweden	
DISCUSSION	
M.S. Chang, David W. Taylor Naval Ship Research and Development Center, Bethesda, USA	538
AUTHORS' REPLY	538
UTILIZATION OF WAVE ENERGY FOR PROPULSION OF SHIPS - WAVE DEVOURING PROPULSION	539
H. Isshiki and M. Murakami, Technical Research Institute, Hitachi Zosen Corp., Osaka, Japan	
Y. Terao, Tokai University, Shizuoka, Japan	
RESISTANCE INCREASE DUE TO SURFACE ROUGHNESS	553
M. Nakato, Hiroshima University, Saijo Higashi, Hiroshima, Japan	
H. Onogi, Tsu Res. Lab. of Nippon Kokkan KK, Tsu City, Japan	
Y. Himeno, University of Osaka Prefecture, Osaka, Japan	
I. Tanaka and T. Suzuki, Osaka University, Osaka, Japan	
DISCUSSION	
P.S. Granville, David W. Taylor Naval Ship Research and Development Center, Bethesda, USA	567
A.J. Musker, Admiralty Research Establishment, Haslar, United Kingdom	568
AUTHORS' REPLY	568
NUMERICAL SIMULATION OF FLOW AROUND BLUFF BODIES AT HIGH REYNOLDS NUMBERS	569
J.J.W. van der Vegt and R.H.M. Huijsmans, Maritime Research Institute Netherlands (MARIN), Wageningen, The Netherlands	
DISCUSSION	
B. Pettersen, Norwegian Institute of Technology, Trondheim, Norway	585
A.J. Hermans, Technische Hogeschool Delft, Delft, The Netherlands	585
AUTHORS' REPLY	585

LIST OF PARTICIPANTS	587
----------------------	-----

INDEX OF CONTRIBUTORS	591
-----------------------	-----

## OPENING CEREMONY

Prof.Dr.-Ing. ODO KRAPPINGER,  
Hamburgische Schiffbau-Versuchsanstalt GmbH, Hamburg, Germany:

Herr Bürgermeister!  
Frau Vizepräsidentin!  
Ladies and Gentlemen!  
Dear Friends!

It is a great pleasure for me to welcome you to the 15th Symposium on Naval Hydrodynamics. We feel privileged to host this meeting of distinguished scientists here in Hamburg. I think that I do not promise too much when I say that a bunch of very interesting and highbrow papers will be presented during this week. In this connection I would like to thank all the colleagues who initiated so many proposals for papers. Thanks go also to the members of the United States and German Papers Committee and last but not least to the authors.

As you all know the world maritime industry is in a serious crisis. In the industry this leads to very hard competition and as a consequence to a strained atmosphere. Fortunately, this situation is not as harmful for this symposium and its participants. Of course, there are more difficulties now with regard to travel funds etc. and the one or other colleague who intended to be here could not come because of this reason. On the other hand there is general agreement that the future of the maritime industry depends - beside others - on today's research. Fundamental research - which is the main concern of this symposium - needs international cooperation. And cooperation means in the first line communication. I can think of no better base for communication than personal relationships or even friendships.

This philosophy has been very successfully practised by the late Georg Weinblum. Therefore the inclusion of the Georg-Weinblum-Memorial-Lecture into the program of this symposium is not only a tribute to his contributions to ship hydrodynamics. It is also a tribute to his ability to make many people working in ship hydrodynamics feel as being members of a big family. This spirit is still existent in the Symposia on Naval Hydrodynamics. We have tried hard to make all provisions that this tradition will be maintained here in Hamburg, the place where Weinblum had spent most of his professional life.

In this we were lucky to have had a lot of support. I would like to express our gratitude to the Office of Naval Research, the National Academy of Sciences, the City of Hamburg and the German Research Association. I also have to thank Dr. Cooper, Dr. Lee and Mr. Hunt for the good cooperation during the time of preparation of the Symposium.

I hope that your stay in Hamburg will be rewarding, professionally as well as socially.

Again: Welcome in Hamburg!

We are very grateful that Bürgermeister Pawelczyk has come to the opening of our Symposium in spite of the fact that he has so many other commitments. We are sorry that he has to leave us shortly after having delivered his address because there is a meeting of the Senat (which is the government of Hamburg).

---

ALFONS PAWELCZYK,  
Second Mayor of Hamburg:

Distinguished Ladies and Gentlemen!

May I cordially welcome you on behalf of the Free and Hanseatic City of Hamburg. I hope you arrived here well in time to have seen also the gay festivities yesterday and the day before. This is the first ONR Symposium on Naval Hydrodynamics to be held in the Federal Republic of Germany. We are of course pleased that it is being conducted in Hamburg. We perceive your choice of this city as an - in our opinion - well deserved appreciation of our Hamburg Ship Model Basin. The HSVA is now 70 years old and eminently successful in its work. It maintains a close cooperation with the Institute of Naval Architecture of the University of Hamburg, founded 32 years ago. You can understand the importance attached by Hamburg to technological development from the fact that we are currently the only state in the Federal Republic of Germany building up a new technical university. The first research projects are already in progress and the further development of this institution has top priority in the decisionmaking of our government, also right now during our budget deliberations. We are convinced that a collaboration of these institutions in all areas, including the one of your interest, will enable Hamburg to maintain a high standard and to generate important impulses also in the future. I feel it is one of my major tasks as the Second Mayor of this city and as Hamburg's plenipotentiary in the federal capital Bonn to make sure that this close cooperation functions well also with respect to the federal agencies. And I know also from those contacts, that your work enjoys a high reputation, which is also underlined by the fact that you are holding this conference here with so many participants.

I wish to thank you heartily for that. I wish for your sake and ours that you will keep Hamburg in good memory, primarily because you will have interesting discussions here and depart with new ideas, but also because you will hopefully gain and retain pleasant impressions of our city. I wish you every success.

Prof.Dr. HEIDE M. PFARR,  
Vice-President of the University of Hamburg:

Ladies and Gentlemen!

On behalf of the University of Hamburg I would like to welcome you to the 15th Symposium on Naval Hydrodynamics. I am proud as Vice-President of the University of Hamburg, and the organizers from the shipbuilding institutions located in Hamburg are proud that this symposium, being held for the first time in the Federal Republic of Germany, is taking place here in Hamburg. This underscores Hamburg's significance as a city involved with the science of shipbuilding.

After going over your program with its four main topics:

- Seakeeping problems
- Propeller-hull interactions
- Nonlinear free-surface interactions
- Frontier problems in hydrodynamics

and reading through the papers, I must confess that I was overcome by an uncomfortable feeling: I had not really understood a thing!

As representatives of a science which is generally considered to be typically male - I was just recently introduced to the male rites of shipbuilding, and women are sparsely represented among the lecturers - you might think that this lack of comprehension is owing to my sex, that women naturally find it difficult to understand complex physical-mathematical-engineering topics. This explanation does not seem to me to be quite right. It is rather a problem - also a didactic one - of expressing complex facts so that they may be generally understood by all. As Vice-President of the University, I experience more and more frequently that - today, when budgets everywhere are becoming tighter - science is being increasingly put under pressure by society to justify itself. Science has to account for what it is doing with the money that society invests in it. And these sums are not so very small: The annual expenditures for the University of Hamburg alone amount to 715 million DM (including the University hospital (UKE), excluding UKE: 307 million). I consider this obligation toward justification to be a legitimate demand made on science. And I believe that science must meet this obligation on the offensive, by actively seeking the way to the public. It must make clear to the public what research is being done and of what use this research can be to society.

You, the participants in this symposium on naval hydrodynamics, are involved in a highly practice-oriented theory of shipbuilding and actually ought to be predestined to fulfill society's demand on this score.

Please do not misunderstand me - I don't mean to criticize your professional program. I just want to express that I feel that a bit more publicity for your symposium would have been beneficial. For example a public lecture, perhaps on the topic - which I formulate as a layman - "Significance of Naval Hydrodynamics for the Reduction of the Energy - Consumption of Ships" or something similar, would certainly have raised public interest and appreciation of your science.

Prof. Georg Weinblum, who died ten years ago and to whom the following first lecture of this symposium will be dedicated, was a man who knew how to unite the theory and practice of shipbuilding in an outstanding manner and how to convince others of the significance of his field. He became the first director of the newly founded Institute for Shipbuilding of the University of Hamburg in 1952. He succeeded in establishing a technical subject - for quite some time the only technical subject! - at a university which, from the historic development of the structure of its subjects, actually seemed to be rather hostile toward technical subjects. Thanks to his initiative, shipbuilding soon became well-anchored (!) at the university.

For a long time students were offered courses in conjunction with the Technical University of Hannover. Today, the training takes place exclusively in Hamburg, in cooperation with the Fachhochschule Hamburg (Technical College) and the newly founded Technical University Hamburg-Harburg. Such cooperation at the university level is today an exception. Many subjects and institutions still have a "separatist attitude" and prefer to isolate themselves.

Georg Weinblum was an exceptional person in still another way - namely in his active commitment toward international relations - for the Institute for Shipbuilding and for shipbuilding in general. In 1971, Weinblum wrote in a brochure: "Characteristic of shipbuilding is its openness to the world; international exchange and cooperation are in this respect the life elements of our science. To promote these things especially in Hamburg was initially the most important task of our institute" (uni forschung Nr. 3, S. 2). The internationality of science that Weinblum describes here is one of the University of Hamburg's special interests. One look around the room at the participants in this symposium proves the correctness of Prof. Weinblum's statement.

Ladies and Gentlemen, I wish you a successful symposium.

Address by Dr. FRANK PRESS,  
National Academy of Sciences, Washington D.C., USA:  
(Read by Dr. RALPH COOPER)

Ladies and Gentlemen of the ship hydrodynamics community!

It is with distinct pleasure that the National Academy of Sciences again joins with the Office of Naval Research, and, on this occasion, the Hamburgische Schiffbau-Versuchsanstalt GmbH in supporting the latest in this prestigious series of symposia. I am sorry that I am unable to welcome you in person to the Fifteenth Symposium on Naval Hydrodynamics. However, I have asked Ralph Cooper, who is now a member of my staff, to read my statement to you.

The formal objective of the First Symposium on Naval Hydrodynamics - held in 1956 - was "to provide an international forum for the exchange of ideas and research results in the field of ship hydrodynamics." For 28 years now that simple, yet ever so fundamental objective, has remained unchanged.

It is the stated objective of the symposium upon which you are about to embark.

In a recent issue of FOREIGN AFFAIRS, Lewis Thomas of the Sloan-Kettering Cancer Research Institute of New York referred to science as "one of the most communal of human endeavors." I agree and would add, by way of elaboration, that science - practiced in its natural and unrestrained state - is one of the most communicative of human endeavors. This week the leading experts from 12 countries - through 34 formal papers and innumerable formal and informal discussions - will share the knowledge accumulated over the past two years. And, those taking part in these discussions will do so from a base of understanding that has evolved, in large measure, from all previous exchanges of this type.

Therefore, I would like to congratulate the principal sponsor, the members of this community, and the institutions you represent for steadfast adherence to your founding objective - the free exchange, on an international basis, of research results and the ideas, thoughts, and questions which emerge from it. It is science, both basic and applied, practiced at its best.

In looking over the four topics you have chosen to provide the theme for the Fifteenth Symposium I was particularly pleased to see that you have included "Seakeeping Problems." Over the past several years the Academy has conducted three studies which strongly supported the selective introduction of the SWATH hull form because of its improved seakeeping characteristics. I was pleased to learn that a number of countries represented here today have plans to either keep abreast of developments in this area or are drawing plans for actual construction. In the area of SWATH development, our Japanese colleagues are to be especially congratulated. Their MESA-80 is already providing valuable operational experience, and will soon be joined by the hydrographic survey ship KAI0.

Finally, I would like to join with the Office of Naval Research in thanking our German colleagues for the excellent job they have done in preparing for the Fifteenth Symposium. The toughest chore always falls on the host in this series as we have learned. I am sure you all join me in expressing our gratitude. My very best wishes to you all for a very successful meeting.

**Preceding Page Blank**

GEORG-WEINBLUM-MEMORIAL-LECTURE

**Preceding Page Blank**

## THE SEVENTH GEORG - WEINBLUM-MEMORIAL-LECTURE

### SURFACE WAVES FROM THE RAY POINT OF VIEW

MARSHALL P. TULIN

#### INTRODUCTION

In commenting on a paper of Bessho (1966), Georg Weinblum noted:

"Science is subject to fashion as much as other human activities. Recently the thin ship and surrogates have completely dominated the field, but in the twenties (and earlier) the pressure system has been considered as being an equally important hydrodynamic model (at least in principle) as the Michell ship, especially suitable for picturing fast shallow-draft and planing vessels. By Dr. Bessho's paper a sound equilibrium has been established. The present speaker had emphasized the similarity of the Hogner and the Michell integral (Zamm, 1930) and thus inspired Sir Thomas Havelock to derive the simple relation between source-sink distributions  $\sigma$  and pressure systems  $p$

$$4\pi\rho g\sigma = c \frac{\partial p}{\partial x} \quad "$$

These days the fashion in ship waves has been very much with so-called low-speed theories, which can be implemented through digital computation. The question has arisen, Keller (1979), as to the nature of true asymptotic low speed theory. In that paper he proposed a ray theory. In the present paper, which I have prepared especially for this lecture, I have chosen to explore the ray theory and to begin by combining it with a very old fashioned subject, and one which early attracted the attention of Weinblum himself, the waves made by a moving pressure patch. In this case, assuming light loading, linearizing assumptions are valid and the theory takes a simple form. It is therefore very useful for sharpening our tools and insight.

After that start we tackle the ship problem, as Keller already has. We made no assumptions concerning the thickness of the ship. We repeat some of his findings. We also find some waves issuing from a limited portion aft and from the ends. We have formulae for these waves. At the ends the situation is, however, ambiguous because of insufficient knowledge of the displacement flow giving rise to the waves.

A few words concerning ray theory. Its antecedents are found in geometrical optics. In dispersive systems it arises with group velocity as a product of asymptotic integration and is inherent in Kelvin (W. Thomson) (1887) and Havelock (1908), and later works, and then much later in Stoker (1957) who considered the wave pattern created by a ship moving in a curved trajectory. All of these assumed no displacement flow in the water. But in problems of optics and acoustics, the inhomogeneity of the medium had long been considered. For dispersive systems, at least for ship waves, this was first discussed and the basic relations given by Ursell (1960), and independently by Whitham (1961). At about the same time, the fundamentals of the interaction between waves and currents were laid out in a series of important papers: Longuet-Higgins and Stewart (1960,1961) and Whitham (1960,1962); see also the discussion in Phillips (1966). The basic assumption of the ray theory is that the waves are short in comparison to the scale over which the flow changes (it is this assumption which is at question near the ends of the ship), so that the waves may be assumed to have locally the same dispersive relation as in undisturbed water (it is this assumption which Eggers (1981) questions at the bow of a ship).

Presidential Professor, Department of Mechanical and Environmental Engineering,  
University of California, Santa Barbara, California 93106

A detailed study of the implications of ray theory for ship waves was begun and later extended by Keller (1974, 1979), while the actual application was begun by Inui and Kajitani (1977) who assumed the waves generated as in linear theory and utilized ray theory to calculate the bending of the rays. Yim (1981) has later made extensive ray tracing studies in the same spirit.

Here we are motivated to understand how ships generate waves, in this case in the true low speed limit; as many questions are eventually raised as are answered.

## 1. WAVES GENERATED BY A STEADY MOVING PRESSURE PATCH IN THREE DIMENSIONS

### Introduction

The problem of the waves generated by a moving real ship contains serious non-linear features. On the other hand, the waves generated by a pressure patch of finite size moving on top of the water surface can perhaps be treated using linearizing assumptions, provided that the magnitude of the pressures are suitably small. And the solution to this problem can yield valuable understanding of wavemaking, just as Kelvin's treatment in 1887 of a concentrated pressure patch. This is certainly the reason why Georg Weinblum (1930) undertook to study this problem. Much later it became of some importance in connection with the performance of air cushion vehicles like the Hovercraft, and was studied by several workers, notably Nick Newman (1962).

Here we study this problem using ray (asymptotic) techniques and obtain some important results; then we go on to the case of a real ship, which is considerably more complicated; but non-linear effects can be treated with interesting results. These ray techniques which we use, first in the linear pressure patch case and then in the non-linear ship case, are generally applicable in the limit of small Froude number.

The usual linearizing assumptions which we employ in the pressure patch problem are: i) the deep water waves propagate locally as progressive waves of small amplitude, for which the dispersion relation between the wave frequency,  $\omega$ , and wave number,  $k$ , is:  $\omega^2 = gk$ ; ii) waves are generated at each point on the free surface under the pressure patch, and the amplitude of the generated waves is proportional to the excess pressure,  $p_0$ , associated with the patch; iii) the waves generated at each point add linearly; iv) the waves, once generated, propagate over the water surface as if it were at rest. The last assumption is decisive and is equivalent to assuming that the moving pressure patch does not induce any significant motion in the water, aside from the waves themselves. This is certainly not true in the case of displacement ships, where the water is forced to go around the ship as well as to issue waves; we shall correct for this vital difference later.

We imagine a patch of constant pressure moving over the water at a speed  $U(t)$ , from right to left along the  $x$ -axis, Figure 1.1. Our technique will be to observe the waves,  $\eta(t)$ , arriving at an observer point,  $P(x,z) = \xi$ , at a distance of many wavelengths from the moving pressure patch. We assume to begin with that these waves can arrive along any ray passing from the observer point to the pressure patch (later we show that only distinct rays contribute at any time,  $t$ ). We designate the rays by their angle of inclination,  $\beta$ , to the horizontal axis. In our present approximation, since no motion occurs in the water to bend the rays, they are straight lines.

### The Far Field Plane Wave Spectrum

An elemental radial wave is generated as if by a concentrated imposition of pressure  $p_0$  (a delta function) at each point of the water over which the pressure patch passes. Those waves generated along a fixed ray bundle (origin at  $\xi$ ) of mean ray angle  $\beta$  and width,  $(\xi - \xi')d\beta$ , and observed at the fixed point,  $\xi(x,z)$ , can be represented as an integration of the generator points,  $\xi'$ , along the mean ray, and over time,  $t' < t$ :

$$\frac{d\eta}{d\beta}(\xi, t, \beta) = R \cdot \int_{\xi_l}^{\xi_u} dt' \int_{\xi_l}^{\xi_u} \frac{p_0}{\rho} [A](\xi - \xi') i e^{i\{k(\xi - \xi') - \omega(t - t')\}} d\xi' ; \quad C_g(k) = \frac{\xi - \xi'}{t - t'} \quad [1.1]$$

where  $\xi_{l,u}$  are the intersections of the ray with the upper and lower boundaries of the patch, and  $C_g = d\omega/dk$ . The function  $[A]$  is found from the asymptotic (ray) theory solution for the wave due to a concentrated imposition of pressure. It is, see Havelock (1908) or Lamb (1932):

$$[A] = g(t - t')^{3/2} \pi (\xi - \xi')^4 = g^{7/2} \pi (\xi - \xi')^3 C_g \quad [1.2]$$



The result of this collection of waves generated within the ray bundle is a plane wave of wave number  $k$  and amplitude,  $\text{Amp}(\beta)$ :

$$\frac{d\eta}{d\beta} = R \cdot [\{\text{Amp}(\beta)\} e^{i[k\xi - \omega t]}]_{\omega}; \text{ far field} \quad [1.3]$$

It was originally pointed out by Thomas Havelock (1934), that the far field wave may be represented by a distribution (spectrum,  $\frac{d\eta}{d\beta}$ ) of such waves:

$$\eta(\xi, t) \cong \int_0^{\pi} \frac{d\eta}{d\beta}(\xi, t, \beta) d\beta \quad [1.4]$$

and the wave resistance (in the case of uniform motion) given simply as:

$$\text{Res.} = \pi \rho U_0^2 \int_{\pi/2}^{\pi} [R \cdot \{\text{Amp}^2(\beta)\} + I \cdot \{\text{Amp}^2(\beta)\}] \cos^3 \beta d\beta \quad [1.5]$$

a result we shall refer to later. In consequence, the problem of determining wave resistance is equivalent to the determination of  $\frac{d\eta}{d\beta}$ , [1.1], in the far field ( $\xi \rightarrow \infty$ ).

#### The Boundary Sources

The integral, [1.1], has no stationary phase points so its asymptotic form can be determined through repeated integration by parts. The result can be represented as a sum of terms with coefficients  $k^{-1}$ ,  $k^{-2}$ , etc. In the present case, where the observer is many wavelengths from the generator point, the first term in this series is dominant and:

$$\frac{d\eta}{d\beta}(\xi, t, \beta) \cong R \cdot \int_0^t \frac{p_0}{\rho k} \{ [A(\xi - \xi_u^*; t - t')] (\xi - \xi_u^*) \cdot e^{i f_u} - [A(\xi - \xi_\ell^*; t - t')] (\xi - \xi_\ell^*) \cdot e^{i f_\ell} \} dt' \quad [1.6]$$

where:  $f_{u,\ell} = k(\xi - \xi_{u,\ell}^*) - \omega(t - t')$ , and  $\xi_{u,\ell}^*$  refer to the intersection of the ray with the patch boundary at time  $t'$ .

We see, [1.6], that waves seem to originate only on the boundary of the pressure patch.

#### Radiation from the Boundary: Ray Theory

The integration of these wave generators (i.e. in  $t'$ ) represented by [1.6] is facilitated by the application of Kelvin's method of stationary phase, see Stoker (1957); this method assumes asymptotic conditions; i.e. that the wave length is much shorter than the range of integration and that  $[A]$  varies slowly enough. We recall for reference, if:

$$b(\xi) = R \cdot \int_{t_1}^{t_2} a(\xi, t') e^{i\psi(\xi, t')} dt'$$

then,

$$b(\xi) \cong R \cdot \sum_p e^{i\{\psi(\xi, t_s) + \pi/4 \text{sgn } \psi_s''\}} a(\xi, t_s) \left[ \frac{2\pi}{|\psi_s''|} \right]^{1/2} + \\ + R \cdot \sum_p e^{i\psi(\xi, t_p)} \cdot a(\xi, t) \frac{\Gamma(1/3)}{\sqrt{3}} \left( \frac{6}{|\psi_s''|} \right)^{1/3} \quad [1.7]$$

where  $\psi' = \frac{\partial \psi}{\partial t'}(t_c) = 0$ , defines the points  $t' = t_c$  where the dominant contribution to the integral arises when  $\psi'' \neq 0$ ; and where  $\psi' = \psi'' = 0$  defines the points  $t = t_c$  where the dominant contribution arises when  $\psi''' = 0$ ; i.e. if  $\psi_s'' \neq 0$  sum only over  $s$ , and when  $\psi_s'' = 0$ , sum only over  $p$ . In this latter case, rays focus by bunching and the resultant wave is more observable. This condition is called a caustic.

Upon applying Kelvin's method to the integration of the boundary waves, [1.6], we find the main contribution arising from points where (stationary phase point):

$$\frac{df_{u,l}}{dt'} = \frac{d}{dt'} \{k(\xi - \xi_{u,l}^*) - \omega(t - t')\} = 0$$

or,

$$\frac{d\xi_{u,l}^*}{dt'} = \omega/k = C_p(k) \quad [1.8]$$

where  $C_p$  is the phase velocity of the wave; this condition defines the wave number of the wave arising at each point of the path boundary; i.e. the phase velocity of the outgoing boundary wave is equal to the velocity of the boundary along the ray.

We have so far considered an arbitrary velocity of the pressure patch. When the patch moves with constant horizontal speed,  $U_0$ , then all of the waves in the resulting pattern must be stationary in body coordinates (the frame of reference moving with the patch) and it follows that the phase speed,  $C_p$ , of the wave traveling along a ray at angle  $\beta$  (Figure 1), is:

$$C_p(k) = -U_0 \cos \beta \quad [1.9]$$

This follows from the fact that the frequency of wave encounter to an observer traveling with velocity  $\vec{V}_{obs}$  is:  $k|\vec{V}_{obs} \cdot \vec{e}^{\beta} - C_p|$ .

Notice that for waves moving outward toward the observer point above the patch,  $C_p > 0$ , so that  $\pi/2 < \beta < \pi$ . These waves may be classified in the usual way: those traveling on rays closest to the vertical (divergent waves) are short, while those on rays closest to the horizontal (transverse waves) are longest.

This condition of stationarity, [1.9], when combined with the stationary phase condition, [1.8], leads to a relationship between the local ray angle,  $\beta(k)$ , and the local patch angle measured from the horizontal,  $\alpha^*$ . First it may be shown taking into account the cutting angle,  $\beta$ , of the ray as it traces out  $\xi_{u,l}(t')$  that:

$$\frac{d\xi_{u,l}^*}{dt'} = \frac{U_0 \tan \alpha^*}{\cos \beta (\tan \beta - \tan \alpha^*)} = \frac{U_0 \sin \alpha^*}{\sin(\beta - \alpha^*)} \quad [1.10]$$

and then combining [1.8-1.10] we finally find that the wave number vector is normal to the patch boundary!:

$$(\beta - \alpha^*) = \pi/2 \quad [1.11]$$

This is a result we might have expected. It is well known that in the case of non-dispersive wave systems (optics or acoustics), that the signal is primarily due to excitation from the point on the body which lies closest to the observer and therefore arrives on the ray normal to the body.

We note: each and every point of a smooth patch boundary produces (at a fixed observer point above the patch) a single wave (single  $k$ , corresponding to  $\beta$ ); however each wave ( $k$ ) receives a contribution from all points sharing the same patch boundary angle,  $\alpha^*$ ; the transverse waves arise particularly from the blunt ends and the divergent waves from the moderately sloped sides. The waves traveling to an observer above the patch will originate from the upper forward and rear aft sectors of the patch boundary, see Figure 1.2. For smooth shapes, then, each wave will be excited at two generator points, one in each of the contributing sectors, provided that a normal to the ray exists (for boundaries with non-blunt ends, the range of  $\beta$  will be limited). Finally a simple relation exists for the phase velocity at any point:  $C_p = U_0 \sin \alpha$ .

The wave energy moves away from the boundary generation points,  $\xi_{u,0}^*$ , along the rays,  $\beta(\alpha^*)$ , at the group velocity,  $\dot{\xi}_g(k)$ . The waves from each generator point will thus be seen by an observer moving with the pressure patch along an angle,  $\gamma$ , to the horizontal, given by the argument of the vector  $\dot{\xi}_g(k) - \dot{U}_0$ . The ray  $\beta$  is thus transformed to body coordinates with the result (we also use [1.11]):

$$\tan \gamma = \frac{-\sin \beta \cos \beta}{1 + \sin^2 \beta} = \tan \alpha^* \cdot \left[ \frac{\cos^2 \alpha^*}{1 + \cos^2 \alpha^*} \right] \quad [1.12]$$

We note that the body rays pass through the pressure patch over the forward part of the hull ( $\gamma < \alpha^*$ ). Of course this is permitted here.

### Caustics

Waves created from different points on the boundary may cross in the water; this is permitted. If they approach tangency while merging (bunching), then a caustic is created; this corresponds

to the zero of  $\left(\frac{d^2 f_{u,l}}{dt^2}\right)$  at a stationary phase point, then the waves correspond to the p-waves of

[1.7]. We differentiate [1.8] again and finally find (we suppress the asterisk on  $\xi_{u,l}$  for simplicity):

$$\frac{d^2 f_{u,l}}{dt^2} = -k \left\{ \frac{2C_g^2}{(\xi - \xi_{u,l})} + \xi''_{u,l} \right\} = -k \left\{ \frac{(\xi'_{u,l})^2}{2(\xi - \xi_{u,l})} + \xi''_{u,l} \right\} \quad [1.13]$$

so that a caustic ( $f''_{u,l} = 0$ ) will form out in the water along every ray originating at a point where  $d^2 \xi_{u,l}/dt^2 < 0$ ; that is everywhere the patch is concave from within. These caustics represent the merging of the rays originating at different points along the patch-boundary. They merge at a finite position along the ray and therefore disappear in the far field; their location is:  $(\xi_c - \xi_{u,l}) = -(\xi'_{u,l})^2 / 2\xi''_{u,l}$ , where:

$$\xi''_{u,l} = +U_0^2 \frac{d\alpha}{dx} \sin \beta = \frac{-U_0^2}{R^*} \quad [1.14]$$

where  $R^*$  is the radius of curvature of the patch, positive when concave from within.

In the far field ( $\xi \rightarrow \infty$ ), then new caustics will appear upon the vanishing of  $\xi''_{u,l}$ , corresponding to points of flatness ( $R^* \rightarrow 0$ ).

### The Resultant Amplitude Spectrum for the Boundary Wave

We allow the patch boundary to have both convex and concave regions with a local point of flatness separating them. Then the far field wave is obtained by combining various relations, [1.1-1.4], using only the waves in [1.7]. The result for  $\text{Amp}(\beta)$ , see the definition according to [1.3], is:

$$\frac{1}{R^*} > 0, \quad \text{Amp}(\beta) = \frac{1}{\sqrt{\pi}} [F_L][\bar{p}_0] \left| \bar{R}^* \right|^{\frac{1}{2}} e^{-i[k(y_{u,l} \csc \beta + x'_{u,l} \cos \beta) \pm \pi/4]} \left. \begin{array}{l} \text{concave} \\ \text{convex} \end{array} \right\}^u \quad [1.15]$$

$$\frac{1}{R^*} = 0,$$

$$\text{Amp}(\beta) = \frac{\Gamma(1/3)}{\pi^{1/6}} [F_L^{2/3} [\bar{p}_0]] \left\{ \left[ (\sin\beta) d^2 \alpha^* / dx^2 \right]^{-1/3} \cdot e^{-i[k(y_{u,\ell} \csc\beta + x'_{u,\ell} \cos\beta)]} \right\}_\ell^u \quad [1.16]$$

(locally)

where:  $x'_{u,\ell}$  is measured aft from the bow;  $\bar{p}_0 = p_0 / \rho U_0^2$ ;  $\bar{R}^* = R^* / L$ ;  $F_L$  (Froude number) =  $U_0 / (gL)^{1/2}$ ; and  $L$  is the length of the patch.

In the neighborhood of a point of flatness, the correct result, [1.16], must be used and the other result, [1.15] (valid elsewhere), appropriately merged with it.

We note: all of the waves are driven by the patch excess pressure,  $\bar{p}_0$ ; interference effects between forward and aft generator points occur and are described by the exponential term in each relation; the strongest wave at low Froude numbers arises from the caustic at the inflection point (local flatness) in the boundary shape,  $O(F_L^{2/3})$ ; for a curved boundary most of the waves are proportional to the (local radius of curvature) $^{1/2}$  and  $O(F_L)$ .

#### The End Waves

In addition to the foregoing boundary waves, which have arisen from the stationary phase contribution to the above integral, we must consider the possibility of end waves arising from integration by parts of the integral over the boundary represented by [1.3]. In this case the result can be represented as a sum of terms with coefficients,  $k^{-1}$ ,  $k^{-2}$ , etc. Again in the far field the first term is dominant. It is:

$$\frac{d\eta}{d\beta} \approx R \cdot \left\{ \frac{p_0 [A] \xi}{\rho k^2} \left[ \frac{1}{C_p - \xi'_u} - \frac{1}{C_p - \xi'_\ell} \right] \cdot i e^{i[k\xi - w(t - t_{b,s})]} \right\}_{t_b}^{t_s} \quad [1.17]$$

where  $C_p$  is given by [1.9],  $\xi'_\ell$  by [1.10], and  $t_s$  is the time required for the pressure patch to cross the ray (we take  $t_b = 0$ ). The far field amplitude function for the end waves is thus:

$$\text{Amp}(\beta) \approx \frac{i \bar{p}_0}{\sqrt{2} \pi} (F_L)^2 [G_s(\beta) \cdot e^{ikL^* \cos\beta} - G_b(\beta)] \quad [1.18]$$

where  $G_{b,s} = \frac{\xi'_u - \xi'_\ell}{(1 - \xi'_u)(1 - \xi'_\ell)}$ ;  $\xi'_{u,\ell} = \xi_{u,\ell} / C_p$ ; and  $L^*$  is the horizontal distance between the initial

forward (bow) and final aft (stern) intersection of a ray with the hull ( $L^* = L$  for rays sufficiently near the vertical, but may be less than  $L$  for rays inclined near the horizontal, whose initial and/or final intersections may be tangent to the boundary at a point inboard from the bow and/or stern).

We note that the end waves are  $O(F_L^2)$  and therefore weaker at low Froude number than the boundary waves. For  $\xi'_{u,\ell} = 1$ , the stationary phase point is realized and the correct value of  $\text{Amp}(\beta)$  is that given by [1.15] or [1.16]. For prolonged flatness at the ends (wedge shapes), special considerations must be made, which we will not undertake here.

The results given here provide the solution of Weinblum's problem for sufficiently small Froude number, allowing the prediction of both wave patterns around the pressure patch and of the wave resistance. Some of the important results are: i) waves are generated on the boundary of the patch and at the ends; ii) for the strongest waves, the boundary wave number vector is normal to the patch boundary, and transverse waves are generated at the blunt ends and divergent waves on the near horizontal sides; iii) boundary waves observable above the patch originate on the forward-upper and near-lower sides of the patch; iv) for smooth boundaries each boundary wave will be excited at two generator points, one in each of the contributing sectors; v) the boundary waves can form caustics in the near field, which can be predicted; vi) the waves from the upper and lower boundary sectors interfere with each other; vii) the amplitude function of the boundary waves is weighted locally by the (radius of curvature) $^{1/2}$  of the patch boundary and is therefore

larger where the surface is flat than where it is highly curved; viii) points of local flatness (inflection) cause stronger waves (caustics) locally than other points; ix) the boundary wave amplitude grows like  $(F_L)$  except for the inflection point wave which grows like  $(F_L^{2/3})$ ; x) the "end" waves originate at points of initial or final intersection (or tangency) of a ray with the pressure patch boundary and grow as  $(F_L^2)$ .

### The Michell Ship as an Extended Pressure Patch

Finally we should point out that the Michell ship may readily be treated as a pressure patch extending to infinity with varying patch pressure corresponding to  $(p_M/\rho)$ , where  $p_M$  is the zero Froude number (double model) pressure in the field about the Michell hull. The far field wave,  $d\eta/d\beta$ , will be found by integration of the pressure sources along a straight ray characteristic,  $\beta$ . When the ray intersects the hull line on the x-axis, then a discontinuity in the pressure gradient,  $\nabla_\beta(p_M/\rho)$  occurs; otherwise the pressure  $p_M$  is smooth.

Upon integration by parts along the ray, waves will originate at the hull boundary, driven by the pressure gradient there:  $\nabla_\beta p = \cos\beta \partial p/\partial x + \sin\beta \partial p/\partial z$ . Except at the ends of the hull,  $\partial p/\partial x$  is continuous across the hull, so that the jump arises from the pressure gradient normal to the hull, and it is this gradient which drives the hull waves, see Figure 1.3. Immediately at the ends, the gradient in  $x$  becomes discontinuous at a stagnation point, and must be accounted for.

We note that upon integrating these boundary generated waves in  $t'$  (along the hull), no stationary phase contributions arise, since the hull is taken on the x-axis (to permit the hull to be distinct from the x axis and otherwise ignore the displacement flow would be inconsistent). Therefore all of the waves made by a smooth Michell hull will arise at the ends as a result of integration by parts.

## 2. THE WAVES GENERATED BY A SHIP

### Introduction

The flow about a ship differs from that under a moving pressure patch in a number of important ways:

- there exists no externally imposed pressure to drive the waves,
- the waves which are created must be prevented from crossing the hull, which is of course impermeable,
- there exists a substantial flow about the ship, which bends the rays, and,
- the waves as they travel along the rays are effected by the displacement flow and alter their characteristics.

### Our Method, Fundamentals.

These differences are formidable and render the problem non-linear. However, most of these differences can be conceptually dealt with, as we show below. (The small letters, a.) etc., refer to the letters above.)

a) We consider that the flow about the ship has been calculated by the method of the "naive" Froude number expansion (the potential is represented as a series of terms whose coefficients are integer powers of  $F$ ). The first term, in which the water surface is flat, represents the zero Froude number flow about the ship. It produces an elevation,  $\eta_0$ , of the water surface which is  $O(F^2)$ . This in turn produces a displacement flow of  $O(F^2)$ . We shall assume that it is this related elevation of the water surface which relaxes and in the process produces a wave pattern. Note that the elevation is simply,  $\eta_0 = p_0/\rho g$ , where  $p_0$  is the pressure in the displacement flow. The latter is the double model flow to zero order in  $F$ , but differs from it in  $O(F^2)$ . We discuss at the end of the paper whether the displacement flow calculated in this way is adequate at the points of the bow and stern.

b) Waves of a given far-field wave number direction,  $\tilde{\beta}$ , which arrive at a distant observer point,  $\xi$ , above the hull, originate at time  $t'$  along some ray,  $S(\beta, t')$ , which intersects the hull surface in the time interval  $(t'_b - t'_s)$ , between contact first with the bow and then with the stern, Figure 2.1.

What conditions must be imposed on the wave vector,  $\vec{k}$ , at the hull? The hull is impermeable; i.e. there can be no energy flux through it. This condition is automatically satisfied when waves originate on the hull whose vector  $\vec{k}$  is parallel to the hull, or if their group velocity,  $c_g$ , is zero. The latter corresponds, we later show, to wave vectors normal to the hull.

Does this mean that no other wave vectors are allowable at the hull? The answer is no. The pair of an outgoing wave vector,  $\vec{k} = k e^{i\beta_0}$ , and an incoming vector,  $k e^{i\beta_i}$ , whose sum is normal to the hull is also allowable. In other words, the outgoing vector is the reflection (optical) from the wall of the incoming vector. Therefore the locus,  $S_0$ , along which energy originates for the observer, must include an incoming portion, too, for which the preceding conditions are satisfied; quite apparently this incoming energy is reflected at the wall toward the observer, see Figure 2.1

As a result of the reflection of the locus at the wall, a discontinuity in the gradient of the pressure occurs on the locus at the wall, and we shall see that this discontinuity drives the waves and they appear as if originating at the hull. This is the same result as emerged in the conceptually simpler case of the Michell ship, discussed earlier.

The question of conditions leading to allowable rays is later discussed in the forthcoming section: The Rays at the Hull.

c) There is a free surface velocity  $\vec{q}_0 = q_0 e^{i\alpha_0}$  associated with the displacement flow, where  $\alpha_0$  is the angle of the flow on the free surface relative to the x-axis; we assume this angle is not significantly different from the corresponding angle for the projection of the free surface velocity on the horizontal plane. This velocity is measured relative to ship (moving) coordinates and is therefore stationary. At a fixed point in water (fixed) coordinates, there corresponds to it a velocity,  $\vec{v}_0 = v_0 e^{i\delta_0} = q_0 e^{i\alpha_0} - U_0$ , which is not stationary, see Figure 2.2.

The wave energy propagates in the water with the sum of the group velocity,  $\vec{c}_g(k)$ , and the convective velocity,  $\vec{v}_0$ . If,  $\vec{c}_g(k) + \vec{v}_0 = u_\mu e^{i\mu}$ , and  $\vec{c}_g(k) + \vec{q}_0 = u_\gamma e^{i\gamma}$ , then the ray angles in fixed coordinates,  $\mu$ , and in ship coordinates,  $\gamma$ , everywhere in the flow are:

$$\tan \mu = \frac{[\sin \alpha_0 (1 + \cos^2 \beta) - \cos \alpha_0 \sin \beta \cos \beta]}{[\cos \alpha_0 (1 + \sin^2 \beta) - \sin \alpha_0 \sin \beta \cos \beta - 2U_0/q_0]} \quad [2.1]$$

$$\tan \gamma = \frac{-\{\sin \beta \cos \beta\} + \tan \alpha_0 \{1 + \cos^2 \beta\}}{\{1 + \sin^2 \beta\} - \tan \alpha_0 \{\sin \beta \cos \beta\}}$$

see Figure 2.3, a most important diagram. To derive [2.1] we have used a result,  $C_g = (-q_0/2)\cos(\beta - \alpha_0)$ , derived from stationarity (see d) below).

d) The waves at any point in the flow must be stationary when observed in ship coordinates. That is:

$$C_p + v_0 \cos(\beta - \delta_0) = -U_0 \cos \beta \quad [2.2]$$

This can be shown to be equivalent to:

$$C_p = (g/k)^{1/2} = -q_0 \cos(\beta - \alpha_0) \quad [2.3]$$

In addition, since  $\vec{k} = \text{grad}(\text{phase})$ , the condition of irrotationality,  $\nabla \times \vec{k}$ , must be satisfied in the wave field. In our notation this can be written:

$$\frac{\partial(k \cos \beta)}{\partial y} - \frac{\partial(k \sin \beta)}{\partial x} = 0 \quad [2.4]$$

When this is expanded and the derivatives  $\partial k / \partial x$ ,  $\partial k / \partial y$  are substituted with values determined by differentiating [2.3], then it is found that:

$$\frac{\partial \beta}{\partial y} \left\{ -q_0 \cos \beta \sin(\beta - \alpha_0) - \frac{C_p}{2} \sin \beta \right\} + \frac{\partial \beta}{\partial x} \left\{ +q_0 \sin \beta \sin(\beta - \alpha_0) - \frac{C_p}{2} \cos \beta \right\} = F$$

$$F = \left\{ -\cos \beta \cos(\beta - \alpha_0) \frac{\partial q_0}{\partial y} + \sin \beta \cos(\beta - \alpha_0) \frac{\partial q_0}{\partial x} - \right.$$

$$\left. q_0 \cos \beta \sin(\beta - \alpha_0) \frac{\partial \alpha_0}{\partial y} + q_0 \sin \beta \sin(\beta - \alpha_0) \frac{\partial \alpha_0}{\partial x} \right\} \quad [2.5]$$

Then it can be shown that the characteristic form of this equation is:

$$\frac{d\beta}{d\ell} = F / [C_g \cos(\beta - \alpha_0) + q_0 \cos(\gamma - \alpha_0)] \quad [2.6]$$

where  $\ell$  is the distance along the ray,  $\gamma$ . This latter equation together with [2.1] and [2.3] allow the tracing of a ray in the ship's flow field. Extensive calculations of this kind have been carried out by Yim (1981).

The local wave frequency on a wave,  $\beta$ , in water coordinates is ( $\omega_0 = (kg)^{1/2}$ ):

$$\omega = \omega_0 + kv_0 \cos(\beta - \delta_0) \quad [2.7]$$

Finally, the wave along a ray in water coordinates can be described in general as:

$$\eta \sim a(s, t) e^{i\psi(s, t)} \sim a(s, t) e^{i \left\{ \int_0^s k_\mu ds - \int_0^t \omega dt \right\}}; \quad \frac{d\omega}{dk_\mu} = \frac{ds}{dt} \quad [2.8]$$

where  $k_\mu$ ,  $\omega$ ,  $q_0$ , and  $\delta_0$ , determined in water coordinates vary along  $s$  and with time too;  $k_\mu$  is the apparent wave number along  $s$ ,  $k_\mu = k \cos(\beta - \mu)$ .

#### The Rays at the Hull

Under what circumstances can an outgoing ray exist at the hull, which will be seen by an observer above the hull? We should require: i) that the ray in ship coordinates,  $\gamma$ , does not lie inside the hull, and ii) that the energy flow outward along the ray, toward the observer; i.e. that  $C_p > 0$ . The first of these requirements is equivalent to: on the upper side of the hull, that  $\gamma^* > \alpha^*$ , and that on the lower side that  $\gamma^* < \alpha^*$ . The second of these requirements is equivalent to:  $\pi/2 \leq (\beta^* - \alpha_0^*) \leq \pi$ , see [2.3]. The asterisks refer to conditions on the hull.

We observe the ray diagrams and note that the second requirement above is met between the two hull lines ( $\gamma^* = \alpha^*$ ), Figure 2.4, and then that the first of these is met only on the upper surface of the hull, Figure 2.3. Therefore, only on the upper surface of the hull can rays originate which will be seen by an observer above the hull. We notice that this is a different result than in the pressure patch case, where we had only the second requirement; but in this case it was allowed for the rays to cross inside the patch boundary, and in the ship case this kind of behavior is forbidden.

Does this mean that any wave angle,  $\beta$ , satisfying the above requirements can exist at each point on the upper hull? The answer is yes. Of course the range of  $\gamma$  possible at a given point will be restricted to a minimum value,  $\gamma^* = \alpha^*$ , and a maximum value corresponding to the peak of the curve  $\gamma$  vs.  $\beta$ ,  $\alpha^*$  being held fixed (this peak corresponds to the caustic curve in Figure 2.4). This conclusion applies as well to the ends as elsewhere, except that at the corner made by a finite entrance or leaving angle, many flow angles may exist, as we discuss in the next section.

Finally we notice that according to the ray diagram, Figure 2.3, there exists no dependence of the local flow speed on the relation between the local angles,  $\gamma$ ,  $\alpha_0$ , and  $\beta$ . Therefore, within the assumptions of ray theory, aspects of the flow geometry determined solely by these variables (not including local wave lengths, which are speed dependent) will not vary with speed except insofar as  $\alpha_0$  is itself speed dependent. Of course the displacement flow is speed dependent; for example, in the high speed limit, the flow would seem to approach the hull with little lateral deviation, reducing  $\alpha_0$  in comparison to the low speed limit.

## The Rays at the Ends

We imagine a bow with a finite entrance angle,  $\alpha_e$ . Directly at the bow then the flow direction changes discontinuously; i.e. the flow direction,  $\alpha_o$ , is zero on the streamline approaching the stem, while it has the angle,  $\pm\alpha_e$ , on the hull streamline itself. In the corner between these streamlines the angle of the flow takes on various angles,  $0 < \alpha_o < \alpha_e$ , which depend on how the corner is approached; i.e. the flow angle,  $\alpha_o$ , at the corner is a function of  $\gamma$ , the ray angle at the corner, see Figure 2.5. What do we know about  $\alpha_o(\gamma)$ ? On the hull itself,  $\gamma = \alpha_e$ . On the approaching streamline,  $\alpha_o = 0$  and  $\gamma = \pi$ . In between we must solve for the flow. As far as the zero Froude number flow is concerned, it seems necessary for the flow at the wedge bow to approach the planar (2 dimensional) wedge flow in the limit of small (thickness/draft). In this case, which we give as an example, a linear relation exists between  $\alpha$  and  $\gamma$ :

$$\begin{array}{l} \text{Wedge bow,} \\ \text{Small (thickness/draft).} \end{array} \quad \gamma = \left[ \frac{\alpha_e - \pi}{\alpha_e} \right] \alpha_o + \pi \quad [2.9]$$

This relation can be superimposed on the ray diagram; we give an example in Figure 2.5. The solution extends between the hull boundary loci. On the upper,  $\beta = \alpha + \pi/2$ , and  $C_o = 0$ . On the lower,  $\beta = \alpha + \pi$  and  $C_o = -\alpha_o/2$ . In between there are two distinct values of  $\beta$  for each value of  $\gamma$  less than  $\gamma_c$ , which is a limiting value and corresponds to a caustic; so all the waves are contained within,  $\alpha_e < \gamma < \delta_c$ . In this respect the wave pattern is qualitatively similar to the Kelvin wave. Notice that on the hull ray,  $\gamma = \alpha_e$ , the wave crests are either normal or parallel to the hull. In the latter case  $C_o = 0$  and the wave does not therefore penetrate the hull. In the former case the wave vector is parallel to the hull and does not penetrate it either.

This problem of determining the kinematical wave pattern at the bow of a ship emphasizes the importance of having a better quantitative understanding of the singular flow at ship bows; but at least the example here illustrates how knowledge of  $\gamma(\alpha_o)$  can be used with the ray diagram to determine the initial wave pattern,  $\beta(\gamma)$ . In addition, since reduction in draft would reduce the disturbance away from the hull, it seems likely that the planar case is more than an example, but represents an upper limit, i.e.  $\alpha_o(\gamma)|_{3D} < \alpha_o(\gamma)|_{2D}$  and in consequence  $\gamma(\alpha_o)|_{3D} < \gamma(\alpha_o)|_{2D}$ .

The limiting ray angle,  $\gamma_c$ , is readily determined by combining  $\gamma(\alpha_o)$ , for example [2.9], with the locus of the caustics in the ray diagram, Figure 2.4. The latter (we are dealing with the locus which intercepts the Kelvin far field curve) is:

$$\gamma = \gamma_K + \alpha_o \quad [2.10]$$

where  $\gamma_K$  is the Kelvin angle,  $19.5^\circ$ . The solution of [2.9] and [2.10] is:

$$\gamma_c = \alpha_e (1 - \gamma_K/\pi) + \gamma_K \quad [2.11]$$

We note that  $\gamma_c > \gamma_K$ . This relation, [2.11] is given as Figure 2.6. We would expect for ships of finite draft that the limiting ray,  $\gamma_c$ , would lie between the two curves labeled hull and bow (theory).

The same considerations apply at the stern if we ignore the viscous wake. If we assume the planar wedge solution there, too, we find:

$$\begin{array}{l} \text{Wedge Stern} \\ \text{Small thickness/draft} \end{array} \quad \gamma = - \left[ \frac{\alpha_e - \pi}{\alpha_e} \right] \alpha_o \quad [2.12]$$

and the intersection of this relation and the caustic locus gives for the caustics at the stern:

$$\gamma_c = \left[ \frac{\alpha_e - \pi}{2\alpha_e - \pi} \right] \cdot \gamma_K \quad [2.13]$$

which is also plotted as Figure 2.6. We note that in this case,  $\gamma_c < \gamma_K$ .

Finally we note that our bow wave results do not at all coincide with the observations of the "non-dispersive" bow waves of the Tokyo school, see Inui (1980) or Miyata (1980). In their experiments on wedge bows, carried out at speeds between 0.5-1.5 m/sec. and drafts between 1-15 cm., the observed "shock" angle increased with draft and with speed. At the lowest speed the observed



shock angle was far in excess of the predictions here; furthermore as the entrance angle decreased to zero the shock angle did not approach the Kelvin angle but an angle of about  $30^\circ$ ; we observe that for these tests (speed = 50 cm/sec.) the local speeds near the bow may have been too close to 23 cm/sec. the minimum phase speed for capillary gravity waves. At the highest speed (Froude number based on draft between 1.5-6) the observed shock angles were much reduced, reducing further with decrease in draft, and did not approach the Kelvin angle as  $\alpha_c$  approached zero. This behavior suggests that the "shock" wave observed by Miyata does not correspond to the limiting gravity wave (caustic) described here. Additional data are required at speeds safely above the capillary regime and at Froude numbers based on draft  $O(10^{-1})$ .

We shall return later at the end of the paper to discuss the vexing problems associated with the ends of the ship. Meanwhile we explore the implications of the ray theory which we have just defined, and which have been largely based on the assumptions of Ursell (1960) and Whitham (1961).

### The Far Field

We may now proceed to examine in further detail the question of how a displacement ship makes waves. Our technique is identical to that observed already in the case of the moving pressure patch, although important differences arise in the results.

From each point in the flow outside the ship an elemental radial wave is generated. Of course this radial wave is distorted in time as the rays from the generation point travel out and are bent; this effect is taken into account by ray tracing according to [2.1], [2.3], and [2.5].

Again, we take a bundle of rays (bent) corresponding to a far field wave number angle,  $\tilde{\beta}$ , originating at an observer point,  $s$ , and width,  $(s-s')d\tilde{\beta}$ , and we represent the resulting plane wave,  $dn/d\tilde{\beta}$ , at  $s$ , as an integration of the elemental waves along the generator points,  $s'$ , and over time,  $t'$ , see Figure 2.1. The ship is moving from right to left:

$$\frac{dn}{d\tilde{\beta}}(s, t, \tilde{\beta}) = R \cdot \int_{-\infty}^t dt' \int_{-\infty}^s \frac{p_D}{\rho} [A](s-s') i e^{i\psi(s-s'; t-t')} ds'; \quad [2.15]$$

where  $\psi$  is defined in [2.8] and:  $dw/dk_\mu = d(s-s')/d(t-t')$ .

We recognize that the locus,  $S(\tilde{\beta})$ , on which waves destined for the fixed observer appear, will vary with time,  $t'$ , approaching the fixed far field observer point,  $s$ , as a ray with a fixed angle,  $\tilde{\beta}$ . This movement of the locus results from the effect of the displacement flow about the ship, which is non-stationary in the observers frame.

The function  $[A]$  in [2.15] refers, as before, to the spreading function for the wave due to a concentrated imposition of pressure,  $p_D/\rho$ . In the absence of a displacement flow this has the form, [1.2], which may also be written:  $[A] = (E)^2(s-s')$ , where  $E$  is proportional to the energy density at the wave number being considered. The displacement flow allows a mechanism for exchange of energy between the wave and the displacement flow, resulting in changes of  $E$  during the travel of the wave group from the hull to the far field. The wave resistance is in reality therefore manifested both in radiation of wave energy to the far field and in changes in the displacement flow. Here we take the point of view that the energy exchange in the near field does not significantly influence the pressure field on the hull and that the wave resistance can be calculated from the far field (pseudo) waves, themselves predicted as if energy exchange does not occur. Of course the pseudo wave amplitude spectrum will not agree with measured spectra, unless the energy exchange happens to be insignificant. In keeping with this point of view, we take  $[A]$  identical with [1.2] putting  $C_0 = C_0^3(\text{hull})$ ; this form conserves the initial energy. Finally, we add, the possibility for predicting the energy exchange in the near field utilizing ray theory does exist and could be implemented, using the conservation equation of Whitham (1962).

This integral, [2.14], can be represented asymptotically (short waves relative to the scale of the flow field) as a wave arising from the hull and perhaps from waves arising in the water at stationary phase points of  $\psi(s, t)$ . We neglect the latter in the present work; it is difficult to see how they might influence the wave resistance.

In keeping with the earlier discussion, we take the locus,  $S(\tilde{\beta})$ , to include its reflection at the hull. We then find, upon integrating by parts over  $s'$  along the entire locus, that the dominant term arises from the pressure gradient at the hull:

$$\frac{dn}{d\tilde{\beta}}(s, t, \tilde{\beta}) \cong R \cdot \int_{-\infty}^t \frac{1}{\rho(k_\mu^*)^2} J^*[\nabla_\mu p_D][A](s-s^*) i e^{i\psi} dt' \quad [2.16]$$

where  $h = \int_{s^*}^s k_\mu ds'' - \int_{t'}^t \omega dt''$ ;  $s^*$  represents the intersection of the ray and hull at time  $t'$ ;

and  $J^*$  represents the jump in the gradient of  $p_D$ , i.e.  $(\nabla_{\mu_i} p_D)^* - (\nabla_{\mu_i} p_D)^*$ . The direction of

the outgoing ray is  $\mu$  and the incoming,  $\mu_i$ ; the latter is determined from the reflection condition on  $k$ , see Figure 2.1. Finally,

$$J^*[\nabla_\mu p_D] = \frac{\partial p}{\partial \sigma} [\cos(\mu_0^* - \alpha_0^*) - \cos(\mu_i^* - \alpha_0^*)] + \frac{\partial p}{\partial n} [\sin(\mu_0^* - \alpha_0^*) + \sin(\mu_i^* - \alpha_0^*)] \quad [2.17]$$

where  $\sigma$  is direction along the hull and  $n$ , normal to it.

The values of  $\mu_{0,i}$  can be determined using [2.1] and the following relation, which follows from the reflection property:

$$(\beta_1^* - \alpha_0^*) = 2\pi - (\beta_0^* - \alpha_0^*) \quad [2.18]$$

### The "Dominant" Waves

This integral, [2.14], may be integrated by applying Kelvin's method of stationary phase, where the main contribution arises from points where  $d^2h/dt'^2 = 0$ , and also through integration by parts. The former produces waves which are stronger than the latter at low Froude numbers.

Applying first Kelvin's method, we can show that

$$dh/dt' = \omega - (k_\mu) \cdot ds^*/dt' \quad [2.19]$$

so that the stationary phase condition becomes:

$$ds^*/dt' = [\omega/k_\mu] = [\omega/k \cos(\beta^* - \mu)] \quad [2.20]$$

Stationarity requires that:  $\omega/k = -U_0 \cos\beta^*$ , so that the stationary phase condition is:

$$ds^*/dt' = -U_0 \cos\beta^* / \cos(\beta^* - \mu) \quad [2.21]$$

We have already given a relationship for  $d\xi_{u,x}/dt'$ , [1.7], and it applies to the hull case too.

$$ds^*/dt' = U_0 \sin\alpha^* / \sin(\mu - \alpha^*) \quad [2.22]$$

These equations taken together, [2.21-2.22], require:

$$\text{Either, } \beta = \alpha_0^* + \pi/2 \quad [2.23]$$

$$\text{or, } \mu = 0, \pi \quad [2.24]$$

In the former case, [2.23], the wave number is normal to the hull boundary exactly as in the case of the pressure patch, the group velocity is therefore zero, see [2.3], and these waves are allowable. Therefore in ship coordinates the ray is initially tangent at each point to the hull ( $\gamma = \alpha_0^*$ ). This condition is represented in the ray diagram, Figure 2.3, by the upper boundary.

Can these rays, initially tangent at their formation, leave the hull? The answer lies with the first order ray equation, [2.5] and [2.6]. It is easy to verify that the solution for  $\beta$  along the ray, with the initial condition,  $\beta^* = \alpha_0^* + \pi/2$ , is everywhere just  $\partial\beta/\partial\ell = \partial\alpha_0/\partial\ell$ , and this means that the ray is not only tangent to the hull at its formation, but coincident with it; therefore none of these waves leave the hull boundary. Keller (1979) had earlier identified these waves ( $C_g \equiv 0$ ) and also concluded that they could not leave the hull.

In the other stationary phase case, [2.19], the ray angle in water coordinates,  $\mu$ , is required to leave the hull parallel to the direction of motion. This leads to two possibilities. First, at a stagnation point, then  $\tan \mu^* = 0$ , see [2.1], while the ray angle,  $\gamma^*$ , can take on a range of values,  $\alpha_0^* < \gamma^* < \gamma_c$ , as we have discussed in a previous section: The Rays at the Ends. Second, in the absence of a stagnation point, the selected rays will emerge from the hull in the horizontal direction; i.e.  $\gamma = 0$ . This is not possible on the forepart of the hull as these rays will pierce the hull, but it is possible over a part of the stern.

The wave number direction,  $\beta^*$ , for these aft waves is given by, see [2.1]:

$$\tan \alpha_0^* = \frac{\sin \beta^* \cos \beta^*}{[1 + \cos^2 \beta^*]} \quad [2.25]$$

which is represented in the ray diagram, Figure 2.3, by the intersection of the curves  $\alpha_0 = \text{const.}$  and the horizontal axis ( $\gamma = 0$ ). Notice that all values of  $\beta$  from  $\pi/2$  to  $\pi$  are represented, two for each value of  $\alpha_0$  smaller than zero and larger than  $-20^\circ$ , which represents a limiting value and is a caustic ( $d\gamma/d\beta = 0$ ). This is the spectrum created on the upper aft part of the ship.

As these rays move aft in the water behind the ship, their angle changes according to the ray diagram. We would expect them to travel upward ( $\alpha_0$  increasing toward zero) from the horizontal axis ( $\gamma = 0$ ) along a trajectory which must be determined from ray tracing, terminating in the far field on the Kelvin boundary ( $\alpha_0 = 0$ ). Of course the final value of  $\beta$  on the ray, i.e.  $\beta$ , will generally be different from the initial value,  $\beta^*$ , and must be determined by ray tracing. The same remark applies, too, in the case of the end waves.

#### The Aft Waves: Their Strength

Upon applying Kelvin's formula, [1.7], to the far field wave integral, [2.16], the strength of the aft waves may be obtained. The far field wave takes the form:

$$\frac{d\eta}{d\beta}(s, t, \beta) \cong R \cdot \left\{ \frac{C_p J^* i}{\rho g \sqrt{\pi} \cos^2 \beta h''} \cdot e^{i[h' + \pi/4 \operatorname{sgn} h'']} \right\}_{x^*} \quad [2.26]$$

where the entire term is to be evaluated at the hull at a particular location, say  $x^*$ , where  $x^*$  is the distance aft of the bow, and is reached by the ray in time  $t'(x^*) = x^*/U_0$ , where we put  $t'(0) = 0$ . Of course the value  $\alpha_0^*(x^*)$  must be allowable, i.e.  $-20^\circ < \alpha_0^* < 0$ . We can calculate  $g''(\mu = 0)$  as follows:

$$h = \int_{s^*(x^*)}^s k_\mu ds'' - \int_{x^*/U_0}^t \omega dt'' \quad [2.27]$$

$$h' = 0 = -k[(s^*)' \cos(\beta - \mu) + U_0 \cos \beta]$$

$$\text{therefore, } (s^*)'_{\mu=0} = -U_0, \text{ and}$$

$$h''(\mu=0) = -k[(s^*)'' \cos \beta - U_0(\mu') \sin \beta] \quad [2.28]$$

$$\text{but, } (s^*)''_{\mu=0} = -U_0 \frac{\cos \alpha_0}{\sin \alpha_0} \cdot \mu' \quad [2.29]$$

and, finally, using [2.24], and  $d\mu/dt' = -U_0 d\mu/dx$ :

$$h''(\mu=0) = -\frac{2kU_0^2}{\sin \beta} d\mu/dx \quad [2.30]$$

In the far field,

$$g \cong [ks - \omega t] + \phi(x^*) \quad [2.31]$$

where  $\phi$  is a phase function which must be determined by ray tracing, after combining [2.31] and [2.26]. Using this result, [2.31], the amplitude function corresponding to [2.25] becomes (we have non-dimensionalized everything):

$$\text{Amp}(\beta) \cong \left\{ \frac{(F_L)^3 (\bar{q}_0 \cos(\beta - \alpha_0))^2 (\sin \beta)^{\frac{1}{2}}}{\sqrt{2\pi} \cos^2 \beta \partial \mu / \partial x^{\frac{1}{2}}} [\bar{J}] e^{i[\phi - \pi/4 \operatorname{sgn} \partial \mu / \partial x]} \right\}_{x^*} \quad [2.32]$$

where  $\partial \mu / \partial x$  can be calculated by differentiating [2.1]. A lengthy calculation arises involving the necessity to determine  $\partial \alpha_0 / \partial x$  and  $\partial \beta / \partial x$ . The former is known from the displacement field and the latter is determined from [2.6], the ray formula. We have to recognize that a caustic may exist ( $\partial \mu / \partial x = 0$ ) in which case the p waves must be substituted for the s waves, see [1.7], and the wave becomes locally stronger. Obviously these aft waves need further detailed (and numerical) study. Finally we note that these waves are  $O(F_L^3)$ .

#### The Point of the Bow

We mean by this phrase, the hull-water intersection in the mid-plane of the ship. Our ray theory predicts two possible sources of waves immediately at the bow or stern ( $x^* = 0$ ): i) in the case where  $q_0(0) = 0$ , then a fan of waves corresponding to  $\mu = 0$  will arise (provided a stagnation point exists there), whose strength is given by [2.27] appropriately evaluated at the bow; these waves are  $O(F_L^3)$ ; ii) waves arising from integration by parts over the hull, giving rise to waves of  $O(F_L^4)$  whose strength also depends on  $J^*(x^*)$ , i.e. on the pressure gradients in the displacement flow at the point of the bow; thus this wave does not depend on the existence of a stagnation point there. These waves can readily be calculated in a similar manner as in the case of the pressure patch, but we do not carry out the calculation here.

The asymptotic theory of bow waves thus predicts that the energy release depends entirely on flow quantities (including their gradients) evaluated immediately at the point of the bow. This is the result of Keller (1979). Now we can even propose formulae for the wave amplitude. But in what situation does this place us?

We have assumed so far that normal wave theory applies: that wave energy propagates with the group velocity advected with the displacement flow, that the group velocity is 1/2 the phase velocity and that waves are conserved. Under what conditions does such theory apply? In connection with the singular region near the bow, the conclusions of K. Eggers (1981) are important. He claims a region near the bow of the double model flow where waves cannot exist. It corresponds to the region  $(\bar{q}_0)^2 < 1/3$ . Other than his investigation, the question of the validity of normal assumptions in regions of small local flow scales does not seem to have been systematically studied.

Here we take the point of view that for such theory to apply, the wave lengths in the field must be smaller than the local scale of the velocity field. We scale the former with  $k^{-1}$  and latter with  $(\frac{1}{q_0} \partial q_0 / \partial r)^{-1}$ . Remember that  $k \sim g C_g^{-2} \sim g q_0^{-2}$ , see [2.3], so that:

$$\frac{\text{Wave Length}}{\text{Local Flow Length}} \sim (F_L)^2 \partial \bar{p}_D / \partial \bar{r} \sim \partial \bar{\eta}_0 / \partial \bar{r} \quad [2.14]$$

where  $\bar{p} = p / \rho U_0^2$ ,  $\bar{r} = r / L$ ,  $\bar{\eta}_0 = \eta_0 / L$ . Therefore, we would conclude that this asymptotic theory applies provided that the slopes of the elevation,  $\eta_0$ , which drives the waves are sufficiently small.

However, in ray theory the entire energy release at the bow depends on conditions immediately at the point of the bow. What is the speed and wave slope in the displacement flow at this point? In particular, is the wave slope small? Are we even able to predict it with existing theories?

In the case of high Froude number based on draft, the situation near a blunt bow was authoritatively discussed by Fernandez (1981) incorporating an inner flow comprising a jet, first proposed by Dagan and Tulin (1972). In the case of low Froude number we have available only the suggestion of the naive Froude number expansion, and even in this case we do not have, as far as I know, actual numerical solutions for practical bow shapes such as wedges alone and wedges incor-

porating bulbs, which we know have a profound effect on the flow at the bow; see, for example, Sharma (1966).

It has in fact been generally proposed to base "low speed" theories including ray theory on a displacement flow calculated according to the naive Froude number expansion. In this case we are forced to have a stagnation point at zero Froude number and  $q_0 \sim r^n$ , where  $n = 1$  if the bow is blunt ( $\alpha_0 = \pi/2$ ) and  $n < 1$  for other wedges (for planar flows  $n = \alpha_0/\pi - \alpha_0$ ). We thus face the vexing situation that, based on the double model flow, either  $\nabla \eta_0$  (second order)  $\sim \nabla p_0 \sim \nabla q_0^2 \rightarrow 0$  at the point of sufficiently blunt bows [no wave energy release to  $O(F_L^3)$ ] or that  $\nabla \eta_0$  is singular, in which case the ray theory does not apply. We are therefore forced to the conclusion that ray theory based on  $\eta_0$  to second order is not useful. Whether the stagnation point and the singular behavior ( $q_0 \sim r^n$ ) is removed in the second order displacement flow remains to be seen; this would only cause a change in  $\eta_0$  at  $O(F_L^4)$ .

Is the naive Froude number expansion even applicable (uniformly convergent) in the neighborhood of the point of the bow? There exists a good chance that it is not. I say that because in nature it is normal on wedge models, see Standing (1974), to find the highest point on the free surface at some distance aft of the point of the bow (as Michell's theory predicts!); is it possible that this behavior is reflected at all Froude numbers on a scale near the bow which decreases with speed, perhaps as  $U_L^2$ , creating an inner flow at the point of the bow for which the naive Froude number expansion is an outer flow?

Finally we seem to face two possibilities. Either: a) the slopes are sufficiently small at the point of the bow that ray theory is applicable and can be used, provided that the displacement flow there is known, or b) the usual ray theory, for one reason or another, is not applicable there. In either case we still have before us to understand, the question how a ship hull generates waves in the asymptotic limit of small Froude number.

#### Concluding Remarks

Using the same procedure for the calculation of the far field spectrum as in the case of the pressure patch, we have shown again that in asymptotic theory the boundary of the ship generates waves; for an observer above the hull only the upper side of the hull can generate waves. One set of these waves must have their wave vectors normal to the ship's hull, just as in the case of the pressure patch. However, because of the condition that the displacement flow follows the ship hull these waves have zero group velocity. They therefore propagate on a ray in ship coordinates tangent to the ship's hull and cannot leave the hull. These results are the same as those of Keller (1979). Another set of waves leave the aft portion of the hull on rays initially parallel to the ship's path, provided that the inclination of the hull is not steeper than  $-20^\circ$ . We provide formulae for calculating the strength of these waves which are in general both transverse and divergent. In principal this set of waves includes a fan at the bow (or stern) provided that a stagnation point exists at the point of the bow; the strength of these waves depends entirely on the gradient of the pressure (elevation) in the displacement at that point, see Figure 2.7. We conclude that our present knowledge is inadequate either to know whether the conventional ray theory is valid near the ends of the hull or if it is, to use it effectively.

We have also examined the geometry of the wave flow which could be expected in the vicinity of a wedge bow or stern, utilizing ray theory. A limiting ray angle is found which correspond to the Kelvin angle ( $19.5^\circ$ ) for vanishing entrance angle, and increases linearly at the bow with increasing entrance angles; it is not dependent on the flow speed, except through changes in the displacement flow. At the stern we find a limiting ray angle which increases very slowly from the Kelvin angle (and not linearly) with the stern angle.

We hope these results will help in future efforts to provide an adequate understanding of the difficult question: how do ships generate waves?

## REFERENCES

- Bessho, M. (1966). "Minimum Wave Resistance of Surface Pressure Distribution," Sixth ONR Symposium on Naval Hydrodynamics (Washington, D.C.), 775-792, ONR/ACR-136, Washington, D.C.
- Dagan, G. and Tulin, M.P. (1972). "Two-Dimensional Free Surface Flow Past Blunt Bodies," Journal of Fluid Mechanics, 51, 529-543.
- Eggers, K. (1981). "Non-Kelvin Dispersive Waves Around Non-Slender Ships," Schiffstechnik, 28, 223-252.
- Fernandez, G. (1981). "Nonlinearity of the Three-Dimensional Flow Past a Flat Blunt Ship," Journal of Fluid Mechanics, 108, 345-361.
- Havelock, T. (1934). "Wave Patterns and Wave Resistance," Trans. Inst. Naval Arch., 76, 430-446.
- Inui, T. and Kajitani, H. (1977). "Study on Local Non-Linear Free Surface Effects in Ship Waves and Wave Resistance," Schiffstechnik, 24, 178-213.
- Inui, T. (1980). "From Bulbous Bow to Free-Surface Shock Wave," The 3rd Georg Weinblum Memorial Lecture, Institut für Schiffbau, Hamburg University, Report No. 402.
- Keller, J.B. (1974). "Wave Patterns of Non-Thin or Full-Bodied Ships," Tenth ONR Symposium on Naval Hydrodynamics (Cambridge, MA), 543-547, ONR/ACR-204, Washington, D.C.
- Keller, J.B. (1979). "The Ray Theory of Ship Waves and the Class of Streamlined Ships," Journal of Fluid Mechanics, 91, Part 3, 465-488.
- Longuet-Higgins, M.S., and Stewart, R.W. (1960). "Changes in the Form of Short Gravity Waves on Long Waves and Tidal Currents," Journal of Fluid Mechanics, 8, 565-583.
- Longuet-Higgins, M.S., and Stewart, R.W. (1961). "The Changes in Amplitude of Short Gravity Waves on Steady Non-Uniform Currents," Journal of Fluid Mechanics, 10, 529-549.
- Miyata, H. (1980). "Characteristics of Nonlinear Waves in the Near-Field of Ships and Their Effects on Resistance," Thirteenth ONR Symposium on Naval Hydrodynamics (Tokyo), 335-353, The Ship-building Research Association of Japan, Tokyo.
- Newman, J.N., and Poole, F.A.P. (1962). "Wave Resistance of a Moving Pressure Distribution in a Canal," Schiffstechnik, 9, 21-26.
- Phillips, O.M. (1966). The Dynamics of the Upper Ocean, Cambridge University Press.
- Sharma, S.D. (1966). "An Attempted Application of Wave Analysis Techniques to Achieve Bow-Wave Reduction," Sixth ONR Symposium on Naval Hydrodynamics (Washington, D.C.), 731-773, ONR/ACR-136.
- Standing, R. (1974). "Phase and Amplitude Discrepancies in the Surface Wave Due to a Wedge-Ended Hull Form," Journal of Fluid Mechanics, 62, Part 4, 625-642.
- Stoker, J.J. (1957). Water Waves: The Mathematical Theory and Applications, Interscience Publishers, Inc., New York, 1957.
- Thomson, W. (1887). "On Ship Waves," Collected Works, 270-306, Cambridge, 1910.
- Ursell, F. (1960). "Steady Wave Patterns on a Non-Uniform Steady Fluid," Journal of Fluid Mechanics, 9, 333-346.
- Weinblum, G. (1930). "Über die Berechnung des wellenbildenden Widerstandes von Schiffen, insbesondere die Hognersche Formel," ZAMM, 10, 453-466.
- Whitham, G.B. (1960). "A Note on Group Velocity," Journal of Fluid Mechanics, 9, 347-352.
- Whitham, G.B. (1961). "Group Velocity and Energy Propagation for Three-Dimensional Waves," Communications on Pure and Applied Mathematics, XIV, 675-691.
- Whitham, G.B. (1962). "Mass, Momentum, and Energy Flux in Water Waves," Journal of Fluid Mechanics, 12, 135-147.
- Yim, B. (1981). "A Ray Theory for Nonlinear Ship Waves and Wave Resistance," Third International Conference on Numerical Ship Hydrodynamics (Paris), 55-70, Bassin d'Essais des Carènes, Paris.

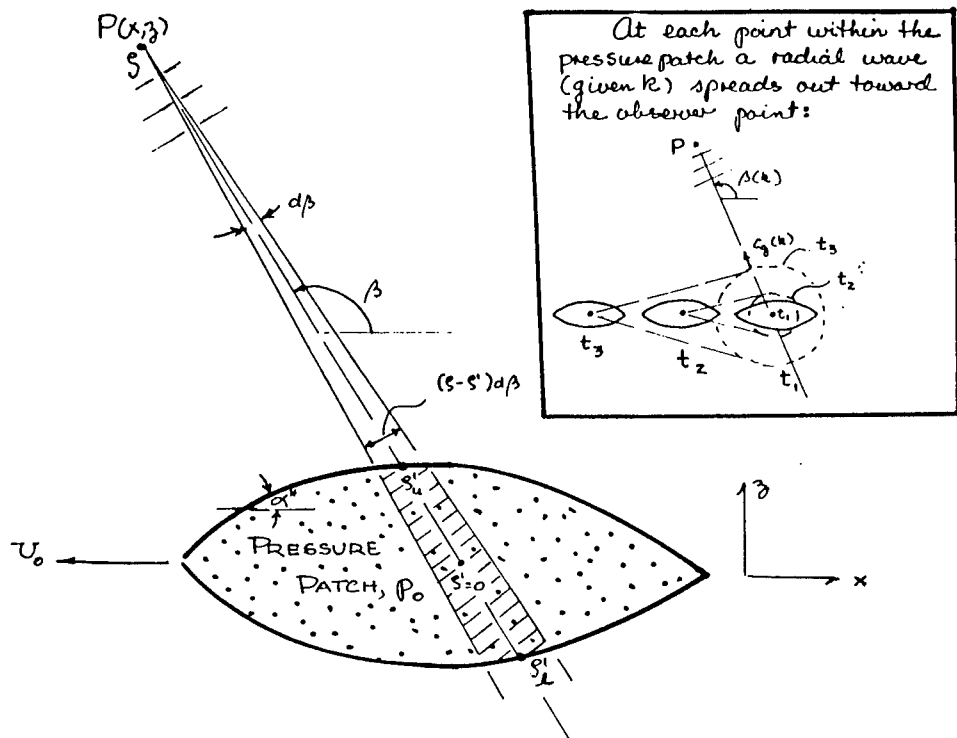


FIGURE 1.1: WAVEMAKING BY A PRESSURE PATCH

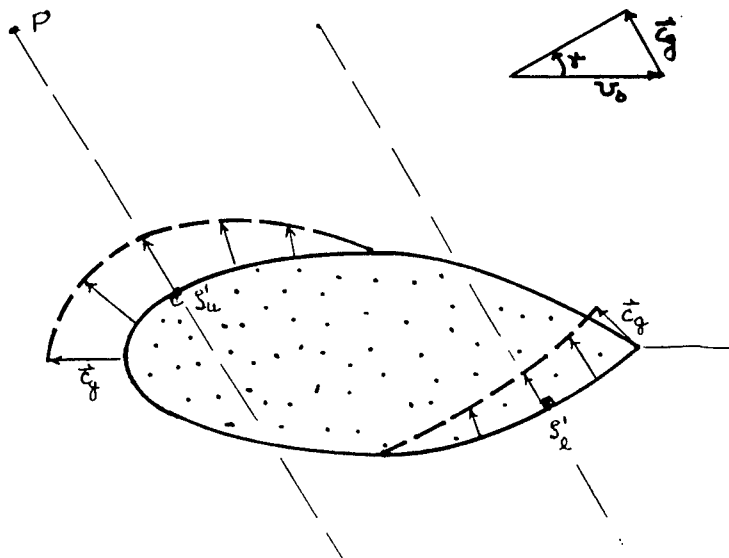


FIGURE 1.2: BOUNDARY WAVE GENERATION

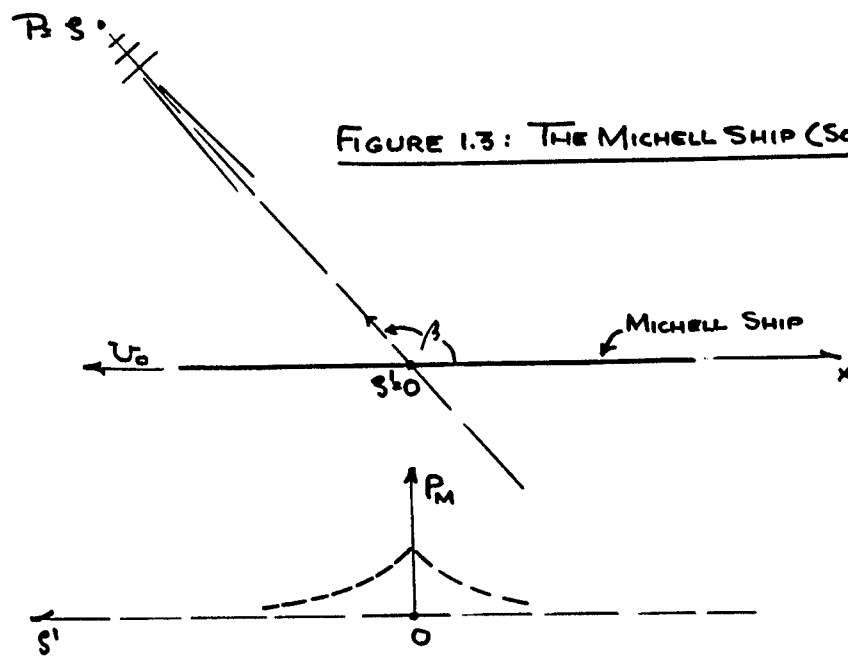
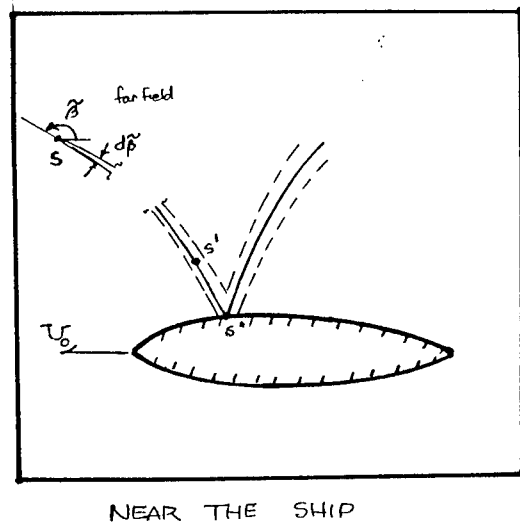
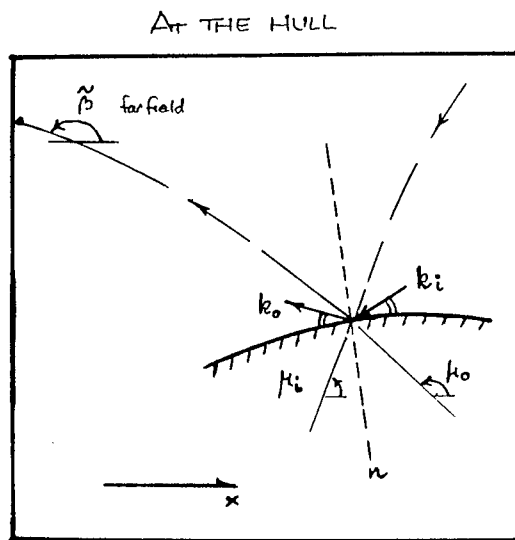


FIGURE 2.1: RAY BUNDLE GEOMETRY





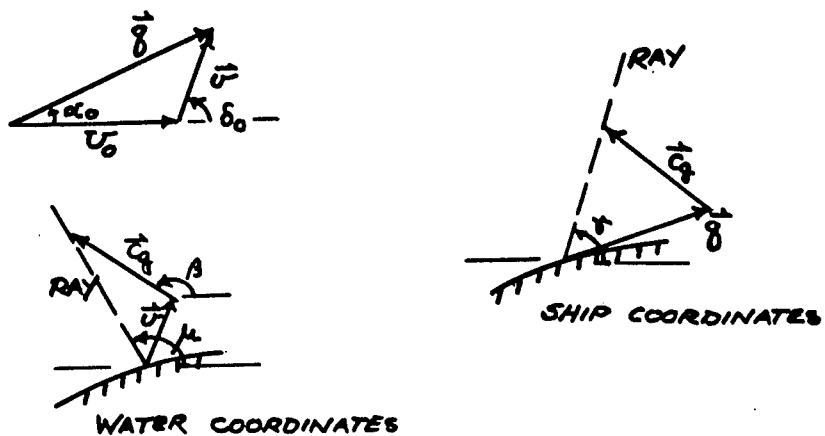
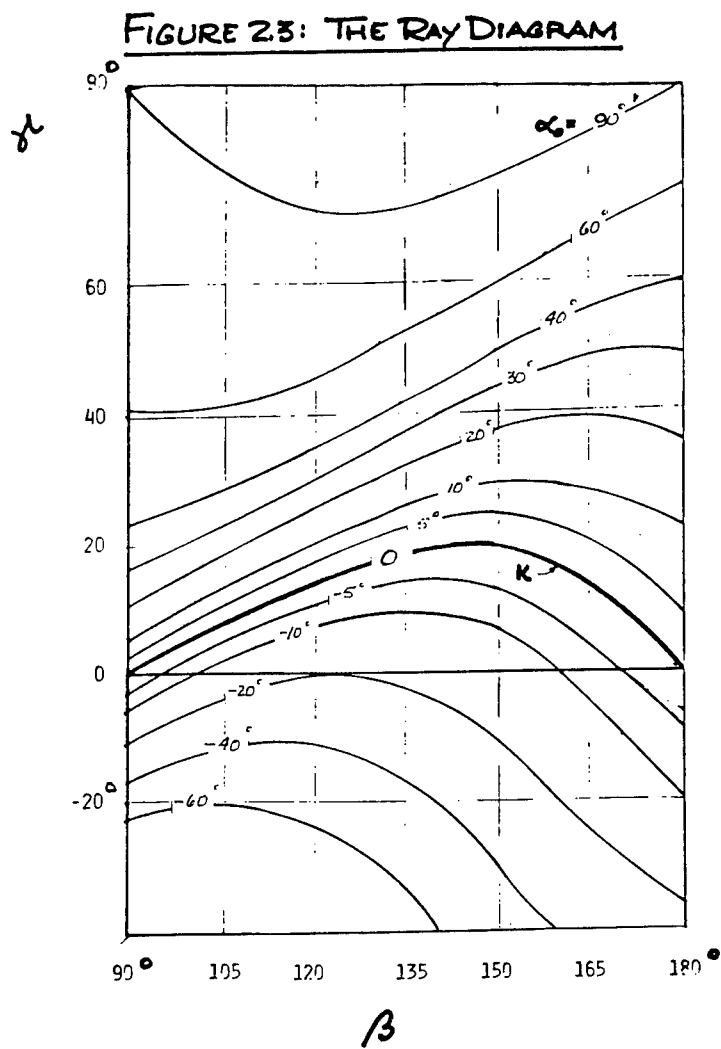
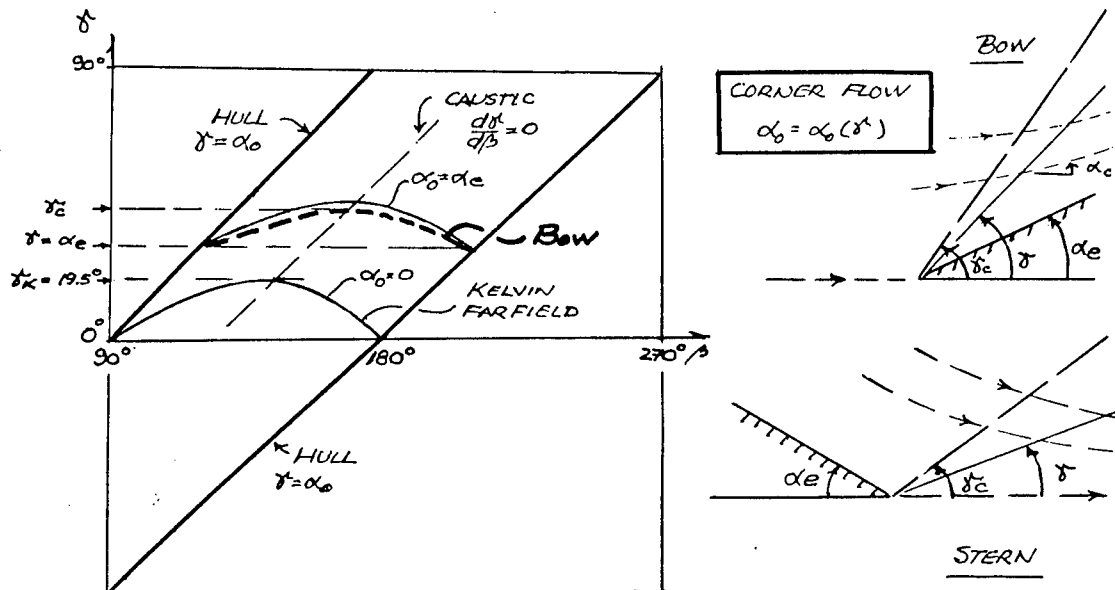
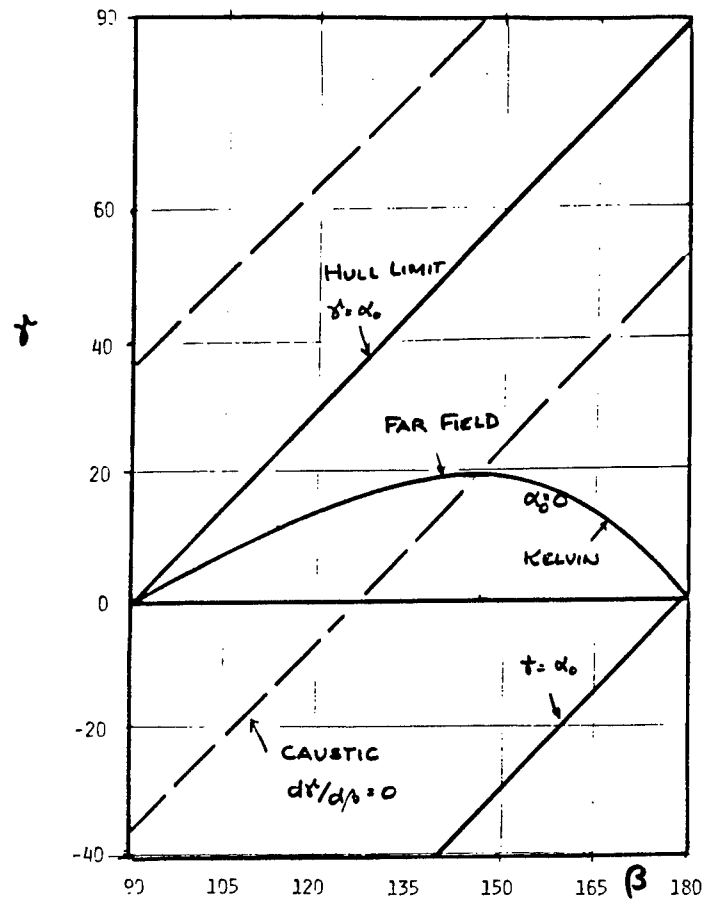


FIGURE 2.2: RAY AND OTHER DEFINITIONS



**FIGURE 2.4: HULL BOUNDARY, CAUSTIC LIMIT**



**FIGURE 2.5: THE END FLOW RAY DIAGRAM (SCHEMATIC)**

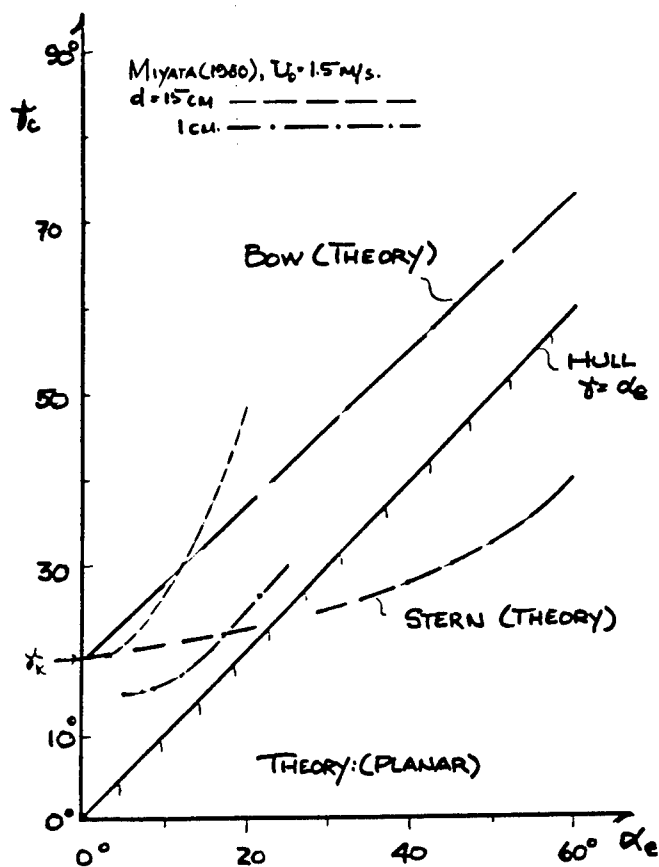


FIGURE 2.6: LIMITING RAY ANGLE,  $\hat{\alpha}_c$

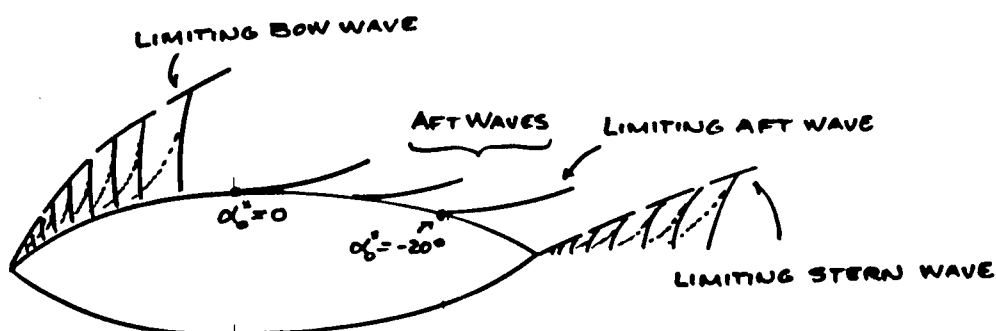


FIGURE 2.7: ASYMPTOTIC SHIP WAVE SYSTEM (SCHEMATIC)

SESSION I  
SEAKEEPING PROBLEMS

## NONLINEAR FORCED MOTIONS OF FLOATING BODIES

W.-M. Lin, J. N. Newman and D. K. Yue

### ABSTRACT

Existing computational models for the numerical solution of nonlinear wave-body interactions have encountered two principal analytical difficulties, first from the singular flow at the intersection of the body and the free surface, and secondly from the difficulty in imposing a radiation condition at infinity. This paper describes complementary studies which address these two separate problems.

A two-dimensional model is constructed for a nonlinear wavemaker in a rectangular domain of finite length and depth. Attention is focussed on the singularity at the intersection of the wavemaker and the free surface. A new algorithm is implemented with the complex potential prescribed at the intersection point. The effectiveness of this scheme is demonstrated by several computational examples including comparisons with experimental observations.

The difficulty associated with a nonlinear radiation condition is avoided by proceeding directly to three dimensions, and matching the finite computational domain to a linear outer solution. The success of this approach is illustrated for transient heaving motions of an axisymmetric cylinder.

### 1. INTRODUCTION

The linear analysis of ship motions in waves has emerged in the past thirty years as one of the most well-studied and useful branches of ship theory. Subject to the basic assumption that the incident waves and resultant body motions are sufficiently small, a rational basis can be established not only for linearizing the boundary conditions, but also for spectral decomposition of the waves and body response. Experiments suggest that the resulting predictions of ship motions, structural loads, and other phenomena of significance are sufficiently accurate for most engineering purposes. Developments in the parallel field of offshore engineering also have made extensive use of the linear theory to predict wave

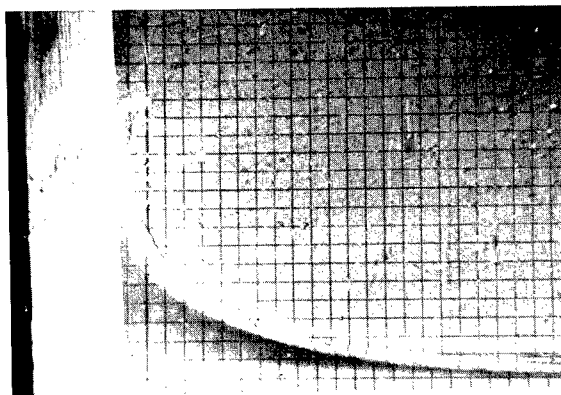


**Figure 1:** Free-surface profile generated by an impulsively moving wavemaker. White vertical object on left side of picture is the wavemaker, rotating counterclockwise about its upper end. Note the small jet moving towards the right from the intersection of the wavemaker and the free surface. (one square=1 cm, water depth=10 cm, time=0.037 sec; from Greenhow and Lin, 1983)

effects on a wide variety of structures.

Despite the success of linear theory, practical engineering problems remain where nonlinear effects are paramount, both in the seakeeping of ships and in the response of offshore structures. The most obvious examples involve precisely the same phenomena where the safety of operations and ultimate survivability are to be analysed. The special importance of these topics lends a note of urgency to efforts to overcome the linear restriction in the theory of ship motions. Indeed, the work reported in this paper was motivated in part by the disaster of the 1979 Fastnet Race, and by our lack of hydrodynamic knowledge to relate the danger for capsizing of small vessels in steep breaking waves to design features of the vessels. Further motivation for research in this area has come from the broaching of fishing vessels, the structural failure of ships due to slamming, and

† Department of Ocean Engineering,  
Massachusetts Institute of Technology, Cambridge, MA 02139

the loss in severe storms of major offshore structures. In all of these cases we require the ability to analyse the seakeeping characteristics of floating bodies when their motions, and the amplitudes of the incident waves, are comparable to the body dimensions.

Accurate nonlinear theories also may be required in cases intermediate between the small-amplitude linear domain and the extremes of survival conditions. More precise predictions for the seakeeping characteristics of ships will ultimately require nonlinear effects to be estimated, if not included. In the field of offshore engineering, much effort has been devoted to the development of nonlinear predictions for the wave loading on structures. Wave resistance is yet another closely-related problem, where progress toward a comprehensive treatment of the nonlinear free-surface condition is essential.

There also is scientific interest in nonlinear free-surface phenomena such as the singular jet shown in Figure 1. When first observed by Greenhow and Lin (1983), this jet was thought to be due to physical processes, such as surface tension, beyond the scope of conventional potential-flow theory. One highlight of the numerical results described here is that this jet is reproduced in the computational simulation when an impulsive wavemaker begins to decelerate.

In an analogous manner to the more familiar linear theory, numerical solutions of nonlinear wave-body problems can be based on the assumptions of irrotational incompressible flow with the velocity potential derived from a discretized boundary-integral method. The most apparent feature of the nonlinear theory is the free-surface boundary condition. Here there has been substantial progress in the development of computational models for the nonlinear dynamics of periodic water waves, in the absence of a floating or submerged body. A semi-Lagrangian time-stepping procedure introduced by Longuet-Higgins and Cokelet (1976) can be used to satisfy both the dynamic and kinematic free-surface conditions, and to trace the trajectories of fluid particles in the free surface. This procedure has been applied to studies of wave-body interactions by Faltinsen (1977) and in a series of papers by Vinje and Brevig (1980, et seq.)

The semi-Lagrangian approach was used by Vinje and Brevig (1980a) to study two-dimensional wave motions in a fluid of finite depth. The solution is obtained in the physical plane, assuming periodicity in space to reduce the computational domain to a finite rectangle. Cauchy's theorem is used to derive a boundary-integral-equation for the complex potential. At each time-step the stream function is prescribed on the boundaries where the normal velocity is known, and the velocity potential is prescribed on the free surface.

In subsequent work Vinje and Brevig have inserted submerged or floating two-dimensional bodies into the computational domain to study the resulting interactions and body motions. To preserve spatial periodicity it is assumed that a

horizontal array of identical bodies are present. The interaction between adjacent bodies is assumed to be weak if their separation is large relative to the duration of the motion in time.

In extending their approach to the case of a floating body, Vinje and Brevig (1980b) consider the points of intersection between the body and free surface as part of the kinematic boundary where the normal velocity is prescribed. At these points, the velocity potential is derived from the integral equation, without regard for the dynamic boundary condition on the free surface, and the intersection points are obtained by extrapolation. The solution obtained in this manner has not been entirely satisfactory. For example, in the study of capsizing of a two-dimensional body by Greenhow et al (1982), experimental data for the locations of the intersection points are required to produce acceptable computations.

Some analytic guidance can be found to describe the singular point at the intersection of a moving body and adjacent free surface. From linear theory it is known that the velocity potential is logarithmically singular at the intersection point if a body in horizontal motion intersects the free surface vertically. It might be thought that this singularity is due to linearization, but the same result is present in nonlinear analytical solutions valid for short times following the impulsive motion of a vertical wavemaker. For example, Peregrine (1972) gives an Eulerian solution for a related steady flow where, at a horizontal distance  $x$  from a moving wall in a fluid of depth  $h$ , the free-surface elevation is proportional to  $\log(\tanh(x/h))$ . The same type of singularity appears in other Eulerian and Lagrangian descriptions reviewed by Greenhow and Lin (1983), and also by Lin (1984). Experimental confirmation for the logarithmic singularity is provided in the former reference, from which Figure 1 is reproduced.

Since a singularity is anticipated at the intersection of the body and free surface, it is understandable that numerical difficulties may be encountered at this point. In order to study this problem in greater detail, we consider in Section 2 a vertical wavemaker with prescribed horizontal motion, situated at one end of a rectangular domain of fluid. The wavemaker extends throughout the finite depth, and moves in uniform translation with transient normal velocity. The bottom of the domain is a horizontal fixed boundary and the end opposite to the wavemaker is a vertical fixed boundary. Attention is focussed on the solution near the intersection of the wavemaker and the free surface, and on the development of an algorithm which can accommodate the flow at this point.

The numerical solution of this problem follows a procedure similar to that of Vinje and Brevig (1980b), with one important modification. Here the intersection point is common to both the wavemaker and the free-surface boundaries, and both the velocity potential and stream function are determined at this point from their

respective boundary conditions. The same scheme is applied at the intersection point on the fixed boundary downstream. This modified method is numerically robust, and can simulate realistic wave motions of large amplitude with obvious nonlinear features including the characteristic steepening of the wave crests, the development of jets near the crests of breaking waves, and also the development of a local jet near the intersection point when the wavemaker is decelerated. The numerical solution, while strictly finite at the intersection point due to discretization, is consistent globally with both experiments and analytic approximations. In most cases the solution can be continued in time without apparent limitations. Encouraging comparisons are shown with the short-time analytic results, and with experimental observations over longer periods of time.

Next we consider the problem of an isolated floating body in an unbounded fluid domain, where the assumptions of spatial periodicity or of a finite domain with fixed boundaries are clearly unsuitable. Instead, an appropriate closure must be developed for the computational domain in the far-field.

Faltinsen (1977) approaches this problem in the context of nonlinear heaving motions of a two-dimensional floating body, using a discretized boundary-integral-equation for the unknown strength of elementary Rankine sources on the body and free surface, and matching the solution to a Rankine dipole in the far-field. Since wave effects are restricted to the domain interior to the fixed matching boundary, the solution is limited to a time duration proportional to the number of unknown points on the free surface. Thus, the number  $N$  of free-surface grid points must increase linearly with time, resulting in  $O(N^2)$  and  $O(N^3)$  increases in the storage requirements and number of arithmetic operations respectively, per time step. The calculations presented by Faltinsen are restricted for this reason to about one cycle of oscillation. In three dimensions the situation is even worse, since  $N$  must increase quadratically with time. Thus, in Isaacson's (1982) Eulerian solution for wave diffraction by a three-dimensional body, where the scattered waves are assumed to vanish at a finite truncation boundary, less than one cycle of motion is simulated in the computations.

If the solution is to proceed for realistic periods of time without an excessively large computational domain, it is necessary to impose an appropriate far-field condition analogous to the radiation condition of outgoing waves in linear theory. Lacking reliable algorithms to express a nonlinear radiation condition, it is logical to follow a hybrid approach where the nonlinear solution in an inner domain near the body is matched to an outer solution consisting of outgoing radiated waves of appropriate amplitude and phase.

The hybrid approach seems destined to fail in two dimensions, since the radiated waves remain nonlinear in the far field. A heuristic

approach might be followed using a linear outer solution, but this is not expected to work due to the imperfect match of the two solutions.

In three dimensions, by comparison, the energy density of the radiated waves attenuates inversely with radial distance, and a linear far-field solution can in principle be assumed outside a matching boundary sufficiently far from the body. Moreover, if the outer solution satisfies the complete transient linear free-surface condition, it can be expected that the solution may be carried out for an unlimited time, given a suitably chosen matching boundary.

Since our practical interest lies ultimately in three dimensions, it seems most appropriate to formulate and solve the nonlinear wave-body problem in this context, rather than attempting to overcome the difficulties associated with the far-field description in two dimensions.

The problem considered in Section 3 is that of an axisymmetric body forced to move vertically in a prescribed transient manner, starting from an initial state of rest. Green's theorem is used to represent the velocity potential in an inner domain bounded by the body surface, the free surface, and a vertical matching cylinder of large radius. Since the solution is axisymmetric, a one-dimensional integral equation can be derived on the trace of these boundaries. The kernel is obtained from a Rankine ring source, and can be expressed in the form of elliptic integrals. Once again the semi-Lagrangian time-stepping procedure is followed to satisfy the complete nonlinear boundary conditions on the free surface. Eulerian points are prescribed on the body surface, and on the matching boundary.

The linearized outer solution can be interpreted as that due to a circular wavemaker coincident with the matching boundary. A special transient free-surface ring source is developed to provide an efficient solution of this problem.

Preliminary results obtained in this manner for the oscillatory heaving motion of a circular cylinder are presented for moderate values of the amplitude, and confirmed by comparison to the linear theory when the amplitude of the body motions is small. An encouraging feature is the absence of reflected waves on the free surface at the matching boundary. More work remains to ascertain the optimum radius for the matching boundary, and the scales of temporal and spatial discretization, to permit effective use of this method for very large amplitudes of heaving motion.

To summarize the present status of this project, numerical approaches have been developed and tested for overcoming the two separate problems of the singularity at the intersection of the body and free surface, and of the far-field description in three dimensions. In both cases the solution appears stable and can proceed indefinitely in time, limited primarily by considerations of computational cost.

Most of our results have been obtained with

a VAX 11/780 computer system. This work has utilized hundreds of hours of CPU time on that system. Encouraging results have been obtained from limited computations performed on a CRAY-1 supercomputer. Future work is planned with the CRAY, to generalize and integrate the two studies reported here, with the ultimate objective a robust and efficient computational model capable of simulating the seakeeping characteristics of realistic floating vessels in waves of large amplitude.

## 2. THE NONLINEAR WAVEMAKER PROBLEM

### 2.1 MATHEMATICAL FORMULATION

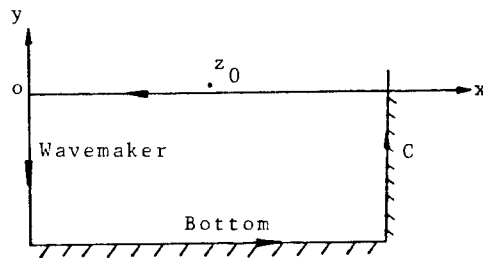


Figure 2: Wave tank and coordinate system.

The fluid in the rectangular domain shown in Figure 2 is assumed to be incompressible, and the motion irrotational. The complex potential  $\beta(z,t) = \phi(z,t) + i\psi(z,t)$ , where  $z = x + iy$ , is applicable for describing the fluid motion. Both the velocity potential  $\phi$  and the stream function  $\psi$  satisfy Laplace's equation so  $\beta$  is analytic in the fluid domain. Cauchy's integral theorem gives

$$\oint_C \frac{\beta}{z - z_0} dz = 0 \quad (1)$$

where  $C$  is a closed contour consisting of the free surface, the wavemaker, the bottom, and a vertical rigid wall downstream. The point  $z_0$  is situated outside  $C$ .

Letting  $z_0$  approach the boundary, it follows that

$$i\alpha_0\beta(z_0) + \oint_C \frac{\beta}{z - z_0} dz = 0 \quad (2)$$

where  $\alpha_0$  is the actual angle between the two elements adjacent to  $z_0$  on  $C$ . For a smooth boundary,  $\alpha_0 = \pi$ .

The contour  $C$  is composed of  $C_\phi$  and  $C_\psi$ , where  $\phi$  is given on  $C_\phi$  and  $\psi$  on  $C_\psi$ . The free surface belongs to  $C_\phi$  and both the velocity potential and the elevation are zero at  $t = 0$  on this boundary. The other three boundaries are recognized as  $C_\psi$ , since the stream function can be calculated from the normal velocity. The stream function is taken to be zero on the bottom and the vertical boundary downstream.

On the wavemaker, the stream function is  $\psi = U(t)(y + 1)$ , where  $U(t)$  is the assigned velocity on the wavemaker. In this section, the length scale is the depth of the tank  $h$  and the time scale is  $(h/g)^{1/2}$ , where  $g$  is the gravitational acceleration. All the other variables are nondimensionalized by the proper combination of  $g$  and  $h$ .

Vinje and Brevig (1980b) show that if the real part of (2) is taken for  $z_0$  on  $C_\phi$  and the imaginary part for  $z_0$  on  $C_\psi$ , the resulting Fredholm integral equations of the second kind have good properties for numerical solution. Thus,

$$\alpha_0\psi(z_0;t) + \text{Re} \left\{ \oint_C \frac{\beta}{z - z_0} dz \right\} = 0 \quad (3)$$

for  $z_0$  on  $C_\phi$ , and

$$\alpha_0\phi(z_0;t) + \text{Re} \left\{ i \oint_C \frac{\beta}{z - z_0} dz \right\} = 0 \quad (4)$$

for  $z_0$  on  $C_\psi$ . From (3) and (4),  $\beta$  can be found on the entire boundary  $C$ .

For the time stepping procedure, fluid particles on the free surface are followed. The position and the velocity of these points are obtained by integrating in time the kinematic free-surface boundary condition

$$\frac{Dz}{Dt} = u + iv = w^* \quad (5)$$

and the dynamic free-surface boundary condition

$$\frac{D\phi}{Dt} = \frac{1}{2} ww^* - y - \frac{p_s}{\rho} \quad (6)$$

where  $*$  denotes the complex conjugate,  $\rho$  the water density,  $p_s$  (taken to be zero in this work) an arbitrary pressure distribution on the free surface, and  $D/Dt$  is the material derivative. The particle velocity  $(u,v)$  is given by

$$w = u - iv = \frac{\partial\beta}{\partial z} \quad (7)$$

No integration is needed for points on the other boundaries, because both the position and the normal velocity are specified.

### 2.2 NUMERICAL SOLUTION

To solve the integral equation for  $\beta$ , the collocation method is used. As shown in Figure 3 nodal points are chosen along the contour  $C$  to divide it into elements. Assuming  $\beta$  varies linearly in  $z$  between nodal points,

$$\beta(z) = \sum_{j=1}^N \Lambda_j \beta_j \quad (8)$$



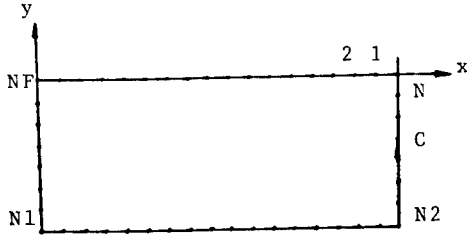


Figure 3: Nodal points on the boundary.

where

$$\begin{aligned} \Lambda_j(z) &= \frac{z - z_{j+1}}{z_j - z_{j+1}} & \text{for } z < z_j < z_{j+1} \\ \Lambda_j(z) &= \frac{z - z_{j-1}}{z_j - z_{j-1}} & \text{for } z < z_j < z_{j-1} \\ \Lambda_j(z) &= 0 & \text{elsewhere} \end{aligned} \quad (9)$$

Substituting (8) into (1) gives the following matrix equation:

$$\oint_C \frac{\beta}{z - z_k} dz = \sum_{j=1}^N \Gamma_{k,j} \beta_j \quad \text{for } k=1, \dots, N \quad (10)$$

where

$$\begin{aligned} \Gamma_{k,j} &= \frac{z_k - z_{j-1}}{z_j - z_{j-1}} \ln \frac{z_j - z_k}{z_{j-1} - z_k} \\ &+ \frac{z_k - z_{j+1}}{z_j - z_{j+1}} \ln \frac{z_{j+1} - z_k}{z_j - z_k} \end{aligned} \quad (11)$$

are the influence coefficients of the matrix equation. The detailed derivation to get (11) and some limiting forms of  $\Gamma_{k,j}$  when  $k = j-1$ ,  $j$ , or  $j+1$  are given in Vinje and Brevig (1980b).

According to (3) and (4), the numerical solution of (10) is found for  $k = 1, 2, \dots, NF-1$

$$\begin{aligned} & - \sum_{j=1}^{NF-1} \text{Im}(\Gamma_{k,j} X_j) + \sum_{j=NF+1}^{N-1} \text{Re}(\Gamma_{k,j} X_j) \\ & = - \sum_{j=1}^{NF-1} \text{Re}(\Gamma_{k,j} \phi_j) + \sum_{j=NF+1}^{N-1} \text{Im}(\Gamma_{k,j} \psi_j) \\ & - \text{Re}\{\Gamma_{k,NF}(\phi_{NF+i\psi_{NF}}) + \Gamma_{k,N}(\phi_N+i\psi_N)\} \end{aligned} \quad (12)$$

and for  $k = NF+1, \dots, N-1$

$$- \sum_{j=1}^{NF-1} \text{Re}(\Gamma_{k,j} X_j) - \sum_{j=NF+1}^{N-1} \text{Im}(\Gamma_{k,j} X_j)$$

$$\begin{aligned} & = \sum_{j=1}^{NF-1} \text{Im}(\Gamma_{k,j} \phi_j) + \sum_{j=NF+1}^{N-1} \text{Re}(\Gamma_{k,j} \psi_j) \\ & - \text{Im}\{\Gamma_{k,NF}(\phi_{NF+i\psi_{NF}}) + \Gamma_{k,N}(\phi_N+i\psi_N)\} \end{aligned} \quad (13)$$

where  $X_j$ ,  $j = 1, 2, \dots, NF-1, NF+1, \dots, N-1$  is the unknown part of the complex potential function, i.e., the stream function for  $j = 1, 2, \dots, NF-1$ , or the velocity potential for  $j = NF+1, \dots, N-1$ .

It should be noted in (12) and (13) that the intersection, point  $NF$ , is common to both the wavemaker and the free-surface boundaries, and both the velocity potential and the stream function are regarded as known at this point in terms of their respective boundary conditions. The same argument applies to point  $N$ , and terms associated with these two points are moved to the right-hand side of the equations.

For the solution of the simultaneous equation system, the Gauss-Seidel iterative method is used. Since the solution is guaranteed to converge for the elliptical type problem and the solution from the previous time step is an excellent initial iterative value for the next time step, the Gauss-Seidel method can save more than 50% of CPU time compared to direct elimination for a typical  $100 \times 100$  matrix.

After solving for the potential function  $\beta$ , (4) and (5) are integrated to march forward in time. It is important to make sure that these two conditions are also satisfied at the points  $NF$  and  $N$ , because the location and the velocity potential at these two points for the next time step can then be calculated from integration instead of being approximated by extrapolation. The pressure at the intersection is zero, according to the dynamic free-surface boundary condition.

The complex velocity  $w(z_0, t)$  has to be calculated along the boundary for time stepping. In general, it takes the form

$$w(z_0, t) = \frac{1}{2\pi i} \oint_C \frac{\beta}{(z - z_0)^2} dz \quad (14)$$

This expression turns out to be singular at the nodal points and a second order differential scheme used in Vinje and Brevig (1980b) is introduced for this calculation.

To integrate (4) and (5) in time, Hamming's fourth order predictor/corrector method with a second order Runge-Kutta starting procedure is used. This scheme is expected to be stable and the detailed description can be found in Vinje and Brevig (1980b).

### 2.3 IMPULSIVE WAVEMAKER MOTION

The first case studied is the impulsive motion of a wavemaker. A wavemaker starts to move with a constant horizontal velocity  $U$  from a state of rest. At  $t = 0^+$ , the velocity is a

step function and the acceleration is infinite. Analytically, a logarithmic singularity is expected at the intersection point of the free surface and the wavemaker. This is confirmed, for sufficiently small time, by the experiments described in Greenhow and Lin (1983). Numerically, this case is very critical, because the high velocity gradient near the intersection point could ruin the numerical scheme. For the actual numerical runs, the length of the tank is taken to be 10 (water depth is 1), the velocity of the wavemaker is 1, and the time is from 0 to 0.2. During this period of time, there is no evidence of wave reflection from the boundary downstream.

Care must be exercised about the element size  $\Delta x$  and the step size  $\Delta t$ . It is found from numerical experiments that the size of the element on each side of the corner points ( $NF$ ,  $N1$ ,  $N2$ ,  $N$ ) should be comparable. The choice of  $\Delta t$  is very critical. As will be seen later, a very thin layer of fluid is formed along the wavemaker face for this impulsive motion problem.  $\Delta t$  must be sufficiently small in order to avoid the fluid particles on the free surface moving across the wavemaker during the time stepping.

The analytical solution suggests that the vertical velocity at the intersection point is infinite at  $t = 0^+$ . To confirm this, (12) and (13) are solved using a wide range of elements on the boundary ( $N = 66, 132, 198, 264, 330, 396, 462, 528$ ). Cosine spacing is used for all of these runs. Figure 4 shows the distribution of the velocity potential on the wavemaker at  $t = 0^+$ . Except for the immediate vicinity of the intersection, the difference between these results is negligible.

An enlarged view of the local region near the intersection point (cf. the small rectangle in Figure 4) is given in Figure 5. It can be seen that the local slope of the potential (i.e., vertical velocity) becomes larger if more elements are used. Note that for the case  $NF = 200$ , the smallest element on the wavemaker is of the order  $10^{-4}$ . The numerical solution becomes closer and closer to the analytical solution if more and more elements are used. On the other hand, the numerical scheme gives an accurate solution away from the intersection even with a small number of elements.

For the subsequent time steps, a comparison between the numerical results and the analytical solution is given in Figure 6. The highest symbol in each curve represents the calculated intersection point. A denser grid near the intersection will result in a very high intersection position but the rest of the free-surface shape is not affected. The analytical solution used here is a leading-order solution in small time, first suggested by Peregrine (1972). This provides a good confirmation of the numerical solution during the first few time steps.

## 2.4 FORCE CALCULATION

To calculate the pressure, it is easier to follow Lagrangian points on the moving boundary. Introducing the material derivative  $D/Dt$  into the Bernoulli's equation, the total pressure takes the form

$$\frac{p}{\rho} = -\frac{D\phi}{Dt} + \frac{1}{2} \nabla\phi \cdot \nabla\phi - y \quad (15)$$

For the pressure distribution on the wavemaker at time  $t = t_n$ ,  $\nabla\phi$  and  $y$  are chosen to be the current value, and  $D\phi/Dt$  is obtained by the central difference formula

$$\frac{D\phi_n}{Dt} = \frac{\phi_{n+1} - \phi_{n-1}}{2\Delta t} \quad (16)$$

The force acting on the wavemaker is calculated by integrating the pressure.

Once again the impulsive wavemaker motion case is studied with  $U = 1$  for  $t > 0$ . The length of the tank is 5,  $\Delta x$  is chosen to be 0.1 on the free surface and 0.05 on the wavemaker. The pressure distributions for several different time steps are given in Figure 7. The upper end of each curve is the actual intersection point calculated by the computer program. The shaded triangle is the hydrostatic pressure below the original free surface. The dynamic pressure under the original mean free surface is nearly constant and the total pressure in the thin jet region is practically zero. This result is not surprising because the jet is so thin that the pressure in this region on the wavemaker is not expected to be too different from the zero pressure on the free surface. But it is interesting to see that in the thin jet region the dynamic pressure cancels out the static pressure which can be very large if the intersection point is very high. The pressure force acting on the wavemaker is insensitive to time.

Since the pressure in the thin jet is negligible, the grid on the free surface can be relatively sparse and the calculated force will have only a small error. But it must be emphasized that both the free-surface and the wavemaker boundary conditions must be satisfied at the intersection point to ensure an accurate global solution.

## 2.5 SIMPLE-HARMONIC WAVEMAKER MOTION

As examples of simple-harmonic wavemaker motion, the wavemaker velocity  $U(t)$  can either be a sine function or a cosine function, that is

$$U(t) = \frac{\omega A}{2} \sin \omega t \quad \text{or} \quad \frac{\omega A}{2} \cos \omega t \quad (17)$$

where  $\omega$  is the frequency, and  $A$  is the double-amplitude of the wavemaker motion. The

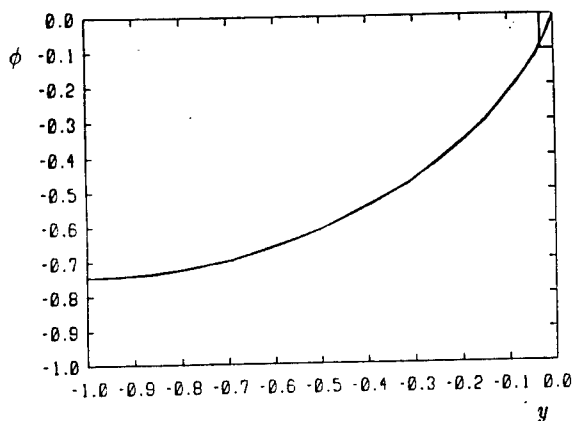


**Figure 4:** Distribution of the velocity potential  $\phi$  on the wavemaker with  $U=1$  at  $t=0^+$ . Figure shown contains 8 curves with  $N = 66, 132, 198, 264, 330, 396, 462, 528$ ;  $NF = 25, 50, 75, 100, 125, 150, 175, 200$ , respectively.

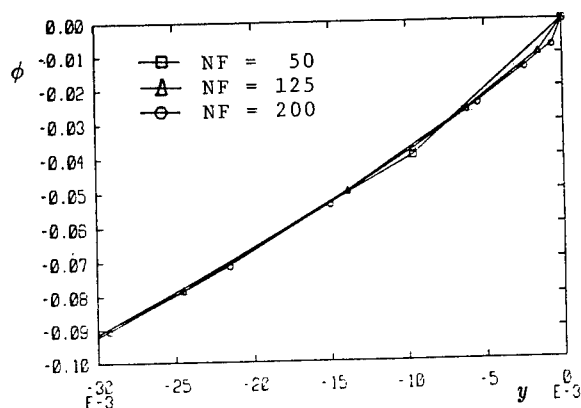


**Figure 5:** Distribution of the velocity potential  $\phi$  on the wavemaker with  $U=1$  at  $t=0^+$ .

former, called "sine motion" in this Section, has zero initial velocity and the mean position of the wavemaker motion is  $A/2$ . The latter, "cosine motion", has an impulsive start and the mean position of the wavemaker motion is at  $x = 0$ . The difference of these two types of wavemaker motion is not important for steady-state linear waves, but is essential for the transient nonlinear waves.

A typical transient wave-front at  $t = 19.1$  is shown in Figure 8. The length of the tank is 20 to minimize reflection from the vertical wall downstream. According to the group velocity calculation, the location of the wavefront of the steady-state linear wave is around  $x = 6.4$ . Behind the front, the wave-amplitude, wavelength, and phase velocity compare well with the linear steady-state theory. The actual front occurs over a distance of several wavelengths due to dispersion.

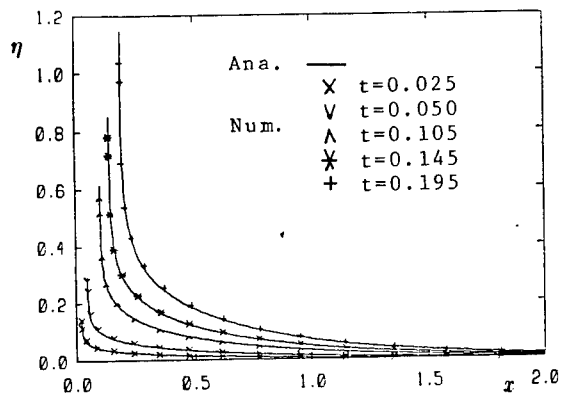


**Figure 6:** Comparison between analytical and numerical results for the free surface elevation  $\eta$ . Wavemaker has impulsive motion with  $U=1$ . Analytical solution is from Peregrine (1972) or Lin (1984).

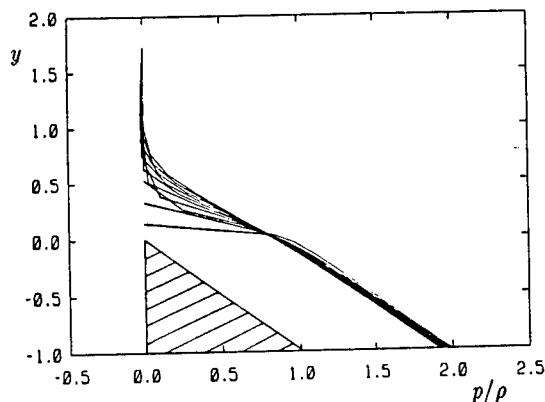
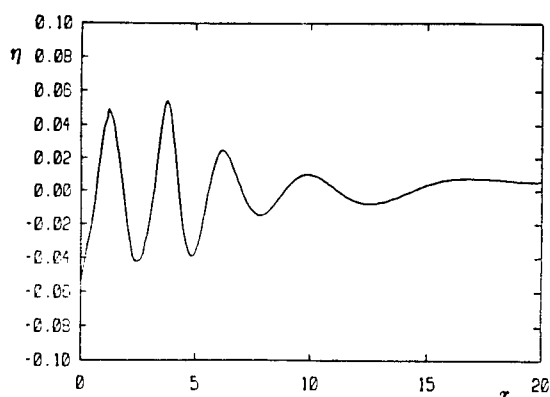


**Figure 7:** Pressure distribution on the wavemaker for the impulsive wavemaker motion case,  $U=1$ ,  $t = 0.05, 0.10, \dots, 0.50$ . Shaded area is the hydrostatic pressure component.

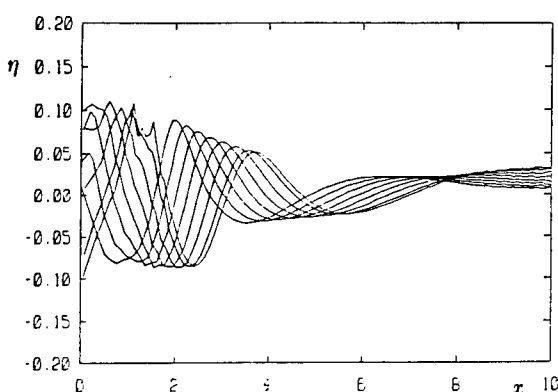
## 2.6 INSTABILITY AND SMOOTHING

Figure 9 shows a sequence of time steps with a larger stroke,  $A = 0.1$ , and  $\omega = 1.5708$ . During the first two cycles (not shown), the wave amplitude decays smoothly. For the third cycle, the disturbance observed on the free surface leads the numerical scheme to break down. Several different combinations of  $\Delta x$  and  $\Delta t$  have been tried, but the numerical scheme always breaks down at approximately the same point. To verify that the precision of the numerical computation is not responsible for this, a computer run has been carried out on the CRAY-1 using double-precision arithmetic and the result is the same.

An analogous instability is discussed by Longuet-Higgins and Cokelet (1976) in their study of breaking waves. After finding that the



**Figure 8:** Free-surface elevation of a sine wavemaker motion with  $\omega=\pi/2$ ,  $A=0.05$ ,  $t=19.1$ .



**Figure 9:** Free-surface elevation of a sine wavemaker motion with  $\omega=\pi/2$ ,  $A=0.10$ ,  $t = 8.4, 8.8, \dots, 11.0$ .

instability is not caused by the time-stepping procedure, and suggesting that it might be related to the amplification of short gravity-waves by horizontal compression at the crest of long waves, they concluded that this instability may be partly physical, and damped by viscosity in a real fluid. To overcome this problem Longuet-Higgins and Cokelet adopted a 5-point smoothing formula. It has been found that if the same scheme is applied here to  $\beta$  and  $z$  every several time steps, the free-surface instability is suppressed and the numerical time stepping can go on without any problem.

## 2.7 EXPERIMENT FOR SIMPLE-HARMONIC WAVEMAKER MOTION

In order to confirm the numerical results, experiments have been conducted to measure the free-surface elevation in a wave tank at the Parson Laboratory, Department of Civil Engineering, M.I.T. The wave tank is 30 m long, 76 cm wide, and the water depth is 60 cm. A power-driven piston wavemaker can perform a specified motion from an outside data source to

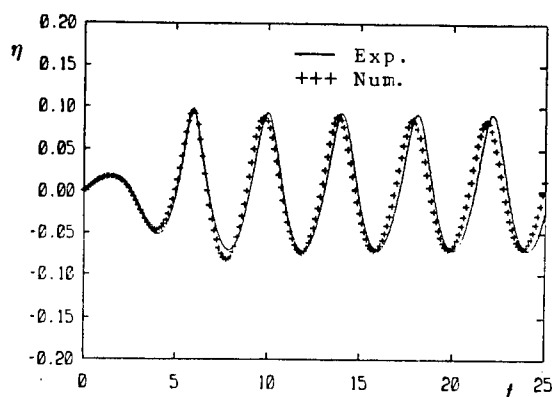


**Figure 10:** Comparison between numerical and experimental results for the free-surface elevation. Wavemaker has cosine motion with  $\omega=1.5539$ ,  $A=0.10$ . Wave probe is located 1.167 away from the mean wavemaker position.

generate two-dimensional waves. In these experiments, the wavemaker has a cosine motion, the frequency  $\omega$  is 1.5539 (nondimensional), and the only parameter changed is the stroke. For the present comparison,  $A$  is chosen to be 0.1 (nondimensional). A wave probe is located 1.1667 from the mean position of the wavemaker. The free-surface elevation at the wave probe and the wavemaker displacement are recorded as functions of time. The data sampling rate is 200 points per second and the duration of each experiment is about 20 seconds.

It is found that the actual wavemaker stroke is about 3% higher than the stroke indicated, and during the first moving cycle of the wavemaker, it overshoots by about 6%. In the experiment, a small disturbance is observed on the wave crest but the wave goes on without any problem. This small disturbance seems to have some relation to the breakdown of the numerical scheme.

A numerical run has also been made with  $\omega = 1.5539$ ,  $A = 0.1$ . A smoothing function is applied every 4 steps for this run. A comparison between the numerical result and the experimental measurement is given in Figure 10. The differences are relatively small. It is not known if these are attributable to the numerical approximation or experimental errors. The comparison in Figure 10 seems to justify the use of the smoothing function, despite its empirical basis.

## 2.8 LARGE-STROKE WAVEMAKER MOTION

Breaking is observed in the experiments if  $A$  exceeds 0.15 (nondimensional). A numerical simulation of this breaking phenomena has been attempted and the results are qualitatively consistent with the experimental observations. An example of cosine motion with  $A = 0.30$  is shown in Figure 11. The free-surface profiles are

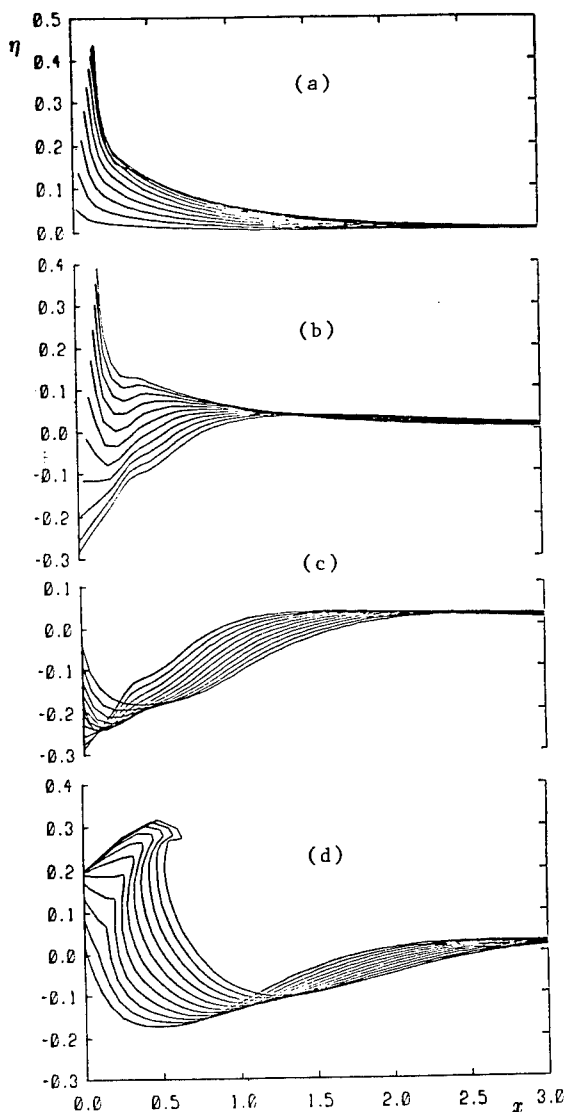


**Figure 11:** Numerical simulation of a breaking wave. Wavemaker has cosine motion with  $\omega=1.5539$ ,  $A=0.30$ . A smoothing function is applied every 4 time steps. (a)  $t = 0.1, 0.2, \dots, 1.1$ ; (b)  $t = 1.2, 1.3, \dots, 2.2$ ; (c)  $t = 2.3, 2.4, \dots, 3.3$ ; (d)  $t = 3.4, 3.5, \dots, 4.4$ .

plotted with time steps indicated in each figure. The smoothing function is applied once for every 4 time steps. The numerical run breaks down a few steps after the last curve plotted, because the free surface intersects itself. For this case, the wave breaks essentially due to the large steepness.

A substantially different picture is shown in Figure 12 for the free surface profiles in the first half cycle of a sine wavemaker motion with  $A = 0.5$ ,  $\omega = \pi$ . A jet shooting out ahead of the intersection point can be seen clearly. This phenomena can not be described properly by using a sparser mesh of grid points.

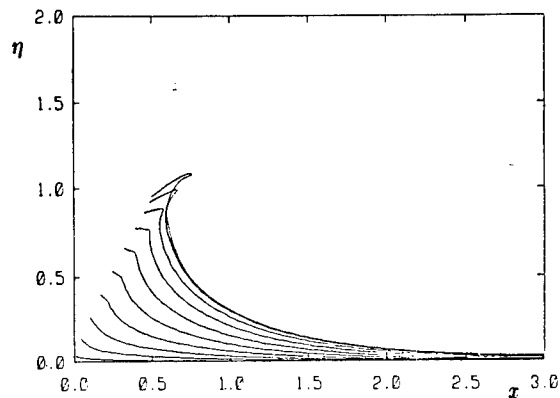


**Figure 12:** Numerical simulation of a jet shooting out near the intersection. Wavemaker has sine motion with  $\omega=\pi$ ,  $A=0.50$ . Smoothing function is applied every 4 time steps.  $t = 0.1, 0.2, \dots, 1.0$ .

This type of jet is believed to be caused by deceleration of the wavemaker. In this sine wavemaker case, the jet starts to develop at about the same time that deceleration of the wavemaker commences at  $t = 1$ . Similar runs for the cosine wavemaker motion have shown no sign of the jet, indicating that the history of the body motion is very important to the free surface behavior near the intersection point.

These striking numerical results are consistent with the experimental observations in Figure 1 in which a similar jet shooting out from the wavemaker near the intersection point is observed. In that experiment the wavemaker velocity is practically constant in time, but since it rotates about a hinge at the top of the wave tank the horizontal velocity decreases with height. Thus the fluid near the intersection point experiences a deceleration. Although the wavemaker motion in the numerical computation is different from that in the experiment, the deceleration effect is similar and it is believed that this accounts for the development of the jet in both cases.

Most of the numerical runs have been done on a VAX 11/780 system with single precision. Some of the critical cases are checked using full precision on a CRAY-1. In all cases, the results agree to four significant figures. The approximate CPU time involved is about 50 seconds on the VAX or 1.3 seconds on the CRAY, per time step, with 150 elements on the boundary.

### 3. THE AXISYMMETRIC HEAVE PROBLEM

#### 3.1 FORMULATION

We formulate potential flow in a fluid volume  $V$  enclosed by a boundary  $\partial V$  consisting of the body surface  $B$ , free surface  $F$ , and a

vertical circular cylindrical matching surface  $S$  at radius  $A$ .  $V$  extends to infinite depth. For  $z$  positive vertically up and  $z = 0$  the still water position, the velocity potential  $\phi(\mathbf{x}, t)$  satisfies:

$$\nabla^2 \phi = 0 \quad \text{in } V(t) \quad (18)$$

$$\nabla \phi \cdot \mathbf{n}(t) = \frac{\partial \phi}{\partial n} = U \quad \text{prescribed, on } B(t) \quad (19)$$

$$|\nabla \phi| \rightarrow 0 \quad z \rightarrow -\infty \quad (20)$$

$$\frac{D\mathbf{x}}{Dt} = \nabla \phi \quad \text{on } F(t) \quad (21)$$

$$\frac{D\phi}{Dt} = -gz + \frac{1}{2} |\nabla \phi|^2 \quad \text{on } F(t) \quad (22)$$

plus a suitable closure boundary condition on  $S$ , and zero initial conditions.

Applying Green's identity to  $\phi$  and the fundamental singularity  $R^{-1} = |P - P'|^{-1}$ , we have

$$\begin{aligned} 2\pi\phi(P, t) \\ = \int_{\partial V(t)} \left( \frac{\partial \phi}{\partial n'} - \phi \frac{\partial}{\partial n'} \right) \frac{1}{R} dP', \quad P \in \partial V \end{aligned} \quad (23)$$

For axisymmetric bodies and motions,  $\phi$  is independent of the angular coordinate  $\theta$  and (23) can be integrated to give

$$\begin{aligned} 2\pi\phi(r, z, t) \\ = \int_{\partial L(t)} r' \left( \frac{\partial \phi}{\partial n'} - \phi \frac{\partial}{\partial n'} \right) G(r, z, r', z') dP', \quad (r, z) \in \partial L \end{aligned} \quad (24)$$

where  $r^2 = x^2 + y^2$ ,  $\partial L(t) = \partial B + \partial F + \partial S$  is the trace of  $\partial V(t)$  on  $(r, z)$ , and  $G$  is the Rankine ring source Green function

$$G = \int_0^{2\pi} \frac{d\theta'}{R} = \frac{4}{\rho} K \left( 1 - \frac{\bar{\rho}^2}{\rho^2} \right) \quad (25)$$

where  $\rho^2 = (z-z')^2 + (r+r')^2$ ,  $\bar{\rho}^2 = (z-z')^2 + (r-r')^2$  and  $K$  is the complete elliptic integral of the first kind (Abramowitz and Stegun, 1964). Note that  $K$  is logarithmically singular at 1, so that as  $(r, z)$  approaches  $(r, z)'$ ,  $\bar{\rho} \rightarrow 0$ , and  $G \sim \log(\bar{\rho})$ , as in two-dimensional flows.

For a given  $\partial L$  at any time, (24) can be used to solve for  $\phi$  or  $\phi_n$  on the boundary given the other. On the outer boundary  $\partial S$ , neither  $\phi$  nor  $\phi_n$  are in principle known, and a closure is obtained by matching to a linearized solution in the exterior.

In general, for any linearized axisymmetric wavefield, the transient potential and its normal velocity on a given cylinder can be related by an equation of the form:

$$\begin{aligned} \phi(A, z, t) &= \int_{-\infty}^0 dz' D_R(z, z') \phi_r(A, z', t) \\ &+ \int_0^t d\tau \int_{-\infty}^0 dz' D_F(z, z', t-\tau) \phi_r(A, z', \tau), \quad z < 0 \end{aligned} \quad (26)$$

Here  $D_R$  is the part due to the Rankine source and its negative image above the  $z = 0$  plane, and  $D_F$  the free-surface contribution, evaluated on  $r = A$ , of the "Green function"  $D(r, z, t; r', z', \tau)$  which satisfies the linearized exterior problem:

$$\nabla^2 D = 0, \quad (r, z, t) \neq (r', z', \tau), \quad r > A, \quad z < 0 \quad (27)$$

$$\frac{\partial D}{\partial r} = \delta(z-z')\delta(t-\tau), \quad r=A, \quad z, z' < 0 \quad (28)$$

$$\frac{\partial^2 D}{\partial t^2} + g \frac{\partial D}{\partial z} = 0, \quad z=0 \quad (29)$$

This result is simplified for values on  $r = A$ , and it can be directly derived that

$$\begin{aligned} D_R(z, z') &= \frac{-2}{\pi A} \int_0^\infty \frac{K_0(kA) \operatorname{sink} z \operatorname{sink} z'}{k K_1(kA)} dk \\ &= \frac{-2}{\pi^2 A} \int_0^\infty \frac{(e^{-k|z-z'|} - e^{-k|z+z'|}) dk}{k^2 [J_1^2(kA) + Y_1^2(kA)]}, \quad z, z' < 0 \end{aligned} \quad (30)$$

and

$$\begin{aligned} D_F(z, z', t-\tau) &= \frac{-4}{\pi^2 A} \int_0^\infty \frac{\sqrt{g/k} \sin(\sqrt{gk}(t-\tau))}{e^{-k|z+z'|} dk} \\ &\quad \frac{e^{-k|z-z'|} dk}{k^2 [J_1^2(kA) + Y_1^2(kA)]}, \quad z, z' < 0 \end{aligned} \quad (31)$$

Here  $J_n$ ,  $K_n$  and  $Y_n$  are Bessel functions as defined by Abramowitz and Stegun (1964). The latter expression of (30) is better suited to computation. As  $|z-z'| \rightarrow 0$ ,

$$D_R(z, z') \sim \frac{1}{\pi} \log|z-z'| \quad (32)$$

while at  $t = \tau$ ,

$$D_F(z, z', 0) = 0 \quad (33)$$

as expected.

Using (26) to eliminate  $\phi$  on  $\partial S$  (in terms of  $\phi_r$ ) from the Green's theorem integral equation (24), we have

$$\begin{aligned}
& \int_{\partial B} dP' (2\pi\delta(P-P') + r' \frac{\partial G}{\partial n'}) \phi(P', t) \\
& - \int_{\partial F} dP' r' G \frac{\partial \phi}{\partial n'} (P', t) \\
& + \int_{\partial S} dz' (2\pi\delta(P-P') + A \frac{\partial G}{\partial n'}) \\
& \cdot \int_{-\infty}^0 dz'' D_R(z', z'') \phi_r(A, z'', t) \\
& = \int_{\partial B} dP' r' G \frac{\partial \phi}{\partial n'} \\
& - \int_{\partial F} dP' (2\pi\delta(P-P') + r' \frac{\partial G}{\partial n'}) \phi(P', t) \\
& - \int_{\partial S} dz' (2\pi\delta(P-P') + r' \frac{\partial G}{\partial n'}) \\
& \cdot \int_{-\infty}^0 dz'' \int_0^t d\tau D_F(z', z'', t-\tau) \phi_r(A, z'', \tau), \quad P \in \partial L \quad (34)
\end{aligned}$$

Following a semi-Lagrangian approach, we select (moving) Eulerian points on  $\partial B(t)$  and  $\partial S$ , and Lagrangian points on  $\partial F(t)$ . At any time  $t$ , the current position  $\partial F(t)$  and the potential  $\phi$  on  $\partial F$  are obtained from previous times by integrating the free-surface conditions (21) and (22) respectively; the body location  $\partial B(t)$  and normal velocity  $\phi_n$  on  $\partial B$  are prescribed, and for known  $\phi_r$  on  $\partial S$  for all earlier times, (34) can be solved as a mixed first and second kind Fredholm integral equation system for  $\phi$  on  $\partial B$ ,  $\phi_n$  on  $\partial F$  and the present  $\phi_r$  on  $\partial S$ . The process is then repeated for the next time step. Note that the potential  $\phi$  on  $\partial S$  is never explicitly required but may be recovered directly by quadrature from (26).

### 3.2 DISCRETIZATION

We subdivide the line  $\partial L$  into linear segments  $\partial L_j$ ,  $j = 1, 2, \dots, J+1$ , and assume  $\phi = \phi_j$ ,  $\phi_n = \phi_{nj}$  to be constants over each segment. The only exception is the last panel on  $\partial S$  which extends to deep water  $\partial L_{J+1} = \{z: -B \leq z < -\infty\}$ . Over this deep infinite segment we assume  $\phi$  and  $\phi_r$  to vary according to that of a dipole at the origin:

$$\phi_{J+1}(A, z, t) = d(t) \frac{z}{(z^2 + A^2)^{3/2}} \quad z \leq -B \quad (35)$$

and

$$\phi_{rJ+1}(A, z, t) = e(t) \frac{z}{(z^2 + A^2)^{5/2}} \quad z \leq -B \quad (36)$$

In principle,  $d(t)$  and  $e(t)$  are related to each other (and to  $\phi(A, z, \tau)$ ,  $\phi_r(A, z, \tau)$ ,  $z < 0$ ,  $0 < \tau < t$ ) by (26)). For simplicity, these unknown strengths are eliminated by requiring continuity with the values on  $\partial L_j$  at every time. Thus, only  $J$  collocation points are required for (34), which are selected at the mid-point of segments  $\partial L_j$ ,  $j = 1, 2, \dots, J$ . Uniform time steps  $t_n = n\Delta t$ ,  $n = 1, 2, \dots$  and  $\phi_j^n = \phi_j(t_n)$  etc., are used. Using the trapezoidal rule, the convolution integral in (34) can be written as

$$\int_0^{t_n} d\tau D_F(t-\tau) \phi_r(\tau) \simeq \Delta t \sum_{l=1}^{n-1} D_F^{n-l} \phi_r^l \quad (37)$$

where the contributions from  $t = t_n$  and  $t = 0$  vanish on account of (33) and the initial condition on  $\phi$  respectively. Thus, we reduce (34) to a system of linear algebraic equations:

$$\begin{aligned}
& \sum_{\partial L_j \in \partial B^n} H_{ij} \phi_j^n - \sum_{\partial L_j \in \partial F^n} G_{ij} \phi_{nj}^n \\
& + \sum_{\partial L_j \in \partial S^n} H_{Sij} \sum_{\partial L_k \in \partial S^n} R_{jk} \phi_{rk}^n \\
& = \sum_{\partial L_j \in \partial B^n} G_{ij} \phi_{nj}^n - \sum_{\partial L_j \in \partial F^n} H_{ij} \phi_j^n \\
& - \Delta t \sum_{l=1}^{n-1} \sum_{\partial L_j \in \partial S^n} H_{Sij} \sum_{\partial L_k \in \partial S^n} F_{jk}^{n-l} \phi_{rk}^l \\
& \quad \text{for } i = 1, 2, \dots, J \quad (38)
\end{aligned}$$

where

$$H_{ij} = 2\pi\delta_{ij} + \int_{\partial L_j} dP_j r_j \frac{\partial G}{\partial n_j} (\bar{P}_i, P_j)$$

$$G_{ij} = \int_{\partial L_j} dP_j r_j G(\bar{P}_i, P_j)$$

$$H_{Sij} = H_{ij} + \delta_{iJ} \frac{(A^2 + B^2)^{3/2}}{-B}$$

$$\int_{-\infty}^B dz' \frac{z'}{(A^2 + z'^2)^{3/2}} A \frac{\partial G}{\partial n'} (\bar{P}_i, P')$$

$$\begin{aligned}
R_{ij} &= \int_{\partial L_k} dP_k D_R(\bar{P}_j, P_k) + \delta_{kJ} \frac{(A^2 + B^2)^{5/2}}{-B} \\
&\cdot \int_{-\infty}^B dz' \frac{z'}{(A^2 + z'^2)^{5/2}} D_R(\bar{P}_j, P')
\end{aligned}$$

$$F_{jk}^{n-l} = \int_{\partial S_k} dP_k D_F(\bar{P}_j, P_k(n-l)\Delta t) \\ + \delta_{kj} \frac{(A^2+B^2)^{5/2}}{-B} \\ \cdot \int_{-\infty}^B dz' \frac{z'}{(A^2+z'^2)^{5/2}} D_F(\bar{P}_j, P_k(n-l)\Delta t)$$

and  $\bar{P}_j$  denote the mid-point of  $\partial L_j$ . At  $t = t_n$ , (38) is solved for  $\phi_j^n$  on  $\partial B^n$ ,  $\phi_{nj}^n$  on  $\partial F^n$ , and  $\phi_{nj}^n$  on  $\partial S^n$ , given the boundary  $\partial L_j^n$ ,  $\phi_{nj}^n$  on  $\partial B^n$ ,  $\phi_j^n$  on  $\partial F^n$  and  $\phi_{rj}^l$ ,  $l = 1, 2, \dots, n-1$  on  $\partial S^n$ . The free-surface Lagrangian positions and potentials are then updated according to (21) and (22):

$$\frac{Dr_j}{Dt} = \langle \cos \alpha \rangle_j \phi_{sj} - \langle \sin \alpha \rangle_j \langle \phi_n \rangle_j \quad (39)$$

$$\frac{Dz_j}{Dt} = \langle \sin \alpha \rangle_j \phi_{sj} + \langle \cos \alpha \rangle_j \langle \phi_n \rangle_j \quad (40)$$

and

$$\frac{D\phi_j}{Dt} = -g \langle z \rangle_j + \frac{1}{2} [ \phi_{sj}^2 + \phi_{nj}^2 ] \quad (41)$$

where  $\langle \rangle$  denotes averaged values over two adjacent panels and the tangential velocity  $\phi_{sj}$  is calculated by centered-differences.

This completes the formulation of the problem. An important note here concerns the position of the last Lagrangian point  $(r, z)_*$  (say) at the matching boundary. A linear closure, in theory, matches  $(r, z)_*$  geometrically to  $(A, 0)$ . In practice, for a realistically limited boundary distance  $A$ ,  $(r, z)_* - (A, 0)$  is never zero or even negligible. Furthermore, the linear formulas (26), (30), (31) are strictly valid for  $z < 0$  only. Here, we simply extrapolate or interpolate for the elevation  $\hat{z}$  at  $r=A$  for a new Lagrangian point. For all the integrals in (34) or (38) involving the Rankine source  $G$  or its derivative,  $\hat{z}$  is used (all other points on  $\partial S$  being fixed) so that  $\partial S = \partial S^n$  is a function of time; but for the integrals containing  $D_R$  or  $D_F$ ,  $\hat{z} = 0$  is prescribed. Thus  $R_{jk}$  and  $F_{jk}^l$ ,  $l = 1, 2, \dots, N$  are independent of the specific flow, and can be calculated at the outset for a given matching surface discretization, and stored. This results in a substantial savings of computational effort for the convolution calculation, especially for very long simulations. For the present scheme to be valid, it is clear that the surface elevation or particle excursion near the matching boundary must be smaller than the order of the grid size there. Otherwise, the matching radius  $A$  must be increased.

### 3.3 NUMERICAL EXAMPLE

As an example, we consider the heaving of a floating truncated vertical circular cylinder of radius  $a$  and mean draft  $a/2$ . For simplicity, the length, time and mass units are chosen so that radius  $a$ , gravity  $g$  and density  $\rho$  equal unity. The radius of the matching boundary is fixed at  $A = 5$ . The last constant strength panel on  $\partial S$  is at  $z = -4$  ( $B=4$ ), and  $z \in [0, -B]$  is subdivided into 24 panels satisfying a nonuniform spacing with segment lengths varying smoothly from  $\Delta \simeq 0.1$  at  $z = 0$  to  $\Delta \simeq 0.4$  at  $z = -B$ . The initial positions of the Lagrangian points on the free surface are spaced evenly at  $\Delta = 0.1$  so that there are 40 panels on  $\partial F$ . The body surface is divided into 20 segments (12 on the bottom and 8 on the side) using a cosine spacing concentrating at the submerged corner. This is motivated by expected large gradients near the corner; the increase in area with radius in integrating for the force; and the need to compute tangential velocities for the pressure calculation. Our experience indicates that disparate grid sizes near an intersection of two boundaries results in poor accuracy and should be avoided.

The vertical velocity of the body is prescribed to be

$$V(t) = h_0 \omega \sin \omega t \quad (42)$$

with the body draft

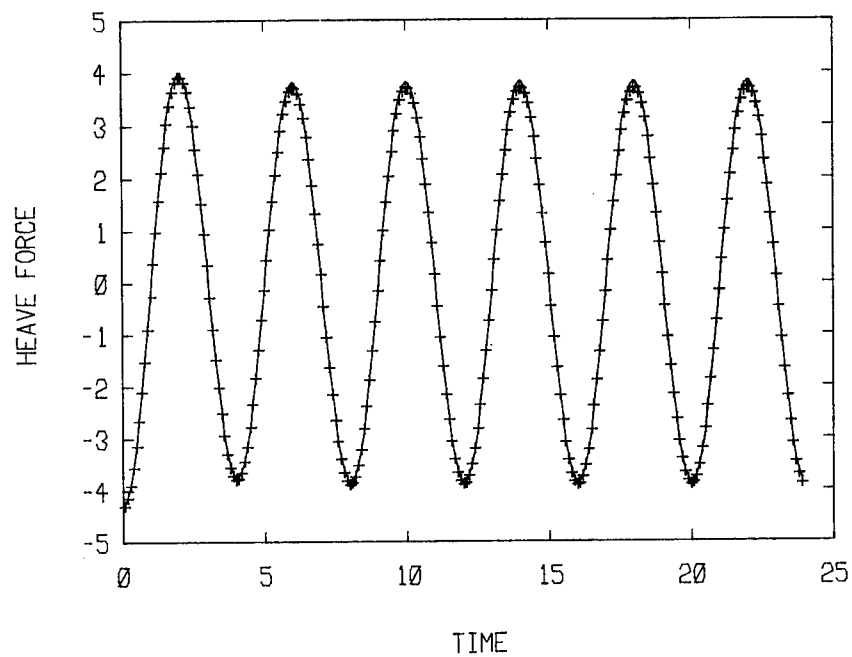
$$h(t) = -1/2 - h_0 \cos \omega t \quad (43)$$

so that  $h_0$  is the half stroke and the cylinder is initially submerged to a depth of  $1/2 + h_0$ .

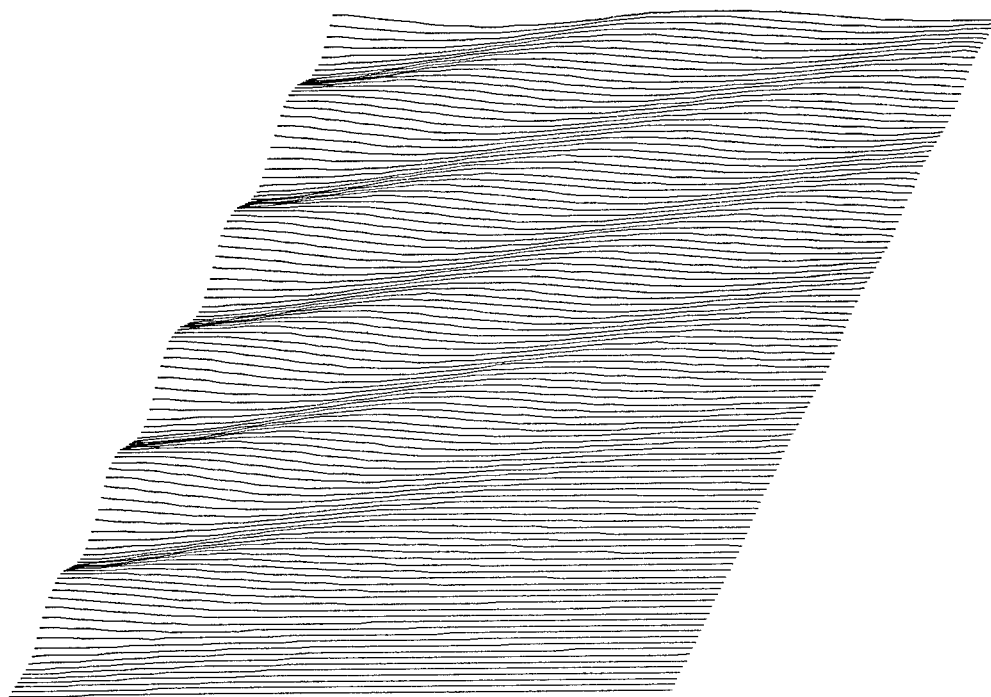
The algebraic system (38) is solved by a direct Gauss elimination scheme with partial pivoting, and the time integration of (39) - (41) is performed using a second-order Runge-Kutta formula. For the following calculations, we fix  $\omega = \pi/2$  (period = 4) and  $\Delta t = 0.1$ .

Figure 13 shows the vertical force on the cylinder (minus the hydrostatic restoring component and normalized by  $h_0$ ) for stroke amplitude  $h_0 = 0.05$ . The comparison is made with the linearized transient result of Newman (1984) which is computed by convolution of the impulse-response function derived from a distribution of ring free-surface singularities on the body surface. For this relatively small amplitude of motion, the nonlinear force follows closely that from the linear calculation. The discernible differences are at the peaks and troughs where the nonlinear values are slightly lower. As with two-dimensional cylinders (Faltinsen, 1977), steady-state for the heave force is reached rapidly for both the linear and nonlinear results. Here, six complete oscillation periods are shown to demonstrate the





**Figure 13:** Heave force history. --- linear transient theory; +++ nonlinear theory for amplitude  $h_0=0.05$ .



**Figure 14:** Nonlinear radial free-surface profiles for  $1 \leq r \leq 5$  and  $0 \leq t \leq 22.6$  at 0.2 intervals. Amplitude  $h_0=0.05$ .

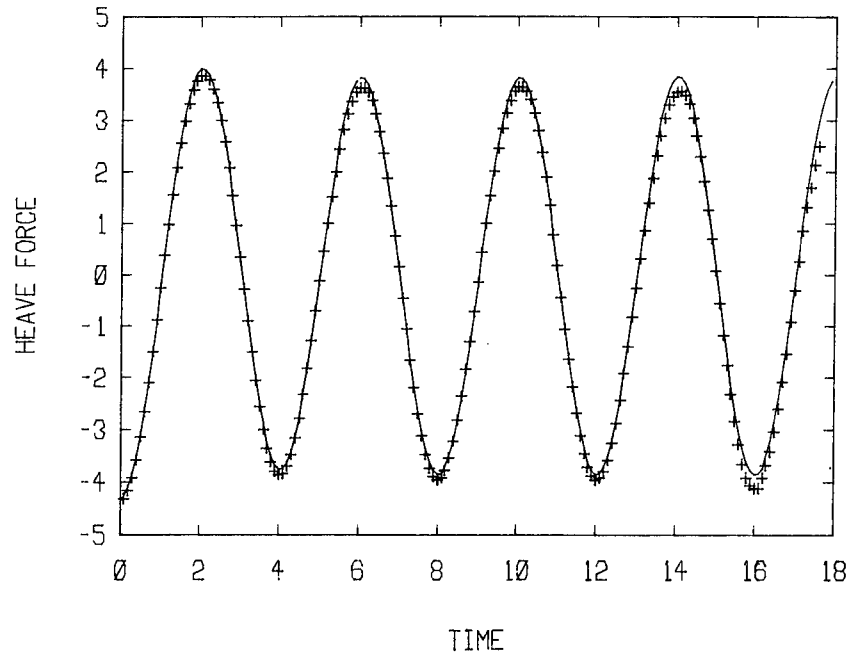


**Figure 15:** Heave force history. --- linear transient theory; +++ nonlinear theory for amplitude  $h_0=0.1$ .

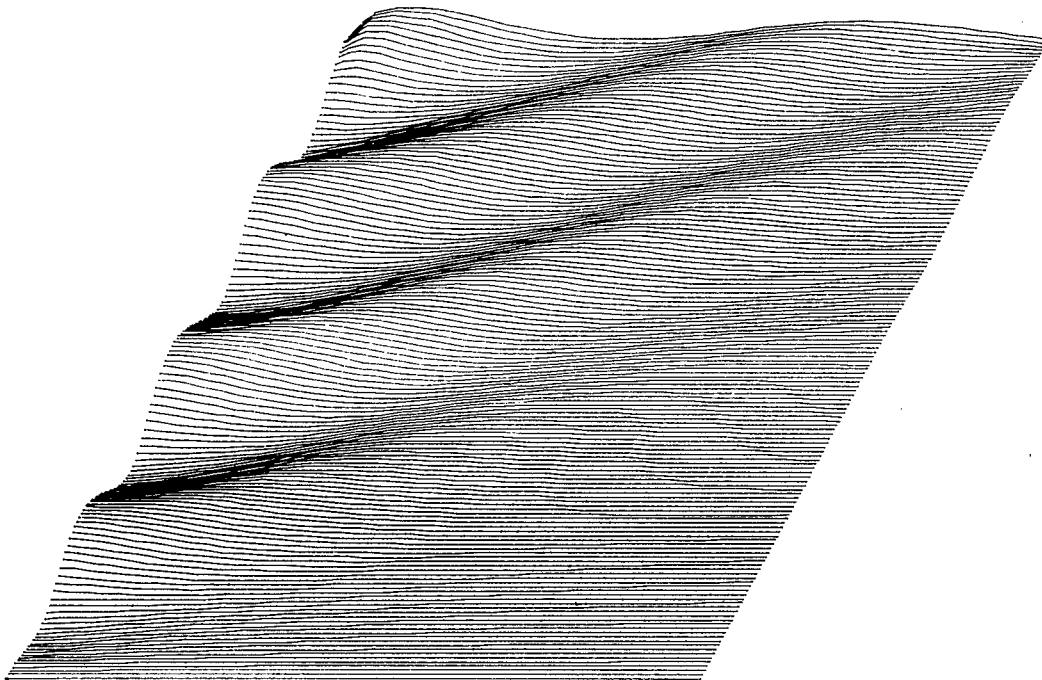


**Figure 16:** Nonlinear radial free-surface profiles for  $1 \leq r \leq 5$  and  $0 \leq t \leq 15.5$  at 0.1 intervals. Amplitude  $h_0=0.1$ .

effectiveness of the numerical closure treatment. A more direct evaluation can be obtained by examining the free surface. This is shown in Figure 14, where the radial free-surface profiles between the body and the matching boundary ( $1 \leq r \leq 5$ ) are plotted at every other time step ( $t = 0.2, 0.4, \dots$ ). (For clarity, each subsequent curve is shifted slightly up and to the right.) Notice that the outer boundary exhibits no sign of reflection or instability over the entire duration while several wavelets seem to have exited. An estimate based on Airy waves at the heave frequency gives a wavelength of about 2.6 and a group propagation distance of over 7.6 (in 6 periods), indicating that the present matching boundary at a distance of 4 from the body is quite efficacious. Figures 15 and 16 show similar results for a somewhat larger heave amplitude,  $h_0 = 0.1$ . In this case, the numerical scheme is stopped after about 4-1/2 periods when instability sets in at the boundary intersection. The force and the free-surface profiles, however, remain valid up to that time. The decrease in the force extrema from the linear theory is greater for the increased heave amplitude, although the differences are still very small. This relatively limited effect of nonlinearity is due largely to three-dimensionality and the wall-sided geometry. We have also obtained preliminary results for several larger heave amplitudes (up to half the draft of the cylinder): the mild decrease in the force continues, and a small but noticeable forward shift of the peaks is observed. For long simulations involving very large amplitudes, the radius  $A$  of the matching surface must be further increased. Other refinements (in discretization, and perhaps use of smoothing and a more careful treatment at the intersection boundaries) are being explored.

Although the results here are preliminary, it is evident that the present method is effective for the long time calculation of nonlinear body-wave interactions in three-dimensions. All the computations are performed on a DEC-VAX 11/780 computer and require approximately 1 minute of CPU for every time step. Larger scale calculations, convergence studies and a more quantitative assessment of the matching boundary using a supercomputer are planned.

#### 4. ACKNOWLEDGEMENTS

This work has been supported by the Office of Naval Research Special Focus Program in Ship Hydrodynamics (Contract N0014-82-K-0198), and by the National Science Foundation Engineering Science Division (Grant MEA-8210649). The authors are indebted to both agencies for their continual support.

#### REFERENCES

- Abramowitz, M. and Stegun, I. A. (1964): Handbook of Mathematical Functions. Dover Publications.
- Faltinsen, O. M. (1977): Numerical Solution of Transient Nonlinear Free-Surface Motion Outside or Inside Moving Bodies. Proceedings, Second International Conference on Numerical Ship Hydrodynamics, U. C. Berkeley.
- Greenhow, M., Vinje, T., Brevig, P. and Taylor J. (1982): A Theoretical and Experimental Study of the Capsize of Salter's Duck in Extreme Waves. J. Fluid Mech., 118, pp. 259-275.
- Greenhow, M. and Lin, W. M. (1983): Nonlinear Free Surface Effects: Experiments and Theory. M.I.T., Dept. of Ocean Engineering, Rept. No. 83-19.
- Isaacson, M. de St. Q. (1982): Nonlinear-wave Effects on Fixed and Floating Bodies. J. Fluid Mech., Vol. 120, pp. 267-281.
- Lin, W.-M. (1984): Nonlinear Motion of the Free Surface Near a Moving Body. Ph.D Thesis, M.I.T., Dept. of Ocean Engineering.
- Longuet-Higgins, M. S. and Cokelet, E. D. (1976): The Deformation of Steep Surface Waves on Water, I: A Numerical Method of Computation. Proc., R. Soc. Lond., Series A, 350, pp. 1-26.
- Newman, J. N. (1984): Transient Axisymmetric Motion of a Floating Cylinder. Unpublished.
- Peregrine, D. H. (1972): Flow Due to Vertical Plate Moving in a Channel. Unpublished.
- Vinje, T. and Brevig, P. (1980a): Breaking Waves on Finite Water Depth, a Numerical Study. SIS Report, Norwegian Hydrodynamic Laboratory, Trondheim.
- Vinje, T. and Brevig, P. (1980b): Nonlinear, Two-Dimensional Ship Motion. SIS Report, Norwegian Hydrodynamic Laboratory, Trondheim.
- Vinje, T. and Brevig, P. (1981): Nonlinear Ship Motion. Proceedings of the 3rd Int. Conf. on Numerical Ship Hydrodynamics, Paris.

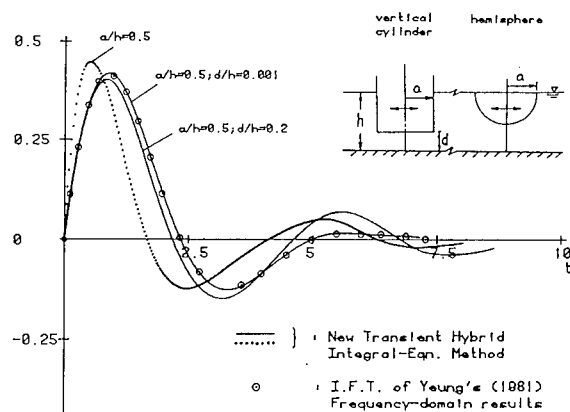
## DISCUSSION

Prof. RONALD W. YEUNG,  
Dept. of Naval Arch. & Offshore Engineering,  
University of California, Berkeley, CA, USA:

In this rather interesting paper, the authors stated two objectives in the Introduction. The first, concerning free-surface and body intersection irregularity, was tackled in a very "neat and clean" way. The second, which concerns matching a nonlinear interior solution with a linear one at a radiation boundary, however is not quite settled. In my opinion, the necessity of locating a matching boundary at sufficiently large distance from the origin so that the waves are small is really not meeting the matching problem "head on". The scheme proposed by the authors cannot work as soon as any "numerically detectable" nonlinear waves of elevation  $> 0$  arrive at the boundary  $\partial S$ . At that instant, the integrals for the time-dependent source functions (31) and (26) are not defined for  $z > 0$ . Thus  $\phi$  and  $(\phi_r)$  cannot be defined for  $z > 0$ , making it not possible to match with a genuine non-linear solution as the authors hope they would.

In the context of linear time-dependent type hybrid matching, I should cite here the results of my Ph.D. student Ming Y. Lee's thesis work. He solved the sway-motion problem of an arbitrary axis-symmetric shape in finite depth water. To verify that his programs indeed work for waves of an arbitrary frequency at any instant of time, he computed the sway-motion step response memory functions. The method permits the matching surface to locate at any arbitrary distance from the cylinder axis. The excellent agreement with the inverse Fourier transform of my AOR (Yeung '81) results in the frequency domain convinces us that all the wave components propagate out properly in our method. Also, I believe the term  $\int_{\partial S} \phi \cdot \mathbf{G} dP$  is missing in (34).

MEMORY-EFFECT FUNCTIONS FOR SWAYING OF  
SEVERAL AXI-SYMMETRICAL BODIES



Taken from: "Unsteady Fluid-Structure Interaction in Water of Finite Depth" by M.-Y. Lee, Ph.D. Thesis, Univ. Calif., Berkeley, 1984.

Prof. ERNEST O. TUCK,  
University of Adelaide, Australia:

Non-linear studies are often difficult to interpret because of numerical detail. I have two questions relating more to fundamental analytical properties.

1. Can the authors distinguish "body" and "free-surface" non-linearities, the former being what one would obtain by replacing the free-surface condition with the linearized one, and the latter by doing the same for the body condition?
2. Do the results settle down to a periodic wave of non-sinusoidal form? If so, is the final form dependent upon the time-history of the start-up? If there is a non-zero "D.C." (i.e. non-zero time average) in the asymptotic steady state as  $t \rightarrow \infty$ , what is the physical interpretation?

Prof. ALLEN T. CHWANG,  
The University of Iowa, Iowa City, USA:

You have presented in your paper numerical solutions for the impulsive motion of a two-dimensional vertical plate and for transient heaving motions of an axisymmetric cylinder. Do you have any numerical results for the impulsive motion of a vertical cylinder? We would be very interested in knowing this because we have obtained analytical solutions and conducted experiments on the impulsive motion of a vertical cylinder; and we would like to compare our solutions with your numerical results, if you have. Our analytic result indicates that the free-surface elevation and the vertical velocity are singular at the intersection of the free-surface and the surface of an impulsively starting vertical cylinder. However, our experimental result indicates otherwise and there is no jet at the cylindrical surface. Referring to your Fig. 15, we would like to know why the nonlinear heave force decreases as heave amplitude increases.

## AUTHORS' REPLY

Professor Yeung has questioned the matching scheme by which we close our three-dimensional solution, from the standpoint that any finite disturbance, however small, will be impossible to match with a linear far-field description. Our view is that the scheme which we have employed has a rational asymptotic basis, and that the numerical results which we have obtained conclusively demonstrate its validity. Any finite discretization of a continuous physical solution may be criticised as inexact, and subject to a variety of possible errors, but it is generally accepted when the numerical approximation has both a rational basis and a successful demonstration of its validity.

The linear time-dependent solution described by Professor Yeung is analogous to our linear study described in the reference by Newman (1984).

The only term missing in our equations is in equation (34), where

$$- \int_{\partial S} dz' AG\phi_p(A, z', t)$$

should be inserted on the left-hand side.

Professor Tuck asks if a distinction can be made between "body" and "free-surface" nonlinearities. This is possible in the formal sense, if and only if the body boundary condition is homogeneous at the free surface. Thus we could make such a decomposition for the heaving vertical cylinder, but not for the wavemaker. We have not performed computations along this line, and cannot speculate as to the relative importance of these two sources of nonlinearities. Regarding the second question, we have not varied the time-history of the start-up. However, the comparisons with linear theory in Figures 13 and 15 imply that the ultimate steady-state would not be sensitive to such a modification. There is an obvious "D.C." shift in the force shown in Figure 15 (a less-obvious shift can be discerned also in Figure 13), relative to the sinusoidal linear result. In both cases the mean shift is negative, and corresponds to the "suction" force associated with the quadratic term in Bernoulli's integral for the pressure. Since other nonlinear contributions are also present, this correspondence is comforting, but not strictly necessary.

In response to Professor Chwang, the present results for the circular cylinder are limited to the case of axisymmetric heave motions. For this mode of motion it is possible to study the impulsive-motion case, but the problem described by Professor Chwang appears to be that of horizontal surge motion. For the latter a more general three-dimensional solution is required, without the assumption of an axisymmetric fluid motion.

# SHIP MOTIONS IN SHALLOW WATER BY UNIFIED THEORY

R. BØRRESEN AND O.M. FALTINSEN

## ABSTRACT

A theoretical formulation of added mass and damping of a ship at forward speed in finite water depth is presented. The "Unified Theory" concept by Newman and Sclavounos has been generalized to finite water depth. Numerical difficulties in calculating the far-field kernel function and the interaction term  $m_3$  between steady forward and oscillatory motion are pointed out. It is difficult to conclude that "Unified Theory" gives better results than "Strip Theory" in finite water depth.

## 1. INTRODUCTION

We consider here as our task to study the motion of a ship in regular, i.e. periodic waves. Much attention has been devoted to this problem through the years. The most common way of analyzing the problem is to use some kind of strip theory. An example is the Salvesen, Tuck-Faltinsen method. The strip theory concept implies that possible wave interaction between sections is not taken care of. Strictly speaking we can only give strip theories some justification as long as the frequency of encounter between waves and the ship is high and as long as we consider the forced motion problem. Strip theories have also limited applicability at high Froude number.

Recently Newman (1978) and Sclavounos (1981) have come up with a "Unified Theory" where they take into account wave interactions between cross-sections along the ship. Newman and Sclavounos' Unified Theory represents an improved ship motion, slender body theory from a rational point of view. It is in principle valid for all frequencies. But there are still possibilities for improvements. One can ask whether they take proper account of the forward speed effect. For instance they use the rigid free surface condition for the steady wave potential near the ship. This has limited applicability for high Froude numbers.

Newman and Sclavounos' Unified Theory was derived for deep water. In the present paper we have generalized their concept to finite water depth. We are only considering forced heave and pitch motions. Numerical results are presented and compared with published numerical and experimental results.

The present article is based on Børresen (1984). The main results of that work is a theoretical formulation for the velocity potential in both the radiation and diffraction problems, that in the large depth limit is conform with the Unified Theory of Newman and Sclavounos. The hydrodynamic problem is solved in two steps. Firstly, section-wise solutions are found utilizing two-dimensional solutions. We suggest the method of Bai & Yeung (1974) to be applied for the heave and pitch motion case presented in this article. Ordinary strip-

theory solutions (e.g. Salvesen et. al. (1970)) can also be constructed with these two dimensional solutions as building bricks.

Both the two-dimensional radiation and diffraction problems can be split up into symmetric and odd problems with respect to the vessel transverse coordinates. By adding homogeneous solutions to the two-dimensional velocity potentials, an interaction between the two-dimensional solutions is obtained. The study of this interaction constitutes the second step in the solution. The formulation of this second step is obtained through a matching between far and near field problem formulations. It is shown in Børresen (1984) that to leading order, this sectionwise interaction exists only for the symmetric problems. This is conform with Newman's (1978) result in deep water.

In previous deep water high frequency slender body theories, sectionwise interactions were present in the diffraction problems, see e.g. Faltinsen (1971). This interaction effect shows up as a diminution of the incoming wave amplitude along the vessel length (not in oblique waves). In the Unified Theory, this interaction is also present, see a thorough discussion on this by Sclavounos (1981). In the diffraction problem investigated by Faltinsen (1971), the interaction accommodates for the fact that along the vessel path there are transverse wave systems which are left behind the vessel. This is also reflected in the Unified Theory in both the diffraction and radiation problems. These vessel generated waves represent radiated energy which is not accounted for in two dimensional solutions. The essence of the Unified Theory is to include this energy radiation through a sectionwise interference based on two dimensional solutions.

The novelty of Newman's (1978) Unified Theory formulation is that wave effects are included in this sectionwise interaction. In fact, Tuck (1964), developed a similar theory, but for calm water. It is shown in Børresen (1984) that for deep water, the zero frequency limit of the Unified Theory recovers Tuck's solution. We have not discussed the complementary zero frequency solution when finite depth effects are included.

R. Børresen, Norwegian Hydrodynamic Laboratories, Trondheim, Norway  
O.M. Faltinsen, Norwegian Institute of Technology, Trondheim, Norway

In the rest of this article we shall address the radiation problems in heave and pitch. The theoretical derivations are founded on the fundamental assumptions of neglecting viscous forces, that the boundary conditions are linearized, that the problem is harmonic in time and that potential theory can be applied.

## 2. THEORY

We consider a ship which moves in the negative x-direction relative an earth fixed coordinate system XYZ (fig. 1). The ship travels with a mean velocity U whilst performing harmonic oscillations in heave and pitch with frequency  $\omega$ . By assuming linearity we can study the heave and pitch motion problems separately.

We shall operate with a coordinate system xyz travelling with the vessels mean speed. The xy-plane describes the undisturbed mean free surface of the water. Within the realm of linear potential theory we are seeking the velocity potentials  $\text{Re}[\phi_j(x,y,z)\exp(i\omega t)]$ . Here  $j=3$  denotes heave and  $j=5$  denotes pitch. The potentials are governed by the three-dimensional Laplace equation

$$\nabla^2 \phi_j = 0 \quad (1)$$

Furthermore, the potentials have to satisfy the boundary condition on the free surface, expressed in its linearized form viz:

$$(i\omega + U\partial/\partial x)^2 \phi_j + g\partial\phi_j/\partial z = 0 \quad (2)$$

The conditions of no intrusion of water through the vessel hull and the ocean bottom have to be satisfied, and finally, to complete the problem formulation, a condition of outwardly radiating waves at infinity have to be specified.

The analytical reduction of the full problem to a strip theory formulation may involve the technique of "matched asymptotic expansions". The essence of this method is to separate the physical domain of the problem into two; the "far-" and "near"-fields. In each of the domains the Laplace equation is to be solved. It is known that boundary conditions have to be prescribed on all boundaries surrounding the fluid. In the overlap region separating the two physical domains, one will have common, but at the outset, unknown conditions.

In the overlap region, one strives at studying the asymptotic expansions of the far and near field problem formulations. By a careful study in the overlap region the asymptotic expansions are matched such as to result in a complete problem formulation in either of the domains.

Newman (1978) utilizes this technique in developing his Unified Theory. He arrives at his final formulation via a careful analysis of the error estimates in the overlap region. We shall deviate slightly from this procedure, but show in the end that we arrive at the same result as Newman did for infinite water depth.

### 2.1 THE FAR FIELD FORMULATION

In the far field the presence of the vessel is simplified by considering translating strings of sources, the length of the strings being equal to the vessel length. We assume that the source strength distribution is given by

$$q(x,t) = R_0 [q_j(x)\exp(i\omega t)] \quad (3)$$

For a single source located in  $(0,0,z_0)$ , oscillating in strength with frequency  $\omega$ , the velocity potential, or Green function  $G(x,y,z)$  is governed by the Poisson equation

$$\nabla^2 G(x,y,z) = 4\pi q(x)\delta(y)\delta(z-z_0) \quad (4)$$

where  $\delta(\ )$  is the Dirac delta function. The free surface and radiation conditions are jointly given by

$$(i\omega + U\partial/\partial x + \mu)^2 G + \partial G/\partial z = 0 \text{ on } z=0 \quad (5)$$

where  $\mu$  is the Rayleigh viscosity, a small positive quantity introduced to ensure a proper radiation condition.

On the flat horizontal bottom at  $z=-h$ , the boundary condition is

$$\partial G/\partial z = 0 \text{ on } z=-h \quad (6)$$

For details on this problem formulation we refer to Ogilvie and Tuck (1969). At present we assume that the Green function is available. The velocity potential of the travelling string of sources is then expressed as

$$\phi_j(x,y,z) = \int_{-\infty}^{\infty} q_j(\xi) G(x-\xi,y,z) d\xi \quad (7)$$

We shall need the Fourier transform which will be denoted with an asterix. The Fourier transform convention which we shall follow is given by

$$q^*(k) = \int_{-\infty}^{\infty} q(x) e^{-ikx} dx \quad (8)$$

$$q(x) = \frac{1}{2\pi} \int_{-\infty}^{\infty} q^*(k) e^{ikx} dk \quad (9)$$

By the convolution theorem we can now write (7) as

$$\phi_j = \int_{-\infty}^{\infty} q_j^*(k) G^*(k;y,z) e^{ikx} dk \quad (10)$$

Through the Fourier transform convention it will be seen that

$$G^*(0;y,z) = \int_{-\infty}^{\infty} G(x,y,z) dx \quad (11)$$

Due to the reciprocity property of the Green function, the integral in (11) is equivalent with the velocity potential in  $(0,y,z)$  due to a distribution of sources parallel with the x-axis and in the x-z plane. This is however equal to the two-dimensional Green function  $G_{2D}(y,z)$ . We separate out this two-dimensional property from the 3D Green function by writing

$$G^*(k; y, z) = f^*(k; y, z) + G_{2D}(y, z) \quad (12)$$

By representing the Dirac delta function as

$$\delta(x) = \frac{1}{2\pi} \int_{-\infty}^{\infty} e^{ikx} dx \quad (13)$$

it is readily verified that (10) can be written as

$$\phi_j = q(x) G_{2D}(y, z) + Q(x, y, z; q) \quad (14)$$

where the functional  $Q(x, y, z, q_j)$  is given by

$$Q(x, y, z; q) = \int_{-\infty}^{\infty} q_j(\xi) f(x - \xi, y, z) d\xi \quad (15)$$

The Fourier transform  $f^*$  of  $f$  in (15) is now defined by equation (12). For the case where the oscillating source string is located at the free surface, the Green functions  $G$  and  $G_{2D}$  together with the kernel function  $f(x, y, z)$  is given in appendix.

Equation (14) does now represent our far field velocity potential. We note here that we are ensured outwardly radiating waves through the boundary condition (5). In this far field formulation the source strength distribution  $q_j(x)$  is as yet unspecified. It will be found through a near field study.

## 2.2 THE NEAR FIELD FORMULATION

For a more thorough elaboration on the near field formulation we merely refer to Newman (1978). His discussion was for infinite water depth. We will generalize this to finite water depth. Following a slenderness assumption, sectionwise solutions along the vessel can be constructed by

$$\phi_j(s) = \bar{\phi}_j(y, z) - U \hat{\phi}_j(y, z) \quad (16)$$

This is not the complete near field solution as we shall see later on. The two-dimensional potentials  $\phi_j$  and  $\bar{\phi}_j$  satisfy the two-dimensional Laplace equation, the free surface condition

$$-\omega^2 \phi + \partial \phi / \partial z = 0 \quad (17)$$

the hull boundary conditions

$$\partial \phi_j / \partial N = i \omega n_j \quad (18)$$

$$\partial \phi_j / \partial N = m_j \quad (19)$$

and the bottom condition. Here  $N$  is the two dimensional unit normal to the hull.  $n_j$  are found from

$$(n_1, n_2, n_3) = \underline{n} \quad (20)$$

$$(n_4, n_5, n_6) = \underline{x}' \times \underline{n}$$

where  $\underline{n}$  is the unit normal to the three-dimensional hull in the direction into the fluid.  $\underline{x}'$  is the vector describing the hull itself.

Furthermore

$$m_3 = -n_2 \bar{\phi}_{yz} - n_3 \bar{\phi}_{yy} \quad (21)$$

$$m_5 = -x m_3 - n_3 \quad (22)$$

where  $\bar{\phi}$  is the steady potential, originating from steady translation of the vessel, i.e.  $\bar{\phi}$  satisfies  $\partial \bar{\phi} / \partial n = n_1$  on the body hull and the bottom condition. The functions  $m_j$  are due to a result by Ogilvie and Tuck (1969).

For large  $|y|$  the potentials  $\phi_j$  and  $\hat{\phi}_j$  can be represented by

$$\phi_j \sim \sigma_j G_{2D}(y, z) \quad (23)$$

$$\hat{\phi}_j \sim \bar{\sigma}_j G_{2D}(y, z) \quad (24)$$

where  $G_{2D}$  is the two-dimensional Green function due to a harmonically oscillating source located in (0,0). The solutions (23) and (24) represent for large  $|y|$ , periodic waves, radiating towards infinity.

Newman (1978) points out that the two-dimensional potentials of (16) are unique and do only depend on the local cross-sectional geometry of the vessel. However, we can construct other sectionwise solutions by adding to the potentials (16) solutions which satisfy the homogeneous boundary condition  $\partial \phi_j / \partial N = 0$  on the hull surface. As discussed by Newman, such homogeneous solutions can in view of the boundary condition (4.14) simply be taken to be  $\phi_j + \bar{\phi}_j$ , where the overbar denotes complex conjugation. Thus we can construct a new set of stripwise solutions by

$$\tilde{\phi} = \phi_j^{(s)} + C_j(x) (\phi_j + \bar{\phi}_j) \quad (25)$$

In view of (23) and (24), the large  $|y|$  approximation of (25) can be written as

$$\tilde{\phi}_j \sim \{ \sigma_j - U \bar{\sigma}_j + C_j (\sigma_j + \bar{\sigma}_j) \} G_{2D} - C_j \bar{\sigma} (G_{2D} - \bar{G}_{2D}) \quad (26)$$

The real part of  $G_{2D}$  is singular for  $(y, z) \rightarrow (0, 0)$ , whilst the imaginary part is regular for all  $y, z$ . It is shown in Børresen (1984) that

$$G_{2D} - \bar{G}_{2D} = 2A \cos l_0 y \quad (27)$$

where  $A$  is given in Appendix A.

## 2.3 UNIFICATION

We have now formulated the potential theoretical problem in two domains. The inner source strength distributions  $\sigma_j$  can in principle be found, we shall later revert to that. However the interaction functions  $C_j(x)$  are as yet unknown. A unification procedure similar to Newman (1978) will be constructed, whereby the far and near field formulations are joined to result in a formulation for  $C_j$ .

Since the general far field formulation (14) and the large  $|y|$  approximation (26) of the



near field formulation both contain the two-dimensional Green function we equate the factors of  $G_{2D}$  in these formulations and have

$$q_j = \sigma_j - U \hat{\sigma}_j + C_j (\sigma_j + \bar{\sigma}_j) \quad (28)$$

In order to complete the unification, the remaining terms should also be equated. However, before doing this, we assume the legitimacy of expanding the regular functional  $Q(x, y, z; q_j)$  in a Taylor series:

$$Q(x, y, z; q_j) = Q(x, 0, 0; q_j) + Q_z(x, 0, 0; q_j)z + \dots \quad (29)$$

where the  $y$ -derivative of  $Q$  is zero due to symmetry. Now we equate the remaining terms of (14) and (26), using this series expansion. If this equating procedure is done for  $z=0$  we have

$$C_j \bar{\sigma}_{2A}|_{z=0} = -Q(x, 0, 0; q_j) \quad (30)$$

(29) and (30) does now give an integral equation for the outer source strength is:

$$q_j + \frac{1}{2A}|_{z=0} (\sigma_j / \bar{\sigma}_j + 1) Q(x, 0, 0; q_j) = \sigma_j - U \hat{\sigma}_j \quad (31)$$

The interaction functions  $C_j$  can then be found from (30).

It is shown in Børresen (1984) that for large depths, the integral equation (31) reduces to that of Newman and Sclavounos (1980).

### 3. THE SINGLE SOURCE PROBLEM

In the course of this work, we found it appealing to study the velocity potential due to the travelling source of oscillating strength. A far field formulation was developed to study this velocity potential. The method of analysis is similar to what Newman (1959) did for infinite water depth. We shall omit the mathematical details in this article, and merely describe the main results verbally.

In a mathematical environment, the results for the large  $R = (x^2 + y^2)^{1/2}$  approximation for  $G$  are given in terms of curves of stationary phase. Such curves have been presented earlier in the case of deep water, see e.g. Eggers (1957). The zero frequency limit of these curves are often denoted the Kelvin wave pattern. It is known that in deep water, the dimensionless parameter  $\tau = \omega U / g$  is a critical parameter for qualitative appearance of the curves of stationary phase, which in fact represent the picture of the wave pattern due to the source. For  $\tau > 0.25$ , the curves of stationary phase of the velocity potential appear as shown in fig. 2, where we have indicated the direction of travel of the individual wave systems. For  $\tau < 0.25$ , the curves of stationary phase appears as shown in fig. 3.

When the effect of finite depth is included, a similar situation appears. However, here also the non dimensional parameter  $U/U_0$  influences the result, where  $U_0 = \sqrt{gh}$  is the critical velocity. The transition from the wave

pattern depicted in fig. 4, to the wave pattern shown in fig. 5, is associated with the change in the ratio between the speed of the source and the maximum velocity of the energy flux of radiated waves. The latter is associated with the frequency  $\omega$  through the dispersion relationship and the group velocity (see Newman (1977)). Thus, the effect of finite depth on the wave pattern will be involved via the dispersion relationship. In Børresen (1984) is shown several examples on the wave pattern depending on  $\tau$  and  $U/U_0$ . The large  $R$  approximation of  $G$  has been used to evaluate  $G$  on the  $x$ -axis. This was done in order to compare with the numerical evaluation of the kernel function  $f(x, 0, 0)$  in equation (15). It can be seen through the relationship (12), that  $f(x, 0, 0)$  represents the velocity potential on the  $x$ -axis except at the singular point  $x=0$ . Thus, the regular part of  $f(x, 0, 0)$  should compare with the large  $R$ -approximation of  $G$  for large  $x$ . It is shown in Børresen (1984) that the two methods of studying the potential on the  $x$ -axis compares favourably for moderate depths.

In figures 6 and 7 are shown two examples of the regular part of the kernel function  $f(x, 0, 0)$ , computed according to the mathematical description given by equation (A.8). Figure 6 shows  $f(x, 0, 0)$  for a combination of  $\tau$  and  $U/U_0$  revealing a wave pattern qualitatively comparable to fig. 4, whilst figure 7 represents the potential on the  $x$ -axis in a situation similar to fig. 5.

### 4. TWO-DIMENSIONAL NEAR FIELD CALCULATIONS

A necessary part of the numerical solution is to solve the two-dimensional added mass and damping problem for finite water depth. There exists different numerical techniques for solving this problem (see for instance Keil (1974), Bai & Yeung (1974)). We have chosen a procedure which is very similar to Yeung's approach. This means we start out with Green's second identity and represent the velocity potential in a point  $(y_1, z_1)$  in the fluid domain as

$$2\pi\phi(y_1, z_1) = \int_S \left[ \frac{\partial\phi}{\partial n} (\log r + \log r_1) - \phi \frac{\partial}{\partial n} (\log r + \log r_1) \right] ds(x, y) \quad (32)$$

where  $S = S_B + S_F + S_\infty + S_-$

Here  $S_B$  is the body surface,  $S_\infty$  and  $S_-$  are vertical control surfaces at  $y = -\infty$ , respectively and  $S_F$  is the mean free surface inside  $S_\infty$  and  $S_-$ . Further

$$r = ((y_1 - y)^2 + (z_1 - z)^2)^{1/2} \quad (33)$$

$$r_1 = ((y_1 - y)^2 + (2h + z_1 + z)^2)^{1/2} \quad (34)$$

Here  $(x, y)$  are points on the integrating surface.

We will study only forced harmonic steady-state heave oscillations and assume the submerged body to be symmetric about the  $z$ -axis. We can then write the velocity potential at  $S_\infty$  as

$$\phi \sim \frac{g\zeta}{\omega} \frac{\cosh k(z+h)}{\cosh kh} e^{i(\omega t - k|y| + \alpha)} \quad (35)$$

where the wave amplitude  $\zeta$  and the phase angle  $\alpha$  are a priori unknowns. By substituting equation (35) into equation (32) we can evaluate the integrals over  $S_\infty$  and  $S_{-\infty}$ . In addition we can use the body boundary condition to rewrite  $\partial\phi/\partial n$  on  $S_B$  in equation (32). Further  $\partial\phi/\partial n$  on  $S_F$  can be rewritten in terms of  $\phi$  by means of the free surface condition.

The problem is now to find  $\phi$  on the free surface and the body surface as well as the wave amplitude  $\zeta$  and the phase angle  $\alpha$  of the generated waves at infinity. This is done by letting  $(y_1, z_1)$  approach points on  $S_B$  and  $S_F$  in equation (32). We then obtain an integral equation for determining  $\phi$  on  $S_B$  and  $S_F$ . By using this integral equation in combination with equation (35) we have sufficient conditions to determine the unknowns.

The numerical procedure we followed is as follows. We used that the flow is symmetric about the  $z$ -axis and divided the body surface for  $y>0$  into  $N_B$  straight line elements. The mean free surface  $S_F$  for  $y>0$  is divided into  $N_F$  straight line elements. We assumed  $\phi$  are constants over each element and satisfied the integral equation at the midpoints of each element. In the numerical evaluation of the integrals over  $S_\infty$  and  $S_{-\infty}$  we used  $N_\infty$  elements. A satisfactory number of algebraic equations are achieved by satisfying the integral equation at the  $N_B$  body elements, the  $N_F$  free surface elements and setting up equation (35) between  $\phi$ ,  $\zeta \cos\alpha$  and  $\zeta \sin\alpha$  on the element furthest away from the body. The resulting linear algebraic equation system can be solved by standard methods.

In addition to find the velocity potential  $\phi$  it is necessary to find the source density  $\sigma$  of a two-dimensional source representing the body in the farfield. We can write

$$\phi \sim \sigma G_{2D} e^{i\omega t} \quad (36)$$

where

$$G_{2D} = -4 \int_0^\infty \frac{dl \cos ly \cosh l(z+h)}{\cosh lh (1 - \tanh lh - \frac{1}{g}(\omega - i\mu)^2)} \quad (37)$$

By an asymptotic expansion of (36) and (37) we find a form of the velocity potential which resembles (35). This enables us to determine  $\sigma$ . We can write

$$\sigma = \frac{g\zeta}{4\pi\omega} e^{i(\alpha - \frac{\pi}{2})} \left( \tanh kh + \frac{kh}{\cosh^2 kh} \right) \quad (38)$$

The numerical procedure has been tested out by Zhao (1984). He found satisfactory agreement with the results by Bai & Yeung (1974) and Keil (1974) for the added mass and damping coefficient. Zhao also found that in the normal case one could use 4-8 elements on  $S_B$ , 20-30 elements on  $S_F$ , 30 elements on  $S_\infty$  and that the  $y$ -coordinate of the vertical control surface  $S_\infty$  could be set equal to 3-5 times the breadth of the body.

Another necessary part of the 3-D numerical solution is to find the two-dimensional steady potential  $\phi$  in the near-field. We have to know that to evaluate  $m_3$ . This means that we have to find the solution to the boundary value problem

$$\begin{aligned} \frac{\partial^2 \bar{\phi}}{\partial y^2} + \frac{\partial^2 \bar{\phi}}{\partial z^2} &= 0 \\ \frac{\partial \bar{\phi}}{\partial z} &= 0 \text{ as } z=0 \text{ and } -h \end{aligned} \quad (39)$$

$\frac{\partial \bar{\phi}}{\partial n} = n_1$  on  $S_B$   
This is done by writing

$$2\pi\bar{\phi}(y_1, z_1) = \int_{S_B} \left( \frac{\partial \bar{\phi}}{\partial n} \bar{\psi} - \bar{\phi} \frac{\partial \bar{\psi}}{\partial n} \right) ds \quad (40)$$

Here

$$\begin{aligned} \bar{\psi} &= \sum_{n=-\infty}^{n=+\infty} (\log \sqrt{(y_1 - y)^2 + (z_1 - z - 2nh)^2} \\ &\quad + \log \sqrt{(y_1 - y)^2 + (z_1 + z - 2nh)^2}) \end{aligned} \quad (41)$$

The numerical solution technique is similar as for the two-dimensional added mass and damping problem. The quantity we want to calculate is

$$m_3 = - \frac{\partial}{\partial n} \frac{\partial \bar{\phi}}{\partial z} \quad (42)$$

This is done by first evaluating  $\frac{\partial \bar{\phi}}{\partial z}$  by using that

$$\frac{\partial \bar{\phi}}{\partial z_1} = \frac{1}{2\pi} \int_{S_B} \left( n_1 \frac{\partial \bar{\psi}}{\partial z_1} - \bar{\phi} \frac{\partial}{\partial z_1} \frac{\partial \bar{\psi}}{\partial n} \right) ds \quad (43)$$

In order to calculate  $m_3$  we evaluate  $\frac{\partial \bar{\phi}}{\partial z_1}$  in two different points along the two-dimensional normal

$$\frac{\partial}{\partial n} \frac{\partial \bar{\phi}}{\partial z_1} \approx \frac{\left( \frac{\partial \bar{\phi}}{\partial z_1} \right)_2 - \left( \frac{\partial \bar{\phi}}{\partial z_1} \right)_1}{n_2 - n_1} \quad (44)$$

In order to control our calculations of  $m_3$  we have compared with the analytical solution for a circular cylinder in infinite fluid. The  $n_1$ -value was constant in this case. Further we have compared with the local solution close to the keel of a rectangular cross-section at very shallow water depth. In the case of constant  $n_1$  this local solution is like a corner flow. It is then possible to show that

$$m_3 = \frac{n_1}{h-D} \quad (45)$$

where  $D$  is the draft of the section. In addition we have compared with the fact that for any water depth and for any symmetric two-dimensional body shape with vertical sides at the water line it is possible to write

$$\int_{S_B} m_3 ds = 2n_1 \quad (46)$$

Here  $n_1$  is evaluated at  $z=0, y=B/2$ . Further  $B$  is the beam of the cross-section. The integration is over the mean wetted body surface.

Zhao (1984) has found that the numerical results for  $m_3$  is very sensitive to how many elements is used, but not very sensitive to how many images are used (see equation (41)) and how large  $n_2 - n_1$  (see equation (44)) is. Zhao found that choosing one of the points used in the calculation of  $m_3$  to coincide with the midpoints did not give satisfactory results. Instead he found it necessary to keep the

points a certain distance from the elements. As an example this distance could be chosen to be 3% of the draft plus 25% of the element length. In practise it seems necessary to use at least 50 elements on half of the cross-sectional surface. This is approximately five times as many elements to calculate  $m_3$  as to calculate the two-dimensional added mass and damping coefficients. The reason why we need more elements to calculate  $m_3$  is that  $m_3$  involves calculating a second derivative of a potential which require higher accuracy than calculating the potential itself. The reason why it is dangerous to keep the control points too close to the elements must be associated with that  $\phi$  is assumed to be a constant along the element. This means that the second derivative of  $\phi$  along the element is zero. Strictly speaking Laplace equation then implies that the second derivative with respect to  $n$  is zero. This leads us into inconsistencies and indicate difficulties in calculating second derivatives. We feel as our numerical results show, that the difficulties in calculating the second derivative is more pronounced locally and that the numerical error dies out when we come a certain distance from the elements. This discussion indicates that we had been better off by assuming higher order elements for instance represented by a second order polynomial and by assuming  $\phi$  to vary like a second order polynomial over each element.

The fact that at least 50 elements seem to be necessary on  $S_B$  in the two-dimensional calculations of  $m_3$  has certain consequences for complete three-dimensional calculations of  $m_3$ . It indicates that approximately 2000 elements is necessary on the ship surface in a three-dimensional calculation of  $m_3$ . This is certainly far beyond what is necessary in a three-dimensional calculations of added mass and damping at zero forward speed.

At the moment we feel that our calculations of  $m_3$  is not completely satisfactory. Our results show that even if we use 50 elements we may in some special cases be 50% wrong in our estimates of  $m_3$ . This indicates that the calculation procedure for  $m_3$  require further studies.

##### 5. THREE-DIMENSIONAL ADDED MASS AND DAMPING COEFFICIENT

In order to find the added mass and damping coefficients for the total ship we can use relationships derived by Ogilvie and Tuck (1969). This means

$$A_{ij} = \text{Re} \left[ \frac{\rho}{\omega^2} \iint_{S_B} (i\omega \phi_j n_i - U m_i \phi_j) ds \right]$$

$$B_{ij} = \text{Im} \left[ \frac{\rho}{(-\omega)} \iint_{S_B} (i\omega \phi_j n_i - U m_i \phi_j) ds \right] \quad (47)$$

If we want to evaluate added mass and damping coefficients on parts of the ships we cannot directly use equation (47). We have to add some terms. Let us say we want to evaluate force on a strip of the ship between a cross-section at  $x=x_n$  and  $x=x_{n+1}$ , we will find that the additional terms are

$$\text{Re} \left[ \frac{\rho}{\omega^2} t_{ij} \right] \quad \text{and} \quad \text{Im} \left[ \frac{\rho}{-\omega} t_{ij} \right]$$

where

$$t_{ij} = U \left[ \phi_j n_i dl \right]_{x=x_n}^{x=x_{n+1}}$$

##### 6. NUMERICAL RESULTS.

We have analyzed numerically the added mass and damping coefficients in heave and pitch for a Series 60 ship with  $C_b = 0.7$ . This is the same ship that Gerritsma and Beukelman (1982) presented experimental results for. For infinite water depth we have compared our numerical results with Newman and Sclavounos (1980) results for zero forward speed and  $Fn=0.2$ . The agreement between our results and Newman and Sclavounos results for zero forward speed is satisfactory. This applies both for the Unified theory and the strip theory. The results of the comparison for  $Fn=0.2$  are somewhat mixed. This is probably connected with the calculation of the  $m_3$ -factor. The  $m_3$ -factor (see equation (42)) is associated with forward speed effects and does not influence the results for zero forward speed. Newman and Sclavounos state that the strip theory approach represent a significant overprediction of  $m_3$  at the ship ends. They avoid this problem by assuming a linear variation of  $m_3$  within 5% of the ship length away from each end and assuming  $m_3=0$  at the ends. We should note when discussing this that it is at the ship ends that  $m_3$  is important. The way we do our calculation is to use the  $m_3$ -values according to our two-dimensional calculation procedure. This is consistent with the theoretical formulation, but may not represent a more correct physical way to represent the flow than Newman and Sclavounos did. Our  $m_3$ -values are calculated at half stations, i.e. we calculate them at st 0.5, st 1.5 ..... , st 19.5. The offsetpoints at the half stations are obtained by a linear interpolation between offsetpoints at two consecutive stations with integer number. The latter information is also used to calculate the  $n_i$  - component of the surface normal vector at the half station. In the calculation of  $m_3$  we have used 56 body elements on one half cross-section. The corresponding number we used in the calculation of two-dimensional added mass and damping was 14.

The results for the added mass and damping coefficients in heave and pitch are presented in Fig. 8. The agreement for the two different computations of the Salvesen Tuck-Faltinsen method is satisfactory. Further if we use  $m_3=0$  in an Unified theory calculation the agreement is generally satisfactory with Newman and Sclavounos' results from Newman and Sclavounos (1980) results. If we examine the force distribution along the ship we find that the difference between our results for  $m_3=0$  and  $m_3 \neq 0$  are most pronounced at the ship ends. By comparing with experimental results it seems like our results for  $m_3 \neq 0$  give worse results than the Unified Theory for  $m_3=0$  and the STF method. The difference between the two latter approaches is generally not significant.

We have also compared with Gerritsma and Beukelman's numerical and experimental results for finite water depth. First we combined the Salvesen - Tuck - Faltinsen method with two-dimensional added mass and damping coefficients on finite water depth. The numerical procedure outlined earlier in the text was used. Our calculated results by STF method was found to be consistent with Gerritsma and Beukelman's results. It is somewhat surprising to see how good strip theory agrees with the experimental results. There occur disagreements, in particular for the lowest tested frequency. We have tried to use unified theory in these cases in order to see if better agreement can be obtained between theory and experiments. Our experience from deep water at forward speed should not indicate this.

In the calculation by the "Unified Theory" the evaluation of the far-field kernel function  $f(x)$  is an essential part. It is shown in Appendix A that  $f(x)$  can be divided into the sum of the infinite water depth kernel function and a correction factor  $g(x)$  for finite water depth (see equation (A.8)). The calculation of the double integral  $p(x)$  in the  $g(x)$ -function is quite troublesome. The  $p(x)$ -function is defined as

$$p(x) = -\frac{1}{\pi} \int_0^\infty du \int_0^\infty d\lambda \left( \frac{\lambda}{\lambda \tanh h - K} - \frac{\lambda}{\lambda - K} \right) e^{ix\lambda \cos u} \quad (48)$$

where

$$K = (\omega + U\lambda \cos u - i\mu)^2 / g \quad (49)$$

The first part of the integral associated with the  $\lambda/(\tanh h - K)$ -term will be referred to as the finite depth part of the integral. The last part of the integral will be called the infinite depth part. Depending on the angle  $u$  there will exist singularities along the real  $\lambda$ -axis. These singularities  $\lambda_i$  are defined by

$$\lambda_i \tanh \lambda_i h - K = 0, \quad i = 1, 2 \quad (50)$$

$$\lambda_i - K = 0, \quad i = 3, 4 \quad (51)$$

If  $\tau > 1/4$ , the  $\lambda_3$  and  $\lambda_4$ -values exist when  $2\pi - u_0 > u > u_0 = \arccos(\frac{1}{4\tau})$ . If  $\tau < 1/4$ ,  $u_0 = 0$ . The  $\lambda_1$  and  $\lambda_2$  values exist for  $2\pi - u_{OF} > u > u_{OF} \geq u_0$ . The  $u_{OF}$ -value has to be found numerically for each water depth, frequency and ship speed. As long as there exist singularities along the real  $\lambda$ -axis, we use residue calculations to find the value of the  $\lambda$ -integral. This means that for  $u_0 < u < u_{OF}$  and  $2\pi - u_{OF} > u > 2\pi - u_0$  we use the residue theory only with the part of the integral which is associated with the deep water solution. By means of the Rayleigh viscosity we find out how to go around the singularities. If

$\lambda \cos u > 0$  we introduce a ray  $C_R$  along the angle  $\pi/4$  in the complex plane. If  $\lambda \cos u < 0$ , the ray  $C_R$  is selected along the angle  $-\pi/4$  in the complex  $\lambda$ -plane. By means of the residue theorem we rewrite the  $\lambda$ -integral as the sum of an integral along the ray  $C_R$  and possible residue contributions from the singularities along the real  $\lambda$ -axis. By doing this we have outruled any other singularities between  $C_R$  and the positive real  $\lambda$ -axis. In the deep water case it is easy to see that this is true by means of the analytic solution for  $\lambda_1$ . In the finite water depth case we have not proved this to be true. But numerical search processes indicate that there does not exist any singularities between  $C_R$  and the positive real  $\lambda$ -axis as long as real-valued singularities exist. Generally speaking one of the solutions of (50), let us say  $\lambda_2$  and one of the solutions of (51), let us say  $\lambda_4$  will have a very high value. But it is easy to see from (48) that the residue contributions from  $\lambda_2$  and  $\lambda_4$  will approximately cancel if  $\lambda_2 h$  is larger than some specific value  $B$ . In our calculations we set  $B=7$ .

The consequence of this cancellation is that we do not have any numerical problems associated with highly oscillatory integrals. When there do not exist real singularities we perform a direct numerical integration of the  $\lambda$ -integral.

We have to be careful in the  $u$ -integration when  $u$  is close to  $u_0$ ,  $u_{OF}$ ,  $2\pi - u_0$ ,  $2\pi - u_{OF}$ . It is the finite depth part of the integral which cause difficulties around  $u = u_{OF}$  and  $u = 2\pi - u_{OF}$ . The infinite depth part cause difficulties around  $u = u_0$  and  $u = 2\pi - u_0$ . To exemplify this let us discuss the finite depth part of the integral around  $u = u_{OF}$ . For  $u = u_{OF} + \epsilon$  where  $\epsilon$  is a small positive quantity, it is possible to show that the singularities  $\lambda_i$ ,  $i=1,2$  can be written as

$$\lambda_i \sim \lambda_0 \pm iA \sqrt{\epsilon}$$

where  $A$  can be analytically determined and  $\lambda_0$  is the double pole at  $u = u_{OF}$ . It is further possible to show that the residue part of the  $\lambda$ -integral of the finite depth part has a square root singularity in the angle  $u - u_{OF}$  near  $u = u_{OF}$ . When  $u = u_{OF} - \epsilon$ , the singularities of the finite depth of the integral will be close to the real axis at

$$\lambda_i \sim \lambda_0 \pm iA \sqrt{\epsilon}$$

We can again show that there is a square root singularity of the finite depth part of the integral close to  $u = u_{OF}$ . The behaviour of the finite depth part around  $u = 2\pi - u_{OF}$  is similar as around  $u = u_{OF}$ . A similar discussion can be done for the infinite depth part of the integral around  $u = u_0$  and  $2\pi - u_0$ .

The numerical problems with the square root singularity in the finite depth part of the integrals around  $u=u_{OF}$  is taken care of by introducing a new local integration variable  $v$  defined by

$$v^2 = u - u_{OF}$$

In the  $v$ -integration there are no singularities. Similarly were done around the other critical  $u$ -values.

The far-field kernel function  $f(x)$  is used in the integral equation given by (31) and (15). The functional  $C(x)$  in (31) can be written as

$$Q(x) = \int_{-\infty}^{\infty} q(\xi) (f_d(x-\xi) + g(x-\xi)) d\xi \quad (52)$$

where  $f_d(x)$  is the deep water kernel (see equation (A8)). In view of the  $1/x$  singular term in  $f_d(x)$  we apply partial integration to (52) such that  $Q$  can be written as

$$Q(x) = \int_{-\infty}^{\infty} q'(\xi) F_d(x-\xi) d\xi + \int_{-\infty}^{\infty} q(\xi) g(x-\xi) d\xi$$

where

$$f_d(x) = \frac{dF_d}{dx}$$

The singularity in  $F_d$  is logarithmic such that the integration in (19) can be performed with ease (see Newman and Sclavounos (1980)). The numerical solution of the integral equation is done by formulating a linear equation system in unknown discrete values of  $q$  along the ship. The equation system is solved by standard matrix inversion.

We have used our "Unified Theory" approach in finite water depth to compare with the experimental results by Gerritsma and Beukelman (1982). Since it is for the lower frequencies that "Unified Theory" differs most from "Strip Theory", we have concentrated on comparisons with the experimental results for the lowest circular frequency  $\omega = 4$  rad/s. Gerritsma and Beukelman indicate that there may be wall effects present in their experimental results for  $F = 0.1$  and low frequencies. We have therefore decided on presenting comparisons for  $F = 0.2$ . The results of the comparisons for the total added mass and damping coefficients in heave and pitch are presented in Fig. 9. We note a noticeable difference in the results by "Unified Theory" and "Strip Theory". With "Strip Theory" we mean the strip theory by Salvesen - Tuck - Faltinsen with two-dimensional added mass and damping coefficients for finite water depth. When we have used the Unified Theory approach we have generally set  $m_3 = 0$ . In the case of  $h/T = 1.5$ , where  $h$  is water depth and  $T$  is ship draught, we have also used  $m_3 \neq 0$ . The difference does not seem

so large as we saw for infinite water depth between the results with  $m_3 = 0$  and  $m_3 \neq 0$ . Relative to experimental results  $A_{33}$ ,  $B_{55}$  and  $A_{35}$  from "Unified Theory" compares better than the "Strip Theory" results. The "Strip Theory" gives best results for  $B_{33}$  and  $B_{35}$ . For the other coefficients there is no clear answer on what theory is in best agreement with experimental results.

## CONCLUSIONS

A theoretical formulation of added mass and damping of a ship at forward speed in finite water depth is presented. The "Unified Theory" concept by Newman and Sclavounos has been generalized to finite water depth. The far-fields solution has been tested with satisfactory results by comparing with asymptotic expressions for single sources. It is pointed out numerical difficulties in calculating the interaction term  $m_3$  between steady forward speed and oscillatory motion. The calculation of the far-field kernel function in finite water depth is complicated. It is difficult to conclude that "Unified Theory" gives better results than "Strip Theory" in finite water depth.

## ACKNOWLEDGEMENT

The authors acknowledge the discussions with Dr. P. Sclavounos on the formulation of the far field solution in finite water depth. The numerical calculation of the added mass and damping coefficients have been performed by Rang Zhao.

## LIST OF REFERENCES.

- Bai, K.J. and Yeung, R.W.: (June 1974), "Numerical Solutions to Free Surface Flow Problems". Proc. Symp. Nav. Hydrodyn. 10th. Office of Naval Research, Cambridge, Massachusetts.
- Beukelman, W. and Gerritsma, J. (1982). "The Distribution of Hydrodynamic Mass and Damping of an Oscillating Shipform in Shallow Water". Report nr. 546, Delft University of Technology. Ship Hydromechanics Laboratory.
- Børresen, R.: February (1984). "The Unified Theory of Ship Motions in Water of Finite Depth". Dr.ing. thesis. Division of Marine Hydrodynamics. The Norwegian Institute of Technology.
- Eggers, K.: (1957) "Über das Wellenbild einer pulsierenden Störung in Translation". Schiff und Hafen, pp. 874-878.
- Faltinsen, O.: (Dec. 1971) "A Rational Strip Theory of Ship Motions, Part II". Ph.D. Thesis University of Michigan, Ann Arbor.

Keil, H. (1974) "Die hydrodynamische Kräfte bei der periodischen Bewegung zweidimensionaler Körper an der Oberfläche flacher Gewässer". Bericht nr. 305, Institut für Schiffbau der Universität Hamburg.

Newman, J.N.: (June 1959) "The Damping and Wave resistance of a Pitching and Heaving Ship". Journal of Ship Research, pp. 1-19.

Newman, J.N.: (1977) "Marine Hydrodynamics". The MIT Press, Cambridge, Massachusetts, USA.

Newman, J.N.: (1978) "The Theory of Ship Motions". Advances in Applied Mechanics, Volume 18, 222-283.

Newman, J.N. and Slavounos, P.: (October 1980) "The Unified Theory of Ship Motions". 13th Symposium on Naval Hydrodynamics, Tokyo.

Ogilvie, T.F. and Tuck, O.: (March 1969) "A Rational Strip Theory of Ship Motions, Part I". The Department of Naval Architecture and Marine Engineering, University of Michigan. Vo. 013.

Salvesen, N., Tuck, E.O. and Faltinsen, O.: (1970) "Ship Motions and Sealoads". Soc. Nav. Archit. Mar. Eng., Trans. 78, 250-287.

Slavounos, P.: (1981) "On the Diffraction of Free Surface Waves by a Slender Ship". Ph.D. Thesis. M.I.T.

Tuck, E.O.: (September 1964) "On Line Distributions of Kelvin Sources". Journal of Ship Research, pp. 45-52.

Zhao, R. "Two-dimensional added mass, damping and exciting forces in water of finite depth", Student Project, Division of marine hydrodynamics, The Norwegian Institute of Technology, April 1984.

## APPENDIX A

The Fourier transform of the three-dimensional Green function due to a travelling, harmonically oscillating source on the free surface is given by

$$G^*(k; y, z) = \lim_{\mu \rightarrow 0} -2 \int_{-\infty}^{\infty} d\ell e^{i\ell y} \frac{\cosh \sqrt{k^2 + \ell^2} (z+h)}{\cosh \sqrt{k^2 + \ell^2} h} \frac{1}{(\sqrt{k^2 + \ell^2} \tanh \sqrt{k^2 + \ell^2} h - (\omega + Uk - i\mu)^2/g)} \quad (A.1)$$

The two-dimensional Green function for the harmonically oscillating source  $G_{2D}(y, z) = G^*(0, y, z)$  is given by

$$G_{2D}(y, z) = \lim_{\mu \rightarrow 0} -4 \int_0^{\infty} \frac{\cos \ell y \cosh \ell (z+h)}{\cosh \ell h (\ell \tanh h - \frac{1}{g}(\omega - i\mu)^2)} d\ell \quad (A.2)$$

The expression  $G_{2D} - \bar{G}_{2D}$  can be found in Børresen (1984) and is given by

$$G_{2D} - \bar{G}_{2D} = 2A \cos \ell_0 y \quad (A.3)$$

where

$$A = 4\pi i \frac{\ell_0 h \cos \ell_0 (z+h)}{\cosh \ell_0 h (\omega^2 h/y + (\ell_0 h / \cosh \ell_0 h)^2)} \quad (A.4)$$

$$\omega^2 = \ell_0 y \tanh \ell_0 h \quad (A.5)$$

The kernel function  $f(x, y, z)$  is defined as

$$f(x, y, z) = \frac{1}{2\pi} \int_{-\infty}^{\infty} f^*(k, y, z) e^{ikx} dk \quad (A.6)$$

with

$$f^*(k, y, z) = G^*(k, y, z) - G_{2D}(y, z) \quad (A.7)$$

In Børresen (1984) it is shown that  $f(x, 0, 0)$  can be written as

$$f(x, 0, 0) = f_d(x, 0, 0) + g(x) \quad (A.8)$$

where

$$f_d(x) = \begin{cases} f_1(x) + f_2(x) & x > 0 \\ f_2(x) & x < 0 \end{cases} \quad (A.9)$$

where

$$f_1(x) = -4i \left\{ \int_{-\infty}^{k_1} \frac{1}{k} dk (h_1(k) - 1) e^{ikx} - 4i \frac{1}{x} (\sin k_1 x + \sin k_2 x) - 2\pi i \delta(x) - \frac{1}{x} (\cos k_1 x + \cos k_2 x) \right\} \quad (A.10)$$

$$f_2(x) = 2i \left\{ \int_0^{k_3} \frac{1}{k} dk (h_1(k) - 1) e^{ikx} + 2i \int_{k_3}^{k_4} \frac{1}{k} dk (ih_2(k) - 1) e^{ikx} \right\} \quad \text{for } \frac{Uw}{g} < 1/4 \quad (A.11)$$

$$f_2(x) = 2i \int_0^{\infty} \frac{1}{k} dk (h_1(k) - 1) e^{ikx} \quad \text{for } \frac{Uw}{g} > 1/4 \quad (A.12)$$

and

$$\begin{aligned} h_1(k) &= \beta(k) / (\beta^2(k) - 1)^{\frac{1}{2}} \\ h_2(k) &= \beta(k) / (1 - \beta^2(k))^{\frac{1}{2}} \\ (k) &= (\omega + Uk)^2 / g |k| \end{aligned} \quad (A.13)$$

$k_1$  and  $k_2$  are the roots ( $k_1 < k_2$ ) of the equation  $\beta(k) = -1$ .  $k_3$  and  $k_4$  are the roots of  $\beta(k) = 1$ , and

$$g(x) = \lim_{\mu \rightarrow 0} -\frac{1}{\pi} \int_0^{2\pi} du \int_0^{\infty} \left( \frac{\lambda}{\lambda \tanh \lambda h - K} - \frac{\lambda}{\lambda - K} \right) e^{ix\lambda \cos u} d\lambda + \delta(x) P \quad (A.14)$$

where

$$P = \lim_{\mu \rightarrow 0} 2 \int_0^{\infty} d\ell / (|\ell| \tanh |\ell| h - K_0) - \lim_{\mu \rightarrow 0} 2 \int_0^{\infty} d\ell / (|\ell| - K_0) \quad (A.15)$$

$$K = (\omega + U\lambda \cos u - i\mu)^2 / g \quad (A.16)$$

$$K_0 = (\omega - i\mu)^2 / g \quad (A.17)$$

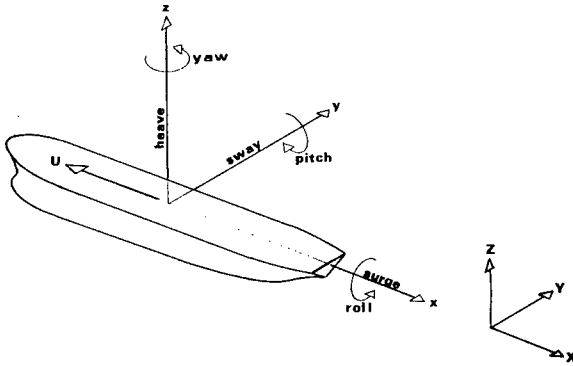


Figure 1. Description of coordinate systems.

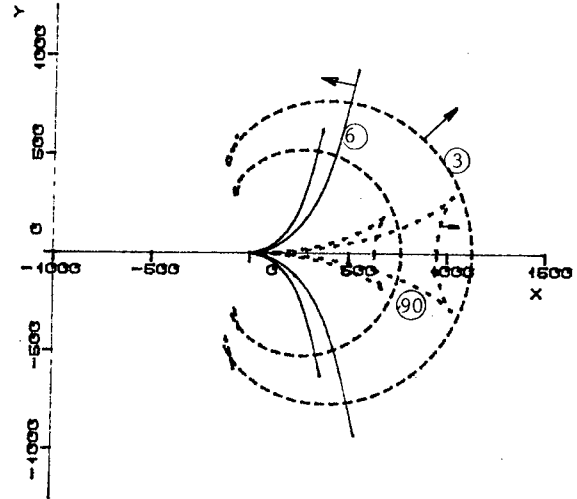


Figure 2. Infinite depth. Sample plot of wave crests for  $\tau = 0.2548$ . The source is located in  $(0,0)$ . Source speed  $U = 5$  m/s, frequency  $\omega = 0.5$  rad/s. The arrows indicate the individual wave formations' direction of travel relative the source. The numbers denotes "crest" number from source point. The x and y dimensions are given in meters.

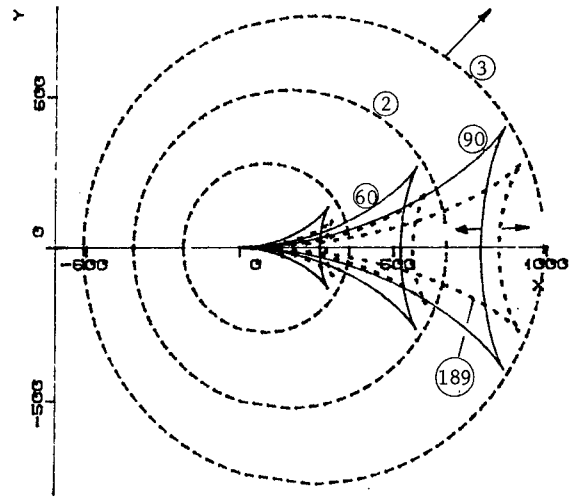


Fig. 3. Infinite depth. Sample plot of wave crests for  $\tau = 0.1529$ . Source speed  $U = 3$  m/s frequency  $\omega = 0.5$  rad/s.

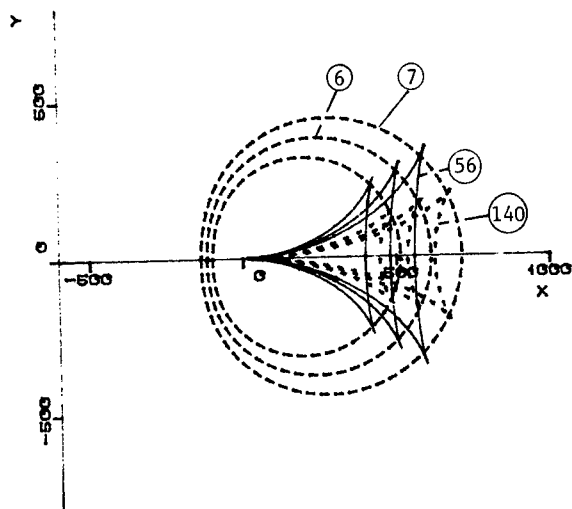


Figure 4. Finite depth. Sample plot of wave crests for  $\tau = 0.2548$ . Source speed  $U = 3$  m/s, frequency  $\omega = 0.5$  m/s.  $U/\sqrt{gh} = 0.6$  where  $h$  is the water depth.

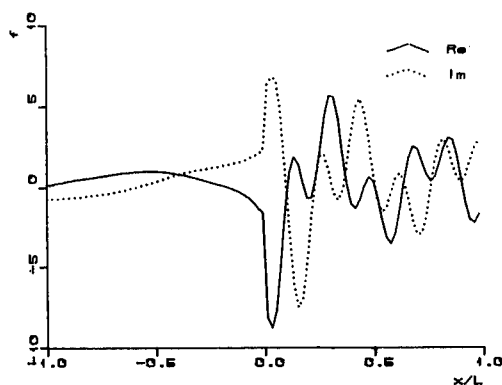


Figure 6. The non singular part of the finite depth kernel function  $f(x)$  for  $\tau = 0.2$ ,  $F_n = 0.2$  and  $L/h = 31.25$ . ( $L$  = vessel length,  $h$  = water depth,  $F_n$  = Froude number).

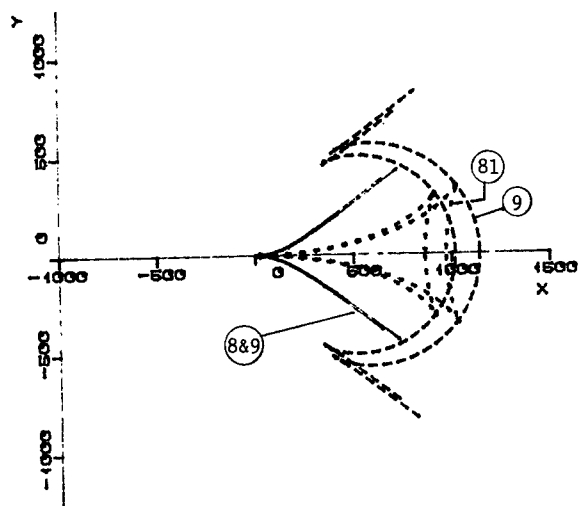


Figure 5. Finite depth. Sample plot at wave crests for  $\tau = 0.2548$ . Source speed  $U = 5$  m/s, frequency  $\omega = 0.5$  m/s,  $U/\sqrt{gh} = 1.0$ .

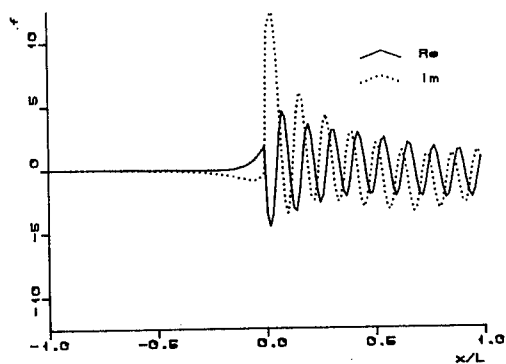


Figure 7. The non singular part of the finite depth kernel function  $f(x)$  for  $\tau = 0.7$ ,  $F_n = 0.2$ ,  $L/h = 31.25$ .



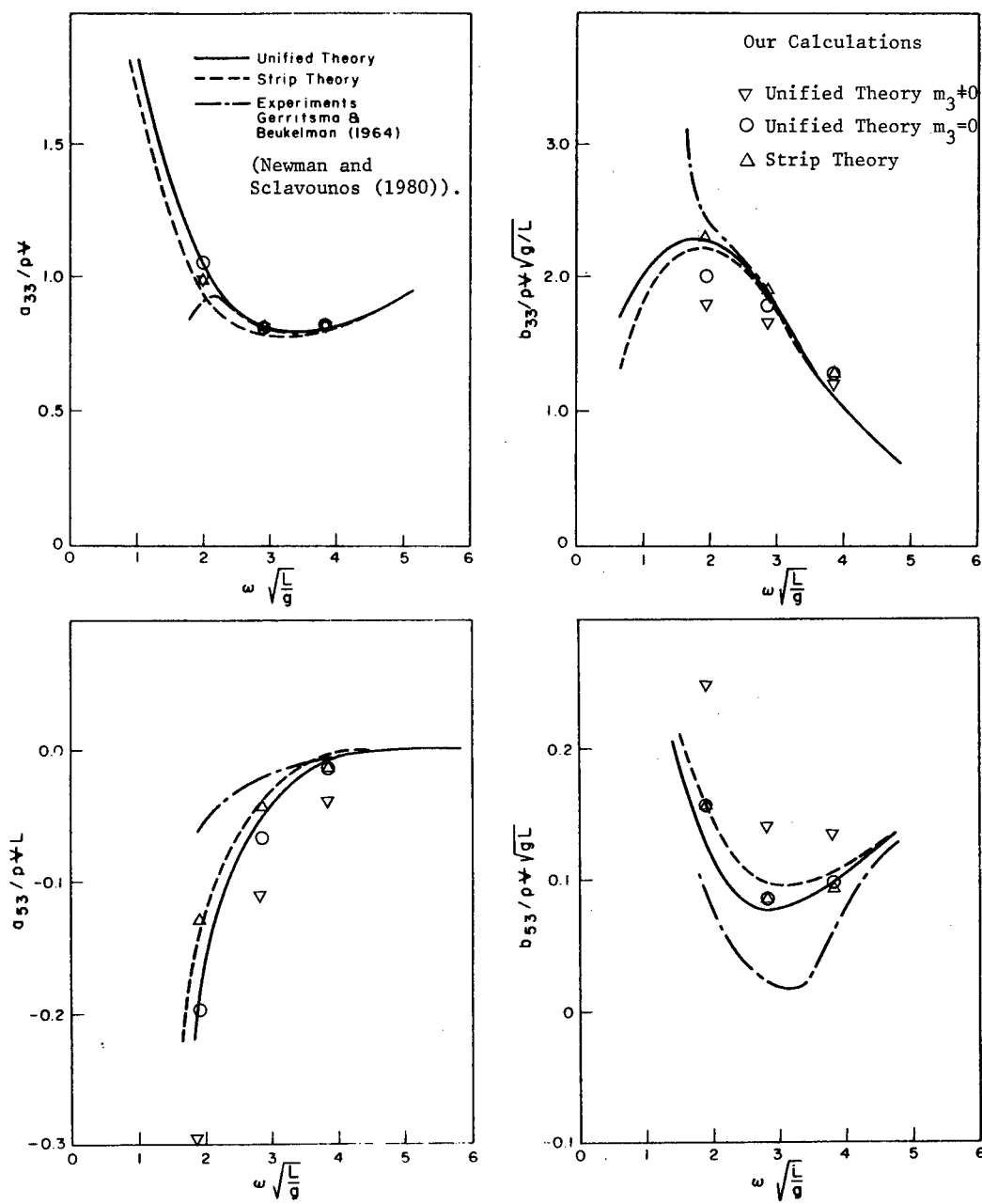


Figure 8. Added mass and damping coefficients of a series 60 hull ( $C_B = 0.7$ ) at  $F_n = 0.2$  (Based on Newman and Slavounos (1980)).

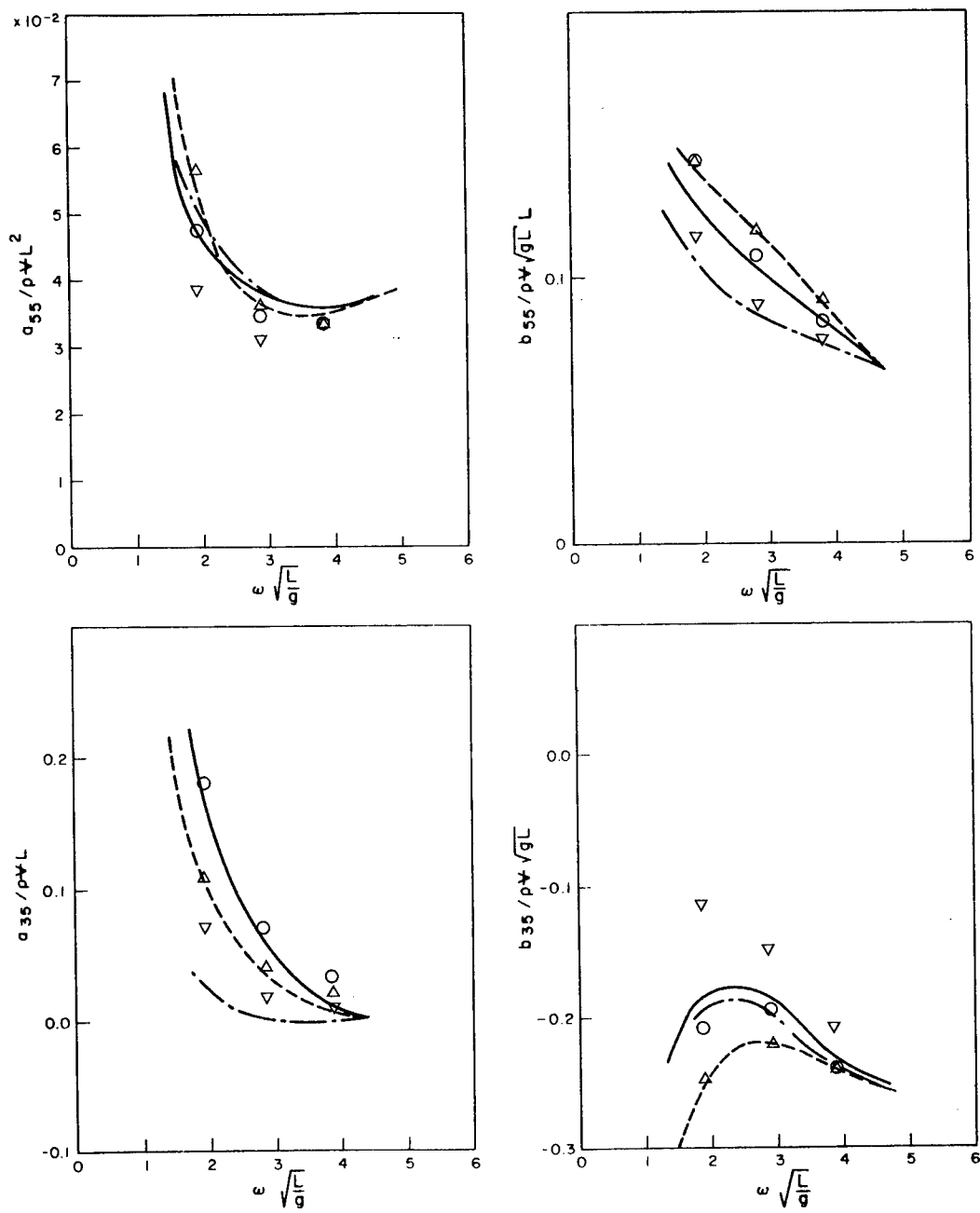


Fig. 8. (continued).

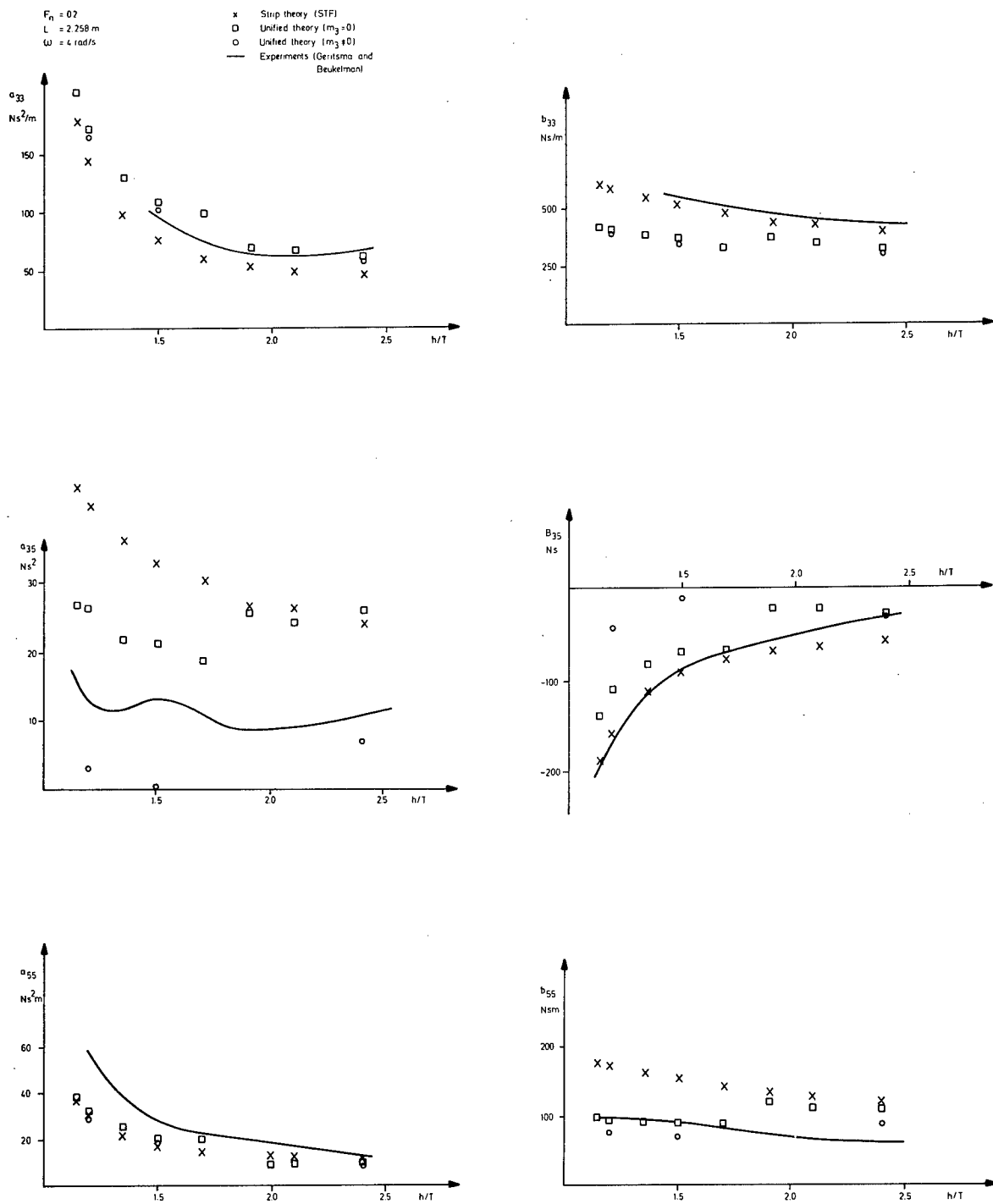


Figure 9. Added mass and damping coefficients of a series 60 hull ( $C_B = 0.7$ ) at  $F_n = 0.2$  depending on depth/draft ratio.

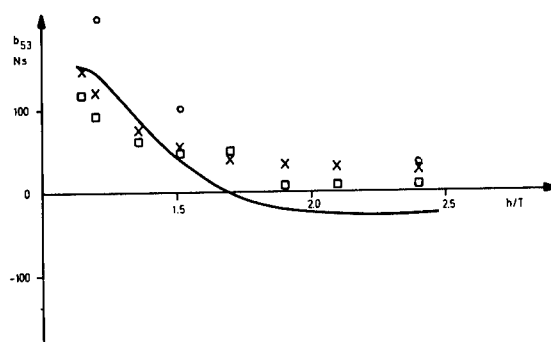
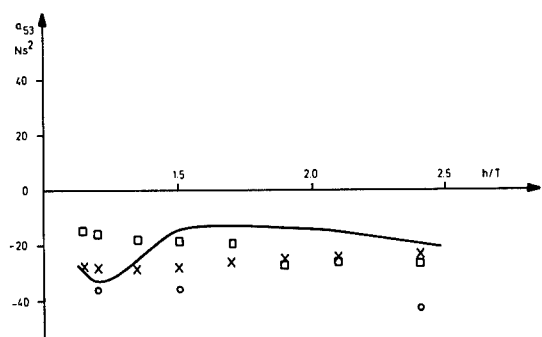


Fig. 9. (continued).

SESSION II  
SEAKEEPING PROBLEMS

# UNSTEADY WAKE VELOCITIES DUE TO WAVES AND MOTIONS MEASURED ON A SHIP MODEL IN HEAD WAVES

A.B. AALBERS AND W. VAN GENT

## ABSTRACT

To specify design criteria for a cavitating propeller of a ship in waves, information about the unsteady velocities in the wake of a frigate type ship model proceeding in waves has been investigated. The NSMB wake field Laser-Doppler velocimeter was used to investigate successively two cases in head waves, viz.:

- model towed, while restrained at static equilibrium draught and trim (captive model);
- model towed, while completely free in its six-degrees of freedom (free model).

The results are decomposed in effects of undisturbed wave orbital motion, ship model motion, i.e. heave, pitch and surge, and disturbances due to the presence of the hull. The latter part is also calculated by means of a three-dimensional diffraction theory. A comparison is made with calm water wake field data.

To investigate the effect on the propeller, loading and cavitation calculations have been performed for various conditions in the unsteady wake.

## 1. INTRODUCTION

### 1.1 General

Current design procedures for propellers make use of the wake data obtained from model tests in calm water. However, for ships operating in areas such as the North Atlantic Ocean where in some seasons Beaufort 7 sea conditions are more the rule than the exception, the propeller designer should consider the unsteady contributions to the wake field which are caused by the waves and the wave induced ship motions. The combined effect of these two contributions has been investigated in the past by means of measuring load fluctuations on the propeller of ship models travelling in waves. In this respect one can refer to information by Van Sluijs (1972) and by Jessup and Boswell (1982).

In ship motion theory it is common that for the calculation of the response in waves the effects of the wave forces on the non-moving hull and the motion induced calm water reaction forces are linearly superimposed. Application of the linear superposition principle to the problem of the unsteady wake, the following contributions may be discerned:

- |  |  |
|--|--|
| - undisturbed wave orbital velocity;                               | For a non-moving (captive) hull in waves |
| - velocity due to wave reflection on the hull;                     |  |
| - radiated wave velocity due to ship motions (motion diffraction); |  |
| - relative motion velocity.  | For a moving hull in calm water          |

If these contributions may be superimposed on the calm water wake field, computer calculations to study the effect of waves and ship motions on the propeller design are possible.

### 1.2 Propeller Load Fluctuations

Measurements were carried out by Van Sluijs (1972) on the shaft thrust fluctuations of an O.B.O. carrier type vessel in regular and irregular waves. It was concluded that the surge motion was an important influence. It was not possible from these tests to determine the extent to which wave particle velocity or ship motion contributed to the thrust fluctuations.

Jessup and Boswell (1982) tested a captive model in waves and carried out forced pitching tests in calm water and waves. From propeller blade load and bearing load measurements and comparisons with calculations they concluded that the wake field contributions due to wave particle velocity and pitch motions may be linearly superimposed. Yet, it should be noted that in their calculations only the pitch induced relative motion and the undisturbed wave orbital motion contributions were considered. Hence, the contributions from other modes of ship motion and the effects of radiation and wave reflection were not taken into account.

A.B. Aalbers and W. van Gent, Maritime Research Institute Netherlands (MARIN)  
Haagsteeg 2, P.O. Box 28, 6700 AA Wageningen, The Netherlands

Helle and Hageman (1979) used the data of Van Sluijs (1972) to calculate velocity fluctuations in the wake field of the O.B.O. carrier. The propeller blade loads due to these velocity fluctuations were considered to have only a marginal effect on the fatigue life of the propeller, taking into account the expected range of sea conditions to be met. In this investigation not only the radiation effects but also the important wave orbital motion contribution were disregarded.

It may be concluded that none of the above mentioned authors give a complete picture for the case of a ship moving in waves.

### 1.3 Design Aspects

The present investigations provide measured and calculated data for the varying part of fluid velocities in the wake field of a frigate type ship in waves. The validity of the superposition assumption was judged by comparing the mean value of the advance speed in waves with the calm water results and by comparing results for a captive model with those for a free moving model. The reliability of the Laser-Doppler velocimeter equipment was investigated by comparing the calm water wake field measured on a scale 1 to 26 model with pitot tube measurements on a geosim model at scale 1 to 17.15.

The measurement accuracy was analyzed using linear error theory. The results are discussed in Section 2.4.

In Section 4 of this paper it is concluded that the calculation method compares well with the measurements. This means that the calculated wake field variations can be used in a propeller design program.

When in a propeller design attention has to be given to the non-uniformity of the ship's wake, the design procedure is based on theoretical approaches. Data on systematic series of propellers are insufficient as a base for wake adapted propeller design. In theoretical computations the local inflow of each propeller blade section is taken into account. In calm water, where the wake field is steady, such computations have become parts of standard procedures for propeller design. These parts can be formulated as direct design criteria or as intermediate analyses of the design of which the results are used as a refined criterium in a subsequent design stage.

In the present case of a ship in waves, the propeller design problem is even more complicated. Besides non-uniformity also unsteadiness of the wake has to be considered. In this paper the treatment of the (low frequency) unsteadiness is considered as an extension of the forementioned standard procedures. This requires a careful assessment of the local values of the velocities and pressures at the propeller disc. This is undertaken in Section 3. Application of the NSMB propeller calculation program for design and analysis is then valid to investigate the consequences for cavitation and dynamic pressures.

## 2. MEASUREMENTS

### 2.1 Model Tests

Regular wave tests were carried out for a frigate type ship model at a linear scale of 1 to 26 in the Seakeeping Laboratory of the NSMB, which is described by Van Lammeren and Vossers (1957). The ship particulars and a small scale body plan are given in Table 1 and Figure 1.

Table 1 - Particulars of Ship and Propellers

Designation	Symbol	Unit	Magnitude
Length between perpendiculars	$L_{pp}$	m	95.0
Breadth moulded	B	m	13.0
Draught even keel	T	m	4.0
Displacement weight	$\Delta$	t	2234.0
Block coefficient	$C_B$	-	0.44
Waterplane coefficient	$C_W$	-	0.77
Midship section coefficient	$C_M$	-	0.70
Centre of gravity aft of Station 10	LCG	m	-2.195
Centre of gravity above base	$\overline{KG}$	m	5.76
Metacentric height	$\overline{GM}$	m	1.50
Longitudinal radius of gyration	$k_{yy}$	m	23.28
Transverse radius of gyration	$k_{xx}$	m	5.20
Natural roll period	$T_\phi$	s	9.3
Natural pitch period	$T_\theta$	s	4.3
Natural heave period	$T_z$	s	4.5
Propeller diameter	D	m	3.96
Pitch ratio at 0.7 D	$P_{0.7/D}$	-	1.35
Expanded blade area ratio	$A_E/A_0$	-	0.47
Number of blades	Z	-	4
Direction of rotation	-	-	Right-handed

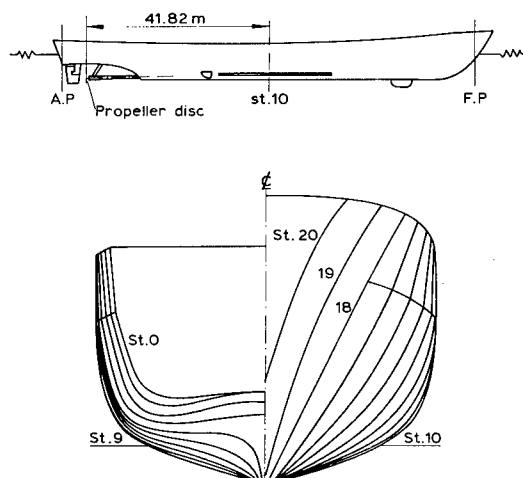


Figure 1 - Profile and Body Plan of Frigate Type Model

Two series of tests were carried out, viz.:

- tests in calm water and regular waves with a captive model;
- tests in calm water and regular waves with a free (towed) model.

In both test series the Laser-Doppler velocimeter (L.D.V.) technique was applied. The ship speed corresponded to 20 kn. (10.288 m/s) in the appropriate cases. A test review is given in Table 2.

Table 2 - Test Review

Speed (kn.)	Wave conditions		Test series	Number of measurement locations in pro- peller disc
	Amplitude (m)	Period (s)		
20	-	-	1	17
20	2	7.0	1	16
20	2	9.0	1	17
20	2	12.2	1	17
20	-	-	2	8
0	1	7.0	2	2
0	1	7.6	2	2
0	1	8.8	2	3
0	1	9.8	2	2
0	1	12.0	2	2
20	1	7.0	2	8
20	1	7.6	2	8
20	1	8.8	2	8
20	1	9.8	2	8
20	1	12.0	2	8

The calm water runs were carried out for two purposes:

- to investigate the reliability of the L.D.V. for wake measurement on the small model (1:26);
- to have a data base for the investigation of the superimposeability of the unsteady (wave induced) contributions to the calm water nominal wake field.

The reliability of the L.D.V. was judged by comparing the results for the small model with five-hole pitot tube measurements on the large model (1:17.15).

## 2.2 Measurement Signals

The measurement signals which were recorded during the two test series are presented in Table 3. For the first test series the standard L.D.V. equipment as described by De Bruin and Versmissen (1979) was used. For the second test series - with the free model - a lightweight L.D.V. system was developed which could be mounted in the model. The principles are shown in Figure 2. The L.D.V.'s can measure water particle velocities in two orthogonal directions in a plane perpendicular to the axis of the laser beam. The measurement method is a forward scatter system in the reference beam mode and the location of measurement is well defined as the focus point (about  $1 \text{ mm}^2$ ) of the triple laser beam.

Table 3 - Measurements

Quantity	Notation	Unit	Signal/noise ratio	Relative accuracy $q_{amp}/Q$	Test series
Ship speed	$V_s$	m/s	>10	1%	1, 2
Wave	$\zeta$	m	>10	2%	1, 2
Heave	$z$	m	>10	2%	2
Surge	$x$	m	>10	2%	2
Pitch	$\theta$	deg.	>10	2%	2
Axial wake velocity	$V_x$	m/s	10 - 5	4%	1, 2
Transverse wake velocity components	$V_z$	m/s	5 - 1	10%	1
	$V_y$	m/s	1	10%	2

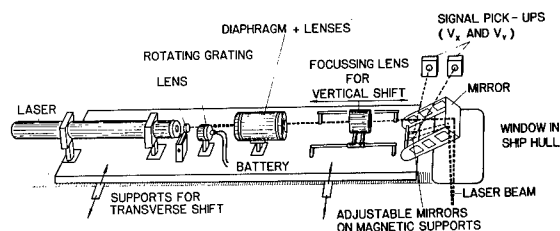


Figure 2 - Lightweight L.D.V. System

In Figure 3 the measurement locations in the propeller disc are indicated. These locations could be adjusted by shifting the reflection mirror arrangement of the L.D.V. system.

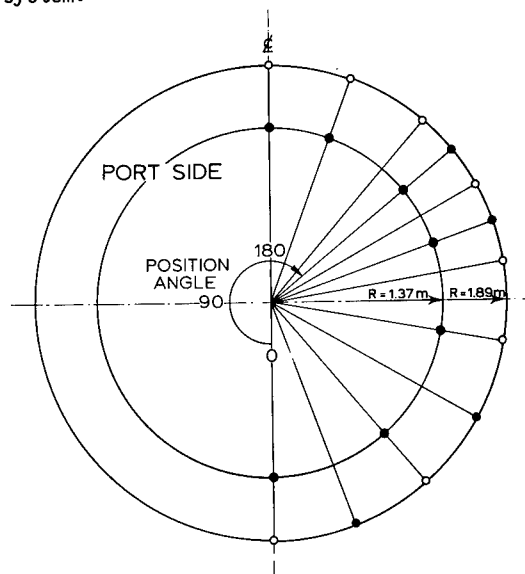


Figure 3 - Locations in the Propeller Disc  
● and o Test Series 1  
o Test Series 2



In the second test series the ship motions were measured by an optical tracking system (for heave and surge) and a gyroscope (for pitch).

During the measurement runs at forward speed, the carriage four-quadrant thyristor electromotor control kept the speed constant at the required value.

The wave height was measured by a resistance type wave probe.

### 2.3 Data Analysis and Reduction

The measurement signals of the tests in waves were subjected to harmonic analysis to determine the amplitude and phase lead of the signal components up to the fifth harmonic. Only the harmonic component with a frequency equal to the wave encounter frequency was considered. The amplitude of the higher harmonics were negligible. Furthermore, the mean value of all signals was determined.

All data was scaled up to prototype values according to Froude's law of similitude.

The sign convention and system of co-ordinates are given in Figure 4. Note that the ship system of co-ordinates is earth-oriented with its origin in the centre of gravity of the ship, while the wake velocity system of co-ordinates is ship-fixed.

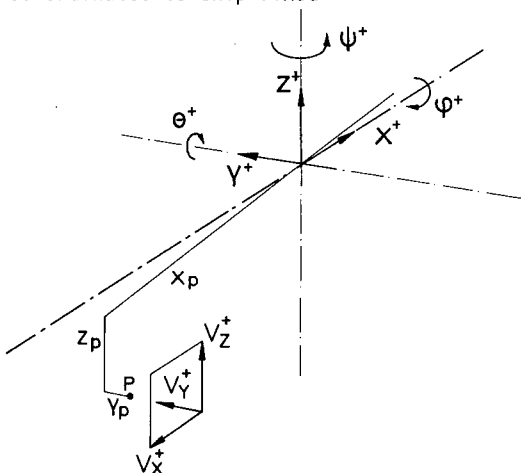


Figure 4 - System of Axes for Ship Motions and for Wake Velocity Components in Measuring Location P ( $x_p$ ,  $y_p$ ,  $z_p$ )

### 2.4 Accuracy of the Measurements

During the tests each signal is digitized and recorded on magnetic computer tape. Table 3 presents for each recorded signal  $Q$  the measurement accuracy and signal to noise ratio denoted by  $q$  and  $s$  respectively.

For the signals on tape which were subjected to the harmonic analysis (see Figure 5), the analysis accuracy in amplitude and phase depends on the signal to noise ratio. The following values are adopted:

$s > 10$	$q_{amp} = 0.01 Q$	$q_{phase} = 5 \text{ deg.}$
$10 < s < 5$	$q_{amp} = 0.10 Q$	$q_{phase} = 10 \text{ deg.}$
$s \approx 1$	$q_{amp} = 0.50 Q$	$q_{phase} = 20 \text{ deg.}$

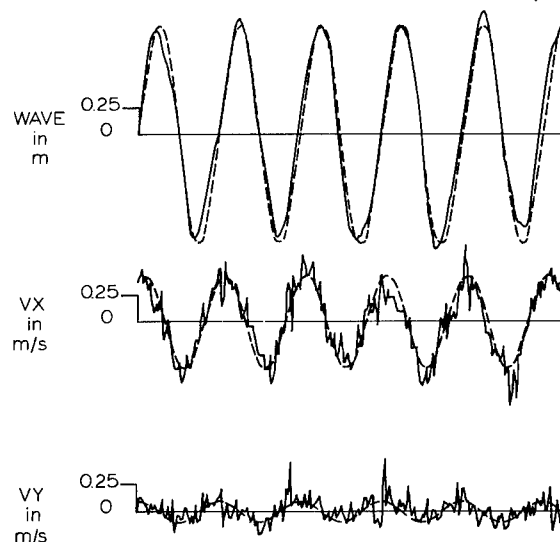


Figure 5 - Example of Fit of First Harmonic

The non-dimensional values for the unsteady advance speed contributions divided by the ship speed are given per unit wave amplitude. The phase lead is given with respect to the wave measurements. The individual accuracy limits from measurement and analysis have to be combined to an overall accuracy limit for the presented quantities. Linear error analysis was applied to obtain the following values:

- Large amplitude wake variations ( $V/V_s \zeta_a > 0.02$ ):  $q_{amp} = 0.11 Q$ ,  $q_{phase} = 12 \text{ deg.}$
- Small amplitude wake variations ( $V/V_s \zeta_a < 0.02$ ):  $q_{amp} = 0.51 Q$ ,  $q_{phase} = 31 \text{ deg.}$

In both test series the transverse wake variations were small in amplitude since the tests were carried out in head waves. Hence, the error margins were relatively large for those signals. For these reasons the discussion of the results in this paper was restricted to mainly the axial wake variations.

At several measurement locations the wave tests were repeated to investigate the reproducibility. In general the reproduction was within the accuracy limits, except at the measurement locations which were in the wake of the struts. Those repeat measurements showed some scatter because the advance speed gradient is relatively large. Hence, small differences in model trim or laser beam focus may lead to 20 or 30 per cent difference in measurement value. In this paper the average value is given in case more than one test result was available.

## 3. THEORY

### 3.1 Motion Response

In order to calculate the motions of a ship in waves, a set of linearized equations of motion are solved in the frequency domain. These equations can be written as follows:

$$\sum_{j=1}^6 [-\omega^2 (M_{kj} + a_{kj}) \cos(\omega t + \epsilon_j) + \omega b_{kj} \sin(\omega t + \epsilon_j) + c_{kj} \cos(\omega t + \epsilon_j)] \xi_{aj} = F_{ak} \cos(\omega t + \delta_k) \quad \text{for } k = 1 \text{ to } 6 \quad (1)$$

in which:

$m_{kj}$  = inertia matrix  
 $a_{kj}$  = added mass matrix  
 $b_{kj}$  = damping matrix  
 $c_{kj}$  = restoring matrix  
 $F_{ak}$  = excitation force amplitude  
 $\xi_{aj}$  = motion amplitude  
 $\omega$  = (circular) oscillation frequency  
 $\delta_j, \epsilon_j$  = phase angles.

The coefficients in the equation of motion follow from the ship particulars and from the hydrodynamic (motion induced) reaction forces and the (wave induced) excitation forces. These forces were calculated by means of a computer program based on three-dimensional diffraction theory described by Van Oortmerssen (1976).

Assuming the fluid irrotational and ideal the flow field around the ship at forward speed may be described by the superposition of a set of linear potential contributions (see Huijsmans and Dallinga (1983)):

$$\phi(\bar{x}, t) = -V_s x + \phi_v(\bar{x}) + \phi(\bar{x}) e^{-i\omega t} \quad (2)$$

in which:

$\bar{x}$  = space co-ordinate in an earth-oriented system of axes with its origin in the centre of gravity G

$t$  = time

$V_s$  = ship speed

$\phi_v(\bar{x})$  = steady flow field potential due to forward speed

$\phi(\bar{x})$  = amplitude of unsteady flow field potential due to waves and ship motions.

For the calculation of the ship motions  $\phi_v(\bar{x})$  will not be considered since it only contributes to the average values (viz. the trim and sinkage). The diffraction theory assumes infinitesimal motions so that the earth-oriented system of axes coincides with a ship-fixed system of axes. The unsteady flow field contributions, i.e. the potentials due to surface waves and diffraction may then be superimposed directly although they are defined in an earth-oriented and in a ship-fixed system of axes respectively:

$$\phi(\bar{x}) = -i\omega \sum_{a=0}^6 \{ \phi_0(\bar{x}) + \phi_7(\bar{x}) \} + -i\omega \sum_{j=1}^6 \phi_j(\bar{x}) \xi_{aj} \quad (3)$$

in which:

$\xi_a$  = wave amplitude  
 $\phi_0(\bar{x})$  = incident wave potential  
 $\phi_7(\bar{x})$  = reflected wave potential  
 $\phi_j(\bar{x})$  = ship motion diffracted wave potentials ( $j = 1 \dots 6$ ).

Salvesen, Tuck and Faltinsen (1970) showed that the motion related velocity potentials  $\phi_j(\bar{x})$  may be expressed explicitly in their zero speed counter parts  $\phi_j^0(\bar{x})$ :

$$\phi_j(\bar{x}) = \phi_j^0(\bar{x}) \quad \text{for } j = 1 \dots 4$$

$$\phi_5(\bar{x}) = \phi_5^0(\bar{x}) + \frac{V_s}{V_e} \phi_3^0(\bar{x})$$

$$\phi_6(\bar{x}) = \phi_6^0(\bar{x}) - \frac{V_s}{V_e} \phi_2^0(\bar{x})$$

Note that the oscillation frequency  $\omega$  of the ship is equal to the encounter frequency  $\omega_e$ , which is related to the wave frequency  $\omega_g$  according to:

$$\omega_e = \omega_g - \kappa V_s \cos \mu \quad (4)$$

in which:

$\kappa$  = the wave number =  $2\pi/\lambda$

$\lambda$  = the wave length

$\mu$  = the wave direction.

In the evaluation the reflected wave contribution  $\phi_7(\bar{x})$  is treated in a similar way as the motion diffraction potentials, so:

$$\phi_7(\bar{x}) = \phi_7^0(\bar{x}) \quad (5)$$

In the three-dimensional diffraction theory program the zero speed potentials are calculated using a source-sinc method in which the ship is represented by a large number of facet elements. The pressure  $p(\bar{x}, t)$  on each element follows from the linearized Bernoulli equation:

$$p(\bar{x}, t) = -\rho \left( \frac{\partial}{\partial t} - V_s \bar{i}_x \cdot \nabla \right) \phi(\bar{x}, t) \quad (6)$$

in which:

$\rho$  = the density of water

$\bar{i}_x$  = the unit vector in x-direction.

The wave induced excitation forces and the hydrodynamic reaction forces are obtained by integrating the linearized pressures over the mean wetted area of the hull. After expressing the reaction forces in terms of added mass and damping coefficients the equation of motion (1) can be solved.

### 3.2 Local Fluid Velocity

In order to obtain the amplitude of the oscillating local fluid velocity at a location  $\bar{x}_p$  in the propeller disc the unsteady potentials are evaluated:

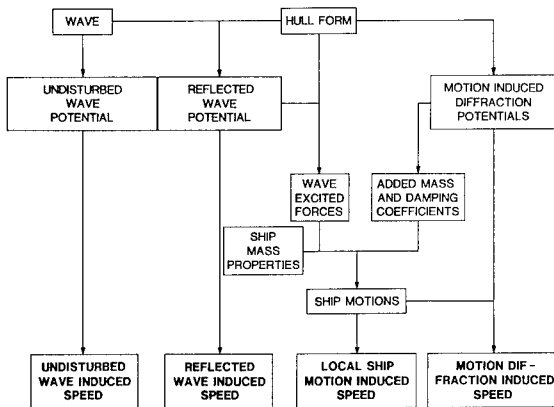
$$\nabla'(\bar{x}_p) = \nabla \phi(\bar{x}_p) \quad (7)$$

in which  $\nabla'(\bar{x}_p)$  is the unsteady fluid velocity amplitude in the earth-oriented system of axes. The measured unsteady fluid velocity is given with respect to a ship-fixed system of axes while the ship motions are finite. So the relative velocity due to the local ship motion with respect to the earth-oriented system of axes has to be included:

$$\nabla(\bar{x}_p) = \nabla \phi(\bar{x}_p) - \dot{\xi}_a(x_p) \quad (8)$$

in which the local ship motion amplitude  $\xi_s(\bar{x})$  is calculated by combining the rigid body motions in a linear way.

The calculation scheme for the velocity amplitudes of the wake field is shown in the review below:



### 3.3 Local Pressures

For the propeller design calculations the pressure at the propeller disc has to be determined in order to establish its cavitation behaviour. To this purpose the Bernoulli equation was evaluated taking into account the unsteady flow as well as the steady flow around the ship.

In an earth-oriented reference frame moving with the ship mean speed the Bernoulli equation for a potential flow is:

$$p(\bar{x}, t) + 0.5 \rho (\nabla \phi(\bar{x}, t))^2 + \rho g z(t) + \rho \frac{\partial}{\partial t} \phi(\bar{x}, t) = \text{constant}$$

in which:

$p(\bar{x}, t)$  = the local pressure

$g$  = the acceleration due to gravity

$\phi(\bar{x}, t)$  = the total fluid potential given in equation (2)

$z(t)$  = the vertical co-ordinate.

The constant at the right-hand side of the equation can be derived from the conditions far ahead of the ship. Assuming the effects of the undisturbed waves to be linear and sinusoidal the velocity potential at infinity becomes:

$$\phi(\infty, t) = \phi_0(\infty, t) - V_s x$$

and the quadratic terms are approximated by:

$$(\nabla \phi(\infty, t))^2 \approx V_s^2 - 2 V_s \nabla \phi_0(\infty, t)$$

The time average of the Bernoulli constant equals the constant for the flow without waves and therefore the constant follows from the condition at the undisturbed free surface level,  $z = 0$ , where:

$$p = p_a = \text{atmospheric pressure}$$

Hence:

$$p(\bar{x}, t) + 0.5 \rho (\nabla \phi(\bar{x}, t))^2 + \rho g z(t) + \rho \frac{\partial}{\partial t} \phi(\bar{x}, t) = p_a + 0.5 \rho (-V_s)^2 \quad (9)$$

The velocity potential in the neighbourhood of the ship consists of two parts, viz. the steady potential denoted as  $\phi_s(\bar{x})$  and the unsteady part denoted as  $\phi_u(\bar{x}, t)$ . The time dependent part was determined in the diffraction theory in a system of axes which - due to infinitesimal ship motions - coincides with a ship-fixed system. For application in the Bernoulli equation the relations between the derivatives of the potentials in body co-ordinates and earth co-ordinates respectively have to be considered. See also Section 3.1 and 3.2. For time derivatives holds:

$$\frac{D}{Dt} \phi_u(\bar{x}, t) = \frac{\partial}{\partial t} \phi_u(\bar{x}, t) + \dot{\xi}(\bar{x}, t) \nabla \phi_u(\bar{x}, t) \quad (10)$$

in which:

$\frac{D}{Dt}$  = derivatives in a body frame

$\frac{\partial}{\partial t}$  = derivatives in an earth frame

$\dot{\xi}(\bar{x}, t)$  = oscillatory ship motion velocity.

In the linear case the second term at the right-hand side of (10) may be neglected, so the time derivatives in the two systems of axes are equal. For the spatial derivatives holds:

$$\nabla' \phi_u(\bar{x}, t) = \nabla \phi_u(\bar{x}, t) + \dot{\xi}(\bar{x}, t) \quad (11)$$

in which the left-hand side represents the earth-oriented spatial derivative. The steady potential in the neighbourhood of the ship is given by:

$$\phi_s(\bar{x}) = -V_s x + \phi_v(\bar{x}) \quad (12)$$

consisting of the contributions due to the speed of the hull and the free surface effect. The steady potential contribution to the fluid velocity at the propeller disc cannot be separated from the velocity defect created by the development of the viscous boundary layer along the ship. As this defect is still difficult to calculate, the velocity due to  $\phi_s$  is preferably taken from experimental results (nominal wake measurements).

Since in the present investigation no pressure measurements in the nominal wake are available an estimate of the effects of the steady free surface wave and of the lack of pressure recovery in the viscous wake has to be made as follows. The Bernoulli equation for steady flow at the free surface is:

$$p_a + 0.5 \rho (\nabla \phi_s(\bar{x}))^2 + \rho g z(\bar{x}) = p_a + 0.5 \rho (-V_s)^2$$

or, after linearization:

$$\nabla \phi_s(\bar{x}) \approx -V_s + g \frac{z(\bar{x})}{V_s} \quad (13)$$

in which:

$\zeta(\bar{x})$  = the local free surface elevation.

The Bernoulli equation for the flow through the propeller disc is:

$$p(\bar{x}) + 0.5 \rho (\nabla \phi_s(\bar{x}) + w)^2 + \rho g z = p_a + 0.5 \rho (-V_s + w)^2 \quad (14)$$

in which:

$w$  = the viscous wake velocity defect

$\nabla \phi_s(\bar{x}) + w$  = the measurable nominal velocity in the wake.

Under the assumption that  $\nabla \phi_s(\bar{x})$  is almost invariant over the propeller disc, combination of (13) and (14) at the undisturbed free surface  $z = 0$  leads to:

$$p(\bar{x}) = p_a + \rho g \zeta(\bar{x}) \frac{\nabla \phi_s(\bar{x}) + w}{-V_s} = p_a + \rho g \zeta(\bar{x}) \quad (15)$$

This indicates that the atmospheric pressure may be corrected for the local free surface elevation.

To arrive at the pressure equation for the total flow through the propeller disc, a modification of (9) is used which reduces to (14) in the steady case:

$$p(\bar{x}) + 0.5 \rho (\nabla \phi_u(\bar{x}, t) + \dot{\xi}(\bar{x}, t) + \nabla \phi_s(\bar{x}) + w)^2 + \rho g z(t) + \rho \frac{\partial}{\partial t} \phi_u(\bar{x}, t) = p_a + 0.5 \rho (-V_s + w)^2 \quad (16)$$

Application of (13) to eliminate  $V_s$  in the right-hand side yields:

$$p(\bar{x}, t) - p_a = \rho [g(\zeta(\bar{x}) - z(t)) - \frac{\partial}{\partial t} \phi_u(\bar{x}, t)] + -0.5 \rho [(V_n + V_u)^2 - V_n^2] \quad (17)$$

in which:

$$V_n = (\nabla \phi_s(\bar{x}) + w) \cdot \bar{T}_x$$

$$V_u = (\nabla \phi_u(\bar{x}, t) + \dot{\xi}(\bar{x}, t)) \cdot \bar{T}_x$$

So,  $-(V_n + V_u)$  is the instantaneous nominal advance speed in axial direction and  $z(t)$  is the instantaneous submergence of the propeller relative to the undisturbed free surface level. Since  $|V_n| \gg |V_u|$  (17) may be simplified to:

$$p(\bar{x}, t) - p_a = \rho [g(\zeta(\bar{x}) - z(t)) - \frac{\partial}{\partial t} \phi_u(\bar{x}, t)] - \rho V_n V_u$$

### 3.4 Propeller Calculation

The above derived expressions for the local velocity and the local pressure were applied in a propeller analysis program. The hydrodynamic loading is based on lifting surface theory and has been described by Van Gent

(1975, 1977); the cavitation and its pressure field is based on free streamline theory and has been described by Noordzij (1976, 1978). The nominal wake field at the propeller disc has been taken from the experiments available for the large model (scale 1 to 17.15). The unsteady contributions to this field were calculated for a range of regular wave conditions. The RPM of the propeller was determined from the trial prediction for this ship, taking into account the wave induced resistance increase in the appropriate regular waves according to the method of Gerritsma and Beukelman (1972). For a stock propeller the performance and cavitation behaviour in waves were compared with those in calm water in order to illustrate the consequences of the unsteady wake.

## 4. RESULTS OF THE MEASUREMENTS AND CORRELATION

### 4.1 Feasibility

Since the size of the model (scale 1 to 26) was small, the calm water nominal wake fields obtained from the L.D.V. measurements at the captive model and the free model were compared with the results obtained from pitot tube measurements on a 1 to 17.15 scale model.

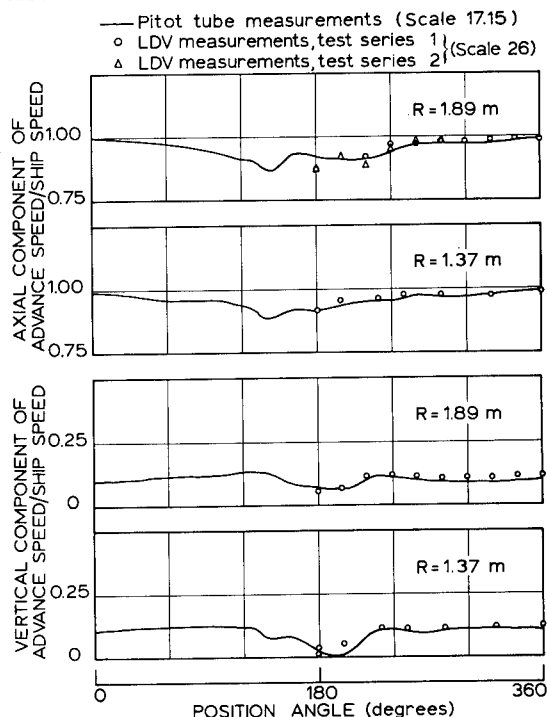


Figure 6 - Comparison of Nominal Wake Measurement Methods - Ship Speed 20 kn.

From the results presented in Figure 6 it follows that:

- The L.D.V. measurements for the axial and the vertical advance speed components agree very well with the pitot tube results.
- The reproducibility of the L.D.V. measurements of test series 1 and 2 is good; the small difference at the position angle of

220 deg. may be attributed to the effect of the struts (see also Section 2.4).

- The axial advance speed component measured very close to the hull (position angle 180 deg. at radius 1.89 m) with the L.D.V. equipment is consistently lower than with the pitot tube.

This may indicate scale effect, i.e. a relatively greater boundary layer thickness of the small model, see Jonk and Van de Beek (1977). Since the good agreement at the other measuring locations close to the hull (position angles 200 and 220 deg.) does not support this supposition, the pitot tube results may be in error for this specific measuring location. Yet, the conclusion may be drawn that the L.D.V. equipment is quite dependable for the intended measurements.

#### 4.2 Superposition

In the theoretical approach it is assumed that the potentials for the calm water wake field and the potentials due to wave action and motions may be linearly superimposed.

The validity of this assumption has been investigated for the two test series by comparing the average advance speed in waves with the calm water results. The way of thinking is that if the average value for an advance speed component in waves differs considerably from the calm water value, the superposition assumption should be rejected. Figure 7 shows that for test series 1 (captive model) as well as for test series 2 (free model) the agreement between the average value in waves and calm water value is excellent. So, in case of the captive model test series the undisturbed and reflected wave potentials  $\phi_0$  and  $\phi_7$  may be superimposed on the calm water wake field potential  $\phi_s$ . Using this in the interpretation of the results of the test series with the free model, the same applies for the motion induced potentials  $\phi_1$  to  $\phi_6$ .

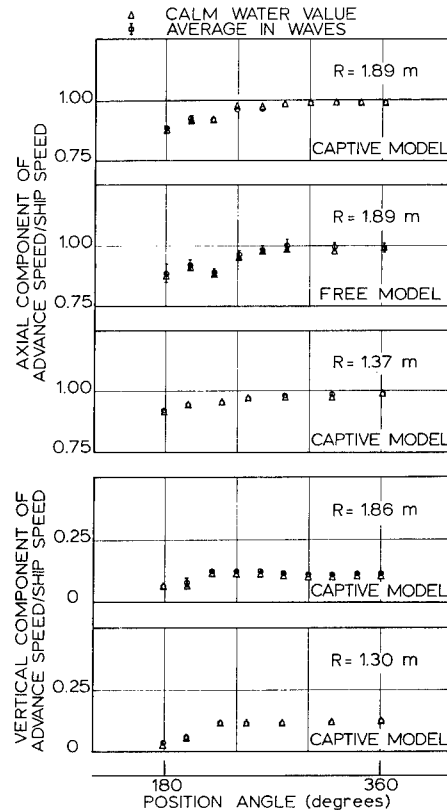
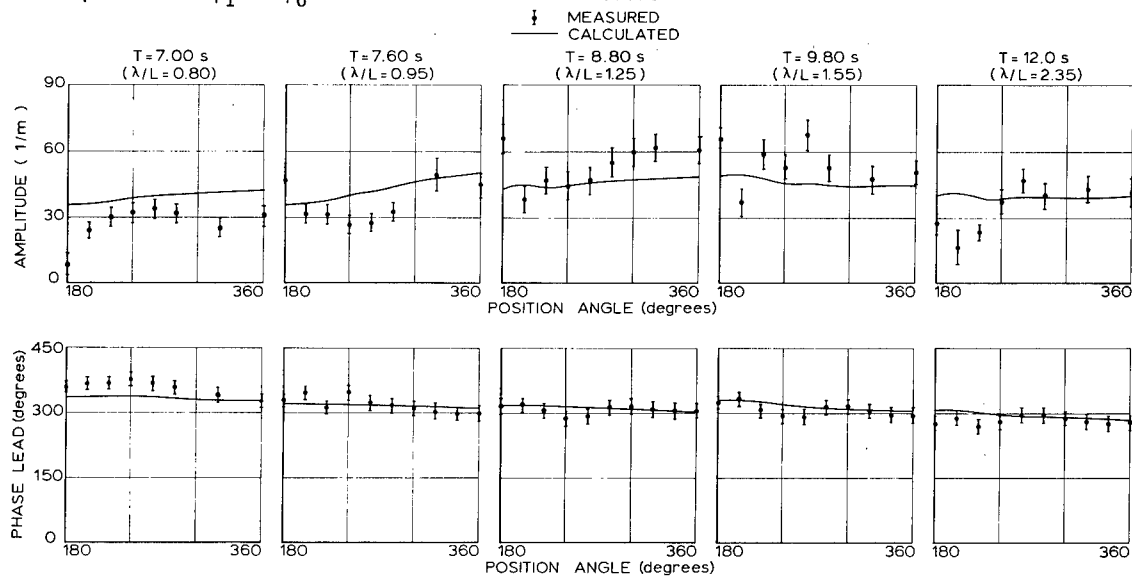


Figure 7 - Average Wake Compared to Calm Water Values

#### 4.3 Unsteady Wake Field

The variations of the axial component of the advance speed for the free model in waves are presented in Figures 8 through 12. The error margins as described in Section 2.4 are indicated as vertical lines on the measurement value.



Figures 8 through 12 - Axial Component of Unsteady Advance Speed/Ship Speed per Unit Wave Amplitude - Ship Speed = 20 kn.

Also indicated in these figures are the results of the calculations with the three-dimensional diffraction theory. In the following the various aspects will be discussed.

#### • Measurement Location

The measured data show more details than the calculated values; at the measurement locations in the wake of the struts (position angles 200, 220 and 240 deg.) the amplitude of the axial components of the advance speed is very sensitive to the location. Considerable differences are found between the measurements and the diffraction theory calculations in which the appendages cannot be taken into account. For other measurement locations the agreement between measurements and calculations is satisfactory.

#### • Wave Length

The amplitude of the axial components of the advance speed are largest for wave length to ship length ratios of 1.25 to 1.55. The measurements and calculations agree in this respect, but not to the same extent. This is caused by the somewhat too low pitch response calculated for those wave lengths. In Figure 13 the pitch response is shown for a range of  $\lambda/L$  values between 0.8 and 2.35.

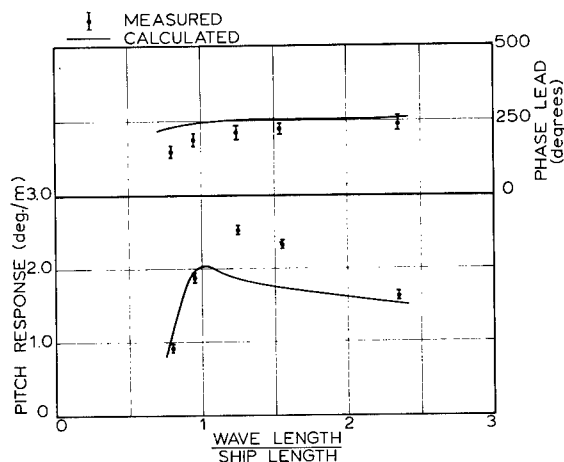


Figure 13 - Pitch Response in Head Waves

As discussed in Section 3.2 the pitch motion together with the surge motion (see Figure 14) contributes in the local finite body motion in axial direction which yields one of the contributions to the axial component of the advance speed. Another contribution originates from the ship motion diffraction. In head waves the contribution due to pitch will be the most important. Considering these two aspects, it may be assumed that if the calculated pitch responses at  $\lambda/L = 1.25$  and  $1.55$  were equal to the measured response the axial component of the advance speed should have been larger.

For shorter waves pitch and local surge reduce, so a smaller amplitude for the axial component of the advance speed results. For

longer waves the reduction of pitch and increment of surge compensate each other to some extent. The reduction in the amplitude of the axial component of the advance speed will mainly be due to the reduced wave orbital velocity.

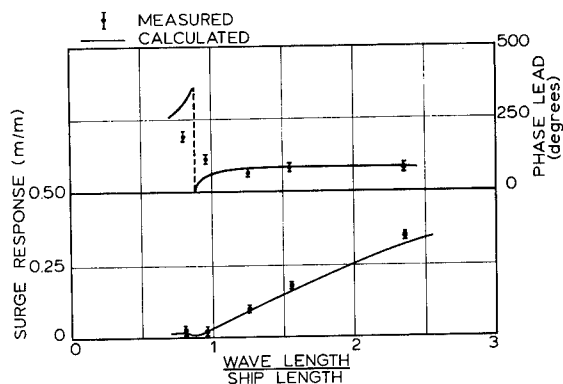


Figure 14 - Surge Response in Head Waves

#### • Amplitude and Phase

Taking into consideration that the pitch induced contributions at  $\lambda/L = 1.25$  and  $1.55$  are underestimated, it may be concluded that the calculated results tend to be somewhat higher than the measured values. This may be caused by the fact that in the diffraction theory calculations the linearized boundary condition on the hull requires only that the normal fluid velocity is zero. Therefore, the boundary layer is not taken into account.

For the phase lead which is given with respect to wave crest passage at the ordinate of the propeller disc the agreement between the measurements and calculations is good. Apparently the wake disturbance due to the struts has only a small effect on the phase.

#### 4.4 Breakdown of Axial Velocity Component

Using the model test data for surge and pitch and the theoretical value of the undisturbed wave orbital velocity corresponding to the measured wave height, the following contributions to the axial advance speed can be isolated:

- the undisturbed wave contribution;
- the local ship motion contribution;
- the sum of the reflected wave and motion diffraction contributions.

Furthermore, taking the test results of series 1 and using the undisturbed wave orbital velocity in the same wave as above for series 2, the last mentioned contribution can be split up into:

- the reflected wave contribution;
- the motion diffraction contribution.

In Figure 15 the measured and calculated contributions are compared with those for  $\lambda/L = 1.25$ . For the undisturbed wave orbital velocity the measurement value results from a test run without ship model using the standard L.D.V. equipment. The agreement is good.

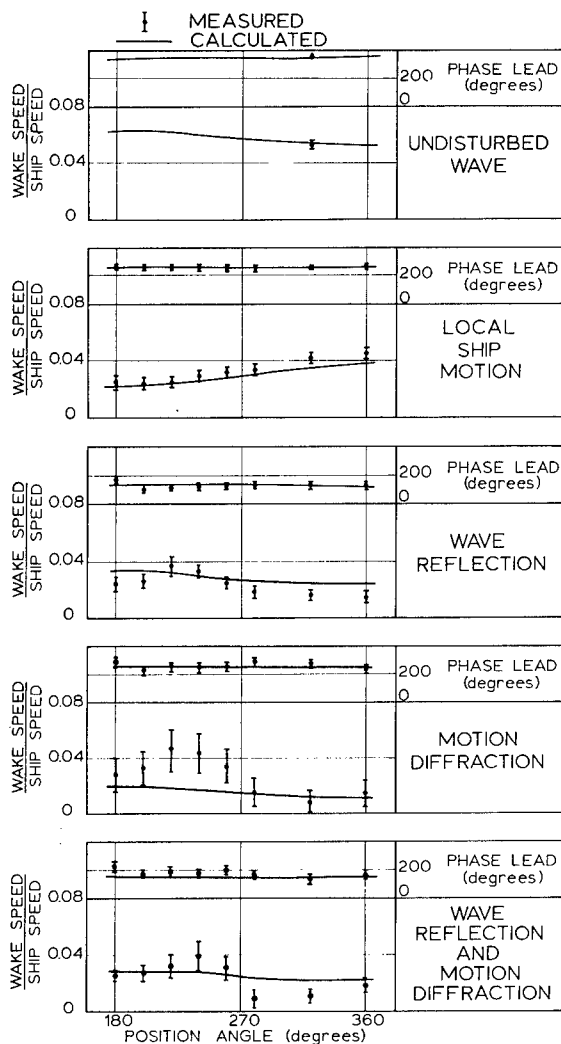


Figure 15 - The Various Contributions to the Axial Component of the Wake Speed Amplitude per Unit Wave Amplitude Ship Speed 20 kn. Wave Period  $T = 8.8$  s ( $\lambda/L = 1.25$ )

For the local ship motion contribution some discrepancies exist between measurement and calculation for the lower measurement locations in the propeller disc. This can be explained by the fact that the calculation underestimates pitch for this wave length, so the pitch contribution in the local surge is less than measured.

The reflected wave contribution as determined from the captive model test series shows a good agreement with the calculations.

Finally the motion diffraction contribution is determined. Due to the successive subtraction of the known contributions from the directly measured value, the error margin is relatively large. Except for the locations in the wake of the struts, the agreement is still good.

In Figure 15 also the sum of the contributions of wave reflection and motion diffraction is given, and measurement and calculation

agree very well.

Considering in general the results of the calculations, the various calculated contributions lay within the error margins of the measurements, so it may be concluded that the calculation method incorporates the prime aspects of the unsteady wake field correctly.

#### 4.5 Correlations for Axial Velocity at Zero Speed

In order to further calibrate the computation method a series of model tests were carried out to measure the wake velocity variations for zero ship speed. The results are presented in Figure 16 and the same tendency as discussed for the cases with forward speed is present: the calculated amplitudes are generally slightly higher than the measurements.

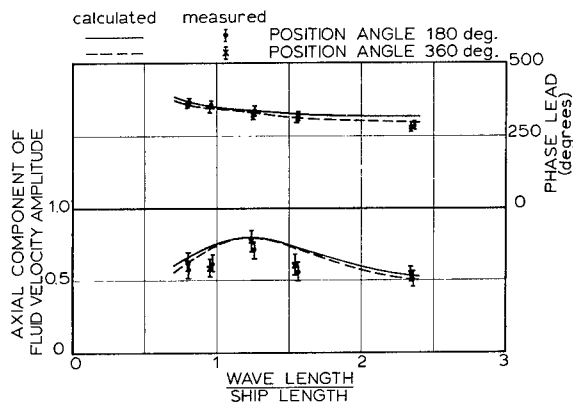


Figure 16 - Fluid Velocity at Propeller Position for Zero Ship Speed and Unit Wave Amplitude

For the condition with  $\lambda/L = 1.25$  some details are given in Table 4. It may be concluded that for the zero forward speed case the calculation method is reliable to determine the ship motions as well as the unsteady wake field.

Table 4 - Comparison between Measurement and Calculation for Unit Wave Amplitude and Zero Ship Speed Wave Period  $T = 8.8$  s ( $\lambda/L = 1.25$ )

Quantity	Notation	Measured		Calculated	
		Amplitude	Phase lead	Amplitude	Phase lead
Surge of ship	$x$	0.45 m	95°	0.46 m	88°
Pitch of ship	$\theta$	1.74 deg.	26°	1.79 deg.	18°
Axial fluid velocity	$V_x$	0.72 m/s	338°	0.79 m/s	333°
Axial fluid velocity contributions due to local motion	$\dot{\xi}_p$	0.39 m/s	292°	0.40 m/s	288°

## 5. APPLICATION IN PROPELLER CALCULATIONS

### 5.1 Review of Calculated Conditions

The conditions for which calculations have been carried out with the propeller program ANPRO are given in Table 5.

Table 5 - Review of Wave and Propeller Conditions in Calculations

Wave length Ship length $\lambda/L$	Wave ampli- tude $\tau_a$ (m)	Phase $\epsilon$ (deg.)	Propeller revolu- tions $N_s$ (Hz)	Cavita- tion number at shaft centre $\sigma_n$
-	-	-	2.367	3.141
0.8	1.0	0	2.487	2.810
0.95	1.0	0	2.557	2.624
1.25	1.0	0	2.515	2.752
1.25	1.0	90	2.515	2.850
1.25	1.0	180	2.515	2.812
1.25	1.0	270	2.515	2.714
1.55	1.0	0	2.435	2.970
2.35	1.0	0	2.382	3.104
1.25	2.0	0	2.898	2.049

The phase  $\epsilon$  indicates the position of the wave crest with respect to the propeller position in the quasi-static calculation. For these conditions the local velocities and local pressures have been calculated according to the relations derived in Section 3.3. The cavitation number  $\sigma_n$  is defined as:

$$\sigma_n = (p(\bar{x}, t) - p_v) / (0.5 \rho N_s^2 D^2)$$

in which:

$p(\bar{x}, t)$  = the local pressure

$p_v$  = the vapour pressure of sea water

$N_s$  = number of propeller revolutions per second

$D$  = propeller diameter.

In Figures 17 and 18 the results of the calculations have been plotted in a diagram of the blade section cavitation number  $\sigma_v$  versus effective angle of attack  $\alpha_e$ , where:

$$\sigma_v = (p(r, \theta) - p_v) / (0.5 \rho V_R^2)$$

in which:

$p(r, \theta)$  = the pressure at the midchord position of the blade section

$V_R$  = the local resultant velocity.

Furthermore:

$\alpha_e$  = the effective angle of attack based on the two-dimensional interpretation of the calculated three-dimensional pressure distribution.

The results given in Figures 17 and 18 apply to the blade section where  $r = 0.8$  of the propeller outer radius. For this section also the characteristics in a uniform inflow have been calculated and the so-called cavitation free conditions are determined. In the figures, the shaded area indicates the operational condi-

tions where the minimum pressures at the pressure or suction side of the profile remain higher than the vapour pressure.

It has to be noted that in the present case the actual conditions are rather away from the cavitation free conditions. This is connected to the fact that the propeller is a stock propeller, which is not optimized as a newly designed propeller would have been. Nevertheless the discussion in the next sections is valid.

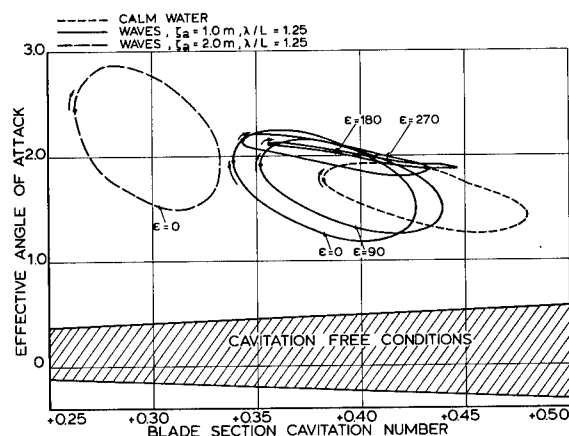


Figure 17 - The Effect of Wave Amplitude and Wave Crest Position on the Cavitation Conditions of the Propeller

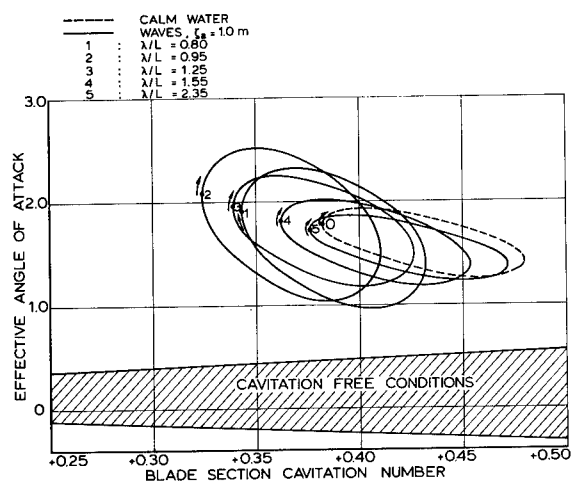


Figure 18 - The Effect of Wave Length on the Cavitation Conditions of the Propeller



## 5.2 Results for $\lambda/L = 1.25$

These results are given in Figures 17 and 19. The four loops in Figure 17 correspond to different phases during a wave period. Apparently there are situations in which the angle of attack variations during a propeller revolution become very much reduced. For comparison also the loop for still water is given (dotted line).

The loops in waves show a slightly smaller variation in cavitation number but the angle of attack variations may cover a larger interval than without waves. The conditions for phase  $\epsilon = 0$  seem representative for the most unfavourable situation. For this phase another wave amplitude has been considered, the results of which are also given in Figure 17. So, three wave amplitudes (0, 1 and 2 m respectively) are compared. Due to the effect of RPM increase in waves, to maintain speed, the operational loops shift to lower cavitation numbers and higher angles of attack. Furthermore, angle of attack variations become stronger.

Figure 19 shows cavitation patterns at the suction side of the propeller for a number of blade positions. The increase in cavitation length due to waves agrees with the above considerations as to Figure 17.

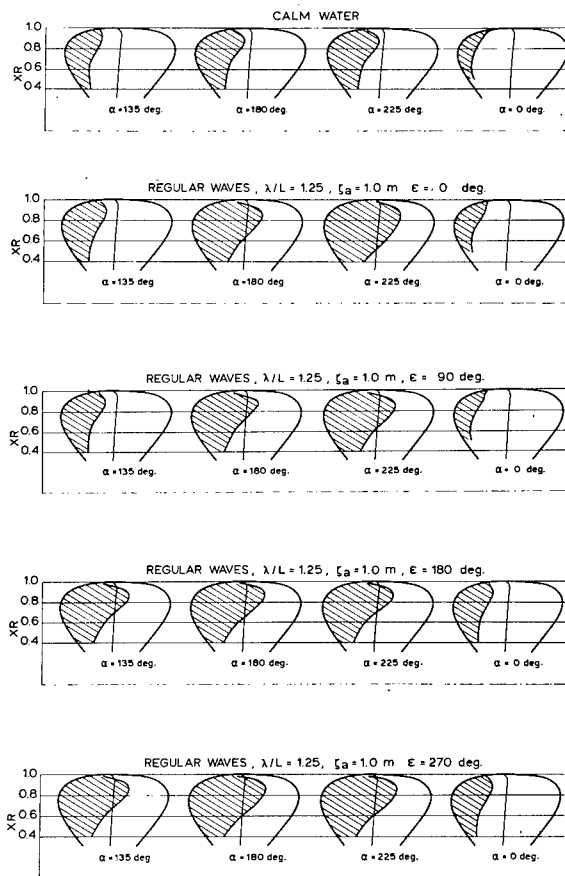


Figure 19 - Predicted Sheet Cavitation on the Propeller

## 5.3 Comparison of Results for Various Wave Periods

In Figure 18 the results for various wave periods (phase  $\epsilon = 0$  deg.) are compared. For the longest wave the loop is quite close to the no-wave conditions. For shorter waves the influence of waves becomes gradually stronger, except for the shortest wave. For this condition the behaviour is different.

According to Figures 13 and 14 the pitch and surge responses are small for the shortest wave. On the other hand, as shown in Figures 8 through 12, the local velocity variations of the wake are not reduced. Furthermore, the local pressures are in the same order of magnitude as for condition III for instance. Apparently the effect of the smaller ship motions are to a large extent compensated by the effects of wave orbital velocity and relative motion of the water surface with respect to the ship. Accordingly, it is concluded that a complete picture of the influence of waves and ship motions on wake velocity and local pressures is necessary before a statement about changes in cavitation condition for the propeller can be made.

Furthermore, from the propeller calculations it follows in general that:

- The angle of attack of a typical propeller blade section becomes higher and shows larger variations in waves than for the calm water condition.
- The cavitation number decreases but the variations become slightly smaller.
- In view of the width of the cavitation free conditions area, it seems impossible to avoid cavitation completely, but by designing the propeller in such a way that the location of the cavitation free conditions is adapted to the conditions in waves, the cavitation performance can be strongly influenced.

## 6. CONCLUSIONS

In the present investigation the effect of waves on the wake velocity variations and the consequences for propeller design have been considered. The following conclusions were drawn:

- Reliable measurement of varying wake velocity can be carried out using Laser-Doppler velocimeter techniques.
- Linearized potential theory calculations for the fluid flow around the ship travelling in waves were carried out and the results were in good agreement with the measurements. Hence, the superposition principle appears to be valid for these calculations.
- In order to obtain reliable information on the effect of waves on the cavitation behaviour of the propeller it is imperative to consider the influence of both waves and ship motions on the local fluid velocities and local pressures to the fullest extent possible.
- For the propeller design it seems impossible to avoid cavitation completely but if the designer takes into account the wave climate

in the area of operation of the ship, it is possible to adapt the propeller in such a way that the long-term cavitation performance is considerably improved.

#### REFERENCES

- Bruin, W. de and Versmissen, A.G.P. (1979): An Application of Laser Doppler Velocimetry in Ship Hydrodynamics. Abstract TH Delft Symposium on "Eigenschappen en Toepassing Laserstraling".
- Gent, W. van (1975): Unsteady Lifting Surface Theory for Ship Screws: Derivation and Numerical Treatment of Integral Equation. Journal of Ship Research, Vol. 19, No. 4.
- Gent, W. van (1977): On the Use of Lifting Surface Theory for Moderately and Heavily Loaded Ship Propellers. NSMB Publication No. 526.
- Gerritsma, J. and Beukelman, W. (1972): Analysis of the Resistance Increase in Waves of a Fast Cargo Ship. International Shipbuilding Progress, Vol. 19, No. 217.
- Helle, H.P.E. and Hageman, L.A.S. (1979): Fatigue Damage Accumulation in Marine Propellers. 4th Lips Symposium, Drunen.
- Huijsmans, R.H.M. and Dallinga, R.P. (1983): Non-linear Ship Motions in Shallow Water. International Workshop on Ship and Platform Motions, Berkeley.
- Jessup, S.D. and Boswell, R.J. (1982): The Effect of Hull Pitching Motions and Waves on Periodic Propeller Blade Loads. 14th Symposium on Naval Hydrodynamics, Ann Harbour, Michigan.
- Jonk, A. and Beek, J. van de (1977): Investigation into the Effect of Model Scale on the Performance of Two Geosim Ship Models, Part I. Publication M19 of the Netherlands Maritime Institute.
- Lammeren, W.P.A. van and Vossers, G. (1957): New Facilities of the NSMB at Wageningen, B. The Seakeeping Laboratory. International Shipbuilding Progress, Vol. 4, No. 29.
- Noordzij, L. (1976): Pressure Field Induced by a Cavitating Propeller. International Shipbuilding Progress, Vol. 23, No. 260.
- Noordzij, L. (1978): Consideration on the Hull Excitation Force Induced by a Cavitating Propeller. International Shipbuilding Progress, Vol. 25, No. 288.
- Oortmerssen, G. van (1976): The Motions of a Ship in Shallow Water. Ocean Engineering, Vol. 3.
- Salvesen, W., Tuck, E. and Faltinsen, O. (1970): Ship Motions and Sea Loads. Transactions SNAME '79.
- Sluijs, M.F. van (1972): Performance and Propeller Load Fluctuations of a Ship in Waves. Publication No. 163S of the Netherlands Ship Research Centre TNO.

# SIMULATION OF COMBINED ENGINE AND RUDDER MANEUVERS USING AN IMPROVED MODEL OF HULL-PROPELLER-RUDDER INTERACTIONS

PETER OLTMANN AND SOM D. SHARMA

## ABSTRACT

Digital simulations of combined engine and rudder maneuvers are presented for two representative ship types, namely a single-screw tanker and a twin-screw center-rudder container carrier. The hydrodynamic coefficients occurring in the dynamical equations have been derived from special four-quadrant force measurements on ship models in the captive mode and partially validated by trajectory measurements in the free-running mode, both by means of the Computerized Planar Motion Carriage at the Hamburg Ship Model Basin (HSVA). Contrary to previous versions, the new mathematical model is not restricted to small changes of initial forward speed and can be applied even to maneuvers involving speed reversal. For this purpose, it was found to be necessary to adopt a compact physically motivated rather than a formal mathematical series approximation of the hydrodynamic forces as functions of motion variables and to explicitly account for the three-way hull-propeller-rudder interactions in the system.

## NOMENCLATURE

### Abbreviations

CPMC	Computerized planar motion carriage
CPRM	Constant propeller rate, model cond.
CPRS	Constant propeller rate, ship cond.
CSRS	Constant steam rate, ship condition
HSVA	<i>Hamburgische Schiffbau-Versuchsanstalt</i> (Hamburg Ship Model Basin)
ITTC	International Towing Tank Conference
MSPP	Model self-propulsion point
SSPP	Ship self-propulsion point

### Symbols

$A_R$	Total rudder area
$A_{RP}$	Rudder area swept by propeller race
$A_f, A_b$	Turbine torque parameters, Sect. 2.3
$A_o$	Propeller disk area
$a, b$	Turbine torque parameters, Sect. 2.3

$a_o, a_7$	Parameters associated with hull cross flow drag coefficient, Sect. 2.2.4
$a_8, a_9$	Turbine torque parameters, Sect. 2.3
$B_f, B_b$	Coefficient of local cross flow drag
$C_{CFD}$	Rudder drag coefficient, Sect. 2.2.7
$C_{DR}^o$	Rudder drag coefficient at $u_p/\bar{u}_R = 0$
$C_{DR}^*$	Frictional drag coefficient
$C_F$	Rudder lift coefficient, Sect. 2.2.7
$C_{LR}^o$	Rudder lift coefficient at $u_p/\bar{u}_R = 0$
$C_{LR}^*$	Propeller torque coeff., Sect. 2.2.6
$C_Q^*$	Propeller thrust coeff., Sect. 2.2.6
$C_T^*$	Parameters associated with lifting forces on the hull, Sect. 2.2.3
$c, d, e, k$	Circumferential velocity of propeller blade at 0.7 radius
$c', d', e'$	Diameter of propeller
$c_p$	Distance between propeller disk and quarter mean chord of rudder
$D$	Force in general
$d$	Center of gravity
$F$	Acceleration due to gravity
$G$	Moment of inertia about $z$ -axis
$g$	Effective moment of inertia about propeller axis
$I_{zz}$	Correction or amplification factor in general
$I_{EP}$	Interaction factors, Sect. 2.2.7
$k$	Amplification factors, Sect. 2.2.7
$k_{HR}, k_{PR}$	Length between perpendiculars
$k_{LR}, k_{DR}$	Half-length
$L$	Mass
$l$	Hydrodynamic moment about $z$ -axis
$m$	Rate of revolutions of propeller
$N$	Coordinate origin fixed in the body
$n$	Propeller torque
$O$	Engine torque
$Q$	Engine fuel rate
$Q_E$	Turbine steam rate
$q_F$	Turning radius
$q_S$	Total hull resistance
$R$	
$R_T$	

Peter Oltmann, Hamburgische Schiffbau-Versuchsanstalt, Postfach 600929, 2000 Hamburg 60, FR Germany  
Som D. Sharma, Institut für Schiffbau der Universität Hamburg, Lämmersieth 90, 2000 Hamburg 60, FRG

$r$	Rate of turn about $z$ -axis (yaw rate)
$s$	Distance along track
$T$	Draft
$T$	Period of zigzag maneuver
$T$	Propeller thrust
$t$	Thrust deduction fraction
$t$	Time
$U$	Along-track velocity of 0
$U_0$	Initial value of $U$
$u_A$	Axial velocity induced by propeller
$u_{A\infty}$	Asymptotic value of $u_A$ at infinity
$u, v$	Components of $U$ along $x, y$ -axes
$u_P$	Speed of advance of propeller
$\bar{u}_R$	Mean flow velocity past rudder
$w$	Taylor wake fraction
$X, Y$	Hydrodynamic forces along $x, y$ -axes
$x, y, z$	Coordinate axes fixed in the body
$x_G, y_G, z_G$	Coordinates of center of gravity
$x_0, y_0, z_0$	Coordinates of 0 in an earth-fixed system, Fig. 1
$\alpha_0$	Overshoot angle in zigzag maneuver
$\beta$	Drift angle
$\beta_R$	Local drift angle at rudder
$\gamma$	Yaw rate angle, Sect. 2.2.3
$\delta$	Rudder angle
$\delta_e$	Effective rudder angle
$\delta_m$	Max. value of $\delta$ in zigzag maneuver
$\epsilon$	Propeller advance angle, Sect. 2.2.6
$\rho$	Mass density of water
$\tau$	Characteristic times of zigzag maneuver, Fig. 2
$\tau_a$	Time to attain switching value $\psi_s$
$\tau_b$	Time to check yaw rate $r$
$\tau_c$	Time for counterturn
$\tau_r$	Reach time
$\tau_L$	Time lag of steering gear
$\psi$	Heading angle
$\psi_s$	Switching value of $\psi$ in zigzag man.

### Notes

As far as possible, ITTC standard symbols and the SI units have been used. Several special rules have been adopted or devised for achieving greater clarity and for generating compound symbols in a systematic and meaningful way. Vertical and italic type has been consistently used (except for Greek letters) to distinguish between abbreviations and numerical variables.

Subscript abbreviations H, P, R and I, L, C have been used singly and multiply to indicate that the subscripted quantity is associated with the hull, propeller and rudder or the ideal-fluid, lifting and cross-flow effects respectively. Subscript variables  $u, v, r$  etc. have been used to identify corresponding coefficients in a polynomial expansion for the subscripted quantity. Other subscripts and superscripts have been used in the conventional manner.

All time-independent system parameters have been ultimately reduced to nondimensional numbers, see Table 3. In many cases this has been done according to the so-called bis-system, i.e. by multiplying the (") superscripted quantity by the necessary powers of certain fundamental units of mass, length and time, namely  $m, L$  and  $\sqrt{L/g}$  respectively.

### 1. INTRODUCTION

Both the demand and the capability of simulating ship maneuvers on digital computers have grown dramatically during the last twenty years, fed by the increasing need of ship operators to define and document maneuverability on the one hand and the ready availability of ever more efficient computers on the other. A specially strong incentive has also come from the now widespread use of real-time ship simulators for the training of nautical personnel.

Any algorithm for the simulation of ship maneuvers must incorporate as a key element an explicit or implicit mathematical model of the hydrodynamics of the maneuvering vessel. For lack of a matured hydrodynamic theory dictating an all-embracing standard format, the number of heuristic mathematical models in use has also proliferated. However, it is fair to say that the three dominant models on the market are due to Abkowitz (1964), Norrbin (1970), and the Mathematical Model Group of the Society of Naval Architects of Japan (JMMG for short) as reported by Ogawa and Kasai (1978).

The highly formal and systematic Abkowitz model treats the hull-water interface essentially as a black box and is based on the notion of a maneuver being a small perturbation of an equilibrium state of steady forward motion at designed speed. Nevertheless, it has proven very successful for the simulation of arbitrary rudder maneuvers at constant engine setting as documented by the pioneering work of Strøm-Tejsten and Chislett (1966) followed by many others including our own group, cf. Oltmann and Wolff (1979) and Wolff (1981). In a modified form it has even been applied to engine maneuvers, by Crane (1973) and Eda (1974) for example, despite the fact that such maneuvers can hardly be considered "small" perturbations of an equilibrium state.

The Norrbin model is less formal, more physically motivated and very broadly conceived, even including approximate corrections for shallow and restricted water effects, cf. Berlekom and Goddard (1972) and Norrbin (1978).

The JMMG model is quite heuristic and pays special attention to hull-propeller-rudder interactions, but is also restricted to maneuvers retaining considerable forward speed. It works alright for rudder maneuvers as exemplified by Matsumoto and Suemitsu (1981). Moreover, a great amount of additional effort has been undertaken in Japan recently to cover also stopping maneuvers, as documented by Tanaka and Miyata (1977), Yoshimura and Nomoto (1978), Fujino et al. (1979) and summarized in the latest Report of the Maneuverability Committee of the 17th ITTC (1984).

The principal purpose of this paper is to

present an alternative mathematical model suitable for the digital simulation of combined engine and rudder maneuvers for a wide range of surface ships. The core of this model is a rather new scheme for the mathematical approximation of the complex hydrodynamic forces generated in response to the motion of a maneuvering hull and to the operation of its primary control organs (rudder and screw propeller). This new approach, necessitated by the inadequate performance of previous models in the vicinity of zero forward speed, has evolved gradually over the last five years. Portions of it have already appeared in print, cf. Sharma and Zimmermann (1981) and Sharma (1982a). However, a comprehensive description of the total model accompanied by examples of simulated maneuvers is being published here for the first time. The main advantages claimed for the new model are applicability to forward and backward motion, explicit accounting of the three-way hull-propeller-rudder interaction, corrections for major scale effects, and the modeling of engine characteristics up to and even beyond speed reversal.

## 2. MATHEMATICAL MODEL

### 2.1. Dynamical Equations

The equations of motion of a surface ship maneuvering in the horizontal plane with three degrees of freedom (namely surge, sway and yaw) can be written down as usual in the following form (see also Fig. 1):

$$\dot{x}_0 = u \cos \psi - v \sin \psi \quad (1)$$

$$\dot{y}_0 = u \sin \psi + v \cos \psi \quad (2)$$

$$\dot{\psi} = r \quad (3)$$

$$(\dot{u} - vr - r^2 x_G) m = X \quad (4)$$

$$(\dot{v} + ur + \dot{r} x_G) m = Y \quad (5)$$

$$\dot{r} I_{zz} + (\dot{v} + ur) x_G m = N \quad (6)$$

The basic assumptions at this stage are that the ship may be treated as a rigid body and that the "vertical" motions of heave, pitch and roll are either negligible or at least decoupled from the "horizontal" motions of surge, sway and yaw. The external force-couple  $X, Y, N$  acting on the ship will in general comprise applied forces as well as complex hydrodynamic and aerodynamic reactions to the time history of the ship's motion and appropriate control actions. The various competing models for the simulation of ship maneuvers currently in vogue differ mainly in which forces they take into account and how these are explicitly related to the numerous variables and parameters of the system.

Consistent with the limited scope of this paper we shall consider here exclusively hydrodynamic response forces of the quasisteady type. These will be discussed in due detail in the following section. However, there are two particular aspects of these forces, pertaining to

the general format and number of the dynamical equations, which are better anticipated here.

Firstly, these forces are found to depend in a significant way on the rudder angle  $\delta$  and the propeller rate  $n$ . The question therefore arises whether the variables  $\delta, n$  can be simply treated as control input or whether additional dynamic equations must be introduced accounting for the inertia of the steering gear and the propulsion plant. The compromise attitude adopted here is that the rudder angle may be considered as a direct control variable subject to simple constraints whereas the following dynamic equation is optionally added to achieve greater flexibility and realism in the simulation of engine maneuvers:

$$2\pi \dot{n} I_{EP} = Q_E - Q \quad (7)$$

Under this option the propeller torque  $Q$  depends mainly on longitudinal velocity  $u$  and propeller rate  $n$ , while the engine torque  $Q_E$  depends essentially on propeller rate  $n$  and some suitable engine input such as the fuel rate  $q_F$ . Hence we end up with seven state variables  $x_0, y_0, \psi, u, v, r, n$  and two control variables  $\delta, q_F$ .

Secondly, the hydrodynamic response forces contain the usual linear acceleration terms dictated by classical hydrodynamic theory. Hence a simple reshuffling of Equations (4-7) is required to get all the acceleration terms and only these on the left hand sides. When the linear acceleration coupling still persisting in Equations (5-6) is also eliminated by solving algebraically for  $\dot{v}, \dot{r}$  the canonical format of the dynamical equations emerges expressing the time rate of change of state as a vector function of state variables, control variables and time-independent parameters. Trajectory simulation for any given initial state and control input is then easily accomplished on a digital computer using any standard algorithm for the numerical integration of a system of ordinary differential equations.

### 2.2. Hydrodynamic Forces

#### 2.2.1. General Outline

It will be helpful to outline the basic philosophy behind our present model of the hydrodynamic response forces before going into its unavoidably complex details. As already stated, our main motivation for developing this new approach was the operational demand for simulation of combined engine and rudder maneuvers often employed in shiphandling and in emergency situations like an impending collision. Hence the primary requirement on the mathematical description of the forces was that it must not break down in the proximity of hull or propeller speed reversal, as is unfortunately the case with most conventional models utilizing longitudinal velocity  $u$  and propeller rate  $n$  as reference quantities for scaling the forces. In view of the overriding importance of this objective, certain other effects have been ignored or simplified for the time being.

Thus the ship is taken to be maneuvering in an otherwise undisturbed, homogeneous, isotropic

environment on horizontally unbounded waters of uniform depth. So the forces need not depend explicitly on the position variables  $x, y, \psi$  or the water depth, effectively decoupling the kinematic Equations (1-3) from the remaining dynamic Equations (4-7). Moreover, possible time history effects are neglected so that, except for certain linear acceleration terms dictated by potential theory, the response forces  $X, Y, N, Q$  can be supposed to depend only on the instantaneous values of just five dynamic variables  $u, v, r, n, \delta$ . Within the domain of validity delimited by these putative premises the model has been kept perfectly general. This has been achieved by introducing the following four angles (see Nomenclature):

$$\beta = \arctan(-v/u) \quad (8)$$

$$\gamma = \arctan(rL/u) \quad (9)$$

$$\delta_e = \delta + \beta_R, \beta_R = \arctan(-v_R/\bar{u}_R) \quad (10)$$

$$\epsilon = \arctan(u_P/\sigma_P) \quad (11)$$

to express all possible relative magnitudes of the five variables  $u, v, r, \delta, n$ , and by insisting that the force descriptions chosen remain valid in all four quadrants of each of these four angles. By way of comparison it may be noted that for simulating simple rudder maneuvers the range of validity required in terms of these angles is only about one tenth as large.

In order to satisfy this fourfold four-quadrant requirement it was found to be necessary to depart in three major respects from the previously used direct input-output models which blindly but elegantly expressed  $X, Y, N$  as formal polynomials of  $u, v, r, \delta$ . Firstly, the forces had to be partly decomposed into contributions associated with the system elements hull, propeller and rudder on the one hand and with the physical mechanisms labeled ideal fluid, hull lifting and cross-flow effects on the other:

$$X = X_I + X_{HL} - R_T + X_P + X_R \quad (12)$$

$$Y = Y_I + Y_{HL} + Y_{HC} + Y_P + Y_R \quad (13)$$

$$N = N_I + N_{HL} + N_{HC} + N_P + N_R \quad (14)$$

Secondly, a number of intermediate variables had to be introduced, mainly to account for interaction effects such as wake, thrust deduction, slipstream, flow rectification etc. between the three system elements. Thirdly, a wider set of physically motivated functions than mere polynomials had to be invoked to achieve reasonable accuracy without sacrificing compactness.

This four-quadrant model has so far been identified and partly validated by means of suitable model experiments in the captive and free-running modes for four representative ship types of which only two will be discussed in this paper, namely a single-screw tanker (see Table 1 and Fig. 3) and a twin-screw center-rudder container carrier (see Table 2 and Fig. 4). It needs to be said that such four-quadrant experiments (specially in the yaw rate angle  $\gamma$ ) were rendered feasible only by the availability

of our Computerized Planar Motion Carriage (CPMC) described previously at these Symposia, cf. Grim et al. (1976) and Oltmann et al. (1980). To our knowledge no comparable set of complete four-quadrant experiments has been elsewhere reported in the literature.

Although our model experiments covered all four quadrants completely and uniformly, see Sharma and Zimmermann (1981), the present analysis has been significantly simplified by taking advantage of the nearly perfect port-and-starboard symmetry inherent in every ship. The only hydrodynamically relevant asymmetry stems from the rotation in the slipstream of a single-screw propeller. We have isolated its effect by comparing the measured forces for corresponding odd and even values of  $\beta, \gamma, \delta$  and lumped it up in just two terms, namely  $Y, N$ . The remaining terms in Eq. (12-14), practically all of which are directly or indirectly affected by the action of the propeller, thus refer to a symmetrized system. Consequently, the forces are either exactly symmetric ( $X$ ) or anti-symmetric ( $Y, N$ ) functions of the angles  $\beta, \gamma, \delta$ , and need to be displayed in the first two quadrants only.

## 2.2.2. Ideal Fluid Effects

According to a famous theorem of potential theory the hydrodynamic forces generated by the irrotational flow of an otherwise undisturbed, unbounded ideal fluid in response to the general motion of an arbitrarily shaped rigid body can be explained in terms of an "added inertia" tensor consisting of a symmetric 6x6 matrix of coefficients determined by the body form alone. An often cited classical derivation of this result can be found in Lamb (1932, p. 160 ff.) and a modern marine hydrodynamic version in Newman (1977, p. 135 ff.). A particularly perspicuous rendering of the complete expressions for these forces on a body moving with six degrees of freedom was given in the present nomenclature by Imlay (1961).

If we ignore the wavemaking at the free surface - a reasonable simplification for low Froude numbers in the present context - the horizontally maneuvering surface ship becomes equivalent to (the lower half of) a mirror-symmetric double-body moving in an unbounded fluid with three degrees of freedom only. The relevant portion of the added inertia tensor then reduces to the following 3x3 matrix:

$$\begin{bmatrix} -X_u^* & -X_v^* & -X_r^* \\ -Y_u^* & -Y_v^* & -Y_r^* \\ -N_u^* & -N_v^* & -N_r^* \end{bmatrix}$$

The symbols are chosen to reflect the immediate interpretation of the individual elements of the inertia tensor as acceleration derivatives, i.e. as factors of proportionality for the forces and moments with which the fluid resists the accelerations of the body. The port and starboard symmetry inherent in almost every hull form entails the further simplifications:

$$X_v^* = Y_u^* = 0, \quad X_r^* = N_u^* = 0 \quad (15)$$

The near fore-and-aft symmetry, also usually prevailing, implies that the remaining coupling coefficients are small compared to the direct effects:

$$Y_{\dot{r}} = N_{\dot{v}} \ll X_{\dot{u}}, Y_{\dot{v}}, N_{\dot{r}} \quad (16)$$

and the slenderness of the hull ( $B, T \ll L$ ) ensures that the longitudinal effects are small compared to the transverse effects:

$$X_{\dot{u}} \ll Y_{\dot{v}}, N_{\dot{r}} \quad (17)$$

A somewhat surprising result of this theory is that although every single element of the inertia tensor may be considered an acceleration derivative the complete final expressions for the forces also contain terms involving velocities. Accordingly, our model comprises the following expressions for the forces associated with "ideal fluid" effects:

$$X_I = X_{\dot{u}} \dot{u} + X_{v\dot{r}} v \dot{r} + X_{\dot{r}\dot{r}} \dot{r}^2 + X_{v\dot{v}} v \dot{v} \quad (18)$$

$$Y_I = Y_{\dot{v}} \dot{v} + X_{\dot{u}\dot{r}} \dot{u} \dot{r} + Y_{\dot{r}\dot{r}} \dot{r}^2 \quad (19)$$

$$N_I = N_{\dot{r}} \dot{r} + N_{\dot{v}} (\dot{v} + u \dot{r}) + (Y_{\dot{v}} - X_{\dot{u}}) u v \quad (20)$$

It is worth noting that these expressions deviate in certain details from the strict potential theory. The latter would require

$$X_{v\dot{r}} = -Y_{\dot{v}}, X_{\dot{r}\dot{r}} = -Y_{\dot{r}} = -N_{\dot{v}}, X_{v\dot{v}} = 0 \quad (21)$$

However, since our goal is not to estimate the true ideal fluid effects - amenable to computation only - but to simulate a part of the real effects observed in model experiment after the pattern of potential theory, this slight generalization comprising eight distinct form-dependent parameters instead of only four allowed by the strict theory seems justified.

The nondimensionalized numerical values of these eight parameters for our tanker form, as identified by suitable experiments, are documented in Table 3. It will be seen that the only serious departure from the mandates of the theory is the significant nonequality of the derivatives  $X_{v\dot{r}}$  and  $-Y_{\dot{v}}$ . Of particular interest in the context of maneuvering are the side force and yaw moment in response to the velocities  $u, v, r$  in steady motion. The ideal fluid contributions to these forces according to the above equations are depicted in nondimensional coefficient form as functions of drift angle and yaw rate angle by the long dashed curves in Figs. 5 and 6 respectively, in relation to the other contributions explained in subsequent sections. It will be noted from Fig. 5 (bottom) that the term  $(Y_{\dot{v}} - X_{\dot{u}})uv$ , sometimes called the Munk moment, plays a dominant role in maneuvering dynamics.

### 2.2.3. Hull Lifting Effects

Although a displacement hull - unlike a hydrofoil or rudder - is not primarily designed to generate circulation and lift, it nevertheless acts like a slender lifting body in inclined flow. The resulting side force and yaw

moment in response to the combined longitudinal and transverse motion play a crucial role in maneuvering. Our model of these lifting effects is based on three simplified principles of airfoil theory, see for instance Prandtl and Tietjens (1934, p. 144 ff.). First, the lift  $F_L$  is proportional to the underwater lateral area, the stagnation pressure of the effective inflow, and the sine of twice the effective angle of attack; it acts normal to the inflow. Second, the lift is accompanied by a parasitic induced drag  $F_D$  proportional to the square of the lift and acting parallel to the inflow. Third, the yaw moment is obtained by multiplying the resulting side force with an effective lever representing the longitudinal distance  $x_F$  of the center of action of the lifting forces  $F$  from the coordinate origin. Under these assumptions the lifting effects can be correctly approximated over four quadrants of the angle of attack by a minimum of three empirical constants for a given hull shape and flow configuration.

Thus the effect of drift ( $u$  and  $v$ ) can be quantified in a straightforward manner by the three equations:

$$F_L = c L T \frac{\rho}{2} (u^2 + v^2) \cos \beta \sin \beta \quad (22)$$

$$F_D = d F_L \cos \beta \sin \beta \quad (23)$$

$$x_F = -\frac{e}{c} L \operatorname{sgn} u \quad (24)$$

incorporating the coefficients  $c, d, e$  as three nondimensional, positive hull-form parameters. The factor  $\operatorname{sgn} u$  accounts for the fact that the hydrodynamic trailing edge responsible for the generation of lift through the Kutta condition lies at the stern for  $u > 0$  and at the stem for  $u < 0$ . The equivalent force-couple resolved along body coordinates becomes:

$$X = F_L \sin \beta - F_D \cos \beta \quad (25)$$

$$Y = F_L \cos \beta + F_D \sin \beta \quad (26)$$

$$N = -\frac{e}{c} L Y \operatorname{sgn} u \quad (27)$$

The situation in yaw ( $u$  and  $r$ ) is analogous but slightly more complicated. Here the steady motion of the hull along a circular arc gives rise to a centripetal lift, somewhat comparable to the action of a cambered body in steady translation. In any case, an additional constant  $k$  is desirable to average the locally variable transverse velocity and define an effective angle of attack at the active trailing edge:

$$\gamma^* = \arctan \left( \frac{k r L \operatorname{sgn} u}{u} \right) \quad (28)$$

which differs subtly from the purely kinematic yaw rate angle  $\gamma$  used to identify the relative magnitudes of  $u$  and  $r$ . The lifting effect of yaw is then expressed by equations analogous to (22-27) substituting  $k r L \operatorname{sgn} u$  for  $-v$ ,  $\gamma^*$  for  $\beta$ , and three new form parameters  $c', d', e'$  for  $c, d, e$ .

As an example, the numerical values of these seven parameters as determined from suit-

able model experiments for our tanker hull are listed in Table 3. Their contributions to side force and yaw moment in response to drift and yaw are plotted in Figs. 5 and 6 as the short-dashed curves for the sake of comparison with the two other effects. Attention is called to the following features. First, in our model the ideal fluid and lifting effects together constitute what are ordinarily called "linear" terms in the expansions for side force and yaw moment about the equilibrium point  $v, r = 0$ . Second, single analytical expressions could serve in four quadrants only because we made the lift proportional to the sine of twice the angle of attack instead of just the angle of attack as is common practice. Third, a constant position for the center of lift (somewhere in the active after body) makes sense only because we have segregated other effects, especially the Munk moment.

The final step required for completing the description of hull lifting effects is the treatment of a combined drift and yaw motion. This synthesis has been effected in a heuristic way by a linear combination of weighted transverse velocities, making sure that the limiting cases come out alright. The final expressions, now directly in terms of the velocities  $u, v, r$ , are as follows:

$$X_{HL} = \frac{\rho}{2} LT \frac{u(c'kr\lg nu - cv)}{\sqrt{u^2 + (kr\lg nu - v)^2}} \times \left\{ (kr\lg nu - v) - \frac{u^2(d'kr\lg nu - dv)}{u^2 + (kr\lg nu - v)^2} \right\} \quad (29)$$

$$Y_{HL} = \frac{\rho}{2} LT \frac{u^2(c'kr\lg nu - cv)}{\sqrt{u^2 + (kr\lg nu - v)^2}} \times \left\{ 1 + \frac{(d'kr\lg nu - dv)(kr\lg nu - v)}{u^2 + (kr\lg nu - v)^2} \right\} \quad (30)$$

$$N_{HL} = -\frac{\rho}{2} L^2 T \frac{u|u|(c'kr\lg nu - cv)}{\sqrt{u^2 + (kr\lg nu - v)^2}} \times \left\{ 1 + \frac{(d'kr\lg nu - dv)(kr\lg nu - v)}{u^2 + (kr\lg nu - v)^2} \right\} \quad (31)$$

We note parenthetically that the use of the above expressions beyond speed reversal ( $u=0$ ) with parameters  $c, d, e$  etc. identified for forward motion ( $u>0$ ) is tantamount to ignoring the minor fore-and-aft asymmetry of the hull, which is generally permissible. However, if higher accuracy is required for reverse motion ( $u<0$ ) only the numerical values of the parameters need be slightly changed, retaining the general format of these expressions.

#### 2.2.4. Hull Cross-Flow Effects

The essentially nonlinear cross-flow forces on the hull in response to its transverse motion are relatively large, for the hull is

purposely designed to have a low longitudinal and a high transverse resistance. They are modeled here according to a simple strip theory along the lines of Norrbin (1978). The elementary side force  $dY_{HG}$  on a hull element of length  $dx$  is assumed to be proportional to the stagnation pressure of the local transverse flow velocity  $(v+rx)$ , the local draft  $T(x)$  and the local coefficient of cross-flow drag  $C_{CFD}(x)$ . So the total side force and yaw moment can be expressed as follows:

$$Y_{HC} = -\frac{\rho}{2} \int_{-l_a}^{l_f} T(x) C_{CFD}(x) (v+rx) |v+rx| dx \quad (32)$$

$$N_{HC} = -\frac{\rho}{2} \int_{-l_a}^{l_f} T(x) C_{CFD}(x) (v+rx) |v+rx| x dx \quad (33)$$

These integrals can be solved in closed form using suitable analytical approximations (e.g. polynomials) for the functions  $T(x)$  and  $C_{CFD}(x)$ .

In special cases (e.g. asymmetric profile, inclined keel, trim or heel) it may be useful to allow for different lengths of afterbody and forebody  $l_a, l_f$  as well as for a variable draft  $T(x)$ . In most cases, however, the following simplifications prevail:

$$l_a = l_f = l, \quad T(x) = \text{const} = T \quad (34)$$

As regards the local variation of cross-flow drag coefficient, it has been found convenient to use a high-order four-term polynomial such as

$$C_{CFD}(x) = a_0 + a_7(x/l)^7 + a_8(x/l)^8 + a_9(x/l)^9 \quad (35)$$

which is well suited to approximate a fairly constant value over the parallel midbody, rising substantially toward the ends with a certain amount of asymmetry (to account for the propeller or a bulb for instance), as illustrated in Fig. 8 for our tanker form. The reason for using just four terms is that the four unknown coefficients  $a_0, a_7, a_8, a_9$  can be fitted exactly to the four measured values of side force and yaw moment coefficients at zero forward speed ( $\beta = 90^\circ$  and  $\gamma = 90^\circ$ ) where pure cross-flow effects can be observed without interference from ideal-fluid or lifting effects.

Note that the above analytical expressions are not used for determining the cross-flow forces *a priori* but in effect for interpolating them continuously over the four quadrants of drift angle and yaw rate angle (as well as their combinations) on the basis of their observed values at zero longitudinal motion and their theoretical values (namely zero) at zero transverse motion ( $\beta = \gamma = 0$ ). As shown by the dash-dotted curves in Figs. 5 and 6 the relative importance of cross-flow forces increases steadily with decreasing longitudinal motion and is maximum at  $\beta = 90^\circ$  and  $\gamma = 90^\circ$ . The dominant effects are a resistive side force in



response to drift and a resistive yaw moment in response to yaw rate. The rather weak coupling manifested as side force in response to yaw rate and yaw moment in response to drift arises, of course, from the small fore-and-aft asymmetry of the hull.

The strictly nonlinear mechanism by which simultaneous drift and yaw unite to generate a combined side force and yaw moment is automatically taken care of by the above formulas. This is illustrated in nondimensional coefficient form in Fig. 7 for all possible combinations of transverse velocity  $v$  and yaw rate  $r$ . In addition, the contribution of each term of the polynomial  $C_{CFD}(x)$  is individually shown. It is seen that the even terms  $a_0, a_2$  (responsible for the direct effects) dominate, while the odd terms  $a_1, a_3$  (responsible for the coupling) largely annihilate each other. It has been found that the total effects are quite insensitive to the polynomial degree chosen for representing  $C_{CFD}(x)$ . For instance, an alternative calculation based on the same experimental data but a third degree polynomial ( $a_0, a_1, a_2, a_3$ ) for interpolation yielded a somewhat unrealistic curve for the associated local drag coefficient but practically the same integrated cross forces for all transverse motions.

### 2.2.5. Hull Resistance

The ordinary hull resistance to pure longitudinal motion is measured in a routine model test and extrapolated to full-scale in the conventional manner by decomposing the nondimensional coefficient of total resistance:

$$C_T = 2R_T / \rho S u^2 \quad (36)$$

into viscous and wave components:

$$C_T(R_n, F_n) = (1+k) C_F(R_n) + C_W(F_n) \quad (37)$$

subject to Reynolds and Froude scaling respectively, and using the 1957 ITTC correlation line to calculate the Reynolds-number dependent frictional coefficient  $C_F$ . In the simulation algorithm, however, a suitable polynomial fit is preferred to avoid numerical problems with the term  $C_F(R_n)$  near zero forward speed:

$$R_T(u) = R_{Tu} u + R_{Tu|u}|u| + R_{Tu|u|u} u^3 \quad (38)$$

The nondimensionalized polynomial coefficients for the tanker form are included in Table 3. Obviously, the numerical values must be different for the model condition and the ship condition owing to the scale effect on viscous resistance. Strictly speaking, the values given were determined for forward motion. However, the formula applies also to backward motion without serious error. If higher precision is desired, a separate set of coefficients may be used for negative speeds or the expression modified to include a small even term in  $u$ .

### 2.2.6. Propeller Forces

Accurate modeling of the propeller forces is of utmost importance for the correct simula-

tion of engine maneuvers, specially those involving thrust, torque and speed reversal, such as the crashback. The forces of primary interest are, of course, the thrust  $T$ , and the torque  $Q$  if the additional dynamical Equation (7) is also used. Obviously, the conventional representation of propeller characteristics in terms of advance coefficient  $J$  and thrust and torque coefficients  $K_T, K_Q$  is unsatisfactory because  $J$  is ambiguous for negative speeds and everything breaks down at  $n=0$ :

$$J = u_p / n D, \quad K_T = T / \rho n^2 D^4, \quad K_Q = Q / \rho n^2 D^5 \quad (39)$$

The proper way to cover all possible combinations of axial and rotational motion is to introduce an advance angle  $\epsilon$  and new force coefficients  $C_T^*, C_Q^*$  in terms of axial and circumferential blade velocities  $u_p, c_p$  at a significant radius:

$$\epsilon = \arctan(u_p / c_p), \quad c_p = 0.7 \pi n D \quad (40)$$

$$C_T^* = 2T / \rho A_o (u_p^2 + c_p^2) \quad (41)$$

$$C_Q^* = 2Q / \rho A_o D (u_p^2 + c_p^2) \quad (42)$$

For any given propeller the functions  $C_T^*(\epsilon)$ ,  $C_Q^*(\epsilon)$  can be determined by experiment and smoothly interpolated in four quadrants by finite Fourier series, as was first demonstrated for the Wageningen B-Screw Series by van Lammeren et al. (1969). However, this mathematically elegant approximation is not very efficient, for as many as  $2 \times 40$  Fourier coefficients are required to achieve adequate accuracy, cf. also Laudan (1974). We therefore advocate a more flexible approach pursuing the principle of parsimony. Our simulation algorithm currently employs a composite approximation. Over the short range of advance angles between the bollard-pull condition ( $\epsilon=0$ ) and the zero-thrust condition ( $\epsilon=20^\circ$ ) where a high percentage accuracy is desired we recommend either tabular interpolation in the open-water diagram or a low-order algebraic or trigonometric polynomial fit. Over the remaining interval one can safely use the following compact functions:

$$C_T^*(\epsilon) = A_T \cos \epsilon |\cos \epsilon| - B_T \sin \epsilon |\sin \epsilon| \quad (43)$$

$$C_Q^*(\epsilon) = A_Q \cos \epsilon |\cos \epsilon| - B_Q \sin \epsilon |\sin \epsilon| \quad (44)$$

custom-tailored to roughly reproduce the global characteristics with just two parameters each.

By way of illustration, the relevant expressions for our tanker propeller are listed in Table 3 and plotted in Fig. 9. It will be noted that no more than five parameters are used for each force. An additional set may be optionally inserted if higher accuracy in backward motion  $-180^\circ < \epsilon < 0^\circ$  is needed.

Such economy is mandatory also in view of future extensions to account for the effect of transverse motions, which has been systematically investigated by our group, cf. Laudan (1977), but not yet incorporated into the simulation model.

Whereas in the previous Sections the com-

plex interactions between the elements hull, propeller and rudder were only implicitly included in so far as the model identification rested on forces measured on the total system, we must now account explicitly for wake and thrust deduction to adapt the open-water characteristics to the behind-hull condition. This is done by the conventional rules:

$$u_P = (1-w)u, \quad X_P = (1-t)T \quad (45)$$

Although our four-quadrant experiments in the behind-hull condition have revealed complicated variations of wake fraction  $w$  and thrust-deduction fraction  $t$  with the advance angle  $\epsilon$ , pending further analysis we have chosen to employ just two distinct values each for forward and backward motion. However, we do apply an important scale-effect correction in extrapolating the wake from model to ship according to the ITTC 1978/84 standard procedures for single and twin screws. For example, the wake fraction of our tanker decreases by about 30% from model to full-scale, see Table 3.

Finally, the side force and yaw moment generated directly and indirectly by the hydrodynamic asymmetry inherent in a single-screw ship must be modeled, cf. Saunders (1957, p. 496 ff.) and Mandel (1967, p. 332 ff.). As discussed in detail elsewhere, this effect is rather weak and sensitive in steady forward motion, cf. Oltmann et al. (1980), but quite strong and consequential in stopping or reversing when the inverted propeller slipstream hits the hull, cf. Sharma (1982b). For the present purpose it has been found sufficient to postulate a linear dependence on thrust:

$$Y_P = Y_{PT} T, \quad N_P = N_{PT} T \quad (46)$$

with the factors of proportionality assuming different values for forward and backward thrust and motion. Typical numbers are given in Table 3 for the tanker. It is almost needless to add that the terms  $Y_P, N_P$  vanish for any symmetric twin-screw arrangement as in our Fig. 4.

#### 2.2.7. Rudder Forces

The rudder being the key element in ship maneuvering deserves the most careful consideration. Our model of the rudder forces is conceptually straightforward but by no means practically so. Essentially, we treat the rudder as a symmetric control surface fully characterized by its empirical lift and drag coefficients in two quadrants, e.g. see Fig. 10. These coefficients, derived from measurements in the behind-ship condition, represent the total system response to rudder application and not merely the forces acting on the (movable part of the) rudder itself. Since the movement of the model rudder is often constrained to about  $\pm 40^\circ$  the gaps may have to be filled by reference to relevant data on similar rudders investigated in the freestream, e.g. see Thieme (1962). Unlike the smooth lifting characteristics of the slender hull, the coefficients of the rudder by virtue of its higher aspect ratio exhibit typical discontinuities reflecting stall. Hence

they must be approximated by multiple piecewise analytical functions or simple tabular interpolation, cf. Table 3.

The practical difficulties in the identification as well as subsequent simulation of rudder forces lie in the determination of the highly variable, complex flow conditions at the rudder. Here the interaction effects of the hull and the propeller come into full play. Let us first consider the relatively simple case of a rudder operating outside the slipstream, as on our container carrier (Fig. 4). Then only the hull influence needs to be taken into account, say through an average wake fraction  $w$ , and a flow rectification factor  $k_{PR}$ , so that the effective longitudinal and transverse velocities at the rudder become simply:

$$u_R = (1-w_R)u, \quad v_R = (v+wx_R)k_{HR} \quad (47)$$

This implies an effective angle of attack  $\delta$  equal to the sum of the geometric rudder angle  $\delta$  and the local drift angle  $\beta_R$ , see Eq. (10), leading to the following expressions for the effective rudder forces resolved along hull coordinates:

$$X_R = \frac{\rho}{2} A_R (u_R^2 + v_R^2) (C_{LR} \sin \beta_R - C_{DR} \cos \beta_R) \quad (48)$$

$$Y_R = \frac{\rho}{2} A_R (u_R^2 + v_R^2) (C_{LR} \cos \beta_R + C_{DR} \sin \beta_R) \quad (49)$$

$$N_R = Y_R x_R \quad (50)$$

However, if the rudder is wholly or partially immersed in the slipstream, as in the case of our tanker (Fig. 3), the additional influence of the propeller must be considered. This requires a tedious procedure involving several steps, of which only a simplified version is given here omitting a few *ad hoc* rules for treating marginal cases. First of all, the asymptotic axial velocity increment in the slipstream at infinity can be estimated from elementary momentum theory:

$$u_{A\infty} = (\text{sgn} u) \sqrt{u_P^2 + (\text{sgn} u) \frac{2T}{\rho A_O}} - u_P \quad (51)$$

Application of a factor  $k_{PR}$ , depending only on the relative distance  $d/D$  of the rudder from the propeller disk after Gutsche (1955), then yields the axial flow velocity at the location of the rudder:

$$u_{RP} = u_P + \left\{ (k_{PR} - \frac{1}{2}) \text{sgn} u + \frac{1}{2} \right\} u_{A\infty} \quad (52)$$

For estimating the area  $A_{RP}$  of the rudder subjected to this velocity, the slipstream diameter  $D_{RP}$  in way of the rudder can be calculated from the condition of continuity:

$$D_{RP}^2 u_{RP} = D^2 (u_P + \frac{1}{2} u_{A\infty}) \quad (53)$$

An average longitudinal flow velocity  $\bar{u}_R$  at the rudder can then be defined by:

$$\bar{u}_R^2 = \{ A_{RP} u_{RP}^2 + (A_R - A_{RP}) u_R^2 \} / A_R \quad (54)$$

Other investigators have, in effect, reported that the influence of the propeller on the rudder is adequately accounted for by simply sub-

stituting  $\bar{u}_R$  for  $u_R$  in Eq. (48-49), cf. Thulin (1974) or Landgraf and Müller (1975). However, our experience indicates a significant residual dependence on thrust loading, which can be expressed as a linear variation with the velocity ratio  $u_P/\bar{u}_R$  within the range (0,1):

$$C_{LR} = (1 + k_{LR} u_P/\bar{u}_R) C_{LR}^0 \quad (55)$$

$$C_{DR} = (1 + k_{DR} u_P/\bar{u}_R) C_{DR}^0 \quad (56)$$

$$N_R = (1 - k_{NR} u_P/\bar{u}_R) Y_{R,x} \quad (57)$$

This effect probably arises from the nonuniform velocity distribution over the rudder, the rotation in the slipstream and the flaplike action of the rudder behind the hull. In any case, three additional factors  $k_{LR}, k_{DR}, k_{NR}$  suffice to take care of this phenomenon. See Table 3 for the tanker. Moreover, the rudder characteristics must now refer to some particular value of the velocity ratio  $u_P/\bar{u}_R$ , for instance zero in Table 3 or one-half in Fig. 10.

Finally, it is worth emphasizing that corrections for scale effects enter into this algorithm directly through the wake fractions and indirectly through the thrust loading which varies to match the hull resistance.

### 2.3. Machinery Characteristics

Obviously the dynamics of the ship's steering gear and propulsion plant have a direct influence on the time history of its maneuvers. It is realized that for certain special tasks such as the finetuning of an autopilot an accurate and detailed knowledge of the transfer function between commanded helm and executed rudder angle is required. However, for a computation of the ship's trajectory in substantial turning or checking maneuvers we think it reasonable to treat the helm angle as a direct input variable subject to some simple constraints, such as a prescribed time lag  $\tau_L$  and given upper bounds on executable rudder angle  $|\delta|$  and rudder rate  $|\dot{\delta}|$ , the standard values being 35 deg and 2.3 deg/s respectively.

As regards the propulsion plant, our simulation model provides two independent options. Most marine engines nowadays have automatic controllers which maintain a constant rate of revolutions in face of varying load (within limits) and trigger a predetermined temporal pattern of RPM change in response to an engine command from the bridge. On some ships the RPM can be explicitly controlled from the bridge. In all these cases we treat RPM as a direct input variable subject to suitable constraints.

On the other hand, there are several situations where the RPM should be treated as an output variable subject to the dynamic equilibrium of the rotating propeller shaft. This occurs when the engine is being operated at constant fuel rate or when the RPM controller is unable to maintain a steady rate against increasing load for lack of power reserve or when the RPM controller is intentionally overridden in an emergency maneuver such as the crashback. For handling these situations our simulation model has an additional (optional) dynamic

equation (see Sect. 2.1.), which presupposes that the engine torque can be expressed as a quasisteady function of fuel rate and RPM. This so-called torque characteristic depends crucially on engine type and is very different for diesel engines and steam turbines. For the latter we adapted a fairly general bilinear formula given by Geisler and Siemer (1974):

$$q_s^* \geq 0: Q_E^* = A_f \left( \frac{q_s^* - a}{1-a} \right) (1-n^*) + B_f \left( \frac{q_s^* - b}{1-b} \right) n^* \quad (58)$$

$$q_s^* < 0: Q_E^* = A_b \left( \frac{q_s^* + a}{1-a} \right) (1+n^*) - B_b \left( \frac{q_s^* + b}{1-b} \right) n^* \quad (59)$$

Here  $q_s^*, Q_E^*$  and  $n^*$  denote nondimensional relative steam rate, engine torque and RPM respectively, each expressed as a fraction of its full rated value. Typical values of the nondimensional parameters  $a, b$  and  $A_f, B_f$  (for the main turbine) and  $A_b, B_b$  (for the astern turbine, formally implied by a "negative" steam rate) are given in Table 3. It so happens that the two prototype ships treated in this paper both had steam turbines.

It should be noted that in free-running tests with ship models in a towing tank the propulsion plant is almost invariably an electric motor with sufficient power reserve and simple RPM control. Hence the model maneuvers are normally executed at constant propeller rate irrespective of the torque characteristics of the prototype. However, devices comprising torque feedback and a programmable micro-computer are now available for driving a model propeller in accordance with a specified engine characteristic.

## 3. SAMPLE RESULTS

### 3.1. Preamble

The usefulness of the foregoing mathematical model will now be examined by dint of sample results obtained for two quite different ships, namely a single-screw tanker and a twin-screw center-rudder container carrier. Their main dimensions are listed in Tables 1 and 2, and the hull lines are displayed in Figs. 3 and 4 respectively. Not only do they represent the two most important classes of merchant ships afloat today, but they are also significantly different in their hull form parameters and propeller-rudder configurations, so as to be ideally suited as test cases for the present purpose.

For each ship three series of definitive maneuvers have been simulated, namely zigzags, turning circles, and crashbacks with and without rudder application. These are generally considered adequate for identifying the turning, checking and stopping capabilities in a comprehensive manner.

Almost every maneuver has been simulated under two distinct conditions, briefly designated CPRM and CSRS. The first condition implies a constant propeller rate corresponding to the model self-propulsion point (MSPP) for the approach speed and no scale effect corrections for model resistance and wake. This computation

is thus equivalent to a direct Froude scaling of free-running maneuvers in a model tank, where the electric drive can hold a constant RPM by virtue of its power reserve. The second condition implies the extrapolation of resistance and wake from model to full-scale according to the standard ITTC procedure and a constant fuel or steam rate corresponding to the ship self-propulsion point (SSPP) at the approach speed. The rate of revolutions then varies during the maneuver depending upon the torque characteristics of the engine and the propeller. For the crashback maneuvers, of course, the steam flux is not held constant but diverted to the astern turbine in the shortest admissible time up to the highest permissible value.

For the convenience of readers and rivals who may wish to reproduce our results or scrutinize our simulation scheme the requisite set of system parameters, besides the pertinent principal particulars, is listed for one of the ships (the tanker) in Table 3. For the same reason an adequate amount of simulation output is presented digitally in Tables 4 and 5 in addition to the customary graphs. It is not claimed, however, that the numbers reported are significant to the last listed digit. A systematic sensitivity survey has not yet been attempted for the subject model.

### 3.2. Tanker

The maneuvering hydrodynamic interest of this tanker hinges on its relatively tiny propeller operating at a high thrust loading behind a full-bodied hull so that the hull-propeller-rudder interactions are pretty pronounced and the scale effects are rather large. All maneuver simulations reported here start with a steady approach speed of 15 kn at either 98.8 RPM (MSPP) or 85.8 RPM (SSPP), the latter corresponding to 76% rated power or 79% rated steam flux.

Let us consider the zigzag maneuvers first. A partial time history of the standard  $20^\circ/20^\circ$  zigzags is plotted in Fig. 11 and selected output of two systematic series of zigzags is shown in Fig. 12, consult also Fig. 2 for definitions. Since the results marked CPRM have been previously validated by reference to trajectories of a freely maneuvering model in the CPMC tracking mode, the interest here lies in the comparison of CPRM and CSRS. Clearly, the differences are rather small, partly because of the self-correcting feedback strategy inherent in a zigzag maneuver and partly because the hydrodynamic scale effect and the differing engine characteristics tend to counterbalance each other. In general, the response times, overshoots, turning rates and transfers are slightly lower under ship conditions.

Turning now to the hard-starboard turning circle time-histories in Fig. 13 and trajectories in Fig. 14, we observe a marked difference between CPRM and CSRS, see also Table 5 for a complete overview of turning characteristics. As might have been expected the final speeds and turning rates are lower for the ship, but it is not self-evident why the drift angle should be larger and the turning circle tighter.

The real value of a simulation algorithm lies in revealing counter-intuitive behavior.

The most interesting results, however, were obtained for the crashbacks, simulated by diverting the full rated steam flux to the astern turbine within 27 seconds, without and with simultaneous rudder application, see Figs. 15 and 16. Three outstanding features are noticed. First, there is a striking tendency to turn to starboard in stopping even with rudder held amidships. Second, simultaneous hard starboard rudder hardly affects the time history but markedly shortens the advance. Third, by far the shortest advance is achieved by rudder hard to starboard while steaming full ahead!

### 3.3. Container Carrier

Our container carrier is a bit beamy but slender and has an out-of-the-rut twin-screw center-rudder configuration (Table 2 and Fig. 4). The simulations reported here all start with a steady approach speed of 16 kn either at 85.8 RPM (MSPP) or at 74.7 RPM (SSPP) corresponding to only 30% rated power or 28% rated steam flux. This modest speed with an enormous power reserve was originally chosen for the sake of correlation with some full-scale maneuver data that happened to be accessible.

The zigzag and turning circle maneuvers are shown in Figs. 17 to 20 in a manner exactly analogous to Figs. 11 to 14 for the tanker. Surprisingly, despite the conspicuous differences in hull form and propeller-rudder arrangement, the zigzag characteristics are almost indistinguishable. The turning circles, of course, show significant differences. The container carrier attains the final steady state much sooner, has no bias to starboard, a turning radius twice as large, and reverts almost exactly to original track after a complete circle. The relation of CPRM to CSRS is the same as for the tanker.

The most dramatic difference from the tanker, however, is observed in the fantastic stopping capability of the overpowered container carrier, compare Figs. 21-22 vs. 15-16. Rudder application further reduces both the stopping time and the stopping distance. In marked contrast to the tanker a hard turning circle produces the same advance as a crashback straight on the track. The shortest advance is achieved by a radical combined engine and rudder maneuver.

The authors trust this pilot probe into the vast space of combined engine and rudder maneuvers now opened to study by simulation shall serve to demonstrate the power and utility of the proposed four-quadrant model. Yet it can only be a tentative prototype likely to undergo many modifications in the foreseeable future.

### ACKNOWLEDGMENT

This paper is an offshoot of a long-term research project concerning the safety of ships against collisions, sponsored by the German Research Association (*Deutsche Forschungsgemeinschaft*) within the framework of a Special Research Pool for Marine Technology (*Sonderforschungsbereich 98 "Schiffstechnik und Schiffsbau"*) at Hamburg and Hanover.

## REFERENCES

- Abkowitz, M.A. (1964): Lectures on ship hydrodynamics - Steering and maneuverability. Hydro- and Aerodynamics Laboratory, Lyngby/Denmark, Report Hy-5.
- Berlekom, W.B.; Goddard, T.A. (1972): Maneuvering of large tankers. Transactions SNAME, Vol. 80, pp. 264-298.
- Crane, C.L. (1973): Maneuvering safety of large tankers: Stopping, turning and speed selection. Transactions SNAME, Vol. 81, pp. 213-242.
- Eda, H. (1974): Digital simulation analysis of maneuvering performance. Proc. 10th ONR Symposium on Naval Hydrodynamics, Cambridge MA/USA, pp. 181-205.
- Fujino, M.; Kirita, A.; Nishihata, A. (1979): On the manoeuvrability of ships while stopping by adverse rotation of propeller - 2nd Report (in Japanese). Journal of Kansai Society of Naval Architects of Japan, Vol. 173, pp. 45-55.
- Geisler, O.; Siemer, G. (1974): Dynamische Belastung von Schiffsdampfturbinenanlagen bei Umsteuermanövern. Schiff & Hafen, Vol. 26, pp. 213-218.
- Grim, O.; Oltmann, P.; Sharma, S.D.; Wolff, K. (1976): CPMC - A novel facility for planar motion testing of ship models. Proc. 11th ONR Symposium on Naval Hydrodynamics, London/UK, pp. 115-131.
- Gutsche, F. (1955): Die Induktion der axialen Strahlzusatzgeschwindigkeit in der Umgebung der Schraubenebene. Schiffstechnik, Vol. 3, pp. 31-33.
- Imlay, F.H. (1961): The complete expressions for "added mass" of a rigid body moving in an ideal fluid. Hydro. Lab. R & D Report 1528, David Taylor Model Basin, Carderock MD/USA.
- Lamb, H. (1952): Hydrodynamics. Cambridge University Press (Reprint of Sixth Edition, 1932), Cambridge/UK.
- Lammeren, W.P.A. van; Manen, J. D. van; Oosterveld, M.W.C. (1969): The Wageningen B-Screw Series. Transactions SNAME, Vol. 77, pp. 269-317.
- Landgraf, J.; Müller, E. (1975): Ruder im Schraubenstrahl. Jahrbuch STG, Vol. 69, pp. 361-371.
- Laudan, J. (1974): Propellerkräfte und -momente beim geradlinigen Stoppmanöver. HSVA-Report No. F4/74, Hamburg.
- Laudan, J. (1977): Zweiquadrantenmessungen bei Schräganströmung hinter einem Schiffsmodell. HSVA-Report No. 1508, Hamburg.
- Mandel, P. (1967): Ship Maneuvering and Control. Chapter VIII, Principles of Naval Architecture, SNAME, New York NY/USA, pp. 463-606.
- Matsumoto, N.; Suemitsu, K. (1981): Experimental prediction method of manoeuvring performance of ships and ocean structures. Nippon Kokan Technical Report No. 32, Tokyo/Japan.
- Newman, J.N. (1977): Marine Hydrodynamics. The M.I.T. Press, Cambridge MA/USA.
- Norrbin, N. (1970): Theory and observations on the use of a mathematical model for ship maneuvering in deep and confined waters. Proc. 8th ONR Symposium on Naval Hydrodynamics, Pasadena CA/USA, pp. 807-904.
- Norrbin, N. (1978): A method for the prediction of the maneuvering lane of a ship in a channel of varying width. Proc. Symp. "Aspects of Navigability of Constraint Waterways, Including Harbour Entrances", Delft/Holland, Vol. 3, Paper 22.
- Ogawa, A.; Kasai, H. (1978): On the mathematical model of manoeuvring motion of ships. International Shipbuilding Progress, Vol. 25, pp. 306-319.
- Oltmann, P.; Wolff, K. (1979): Vergleichende Untersuchung über das Manövrierverhalten des MARINER-Standardschiffes. Institut für Schiffbau, Hamburg, Report No. 385.
- Oltmann, P.; Sharma, S.D.; Wolff, K. (1980): An investigation of certain scale effects in maneuvering tests with ship models. Proc. 13th ONR Symposium on Naval Hydrodynamics, Tokyo/Japan, pp. 779-801.
- Prandtl, L.; Tietjens, O.G. (1957): Applied Hydro- and Aeromechanics. Dover Publications, New York NY/USA (Reprint of 1934 Edition).
- Saunders, H.E. (1957): Hydrodynamics in Ship Design, Vol. 1. SNAME, New York NY/USA.
- Sharma, S.D. (1982a): Schrägschlepp- und Drehversuche in vier Quadranten - Teil 2. Schiff & Hafen, Vol. 34, pp. 219-222.
- Sharma, S.D. (1982b): Bemerkungen über die Steuerwirkung von Propellern. Jahrbuch STG, Vol. 76, pp. 111-117.
- Sharma, S.D.; Zimmermann, B. (1981): Schrägschlepp- und Drehversuche in vier Quadranten - Teil 1. Schiff & Hafen, Vol. 33, pp. 123-125.
- Smitt, L.W.; Chislett, M.S. (1974): Large amplitude PMM tests and maneuvering predictions for a Mariner class vessel. Proc. 10th ONR Symposium on Naval Hydrodynamics, Cambridge MA/USA, pp. 131-157.
- Strøm-Tejse, J.; Chislett, M.S. (1966): A model testing technique and method of analysis for the prediction of steering and maneuvering qualities of surface ships. Proc. 6th ONR Symposium on Naval Hydrodynamics, Washington DC/USA, pp. 317-381.
- Tanaka, M.; Miyata, H. (1977): Simulation program for maneuverability of ships and its application. Japan Shipbuilding & Marine Engineering, Vol. 11, No. 4, pp. 5-14.
- Thieme, H. (1962): Zur Formgebung von Schiffsrudern. Jahrbuch STG, Vol. 56, pp. 381-426.
- Thulin, S.A.R. (1974): Discussion to Smitt and Chislett (1974). Proc. 10th ONR Symposium on Naval Hydrodynamics, Cambridge MA/USA, pp. 153-156.
- Wolff, K. (1981): Ermittlung der Manöviereigenschaften fünf repräsentativer Schiffstypen mit Hilfe von CPMC-Modellversuchen. Institut für Schiffbau, Hamburg, Report No. 412.
- Yoshimura, Y.; Nomoto, K. (1978): Modeling of manoeuvring behaviour of ships with a propeller idling, boosting and reversing (in Japanese). Journal of The Society of Naval Architects of Japan, Vol. 144, pp. 57-69.

Note: Tables 1 to 5, Figures 1 to 22 and an Addendum follow.

Table 1 Main dimensions  
of the tanker  
(HSVA Model 2507, Scale 1 : 35)

Length between perpendiculars	290.000 m
Length of waterline	296.446 m
Beam	47.500 m
Draft forward	16.196 m
Draft aft	15.964 m
Block coefficient	0.805
LCB fwd of midship section	7.243 m
Radius of gyration (z-axis)	66.360 m
Number of propellers	1
Diameter	7.910 m
Pitch ratio	0.745
Expanded area ratio	0.600
Number of blades	5
Sense of rotation	right
Number of rudders	1
Rudder area	73.500 m <sup>2</sup>
Chord length	7.150 m
Aspect ratio	1.438
Turbine plant:	
Rated power	20 608.0 kW
Rated speed	95.0 RPM
Effective moment of inertia about propeller axis	766.2 tm <sup>2</sup>

Table 2 Main dimensions  
of the container carrier  
(HSVA Model 2657, Scale 1 : 34)

Length between perpendiculars	273.000 m
Length of waterline	279.351 m
Beam	32.200 m
Draft forward	12.200 m
Draft aft	12.200 m
Block coefficient	0.611
LCB aft of midship section	5.435 m
Radius of gyration (z-axis)	61.880 m
Number of propellers	2
Diameter	6.150 m
Pitch ratio	1.200
Expanded area ratio	0.860
Number of blades	5
Sense of rotation	outward
Number of rudders	1
Rudder area	59.350 m <sup>2</sup>
Chord length	5.850 m
Aspect ratio	1.734
Turbine plant:	
Rated power	2 × 29 233.4 kW
Rated speed	136.0 RPM
Effective moment of inertia about propeller axis	2 × 948.1 tm <sup>2</sup>

Table 3 System parameters of the tanker for maneuver simulation

#### Hydrodynamic Characteristics

##### Ideal Fluid Effects:

$$\begin{aligned} X''_{\dot{u}} &= -0.0737 & X''_{v\dot{r}} &= 0.6482 \\ X''_{r\dot{r}} &= 0.0423 & X''_{v\dot{v}} &= -0.0261 \\ Y''_{\dot{v}} &= -0.7810 & Y''_{\dot{r}} &= -0.0488 \\ N''_{\dot{r}} &= -0.0394 & N''_{\dot{v}} &= -0.0357 \end{aligned}$$

##### Hull Resistance:

	(Model)	(Ship)
$R''_{Tu}$	0.00162	0.00109
$R''_{Tu u }$	0.04034	0.02364
$R''_{Tuuu}$	0.07659	0.03594

##### Interaction Factors:

$$\begin{aligned} w_R \approx w &= 0.530 \text{ (Model)} \\ w_R \approx w &= 0.370 \text{ (Ship)} \\ t &= 0.191 \\ Y''_{PT+} &= -0.030 & N''_{PT+} &= 0.015 \\ Y''_{PT-} &= 0.410 & N''_{PT-} &= -0.105 \\ k_{HR} &= 1.000 & k_{PR} &= 0.870 \end{aligned}$$

#### Machinery Characteristics

##### Steering Gear:

$$\begin{aligned} |\delta| &< 40.0 \text{ deg} & \tau_L &= 0.00 \text{ s} \\ |\dot{\delta}| &\leq 2.32 \text{ deg/s} \end{aligned}$$

##### Hull Cross-Flow Effects:

$$\begin{aligned} \alpha_O &= 0.207 & \alpha_7 &= 5.310 \\ \alpha_8 &= 3.218 & \alpha_9 &= -6.732 \end{aligned}$$

##### Hull Lifting Effects:

$$\begin{aligned} c &= 0.240 & c' &= 0.500 \\ d &= 1.000 & d' &= 1.000 \\ e &= 0.064 & e' &= 0.100 \\ k &= 0.400 \end{aligned}$$

##### Propeller Coefficients:

$$\begin{aligned} 0^\circ \leq \epsilon \leq 21^\circ: & C_T^* = -0.833 + 1.020 \cos \epsilon - 0.332 \sin \epsilon \\ & 10C_Q^* = -1.171 + 1.378 \cos \epsilon - 0.235 \sin \epsilon \\ 21^\circ \leq \epsilon \leq 180^\circ: & C_T^* = 0.099 \cos \epsilon |\cos \epsilon| - 0.671 \sin \epsilon |\sin \epsilon| \\ & 10C_Q^* = 0.158 \cos \epsilon |\cos \epsilon| - 0.824 \sin \epsilon |\sin \epsilon| \end{aligned}$$

##### Rudder Coefficients:

$\delta_e = 0 \text{ deg}$	$C_{LR}^O = 0.0000$	$C_{DR}^O = 0.0000$	$k_{LR} = 5.30$
$= 15 \text{ deg}$	$= 0.2401$	$= 0.0428$	$k_{DR} = 2.50$
$= 30 \text{ deg}$	$= 0.4539$	$= 0.1875$	$k_{NR} = 0.12$
$= 45 \text{ deg}$	$= 0.5789$	$= 0.4250$	$x_R'' = -0.50$
$= 50 \text{ deg}$	$= 0.2960$	$= 0.3057$	
$= 90 \text{ deg}$	$= 0.0329$	$= 0.5096$	

Table 4

Computed zigzag maneuver characteristics  
of the tanker at an approach speed  $U_0 = 15$  kn

Top: Constant propeller rate, model condition  
Bottom: Constant steam rate, ship condition

Rudder angle	Course change	Time to attain course change	Time to check yaw to starboard	Time for counterturn	Time to return to base course	Time to check yaw to port	Period of zigzag	Overswing to starboard	Overswing to port	Maximum transfer	Turning rate to starboard	Turning rate to port
$\delta_m$	$\psi_s$	$\tau_a$	$\tau_{b1}$	$\tau_c$	$\tau_r$	$\tau_{b2}$	$T$	$\alpha_{O1}$	$\alpha_{O2}$	$y_{O\max}$	$ \dot{r} _{\max1}$	$ \dot{r} _{\max2}$
deg	deg	s	s	s	s	s	s	deg	deg	m	deg/s	deg/s
5.0	10.0	85.5	66.5	142.0	294.0	60.0		4.8	4.8	333.4	0.189	0.203
10.0	10.0	61.3	40.2	95.3	196.8	42.4	351.9	4.9	5.5	211.8	0.267	0.294
15.0	10.0	51.0	34.0	78.1	163.1	36.7	291.2	5.8	6.6	179.7	0.332	0.367
20.0	10.0	45.3	32.7	69.6	147.5	34.8	261.6	7.2	7.9	170.1	0.389	0.429
25.0	10.0	41.8	33.0	65.0	139.8	34.8	246.5	8.7	9.4	170.3	0.440	0.483
30.0	10.0	39.6	34.3	62.3	136.2	35.6	239.2	10.3	11.0	176.3	0.485	0.532
35.0	10.0	38.0	36.1	61.2	135.3	37.3	237.0	12.1	12.6	185.4	0.526	0.573
40.0	10.0	37.1	38.7	60.9	136.7	40.1	240.6	13.9	14.2	199.4	0.562	0.607
20.0	20.0	69.1	36.8	99.9	205.8	36.7	368.4	8.5	8.2	386.4	0.442	0.433
5.0	10.0	88.5	48.0	131.0	267.5	50.5		3.4	3.9	267.1	0.176	0.192
10.0	10.0	61.6	33.2	89.2	184.0	37.0	332.0	4.1	4.8	183.7	0.259	0.284
15.0	10.0	50.7	29.8	73.8	154.3	33.1	277.8	5.2	5.9	160.2	0.327	0.358
20.0	10.0	44.8	29.6	66.2	140.5	32.4	252.1	6.6	7.3	154.3	0.387	0.420
25.0	10.0	41.3	30.6	61.9	133.8	33.0	239.7	8.2	8.9	156.9	0.439	0.476
30.0	10.0	38.9	32.3	59.8	131.0	34.3	234.4	9.8	10.5	163.6	0.487	0.523
35.0	10.0	36.6	35.2	58.8	130.5	36.3	233.9	11.6	12.0	173.5	0.529	0.564
40.0	10.0	36.5	36.8	58.8	132.2	40.0	240.3	13.4	13.7	186.7	0.566	0.598
20.0	20.0	69.0	32.8	96.5	198.3	34.5	365.0	7.6	7.5	355.9	0.432	0.419

Table 5

Computed turning circle characteristics  
of the tanker at an approach speed  $U_0 = 15$  kn

Top: Constant propeller rate, model condition  
Bottom: Constant steam rate, ship condition

Rudder angle $\delta$ deg	Advance $x_0$ at $\psi = 90^\circ$ m	Transfer $y_0$ at $\psi = 90^\circ$ m	Maximum advance m	Tactical diameter m	Time $t$ at $\psi = 90^\circ$ s	Time $t$ at $\psi = 180^\circ$ s	Maximum transfer m	Final values in steady turn				
								Turning radius $R$ m	Drift angle $\beta$ deg	Turning rate $\dot{\alpha}$ deg/s	Track speed $U$ kn	Speed ratio $U/U_0$ 1
5.0	2603	-1835	2609	3864	478	898	-3870	1884	-4.48	-0.212	13.55	0.903
-5.0	2301	1598	2307	3382	421	793	3389	1625	5.15	0.239	13.18	0.879
10.0	1796	-1201	1804	-2595	330	632	-2603	1230	-6.75	-0.289	12.06	0.804
-10.0	1684	1113	1693	2410	309	591	2419	1123	7.37	0.307	11.70	0.780
15.0	1458	-928	1469	-2041	268	521	-2052	930	-8.81	-0.337	10.63	0.709
-15.0	1395	878	1406	1934	256	497	1946	863	9.48	0.351	10.28	0.685
20.0	1263	-766	1275	-1708	233	458	-1721	742	-10.93	-0.370	9.31	0.621
-20.0	1220	733	1233	1636	225	441	1649	691	11.69	0.383	8.98	0.599
25.0	1134	-655	1148	-1479	210	416	-1494	606	-13.17	-0.393	8.08	0.539
-25.0	1102	631	1117	1425	203	403	1440	565	14.07	0.406	7.78	0.519
30.0	1042	-574	1058	-1309	194	388	-1327	502	-15.62	-0.410	6.98	0.465
-30.0	1017	556	1033	1266	188	376	1285	468	16.70	0.422	6.70	0.447
35.0	973	-512	992	-1176	182	368	-1196	418	-18.38	-0.422	5.99	0.399
-35.0	953	497	970	1141	177	357	1162	388	19.69	0.435	5.73	0.382
40.0	921	-463	941	-1069	173	358	-1092	349	-21.63	-0.428	5.07	0.338
-40.0	903	450	923	1039	169	344	1063	322	23.30	0.444	4.85	0.323
5.0	2674	-1963	2679	-4126	500	957	-4132	2006	-4.20	-0.191	13.00	0.867
-5.0	2486	1804	2491	3796	463	887	3802	1814	4.62	0.206	12.68	0.845
10.0	1820	-1253	1828	-2700	340	664	-2708	1254	-6.64	-0.256	10.89	0.726
-10.0	1754	1197	1763	2579	327	638	2588	1172	7.10	0.266	10.58	0.705
15.0	1467	-956	1478	-2098	274	546	-2109	919	-8.98	-0.291	9.07	0.605
-15.0	1430	926	1441	2030	267	530	2042	867	9.53	0.299	8.79	0.586
20.0	1265	-783	1278	-1744	237	480	-1758	710	-11.42	-0.312	7.52	0.501
-20.0	1241	763	1253	1698	232	468	1712	671	12.09	0.320	7.28	0.485
25.0	1132	-667	1147	-1504	213	438	-1520	567	-14.08	-0.325	6.25	0.417
-25.0	1114	652	1129	1469	209	428	1486	530	14.95	0.335	6.02	0.401
30.0	1038	-582	1055	-1327	197	409	-1346	458	-17.00	-0.335	5.20	0.347
-30.0	1024	571	1041	1299	193	401	1319	429	18.05	0.345	5.02	0.335
35.0	968	-517	986	-1190	184	389	-1212	376	-20.30	-0.341	4.35	0.290
-35.0	956	508	975	1167	182	382	1189	352	21.60	0.352	4.20	0.280
40.0	915	-465	935	-1081	175	376	-1106	308	-24.12	-0.345	3.60	0.240
-40.0	904	458	925	1061	173	369	1087	288	25.80	0.356	3.48	0.232



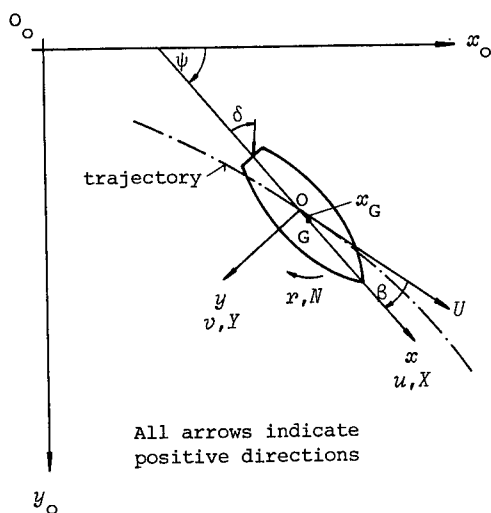


Fig. 1 Coordinate system

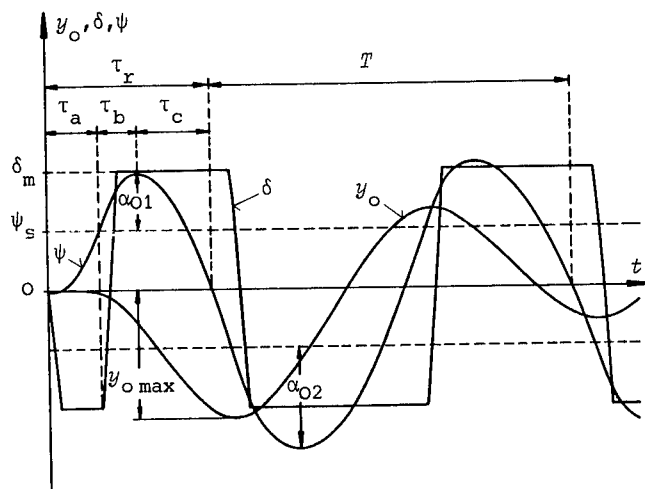


Fig. 2 Characteristic parameters of zigzag maneuver

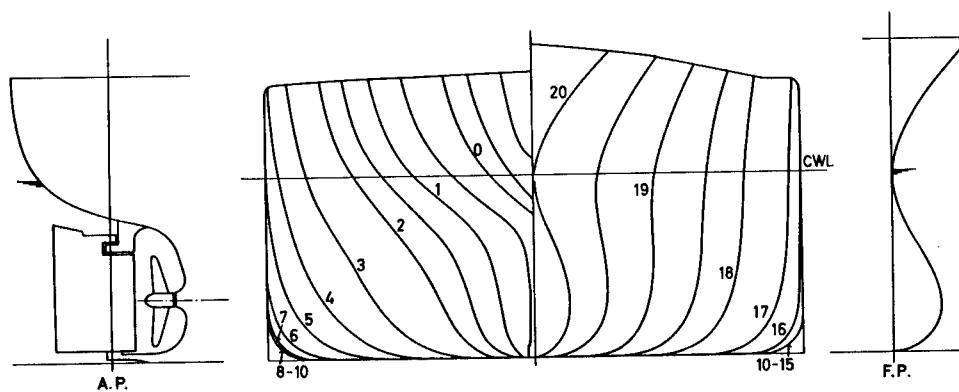


Fig. 3 Body plan and profile of tanker (HSVA Model 2507)

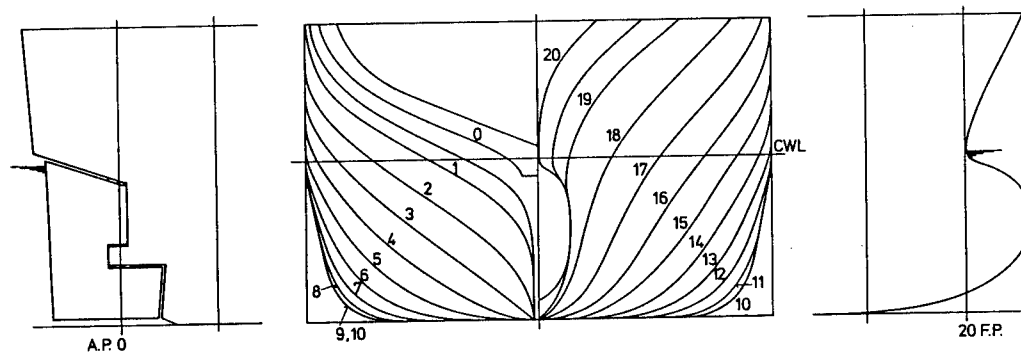


Fig. 4 Body plan and profile of container carrier (HSVA Model 2657)

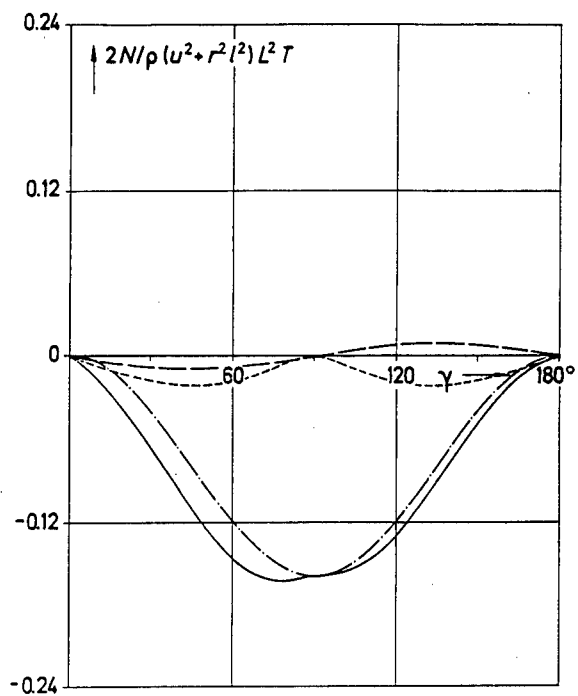
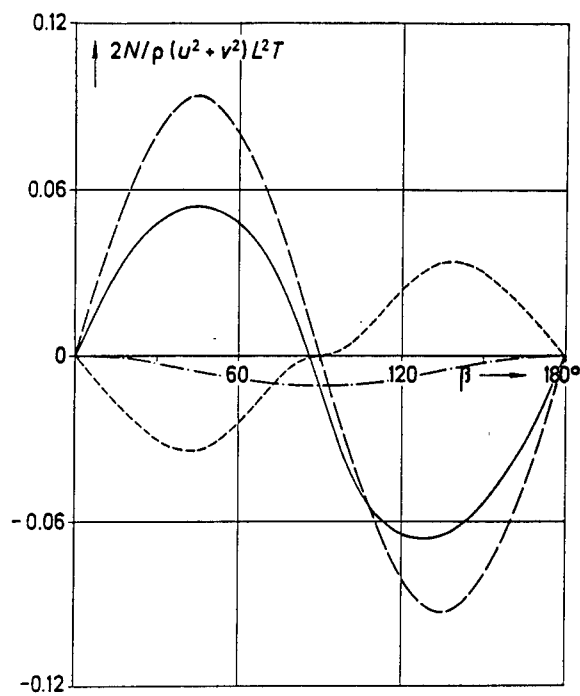
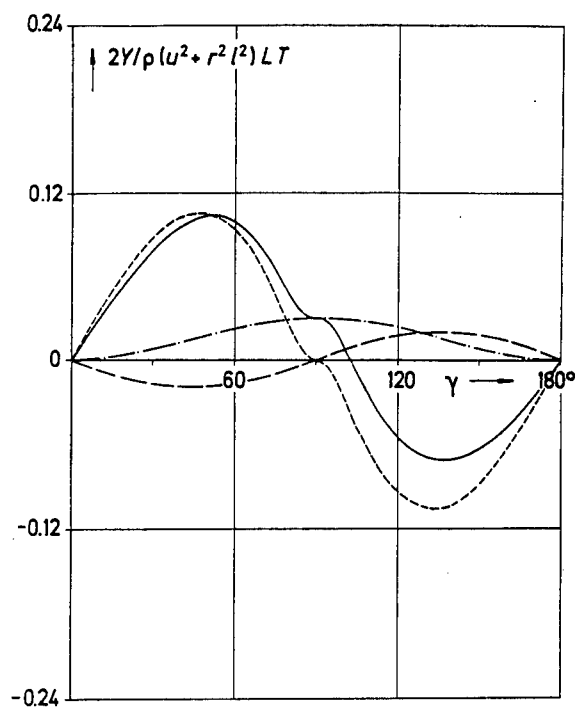
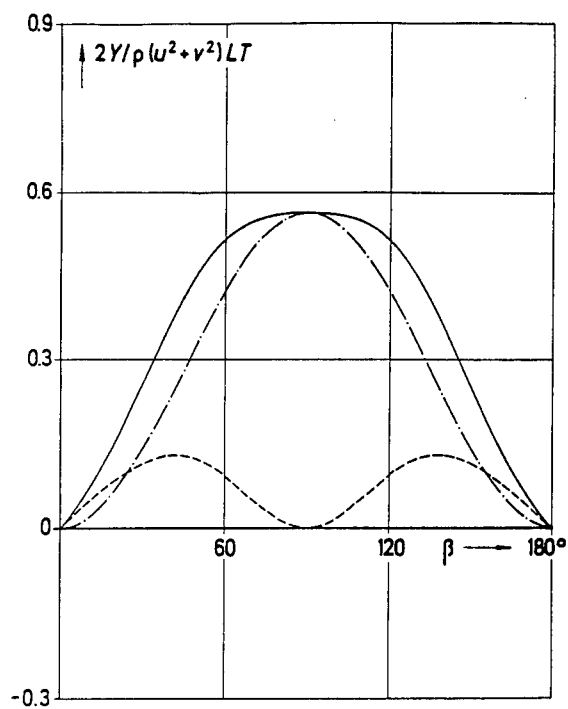


Fig. 5 Side force (top) and yaw moment (bottom) on the tanker resulting from pure drift

Fig. 6 Side force (top) and yaw moment (bottom) on the tanker resulting from pure yaw

Common legend

- — — — — Ideal fluid effects
- - - - - Lifting effects
- · - · - Cross flow effects
- — — — — Total

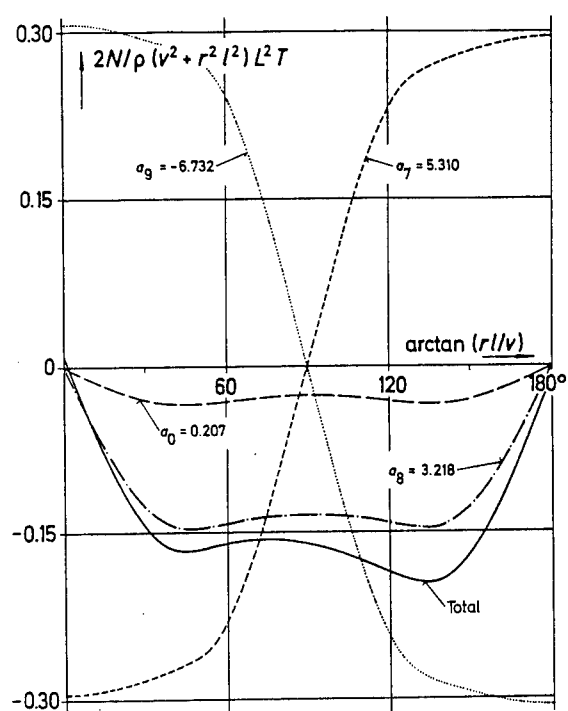
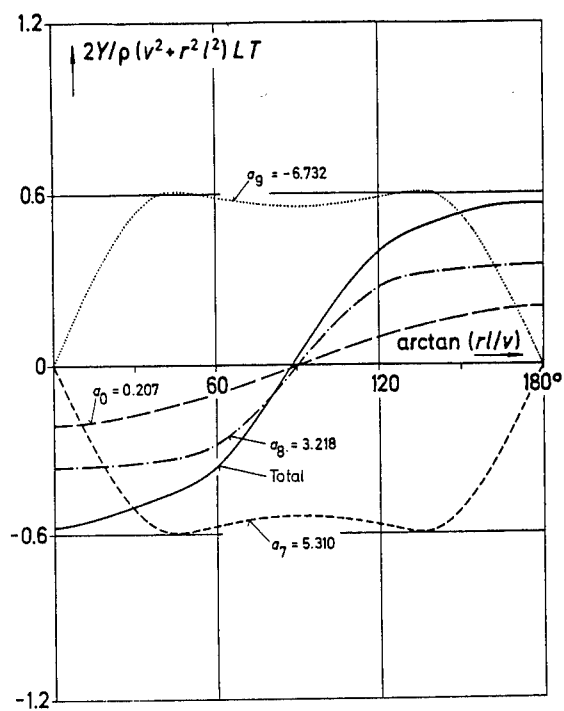


Fig. 7 Side force (top) and yaw moment (bottom) on the tanker resulting from pure cross flow as measured at zero forward speed

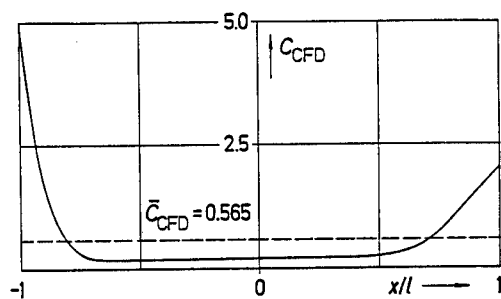


Fig. 8 Local drag coefficient associated with observed cross flow effects on tanker

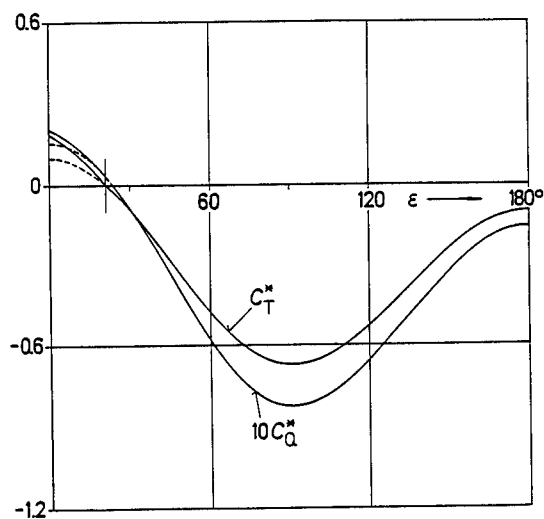


Fig. 9 Thrust and torque characteristics of the tanker propeller

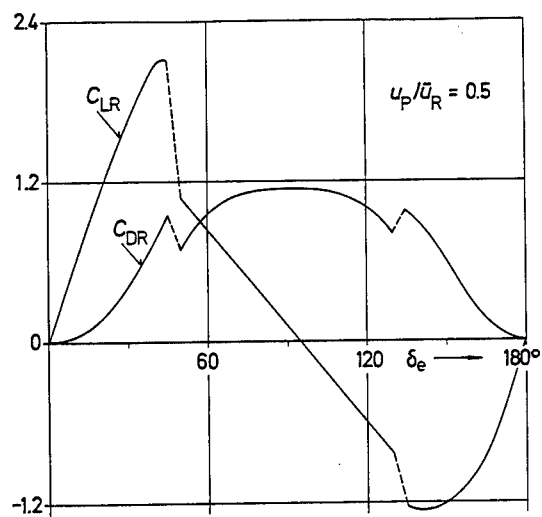


Fig. 10 Lift and drag characteristics of the tanker rudder

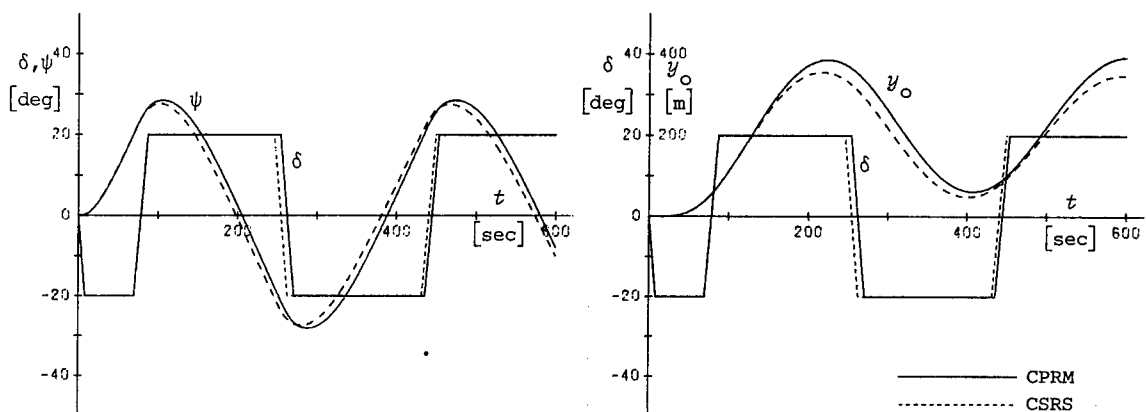


Fig. 11 Simulated 20°/20° zigzag maneuver of the tanker (CPRM versus CSRS)

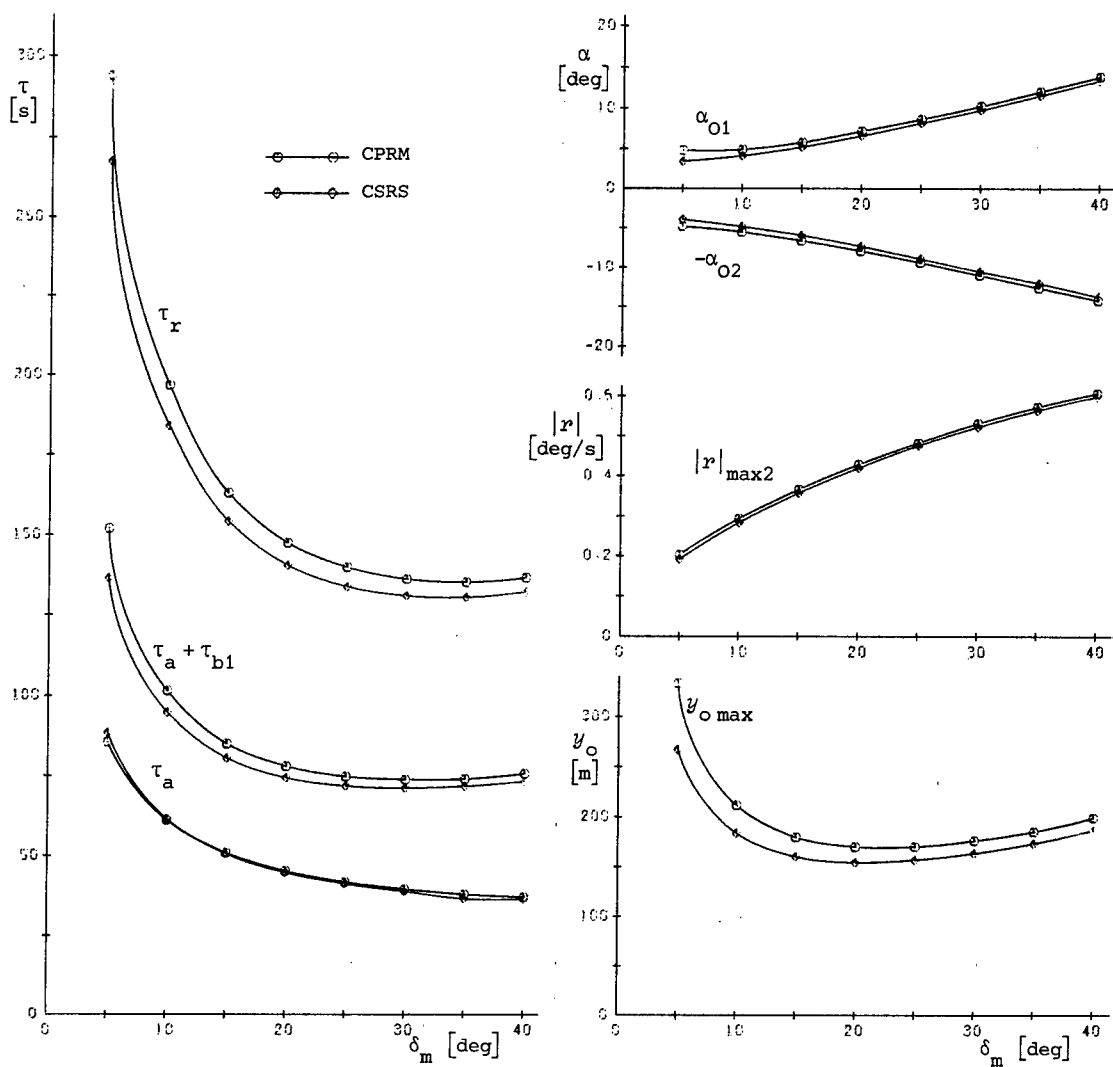


Fig. 12 Selected zigzag maneuver characteristics of the tanker (CPRM versus CSRS)

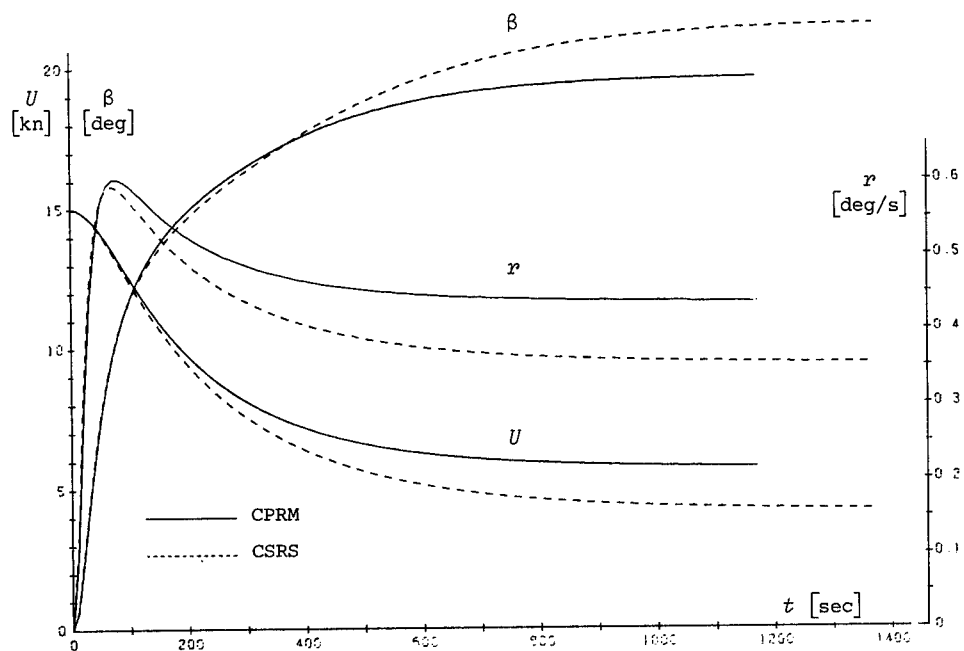


Fig. 13 Simulated turning circle ( $\delta = -35^\circ$ ) maneuver of the tanker (CPRM versus CSRS)

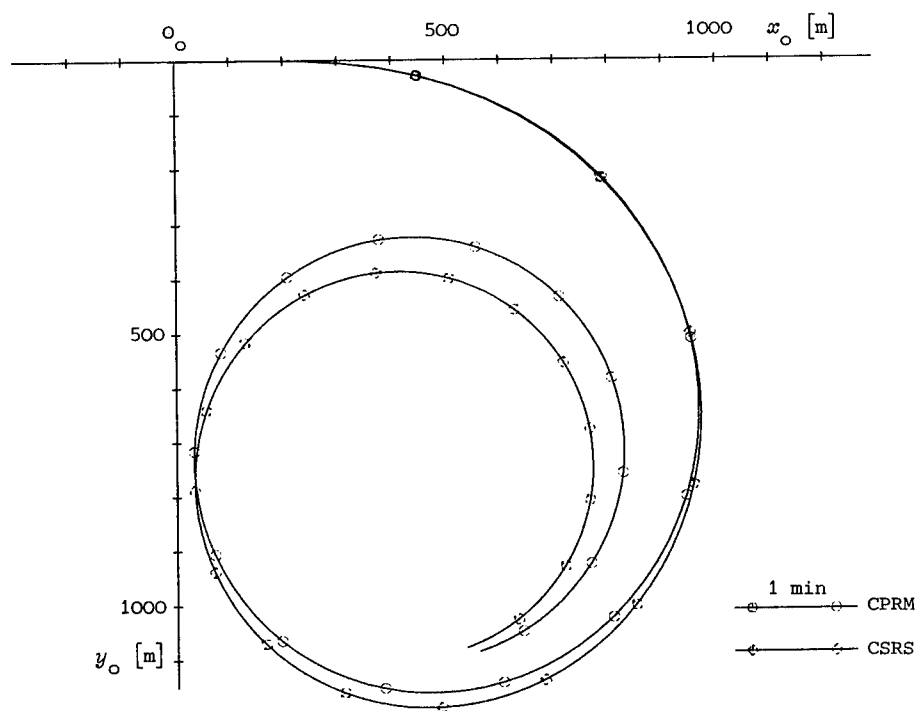


Fig. 14 Simulated turning circle ( $\delta = -35^\circ$ ) trajectory of the tanker (CPRM versus CSRS)

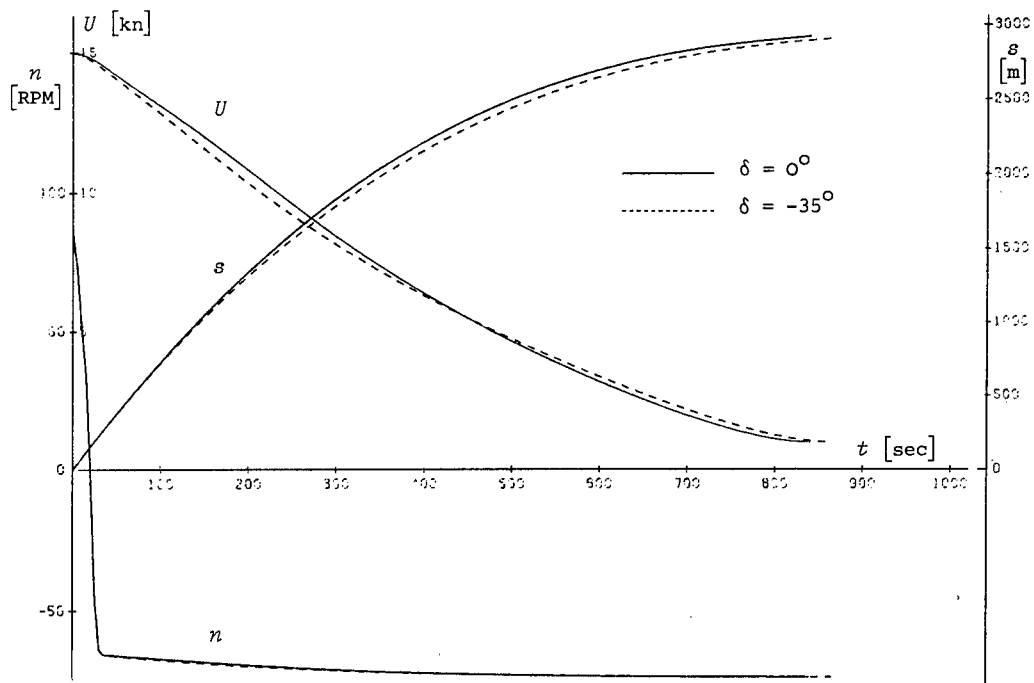


Fig. 15 Simulated crashback maneuvers of the tanker with and without rudder application

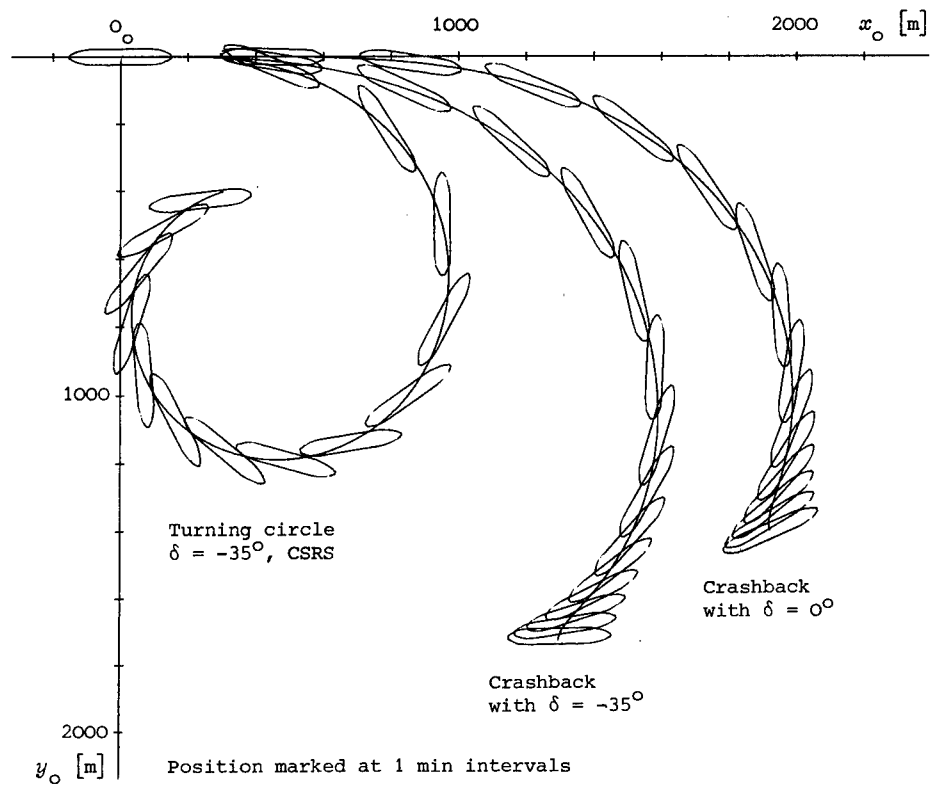


Fig. 16 Comparison of crashback and turning circle trajectories for the tanker

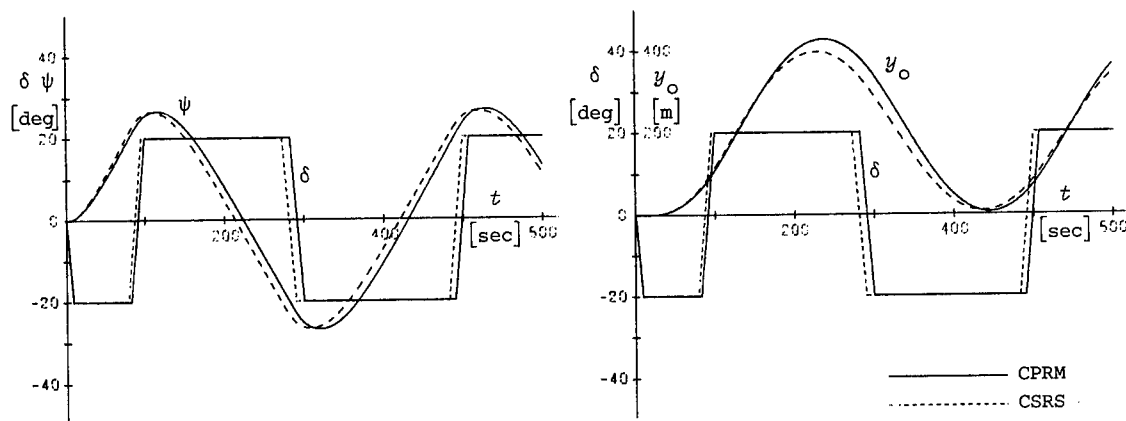


Fig. 17 Simulated 20°/20° zigzag maneuver of the container carrier (CPRM versus CSRS)

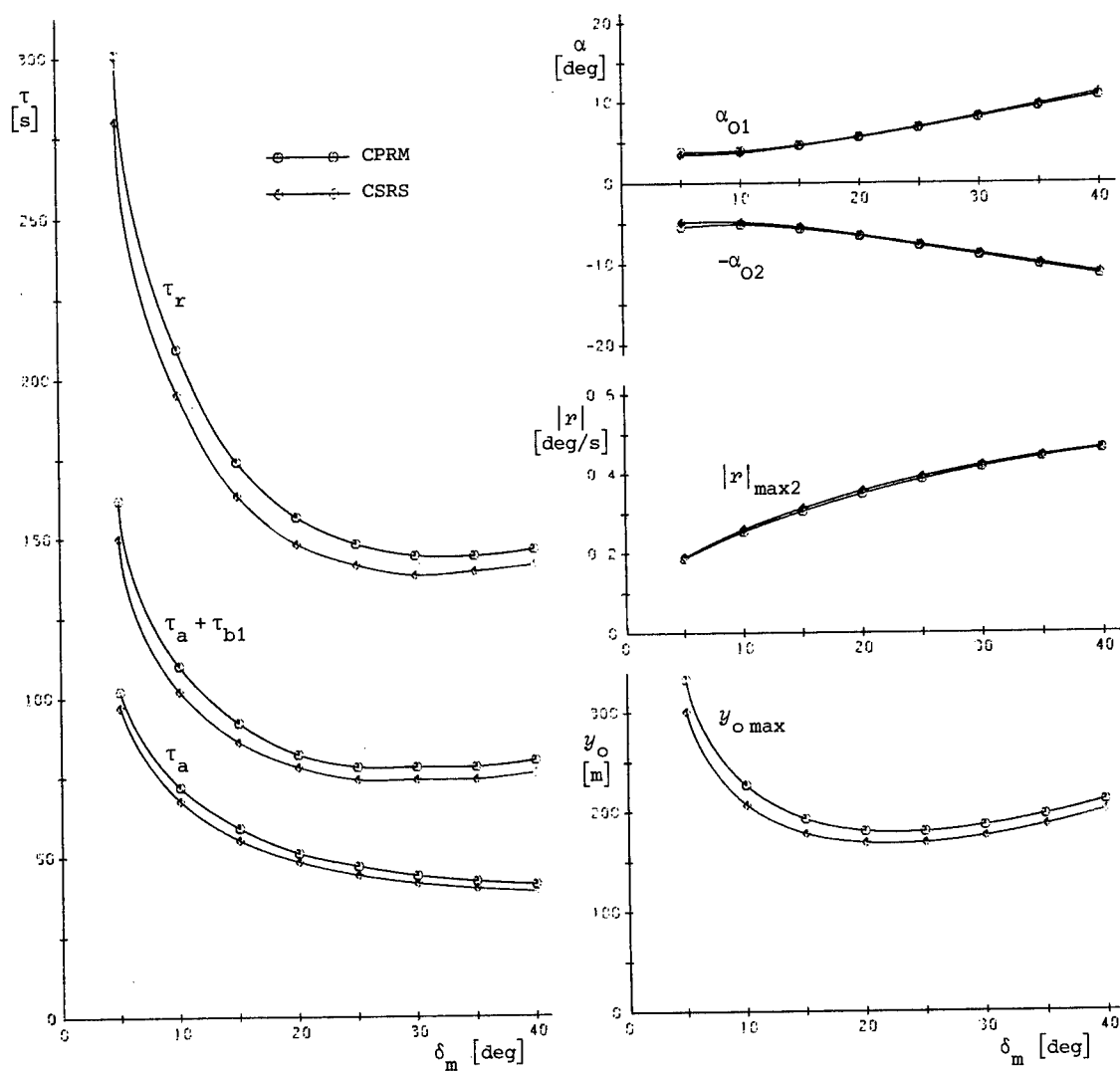


Fig. 18 Selected zigzag maneuver characteristics of the container carrier (CPRM versus CSRS)

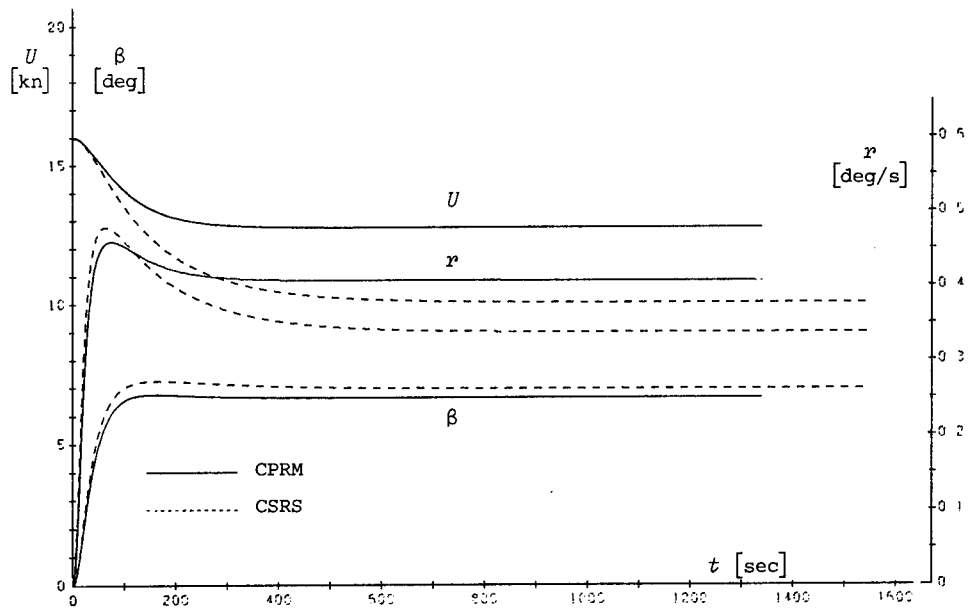


Fig. 19 Simulated turning circle ( $\delta = -35^\circ$ ) maneuver of the container carrier (CPRM versus CSRS)

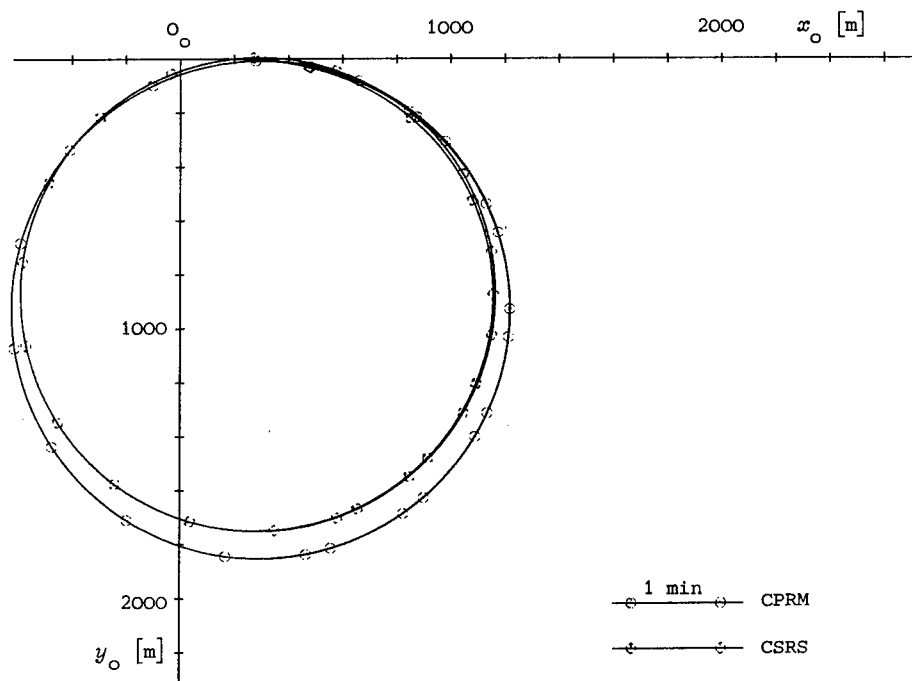


Fig. 20 Simulated turning circle ( $\delta = -35^\circ$ ) trajectory of the container carrier (CPRM versus CSRS)



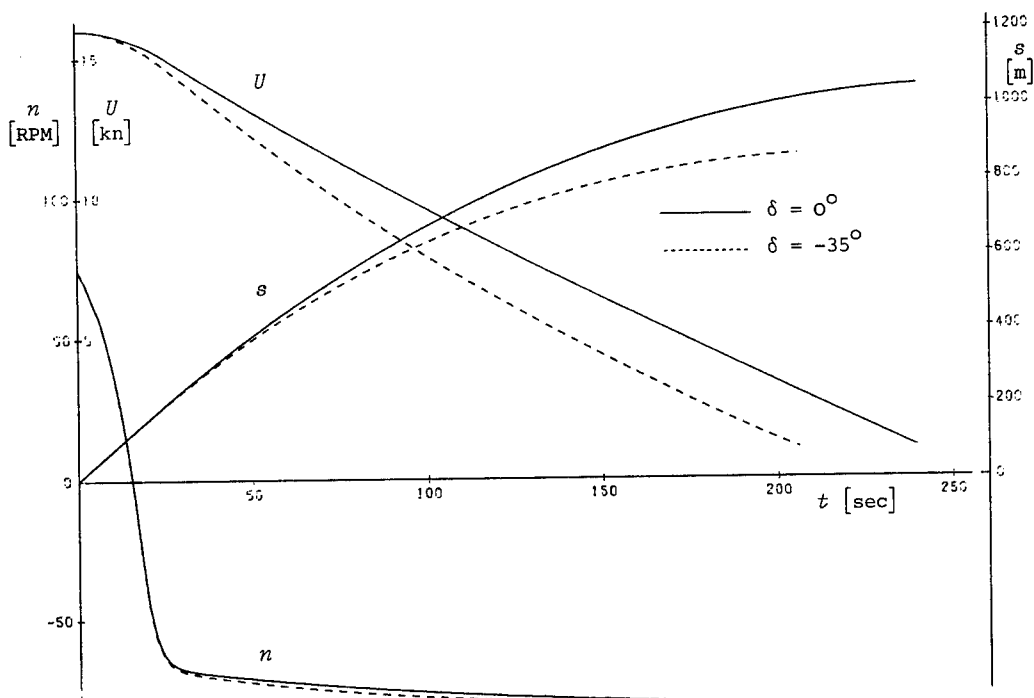


Fig. 21 Simulated crashback maneuvers of the container carrier with and without rudder application

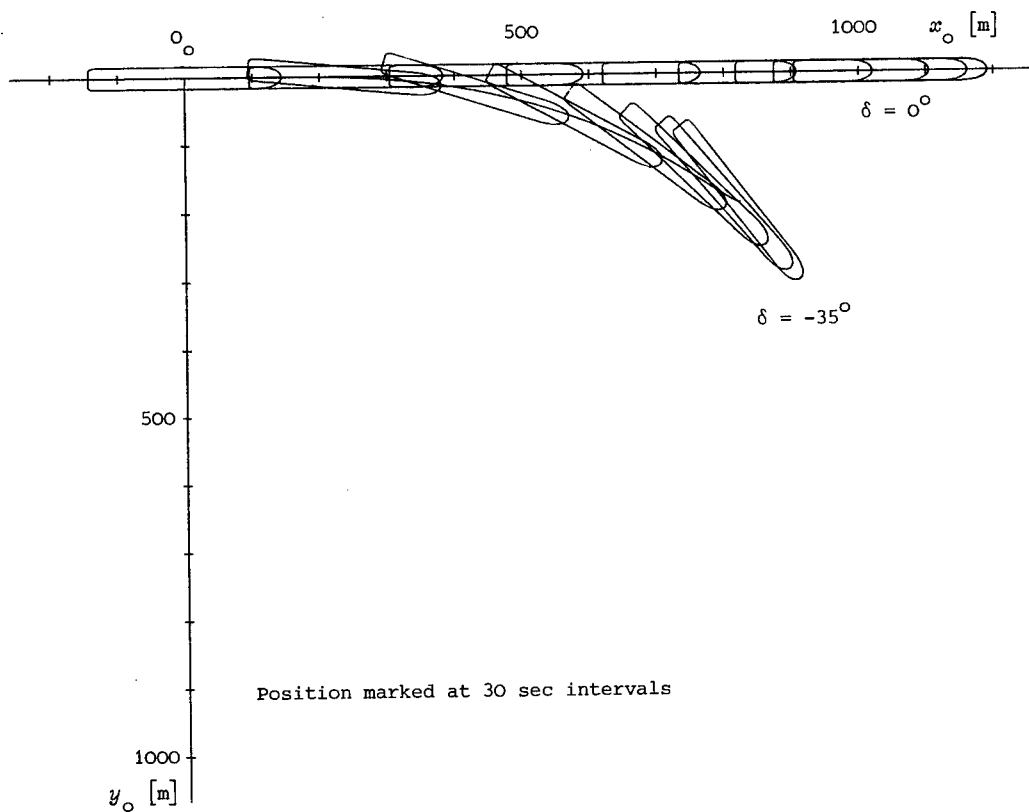


Fig. 22 Simulated crashback trajectories of the container carrier with and without rudder application

## ADDENDUM

The integral occurring in Section 2.2.4, Hull Cross-Flow Effects has the following general solution:

$$\begin{aligned}
 \int_{-l}^l x^n (v + rx) |v + rx| dx &= 2l^{n+1} \left\{ \frac{v^2}{n+1} + \frac{r^2 l^2}{n+3} \right\} \operatorname{sgn} v & [v^2 \geq r^2 l^2, n \text{ even}] \\
 &= \frac{4l^{n+1}}{n+2} v r l \operatorname{sgn} v & [v^2 \geq r^2 l^2, n \text{ odd}] \\
 &= \frac{4l^{n+1}}{n+2} \left\{ r l + \frac{v^{n+2}}{(n+1)(n+3)(rl)^{n+1}} \right\} v \operatorname{sgn} r & [v^2 < r^2 l^2, n \text{ even}] \\
 &= l^{n+1} \left\{ \frac{2v^2}{n+1} + \frac{2r^2 l^2}{n+3} - \frac{4v^{n+3}}{(n+1)(n+2)(n+3)(rl)^{n+1}} \right\} \operatorname{sgn} r & [v^2 < r^2 l^2, n \text{ odd}]
 \end{aligned}$$

Substitution of Eq. (34-35) into Eq. (32-33) then yields the following specific expressions for side force and yaw moment in response to cross flow:

$$\begin{aligned}
 Y_{HC} &= -\frac{\rho}{2} L T \left\{ \alpha_0 \left( v^2 + \frac{r^2 l^2}{3} \right) + \alpha_7 \frac{2}{9} v r l + \alpha_8 \left( \frac{v^2}{9} + \frac{r^2 l^2}{11} \right) + \alpha_9 \frac{2}{11} v r l \right\} \operatorname{sgn} v & [v^2 \geq r^2 l^2] \\
 &= -\frac{\rho}{2} L T \left\{ \alpha_0 \left( r l + \frac{v^2}{3 r l} \right) v + \alpha_7 \frac{1}{2} \left( \frac{v^2}{4} + \frac{r^2 l^2}{5} - \frac{v^{10}}{180 r^8 l^8} \right) \right. \\
 &\quad \left. + \alpha_8 \frac{1}{5} \left( r l + \frac{v^{10}}{99 r^9 l^9} \right) v + \alpha_9 \frac{1}{2} \left( \frac{v^2}{5} + \frac{r^2 l^2}{6} - \frac{v^{12}}{330 r^{10} l^{10}} \right) \right\} \operatorname{sgn} r & [v^2 < r^2 l^2] \\
 N_{HC} &= -\frac{\rho}{2} L^2 T \left\{ \alpha_0 \frac{1}{3} v r l + \alpha_7 \frac{1}{2} \left( \frac{v^2}{9} + \frac{r^2 l^2}{11} \right) + \alpha_8 \frac{1}{11} v r l + \alpha_9 \frac{1}{2} \left( \frac{v^2}{11} + \frac{r^2 l^2}{13} \right) \right\} \operatorname{sgn} v & [v^2 \geq r^2 l^2] \\
 &= -\frac{\rho}{2} L^2 T \left\{ \alpha_0 \frac{1}{4} \left( v^2 + \frac{r^2 l^2}{2} - \frac{v^4}{6 r^2 l^2} \right) + \alpha_7 \frac{1}{10} \left( r l + \frac{v^{10}}{99 r^9 l^9} \right) v \right. \\
 &\quad \left. + \alpha_8 \frac{1}{4} \left( \frac{v^2}{5} + \frac{r^2 l^2}{6} - \frac{v^{12}}{330 r^{10} l^{10}} \right) + \alpha_9 \frac{1}{12} \left( r l + \frac{v^{12}}{143 r^{11} l^{11}} \right) v \right\} \operatorname{sgn} r & [v^2 < r^2 l^2]
 \end{aligned}$$

Our simulation algorithm actually uses these analytical formulas, but numerical quadrature would be an equally admissible alternative.

## DISCUSSION

JERZY MATUSIAK,  
Technical Research Centre of Finland,  
Espoo, Finland:

I would like to congratulate the authors on their very interesting paper. I have just one question to ask: Did you have a possibility to compare the results of your digital simulation with the results of free-running model experiments or fullscale manoeuvring measurements?

Dr. VLADIMIR ANKUDINOV,  
Tracor Hydronautics, Inc.,  
Laurel, MD, USA:

I believe the paper is a very welcome addition to data in this particular field. As far as Tracor Hydronautics is concerned we have been using four-quadrant hydrodynamical model and square absolute representation for higher order terms (in contrast to the "third order Taylor expansion" method) for a number of years. Based on the physical considerations and our experience with extensive PMM test results, it is recommended to express sway (or yaw) forces and moments in two different regions. In the first region of relatively small drift angles the lifting-surface effects proportional to the instantaneous sway and yaw velocities are dominant. At large drift angles hydrodynamic forces and moments are dominated by cross-flow drag

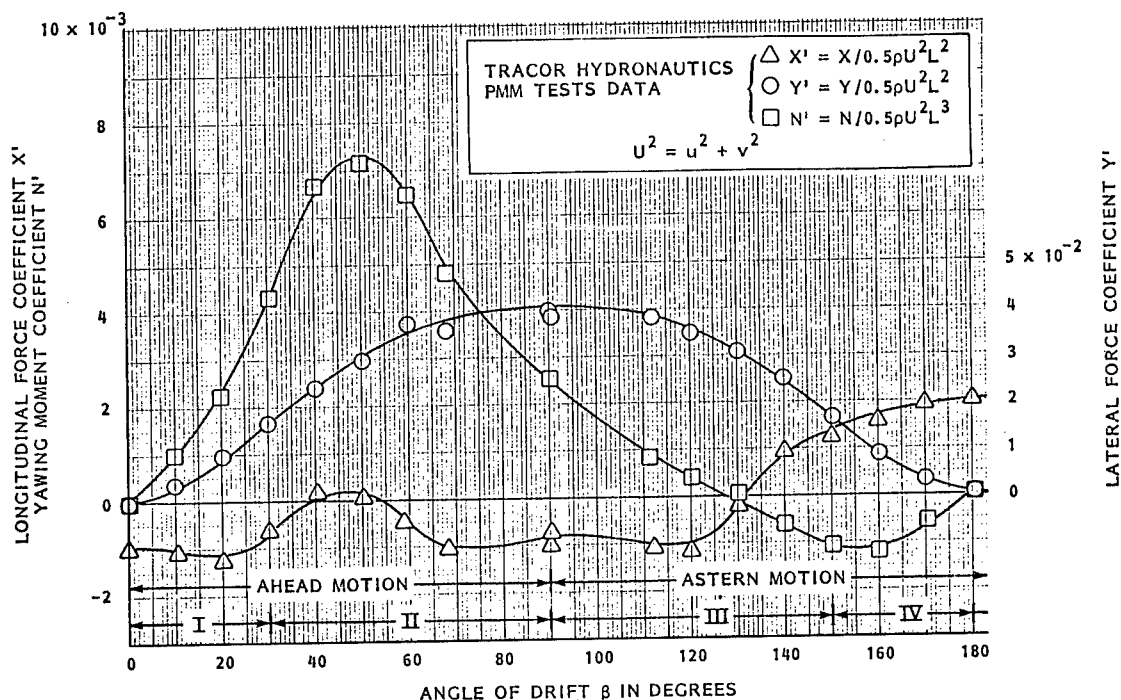


Fig. A1 Variation of longitudinal force, lateral force, and yawing moment coefficients with a large range of angle of drift, for a fine form ship hull

which is essentially proportional to velocity squared. If sway force,  $Y$ , and sway moment,  $N$ , are continuous functions in the whole range of drift angles, as shown on Figure A1, by matching regions I and II for ahead motion (and III and IV in astern motion) the cross flow terms at small drift angles,  $\beta$ , can be determined.

In any region

$$Y = 0.5\rho L^2 U^2 [Y'_v \cos\beta \sin\beta + Y'_{|v|} |\sin\beta| |\sin\beta|]$$

$$N = 0.5\rho L^3 U^2 [N'_v \cos\beta \sin\beta + N'_{|v|} |\sin\beta| |\sin\beta|]$$

and therefore, by matching two regions somewhat conventionally at 30 degrees:

$$(Y'_v \cos 30^\circ \sin 30^\circ + Y'_{|v|} \sin^2 30^\circ) = [Y'_{|v|}]_{\text{large}\beta} \sin^2 30^\circ$$

$$(N'_v \cos 30^\circ \sin 30^\circ + N'_{|v|} \sin^2 30^\circ) = [N'_{|v|}]_{\text{large}\beta} \sin^2 30^\circ$$

where

$$[Y'_{|v|}]_{\text{large}\beta} = \int_L C_{CFD} T(x) dx / L^2$$

$$[N'_{|v|}]_{\text{large}\beta} = \int_L C_{CFD} T(x) x dx / L^3,$$

the values of  $Y'_{|v|}$  and  $N'_{|v|}$  of the region I can be estimated.

Similarly for yaw motion, considering

$$r' = \frac{rL}{U} \quad \text{and} \quad \frac{r(0.5L)}{U} = \sin\beta_r$$

the matching condition at  $r' = 1$  ( $\beta_r = 30^\circ$ )

$$N_{\text{yaw}} = 0.5\rho L^3 U^2 [N'_r r' + N'_{|r|} |r'| |r'|]$$

$$= 0.5\rho L^3 U^2 [(N'_r |r'|)_{\text{large}r} r' |r'|]$$

where

$$(N'_r |r'|)_{\text{large}r} = \int_L C_{CFD} T(x) x^2 dx / L^4,$$

provides the value of  $N'_{|r|}$  for small yaw rates,  $r'$ .

My second point concerns the interaction between ship hull and rudder. In Tracor Hydro-nautics simulation models the forces generated by the rudders,  $Y_{\text{rud}}$ , are based on inflow velocity  $U_R$ , which is a function of forward speed  $u$  and propeller rotational speed  $n$ , so that

$$Y_{\text{rud}} = 0.5\rho L^2 U_R^2 [Y'_{\delta_r} \delta_r],$$

$$U_R^2 = [du^2 + eu(nD_p)^2 + f(nD_p)^2],$$

where  $D_p$  is the propeller diameter, and non-dimensional coefficients  $d$ ,  $e$  and  $f$  are defined in four quadrants of  $u$ ,  $n$  combinations. For typical maneuvers (propeller is overloaded) the contribution of  $f$  term is dominant.

The hull/rudder interaction forces then are expressed simply as

$$Y_{\text{hull/rud}} = 0.5 \rho L^2 C_R Y_{\delta_x}^* U_R v,$$

$$N_{\text{hull/rud}} = Y_{\text{hull/rud}} x_{\text{rud}},$$

where  $x_{\text{rud}}$  is a longitudinal distance between CG and rudder. As a first approximation, the interaction coefficient,  $C_R \approx 1.0$ .

For ships operating at sea the effect of free-surface waves (including forward speed, frequency and final amplitude dependence) and its interaction with lifting effects and viscous separation should be considered. Figure A2 shows results of our simulations for Mariner Ship in calm water and irregular seas, cf. Ankudinov (1983). At significant wave heights,  $H_{1/3}$ , larger than 8-10 feet, the ship is practically unsteerable.

Reference:

Ankudinov, V. (1983): Simulation Analysis of Ship Motions in Waves. Proceedings of International Workshop on Ship and Platform Motions, University of California, Berkeley, CA, USA, pp. 384-403.

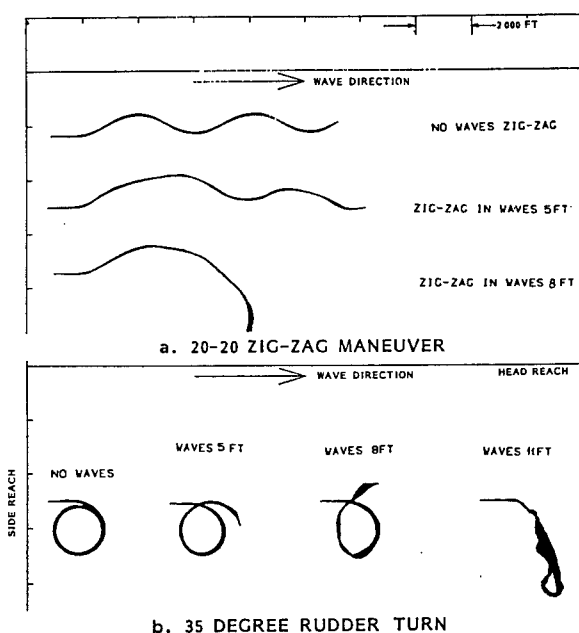


Fig. A2 Simulated maneuvers of Mariner ship in calm water and in irregular waves for 15 knots approach speed

## AUTHORS' REPLY

First of all we would like to thank both discussers for their congenial remarks.

In reply to Mr. Matusiak's question, our simulations have been partially validated in each case by comparison with the results of systematic series of zigzag maneuvers performed in the towing tank with the ship model operating in the free-running mode at constant propeller re-

volutions (CPRM). For lack of suitable facilities we have so far been unable to conduct turning circle or engine maneuvers in the tank. Moreover, we have conducted a detailed comparison with full-scale trials of the MARINER model as reported in a previous paper, cf. Oltmann et al. (1980). Although that simulation was based on an earlier, significantly different algorithm, it did provide some validation for our scale effect corrections to hull-propeller-rudder interaction. Finally, a rough, order-of-magnitude comparison has been made with some full-scale trials of the container carrier HAMBURG EXPRESS to support our simulation of engine characteristics. Thus almost all modules of the simulation algorithm have been directly or indirectly validated by some maneuver trajectories. Yet we are still looking forward to a real test of our simulation model by comparison with a comprehensive set of high precision maneuvering trials, all performed with the same ship.

Dr. Ankudinov's contribution is an interesting enrichment of our paper for it reveals a rather different approach to four-quadrant modeling. We have tried to construct single expressions which by virtue of their structure are essentially valid in all four quadrants and have succeeded in doing so at least for the major hull forces, thus eliminating the need for matching and patching piecewise approximations advocated by Dr. Ankudinov.

Parenthetically, we would like to point out, for the convenience of the reader, a couple of presumably typographical errors in Dr. Ankudinov's discussion. In our opinion, his first two Equations should begin with a minus sign on the R.H.S. since by definition  $v = -U \sin \beta$ . Moreover, his Equation for the nonlinear yawing moment in response to pure yaw should correctly read

$$(N'_{\dot{r}} | \dot{r} |)_{\text{larger}} = - \int_L C_{CFD} T(x) x^2 |x| dx / L^5.$$

More importantly, we doubt whether the true nonlinear coupling of sway and yaw motion in the crossflow forces implicit in our Equations (32-33) - and made explicit in the Addendum - can be properly modeled by polynomials with only positive powers of  $v, |v|, r, |\dot{r}|$  as used by Dr. Ankudinov. In short, we have good reasons for preferring our own basic model of hull forces. But we hasten to recognize that we still have to incorporate features such as shallow water and seaway effects which Dr. Ankudinov already appears to have successfully done.

In view of the latest worldwide developments in maneuvering simulation we suggest that the time is now ripe for organizing a workshop to obtain an objective assessment of the performance of the new generation of four-quadrant models by comparing them for standardized maneuvers of certain benchmark ships.

# ON THE SHIP MOTION REDUCTION BY ANTI-PITCHING FINS IN HEAD SEAS

MASATOSHI BESSHO AND YUSAKU KYOZUKA

## ABSTRACT

This is a study on a heave-free and/or pitch-free ship with pairs of fins, that is, a ship which is free from the heaving and/or pitching oscillation in head sea at a given wave-length. For this purpose, it is sufficient to cancel the wave-exciting force and/or moment by using pairs of fins to make a ship with fin wave-free for heave and/or pitch motion. Thus, there are two equations in complex variables for the heave and pitch-free.

On the other hand, a pair of fins has three variables to be determined which are the area, the aspect-ratio and the location of fins to be attached. Two pairs of fins are sufficient to make a ship heave-free and pitch-free, but two parameters are left undetermined. In the same way, a pair of fins is sufficient to make a ship heave-free or pitch-free.

The above discussion is purely mathematical and the particulars of fins thus obtained must be checked to be feasible for a practical application. For this purpose, taking a container-cargo ship for an example, the calculations are carried out for two cases. And it is confirmed by experiments that the theory agrees well with experimental results.

## NOMENCLATURE

$A_f = C_f S_f$  : area of fin (of one side)  
 $A.R.$  : aspect-ratio of fin (of one side)  
 $A_w$  : water plane area of ship  
 $a$  : amplitude of in-coming wave  
 $C_{fj}$  : chord length of j-th fin  
 $C_L$  : lift coefficient of fin  
 $C_T$  : total resistance coefficient  
 $c = \omega_0 / K$  : phase velocity of wave  
 $Fn = V / \sqrt{gL}$  : Froude number  
 $g$  : gravity constant  
 $h$  : amplitude of heaving oscillation at center of gravity of ship  
 $I_1, I_2$  : amplitude of heaving and pitching velocity  
 $K = 2\pi / \lambda = \omega_0^2 / g$  : wave number of in-coming wave  
 $L$  : length of ship or lift of fin  
 $l_j$  : position of j-th fin  
 $l_w^j = |V_2 / V_1|$  : lever of wave-exciting moment  
 $m$  : added mass of fin

$N$  : two dimensional damping coefficient  
 $R$  : resistance increase in waves  
 $T_f$  : thrust by fin  
 $V$  : ship velocity  
 $V_1, V_2$  : wave-exciting force and moment  
 $v_{wj}$  : vertical velocity of water at j-th fin  
 $v_{rj}$  : vertical velocity of j-th fin relative to water  
 $W$  : dissipated power of radiating wave  
 $Z_{ij}$  : i-th mode hydro- and mechanical impedance of j-th mode motion  
 $z_j$  : impedance of j-th pair of fin  
 $\omega_0$  : circular frequency of in-coming wave  
 $\omega = \omega_0 + KV$  : encounter frequency  
 $\psi$  : pitching amplitude  
 $\alpha_j = \arg[V_j]$  : phase of wave-exciting force or moment

## 1. INTRODUCTION

The study of ship motion reduction with fins has a long history and many works have been carried out. But there are comparatively few works which deal with anti-pitching fins.

At first, M.A.Abkowitz[3] reported that the pitching oscillation can be reduced to a half by a pair of fins with the area of 3 to 7 % of the ship water plane area. M.Matsui[4] reported that the active control anti-pitching fin for a small passenger ship can reduce pitching completely at some wave-length. The added mass effect of fins is neglected in the above two studies. Ir.J.H.Vugts[5] studied the passive and active fins including the added mass effect and showed a good agreement with experiments and theoretical calculations by the strip method.

M.A.Abkowitz and M.Matsui et al. suggested that the motion reduction effect of fins result from large eddy damping. This is true and may be the largest role of fins. On the other hand, the reduction of ship motions by fins can be also explained by the reduction of wave-exciting moment.

It is well known that the semi-submerged ship has a good sea-keeping quality. This is result of its wave-free property, that is, the wave-exciting force vanishes at a certain wave-length. However, the motions of a ship are not

† Dept. Mech. Eng., National Defense Academy, Yokosuka, Japan 239.

always reduced when the wave-exciting force vanishes because the damping coefficient also vanishes consequently.[1,2]

If it is possible to make a ship wave-free only in one direction, for example, head seas, it must allow us to have heave-free and/or pitch-free ship. The preceding works tried to reduce only pitching motion. On the contrary, we have tried to obtain the fins which make a ship heave-free and/or pitch-free at a given wave-length. The solution have been obtained by the wave-free condition; that is, cancellation of the wave-exciting force and/or moment by the appropriate combinations of fins.

The calculation is based on the reliable ordinary method which gives correct prediction of sea-keeping properties. Taking a container-cargo ship as an example, we have carried out the calculation and studied the practical feasibility and found that there exists actually such a fin in a fairly broad range of wave-length.

Lastly, we have verified the prediction to be reliable by experiments.

## 2. SHIP MODEL AND FINS

Let us calculate fin particulars to make a ship heave and/or pitch-free in head seas. For this purpose, we make use of the ordinary strip method with the coordinate systems as shown in Figure 1.[1,2].

We calculate the motions of a container ship. Figure 2 and Table 1 show the body plan and principal dimensions of the ship respectively. Her service speed is  $F_n=0.26$ , but the calculation was carried out for  $F_n=0.18$  because of the short length of the model testing basin. But the difference of the Froude number would not change the calculation results greatly. The calculation shows that the fin area decreases slightly as the ship speed increases. Also the type of ship has effects on the fin particulars and we have studied various types of ships changing their hull forms systematically.[14] Of course, there are some differences in their results but they are quantitative and not qualitative so that we will discuss here only the above model.

Now, we must estimate the force acting on fins. Firstly, we assume that the force acts on one point of the ship and its moment about mid-chord of the fin is negligible. Then, the lift  $L$  and added mass  $m$  of the fin are estimated as follows, because the reduced frequency must be very small in practical case.

$$\left. \begin{aligned} L &= \frac{\rho}{2} V v S_f C_f C_L' \\ C_L' &= \frac{2\pi}{1 + \frac{1}{A.R.}} \quad , \quad A.R. = S_f / C_f \\ m &= \frac{\pi}{4} \rho C_f^2 S_f \end{aligned} \right\} (1)$$

where  $v$  is a relative vertical velocity of fin to the water. The effect of aspect-ratio is assumed as the same of the one of elliptic wing taking into account mirror image effect to the ship hull and the lift coefficient is due to

theory of flat plate wing so that it must be corrected at the stage of practical application.

In the followings, dividing these quantities by the velocity  $v$  and combining them we make use of an impedance form. For a pair of fins the impedance may be written as:

$$\begin{aligned} z &= z_c + i z_s \\ &= \frac{2L}{v} + 2i\omega m = \frac{\pi \rho V A_f}{1 + \frac{1}{A.R.}} + \frac{i\pi}{2} \rho \omega C_f A_f \quad (2) \end{aligned}$$

## 3. TWO PAIRS OF FINS FOR HEAVE- AND PITCH-FREE

In general, in treating mechanical oscillation problem, it is simple, convenient and even fertile to make use of analogy to the electric circuit theory.[12] Hence, we express the equation of motion as follows:

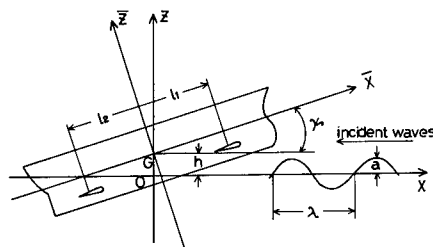


Figure 1 Coordinate system

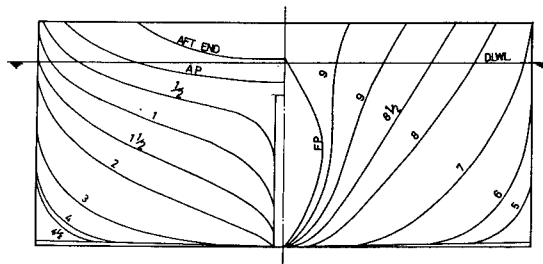


Figure 2 Body plan of the ship

Table 1 Principal dimensions of the ship

	Ship'	Model
Length between perpendiculars (m)	250	3
Breadth moulded (m)	32	0.384
Draft loaded (m)	11.5	0.138
Block coefficient		0.632
Midship coefficient		0.964
Volume of displacement (m <sup>3</sup> )	58126	0.1004
Waterplane area (m <sup>2</sup> )	6870	0.9893
Wetted surface area (m <sup>2</sup> )	10073	1.4505
Radius of gyration / Lpp		0.25
$\bar{X}G$ / Lpp	*	-0.01824
$\bar{X}F$ / Lpp	**	-0.0578

\*  $\bar{X}G$  : distance of C.G. from

\*\*  $\bar{X}F$  : distance of center of flotation from

$$\left. \begin{aligned} Z_{11}I_1 + Z_{12}I_2 &= V_1 \\ Z_{21}I_1 + Z_{22}I_2 &= V_2 \end{aligned} \right\} \quad (3)$$

where  $I_1$  and  $I_2$  are the complex velocities of heaving and pitching oscillation respectively.  $Z_{ij}$  denotes the hydrodynamical and mechanical impedance.  $V_1$  and  $V_2$  are the wave exciting force and moment, which are calculated from the strip method by ordinary process.[1,2]

Here, we use an analogy in which the velocity and force or moment correspond to electric current and voltage, so that mass, spring constant and damping coefficient correspond to inductance, capacitance and resistance respectively.

Now, let us consider to suppress completely heaving and pitching oscillations. As easily seen, it is sufficient when the following conditions exist.

$$V_1 = V_2 = 0. \quad (4)$$

These conditions mean the ship form is wave-free, and the ship does not radiate waves to the forward direction when heaving and pitching.[1,2] Although such ship form is not yet known well, but we may fit some appendage to cancel out the wave exciting force and moment. For such appendage, let us choose two pairs of fins. The fore and aft fins are attached to the bow and stern respectively and their distances from the C.G. are  $l_1$  and  $l_2$ . Let us denote the impedances of the fore- and aft-fins as  $z_1$  and  $z_2$  respectively.

Then, the equations (3) become:

$$\left. \begin{aligned} Z_{11}'I_1 + Z_{12}'I_2 &= V_1' \\ Z_{21}'I_1 + Z_{22}'I_2 &= V_2' \end{aligned} \right\} \quad (5)$$

where

$$\left. \begin{aligned} Z_{11}' &= Z_{11} + z_1 + z_2, \\ Z_{12}' &= Z_{12} + (l_1 + \frac{iV}{\omega})z_1 + (\frac{iV}{\omega} - l_2)z_2, \\ Z_{21}' &= Z_{21} + l_1z_1 - l_2z_2 \\ Z_{22}' &= Z_{22} + l_1(l_1 + \frac{iV}{\omega})z_1 + l_2(l_2 - \frac{iV}{\omega})z_2 \end{aligned} \right\} \quad (6)$$

$$\left. \begin{aligned} V_1' &= V_1 + z_1v_{w1} + z_2v_{w2}, \\ V_2' &= V_2 + l_1z_1v_{w1} - l_2z_2v_{w2}. \end{aligned} \right\} \quad (7)$$

where  $v_{wj}$  is the upward orbital velocity of wave at the fin position and

$$v_{wj} = i\omega_0 a e^{Kz_j \pm iKl_j} \cdot \begin{Bmatrix} + \\ - \end{Bmatrix} \text{ for } j = \begin{Bmatrix} 1 \\ 2 \end{Bmatrix} \quad (8)$$

As in eq.(4), the oscillation-free conditions are

$$V_1' = V_2' = 0. \quad (9)$$

In a purely mathematical sense, these equations give four relations between real variables and we have six variables with regard to two pairs of fins, that is, their positions, areas and aspect-ratios. Therefore, we have two redundancies which may be determined arbitrarily.

Now, putting

$$\left. \begin{aligned} V_1 &= |V_1|e^{i\alpha_1}, \\ V_2 &= l_w |V_1|e^{i\alpha_2} \end{aligned} \right\} \quad (10)$$

$$\left. \begin{aligned} l_1 + l_2 &= 2l_m, \\ l_1 - l_2 &= 2l_c. \end{aligned} \right\} \quad (11)$$

We have from eqs.(9) with eqs.(7),

$$\frac{l_w - l_c + l_w \cos(\alpha_2 - \alpha_1) + il_w \sin(\alpha_2 - \alpha_1)}{l_m + l_c - l_w \cos(\alpha_2 - \alpha_1) - il_w \sin(\alpha_2 - \alpha_1)} = \frac{z_1}{z_2} e^{2iKl_m} \quad (12)$$

At first, for the convenience sake, let us assume two same fins are fitted. Then, we may verify the condition (12) becomes

$$\left. \begin{aligned} l_c &= l_w \cos(\alpha_2 - \alpha_1) \\ l_w \sin(\alpha_2 - \alpha_1) &= l_m \tan Kl_m, \end{aligned} \right\} \quad (13)$$

and then, putting these condition in the one of eqs.(7), we may calculate the impedance:

$$z_1 = z_2 = \frac{i\sqrt{l_m^2 + l_w^2}}{2\omega_0 a l_m} V_1 e^{-Kz_1 - iKl_c}. \quad (14)$$

For an actual calculation, we must search at first one of the root  $l_m$  of the second equation of eqs.(13) for a given wave number. Then, we may calculate  $l_c$  and  $z_1$  from eqs.(13) and (14). Here,  $z_1$  must lie in the first quadrant of the complex plane by the eq.(2). Hence, if it does not lie in the first quadrant, we must search another root which gives appropriate impedance.

From the impedance thus obtained, we may calculate its aspect-ratio and area as follows. Namely, cancelling the fin area from the real and imaginary part of the impedance of eq.(2), we have

$$\frac{z_c^3}{z_s^2} = \frac{32\pi\rho V^3 (A.R.)^4}{\omega^2 (1+A.R.)^3} \quad (15)$$

Solving this equation, we may determine the aspect-ratio and then calculate the fin area

from the real or imaginary part of the impedance.

Carrying out this calculation for the present model, we have results shown in Table 2 and show an example of the responses of the ship in waves in Figure 3. Thus, it seems that the appropriate combination of two pairs of fins to suppress completely heaving and pitching oscillations at any wave length exists.

However, this is only one case, so that we may not generalize this result to any ship, and moreover we can see in this result two difficulties. The one is that the aft fin lies far aft of ship's stern so that the actual installation might be impossible. The other is that there are cases to need fins of the very small aspect-ratio.

Table 2 Calculated particulars of two-pairs of fixed fins to stabilize heaving and pitching motions (model ship,  $F_n=0.18$ )

$\lambda/L$	Fin Position		Fin Particular		
	$l_1(m)$	$l_2(m)$	$A_f(m^2)$	$C_f(m)$	A.R.
0.9	-3.097	4.653	.053	.417	.305
0.95	-5.986	9.314	.016	.336	.142
1.0	-1.671	5.751	.048	.288	.577
1.05	0.486	3.707	.052	.500	.208
1.1	1.249	3.024	.069	.149	3.110
1.2	1.805	2.643	.078	.428	.425
1.4	2.236	2.643	.085	.645	.204
1.6	2.539	2.835	.098	.780	.161
1.8	2.823	3.076	.113	.886	.144
2.0	3.106	3.339	.127	.974	.134

	$A_f(m^2)$	$C_f(m)$	A.R.	$l_1(m)$	$l_2(m)$	cal.
Without Fin						
2P. Fixed	0.015	0.307	0.154	-5.99	9.31	----

design point :  $\lambda/L = 0.95$

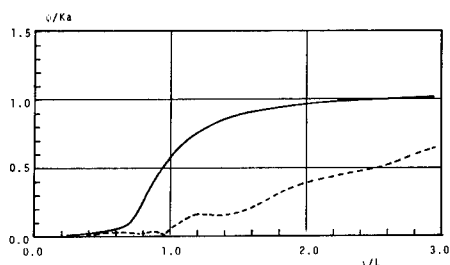
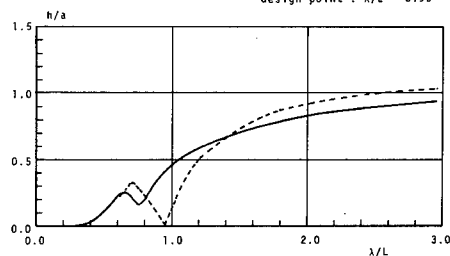


Figure 3 Amplitude responses of heave and pitch ;  $F_n=0.18$

We assume at first the force acting on the fins at one point so that these fins could not effect like calculations. In fact, we can verify this by calculations of a long distributed fins and this confirms at the same time that bilge keels hardly change the ship responses in waves.

On the contrary, we may put fin positions preliminarily in the condition of eqs.(9). Then, that condition may determine the ratio of impedances of two fins. However, we did not try such calculation. But in this procedure, we may hope at least to avoid the above difficulty to determine the fin positions.

In any way, we must notice that these fins obtained in this study have very much larger area than the one studied before. This is, of course, the largest difficulty to the practical application.

#### 4. ONE PAIR OF FINS FOR PITCH-FREE

In a similar way as the preceding case, we may design one pair of fins for heave-free or pitch-free.

Now, we put the equation of motion as follows:

$$\left. \begin{aligned} Z_{11}' I_1 + Z_{21}' I_2 &= V_1' \\ Z_{21}' I_1 + Z_{22}' I_2 &= V_2' \end{aligned} \right\} \quad (16)$$

$$\left. \begin{aligned} Z_{11}' &= Z_{11} + z \\ Z_{12}' &= Z_{12} + (1 + \frac{iV}{\omega})z \\ Z_{21}' &= Z_{21} + lz \\ Z_{22}' &= Z_{22} + l(1 + \frac{iV}{\omega})z \end{aligned} \right\} \quad (17)$$

$$\left. \begin{aligned} V_1' &= V_1 + z v_w \\ V_2' &= V_2 + l z v_w \end{aligned} \right\} \quad (18)$$

where  $z$  is the impedance and  $l$  is the distance between the attached fins and the C.G..

Cancelling each coupling term from eqs.(16), we have

$$\left. \begin{aligned} \frac{\Delta'}{Z_{22}'} I_1 &= V_1^* \\ \frac{\Delta'}{Z_{11}'} I_2 &= V_2^* \\ \Delta' &= Z_{11}' Z_{22}' - Z_{12}' Z_{21}' \end{aligned} \right\} \quad (19)$$



$$\begin{aligned}
 V_1^* &= V_1' - V_2' \frac{Z_{12}'}{Z_{22}'} \\
 &= \frac{1}{Z_{22}'} [V_1 Z_{22} - V_2 Z_{12} + \\
 &\quad z \{ (1 + \frac{iV}{\omega}) (1 V_1 - V_2) + v_w (Z_{22} - 1 Z_{12}) \}] \\
 V_2^* &= V_2' - V_1' \frac{Z_{21}'}{Z_{11}'} \\
 &= \frac{1}{Z_{11}'} [V_2 Z_{11} - V_1 Z_{21} + \\
 &\quad z \{ (V_2 - 1 V_1) + v_w (1 Z_{11} - Z_{21}) \}] .
 \end{aligned} \quad (20)$$

Therefore, the heave-free condition clearly is

$$V_1^* = 0, \quad (21)$$

and the pitch-free one is

$$V_2^* = 0. \quad (22)$$

For the heave-free at  $l_p$  forward the C.G.

$$I_1 + l_p I_2 = 0, \text{ for } V_1^* Z_{22}' + V_2^* Z_{11}' = 0. \quad (23)$$

Hereafter, we confine ourselves to the pitch-free case merely for a simplicity, and the heave-free case may be treated almost in the same way.[13] Then, for a given wave number and fin-position, we may obtain the fin impedance from eq.(22) with eq.(20).

As before, if the impedance lie in the first quadrant in the complex plane, we may calculate its aspect-ratio by eq.(15) and then its area. Otherwise, there does not exist the pitch-free fin in this case.

Table 3 is a result of such calculation and Figure 4 shows an example of responses in waves. As seen in the table, the fin area becomes smaller, the position approaches near mid-ship and at the same time its aspect-ratio becomes extraordinarily small, so that the fin could not have anti-pitching effect as remarked before. Thus, the only preferable position of the fins may be near the F.P. .

The responses in waves are remarkably lower than the one without fin. This seems only because of a very much large area of fin. Namely, the necessity of large fin area is the greatest difficulty for a practical application. Naturally, we may suppose this area of fin depends on the type of ship form, so that we add the same calculation with respect to various types of ships and found that the necessary fin area for pitch-free becomes smaller, when the water plane area becomes smaller; in another words, the vertical prismatic coefficient becomes greater.[14]

Therefore, the limiting ship form becomes similar as the so-called semi-submerged ship. But, in that type of ship, the responses in waves are generally larger than the ones of ordinary type of ships because of its smaller

wave-damping of the main hull.

Lastly, both the magnitude and phase of quantities appeared is important in these calculation, so that it is convenient and helpful to our understanding to plot them in the complex plane as shown in Figures 5 and 6. In the case of one pair of fins, it is preferable to plot  $V_1^*$  instead of  $V_1$ . These figures give us a clear geometrical image with respect to the effect of fin.

Table 3 Calculated particulars of a pair of fixed fins to stabilize pitching motion (model ship,  $Fn=0.18$ )

Fins Posi. (m)	Fin's Dim.	$\lambda/L$						
		1.05	1.1	1.2	1.4	1.6	1.8	2.0
1.1	$A_f (m^2)$	*	*	*	*	0.042	0.066	0.081
	$C_f (m)$	*	*	*	*	1.366	1.000	0.937
	A.R.	*	*	*	*	0.022	0.066	0.092
1.2	$A_f$	*	*	*	*	0.046	0.065	0.077
	$C_f$	*	*	*	*	1.000	0.820	0.794
	A.R.	*	*	*	*	0.046	0.096	0.122
1.3	$A_f$	*	*	*	0.040	0.062	0.072	0.081
	$C_f$	*	*	*	1.015	0.701	0.679	0.688
	A.R.	*	*	*	0.039	0.126	0.157	0.171
1.4	$A_f$	*	0.050	0.061	0.069	0.076	0.083	0.090
	$C_f$	*	0.884	0.655	0.593	0.598	0.618	0.641
	A.R.	*	0.064	0.143	0.197	0.213	0.218	0.219
1.5	$A_f$	0.077	0.075	0.072	0.074	0.076	0.084	0.089
	$C_f$	0.746	0.627	0.550	0.526	0.540	0.564	0.590
	A.R.	0.138	0.189	0.238	0.267	0.268	0.263	0.256

Note) \* means no solution

	$A_f (m^2)$	$C_f (m)$	A.R.	$l (m)$	Cal.
Without Fin	—	—	—	—	—
1P. Fixed	0.074	0.627	0.189	1.5	---

design point :  $\lambda/L = 1.1$

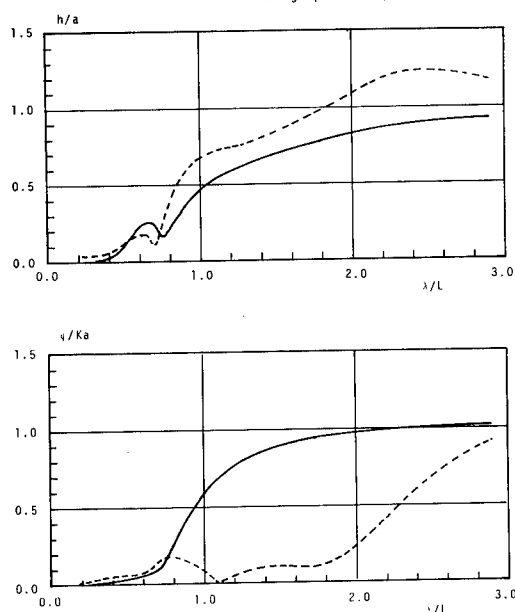


Figure 4 Amplitude responses of heave and pitch ;  $Fn=0.18$

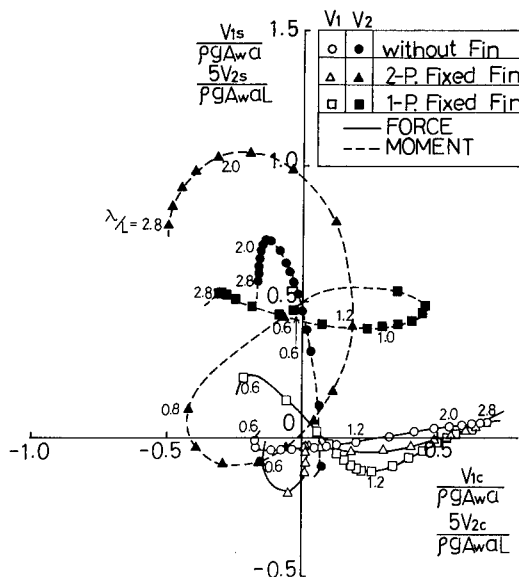


Figure 5 Vector representations of wave-exciting force and moment

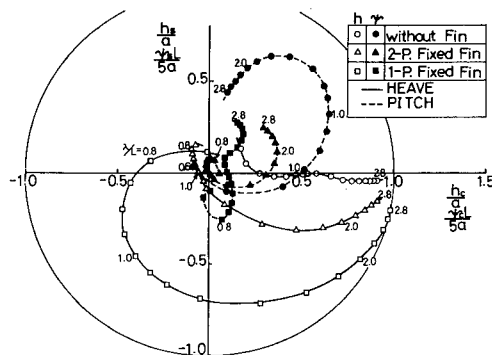


Figure 6 Vector representations of heave and pitch motions

## 5. EXPERIMENTS

To confirm the reliability of the foregoing theory, we carried out experiments using three-meter models shown in Table 1 at Meguro Ship-Model Basin of Defense Agency. The first test was carried out for a naked hull without fin, the second with two pairs of fins and the third with one pair of fins arranged as shown in Figure 7.

Before the tests in waves, resistance tests were carried out in calm water. Figure 8 shows the results. A large added resistance by fin is remarkable and the added resistance coefficient divided by the fin area is about 0.012 for one pair of fins and 0.019 for two pairs respectively. These values are extraordinarily higher than the value of 0.006 obtained by wind-tunnel test results at  $Re = 10^6$ . [8] These differences would be explained as that the relative angle of attack of fins to

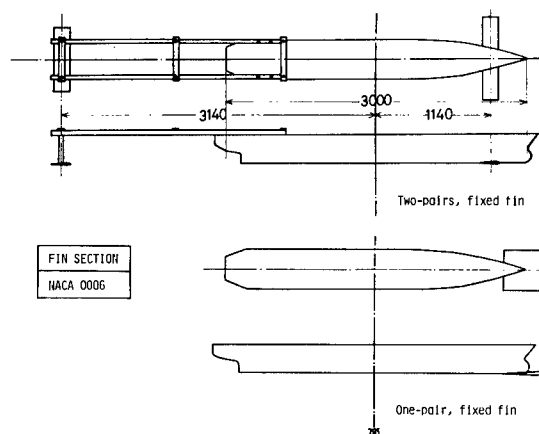


Figure 7 Arrangements of fins

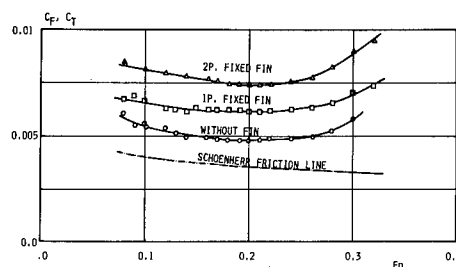


Figure 8 Resistance in calm sea

the water might have a certain value. In any way, this is no doubt one of the greatest practical difficulty.

Then, we carried out test in waves. The responses are shown in Figures 9 and 10 with fin particulars. These fins are selected merely for simplicity sake and do not give strictly heave and/or pitch-free but it might give a sufficient sea-keeping quality as seen in the figures. The agreement with theory and experiments seems fairly well but there are a little differences between them. Then, multiplying factor 0.8 to the fin's impedance, we have responses of chain lines in these figures. This correction seems not always right but do for pitching response for one pair of fins in Figure 10.

The resistance increases in waves are also measured by a gravity dynamometer and shown in Figures 11 and 12. The solid and dotted lines are theoretical values calculated by Gerritsma's formula [2] for the only main hull. The test results show that the resistance increase reduces fairly the amount near the wave length equal to the ship length and this is observed also by G.P. Stefan. [7] The one of the reason may be a motion reduction by fin because the resistance increase is proportional to the relative vertical velocity of ship to water and this is seen from theoretical values in Figure 11. The other may be a thrust produced by oscillating fin [10] but we have little knowledge about this side of phenomena, so that we leave this in the future and show only a rough approximation in Appendix.

	$A_F(m^2)$	$C_F(m)$	A.R.	$l_1(m)$	$l_2(m)$	Cal.	Exp.
Without Fin						—	●
2P. Fixed	0.050	0.160	1.938	1.14	3.14	---	○
2P. Fixed	0.040	0.144	do.	do.	do.	---	---

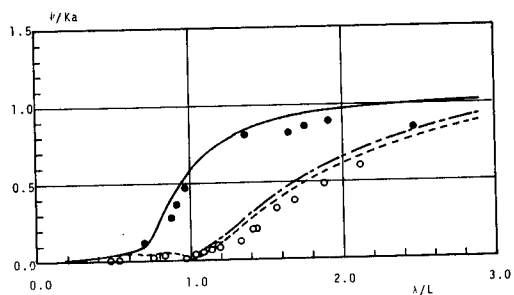
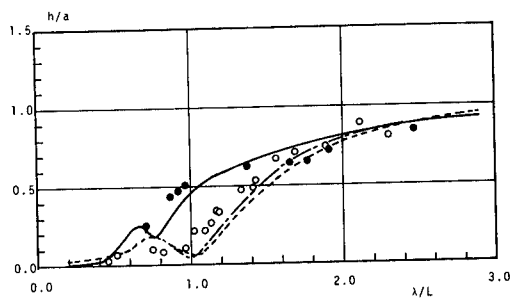


Figure 9 Experimental results of amplitude responses of a ship in waves (two-pairs)

	$A_F(m^2)$	$C_F(m)$	A.R.	$l(m)$	Cal.	Exp.
Without Fin					—	●
1P. Fixed	0.080	0.40	0.5	1.50	---	○
1P. Fixed	0.065	0.36	do.	do.	---	---

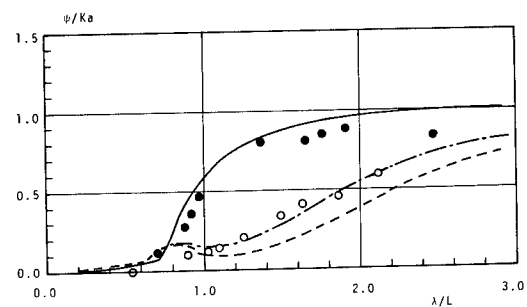
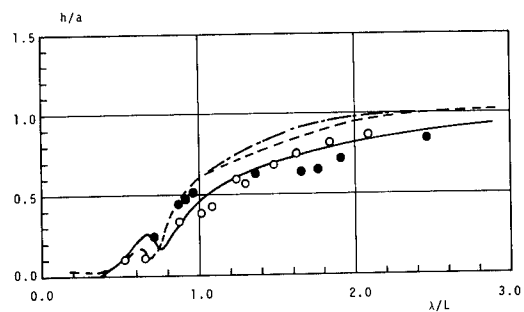


Figure 10 Experimental results of amplitude responses of a ship in waves (one-pair)

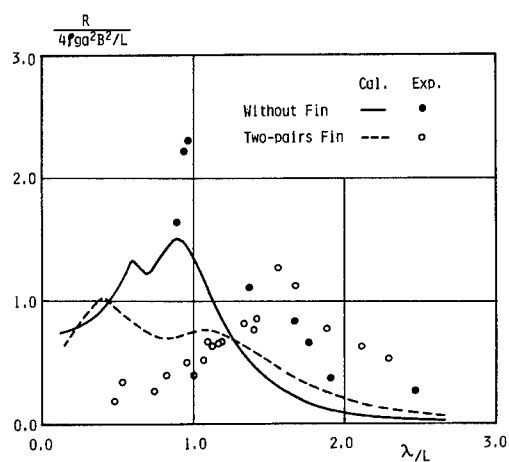


Figure 11 Resistance increase in waves (two-pairs)

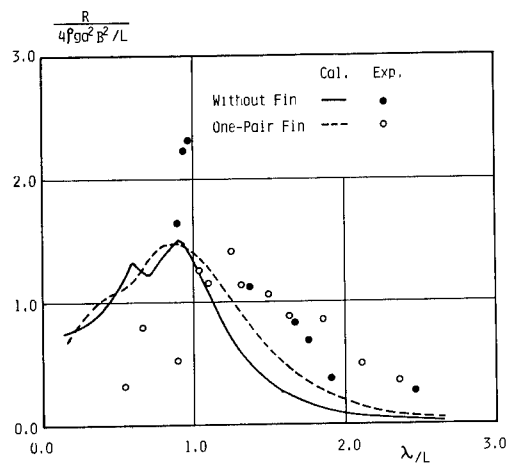


Figure 12 Resistance increase in waves (one-pair)

## 6. CONCLUSION

We have discussed the fins necessary to suppress completely the heaving and/or pitching oscillation at a given wave length in head seas and have the following conclusions.

(1) Two pairs of fins may be sufficient almost always to make a ship heave- and pitch-free. Although there are left two arbitrarinesses, we can calculate the position, area and aspect-ratio of fin assuming the same fin fitted. However, the position of fin lies far from the A.P. in almost all cases.

(2) A pair of fins would make a ship either heave-free or pitch-free. In this paper, we have dealt with the pitch-free case and calculated the particulars of fins for a given position near F.P.. However, such fins do not exist in shorter wave range but do in the range longer than resonance. This range shifts slightly if the hull forms of ships are different.

(3) In both cases, the fins thus obtained are much larger than the one studied in the past. The aspect-ratio sometimes becomes very much smaller but these solutions are false because such fins do not act effectively.

(4) The experiments were carried out and the experimental results agree well with the theory.

Now, the greatest difficulty may be, of course, such a large area of fin. Therefore, we have carried out the same calculation with respect to various types of ship and found that the fin area decrease when the vertical prismatic coefficient increases. Thus, a semi-submerged ship needs only a small area of fin but the responses in waves are much larger than the ordinary ship except the designed wave length. These observations suggest a dominant role of the damping force for reduction of oscillations.

## ACKNOWLEDGEMENT

We thank Messrs. M.Hayashida, S.Yamauchi and M.Miyazaki for their assistances carrying out the study. Also, we thank Meguro Ship Model Basin of Defense Agency and Hiratsuka Technical Institute Laboratory of Sumitomo Heavy Industry Co.Ltd. for their experimental support.

## REFERENCES

- 1) J.T.T.C. (Jul. 1969): Text of Symp. on Sea-Keeping Performance.
- 2) J.T.T.C. (Dec. 1977): Text of the second Symp. on Sea-Keeping Performance.
- 3) Abkowitz, M.A. (1959): The Effect of Anti-Pitching Fins on Ship Motion, S.N.A.M.E.
- 4) Matsui, M. et al. (1966): On the Controlled Anti-Pitching Fin, J.S.N.A. Japan, Vol.119.

- 5) Vugts, Ir.J.H. (1967): Pitching and Heaving with Fixed and Controlled Bow Fins, I.S.P., No.153.
- 6) Fein, J.A. et al. (1980): The Sea-Keeping Characteristics of a SWATH Ship, 13th O.N.R. Symp. Tokyo.
- 7) Stefun, G.P. (Oct.1959): Model Experiments with Fixed Bow Anti-Pitching Fins, J.S.R., Vol.3, No.2.
- 8) Abbott, I.H. and von Doenhoff, A.E. (1959): Theory of Wing Section, Dover Pub.
- 9) Lee, C.M. (1983): Preliminary Studies Leading to Seakeeping Hull Design, PRADS'83, Tokyo-Seoul.
- 10) Jacobsen, E. (Sep. 1981): The Foil Propeller, Wave Power for a Propulsion, 2nd Symp. on Wave and Tidal Energy, Cambridge, England.
- 11) Bessho, M. (1965): On Wave-Free Distribution in the Oscillating Problems, J.S.N.A. Japan, Vol.117.
- 12) Bessho, M. (Apr. 1982): Introduction to Water Wave Engineering, Bull. S.N.A. Japan, No.634.
- 13) Bessho, M. et al. (Jun. 1983): On the Ship Motion Reduction by Anti-Pitching Fins in Head Seas, J.S.N.A. Japan, Vol.153.
- 14) Bessho, M. et al. (Jun. 1984): On the Ship Motion Reduction by Anti-Pitching Fins in Head Seas (Second Report), J.S.N.A. Japan, Vol.155.

## APPENDIX

### Resistance Increase in Waves and Thrust of Fin

The resistance increase  $R$  in waves may be estimated by Gerritsma's formula[1]:

$$R = W / (c + V) \quad (A.1)$$

where

$$W = \frac{1}{2} \int_L N |v_r|^2 dx \quad (A.2)$$

and  $c$  is the phase velocity of wave.  $N$  and  $v_r$  denote the wave damping of the ship section and the vertical relative velocity respectively.  $W$  is the radiated wave power by a ship which is absorbed from the in-coming wave, so that this resistance results from the momentum loss of the in-coming wave.

Therefore, in the case of fin we could make use of this formula in this sense, that is,

$$R_f = \frac{\pi \rho V A_f |v_r|^2}{(c+V)(1+\frac{1}{A.R.})} \quad (A.3)$$

for a pair of fins, making use of eq.(2).

On the other hand, the oscillating fin may have a thrust.[10] Assuming quasi-steady process because of small reduced frequency for practical case, we may estimate it as follows. Namely, since the thrust of a pair of fins is the time mean of the x-component of the lift by eq.(1), we may have approximately

$$T = \frac{1}{2}(2L) \left| \frac{v_r}{V} \right|^2 = \frac{\pi \rho A_f |v_r|^2}{(1 + \frac{1}{A.R.})^2} \quad (A.4)$$

Of course, this must be multiplied some reduction factor, but represents its property qualitatively. Figures 13 and 14 are the calculated results corresponding to the experiments. The order of magnitude agrees well with the experiments but differs in phase.

In any way, if we expect a thrust of fin it is clear from these consideration that the aspect-ratio and the relative velocity to water must be large.

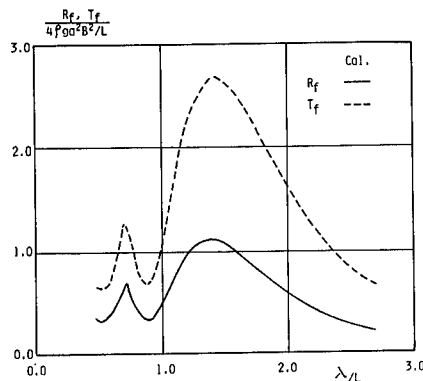


Figure 13 Resistance increase and thrust of fins (two-pairs)

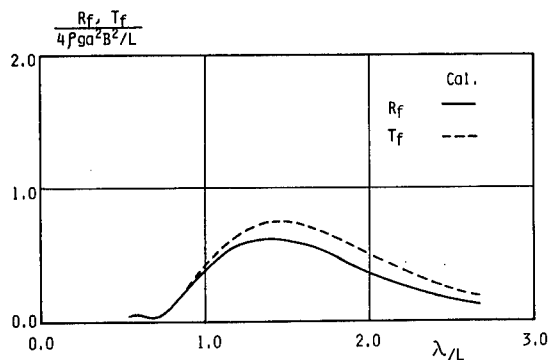


Figure 14 Resistance increase and thrust of fins (one-pair)

## DISCUSSION

Dr.-Ing. HIROSHI ISSHIKI,  
Technical Research Institute, Hitachi Zosen  
Corp., Osaka, Japan:

I would like to express my sincere respect for this very interesting and also very unique research.

I would like to ask two points. One point is related to the size of fins attached to a ship. Your fins seem to be rather big or, honestly speaking, too big as you may admit. Do you have any ideas to reduce the fin size, for example, by introducing springs or something like that?

The other point is your estimation of thrust generated by fins. It shows very interesting results, but seems to be rather incorrect. If correct, resistance increase in waves may become negative in some cases. This is against your experimental results. I would like to ask if you have any ideas how to improve the accuracy of your thrust estimation.

Dr. ROBERT MCGREGOR,  
University of Glasgow, United Kingdom:

This is a most interesting paper which parallels some work we are involved with at the University of Glasgow on SWATH ships. That topic, however, is being discussed by a colleague.

In addition to the analytic references (3,4) there was a full-scale trial of anti-pitching fins in Britain around 1960. The work was carried out by the Ship Division of NPL (now NMI) on two Royal Navy Minesweepers. The basis of the experiment was that one ship was fitted with a fixed reverse delta fin at the bow whereas the other was unmodified. The two vessels were then run together on parallel courses and the motions compared. The fin was generally successful in reducing the pitching motions by a substantial amount. However, the bow of the shallow draught vessels like minesweepers frequently emerges from the water. This exposed the bow fins to many slams and consequential damage.

It may be argued that minesweepers were a poor choice and that the containership hull in the present paper is more appropriate. Nevertheless, such ships do slam and intolerably high loads may be experienced, particularly if the vessel is to operate in high currents such as the Kuroshio. This seems to be strong practical reason for interest in such fins on semi-submerged vessels such as SWATH where a fin broach is much less likely.

In the experiments, were the waves large enough for any slamming to occur?

On a more detailed level the expression for  $C_L$  in Equation (1) has been questioned as to its accuracy when AR is very low and the formula

$$C_L' = \frac{1.8 \cdot \pi \cdot AR}{\sqrt{AR^2 + 4} + 1.8}$$

is sometimes preferred in such circumstances. There are also changes to  $C_M$  and  $C_D$ .

Finally, in the case of semi-submerged vessels, the added masses and damping are strongly frequency dependent. Could the authors say a little about whether similar complexities were found necessary?

JUNE-YOUNG WU,  
University of Glasgow, United Kingdom:

I enjoyed this paper very much. I agree that the bow fins are effective in pitch damping. Research on SWATH ship motion is being carried out in the Dept of Naval Architecture and Ocean Engineering Hydrodynamics Laboratory at the University of Glasgow. From these tests it can be easily seen that there is a large trim by the bow at higher speeds even in calm water and there can be instabilities in waves. In order to solve this problem, we did a fin size determination (1) based on the heave and pitch coupled equations of motion.

This paper reports a valuable contribution to the optimisation of fin position, fin area and the aspect ratio to minimise pitch motion based on a given speed and wave length. The results seem very satisfactory. However, for practical use, did the authors try to use the fin angle as a variable factor for a fixed fin position and aspect ratio? Since the lift coefficient is proportional to the angle of attack, the lift will increase and the pitching moment righting arm (fin position) need not be as large as figure 7 showed.

If possible, I would suggest that there is an active fin control otherwise the anti-pitching fin at the bow may experience a larger angle of attack owing to the induced angular velocity when pitching at large amplitude. Additionally, active fins may be controlled to prevent the lift breakdown from separation and stall.

Reference:

- (1) Wu, J.-Y. (1984): A Study on Fin Size for Anti-Pitching and Anti-Heaving in a SWATH. Report No NAOE-84-52, Dept of Naval Architecture and Ocean Engineering, University of Glasgow, Glasgow, UK.

## AUTHORS' REPLY

We would like to thank all discussers for their valuable comments.

In response to Mr. Wu's discussion, our model is a container ship, so that the trim is not severe both in calm water and in waves. However, I agree with the discussor's opinion that the angles of fin should be included as a variable factor. The resistance in calm water is very large when the fin is attached in our experiments. Therefore, active-controlled fins would be preferable for practical use.

To Dr. McGregor, the amplitudes of the incident waves were less than 10 cm, so that slamming did not occur in our experiments. The slamming and the wave-loads on the fins should be necessarily considered at the practical design stages. However, this paper is a feasibility study of the anti-pitching fins and we did not pay attention to such severe conditions.

The formula for  $C_L$  is assumed to be the same for any A.R. of fin merely for simplicity. I agree with the discussor's opinion that the formula for  $C_L$  should be modified when A.R. is very small.

To the third question, we have applied the present method to some models, one of which is nearly a semi-submersible, in Reference (14). Therefore, we believe that the present method could be applicable to a semi-submerged vessel without modifications.

To Dr. Isshiki, we also think that the large area of fin is one of the greatest difficulties for its practical use. Therefore, we should select a type of ship on which the small fin could act efficiently. An active-controlled fin attached to a semi-submerged vessel would be the best way for that purpose. Further, the fins should be preferably retractable into the hull when the water is calm.

To the second question, the formula for the thrust of fin (A.4), must include the effects of mutual interactions between main hull and fins, and reduced frequency. In any way, we need more experimental data.

# MULTIPLE SCATTERING OF SURFACE WATER WAVES AND THE NULL-FIELD METHOD

PAUL A. MARTIN

## ABSTRACT

Two rigid cylinders of infinite length are floating in the free surface of deep water with their generators parallel. The cylinders are held fixed and a given time-harmonic wave of small amplitude is incident upon them. The corresponding linear two-dimensional boundary-value problem for a velocity potential is treated using the null-field method. This method is exact. In the resulting equations, the effects of scattering by each cylinder in isolation (via the so-called 'T-matrix' for each cylinder), and of the spacing between the cylinders, are clearly separated; computationally, this is a very desirable feature. The method is used in two ways: first, it is shown that the 'wide-spacing' approximation is recovered when the exact equations are solved in an appropriate asymptotic limit. Second, the exact equations are truncated, and numerical solutions obtained for the model problem of scattering of regular surface waves by a pair of identical half-immersed circular cylinders (i.e. a catamaran). Comparisons with the wide-spacing approximation are also given. Extensions to three dimensions and to water of constant finite depth are mentioned.

## 1. INTRODUCTION

In recent years, there has been much interest in multiple-scattering problems, in which surface water waves interact with two (or more) partially-immersed rigid bodies. Such problems arise when studying, e.g., the interaction between neighbouring ships, wave-power devices, or elements of a single larger structure. The corresponding linear boundary-value problem (for time-harmonic waves) is easily formulated and can be solved by integral-equation methods, but this direct approach can be computationally expensive, especially for problems involving several three-dimensional bodies. Thus, Ohkusu (1975) wrote: 'For the purpose of calculating hydrodynamic forces..., it is essential that only the hydrodynamic properties of each element be given. A method having such a merit will facilitate the calculation for a body having many elements and may be applied to the

design arrangement of the elements'. This philosophy has led to various approximate techniques for treating multiple-scattering problems, e.g. Budal's theory of 'point absorbers' (1977), Simon's 'plane-wave' approximation (1982), and Ohkusu's 'wide-spacing' approximation (1970, 1975). In the present paper, we shall describe another method that only uses solutions of single-body problems, but which is exact. This work uses the null-field method, and is an extension of the author's work on single-body problems (Martin, 1981, 1984a) and of some corresponding work in acoustics by Peterson and Ström (1974).

The plan of the paper is as follows. After a literature survey in §2, we study (in §3) the two-dimensional problem of scattering by a single rigid cylinder which is floating in the free surface of deep water; this plane problem is labelled  $S_1$  below. We give a precise formulation of  $S_1$ , briefly review the use of integral-equation methods for its solution, and state the well-known Kreisel-Meyer relations (these relate the complex reflection and transmission coefficients for  $S_1$ ). Next, we describe the null-field method and introduce the T-matrix for  $S_1$ ; the construction of this matrix was first discussed by Waterman (1965) in the context of electromagnetic scattering problems, and the null-field/T-matrix method is now used widely in several branches of mathematical physics (see, e.g. Varadan and Varadan, 1980).

In §4, we consider a pair of floating cylinders. We formulate the corresponding boundary-value problem (labelled  $S_2$  below), and note the absence of a uniqueness theorem for  $S_2$ . We derive the null-field equations for  $S_2$ ; these can be solved for the boundary values of the potential. Under certain geometrical restrictions, the null-field equations can be reduced to matrix equations, involving the matrices  $Q$  and  $\bar{Q}$  which arise when  $S_1$  is solved for each cylinder in isolation (see §§3.2, 3.3); they also involve a matrix  $S$  which occurs in an addition theorem for Ursell's multipole potentials ( $S$  depends only on the spacing between the cylinders). If attention is focussed on the potential in the water, the matrix equations can be recast in terms of the matrix  $S$  and two T-matrices, one for each cylinder. We

Dr. P.A. Martin, Department of Mathematics, University of Manchester, Manchester M13 9PL, England.

solve this system of equations in two ways: first, we solve them asymptotically, and show that Ohkusu's wide-spacing approximation is recovered in an appropriate limit. (The wide-spacing approximation is a heuristic approach for solving  $S_1$ , in which only wave-like interactions between the cylinders are taken into account.) Second, we solve them numerically for the model problem of scattering of regular surface waves by a pair of identical half-immersed circular cylinders, and compare our results with those obtained using the wide-spacing approximation. We conclude with a discussion of some possible extensions and generalisations of the null-field method.

## 2. LITERATURE SURVEY

The literature on scattering of water waves by two, or more, rigid bodies is quite extensive, but does not seem to have been surveyed previously. Here, we shall restrict ourselves to two-dimensional interactions between a pair of cylinders. (For an interesting account of the history of twin-hull ships, see Corlett, 1969.)

### 2.1 The Method of Multipoles

Apart from some work on scattering by two thin vertical barriers (see Evans and Morris (1972) for references), the first problem to be studied extensively was the radiation problem for two half-immersed circular cylinders. Thus, Ohkusu (1969) and Wang and Wahab (1971) extended Ursell's multipole method (1949) for one cylinder to analyse the heaving motion of a catamaran, consisting of two identical, rigidly-connected, half-immersed circular cylinders (we call this 'semicircle-catamaran problem'). For this symmetrical problem, the velocity potential at a point  $P$  in the fluid can be represented as

$$\phi(P) = \sum_{n=1}^{\infty} a_n \{ \phi_n(r_P) + (-1)^n \phi_n(r'_P) \},$$

where  $\phi_n$  are the multipole potentials defined in Appendix A. This representation satisfies all the conditions of the problem, except the boundary condition on the wetted surfaces of the cylinders; applying this condition allows the coefficients  $a_n$  to be determined. Ohkusu (1969) and Wang and Wahab (1971) computed the wave amplitude at infinity and the virtual-mass coefficient, and found good agreement with the corresponding values obtained from their experiments. Ohkusu (1970) has also made similar calculations for the swaying and rolling motions of the same catamaran, whilst Spencer and Sayer (1981) have analysed the motions of two freely-floating identical circular cylinders.

The multipole method has also been used to treat problems involving totally-submerged circular cylinders. Thus, Wang (1970, 1981) has presented extensive numerical results for two identical cylinders, each submerged to the same depth. More recently, O'Leary (1984) has shown how the method can be used for an arbitrary number of totally-submerged circular cylinders; each cylinder can have any radius and any depth

of submergence. Essentially, her method uses an addition theorem for the submerged multipole potentials, so that the boundary condition on each cylinder can be imposed; an addition theorem for  $\phi_n$  has previously been given by Bencheikh (1982) and Martin (1984b); see §4.2. O'Leary also gave numerical results for several configurations of two and three identical cylinders.

### 2.2 Integral-equation Methods

Several authors have used integral-equation methods to treat multiple-scattering problems. Most of these authors represented  $\phi$  as a distribution of simple wave sources over the wetted surfaces of the cylinders, and then solved the corresponding integral equation of the second kind for the unknown source density (see §4.1.). Thus, Nordenström et al. (1971), Kim (1972), Lee et al. (1973) and Katory et al. (1980) have all solved the semicircle-catamaran problem for deep water, whilst Chung and Coleman (1975) have solved it for water of constant finite depth. The agreement between these solutions, those obtained using the method of multipoles, and those determined by experiment is generally very good. Other geometries have also been investigated, e.g. two different rectangles (Kim, 1972; Katory et al., 1980), two triangles (Lee et al., 1973), and bulbous-form catamarans (Kim, 1972; Maeda, 1975).

Integral-equation methods have also been used for totally-submerged cylinders. Thus, Schnute (1971) has solved an equation for the total potential (see §4.1), for two circular cylinders; he reduces it to a system of algebraic equations, but does not give numerical results. Chakrabarti (1979) has solved an equation for the diffraction potential, and has presented numerical results for several configurations of two identical circular cylinders.

Integral equations can also be obtained by applying Green's theorem to  $\phi$  and the simple logarithmic source potential. These equations have simple kernels but the range of integration includes the free surface, the bottom, and two vertical control surfaces at some distance from the floating cylinders. The radiation condition (6), or an approximation to it, is imposed on these vertical surfaces, and the bottom is included so as to obtain a finite range of integration. For details of the method, see Mei (1978) or Yeung (1982). This method has been used by Ho and Harten (1975) to analyse the motion of one or two rectangular cylinders oscillating near a vertical wall, and by Ijima et al. (1976) to compute the transmission coefficient for the semicircle-catamaran problem.

### 2.3 Other Methods

Leonard et al. (1983) have used a finite-element method to solve the semicircle-catamaran problem for water of constant finite depth, and the corresponding problem with freely-floating cylinders. It may be observed that their results for the catamaran are in good qualitative agreement with those of Chung and Coleman (1975).

Two approximate methods have been used to



treat two-dimensional multiple-scattering problems. Alker (1978) has used the method of matched asymptotic expansions to study the scattering of short waves by two partially-immersed cylinders that do not make plane vertical intersections with the free surface. He has shown, e.g., that for a symmetric pair of cylinders, there is an infinite number of frequencies at which there is no reflected wave.

Secondly, Ohkusu (1970) has used a 'wide-spacing' approximation, in which only wave-like interactions between the cylinders are taken into account. This leads to an approximate solution to the multiple-scattering problem in terms of the solutions to various single-cylinder problems. An alternative treatment has been given by Srokosz and Evans (1979); see Appendix C. For the semicircle-catamaran problem, Ohkusu (1970) obtained good agreement with the exact solution (Ohkusu, 1969; Wang and Wahab, 1971), even when the assumption that the spacing between the cylinders is large compared to the wavelength is not valid. (This assumption is made precise in §4.4.) Other applications have been made by Ohkusu (1970, 1975, 1976), Ohkusu and Takaki (1971), Srokosz and Evans (1979) and Masubuchi and Shinomiya (1981).

### 3. SCATTERING BY ONE CYLINDER

Consider a rigid horizontal cylinder which is partially immersed in the free surface of a fluid. We suppose that the cylinder is fixed, and that the fluid is incompressible, inviscid and of infinite depth. We take Cartesian coordinates  $(x, y, z)$ , with the  $z$ -axis horizontal and the  $y$ -axis vertical ( $y$  increasing with depth) such that the free surface occupies a portion of the plane  $y = 0$ . For simplicity, we consider beam seas (waves with crests parallel to the  $z$ -axis) whence the fluid motion can be considered to be two-dimensional, i.e. independent of  $z$ . We assume that the fluid motion is irrotational, whence a velocity potential exists. If we further assume that the motion has a harmonic time-dependence (with radian frequency  $\omega$ ), then we can write the velocity potential as the real part of  $\phi(P)e^{-i\omega t}$ ; henceforth, we shall suppress the factor  $e^{-i\omega t}$ . For waves of small amplitude, the total potential  $\phi$  solves the following linear two-dimensional boundary-value problem:

Scattering boundary-value problem  $S_1$ .

Determine a function  $\phi(P)$ , such that  $\phi$  satisfies Laplace's equation

$$\left(\frac{\partial^2}{\partial x^2} + \frac{\partial^2}{\partial y^2}\right)\phi(P) = 0 \quad \text{in } D, \quad (1)$$

the free-surface condition

$$K\phi + \frac{\partial \phi}{\partial y} = 0 \quad \text{on } F, \quad (2)$$

the boundary condition

$$\frac{\partial \phi(P)}{\partial n_p} = 0 \quad \text{on } \partial D, \quad (3)$$

and the condition that the fluid motion vanishes as  $y \rightarrow \infty$ ,

$$|\text{grad } \phi| \rightarrow 0 \quad \text{as } y \rightarrow \infty. \quad (4)$$

In addition, if we define the diffraction potential  $\phi_D$  by

$$\phi_D = \phi - \phi_I, \quad (5)$$

then  $\phi_D$  must satisfy the radiation condition

$$\left(\frac{\partial}{\partial r_p} - iK\right)\phi_D \rightarrow 0 \quad \text{as } r_p \rightarrow \infty. \quad (6)$$

Here, we denote the fluid domain (in the  $xy$ -plane) by  $D$ , the mean free surface by  $F$  and the wetted surface of the cylinder by  $\partial D$ ; capital letters  $P, Q$  denote points of  $D$ ; lower-case letters  $p, q$  denote points of  $\partial D$ ; the origin  $O$  is assumed to lie in  $F_-$ , the portion of the line  $y=0$  which is inside the body;  $D_-$  denotes the interior of the body, i.e. the region with boundary  $\partial D \cup F_-$ ;  $r_p$  is the position vector of  $P$  with respect to  $O$ ;  $r_p = |r_p|$ ; and  $\partial/\partial n_p$  denotes normal differentiation at the point  $p$ , in the direction from  $\partial D$  into  $D$ . Also,  $K = \omega^2/g$ , where  $g$  is the acceleration due to gravity, and  $\phi_I$  is the velocity potential of the given incident wave.  $\phi_I$  satisfies (1) everywhere in  $y > 0$  (except possibly at a finite number of isolated points in  $D$ ) and (2) everywhere on  $y = 0$ . For example,  $\phi_I$  may correspond to a radiating (line) source in  $D$ , or to a train of regular surface waves.

Let  $\partial D^*$  denote the union of  $\partial D$  and its mirror image in  $F$ . We say that  $\partial D$  has properties  $J$  if  $\partial D^*$  is convex and twice-differentiable. John (1950) has shown that if  $\partial D$  has properties  $J$ , then  $S_1$  has precisely one solution. Actually, John's uniqueness theorem holds if

- (i) all vertical lines drawn down from  $F$  do not meet  $\partial D$ ; his existence theorem holds if, in addition to (i),
- (ii)  $\partial D$  is twice-differentiable and meets  $F$  at right angles.

More recently, Simon and Ursell (1984) have generalised John's uniqueness theorem to cover cases in which (i) is not satisfied, e.g. certain bulbous sections are now covered; if (ii) still holds, then integral-equation methods will yield a corresponding existence theorem.

In many applications, the incident potential  $\phi_I$  corresponds to a train of regular surface waves; for such a wavetrain propagating from  $x = +\infty$  towards the cylinder, we have

$$\phi_I \equiv \phi_I^+ = (gA_+/\omega)e^{-Ky-iKx}, \quad (7)$$

where  $|A_+|$  is the amplitude of the wave. This wave will be partially reflected and partially transmitted; we define (complex) reflection and transmission coefficients,  $r_+$  and  $t_+$  respectively, by

$$\frac{\omega}{gA_+} \phi(P) \sim \begin{cases} e^{-Ky}(e^{-iKx} + r_+ e^{iKx}) & \text{as } x \rightarrow +\infty, \\ t_+ e^{-Ky-iKx} & \text{as } x \rightarrow -\infty. \end{cases} \quad (8)$$

Similarly, for a wave propagating from  $x = -\infty$ , we have

$$\phi_I \equiv \phi_I^- = (gA_-/\omega)e^{-Ky+iKx} \quad (9)$$

and

$$\frac{\omega}{gA_-} \phi(P) \sim \begin{cases} t_- e^{-Ky+iKx} & \text{as } x \rightarrow +\infty, \\ e^{-Ky}(e^{iKx} + r_- e^{-iKx}) & \text{as } x \rightarrow -\infty. \end{cases} \quad (10)$$

It is well known that  $r_{\pm}$  and  $t_{\pm}$  satisfy the following relations:

$$t_+ = t_- = t, \text{ say}; \quad (11)$$

$$|r_+| = |r_-| = |r|, \text{ say}; \quad (12)$$

$$|r|^2 + |t|^2 = 1; \quad (13)$$

and

$$tr_+^* + t^*r_- = 0, \quad (14)$$

where the asterisk denotes the complex conjugate. Using (12), (14) can be rewritten as

$$2 \arg(t) - \arg(r_+) - \arg(r_-) = \pi \text{ modulo } 2\pi. \quad (15)$$

Collectively, we shall call (11), (12), (13) and (14) the Kreisel-Meyer relations; they are derived systematically by Newman (1977) for water of constant finite depth. Kreisel (1949) obtained (12) and (13), and their generalisations to the situation where the asymptotic depths of water are different at  $x = \pm\infty$ . R. Meyer, in an appendix to a paper by Biesel and Le Méhauté (1955), proved (11), (12), (13) and (14).

### 3.1 Integral-equation Methods

Typically,  $S_1$  is solved by integral-equation methods; for a summary, see, e.g. Martin (1981), Mei (1978) or Yeung (1982). To derive an integral equation, we need a fundamental solution:

$$G(P, Q) \equiv G(x, y; \xi, \eta) = \frac{1}{2} \log \frac{(x-\xi)^2 + (y-\eta)^2}{(x-\xi)^2 + (y+\eta)^2} - 2 \int_0^\infty e^{-k(y-\eta)} \cos k(x-\xi) \frac{dk}{k-K}. \quad (16)$$

$G$  satisfies (1) (except at  $P = Q$ ), (2), (4) and (6); it is the potential at  $P$  due to a wave source at  $Q$  (in the absence of the body).

If we apply Green's theorem twice, once in  $D$  to  $\phi_D$  and  $G$ , and once in  $D_-$  to  $\phi_I$  and  $G$ , and add the resulting equations, we obtain (cf. Martin, 1982)

$$2\pi\phi_D(P) = - \int_{\partial D} \phi(q) \frac{\partial}{\partial n_q} G(P, q) ds_q, \quad P \in D, \quad (17)$$

$$\pi\phi(P) + \int_{\partial D} \phi(q) \frac{\partial}{\partial n_q} G(P, q) ds_q = 2\pi\phi_I(P), \quad P \in \partial D \quad (18)$$

and

$$2\pi\phi_I(P) = \int_{\partial D} \phi(q) \frac{\partial}{\partial n_q} G(P, q) ds_q, \quad P \in D_-. \quad (19)$$

(18) is a Fredholm integral equation of the second kind for  $\phi(q)$ ; it is uniquely solvable except at a certain discrete set of values of the wavenumber  $K$ , called the irregular values. Irregular values are not physical ( $S_1$  is uniquely solvable for all values of  $K$ ), but are a consequence of the method of solution. They can be removed in several ways; see, e.g. Ursell (1981).

(17) is an integral representation for  $\phi_D(P)$  as a distribution of wave dipoles over  $\partial D$ , whilst (19) is an integral relation satisfied by  $\phi_I$  at all points in  $D_-$ . We shall use (19) as the basis of our derivation of the system of null-field equations. We shall also require the following bilinear expansion of  $G$  (Ursell, 1981):

$$G(P, Q) = \sum_{m=1}^{\infty} \alpha_m(r_P) \phi_m(r_Q), \quad r_P < r_Q. \quad (20)$$

where the functions  $\alpha_m$  and  $\phi_m$  are defined in Appendix A; each is harmonic and satisfies the free-surface condition (2);  $\alpha_m$  are regular, whilst the multipole potentials  $\phi_m(r_P)$  are singular at 0 and satisfy the radiation condition (6). Henceforth, we shall use a summation convention: sum over repeated suffices from 1 to  $\infty$ . Thus (20) becomes

$$G(P, Q) = \alpha_m(r_P) \phi_m(r_Q), \quad r_P < r_Q.$$

### 3.2 The Null-field Method

Let  $C_-$  be the inscribed semicircle to  $\partial D$ , centered on 0. If we restrict  $P$  (in  $D_-$ ) to lie inside  $C_-$ , we can substitute (20) into (19) giving

$$2\pi\phi_I(P) = d_m \alpha_m(r_P), \quad (21)$$

where

$$d_m = \int_{\partial D} \phi(q) \frac{\partial}{\partial n_q} \phi_m(r_q) ds_q \quad (m=1, 2, \dots). \quad (22)$$

The constants  $d_m$  are known; they are given in terms of  $\phi_I$  by

$$\int_{\partial D} \{ \phi_I(q) \frac{\partial}{\partial n_q} \phi_m(r_q) - \phi_m(r_q) \frac{\partial}{\partial n_q} \phi_I(q) \} ds_q. \quad (23)$$

For example, if  $\phi_I = \phi_I^+$ , comparison of (7), (21) and (A.1) shows that

$$d_1 = -id_2 = i\pi(gA_+/\omega), \quad d_m = 0 \quad \text{for } m > 2. \quad (24)$$

(22) are called the null-field equations; they form an infinite system of moment-like equations from which  $\phi(q)$  is to be determined. It is known that the null-field equations are uniquely solvable for all values of  $K$ —irregular values do not occur with the null-field

method (Martin, 1981).

To solve the null-field equations, we begin by choosing a basis for representing functions defined on  $\partial D$ ; let  $\{\phi_n(q)\}$  ( $n=1,2,\dots$ ) be such a basis. Thus, we may write

$$\phi(q) = a_n \phi_n(q) \quad (25)$$

where  $a_n$  ( $n=1,2,\dots$ ) are unknown coefficients. Substituting (25) into (22) gives

$$Q_{mn} a_n = d_m \quad (m=1,2,\dots), \quad (26)$$

where

$$Q_{mn} = \int_{\partial D} \phi_n(q) \frac{\partial}{\partial n_q} \phi_m(r_q) ds_q. \quad (27)$$

If we truncate the system (26), we obtain a numerical method for solving the null-field equations; this method has been used to solve the radiation problem associated with the heaving oscillations of a half-immersed elliptic cylinder (Martin, 1981). A different method for solving (26) has been used by Martin (1984a); this numerical method is only applicable when  $\phi_I = \phi_I^+$  or  $\phi_I = \phi_I^-$ .

### 3.3 The T-matrix

Once  $\phi(q)$  has been found by solving the null-field equations,  $\phi_D(P)$  is given by (17). Let  $C_+$  be the escribed semicircle to  $\partial D$ , centred on  $O$ . If we restrict  $P$  (in  $D$ ) to lie outside  $C_+$ , we can substitute (20) into (17) giving

$$2\pi\phi_D(P) = c_m \phi_m(r_p) \quad (28)$$

where

$$c_m = - \int_{\partial D} \phi(q) \frac{\partial}{\partial n_q} \alpha_m(r_q) ds_q \quad (m=1,2,\dots). \quad (29)$$

Substituting (25) into (29), we obtain

$$c_m = - \hat{Q}_{mn} a_n \quad (m=1,2,\dots) \quad (30)$$

where

$$\hat{Q}_{mn} = \int_{\partial D} \phi_n(q) \frac{\partial}{\partial n_q} \alpha_m(r_q) ds_q. \quad (31)$$

Does the series on the right-hand side of (28) represent  $\phi_D(P)$  (where  $\phi_D + \phi_I$  solves  $S_1$ ) throughout  $D$  (and not just outside  $C_+$ )? The assumption that it does is called the Rayleigh hypothesis in acoustic scattering. The Rayleigh hypothesis does not seem to have been investigated in the context of water-wave problems; however, we can expect that whether it is correct or not will depend on the shape of  $\partial D$ ; cf. Millar (1973), van den Berg and Fokkema (1979).

Now, the system (26) is uniquely solvable, i.e.  $Q^{-1}$ , the inverse of the infinite matrix  $Q$ , exists. Thus, eliminating  $a_n$  between (26) and (30), we obtain

$$c_m = T_{mn} d_n \quad (m=1,2,\dots) \quad (32)$$

where

$$T_{mn} = - \hat{Q}_{m\ell} \theta_{\ell n}^{-1} \quad (33)$$

is known as the T-matrix. Given  $T$ , we can determine the diffraction potential,  $\phi_D$ , outside  $C_+$  for any given incident potential,  $\phi_I$ , without computing the values of  $\phi$  on  $\partial D$ .

Let us now forget about the derivation of the T-matrix, and merely assume that the coefficients  $c_m$  and  $d_m$  occurring in the representations (21) and (28), respectively, are related through a matrix  $T_{mn}$  by (32). What properties does such a matrix have? To begin with, the unique-solvability of  $S_1$  implies that  $T$  exists and is unique. This, in turn, implies that  $T$  is independent of the choice of basis  $\{\phi_n\}$ , although this choice may be important in numerical calculations when  $T$  must necessarily be truncated.

Secondly, reciprocity considerations show that  $T$  is symmetric,

$$T_{mn} = T_{nm}. \quad (34a)$$

Thirdly, energy considerations show that  $T$  satisfies

$$\frac{2}{\pi} \operatorname{Im}(T_{mn}) + T_{1m} T_{1n}^* + T_{2m} T_{2n}^* = 0. \quad (34b)$$

(34) are derived by Martin (1984c). They are useful because they provide independent checks on numerical calculations. Also, by choosing particular values for  $m$  and  $n$ , we can recover all of the Kreisel-Meyer relations, e.g.,  $T_{12} = T_{21}$  implies that  $t_+ = t_-$ ; in fact, we have (see Martin, 1984c)

$$\pi i T_{11} = 1 - t + \frac{1}{2}(r_- + r_+), \quad (35a)$$

$$\pi i T_{22} = 1 - t - \frac{1}{2}(r_- + r_+), \quad (35b)$$

and

$$\pi T_{12} = \pi T_{21} = \frac{1}{2}(r_- - r_+). \quad (35c)$$

## 4. SCATTERING BY TWO CYLINDERS

Suppose, now, that a second rigid cylinder is partially immersed in the free surface, with its generators parallel to those of the first cylinder. As before, we denote the fluid domain (in the  $xy$ -plane) by  $D$  and the mean free surface by  $F$ . We distinguish all quantities pertaining to the second cylinder by a prime, e.g.  $\partial D'$  denotes its wetted surface. Let  $\partial D'' = \partial D \cup \partial D'$ ; lower-case letters  $p, q$  denote points of  $\partial D''$ . The analogue of  $S_1$  for two fixed cylinders is the following problem: Scattering boundary-value problem  $S_2$ .

Determine a function  $\phi(P)$ , such that  $\phi$  satisfies Laplace's equation (1) in  $D$ , the free-surface condition (2) on  $F$ , the boundary condition

$$\frac{\partial \phi(p)}{\partial n_p} = 0 \quad \text{on } \partial D'', \quad (36)$$

and the condition (4) as  $y \rightarrow \infty$ . In addition,  $\phi_D = \phi - \phi_I$  must satisfy the radiation condition (6).

In order to make some progress with the analysis of  $S_2$ , we make the following Uniqueness assumption.  $S_2$  has at most one solution, i.e. the only solution of the homogeneous problem ( $\phi_I = 0$ ) is the trivial solution,  $\phi \equiv 0$ .

To the author's knowledge, this result has not been proved. John's proof (1950) for one cylinder does not seem to extend to two cylinders. A proof may also impose some restrictions on the geometry: here, we shall suppose that  $\partial D$  and  $\partial D'$  each have properties J.

Although we do not have a uniqueness theorem for  $S_2$ , uniqueness can be proved for some other configurations. Thus, John's proof succeeds for two (or more) floating three-dimensional bodies (each having a wetted surface which is bounded and has properties J); the essential difference between this problem and  $S_2$  is the connectivity of the free surface (note that John's proof also fails for a single floating torus). We also have three results for totally-submerged bodies: Schnute (1971) has proved uniqueness for a pair of widely-spaced circular cylinders, and theorems due to Maz'ja (see Hulme, 1984) and Simon and Ursell (1984) guarantee uniqueness for any two (or more) cylinders, subject to certain geometrical restrictions.

Before describing some methods for solving  $S_2$ , we introduce some more notation. Let  $F'_1$  denote the portion of the line  $y = 0$  inside the second cylinder, and let  $D'_1$  denote the interior region bounded by  $F'_1$  and  $\partial D'$ . Choose a second origin  $O' \in F'_1$  and let  $r'_p$  denote the position vector of  $P$  with respect to  $O'$  (see Fig.1).  $\phi_m(r'_p)$  denotes the  $m$ -th multiple potential centered on (i.e. singular at)  $O'$ ;  $\alpha_m(r'_p)$  is defined similarly.

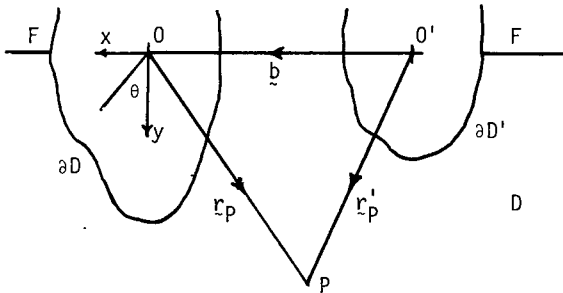


Figure 1. The two cylinders.

#### 4.1 Integral-equation Methods

Integral equations can be, and have been, used to solve  $S_2$  (see §2.2); one example is equation (18), with  $\partial D$  replaced by  $\partial D''$  (this is the equation solved by Schnute, 1971); another is

$$\pi\mu(p) + \int_{\partial D''} \mu(q) \frac{\partial}{\partial n_p} G(p, q) ds_q = - \frac{\partial}{\partial n_p} \phi_I(p), \quad (37)$$

which is obtained by supposing that  $\phi_D(p)$  can be represented as a distribution of sources over  $\partial D''$ ,

$$\phi_D(p) = \int_{\partial D''} \mu(q) G(p, q) ds_q. \quad (38)$$

However, if the uniqueness assumption is correct, then these equations will suffer from difficulties at irregular values of  $K$ , although no such difficulties have been reported in the literature. Irregular values can be eliminated by using a different source function (Martin, 1984b), but this does not seem to be the most efficient way of solving  $S_2$ . In fact, we shall not give further consideration to integral-equation methods.

#### 4.2 The Null-field Method

If we apply Green's theorem thrice, once in  $D$  to  $\phi_D$  and  $G$ , once in  $D_-$  to  $\phi_I$  and  $G$ , and once in  $D'_1$  to  $\phi_I$  and  $G$ , and add the resulting equations, we obtain

$$2\pi\phi_D(P) = - \int_{\partial D''} \phi(q) \frac{\partial}{\partial n_q} G(P, q) ds_q, \quad P \in D, \quad (39)$$

and

$$2\pi\phi_I(P) = \int_{\partial D''} \phi(q) \frac{\partial}{\partial n_q} G(P, q) ds_q, \quad P \in D_- \cup D'_1. \quad (40)$$

Consider (40) for  $P \in D_-$ . Following the derivation in §3.2, we restrict  $P$  to lie inside  $C_-$ ; we observe that for all points  $q \in \partial D''$ ,  $r_q > r_p$  and so we can use (20); and we use the representation (21) for  $\phi_I$  to obtain

$$d_m = \int_{\partial D''} \phi(q) \frac{\partial}{\partial n_q} \phi_m(r_q) ds_q \quad (m=1,2,\dots) \quad (41a)$$

Similarly, let  $C'_1$  be the inscribed semicircle to  $\partial D'$  centred on  $O'$ . If we now consider (40) for  $P \in D'_1$  and restrict  $P$  to lie inside  $C'_1$ , we obtain

$$d'_m = \int_{\partial D''} \phi(q) \frac{\partial}{\partial n_q} \phi_m(r'_q) ds_q \quad (m=1,2,\dots), \quad (41b)$$

where  $d'_m$  ( $m=1,2,\dots$ ) are the coefficients in a second representation for  $\phi_I$ ,

$$2\pi\phi_I(P) = d'_m \alpha_m(r'_p). \quad (42)$$

The coefficients  $d_m$  and  $d'_m$  ( $m=1,2,\dots$ ) are assumed to be known; moreover, they are related, since (21) and (42) are two representations of the same incident potential (see, e.g. (68)).

(41) are the null-field equations for  $S_2$ . It can be proved that if the uniqueness assumption is correct, then the null-field equations are uniquely solvable for all real values of  $K$ .

To solve the null-field equations, we represent  $\phi(q)$  on  $\partial D$  by (25), and on  $\partial D'$  by

$$\phi(q) = a'_n \phi'_n(q), \quad (43)$$

where  $\{\phi'_n(q)\}$  is a second set of basis functions and  $a'_n (n=1,2,\dots)$  are unknown coefficients. Substituting (25) and (43) into (41a), we obtain

$$d_m = Q_{mn} a_n + a'_n \int_{\partial D'} \phi'_n(q) \frac{\partial}{\partial n_q} \phi_m(r_q) ds_q \quad (m=1,2,\dots), \quad (44)$$

where  $Q_{mn}$  is given by (27). The integral in (44) is over  $\partial D'$ . We would like to express it in terms of known integrals over  $\partial D'$ . To do this, we must replace  $\phi_m(r_q)$  by functions centred on  $O'$ ; since  $\phi_m(r_q)$  is regular near  $O'$ , it has an expansion in terms of  $\alpha_m(r'_q)$ . In fact, we have the following

Addition theorem.

$$\phi_m(r_p) = S_{mn}(-b) \alpha_n(r'_p), \quad (45)$$

where  $r'_p = r_p + b$  and  $r'_p < b = |b|$ . The matrix  $S$  is defined in Appendix B; it satisfies

$$S_{mn}(-b) = S_{nm}(b). \quad (46)$$

This theorem can be proved either by introducing complex variables (Bencheikh, 1982) or by using integral representations; both proofs are sketched by Martin (1984b).

Let  $C'_+$  be the escribed semicircle to  $\partial D'$ , centred on  $O'$ . If  $O$  lies outside  $C'_+$ , then we can substitute (45) into (44) giving

$$d_m = Q_{mn} a_n + S_{mk}(-b) \hat{Q}'_{kn} a'_n \quad (m=1,2,\dots) \quad (47a)$$

where

$$\hat{Q}'_{mn} = \int_{\partial D'} \phi'_n(q) \frac{\partial}{\partial n_q} \alpha_m(r'_q) ds_q. \quad (48)$$

Similarly, if  $O'$  lies outside  $C_+$ , we can reduce (41b) to

$$d'_m = S_{mk}(b) \hat{Q}_{kn} a_n + Q'_{mn} a'_n \quad (m=1,2,\dots) \quad (47b)$$

where

$$Q'_{mn} = \int_{\partial D'} \phi'_n(q) \frac{\partial}{\partial n_q} \phi_m(r'_q) ds_q. \quad (49)$$

The coupled system (47) is to be solved for  $a_n$  and  $a'_n (n=1,2,\dots)$ . Truncating this system leads to a numerical method for solving the null-field equations. The corresponding acoustic problem (scattering by a pair of sound-hard cylinders) has been solved in this way by Bates and Wall (1977). Note that the matrices  $Q$  and  $\hat{Q}$  ( $Q'$  and  $\hat{Q}'$ ) occur in the solution of  $S_1$  for the first (second) cylinder in isolation.

### 4.3 The Potential in $D$

Once  $\phi(q)$  has been found by solving the null-field equations,  $\phi_D(P)$  is given by (39). If we restrict  $P \in D$  to lie outside  $C_+$  and  $C'_+$ , we can substitute (20) into (39) giving

$$2\pi\phi_D(P) = c_m \phi_m(r_p) + c'_m \phi'_m(r'_p) \quad (50)$$

where

$$c_m = - \int_{\partial D} \phi(q) \frac{\partial}{\partial n_q} \alpha_m(r_q) ds_q \quad (51)$$

$$= - \hat{Q}_{mn} a_n = T_{mk} Q_{kn} a_n, \quad (52)$$

$$c'_m = - \int_{\partial D'} \phi(q) \frac{\partial}{\partial n_q} \alpha_m(r'_q) ds_q \quad (53)$$

$$= - \hat{Q}'_{mn} a'_n = T'_{mk} Q'_{kn} a'_n, \quad (54)$$

and  $T'$  is the  $T$ -matrix for the second cylinder. Henceforth, we shall concentrate on finding  $c_m$  and  $c'_m$  (rather than  $a_n$  and  $a'_n$ ). Multiply (47a) by  $T_{lm}$  and sum over  $m$  to give

$$c_\ell - X_{\ell k} c'_k = t_\ell \quad (\ell=1,2,\dots), \quad (55)$$

where

$$X_{mn} = T_{mk} S_{kn}(-b) = S_{nk}(b) T_{km} \quad (56)$$

and

$$t_m = T_{mn} d_n. \quad (57)$$

Similarly, from (47b), we obtain

$$c'_\ell - X'_{\ell k} c_k = t'_\ell \quad (\ell=1,2,\dots), \quad (58)$$

where

$$X'_{mn} = T'_{mk} S_{kn}(b) = S_{nk}(-b) T'_{km} \quad (59)$$

and

$$t'_m = T'_{mn} d'_n. \quad (60)$$

Eliminating  $c'_m$  between (55) and (58) gives

$$c_m - K_{mn} c_n = f_m \quad (m=1,2,\dots) \quad (61a)$$

where

$$K_{mn} = X_{mk} X'_{kn} \quad \text{and} \quad f_m = t_m + X_{mn} t'_n. \quad (62)$$

(61a) is an infinite system of linear algebraic equations from which  $c_m (m=1,2,\dots)$  can be determined. Similarly,  $c'_m$  can be determined from

$$c'_m - X'_{mk} X_{kn} c_n = t'_m + X'_{mn} t_n \quad (m=1,2,\dots), \quad (61b)$$

or by substituting the solution of (61a) into (58).

We remark that (61) are convenient for numerical computations. The effects of scattering by each cylinder in isolation (i.e. the matrices  $T$  and  $T'$ ), and those of the spacing between the cylinders, are clearly separated: changing the spacing merely requires that  $S$  has to be recomputed. In §4.5, we solve  $S_2$  for a semicircle-catamaran by solving (61), numerically.

In essence, the analysis of the present section follows that given by Peterson and Ström (1974) for the corresponding problem in acoustics. Similar equations have been obtained by Bencheikh (1982).

#### 4.4 Asymptotic Solutions; Wide Spacings

(61) can also be solved asymptotically. Suppose that the second cylinder is absent: thus  $T'_{mn} = 0$ , whence  $t'_m = 0$ ,  $X'_{mn} = 0$ ,  $c'_m = 0$  and  $c_m = t_m = T_{mn}d_n$ , in agreement with (32). This suggests that if the second cylinder is small (compared with the first cylinder and the wavelength), then approximations to  $c_m$  and  $c'_m$  could be found by substituting an appropriate approximation to  $T'_{mn}$ ; however, this will not be pursued here.

Different approximations to  $c_m$  and  $c'_m$  are obtained by assuming that the spacing between the cylinders is large, i.e. by substituting an appropriate approximation to  $S_{mn}$  into (61). Let  $a$  be a typical dimension of both cylinders, and set  $\tau = a/b$  ( $b = |b|$  = distance between 0 and 0'). We assume that

$$Kb \gg 1 \quad \text{and} \quad \tau \ll 1. \quad (63)$$

We have (see Appendix A)

$$\phi_1(b) = \pi e^{iKb} + O((Kb)^{-3})$$

and

$$\phi_2(b) = \pi i e^{iKb} + O((Kb)^{-2}),$$

as  $Kb \rightarrow \infty$ . Also,

$$a^{2m+1} \phi_{2m+1}(b) = \tau a^{2m} \phi_{2m+2}(b) = (-1)^m \tau^{2m+1}, \quad m \geq 1.$$

If we ignore all 'local' effects, i.e. we only include the wave terms in  $\phi_1$  and  $\phi_2$ , the matrix  $S_{mn}(b)$  becomes very simple (see Appendix B):

$$S_{11} = S_{22} = iS_{12} = -iS_{21} = -i\lambda, \quad S_{mn} = 0 \quad m, n > 2,$$

where  $\lambda = \frac{1}{2}\pi e^{iKb}$ . Using these approximations, we obtain the following:

$$X_{m1} = -\lambda(iT_{m1} + T_{m2}), \quad X_{m2} = \lambda(T_{m1} - iT_{m2}),$$

$$X'_{m1} = -\lambda(iT'_{m1} - T'_{m2}), \quad X'_{m2} = -\lambda(T'_{m1} + iT'_{m2}),$$

$$X_{mn} = 0, \quad X'_{mn} = 0 \quad \text{for } n > 2,$$

$$K_{11} = iK_{12} = X_{12}(X'_{12} + X'_{21}),$$

$$K_{22} = -iK_{21} = X_{21}(X'_{12} + X'_{21}),$$

$$\text{and } K_{mn} = 0 \quad \text{for } n > 2.$$

Substituting into (61a), we obtain

$$(1 - K_{11})c_1 - K_{12}c_2 = f_1 \quad (64a)$$

$$-K_{21}c_1 + (1 - K_{22})c_2 = f_2 \quad (64b)$$

$$c_m = K_{m1}c_1 + K_{m2}c_2 + f_m, \quad m > 2. \quad (65)$$

Thus, the infinite system (61a) reduces to a  $2 \times 2$  system (64) for  $c_1$  and  $c_2$ , and a formula for  $c_m$ ,  $m > 2$ . Solving (64) gives

$$\Delta c_1 = (1 - K_{22})f_1 + K_{12}f_2 \quad (66a)$$

$$\text{and } \Delta c_2 = (1 - K_{11})f_2 + K_{21}f_1, \quad (66b)$$

where

$$\begin{aligned} \Delta &= (1 - K_{11})(1 - K_{22}) - K_{12}K_{21} \\ &= 1 - (X_{12} + X_{21})(X'_{12} + X'_{21}) \\ &= 1 - r_+ r'_+ e^{2iKb}, \end{aligned} \quad (67)$$

$r'_+$ ,  $t'_+$  are the reflection and transmission coefficients for the second cylinder in isolation, and we have used (35).

Let us now consider a specific incident wave, namely, a regular wavetrain propagating from  $x = +\infty$ , with velocity potential  $\phi_1^+$  given by (7); the coefficients  $d_m$  are given by (24), whilst

$$d'_m = e^{iKb} d_m \quad (m = 1, 2, \dots). \quad (68)$$

Substituting into the right-hand sides of (66), we obtain

$$\mu(c_1 + ic_2) = r_+ - e^{2iKb} r'_+ \{r_+ r_- + t(1-t)\} \quad (69a)$$

and

$$\mu(c_1 - ic_2) = 1 - t - e^{2iKb} r'_+ r_-, \quad (69b)$$

where  $\mu = \omega \Delta / (2gA_+)$ . Similarly,

$$\mu(c'_1 + ic'_2) = e^{iKb} t r'_+ \quad (69c)$$

and

$$\mu(c'_1 - ic'_2) = e^{iKb} t(1-t'). \quad (69d)$$

We define reflection and transmission coefficients,  $R_+$  and  $T_+$ , respectively, by (8) with  $r_+(t_+)$  replaced by  $R_+(T_+)$ ; they are given by

$$R_+ = \frac{1}{2}(c_1 + ic_2 + e^{iKb}(c'_1 + ic'_2)) \quad (70a)$$

$$\text{and } T_+ = 1 - \frac{1}{2}(c_1 - ic_2 + e^{-iKb}(c'_1 - ic'_2)). \quad (70b)$$

Substituting our approximations (69) into (70), we obtain

$$\Delta R_+ = r_+ - e^{2iKb} r'_+ \{r_+ r_- - t^2\} \quad (71a)$$

$$\text{and } \Delta T_+ = t t'. \quad (71b)$$

Similarly, for a regular wavetrain propagating from  $x = -\infty$ , we can define reflection and transmission coefficients by (10); using (69), we find the approximations

$$\Delta R_- = e^{-2iKb} r'_- - r_- \{r'_+ r'_- - (t')^2\} \quad (71c)$$

$$\text{and } \Delta T_- = tt' \quad (71d)$$

(71) are precisely the formulae obtained using the 'wide-spacing' approximation (see Appendix C). Here, we can see precisely the assumptions that have been made, namely (63), in order to arrive at (71). The first assumption ( $Kb \gg 1$ ) means that the wavelength is much shorter than the spacing between the cylinders. The second assumption ( $\tau \ll 1$ ) means that each cylinder is small compared to the spacing, i.e. it is purely geometrical in nature.

Finally, we remark that it can be verified that the approximations (71) do indeed satisfy the Kreisel-Meyer relations (§3).

#### 4.5 A Numerical Example

We consider the semicircle-catamaran problem, i.e. scattering by a pair of fixed half-immersed circular cylinders. Let each have radius  $a$ , and locate the two origins,  $0$  and  $0'$ , at their centres. For the incident wave, we chose a regular wavetrain propagating from  $x = +\infty$ , with velocity potential  $\phi_+^i$  given by (7); hence we non-dimensionalised  $\phi$  using  $gA_+/\omega$ .  $q \in \partial D$  has coordinates  $x = asin\theta$ ,  $y = a\cos\theta$  with  $-\frac{1}{2}\pi \leq \theta \leq \frac{1}{2}\pi$ . The T-matrix. The cylinders are identical, whence  $T_{mn} = T'_{mn}$ . We non-dimensionalised  $\alpha_m$  and  $\phi_{mn}$  using powers of  $a$ . From symmetry considerations, we chose

$$\phi_{2m-1}(\theta) = \sin(2m-1)\theta \text{ and } \phi_{2m}(\theta) = \cos(2m-2)\theta \\ (m=1,2,\dots),$$

whence, e.g.  $Q_{2m,2n-1} = Q_{2m-1,2n} = 0$ . The non-zero elements of  $Q$  and  $\hat{Q}$  can be evaluated exactly (it is not necessary to use numerical quadrature in this simple example). Each infinite matrix was truncated to an  $N \times N$  matrix (typically,  $N = 24$ ) and an approximation to the T-matrix was computed. Two checks on this approximation were made: first, the relations (34) were verified; second, from (35), we have (by symmetry,  $r_+ = r_- = r$ , say)

$$t = 1 - \frac{1}{2}\pi i(T_{11} + T_{22}) \quad (72)$$

$$\text{and } r = \frac{1}{2}\pi i(T_{11} - T_{22}), \quad (73)$$

and these can be compared with other calculations, e.g. Martin and Dixon (1983) tabulate  $r$  and  $t$  for various values of  $Ka$ .

The S-matrix. The non-dimensionalisation of  $S$  is prescribed by that used for  $Q$  and  $\hat{Q}$ . The addition theorem was verified, using an  $N \times N$  truncation for  $S$ .  $R_+$  and  $T_+$ . Approximations to  $c_m$  and  $c'_m$  ( $m=1,2,\dots,N$ ) were computed by solving (61), and then  $R_+$  and  $T_+$  were computed from (70). It was verified that  $R_+$  and  $T_+$  satisfy the Kreisel-Meyer relations, which take the form

$$|R_+|^2 + |T_+|^2 = 1 \quad (74)$$

$$\text{and } \arg(R_+) - \arg(T_+) - Kb = \frac{1}{2}\pi \text{ modulo } \pi. \quad (75)$$

(Note that the geometry is symmetric about  $x = -\frac{1}{2}b$ , but the incident wave (7) is specified relative to  $0$  (cf. Srokosz and Evans, 1979); this accounts for the term  $Kb$  in (75). Thus, increasing  $b$  means that the position of the first (i.e. front) cylinder remains fixed relative to the incident wave, and the second (i.e. rear) cylinder recedes (towards  $x = -\infty$ ).)

In Fig. 2, we plot  $|R_+|$  as a function of  $Ka$  for  $\tau = 0.25$  and  $\tau = 0.4$ ; the corresponding gaps between the cylinders are  $2a$  and  $\frac{1}{2}a$ , respectively. For comparison, we also give  $|R_+|$  for a single cylinder ( $\tau = 0$ ). It is interesting to compare the curve for  $\tau = 0.25$  with a corresponding curve for scattering by two thin vertical plates (each immersed to a depth  $a$ ) obtained by Srokosz and Evans (1979; Fig. 3a). This latter curve is also for a gap (between the plates) of  $2a$ . The two curves are broadly similar, and both have a zero near  $Ka = 0.5$ .

In Fig. 3, we plot  $|R_+|$  as a function of  $\tau$  for  $Ka = 0.2$  and  $Ka = 0.5$ . In Table 1, we give values of  $|R_+|$  and  $\arg(R_+)$  for  $0.1 \leq Ka \leq 1.0$  and  $0 \leq \tau \leq 0.5$  (when  $\tau = 0.5$ , the cylinders are touching); for each pair ( $Ka$ ,  $\tau$ ), the upper number is obtained using the present method (with  $N = 24$ ) and the lower number is obtained using the wide-spacing approximation, (71a) (leading characters are replaced by asterisks when they agree with the upper number). The agreement is seen to be good, with the largest error ( $\approx 10\%$ ) occurring when  $Ka = 0.2$ ,  $\tau = 0.5$ .

From the wide-spacing approximation (71a), we deduce that  $R_+ = 0$  whenever

$$Kb + \arg(r) = 0 \text{ modulo } \pi, \quad (76)$$

where  $\arg(r)$  is a function of  $Ka$ . (We have  $\Delta T_+ = (1 - |r|^2)\exp\{2i\arg(t)\}$ ; when (76) holds,  $\Delta = 1 - |r|^2$ , whence  $|T_+| = 1$  and  $R_+ = 0$ .) In fact, the approximation (71a) has an infinite number of zeros, both as a function of  $\tau$  for fixed  $Ka$ , and as a function of  $Ka$  for fixed  $\tau$ . In particular, when  $Ka = 0.2$  (from the last column of Table 1,  $\arg(r) = -1.768$ ), (71a) predicts that  $R_+$  first vanishes at  $\tau \approx 0.113$ ; this agrees well with the graph in Fig. 3. Similarly, when  $Ka = 0.5$ , (71a) predicts that the first two zeros of  $R_+$  are at  $\tau \approx 0.270$  and  $\tau \approx 0.101$ .

If  $\tau$  is fixed, (76) gives an estimate for the zeros of  $R_+$  as a function of  $Ka$ . Thus, when  $\tau = 0.4$ , we can use Table 1 to show that  $R_+$  has a zero between  $Ka = 0.9$  and  $Ka = 1.0$ ; similarly, when  $\tau = 0.25$ , the first zero occurs between  $Ka = 0.4$  and  $Ka = 0.5$ . Again, these observations accord with the calculations presented in Fig. 2.

The pressure on the front cylinder. In Fig. 4, we plot dimensionless forms of  $|T_+(q)|$  for  $q(\theta) \in \partial D$ , with  $\theta$  varying between  $90^\circ$  (front face, i.e. facing the incident wave) and  $-90^\circ$  (rear face, i.e. facing the second cylinder). (The hydrodynamic pressure is proportional to the potential.) There are three curves, corresponding to (i) the present method, (ii) the wide-spacing approximation (given by (C.3)) and (iii) a single cylinder in isolation. We

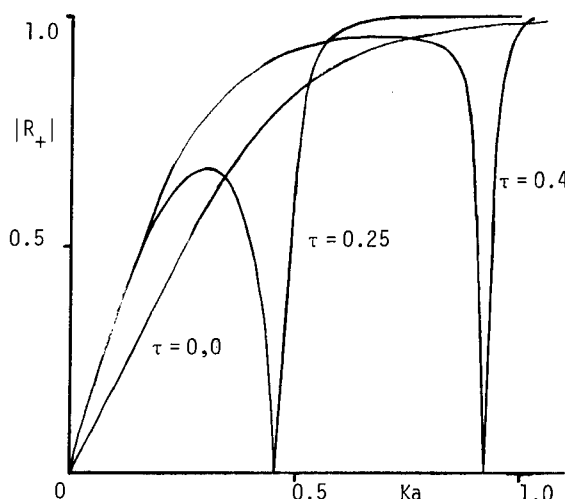


Figure 2. The reflection coefficient as a function of  $Ka$ , for  $\tau=0.4$ ,  $\tau=0.2$  and  $\tau=0.0$ .

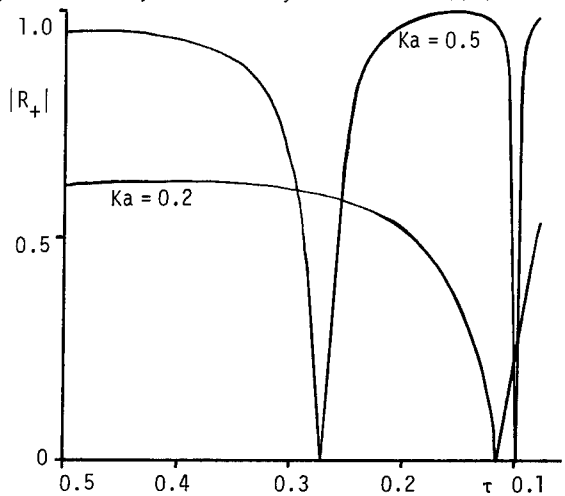


Figure 3. The reflection coefficient as a function of  $\tau$ , for  $Ka = 0.2$  and  $Ka = 0.5$ .

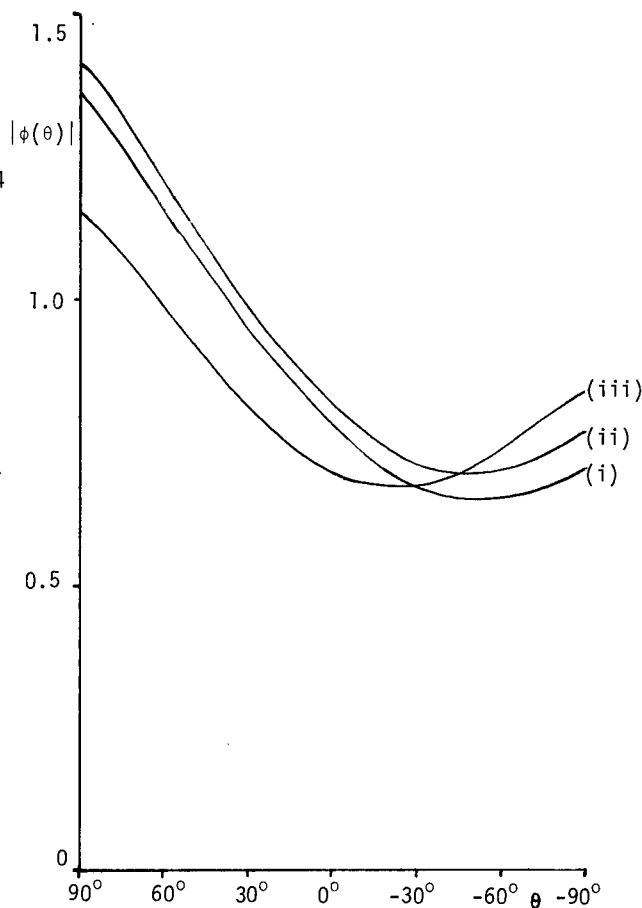


Figure 4. The normalised total potential on the front cylinder, for  $Ka=0.2$ ,  $\tau=0.45$ . (i): the null-field method; (ii): the wide-spacing approximation; and (iii) a single cylinder in isolation.

Table 1. The complex reflection coefficient; for each pair  $(Ka, \tau)$ , the upper and lower numbers are obtained using the null-field method and the wide-spacing approximation, respectively. In the lower number, leading characters are replaced by asterisks when they agree with the upper number.

$Ka$	$\tau=0.5$		$\tau=0.4$		$\tau=0.3$		$\tau=0.2$		$\tau=0.1$		$\tau=0.0$	
	$ R_+ $	arg $R_+$	$ R_+ $	arg $R_+$	$ R_+ $	arg $R_+$	$ R_+ $	arg $R_+$	$ R_+ $	arg $R_+$	$ R_+ $	arg $R_+$
0.1	0.3422	-1.639	0.3466	-1.593	0.3483	-1.517	0.3393	-1.363	0.2469	-0.880	0.1942	-1.708
	***736	****50	***722	***604	***681	***26	***530	***70	***539	****3	—	—
0.2	0.6177	-1.610	0.6210	-1.536	0.6076	-1.405	0.5230	-1.115	0.2178	-3.028	0.3958	-1.768
	***768	****20	***673	****44	***419	***13	***461	***21	***11	****5	—	—
0.3	0.7980	-1.591	0.7930	-1.505	0.7494	-1.332	0.4262	-0.763	0.8613	-1.978	0.5857	-1.791
	***8560	****8	***8384	***11	***851	***40	***550	****9	***577	****3	—	—
0.4	0.8960	-1.619	0.8840	-1.529	0.7941	-1.281	0.5330	-2.818	0.9379	-1.608	0.7369	-1.812
	***9392	****29	***9195	****38	***8294	***93	***166	****1	***47	****5	—	—
0.5	0.9455	-1.692	0.9294	-1.598	0.6796	-1.091	0.9648	-2.086	0.0035	+2.867	0.8403	-1.855
	***742	***706	***559	***611	***7309	***120	***02	****0	***196	****7	—	—
0.6	0.9704	-1.799	0.9513	-1.693	0.6269	-2.854	0.9952	-1.986	0.9918	-2.001	0.9046	-1.928
	***888	***816	***719	***712	***5839	***71	***35	****2	***22	****2	—	—
0.7	0.9833	-1.928	0.9591	-1.797	0.9855	-2.220	0.9990	-2.036	0.9979	-2.011	0.9427	-2.028
	***950	***47	***776	***824	***13	***12	***82	****3	***81	****2	—	—
0.8	0.9903	-2.073	0.9485	-1.869	0.9987	-2.217	0.9997	-2.141	0.9960	-2.071	0.9650	-2.150
	***77	***91	***726	***918	***74	****2	****3	****39	****4	****3	—	—
0.9	0.9941	-2.229	0.6858	-1.506	0.9999	-2.316	0.9999	-2.273	0.9987	-2.337	0.9783	-2.288
	***89	***47	***649	***762	****4	***3	****6	****1	****6	****6	—	—
1.0	0.9963	-2.392	0.9820	-2.656	1.0000	-2.451	0.9999	-2.419	0.9999	-2.443	0.9862	-2.439
	***95	***409	***754	***61	0.9998	****0	****7	****7	****7	****7	—	—



chose  $Ka = 0.2$  and  $\tau = 0.45$ , since, based on the results in Table 1, we expected significant discrepancies between (i) and (ii). In fact, we see that the wide-spacing approximation (ii) overestimates, with the largest error ( $\approx 9\%$ ) occurring near  $\theta = -90^\circ$ , and the smallest ( $\approx 4\%$ ) occurring near  $\theta = 90^\circ$ . The single-cylinder curve varies between an overestimate ( $\approx 20\%$ ) near  $\theta = -90^\circ$  to an underestimate ( $\approx 15\%$ ) near  $\theta = 90^\circ$ .

If we fix  $Ka$  and reduce  $\tau$  (whence  $Kb$  increases), the agreement between (i) and (ii) improves; e.g. with  $Ka = 0.2$  and  $\tau = 0.09$  ( $Kb = 20/9$ ), the errors at  $\pm 90^\circ$  are both less than 1%. However, if we fix  $\tau$  and increase  $Ka$  (whence  $Kb$  also increases), then the agreement may or may not improve; e.g. with  $Ka = 1.0$  and  $\tau = 0.45$  (again,  $Kb = 20/9$ ), the errors at  $-90^\circ$  and  $+90^\circ$  are 15% and 1%, respectively. These numerical observations verify that both assumptions (63) are important.

Finally, we mention Ohkusu's comparison (1970, 1975) between his exact solution (1969) and the wide-spacing approximation for the forced motions of a semicircle-catamaran. In the present notation, he found that they agreed 'almost completely... at least for  $\tau \leq \frac{1}{2}$  unless  $Ka$  is very small'; this conclusion conforms with our analysis in §4.4.

## 5. DISCUSSION AND CONCLUSIONS

In this paper, we have used the null-field method to solve a multiple-scattering problem, namely, the interaction of water waves with two long horizontal cylinders, floating in the free surface of deep water. The method is exact; it yields a viable numerical approach for solving such problems; and it meets the requirements of the philosophy put forward in §1. Of course, it is not as simple as a method based on the wide-spacing approximation, although it could be useful when that approximation is not valid (see §4.4).

We conclude by noting that the null-field method could be modified in several ways:

- (i) It should be possible to extend the method to water of constant finite depth, and to three dimensions (see Martin, 1981), although the corresponding addition theorems are not yet available.
- (ii) The geometrical restriction required to reduce (41) to (47) would be altered if the multipole potentials  $\phi_m$  were replaced by a different set, pertinent to elliptic coordinates, say (cf. Bates and Wall, 1977).
- (iii) The number of cylinders could be increased; see, e.g. Peterson and Ström (1974; §3) and Bates and Wall (1977; §7).

## REFERENCES

- Alker, G. (1978): The Radiation and Scattering of Short Surface Waves by a Number of Cylinders. *Quarterly Journal of Mechanics and Applied Mathematics*, Vol. 31, pp.391-408.
- Bates, R.H.T. and Wall, D.J.N. (1977): Null Field Approach to Scalar Diffraction I. General Method. *Philosophical Transactions of the Royal Society of London, Series A*, Vol. 287, pp.45-78.
- Bencheikh, L. (1982): Scattering of Water-waves by Two Cylinders, using the Null-field Method. M.Sc. Dissertation, University of Manchester.
- Biesel, F. and Le Méhauté, B. (1955): Étude Théorique de la Reflexion de la Houle sur Certains Obstacles. *La Houille Blanche*, Vol.10, pp.130-140.
- Budal, K. (1977): Theory for Absorption of Wave Power by a System of Interacting Bodies. *Journal of Ship Research*, Vol.21, pp.248-253.
- Chakrabarti, S.K. (1979): Wave Interaction with Multiple Horizontal Cylinders. *Applied Ocean Research*, Vol.1, pp.213-216.
- Chung, Y.K. and Coleman, M.I. (1975): Hydrodynamic Forces and Moments for Oscillating Cylinders. *Proceedings, Civil Engineering in the Oceans, III, American Society of Civil Engineers*, Vol.2, pp.899-913.
- Corlett, E.C.B. (1969): Twin Hull Ships. *Transactions of the Royal Institution of Naval Architects*, Vol.111, pp.401-438.
- Evans, D.V. and Morris, C.A.N. (1972): Complementary Approximations to the Solution of a Problem in Water Waves. *Journal of the Institute of Mathematics and its Applications*, Vol.10, pp.1-9.
- Ho, R.-T. and Harten, A. (1975): Green's Function Techniques for Solutions of Floating Body Problems. *Proceedings, Civil Engineering in the Oceans, III, American Society of Civil Engineers*, Vol.2, pp.939-958.
- Hulme, A. (1984): Some Applications of Maz'ja's Uniqueness Theorem to a Class of Linear Water Wave Problems. *Mathematical Proceedings of the Cambridge Philosophical Society*, Vol.95, pp.165-174.
- Ijima, T., Chou, C.R. and Yoshida, A. (1976): Method of Analyses for Two-dimensional Water Wave Problems. *Proceedings, 15th Coastal Engineering Conference, American Society of Civil Engineers*, pp.2717-2736.
- John, F. (1950): On the Motion of Floating Bodies II. Simple Harmonic Motions. *Communications on Pure and Applied Mathematics*, Vol.3, pp.45-101.
- Katory, M., Lacey, A.A. and Tam, P.K.Y. (1980): Application of Theoretical Hydrodynamics to the Design of Arbitrarily Shaped and Multibodied Marine Structures. *Transactions of the Royal Institution of Naval Architects*, Vol.122, pp.253-267.
- Kim, C.H. (1972): The Hydrodynamic Interaction between Two Cylindrical Bodies Floating in Beam Seas. Report SIT-OE-72-10, Stevens Institute of Technology, Hoboken, New Jersey.
- Kreisel, G. (1949): Surface Waves. *Quarterly of Applied Mathematics*, Vol.7, pp.21-44.
- Lee, C.M., Jones, H.D. and Curphey, R.M. (1973): Prediction of Motion and Hydrodynamic Loads of Catamarans. *Marine Technology*, Vol.10, pp.392-405.
- Leonard, J.W., Huang, M.-C. and Hudspeth, R.T. (1983): Hydrodynamic Interferences between Floating Cylinders in Oblique Seas. *Applied Ocean Research*, Vol.5, pp.158-166.

- Maeda, H. (1975): Hydrodynamical Forces on a Cross-section of a Stationary Structure. The Dynamics of Marine Vehicles and Structures in Waves (ed. R.E.D. Bishop and W.G. Price), Institution of Mechanical Engineers, pp.80-90.
- Martin, P.A. (1981): On the Null-field Equations for Water-wave Radiation Problems. *Journal of Fluid Mechanics*, Vol.113, pp.315-332.
- Martin, P.A. (1982): Acoustic Scattering and Radiation Problems, and the Null-field Method. *Wave Motion*, Vol.4, pp.391-408.
- Martin, P.A. (1984a): On the Null-field Equations for Water-wave Scattering Problems. *IMA Journal of Applied Mathematics*, to appear.
- Martin, P.A. (1984b): Integral-equation Methods for Multiple-scattering Problems II. *Water Waves. Quarterly Journal of Mechanics and Applied Mathematics*, to appear.
- Martin, P.A. (1984c): On the T-matrix for Water-wave Scattering Problems. *Wave Motion*, submitted.
- Martin, P.A. and Dixon, A.G. (1983): The Scattering of Regular Surface Waves by a Fixed, Half-immersed, Circular Cylinder. *Applied Ocean Research*, Vol.5, pp.13-23.
- Masubuchi, M. and Shinomiya, Y. (1981): Dynamic Analysis of Ocean Wave Energy Converter with Multiple-floating Bodies. *Bulletin of the Japanese Society of Mechanical Engineers*, Vol.24, pp.2036-2042.
- Mei, C.C. (1978): Numerical Methods in Water-wave Diffraction and Radiation. *Annual Review of Fluid Mechanics*, Vol.10, pp.393-416.
- Millar, R.F. (1973): The Rayleigh Hypothesis and a Related Least-squares Solution to Scattering Problems for Periodic Surfaces and Other Scatterers. *Radio Science*, Vol.8, pp.785-796.
- Newman, J.N. (1977): The Interaction of Stationary Vessels with Regular Waves. *Proceedings, 11th Symposium on Naval Hydrodynamics*, Institution of Mechanical Engineers, pp.491-501.
- Nordenström, N., Faltinsen, O. and Pedersen, B. (1971): Prediction of Wave-induced Motions and Loads for Catamarans. Preprint, Off-shore Technology Conference, Paper Number OTC 1418.
- Ohkusu, M. (1969): On the Heaving Motion of Two Circular Cylinders on the Surface of a Fluid. Reports of Research Institute for Applied Mechanics, Kyushu University, Vol.17, No.58, pp.167-185.
- Ohkusu, M. (1970): On the Motion of Multihull Ships in Waves (I). Reports of Research Institute for Applied Mechanics, Kyushu University, Vol.18, No.60, pp.33-60.
- Ohkusu, M. (1975): Hydrodynamic Forces on Multiple Cylinders in Waves. The Dynamics of Marine Vehicles and Structures in Waves (ed. R.E.D. Bishop and W.G. Price), Institution of Mechanical Engineers, pp.107-112.
- Ohkusu, M. (1976): Ship Motions in Vicinity of a Structure. *Proceedings, Behaviour of Off-shore Structures*, Norwegian Institute of Technology, Vol.1, pp.284-306.
- Ohkusu, M. and Takaki, M. (1971): On the Motion of Multihull Ships in Waves (II). Reports of Research Institute for Applied Mechanics, Kyushu University, Vol.19, No.62, pp.75-94.
- O'Leary, M. (1984): Radiation and Scattering of Surface Waves by a Group of Submerged, Horizontal, Circular Cylinders. *Applied Ocean Research*, submitted.
- Peterson, B. and Ström, S. (1974): Matrix Formulation of Acoustic Scattering from an Arbitrary Number of Scatterers. *Journal of the Acoustical Society of America*, Vol.56, pp.771-780.
- Schnute, J.T. (1971): The Scattering of Surface Waves by Two Submerged Cylinders. *Proceedings of the Cambridge Philosophical Society*, Vol.69, pp.201-215.
- Simon, M.J. (1982): Multiple Scattering in Arrays of Axisymmetric Wave-energy Devices. Part 1. A Matrix Method Using a Plane-wave Approximation. *Journal of Fluid Mechanics*, Vol.120, pp.1-25.
- Simon, M.J. and Ursell, F. (1984): Uniqueness in Linearised Two-dimensional Water-wave Problems. *Journal of Fluid Mechanics*, to appear.
- Spencer, R. and Sayer, P. (1981): The Wave-induced Motions of Adjacent Floating Vessels. *Proceedings, Hydrodynamics in Ocean Engineering*, Norwegian Institute of Technology, Vol.2, pp.781-798.
- Srokosz, M.A. and Evans, D.V. (1979): A Theory for Wave-power Absorption by Two Independently Oscillating Bodies. *Journal of Fluid Mechanics*, Vol.90, pp.337-362.
- Ursell, F. (1949): On the Heaving Motion of a Circular Cylinder on the Surface of a Fluid. *Quarterly Journal of Mechanics and Applied Mathematics*, Vol.2, pp.218-231.
- Ursell, F. (1961): The Transmission of Surface Waves under Surface Obstacles. *Proceedings of the Cambridge Philosophical Society*, Vol.57, pp.638-668.
- Ursell, F. (1981): Irregular Frequencies and the Motion of Floating Bodies. *Journal of Fluid Mechanics*, Vol.105, pp.143-156.
- van den Berg, P.M. and Fokkema, J.T. (1979): The Rayleigh Hypothesis in the Theory of Diffraction by a Cylindrical Obstacle. *IEEE Transactions on Antennas and Propagation*, Vol.AP-27, pp.577-583.
- Varadan, V.K. and Varadan, V.V. (ed.) (1980): *Acoustic, Electromagnetic and Elastic Wave Scattering-Focus on the T-matrix Approach*. Pergamon Press, New York.
- Wang, S. (1970): On the Hydrodynamic Forces of Twin-hull Vessels. *Proceedings, 12th Coastal Engineering Conference*, American Society of Civil Engineers, pp.1701-1721.
- Wang, S. (1981): Wave Radiation due to Oscillation of Two Parallel Spaced Cylinders. *Ocean Engineering*, Vol.8, pp.599-621.
- Wang, S. and Wahab, R. (1971): Heaving Oscillations of Twin Cylinders in a Free Surface. *Journal of Ship Research*, Vol.15, pp.33-48.
- Waterman, P.C. (1965): Matrix Formulation of Electromagnetic Scattering. *Proceedings of the IEEE*, Vol.53, pp.805-812.

Yeung, R.W. (1982): Numerical Methods in Free-surface Flows. Annual Review of Fluid Mechanics, Vol.14, pp.395-442.

#### APPENDIX A. Multipole Potentials

From Ursell (1981), we have (20) with

$$\phi_2(r_p) = \int_0^\infty -ky \cos kx \frac{dk}{k-K}, \quad \phi_1(r_p) = \frac{-1}{K} \frac{\partial}{\partial x} \phi_2,$$

$$\phi_{2m+2}(r_p) = \frac{\cos 2m\theta}{r^{2m}} + \frac{K}{2m-1} \frac{\cos(2m-1)\theta}{r^{2m-1}},$$

$$\phi_{2m+1}(r_p) = \frac{\sin(2m+1)\theta}{r^{2m+1}} + \frac{K}{2m} \frac{\sin 2m\theta}{r^{2m}},$$

$$\alpha_2(r_p) = -2e^{-Ky} \cos Kx, \quad \alpha_1(r_p) = -2e^{-Ky} \sin Kx, \quad (A.1)$$

$$\alpha_{2m+2}(r_p) = \frac{-2(2m-1)!}{K^{2m}} \sum_{q=2m}^{\infty} \frac{(-Kr)^q}{q!} \cos q\theta,$$

$$\alpha_{2m+1}(r_p) = \frac{2(2m)!}{K^{2m+1}} \sum_{q=2m+1}^{\infty} \frac{(-Kr)^q}{q!} \sin q\theta,$$

$m=1,2,\dots$ , and the point  $P \equiv (x,y)$  has circular polar coordinates given by  $x=r\sin\theta$ ,  $y=r\cos\theta$  (with  $r=r_p$ ). Note that  $\phi_{2m}$  and  $\alpha_{2m}$  ( $\phi_{2m-1}$  and  $\alpha_{2m-1}$ ) are even (odd) functions of  $x$  ( $m=1,2,\dots$ ). Note also that  $\phi_m(r_p) \equiv \phi_m(r,\theta)$  is singular at 0, i.e. at  $r=0$ .

For large  $|x|$ , we have

$$\phi_1 \sim \pm \pi \exp(-Ky \pm iKx), \quad \phi_2 \sim \mp i \exp(-Ky \pm iKx) \quad (A.2)$$

as  $x \rightarrow \pm \infty$ .

For  $m > 2$ ,  $\phi_m$  is a wavefree potential, i.e. it decays algebraically as  $|x| \rightarrow \infty$ . The precise error terms in (A.2) are given by Ursell (1961).

#### APPENDIX B. The Addition Theorem

$$\phi_m(r'_p) = \sum_{n=1}^{\infty} S_{mn}(b) \alpha_n(r_p).$$

where  $r'_p = r_p + b$ ,  $|r_p| < |b|$  and the matrix  $S$  is defined as follows.

$$S_{11} = -\frac{1}{2}(\phi_2 + K^{-2}\phi_4), \quad S_{21} = -S_{12} = \frac{1}{2}\phi_1, \quad S_{22} = -\frac{1}{2}\phi_2$$

$$S_{1,2n+1} = S_{2n+1,1} = -((n + \frac{1}{2})/K) \phi_{2n+4}$$

$$S_{1,2n+2} = -S_{2n+2,1} = -(n/K) \phi_{2n+1}$$

$$S_{2,2n+1} = -S_{2n+1,2} = \frac{1}{2}\phi_{2n+1}$$

$$S_{2,2n+2} = S_{2n+2,2} = -\frac{1}{2}\phi_{2n+2}$$

$$S_{2m+1,2n+1} = -\frac{1}{2} \left\{ \binom{2q+1}{2m} (2n+1) \phi_{2q+4} - \binom{2q-1}{2m} \frac{K^2}{2n} \phi_{2q+2} \right\}$$

$$S_{2m+2,2n+2} = -\frac{1}{2} \left\{ \binom{2q-1}{2m-1} 2n \phi_{2q+2} - \binom{2q-3}{2m-1} \frac{K^2}{2n-1} \phi_{2q} \right\}$$

$$S_{2m+1,2n+2} = -S_{2n+2,2m+1}$$

$$= -\frac{1}{2} \left\{ \binom{2q}{2m} 2n \phi_{2q+1} - \binom{2q-2}{2m} \frac{K^2}{2n-1} \phi_{2q-1} \right\},$$

$q=m+n$ ,  $m \geq 1$ ,  $n \geq 1$ , and  $\binom{n}{k} = \frac{n!}{k!(n-k)!}$ .

All functions have argument  $b$ , i.e.  $\phi_m \equiv \phi_m(b) = \phi_m(b, \frac{1}{2}\pi)$ . It may be verified that (46) is satisfied.

#### APPENDIX C. The Wide-spacing Approximation

The derivation below is modelled closely on that given by Srokosz and Evans (1979; §5.3). Write  $S_1 \equiv S_1(\partial D; \phi_I)$  to emphasise the dependence on the particular geometry and incident potential.

Let  $\phi_{\pm}(x,y)$  solve  $S_1(\partial D; \exp\{-Ky \mp iKx\})$  and define corresponding reflection and transmission coefficients,  $r_{\pm}$  and  $t_{\pm}$ , by (8) and (10), with  $A_{\pm} = \omega/g$ . Similarly, let  $\phi_{\pm}^*(x,y)$  solve  $S_1(\partial D^*; \exp\{-Ky \mp iKx\})$ , with corresponding coefficients  $r_{\pm}^*$  and  $t_{\pm}^*$ . Finally, let  $\phi(x,y)$  solve  $S_2$ , with  $\phi_I = \exp\{-Ky - iKx\}$ , and define  $R_+$  and  $T_+$  by

$$\phi(x,0) \sim \begin{cases} e^{-iKx} + R_+ e^{iKx}, & \text{as } x \rightarrow +\infty \\ T_+ e^{-iKx}, & \text{as } x \rightarrow -\infty. \end{cases} \quad (C.1)$$

Now, we suppose that near the first (i.e. front) cylinder (see Fig.1)

$$\phi(x,y) = \alpha \phi_+(x,y) + \beta \phi_-(x,y) \quad (C.3)$$

$$\sim \begin{cases} \alpha(e^{-iKx} + r_+ e^{iKx}) + \beta t_- e^{iKx} & \text{as } x \rightarrow +\infty \\ \alpha t_+ e^{-iKx} + \beta(e^{iKx} + r_- e^{-iKx}) & \text{as } x \rightarrow -\infty, \end{cases} \quad (C.4)$$

on  $y=0$ , where  $\alpha$  and  $\beta$  are unknown complex constants. Comparing (C.4) with (C.1), we find that  $\alpha = 1$  and

$$R_+ = r_+ + \beta t_- . \quad (C.6)$$

Also, we suppose that near the second (i.e. rear) cylinder,

$$\phi(x,y) = \gamma \phi_+^*(x+b, y) \quad (C.7)$$

$$\sim \begin{cases} \gamma(e^{-iK(x+b)} + r_+^* e^{iK(x+b)}) & \text{as } x \rightarrow +\infty \\ \gamma t_+^* e^{-iK(x+b)} & \text{as } x \rightarrow -\infty \end{cases} \quad (C.8)$$

on  $y=0$ , where  $\gamma$  is another complex constant. Comparing (C.9) with (C.2), we find that

$$T_+ = \gamma t_+^* e^{-iKb} . \quad (C.10)$$

To find  $\beta$  and  $\gamma$ , we assume that there is a region between the two cylinders where (C.5) and (C.8) match; equating the coefficients of

$\exp\{\pm iKx\}$ , we obtain

$$\beta = \gamma r'_+ e^{iKb} \quad \text{and} \quad t_+ + \beta r_- = \gamma e^{-iKb}$$

i.e.

$$\Delta\beta = r'_+ t_+ e^{2iKb} \quad \text{and} \quad \Delta\gamma = t_+ e^{iKb},$$

where  $\Delta$  is given by (67). Substituting for  $\beta$  and  $\gamma$  in (C.6) and (C.10), we obtain the formulae (71a,b). Formulae for  $R_-$  and  $T_-$ , (71c,d), can be obtained in a similar manner.

SESSION III  
SEAKEEPING PROBLEMS

# ADDED RESISTANCE IN WAVES OF HULL FORMS WITH BLUNT BOW

MAKOTO OHKUSU

## ABSTRACT

Added resistance of a ship running in incident waves short compared with its length is thought to be dominated by diffraction of the incident waves on the ship's hull. Physics of resistance increase, however, in short waves for blunt bow hull forms has not been fully understood.

In this report we describe firstly the measurements of diffraction wave pattern, of blunt bow hull forms towed in regular head waves, leading us to conclude that added resistances computed from the energy transported with the measured diffraction wave pattern away from the hulls are only half as much as added resistances measured with force gages. Except small viscosity effect, the other half of energy is possibly dissipated with waves not recognized far from the hulls and generated with other mechanism than linear theory predicts. This possibility was confirmed on the observations of diffraction waves propagating some distance forward of a 2-D body until vanishing by breaking even if  $\omega_e V/g$  is larger than 0.25 ( $\omega_e$ : encounter frequency of incident waves,  $V$ : ambient flow velocity far in front or body's forward speed). Those waves may be given rise to by their interaction with steady flow field prominent close to blunt bow caused by forward speed.

Secondly a computation is proposed for getting the difference between the added resistances derived from wave pattern and measured with force gages.

## 1. INTRODUCTION

It is well known that resistance increase due to waves of a ship with a full hull form is of larger magnitude than theoretically expected (Strøm-Tejsen et al., 1973) if the length of incident waves is short compared with

the ship's dimensions. Added resistance in short waves is one of the factors governing our evaluation of large ship's performance in a seaway. Large added resistance of full hull forms at short wave length is supposed to be due to the diffraction of incident waves on their bow part. We could not evaluate correctly this diffraction effect on added resistance until recently.

Fujii and Takahashi (1975) carried out a series test of full hull forms for added resistance in head and oblique waves, concentrating on it at short wave length and found that it highly correlates with the bluntness coefficient defined as a mean square value of the inclination of the water line in ship's fore part with respect to its center line. Interpreting this finding in the light of wave diffraction theory for a cylindrical form, which is restrained in incident waves without advance speed, they derived an empirical formula of practical use giving the resistance increase of a blunt bow ship in short waves as a diffraction wave resistance.

Faltinsen et al. (1980) gave an asymptotic formula predicting added resistance when wave length approaches zero. His formula is remarkable in taking into account even approximately the interaction of diffraction waves with steady but non-uniform current around the hull.

Technique of measuring and analyzing the unsteady waves around ship models running into waves was developed by Ohkusu (1977, 1980). With this technique it is now possible to experimentally examine the diffraction waves around a ship of full hull form when running into the incident waves of short wave length. Analysis of the measured diffraction waves leads to the direct derivation of added resistance as a wave making resistance, caused by the transport of energy by the diffraction waves. The added resistance thus measured might

M. Ohkusu, Research Institute for Applied Mechanics, Kyushu University 87,  
Kasuga, 816 Japan

be called wave pattern added resistance in contrast with that measured as a force on a ship model.

The purpose of the present study is to study experimentally the added resistance of full hull form, particularly with blunt bow with the measured diffraction waves, the wave pattern added resistance and observations of the wave field close to the bow part and to try to understand hydrodynamics of the added resistance at short wave length.

## 2. ANALYSIS OF DIFFRACTION WAVE PATTERN AROUND SHIP

### 2.1 Theoretical Formulation

A ship, when running in waves, generates time dependent waves as well as stationary ones. The time dependent waves are regarded as a superposition of radiation waves and diffraction waves, if we can linearize the time dependent flow around the ship, the former is supposed to be caused by the ship forced to undergo the oscillatory motions and advancing with forward velocity on otherwise a calmwater. The latter, which is our concern here, is produced when incident waves scatter on the surface of the ship running but its oscillatory motions suppressed.

Energy flux of the superposition of radiation and diffraction waves away from the ship running and freely oscillating in waves is compensated by work done by added resistance of the ship. Energy flux of the diffraction waves alone will give the added resistance due to the diffraction waves. This is not an imaginary quantity, but really the added resistance of the ship when it runs in short waves where its oscillatory motions are of very small magnitude and the radiation waves hardly contribute to the unsteady wave field.

Hull forms with blunt bow are supposed to produce large diffraction waves, particularly in short waves, resulting large added resistance. However, at present, it seems we have few experimental data directly proving that the larger diffraction really occurs close to the bow. If we measure the diffraction waves for a ship of blunt bow towed in incident waves of short wave length and describe them in a form by which we are able to understand their function in the added resistance, we might be able to get some correct knowledge on the diffraction waves of the blunt bow hull form and to clarify the relation of the wave pattern added resistance directly derived from the measured diffraction waves to the added resistance measured as a force on the hull. The unsteady waves around a ship model, diffraction waves or a superposition of

both diffraction and radiation waves, are expressed, at the location  $(x, y)$  in the reference frame moving with the model as illustrated in Fig.1, by

$$\begin{aligned} & [\zeta_c - i\zeta_s] e^{i\omega t} \\ &= \frac{2\omega}{g} \left[ \int_{-\pi/2}^{\theta-\pi/2} - \int_{\pi/2}^{\theta+\pi/2} \right] F_1(\theta) \\ & \times \exp[-ik_1 x \cos\theta - ik_1 y \sin\theta + i\omega t] \\ &+ \frac{2\omega}{g} \int_{\theta-\pi/2}^{\theta+\pi/2} F_2(\theta) \exp[-ik_2 x \cos\theta \\ & - ik_2 y \sin\theta + i\omega t] \end{aligned} \quad (1)$$

$$k_{1,2} = \frac{1 - 2\Omega \cos\theta \pm \sqrt{1 - 4\Omega \cos\theta}}{2U^2/g \cos\theta} \quad (2)$$

where  $\omega$  is the frequency of encounter with the incident waves,  $U$  is the forward speed of the model,  $\Omega = U\omega/g$  and  $\theta = \tan^{-1}(y/x)$ ,  $\omega = \omega_0 + k_0 U$ .

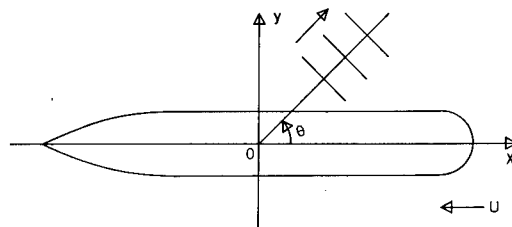


Figure 1. Coordinate System

Kochin function  $H_j(\theta)$  ( $j=1, 2$ ), proportional to the amplitude function  $F_j(\theta)$  of waves propagating into the  $\theta$  direction as found in the equation (1), provides the energy flux of those waves to give the added resistance as integrated with respect to every direction (Maruo, 1963).

$$\begin{aligned} \Delta R &= 4\pi\rho \left[ \int_{\alpha_0}^{\pi/2} - \int_{\pi/2}^{\pi} \right] \\ & \frac{|H_1(\theta)|^2 k_1 (k_1 \cos\theta + k)}{\sqrt{1 - 4\Omega \cos\theta}} d\theta \end{aligned}$$

$$+ 4\pi\rho \int_{\alpha_0}^{\pi} \frac{|H_2(\theta)|^2 k_2 (k_2 \cos\theta + k)}{\sqrt{1 - 4\Omega \cos\theta}} d\theta \quad (3)$$

$$H_j(\theta) = \frac{F_j(\theta) \sqrt{1 - 4\Omega \cos\theta}}{k_j (1 + k_j / k\Omega \cos\theta)} \quad (4)$$

where  $k = \omega_0^2/g$  and  $\alpha_0 = \cos^{-1}(1/4\Omega)$ .  $\Delta R$  is the diffraction wave resistance or the total added resistance according as  $H_j(\theta)$  are those of the diffraction waves or of the total unsteady waves including the radiation waves as well. The equation assumes that the wave field is port and starboard symmetrical, that is, the equation is for the ship running in head waves.

Ohkusu (1977, 1980) proposed a method to derive  $H_j(\theta)$  from the measured wave elevation around a ship model, running in regular waves with its motion suppressed or freely oscillating.

$H_j(\theta)$  obtained with this method is a quantity describing the characteristics of the diffraction waves to be compared with theoretical prediction. We can also square and integrate the measured  $H_j(\theta)$  by means of the equation (3) to get the added resistance of the model without relying upon the measurement of a force on it. Hereafter we call this added resistance derived from the measured wave field as wave pattern added resistance.

The method is described briefly as follows (for detail, refer to Ohkusu, 1980).

Provided  $\zeta_c$  and  $\zeta_s$  in (1) on the line of  $y=\text{const.}$  i.e. the amplitude of the cosine and the sine component of the sinusoidal movement of wave surface along a line parallel to the course of the model are measured, the Fourier transform of them with respect to  $x$  gives the Kochin function  $H_j(\theta)$  for  $\theta > 0$ .

$$H_1(\theta) = \frac{g}{4\pi\omega} \text{sgn}[\cos\theta] \\ \times \sin\theta \frac{\exp[i \text{sgn}(\cos\theta) k_1 y \sin\theta]}{(1 + k_1/k\Omega \cos\theta)} \\ \times \int_{-\infty}^{\infty} [\zeta_c(x, y) - i\zeta_s(x, y)] \\ \times \exp[ik_1 x \cos\theta] dx + o(1/y)$$

$$H_2(\theta) = \frac{g}{4\pi\omega} \\ \times \sin\theta \frac{\exp[ik_2 y \sin\theta]}{(1 + k_2/k\Omega \cos\theta)} \\ \times \int_{-\infty}^{\infty} [\zeta_c(x, y) - i\zeta_s(x, y)] \\ \exp[ik_2 x \cos\theta] d\theta + o(1/y) \quad (5)$$

This expressions for  $H_j(\theta)$  are for the port and starboard symmetrical wave pattern.

As a ship model moves forward in incident waves, a single wave probe placed in the model basin changes its position in the reference frame moving with that model. Accordingly what is recorded by this probe is the wave elevation at different location relative to the model on different time. Since we need to record it at least for a period to know the amplitude and the phase of the wave surface's up and down movement at every location, a single wave probe is not sufficient for our purpose. Each of several wave probes placed along a line parallel to the model ship's track with an appropriate spacing comes to an identical location, which can be any point on the line, in the reference frame moving with the model, at different moments. It means wave records with them provide equivalently wave elevations at the identical location on several moments at intervals. Even wave elevations at a location not continuously recorded but at intervals are sufficient to know the amplitude and the phase of water surface movement at this location, since the movement is supposed to be sinusoidal, with a period of encounter with the incident waves. Procedure for excluding the incident wave elevations from the data thus obtained to get  $\zeta_c$  and  $\zeta_s$ , i.e. the pure diffraction waves is described by Ohkusu (1980).

It is usually impossible to get the information on the wave elevation at further than a certain distance behind the model since the tank width is limited. Wave elevation after that distance is assumed to be expressed by an asymptotic form matched to the tail part of the measured wave record. With this asymptotic expression for the wave field far behind we are able to carry out the Fourier integral to the negative infinity of  $x$ .

## 2.2 Results of Analysis of Measured Diffraction Waves

Models of S175(L=3m), the Series 60,  $C_B=0.80$ (L=3m) and CCl(L=2m) were towed



in regular waves with their motions suppressed and the diffraction waves were measured to be analyzed with the procedure described in the previous section.

S175 is a container ship's hull form which has been used for the 15th ITTC's comparative computation of its motions in waves and CCI is the fullest hull of those three models whose water line form is semi-circular for its bow part. This model is stream lined for its stern part after a long parallel part as illustrated in Fig.1. CCI's length to breadth ratio  $L/B$  is 6.67 and its draft is made so deep as  $d/B=2.0$  in order to exaggerate the diffraction of incident waves especially at its bow part.

An example of  $\zeta_C$  (referred to as Cos. component),  $\zeta_S$  (Sin component) and stationary wave elevation along the line ( $y/L=0.25$ ) is illustrated in Fig.2. This is for a model of the Series 60,  $C_B=0.80$  at  $Fn=0.20$  and  $\lambda/L=0.60$ .  $\zeta_C$  and  $\zeta_S$  are non-dimensionalized by amplitude of incident waves (2.53cm). Two stationary wave patterns are compared in this figure, one of which is that when the model is towed on a calm water without any incident waves. The other is under the influence of the interaction, if any, with the incident and the diffraction waves, i.e. the stationary wave elevation around the model towed in the incident waves.

Except far behind the model, where wave height is so low that we can not separate the stationary ones from the prominent unsteady waves with enough accuracy, it seems that both agree with each other. This means that the presence of the unsteady wave motions does not change the stationary wave field at least in the far field of a ship.

Wave length of the diffraction waves propagating into the direction of  $\theta=180^\circ$  right behind the model is found to be identical with the theoretically expected even for the closer position  $y/L=0.1$ , and their amplitudes are almost identical regardless of  $y/L$  as later described. Therefore we can conclude that the wake behind the hull has little effect on the diffraction waves.

Several examples of  $H_j(\theta)k_j 4\pi\omega/g\delta$  ( $j=1,2$ ) (for S175 and the model of the Series 60,  $C_B=0.80$ ) obtained through the Fourier transform of the wave data, an example of which is shown in Fig.2, where  $\delta$  denotes the amplitude of incident regular waves, are illustrated Figs.3 to 8. All the results in those figures are for short wave length of the incident waves and derived from the wave elevation measured very close to the hull surface of the models, that is  $y/L=0.1 \sim 0.17$  where  $y$  refers the distance from the model's center to the locations of the line along which the diffraction waves were measured.  $H_2(\theta)$  not only its absolute value but also its

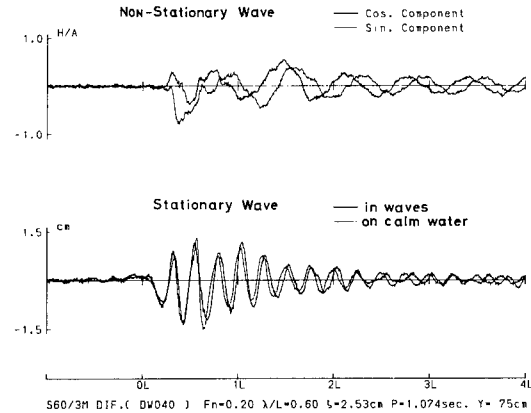


Figure 2. Wave Pattern along  $y=\text{constant}$  (Series 60  $C_B=0.8$ )

phase angle, is confirmed to show surprisingly little deviation from those of the waves measured at  $y/L=0.5$ . Particularly the deviation is the less for the more slender hull form.  $H_1(\theta)$  at  $y/L=0.1$  is, however, a little larger than that at  $y/L=0.5$ . The wave pattern due to  $H_1(\theta)$  is theoretically supposed to be recognized only in the vicinity of the  $x$  axis just like the Kelvin wave pattern we find around a ship running on a calm water and accordingly accuracy of the measured  $H_1(\theta)$  is the higher the closer  $y$  is located to the  $x$  axis. However  $H_1(\theta)$  is generally of much smaller magnitude as compared to  $H_2(\theta)$  and has so little contribution to the added resistance integral as to be disregarded. So we do not go far into  $H_1(\theta)$  matter in this paper.

Theoretical values of  $H_j(\theta)$  are computed using a slender body theory (Adachi, 1978) which assumes the incident wave length as short as the transverse dimension of hull forms.  $H_2(\theta)$  is provided by integrating waves propagating into the  $\theta$  direction from the line of sources along the  $x$  axis. Waves emanating to the direction of  $\theta$  from each point on the line source will cancel or intensify each other according to the rapid variation of their phase relationship with respect to the location of the point on the line provided the length of those waves is short. Theoretically computed  $H_1(\theta)$  for all the directions and  $H_2(\theta)$  for  $\theta \gtrsim 90$  i.e. the amplitude of waves emanating forward from the ship fluctuates rapidly even with a small variation in  $\theta$ . In such  $\theta$  region theoretical lines shown in Figs.3 to 8 are connecting only the maximum values.

Generally speaking the theoretical amplitude function agree with the measured one. The agreement is rather surprising, considering the assumptions of the slender body theory used to compute

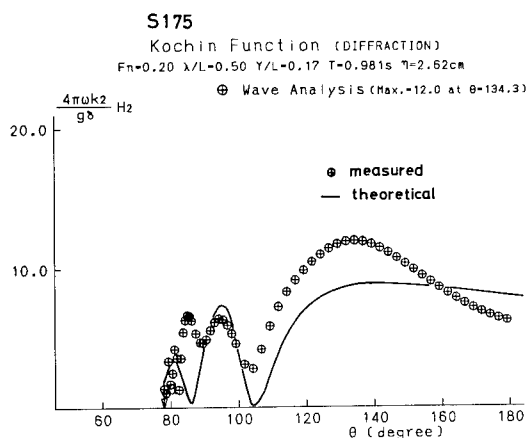
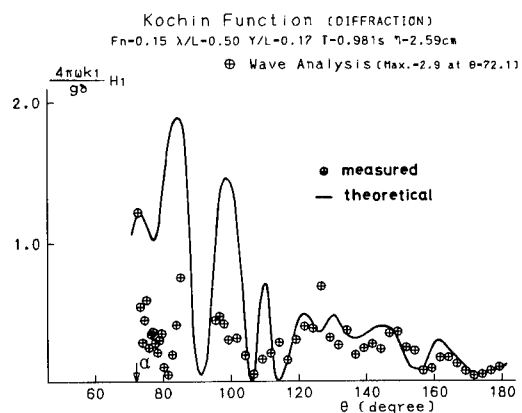


Figure 5. Amplitude Function of Diffraction Wave

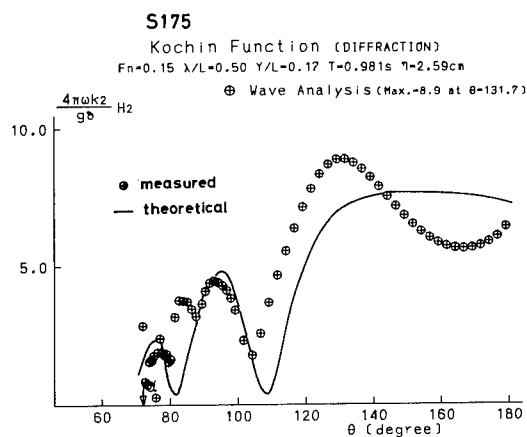


Figure 3. Amplitude Function of Diffraction wave

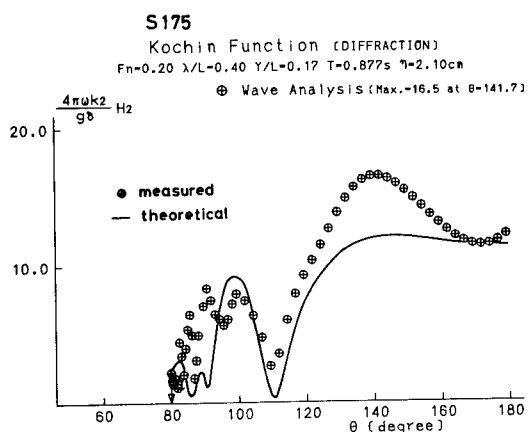
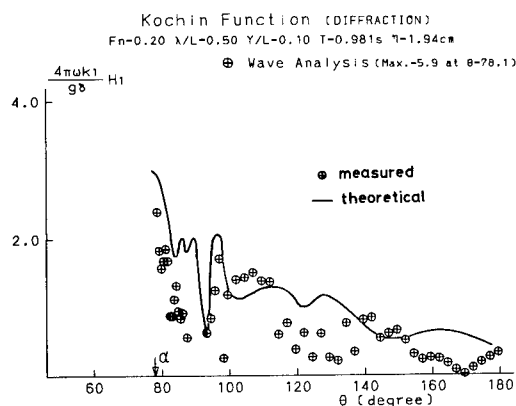


Figure 4. Amplitude Function of Diffraction Wave

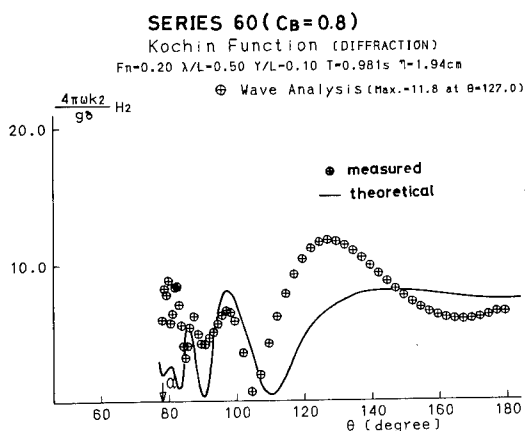


Figure 6. Amplitude Function of Diffraction Wave

the theoretical and the short wave length of  $H_1(\theta)$ . We do not show the results for the model CC1 since the predictions by the slender body theory are too poor and much less in its magnitude than the

measured one because of the deep draft of the hull form.

The measured  $H_2(\theta)$  is not, of course, completely identical in their details with the theoretical one. The

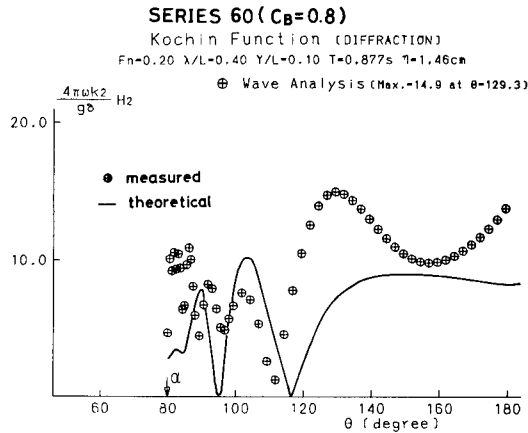


Figure 7. Amplitude Function of Diffraction Wave

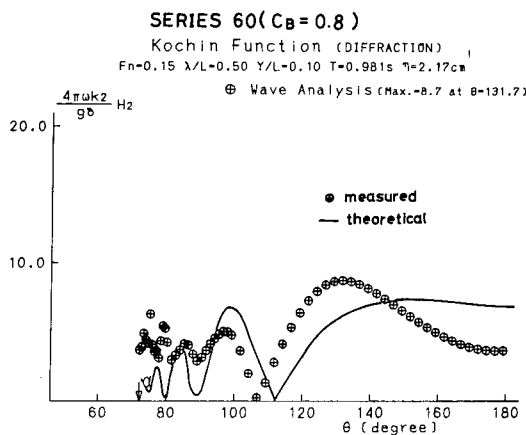
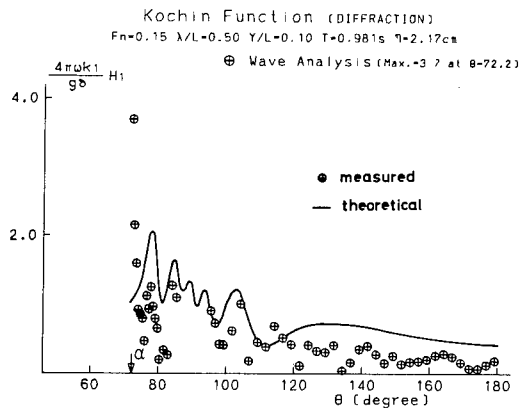


Figure 8. Amplitude Function of Diffraction Wave

difference that the measured is greater for the full hull form than the theoretical especially in  $\theta$  close to  $\alpha_0$  the limit angle beyond which no waves propagate.

This is because most energy of the waves in those directions comes from the bow part for short wave length and the slender body theory naturally can not predict the diffraction waves from the blunt bow. Big  $H_2(\alpha_0)$  suggests the presence of the diffraction waves propagating locally into the direction of  $\theta < \alpha_0$ , even if asymptotically otherwise.

In Figs.9 and 10, "wave pattern added resistance" and added resistance of the diffraction wave resistance are compared for the model of the Series 60,  $C_B=0.80$ . The former denoted as "diffraction (wave pattern)" was obtained directly from the diffraction wave pattern around the model by following the procedure described in the previous section. Measured  $H_1(\theta)$ 's contribution to the added resistance, i.e. value of the second term on the right side of the equation (3) is so small compared with  $H_2(\theta)$ 's as to be ignored. Added resistance without restriction denotes one on the model freely moving in waves without any restraint, which was measured by a hanging weight dynamometer. The added resistance with no restraint is of almost identical magnitude with diffraction resistance measured as a force on the hull restrained. The wave

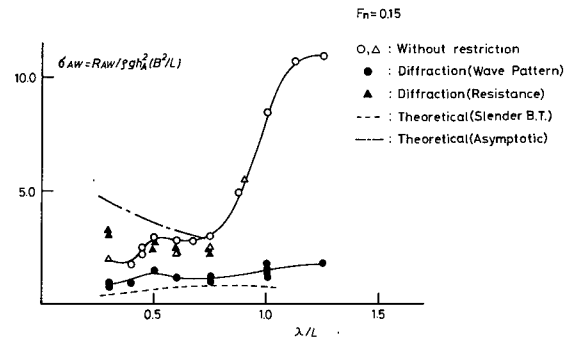


Figure 9. Added Resistance Coefficient (Series 60,  $C_B=0.80$ )

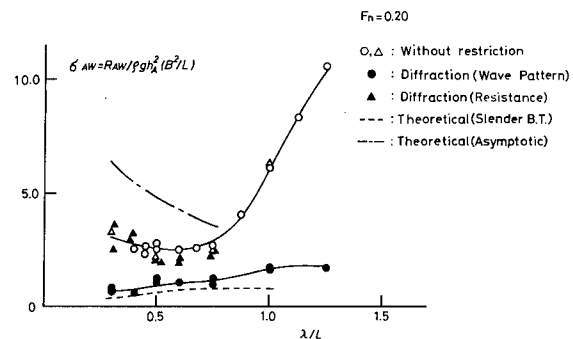


Figure 10. Added Resistance Coefficient (Series 60,  $C_B=0.80$ )

pattern added resistance of the model of the Series 60,  $C_B=0.80$  is of half or less magnitude as its added resistance (added resistance, if simply stated so, denotes that measured as a force on a hull hereafter).

Nakamura et al. (1983) did the similar experiment on a model which is of semi-circular bow form in water line forward from the station No.9 just like the CC1 model but with less draft. They found the similar or larger difference between the wave pattern added resistance and the added resistance.

The wave pattern added resistance of the model S175 does not have such a big discrepancy between the added resistance as the full hull forms as illustrated in Fig.11.

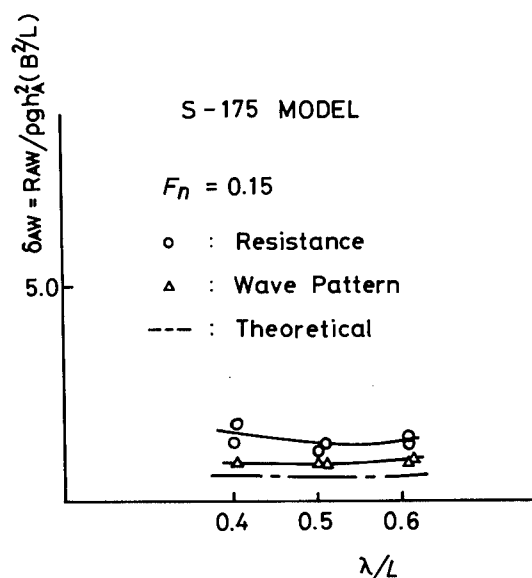


Figure 11. Added Resistance Coefficient (S-175)

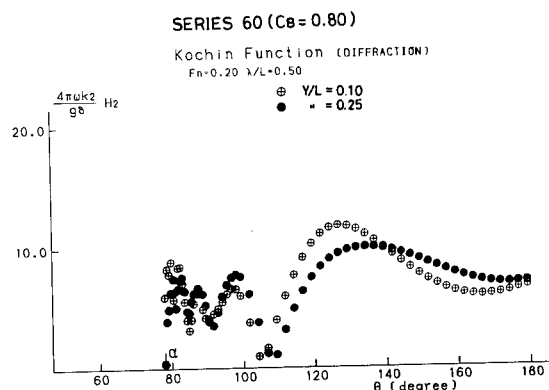


Figure 12. Comparison of Amplitude Function at Different Distances from Hull Surface

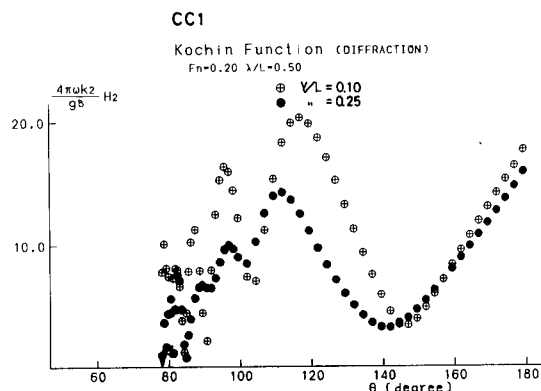


Figure 13. Comparison of Amplitude Function at Different Distances from Hull Surface

Theoretical added resistance illustrated in Figs.9 through 11 by dotted lines are calculated integrating the equation (3) with theoretical  $H_j(\theta)$  ( $j=1, 2$ ) as shown in Figs.3 to 8.

Comparison of  $H_2(\theta)$  obtained analyzing the wave elevation data at two different distances from the hull surface ( $y/L=0.1$  and  $0.25$ ) are shown in Figs.12 and 13. For the less full hull form (the Series 60,  $C_B=0.80$ ) we have almost no difference between them. Even if we added the  $H_2(\theta)$  at  $y/L=0.5$  to Fig.11, this conclusion would not be altered. Agreement between the  $H_2(\theta)$  at different  $y/L$  is still more complete for the more slender model S175, although we do not show the results here.

On the other hand the fullest CC1 model has much different  $H_2(\theta)$  for  $y/L=0.1$  and  $0.25$ , except that of waves propagating right behind the model. This difference in  $H_2(\theta)$  corresponds to the difference in the wave pattern added resistance that the bigger one is twice as large as the smaller one. Considering the incident wave's length is small enough and the model has so long parallel part and deep draft, that the parallel part generates little waves, most energy of the diffraction waves emanating to the direction of  $\alpha < \theta < 90^\circ \sim 100^\circ$  may come from the bow part. Part of energy of the diffraction waves propagating to those directions might be dissipated in the other form than the wave energy with some mechanism we do not know and we are not able to take account of it in the wave pattern added resistance. Energy corresponding to the difference between the wave pattern added resistance and the added resistance is assumed to be due to this dissipation.

Increase of frictional resistance due to the presence of the incident waves may be of the order of magnitude less than  $u^2/u^2$  relative to that on calm water, where  $u$  is the maximum orbital velocity of the incident waves.  $u^2/u^2$  is about

several hundredths for the conditions of our experiments but the difference between the wave pattern added resistance and the added resistance is not less than one tenth of the resistance on calm water.

### 3. OBSERVATION OF DIFFRACTION WAVES IN FRONT OF A 2-D MODEL AND BOW OF A FULL HULL FORM

In order to observe the diffraction waves propagating upstream against the ambient flow even for  $U\omega_e/g > 0.25$ , if any, whose possibility to cause the difference between wave pattern added resistance and added resistance was pointed out earlier by Nakamura et al. (1983), a horizontal cylinder with an elliptical section ( $b=24\text{cm}$ ,  $a=20\text{cm}$ ) was towed in regular incident waves, to the direction perpendicular to its axis, with its motion restrained. Model basin's width, in this experiment coincides almost with length of the cylinder 1.5m and the flow field around it therefore can be regarded as completely 2-dimensional.

We are concerned with the waves ahead of the cylinder. Waves behind the cylinder is highly influenced by the effect of separation and does not provide useful informations for our purpose.

In the experiments it was observed that diffraction waves propagate obviously forward upstream even for  $U\omega_e/g$  much greater than 0.25. Those waves propagate some distance forward and become so steep to break. Ahead beyond this distance no waves except the incident waves are present because  $U\omega_e/g$  is greater than 0.25.

Waves were measured by means of several wave probes advancing with the cylinder into the direction perpendicular to its axis. Far ahead of the cylinder we have no waves except the incident waves as already stated. An incident wave probe at the most forward position is located ahead enough to record the incident waves alone. The incident waves are regular and the time series of the incident wave elevations at the locations of other wave probes, where the diffraction waves are supposed to exist, can be extrapolated with a sufficient accuracy from the records with the incident wave probe. These extrapolated incident wave elevations are subtracted from the wave records including both the incident and the diffraction waves at other wave probes to provide the records of the diffraction waves alone there. The time series of the diffraction waves thus derived normally include the components of the higher harmonics of  $\omega_e$ , the encounter frequency with the incident waves, since the wave motions are of complicated variation close to the breaking point. Harmonic analysis of those records gives the am-

plitude and the phase of the wave motions of the frequency  $\omega_e$  as well as the stationary wave elevation.

The 2-D wave pattern ahead of the cylinders can be drawn in the course of time by means of those data. Two examples of them, non-dimensionalized with the amplitude of the incident waves, are illustrated every  $\omega_e t = 30^\circ$  in Figs. 14 and 15, where circles are the measured data at the locations of the wave probes and lines are drawn connecting them.

Obviously diffraction waves propagate forward even at such a high velocity of the cylinder  $U\omega_e/g = 0.47$  and  $0.61$ . They break to disappear after progressing  $50 \sim 60\text{cm}$ , about one and half wave length observed. Steepness of those diffraction waves is not less than  $1/10$  at the location close to the cylinder, noting  $\zeta$  the amplitude of the incident waves is about  $1\text{cm}$  and the wave length is nearly  $40 \sim 50\text{cm}$ .

Linear theory of short waves riding on steady current, slowly varying with the distance along the stream (Peregrine, 1976) might be used to describe those waves even though the scale of the current variation, supposed to be of the order of the cylinder's draft  $\times 2$ , is not so large as compared with the observed wave length and the current around the cylinder is not necessarily depthwise uniform.

The diffraction waves propagate

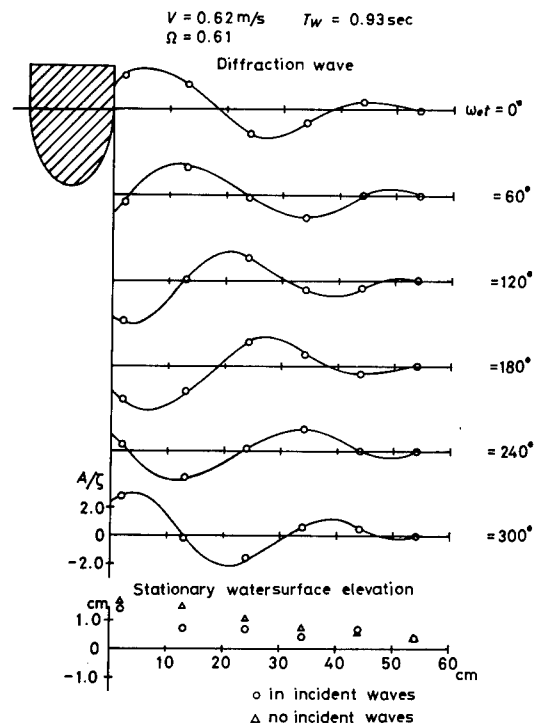


Figure 14. Diffraction Waves Ahead of a 2-D Body

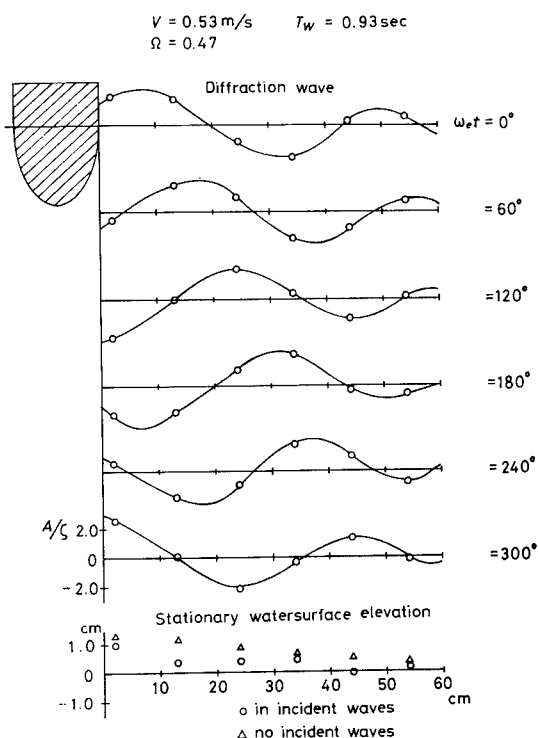


Figure 15. Diffraction Waves  
Ahead of a 2-D Body

upstream against the current whose magnitude approaches to  $u$ , the advance speed of the cylinder. Accordingly the waves propagate further ahead from the cylinder, they continually shorten and increase in steepness so that small amplitude theory becomes invalid. Practically they break and little or no energy is propagated beyond a point where the current velocity coincides with their group velocity. This current velocity is conveniently called the stopping velocity  $u(-1/4c, c$ : the phase velocity of the waves when they are on still water very close to the cylinder, given by  $g/\omega_e$ ). The wave number  $k_1$  at the stopping velocity equals to  $4k$ , where  $k(=\omega_e^2/g)$  is the wave number corresponding to  $c$ . At the stopping velocity the amplitude of the waves is singular and the waves break necessarily before reaching the stopping velocity.

In Fig.14 the computed  $k$  is 9.45, which corresponds to the wave length  $\lambda = 0.66\text{m}$  and the wave length  $\lambda_1$  at the distance close to the stopping velocity is 0.17m. For the second case shown in Fig.15,  $\lambda = 0.73\text{m}$  and  $\lambda_1 = 0.18\text{m}$ . It does not clearly appear that wave length shortens as the waves approach to the breaking point. The length of the propagating waves clearly observed in both figures is between  $\lambda$  and  $\lambda_1$ . The locations of the stopping velocity deter-

mined by the computed  $c(1.02$  and  $1.06 \text{ m/s})$  and the measured current velocity close to the free surface are 22cm and 25cm respectively ahead of the cylinder. The diffraction waves propagate against the current more than 30cm beyond the stopping velocity predicted by the linear theory.

Amplitude of the diffraction waves particularly close to the cylinder looks more twice as great as that of the incident waves.

Faltinsen's method to give amplitude  $A$  of the diffraction waves relative to that  $\zeta$  of the incident waves (Faltinsen, 1980) assuming that the incident waves are not influenced by non-uniform current around a body since its length is long as compared with the current scale, but the diffraction waves interact with the current (its velocity is zero on the body in our case). For the 2-D case with which we are concerned, the amplitude ratio is given by the equation (6) with  $k_1$  and  $\theta$  substituted by  $k$  and  $\pi/2$  respectively. That is

$$A/\zeta = \frac{2k_0}{k + k_0} \sqrt{\frac{k_1}{k_0}} \quad (6)$$

where  $k_0(=\omega_0^2/g)$  is the wave number of the incident waves for ahead of the cylinder. For the conditions of Fig.14, this equation gives  $A/\zeta = 0.9$  much less than the observed. On the other hand if we assume the total reflection on the body, then the conservation principle of wave action (Longuet-Higgins and Stewart, 1961, Whitham, 1974) describes the reflected waves as follows.

$$\frac{\zeta^2(u + \omega_0/2k_0)}{\omega_0} = \frac{A^2\omega/2k}{\omega} \quad (7)$$

This equation leads to  $A/\zeta \approx 1.9$  for the cases of Figs.14 and 15, which seem to be close to their observed values.

In the lower part of those figures the stationary wave elevation in front of the cylinder towed in the incident waves are compared with those when it is towed on a calm water with the identical velocity. The mean water level is depressed if the incident waves and accordingly the diffraction waves exist. Interaction of waves and non-uniform current including that of long waves such as the incident waves in our case is well known to lead to the mean water level displacement and part of the displacement is caused by spatial variation of the wave momentum flux. Our results of experiment show that the depression is larger at the highest diffraction waves and it returns to the original level after breaking. This phenomenon is supposed to be described by the similar mechanism as the set down and set up

of the waves coming to the shallow water to break.

Fig.16 shows the measured depression, just similar to the 2-D case due to the existence of the waves, of the mean water surface in front of the bow of CCl model along the center line. From this figure we can infer that reflected waves from the bow interact with the non-uniform current around it and the incident waves to change the stationary flow field in the vicinity of the bow. And the similarity of the depression of the mean water level to that of the 2-D let us expect that the diffraction waves propagate some distance ahead of the bow just like the 2-D waves.

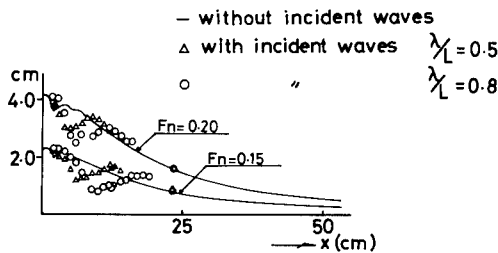


Figure 16. Stationary Waves Ahead of CCl's Bow

In Fig.17 is illustrated the variation of the measured form of the diffraction waves in the course of time, ahead of the bow and along the center line of CCl model. They are obtained with just the same procedure as in Fig.14. It seems that waves propagate forward to disappear beyond some distance but not so obviously as in the 2-D case.

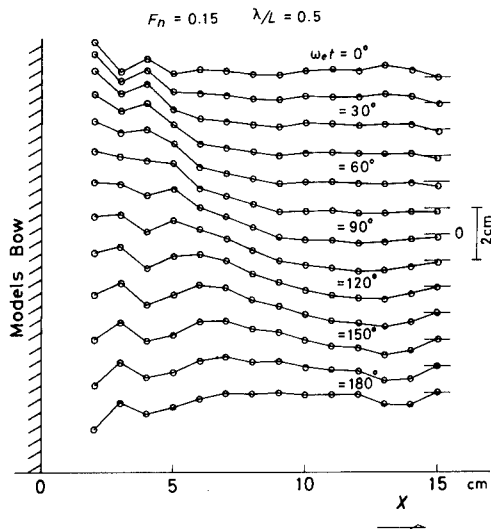


Figure 17. Diffraction Waves Ahead of the CCl's Body

#### 4. PREDICTION OF ADDED RESISTANCE DUE TO DIFFRACTION WAVES

Faltinsen's idea (1980) predicting resistance increase caused by the reflection of waves on the surface of ship's hull is based on ray theory assuming very small wave length as compared with other length scales such as draft, length of the hull and current scale. Ray of incident waves reaches to the hull surface, without any deformation even in the non-uniform current around the hull, and is reflected there. Direction of ray and wave number of the reflected waves are determined with free surface condition and reflection condition considering the non-uniform current, whose scale is assumed to be many times larger than wave length of the reflected waves and therefore is to be considered uniform around the reflection point. Practically Faltinsen assumed the current is directed along the water line of the hull and its magnitude is  $u \cos \theta$  as shown in Fig.18 where  $\theta$  is the inclination of the tangent at the point of the reflection. With the boundary condition that the reflected waves propagating outward should have an identical wave number along the  $s$ -axis with that of the incident waves and the free surface condition on the uniform flow  $u \cos \theta$ , the wave number  $k_1$  and the angle of the reflected ray  $\beta$  are given as follows

$$k_1 = (\omega_e - u k_0 \cos^2 \theta)^2 / g$$

$$\beta = \pi - \{ \theta + \tan^{-1} (\sqrt{k_1^2 - k_0^2 \cos^2 \theta} / k_0 \cos \theta) \} \quad (8)$$

where  $\omega_e$  is the encounter frequency,  $k_0$  the wave number of the incident waves. We have to notice that  $k_1$  is not by any means less than  $k_0 \cos \theta$ , since

$$k_1 = (\omega + u k_0 \sin^2 \theta)^2 / g > \omega^2 / g = k_0$$

where  $\omega$  is the frequency of the incident waves relative to the water. It means that reflected waves from any point on the hull surface propagate outward.

In the linear theory, which assumes the uniform ambient flow  $u$  everywhere even close to the hull surface, it is well known that no waves propagate into the direction satisfying  $1 - 4\Omega \cos \beta < 0$  provided  $\Omega = u \omega_e / g$  is larger than 0.25.  $\alpha_0$  defined in the section 2 is the limit of  $\beta$  beyond which no waves propagate.

Nevertheless in Faltinsen's ray theory the reflected waves interact with the steady current field,  $u \cos \theta$  along the water line, close to the hull surface and can emanate against the ambient flow even to the direction  $\beta=0^\circ$  for the blunt bow, since  $\theta=\pi/2$  at the apex and  $u \cos \theta$  equals to zero around there.

That is, very low velocity around the bow makes it possible for waves to propagate forward even if  $u\omega_e/g$ , based on the current field away from the hull, is larger than 0.25. This phenomenon was observed in the 2-D experiments described in the previous section. So Faltinsen's reflection condition given by the equation (8) is considered to be proved experimentally reasonable, although the 3-D flow might be a little different from the 2-D one.

The characteristics of reflected waves for the 2-D case are rather simpler as already described. It was observed that the waves, progressing forward if they are close to the body, are not able to reach far from it because the current velocity becomes higher than that satisfying  $u\omega_e/g = 0.25$  as they propagate forward and eventually they break at or before the stopping velocity.

Reflected waves emanating from the bow of a ship and satisfying the condition (8) on the hull surface are not described such a simple way. Direction of the reflected waves will change, that is, the waves are refracted, interacting with the non-uniform current as they propagate outward away from the hull surface. Naito et al. (1982) proposed to describe the propagation of the reflected waves in the assumed slowly varying current around a ship with the use of an averaged Lagrangian developed by Whitham (1974). The steady and non-uniform current field around the hull is assumed in their computation to be that with a double model approximation to the free surface condition. They found that reflected waves from the apex part of the bow break.

With the objective of understanding the deformation of reflected waves around the CCI model's bow, we computed changes of their direction and their amplitude along Naito's idea in principle but with a simpler flow model. We assumed the flow field is  $u \cos \theta$  along the water line if close to the hull surface but shift abruptly to the uniform ambient flow  $u$  of the  $-x$  direction. Reflected waves start from every point on the bow surface with the direction and the wave number satisfying the conditions (8) will be refracted when entering the uniform flow field  $u$ . Refraction of waves in a current making an oblique angle with the wave direction is easily computed (Longuet-Higgins and Stewart, 1961). Increase or decrease of their amplitude associated with the refraction was computed by the principle of the wave action being constant before and after the refraction, which is expressed by

$$\nabla(\epsilon_g + \vec{v})(\zeta^2/\sigma) = 0$$

where  $\vec{v}$  the flow field vector,  $\epsilon_g$  the

group velocity of the waves,  $\zeta$  the amplitude and  $\sigma$  the frequency of the waves relative to the water.

In Fig.19 are depicted directions of the reflected waves just after leaving the bow surface (denoted as  $\beta$  in near-field) vs. directions of the same waves after arriving in the uniform flow field  $u$  ( $\beta$  in far-field). Their steepness in the far-field is illustrated vs.  $\beta$  in the near-field. This figure clearly shows that all the waves with small  $\beta$  in near-field, that is, waves emanating from the apex part of the bow, concentrate to propagate into a direction  $\alpha_0$  ( $\approx 72^\circ$  for  $F_N=0.15$ ,  $\lambda/L=0.5$ ). Naturally their steepness becomes so great that some part of their energy will dissipate into other form of energy than waves. In this computation steepness of the incident waves is assumed to be 0.02.

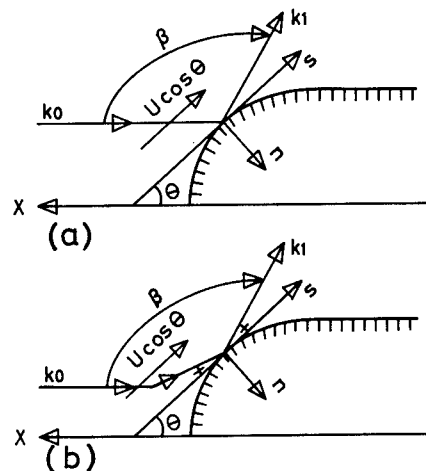


Figure 18. Reflection of Incident Waves

Distribution of the measured amplitude of diffraction waves on several lines of  $y/L = \text{const.}$  are shown together in Fig.20. Very steep waves appear particularly for the CCI model in the front part of the waves if the line of  $y/L = \text{const.}$  is close to the hull surface. This steep waves disappear a little away from the hull surface.

Reflected waves from the bow part will reach to the far field after modifications of their amplitude, direction of propagation and wave length under the influence of the non-uniform current close to the hull surface. Added resistance derived from the wave field close to the hull surface is supposed to be of different magnitude from that in the far field which is the wave pattern added resistance. However we have at present no theory to provide diffraction waves in the far-field with taking into account the effects due to the non-uniform current prominent close to the blunt bow.

Assuming wave length to be very



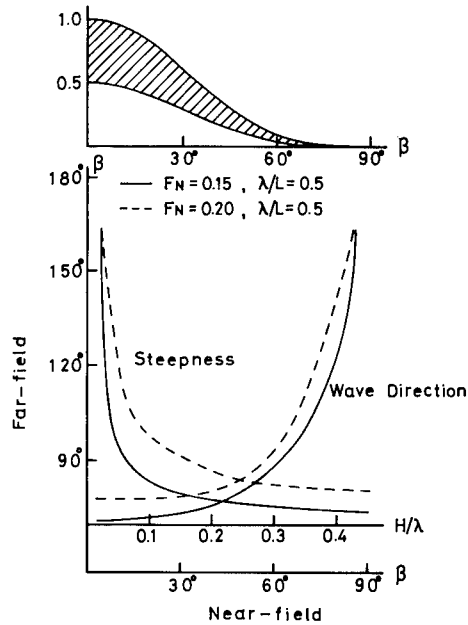


Figure 19. Steepness and Direction of Waves

short as compared with other length scales, the 2-D approach is possible to get the added resistance due to the wave field close to the blunt bow part of a ship just as Faltinsen (1980) did. If we could know what part of reflected waves contributing the added resistance thus computed is able to reach far, we might roughly evaluate the difference between added resistance and wave pattern added resistance. Along this line Nakamura et al. (1983) computed the difference excluding some part of the bow apex from an integral of the stationary pressure given by Faltinsen (1980). The bow part excluded from the integral corresponds to that from which reflected waves emanate but break before arriving to the far-field in their computation (Naito et al., 1982).

Faltinsen (1980) assumes naturally the incident waves are not influenced by the local flow close to the bow as illustrated in Fig. 18 (a) and therefore two wave systems with different wave length are present there. Since no other energy dissipation is assumed, the conservation of energy is not realized with only the incident waves and the reflected waves of different wave lengths. Added resistance derived on this assumption has accordingly ambiguity that added resistance is determined regardless of amplitude of the reflected waves, that means different amplitude of the reflected waves give the same added resistance.

To avoid this ambiguity, we assume that the incident waves are also deform-

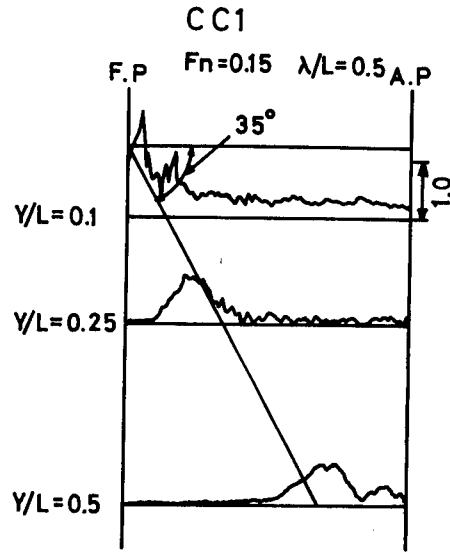


Figure 20. Amplitude Distribution of Diffraction Waves

ed in their direction as shown Fig. 18 (b) with the current along the water line prominent close to the hull surface. With this assumption the incident waves satisfy the same free surface condition and are of the same wave number as the reflected waves. The reflection is prescribed by Snell's Law. Then velocity potential is given by

$$\Phi = \frac{g\zeta_a}{\sqrt{gk_1}} \sqrt{\frac{k_1^2}{k_{1n}k_0} \left(1 + \frac{2\omega U}{g}\right) \sin\theta} e^{k_1 z} \times [\cos(k_{1s} s + k_{1n} n - \omega_e t) + f \cos(k_{1s} s - k_{1n} n - \omega_e t + \epsilon)] \quad (9)$$

where  $\zeta_a$ ,  $f\zeta_a$  the amplitude of the incident and the reflected waves respectively,  $k_1$  the wave number satisfying the equation (8) and  $k_{1s}$ ,  $k_{1n}$  the components of the  $k_1$  into the directions  $s$

and  $n$ . The square-root term on the equation (9) is amplification factor of  $\zeta_a$  associated with the change of the incident waves in their direction. This is again provided with the wave action being constant before or after the refraction.

Sum of momentum flux through the  $n=-\infty$  plane and the body surface being zero, added resistance is given by

$$\Delta R = \frac{1}{2} \rho g \zeta_a^2 \left(1 + \frac{2\omega U}{g}\right) \times \int \left(\frac{1}{2} + \frac{\varepsilon^2}{2}\right) \frac{k_1 n}{k_0} \sin^2 \theta \, d\ell \quad (10)$$

where the integration is along the non-shadow part on the incident waves of the water line curve. Conservation of energy generally prescribes  $\varepsilon=1$ . So added resistance is supposed to be given by the equation (10) with  $\varepsilon=1$  being substituted. However if the amplitude of reflected waves is assumed to be reduced untill they propagate a little further from the body surface, we get less added resistance with substituting some value corresponding to the reduced amplitude into  $\varepsilon$ . For example  $\varepsilon$  will be given through the computation of steepness as done in Fig.19, if energy corresponding to the steepness more than 0.1 is assumed not to exist as wave energy and it is equivalent to the reduction of  $\varepsilon$ .

Added resistance of a model of the Series 60,  $C_B=0.80$  computed by this equation with  $\varepsilon=1$  being substituted is depicted by chain line in Figs.9 and 10.

The equation tells that waves propagating forward contribute at most only 50% for the added resistance and the wave pattern added resistance is much more than a half of the added resistance. However it is not in experiments.

Theoretical model for computing the difference between added resistance and wave pattern added resistance should be investigated further.

## 5. CONCLUDING REMARKS

We found a big discrepancy in magnitude between added resistance measured as a force on a ship model and wave pattern added resistance derived from the measured wave pattern around the model if it is of full hull form with blunt bow. Some part of this discrepancy is supposed, based on several observations of diffraction waves and analysis of wave pattern, to be caused by the interaction of diffraction waves with the non-uniform current around the bow.

Simple theoretical model of this interaction did not provide quantitatively satisfactory results. Obvious approach to achieving further progress is to use numerical method to solve the complete problem of wave diffraction on

the body surface in the non-uniform current.

## REFERENCES

- Adachi, F. (1978): On the Calculation of Wave Exciting Forces on Ship Translating in Head Sea Waves. Journal of the Society of Naval Architects of Japan, Vol.143, pp.34-40.
- Faltinsen, O.M. et al. (1980): Prediction of Resistance and Propulsion of a Ship in a Seaway. Proc. of 13th ONR Symposium, pp.505-523.
- Fujii, H. and Takahashi, T. (1975): Experimental Study on the Resistance Increase of a Large Full Ship in Regular Oblique Waves. Journal of the Society of Naval Architects of Japan, Vol.137, pp.132-137.
- Longuet-Higgins, M.S. and Stewart, R.W. (1961): The Changes in Amplitude of Short Gravity Waves on Steady Non-Uniform Currents. Journal of Fluid Mechanics, Vol.10, pp.529-549.
- Maruo, H. (1963): Resistance in Waves. 60th Anniversary Series of the Society of Naval Architects of Japan, Vol.8, pp.67-102.
- Nakamura, S. et al. (1983): Experimental Study on Resistance Increase of a Ship with Blunt Bow in Regular Head Waves. Journal of the Kansai Society of Naval Architects of Japan, Vol.190, pp.73-81.
- Nakamura, S. et al. (1983): On Resistance Increase of a Ship with Blunt Bow in Regular Head Waves. Report of Research Committee of the Society of Naval Architects of Japan.
- Naito, S. et al. (1982): Propagation of Diffraction Waves around a Full Hull Form. Report of Research Committee of the Society of Naval Architects of Japan.
- Ohkusu, M. (1977): Analysis of Waves Generated by a Ship Oscillating and Running on a Calm Water with Forward Velocity. Journal of the Society of Naval Architects of Japan, Vol.142, pp.36-44.
- Ohkusu, M. (1980): Added Resistance in Waves in the Light of Unsteady Wave Pattern Analysis. 13th ONR Symposium, pp.413-424.
- Peregrine, D.H. (1976): Interaction of Water Waves and Currents. Advance in Applied Mechanics, Vol.16, pp.10-117.
- Strom-Tejsten, J. et al. (1973): Added Resistance in Waves. Trans. SNAME. pp.109-142.
- Whitham, G.B. (1974): Linear and Non-linear Waves. Wiley, New York.

## DISCUSSION

Prof. SERGE BINDEL,  
Ecole Nationale Supérieure de Techniques  
Avancées, Paris, France:

May I make a personal remark regarding the difference between the measured added resistance on the model and the wave pattern added resistance for a full hull form with a blunt bow. It seems to me that a significant part of that difference may be due to the breaking of the waves. Such a breaking is well known for full ships moving steadily in calm water. The superposition of the three wave fields, i.e. steady waves, incident waves and diffraction waves surely leads to an increased risk of breaking. This part of the wave energy is not radiated but dissipated inside the fluid itself, producing a head loss for this reason. I am not sure that the solution for achieving further progress is to improve numerical methods at this stage. In my opinion it would be probably more useful to try to measure the head loss due to wave breaking, but that is of course difficult in the case of an unsteady flow.

## AUTHOR'S REPLY

I pointed out in this paper that the difference between added resistance and wave pattern added resistance might be described partly by the breaking of waves propagating forward from the bow of ship. I presented several experimental evidences supporting this description. However I am still not satisfied with those evidences and I need evidence showing this description is obviously correct. Numerical computation of diffraction waves, by whatever means, with stationary current field around the bow incorporated even approximately will show if such steep waves as to break occur actually or not. Naturally, measurement of flow field, if it were done accurately enough, would provide us an answer.

# NONLINEAR DEVELOPMENT OF HEAD SEAS ALONG A LARGE SLENDER BODY

CHIANG C. MEI AND EDMOND LO

## ABSTRACT

The nonlinear evolution of a steady wave train passing a slender but large body cruising on the sea surface is studied theoretically. The body is assumed to be long enough for third-order nonlinearity to affect the leading-order wave amplitude significantly. The current induced by the forward speed of the body is also accounted for. By means of multiple scales the diffraction of nonlinear waves is found to be governed by a cubic Schrodinger equation whose coefficients depend on the local current distribution. Numerical results are presented for a range of wave slopes while the ship can either move into or away from the incident waves. It is also shown that the drift force is at most third order in incident wave amplitude.

## INTRODUCTION

Wave diffraction by a large body is of interest not only in the structural design of floating vessels but also in the mechanics of icebergs. Hult and Ostrander (1974) observe that icebergs in the open southern ocean tend to be much smaller than those seen within the shelter of Antarctic pack ice, and suggest that wave-induced flexural failure may be partially responsible. Both theoretical estimates (Squire (1981), Kristensen and Squire (1983)) and field observations (Goodman et al (1980), Orheim (1980), Orheim et al (1982), and Wadhams and Kristensen (1983)) have been reported. Interests in this problem stem from proposals to develop technology for towing icebergs (Weeks and Mellow, 1978).

At present wave diffraction by floating bodies without forward speed can be efficiently predicted only if all nonlinear effects are ignored (see, e.g., Wehausen (1972), Mei (1983)). For bodies of arbitrary shape, a variety of numerical methods now exist (see surveys by Mei (1980), Yeung (1982)). For slender bodies such as ships, approximate schemes such as two-dimensional strip theory and matched asymptotic expansions are available (see surveys by Ogilvie (1977,

Newman (1978)).

An important problem for the slender body is the case of head-sea diffraction, for which the linearized theory is already not simple (Faltinsen (1972), Maruo and Sasaki (1974)). In Faltinsen's matched asymptotic treatment of a stationary ship, the outer solution is constructed via a line distribution of oscillating sources; the inner approximation of the outer solution is quite involved. Haren and Mei (1980) show that this difficult step can be bypassed by employing the **parabolic approximation**. Perhaps a more important advantage of the parabolic approximation is that inclusion of third-order nonlinearity is quite straightforward. The simple example of a wedge with vertical walls extending the entire sea depth has been studied in this manner by Yue and Mei (1980). Further extension of parabolic approximation to refraction and diffraction of nonlinear waves by slowly varying depth has been made by Kirby and Dalrymple (1983). In contrast, the usual Stokes expansion is already formidable at second order if a body is present.

From the numerical point of view, all existing methods for the linearized diffraction theory for a general **large body** without forward speed are costly; direct application or extension of them for second-order improvement in the usual manner of Stokes expansion is both tedious and expensive. For a long slender body, however, the parabolic approximation can again be extended to include third-order effects; this is demonstrated in the present paper. Specifically the present theory is based on the assumptions of low speed and slender body such that

$$F = \frac{U}{\sqrt{gL}} = O\left(\frac{B}{L}\right) \ll 1 \quad (1)$$

where  $F$  = Froude number,  $U$  = current of ship speed,  $L$  = half length,  $B$  = half beam. In addition the incident wave is both small and short in the sense that

Dept. of Civil Engineering, Massachusetts Institute of Technology, Cambridge, Mass. 02139, USA

$$ka_0 = \frac{\omega^2 a_0}{g} = 0(kB)^{-1} = 0\left(\frac{B}{L}\right) < 1 \quad (2)$$

Strictly speaking these several parameters need not be of the same order of magnitude, but our choice leads to the most interesting physical circumstance in which nonlinearity and dispersion are comparable. Our attention is focused on the diffraction near the body. Ship waves which are stationary with respect to the body due to no-zero  $U$  are not treated. Applying the ray approximation under condition (1), Keller (1979) estimates that there are ship waves whose amplitude is at most of the order

$$a_0 = 0(F^2 L) \quad (3)$$

Equation (2) then implies

$$a_0 = 0(a_s) \epsilon \quad (4)$$

However, Keller also reasons that these waves are generated mainly at the bow and the stern, and are significant only far away  $0(L)$  from the ship. Quantitative calculations of the bow and stern waves have not been carried out by this scheme so that the ray theory is yet incomplete. In any case rays of the bow and stern waves point away from the body at a finite angle ( $\approx 19^\circ$ ); their encounter with the incident waves is brief, and the mutual influence should therefore be weak. Therefore we expect our theory, which does not account for the ship waves, to be correct to the leading order near the main part of the body but away from the bow and the stern. Linear corrections can be superimposed near the two ends once the ship waves there are computed.

By means of multiple-scale expansions, the evolution equation governing the modulation of the wave envelope is derived. The solution is affected by the steady, nonuniform current field which is solved to the leading order as a double-body problem in an infinite fluid. Numerical results are obtained for a paraboloid of revolution, advancing with or opposite to the waves.

#### FORMULATION

We choose a coordinate system moving with the slender body, as depicted in Fig. 1. A current of speed  $U$  at infinity is directed along the  $x$ -axis, being positive if it is from left to right. The maximum beam and draft of the body is  $2B$ , while the length is  $2L$ . A train of incident waves of length  $2\pi/k$  and amplitude  $a_0$  propagates along the  $x$ -axis from  $x \rightarrow -\infty$  to  $\infty$ . We shall assume that the water depth is much greater than the wavelength. Denoting by

$$\epsilon = ka_0 \ll 1 \quad (5)$$

the incident wave slope, Eqs. (1) and (2) imply that

$$kB = 0(\epsilon^{-1}) \quad kL = 0(\epsilon^{-2}) \quad (6)$$

$$kU^2/g = 0(1)$$

or, in physical terms: wave amplitude  $\ll$  wavelength  $\ll$  body width or draft  $\ll$  body length, and current speed  $= 0$  (phase speed). To see the practical relevance of these assumptions we take two sample cases. If a supertanker of length  $2L = 320$  m and beam  $2B = 64$  m is in a wave of period  $T = 4$  sec, as seen in the rest frame, then  $kL \approx 40$ .  $M = 1$  corresponds to  $F = 0.158$  and  $U = 6.3$  m/sec  $= 23$  km/hr. This is in a speed range common to supertankers. On the other hand, for an elongated iceberg of  $2L = 2000$  m,  $2B = 400$  m in a long swell of  $T = 10$  sec, we have  $kL = 40$ . If it is towed at the speed  $U = 5$  m/sec, we can have  $M = 0.03$ .

In this coordinate system the governing condition for the perturbed velocity potential  $\phi'(x', y', z', t')$  is

$$\phi'_{x'x'} + \phi'_{y'y'} + \phi'_{z'z'} = 0 \quad -\infty < z' < \zeta' \quad (7)$$

On the body, described by  $y' = Y'(x', z')$ , the kinematic condition is

$$\phi'_{y'} = (U + \phi'_{x'})Y'_{x'} + \phi'_{z'}Y'_{z'} \quad y' = Y'(x', z') \quad (8)$$

On the free surface  $z' = \zeta'(x', y', t')$  the kinematic and dynamic conditions are

$$\phi'_{z'} = \zeta'_t + (U + \phi'_{x'})\zeta'_{x'} + \phi'_{y'}\zeta'_{y'} \quad (9)$$

$$g\zeta' + \phi'_{tt'} + U\phi'_{xt'} + \frac{1}{2}(\nabla'\phi')^2 = 0 \quad (10)$$

Before proceeding further, we note that the assumed slenderness  $B/L = 0(\epsilon)$  implies that the current-induced velocity perturbation  $\phi'_{y'}$  is of the order  $\epsilon U$  according to (8). Because of the small wave slope the velocity perturbation induced by the incident waves is also of the order  $\epsilon U$  when use is made of the assumption  $M = 0(1)$ .

We now introduce the normalized variables

$$(x', y', z') = (x, y, z)/k \quad t' = t/\sqrt{gk} \quad (11)$$

$$\phi' = \phi\sqrt{g/k}/k \quad \zeta' = \zeta/k$$

The dimensionless governing equations are

$$\phi_{xx} + \phi_{yy} + \phi_{zz} = 0 \quad -\infty < z < \zeta \quad (12)$$

$$\phi_y = \frac{b}{\epsilon} [(M + \phi_x)Y_x + \phi_z Y_z] \quad y = \frac{b}{\epsilon} Y(x, z) \quad (13)$$

$$\phi_z = \zeta_t + (M + \phi_x)\zeta_x + \phi_y \zeta_y \quad (14)$$

$$g\zeta + \phi_{tt} + M\phi_x + \frac{1}{2}(\nabla\phi)^2 = 0 \quad z = \epsilon\zeta(x, y, t) \quad (15)$$

where

$$M = U\sqrt{K/g} = F/\sqrt{K} = O(1) \quad (16)$$

$$b = \epsilon k B = O(1) \quad (17)$$

#### THE PERTURBATION EXPANSIONS

In terms of the dimensionless coordinates  $x, y$ , and  $z$  the body width and draft are of the order  $\epsilon^{-1}$ , while the length is of the order  $\epsilon^{-2}$ . Therefore we introduce the additional slow variables:

$$x_2 = \epsilon^2 x, \quad y_1 = \epsilon x, \quad z_1 = \epsilon z \quad (18)$$

For simplicity we do not allow slow modulation in time and in the  $x$  direction on the scale  $\epsilon^{-1}$ , i.e., there is no  $t_1, t_2$ , and  $x_1$ . This assumption precludes the interesting case of wave instability along an advancing body.

Since the current-induced velocity potential is, in physical variables,  $\phi = O(\epsilon UB)$ , we must allow for a term  $\phi^{(0)}$  of order unity in the expansion, i.e.,

$$\phi = \phi^{(0)} + \epsilon \phi^{(1)} + \epsilon^2 \phi^{(2)} + \epsilon^3 \phi^{(3)} + \dots \quad (19)$$

Furthermore, because of the large size of the body,  $\phi^{(0)}$  only depends on the slow variables  $(x_2, y_1, z_1)$ ; dependence on  $x, y, z$  and  $t$  can only be associated with  $\phi^{(n)}$ ,  $n > 1$ , i.e.,

$$\begin{aligned} \phi^{(0)} &= \phi^{(0)}(x_2, y_1, z_1) \\ \phi^{(n)} &= \phi^{(n)}(x, y, z, t; x_2, y_1, z_1) \end{aligned} \quad (20)$$

Dictated by Bernoulli's equation, the free surface displacement corresponding to  $\phi^{(0)}$  is only  $O(\epsilon^2)$ . Denoting by

$$\nabla = \left( \frac{\partial}{\partial x}, \frac{\partial}{\partial z} \right) \quad (21)$$

$$\nabla_1 = \left( \frac{\partial}{\partial y_1}, \frac{\partial}{\partial z_1} \right)$$

we have, from the Laplace equation,

$$\nabla^2 \phi^{(1)} = 0 \quad (22a)$$

$$\nabla^2 \phi^{(2)} = -\nabla_1^2 \phi^{(0)} - 2\phi_{zz_1}^{(1)} \quad (22b)$$

$$\nabla^2 \phi^{(3)} = -\nabla_1^2 \phi^{(0)} - 2(\phi_{xx_2}^{(1)} + \phi_{zz_1}^{(2)}) \quad (22c)$$

On the body boundary which is now expressed by  $y_1 = bY(x_2, z_1)$  the kinematic condition gives

$O(\epsilon)$ :

$$\phi_{y_1}^{(0)} = b[MY_{x_2} + Y_{z_1}(\phi_z^{(1)} + \phi_{z_1}^{(0)})] \quad (23a)$$

$O(\epsilon^2)$ :

$$\phi_{y_1}^{(1)} = b[Y_{x_2}\phi_x^{(1)} + Y_{z_1}(\phi_z^{(2)} + \phi_{z_1}^{(1)})] \quad (23b)$$

$O(\epsilon^3)$ :

$$\phi_{y_1}^{(2)} = b[Y_{x_2}(\phi_x^{(2)} + \phi_{x_2}^{(0)}) + Y_{z_1}(\phi_z^{(3)} + \phi_{z_1}^{(2)})] \quad (23c)$$

Without serious loss of practicality we shall assume from here on that the body surface is vertical along the water line, i.e.,

$$Y_{z_1} = 0 \quad \text{on} \quad y_1 = bY(x_2, 0) \quad (24)$$

After expanding the free surface height as

$$\zeta = \epsilon \zeta^{(1)} + \epsilon^2 \zeta^{(2)} + \epsilon^3 \zeta^{(3)} + \dots \quad (25)$$

where

$$\zeta^{(n)} = \zeta^{(n)}(x, y, t; x_2, y_1) \quad (26)$$

and Taylor-expanding the kinematic condition about  $z = 0$ , we get,

$O(\epsilon)$ :

$$\phi_z^{(1)} + \phi_{z_1}^{(0)} = \zeta_t^{(1)} + M\zeta_x^{(1)} \quad (27a)$$

$O(\epsilon^2)$ :

$$\phi_z^{(2)} + \phi_{z_1}^{(1)} + \zeta^{(1)}\phi_{zz}^{(1)} = \zeta_t^{(2)} + M\zeta_x^{(2)} + \zeta_x^{(1)}\phi_x^{(1)} \quad (27b)$$

$O(\epsilon^3)$ :

$$\begin{aligned} \phi_z^{(3)} + \phi_{z_1}^{(2)} + \zeta^{(2)}\phi_{zz}^{(1)} + \zeta^{(1)}(\phi_{zz}^{(2)} + 2\phi_{zz_1}^{(1)} + \phi_{z_1 z_1}^{(0)}) \\ + \frac{1}{2}(\zeta^{(1)})^2\phi_{zzz}^{(1)} = \zeta_t^{(3)} + M(\zeta_x^{(3)} + \zeta_x^{(1)}) \\ + \zeta_x^{(2)}\phi_x^{(1)} + \zeta_x^{(1)}(\phi_x^{(2)} + \phi_{x_2}^{(0)}) \\ + \zeta^{(1)}\zeta_x^{(1)}\phi_{xz}^{(1)} + \zeta_{y_1}^{(1)}\phi_{y_1}^{(0)} \end{aligned} \quad (27c)$$

Similarly the dynamic boundary condition on the free surface leads to:

$$O(\epsilon):$$

$$\phi_t^{(1)} + M\phi_x^{(1)} + \zeta^{(1)} = 0 \quad (28a)$$

$$O(\epsilon^2):$$

$$\begin{aligned} \phi_t^{(2)} + M\phi_x^{(2)} + \zeta^{(2)} + M\phi_{x_2}^{(0)} + \zeta^{(1)} \left( \frac{\partial}{\partial t} + M \frac{\partial}{\partial x} \right) \phi_z^{(1)} \\ + \frac{1}{2} [(\phi_x^{(1)})^2 + (\phi_y^{(0)})^2 + (\phi_{z_1}^{(0)} + \phi_z^{(1)})^2] = 0 \end{aligned} \quad (28b)$$

$$O(\epsilon^3):$$

$$\begin{aligned} \phi_t^{(3)} + M\phi_x^{(3)} + \zeta^{(3)} + M\phi_{x_2}^{(1)} \\ + \zeta^{(1)} \left[ \left( \frac{\partial}{\partial t} + M \frac{\partial}{\partial x} \right) (\phi_z^{(2)} + \phi_z^{(1)}) \right] \\ + \zeta^{(2)} \left( \frac{\partial}{\partial t} + M \frac{\partial}{\partial x} \right) \phi_z^{(1)} \\ + \frac{1}{2} (\zeta^{(1)})^2 \left( \frac{\partial}{\partial t} + M \frac{\partial}{\partial x} \right) \phi_{zz}^{(1)} \\ + \phi_x^{(1)} (\phi_{x_2}^{(0)} + \phi_{x_2}^{(2)}) + \zeta^{(1)} \phi_x^{(1)} \phi_{xz}^{(1)} \\ + \phi_{y_1}^{(0)} \phi_{y_1}^{(1)} + (\phi_{z_1}^{(0)} + \phi_{z_1}^{(1)}) (\phi_{z_1}^{(1)} + \phi_z^{(2)}) \\ + \zeta^{(1)} (\phi_z^{(1)} + \phi_{z_1}^{(0)}) \phi_{zz}^{(1)} = 0 \end{aligned} \quad (28c)$$

#### APPROXIMATE EQUATIONS FOR THE CURRENT POTENTIAL AND THE WAVE ENVELOPE

As in the case without a body and topography, an evolution equation is expected for the amplitude of the first-order, first harmonic wave after examining the perturbation equations at orders  $O(\epsilon^2)$  and  $O(\epsilon^3)$ . In this case, the leading-order perturbation potential for the deflected current is also an outcome of the same procedure.

At  $O(\epsilon)$  we assume the solution to be in the form

$$\phi^{(1)} = \phi^{(10)} + (\phi^{(11)} e^{i\theta} + \text{c.c.}) \quad (29)$$

where

$$\theta = x - \Omega t \quad (30)$$

$$\phi^{(10)} = \phi^{(10)}(z, x_2, y_1, z_1) \quad (31a)$$

$$\phi^{(11)} = \phi^{(11)}(z, x_2, y_1, z_1) \quad (31b)$$

and c.c. represents the complex conjugate of the preceding term. The zeroth harmonic  $\phi^{(10)}$  satisfies

$$\phi_{zz}^{(10)} = 0 \quad -\infty < z < 0 \quad (32)$$

and

$$\phi_z^{(10)} = -\phi_{z_1}^{(0)} \quad \text{on } z = 0 \quad (33)$$

We require  $\phi^{(10)}$  to be finite for  $z \rightarrow -\infty$ . To assure this we must have

$$\phi_{z_1}^{(0)} = 0 \quad \text{on } z = z_1 = 0 \quad (34)$$

Thus,

$$\phi_z^{(10)} = 0 \quad \text{or} \quad \phi^{(10)} = \phi^{(10)}(x_2, y_1, z_1) \quad (35)$$

also. Now from (23a) we get for  $\phi^{(11)}$ :

$$\phi_{zz}^{(11)} - \phi^{(11)} = 0 \quad z < 0 \quad (36)$$

$$\phi_z^{(1)} + \phi_{z_1}^{(0)} + \left( \frac{\partial}{\partial t} + M \frac{\partial}{\partial x} \right)^2 \phi^{(1)} = 0 \quad z = 0 \quad (37)$$

Making use of (34), we find

$$\phi_z^{(11)} - (M - \Omega)^2 \phi^{(11)} = 0 \quad z = 0 \quad (38)$$

It is easy to find that

$$\phi^{(1)} = \phi^{(10)} + \frac{1}{2} e^z (-iAe^{i\theta} + \text{c.c.}) \quad (39)$$

$$\zeta^{(1)} = \frac{1}{2} (Ae^{i\theta} + \text{c.c.}) \quad (40)$$

where  $A(x_2, y_1)$  is the amplitude of the first-order, first harmonic. The dispersion relation is

$$\Omega - M = 1 \quad (41)$$

or equivalently,

$$\omega - Uk = \sqrt{gk} \quad (42)$$

in dimensional form, as is well known from the linearized theory. Here  $\sqrt{gk}$  is the wave frequency in the absolute frame of reference, while  $\omega$  is the frequency of the same wave seen by the moving body. In view of (35) and of the exponential decay with depth of  $\phi^{(11)}$ , the product  $y_{z_1} \phi_z^{(11)}$  vanishes and the condition (23a) on the body reduces to

$$\phi_{y_1}^{(0)} = b(M y_{x_2} + y_{z_1} \phi_{z_1}^{(0)}) \quad \text{on } y_1 = b y(x_2, z_1) \quad (43)$$

Now the normal to the body contour at any fixed  $x_2$  is

$$\vec{n}_1 = (1, -bY_{z_1})[1 + (bY_{z_1})^2]^{-1/2} \quad (44)$$

which is taken to be positive if pointing into the fluid. Equation (43) can be written

$$\frac{\partial \phi^{(0)}}{\partial n_1} = MbY_{x_2} \frac{dz_1}{ds_1} \quad (45)$$

where

$$ds_1 = dz_1[1 + (bY_{z_1})^2]^{1/2} \quad (46)$$

Integrating along the body contour we get

$$\int \frac{\partial \phi^{(0)}}{\partial n_1} ds_1 = M \int bY_{x_2} dz_1 = MS'(x_2) \quad (47)$$

where  $S$  denotes the cross-sectional area at  $x_2$ . Well known in aerodynamics, this result means that the change of cross-sectional area induces a radial flux.

At the order  $O(\epsilon^2)$ , Eq. (22b) is simplified to

$$\nabla^2 \phi^{(2)} = -\nabla_1^2 \phi^{(0)} \quad (48)$$

On the body boundary, we have from Eq. (13)

$$\phi_{y_1}^{(1)} = b(Y_{x_2} \phi_x^{(1)} + Y_{z_1} \phi_{z_1}^{(1)}) \quad y_1 = bY \quad (49)$$

From the two conditions on the free surface we find

$$\begin{aligned} & \phi_z^{(2)} + \left(\frac{\partial}{\partial t} + M \frac{\partial}{\partial x}\right)^2 \phi^{(2)} \\ &= -\phi_{z_1}^{(1)} - \zeta^{(1)} \phi_{zz}^{(1)} + \zeta_x^{(1)} \phi_x^{(1)} \\ & - \left(\frac{\partial}{\partial t} + M \frac{\partial}{\partial x}\right) \left\{ \zeta^{(1)} \left(\frac{\partial}{\partial t} + M \frac{\partial}{\partial x}\right) \phi_z^{(1)} \right. \\ & \left. + \frac{1}{2} [(\phi_x^{(1)})^2 + (\phi_y^{(1)})^2] \right\} \end{aligned} \quad (50)$$

The second-order solution must be of the form:

$$\begin{aligned} \phi^{(2)} = & \phi^{(20)} + (\phi^{(21)} e^{i\theta} + \text{c.c.}) \\ & + (\phi^{(22)} e^{2i\theta} + \text{c.c.}) \end{aligned} \quad (51)$$

From (23b) we have

$$\phi_{zz}^{(20)} = -\nabla_1^2 \phi^{(0)} \quad (52)$$

In order that  $\phi^{(20)}$  is bounded as  $z \rightarrow -\infty$ , we insist that

$$\nabla_1^2 \phi^{(0)} = 0 \quad z_1 < 0 \quad (53)$$

We now have three conditions defining  $\phi^{(0)}$ : (53), (43), and (34). Clearly  $\phi^{(0)}$  is the inner approximation of a slowly advancing slender ship; it may also be regarded as the inner approximation of a flow in an infinite fluid around a body which is symmetric about the plane  $z = 0$  and is moving along its longitudinal axis, i.e., the **double-body problem** for which the numerical solution is straightforward for any body shape.

Substituting (51) into (48) we get

$$\phi_{zz}^{(21)} - \phi^{(21)} = 0 \quad z < 0 \quad (54)$$

and

$$\phi_{zz}^{(22)} - 4\phi^{(22)} = 0 \quad z < 0 \quad (55)$$

From the boundary condition on the body we get

$$\phi_{y_1}^{(10)} = bY_{z_1} \phi_{z_1}^{(10)}$$

i.e.,

$$\phi_{n_1}^{(10)} = 0 \quad \text{on} \quad y_1 = bY(x_2, z_1) \quad (56)$$

and

$$A_{y_1} = ibAY_{x_2} \quad \text{on} \quad y_1 = bY(x_2, 0) \quad (57)$$

Note that only the value of  $Y_{x_2}$  at  $z_1 = 0$  enters (57) since  $\phi^{(11)}$  is exponentially small for  $z_1 = O(1)$ . On the free surface (50) leads to

$$\phi_z^{(20)} = -\phi_{z_1}^{(10)} \quad z = 0 \quad (58a)$$

$$\phi_z^{(21)} - \phi^{(21)} = 0 \quad z = 0 \quad (58b)$$

$$\phi_z^{(22)} - 4\phi^{(22)} = 0 \quad z = 0 \quad (58c)$$

Again boundedness at  $z \rightarrow -\infty$  requires that

$$\phi_z^{(20)} = \phi_{z_1}^{(10)} = 0 \quad \text{on} \quad z = z_1 = 0 \quad (59)$$

The boundary-value problems for  $\phi^{(21)}$  and  $\phi^{(22)}$  are homogeneous, so that  $\phi^{(21)}$  can be absorbed in  $\phi^{(11)}$ , i.e., it can be discarded;  $\phi^{(22)}$  is identically zero. Thus

$$\phi^{(2)} = \phi^{(20)}(x_2, y_1, z_1) \quad (60)$$

The second-order displacement can be found



$$\zeta^{(2)} = [-M\phi_{x_2}^{(0)} - \frac{1}{2}(\phi_y^{(0)})^2]_{z=0} + \frac{1}{4}(A^2 e^{2i\theta} + \text{c.c.}) \quad (61)$$

At order  $O(\epsilon^3)$  we only need the first harmonic of  $\phi^{(3)}$ . From the Laplace equation we have

$$\phi_{zz}^{(31)} - \phi^{(31)} = -e^z(A_{x_2} - \frac{i}{2}A_{y_1 y_1}) \quad z < 0 \quad (62)$$

and from the free surface conditions we find after lengthy algebra that

$$\phi_z^{(31)} - \phi^{(31)} = \frac{i}{2}|A|^2 A + \frac{i}{2}A(2\phi_{x_2}^{(0)} + i\phi_{z_1 z_1}^{(0)}) + MA_{x_2} + \phi_{y_1}^{(0)}A_{y_1} \quad z = 0 \quad (63)$$

At the bottom, we have of course  $\phi_z^{(31)} \rightarrow 0$ . Applying Green's formula to  $\phi^{(11)}$  and  $\phi^{(31)}$ , and using their governing conditions, we obtain finally the evolution equation for the wave envelope A:

$$-i(1+2M)A_{x_2} - \frac{1}{2}A_{y_1 y_1} - 2i\phi_{y_1}^{(0)}A_{y_1} + |A|^2 A + A(i\phi_{z_1 z_1}^{(0)} + 2\phi_{x_2}^{(0)}) = 0 \quad (64)$$

All the derivatives of  $\phi^{(0)}$  above are evaluated on  $z_1 = 0$ . This is a cubic Schrodinger equation, which is parabolic. On the body Eq. (57) serves as the boundary condition. The **initial condition** is specified at some line  $x_2 = \text{constant}$  sufficiently far upwave so that both the incident wave and the incident current are undisturbed. At  $y_1 \rightarrow \pm\infty$ ,  $\phi^{(0)}$  and  $A_{y_1}$  must vanish. Thus,

$$A \rightarrow A_0 \exp(-\frac{ix_2}{1+2M}) \quad \text{or} \quad x_2 \rightarrow -\infty \quad (65a)$$

$$y_1 \rightarrow \pm\infty \quad (65b)$$

with  $|A_0| = 1$ . Equation (65) is just the Stokes wave on a constant current.

In the special case without current  $M = \phi^{(0)} = 0$ , the governing equation agrees with Yue and Mei (1980, after letting  $kh \rightarrow \infty$ ).

When the current opposes the waves and is equal to the group velocity of the incident waves,  $M = -1/2$ , the first term in (64) disappears. This corresponds to the so-called stopping velocity against which waves of length  $2\pi/k$  cannot propagate (see Longuet-Higgins and Stewart, 1962, for the case of pure refraction). There are several ways to avert this singularity. For example we may allow modulation in  $x$  and  $t$  along scales  $O(\epsilon^{-1})$ . These are left for future studies and the neighborhood of  $M = -1/2$  will be excluded here.

By letting

$$A = \hat{A} e^{-2i\phi^{(0)}} \quad (66)$$

and using (53) the envelope equation can be transformed to

$$(1+2M)\hat{A}_{x_2} - \frac{i}{2}\hat{A}_{y_1 y_1} + i|\hat{A}|^2 \hat{A} - i\hat{A}[4M\phi_{x_2}^{(0)} + (\phi_{y_1}^{(0)})^2] = 0 \quad (67)$$

This form is numerically more preferable because it avoids the second derivative  $\phi_{z_1 z_1}^{(0)} = -\phi_{y_1 y_1}^{(0)}$ , whose evaluation requires high accuracy in the numerical solution of  $\phi^{(0)}$ . The boundary condition on the body is

$$\hat{A}_{y_1} = i\hat{A}(\gamma_{x_2} + 2\phi_{y_1}^{(0)}) \quad \text{on } y_1 = b\gamma(x_2, 0) \quad (68)$$

while the Stokes wave at infinity becomes

$$\hat{A} \rightarrow A_0 \exp[-i(\frac{x_2}{1+2M} + 2\phi^{(0)})] \quad (69)$$

#### THE CURRENT POTENTIAL FOR A PARABOLOID OF REVOLUTION

We assume for simplicity that the depth is very large in the coordinate  $x_2, y_1, z_1$ , and the slender body is half of a body of revolution. Then the solution to the three-dimensional slender double-body problem is:

$$\phi^{(0)} = -\frac{M}{2\pi} \int_{-l}^l \frac{d\xi_2 S'(\xi_2)}{\sqrt{(x_2 - \xi_2)^2 + \epsilon^2(y_1^2 + z_1^2)}} \quad (70)$$

where

$$l = \epsilon^2 kL \quad \text{and} \quad S = \frac{\pi}{2} bR^2(x_2) \quad (71)$$

is the area of the semicircular cross section of radius  $R$ . This solution is **uniformly valid** to the leading order in the slenderness ratio, except in the vicinities of the bow and the stern (see, e.g., Cole, 1969). Its inner approximation near the body can be derived and this should in principle suffice for the computation of the wave envelope  $A$ . However, in applying the boundary condition (65b) in the numerical scheme,  $y_1$  must be very large where the inner solution blows up logarithmically. Hence in actual computations the more complete potential (70) is used.

We further restrict the body to be a paraboloid of revolution, i.e.,

$$R(x_2) = 1 - (\frac{x_2}{l})^2 \quad (72)$$

The integral in (70) can be explicitly evaluated

$$\begin{aligned} \phi^{(0)} \left( M \frac{b^2}{l} \right)^{-1} &= \left\{ \frac{x_2}{l} \left[ 1 - \left( \frac{x_2}{l} \right)^2 + \frac{3}{2} \left( \frac{\epsilon r_1}{l} \right)^2 \right] \times \right. \\ &\quad \left. \sinh^{-1} \left( \frac{1-x_2/l}{\epsilon r_1/l} \right) + \frac{1}{6} \sqrt{\left( 1 - \frac{x_2}{l} \right)^2 + \left( \frac{\epsilon r_1}{l} \right)^2} \right. \\ &\quad \left. \left[ -11 \left( \frac{x_2}{l} \right)^2 - 5 \frac{x_2}{l} + 4 + 4 \left( \frac{\epsilon r_1}{l} \right)^2 \right] \right\} \\ &\quad - \{x_2 \rightarrow -x_2\} \end{aligned} \quad (73)$$

where the second  $\{ \}$  is obtained from the first by changing  $x_2$  to  $-x_2$ . Now the derivatives  $\phi_{x_2}^{(0)}$  and  $\phi_{y_1}^{(0)}$  are needed in Eq. (68).

$$\begin{aligned} \phi_{x_2}^{(0)} \left( M \frac{b^2}{l} \right)^{-1} &= \left\{ \left[ 1 - 3 \left( \frac{x_2}{l} \right)^2 + \frac{3}{2} \left( \frac{\epsilon r_1}{l} \right)^2 \right] \times \right. \\ &\quad \sinh^{-1} \left( \frac{1-x_2/l}{\epsilon r_1/l} \right) - \frac{x_2}{l} \left[ 1 - \left( \frac{x_2}{l} \right)^2 \right. \\ &\quad \left. + \frac{3}{2} \left( \frac{\epsilon r_1}{l} \right)^2 \right] \sqrt{\left( 1 - \frac{x_2}{l} \right)^2 + \left( \frac{\epsilon r_1}{l} \right)^2} \\ &\quad \left. - \frac{(1-x_2/l)}{6 \sqrt{\left( 1 - \frac{x_2}{l} \right)^2 + \left( \frac{\epsilon r_1}{l} \right)^2}} \left[ -11 \left( \frac{x_2}{l} \right)^2 \right. \right. \\ &\quad \left. \left. - 5 \frac{x_2}{l} + 4 + 4 \left( \frac{\epsilon r_1}{l} \right)^2 \right] \right. \\ &\quad \left. - \frac{1}{6} \sqrt{\left( 1 - \frac{x_2}{l} \right)^2 + \left( \frac{\epsilon r_1}{l} \right)^2} \left[ 22 \frac{x_2}{l} + 5 \right] \right\} \\ &\quad + \{x_2 \rightarrow -x_2\} \end{aligned} \quad (74)$$

$$\begin{aligned} \phi_{y_1}^{(0)} \left( M \frac{b^2}{l} \right)^{-1} &= \left\{ -\frac{x_2}{l} \left[ 1 - \left( \frac{x_2}{l} \right)^2 + \frac{3}{2} \left( \frac{\epsilon r_1}{l} \right)^2 \right] \times \right. \\ &\quad \frac{(1-x_2/l)}{r_1/l \sqrt{\left( 1 - \frac{x_2}{l} \right)^2 + \left( \frac{\epsilon r_1}{l} \right)^2}} \\ &\quad \left. + \epsilon^2 \frac{r_1}{l} \left[ 3 \frac{x_2}{l} \sinh^{-1} \left( \frac{1-x_2/l}{\epsilon r_1/l} \right) \right. \right. \\ &\quad \left. \left. + \frac{4}{3} \sqrt{\left( 1 - \frac{x_2}{l} \right)^2 + \left( \frac{\epsilon r_1}{l} \right)^2} \right] \right\} \end{aligned}$$

$$\begin{aligned} &+ \frac{\left( -11 \left( \frac{x_2}{l} \right)^2 - 5 \frac{x_2}{l} + 4 + 4 \left( \frac{\epsilon r_1}{l} \right)^2 \right)}{6 \sqrt{\left( 1 - \frac{x_2}{l} \right)^2 + \left( \frac{\epsilon r_1}{l} \right)^2}} \Bigg\} \\ &\quad - \{x_2 \rightarrow -x_2\} \end{aligned} \quad (75)$$

It can be shown that, on the body, both derivatives contain

$$\begin{aligned} &\sinh^{-1} \frac{1-x_2/l}{\epsilon r_1/l} + \sinh^{-1} \frac{1+x_2/l}{\epsilon r_1/l} \\ &= -2 \ln \frac{\epsilon b}{2} \sqrt{1 - \left( \frac{x_2}{l} \right)^2} \end{aligned} \quad (76)$$

which is singular at the pointed tips  $x_2 = \pm l$ . These singularities can be removed by a more refined local analysis involving the flow around an infinite cone. The refinement can be expressed as a correction factor  $f$  (Van Dyke, (1956)), with the corrected velocities being

$$[\phi_{x_2}^{(0)}]_{\text{corrected}} = \frac{M}{\epsilon} (f-1) + f \phi_{x_2}^{(0)} \quad (77)$$

$$[\phi_{y_1}^{(0)}]_{\text{corrected}} = f \phi_{y_1}^{(0)} \quad (78)$$

where

$$f = \left[ \frac{(Q_1)^{\frac{2}{9}\delta}}{1 + \frac{2}{9}\delta^2 \ln(Q_1)} \right] \left[ \frac{(Q_2)^{\frac{2}{9}\delta}}{1 + \frac{2}{9}\delta^2 \ln(Q_2)} \right] \quad (79)$$

Here,  $\delta = \tan(2B/L)$  is the half cone angle and

$$Q_{1,2} = \sqrt{\left( 1 \pm \frac{x_2}{l} \right)^2 + \left( \frac{\epsilon r_1}{l} \right)^2} \quad (80)$$

is the distance from the tip at  $x_2 = \pm l$ .

We remark that the known exact solution for an ellipsoid can in principle be used as an alternative model body. Although no separate correction is needed at the ends, the exact solution would involve numerical evaluation of an integral at all points on the free surface. Thus the approximate analytical solution is chosen here.

#### COMPUTATION AND NUMERICAL RESULTS

In computations it is convenient to renormalize as follows:

$$\bar{x}_2 = x_2/\ell = x/L \quad (81)$$

$$(\bar{y}_1, \bar{z}_1) = \frac{b}{\ell} (y_1, z_1) = \frac{B}{L} k(y', z')$$

so that the body spans from  $\bar{x}_2 = -1$  to  $\bar{x}_2 = 1$ . The dimensionless current potential  $\phi^{(0)}$  depends only on  $M$ ,  $B/L$ , and  $kB$ . The envelope equation is now

$$(1 + 2M) \frac{\ell}{b^2} \hat{A}_{\bar{x}_2} - \frac{i}{2} \hat{A}_{\bar{y}_1} \bar{y}_1 + i \left(\frac{\ell}{b}\right)^2 |\hat{A}|^2 \hat{A} - i \left[ 4M \frac{\ell}{b^2} \phi_{\bar{x}_2}^{(0)} + 2 \left( \phi_{\bar{y}_1}^{(0)} \right)^2 \right] \hat{A} = 0 \quad (82)$$

with the auxiliary conditions:

$$\hat{A}_{\bar{y}_1} = i \hat{A} \left( \bar{y}_{\bar{x}_2} + 2 \phi_{\bar{y}_1}^{(0)} \right) \quad \text{on} \quad \bar{y}_1 = \frac{b^2}{\ell} \gamma(\bar{x}_2, 0) \quad (83)$$

$$\hat{A} \rightarrow A_0 \exp \left( - \frac{i \ell \bar{x}_2}{1 + 2M} - 2i \phi^{(0)} \right) \quad \text{on} \quad \begin{matrix} \bar{x}_2 \rightarrow -\infty \\ \bar{y}_1 \rightarrow \pm\infty \end{matrix} \quad (84)$$

There are 3 dimensionless parameters  $M$ ,  $\ell$ , and  $b$ . Note that the ratio  $\ell/b^2 = (L/kB^2)$  is independent of the wave amplitude while  $\ell = (ka)^2 kL$  and  $\ell/b = ka_0 L/B$  are not. In a physical problem, these parameters are obtained from the independently prescribed values of  $U$ ,  $k$ ,  $a_0$ ,  $B$ , and  $L$ .

We have solved the initial-boundary-value problem numerically by a Crank-Nicholsen finite difference scheme, with second-order differencing in  $\bar{x}_2$  and  $\bar{y}_1$ , as described in Yue and Mei (1980). Because of symmetry only one half of the domain  $\bar{y}_1 > 0$  is needed. The initial line is set at  $\bar{x}_2 = -11$  (five body lengths upwave) where  $\hat{A}$  is taken to be 1. The side computational boundaries are  $\bar{y}_1 = 0$  and  $\bar{y}_1 = 66$ . Further increase in the range of  $\bar{y}_1$  does not alter the numerical result appreciably. At any  $\bar{x}_2$  step we use the following conservation law (derivable from (82))

$$\begin{aligned} \left[ \frac{\partial}{\partial \bar{x}_2} \int_0^\infty |\hat{A}|^2 d\bar{y}_1 \right]_{\bar{x}_2} &> 1 \\ &= \left[ \frac{\partial}{\partial \bar{x}_2} \int \frac{b^2}{\ell} \gamma(\bar{x}_2, 0) |\hat{A}|^2 d\bar{y}_1 \right]_{\bar{x}_2} < 1 \end{aligned} \quad (85)$$

to check errors due to discretization, round-off, and finite boundaries. An error less than 3% is always achieved.

Computations have been performed for a body with the slenderness ratio  $B/L = 0.2$ , for various combinations of the following sets of inputs:

Incident wavelength:  $kL = 40, 80$

Incident wave amplitude:  
 $\epsilon = ka_0 = 0, 0.1, 0.2$

Head seas:  $M = 0, 1/4, 1/2, 3/4, 1$

Tail seas:  $M = -1/4, -3/4, -1$

We use the expression  $\epsilon = 0$  to represent the linear parabolic approximation; it is computed from (82) by omitting the cubic term. The current potential  $\phi^{(0)}$  is kept whenever  $M \neq 0$ . Note also that the singular case of  $M = -1/2$  is excluded.

We first examine the case of a stationary body  $M = 0$ . In Fig. 2 the variation of  $|\hat{A}|$  along the waterline of the body is shown for  $kL = 40$  and  $\epsilon = 0, 0.1, 0.2$ . For all three wave slopes the common feature is the increase of  $|\hat{A}|$  to its maximum around the quarter length behind the bow at  $\bar{x}_2 = -1$ . As the wave slope increases, the maximum decreases. Non-linearity has similar effects when the body advances into the waves ( $M > 0$ , head seas); plots are omitted.

The effect of the incident wavelength relative to the ship length is shown in Fig. 3 for a stationary ship. Again the linear limit is also plotted for comparison. Shorter waves tend to reach a greater maximum amplitude along the ship at a point closer to the bow.

Figures 4a and b show the effects of ship speed on the evolution of the waves along the water line for  $\epsilon = 0.2$  and  $0.1$ . For comparison the linear limit is shown in Fig. 4c. Thus for head seas ( $M > 0$ ) increasing ship speed steepens the waves along the body; the maximum of  $|\hat{A}|$  therefore increases. This trend is maintained even for tail seas as long as the ship speed is numerically less than the wave-stopping speed, i.e.,  $0 > M > -1/2$ . Thus as  $-M$  increases in magnitude, the wave slope is reduced everywhere. However, for  $M < -1/2$  the maximum occurs in the fore section  $0 < \bar{x}_2 < 1$  and a minimum in the aft section  $-1 < \bar{x}_2 < 0$ . Either for a greater ship speed or for steeper incident waves, the maximum of  $|\hat{A}|$  increases.

In order to see the overall diffraction pattern near the ship, we show in Figs. 5a, b, and c three-dimensional perspectives of the wave envelope for  $M = 0, 1$ , and  $-1$ , respectively. Relative to the stationary case, cruising into the waves has the effect of compressing laterally the diffraction field; i.e., the current sweeps the diffracted waves downstream. On the other hand, cruising away from the waves helps spread the diffraction field laterally.

From the computed  $\hat{A}$  the pressure field can be straightforwardly calculated to the third order in  $\epsilon$ , which can be used for computing the stresses in the slender body.

#### DRIFT FORCE

On a floating body, incident waves exert a steady drift force, which is second order in wave amplitude, in the direction of the

incident waves. It is known that the wave drag on a slender vessel is small at low Froude numbers, being of the order

$$D = O(\rho U^2 a_s^2) \quad (86)$$

Now the drift force is in general of the order

$$F = O(\rho g a_0^2 B) = O\left(\frac{\rho g}{k^3}\right)(ka_0)^2 kB = O\left(\epsilon \frac{\rho g}{k^3}\right) \quad (87)$$

The ratio is

$$\frac{F}{D} = O\left(\frac{gB}{U^2} \left(\frac{a_0}{a_s}\right)^2\right) = O(\epsilon) \ll 1 \quad (88)$$

The drift force is the time average of the pressure force on the body

$$F = \langle \iint_{S(x)} dS n_x p \rangle \quad (89)$$

where  $n_x$  is the x-component of the unit normal pointing into the body. Let us divide the wetted surface into two parts  $\bar{S}$  and  $\bar{S}$  with the first part lying below  $z = 0$  and the second part near the water line  $\Gamma$  between  $z = 0$  and  $z = \zeta$ , i.e.,

$$F = F_1 + F_2 \equiv \iint_{\bar{S}} dS n_x \langle p \rangle + \int_{\Gamma} ds \langle \int_0^{\zeta} dz p \rangle \quad (90)$$

Since the side walls are assumed to be vertical near the waterline and the pressure is exponentially small at depth about a wavelength below the free surface, we only need to evaluate  $n_x$  at the waterline:

$$n_x = BY_x \sqrt{1 + (BY_x)^2} = \epsilon b Y_{x_2} \sqrt{1 + (\epsilon b Y_{x_2})^2} \quad (91)$$

where  $Y = Y(x, 0)$ . The first part of the drift force is then

$$F_1 \approx \int_{\Gamma} ds \int_{-\infty}^0 dz n_x \langle p \rangle = 2 \int_{-L}^L dx BY_x \int_{-\infty}^0 dz \langle p \rangle \quad (92)$$

or, in dimensionless form:

$$F_1 = \frac{2b}{\epsilon} \frac{\rho g}{k^3} \int_{-L}^L \frac{Y}{x_2} dx_2 \int_{-\infty}^0 dz \langle p \rangle \quad (93)$$

For brevity we write  $( )_n$  instead of  $( )^{(n)}$ , i.e.,

$$P = kp/\rho g = P_0 + \epsilon P_1 + \epsilon^2 P_2 + \epsilon^3 P_3 + \dots \quad (94)$$

Then

$$-P_0 = z \quad (95a)$$

$$-P_1 = \phi_{1t} + M\phi_{1x} \quad (95b)$$

$$-P_2 = \phi_{2t} + M(\phi_{2x} + \phi_{0x_2}) + \frac{1}{2}(\phi_{1x}^2 + \phi_{1z}^2 + \phi_{0y_1}^2 + \phi_{0z_1}^2) \quad (95c)$$

$$-P_3 = \phi_{3t} + M(\phi_{3x} + \phi_{1x_2}) + \phi_{1x}(\phi_{0x_2} + \phi_{2x}) + \phi_{0y_1}\phi_{1y_1} + (\phi_{0z_1} + \phi_{1z})\phi_{2z} \quad (95d)$$

Making use of (39) and (60) we get the time averages:

$$-\langle P_0 \rangle = z, \quad (96a)$$

$$-\langle P_1 \rangle = 0 \quad (96b)$$

$$-\langle P_2 \rangle = M\phi_{0x_2} + \frac{1}{2}(\phi_{0y_1}^2 + \phi_{0z_1}^2) + \frac{1}{2}\langle \phi_{1x}^2 + \phi_{1z}^2 \rangle \quad (96c)$$

$$-\langle P_3 \rangle = 0 \quad (96d)$$

The contribution to  $F_1$  by  $\phi_0$  through  $\langle P_2 \rangle$  is zero. Since

$$\frac{1}{2}\langle \phi_{1x}^2 + \phi_{1z}^2 \rangle = \frac{1}{2}e^{2z}|A|^2 \quad (97)$$

we get,

$$F_1 \approx -\frac{\epsilon b}{2} \frac{\rho g}{k^3} \int_{-L}^L dx_2 Y_{x_2} |A|^2 + O(\epsilon^3) \quad (98)$$

where  $A$  is to be evaluated at the waterline  $\Gamma$ .

In dimensionless form the second part of the drift force is

$$F_2 = \frac{2b}{\epsilon} \frac{\rho g}{k^3} \int_{-L}^L dx_2 Y_{x_2} \langle \int_0^{\zeta} dz p \rangle \quad (99)$$

We need only evaluate the inner integral up to  $O(\epsilon^3)$  by first expanding  $P$  about  $z = 0$ :

$$\begin{aligned}
\langle \int_0^{\zeta} dz P \rangle &= P_{\zeta} + P_2 \zeta^2/2 + O(\epsilon^4) \\
&= \langle (\epsilon P_1 + \epsilon^2 P_2)(\epsilon \zeta_1 + \epsilon^2 \zeta_2) \rangle \\
&\quad + \langle (-1 + \epsilon P_{1z}) \epsilon^2 \zeta_1^2/2 \rangle + O(\epsilon^4) \\
&= \epsilon^2 \langle P_1 \zeta_1 - \zeta_1^2/2 \rangle + \epsilon^3 \langle P_1 \zeta_2 + P_2 \zeta_1 + \\
&\quad P_{1z} \zeta_1^2/2 \rangle + O(\epsilon^4) \quad (100)
\end{aligned}$$

The leading-order coefficient is

$$\langle P_2 \zeta_1 - \zeta_1^2/2 \rangle = \langle \zeta_1^2/2 \rangle = |A|^2/4 \quad (101)$$

Because  $\zeta_2$  and  $P_2$  do not have first harmonics, the coefficient of  $\epsilon^3$  vanishes; hence

$$F_2 = \frac{\epsilon b}{2} \frac{\rho g}{k^3} \int_{-L}^L dx_2 Y_{x_2} |A|^2 + O(\epsilon^3) \quad (102)$$

which cancels  $F_1$ . Thus the total drift force

$$F = F_1 + F_2 = O(\epsilon^3) \rho g/k^3 \quad (103)$$

is insignificant. To compute the drift force at  $O(\epsilon^3)$  would require the knowledge of  $P_4$ , corresponding to  $O(\epsilon^4)$ . The reason for this small force is the body slenderness and the weakness of wave scattering. In contrast, the drift force on a small but non-slender vessel can be  $O(\epsilon^2)$  and hence greater.

#### ACKNOWLEDGEMENT

We thank the U. S. Office of Naval Research (Ship Hydrodynamics Program) and the U. S. National Science Foundation (Fluid Mechanics Program) for supporting this study.

#### REFERENCES

- Cole, J.D. (1968): Perturbation Methods in Applied Mathematics. Blaisdell Pub. Co., 260 pp.
- Faltinsen, O.M. (1972): Wave Force on a Restrained Ship in Head-Sea Waves. Proc. 9th Symp. Naval Hydrodynamics, Paris, France, pp. 1763-1840.
- Goodman, D.J., Wadhams, P. and Squire, V.A. (1980): The Flexural Response of a Tabular Ice Island to Ocean Swell. Ann. Glacio., Vol. 1, pp. 23-28.
- Haren, P. and Mei, C.C. (1981): Head-Sea Diffraction by a Slender Raft with Application to Wave-Power Absorption. Journal of Fluid Mechanics, Vol. 104, pp. 505-526.
- Hult, J.L. and Ostrander, N.C. (1974): Applicability of ERTS to Antarctic Iceberg Resources. Third Earth Resources Tech. Satellite-1 Symp. S.C. Freden & M. A.

- Becker (eds.), Vol. 1B, NASA Spec. Publ. SP251, pp. 1467-1490.
- Keller, J.B. (1979): The Ray Theory of Ship Waves and the Class of Streamline Ships. Journal of Fluid Mechanics, Vol. 91, pp. 465-488.
- Kirby, J.T. and Dalrymple, R.A. (1984): A Parabolic Equation for the Combined Refraction - Diffraction of Stokes Waves by Mildly Varying Topography. Journal of Fluid Mechanics, Vol. 136, pp. 453-466.
- Kristensen, M. and Squire, V.A. (1983): Modelling of Antarctic Tabular Iceberg in Ocean Waves. Ann. Glacio., Vol. 4, pp. 152-157.
- Longuet-Higgins, M.S. and Stewart, R.W. (1961): The Changes in Amplitudes of Short Gravity Waves on Steady Non-Uniform Currents. Journal of Fluid Mechanics, Vol. 10, pp. 529-549.
- Maruo, H. and Sasaki, N. (1974): On the Wave Pressure Acting on the Surface of an Elongated Body Fixed in Head Sea. J. Soc. Naval Arch., Japan, Vol. 136, pp. 34-42.
- Mei, C.C. (1978): Numerical Methods in Water Wave Diffraction and Radiation. Annual Review of Fluid Mechanics, M.D. VanDyke, J.V. Wehausen (eds.) Vol. 10.
- Mei, C.C. (1983): The Applied Dynamics of Ocean Surface Waves. Wiley-International, NY.
- Newman, J.N. (1978): The Theory of Ship Motions. Adv. Appl. Mech., Vol. 18, pp. 221-283.
- Ogilvie, T.F. (1977): Singular Perturbation Problems in Ship Hydrodynamics. Adv. Appl. Mech., Vol. 17, pp. 91-188.
- Orheim, O. (1980): Physical Characteristics and Life Expectancy of Tabular Antarctic Icebergs. Ann. Glacio., Vol. 1, pp. 11-18.
- Orheim, O., Wadhauser, P., and Kristensen, M. (1982): Iceberg Response to Sea State. Iceberg Research, Vol. 1, pp. 10-15.
- Squire, V.A. (1981): Numerical Simulation of Ice Floes in Waves, Tech. Report 81-1, Scott Polar Res. Inst., Cambridge.
- Van Dyke, M.S. (1954): Subsonic Edges in Thin Wind and Slender Body Theory. Nat. Advis. Comm. for Aeronautics, Tech. Note 3343.
- Wadhams, P. and Kristensen, M. (1983): The Response of Antarctic Iceberg to Ocean Waves. J. Geophys. Res. Vol. 88, pp. 6053-6065.
- Weeks, W.F. and Mellow, M. (1978): Some Elements of Iceberg Technology, Iceberg Utilization, A.A. Hauseiny (ed), Pergamon Press, pp. 45-98.
- Wehausen, J.V. (1971): The Motion of Floating Bodies. Annual Rev. of Fluid Mech., Vol. 3, pp. 237-268.
- Yeung, R.W. (1982): Numerical Methods in Free Surface Waves. Ann. Rev. Fluid Mech., Vol. 14, pp. 395-442.
- Yue, D.K.P., and Mei, C.C. (1980): Forward Diffraction of Stokes Waves by a Thin Wedge. Journal of Fluid Mechanics, Vol. 99, pp. 33-52.

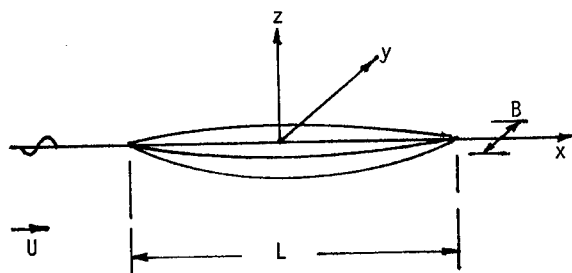


Figure 1. Definition sketch.

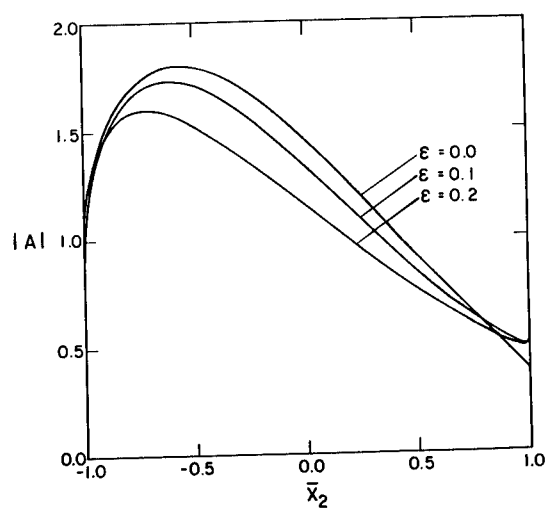


Figure 2. Wave amplitude along the ship waterline. Ship speed = 0,  $kL = 40$ ,  $B/L = 0.2$ .

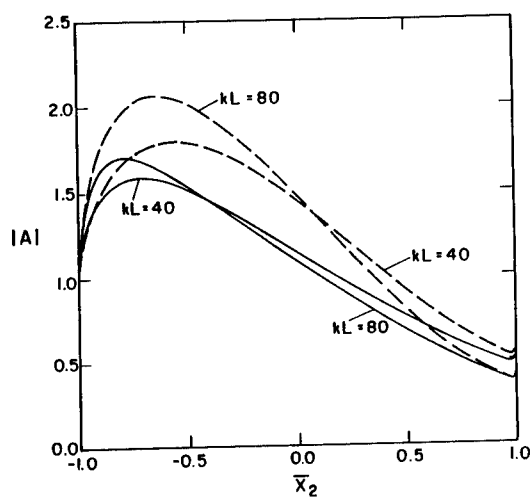
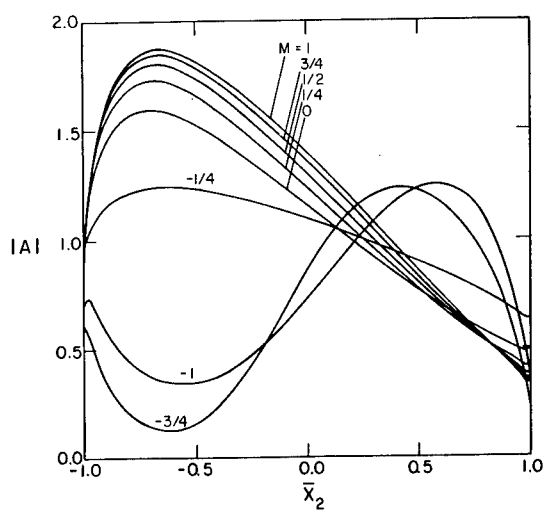
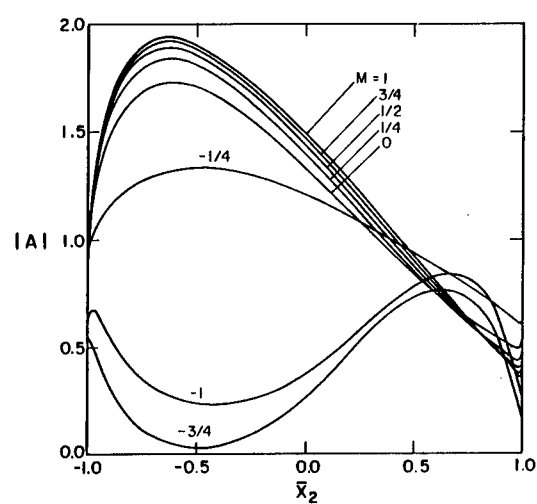


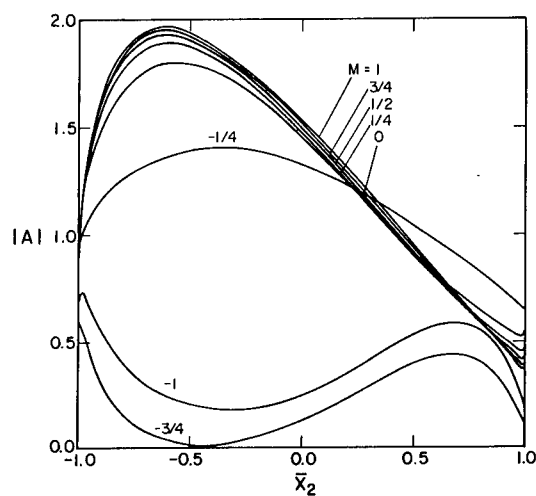
Figure 3. Wave amplitude along the ship waterline.  $B/L = 0.2$ . Solid curve: nonlinear with  $ka_0 = 0.2$ . Dashed curve: linear.



(a)



(b)



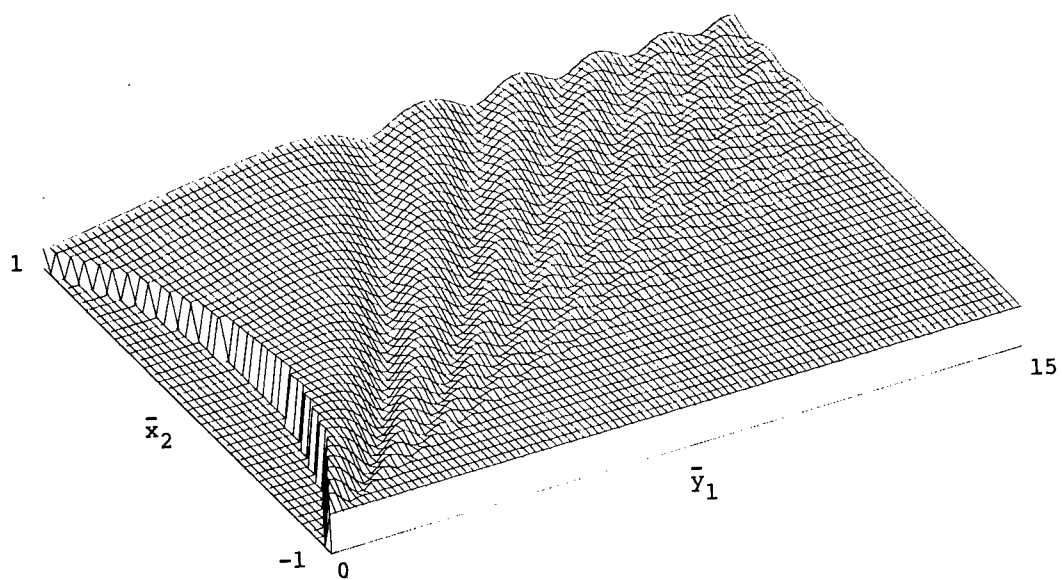
(c)

Figure 4. Wave amplitude along the ship waterline.  $B/L = 0.2$ ,  $kL = 40$  for various ship speeds.

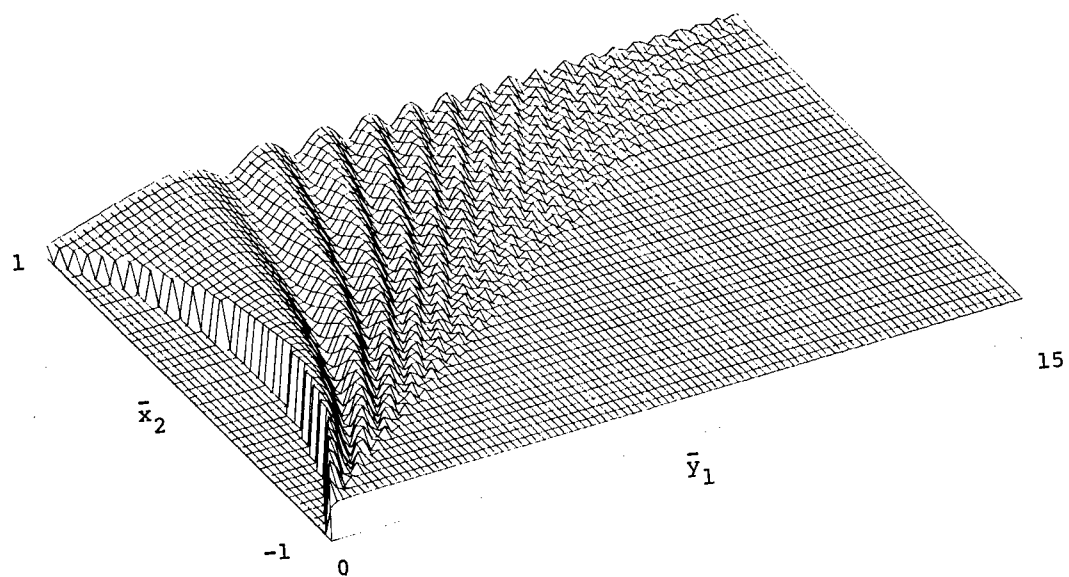
(a):  $\epsilon = ka_0 = 0.2$

(b):  $ka_0 = 0.1$

(c):  $ka_0 = 0$



(a)

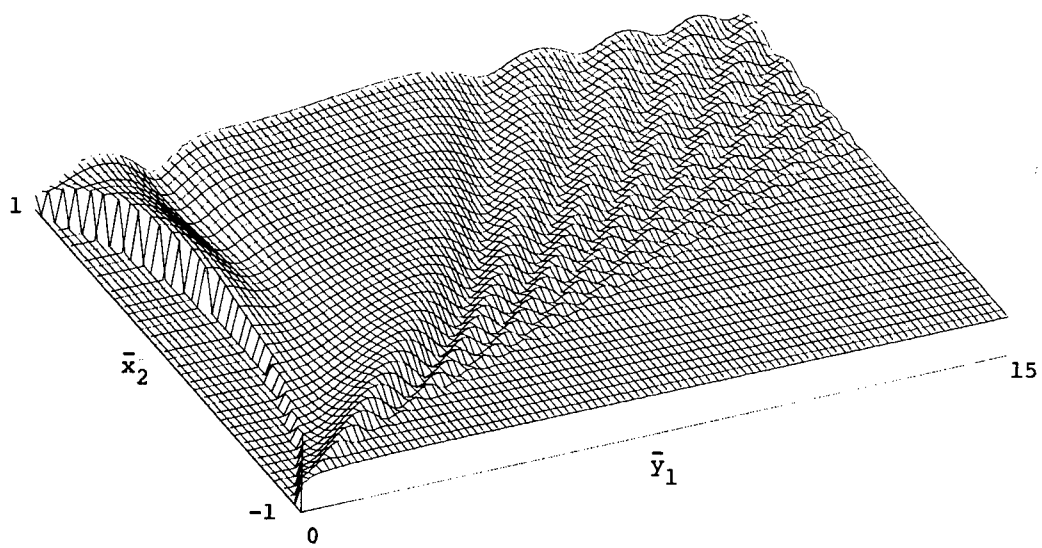


(b)

Figure 5. Perspectives of wave envelope near a slender body.  $B/L = 0.2$ ,  $kL = 40$

(a):  $M = 0$   
 (b):  $M = 1$





(c)

Figure 5. Perspectives of wave envelope near a slender body.  $B/L = 0.2$ ,  $kL = 40$

(c):  $M = -1$

# THE EFFECT OF BOW SHAPE AND NONLINEARITIES ON THE PREDICTION OF LARGE AMPLITUDE MOTIONS AND DECK WETNESS

JOHN F. O'DEA AND DAVID A. WALDEN

## ABSTRACT

Ship motions in waves are usually calculated in the frequency domain using linearized free surface hydrodynamics. However, the sea conditions in which limits to ship operations or survival are reached, can cause motions of sufficiently large magnitude that linear predictions are inadequate. In order to examine the importance of nonlinearities in large amplitude motions, a series of experiments has been conducted with a model of a frigate in steep head waves. Variations were made in above-water bow shape, and measurements were made of absolute and relative motion near the bow, and water on deck. The results are compared to approximate prediction methods, in which an attempt has been made to account for the most important nonlinearities.

## 1. INTRODUCTION

In analyzing and predicting ship motions in waves, it is customary to use a linearization of the actual physical motions. The process of linearization involves some or all of the following assumptions: that the wave and resulting motions are small in some sense (such as compared to a hull characteristic dimension), that the wavelengths are also small, that the hull has vertical sides, and that viscous effects are negligible. The result is a description of hull response in terms of its linear transfer functions. The knowledge of the transfer functions, in turn, permits the use of the powerful and general linear systems techniques and random process theory to predict the statistical behavior of ships in realistic random seas. This approach has proved adequate in many cases, for prediction of ship motions in waves.

However, it may not always be acceptable to completely linearize the ship response characteristics, since such a procedure may lead to poor quantitative predictions or, in some cases, may ignore an essential qualitative aspect of importance. An example of the former problem is the case of ship rolling, in which it is recognized that nonlinear, viscous roll damping dominates the linear,

free surface wave damping predicted by normal ship motion theory. An example of the latter type of problem is that of slow drift oscillations, in which the response of interest occurs at frequencies other than those of the excitation, a result not predicted by the linear theory. Both of the problems just mentioned share the qualitative nature that a linear term was either very small (in roll damping) or even zero (sway restoring coefficient, in the absence of moorings). This caused a nonlinear effect, which might otherwise be considered unimportant, to have a dominant effect.

Deck wetness has long been known to be a particularly difficult phenomenon to deal with. Even the terms used in its description are notable for their lack of clarity; mild wetness, severe wetness, heavy spray, green water. Deck wetness can be looked at from a number of angles, depending on the interests of a particular investigator. Spray can affect operator visibility and deck operations. Impact forces on deck and superstructure have structural implications. Amount and movement of water on deck can affect stability in smaller vessels. This is further related to the siting and location of freeing ports on such vessels. The complexity associated with many of the aspects of deck wetness gives rise to grave doubts about the possibility of developing any linear frequency domain description. It is known that spray occurrence cannot be adequately predicted from model experiments because of the effect of surface tension and wind. In this paper, only the occurrence of heavy wetness, defined to be a continuous layer of water over the deck, will be measured and analyzed.

In the case of vertical plane motions (pitch and heave) of a conventional, monohull ship, it is known that the linear forces and moments are in general very large. So it is not surprising that satisfactory predictions of these modes are often obtained with linear techniques. However, there are cases where, again, a small nonlinearity may assume great importance. Examples are heave or pitch resonance, where the large inertia and hydrostatic restoring loads effectively cancel each other; and the springing motion of a long slender

\* David W. Taylor Naval Ship Research and Development Center, Bethesda, Maryland 20084, USA

ship, where higher harmonic loads introduced by nonlinear hydrodynamic interactions can cause significant hull stresses to which a stiffer ship would not respond.

There is also the case of vertical plane motions in steep head waves. When motions in such waves are so large as to cause the keel to emerge, or the deck to immerse, it is to be expected that linear predictions would have noticeable inadequacies. The hydrostatic loads will certainly be a function of the entire hull shape, rather than just the characteristics of the static waterplane as assumed by linear theory. The hydrodynamic loads will also be a function of the actual immersed hull form (and possibly depend on the past history of motion, or memory effect, as well), and impact loads on both the bottom of the hull and its sloping sides above the static waterline can also be expected. In fact, the flow near the bow may be subject to nonlinear flow even in waves of moderate steepness. This is because the relative vertical motion between the bow and wave surface can often be four or five times the wave amplitude, as a result of the phasing between pitch, heave, and the local incident wave, and disturbances caused by diffracted and radiated waves (Lee et al. (1982)).

It is the purpose of this paper to explore the limits of validity of linear seakeeping predictions with a series of experimental measurements in waves of varying steepness and comparison to both linear and nonlinear predictions. Since bow impact loading and deck wetness can strongly affect ship operability, and since these phenomena can be strongly influenced by nonlinearities in the rigid body motions, the experiments have included measurements of relative motion, deck wetness and forces on a portion of the bow.

## 2. CALCULATION OF MOTIONS, FORCES AND DECK WETNESS

### 2.1 Linear Calculations

The calculation of ship motions and loads with linear strip theory has been fairly well standardized for some time. The standard approach is thoroughly documented by Salvesen et al. (1970). Differences among various strip theory computer programs arise in the method of evaluating the various coefficients (Faltinsen (1974)) and in various empirical ways of including viscous effects. Three-dimensional programs, which do not require a vehicle to be slender, have recently become available, but are generally restricted to zero speed.

One fact common to all linear prediction theories is that the shape of the hull above the waterline does not enter into the calculation at all. Because of the recognized need to include nonlinear effects in vertical plane motions, there have been a number of attempts in recent years to develop methods for computing nonlinear responses, particularly with respect to the structural loads imposed on the hull.

### 2.2 Nonlinear Calculations

Linear free surface problems are approached by the use of expansion of the various boundary conditions in powers of a small perturbation parameter, and retaining only the linear terms. Similarly, the first successful calculations of nonlinear effects were obtained by retaining quadratic terms in the boundary condition expansions (Ogilvie (1963), Lee (1968)). More recently, with the availability of more powerful digital computers, numerical techniques have been developed for computation of free surface problems with fully nonlinear boundary conditions (Faltinsen (1977), Vinje et al. (1982)). These latter methods make no requirement that the motions or wave steepness be small in any sense, while in the second-order perturbation approach there remains the assumption that the quantities remain sufficiently small to permit truncation of the expansion at the quadratic terms. In either case, the nonlinear computations which have been done with a degree of rigor have been generally limited to two-dimensional cases.

The calculation of nonlinear effects on three-dimensional ship hulls has been applied most extensively to the problem of mean horizontal loads, i.e., drift forces and added resistance. This problem, involving perturbation expansion to second order, can still be analyzed in the frequency domain, as is done with most linear seakeeping analysis. When large motions or very steep waves are to be included, one must resort to a time domain approach and various approximations to the very complicated fluid dynamic boundary value problem involved. A number of time domain methods have been reported in recent years, and while each might be criticized for lack of mathematical rigor in various parts of their formulation, it is unlikely that an exact, rigorous, yet practical computational approach will be available in the near future. Meanwhile, since it is still desirable to obtain an improved understanding of motions in very severe waves, the most reasonable approach now available seems to be to assess the accuracy of approximate computations against physical model experiments.

One of the first nonlinear, time-domain techniques was developed by Paulling and Wood (1973), primarily for the purpose of investigating capsizing. Other methods have been developed by Meyerhoff and Schlachter (1980), Chuang et al. (1977), Jensen and Pedersen (1978), Yamamoto et al. (1980, 1982) and Salvesen (1982). All involve similar approaches, in which the hydrodynamic force on a ship section is represented as, for example:

$$F(x,t) = \left[ \frac{D}{Dt} \left[ M(x,t) \frac{DZ}{Dt} \right] + N(x,t) \frac{DZ}{Dt} + \rho g A(x,t) Z \right] \quad (1)$$

$$\text{where } \frac{D}{Dt} = \frac{\partial}{\partial t} - V \frac{\partial}{\partial x},$$

and  $V$  is ship forward speed,  $Z$  is vertical

motion of ship section relative to the water, and M, N and A are the added mass, damping and cross-sectional area respectively. The sectional loads are integrated along the hull length to produce heave force and pitch moment, and are combined with the hull inertial characteristics in a simulation of motion time histories. In contrast to linear theory, the coefficients are assumed to be time-varying, depending on the local wave elevation at each station. Since this is a relative elevation between the incident wave and the absolute vertical motion at each station (not known a priori), the need to do a time-domain simulation is apparent.

The manner in which the coefficients are assumed to change differs somewhat among the various approaches. Jensen and Pedersen (1978) and Salvesen (1982) followed a perturbation approach, in which some of the second order terms were included to account for quadratic effects (particularly mean value changes and second harmonics). The other authors have instead recalculated the added mass, damping and buoyancy at each time increment. In each case, the excitation is estimated primarily by a nonlinear calculation of the Froude-Kriloff force and moment, and diffraction effects are taken into account only approximately, by using the motion, velocity and acceleration relative to the incident wave flow field.

The only portion of the hydrodynamics which these methods can calculate more or less exactly, is the Froude-Kriloff portion due to the incident wave, and even here there is a limitation imposed by the assumed form of the incident wave potential (i.e., linear potential, second order Stokes wave, etc.). All calculations of inertial and damping effects are at best very approximate, since none yet seem to have incorporated exact nonlinear two-dimensional calculations such as those of Faltinsen (1977) or Vinje (1982) into the strip theory calculations. Some methods calculate the sectional added mass and damping in the frequency domain, as in the usual linear strip theory, but use the instantaneous immersed section shape, while others use the infinite frequency limit in the calculations. Thus, it is difficult to determine whether the most important nonlinear effects are being included, or whether the neglect of parameters such as the nonlinear free surface condition (either exact or carried to a perturbation term beyond linear) might cause serious deficiencies.

### 2.3 Calculation of Bow Flare Loads

As mentioned previously, the relative vertical motion between a ship's bow and the water surface can be quite large even in waves of moderate steepness. Many ships have considerable flare in their forward sections, and consequently the local immersed section shape can change very rapidly. This can lead to bow flare impact loads above the static waterline which may contribute significantly to hull girder as well as local structural loads. This effect is implicitly included in the nonlinear motion calculation methods described above.

Gran et al (1976) have examined this effect explicitly and proposed a simplified two-dimensional approach to calculating loads due to bow flare. It is assumed that the hydrodynamic inertial loading is the dominant part, and that the peak force occurs in a time interval when the vertical acceleration is negligible. It is further assumed that the rate change of geometric sectional proportions is small, with the final result that the two-dimensional sectional impact force due to bow flare is estimated as

$$F = \pi \rho C_V \left( \frac{dz}{dt} \right)^2 b \frac{db}{dz} \quad (2)$$

where b is the instantaneous section half-beam and  $C_V$  is the dimensionless added mass coefficient.

### 2.4 Calculation of Deck Wetness

The calculation of deck wetness involves relative motion at the bow and freeboard. As summarized in Bales (1979), the relative motion can be described as the sum of absolute ship motion and incident wave elevation, dynamic swell-up due to the oscillation at the free surface and incident wave distortion due to the presence of the hull. Deck wetness by its very nature requires large motions and one would expect nonlinearities in the absolute ship motions involved. The same hold true for the other components of relative motion. Recent work on components of relative motion is described in Lee et al. (1982).

Freeboard has been considered by a number of investigators to be the geometric freeboard plus a number of additional factors to account for trim and sinkage, ship's wave profile and the effect of ship's above-water sectional characteristics. The latter was termed effective freeboard by Newton (1960).

Most investigations of deck wetness have been experimental. Among the most important studies are those of Tasaki (1960). His corrections for swell-up due to ships wave and dynamic swell up due to relative motion based on model tests of tankers have been included in the work of many others. Takezawa et al (1977) described experiments on an ore carrier model using deck mounted pressure gauges. They could not successfully relate deck wetness and impulsive pressure.

Lloyd (1983) has reported on a number of experiments involving variant bow forms and measurements of impact pressures on the fo'c'sle. He concludes most bow modifications resulted in relatively little effect on the degree of wetness measured.

There is, at present, no satisfactory analytic method for the calculation of deck wetness. The difficulties in formulating a general method for predicting any of the components described above are apparent. State-of-the-art methods, for example Blok and Huisman (1984), require generalizing from limited amounts of model test data to derive empirical corrections. Questions exist

concerning the generalization of such empirical corrections to differing ship types and sizes. Further questions can be raised concerning existing methods about the accuracy of using calm water sinkage and trim and bow wave profile results for predictions involving extreme motions and large waves. O'Dea (1983) describes experimental and analytic results on the shifts of mean sinkage and trim in waves.

### 3. MODEL EXPERIMENTS

In order to determine the validity of linear motion calculations, and of approximate nonlinear calculations, an experimental program was conducted in the Harold E. Saunders Maneuvering and Seakeeping (MASK) Basin of the David W. Taylor Naval Ship Research and Development Center. A model of a modern frigate was used. Its body plan and principal characteristics are shown in Figure 1. The model was attached to the towing carriage through a heave staff and pitch/roll gimbal. Surge, sway, and yaw were restrained. All experiments were conducted in regular head waves. The model was constructed so as to allow the bow above the waterline to be removed and replaced with another shape, following initial experiment design investigations by Bales and Jones (1980). The forward portion of the bow above the static waterline and forward of station 2.5 was mounted on a force gauge system to measure flare loads, while the deck above this section was fitted with five resistance-type wave probes to measure depth of water at several locations on the deck. Relative motion around the bow was measured by seven resistance wire probes mounted outboard of the hull. These probes were stretched between outriggers which were designed to prevent interference with measurement of deck or flare loading of the forward section. An accelerometer was mounted in the hull at a longitudinal location corresponding to the center of gravity of the removable bow section (approximately station 1.5). The acceleration measurement was used to correct the force measurements for inertial effects.

In addition to the original above-water bow shape (designated the "parent" form), four additional bow forms were tested. These are shown in Figure 2. Bows 1 and 2 correspond to decreased and increased flare relative to the parent, primarily between stations 0 and 3, and Bows 3 and 4 consist of a deep and a shallow knuckle in the side of the hull. The knuckle sections have the same freeboard and offset at the deck as the parent, but the knuckle is formed by dropping the side vertically a certain distance, at which there is a discontinuity in slope and the section below the knuckle is faired smoothly into the underwater hull shape at the static waterline. The length of the vertical drop at station 2 is 25 percent of the local freeboard for the shallow knuckle, and 50 percent for the deep knuckle.

Measurements were collected digitally by a carriage mounted computer. The data were initially analyzed with the normal harmonic analysis programs used for standard seakeeping

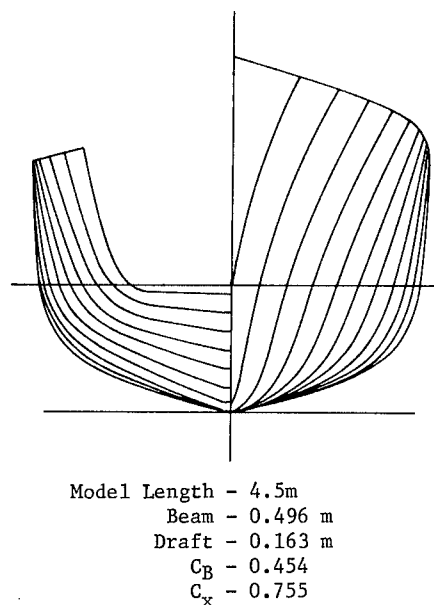


Figure 1 - Model Principal Characteristics and Body Plan

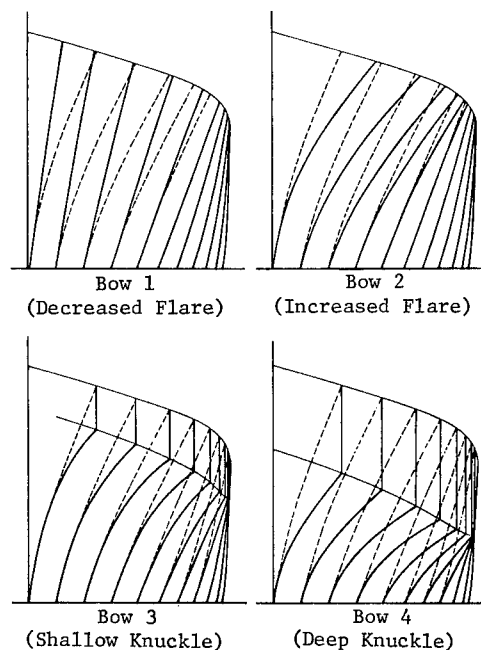


Figure 2 - Body Plans of Alternate Bow Shapes  
(- - - - - Parent)

experiments. All experiments were done in regular waves, and all measurements were remarkably repeatable in their periodicity. However, many signals were by no means pure sinusoids, so further analysis included calculation of higher harmonics, and peak analysis of time histories to determine characteristics of events such as flare forces and deck wetness. In the case of flare forces, the measured forces on the bow section (located

above the static waterline and ahead of station 2.5) had to be corrected for both the inertial loading of the mass of this section and the weight of water on deck estimated from the deck wetness probes.

#### 4. RESULTS

Experiments were initially conducted for speeds corresponding to  $F_n = 0.15$  and  $0.30$ , over a range of wavelengths,  $0.8 < \lambda/L < 3.0$ , with two nominal wave steepness values (ratio of wave height  $H$  to wavelength  $\lambda$ ) of approximately  $H/\lambda = 0.01$  and  $H/\lambda = 0.03$ . The pitch and heave transfer function results of these experiments for the parent hull are shown in Figures 3 and 4. As expected, there were no

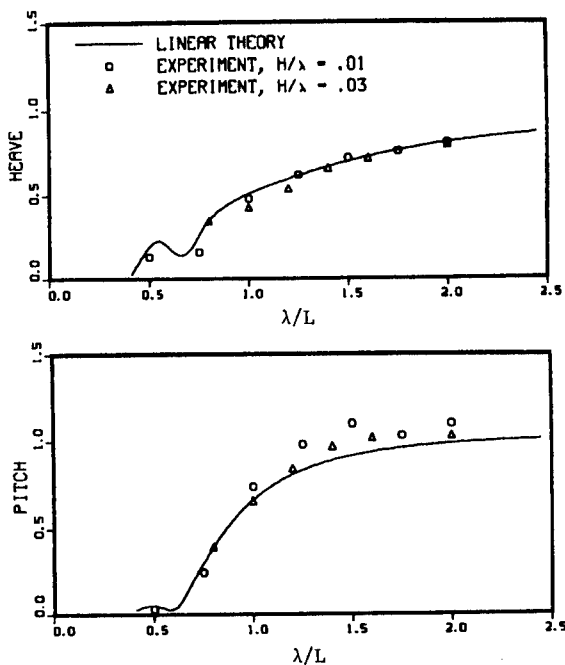


Figure 3 - Heave and Pitch Transfer Functions ( $F_n = 0.15$ )

large nonlinearities as demonstrated by a difference in transfer functions caused by changing steepness, nor were there significant differences noticed among bow shapes. In the neighborhood of  $\lambda/L = 1.0$ , where both the absolute and relative vertical motions reach large peaks in a rather narrow range of wavelength, as shown in Figure 5, there was noticed a slight tendency for the pitch transfer function to decrease slightly at the greater wave steepness. Consequently it was decided to carry out more experiments in steeper waves at one value of speed and wavelength for all the bow shapes. This was done at a Froude number of  $0.30$  and a wavelength equal to  $1.2$  times the model length. Wave steepness was varied from  $H/\lambda = 0.02$  up to  $H/\lambda = 0.07$  (a near-survival condition for the ship model itself). Calculation of ship motions were made using linear strip theory, Salvesen et al. (1970), and the nonlinear

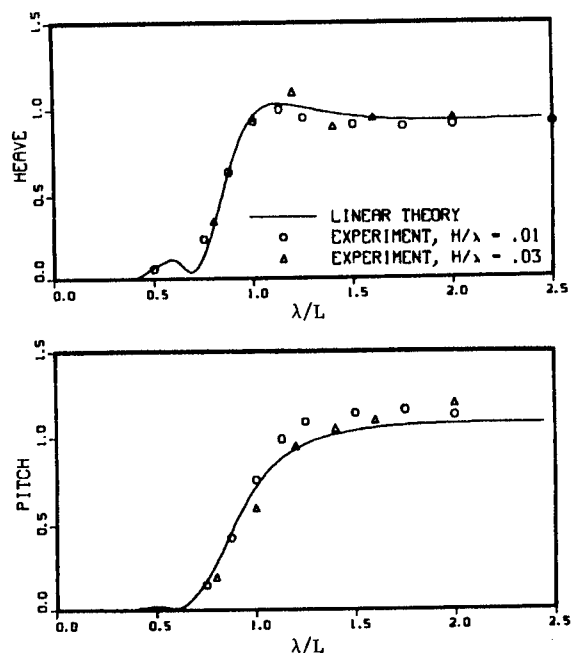


Figure 4 - Heave and Pitch Transfer Functions ( $F_n = 0.30$ )

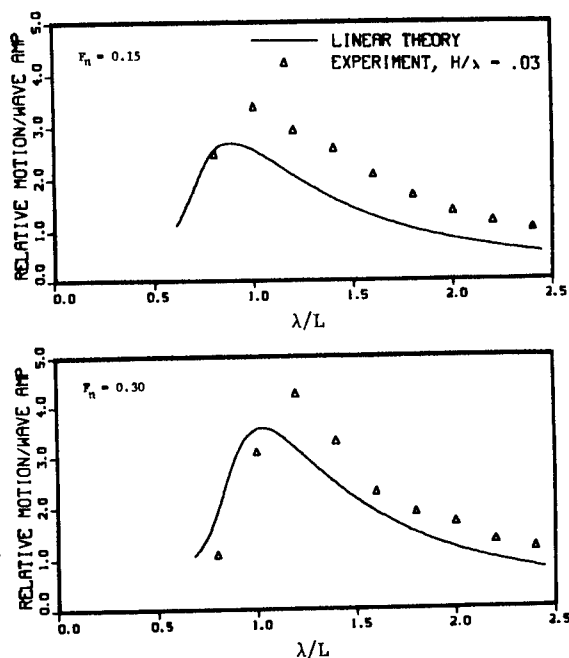


Figure 5 - Relative Motion Transfer Function at Station 2 (Parent),  $H/\lambda = 0.03$

program described by Paulling and Wood (1973). The latter program was intended to investigate ship rolling. However, it is a general six-degree of freedom program for arbitrary heading, and the approximations used in it are similar to those of the other nonlinear, time domain approaches described in section 2.2.

Also, when wave amplitude is minimized, the calculated pitch and heave motions from this program converge exactly to the transfer functions calculated with linear strip theory.

#### 4.1 Motions

Photographs of a typical time sequence of bow motion are shown in Figure 6. In the first photo the bow has risen almost clear of the water surface, and the outriggers both above the deck and below the keel (used for attaching relative motion probes) are visible. Also visible rising from the deck are the five deck wetness probes. The next photo shows water

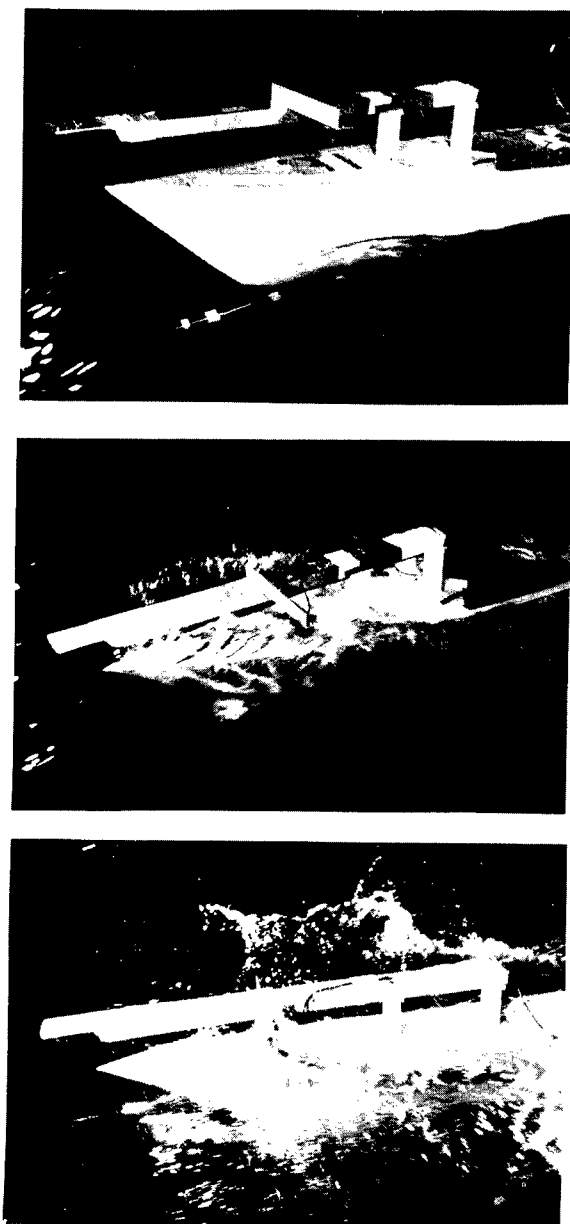


Figure 6 - Photographs of Bow Motion ( $F_n = 0.30$ ,  $\lambda/L = 1.2$ ,  $H/\lambda = 0.03$ )

coming over the bow in a sheet as the bow plunges into the wave, and the final photo shows the bow in the process of re-emerging with the water breaking into spray.

A typical time history record of incident wave, heave and pitch motions, bow acceleration, relative bow motion and deck wetness is shown in Figure 7, for the same condition as Figure 6 ( $F_n = 0.30$ ,  $\lambda/L = 1.2$ ,  $H/\lambda = 0.03$ ). The time traces of incident waves, heave and pitch appear sinusoidal, although a harmonic analysis would reveal some distortion at this steepness. The relative motion measurement is clipped in the bow up portion of each cycle, indicating that the keel is well clear of the water at that point, while the deck wetness

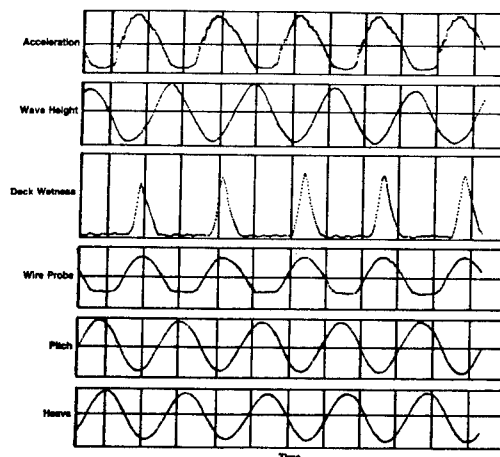


Figure 7 - Sample Time Histories of Model Responses ( $F_n = 0.30$ ,  $\lambda/L = 1.2$ ,  $H/\lambda = 0.03$ )

signal registers at the extreme bow down portion of each cycle. The vertical acceleration at the bow displays considerable distortion, much more than would be expected by a visual examination of the pitch and heave motions. The explanation for this is that any harmonic distortion in displacement is exaggerated in velocity in proportion to the harmonic multiple involved, and in acceleration the effect is increased by the square of the harmonic multiple. That is, for a motion signal that is distorted by 10 percent due to a second harmonic, the velocity will have a 20 percent distortion and the acceleration will have a 40 percent distortion. Higher harmonics can thus significantly distort the time history of bow acceleration, even if they represent only a very few percent of the motion itself.

Linear motion theory predicts that response to a pure sinusoid will also be a pure sinusoid, and that the amplitude and phase relationships between input and output will be independent of the magnitude of the input. Therefore, the variation of the first harmonic of response with wave amplitude, and the presence of higher harmonics, provide useful indications of the degree of nonlinearity present.

One of the most remarkable experimental results of varying wave steepness was the large reduction of the pitch transfer function as shown in Figure 8, amounting to 40 percent at the steepest condition tested. That is, the first harmonic of pitch became a smaller percentage of wave slope as slope was increased. This trend was well predicted by the nonlinear calculation. It is interesting to note that this effect was the same for all the bow shapes. At the same time, the calculations predicted a less pronounced variation of heave transfer function with wave steepness. This trend was not discernible in the experimental data, which were somewhat more scattered for heave than for pitch.

The phase angles of the first harmonics of heave and pitch also change with wave steepness. This is shown in Figure 9. The phase angles are defined as leads with respect to maximum wave elevation at the ship center of gravity, with positive pitch defined as bow up. The calculated phase shifts are seen to be in good agreement with the measured values for both heave and pitch.

In addition to the changes in the first harmonics of motion responses, an increase in wave steepness is accompanied by a significant

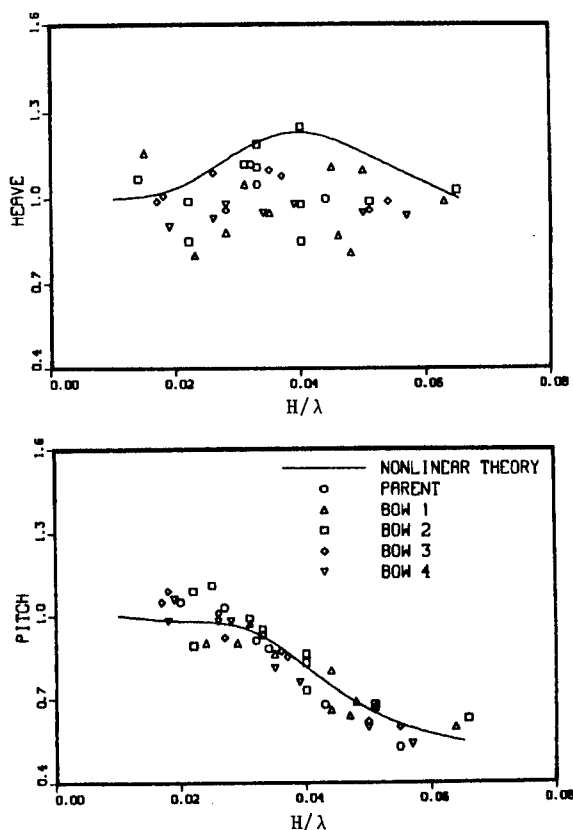


Figure 8 - Variation of Magnitude of Transfer Functions with Wave Steepness ( $F_n = 0.30$ ,  $\lambda/L = 1.2$ )

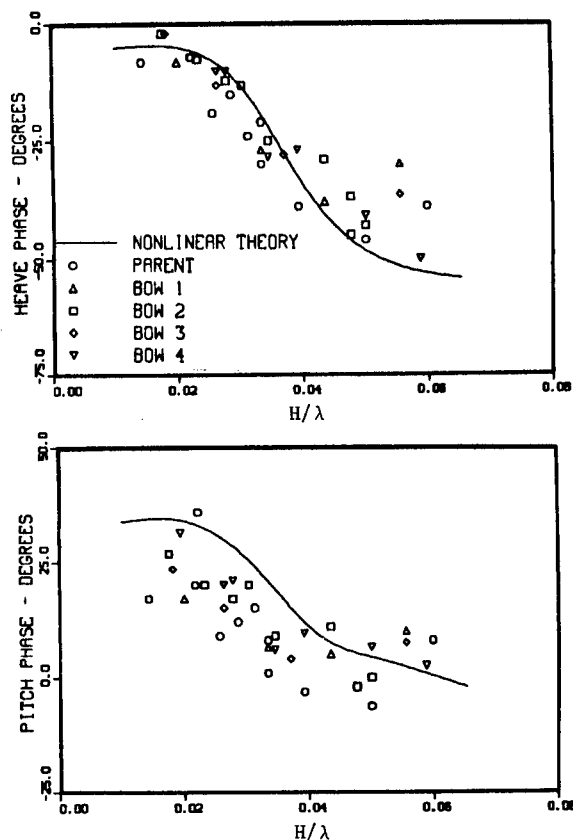


Figure 9 - Variation of Phase of Transfer Functions with Wave Steepness ( $F_n = 0.30$ ,  $\lambda/L = 1.2$ )

growth of higher harmonics, and a shift in mean values. The variation of mean and second harmonic of heave and pitch is shown in Figure 10. As in the case of first harmonics, there is no apparent difference caused by variation of above-water bow shape. However, the distortion caused by higher order harmonics was most prominent for Bow 4 (deep knuckle). As shown in Figure 11, the pitch and bow acceleration are noticeably distorted in this case. (The high frequency component in the acceleration, about 10 Hz, is caused by flexural vibration of the model hull which had relatively low longitudinal stiffness.) One cycle of the pitch time history is shown in Figure 12. Harmonic analysis of the signal indicated that five harmonics had to be included to closely represent the time history, as shown. Also shown in the figure is the amplitude of the pure first harmonic motion which is predicted by linear theory. The distortion of the pitch motion is apparently caused by the large impulsive loading on the above-water bow, as discussed below, and since the absolute vertical motion at the bow is primarily due to pitch, the acceleration is also distorted.



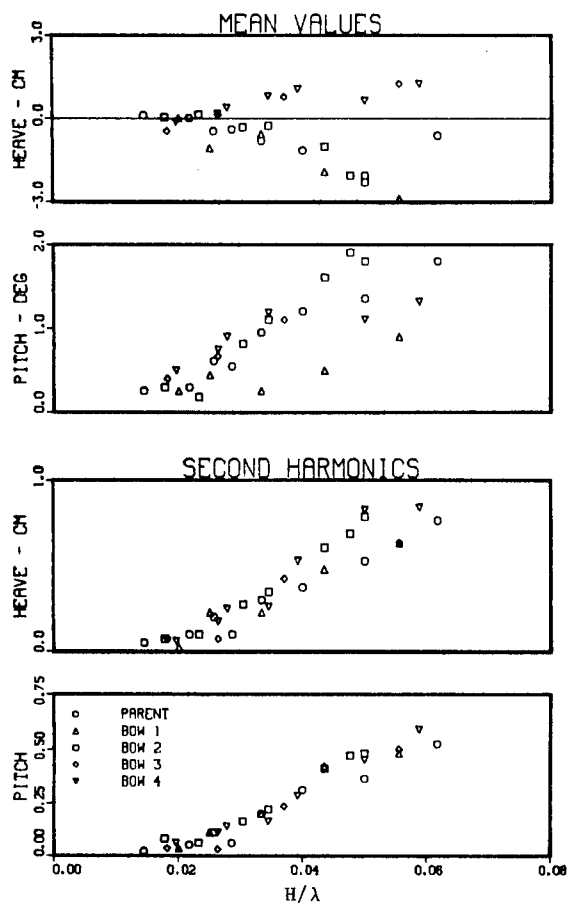


Figure 10 - Mean Value and Second Harmonic of Heave and Pitch Motions ( $F_n = 0.30$ ,  $\lambda/L = 1.2$ )

#### 4.2 Bow Flare Forces

The force on the instrumented portion of the bow, forward of station 2.5 and above the static waterline, can be considered to consist of three components: an inertial component associated with acceleration of the mass of the section; a downward force due to water on the deck; and an upward force on the bow flare. The latter component was the one of interest in these experiments; therefore, an analysis method was devised to separate and remove the other two components. The inertial correction is straightforward. The mass of the section supported by the force gauges is easily measured, and the vertical acceleration at its centroid can be either measured directly or calculated from the pitch and heave motions. To account for the rotational inertia effect (pitch acceleration), the moment of inertia of the section had to be estimated; however, this component was quite small compared to the translational inertia component. The component of force due to water on deck was not negligible. It was estimated by taking the average water depth measured by the wetness probes and multiplying by the deck area. This is, of

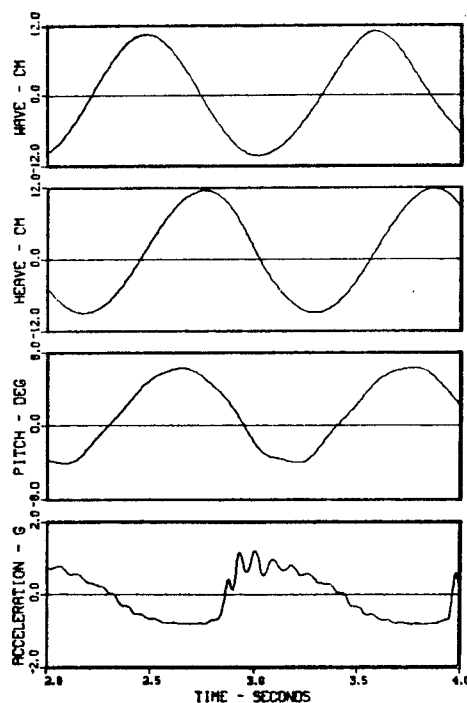


Figure 11 - Time Histories of Responses for Bow 4 ( $F_n = 0.30$ ,  $\lambda/L = 1.2$ ,  $H/\lambda = 0.04$ )

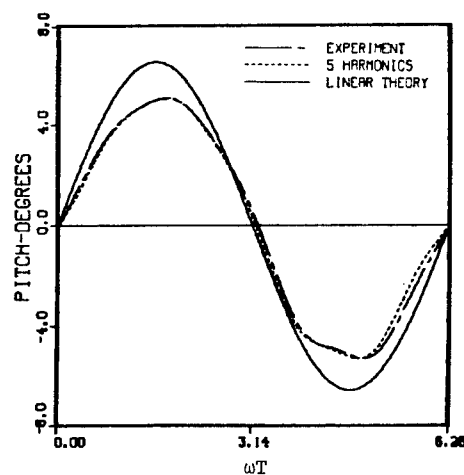


Figure 12 - Time History of Pitch Motion for Bow 4 ( $F_n = 0.30$ ,  $\lambda/L = 1.2$ ,  $H/\lambda = 0.04$ )

course, a very approximate correction, since there is no reason to expect that water on deck acts as a static mass. However, because the peak flare force and peak water on deck generally occur at different points in the wave encounter cycle, this method of compensating for deck loads was considered satisfactory.

Examples of the time history of the upward bow force, calculated as described above, are shown in Figure 13. The model-scale encounter

period was approximately 1.1 seconds for this case, so the peak loads generally have a duration of less than one tenth of a cycle. Neither the parent nor the reduced flare bow (Bow 1) exhibit an impulsive loading in this case, while Bows 2, 3, and 4 show a peak which is progressively larger and of shorter duration. The variation of peak force with wave steepness is shown in Figure 14. Again, the parent and Bow 1 show similar magnitudes and the variation is approximately linear with steepness. The other bow shapes show considerably larger forces, which in the most severe case approach one-half of the hull displacement. While this peak may be of short duration, the impulse of the force can cause very noticeable distortion of motion, such as is shown in Figure 12.

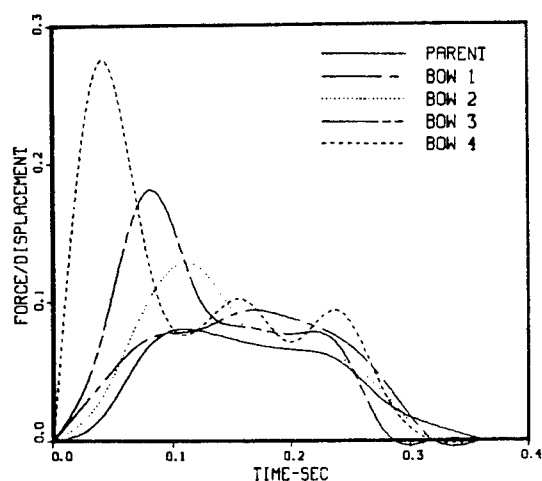


Figure 13 - Example of Peak Bow Force Time Histories ( $F_n = 0.30$ ,  $\lambda/L = 1.2$ ,  $H/\lambda = 0.04$ )

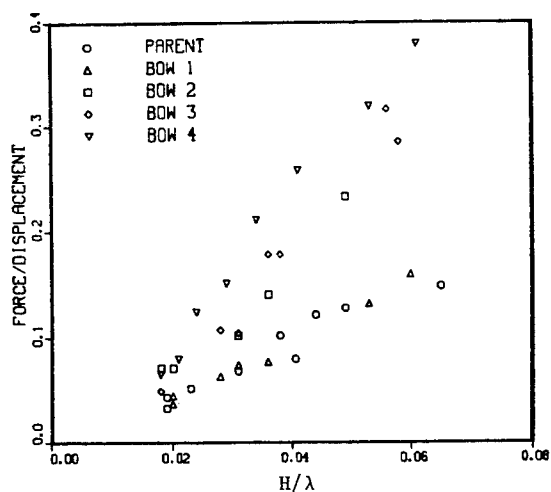


Figure 14 - Variation of Peak Bow Force with Wave Steepness ( $F_n = 0.30$ ,  $\lambda/L = 1.2$ )

The peak forces were also calculated using Equation (2). It was found that using the values of the added mass coefficient  $C_v$  given by Gran (1976) for the section shapes of the bow of this hull, considerably overestimated the peak loads. The values of  $C_v$  given by Gran are for an infinite fluid, corresponding to infinite frequency of oscillation. However, the added mass at the actual frequency is much lower, and use of this quantity gives predictions which are closer to the measurements, as illustrated in Table 1 for the case of the Parent and Bow 4, which had the largest flare loading. Further improvement in prediction of flare loads may require a more detailed calculation of pressures, including three dimensional effects, as discussed by Hwang et al. (1983).

TABLE 1 - COMPARISON OF CALCULATED AND MEASURED PEAK FLARE FORCES

( $F_n = 0.30$ ,  $\lambda/L = 1.2$ ,  $H/\lambda = 0.04$ )

	Parent	Bow 4
Measured*	0.10	0.27
Calculated	0.13	0.37
Calculated ( $\omega = \infty$ )	0.25	0.70

\*All values are divided by model displacement.

#### 4.3 Deck Wetness

The experiments described in the previous section have also been analyzed to investigate the effect of above waterline bow shape on deck wetness. The data of particular interest is that obtained from the five wetness probes mounted on the deck. As described, the regular wave results were found to be quite repetitive from cycle to cycle. This was also found to be the case for the deck wetness measurements as can be seen in Figure 7.

The results shown in Figure 15 are for head seas, Froude number of 0.3 and wavelength to ship length ratio of 1.2. Shown are data for the parent, increased flare and decreased flare variants. Note that flare here refers to beam at the deck edge. The flare angle at the waterline is the same for all variants. The average of the peak water elevation on deck measured by the five deck wetness probes is given as a function of wave height. The advantage of increased flare in reducing wetness can be seen. The increased flare variant has somewhat less wetness, while the decreased flare variant shows considerably greater wetness.

Figure 16 shows average wetness for the parent, deep knuckle and shallow knuckle variants. In this case, no significant differences can be seen. This confirms results obtained in previous investigations that for cases of extreme wetness, where the knuckle is submerged, it provides no reduction of deck wetness. Since the probes used in this experiment do not respond to spray, no conclusions can be drawn on the effectiveness of knuckles on the reduction of less severe wetness incidences.

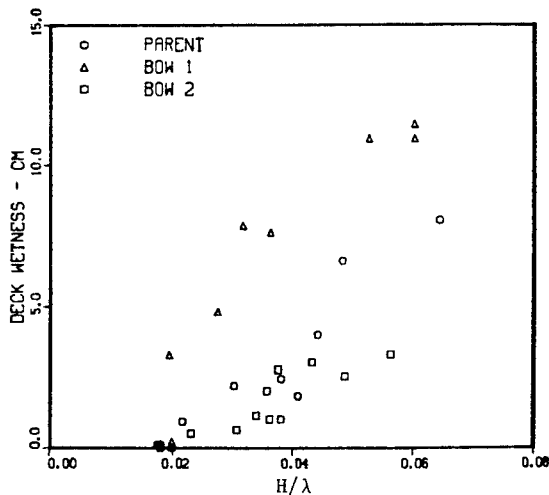


Figure 15 - Variation of Deck Wetness with Wave Steepness (Decreased Flare, Parent, and Increased Flare)

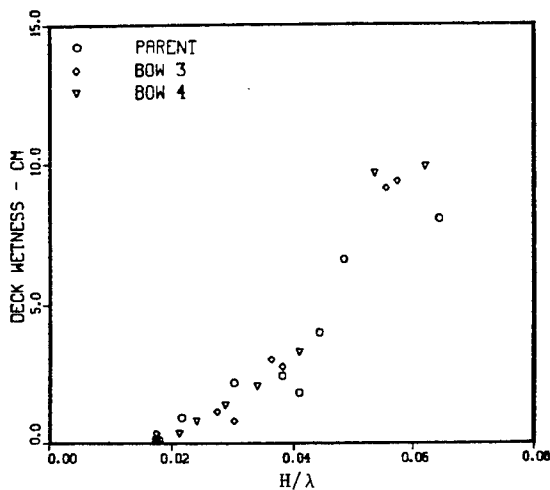


Figure 16 - Variation of Deck Wetness with Wave Steepness (Deep Knuckle, Shallow Knuckle and Parent)

It can also be seen from Figures 15 and 16 that the onset of deck wetness appears to be independent of bow shape. Again, it should be noted that wetness refers to a measurable depth of water on deck and does not include spray.

Figure 17 shows the height of water above deck level plotted at the location of the measurement. Also shown are the deck edge and the waterline. Figure 18 shows the same data in a contour plot. This data is for the parent in head seas, Froude number of 0.3, wave height to wavelength of 0.03 and wavelength to ship length of 1.2. The data is for the time at

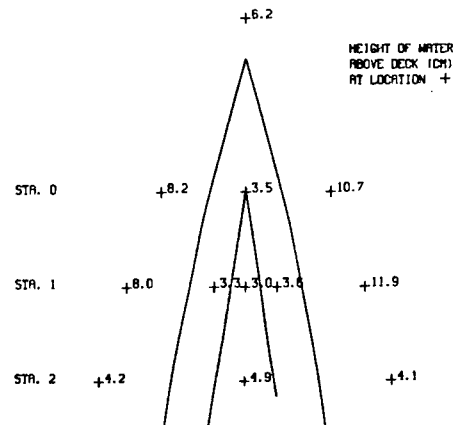


Figure 17 - Deck Wetness and Relative Wave Height Values

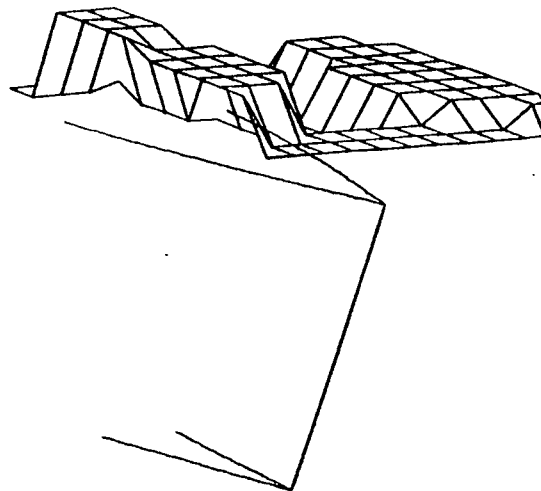


Figure 18 - Deck Wetness and Relative Wave Height Contours

which average depth of water for the five deck probes is maximum. It can be seen that the relative height outboard considerably exceeds the level of the water on deck. Some slight port-starboard differences can be seen even in what should be a symmetric case, a result of experimental variability.

## 5. CONCLUSIONS

(1) The results have shown, that for cases where the wave frequency of encounter coincides with the peak absolute and relative motion responses in head waves, linear theory is able to predict the rigid body motions with acceptable accuracy up to a wave steepness of approximately  $H/\lambda = 0.03$ . For longer and

shorter waves, linear theory may be acceptable in steeper waves. In the case of very steep waves in the frequency range of maximum ship response, the transfer functions of rigid body response may change appreciably, accompanied by the growth of higher harmonics and distortion of the motion time history. Vertical acceleration at the bow is particularly sensitive to harmonic distortion in the motion.

(2) A time-domain simulation of nonlinear motions was able to reproduce the basic properties found in the experimental motion measurements, i.e., a change in the first harmonic, together with a mean shift and growth of second and higher harmonics. However, the calculations were quantitatively correct only in the first harmonic calculations. It is important to note that the change in the transfer functions with wave steepness is not predicted by linear theory, nor would it be predicted by any perturbation procedure carried out consistently to second order. An expansion carried to at least cubic terms would be necessary to predict this phenomenon. Thus, it is unlikely that nonlinear, frequency domain techniques such as are used in drift force calculations, will be useful in predicting nonlinear pitch and heave in steep head waves.

(3) The variations in above-water bow shape used in the experiments did not produce large variations in rigid body motions. However, there were noticeable differences in the peak flare forces measured in the instrumented part of the bow. The peak upward force on this section, which represented only the forward one-eighth of the length above the static waterline, approached one-half of the hull displacement for the deep knuckle and increased flare bow shapes in very steep waves. Since the peak flare load lasts only a small fraction of each encounter cycle, the resulting impulse does not significantly change the first harmonic of motion. However, this impulse can cause higher harmonics resulting in distortion of the time history of motion, particularly pitch, and the harmonic distortion is magnified in the vertical bow acceleration. Also, such large forces may indicate severe structural loads both locally and in the main hull girder.

(4) Figures 15 and 16 have shown that deck wetness, as measured by depth of water on deck, varies nonlinearly with wave steepness. Figures 17 and 18 show significant difference between relative motion and depth of water on deck. It appears that, in addition to the known difficulties in the prediction of the effect of bow shape on spray, the calculation of depth of water on deck may be equally as complex. An adequate analytical prediction of deck wetness will require a time domain calculation. This will allow the incorporation and the interaction of the large number of physical phenomena involved.

(5) All the work described in this paper has dealt with regular wave results, primarily at one particular speed and wavelength. It is important to consider the implications for predicting responses in realistic, severe, irregular seas. Because ships are usually considered, at worst, weakly nonlinear systems,

much effort has been devoted in the past to perturbation methods in which only the linear or quadratic portions were retained. The experimental results presented show clearly that considerably higher order effects such as apparent cubic effect responsible for reducing the pitch transfer function, and fourth and fifth harmonics in the time history of pitch, can occur in steep waves with large motion responses. It is possible that approximate nonlinear methods used in the frequency domain, such as describing functions, could represent at least some of this behavior. In this way, an improved estimate of the most basic statistical quantities, such as RMS, might be made. However, the fact that the actual responses are nonlinear would make any attempts to predict extreme values from the usual relationships very questionable.

An alternate method is to carry out computer time-domain simulations, with random input, and of sufficient length to obtain reasonable statistical measures of performance. The nonlinear methods presently available appear able to simulate the most prominent aspects of nonlinear response, although not all the detailed distortions and harmonics which exist. Since the present state of this approach handles the nonlinear Froude-Kriloff forces and moments with the most care, it is likely that further improvement will require more exact treatment of the hydrodynamic problems of incident wave diffraction and wave radiation by a hull undergoing large amplitude oscillation. Although present time-domain techniques already require considerable computing effort, the advent of ever-faster computers may make more exact simulations feasible, if not inexpensive, in the not-too-distant future.

## 6. ACKNOWLEDGMENTS

This work was funded by the Independent Exploratory Development Program of DTNSRDC, and by the Naval Sea Systems Command under the General Hydromechanics Research Program administered by DTNSRDC. The authors wish to acknowledge the work of Harry D. Jones, who was responsible for carrying out the extensive experimental program and developing new analysis techniques. The original work on bow flare was initiated at DTNSRDC by the late N. K. Bales.

## REFERENCES

- Bales, N.K. (1979): Minimum Freeboard Requirements for Dry Foredecks: A Design Procedure. SNAME STAR Symposium, pp. 39-62.
- Bales, N.K. and H.D. Jones (1980): Measurement and Reduction of Model-Scale Data on Flare Slamming and Deck Wetness. Proc. 19th ATTC, pp. 209-226.
- Blok, J.J. and J. Huisman (July/August 1984): Relative Motions and Swell-Up for a Frigate Bow. RINA Naval Architect, pp. 227-244.

- Chuang, S.-L., E.A. Schroeder and S. Wybraniec (May 1977): Seaworthiness Digital Computer Program ROSAS. DTNSRDC Report 77-001.
- Faltinsen, O.M. (1974): A Numerical Investigation of the Ogilvie-Tuck Formulas for Added-Mass and Damping Coefficients. *Journal of Ship Research*, Vol. 18, pp. 73-90.
- Faltinsen, O.M. (1977): Numerical Solutions of Transient Nonlinear Free Surface Motion Outside or Inside Moving Bodies. Second International Conference on Numerical Ship Hydrodynamics, pp. 347-357.
- Gran, Sverre, Harald Olsen and Finn Tellsgard (1976): Hull Responses to Hydrodynamic Forces on Bow Flare. *Norwegian Maritime Research*, Vol. 4, pp. 29-40.
- Hwang, J.H., Y.J. Kim, K.S. Min and S.I. Ahn (1983): Prediction of Bow Flare Impact Pressure by Momentum Slamming Theory. International Workshop on Ship and Platform Motions, Berkeley, pp. 183-201.
- Jensen, J. Juncher and P. Terndrup Pedersen (1978): Wave Induced Bending Moments in Ships - A Quadratic Theory. *Transactions RINA*, Vol. 120, pp. 151-165.
- Lee, C.M. (Dec 1968): The Second-Order Theory of Heaving Cylinders in a Free Surface. *Journal of Ship Research*, Vol. 12, pp. 313-328.
- Lee, C.M., J.F. O'Dea and W.G. Meyers (1982): Prediction of Relative Motion of Ships in Waves. 14th Symposium on Naval Hydrodynamics, pp. 417-452.
- Lloyd, A.R.J.M. (1983): Deck Wetness Experiments. *Proc. 20th ATTC*, pp. 969-999.
- Meyerhoff, W.K. and G. Schlachter (1980): An Approach for the Determination of Hull Girder Loads in a Seaway Including Hydrodynamic Impacts. *Ocean Engineering*, Vol. 7, pp. 305-326.
- Newton, R.N. (1960): Wetness Related to Freeboard and Flare. *Transactions RINA*, Vol. 102, pp. 49-81.
- O'Dea, J.F. (1983): Wave Induced Mean Shift in Vertical and Absolute Relative Motion. International Workshop on Ship and Platform Motions, Berkeley, pp. 32-48.
- Ogilvie, T.F. (1963): First and Second-Order Forces on a Cylinder Submerged Under a Free Surface. *Journal of Fluid Mechanics*, Vol. 16, pp. 451-472.
- Paulling, J.R. and Paul D. Wood (1973): Numerical Simulation of Large-Amplitude Ship Motions in Astern Seas. SNAME Technical and Research Symposium S-3, "Seakeeping 1953-1973," pp. 93-109.
- Salvesen, Nils, E. O. Tuck and Odd Faltinsen (1970): Ship Motions and Sea Loads. *Transactions SNAME*, Vol. 78, pp. 250-279.
- Salvesen, N. (April 1982): Nonlinear Large-Amplitude Low-Frequency Ship Motions. U.S. Naval Academy Report EW-10-82.
- Takezawa, S., K. Kobayashi and K. Sawada (1977): On the Deck Wetness and Impulsive Water Pressure Acting on the Deck in Head Seas. *Journal Zosen Kiokai*, SNAJ, Vol. 142, pp. 86-96.
- Tasaki, R. (1960): On the Shipping Water in Head Waves. *Journal Zosen Kiokai*, SNAJ, Vol. 107, pp. 47-61.
- Vinje, T., Xie Magong and Per Brevig (1982): A Numerical Approach to Nonlinear Ship Motion. 14th ONR Symposium on Naval Hydrodynamics, pp. 245-278.
- Yamamoto, Y., M. Fujino and T. Fukasawa (1980): Motion and Longitudinal Strength of a Ship in Head Sea and the Effects of Nonlinearities. *Naval Architecture and Ocean Engineering*, SNAJ, Vol. 18, p.p. 91-100.
- Yamamoto, Y., T. Fukasawa, M. Arai and E. Kajita (1982): Nonlinear Effects for Ship Motions in Heavy Seas. *International Shipbuilding Progress*, Vol. 29, pp. 118-124.

## DISCUSSION

Dr. TOICHI FUKASAWA,  
University of Tokyo, Japan:

Since the law of similitude for Reynolds number is not satisfied in case of the Seakeeping Tests, the aspect of breaking of water on deck is much different between the model test and full scale. When we estimate the load due to green water on deck in actual ship is the estimation based on the model test valid or not?

Prof. WILLIAM C. WEBSTER,  
University of California, Berkeley, CA, USA:

At the University of California, Berkeley, we have conducted experiments very similar to those reported by the authors, but for Series 60 block 0.60 hulls. Our hulls included a parent plus three other bows (one with no flare, one with large flare and one with a knuckle). Our results

showed somewhat different trends from those reported by the authors; however, we tested in waves of much smaller steepness,  $H/\lambda = 0.025$ . We found that the mean heave increased with flare but mean pitch did not. The second harmonic amplitudes for pitch increased with flare but the second harmonic in heave did not. These results are different from those presented by the authors, but the reasons for this are not clear. Perhaps the difference between the bow rake of the frigate tested by the authors and that of the Series 60 is responsible.

Prof. THEODORE LOUKAKIS,  
National Technical University, Athens, Greece:

The authors have to be congratulated for the vast amount of interesting and important work contained in their paper. There is however a point to be made with regard

to experiments for "seakeeping events" (e.g. deck wetness) in regular waves. As is well known, the results of tests in low amplitude regular waves when combined with the usual statistical tools do not result in accurate predictions for seakeeping events in a seaway. Therefore it is difficult for me to see how experiments in very steep regular waves will improve the aforementioned predictions. Maybe the investigation of the effects of different bow shapes on deck wetness could be more fruitful if performed by long experiments in seaways with the same non-dimensional spectrum but varying energy content.

Prof. SERGE BINDEL,  
Ecole Nationale Supérieure de Techniques  
Avancées, Paris, France:

In seakeeping problems there are in my opinion two types of non-linearities:

- non-linearities as a whole, that is non-linearities affecting the general behaviour of the ship, for example pitch or heave,
- and local non-linearities affecting some particular phenomena like wetness.

It is obvious that if the general behaviour of the ship is nonlinear, all the phenomena are nonlinear. But the converse is not true and it is possible to have to solve nonlinear local equations and at the same time to keep linear general equations. For example the value of the steepness  $H/\lambda$  of the wave for which there is an influence of non-linearity on transfer and phase function is about 0.03, but the deck wetness appears for  $H/\lambda = 0.02$ .

May I suggest that, keeping linear equations for the whole motion, research be concentrated in a first stage on the deformation of the local flow at the bow in order to solve the problem of wetness and afterwards, if necessary, the general non-linearities be taken into account.

Dr. ROBERT MCGREGOR  
University of Glasgow, United Kingdom:

This is a fascinating paper tackling a notoriously difficult problem. The particular point I would like to enquire about is the use of resistance probes to measure deck wetness. While the presence of green water on deck may be expected to scale satisfactorily it is well known that spray does not scale. Surely, under such circumstances resistance probes are prone to give false readings at certain parts of the pitch-wave cycle. It would seem that pressure measurements have a greater potential for accuracy providing such relatively temperamental devices can be made to operate reliably. Is this basis of the choice - that, until Lloyd (1983) and more recently, pressure transducers have not worked well when subjected to violent motions?

Is the motivation in measuring deck wetness primarily concerned with the loading of the liquid on deck and how this influences the overall seakeeping or is it purely concerned with the operability or survivability of forward positioned weapons? If the former, surely

this emphasises the desirability of sensing pressures. If the latter, then have further experiments investigated impact loads (survivability) and visibility (operability)?

## AUTHORS' REPLY

We wish to thank all the discussers for their interest and valuable contributions, and will try to respond to all the questions raised. In response to Professor Fukasawa's question about scaling effect, we believe that in the case of heavy, green water on deck, the load is primarily inertial and may be predictable from model experiments. In the case of the incident wave breaking into a spray type of deck wetness, then certainly surface tension, and possibly viscosity, will prevent dynamic similarity between model and ship.

Professor Webster has reported on some additional interesting experimental evidence of mean and second harmonic effects. It is not too surprising that these results differ from ours, for two reasons. First, these are relatively small quantities and thus difficult to measure. Second, these trends are expected to be functions of the first order rigid body motions (both amplitude and phase) which are in turn a function of the hull shape. Thus the trends may be different for each hull. Another example of mean shifts in waves was reported by O'Dea at the International Workshop on Ship and Platform Motions in Berkeley last year. Those results, for a containership, show increases in both heave and pitch in head waves. Regarding Professor Loukakis' question concerning the applicability of results in steep regular waves to the random sea situation, we of course agree that it would be desirable to carry out very long experiments in random waves of varying steepness. Such experiments would be very taxing on experimental resources and data analysis, and our intention in these experiments was to give some insight into the physical mechanisms of nonlinear responses in an environment where the only element of randomness was that of experimental error or scatter. We hope this will lead to improving our mathematical models for predicting response in random waves. We might also add that Dr. Lloyd of ARE, while a visiting professor at the U.S. Naval Academy, has carried out experiments on the same basic hull form (but with a different series of bow shapes) in random waves. The results of his experiments should clarify the effect of bow shape on deck wetness in random waves.

Finally, the chairman, Professor Bindel, raises a very interesting point. It appears to be true that the linear transfer functions are valid up to the point where deck wetness and flare forces begin to be measurable. Therefore, linear theory may be adequate in predicting the threshold of such occurrences or the frequency of occurrence in random waves. However, if the intention is to predict the severity of such occurrences (i.e. flare force magnitude or depth of water on deck) these nonlinearities will be significant.

We agree with Dr. McGregor that the use of resistance probes gives a somewhat qualitative measurement of deck wetness, since these probes are not expected to record the presence of spray. However, as he points out, spray could not be scaled correctly from a model test even if it could be measured. We also agree that it would be desirable to measure pressure, but it should be noted that such measurements would be sensitive to the arrangement of the deck and structures on it. For instance, Lloyd has made measurements on a vertical surface similar to the forward side of a deck house and the pressure in that case may be expected to be most sensitive to the horizontal component of relative velocity and acceleration, while a pressure transducer mounted flush in a flat deck may be more sensitive to the vertical component. In any case, our intention was to explore the possibility of using resistance probes for wetness measurements, rather than to determine specific loads on deck. If the latter were the purpose, it would seem necessary to model the detailed shape of major components on the deck and measure pressures or forces on such components.

# THE UNIFIED SLENDER-BODY THEORY: SHIP MOTIONS IN WAVES

PAUL D. SCLAVOUNOS

## ABSTRACT

The heave and pitch motions of ships with forward speed in waves are evaluated using the unified slender-body theory. The radiation and diffraction problems are solved independently. Near the ship hull two-dimensional strip-like solutions are supplemented with homogeneous components which account for hydrodynamic interactions along the ship length. Their strength is determined from the asymptotic matching with a three-dimensional outer solution which is represented by a line distribution of sources on the ship axis. Computations are presented for the heave added-mass and damping coefficients, exciting forces and motions of two realistic ship hulls. Comparisons with strip theory and experiments confirm the unified theory predictions.

## 1. INTRODUCTION

The forces experienced by a ship advancing with forward speed in waves have been the subject of numerous studies since the early days of ship hydrodynamics. Essential has been the assumption that the ship hull is thin or slender. This formally justifies the use of linear wave theory for incident waves of small amplitude and permits the superposition of the forced-motion radiation problem and of the diffraction problem where the ship interacts with the incident waves while fixed at its mean advancing position.

Strip theory is the method used in today's practice for the prediction of the seakeeping performance of ships. Filtered from the pioneering work of Korvin-Kroukovsky and subsequent refinements, the version most often cited in the literature is that of Salvesen, Tuck and Faltinsen (STF)(1970). The radiation problem near the ship hull is approximated by a sequence of non-interacting flows. Each satisfies the two-dimensional Laplace equation, free-surface condition and a condition of outgoing waves. Rational justification of the strip-theory framework has been given by Ogilvie and Tuck (1969) for high frequencies of oscillation. Forward-speed effects are accounted for in the frequency of encounter and in the body-boundary normal velocity for the pitch and

yaw motions. The latter is due to the vertical velocity relative to an inertial frame induced by the angle of rotation of a translating ship. The exciting forces are evaluated by employing a two-dimensional form of the Haskind reciprocity relations. Ship motions and derived responses predicted by strip theory are known to be often inadequate at low frequencies of oscillation and high forward speeds, and second-order forces in short waves.

The present paper reports on the performance of the unified slender-body theory which is uniformly valid from low to high frequencies and for all angles of wave incidence. The theoretical framework is developed in Newman (1978). In the radiation problem the Laplace equation, the free-surface and body-boundary conditions in the near field are replaced by their two-dimensional form. This is justified by the ship geometry slenderness and the body-boundary normal velocity which dictate that the longitudinal flow gradients are small relative to the transverse gradients. No radiation condition is enforced in the near field. This permits the inner solution to be constructed by the superposition of the strip-theory velocity potential and a homogeneous component, a priori of unknown strength, which accounts for the longitudinal flow interactions. Far from the ship, the flow is three-dimensional and is approximated by a distribution of three-dimensional wave sources on the ship axis. The techniques of matched asymptotic expansions are used to enforce the compatibility of the two complementary solutions. This procedure leads to an integral equation for the outer source strength, the solution of which also determines the strength of the near-field homogeneous solution.

Computations are presented of the heave and pitch added-mass and damping coefficients of two realistic ship hulls, complementing earlier results obtained by Newman and Sclavounos (1980). The relative importance of the forward-speed effects which arise from the free surface and the body-boundary conditions has been studied. The former are present in the homogeneous component which complements the strip theory velocity potential. Their effect on the hydrodynamic coefficients has been found qualitatively very similar to that in known fully three-dimensional solutions. At  $\tau = \omega U/g = 1/4$

Paul D. Sclavounos, Massachusetts Institute of Technology, Department of Ocean Engineering,  
Cambridge, Mass., USA



where  $\omega$  is the frequency of oscillation and  $U$  the forward speed, a singularity is visible in all coefficients but the heave and pitch added masses  $a_{33}$  and  $a_{55}$ . A consistent linearization of the ship hull normal velocity leads to two identifiable forward-speed terms. The first is present only in the pitching motion and is associated with the hull angle of attack. The second, usually referred to as the  $m$ -term, contains the interactions of the steady state and oscillatory flows and depends on gradients of the steady-state velocity potential. This has been approximated by the double-body flow, consistently with the slenderness assumptions in unified theory. The full boundary condition is derived in Timman and Newman(1962) and Ogilvie and Tuck(1969). Computations of the  $m$ -term revealed that its magnitude grows towards the ship ends and may be unrealistically overpredicted if the double-body flow is approximated in a two-dimensional manner, as in the classical slender-body theory of aerodynamics. The detrimental effects of inaccurate  $m$ -terms near the ends on the heave and pitch damping coefficients  $b_{33}$  and  $b_{55}$  have been illustrated by a numerical experiment which motivated their omission in the evaluation of the hydrodynamic forces. Their proper account relies on the solution of the three-dimensional double-body flow which is expected to predict more accurately gradients near the ends. Numerical tests with artificially smeared  $m$ -terms near the ends (not reported here) suggest that the present unified theory predictions improve. Comparisons with experiments confirm the unified theory refinements and indicate substantial differences with strip theory at low frequencies of oscillation.

The vertical wave exciting force and moment are evaluated from the direct solution of the diffraction problem obtained by Sclavounos (1984). Near the ship hull, slenderness approximations are introduced in the flow equations after the factorization of their oscillatory behaviour along the ship length. Neglecting the longitudinal gradients of the slowly varying velocity potential, the two-dimensional modified Helmholtz equation is obtained in the fluid domain, subject to homogeneous body-boundary and free-surface conditions. The resulting boundary-value problem is driven by the absolute wave frequency as opposed to the frequency of encounter in the corresponding radiation problem. By enforcing a zero normal velocity on the ship hull for the sum of the incident and diffraction velocity potentials, a normalized homogeneous solution is first constructed by employing the real part of the Green function studied by Ursell (1968) which, unlike its imaginary part, is regular in the limit of head waves. A more general near-field solution follows by multiplying the normalized solution by an arbitrary complex interaction function which depends parametrically on the longitudinal coordinate and accounts for forward-speed and three-dimensional effects like its counterpart in the radiation problem. Its magnitude is determined by matching the near-field solution with its far-field three-dimensional complement

represented again by a distribution of wave sources on the ship axis. A second integral equation is so obtained and solved for the outer source strength and the magnitude of the interaction coefficient, producing results which are uniformly valid for all frequencies of practical interest and all wave headings.

Computations of the heave and pitch exciting forces have been carried out in head waves. The predicted values of the exciting-force amplitudes and phases are in better agreement with experiments relative to the Haskind relations used in the STF strip theory.

The integral equations in the radiation and diffraction problems share a common kernel. The wave systems associated with it are illustrated for values of the parameter  $\tau >$  and  $< 1/4$ . Due to the different nature of the integral equation in each  $\tau$ -region, a numerical scheme has been carefully selected to ensure the stability of the solution over a wide range of frequencies and Froude numbers. Useful insight has been provided for the design of a stable numerical scheme in the three-dimensional forward-speed problem where the sources are distributed over the ship hull rather than on its axis.

The modulus and phase of the heave and pitch motions have been computed for a Series 60 ( $C_b = 0.7$ ) and a destroyer ( $C_b=0.55$ ) hull. Comparisons with experiments and strip theory, suggest that the two theories are comparably accurate for the cases tested. An extension of unified theory to the ship motion problem in finite-depth water is reported by Børresen and Faltinsen (1984) at the present conference.

A study on similar lines has been conducted by Maruo and Matsunaga (1983) based on a small- $\tau$  approximation in both the radiation and diffraction problems. Yeung and Kim (1981) presented an alternative formulation of the heave and pitch radiation problem. The oscillatory flow is viewed from a cross-flow plane fixed in space as a transient two-dimensional disturbance caused by the oscillatory motion of the ship hull passing through. It corresponds to the use of the three-dimensional free-surface condition and the two-dimensional Laplace equation. An extension has been obtained by Kim(1982) which approximates the three-dimensional wave source potential for a slender ship, and requires the solution of an integral equation over its hull similar to the one obtained in the exact three-dimensional formulation.

At zero speed unified theory has been extensively tested and found to be in excellent agreement with three-dimensional numerical solutions. Computations have been presented by Mays(1978), Newman and Sclavounos(1980) and Sclavounos(1981).

In spite of the recent developments in slender-ship theory, the numerical solution of the three-dimensional linear forward-speed problem remains essential for our understanding of the ship motion problem, as well as for the validation first of linear theory and thereof of slender-body approximations. This task has been undertaken by Chang (1977) and Inglis and

Price (1981). Evident in all three studies is the need for a more fine discretization of the body geometry. Unlike zero-speed problems, the discretization of the ship surface is dictated not by the geometry gradients but by the shortest characteristic wavelength of the wave systems associated with the wave source potential. Assuming that potential difficulties with the stability of the numerical scheme are resolved, and in spite of the size and complexity of the computational effort involved, it is the author's view that continued efforts in that direction are a very worthwhile undertaking.

## 2. SUMMARY OF THE THEORY

A coordinate system  $(x, y, z)$  is selected as in Figure 1 fixed relative to the ship mean advancing position with its origin at midships.

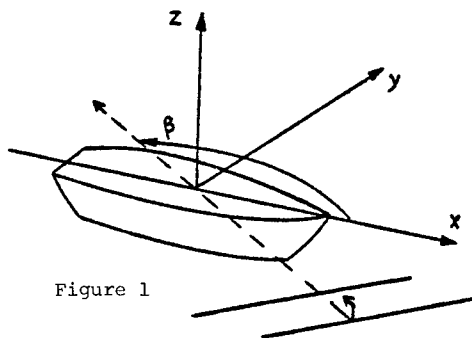


Figure 1

The ship is assumed to undergo small oscillations around its mean position due to the action of a train of regular plane progressive waves. The flow, assumed ideal and irrotational, is described by the velocity potential  $\phi$  which satisfies the three-dimensional Laplace equation

$$\phi_{xx} + \phi_{yy} + \phi_{zz} = 0 \quad (2.1)$$

in the fluid domain. Linearization justifies the decomposition

$$\phi = -Ux + U\bar{\phi} + \text{Re} \{ [ A(\varphi_0 + \varphi_7) + \xi_3 \varphi_3 + \xi_5 \varphi_5 ] e^{i\omega t} \} \quad (2.2)$$

where  $\bar{\phi}$  is the steady-state disturbance velocity potential,  $A$  the incident-wave amplitude,  $\xi_j$ ,  $j=3,5$  the complex amplitudes of the heave and pitch motions, and  $\omega$  the frequency of encounter assumed positive. The incident-wave velocity potential is given by

$$\varphi_0 = \frac{ig}{\omega_0} e^{i\omega_0 z - i\nu x \cos\beta - i\nu y \sin\beta} \quad (2.3)$$

where  $\omega_0$  is the absolute wave frequency,  $\nu = \omega_0^2/g$ ,  $\beta$  the angle of wave incidence defined in Figure 1. and  $g$  the acceleration of gravity.

To be determined, are the heave, pitch and diffraction velocity potentials  $\varphi_j$ ,  $j=3,5$  and 7 respectively which are governed by the three-dimensional linear free-surface condition

$$(i\omega - U \frac{\partial}{\partial x})^2 \varphi_j + g \varphi_{jz} = 0, \quad \text{on } z=0 \quad (2.4)$$

and are subject to the condition of outgoing waves at infinity and vanishing velocity at  $z = -\infty$ . On the ship hull

$$\frac{\partial}{\partial n} (\varphi_0 + \varphi_7) = 0 \quad (2.5)$$

$$\frac{\partial}{\partial n} \varphi_j = i\omega n_j + U m_j, \quad j = 3, 5 \quad (2.6)$$

and  $\vec{n} = (n_1, n_2, n_3)$ ,

$$\vec{x} \times \vec{n} = (n_4, n_5, n_6) \quad (2.6a)$$

$$(m_1, m_2, m_3) = -(\vec{n} \cdot \nabla) \bar{\phi},$$

$$(m_4, m_5, m_6) = -(\vec{n} \cdot \nabla) (\vec{x} \times \nabla \bar{\phi}), \quad (2.6b)$$

with the unit vector  $\vec{n}$  pointing out of the fluid domain. The speed-dependent term in (2.6) is derived in Timman and Newman (1962) and Ogilvie and Tuck (1969).

The following two sections summarize the unified theory approximations of the three-dimensional boundary-value problem (2.1)–(2.6) for slender ships. The details of the derivations can be found in Newman (1978) and Slavounos (1984) for the radiation and the diffraction problems respectively.

### 2.1 The radiation problem

Let  $\epsilon$  be the ship beam/length ratio. For small  $\epsilon$ , gradients of the flow in the  $x$ -direction are neglected near the ship hull. Thus the heave and pitch velocity potentials satisfy

$$\varphi_{jyy} + \varphi_{jzz} = 0 \quad (2.7)$$

$$\varphi_{jz} - K \varphi_j = 0 \quad \text{on } z=0 \quad (2.8)$$

where

$$\varphi_{3n} = i\omega n_3 + U m_3, \quad j = 3 \quad (2.9a)$$

$$\varphi_{5n} = i\omega n_5 + U m_5, \quad j = 5 \quad (2.9b)$$

$$n_5 = -x n_3, \quad m_3 = -\bar{\phi}_{nz}, \quad m_5 = -x m_3 + n_3 \quad (2.10)$$

and  $K = \omega^2/g$ .

Consistently with the slenderness approximations, the steady-state disturbance velocity potential  $\bar{\phi}$  is assumed to satisfy the two-dimensional Laplace equation in the

fluid domain, the rigid-wall free-surface condition, and is subject to

$$\bar{\phi}_n = n_1 \quad (2.11)$$

on the ship hull.

Unique solutions to (2.7)-(2.10) for  $j = 3$  and 5 exist if a radiation condition is imposed for large  $K|y|$ . They can be written in the form

$$\psi_j = \phi_j + U \hat{\phi}_j \quad (2.12)$$

On the ship hull the strip theory velocity potentials  $\psi_j, \hat{\phi}_j$  satisfy

$$\phi_{jn} = i\omega n_j \quad (2.13)$$

$$\hat{\phi}_{jn} = m_j \quad (2.14)$$

and at a large transverse distance

$$\phi_j \sim 1/2 i \sigma_j e^{Kz - iK|y|} \quad (2.15)$$

$$\hat{\phi}_j \sim 1/2 i \hat{\sigma}_j e^{Kz - iK|y|} \quad (2.16)$$

The observation that  $\phi_j + \phi_j^*$  constitutes a nontrivial homogeneous solution of (2.7)-(2.10), allows the generalization of the inner solution in the form

$$\psi_j = \phi_j + U \hat{\phi}_j + C_j(x) (\phi_j + \phi_j^*) \quad (2.17)$$

where  $C_j(x)$  is a function, a priori unknown, which depends parametrically on the  $x$ -coordinate and is expected to account for longitudinal flow interactions in the near field. Its magnitude is determined from the asymptotic matching with a three-dimensional outer solution represented by a distribution of wave sources on the ship axis

$$\psi_j = \int_L q_j(\xi) G(x-\xi, y, z) d\xi \quad (2.18)$$

The function  $G(x-\xi, y, z)$  denotes the velocity potential at  $(x, y, z)$  due to a pulsating and translating source located at  $(\xi, 0, 0)$ . Its derivation is given in Wehausen and Laitone (1960). The source strength  $q_j(x)$  and the interaction function  $C_j(x)$  are determined by a two-term matching of the outer expansion of the inner solution (2.17) to the inner expansion of the outer solution (2.18). The result of this procedure is an integral equation for  $q_j(x)$

$$q_j(x) - \frac{1}{2\pi i} \left( \frac{\sigma_j}{\sigma_j^*} + 1 \right) L_R(q_j, x) = \sigma_j + U \hat{\sigma}_j \quad (2.19)$$

where

$$L_R(q, x) = [\pi i + 2\gamma + 2 \ln(\omega L/U)] q(x) - 2 \int_x^{L/2} q'(\xi) \ln \frac{\xi-x}{L} d\xi + \int_L q(\xi) W(x-\xi) d\xi \quad (2.20)$$

followed by two equivalent definitions for  $C_j(x)$

$$C_j(x) = \frac{q_j - (\sigma_j + U \hat{\sigma}_j)}{\sigma_j + \sigma_j^*} \quad (2.21)$$

$$= \frac{1}{2\pi i \sigma_j^*} L_R(q_j, x) \quad (2.22)$$

The kernel  $W(x)$  is finite but discontinuous across  $x=0$  and is defined as follows

$$W(x) = W_1(x) + W_2(x) \quad x < 0, \\ = W_2(x) \quad x > 0, \quad (2.23)$$

where  $W_1(x)$  is composed of

$$W_1(x) = W_1^{(1)}(x) + W_1^{(2)}(x) \quad (2.24)$$

with

$$W_1^{(1)}(x) = i \int_{-\infty}^{k_1} e^{-ikx} [(1 - k^2/\kappa^2)^{-1/2} - 1] dk - \frac{e^{-ik_1 x} - 1}{x} \quad (2.24a)$$

$$W_1^{(2)}(x) = -i \int_{k_2}^0 e^{-ikx} (1 - k^2/\kappa^2)^{-1/2} dk \quad (2.24b)$$

For  $\tau < 1/4$ ,

$$W_2(x) = W_2^{(3)}(x) + W_2^{(34)}(x) + W_2^{(4)}(x) \quad (2.25)$$

$$W_2^{(3)}(x) = -\frac{i}{2} \int_0^{k_3} e^{-ikx} (1 - k^2/\kappa^2)^{-1/2} dk \quad (2.25a)$$

$$W_2^{(34)}(x) = \frac{1}{2} \int_{k_3}^{k_4} e^{-ikx} (k^2/\kappa^2 - 1)^{-1/2} dk \quad (2.25b)$$

$$W_2^{(4)}(x) = -\frac{i}{2} \int_{k_4}^{\infty} e^{-ikx} [(1 - k^2/\kappa^2)^{-1/2} - 1] dk - \frac{1}{2} \frac{e^{-ik_4 x} - 1}{x} \quad (2.25c)$$

and for  $\tau > 1/4$ ,

$$W_2(x) = -\frac{i}{2} \int_0^{\infty} e^{-ikx} [(1 - k^2/\kappa^2)^{-1/2} - 1] dk \quad (2.26)$$

where  $\kappa = (\omega + U\kappa)^2/g$ .

The branch points  $k_i$ ,  $i=1, \dots, 4$  are defined by

$$k_{1,2} = -(g/2U^2) [1+2\tau \pm (1+4\tau)^{1/2}], \quad (2.27a)$$

$$k_{3,4} = (g/2U^2) [1-2\tau \mp (1-4\tau)^{1/2}], \quad (2.27b)$$

with  $\tau = \omega U/g$ . The derivation of  $W(x)$  follows from the corresponding definitions derived in Newman and Schlavounos (1980) [eq. 30, 39-41] by subtracting the singular behaviour of the kernel and integrating by parts.

The limits  $\omega \rightarrow 0$  and  $U \rightarrow 0$  both correspond to  $\tau \rightarrow 0$ . It follows from their definition (2.27) that the roots  $k_i$  tend to

$$k_{1,4} \rightarrow \mp g/U^2, \quad k_{2,3} \rightarrow \mp \omega^2/g \quad (2.28)$$

as  $\tau \rightarrow 0$ . The corresponding limits of the kernel  $W(x)$  can be obtained from its definition (2.23) -(2.26). Without quoting the final results, at  $U = 0$  the kernel can be expressed in terms of the  $H_0$ ,  $J_0$ , and  $Y_0$  Struve and Bessel functions as derived by Ursell (1962). In the complementary limit  $\omega = 0$  the kernel derived by Tuck (1963) in the wave resistance problem of a slender ship is recovered. In the limit  $\omega \rightarrow 0$  the  $\ln(\omega)$  term in (2.20) is cancelled by an equal and opposite contribution which arises in the two-dimensional inner solution (2.17).

Plots of the kernel  $W(x)$  and an analysis of the associated wave systems, are presented in Section 4, together with a discussion of the numerical solution of the integral equation (2.19) and its analog [eq. (2.39)] in the diffraction problem.

## 2.2 The diffraction problem.

In the diffraction problem slenderness approximations are justified after the factorization of the oscillatory component of the flow in the  $x$ -direction. Based on the definition (2.3) of the incident-wave velocity potential we set

$$\psi_0 = \frac{ig}{\omega_0} e^{-ivx} \cos \beta \psi_0(y, z) \quad (2.29)$$

$$\psi_7 = \frac{ig}{\omega_0} e^{-ivx} \cos \beta \psi_7(y, z; x). \quad (2.30)$$

Neglecting the  $x$ -derivatives of the symmetric component of the potential  $\psi_7$  the following set of equations are obtained

$$\psi_{7yy} + \psi_{7zz} - v^2 \cos^2 \beta \psi_7 = 0 \quad (2.31)$$

$$\psi_{7z} - v \psi_7 = 0, \quad \text{on } z = 0. \quad (2.32)$$

$$\psi_{7n} = -\psi_{0n}, \quad \text{on the ship hull.} \quad (2.33)$$

By definition the sum  $\psi_7 + \psi_0$  is a homogeneous solution of the near-field problem. Thus a general solution can be written as the product of a normalized homogeneous solution  $\psi_H$  by an arbitrary function  $C_7(x)$ , which accounts for the longitudinal flow interactions like its counterpart in the radiation problem. Its magnitude is to be determined from the asymptotic matching with the outer solution. Thus we set

$$\psi_7 + \psi_0^S = C_7(x) \psi_H(y, z; x). \quad (2.34)$$

The homogeneous solution  $\psi_H$  is constructed by enforcing the interaction of two unit-amplitude and equal-phase waves incident upon the body section from opposite directions, defined by

$$\psi_0^S = \frac{1}{2} e^{vz} - ivy \sin \beta + \frac{1}{2} e^{vz} + ivy \sin \beta. \quad (2.35)$$

Denoting the resulting disturbance velocity potential by  $\psi_P$  we obtain

$$\psi_H = \psi_0^S + \psi_P. \quad (2.36)$$

By a rearrangement of terms it is possible to bring the inner diffraction velocity potential into a form similar to the inner solution of the radiation problem given by (2.17)

$$\psi_7 = \psi_P + [C_7(x) - 1] (\psi_0^S + \psi_P). \quad (2.37)$$

It is here essential to require that the velocity potential  $\psi_P$  be purely real. This permits to solve for  $\psi_P$  by using the real part of the relevant Green function which, unlike its imaginary part, is regular for all headings. Its derivation and properties are discussed by Ursell (1968). The asymptotic behaviour of  $\psi_P$  for large  $|y|$  is of the form

$$\psi_P \sim \frac{1}{2} \sigma_7(x) e^{vz} \frac{\sin(v|y| \sin \beta)}{\sin \beta} \quad (2.38)$$

where  $\sigma_7(x)$  is a real two-dimensional source strength determined from the numerical solution for  $\psi_P$ .

It is noted that the near-field potential  $\psi_7$  is driven by the absolute wave frequency

$\omega_0$ . Here forward-speed effects are present only in the complex interaction coefficient  $C_7(x)$  which draws this information from the asymptotic matching with the three-dimensional outer velocity potential.

The far-field diffraction velocity potential is again represented by a distribution of three-dimensional wave sources on the ship axis, given by (2.18), with  $q_j(x)$  replaced by the diffraction source strength  $q_7(x)$ . The asymptotic matching with the inner solution leads to an integral equation for  $q_7(x)$ , companion to that derived for  $q_j(x)$  in the radiation problem

$$q_7(x) + \frac{\sigma_7}{2\pi} L_D(q_7, x) = e^{-i\omega x \cos \beta} \sigma_7(x) \quad (2.39)$$

where

$$L_D(q, x) = [2\gamma + 2 \ln(\omega_0 L/U) + \csc \beta \cosh^{-1} |\sec \beta| - \ln 2 |\sec \beta|] q(x) - 2 \int_x^{L/2} q'(\xi) \ln \frac{\xi-x}{L} d\xi + \int_L q(\xi) W(x-\xi) d\xi \quad (2.40)$$

and two equivalent definitions for  $C_7(x)$

$$C_7(x) = \frac{q_7}{\sigma_7} e^{i\omega x \cos \beta} \quad (2.41)$$

$$= 1 - \frac{e^{i\omega x \cos \beta}}{2\pi} L_D(q_7, x) \quad (2.42)$$

where the kernel  $W(x)$  is again defined by (2.23)-(2.26). The two terms in (2.40) which depend on the angle of wave incidence can be shown to be regular for all headings with values 0 and  $1-\ln 2$  as  $\beta = \pi/2$  and 0 respectively. The properties and numerical solution of the integral equations (2.19) and (2.39) will be discussed in Section 4.

### 3. ANALYSIS OF THE m-TERMS

The determination of the velocity potential  $\hat{\phi}_1$  requires the prior evaluation of  $m_3$  defined in (2.10). An alternative definition better suited for computations has been derived by Nestegard (1984) in the form

$$m_3 = \frac{d}{ds} (n_3 \bar{\phi}_s + n_2 n_1) \quad (3.1)$$

where the subscript  $s$  denotes the derivative with respect to the section arc length. Consistently with the slenderness approximations introduced in the radiation and diffraction problems, the steady-state disturbance velocity potential  $\hat{\phi}$  is governed by the two-dimensional Laplace equation, the body-boundary condition (2.11) and a zero-flux free-surface condition. Its values on the body are obtained

by applying Green's theorem followed by the numerical solution of the resulting integral equation. Numerical differentiation is used next, in connection with the definition (3.1), to determine the values of  $m_3$ . Acceptable accuracy has been obtained by using 20-30 segments per section. The velocity potentials  $\phi_1$ ,  $\hat{\phi}_1$  and the corresponding source strengths  $\sigma_1$ ,  $\hat{\sigma}_1$  are next determined using the two-dimensional numerical scheme of Nestegard and Sclavounos (1984).

Useful for the solution of the integral equations (2.19) and (2.39), outlined in Section 4, are the limiting values of the source strengths  $\sigma_1$ ,  $\hat{\sigma}_1$  and  $\sigma_7$  at the ship ends. For conventional ship forms with small waterline beam distribution  $B(x)$  near the ends they can be determined by considering the low-frequency limits of the associated two-dimensional problems. To leading order for small  $KB(x)$ , the source strength  $\sigma_3$  has been approximated by Newman and Tuck (1964) in the form

$$\sigma_3(x) \sim -2 \int_C \phi_{3n} ds = -2 i\omega B(x) \quad (3.2)$$

The corresponding result for  $\hat{\sigma}_3$  follows from (2.11), (2.14), and (3.1) by an integration by parts of the integral of  $m_3$  over the body section, or

$$\hat{\sigma}_3(x) \sim -2 \int_C \hat{\phi}_{3n} ds = -2 \int_C m_3 ds = 4n_1 \approx 2B'(x) \quad (3.3)$$

The ship is assumed to be wall-sided and the value of  $n_1$  on the waterline is replaced by half the beam slope with errors quadratic in the ship slenderness. For a Series 60 hull, the source strengths  $(-x+U/i\omega)\sigma_3/(i\omega BL)$  and  $xU\hat{\sigma}_3/\omega BL$  along the ship length, where  $B$  is the ship beam, are illustrated in Figures 2a and 2b respectively for a non-dimensional frequency  $\omega(L/g)^{1/2} = 1$  and a Froude number 0.2. Near the ends the value of the imaginary part of the latter is non-zero, as suggested by (3.3). Numerical tests for prolate spheroids indicate that the  $m$ -term source strengths are overpredicted by the slender-body approximation used here, and suggest that the use of the three-dimensional double body flow is essential. The effect of the  $m$ -term overprediction near the ends on the damping coefficients  $b_{33}$  and  $b_{55}$  is illustrated in Section 5.

The corresponding behaviour of the diffraction source strength near the ends is given by

$$\sigma_7(x) \sim -2 \int_C \psi_{7n} ds = 2 v_B(x) \quad (3.4)$$

The numerical scheme used to solve for the diffraction velocity potential  $\psi_p$  and the source strength  $\sigma_7$  is outlined in Sclavounos (1981).

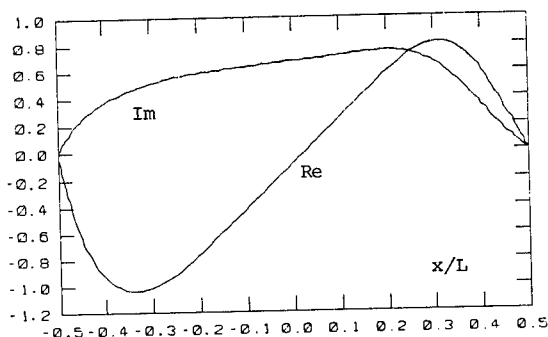


Figure 2 a

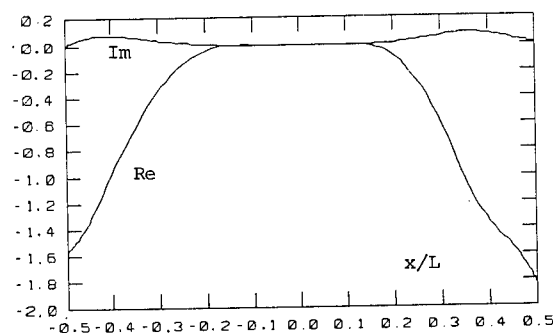


Figure 2 b

#### 4. THE SOLUTION OF THE INTEGRAL EQUATIONS

The integral equations (2.19) and (2.39) may be both set in the form

$$q(x) + A(x) \left[ C q(x) - 2 \int_x^{L/2} q'(\xi) \ln \frac{\xi-x}{L} d\xi + \int_L q(\xi) W(x-\xi) d\xi \right] = S(x) \quad (4.1)$$

where for the radiation problem

$$A(x) = -\frac{1}{2\pi i} \left( \frac{\sigma_j}{\sigma_j^*} + 1 \right) \quad (4.2)$$

$$C = \pi i + 2\gamma + 2 \ln(\omega L/U) \quad (4.3)$$

$$S(x) = \sigma_j(x) + U \hat{\sigma}_j(x) \quad (4.4)$$

and for the diffraction problem

$$A(x) = \frac{\sigma_j}{2\pi} \quad (4.5)$$

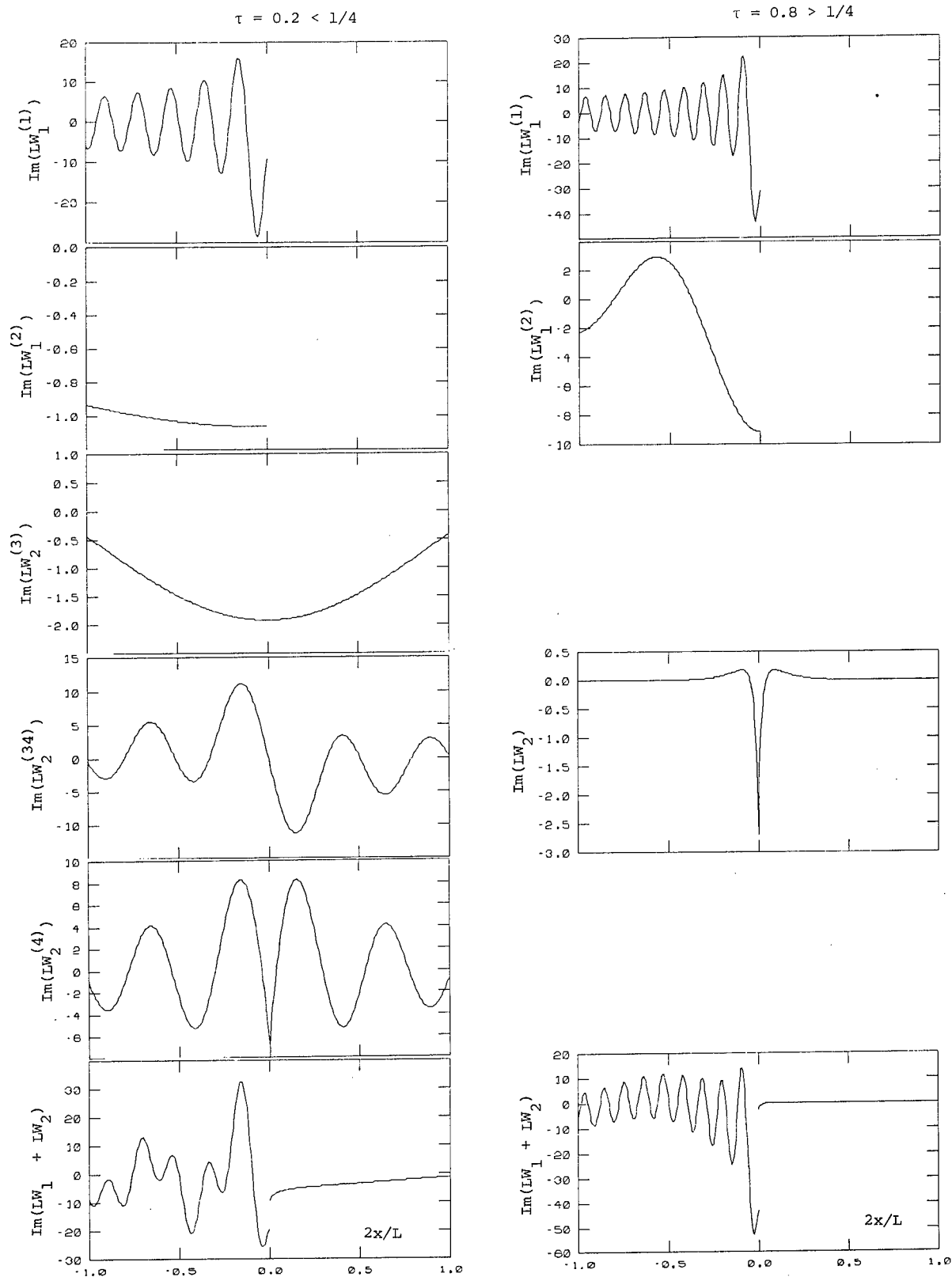
$$C = 2\gamma + 2 \ln(\omega_0 L/U) + \csc \beta \cosh^{-1} |\sec \beta| - \ln 2 |\sec \beta| \quad (4.6)$$

$$S(x) = e^{-i\nu x \cos \beta} \sigma_j(x) \quad (4.7)$$

The kernel  $W(x)$  is common to both problems and is defined by (2.23)-(2.26). As functions of  $2x/L$ , the imaginary parts of  $W_1^{(1)}(x)$ ,  $W_1^{(2)}(x)$  and their sum  $W_1(x)$  defined in (2.24), are plotted in Figures 3a and 3b at a Froude number 0.2 and two non-dimensional frequencies  $\omega(L/g)^{1/2} = 1$  and 4, corresponding to values of  $\tau = 0.2$  and 0.8 respectively. The disparate wavelengths of the associated wave systems are evident at both frequencies. It is noted that at a constant Froude number the root  $k_1$  increases in modulus with increasing frequency, being always greater than the characteristic wavenumber  $g/U^2$  of the transverse wave system generated by a translating source of constant strength. Thus a finite frequency of oscillation in effect shortens the trailing transverse waves due to the root  $k_1$ . The opposite is true for the waves due to  $k_2$ , which are longer relative to their zero-speed limit, since  $|k_2| < \omega^2/g$  at a non-zero frequency of oscillation.

For  $\tau < 1/4$  the component  $W_2(x)$  of  $W(x)$  is defined in (2.25) and consists of three components given by (2.5a,b,c). For  $\tau = 0.2$ , their imaginary parts are plotted in Figure 3a. Two characteristic wavelengths may be identified driven by the roots  $k_3$  and  $k_4$ . The component  $W_2^{(3)}$  is driven by  $k_3^{(4)}$  by both  $k_3$  and  $k_4$  and  $W_2^{(4)}$  by  $k_4$  alone. It may be verified that the rapid oscillations associated with  $k_4$  in the last two components are of opposite phase upstream ( $x > 0$ ) and in phase downstream ( $x < 0$ ). Conversely, the slowly varying oscillations due to  $k_3$  in the first two components are in phase upstream and of opposite phase downstream. The result is that in their sum,  $W_2(x)$ , one wave system is present upstream, associated with the root  $k_3$ , and one downstream associated with the root  $k_4$ . This property is illustrated in Figure 3a. For  $\tau = 0.8$ ,  $W_2(x)$  is defined by (2.26) and plotted in Figure 3b. The kernel  $W(x)$ , obtained by combining  $W_1(x)$  and  $W_2(x)$  as suggested by (2.21), is presented at the bottom of Figures 3a and 3b for  $\tau < 1/4$  and  $\tau > 1/4$  respectively.

An inspection of  $W(x)$  indicates that for  $\tau = 0.8$  its values upstream are essentially zero except for small  $2x/L$ . For  $\tau = 0.2$  on the other hand its values for  $x \geq 0$  are of comparable magnitude. This suggests that the nature of the integral equation (4.1) changes from Fredholm type to a form that resembles a Volterra type as the value of  $\tau$  crosses 0.25. Thus the numerical scheme used for its numerical solution needs to be stable for both equation types. In Newman and Slavounos (1980) a piecewise linear approximation of the source strength has been utilized and the equation has been satisfied at equally spaced collocation points. Further testing of this scheme with the integral equation (4.1) which involves the value of  $q(x)$  rather than its derivative multiplying the non-singular kernel  $W(x)$ , indicated that instabilities may occur for large values of  $\tau$ . Stable solutions of (2.19) and (2.39) have been obtained by instead



Figures 3a,b: The unified theory kernel  $W(x)$ , (eq. (2.23-2.26)) and associated wave systems for two values of  $\tau$ , 0.2 (Figure 3a) and 0.8 (Figure 3b), and  $Fr = 0.2$ .

adopting an expansion for  $q(x) - S(x)$  in terms of Chebyshev polynomials over the ship axis. This takes the form

$$y(x) = q(x) - S(x) = \sum_{k=0}^K Y_k T_k(2x/L). \quad (4.8)$$

The selection of the difference  $q(x) - S(x)$  as the unknown function is motivated by its vanishing value at the ends of ships with vanishing beam distribution on the waterline, and leads to a faster convergence of the expansion (4.8). The coefficients  $Y_k$  may be determined by substituting (4.8) in (4.1) and enforcing the resulting equation at a set of collocation points usually selected to be the  $K+1$  zeroes of the Chebyshev polynomial  $T_{K+1}(2x/L)$ . Here a Galerkin technique has been implemented which instead requires that the discretized equation is multiplied by  $(1-t)^{-1/2} T_l(t)$  for  $l = 0, 1, \dots, K$  where  $t = 2x/L$ , and integrated over its range. In its final discrete form, equation (4.1) with  $y(x)$  as the unknown becomes

$$\delta_{\ell} Y_{\ell} + \sum_{k=0}^K Y_k (A_{k\ell} + L_{k\ell} + W_{k\ell}) = - \sum_{k=0}^K S_k (A_{k\ell} + L_{k\ell} + W_{k\ell})$$

$$\delta_{\ell} = \begin{cases} 2, & \ell = 0 \\ 1, & \ell > 0 \end{cases} \quad \ell = 0, 1, \dots, K \quad (4.9)$$

where  $S_k$  are the coefficients of the Chebyshev series of  $S(x)$  and

$$A_{k\ell} = \frac{2}{\pi} C \int_{-1}^1 dt \frac{T_{\ell}(t)}{(1-t^2)^{1/2}} T_k(t) A(t) \quad (4.10a)$$

$$L_{k\ell} = - \frac{4}{\pi} \int_{-1}^1 dt \frac{T_{\ell}(t)}{(1-t^2)^{1/2}} A(t) \int_t^1 dt' T'_k(t') \ln \frac{t'-t}{2} \quad (4.10b)$$

$$W_{k\ell} = \frac{1}{\pi} \int_{-1}^1 dt \frac{T_{\ell}(t)}{(1-t^2)^{1/2}} A(t) \int_{-1}^1 dt' T_k(t') W\left(\frac{t-t'}{2}\right). \quad (4.10c)$$

The Gauss-Chebyshev quadrature has been used for the evaluation of all integrals with respect to the  $t$  variable. For the integrals with respect to the  $t'$  variable in (4.10b) recurrence relations have been derived for  $k = 2, \dots, K$ , where the first two terms are available in closed form. Finally, the corresponding integrals in (4.10c) are evaluated by first approximating the kernel  $W(t)$  in a piecewise linear manner over a sufficiently dense grid on the ship axis. The resulting products of linear functions with the Chebyshev polynomials  $T_k(t')$  are evaluated analytically. A sufficiently accurate solution has been obtained by selecting 20-30 polynomials.

## 5. HYDRODYNAMIC FORCES AND MOTIONS

The solution of the integral equations (2.19) and (2.39) lead to the evaluation of the interaction coefficients  $C_j(x)$  defined by (2.21)-(2.22) and (2.41)-(2.42) for the radiation and diffraction problems respectively. The relations, (2.22) and (2.42) have been found to be more stable numerically near the ship ends. In the radiation problem the hydrodynamic impedance forces due to the ship forced oscillations are expressed in terms of the added mass and damping coefficients  $a_{ij}$  and  $b_{ij}$ ,  $i, j = 3, 5$ . Substituting the near-field definition of the radiation velocity potential (2.17) in the linearized Bernoulli equation, and integrating over the ship hull using Tuck's theorem [Ogilvie and Tuck (1969)],  $a_{ij}$  and  $b_{ij}$  are obtained in the form

$$\omega^2 a_{ij} - i\omega b_{ij} = -i\omega\rho \iint_S n_i \phi_j dS$$

$$- \rho U \iint_S (i\omega n_i \hat{\phi}_j - m_i \phi_j) dS + \rho U^2 \iint_S m_i \hat{\phi}_j dS$$

$$- \rho \iint_S C_j(x) (i\omega n_i - U m_i) (\phi_j + \phi_j^*) dS. \quad (5.1)$$

The first integral in (5.1) contains contributions which, other than the frequency of encounter, are speed-independent. The next two arise from the speed-dependent terms in the body-boundary condition and contain the contribution from the angle-of-attack and the  $m$ -terms. The last integral contains the unified-theory corrections.

An assesment of the importance of the  $m$ -terms, along with the potential inaccuracies introduced by their overprediction near the ends, has been carried out. The heave and pitch damping coefficients  $b_{33}$  and  $b_{55}$  have been selected for this numerical experiment and their values have been determined by integrating the energy flux radiated at infinity by the strip theory source strength distributions  $\mathcal{S}_3$  and  $\mathcal{S}_5$  over the axis of the Series 60 hull at  $Fr=0.2$ . It is shown in Slavounos(1983) that the damping coefficient associated with a distribution  $q(x)$  of three-dimensional wave sources over a segment on the free surface is given by

$$b = -\frac{\rho}{4\pi\omega} \operatorname{Im} \int_L dx q^*(x) \left[ \int_L d\xi q(\xi) W(x-\xi) - 2 \int_x^{L/2} d\xi q'(\xi) \ln \frac{\xi-x}{L} \right] \quad (5.2)$$

where the kernel  $W(x)$  is defined in (2.23)-(2.26). Figures 4a and 4b present the heave damping coefficient obtained by (5.2) with  $q(x)$  replaced with the strip theory source strengths  $\mathcal{S}_3$  and  $\mathcal{S}_3 + U \mathcal{S}_5$  respectively. The predictions of strip theory and experimental measurements by Gerritsma and Beukelman(1967) are also shown. The corresponding results for the pitch damping coefficient are presented in Figures 5a and 5b. The inclusion of the  $m$ -terms



appears to lead to a substantial overprediction of the damping coefficients which is attributed to the unrealistically large values of the source strengths  $\hat{G}$ , near the ship ends, illustrated in Figure 2b. It was thus decided to omit the  $m$ -terms in the evaluation of the added-mass and damping coefficients. Research currently under way investigates the proper account of the  $m$ -terms. It is expected that their inclusion will improve the present unified theory predictions. The results will be reported by Nestegard(1984).

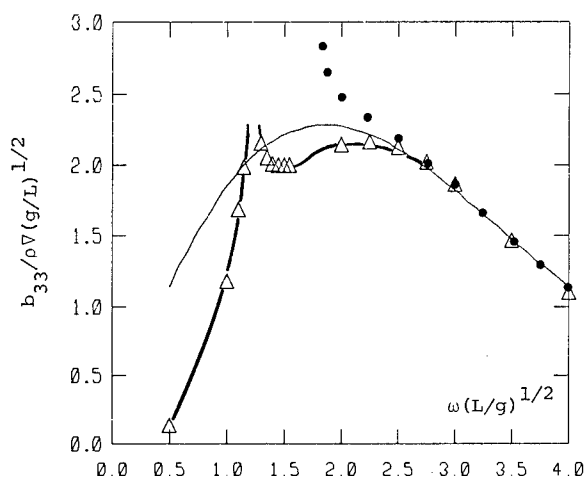


Figure 4a : Heave damping coefficient, Series 60.  
 — : Strip theory.  
 —△— : Equation (5.2),  $q(x) = \sigma_3(x)$   
 • : Experiments, Gerritsma and Beukelman.

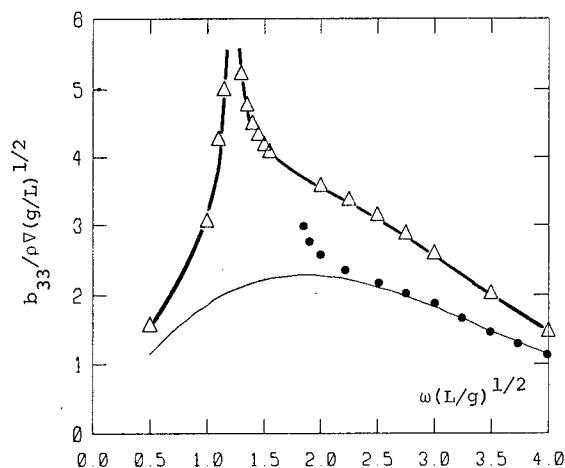


Figure 4b : Heave damping coefficient, Series 60.  
 —△— : Equation (5.2),  $q(x) = \sigma_3(x) + U \sigma_3(x)$ .

The preceding numerical experiment also illustrates the difference between the predictions of the damping coefficients obtained by evaluating the energy-flux at infinity due to the distribution of the strip-theory source strengths on the ship axis, and

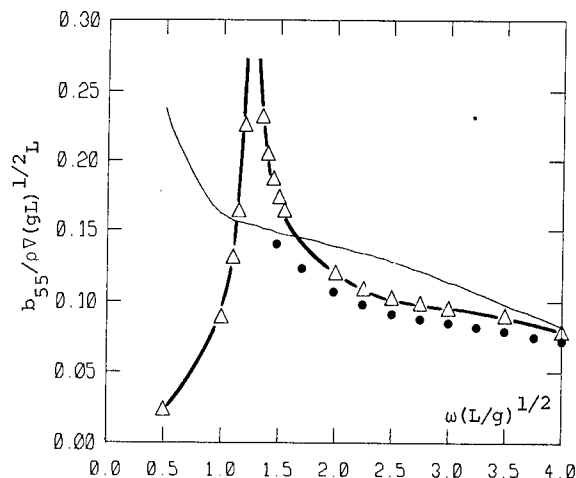


Figure 5a : Pitch damping coefficient.  
 —△— : Equation (5.2),  $q(x) = (-x + U/i\omega) \sigma_3(x)$ .

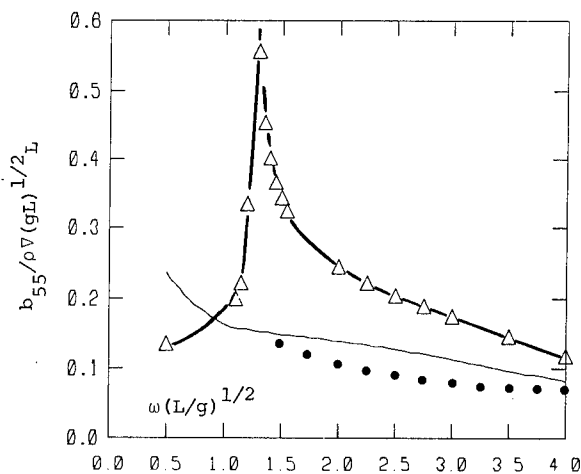


Figure 5b : Pitch damping coefficient.  
 —△— : Equation (5.2),  
 $q(x) = -x(\sigma_3 + U \sigma_3) + (U/i\omega) \sigma_3$

by the pressure integration over the ship hull. The former contain three-dimensional effects missing in the conventional strip theory predictions, indicated by the singularity at  $\tau = 1/4$  and the low-frequency behaviour. In unified theory the two predictions have been shown by Sclavounos(1984) to be identical. This result has been confirmed numerically by comparing the predictions of  $b_{33}$  and  $b_{55}$  obtained from (5.1) and (5.2).

Figure 6 presents the unified-theory predictions of the added-mass and damping coefficients obtained from (5.1), with the  $m$ -terms omitted, for a Series 60 hull ( $C_b=0.7$ ) advancing at a Froude number 0.2. Comparisons are made with the STF strip theory and experiments by Gerritsma and Beukelman(1967). The same coefficients have been computed for a destroyer ( $C_b=0.55$ ) at  $Fr=0.35$ , for which

experimental measurements have been carried out by Smith(1966). These are illustrated in Figure 7. Substantial differences between the unified and strip theory predictions exist for low frequencies and near the  $\tau = 1/4$  singularity. Unified theory is in general in better agreement with experiments than strip theory with the exception of the cross-coupling coefficients  $a_{35}$  and  $a_{53}$ . The existence of a singular behaviour of certain coefficients at  $\tau=1/4$  should not be viewed as a defect of unified theory or more generally of three-dimensional theories. Experiments carried out by Maruo and Matsunaga(1983) suggest that the pitch damping coefficients  $b_{33}$  and  $b_{55}$  display a clearly identifiable peak at  $\tau=1/4$ .

The exciting forces are obtained by the substitution of the sum of the incident and diffraction velocity potentials given by (2.34) in Bernoulli's equation, followed by an integration over the ship hull and the use of Tuck's theorem. This procedure leads to an expression for exciting force which depends on the m-terms. An alternative definition may be obtained by using

$$\frac{\partial}{\partial t} = i\omega - U \frac{\partial}{\partial x} \quad (5.3)$$

and neglecting gradients of the slowly varying components of the flow in the x-direction relative to the x-derivative of the rapidly oscillatory component of the diffraction velocity potential. It can be confirmed that the application of (5.3) in the radiation problem, in the absence of the velocity potential  $\phi_3$ , leads to (5.1) without the m-terms. The resulting exciting force takes the form

$$X_j = \rho g A \iint_S n_j C_7(x) (\psi_0 + \psi_7) e^{-i\nu x \cos \beta} ds \quad (5.4)$$

where the quantities involved are defined in section 2.2. The corresponding expressions in the STF strip theory are obtained by applying a two-dimensional form of the Haskind relations. They are given by

$$X_j^{(s)} = -\rho A \iint_S (\psi_0 i\omega_0 n_j - \psi_j^{(s)} \bar{\psi}_{0n}) ds \quad (5.5)$$

$$\psi_3^{(s)} = \phi_3$$

$$\psi_5^{(s)} = -x \phi_3 - \frac{U}{i\omega} \phi_3$$

where the velocity potential  $\phi_3$  is defined in Section 2.

Computations of the modulus and phase of the heave and pitch exciting forces of the Series 60 hull and the destroyer in head waves at the same Froude numbers are shown in Figures 8 and 9. The unified theory predictions of the exciting force modulus are in very good agree-

ment with experiments and comparably accurate to strip theory. Unified theory, however, performs substantially better than strip theory in the phase prediction.

Following the evaluation of the hydrodynamic forces, the heave and pitch ship motions are easily obtained as the solution of the complex linear system

$$\sum_{i=3,5} \{ -\omega^2 (a_{ij} + M_{ij}) + i\omega b_{ij} + C_{ij} \} \xi_i = X_j. \quad (5.6)$$

The ship particulars have been selected as in the model experiments with the center of gravity coinciding with the center of buoyancy. The heave and pitch motion amplitudes and phases for the two hulls are presented in Figures 10 and 11 for the Series 60 hull and the destroyer respectively. Unified theory tends to overpredict the heave amplitude but performs better than strip theory in the prediction of the motion phases.

## 6. CONCLUSIONS

A summary of the analysis and computations of the hydrodynamic forces and motions as predicted by the unified slender body theory have been presented. Based on the experimental measurements it may be concluded that in the radiation problem the unified theory provided an improvement over the Salvesen, Tuck and Faltinsen strip theory, with the exception of the cross-coupling added-mass coefficients  $a_{35}$  and  $a_{53}$ . Substantial differences between the two theories have been observed near the  $\tau=1/4$  singularity and at low frequencies where unified theory is expected to be superior. In the exciting force predictions unified theory is in better agreement with experiments. This is especially notable in the phase prediction. The heave amplitude predicted by unified theory is larger than the strip theory prediction and experiments. For the phases the unified theory predictions appear to be more accurate, especially for heave. Head wave results have been presented in the present paper. As is evident from the outline of the diffraction problem the theory applies for all headings. The performance of unified theory in the form presented here (i.e. without the m-terms) is expected to be more reliable and in general more accurate than strip theory for the prediction of the wave forces, motions, derived responses and second-order forces. If, for example, the relative motion at the ship bow is needed, a less accurate heave motion-amplitude prediction by unified theory combined with more accurate phase and local wave elevation predictions relative to strip theory, may lead to a more accurate final estimate of the relative motion amplitude. Further testing and applications for the stated problems are planned.

The computational effort involved in unified theory is estimated to be less than three times that of strip theory, including the solution of the diffraction problem, thus its use in practice appears quite attractive.

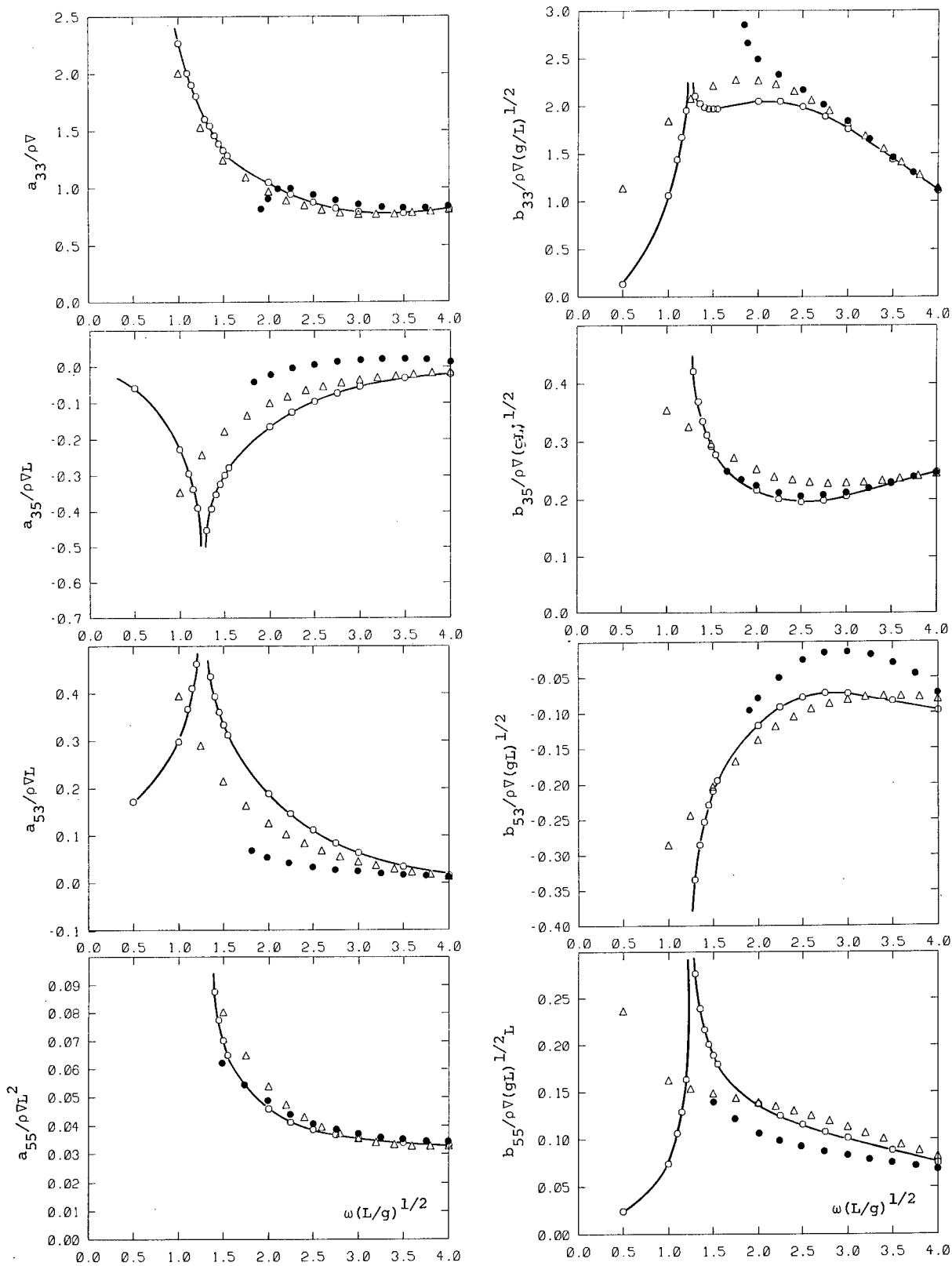


Figure 6 : Hydrodynamic coefficients for a Series 60 hull ( $C_b=0.7$ ) at  $Fr = 0.2$ .  
—○— unified theory,  $\Delta$  strip theory,  $\bullet$  Experiments by Gerritsma and Beukelman.

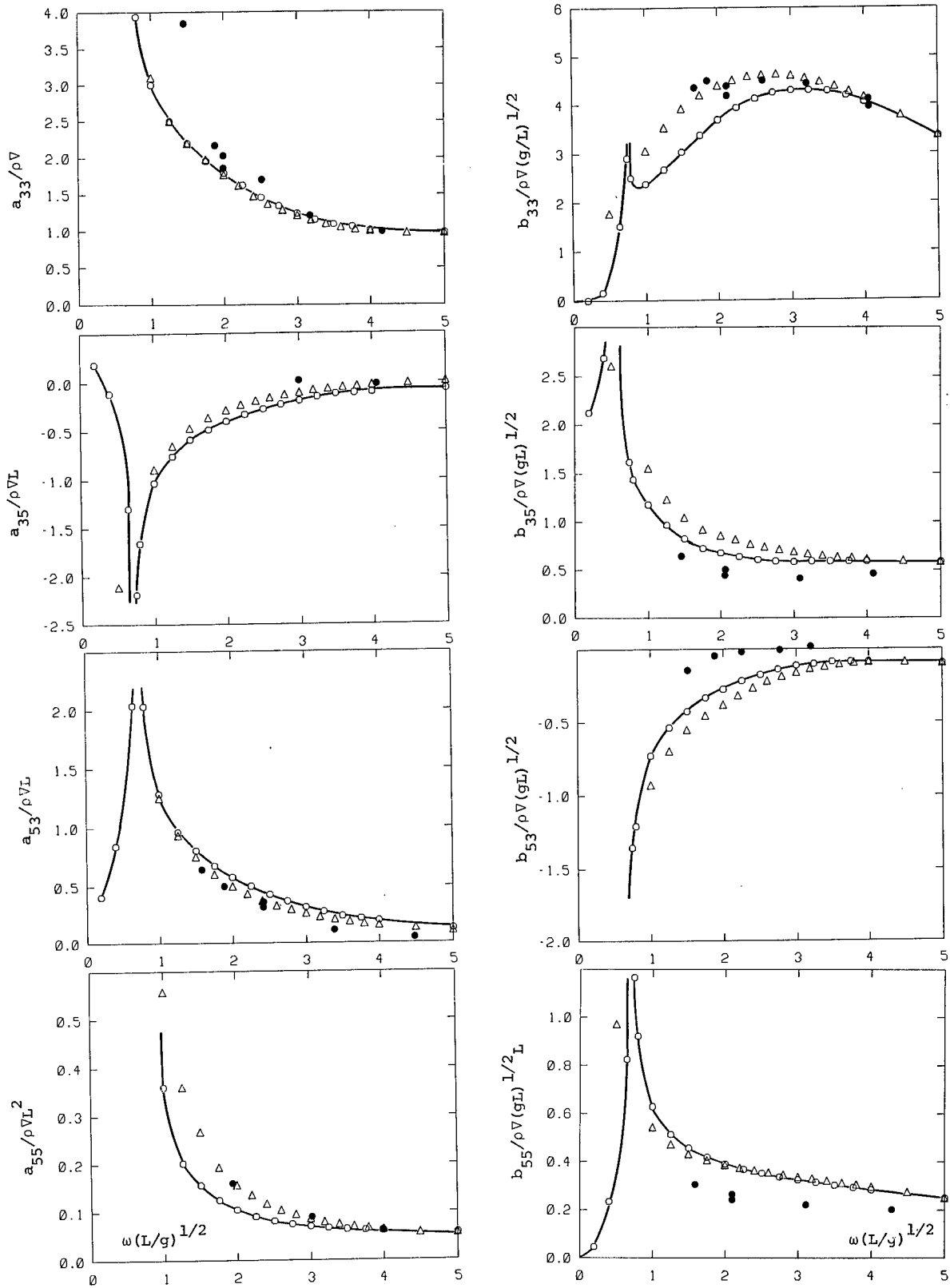


Figure 7 : Hydrodynamic coefficients for a destroyer (Cb=0.55) at Fr = 0.35.

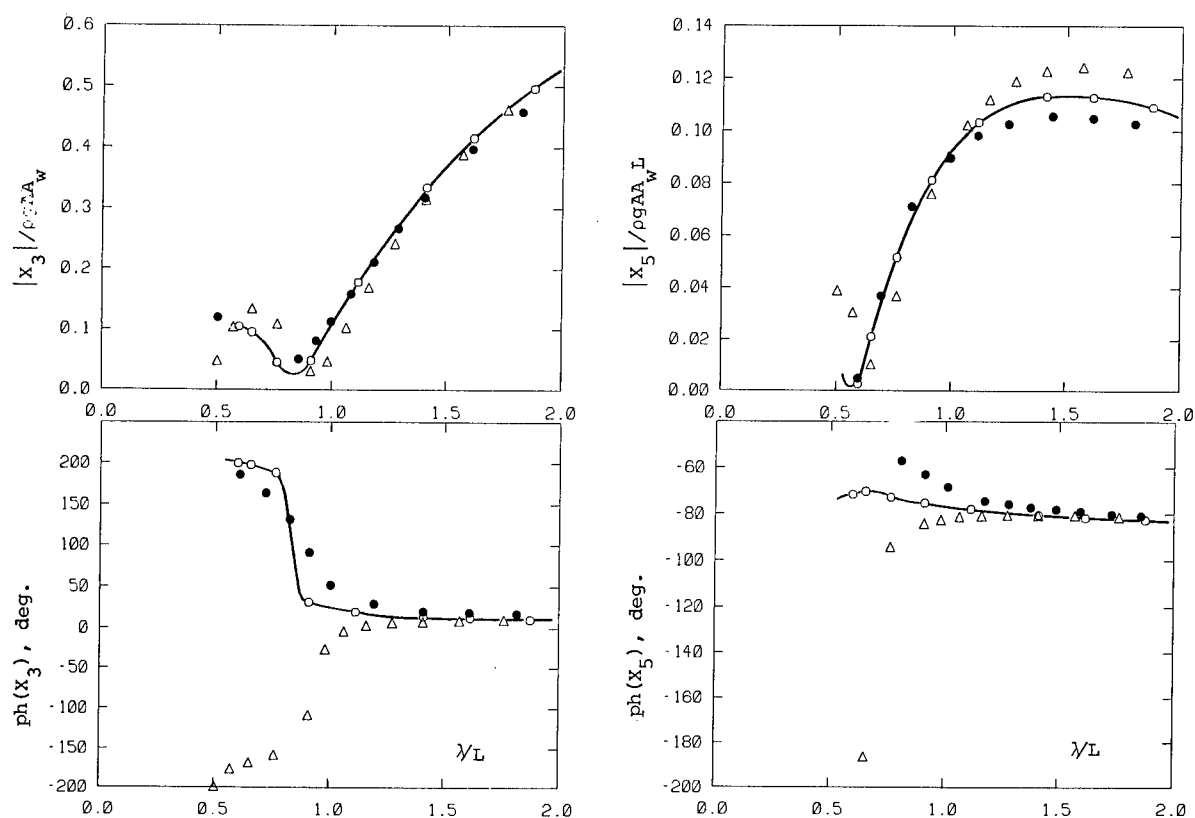


Figure 8 : Exciting forces for the Series 60 hull in head waves at  $Fr = 0.2$ .

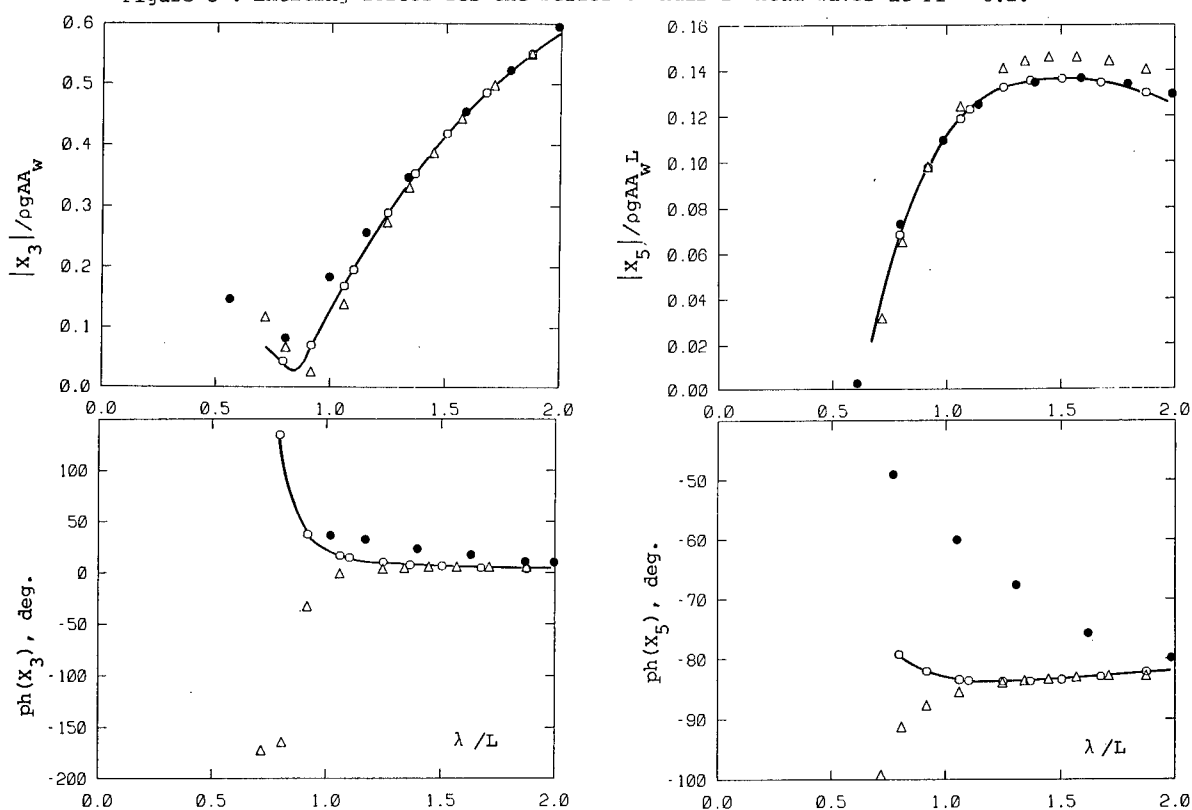
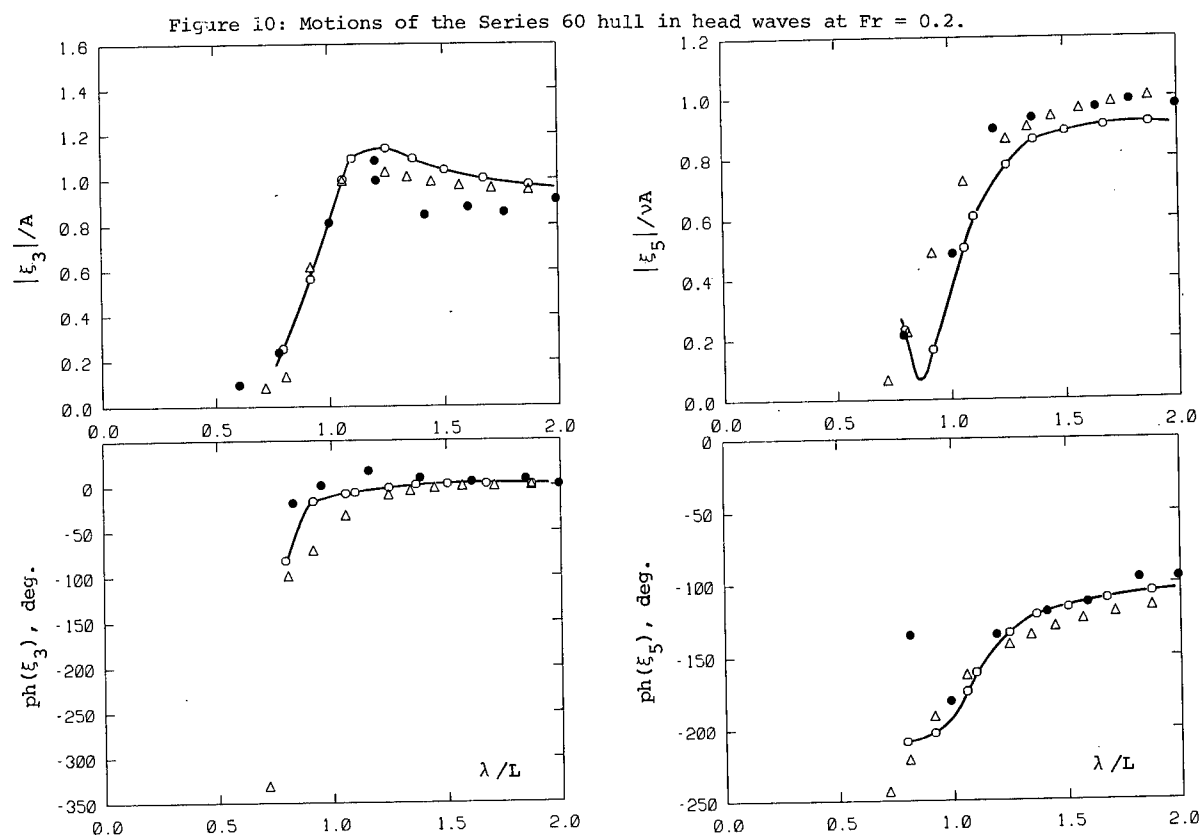
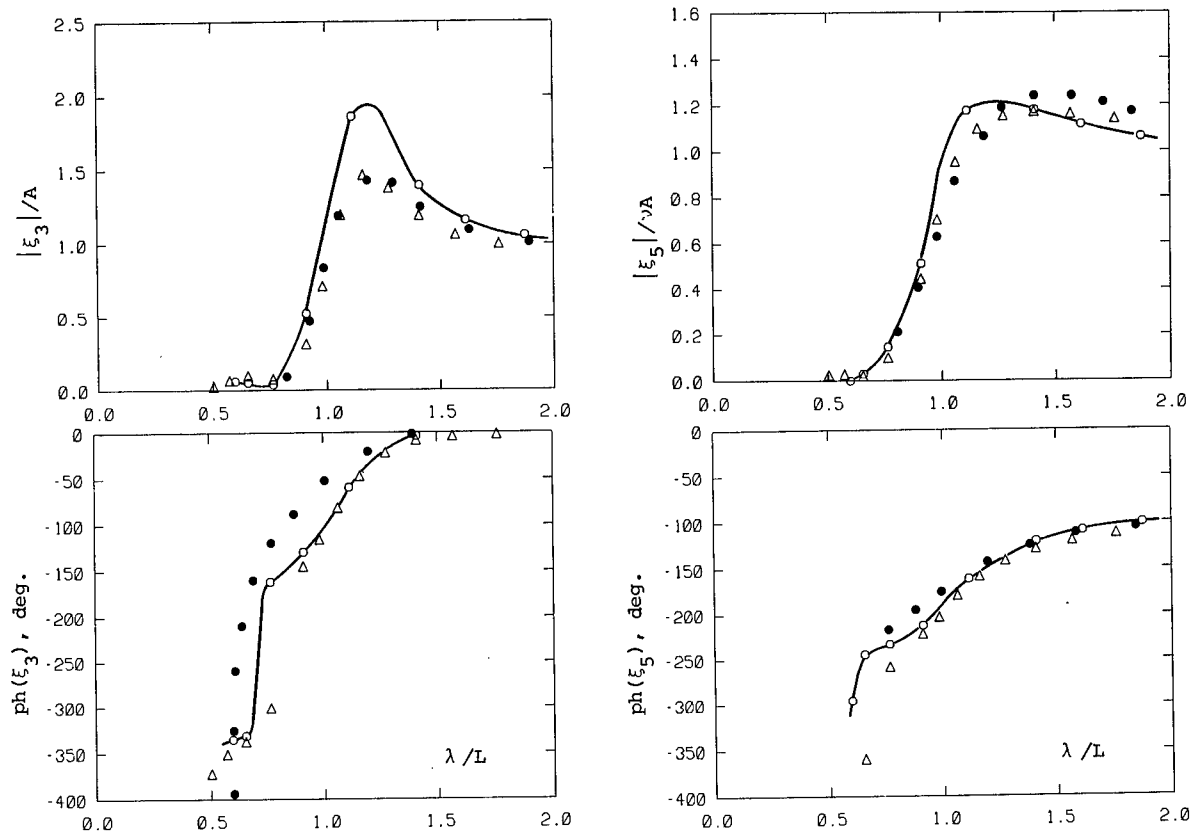


Figure 9 : Exciting forces for the destroyer in head waves at  $Fr = 0.35$ .



## ACKNOWLEDGEMENTS

The author wishes to thank Professor J. N. Newman for numerous educational discussions since the early stages of the the present study. The financial support from the Office of Naval Research, the National Science Foundation and the Naval Sea System Command's General Hydromechanics Research Program administered by the David W. Taylor Ship Research and Development Center are gratefully acknowledged. The computational assistance of Mr. A. Nestegard, Mr. T. Korsmeyer and Mr. P. F. Wang is appreciated.

## REFERENCES

- Børresen, R. and Faltinsen, O. M. (1984). Ship motions in shallow water by unified theory. Proc. 15th Nav. Hydrodyn. Conf., Hamburg.
- Chang, M.-S. (1977). Computations of three-dimensional ship motions with forward speed. Proc. 2nd Int. Conf. Num. Ship Hydrodyn., Berkeley.
- Gerritsma, I. J. and Beukelman, W. (1967). Analysis of the modified strip theory for the calculation of ship motions and wave bending moments. Rep. No. 96S, Neth. Ship Res. Center.
- Inglis, R. B. and Price, W. G. (1981). A three-dimensional ship motion theory-comparison between theoretical predictions and experimental data of the hydrodynamic coefficients with forward speed. Trans. Roy. Inst. Nav. Arch. W2.
- Kim, S. H. (1982). Slender ships with forward speed - A new approach and a new theory. Ph.D Thesis, MIT Cambridge Massachusetts.
- Maruo, H. and Matsunaga, K. (1983). The slender body approximation in radiation and diffraction problems of a ship with forward speed. SSMH,83 Conference, Varna, Bulgaria.
- Mays, J. H. (1978). Wave radiation and diffraction from slender bodies. Ph.D. Thesis, MIT Cambridge Massachusetts.
- Nestegard, A. and Sclavounos, P. D. (1984). A numerical solution of two-dimensional deep-water wave-body problems. JSR Vol. 28, No. 1, March, 48-54.
- Nestegard, A. (1984). End effects in the forward-speed radiation problem for ships. To appear.
- Newman, J. N. (1978). The theory of ship motions. Adv. Appl. Mech., Vol. 18, 221-283.
- Newman, J. N. and Tuck, E. O. (1964). Current progress in the slender-body theory of ship motions. Proc. 5th Symp. Nav. Hydrodyn., Norway.
- Newman, J. N. and Sclavounos, P. D. (1980). The unified theory of ship motions. Proc. 13th Symp. Nav. Hydrodyn., Tokyo.
- Ogilvie, T. F. and Tuck, E. O. (1969). A rational strip theory for ship motions, Part 1. Rep. No. 013, Dept. of Naval Arch. Marine Eng. Univ. of Michigan.
- Salvesen, N., Tuck, E. O. and Faltinsen, O. M. (1978). Ship motions and sea loads. Trans. SNAME, Vol. 78, 250-287.
- Sclavounos, P. D. (1981). The interaction of an incident wave field with a floating slender body at zero speed. Proc. 3rd Int. Conf. Num. Ship Hydrodyn., Paris.
- Sclavounos, P. D. (1983). Energy relations in slender ship theory. Proc. Int. Workshop Ship and Platf. Motions, Berkeley.
- Sclavounos, P. D. (1984). The diffraction of free-surface waves by a slender ship. JSR Vol 28., March, 29-47.
- Smith, W. E. (1966). Equation of motion coefficients for a pitching and heaving destroyer model. Rep. No. 154, Delft Univ. of Technology.
- Timman, R. and Newman, J. N. (1962). The coupled damping coefficients of symmetric ships. JSR, Vol. 5, No. 4.
- Tuck, E. O. (1963). The steady motion of a slender ship. Ph.D. Thesis, Univ. of Cambridge.
- Wehausen, J. V. and Laitone, E. V. (1960). Surface waves. In Handbuch der Physik, Vol. 9, 446-778, Springer-Verlag, Berlin.
- Ursell, F. (1962). Slender oscillating ships at zero forward speed. JFM, Vol. 19, 496-516.
- Ursell, F. (1968). The expansion of water-wave potentials at great distances. Proc. Cambridge Philos. Soc. 64, 811-826.
- Yeung, R. W. and Kim, S. H. (1981). Radiation forces on a ship with forward speed. Proc. 3rd Int. Conf. Num. Ship. Hydrodyn., Paris.

## DISCUSSION

Dr. JACEK STANISLAW PAWLOWSKI,  
National Research Council Canada, Ottawa,  
Canada:

I would like to congratulate Professor Sclavounos on the presentation of a most interesting paper. For those who for many years now have been using strip theory as a working tool it is interesting and encouraging to observe further developments of the slender body approach to the prediction of ship's behaviour in waves, developments which lead to the formulation of a fully mature hydrodynamic theory. However, it would perhaps be even more interesting and encouraging to see the consequences of the theoretical improvement in terms of a wide range of better predictions of ship's behaviour.

It is well known that although strip theory provides quite good estimates of ship motions, with the exception of those at low frequencies, it is not equally accurate in predicting local properties of the flow around ship's hull, which is exemplified by estimates of cross-sectional radiation and diffraction forces showing much poorer agreement with experimental values, see e.g. References (1, 2, 3, 4). The theoretical refinements of the unified slender body theory aim at taking into account effects of the flow between cross-sectional planes and therefore they should be expected to improve cross-sectional estimates of strip theory. Besides, accurate estimates of cross-sectional forces are of significant practical importance for structural considerations.

In view of the comparisons of motions and global force characteristics presented in the paper, as calculated by unified slender body theory, strip theory and found experimentally, not showing a decisive superiority of the unified theory predictions, I wonder if the author attempted comparisons of cross-sectional estimates and if so, with what results.

### References:

- (1) Gerritsma, J.; Beukelman, W. (1964): The distribution of the hydrodynamic forces on a heaving and pitching ship model in still water. 5th ONR Symposium on Naval Hydrodynamics, Bergen, Norway, pp. 219-251.
- (2) Gerritsma, J.; Beukelman, W. (1967): Analysis of the modified strip theory for the calculation of ship motions and wave bending moments. International Shipbuilding Progress, Vol. 14, No. 156, pp. 319-336.
- (3) Wereldsma, R.; Moeyes, G. (1976): Wave and structural experiments for elastic ships. 11th ONR Symposium on Naval Hydrodynamics, London, UK, pp. 567-586.

- (4) Beukelman, W.; Gerritsma, J. (1982): The distribution of hydrodynamic mass and damping of an oscillating ship form in shallow water. International Shipbuilding Progress, Vol. 29, No. 339, pp. 297-315.

## AUTHORS' REPLY

Dr. Pawlowski raises a valid and interesting point. It appears that a rational way to evaluate the performance of a slender-body theory for the prediction of the seakeeping behavior of a ship in waves is to compute the sectional force distribution along the ship length and compare with experiments. Information can be so obtained not only for the hydrodynamic coefficients and exciting forces but for the structural loads as well. The author appreciates Dr. Pawlowski's remark and reserves the presentation of further results for the future.



# A NEW DEVELOPMENT IN THE THEORY OF OSCILLATING AND TRANSLATING SLENDER SHIPS

RONALD W. YEUNG AND SEA H. KIM

**ABSTRACT** A brief review of some of the existing nearfield approximations used in developing ship-motion theories is first given. The inability of a strip-type solution to generate the proper speed-modified wave characteristics is pointed out. In the context of linear theory, a new and comprehensive slender-ship theory with no restrictions on forward speed and frequency of oscillation is developed. A novel approach of asymptotically matching a partly unknown "generalized inner Green function" with an outer three-dimensional Green function is used. The new inner solution satisfies a speed-dependent free-surface condition, and has wave characteristics compatible with three-dimensional flow. The zero-speed version of Newman's (1978) unified theory is recovered as a special case of this general theory. In the limit of vanishing oscillation frequency, a new slender-ship formulation of the Neumann-Kelvin wave-resistance problem is obtained. In the high-frequency limit with forward speed, the "pseudo-time" formulation of Yeung & Kim (1981) can be deduced. Useful properties of this new theory are also summarized.

## 1. INTRODUCTION

The use of the strip theory in ship-motion calculations is well known. Conceived initially by Korvin-Kroukovsky (1955) as an extension of the slender-body theory in aerodynamics, the idea consisted of obtaining the hydrodynamic properties of each ship section by using a zero-speed time-harmonic flow solution. The theory has undergone a number of important changes since its original conception. Among them, are two forward-speed versions offered by Salvesen, Tuck, and Faltinsen (1970, "STF") and Ogilvie and Tuck (1969, "O&T"); both works contained more systematic derivations of the original theory and had uncovered a number of missing terms that were not apriori obvious from the physical standpoint. More recently, Newman (1978) has proposed a "unified theory" which brings in a certain amount of three-dimensional correction to the basic strip solution. This theory is emerging as one that can be adapted well into a number of conventional strip-theory computer programs.

Notwithstanding the moderate success in motion calculations provided by some of the more popular strip theories, a number of unsettling questions of a hydrodynamic nature remain. Firstly, the role played by the neglected forward-speed terms in the free-surface condition is not well understood. In three-dimensional flow, these terms would have combined with the oscillatorily time-dependent terms to

generate rather intricate wave effects. In strip theories, these terms are ignored (except for the O&T version) on the free surface but those of the body boundary condition are retained. Secondly, since strip theories can produce only two-dimensional waves that are unaffected by the ship's forward motion, some restrictions must apply to the speed. At low speeds, steady disturbances of relatively short wave lengths would be generated and their longitudinal gradients may not be negligible. At high speeds, the convective nature of the flow is conceivably important again. What then are these limits? Thirdly, if the effects of forward speed were important, the convective nature of the flow must be accounted for; how can this be carried out in a two-dimensional fashion without having to solve the actual three-dimensional problem? It appears that these and other questions are somewhat tied up with the possibility of developing a general slender-body theory that can properly account for the presence of waves generated by the combined effects of oscillation and forward speed. Presumably, one such slender-body theory would tell us what the correct form of "strip-theory" should be in the presence of forward speed.

It is not the intent of this paper to provide the answers to all of the above questions. However, we feel that the new slender-body theory presented here may resolve analytically some of the questions raised. Unlike all of the cited work above, we were not

Dept. of Naval Archit. & Offshore Eng., University of California, Berkeley, Calif. 94720, USA

bounded by the necessity of obtaining a "strip-form" similar to Korvin-Kroukovsky's work. A drastically different approach that can accommodate the convective effects in the free-surface condition is used here at the outset. The idea was initiated by the slender-body theory of Yeung and Kim (1981), which utilized the complete linearized free-surface condition. The treatment of the convective terms was accomplished by interpreting the downstream coordinate as a time variable and by solving a locally two-dimensional initial-value problem. Since the flow solution was "swept" downstream, there existed no upstream influence and the solution was only quasi-three-dimensional. However, the solution contained divergent waves that were similar to those of Chapman's (1976) work for the steady forward-motion problem.

Encouraged by the numerical results presented in our earlier work, we had since set forth to obtain a more comprehensive formulation that accounts for some genuine three-dimensional effects. The new slender-body theory described in this paper shows that it is indeed possible to incorporate the appropriate three-dimensional effects by introducing a "generalized" inner Green function in the nearfield. This Green function has an unknown part that needs to be determined by asymptotically matching with the nearfield approximation of farfield (three-dimensional) behavior. In so doing, we obtain a nearfield solution that contains precisely the same type of wave characteristics, i.e. both divergent and transverse wave fields, that are compatible with those generated by an oscillating and translating three-dimensional source. Our new formulation is necessarily computationally more involved than existing strip theories, but it stands out as a comprehensive theory of the first-order problem, in which no restrictions need to be placed on the frequency of oscillation  $\omega$  and the forward speed  $U$  of the ship. In fact, we show analytically that in the limit of  $U \rightarrow 0$ ,  $\omega \neq 0$ , our new theory recovers the results of Newman's (1978) unified theory, which is known to be consistent for the case of zero forward speed. In another limit,  $\omega \rightarrow 0$ ,  $U \neq 0$ , we obtain a new formulation of the steady-state wave-resistance problem. By making further and more restrictive approximations, this new wave-resistance formulation can be shown to be related to two existing but different slender-ship theories: Tuck (1964) and Maruo (1982). Further, if we assume the frequency of oscillation is high at the outset, the new theory confirms that the downstream-type solution treatment in the original work of Yeung & Kim (1981) is appropriate. In other words, the upstream influence is weak.

In order to provide a better perspective of the approach taken here, it is worthwhile to give in more concrete terms, a short comparison

of the approximations used by the various strip theories mentioned above. We will carry this out in §2 after the governing equations are recalled. More extensive reviews of the subject may be found in Ogilvie (1977) and Newman (1978). §3 to §5 provide an outline of the highlights of the developments of our new theory. A more exhaustive exposition can be found in Kim and Yeung (1984) as well as Kim (1982). The behavior of the two special-limit case studies alluded to above are explained in §6. For simplicity, only heave and pitch motions are considered here. There exist no fundamental obstacles to generalizing the present treatment to other modes of motion. The diffraction problems may be approached in a similar manner and are left for future work.

## 2. GOVERNING EQUATIONS AND EXISTING APPROXIMATIONS

Consider a ship advancing with constant speed  $U$  and undergoing small-amplitude motions of angular frequency  $\omega$  in deep water. We choose a steady frame of reference with the  $x$ -axis pointing in the direction of the forward motion, and the  $z$ -axis pointing upwards. The  $Oxy$  plane thus coincides with the undisturbed free surface. Let  $\bar{S}$  denote the hull surface in the time-averaged sense in this coordinate system and  $\vec{n}$  be a unit normal inwards to  $\bar{S}$  (see Figure 1). The oscillatory motions will be represented by  $\alpha_j(t) = \text{Re}_i \xi_j e^{i\omega t}$ ,  $i = \sqrt{-1}$ , where  $j$  is the mode index,  $j=1, \dots, 6$ , in particular,  $j=3$ , for heave,  $j=5$  for pitch,  $\xi_j$  the motion amplitude and  $\text{Re}_i$  represents that the real part of the expression is to be taken.

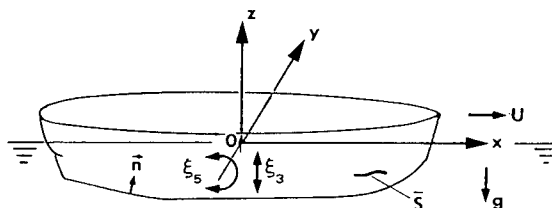


Figure 1. Coordinate system.

Assuming irrotational flow in an inviscid fluid, we introduce a total velocity potential  $\phi(\vec{x}, t)$  which satisfies Laplace's equation  $\nabla^2 \phi = 0$  and includes disturbances generated by the oscillatory motion, the steady forward motion as well as the relative incident stream:

$$\phi(\vec{x}, t) = U(\phi_s - x) + \text{Re}_i \sum_j \phi_j(\vec{x}) \xi_j e^{i\omega t} \quad (2.1)$$

where  $\phi_s$  is the steady-state potential

associated with the forward motion and  $\phi_j$  the spatial potential associated with oscillatory motion of the  $j$ -th mode. It is convenient to introduce a relative fluid velocity  $\vec{W}(x)$  associated with the steady motion:

$$\vec{W} = U\nabla(\phi - x) \quad (2.2)$$

The kinematic boundary condition on the instantaneous position of the hull can be linearized about  $\bar{S}$  (cf. Timman & Newman, 1962) and when applied with (2.1) yields the following condition for  $\phi_j$ ,

$$\phi_{sn} = n_1 \quad \text{on } \bar{S} \quad (2.3a)$$

$$\phi_{jn} = i\omega n_j + Um_j \quad \text{on } \bar{S} \quad (2.3b)$$

where

$$(n_1, n_2, n_3) \equiv \vec{n}, \quad (n_4, n_5, n_6) \equiv \vec{x} \times \vec{n}; \quad (2.4a)$$

$$(m_1, m_2, m_3) \equiv \vec{m} = -(\vec{n} \cdot \nabla) \vec{W}, \quad (2.4b)$$

$$(m_4, m_5, m_6) \equiv -(\vec{n} \cdot \nabla)(\vec{x} \times \vec{W}).$$

In terms of  $\phi$ , the following combined free-surface condition on the exact free surface elevation  $z=\zeta(x,y,t)$  can be derived:

$$\phi_{tt} + 2\nabla\phi \cdot \nabla\phi_t + \frac{1}{2}(\nabla\phi \cdot \nabla)|\nabla\phi|^2 + g\phi = 0, \quad \text{on } z = \zeta. \quad (2.5)$$

where  $g$  is the gravitational acceleration. If the decomposition (2.1) is substituted into (2.5) and assuming linearization about  $z=0$  is possible, the steady state potential  $\phi_s$ , to leading order, satisfies

$$\phi_{sxx} + K_0 \phi_{sz} = 0, \quad K_0 = g/U^2, \quad \text{on } z = 0 \quad (2.6)$$

If the appropriate radiation condition is introduced, (2.3) and (2.6) define the so-called Neumann-Kelvin problem for steady ship waves. The corresponding free-surface condition for the oscillatory-motion potential  $\phi_j$  is more complex, particularly if one allows for possible interaction with the steady potential whose magnitude is not necessarily the same order as the oscillatory ones. The condition is given by

$$(i\omega - U \frac{\partial}{\partial x})^2 \phi_j + g\phi_{jz} = U(i\omega - U \frac{\partial}{\partial x}) \phi_j (K_0 \phi_{sxx} + \phi_{sz}) - 2U(i\omega - U \frac{\partial}{\partial x})(\nabla\phi_s \cdot \nabla\phi_j) \quad \text{on } z=0 \quad (2.7)$$

where all terms with constant coefficients are transposed to the left-hand side and all terms of  $O(\phi_j^2)$  and  $O(\phi_s^2)$  are neglected. If interactions of the steady-state and the oscillatory potentials are further neglected, (2.7) is homogeneous, otherwise the right-hand side behaves like a pressure distribution applied on the free surface. In as much as the steady-state potential  $\phi_s$  is not immediately amenable to reliable numerical description even with present state-of-the-art computational techniques, and that there is already considerable amount of complexity in tackling just the homogeneous equation of (2.7) alone, it is a little premature to consider the inclusion of these interaction terms at this time. Nevertheless, it is displayed here to illustrate one of the higher-order approximations used in the U&T theory.

With the right-hand side of (2.7) taken as zero, one might consider the boundary-value problems of  $\phi_s$  and  $\phi_j$  in the following common form:

$$\nabla^2 \phi_j = 0 \quad \text{for } z < 0 \quad (2.8a)$$

$$[(i\omega)^2 - 2i\omega U \frac{\partial}{\partial x} + U^2 \frac{\partial^2}{\partial x^2} + \mu] \phi_j + g\phi_{jz} = 0, \quad \text{on } z = 0, \quad \mu \rightarrow 0^+ \quad (2.8b)$$

$$\phi_{jn} = f(s) \quad \text{on } \bar{S} \quad (2.8c)$$

$$\nabla\phi_j \rightarrow 0 \quad \text{as } z \rightarrow -\infty \quad (2.8d)$$

where  $j=s$  corresponds to the steady-state problem with  $\omega$  set equal to zero, and  $f(s)$  is defined by (2.3). Here the appropriate radiation condition has been imposed by introducing an artificial Rayleigh viscosity  $\mu$ .

### Slender-Ship Approximations

In the context of slender-body theories, the transverse dimensions of the ship are assumed to be of  $O(\epsilon)$  relative to the length of the ship; or equivalently,  $L=O(1)$ ,  $B, T=O(\epsilon)$ , where  $L$  is the length,  $B$  the beam, and  $T$  the draft of the ship. For the time scale,  $g$  can be used for nondimensionalization. With that as the understanding, it is easy to show that a statement of  $U=O(1)$  would imply  $U/\sqrt{gL}=O(1)$  and  $\omega=O(\epsilon)$  would imply  $\omega^2 B/g=O(\epsilon^3)$  etc. Of course, in asymptotic theories of the kind that we are pursuing here, it is difficult to specify a transitional value where a parameter may switch from  $O(\epsilon)$  to  $O(1)$ . Nevertheless, it is helpful to use that as a guide to identify the more important terms in the governing equations.

In an inner region, which is defined by  $R = \sqrt{y^2 + z^2} = O(\epsilon)$ , i.e. close to the hull, it is assumed that the longitudinal flow gradient is

small compared with the transverse ones. Thus

$$\frac{\partial}{\partial x} = O(1), \quad \frac{\partial}{\partial y}, \quad \frac{\partial}{\partial z} = O(\epsilon^{-1}) \quad (2.9)$$

If  $\Phi(\vec{x})$  represents the inner or nearfield approximation of the potentials  $\phi_j$ ,  $j=3,5$ , or  $s$ , the boundary-value problems of (2.8) reduce to:

$$\nabla_{2D}^2 \Phi = \left[ \frac{\partial^2}{\partial y^2} + \frac{\partial^2}{\partial z^2} \right] \Phi(y, z; x) = 0 \quad \text{for } z < 0 \quad (2.10)$$

$$\left[ (i\omega)^2 - 2i\omega U \frac{\partial}{\partial x} + U^2 \frac{\partial^2}{\partial x^2} \right] \Phi + g \Phi_z = 0 \quad \text{on } z = 0 \quad (2.11)$$

$$\Phi_N = V_N(y, z; x) \quad \text{on } \mathcal{B}(x) \quad (2.12)$$

$$\nabla \Phi \rightarrow 0(1) \quad \text{for } z \gg 0(1) \quad (2.13)$$

where  $\mathcal{B}(x)$  is the sectional contour at station  $x$ , and  $N$  the two-dimensional unit normal on  $\mathcal{B}(x)$ , (see Figure 2). The boundary condition  $V_N$  in (2.12) is still given by (2.3), viz.

$$\Phi_{jN} = \begin{cases} n_1 & \text{on } \mathcal{B}(x), \text{ for } j=s \end{cases} \quad (2.14a)$$

$$\begin{cases} i\omega N + U m_j & \text{on } \mathcal{B}(x), \text{ for } j=3,5 \end{cases} \quad (2.14b)$$

However, the quantities  $m_3$  and  $m_5$  can be approximated by discarding the longitudinal derivatives of  $\phi_s$ . Hence,

$$n_2 \approx N_2, \quad n_3 \approx N_3, \quad n_5 \approx -xN_3 \quad (2.15a)$$

$$m_3 \approx -N_2(\phi_s)_{yz} - N_3(\phi_s)_{zz} \quad (2.15b)$$

$$m_5 \approx N_3 + x m_3 \quad (2.15c)$$

It is noteworthy that we have kept all terms in the linearized free-surface condition in (2.11) since it is the intent of this work to treat  $U$  and  $\omega$  as arbitrary parameters. Also

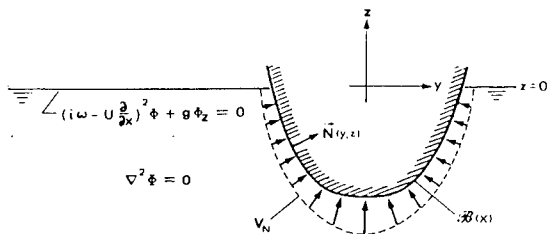


Figure 2. Two-dimensional boundary-value problem for  $\Phi$ .

note that the artificial viscosity  $\mu$  in (2.8b) has been discarded since the inner observer does not have a full perception of the overall radiation field.

In the outer region, where the transverse coordinates  $(y, z)$  are such that  $R=O(1)$ , the flow field is governed by (2.8a,b,d). The body condition (2.8c), however, is not applicable since geometric details of the hull cannot be distinguished by the far-field observer.

## 2.2 Existing Theories

We shall now give a brief discussion of a number of existing theories by examining the approximation used in further simplifying the nearfield free-surface condition.

### Ordinary Slender-Body Theory

This was one of the first attempts to utilize the slender-body theory in ship-motion problems (Newman & Tuck, 1964; Joosen, 1964). The theory was successful only for the zero forward-speed case. The assumption of  $\omega=O(1)$  is made. By (2.9), the free-surface condition becomes a rigid-wall condition:

$$\Phi_z = 0 \quad \text{on } z = 0 \quad (2.16a)$$

As a consequence, the inner region contains no wave-like motion. The body boundary condition (2.14b) yields a source-like solution that is similar to those in slender-body aerodynamics. Namely,

$$\Phi_j(y, z; x) = -\frac{i\omega}{\pi} \left\{ \frac{1}{x} \right\} B(x) \log R + f_j(x), \quad \text{for } j = \begin{cases} 3 \\ 5 \end{cases} \quad (2.16b)$$

where  $B(x)$  is the local beam at waterline and  $f_j(x)$  is a longitudinal interaction function that is obtained by matching the inner solution with the nearfield behavior of the outer representation. This long-wave theory yields radiation forces that are negligible compared with the hydrostatic restoring forces, and wave-exciting forces that are dominated by Froude-Krylov forces.

### Strip Theory

This is the short wave-length theory initially proposed by Korvin-Kroukovsky (1955), and refined later by Korvin-Kroukovsky & Jacobs (1957), Gerritsma & Beukelman (1967), (STF, 1970), among others. This is normally "justified" by assuming that  $\omega=O(\epsilon^{-1/2})$ ,  $U=O(1)$ , and since  $\partial/\partial z$  in (2.11) is by assumption  $O(\epsilon^{-1})$ , the free-surface condition reduces to one identical to the case of no forward motion:

$$-\omega^2\Phi + g\Phi_z = 0 \quad \text{on } z = 0 \quad (2.17)$$

A strictly two-dimensional ("strip") solution  $\Phi^{2D}(y,z;x)$  can now be constructed using (2.17) and the boundary condition (2.14b) on  $\mathcal{B}(x)$ . This, of course, assumes implicitly that all waves radiate outwards. Once  $\Phi$  is assumed to be approximated by  $\Phi^{2D}$ , added mass and damping can be calculated, and they are dependent on  $U$  only through the body boundary condition (2.14b). In most strip theories, say STF (1970), the effects due to the steady-state forward-motion potential  $\Phi_s$  in (2.15b,c) are neglected. STF (1970) obtained the wave exciting forces by applying Khaskind's (1957) relation in a two-dimensional fashion for each section. The strip theory as described does not have any three-dimensional effects representing interactions between sections nor any forward-speed effects on the free-surface condition. It is known to be incorrect in the low-frequency limit. However, since the hydrostatic components of the body and wave forces dominate in this limit, the errors due to the hydrodynamic effects are fortunately not disastrous.

### Rational Strip Theory of O&T (1969)

Ogilvie & Tuck devised a rather rational procedure of examining the approximation involved in the strip theories of 60's. The result of some of their analysis was somewhat incorporated (in part) in the STF theory. However, it is a very distinct theory by itself. Starting with the assumption that  $\omega = O(\epsilon^{-1/2})$ ,  $U = O(1)$ , Ogilvie & Tuck noted that the two terms in the body condition (2.14b) are of order  $\epsilon^{-1/2}$  and 1 respectively. Or equivalently,  $\Phi$  was expected to be a power series of increasing order  $\epsilon^{1/2}$ , with the leading term being  $\epsilon^{1/2}$  (since  $\partial/\partial N = O(1/\epsilon)$ ). Accordingly,  $\Phi$  might be decomposed as:

$$\Phi(y,z;x) = \Phi^0(y,z;x) + \hat{\Phi} + \tilde{\Phi} \quad (2.18)$$

with the body boundary condition being

$$\Phi_N^0 = i\omega N_j, \quad \hat{\Phi}_N = U m_j, \quad \tilde{\Phi}_N = 0 \quad (2.19)$$

Here the term  $\tilde{\Phi}$  was introduced to account for possible higher order effects on the free surface, and  $\Phi^{2D} = \Phi^0 + \hat{\Phi}$  is the usual strip solution. Ogilvie & Tuck proceeded to examine the non-linear free surface condition (2.5) systematically. The first two orders of their analysis may be recovered from (2.7) by keeping the  $i\omega U \partial/\partial x$  terms and discarding the  $U^2 \partial^2/\partial x^2$  ones. The result is:

$$-\omega^2\Phi_j + g\Phi_{jz} = 2i\omega U \left[ \Phi_{jx} - \Phi_j \Phi_{sy} - \frac{1}{2} \Phi_j \Phi_{syy} \right], \quad \text{on } z = 0, \quad j \neq s \quad (2.20)$$

which is obtained with the additional assumption that  $\Phi_s$  satisfies a rigid free-surface condition,  $(\Phi_s)_z = 0$ .

Thus (2.20) is basically the same form as (2.17) except that it is non-homogeneous. In a systematic perturbation procedure, the right-hand side of (2.20) would be treated as higher order with  $\Phi_j$  replaced by  $\Phi^0$ . Hence, the homogeneous solution of (2.20) yields a strip solution  $\Phi^{2D}$  no different from that of the STF theory discussed earlier. The added-mass and damping expressions, however, differ since the O&T theory ignores  $U^2$  terms relative to those of  $i\omega U$ . Ogilvie also very skillfully solved the pressure distribution problem associated with  $\tilde{\Phi}$ , which represents the leading-order forward-speed correction of the free-surface condition that was ignored in almost all previous strip theories. The final results were simplified rather remarkably. The heave/pitch coupling added-mass and damping are modified from those of the strip theory by the addition of two line-integrals on the free surface that are quadratic quantities in  $\Phi^0$ . These were calculated by Faltinsen (1974) for a number of practical hulls and were found to provide sizable improvement over the predictions of conventional strip theory when compared with experimental values.

Ogilvie & Tuck's analyses shed much light on the effect of forward-speed on the free-surface condition. However, since it was decided at the outset that the inner problem should take a form similar to that of the strip theory, the effects of forward speed can only occur as higher order. Since these effects were found to be significant, it seems questionable to transpose the convective terms of the free-surface condition to the right-hand side of (2.17).

### The Unified Theory of Ship Motions

In his review paper of 1978, Newman proposed a unified theory that improves the popular strip theory, say of STF, in the high-frequency regime and reduces to the ordinary slender-body theory in the low-frequency limit. It was not recognized until that point that the free-surface condition (2.17) and the boundary condition (2.14b) could have homogeneous solutions. The following form of the inner solution was proposed:

$$\Phi(y,z;x) = \Phi^{2D}(y,z;x) + C(x)(\Phi^0 + \overline{\Phi^0}) \quad (2.21)$$

where the over-bar indicates the complex conjugate with respect to the imaginary number associated with time,  $i$ , and the function  $C(x)$  contains longitudinal interaction effects. By analyzing the nearfield behavior of the three-dimensional Green function satisfying the conditions (2.8,a,b,&d), and matching with the

outer behavior of the inner potential  $\Phi$ , Newman obtained an integral equation for  $C(x)$ . Once  $C(x)$  is solved, (2.21) is known completely.

In this theory, the inner and outer wave fields are compatible for the case of zero forward speed. Very impressive results were obtained by Mays (1978) who compared his calculations with actual three-dimensional solutions for bodies of beam to length ratio as large as 1/4, and for a wide range of frequencies. For the case of forward speed, since the inner solution of the form (2.21) is still basically one corresponding to a single wave length, it is not compatible with waves generated in a three-dimensional flow with forward speed. This difficulty showed up in Newman's (1978) matching procedure when some of the wave components from the outer approximation were forced to be the same wave length as those from the inner problem. It would seem that the three-dimensional flow should dictate the inner behavior rather than be dictated by the inner flow. This difficulty cannot be easily rectified in Newman's formulation since the inner region is assumed to be non speed-dependent to start with. The diffraction problem was pursued by Sclavounos (1981).

#### The Forward-Speed Theory of Yeung & Kim

Yeung & Kim (1981) presented a slender-ship theory which included all of the forward-speed terms in (2.11). The interpretation of a term like  $U\partial/\partial x$  in a two-dimensional problem was not intuitively obvious. They introduced a "pseudo-time" variable

$$t^* = -(x-L/2)/U, \quad (2.22)$$

which represents the time for a fluid particle to be convected downstream from the bow. By rewriting

$$\Phi(y,z;x) = e^{-i\omega t^*} \phi_o(y,z;t^*) \quad (2.23)$$

they showed that the "pseudo-time" potential  $\phi_o$  satisfies

$$\nabla_{2D}^2 \phi_o(y,z;t^*) = 0 \quad \text{for } z < 0 \quad (2.24a)$$

$$\phi_{ot^*} + g\phi_{oz} = 0 \quad \text{on } z = 0 \quad (2.24b)$$

$$\phi_{oN} = e^{i\omega t^*} V_N(y,z;x(t^*)) \quad \text{on } \mathcal{B}(t^*) \quad (2.24c)$$

(2.24) now defines a two-dimensional time-dependent problem on a boundary contour that changes in time. The numerical solution of these equations are considerably harder than those of conventional strip theory, but is still fairly manageable by today's computational standards, provided the initial conditions

are specified. Yeung & Kim assumed that both potential and the free-surface elevation vanish ahead of the bow. The resulting one dimensional integral equation was solved time-wise in the downstream direction.

This theory has only quasi-three-dimensional effects. The downstream sections experience a wave field generated by all the upstream ones, but not vice versa. At its worst, one would expect it to do better than conventional strip theory, since both contain no genuine three-dimensional interactions. However, the pseudo-time formulation contains convective effects on the free-surface and diffraction effects on the hull that are glaringly absent in strip theory. Further, in the limit of  $U \rightarrow 0$ , it is not difficult to show that each section achieves its steady-state time-harmonic solution as those of strip theory at zero speed. Regular strip theory at zero speed is thus recovered as a special case. One may therefore consider this to be a general "forward-speed strip theory". Numerical results presented in Yeung & Kim (1981) seemed to confirm this. The improvements over strip-theory results in the hydrodynamic coupling coefficients of heave and pitch were particularly striking for a number of realistic hull forms. Loeser et al. (1982) followed the Yeung & Kim formulation but used a different numerical method to solve the inner problem. Their calculations for a spheroid submerged under a free surface agreed well with an approximate three-dimensional theory of Newman (1961). Their numerical results for a surface piercing body were however invalid since some important contributions arising from the intersection of the hull and the free surface were ignored.

In spite of the rather encouraging results of this new "pseudo-time theory", questions remain on the validity of imposing a zero-disturbance condition ahead of the bow. In fact, it is known for  $\tau = \omega U/g < 1/4$ , that transverse waves exist ahead of a pulsating and oscillating source. This suggests, therefore, a certain degree of upstream influence would exist. A careful examination of the numerical results of Yeung & Kim (1981) indicates that for a given  $U$ , the quality of the prediction appears to worsen as the frequency decreases below  $\tau = 1/4$ .

To acquire some additional insight of the difficulty involved, let's consider the wave patterns generated by a three-dimensional pulsating and translating source satisfying (2.8a,b,d). The overall results are charted in Figure 3, where the critical frequency  $\tau = 1/4$  marks the boundary between two fundamentally different sets of wave patterns. This is reproduced from Becker (1958) for clarity. The wave numbers associated with these wave systems near the x-axis can be obtained by stationary phase analyses. It is not difficult to arrive

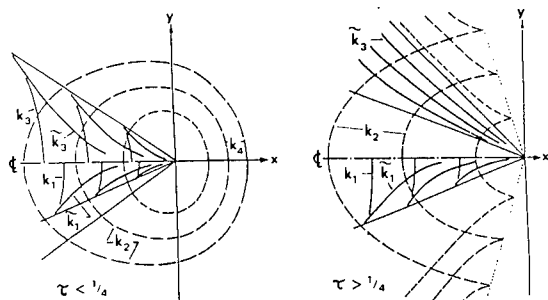


Figure 3. Wave patterns due to a pulsating and translating source.

at the following results:

$$k_{1,2} = -\frac{K_0}{2}[1 + 2\tau \pm (1 + 4\tau)^{1/2}] \quad \text{for } \tau > 0 \quad (2.25a)$$

$$k_{3,4} = \frac{K_0}{2}[1 - 2\tau \mp (1 + 4\tau)^{1/2}] \quad \text{for } 0 \leq \tau \leq 1/4$$

$$\tilde{k}_{1,3} = \mp \frac{K_0 x^2}{4y^2} + \frac{\omega x}{U|y|} \quad \text{for } \tau > 0 \quad (2.25b)$$

where the  $k_i$ ,  $i=1..4$ , represent transverse waves, and  $\tilde{k}_{1,3}$  divergent waves. Thus, in general there are 4 to 6 wave patterns, depending on  $\tau$ , radiating mostly downstream, and athwartship, but occasionally also upstream (for  $\tau < 1/4$ ). The pseudo-time solution can represent the presence of divergent waves,  $\tilde{k}_{1,3}$  but not any of the disturbances associated with transverse waves. The flow model cannot be considered complete unless these waves and their diffraction effects along the hull are properly accounted for. In the same context, all of the foregoing inner approximations that utilize a strip-theory type solution cannot be made compatible to this maze of wave patterns in the presence of forward speed.

### 3. INNER AND OUTER GREEN FUNCTIONS

In order to construct the solution of the inner problem (2.10-2.13) that satisfies the complete linearized free-surface condition, it is instructive to examine the behavior of the outer Green function and certain inner Green functions. The following definition of Fourier-transform pair in the  $x$ -direction will be used:

$$A^*(k) = \int_{-\infty}^{\infty} dx A(x) e^{ikx} \quad (3.1a)$$

$$A(x) = \frac{1}{2\pi} \int_{-\infty}^{\infty} dk A^*(k) e^{-ikx} \quad (3.1b)$$

### 3.1 Inner Green Functions

Consider a pair of Green functions associated with the inner problem (2.10-2.13) that satisfy the following conditions:

$$\nabla_{y,z}^2 G^{\pm}(y,z,\eta,\zeta;x,\xi) = \delta(x-\xi)\delta(y-\eta)\delta(z-\zeta), \quad \text{for } z < 0 \quad (3.2)$$

$$(\pm i\omega \mp U \frac{\partial}{\partial x} + \mu)^2 G^{\pm} + gG_z^{\pm} = 0 \quad \text{on } z = 0, \mu \rightarrow 0^+ \quad (3.3)$$

where  $\delta$  is the Dirac delta function. The superscript "+" case corresponds directly to the problem defined by (2.10-13). The "-" case corresponds physically to a reverse-time, reverse-flow problem which, though may seem artificial at the moment, is intimately related to the absence of a strict definition of  $\mu$  in the entire inner problem (see 2.11). Our introduction of  $\mu$  in (3.3) requires the consideration of the "-" case. The exact role played by  $G^-$  will be explained momentarily.

To define  $G^{\pm}$  completely, we need to introduce the following "initial" conditions corresponding to vanishing motion upstream of the source ( $x > \xi$ ) and downstream of the source ( $x < \xi$ ) for the  $\pm$  cases, respectively:

$$G^{\pm}(y,0,\eta,\zeta;x-\xi) = 0, \quad \text{for } \begin{matrix} x \geq \xi \\ x \leq \xi \end{matrix} \quad (3.4)$$

We write  $G^{\pm}$  as:

$$G^{\pm} = \frac{\delta(x-\xi)}{2\pi} \ln(R/R_1) + H^{\pm}(y,z,y,\zeta;x-\xi), \quad (3.5)$$

where

$$\begin{aligned} R &= [(y-\eta)^2 + (z-\zeta)^2]^{1/2}, \\ R_1 &= [(y-\eta)^2 + (z+\zeta)^2]^{1/2}. \end{aligned} \quad (3.6)$$

The first term of (3.5) satisfies (3.2) and the harmonic function  $H^{\pm}$  can be determined by using Fourier transform to satisfy (3.3). The final expressions are given by:

$$\begin{aligned} G^{\pm} &= \frac{\delta(x-\xi)}{2\pi} \ln(R/R_1) + \frac{K_0}{\pi} u[\mp(x-\xi)] e^{i\omega(x-\xi)/U} \times \\ &\quad \int_0^{\infty} \frac{d\ell}{\sqrt{K_0\ell}} e^{\ell(z+\zeta)} \cos \ell(y-\eta) \sin \sqrt{K_0\ell}(x-\xi), \end{aligned} \quad (3.7)$$

where  $u[x]$  is the Heaviside function. It is easy to recognize that  $G^+$  is simply the two-dimensional time-dependent Green function that satisfies homogeneous initial conditions and has the usual "time" variable  $\tau$  replaced by  $(\xi-x)/U$  (see Yeung & Kim, 1981). In fact, the pseudo-time inner solution  $\Phi$  associated with the pseudo-time problem in (2.23) can be con-

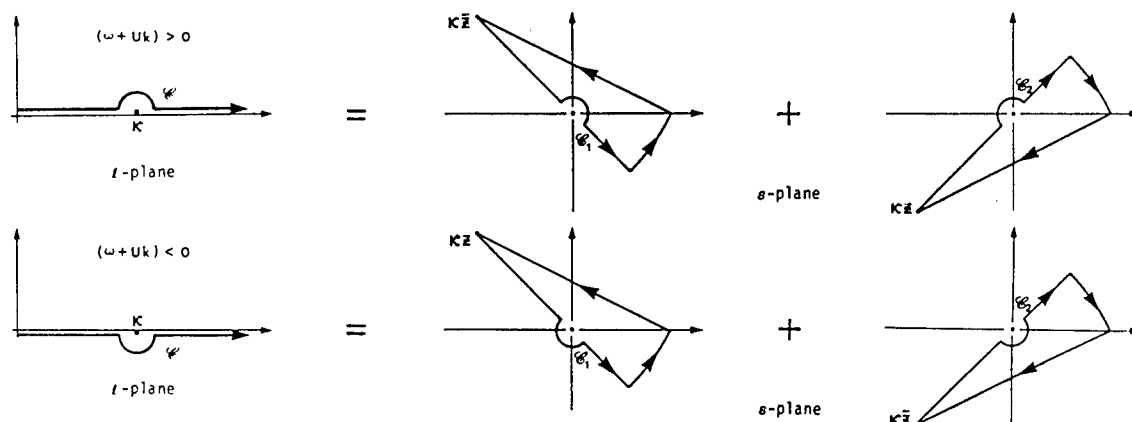


Figure 4. Path integrals for  $G^*$ .

constructed directly from  $G^+$ . We will refer to (3.7) as the pseudo-time forward-flow and reverse-flow Green functions.

Returning now to the original inner problem (2.10-13), we will introduce a generalized inner Green function  $G^{(i)}$  defined by:

$$G^{(i)}(y, z, \eta, \zeta; x - \xi) = G^+ + E(y, z, \eta, \zeta; x - \xi) \quad (3.8a)$$

$$= \frac{\delta(x - \xi)}{2\pi} \ln R/R_1 + H^+ + E \quad (3.8b)$$

where  $E$  is an unknown harmonic function in  $(y, z)$ . The determination of  $E$  is non-trivial since it must satisfy the speed-dependent free-surface condition (2.11). A moment of reflection on the integral representation (3.7) of  $G^+$  will show that its point of stationary phase (cf. Copson, 1965) occurs at:

$$\sqrt{l} = -\sqrt{K_0} x/2y.$$

This yields waves of the form

$$H^+ \sim \left(\frac{4\pi}{K_0 y}\right)^{1/2} \exp\left\{\frac{K_0 x^2}{4y^2}(z + \zeta)\right\} e^{i\omega(x - \xi)/U} \sin\left(\frac{K_0 x^2}{4y} - \frac{\pi}{4}\right) \quad (3.9)$$

which corresponds to the divergent waves of (2.25b). Thus, the function  $E$  is introduced here to account for other disturbances that may be present, including those that would eventually become transverse waves at sufficiently large longitudinal distance from the source.

#### Asymptotic Behaviour of Inner Green Functions

In developing expressions for the far-field behavior of  $G^\pm$ , we assume in this section that the source is located on the  $x$ -axis; i.e.  $\eta = \zeta = 0$ . For simplicity, we therefore introduce the notation:

$$G^\pm(y, z; x) \equiv G^\pm(y, z, 0, 0; x) = H^\pm \quad (3.10)$$

Furthermore, we define:

$$\bar{z} = z + i|y| = -Re^{-i\theta} \quad (3.11)$$

$$\kappa = (\omega + Uk)^2/g \quad (3.12)$$

It is convenient to work with the Fourier space rather than  $x$  directly. The Fourier transforms of  $G^\pm$  are given by contour integrals in the complex  $l$ -plane as follows:

$$G^{\pm*}(y, z; k) = -\frac{1}{\pi} \int_0^\infty dl \frac{e^{lz} \cos ly}{l - (\omega + Uk \mp i\mu)^2/g}, \quad \mu \rightarrow 0^+. \quad (3.13)$$

Note that  $\overline{G^{-*}} = G^{+*}$ . Thus, it is only necessary to consider, say,  $G^{+*}$ . Introducing the complex representation for  $\cos ly$ , we can deform the contour integral  $\mathcal{C}$  in the  $l$ -plane into two contours,  $\mathcal{C}_1$  and  $\mathcal{C}_2$ , in the  $s$ -plane, where  $s = (\kappa - l)\bar{z}$  or  $(\kappa - l)\bar{z}$ . The actual paths depend on the sign of  $\omega + Uk$  (see Figure 4). Applying the Residue theorem, it is relatively easy to show that

$$G^{+*} = -\frac{1}{\pi} \operatorname{Re} \{ e^{\kappa(z+i y)} E_1[\kappa(z+i y)] \} + i \operatorname{sgn}(\omega + Uk) \exp\{\kappa[z - i|y| \operatorname{sgn}(\omega + Uk)]\} \quad (3.14)$$

where  $E_1(\Omega)$  is the exponential integral defined in Abramowitz and Stegun (1964):

$$E_1(\Omega) = \int_\Omega^\infty \frac{e^{-s}}{s} ds, \quad \arg \Omega < \pi \quad (3.15)$$

The asymptotic properties of  $G^{\pm*}$  can be readily obtained by using known expansions of the exponential integral. For small values of  $\kappa R$ ,

$$G^{\pm*}(y, z; k) = \frac{1}{\pi} (1 + \kappa z) [\ln \kappa R + \gamma \pm \pi i \operatorname{sgn}(\omega + Uk) - \kappa z + \kappa y \theta] + O(\kappa^2 R^2) \quad (3.16)$$



where  $\gamma$  is Euler's constant. For large values of  $\kappa R$ , we obtain:

$$G^{\pm*}(y, z; k) = \pm \text{sgn}(\omega + Uk) \exp\{\kappa[z \mp i|y| \text{sgn}(\omega + Uk)]\} + \frac{\cos \theta}{\pi \kappa R} + O((\kappa R)^{-2}) \quad (3.17)$$

### 3.2 The Outer Green Function

In view of the boundary condition (2.8c), we expect the velocity potential,  $\phi_j$ ,  $j=s, 3$ , or 5 to be defined by line distribution of "sources" on the  $x$ -axis:

$$\phi_j = \int_{-\infty}^{\infty} d\xi q_j(\xi) G^{(o)}(x-\xi, y, z) \quad (3.18)$$

where  $q_j(\xi)$  is the unknown source strength, and  $G^{(o)}$  the outer Green function. Effects of forward motion make it unclear that  $q_j(\xi)$  should vanish immediately outside of the ship length  $x = [-L/2, L/2]$ . Thus, we make no a priori assumption on the limits of the integration. The outer Green function  $G^{(o)}$  satisfying (2.8a,b,d) and located on the free surface can be found in Wehausen & Laitone (1960):

$$G^{(o)}(x, y, z) = \frac{-1}{4\pi^2} \int_{-\infty}^{\infty} dk \int_{-\infty}^{\infty} d\ell \frac{e^{(k^2 + \ell^2)^{1/2} z - i(kx + \ell y)}}{(k^2 + \ell^2)^{1/2} - (\omega + Uk - i\mu)^2/g} \quad \mu \rightarrow 0^+ \quad (3.19)$$

Its Fourier transform  $G^{(o)*}$  is given by:

$$G^{(o)*}(y, z; k) = -\frac{1}{\pi} \int_0^{\infty} d\ell \frac{\exp[(k^2 + \ell^2)^{1/2} z] \cos \ell y}{(k^2 + \ell^2)^{1/2} - (\omega + Uk - i\mu)^2/g} \quad (3.20)$$

We need an inner expansion of (3.20) for small values of  $R = (y^2 + z^2)^{1/2}$ . Similar expansions have been studied by Ursell (1962) for  $U=0$ , and Newman (1978) for  $U \neq 0$ . It is necessary to make a distinction of the order of magnitude of  $\omega$  and  $U$ , thus  $\kappa$ , in constructing these expansions. If both  $\omega$  and  $U$  are  $O(1)$ ,  $\kappa R$  can be considered small. If  $U=O(1)$  but  $\omega \gg 1$ , for  $R \ll 1$ , a separate expansion is necessary. This can be carried out by using a procedure similar to Ogilvie & Tuck (1969). A more detailed discussion of this can be found in Kim (1982). The asymptotic analysis yields the following results for  $R \ll 1$ :

$$G^{(o)*} = \frac{(1+\kappa z)}{\pi} \left[ \frac{\pi i \text{sgn}(\omega + Uk) + \alpha}{\alpha' - \pi} \right] |1 - k^2/\kappa^2|^{1/2} + \gamma + \ln \frac{|k|R}{2} - \kappa z + \kappa y \theta + O(k^2 R^2, \kappa^2 R^2) \quad \text{for } \kappa R \ll 1 \quad (3.21a)$$

$$G^{(o)*} = i \text{sgn}(\omega + Uk) \exp[\kappa(z - i|y| \text{sgn}(\omega + Uk))] + \frac{\cos \theta}{\pi \kappa R} + O(k^2/\kappa^2, k^2 y/\kappa, (\kappa y)^{-2}) \quad \text{for } \kappa R \gg 1 \quad (3.21b)$$

Here the quantities  $\alpha$  and  $\alpha'$  are defined by:

$$\alpha = \cosh^{-1}(\kappa/|k|), \quad \alpha' = \cos^{-1}(\kappa/|k|), \quad (3.21c)$$

for  $\kappa/|k| > 1$  and  $\kappa/|k| < 1$ , respectively.

These expressions can now be used to match the inner and outer Green functions in Fourier space. First, comparing (3.21b) & (3.17) we obtain:

$$G^{(o)*} = G^{+*} + O(k^2/\kappa^2, k^2 y/\kappa, (\kappa y)^{-2}) \quad (3.22)$$

which states that the pseudo-time forward-flow potential is compatible with the three-dimensional flow at high frequencies. If the expansion (3.16) of  $G^{+*}$  is now introduced into (3.21a) the resulting expression can be rearranged to deduce the following:

$$G^{(o)*} = G^{+*} - \frac{f^*(k, \kappa)}{2\pi i} [G^{+-} - G^{-}]^* + O(k^2 R^2, \kappa^2 R^2) \equiv G^{+*} + F^*(y, z; k) + O(k^2 R^2, \kappa^2 R^2) \quad (3.23)$$

where the 'modulation' function  $f^*$  in the Fourier space is given by:

$$f^*(k, \kappa) = - \left\{ \begin{array}{l} \pi i + \text{sgn}(\omega + Uk) \cosh^{-1}(\kappa/|k|) \\ [-\pi + \cos^{-1}(\kappa/|k|)] \text{sgn}(\omega + Uk) \end{array} \right\} |1 - k^2/\kappa^2|^{1/2} + \text{sgn}(\omega + Uk) \times \ln(2\kappa/|k|) + \pi i \quad (3.24)$$

with the top and bottom expression in  $\{ \}$  corresponding to  $\kappa/|k| > 1$  and  $< 1$  respectively. For large values of  $k/\kappa$ , it is straightforward to show that the expression for  $f^* \sim O(k^2/\kappa^2)$  and  $[G^{+-} - G^{-}]^* \sim O(1)$ . Thus, to the order of accuracy indicated in (3.22), we may consider (3.23) as the general expression for arbitrary  $\kappa$ . It is interesting that disturbances other than those associated with the divergent wave system  $G^{+}$  can be constructed by superposing the forward-flow and reverse-flow pseudo-time Green functions and convolving their difference by a wave function that depends only on the longitudinal coordinate.

Equation (3.23) is one of the principal results of our theory. If we recall the definition of the generalized inner Green function (3.8), we see that the missing waves described by  $E$  are now defined by  $F$ . More specifically,

$$E^*(y, z, \eta, \zeta; x - \xi) = F^* \\ = \frac{-f^*(k, \kappa)}{2\pi i} [G^+ - G^-]^* \quad (3.25)$$

$$G^{(1)} = G^+ + F, \quad F = \begin{cases} O(1) & \text{for } \nu R \ll 1 \\ O((\nu R)^{-2}) & \text{for } \nu R \gg 1 \end{cases} \quad (3.26)$$

$$(3.27)$$

where  $F$  is the inverse Fourier transform of (3.25). A more detailed description of the error in physical space can be found in Kim & Yeung (1984). As defined by (3.26),  $G^{(1)}$  contains all of the essential features in a three-dimensional flow near the hull. The vanishing of  $F$  for  $\omega \gg 1$  indicates that the pseudo-time theory of Yeung & Kim (1981) discussed in § 2 is the appropriate approximation in the presence of forward speed, but not one based on the time-harmonic strip solution.

#### 4. THE GENERALIZED INNER GREEN FUNCTION AND THE NEW INNER SOLUTION

With the function  $F$  now explicitly given by (3.23) and (3.24), we can proceed to construct the inner solution. However it is worthwhile to examine and simplify  $F$  further. The pseudo-time forward-flow potential  $G^+$  has already been studied and used extensively in Yeung (1981), and Yeung & Kim (1981). We focus most of our attention here on  $F$ .

##### 4.1 Properties and Expressions of $F$

Because of the various approximations used in arriving at  $F$ , it is not immediately obvious that  $F$  satisfies the two-dimensional Laplace equation and the complete speed-dependant linearized free-surface condition (2.11). It is only necessary to show this in Fourier space. (2.10) and (2.11) require that

$$\nabla_{y,z}^2 F^*(y, z; k) = 0 \quad (4.1)$$

$$(\omega + Uk)^2 F^* - g F_z^* = 0 \quad (4.2)$$

However, by definition,

$$F^* = \frac{-f^*(k, \kappa)}{2\pi i} [G^{+*} - G^{-*}] \quad (4.3)$$

where the bracketed term itself satisfies (4.1) and (4.2) by design. Hence,  $F^*$  clearly satisfies (4.1), and also (4.2) upon noting that  $f_z^* = 0$ . This is a rather remarkable property of our new kernel function.

The exact expression of  $F(y, z; x)$ , or  $E(y, z; x)$  in (3.8), is

$$F(y, z; x) = \frac{-1}{2\pi^2} \int_{-\infty}^{\infty} dk e^{-ikx} D(k, \tau) e^{kz} \cos ky, \quad (4.4)$$

where, according to (3.24),  $D(k, \tau)$  is given by:

$$D(k, \tau) = \text{sgn}(\omega + Uk) f^*(k, \kappa) \quad (4.5)$$

with

$$\tau = \omega U / g, \quad \kappa = (\omega + Uk)^2 / g = K_0(\tau + k/K_0)^2 \quad (4.6a, b)$$

The complicated expression of (4.5) makes the evaluation of  $F$  a non-trivial task. In considering a related integral in the unified theory with forward speed, Sclavounos (1981) devised a clever way of evaluating (4.4) for the case of  $y=z=0$ . His procedure was generalized by Kim (1982) to include the factor of  $\exp(\kappa z) \cos(ky)$ . The analysis was quite lengthy, and only the final results, which are considerably simpler than (4.4) and (4.5), are reported below. First, we define the following wave function:

$$w(kx, \kappa y, \kappa z) = e^{-ikx} e^{kz} \cos ky \quad (4.7)$$

Then  $F(y, z; x)$  can be written as:

$$F(y, z; x) = \begin{cases} F_1(y, z; x) + F_2(y, z; x), & x < 0 \\ F_2(y, z; x), & x > 0 \end{cases} \quad (4.8)$$

where

$$F_1(y, z; x) = \frac{i}{\pi} \left[ \int_{-\infty}^{k'_1} - \int_{k'_2}^0 \right] dk w \left\{ 1 - \left[ 1 - \frac{k^2}{\kappa^2} \right]^{-1/2} \right\}, \\ + \frac{i}{\pi} \left[ \int_{k'_1}^{\omega/U} - \int_{-\omega/U}^{k'_2} \right] dk w; \quad \tau > 0 \quad (4.9)$$

$$F_2(y, z; x) = \frac{-i}{2\pi} \left[ \int_0^{k'_3} + \int_{k'_4}^{\infty} \right] dk w \left\{ 1 - \left[ 1 - \frac{k^2}{\kappa^2} \right]^{-1/2} \right\} \\ - \frac{i}{2\pi} \int_{k'_3}^{k'_4} dk w \left\{ 1 - \left[ \frac{k^2}{\kappa^2} - 1 \right]^{-1/2} \right\},$$

$$0 < \tau < 1/4 \quad (4.10a)$$

$$F_2(y, z; x) = \frac{-i}{2\pi} \int_0^{\infty} dk w \left\{ 1 - \left[ 1 - \frac{k^2}{\kappa^2} \right]^{-1/2} \right\}, \\ \tau > 1/4 \quad (4.10b)$$

Here, the limits of integration are given by the equation

$$(\omega + Uk'_1)^4/g^2 = k'^2_1, \quad i = 1, \dots, 4 \quad (4.11)$$

Or equivalently,

$$k'_{1,2} = -\frac{K}{2} \{1 + 2\tau \pm (1 + 4\tau)^{1/2}\}, \quad \tau > 0 \quad (4.12)$$

$$k'_{3,4} = \frac{K}{2} \begin{cases} 1 - 2\tau \mp (1 - 4\tau)^{1/2}, & 0 < \tau < 1/4 \\ 1 - 2\tau \mp i(4\tau - 1)^{1/2}, & \tau > 1/4 \end{cases} \quad (4.13a,b)$$

The expressions given by (4.8-4.10) are easily one order of magnitude simpler than the original three-dimensional Green function (3.19), thus making it worthwhile to pursue a slender-body theory.

Finally, it is noteworthy that the wave numbers given by (4.12) and (4.13a) are precisely the same as those associated with the transverse waves noted in §2, Eq. (2.25a). To see this, one simply has to observe that the function  $F(0, z; x \ll -1)$  is, to leading order, sinusoids with  $k$  evaluated at the limits of integration  $k'_i$ . However,  $F$  contains more information than these transverse waves since it describes completely how the disturbances would vary for  $x=0(1)$  and for  $y$  not directly on the track of the source function, all with the effects of forward speed included!

#### 4.2. The Inner Solution

The new inner solution differs, in principle, from that of Yeung & Kim (1981) only by the additional term  $F$  in the inner Green function. The procedure for constructing  $\Phi$  is the same. Let's apply Green's second identity in a sectional plane (see Figure 5) to the inner potential  $\Phi(Q; \xi)$  and the generalized inner Green function  $G^{(1)}(P, Q, x - \xi)$ , the latter given

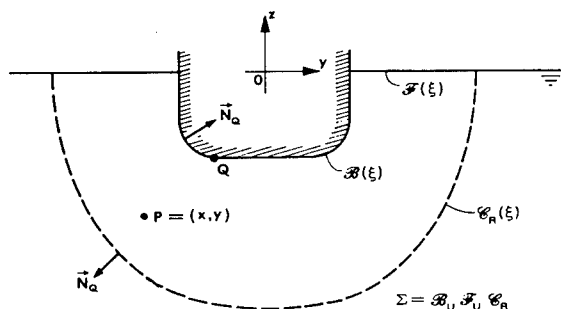


Figure 5. Domain of application of Green's Theorem at section  $\xi$ .

by (3.26), (3.7), and (4.4). Let  $P=(x, y)$ ,  $Q=(\xi, \eta)$ . The boundary contour consists of the body contour  $B(\xi)$ , the linearized free surface  $B_R(\xi)$  and a large contour at infinity  $C_R(\xi)$ . The result is given by

$$\delta(x - \xi)\Phi(P; \xi) = \int_{B(\xi) + B_R(\xi) + C_R(\xi)} ds_Q \left[ \Phi(Q; \xi) \frac{\partial}{\partial N_Q} - \Phi_N \right] G^{(1)}(P, Q; x - \xi) \quad (4.14)$$

The contribution from  $C_R(\xi)$  can be shown to vanish. Integration with respect to  $\xi$  from  $[-L/2, L/2]$  then yields

$$\begin{aligned} \Phi(P; x) &= \frac{1}{2\pi} \int_{B(x)} ds_Q \left[ \Phi(Q; x) \frac{\partial}{\partial N} - \Phi_N \right] \ln(R/R_1) \\ &+ \int_{-L/2}^{L/2} d\xi \int_{B(\xi)} ds_Q \left[ \Phi(Q; \xi) \frac{\partial}{\partial N} - \Phi_N \right] [H^+(P; Q, x - \xi) + F] \\ &- \frac{U^2}{g} \oint_{\mathcal{C}} \left[ \Phi(Q; \xi) \frac{\partial}{\partial \xi} - \Phi_\xi + \frac{2i\omega}{U} \Phi \right] [H^+ + F] d\eta, \end{aligned} \quad (4.15)$$

$P \notin Q$

where  $\mathcal{C}$  is a clockwise contour representing the intersection of the hull and the plane  $z=0$ . In arriving at (4.15), we have made use of the fact that both  $\Phi$  and  $G^{(1)}$  satisfy the complete linearized free-surface condition (2.11) on  $\mathcal{F}$ . Thus,

$$\begin{aligned} \left( \Phi \frac{\partial}{\partial \xi} - \Phi_\xi \right) G^{(1)} \Big|_{\xi=0} &= -\frac{U^2}{g} \frac{\partial}{\partial \xi} \left[ \left( \Phi \frac{\partial}{\partial \xi} - \Phi_\xi + \frac{2i\omega}{U} \Phi \right) G^{(1)} \right] \end{aligned} \quad (4.16)$$

which reduces to the line integral over  $\mathcal{C}$  after taking advantage of Stoke's Theorem and assuming vanishing motion at sufficiently large values of  $|x|$ . (4.15) was derived based on the assumption that  $P \notin B$ . If we let  $P$  approach  $B$ , the unity factor on the left hand side of (4.15) should be replaced by 1/2 for a smooth contour. This then yields an integral equation for  $\Phi$  on  $B(x)$ , since  $\Phi_N$  is given. Details on its numerical treatment have been discussed in Yeung & Kim (1981). We note that if  $F \rightarrow 0$ , the limit of integration for  $\xi$  reduces to  $\xi = [x, L/2]$ , because of the step function property of  $H^+$  in (3.7). This reduces to the pseudo-time slender-ship theory. In its most general form, our new theory states that full interaction among the various sections of the ship is to be expected unless  $F$  vanishes (which is the case when  $\omega \gg 1$ ). The type of interaction accounted for here is of an approximately three-dimensional kind that includes forward-speed

effects in the free-surface condition.

### 4.3. Effective Line-Source Distribution

One question remains to be settled in our new theory. The most general form of the solution obtained by solving (4.15) in the inner field involves a sectional contour distribution of our "generalized inner sources and dipoles" under the plane  $z=0$ . In matching the asymptotic behaviours of the inner and the outer Green functions in §3, we have made the assumption that the inner solution, as seen from the outer field, can be represented by a line distribution of sources on the free-surface. It is not obvious, for this new type of Green function, that a submerged distribution is always equivalent to a point singularity on the free surface. The equivalence relation is known only in time-harmonic zero-speed problems, but not for our case here.

To resolve this uncertainty, let's consider the following question. Suppose (4.15) is solved. We ask if it would be possible to find an equivalent distribution  $\sigma(x)$ , so that the wave field will be equivalent to those of (4.15) for large transverse distance  $R$ . The analysis of this problem is detailed in Kim & Yeung (1984). The answer to the question is "yes" and the equivalent source strength  $\sigma(x)$  turns out to be:

$$\begin{aligned} \sigma(x) = & \int_{-L/2}^{L/2} d\xi \int_{\mathcal{B}(\xi)} ds_Q [\Phi(Q;\xi) \frac{\partial}{\partial N} - \Phi_N] M(Q;x-\xi) \\ & - \frac{U^2}{g} \oint_{\mathcal{C}} d\eta [\Phi(\eta,0;\xi) - \Phi_\xi + \frac{2i\omega}{U} \Phi] M(\eta,0;x-\xi) \\ & - \infty < x < \infty \end{aligned} \quad (4.17)$$

where the weighting function  $M$  is given by:

$$\begin{aligned} M(\eta,\zeta;x-\xi) = & \frac{1}{2\pi} \int_{-\infty}^{\infty} dk e^{ik(x-\xi)} e^{k\zeta} \cos k\eta \\ = & \operatorname{Re}_j \left[ \frac{-K_0}{4\pi(\zeta+j\eta)} \right]^{1/2} \exp \left[ \frac{K_0(x-\xi)^2}{4(\zeta+j\eta)} \right] e^{i\omega(x-\xi)/U} \end{aligned} \quad (4.18)$$

The existence of the function  $\sigma(x)$  justifies our earlier assumptions. In fact, by (3.18),

$$\sigma(x) = q_j(x)$$

since the Green functions were matched by construction. Note that the distribution does not, in general, vanish outside of the part of  $x$ -axis occupied by the ship,  $|x| \leq L/2$ . This explains our choice of limits of integration in

(3.18). However, if we let  $U \rightarrow 0$ , it is possible to reduce (4.17) and (4.18) to a simpler form by using generalized functions. The result is:

$$\lim_{U \rightarrow 0} \sigma(x) = \begin{cases} \int_{\mathcal{B}(x)} ds_Q [\Phi(Q;x) \frac{\partial}{\partial N} - \Phi_N] e^{i\omega \zeta} \cos \eta \zeta & |x| < L/2 \\ 0 & |x| > L/2 \end{cases} \quad (4.19)$$

where  $\omega = \omega^2/g$ . These last two expressions are well known, but they are invalid in the presence of forward speed.

### 5. HYDRODYNAMIC PRESSURE AND FORCES

To obtain the hydrodynamic force acting on the hull, we use Euler's integral. Let  $\rho$  be the fluid density. After introducing the description (2.1) and neglecting terms of  $O(\phi_j^2)$ , we may write the linearized hydrodynamic pressure as:

$$p(\vec{x}) = -\rho \left\{ i\omega \xi_j \phi_j + \xi_j \vec{W} \cdot \nabla \phi_j + U^2 \frac{\partial \phi_j}{\partial x} + \frac{1}{2} \vec{\alpha} \cdot \nabla \vec{W}^2 \right\} \quad \text{on } \bar{S} \quad (5.1)$$

where  $\vec{W}$  was defined earlier by (2.2) and  $\vec{\alpha}$ , the vector displacement of the ship's wetted surface, is given by:

$$\vec{\alpha} = (z\xi_5, 0, \xi_3 - x\xi_5) \quad (5.2)$$

assuming only heave and pitch motions exist. The last term in (5.1) gives a force proportional to the unsteady displacement of the ship, and hence an additional buoyancy force to the hydrostatic restoring force. Since we are now interested in the linearized pressure forces associated with the wave-resistance, the added-mass, and the damping, we will use (5.1) without the last term.

Following the conventional definition of added-mass and damping coefficients, the unsteady hydrodynamic pressure  $p^{(u)}$ , can be written in the form:

$$\begin{aligned} F_i = & \iint_{\bar{S}} dS p^{(u)} n_i = -\rho \sum_j \xi_j \iint_{\bar{S}} dS (i\omega \phi_j + \vec{W} \cdot \nabla \phi_j) n_i \\ = & \omega^2 \sum_j \xi_j (a_{ij} + b_{ij}/i\omega) \quad , \quad i = 3,5 \quad j = 3,5 \end{aligned} \quad (5.3)$$

where the quantities  $a_{ij}$  and  $b_{ij}$  are the added-mass and damping coefficients associated with the force (moment) in the  $i$ -th direction due to the  $j$ -th mode of motion.

The wave-resistance of the ship is obtained by integrating the linearized steady part of the hydrodynamic pressure in (5.1):

$$R_w = - \iint_{\bar{S}} dS p(s) n_1 = \rho U^2 \iint_{\bar{S}} dS n_1 \frac{\partial \phi_s}{\partial x} \\ = (\rho U^2 L^2) \gamma_w \quad (5.4)$$

where  $\gamma_w$ , defined as  $\gamma_w = R_w / \rho U^2 L^2$ , is the nondimensional wave-resistance.

An alternative expression for  $F_i$ , which is convenient for simplifying the integrals (5.3) involving  $\vec{W}$ , can be obtained using Tuck's theorem (Ogilvie and Tuck, 1969):

$$\iint_{\bar{S}} dS (\vec{W} \cdot \nabla \phi) \vec{n} = \iint_{\bar{S}} dS \phi (\vec{n} \cdot \nabla) \vec{W} - \oint_{\mathcal{C}} (d\vec{\ell} \times \phi \vec{W}) \quad (5.5)$$

$$\iint_{\bar{S}} dS (\vec{W} \cdot \nabla \phi) (\vec{x} \times \vec{n}) = \iint_{\bar{S}} dS \phi (\vec{n} \cdot \nabla) (\vec{x} \times \vec{W}) \\ - \oint_{\mathcal{C}} (d\vec{\ell} \times \phi \vec{W}) \times \vec{x} \quad (5.6)$$

where  $d\vec{\ell}$  denotes the infinitesimal arc-length vector tangent to  $\mathcal{C}$  on the undisturbed free surface. We note that the line integrals in (5.5) and (5.6) may be ignored for a slender ship, for it is of higher order than the remaining surface integral by a relative order  $\epsilon$ . Thus, we obtain

$$a_{ij} + b_{ij} / i\omega = -(\rho / \omega^2) \iint_{\bar{S}} dS (i\omega n_1 - U m_1) \phi_j \quad (5.7)$$

Let  $\psi_j$  and  $\hat{\psi}_j$  be inner potentials determined by the numerical solution of (4.15), with the following hull boundary conditions on  $\mathcal{B}(x)$ :

$$\frac{\partial \psi_j}{\partial N} = n_j \quad (5.8a)$$

$$\frac{\partial \hat{\psi}_j}{\partial N} = m_j \quad (5.8b)$$

Then, in view of the boundary conditions (2.14b), the unsteady velocity potential can be expressed in the form,

$$\phi_j(\vec{x}) = i\omega \psi_j + U \hat{\psi}_j \quad (5.9)$$

Substituting (5.9) into (5.7), we obtain

$$a_{ij} + b_{ij} / i\omega = f_{ij}^{(1)} + f_{ij}^{(2)} + f_{ij}^{(3)} \quad (5.10)$$

with

$$f_{ij}^{(1)} \equiv \rho \iint_{\bar{S}} dS n_1 \psi_j \quad (5.11a)$$

$$f_{ij}^{(2)} \equiv \rho (U / i\omega) \iint_{\bar{S}} dS (n_1 \hat{\psi}_j - m_1 \psi_j) \quad (5.11b)$$

$$f_{ij}^{(3)} \equiv \rho (U / i\omega)^2 \iint_{\bar{S}} dS m_1 \hat{\psi}_j \quad \begin{matrix} i=3,5 \\ j=3,5 \end{matrix} \quad (5.11c)$$

Now the expressions in (5.10)-(5.11) will be discussed in more detail. From Green's theorem applied to  $\psi_i$  and  $\psi_j$ , with the boundary conditions (5.8), we can show that

$$0 = \int_{\Sigma(x)} dS (N_j \psi_i - N_i \psi_j) = \int_{\Sigma(x)} dS (\psi_i \psi_{jN} - \psi_j \psi_{iN}) \quad (5.12)$$

where the closed contour  $\Sigma(x)$  is the boundary of the simply connected domain shown in Figure 5,  $\mathcal{B}(x) + \mathcal{F}(x) + \mathcal{C}_R(x)$ . The integral over  $\mathcal{C}_R(x)$  vanishes if we let  $\mathcal{C}_R$  tend to infinity. Since both  $\psi_i$  and  $\psi_j$  satisfy the free-surface condition (2.11) it follows that

$$f_{ij}^{(1)} - f_{ji}^{(1)} = \rho \iint_{\bar{S}} dS (N_i \psi_j - N_j \psi_i) \\ = (\rho/g) \int_{-L/2}^{L/2} dx \int_{\mathcal{F}(x)} dy (U^2 \frac{\partial^2}{\partial x^2} - 2i\omega U) (\psi_j \psi_{ix} - \psi_i \psi_{jx}) \quad (5.13)$$

The integral over the free surface, in general, does not vanish. Since the velocity potential in the present theory retains a similar line integral (see equation (4.15)), a consequence of the complete linearized free-surface condition used in the formulation of the inner problem, we cannot justify the omission of this integral. By using a similar analysis to what we did above, we can also show that

$$f_{ij}^{(2)} - f_{ji}^{(2)} = \rho \int_{-L/2}^{L/2} dx \int_{\mathcal{F}(x)} dy (U^2 \frac{\partial^2}{\partial x^2} - 2i\omega U) \times \\ [\hat{\psi}_j \psi_{ix} - \psi_i \hat{\psi}_{jx} - \psi_j \hat{\psi}_{ix} + \hat{\psi}_i \psi_{jx}] \quad (5.14)$$

$$f_{ij}^{(3)} - f_{ji}^{(3)} = \rho \int_{-L/2}^{L/2} dx \int_{\mathcal{F}(x)} dy (U^2 \frac{\partial^2}{\partial x^2} - 2i\omega U) \times \\ [\hat{\psi}_j \hat{\psi}_{ix} - \hat{\psi}_i \hat{\psi}_{jx}] \quad (5.15)$$

If we had assumed the same approximations used in the derivation of the reverse-flow theorem of Timman and Newman (1962), we could have shown that

$$f_{ij}^{(1)+} = f_{ji}^{(1)-} \quad (5.16a)$$

$$f_{ij}^{(2)+} = f_{ji}^{(2)-} \quad (5.16b)$$

$$f_{ij}^{(3)+} = f_{ji}^{(3)-} \quad (5.16c)$$

where the superscript "+" denotes the direction of the forward velocity with time still taken in the forward sense. Since these approximations are not assumed in the present formulation, the applicability of the reverse-flow theorem to the present result is questionable.

In an intuitive approach, if the gradients of the steady-state disturbance velocity field are considered negligible, then the only non-zero element of  $m_j$  ( $j=3,5$ ) is  $m_5$ , which is identified to  $n_3$ . Thus it leads to  $\hat{\psi}_3=0$  and  $\hat{\psi}_5=\psi_3$ . With these simplifications in (5.10)-(5.11), we obtain

$$a_{33} + b_{33}/i\omega = f_{33}^{(1)} \quad (5.17a)$$

$$a_{53} + b_{53}/i\omega = f_{53}^{(1)} - (U/i\omega)f_{33}^{(1)} \quad (5.17b)$$

$$a_{35} + b_{35}/i\omega = f_{35}^{(1)} + (U/i\omega)f_{33}^{(1)} \quad (5.17c)$$

$$a_{55} + b_{55}/i\omega = f_{55}^{(1)} - (U/i\omega)[f_{35}^{(1)} - f_{53}^{(1)}] - (U/i\omega)^2 f_{33}^{(1)} \quad (5.17d)$$

These equations are 'structurally' very similar to the strip theory results for heave and pitch derived by Salvesen et al. (1970). But the coefficients  $f_{ij}^{(1)}$  in (5.17) are now three-dimensional ones which include the three-dimensional interactions, while those of the conventional theories are their corresponding two-dimensional values.

## 6. TWO ANALYTICAL LIMITS OF THE NEW THEORY

Two analytical limits of our theory will be discussed for the purposes of comparison with other existing ones. The first study corresponds to  $\omega \neq 0, U=0$ , the problem associated with a stationary slender body undergoing forced harmonic oscillation. The present theory reduces to the zero-speed case of Newman's (1978) unified theory, which is known to be consistent. The second study corresponds to  $\omega=0, U \neq 0$ . This is the well-known Neumann-Kelvin problem associated with the wave-resistance prediction of ships. Our theory yields a completely new slender-ship formulation for this problem. Since more details on the treatment of these limits are available in Kim &

Yeung (1984), we will not develop the equations in detail, and only the major results are summarized.

### 6.1 Stationary Ship In Forced Oscillations $\omega \neq 0, U=0$

We first recall that one of the key results developed here consists of a generalized inner Green function of the form given by (3.26). Alternatively, in Fourier space,

$$G^{(i)*}(y, z; \eta, \zeta; k) = G^{+*}(y, z; \eta, \zeta; k) - \frac{f^*(k, \kappa)}{2\pi i} [G^{+*} - G^{-*}] \quad (6.1)$$

where  $G^{\pm}$  are the pseudo-time forward- and reverse-flow potentials given by (3.7). If  $U$  is taken as zero, (3.5) and (3.13) yields

$$G^{+*}(y, z; \eta, \zeta; 0) = \frac{1}{2\pi} \ln R/R_1 + H^{+*}(y-\eta, z+\zeta; 0) \quad (6.2a)$$

$$= G_{2D}^{+}(y, z; \eta, \zeta) = G_{2D}^{+}(P; Q) \quad (6.2b)$$

where  $G_{2D}^{+}$  is the "standard" two-dimensional time-harmonic Green function satisfying an outgoing-wave radiation condition. In simple terms, the Fourier transform of the pseudo-time forward-flow Green function at zero longitudinal wave number is the two-dimensional time-harmonic source! Whence, we may write in the place of (6.1)

$$G^{(i)*}(y, z; \eta, \zeta; k) = G_{2D}^{+}(P, Q) - \frac{f^*(k, \nu)}{2\pi i} [G_{2D}^{+} - G_{2D}^{-}], \quad U=0, \quad (6.3)$$

where the combination  $G_{2D}^{+} - G_{2D}^{-}$  is given simply by

$$G_{2D}^{+} - G_{2D}^{-} = 2ie^{\nu z} \cos(\nu y) \quad (6.4)$$

Thus, the zero-speed generalized inner Green function in the context of our theory reduces to

$$G^{(i)} = \delta(x-\xi) \left[ \frac{1}{2\pi} \ln R/R_1 + H_{2D}^{+} \right] - \frac{f(x-\xi)}{2\pi i} [G_{2D}^{+} - G_{2D}^{-}] \quad (6.5)$$

with  $H_{2D}^{+}$  being the harmonic part of  $G_{2D}^{+}$ . Here, inversion of  $f^*(k, \nu)$  yields  $f(x-\xi)$  and the expression was given by Newman and Sclavounos (1981) as:

$$f(x) = \frac{1}{2} \left\{ \frac{1}{|x|} - \frac{\pi \nu}{2} [H_0(\nu x) + Y_0 + 2iJ_0] \right\} \quad (6.6)$$

where  $H_0, Y_0$ , and  $J_0$  are the Struve function, Bessel function of the second and first kind, all order zero, respectively.

The integral equation satisfied by the inner potential  $\Phi$ , according to (3.8b) and (4.15), is now given by:

$$\begin{aligned} \frac{1}{2}\Phi(P; x) = & \int_{\mathcal{B}(x)} ds_Q (\Phi(Q; x) \frac{\partial}{\partial N} - \Phi_N) G_{2D}^+(P, Q) \\ & - \frac{1}{2\pi i} \int_{-L/2}^{L/2} d\xi f(x-\xi) \int_{\mathcal{B}(\xi)} ds_Q (\Phi(Q; \xi) \frac{\partial}{\partial N} - \Phi_N) [G_{2D}^+ - G_{2D}^-] \\ & P \in \mathcal{B}(x) \end{aligned} \quad (6.7)$$

Note that the Green function  $G^\pm$  does not depend on  $x$  and the three-dimensional interaction effects are represented by  $f$  in the last term. Imbedded in this integral equation is the formulation of the unified theory. To see this, we can introduce the decomposition of Newman's (for  $U=0$ ) as given by (2.21):

$$\Phi(P, x) = \Phi^0 + C(x)(\Phi^0 + \bar{\Phi}^0) \quad (6.8)$$

where  $\Phi^0(x)$  is the strip solution at section  $x$  satisfying the integral equation:

$$\begin{aligned} \frac{1}{2}\Phi^0(P, x) = & \int_{\mathcal{B}(x)} ds_Q [\Phi^0(Q, x) \frac{\partial}{\partial N} - \Phi_N^0] G_{2D}^+(P, Q) \\ & P \in \mathcal{B}(x) \end{aligned} \quad (6.9)$$

After substituting (6.8) into (6.7), some manipulations yield:

$$-2\pi i C(x) \bar{\sigma}^0(x) = \int_{-L/2}^{L/2} d\xi \sigma(\xi) f(x-\xi) \quad (6.10)$$

where  $\sigma^0$  is the strip-theory source strength, and  $\sigma$  the effective (three-dimensional) source strength given by (4.19). Equation (6.10) is identical to Newman's (1978) equation (6.34). Thus the unified theory for  $U=0$  is recovered as a special case of our more comprehensive treatment that includes forward-speed effects. It is worthwhile to add that (6.5) can also be directly obtained from the physical  $x$ -space by using the definition of  $F$ : (4.8-4.10).

For  $U \neq 0$ , a proper inclusion of forward-speed effects on the free-surface in the near field renders (6.8) invalid. The function  $F(y, z; x)$  cannot be simply taken as a product of  $f(x)$  and another function dependent only on  $y, z$ . To obtain the solution of  $\Phi$ , (4.15) must be taken in its original form. From the viewpoint of our formulation, the forward-speed version of Newman's (1978) unified theory can

also be deduced if one simply substitutes  $G_{2D}^+(y, z; \eta, \xi)$  for the term  $G^{\pm*}(y, z; \eta, \xi; k)$  in (6.1). This approximation eliminates all of the forward-speed effects in  $G^\pm$ , and is unnecessarily restrictive. The present theory has more compatible wave effects.

## 6.2 Steady Motion of a Slender Ship; $\omega=0, U \neq 0$

In this limit, the function  $G^{(i)}$  in (3.8) can be written as

$$G^{(i)}(P, Q; x-\xi) = \frac{\delta(x-\xi)}{2\pi} \ln \frac{R/R_1}{1} H_0^+(P, Q; x-\xi) + F(P, Q; x-\xi), \quad (6.11)$$

where  $H_0^+$  is given by (3.7) with  $\omega$  set equal to 0. To obtain  $F$ , one simply notes that the equations for the wave numbers (4.12-4.13a) are now given by:

$$k'_{1,4} = \mp K_0, \quad k'_{2,3} = 0, \quad K_0 = g/U^2 \quad (6.12)$$

Hence the interaction kernel function  $F$  of (4.8) reduces to the following representation. Let

$$w_0(k; K_0 x, K_0 y, K_0 z) = e^{-ikK_0 x} e^{k^2 K_0 z} \cos(k^2 K_0 y), \quad (6.13)$$

then

$$F_1(y, z; x) = \frac{K_0}{\pi} \left[ \int_0^\infty dk \operatorname{Im}(w_0) + \int_1^\infty dk \frac{k}{(k^2-1)^{1/2}} \operatorname{Im}(w_0) \right] \quad (6.14a)$$

$$F_2(y, z; x) = \frac{K_0}{\pi} \left[ \int_0^\infty dk \operatorname{Im}(w_0) - \int_0^1 dk \frac{k}{(1-k^2)^{1/2}} \operatorname{Re}(w_0) \right] \quad (6.14b)$$

These results, valid in the context of slender-ship approximation, are considerably simpler than the three-dimensional (Havelock) Green function, which corresponds to (3.19) here.  $G^{(0)}$  normally needs to be expressed in terms of a real double integral, or a single integral of more complex special functions.

The integral equation corresponding to (4.15) is now given by

$$\begin{aligned} \frac{1}{2}\Phi_s(P; x) = & \frac{1}{2\pi} \int_{\mathcal{B}(x)} ds_Q [\Phi_s(Q; x) \frac{\partial}{\partial N} - \Phi_{sN}] \ln R/R_1 \\ & + \int_{-L/2}^{L/2} d\xi \int_{\mathcal{B}(\xi)} ds (\Phi_s(Q, \xi) \frac{\partial}{\partial N} - \Phi_{sN}) [H_0^+(P, Q; x-\xi) + F] \\ & - K_0 \oint_{\mathcal{C}} d\eta [\Phi_s(\eta, 0, \xi) \frac{\partial}{\partial \xi} - \Phi_{s\xi}] [H_0^+(P; \eta, 0; x-\xi) + F] \end{aligned} \quad (6.15)$$

where  $\oint$  denotes the fact that the limits of integration for the term  $H_0^+$  are given by  $[x, L/2]$ . The function  $F$  in (6.15) provides the only upstream influence. However, it also generates important downstream effects. If (6.15) is solved in its entirety, all "wave-diffraction" effects along the ship hull will be properly accounted for. A number of simplifying treatments of (6.15) are possible but we will not be concerned with them here.

It is of interest to compare our new theory with a number of other existing approximations. First, if we simply set the transverse coordinates  $y$  and  $z$  in (6.13) to zero,

$$F(0,0,x) = -1/\pi x + \left\{ \text{sgn}(x)/2\pi x + \frac{1}{4\partial x} \{ H_0(-K_0 x) + [2 - \text{sgn}(x)] Y_0(K_0 |x|) \} \right\} \quad (6.16)$$

The  $\{\}$  term here is the longitudinal interaction function first derived by Tuck (1964) in his slender-body theory for wave resistance. The first term of (6.16) is annihilated by a similar one from  $H_0^+$ .  $F(0,0;x)$ , however, does not satisfy the speed-dependent linearized free-surface condition (2.11, with  $\omega=0$ ) in the nearfield. Tuck was not concerned with that because he assumed a rigid-wall condition for  $\Phi_S$ . His slender-body theory results in an effective source strength that depends only on the longitudinal derivative of the cross-section area. Or equivalently, the wave-making characteristics associated with the sectional shape cannot be properly modeled.

Chapman (1976), Daoud (1975), and Hirata (1975) used the first two terms of (6.11) in a pseudo-time fashion described earlier to study the flow about a plate and a wedge. These works were all known to produce only divergent waves. The function which accounts for transverse-wave effects downstream was absent and unknown. A re-examination of the matching error in (3.22) will indicate that  $F$  is negligible only under the assumption of  $U \gg 0(1)$ , corresponding to a high-Froude number approximation.

In a recent work, Maruo (1982) proposed a slender-body approximation that can be considered basically as equivalent to (6.11), but with  $F$  given by Tuck's expression, i.e. equation (6.16). This is inconsistent since  $F(0,0,x)$  does not satisfy the same free-surface conditions as  $H_0^+$ .

None of the works cited include the free-surface line integral  $\oint$  in (6.15). It was pointed out by Yeung & Kim (1981) in their pseudo-time formulation that its contribution was important in the forced-motion problems. We expect it to be even more so in the wave-resistance problem since the boundary condition (2.14a) is non-homogeneous at the waterline. Various authors, see e.g. Koch and Noblesse (1979) have documented the importance of its

inclusion in attempts to solve the three-dimensional Neumann-Kelvin problem.

The above comparisons indicate that our new slender-ship formulation for wave-resistance is the most comprehensive, at least to-this-date. It has the capability to represent wave motions of the kind that are compatible with three-dimensional flow, capability to account for longitudinal interaction between ship sections, but does not involve the complicated three-dimensional Green function in its entire form. The outlook for good quantitative predictions appears promising.

## 7. SUMMARY AND CONCLUSIONS

In a re-examination of the hydrodynamic problem of a slender ship undergoing oscillatory and steady forward motions, we have pointed out a number of deficiencies in using a strip-theory type solution near the hull. This paper presents a new theory that will account for the forward-speed effects in a rational way. The formulation is markedly different from all existing ones.

At the outset, we employ the complete linearized free-surface condition in the nearfield. This removes most, if not all, of the undesirable restrictions on the ship speed and the frequency of oscillation. Guided by the "pseudo-time" interpretation of the speed-dependent terms described in Yeung & Kim (1981), we seek a two-dimensional inner solution that can accommodate three-dimensional wave effects. This is accomplished by introducing a new concept: A generalized inner Green function  $G^{(i)}$  that is to be determined from matching.  $G^{(i)}$  has two terms, a "pseudo-time" forward-flow potential that is associated with divergent waves and the usual logarithmic singularity, and an unknown harmonic term  $F$  that is related to transverse waves. Asymptotic matching of  $G^{(i)}$  and the three-dimensional outer Green function in the Fourier space provides the necessary information for  $F$ . The complete expression of  $G^{(i)}$  is given by (3.8b, 3.26, 4.8) which constitutes one of the main results of this theory. This new Green function has rather remarkable properties. It satisfies two-dimensional Laplace's equation, the speed-dependent free-surface condition, and contains wave characteristics that are compatible with three-dimensional flow.

An integral equation has been derived using  $G^{(i)}$  for the inner potential on the ship hull. Numerical solution of this equation is necessarily more complicated than that of the usual strip theory. Nevertheless, it is still quite manageable since the kernel function is defined by only a single integral. An expression for the farfield line-source strength of the inner solution is given in this paper, eq. (4.17). This effective source strength becomes



essentially the three-dimensional source strength in the outer field since the Green functions are matched by construction. Also given in the paper are the appropriate expressions for calculating added mass, damping, and wave resistance, the last for the case of steady forward motion.

The analytical procedure given in this paper has provided us a comprehensive slender-ship theory that is valid over a wide range of speed and frequency parameters. The power of the present approach seems well demonstrated by its ability to include the Neumann-Kelvin wave-resistance problem as a special case of a "ship-motion" formulation. This is rather unorthodox. The practical usefulness of the new theory awaits experimental confirmation of forthcoming numerical calculations. However, a number of exciting results have already been deduced analytically. It is worthwhile to summarize these below:

1) For a body moving in or near a free surface with a mean forward speed, the line distribution of singularities representing its farfield behaviour generally extends beyond the actual length of the body itself. The distribution reduces to the length of the body if the forward speed vanishes.

2) In the limit of vanishing forward speed, the zero-speed version of Newman's (1978) unified theory is recovered from the present theory. The forward-speed version of the unified theory, however, was constructed from strip-type solutions. As such, its inner solution does not contain wave characteristics that are entirely compatible with those of the three-dimensional field. The new theory has this compatibility.

3) The "pseudo-time" formulation of Yeung & Kim (1981) may be considered as a "forward-speed" strip solution, which has no effects due to up-stream influence. This is justifiable in the context of the new formulation if the frequency of oscillation is assumed to be high.

4) A new slender-ship wave-resistance theory has been obtained by taking the frequency of oscillation of the general theory as zero. The kernel function  $F$  provides the necessary three-dimensional interaction that has been omitted in a number of existing approximations. This theory appears to contain all of the important features relevant to wave-resistance calculations, but without the necessity of using the actual three-dimensional Green function.

#### ACKNOWLEDGEMENTS

The genesis of this work was completed in 1982 under the support of the Office of Naval

Research (Task NR62-611, Contract N00014-78-C-0390) and the National Science Foundation (Grant MEA 771-7817), to whom we would like to express our appreciation. Additional analyses and preparation of this paper have been supported by the Office of Naval Research under contract N00014-84-K-0026. A summary report of this new theory was given earlier by one of us in the Proceedings of the International Workshop on Ship & Platform Motions (Kim, 1983).

#### REFERENCES

- Abramowitz, M. and Stegun, I. eds. (1964): "Handbook of Mathematical Functions." U.S. Gov. Print. Off., Washington, D. C.
- Becker, E. (1958): Das Wellenbild einer unter der Oberfläche eines Stromes schwerer Flüssigkeit pulsierender Quelle. Z. angew. Mat. Mech. **38**, 391-399.
- Chapman, R. B. (1976): Free-surface Effects for Yawed Surface-piercing Plate. J. Ship Res. **20**, 125-136.
- Copson, E. T. (1965): "Asymptotic Expansions." Cambridge Univ. Press, Cambridge.
- Daoud, N. (1975): "Potential Flow Near to a Fine Ship's Bow." Rept. No. 177. Dept. Nav. Archit. & Mar. Eng., Univ. of Michigan, Ann Arbor.
- Faltinsen, O. (1974): A Numerical Evaluation of the Ogilvie-Tuck Formulas for Added Mass and Damping Coefficients. J. Ship Res. **18**, 73-85.
- Gerritsma, J. and Beukelman, W. (1967): Analysis of the Modified Strip Theory for the Calculation of Ship Motions and Wave Bending Moments. Int. Shipbuild. Prog. **14**: (156), 319-337.
- Hirata, M. H. (1975): The Flow Near the Bow of a Steadily Turning Ship. J. Fluid Mech. **71**, 283-291.
- Joosen, W. P. A. (1964): "Oscillating Slender Ships at Forward Speed", Publ. No. 268. Neth. Ship Model Basin, Wageningen.
- Khaskind, M. D. (1957): The Exciting Forces and Wetting of Ships in Waves. Izv. Akad. Nauk SSSR. Otd. Tekh. Nauk **66-79**; Translation: (1962) David Taylor Model Basin Trans., Bethesda, Maryland.
- Kim, S. H. (1982): Slender Ships with Forward Speed - A New Approach and A New Theory. Ph.D. Thesis, Mass. Inst. of Technology, Cambridge, Mass.
- Kim, S. H. (1983): Oral Discussion on a New Slender-Ship Theory. Proc. Int. Workshop on Ship & Platform Motions, 512-518, Dept. of Nav. Arch. & Offsh. Eng., Univ. of Calif., Berkeley, California.
- Kim, S. H. and Yeung, R. W. (1984): A New Theory for Oscillating Slender Ships in Forward Motion. Manuscript to be submitted to J. Ship Res.
- Koch, P. and Noblesse, F. (1979): Wave Resistance of the Wigley and Inui Hull Forms Pre-

- dicted by Two Simple Slender-Ship Wave-Resistance Formulas. Proc. Workshop Ship Wave Resist. Comp., D. W. Taylor Nav. Ship Res. Ctr., Bethesda, Maryland.
- Korvin-Kroukovsky, B. V. (1955): Investigation of Ship Motions in Regular Waves. Soc. Nav. Archit. & Mar. Eng., Trans. **63**, 386-435.
- Korvin-Kroukovsky, B. V. and Jacobs, W. R. (1957): Pitching and Heaving Motions of a Ship in Regular Waves. Soc. Nav. Archit. & Mar. Eng., Trans. **65**, 590-632.
- Lighthill, M. J. (1958): "An Introduction to Fourier Analysis and Generalized Functions." Cambridge Univ. Press, Cambridge.
- Loeser, D. J., Yue, D. K., and Salvesen, N. (1982): Slender-Body Calculations of Large-Amplitude Ship Motions. Proc. Symp. Naval Hydrodyn. 14th, 383-416, Nat'l. Academy Press, Washington, D.C.
- Maruo, H. (1982): "New Approach to the Theory of Slender Ships with Forward Velocity." Bull. Faculty Eng., Yokohama Natl. Univ. **31**, Yokohama, Japan.
- Mays, J. H. (1978): Wave Radiation and Diffraction by a Floating Slender Body. Ph.D. Thesis, Mass. Inst. of Tech. Cambridge, Massachusetts.
- Newman, J. N. (1961): "The Damping of an Oscillating Ellipsoid Near a Free Surface." J. Ship Res. **5**, (3) 44-58.
- Newman, J. N. (1970): Application of Slender-body Theory in Ship Hydrodynamics. Ann. Rev. Fluid Mech. **2**, 67-94.
- Newman, J. N. (1978): The Theory of Ship Motions. Adv. Appl. Mech. **18**, 221-283.
- Newman, J. N. and Sclavounos, P. D. (1980): The Unified Theory of Ship Motions. Proc. Symp. Nav. Hydrodyn. 13th, Tokyo, Japan.
- Newman, J. N. and Tuck, E. O. (1964): Current Progress in the Slender-body Theory of Ship Motions. Proc. Symp. Nav. Hydrodyn. 5th ACR-112, 129-167, Off. Nav. Res., Washington D.C.
- Ogilvie, T. F., and Tuck, E. O. (1969): A Rational Strip Theory for Ship Motions, Part 1." Rept. No. 013. Dept. Nav. Archit. & Mar. Eng., Univ. of Michigan, Ann Arbor.
- Ogilvie, T. F. (1977): Singular-perturbation Problems in Ship Hydrodynamics. Adv. Appl. Mech. **17**, 91-188.
- Salvesen, N., Tuck, E. O., and Faltinsen, O. (1970): Ship Motions and Sea Loads. Soc. Nav. Archit. & Mar. Eng., Trans. **78**, 250-287.
- Sclavounos, P. D. (1981): On the Diffraction of Free Surface Waves by a Slender Ship. Ph.D. Thesis, Mass. Inst. of Tech., Cambridge, Massachusetts.
- Timman, R. and Newman, J. N. (1962): The Coupled Damping Coefficients of Symmetric Ships. J. Ship Res. **5**:(4), 34-55.
- Tuck, E. O. (1964): A Systematic Asymptotic Expansion Procedure for Slender Ships. J. Ship Res. **8**:(1), 15-23.
- Ursell, F. (1962): Slender Oscillating Ships at Zero Forward Speed. J. Fluid Mech. **19**, 496-516.
- Wehausen, J. V., and Laitone, E. V. (1960): Surface Waves; in "Handbuch der Physik" (S. Flugge, ed.), Vol. 9, 446-778. Springer-Verlag.
- Yeung, R. W. and Kim, S. H. (1981): Radiation Forces on Ships with Forward Speed. Proc. Int. Conf. Numer. Ship Hydrodyn., 3rd, 499-515, Bassin d'Essais des Carenes, Paris, France.

## DISCUSSION

P.D. KAKLIS,  
National Technical University of Athens,  
Athens, Greece:

The authors have to be congratulated on a very substantial paper, in which, among others, use has been made of the complete linearized free surface condition for the formulation of the inner problem.

At the National Technical University of Athens, the problem of a steadily translating slender body is presently being treated using a new asymptotic formalism (Kaklis, 1984 b), and modern mathematical tools, mainly the calculus of generalized functions.

Since the authors' formulation for the case of  $\omega = 0$  reduces to the aforementioned problem, we read their paper with great interest. As a consequence, we are afraid that we would have to question the method by which the matching of the "generalized" inner Green function  $G^{(i)}$  with the corresponding outer  $G^{(o)}$ , is performed.

More specifically, the mathematical argumentation given in the sequel shows that, at least for the special case  $\omega = 0$ ,  $U \neq 0$ , the integrations with respect to  $l$  and  $k$  in relations (A2.28) of Kim (1983, appendix 2) cannot be interchanged, as is implicitly being done in order to obtain relation (A3.1.a), (ibid, appendix 3). This, analytically non-permissible, manipulation leads to equation (3.13) of the paper under discussion whose validity is questioned.

In this respect, it should be noted that the inconsistency of (3.13) has non-trivial consequences, e.g.

- The right-hand side of relation (3.14) of the paper under discussion possesses a singularity of logarithmic strength as  $r = \sqrt{y^2 + z^2} \rightarrow 0$ , (see theorem 1 below). Nevertheless, on the basis of theorem 2 given in the sequel, it can be inferred that the left-hand side of the relation (3.14) is a function free from singularities as  $r \rightarrow 0$ , at least when  $z = 0$ .
- The kernel of integral equation (6.15) has to be modified by adding to  $F$  an appropriate homogeneous solution  $\Delta$  of the problem satisfied by  $G^{(i)}$ . Let us note that, as  $r \rightarrow 0$ , the function  $\Delta$ , thought of in some generalized sense with respect to  $x$ , has support contained in the plane  $x = 0$ . (See Kaklis (1984 a), theorem 4.3.2, corollary 4.3.1). The previous remark bears out the assertion that a proper construction of  $G^{(i)}$  has to be performed in the context of generalized functions.

Finally, it is expected that the aforementioned analytical shortcoming will influence the asymptotic scheme in general, i.e. when  $\omega \neq 0$ .

In paragraph 3.1 a Green function, suitable for the flow representation in the inner region, is defined as below (see relations (3.7, 3.8a, 3.8b)):

$$G^{(i)}(x, y, z; \xi, \eta, \zeta) = (2n)^{-1} \delta(x - \xi) \ln(R/R_1) + H^+ + E \quad (1)$$

where  $R = \sqrt{(y - \eta)^2 + (z - \zeta)^2}$ ,  $R_1 = \sqrt{(y - \eta)^2 + (z + \zeta)^2}$ ,  $(2)$

$$H^+(x, y, z; \xi, \eta, \zeta) = -\frac{K_0}{\pi} u(\xi - x) e^{i\omega(x - \xi)/U} \int_{R^+} \frac{dl}{\sqrt{K_0}} e^{lz} \cos(l(y - \eta)) \sin(\sqrt{K_0} T(\xi - x)), \quad (3)$$

$K_0 = gU^{-2}$ ,  $u(x)$  is the Heaviside function,  $\delta(x - \xi)$  is the well known delta function of Dirac, and, finally,  $E(x, y, z; \xi, \eta, \zeta)$  is a function which will be determined by matching  $G^{(i)}$  with the inner expansion of the outer Green function  $G^{(o)}$ . For simplicity we consider the case  $\omega = 0$ ,  $\xi = \eta = \zeta = 0$  and introduce the notation

$$G^+(x, y, z) = G^+(x, y, z; \xi = \eta = \zeta = 0, \omega = 0) = H^+(x, y, z; \xi = \eta = \zeta = 0, \omega = 0). \quad (4)$$

Then, the accomplishment of the matching procedure relies essentially on the use of the equation (see relation (3.13))

$$F_x G^+(k, y, z) = -\frac{1}{\pi} \int_{R^+} dl \frac{e^{lz} \cos(l y)}{1 - (Uk - i\mu)^2/g}, \quad \mu \rightarrow 0^+ \quad (5)$$

where the prefix  $F_x$  denotes the operation of the Fourier transform with respect to  $x$ .

We shall now comment on the validity of relation (5). For this purpose we shall cite a number of results obtained by Kaklis (1984 a) in the investigation of the problem

$$G_{Dyy} + G_{Dzz} = 0, \quad x' = (x, y) \in R^2, \quad z \in (-\infty, 0), \quad (6.a)$$

$$(P_{GD}) \frac{1}{K_0} G_{Dxx} + G_{Dz} = \delta(x, y), \quad x' \in R^2, \quad z = 0, \quad (6.b)$$

$$\nabla G_D \rightarrow 0, \quad z \rightarrow -\infty \quad (6.c)$$

In order to construct a set of solutions of  $(P_{GD})$  free from restrictive conditions at infinity  $|x'|^2 = x^2 + y^2 \rightarrow \infty$ , it will be proved convenient to imbed  $G_D(x, y, z)$  into an appropriate space of vector-valued generalized functions (abbreviated by v.v.g.f.). More specifically we assume that

$$G_D(x; z) \in S^{0'}(R^2; C^2((-\infty, 0)) \cap C^1((-\infty, 0))), \quad (7)$$

where  $S^{0'}(R^2)$  is the set of all continuous linear functionals on  $S^0(R^2)$ , which is the space of all  $C^\infty$  functions  $\phi(x')$  satisfying the inequalities

$$\left| x^{p_1} y^{p_2} \frac{\partial^{|q|} \phi(x')}{\partial x^{q_1} \partial y^{q_2}} \right| < C_{p_1 p_2} B^{|q|}, \quad |q| = q_1 + q_2. \quad (8)$$

Here  $p = (p_1, p_2)$ ,  $q = (q_1, q_2)$  are arbitrary multi-indices and the constants  $B, C_{p_1 p_2}$  depend on the function  $\phi(x')$ .

In connection with the space of v.v.g.f. defined above, we introduce the following

**Definition 1:** An element  $G_D(x'; z)$  of  $S^{0'}(R^2; C^0((-\infty, 0)) \cap C^1((-\infty, 0)))$  will be called an abstract degenerate Green function if

$$(G_{Dyy} + G_{Dzz}, \phi(x')) = 0, \quad z \in (-\infty, 0), \quad (9.a)$$

$$(P_{GD}) \left( \frac{1}{K_0} G_{Dxx} + G_{Dz}, \phi(x') \right) = (\delta(x'), \phi(x')), \quad z = 0, \quad (9.b)$$

$$(\nabla G_D, \phi(x')) \rightarrow 0, \quad z \rightarrow -\infty, \quad (9.c)$$

where  $(g, \phi), g \in S^{01}(\mathbb{R}^2), \phi \in S^0(\mathbb{R}^2)$ , denotes the duality pairing in  $S^{01} \times S^0$ .  
Existence theorem: (See Kaklis (1984 a), theorem 3.1). Two families of abstract degenerate Green functions  $G_{D\alpha}, \alpha=1,2$ , are defined by the formulae

$$(G_{D\alpha}, \phi) = \frac{1}{4\pi^2} \langle F_{xy} G_{D\alpha}^P, F_{xy} \phi \rangle + \frac{1}{4\pi^2} \langle F_{xy} G_{D\alpha}^H, F_{xy} \phi \rangle, \quad (10)$$

where

$$\langle F_{xy} G_{D1}^P, F_{xy} \phi \rangle = \int_{\mathbb{R}} dk \text{ P.V.} \int_{\mathbb{R}} dl \frac{e^{-|l|z}}{|l| - \frac{k^2}{K_0}} F_{xy} \phi(k, l), \quad (11.a)$$

$$\langle F_{xy} G_{D2}^P, F_{xy} \phi \rangle = \int_{\mathbb{R}} dl \text{ P.V.} \int_{\mathbb{R}} dk \frac{e^{-|l|z}}{|l| - \frac{k^2}{K_0}} F_{xy} \phi(k, l), \quad (11.b)$$

$$\langle F_{xy} G_{D\alpha}^H, F_{xy} \phi \rangle = \langle e^{\frac{k^2 z}{K_0}} C_+(k), F_{xy} \phi(k, \frac{k^2}{K_0}) \rangle + \langle e^{\frac{k^2 z}{K_0}} C_-(k), F_{xy} \phi(k, -\frac{k^2}{K_0}) \rangle, \quad (11.c)$$

and  $C_{\pm}(k)$  are arbitrary elements in  $K'(\mathbb{R})$  of order zero. Let us note that  $K'(\mathbb{R}^n)$  is the set of all continuous linear functionals on  $K(\mathbb{R}^n)$ , which is the space of all  $C_0^{\infty}(\mathbb{R}^n)$  functions,  $\langle g, \phi \rangle, g \in S^{01}, \phi \in S^0$ , indicating the duality pairing in  $S^{01}(\mathbb{R}^n) \times S^0(\mathbb{R}^n)$ ,  $n \in \mathbb{N}$ . Finally the prefix  $F_{xy}$  indicates the operation of generalized Fourier transform with respect to  $x, y$ .  
Regularity theorem: (See Kaklis (1984 a), theorem 4.1.1). The abstract degenerate Green functions  $G_{D\alpha}^P(x'; z) \in S^0(\mathbb{R}^2; C^{\infty}((-\infty, 0)))$ ,  $\alpha=1,2$ , are regular and the following relations are valid:

$$G_{D1}^P(x'; z) = \frac{1}{\pi^2} \int_{\mathbb{R}^+} dk \cos(kx) \text{Re}(e^{k(z+iy)} E_1(k(z+iy))) - \frac{1}{\pi} \int_{\mathbb{R}^+} dk e^{kz} \sin(k|y|) \cos(kx), \quad (12.1)$$

and

$$G_{D2}^P(x'; z) = \frac{K_0}{\pi} \int_{\mathbb{R}^+} dl \cos(l y) \sqrt{K_0} e^{l z} \sin(\sqrt{K_0} l |x|), \quad (12.2)$$

where the integrals in (12.1), (12.2) exist in the Riemann sense and  $E_1$  denotes the Exponential integral function.

We shall now state two theorems which are concerned with the investigation of the singular behaviour of  $F_{xy} G_{D\alpha}^P$ ,  $\alpha=1,2$ , as  $r \rightarrow 0$ .

Theorem 1: (See Kaklis (1984 a), theorem 4.3.1). An asymptotic, with respect to  $r$ , approximation of  $F_{xy} G_{D1}^P$  is given by the formula

$$F_{xy} G_{D1}^P(k, r, \theta) = -\frac{1}{\pi} \ln r + o(1), \quad \theta = \arctan(z/y),$$

for each  $k$  such that  $|k| \in (0, \infty)$ .

Theorem 2: (See proof of lemma 4.2.5 in Kaklis (1984 a)). An asymptotic, with respect to  $r$ , approximation of  $G_{D2}^P(x, y, 0)$  is given by the formula

$$G_{D2}^P(x, y, z=0) = \frac{1}{2} \sqrt{\frac{K_0}{2\pi|y|}} (\sin^2 - \cos^2) + o(1), \quad x \neq 0,$$

where  $u = \sqrt{K_0}|x|/(2\sqrt{|y|})$ .

Taking into consideration the previous estimate it can be deduced that

$$F_{xy} G_{D2}^P(k, y, z=0) = o(1) \quad \text{as } |y| \rightarrow 0,$$

uniformly with respect to  $k$ .

Performing a smoothness analysis of  $G_{D\alpha}^P$ ,

$\alpha=1,2$ , (See Kaklis (1984 a), theorem 4.2.1, 4.2.2 and remark 4.2.1), we obtain the following

Theorem 3: Comparing the smoothness properties of  $G_{D1}^P, G_{D2}^P$ , we notice the physically interesting superiority of the first one, due to the discontinuity of the first kind presented by  $G_{D2}^P$  on the plane

$$\Omega_0 = \{(x, y, z) \in \mathbb{R}^3 : x=0, y \in \mathbb{R}, z \in (-\infty, 0)\}.$$

Furthermore we have

Theorem 4: (See Kaklis (1984 a), remark 3.8, corollary 4.2.1).

There exist elements  $\phi(x') \in S^{01}(\mathbb{R}^2)$  such that

$$(\Delta(x', z), \phi(x')) = (G_{D1}^P(x', z) - G_{D2}^P(x', z), \phi(x')) = 0,$$

where  $(F_{xy} \Delta, F_{xy} \phi)$  is, for each  $z \in (-\infty, 0)$ , a generalized function in  $K'(\mathbb{R}^2)$  with support contained in the manifold

$$L = \{(k, l) \in \mathbb{R}^2 : |l| - \frac{k^2}{K_0} = 0, k \in \mathbb{R}\}.$$

Theorem 4 states simply that the integrations with respect to  $k, l$  in (11.a), (11.b) cannot be interchanged. On the contrary, in order to obtain equation (5) the authors use Fubini's theorem without assuring the necessary conditions for its application. (See also Kim, 1983, Appendices 2, 3). Hence relation (5), that is (3.13) in the paper, is invalid.

The inconsistency just stated can be overcome by adding to the inner Green function  $G_{D1}^P$  the homogeneous solution  $\Delta_{12}$  of  $(P_{GD})$ . Let us note that, in view of the Regularity theorem,  $\Delta_{12}(x, y, z)$  is a regular generalized function with respect to  $x, y$ , for each  $z \in (-\infty, 0)$ . However, it cannot be claimed that  $\Delta_{12}$  may be represented according to relation (11.c) since the set generated by the latter is strictly interior to the set of homogeneous solutions of  $(P_{GD})$ .

Alternatively, using the degenerate Green function  $G_{D1}^P$  we cannot construct an inner Green function, which is asymptotically close to the Kelvin source  $G_K$  in the following sense:

Theorem on the existence of an abstract Degenerate Kelvin source:

(See Kaklis (1984 a), theorem 5.1.1). There exists in  $K'(\mathbb{R})$  a pair of zeroth order generalized functions  $C_{\pm}(f_1)$  such that the v.v.g.f.

$$G_{D,K} = G_{D_1}^P + G_D^H (C_1^+(f_1) = C_1^+(f_2)) \in S^{0,1}(R^2; C^\infty((-\infty, 0))),$$

henceforth referred to as an abstract Degenerate Kelvin source, satisfies the estimates

$$(G_{D,K} - G_K, \phi) = o(1) \text{ as } r \rightarrow 0,$$

$$(\nabla G_{D,K} - \nabla G_K, \phi) = o(1) \text{ as } r \rightarrow 0.$$

Finally, a regularity and smoothness study of  $G_{D,K}$  leads to results analogous to those obtained for  $G_{D_1}^P$  (See Kalis (1984 a), theorems 5.2.1, 5.2.2).

#### References:

- Kim, S.M. (1983): Slender Ships with forward Speed - A New Approach and a New Theory. Dissertation, Massachusetts Institute of Technology, Cambridge, MA, USA.  
 Kaklis, P.D. (1984 a): A Set of Degenerate Green Functions Related to the Kelvin Source. Report No 1-1984, Dept. of Naval Architecture and Marine Engineering, National Technical University of Athens, Athens, Greece.  
 Kaklis, P.D. (1984 b): A New Asymptotic Formalism for the Study of the Flow Created by a Floating Slender Body Moving with Constant Forward Speed. Report No 3-1984, Dept. of Naval Architecture and Marine Engineering, National Technical University of Athens, Athens, Greece.

Dr. JACEK S. PAWLOWSKI,  
 National Research Council,  
 Ottawa, Canada:

I would like to congratulate the authors on their bold attempt to present a theory which combines radiation and forward motion problems in one formulation. However, recognizing the value of the effort, I must observe that there seem to be reasons to believe that slender body approach is not well suited for such a purpose.

The forward motion problem can be considered on its own in a general formulation and interaction terms with the induced flow can be included in a general formulation of the radiation problem. It is possible to introduce considerable simplifications in both problems as long as every simplification remains compatible with the basic properties of the problem to which it is applied.

Slender body approach involves two kinds of simplifying assumptions:

- a) Those concerned with the geometry of the ship hull which take the form:

$$B/L \equiv \epsilon, \beta \equiv B/D = O(1), D/B = O(1)$$

$$n_1 = O(\epsilon), n_2 = O(1), n_3 = O(1),$$

where  $L, B, D$  have the meaning of main dimensions and  $n_1, n_2, n_3$  represent the components of the normal to the ship surface,  $\epsilon$  represents the small parameter.

- b) Those establishing order of smallness relations between spatial derivatives of the velocity potential; introducing normalized spatial coordinates:

$$x \equiv \tilde{x}L, y \equiv \tilde{y}B, z \equiv \tilde{z}D$$

These relations are expressible as:

$$\frac{\partial}{\partial \tilde{x}} \tilde{\phi} = O(\tilde{\phi}), \frac{\partial}{\partial \tilde{y}} \tilde{\phi} = O(\tilde{\phi}), \frac{\partial}{\partial \tilde{z}} \tilde{\phi} = O(\tilde{\phi})$$

with  $\tilde{\phi}$  representing the normalized velocity potential.

Let us consider the application of this last assumption to the forward motion problem. The following normalized form of the linear free surface condition (corresponding to the equation (2.6) in the paper) is obtained:

$$(F_n^2 \epsilon \frac{\partial^2}{\partial \tilde{x}^2} + \beta \frac{\partial}{\partial \tilde{z}}) \tilde{\phi}_s = 0 \quad \text{on} \quad \tilde{z} = 0 \quad (1)$$

with

$$\phi_s \equiv B \tilde{\phi}_s, U = F_n \sqrt{gL}$$

and  $g$  representing the acceleration of gravity. The consistency of the equation (1) with respect to the order of smallness requires that:

$$F_n^2 = O(\epsilon^{-1}) \quad (2)$$

which constitutes a high speed assumption.

Taking  $\epsilon = 1/8$  it is found that

$$F_n \approx \frac{1}{\sqrt{\epsilon}} = 2.82.$$

This Froude number is approximately ten times greater than Froude numbers at which displacement ships operate and thus it indicates that the assumptions b) may be not applicable.

Taking into account that in the inner region of the flow around a ship moving with constant forward speed the crests of the generated wave system are almost perpendicular to the centre-plane, it is realized that in spite of geometrical relations the significance of longitudinal components of fluid velocity induced by perturbation potential  $\phi_s$  should be preserved. This e.g. can be accomplished by introducing the assumptions:

$$\epsilon \frac{\partial}{\partial \tilde{x}} \tilde{\phi}_s = O(\tilde{\phi}_s), \frac{\partial}{\partial \tilde{y}} \tilde{\phi}_s = O(\tilde{\phi}_s), \frac{\partial}{\partial \tilde{x}} \tilde{\phi}_s = O(\tilde{\phi}_s) \quad (3)$$

The consistency of the equation (1) then leads to the low speed assumption:

$$F_n = O(\epsilon^{1/2}), \quad (4)$$

and the "naive" estimation gives for  $\epsilon = \frac{1}{8}$ :

$$F_n \approx \sqrt{\epsilon} = 0.353.$$

However the relations (3) do not justify the reduction of the Laplace equation:

$$(\epsilon^2 \frac{\partial^2}{\partial \tilde{x}^2} + \frac{\partial^2}{\partial \tilde{y}^2} + \beta \frac{\partial^2}{\partial \tilde{z}^2}) \tilde{\phi}_s = 0$$

to the two dimensions of  $\tilde{y}$  and  $\tilde{z}$  plane.

The slender body assumptions can be adopted for ship oscillations with the exception of the surge mode. Introducing normalized potentials:

$$\phi_j = B \tilde{\phi}_j, j = 2, 3; \quad \phi_j = B^2 \tilde{\phi}_j, j = 4, 5, 6,$$

and normalized frequency  $\omega \equiv \tilde{\omega} \sqrt{g/L}$ , equations corresponding to the equations (2.10) - (2.12) in the paper are expressible in the normalized form:

$$\left( \frac{\partial^2}{\partial \tilde{y}^2} + \beta^2 \frac{\partial^2}{\partial \tilde{z}^2} \right) \tilde{\phi}_j = 0 \quad \text{in the fluid}$$

$$\left( N_2 \frac{\partial}{\partial \tilde{y}} + N_3 \beta \frac{\partial}{\partial \tilde{z}} \right) \tilde{\phi}_j = N_j + \frac{F_n}{\tilde{\omega} \epsilon} \tilde{m}_j \quad \text{on } \bar{S} \quad (5)$$

$$\left[ 1 + 2i \frac{F_n}{\tilde{\omega} \epsilon} \frac{\partial}{\partial \tilde{x}} - \left( \frac{F_n}{\tilde{\omega} \epsilon} \right)^2 \epsilon^2 \frac{\partial^2}{\partial \tilde{x}^2} - \frac{1}{\tilde{\omega}^2 \epsilon} \beta \frac{\partial}{\partial \tilde{z}} \right] \tilde{\phi}_j = 0 \quad (6)$$

on  $\tilde{z} = 0$

The consistency of the equations (6) requires the introduction of the high frequency assumption:

$$\tilde{\omega}^2 = 0(\epsilon^{-1}), \quad (7)$$

which gives  $\frac{1}{\tilde{\omega}^2 \epsilon} = 0(1)$  and, together with (4),

$$\frac{F_n}{\tilde{\omega} \epsilon} = 0(1)$$

Since  $\tilde{m}_j = 0(\tilde{\phi}_j) = 0(\epsilon)$ , the terms dependent upon forward speed in (6) are of higher order of smallness. These terms are different from the ones proposed in the discussed paper as they must include some of the derivatives  $\epsilon \partial \phi_j / \partial \tilde{x}$ , e.g. in  $\tilde{m}_5$ .

Summing up, the application of slender body assumptions b) appears to be unjustified for the forward motion problems. Therefore the possibility of reducing the Laplace equation in that problem to two dimensions is questionable. For the same reason certain terms involving longitudinal velocity components should not be neglected in the impermeability condition of the radiation problem. The consistency of the free surface conditions in both problems is achieved for slow motion (4) and high frequency (7) assumptions.

#### AUTHORS' REPLY:

We thank Professor Loukakis for bringing to our attention the recently completed work of his student on a closely related subject: approximation of the 3-D Kelvin source. The claim made by the discussers, in plain terms, was that Eq. (3.13) of our paper was not the Fourier Transform of Eq. (3.7) with respect to  $x$ . We shall repudiate their claim by showing that (3.13) is indeed the Fourier Transform and that its inverse exists and is given by (3.7).

It is only necessary to consider the case of  $\omega = 0$  in connection with this discussion. In the context of (3.10), the wave function  $H_0^+$  in (3.7) is given by:

$$H_0^+(y, z; x) = \frac{K_0}{\pi} u(-x) \int_0^\infty \frac{d\ell}{\sqrt{K_0} \ell} e^{\ell z} \cos \ell y \sin \sqrt{K_0} \ell x, \quad z < 0, y \neq 0 \quad <1>$$

which satisfies all of the stated conditions in §3.1. In the development of our theory, we needed a transformed expression of <1> for some transverse distance  $|y|(>0)$  in the inner field for matching purposes. As in many water-wave problems, the absolute integrability constraint imposed by the standard Fourier theorem can be relaxed by the use of complex Fourier Transform. Thus, we recall the following transform pair:

$$f^*(k') = \int_{-\infty}^0 dx f(x) e^{ik'x}, \quad \text{Im}(k') < 0 \quad <2a>$$

$$f(x) = \frac{1}{2\pi} \int_{-\infty - i\gamma}^{\infty - i\gamma} dk' f^*(k') e^{-ik'x}, \quad \gamma \geq \mu > 0 \quad <2b>$$

where  $e^{\mu x} f(x)$  provides absolute integrability for  $f(x)$  in  $[-\infty, 0]$ . Upon using <2a> on <1>, we obtain

$$H_0^{+*}(y, z; k') = \frac{K_0}{\pi} \int_{-\infty}^0 dx e^{ik'x} \int_0^\infty \frac{d\ell e^{\ell z}}{\sqrt{K_0} \ell} \cos \ell y \sin \sqrt{K_0} \ell x \quad <3a>$$

$$= \frac{-1}{\pi} \int_0^\infty \frac{d\ell e^{\ell z} \cos \ell y}{\ell - k'^2/K_0}, \quad z < 0, \text{Im}(k') < 0 \quad <3b>$$

where interchangeability of the  $x$ - $\ell$  integration is guaranteed by Fubini's Theorem since the double integral is absolutely convergent, and the subsequent  $x$  integration is elementary. Note that Equation <3b> here is equivalent to

(3.13) of our paper since the inversion path according to <2b> is given by  $k^1 = k - i\mu$ . We have therefore established (3.13):

$$H_0^+(y, z; k) = \frac{-1}{\pi} \int_0^\infty d\ell \frac{e^{\ell z} \cos(\ell y)}{\ell - (k - i\mu)^2 / K_0} \quad <4>$$

with  $\mu$  serving the role of identifying the path of integration for the inverse operation.

Consider now the inversion of <4>:

$$H_0^+(y, z; x) = \frac{-1}{\pi} \int_{-\infty}^\infty dk e^{\mu x - i k x} \int_0^\infty d\ell \frac{e^{\ell z} \cos(\ell y)}{\ell - (k - i\mu)^2 / K_0}, \quad \mu \rightarrow 0 \quad <5a>$$

$$\begin{aligned} &= \frac{K_0}{2\pi} \int_0^\infty dk e^{k^2 z / K_0} \sin\left[\frac{k^2}{K_0}|y| + kx\right] \\ &- \frac{1}{\pi^2} \int_0^\infty dk \cos(kx) \int_0^\infty d\ell e^{\ell|y|} \times \quad <5b> \\ &\times \frac{\ell \cos \ell y + (k^2 / K_0) \sin \ell z}{\ell^2 + k^4 / K_0^2} \end{aligned}$$

where the  $\ell$ -plane in <5a> has a pole as shown in Figure 4. Eqn. <5b> results from <5a> after deforming the integration paths along the real axes to the imaginary ones, with the residue contribution properly included. For the order of integration indicated, we denote the double integral in <5b> as  $I^{kl}$ , which is equivalent to

$$\begin{aligned} I^{kl} &= \frac{-\sqrt{K_0}}{2\pi^2} \int_0^\infty d\rho \frac{\cos \sqrt{K_0} \rho}{\sqrt{\rho}} \int_0^\infty d\ell e^{-\ell|y|} \times \\ &\times \frac{\ell \cos \ell y + \rho \sin \ell z}{\ell^2 + \rho^2} \quad <6> \end{aligned}$$

The absolute integrand of  $I^{kl}$  is of the order  $R^{-3/2} \exp(-R|y| \cos \theta)$  for large  $R$ , where  $\text{Re } i\theta = \ell + i\rho$ . For small  $R$ , the contribution from the neighborhood of  $(\ell, \rho) = (0, 0)$  to  $I^{kl}$  is of  $O(R^{1/2})$ , which vanishes as  $R \rightarrow 0$ . The constraint of  $|y| > 0$  is unimportant since we are only concerned with using the Fourier representation for matching in an intermediate region with the outer representation. Thus, the double integral  $I^{kl}$  exists and is absolutely convergent. Moreover, by Fubini's Theorem,  $I^{kl}$  is representable by either form of the iterated integrals. Hence  $I^{kl} = I^{lk}$ . The subsequent integration of the  $k$ -integral by contour integration is fairly straightforward. Care must, however, be exercised in the choice of the contours which depend on the sign of  $x$ . The final result is given by:

$$I^{kl} = I^{lk} = \frac{-K_0}{2\pi} \int_0^\infty d\ell \frac{e^{\ell z}}{\sqrt{K_0} \ell} \sin(\ell|y| \pm \sqrt{K_0} \ell x), \quad x \geq 0 \quad <7>$$

The double integral now combines with the residue (first) term in <5b> to yield zero upstream disturbances. Hence

$$H_0^+(y, z; x) = \frac{K_0}{\pi} u(-x) \int_0^\infty \frac{d\ell}{\sqrt{K_0} \ell} e^{\ell z} \cos \ell y \sin \sqrt{K_0} \ell x \quad <8>$$

which completes the proof.

We note that the same results could have been obtained if the  $k$ - $\ell$  integrals were interchanged at <5a> although the absolute integrability requirement was "apparently" not met. It should be noted that interchangeability of the order of integration in a double integral is not always contingent upon the satisfaction of Fubini's theorem. There exist many double integrals that are not absolutely integrable yet permit interchangeability. A case in point is the following principal-valued integral which is clearly not absolutely convergent in the Fubini sense:

$$J = \int_0^1 dk \oint_0^1 d\ell \frac{\ell^2}{k - \ell} \quad <9>$$

$J$ , as a double integral, exists in the principal-value sense. It is elementary, however, to show that

$$J^{kl} = -\frac{1}{2} = J^{lk} \quad <10>$$

There is a considerable amount of aerodynamic literature in lifting-surface theory that takes advantage of such an interchangeability property.

In summary, we have demonstrated here that the "analytical non-permissibility" leading to (3.13) as described in the discussers' introduction simply does not exist. The development used by us is mathematically correct. In particular, we have shown that the requirement in Fubini's theorem for interchangeability is satisfied. This leads us to question the validity of Theorem 4 cited by the Discussers (Kaklis, 1984a). It is not clear to what extent the invalidity of Theorem 4 was affected by a missing factor of 1/2 in the discussers' Eqn. (12.2).

In writing this paper, we tried to strike a balance between the physical importance of the structure of the newly proposed inner solution and a modest degree of mathematical rigor based on asymptotic analysis. The inner solution developed has a strong sense of

directionality associated with forward motion. The pseudo-time dependent Green function (3.7) reflects this property; the directionality of the 3-D interaction term  $F$ , which is associated with the residue term in  $\langle 5b \rangle$  (see also (3.17) and (3.25)), relies on matching with the outer representation. We have not examined, however, the question of completeness of the inner solution. This is a very worthwhile question to look into. At the time of writing of this reply, the recent reports of Dr. Kaklis are not available. We look forward to reading any new contributions he can offer in this matter. We note in passing, however, that the particular solution  $G_{D1}^p$  proposed in the last theorem cited by the discussers corresponds only to the principal-value integral portion of our Eqn. (3.14). As such, it contains no directionality of motion and would therefore generate divergent waves propagating upstream as well as downstream. This is physically unacceptable since it implies that the port bow would experience Kelvin-wave effects coming from the starboard stern!

We now turn to Dr. Pawłowski's comments. The scaling advocated by him is a standard one. It is a little cumbersome to carry all of the nondimensional quantities along in our papers (particularly as authors, we have to type and squeeze in all equations reasonably neatly within the 47 columns of spaces!). In any event, we have already stated right under the heading of "Slender-ship Approximations" in §2.1 that such nondimensionalizations are implicitly used. Eqn. (2), for example, of the discussor can be obtained by inspection of (2.11), with  $\omega = 0$ . One must be cautious not to interpret a statement like (2) too literally as Dr. Pawłowski had done when he claimed that (2) implied  $F_n \sim 2.82$ . In the presence of waves, the choice of the longitudinal scale is perhaps not so obvious. If the transverse wavelength  $\lambda$  has been chosen instead of  $L$ , the non-dimensional  $x$ -derivative in Eqn. (1) of Dr. Pawłowski would have a coefficient of  $O(1)$  since  $B/\lambda$  for most displacement ship are typically bigger than  $1/4$  or so for their designed speeds.

To push our point even further, it is entirely possible that a train of Kelvin waves of the form  $\exp(\ell z) \cos(\ell y) \sin \sqrt{K_0} \ell x$ ,  $\ell = O(1)$ , (cf. Eqn. (3.7) of our paper,  $\omega = 0$ ) can propagate along and diffract near the ship axis. Now this behavior satisfies both the full linearized free-surface condition as well as the two-dimensional Laplace equation, and is a situation that the discussor is apparently unaware of.

In doing slender-body ship-hydrodynamics problems, it is a little too easy to fall into a pattern and perhaps pitfalls set up for us by classical aerodynamics, which has only one length scale associated with body geometry. As pointed out in the Introduction section of our paper, the presence of additional length scales associated with the wave fields and their complicated interaction with forward speed suggests a need for another approach. We achieve this by requiring the wave characteristics of the inner and outer Green functions be asymptotically compatible. In many ways, we feel this rather original and unconventional methodology has a lot to offer.

We shall conclude our replies here by presenting a flow diagram (Figure 6). It shows how a number of existing and cited slender-ship theories may be considered as deducible from our proposed solution structure by either doing limiting operations and/or by additional approximations. We hope that this would contribute to the understanding of the nature, and perhaps at times the incompleteness, of the approximations used by some of the theories, all viewed under a common framework.

Relationship Among Various Slender-Ship Theories

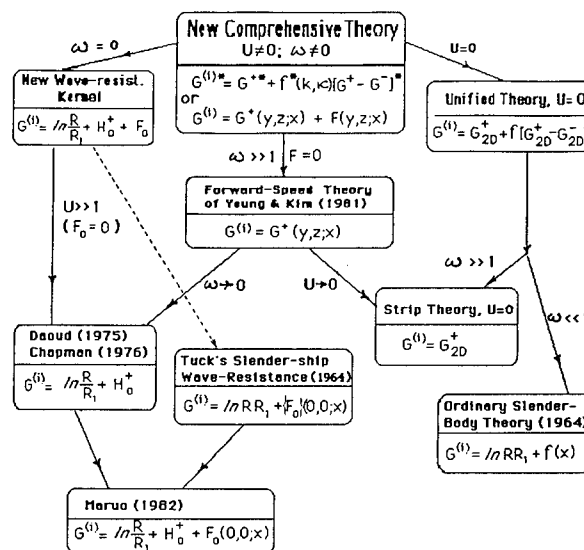


Figure 6



SESSION IV  
PROPELLER-HULL INTERACTIONS

# LOCAL PROPELLER BLADE FLOWS IN UNIFORM AND SHEARED ONSET FLOWS USING LDV TECHNIQUES

STUART D. JESSUP, CARL SCHOTT,  
MICHAEL JEFFERS AND SUKEYUKI KOBAYASHI

## ABSTRACT

Laser Doppler Velocimetry techniques were used to measure local propeller blade flows in the DTNSRDC 24-inch water tunnel. Velocity measurements were made upstream, downstream, and between blades. Measurements were made near the blade surface to identify potential flow surface pressure coefficients and streamwise boundary layer profiles. Blade surface flow visualization was correlated with the measured boundary layer characteristics. Blade pressure distributions and streamwise boundary layer growth were compared with theory. Exploratory velocity measurements were made ahead of a propeller operating in an axisymmetric sheared inflow, and velocity and thrust correlations were made with theory. Measured velocities about the propeller showed good agreement with potential theory ahead of the propeller with discrepancies occurring downstream of the propeller due to viscous effects. Measured boundary layer growth at mid-span of the propeller blade was approximated well by two-dimensional boundary layer theory. Boundary layer profile measurements verified the location of transition determined from flow visualization techniques.

## NOMENCLATURE

$D$  = propeller diameter  
 $c$  = chord length of propeller blade section  
 $C_p$  = blade surface pressure coefficient,  
 $(P - P_o)/\frac{1}{2} \rho V_r^2$ , or  $1 - (\frac{V_b}{V_r})^2$   
 $f$  = camber of propeller blade section  
 $H$  = boundary layer shape factor,  $\delta^*/\theta$   
 $J$  = advance coefficient,  $V_A/nD$   
 $K_T$  = thrust coefficient,  $T/\rho n^2 D^4$   
 $K_Q$  = torque coefficient,  $Q/\rho n^2 D^5$   
 $n$  = propeller rotation speed, revol./second  
 $p$  = propeller blade section pitch  
 $P$  = pressure  
 $P_o$  = reference pressure

$Q$  = torque  
 $R$  = radius of propeller  
 $r$  = radial distance from axis of propeller  
 $T$  = thrust  
 $V_A$  = speed of advance  
 $V_b$  = velocity in the angle  $\phi$  direction relative to the moving blade coordinate system,  
 $V_\phi + 2\pi nr \cos \phi$   
 $V_r$  = resultant inflow velocity to blade section  
 $(V_A^2 + (2\pi nr)^2)^{1/2}$   
 $V_S$  = representative ship speed in sheared wake  
 $DJ/n$  where  $J$  is determined from design  $K_T$  and open water performance data.  
 $V_t$  = tangential velocity, positive in direction of rotation, average value at each blade angular position  
 $V_\phi$  = velocity in the direction of angle  $\phi$ ,  
average value at each angular position,  
 $V_x \cos \phi + V_t \sin \phi$ ,  
 $V_\phi = \frac{1}{n} \sum_{i=1}^n V_\phi(i)$   
 $V_b(i)$ ,  
 $V_\phi(i)$  = velocity in the direction of angle  $\phi$ ,  
individual value at each angular position  
 $x$  = axial position relative to propeller center plane, positive downstream  
 $x_c$  = fraction of chord length  
 $x_r$  = fraction of propeller radius  
 $y$  = distance normal from surface  
 $\beta$  = surface streamline angle with respect to potential flow streamline direction  
 $\delta^*$  = streamwise boundary layer displacement thickness  
 $\rho$  = fluid density

David W. Taylor Naval Ship Research and Development Center, Bethesda, Maryland, USA

- $\phi$  = LDV velocity measurement direction,  
 angle from vertical, positive upstream  
 $\phi_p$  = propeller blade section pitch angle  
 $\theta$  = streamwise boundary layer momentum  
 thickness  
 $\nu$  = kinematic viscosity  
 (—) = bar signifies mean value

## 1. INTRODUCTION

Recent advances in Laser Doppler Velocimetry have provided the ability to measure time-varying velocities near operating propellers. Pioneering work by Min (1978) established techniques and provided field point velocity measurements ahead of and behind operating propellers. Correlations made with Kerwin and Lee's (1978) numerical lifting surface theory, PUF-2, showed good predictions of field point velocity distributions ahead of the propeller and outside the slipstream. Inside the slipstream, downstream of the propeller, predictions showed significant discrepancies with measurements that were attributed to displacement effects due to the viscous wakes of the blades and inaccuracies in the numerical modeling of the downstream vortex system. Using the same LDV system, Kobayashi (1981) calculated the section drag of the blades from detailed measurements of the viscous wakes. Kerwin (1982) presented further correlations of field point velocities about operating propellers using a refined measuring technique resulting in improved spatial resolution. Comparisons were made with Greeley's (1982) improved lifting surface model, PSF-2, showing agreement similar to Min's results. Program FPV-10, reported by Kerwin (1979) was used to generate field point velocities from PSF-2.

All the LDV measurements described were conducted using a one component, dual beam, forward-scatter on-axis system. Transmitting and receiving optics were positioned on opposite sides of the water tunnel with a direct line of sight across the tunnel necessary to perform the measurements. This arrangement restricted the measurements to regions outside the swept area of the rotating propeller.

This paper describes measurements made about rotating propellers using a one component, dual beam, on-axis, backscatter LDV system. Measurements were made within the swept area of the propeller disk, in the potential flow regions between the blades, and within the blade boundary layer. High spatial resolution was obtained with small measuring volume optics in conjunction with precise angular positioning of the propeller. Flow visualization using oil dot techniques was conducted to correlate with measured blade boundary layer characteristics. Exploratory measurements were also made ahead of a propeller operating in an axisymmetric sheared wake to investigate effective wake and resulting propeller performance. The results of these experiments contribute to the understanding of

the potential flow and boundary layer characteristics of typical propeller blade sections, and provide insight into the boundary layer displacement effects on the blade, and propeller operation in sheared wakes.

## 2. EXPERIMENTAL TECHNIQUES

### 2.1 Test Facility

Tests were conducted in the DTNSRDC 24-inch diameter (0.61m) water tunnel incorporating an open jet test section and a downstream drive system. A window insert was installed in the open test section as shown in Figure 1 to permit a close proximity of the LDV

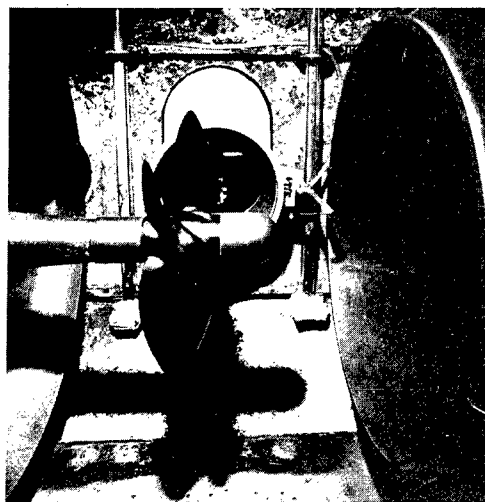


Figure 1 - DTNSRDC 24 Inch Water Tunnel Open Jet Test Section With Tunnel Window Insert for LDV Measurements

optics to the blades of the propeller. This was necessary to minimize the focal length of the LDV optics system for maintaining a minimum measuring volume size. The extended window was positioned approximately 13 inches (33 cm) from the tunnel centerline and was estimated to induce an asymmetry to the uniform flow test section of less than 2%.

The primary propeller tested was DTNSRDC Model 4119. This is a 12 inch (30.5 cm) diameter three-bladed propeller described by Denny (1968), designed for uniform flow as a double thickness version of DTNSRDC propeller Model 4118. The propeller was tested at 7 and 14 rps at a nominal design  $J$  of 0.833 corresponding to a propeller Reynolds number of 0.7 and 1.4 million. Propeller geometry is shown in Table 1.

A relatively large, 150 Hp, dynamometer system was chosen for the tests to maximize shafting rigidity. This was necessary because of the large distance between the propeller and the location of the encoder measuring shaft angular position. It was thought that a rigid shaft arrangement would maximize the consistency of the angular position measurement. Consequently, a compromise was made in the accuracy of thrust and torque measurements, since only 10 percent of the load capacity of the dynamometer was utilized.

TABLE 1 - GEOMETRY OF DTNSRDC MODEL  
PROPELLER 4119

Diameter, D : 1.000 ft (0.305m)

Rotation, Right Hand

Number of Blades, : 3

Hub-Diameter Ratio,  $D_h/D$  : 0.20

Skew, Rake : None

Design Advance Coefficient, J : 0.833

Section thickness form: NACA66 (DTNSRDC Modified)

Section Mean Line : NACA,  $a = 0.8$

$r/R$	$c/D$	$P/D$	$\phi_P$ (Degrees)	$t/c$	$f/c$
0.2	0.320	1.105	60.38	0.20550	0.01429
0.3	0.3625	1.102	49.47	0.15530	0.02318
0.4	0.4048	1.098	41.15	0.11800	0.02303
0.5	0.4392	1.093	34.84	0.09016	0.02182
0.6	0.4610	1.088	29.99	0.06960	0.02072
0.7	0.4622	1.084	26.24	0.05418	0.02003
0.8	0.4347	1.081	23.28	0.04206	0.01967
0.9	0.3613	1.079	20.88	0.03321	0.01817
0.95	0.2775	1.077	19.84	0.03228	0.01631
1.0	0.0	1.075	18.89	0.03160	0.01175

Propeller test conditions were set using thrust identity, where the propeller rpm was set and tunnel water speed was varied to produce measured open water thrust. Preliminary measurements of field point velocities ahead of Propeller 4119 showed a 3% difference in circumferential average axial velocity when compared with predicted values using PSF-2. This discrepancy was believed to be due to the combined effects of measured thrust error, a 1% difference in measured tunnel test section velocity compared to open water advance speed, and the approximate 2% reduction in tunnel test section velocity in the vicinity of the tunnel window insert. Therefore, all correlations were made assuming a 3% reduction in advance speed from the design condition, resulting in an assumed advance coefficient of 0.806. The comparison of the predicted and measured field point velocity distributions at the nominal and assumed advance coefficients are shown later in the paper.

## 2.2 Laser Doppler Velocimetry System

The LDV system used was a relatively conventional TSI, Inc. one component dual beam system operating in the on-axis back scatter

mode. A Spectra-Physics 2 watt ion-argon laser was used, utilizing the green 514.5 nm wavelength line. The single beam was split into two coherent beams through a beam splitter. One beam was frequency shifted to distinguish velocity direction. A 2.27x beam expander was used with a 250 mm focal length lens with 50mm beam separation. This arrangement resulted in a measuring volume .0028 inches (.072mm) in diameter and .030 inches (.75mm) long with 28 fringes across the measuring volume. With the on axis arrangement, the received scattered light past back through the same optical system through a field stop for filtering extraneous scattered light, and then to a photomultiplier. The optical system was afixed to rotating mounts so the beam orientation and thus the direction of velocity measurement could be rotated about the beam axis. Figure 2 depicts the LDV system.

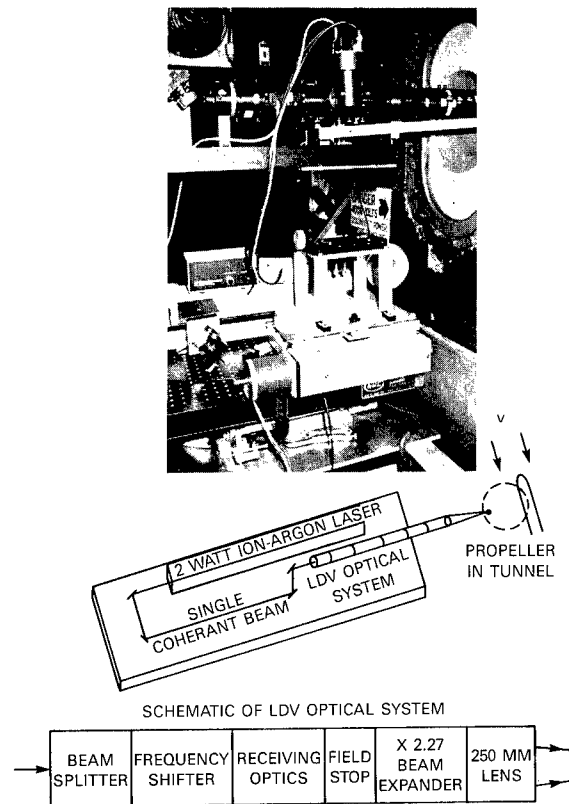


Figure 2 - Laser Doppler Velocimetry System, Single Component, Dual Beam, On-Axis Back Scatter

The doppler signal from the photomultiplier output was processed with both a frequency tracker and a burst counter. Signals were initially band pass filtered to reduce noise. The tracker was used for alignment purposes, processing qualitative results, and identifying blade passage speed. The counter was used for quantitative data processing in conjunction with the computer.

For this test in the water tunnel the data processing rate of individual velocity measurements was relatively good, from 200 to 2000 processed measurements per second. The

data rate was dependent on optical alignment, velocity measurement direction, and tunnel seeding. Routinely, the tunnel water was filtered to 5 micron particle size and then seeded with 1.5 micron size silicon Carbide seeding material. The rate of the processed velocity measurements were considered random in nature so that data collection procedures responded to individual measurements and not to a prescribed time or blade angular position based on propeller rotation.

### 2.3 LDV System Positioning, Calibration and Accuracy

Positioning of the LDV system was performed with a manually controlled, three-directional traverse system as shown in Figure 2. Translations along the propeller shaft axis were performed by moving the entire LDV system, while vertical and horizontal translations from the propeller shaft axis were performed by moving the optical system relative to the single beam laser source. Vertical traverse was performed with an optical scissors jack. Position was measured manually with dial and vernier calipers to a resolution of 0.001 inches (.025mm).

The position of the LDV measuring volume was referenced to the geometry of the propeller inside the tunnel. The vertical position of the LDV measuring volume was referenced to the upper and lower edges of the propeller hub. The axial position was referenced to a mid-chord line drawn on a propeller blade while the propeller was stationary and was checked by positioning the measuring volume at the leading or trailing edges while the propeller was rotating. This was easily performed due to the large doppler signal produced when the measuring volume intersected the blade surface and provided a correction due to shaft system extension under load. The horizontal position from the propeller shaft centerline was referenced to lines of constant radius drawn on the propeller while stationary in the tunnel.

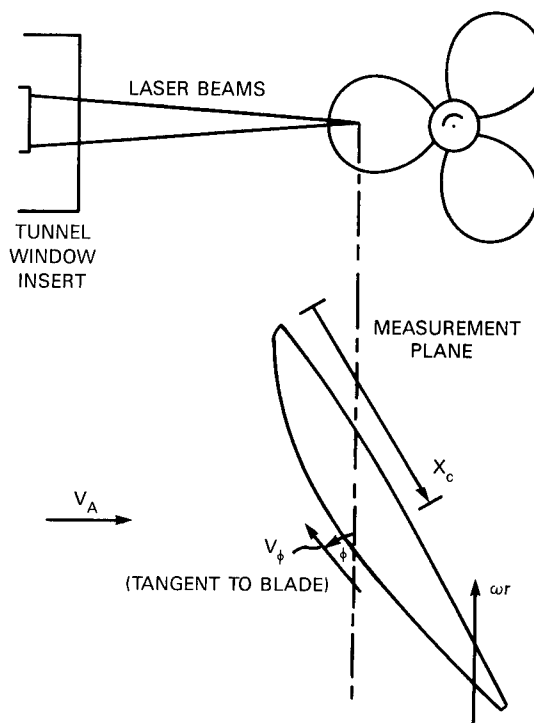
Calibrations were performed by measuring the surface speed of a disk rotating in place of the propeller in the water tunnel. Calculated and measured calibration factors differed by 3% with the difference thought to be due to deviations in the two beam separation distance at the lens.

Calibrations were checked through out the experiment by measuring the blade surface speed while rotating at test conditions. The magnitude of blade speed was most accurately determined using the tracker processor because of its narrow band width and the large offset between blade surface speed and the measured water velocity in the vicinity of the blades. On an average basis the check calibrations were within 1% of the original calibrations but varied up to 3.4% amongst all the measurements. This variation was due primarily to errors in the positioning horizontal to the propeller axis and the angle setting of the two laser beams from the vertical.

### 2.4 Procedure for Measuring Local Blade Velocities

A procedure was derived for measuring the streamwise velocity component near the blade surface using the one component LDV system. The streamwise direction is that tangent to a line of constant radius drawn on the blade. The dual beam LDV system measured the velocity in the plane of the two intersecting beams, perpendicular to the line bisecting the two beams. Figure 3 depicts the measurement of the blade streamwise velocity component.

Figure 3 - Measurement of Blade Streamwise Velocity



The measuring volume located at the intersection of the two beams was positioned at the horizontal centerline plane of the propeller. As the propeller rotated, the blade cut through the measuring volume at some point on the blade. The two beams were rotated about the optical center to orient the direction of velocity measurement to be tangent to one side of the blade as it passed through the measuring volume. This arrangement resulted in a traverse diagonally through the blade surface boundary layer, measuring the velocity parallel to the blade surface at the point where the measuring volume intersected the blade. The mechanism for the boundary layer traverse was simply the rotation of the blade, since the LDV measuring volume remained stationary.

The angle that the two beams were rotated from the vertical,  $\phi$ , was obtained analytically from the design propeller geometry. This angle was similar to the pitch angle of the blade section with a deviation with distance from the mid-chord line.

## 2.5 Measurement of Blade Angular Position

Each velocity measurement processed by the LDV system had to be associated with a given propeller blade angular position. When the tracker was used for qualitative measurements, the time sweep of a storage oscilloscope was used in conjunction with a single pulse per revolution from a magnetic pick-up to reference individual measurements to a known blade angular position. Figure 4 depicts a typical velocity distribution through the rotating propeller disk.

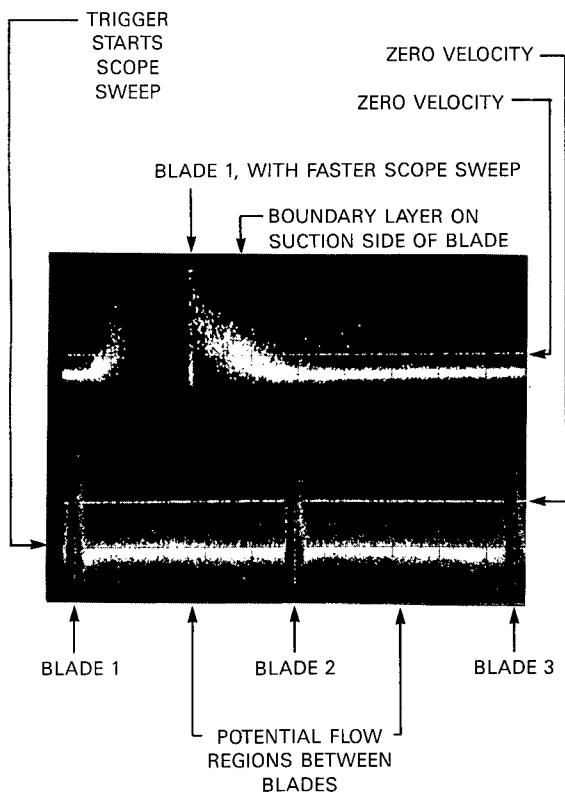


Figure 4 - Sample of Oscilloscope Traces of Streamwise Velocity Measurements

A digital output absolute positioning optical rotary encoder (BEI, #5V680HB) was used to measure blade angular position when quantitative data was collected by computer. A natural binary 12 bit resolution was output from the encoder corresponding to 4096 angular positions per revolution. An angular speed limit of 10 rps was prescribed with this resolution due to a 40 KHZ frequency response of the optical components in the encoder, but a working limit of at least 15 rps was attained.

## 2.6 Computer Data Collection and Analysis

Processed LDV velocity measurement data from the burst counter were collected with a Perkin Elmer (Interdata) 7-16, 16 bit minicomputer. With each velocity measurement collected, an associated shaft angular position was

read from the shaft encoder. Velocity and position data sets were transferred to 9 track-digital tape. A typical run, requiring ten minutes of test time consisted of 168,000 data sets with approximately 40 velocity measurements at each of 4096 angular positions.

Data on digital tape was transferred to a CDC 176 mainframe computer and stored on a cartridge type mass storage system. The velocity data were sorted by angular position and the mean velocity, standard deviation and number of data points at each angular position were retained for each analyzed run. A computer program was developed to analyze the velocity data in the regions close to the blade in a reference frame moving with the blades. The program calculated the blade pressure coefficient from the potential flow regions above the blade surface and calculated boundary layer characteristics of displacement thickness, shape factor, turbulence intensity and velocity profile.

When the measuring volume intersected the blade surface a relatively large signal was returned to the LDV processor. This resulted in a substantially larger number of data samples collected at the angular position corresponding to the blade surface. This phenomenon was used to locate the angular position of the blade surface to within one angular

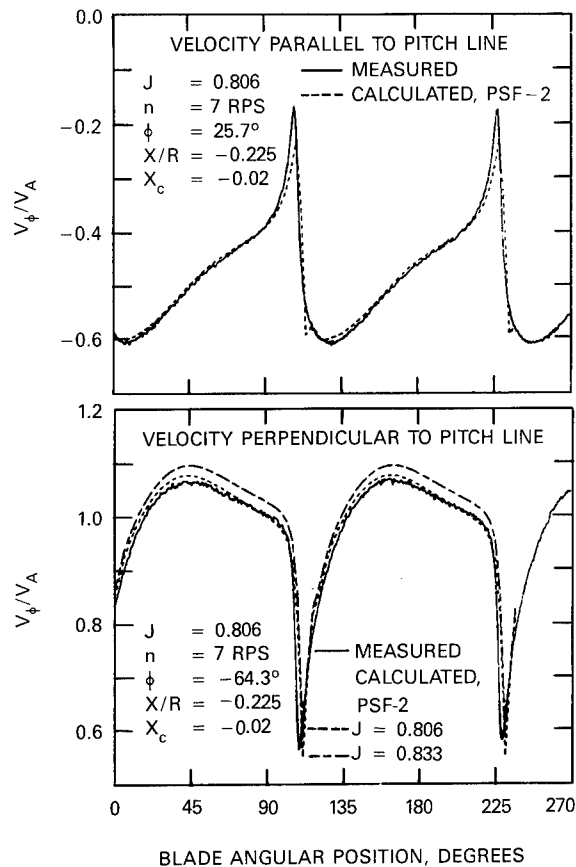


Figure 5 - Comparison of Measured and Predicted Field Point Velocity Distribution Slightly Ahead of the Leading Edge at 0.7R of Propeller 4119

location.

The accuracy of the angular position corresponding to the blade surface had a significant effect on the accuracy of the measured boundary layer parameters. Near the leading edge, where only about six angular positions were contained within the boundary layer, a variation of one angular position produced a dramatic change in  $\delta^*$  and  $H$ . To improve surface angle resolution, in cases where a large number of data samples were shared by two adjacent positions, boundary layer parameters were calculated for each of the adjacent surface angles and then averaged. From this procedure, surface angular resolution was improved to one half an angular location with a resulting estimated error in  $\delta^*$  of  $\pm 0.00021^\circ/\text{C}$ .

### 3. DISCUSSION OF EXPERIMENTAL RESULTS

#### 3.1 Local Blade Flow Measurements About Propeller 4119

Initial measurements were made upstream of the propeller near the leading edge of the blades. As previously reported by Min (1978) and Kerwin (1982) LDV measurements of field point velocities in the potential flow regions ahead of the propeller correlated well with numerical predictions using lifting surface theory. Figure 5 shows the measured field point velocity distribution of propeller 4119 slightly ahead of the leading edge at the 0.7 radius. The measurements correspond to a vector decomposition of the traditionally measured axial and tangential velocity components into directions parallel and perpendicular to the blade section pitch line. Comparisons made with the propeller numerical lifting surface performance prediction program (PSF-2) showed good agreement with measurements. A reference phase for the field point velocity predictions was determined by shifting the phase of the predicted velocity distribution in Figure 5 to match the measured result. Figure 6 shows a composite of the blade to blade velocity distributions traversed axially through the propeller disk across the blade chord. The measurement direction is oriented parallel to the suction side blade surface at the intersection of the LDV measuring volume and the suction side surface. The velocity profiles shown are nondimensionalized on  $V_r$ , the resultant inflow velocity at the given radial section. Velocity  $V_b$  represents the measured velocity  $V_\phi$  transformed to the moving blade reference frame, where  $V_b = V_\phi + 2\pi n r \cos \phi$ .

The blanked-out regions in the plots correspond to the measuring point intersecting the interior of the blade. Measurements near the suction side of the blade are to the right of the blanked region and the pressure side is to the left. Over most of the chord length the velocity jump across the blade can be seen. Near the leading edge on the pressure side of the blade the flow is generally retarded near the stagnation point, but is accelerated near the blade surface downstream of the stagnation point. On the suction side near the trailing

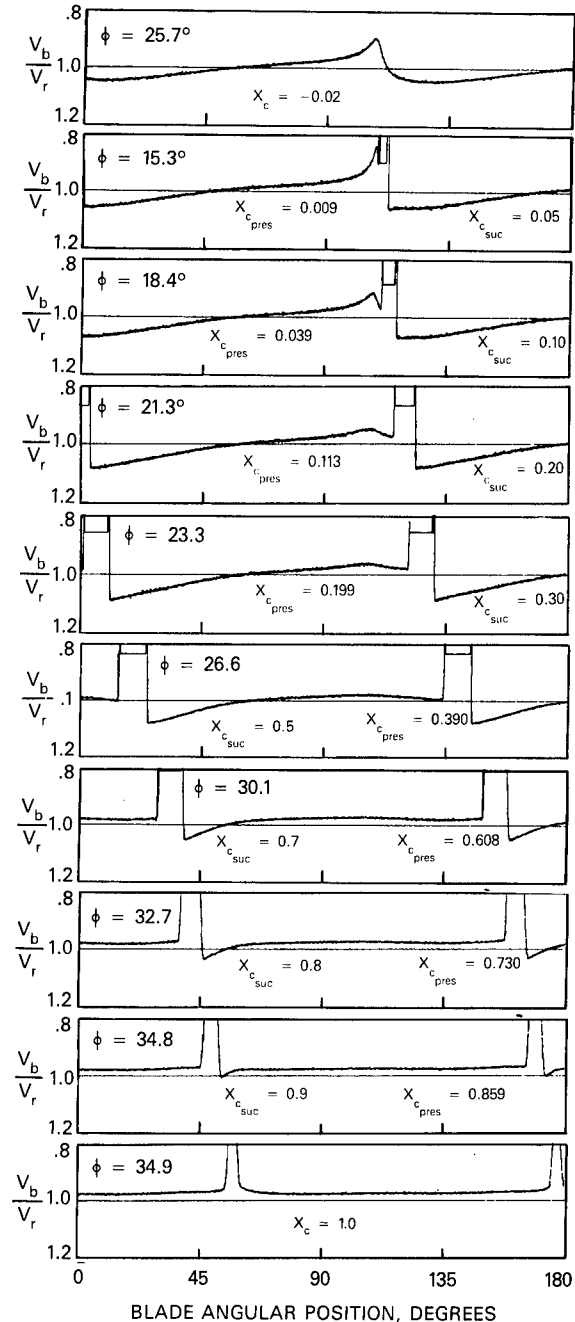


Figure 6 - Measured Streamwise Potential Flow Velocity Profiles Through 0.7R of Propeller 4119

edge the surface velocity decelerates without any apparent flow separation.

The viscous boundary layers developed along each side of the blade are confined to the thin regions very close to the blade surfaces. Even near the trailing edge, the relatively thick boundary layers appear to have little effect on the overall potential flow velocity fields.

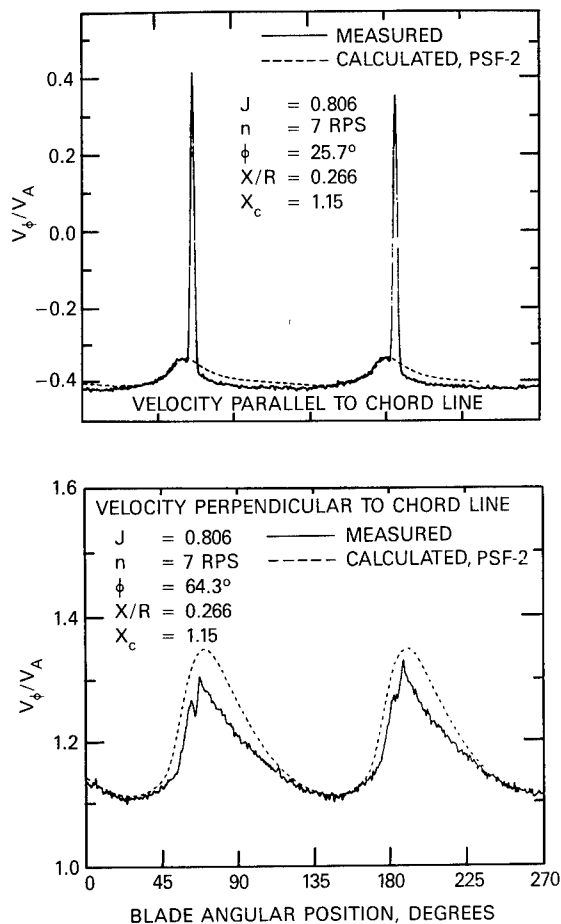


Figure 7 - Comparison of Measured and Predicted Field Point Velocity Distribution Slightly Behind Trailing Edge at 0.7R of Propeller 4119

Figure 7 shows correlations of measurements with predictions downstream of the trailing edge. The influence of the viscous wake on the measured downstream field point velocity distribution can be seen. The viscous blade wake appears to increase the streamwise velocity parallel to the chordline, relative to the moving blade, while the velocity perpendicular to the chordline is reduced from the potential flow prediction. In the region between the blades, toward the pressure side of the blade, correlation with potential flow predictions is good.

### 3.2 Measured Blade Surface Pressure Distributions Derived from LDV Measurements

Blade surface pressure distributions were derived from the LDV measurements and compared to numerical lifting surface predictions. From the data shown in Figure 6, the potential flow velocity measured parallel to the blade surface,  $V_{\phi}$ , was extracted at the edge of the boundary layer, and referenced to the moving blade coordinate systems,  $(V_b)$ . The pressure coefficient was then calculated using

Bernoulli's equation for irrotational, uniform onset flow, nondimensionalized on the resultant inflow velocity,  $V_r$ .

$$C_p = 1 - (V_b/V_r)^2$$

Pressure distributions were derived from the measured results at the 0.7 radii of Propeller 4119. The streamwise blade surface angles,  $\phi$ , were set to measure velocities tangent to the suction side of the blade. Pressure side pressure distributions were approximated from the suction side measurements. The technique has the capability to extract the potential flow surface velocities of each blade of the propeller. In this case, the measured pressure coefficients represent the average value for all blades.

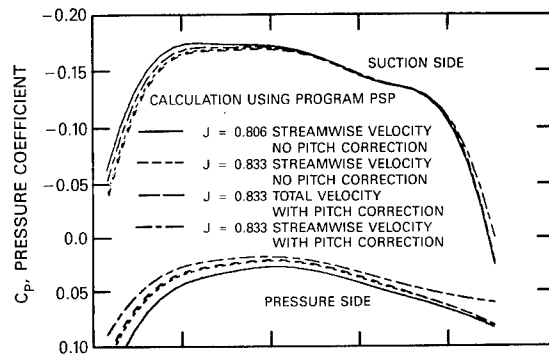


Figure 8a - Calculation for Different Input Parameters

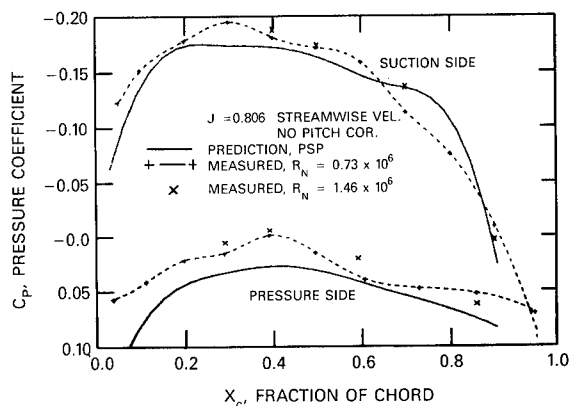


Figure 8b - Comparison of Measured and Calculated Results

Figure 8 - Pressure Distribution Derived From Measured Streamwise Potential Flow Velocity at 0.7R, Propeller 4119,  $J = 0.806$  With Correlation to PSP Predictions

Figure 8 shows the measured pressure coefficients at the 0.7 radius along with comparisons with numerical lifting surface theory (Kim and Kobayashi, 1984). Kim and Kobayashi's procedure signified by program PSP, uses the prediction procedure of Greely and Kerwin (1982) represented by program PSF-2 which also provided the field point velocity predictions. For these comparisons, PSP was modified to calculate pressure distributions based on the streamwise velocity components only, to be compatible with the LDV measurements. Figure 8a shows the variation in



pressure distribution predictions for variations in relevant PSP computer code input parameters. Little change resulted from computations based on the streamwise only and the total velocity along the blade surface at the 0.7 radius. The pitch correction adopted in PSF-2 is an empirical correction reducing pitch to account for viscous effects, and it was not considered in the correlation with measured results.

Figure 8b shows the experimental results compared to calculations. More extensive experimental results were recorded at the low Reynolds number of  $7.3 \times 10^5$ . Data show a reasonably faired distribution over the chord with some anomalies at midchord that could be due to experimental error or local unfaired geometry. The experimental distribution matches prediction reasonably well. The most obvious and accountable discrepancy occurs on the suction side of the blade over the latter part of the chord. There the calculated result underpredicts the measured value. This discrepancy is believed to be a boundary layer displacement thickness effect. The pressure distribution on the pressure side of the blade appears to be further from prediction than that on the suction side. This may be because the blade surface angle  $\phi$  was set to measure velocities tangent to the suction surface. Hence, significant errors may have resulted near the leading and trailing edges where the suction and pressure side surface angles were different.

Measurements taken at the higher Reynolds number ( $1.46 \times 10^6$ ) show a closer agreement with the potential flow predictions as expected, due to the smaller influence of displacement thickness, especially in the region aft of midchord.

TABLE 2 - PERFORMANCE PREDICTIONS FOR PROPELLER 4119

	J	$K_T$	$10 K_Q$
Measured Open Water Test	0.833 0.806	0.150 0.157	0.285 0.293
PSF-2 With Pitch Correction	0.833 0.806	0.151 0.162	0.282 0.298
PSF-2 Without Pitch Correction	0.833 0.806	0.153 0.164	0.287 0.303

### 3.3 Comparison of Measured and Predicted Thrust and Torque

Table 2 shows comparisons of measured and predicted thrust and torque for propeller 4119 at design J. Predictions using PSF-2 with a pitch correction for viscous effects were very close to measured open water test results, within 1% difference on thrust. The water tunnel test conditions were set by thrust identity based on the open water test results at a design J of 0.833. An effective J of 0.806 was established based on asymmetry in the inflow and possible errors in thrust measurement.

Predictions at this advance coefficient showed a significant discrepancy with the open water data. Further tests will include measurements of the inflow asymmetry and more careful load measurements to establish quantitative effects of viscosity on performance.

### 3.4 Boundary Layer Measurements

Boundary layer profiles were extracted from the streamwise velocity measurements at angular positions close to the blade surfaces. With the resolution of 4096 positions per revolution, data points through the boundary layer varied from four near the leading edge to sixty at the trailing edge. A diagonal traverse was obtained through the boundary layer at an angle of  $(90 - \phi)$  degrees from the normal vector from the surface. This effectively increased the resolution of the data normal to the blade surface, but introduced error due to streamwise gradients in the boundary layer profile. Because the boundary layer was relatively thin, streamwise variations were ignored.

Figure 9 shows boundary layer profiles along the suction side blade chord at the 0.7 radius of Propeller 4119 at the effective advance coefficient of 0.806 for the low Reynolds number case ( $7.3 \times 10^5$ ). The vertical scale for each profile represents distance normal to the surface. The boundary layer developed in a fashion typical of a planar wing section, with laminar flow occurring up to around midchord. The point of transition is somewhat ill-defined because of insufficient chordwise resolution and possible chordwise fluctuation in the transition point which would be time-averaged over the duration of run. Typical turbulent boundary layer development occurs at the trailing edge region.

Measured boundary layer parameters were compared to calculations using a two-dimensional procedure of Cebeci (1978). A faired pressure distribution from the measured results in Figure 8 was supplied as input to the calculation procedure. Figure 10 shows comparisons of the measured and calculated values of displacement thickness,  $\delta^*$ , and shape factor, H. The calculations were performed using prescribed transition locations of  $x_c$  equal to 0.5 and 0.6.

The correlation of displacement thickness shown in Figure 10a was reasonably good in the laminar flow region, with an underpredicted growth in boundary layer thickness in the turbulent region aft of midchord. Near the leading edge the measured displacement thickness of blade one was greater than calculated, possibly due to localized leading edge separation. Blade three was noticeably closer to the calculated values aft of midchord, which indicates blade-to-blade differences in geometry that will result in noticeable differences in boundary layer development.

The measured shape factor distribution over the chord resembles the calculated distribution in a general sense as shown in Figure 10b. Through the transition region the measured shape factors decreased less abruptly than predicted. Also there is significant

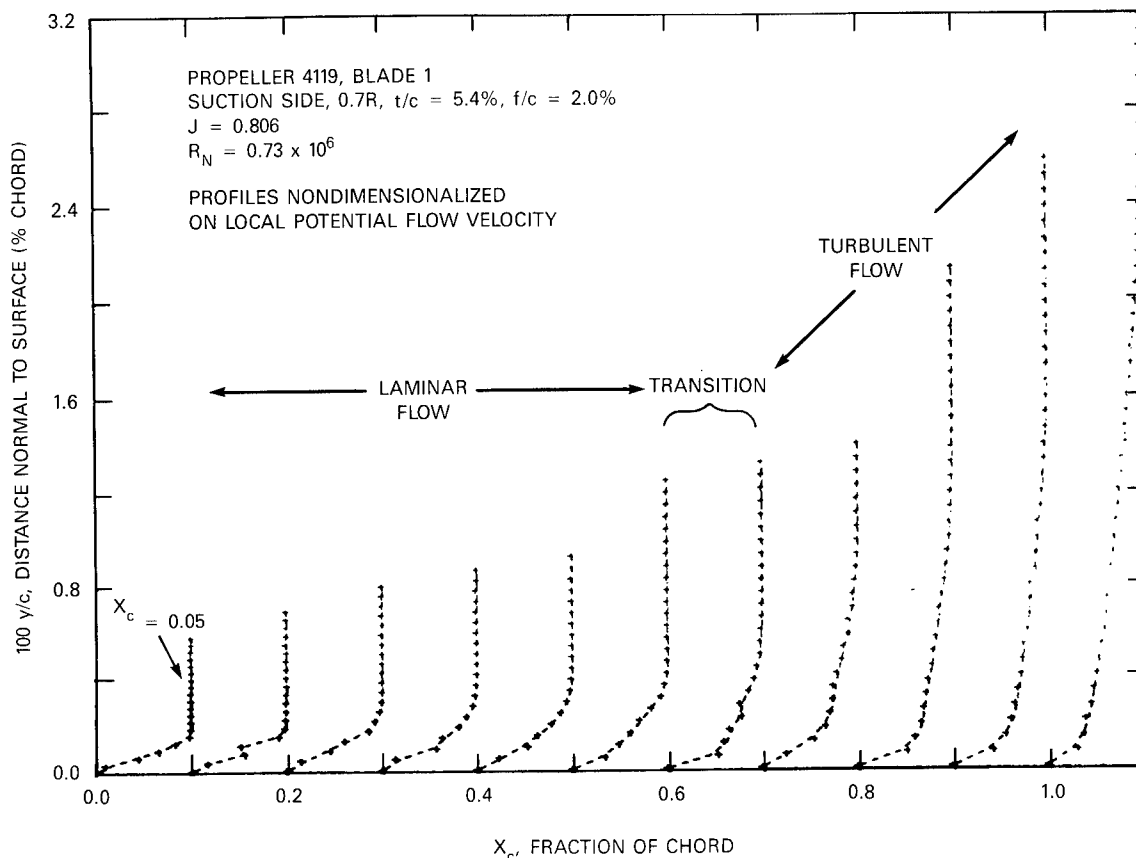


Figure 9 - Measured Streamwise Boundary Layer Growth on Propeller 4119 0.7R, Suction Side

scatter, blade to blade, in the transition region. The discrepancies observed between measured and calculated values of  $\delta^*$  and  $H$  could be due to three dimensional boundary layer effects that are not accounted for in the two dimensional calculations. Unfortunately, the error associated with the location of the boundary surface prohibits detailed analysis of the blade boundary layer. Improved blade angle resolution will result in more precise measured boundary layer profiles.

### 3.5 Measurement of Turbulence Intensity

A measurement of the turbulence intensity in the streamwise component of the blade boundary layer was obtained from the standard deviation of the measured velocity samples recorded at each blade angular position. The turbulence intensity,

$$\frac{\sqrt{(V_{\phi}(i) - V_{\phi})^2}}{V_{\phi}}$$

was referenced to the moving blade and non-dimensionalized by  $V_r$ , the resultant inflow to the blade section. A typical distribution of turbulence intensity across a turbulent boundary layer measured on Propeller 4119 is shown in Figure 11. The maximum turbulent intensity of about 10 percent is comparable to typical airfoil data. The turbulence intensity in the potential flow region away from the blade surface is approximately 1.5 percent relative to the moving blade.

When the turbulence intensity is nondimensionalized on advance speed,  $V_A$ , substantially larger turbulence levels occur. In this case values in Figure 11 would be uniformly increased by a factor of 2.8 resulting in maximum turbulence intensities of about 25 percent. The relatively high turbulence levels (relative to freestream speeds) that would be measured downstream of the propeller are produced by typical turbulent boundary layer growth on blade surfaces moving at speeds substantially higher than the freestream velocity. Therefore, with the absence of blade flow separation, propellers operating at higher advance coefficients would generally produce less downstream turbulence in the blade viscous wakes.

### 3.6 Flow Visualization of the Blade Surface Streamlines

After completion of the LDV measurements about Propeller 4119 blade surface flow visualization studies were conducted at the two Reynolds numbers tested. An oil dot technique was used in which a mixture of 90 weight gear oil and orange fluorescent pigment was applied with a drafting pen in a matrix of dots on the blade surface. The propeller was then run up to speed in the tunnel allowing the oil to spread from the dots at the desired test condition for approximately 30 seconds to a minute. When the propeller rotation and tunnel speed were ini-

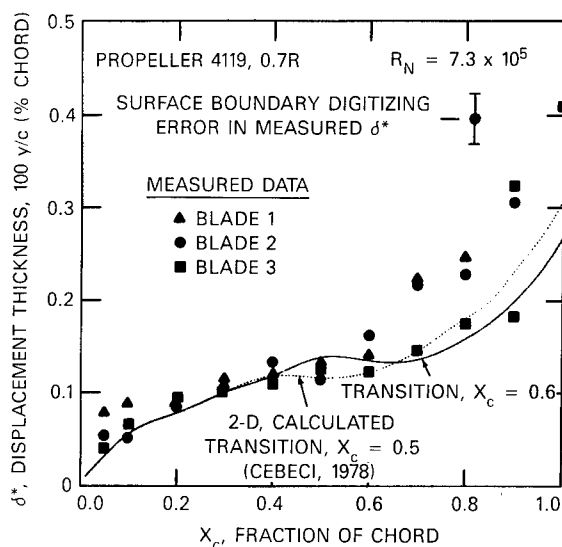


Figure 10a - Displacement Thickness

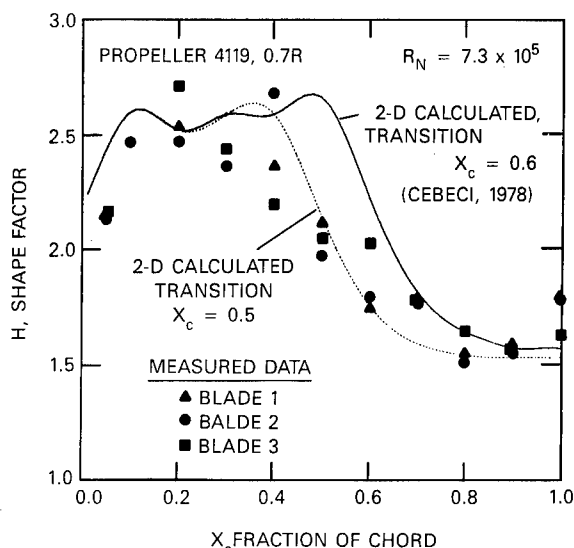


Figure 10b - Shape Factor

Figure 10 - Comparison of Measured Boundary Layer Parameters With 2-D Calculations

tially started, the tunnel speed generally lagged behind shaft rotation, so that the propeller operated at low advance speed in a transient fashion. Therefore, the initial 20 percent of the extended oil line was generally ignored. After the oil had extended completely from the dot, it was sufficiently fixed on the blade so that the running down of the shaft and water speed did not influence the oil pattern on the blade.

Figure 12 shows the results of the blade surface flow visualization conducted on Propeller 4119. Significant outward radial flow was observed over most of the blade, with a change in the surface streamline direction

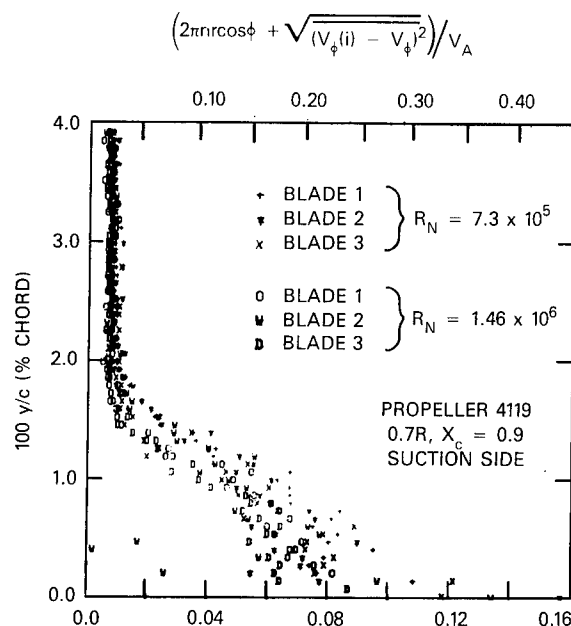


Figure 11 - Streamwise Turbulence Intensity Through the Blade Boundary Layer

occurring towards the trailing edge.

Surface flow patterns of this sort have been investigated by Meyne (1972) and Kuiper (1978) and have been related to laminar and turbulent boundary layer development on a rotating disk. In laminar flow the surface streamline direction,  $\beta$ , on a rotating disk is 40 degrees from the circumferential direction, while in turbulent flow the angle is reduced to 11 degrees. The large difference in surface flow direction between laminar and turbulent boundary layer flow has been used qualitatively to determine regions on the propeller blades where laminar and turbulent flow occur. Large outward radial surface flow is associated with laminar boundary layer occurrence. When the surface flow direction changes to be oriented closer to the circumferential direction, the transition to a turbulent boundary layer is thought to occur.

The interpretation of surface flow direction should be considered relative to the local direction of the potential flow streamlines. In the midspan region of the blade the potential flow direction is approximately in the circumferential direction, so that qualitative boundary layer characteristics can be determined. Near the tip of the blade, strong radial flow velocities occur making qualitative interpretation difficult. If the potential flow streamlines were known, one could determine the angle  $\beta$  between the potential flow streamline and the surface streamlines from Figure 12.

Figures 12a and 12b show the surface streamline directions on the suction side of Propeller 4119 at the low Reynolds number

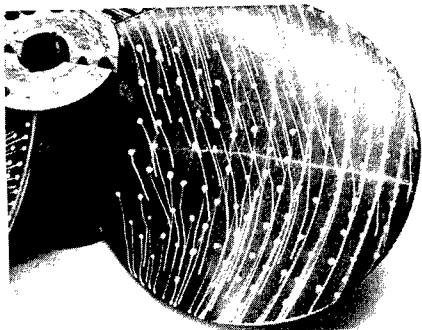


Figure 12a - Suction Side,  $R_N = 7.3 \times 10^5$

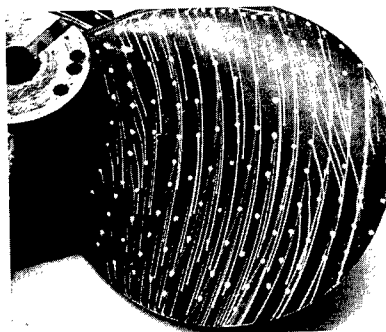


Figure 12d - Suction Side,  $R_N = 7.3 \times 10^5$   
With Leading Edge Trip Wire

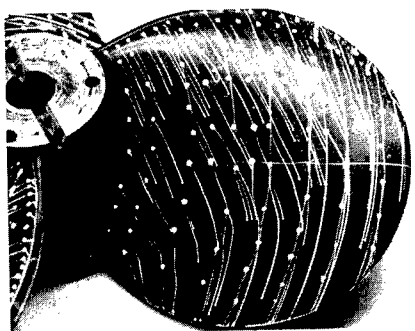


Figure 12b - Suction Side,  $R_N = 7.3 \times 10^5$

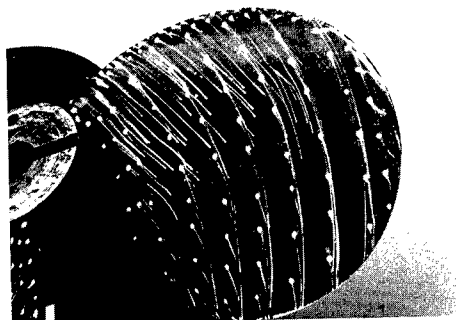


Figure 12e - Suction Side,  $R_N = 1.46 \times 10^6$

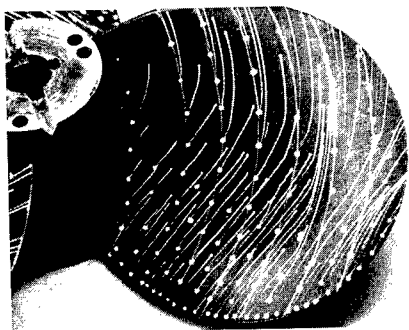


Figure 12c - Pressure Side,  $R_N = 7.3 \times 10^5$

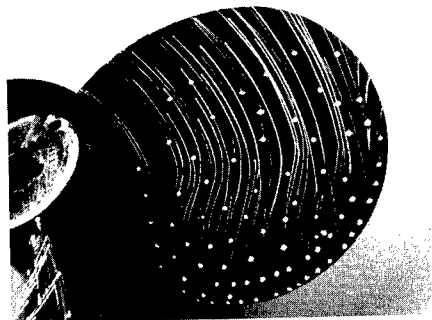


Figure 12f - Pressure Side,  $R_N = 1.46 \times 10^6$

Figure 12 - Blade Surface Flow Visualization on Propeller 4119 Using Oil Dot Technique

tested,  $7.3 \times 10^5$ . Significant laminar flow appears with transition occurring around midchord at the 0.7 radius. This result correlates well with the measured boundary layer profiles shown in Figure 9. Figure 12e shows the surface flow on the suction side at the higher Reynolds number tested,  $1.46 \times 10^6$ . At 0.7 radius transition is estimated to occur around 30 percent chord. Transition has migrated forward as expected but significant laminar flow still occurs at the inner radii.

Figure 12c and 12f show the surface flow on the pressure side of the blade at the two Reynolds numbers tested. Again, significant laminar flow occurs over much of the blade at low Reynolds number, with transition shifting

towards the leading edge at the higher Reynolds number run.

Figure 12d shows the blade surface flow on the suction side of the blade at the low Reynolds number condition with a 0.010 inch (.25mm) diameter trip wire attached near the leading edge from the 0.3 radius to the 0.7 radius. Downstream of the trip wire turbulent flow appeared to occur, but laminar flow persisted outboard of the trip wire from the 0.7 to 0.8 radii. No boundary layer measurements were made when trip wires were applied to the blades. In the future the LDV techniques described could be used to quantify the effects of boundary layer trips to simulate full scale Reynolds number flow similar to work done by McCarthy, et al. (1976) on axisymmetric bodies.

### 3.7 Qualitative Boundary Layer Measurements at Off Design Conditions

During the initial exploratory tests with the propeller boundary layer LDV system, qualitative measurements using a storage oscilloscope were conducted on propellers operating at off design conditions. An unskewed four bladed propeller, with wide, thin blades was used for these initial tests. Design J for this propeller was approximately 0.9 and qualitative measurements were obtained at J values of 0.38, 0.6 and 1.03.

Figure 13 - Qualitative Velocity Measurements in the Pitch Line Direction on a Four Bladed Propeller at Off Design Conditions at 0.7 Radius

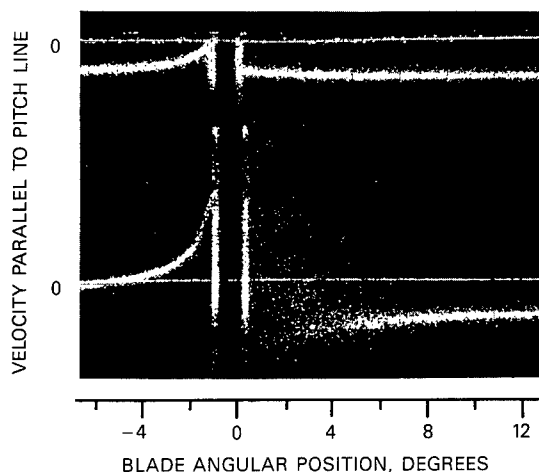


Figure 13a - 2% Chord on Suction Side of Blade  
Top, J = 1.03, Bottom, J = 0.38, Boundary Layer Flow

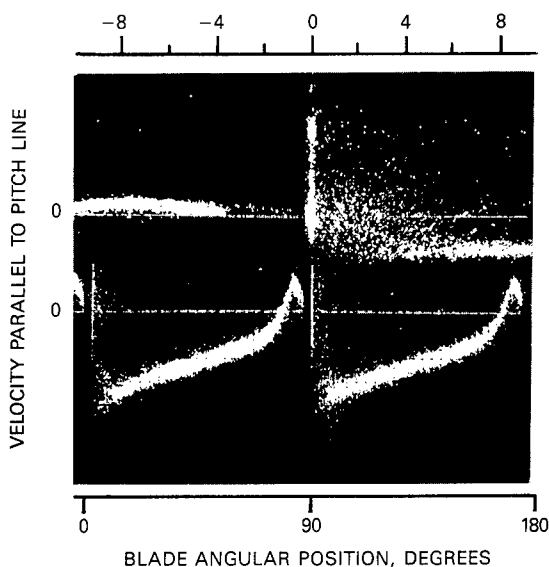


Figure 13b - 10% Chord on Suction Side of Blade,  
J = 0.38 Top, Boundary Layer Flow, Bottom,  
Blade to Blade Potential Flow

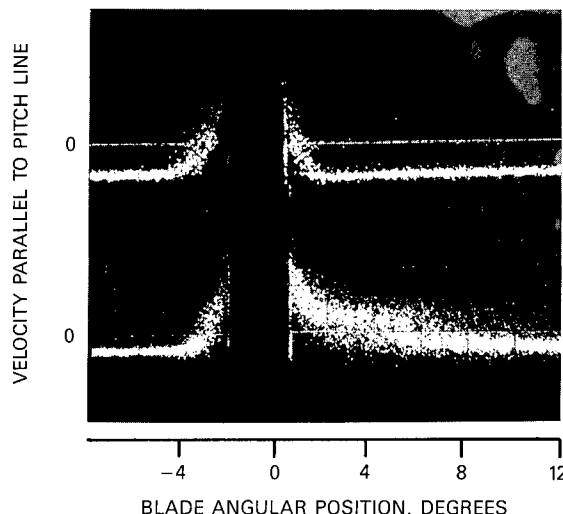


Figure 13c - 87% Chord on Suction Side of Blade  
Boundary Layer Flow, Top, J = 1.03, Bottom J = 0.38

Velocity measurements near the leading edge of the blade at the low advance coefficients of 0.38 and 0.6 showed localized leading edge separation. During these tests, velocity was measured in the forward direction parallel to the pitch line of the propeller. Figure 13a shows the local blade velocity at a position corresponding to 2 percent chord on the suction side of the blade at the 0.7 radius. At the high J=1.03, low loading condition, the angle of attack of the section is small and the flow is attached on both sides of the blade. At the low J condition, the section is at a relatively high angle of attack inducing a large velocity difference between the suction and pressure sides of the blade. The potential flow velocity approaching the suction side of the blade appears to disintegrate producing large fluctuations in velocity near the surface, associated with a region of separated flow. Figure 13b shows velocity profiles corresponding to the 10 percent chord position on the suction side. The top trace shows the local boundary layer flow indicating, again, large velocity fluctuations on the suction side of the blade. It is not obvious whether the boundary layer is attached or separated on the suction side at this chord position. The blade to blade potential flow in the lower trace shows the disintegration of the potential flow velocity near the suction side surface. Figure 13c shows the boundary layer flow at the 87 percent chord position at the high and low J conditions. At low J, in the lower trace, the suction side boundary layer appears turbulent and attached with a lower level of velocity fluctuations than observed close to the leading edge. The upper trace, corresponding to the J=1.03 condition, shows a much thinner turbulent boundary layer resulting from a more favorable chordwise pressure distribution and a smaller or no region of leading edge separation.

The effects of leading edge separation were discussed extensively by Greeley and Kerwin (1982) in relation to propellers. Generally, a long separation bubble extending over an appreciable fraction of the chord will reduce the suction peak predicted at the leading edge from potential flow theory. From Figure 13b, this appeared to be occurring. To check this, qualitative comparisons were made between measured and predicted velocity profiles through the 4 percent chord position of the four bladed propeller tested. Figure 14 shows the qualitative comparisons of measured results with PSF-2 (Greeley, 1982). The potential flow calculation shows significant peak velocities on both the suction and pressure sides of the blade. The measured result shows no suction side peak, implying a separation bubble occurring and reducing the magnitude of the potential flow velocity near the leading edge.

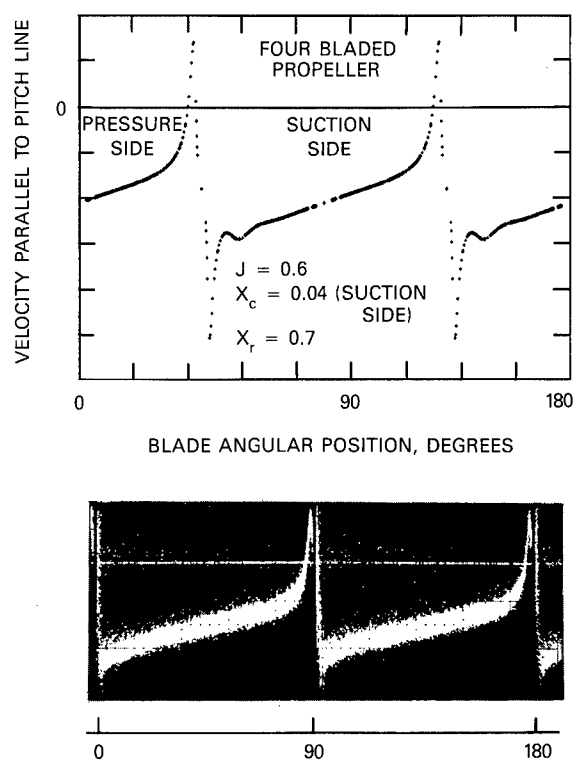


Figure 14 - Qualitative Comparison of Measured Velocity Parallel to Pitch Line With Calculated Values Using PSF-2 and FPV-10 at 4% Chord

From the measured result, an approximate suction side surface velocity could be generated by straight line extrapolation of the potential flow velocity approaching the suction side of the blade.

### 3.8 Field Point Velocity Measurements With Sheared Onset Flow.

Velocity measurements were made ahead of a propeller operating in a sheared axisymmetric onset flow. This investigation was intended to compare measured performance with predictions

using program PSF-2 of Greeley (1982) applied to a radially varying inflow.

The axisymmetric sheared wake was generated in the DTNSRDC 24-inch water tunnel using a 3 foot (0.9m) long, 6 inch (15.2 cm) diameter cylinder with an attached tail cone faired into the hub of the propeller. Also, an additional wake generator was used comprised of nine concentric rings 0.125 inches (3.2 mm) thick and 5 inches (12.7 cm) long mounted around the cylinder approximately 1.5 diameters ahead of the propeller. DTNSRDC Model Propeller 4645, a skewed, seven bladed, wake adapted propeller similar to that described by Wilson (1982) and Valentine and Chase (1976) was used for these tests.

Test conditions in the tunnel were set using thrust identity with an approximate design thrust coefficient,  $K_T = 0.28$ . Field point velocity measurements of axial and tangential velocity,  $V_x$  and  $V_t$ , were performed ahead of the operating propeller at an axial plane as close to the propeller as possible. Because of the aft rake of the blade sections, this resulted in measurements at the leading edge at the 0.3 radius and progressively further from the leading edge with increasing radius. A nominal inflow wake was determined by removing the propeller and measuring the axial inflow velocity,  $V_x$ , at the same measurement plane and at the same tunnel impeller rotation speed.

Programs PSF-2 and FPV-10 were used to predict the propeller's performance and field point velocities across the propeller disk.

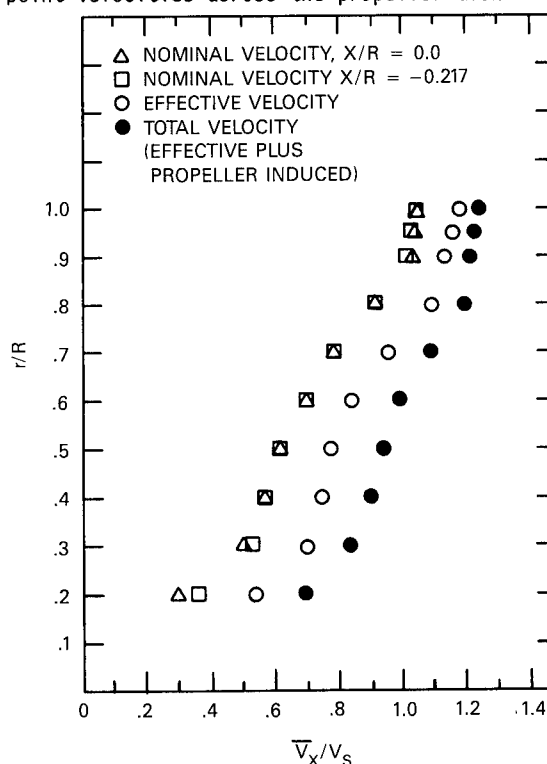


Figure 15 - Calculation of Effective Wake From Predicted and Measured Circumferential Average Velocities Ahead of Propeller 4645 in a Sheared Wake

The effective wake into the propeller was determined using PSF-2 and FPV-10 together with the experimental data obtained ahead of the propeller. Initially, the measured nominal wake was used as input to PSF-2 and FPV-10. The resultant calculated circumferential average propeller induced velocity at each radius was then subtracted from the measured total velocity leaving the estimated effective wake. This procedure was repeated for three iterations until the computed total velocity matched the measured values. Figure 15 shows the nominal, total and final effective wake distributions. It has been shown by Huang (1976) that the nominal and effective wake converge at a point beyond the propeller tip. The present results do not show this trend, possibly because of the confined flow in the water tunnel.

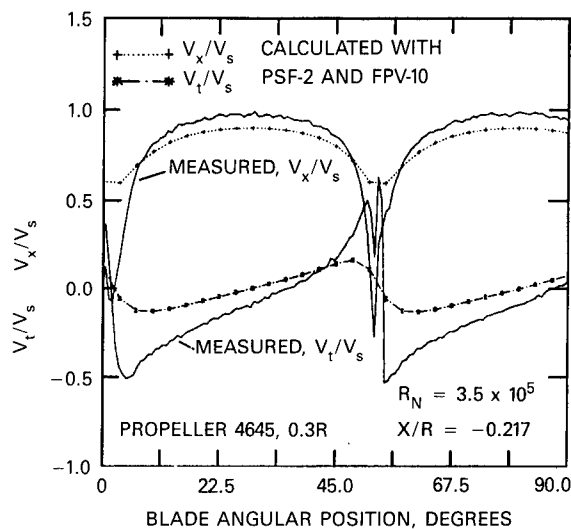


Figure 16a - Measurements at 0.3R

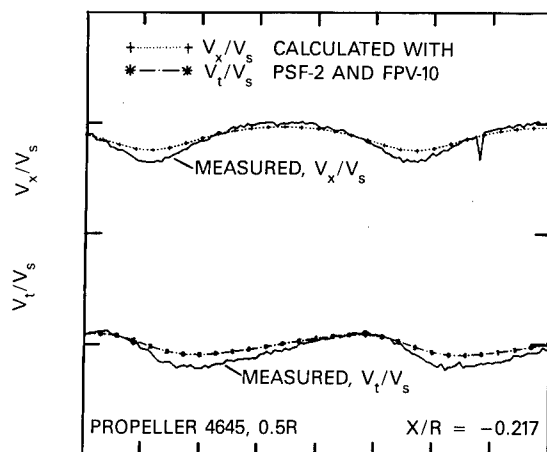


Figure 16b - Measurements at 0.5R

Figure 16 - Comparison of Measured and Calculated Field Point Velocity Distributions Ahead of Propeller 4645 Operating in a Sheared Wake

Predictions of the field point velocity distributions were compared with measured total velocity across the propeller disk. Figure 16a shows comparisons of  $V_x$  and  $V_t$  at 0.3 radius. The calculation underpredicts the circumferential variation of both velocity components. A possible explanation is the inaccuracies of thin wing theory in accounting for the influence of blade thickness close to the leading edge. At the 0.3 radius, the blade section was relatively thick and the measurements were obtained at the leading edge. Figure 16b shows comparisons at 0.5 radius. There, the blade section was thinner, and the measurement was sufficiently distant from the leading edge to avoid inaccuracies in the modeling of thickness effects, but the calculated result also underpredicted the measured peak to trough circumferential variation.

Comparison was also made of measured and predicted thrust. Initially, predictions were made of the measured open water performance of Propeller 4645 showing agreement to within 2 percent near its design condition. With the same empirical wake input parameters as in uniform flow, the effective wake in shear flow was input resulting in a 12 percent overprediction of the measured thrust set in the tunnel. This was inconsistent with the underprediction of the circumferential variation of the field point velocity ahead of the propeller. The field point velocity correlation suggested that the predicted loading should be higher, while the predicted thrust was already too high. There may have been experimental errors in the thrust measurement, and possible asymmetry in the sheared inflow wake, but it's unlikely these would explain the large discrepancy observed. Possible reasons for the discrepancies are hypothesized as follows:

1. Lack of consideration of the three dimensional nature of the induced velocity components associated with the effective wake in shear flow.
2. Improper modeling of the flow through the propeller in sheared wakes using program PSF-2, especially the downstream wake structure.
3. At inner radii, use of thin wing theory to model thickness effects in PSF-2.

#### 4. CONCLUDING REMARKS

The primary contribution of this paper is the introduction of a local flow measuring technique with a great potential to investigate a variety of propeller problems. A high resolution one component back scatter LDV system has been developed to measure flows about operating propellers. A small LDV measuring volume, high resolution optical shaft encoding, and computer data acquisition and analysis have permitted detailed velocity measurements forward, aft, and within the blade boundary layers of operating propellers. The following conclusions can be made concerning the experimental results described in this paper:

1. Good correlation of measured and predicted (Greeley 1982) field point velocities have been further validated ahead of operating propellers in uniform flow. Correlation of field point velocities in the slip stream show discrepancies believed to be due to boundary layer displacement effects not modeled by the prediction method.

2. Blade surface pressure distributions can be derived from LDV measurement of potential flow velocity at the blade surface. Correlations with calculations (Kim, 1984) have shown reasonable agreement with noticeable Reynolds number effects on pressure distribution that are attributed to displacement thickness effects.

3. Streamwise boundary layer measurements on the suction side of Propeller 4119 have shown substantial laminar flow at model scale Reynolds numbers. Location of transition determined from measured boundary layer profiles correlated well with oil dot surface flow visualization techniques. Measured boundary layer growth at mid-span of the blade was approximated well with two-dimensional boundary layer theory using the measured pressure distribution.

4. Measured streamwise turbulence intensity through the turbulent boundary layer shows a typical magnitude relative to the moving blade reference frame.

5. Local blade flow measurements at off-design, low J conditions show leading edge separation with a resulting reduction in potential flow suction peaks.

6. Field point velocity and thrust measurements for a propeller operating in a sheared wake show an inconsistency between measured and calculated results possible due to improper wake modeling in sheared flow and/or the three dimensionality of the effective wake.

#### REFERENCES

- Cebeci, T. (1978): A Computer Program For Calculating Incompressible Laminar and Turbulent Boundary Layers on Plane and Axisymmetric Bodies with Surface Roughness. Report No. TR-78-1, California State University at Long Beach, Long Beach, California.
- Denny, S. (1968): Cavitation and Open Water Performance Tests of a Series of Propellers Designed By Lifting-Surface Methods. David W. Taylor Naval Ship Research and Development Center, Report No. 2878.
- Greeley, S. and Kerwin, J.E. (1982): Numerical Methods for Propeller Design and Analysis in Steady Flow. SNAME TRANSACTIONS, Vol. 90.
- Huang, T.T. and Groves, N.C. (1980): Effective Wake: Theory and Experiment, 13th ONR Symposium on Naval Hydrodynamics, Tokyo, Japan.
- Kerwin, J.E. and Lee, C.S. (1978): Prediction of Steady and Unsteady Marine Propeller Performance by Numerical Lifting Surface Theory. SNAME TRANSACTIONS, Vol. 86.
- Kerwin, J.E. (1979): Propeller Field Point Velocity Program FPV-10. MIT Dept. of Ocean Engineering, Cambridge, Mass.
- Kerwin, J.E. (1982): Flow Field Computation for Non-Cavitation and Cavitating Propellers. 14th ONR Symposium on Naval Hydrodynamics, Ann Arbor, Michigan.
- Kerwin, J.E. (1979): Propeller Field Point Velocity Program FPV-10. MIT Dept. of Ocean Engineering, Cambridge, Mass.
- Kerwin, J.E. (1982): Flow Field Computation for Non-Cavitation and Cavitating Propellers. 14th ONR Symposium on Naval Hydrodynamics, Ann Arbor, Michigan.
- Kim, K.H. and Kobayashi, S. (1984): Pressure Distribution on Propeller Blade Surface Using Numerical Lifting-Surface Theory. SNAME Propellers '84 Symposium, Virginia Beach, Virginia.
- Kobayashi, S. (1981): Experimental Methods for Production of the Effect of Viscosity on Propeller Performance. Report No. 81-7. MIT Dept. of Ocean Engineering, Cambridge, Mass.
- Kuiper, G. (1978): Scale Effects on Propeller Cavitation Inception. 12th ONR Symposium on Naval Hydrodynamics, Washington, D.C.
- McCarthy, J.H., et al. (1976): The Roles of Transition, Laminar Separation, and Turbulence Stimulation in the Analysis of Axisymmetric Body Drag. 11th ONR Symposium on Naval Hydrodynamics, London.
- Meyne, K. (1972): Untersuchung der Propellergrenzschichtströmung und der Einfluss der Reibung auf die Propellerkenngrößen (Investigation of Propeller Boundary-Layer Flow and Friction Effects on Propeller Characteristics). Jahrbuch der Schiffbautechnischen Gesellschaft, Band 66, Also DTNSRDC translation 352.
- Min, K.S. (1978): Numerical and Experimental Methods for the Prediction of Field Point Velocities Around Propeller Blades. Report No. 78-12, MIT Dept. of Ocean Engineering, Cambridge, Mass.
- Valentine, D.T. and Chase, A. (1976): Highly Skewed Propeller Design For A Naval Auxiliary Oiler (AO177). David W. Taylor Naval Ship Research and Development Center, Report No. DTNSRDC/SPD-544-12.
- Wilson, M.B., et al. (1982): Causes and Corrections for Propeller-Excited Airborne Noise on a Naval Auxiliary Oiler. SNAME TRANSACTIONS, Vol. 90.



## DISCUSSION

JÖRG BLAUROCK,  
Hamburg Ship Model Basin, Hamburg, Germany:

First I wish to congratulate the Authors on their excellent paper.

My impression is that you have solved some serious technical problems to enable the determination of the pressure distribution on the blades of a rotating propeller by means of LDA.

But now I will pass on to a detail of your paper. On Fig. 12d we see mainly turbulent flow, caused by the trip wire attached near the leading edge, whilst on the blade without trip wire (Fig. 12a) at the same Reynolds number the fore part of the suction side is covered mainly by laminar flow.

Likely the turbulent flow will represent the full scale condition well. But as we all know it is important and necessary to manufacture just the leading edge of the blade as accurate as possible. Now you put a wire of 0.25 mm diameter at the leading edge. This seriously changes the geometry and hence influences the pressure distribution in the forward part of the blade significantly. This consequently will cause further problems when this tool will be used for cavitation tests too.

My question therefore is, did you use this trip wire only for the purpose of this research work or will this become a standard procedure at your institute?

WENDY EVE BALL,  
Admiralty Research Establishment, Haslar,  
United Kingdom:

I would like to thank the authors for a very interesting paper. I note that in one of your experiments you used a leading edge trip wire to create a turbulent boundary layer on the model blade. I would be interested for comments by the authors on boundary layer tripping techniques and whether they intend to do further work in this field.

MING S. CHANG and NANCY C. GROVES,  
David W. Taylor Naval Ship R&D Center,  
Bethesda, MD, USA:

The authors are to be congratulated on their paper. Their pioneering efforts in the measurements of propeller flow characteristics have provided both interesting and useful data. Their discussions on Laser Doppler Velocimetry techniques will be helpful to other experimentalists venturing into this difficult area. Their boundary-layer results are a welcome addition to the scarce data base which results for flow measurements on propeller blades and their shear flow measurements should stimulate interest in an area so often neglected. We have two comments for the authors:

1. We found your flow visualization results in Figure 12 quite interesting since we

have computed the flow on Propeller 4119 using our boundary-layer code. Our crude measurements from Figures 12a and 12b of the limiting streamline angle at the 0.7 radius give angles of 25-30 degrees just ahead of transition. Our calculations predict this angle to be 35 degrees at this location. Would it be possible for you to give a more accurate estimate of this angle? Also, Figure 12d shows a surprising phenomenon occurring at the tip when a trip wire is placed between  $0.3 < r/R < 0.7$ . The flow appears to be turbulent downstream of the trip wire and yet laminar outboard of the trip wire. This would be a challenging test case for our boundary-layer calculation program; we plan to modify the code so that transition is a function of radius. It will be interesting to determine if we can predict this behavior.

2. Our second comment refers to your measurements with a sheared onset flow. We agree that the lack of convergence of the nominal and effective wakes beyond the propeller tip, as shown in Figure 15, could be the result of the confined flow in the tunnel. Had the tunnel effects been subtracted in the calculation of the effective wake, the effective wake at the tip would have been reduced. Also, do you have any physical explanation for the nonzero average measured tangential velocity and for the negative value in the measured axial velocity in Figure 16?

## AUTHORS' REPLY

Initially, we would like to thank all the discussers who commented on our paper. First, we would like to respond to the questions of Ms. Ball and Mr. Blaurock. The reason the tip wire was used to trip the blade boundary layer in Figure 12d was purely for convenience. The wire has a uniform diameter and is very easy to apply at the leading edge. For studies of detailed leading edge flow or leading edge cavitation the wire trips may distort the flow significantly but tripping may not be necessary when cavitation occurs due to occurrence of leading edge separation. A possible advantage of wire trips may be in the ability to predict their parasitic drag for use in high Reynolds number design J, thrust and torque predictions. It is believed that at design condition, where the sections are operating at shock free entry, potential flow modifications due to the trip would be unimportant. Studies of blade boundary layer trips and cavitation are planned at DTNSRDC by Dr. Young Shen, possibly incorporating the LDV techniques discussed in this paper.

Dr. Breslin addressed the existence of a three-dimensional stagnation point at the leading edge of the blade. Only blade streamwise measurements were presented in this paper so that only a streamwise two-dimensional type stagnation point could be observed. In Figure 6 the second plot from the top shows the streamwise velocity relative to the blade on the pressure side at  $x_c = 0.009$ . Near the pressure side surface an extreme velocity gradient is ob-

served that is associated with the streamwise stagnation point. This gradient in velocity decreases along the chord. It is believed that more detailed measurements in this region could more precisely map the streamwise stagnation flow.

To investigate the radial flow stagnation point, a different LDV optical arrangement is required. To maintain a small measuring volume in the direction where extreme radial velocity gradients occur, it is required to transmit the laser beams into the water tunnel at angles up to 40 degrees from a plane perpendicular to the tunnel axis. An optical arrangement of this sort has been developed and tested this past year, and in later years will be used to map the radial stagnation flow. It's our belief that the radial stagnation point will occur at the furthest forward leading edge point. On propeller 4119 this would correspond to somewhere around 0.7 R. For propellers with skew, the furthest forward leading edge point will generally be more pronounced. It is also thought that a stagnation line emanating from the three dimension stagnation point would dominate the stagnation geometry and would lead to typical two dimensional stagnation flow over most of the blade similar to Figure 6 in the paper.

Dr. Maruo asked if we had observed cases of laminar separation associated with radial surface flow converging to a radial separation line. In flow visualization tests, primarily on skewed propellers, we have observed this type of surface flow that we have attributed to laminar separation. In one case it was very localized at the 0.4 to 0.5 radius at around 0.8 chord. When the boundary layer was tripped at the leading edge, the surface flow lines maintained a pattern similar to that in Figure 12d implying the elimination of laminar separation. In other cases, the observed separation line continued over most of the radius at about 0.8 c. Tripping the boundary layer only caused the separation line to occur slightly further toward the trailing edge. For this case it was assumed that turbulent separation was occurring.

We would guess that these types of separation patterns are a result of very strong adverse pressure gradients in the streamwise and or radial direction. Predictions of streamwise pressure distributions using program PSP of Kim (1984) for the propellers described above show pressure minimums at around 0.7 to 0.8 chord followed by extreme adverse pressure gradients continuing to the trailing edge. It is believed that these unfavorable pressure distributions are associated with skewed propellers (that is not observed on propeller 4119). Radial boundary layer growth appears to be very extreme in these regions and is likely to be strongly coupled to the streamwise boundary layer behavior. We would recommend calculating the blade pressure distributions on propellers that appear to produce laminar or turbulent boundary layer separation and compare these to propellers that have good boundary layer characteristics. This may provide some understanding of the propeller para-

meters, such as skew, thickness, and camber, that will result in poor viscous performance. In the future we hope to exercise Nancy Groves' program (15th ONR) to investigate separation.

Dr. Ming Chang and Ms. Nancy Groves asked about estimates of the limiting streamline angle,  $\beta$ , from visualization shown in Figure 12. In our paper, we described the angle  $\beta$  with respect to the potential flow streamline direction. Therefore it was felt that estimation of these angles would be inappropriate without the radial potential flow being known. Fortunately,  $\beta$  in Groves' paper is referenced to the coordinate,  $\xi$ , in the chordwise direction. Therefore it is planned to carefully measure the  $\beta$  angle from enlargements of Figures 12 a and b.

Dr. Chang and Ms. Groves also questioned the results measured in sheared onset flows. The lack of convergence of the nominal and effective wakes at the propeller tip was attributed to effects of the confined tunnel. The results shown in Figure 15 had not been corrected for these assumed tunnel effects. A measure of the volumetric flow through the tunnel with and without the propeller operating should permit this correction to be made and it will be pursued at a later time.

The concern about the non-zero average of the tangential velocity shown in Figure 16 is also a concern to us. It is possible that in a sheared viscous flow this component ahead of the propeller may not be zero, but we tend to believe that this discrepancy is due to experimental error due to flow asymmetry, improper measuring volume location or direction orientation, or an offset error in LDV signal processing.

We would like to emphasize that the measurements made in sheared onset flow were intended to be exploratory in nature. We think that only qualitative conclusions are appropriate, one being that more work in this area is needed and welcomed.

# CORRELATION OF WAKE MEASUREMENTS AT MODEL AND FULL SCALE SHIP

JÜRGEN KUX AND JOCHEN LAUDAN

## ABSTRACT

Results from measurements of the velocity in the wake of two ships of different block coefficient at full scale and at model scale in the towing tank at comparable conditions are presented. In both scales Laser Doppler Velocimetry (LDV) was applied using two specially designed LDV systems which are briefly described. At the model all three velocity components were determined in three transversal planes while in the full scale experiments only the axial component in one single plane was measured. A coarse picture of the distribution of the axial turbulence intensity at full scale can be derived. Based on the data set obtained the validity of different scaling procedures was tested. For the slender ship the velocity fields of ship and model match quite well after extrapolation while the correlation for the full ship form is not satisfactory. Different approaches of velocity field analysis are proposed. Space derivatives of the experimental values are computed and allow to depict the distribution of vorticity and similar characteristics of the wake. Boundary layer calculation results are shown for comparison.

## NOMENCLATURE

$\vec{a}, a_i$	acceleration
$A_o$	propeller disc area
$B/T$	breadth to draught ratio
$C_B$	block coefficient
$C_{BA}$	block coefficient of afterbody
$C_F$	frictional resistance coefficient
$C_{Th}$	thrust loading coefficient $= T/0.5\rho V_o^2 A_o$
$d$	deformation rate
$d_{ij}$	components of $S$
$D$	diameter of propeller
$F_n$	Froude number
$k$	three dimensional form factor
$K_Q$	torque coefficient $Q/\rho n^2 D^5$
$K_T$	thrust coefficient $T/\rho n^2 D^4$
$L_{pp}$	length between perpendiculars
$n$	rate of propeller revolution
$R$	radius of propeller
$R_n$	Reynolds number

$S$	symmetric part of $V$
$t$	thrust deduction fraction
$T$	thrust
$\vec{v}, v_i$	velocity vector
$V, v_{ij}$	tensor (second rank) of velocity gradient
$V_o$	speed of ship or model
$w_d$	displacement wake fraction
$w_f$	frictional wake fraction
$w_T$	wake fraction determined from thrust identity
$w_w$	wave wake fraction
$x, y, z$	rectangular cartesian coordinates fixed to the ship. The x-axis is forward and parallel to the baseline, the y-axis is to starboard and the z-axis vertically downwards. The origin, defining the propeller plane, lies in the intersection of shaft axis and generator line.
$\Delta C_F$	roughness allowance
$\Delta$	Laplacian
$\delta$	thickness of boundary layer
$\delta_{ij}$	Kronecker symbol
$\lambda$	scale ratio
$\lambda$	eigenvalue of $V$
$\nu$	kinematic viscosity
$\epsilon_{ijk}$	totally antisymmetric tensor
$\rho$	mass density of water
$\Omega, \omega_{ij}$	antisymmetric part of $V$
$\vec{\omega}, \omega_i$	vorticity vector
$\omega$	magnitude of $\vec{\omega}$
$II$	second principal invariant of tensor $V$
$v$	

## 1. INTRODUCTION

A satisfactory calculation method for the prediction of the wake field on a theoretical basis is nowadays not yet available. A better understanding of the wake flow therefore is of theoretical interest. Besides this the practical interest is raised by the fact that in order to design optimized propellers the know-

Jürgen Kux, Institut für Schiffbau, Lammersbeth 90, D-2000 Hamburg 60  
Jochen Laudan, Hamburgische Schiffbau-Versuchsanstalt GmbH, Postfach 60 09 29, D-2000 Hamburg 60

ledge on the ship wake is a most important prerequisite. The mean velocity values of the effective wake averaged in circumferential direction determine the pitch distribution of the blades and the power prediction as the propeller is designed while cavitation and vibration effects depend on the local, i.e. radial and tangential variation of the wake.

As prediction methods for the wake field are not available, not even by some continuation of a boundary layer calculation, more success is expected from scaling procedures which transform a measured model wake to full scale. The procedures so far proposed are not based on a theoretical derivation but consider thickness of the hull boundary layer (taken to be a flat plate boundary layer) as expected at different scales. These procedures were developed with the main purpose (except Hoekstras method) to support at design the choice of the appropriate rate of propeller revolution for the full scale case. Therefore their predicting power for the wake velocity field has to be tested by measurements behind ship hulls at model and full scale under comparable conditions. We report on such measurements and some results in this paper, measurements which were performed on two ships and their models in the frame of a research project funded by the German Federal Ministry of Research and Technology BMFT.

This contribution presents results of activities in the field of wake investigation as obtained by the Hamburgische Schiffbau-Versuchsanstalt (HSVA) and by the Institut fuer Schiffbau (IfS), including the measurements referred to above, an evaluation of scaling procedures and some approaches of wake velocity field analysis. The latter rely on the knowledge of the spatial derivatives of the velocity vector which may be computed if velocity data is available from the experiment in a net of points in space of adequate density.

## 2. CHARACTERISTICS OF SHIPS AND MODELS INVESTIGATED

Measurements were carried out at two ships of different block coefficient: "Sydney Express" from HAPAG-Lloyd and "St. Michaelis" from Hamburg-Suedamerikanische Dampfschiff-fahrtsgesellschaft.

The "Sydney Express" is a container ship with a length/breadth ratio of  $L/B = 6.9$  and a block coefficient of  $C_B = 0.61$ . Fig. 1 shows the body plan, the main dimensions are given in Table 1. The ship is equipped with a semi-balanced rudder. At a scale of 1:28, a plastic model was manufactured. For turbulence stimulation a sand strip was attached to the forebody at a distance of  $0.025 L_{pp}$  after the forward perpendicular. Propeller data are also given in Table 1. The distance from the propeller plane to frame 0 is 3.7 m for full scale.

The "St. Michaelis" is a product tanker with a length/breadth ratio of  $L/B = 5.4$  and a block coefficient of 0.80. Fig. 2 shows the body plan, the main dimensions are given in Table 2.

A model was manufactured of wood at a scale of 1:25.5. Ship and model are fitted out

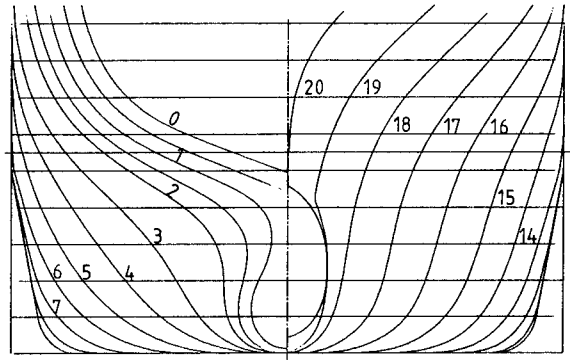


Fig. 1 "Sydney Express", Body Plan

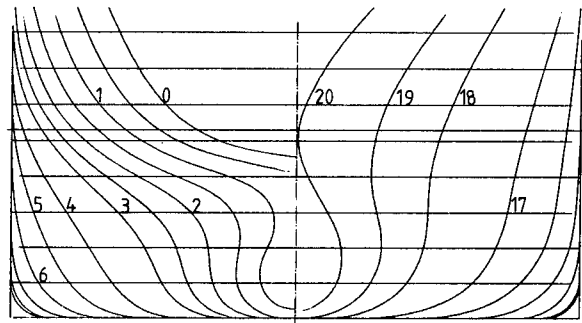


Fig. 2 "St. Michaelis", Body Plan

with a semi-balanced rudder. Turbulence stimulation is done by a sand strip on the forebody at a distance of  $0.025 L_{pp}$  after the forward perpendicular. Again propeller data are also given in Table 2. The propeller plane lies 3.5 m in front of frame 0 for full scale.

## 3. MEASUREMENT OF THE VELOCITY FIELD IN THE WAKE FLOW

### 3.1 Model Wake

#### 3.1.1 Description of Measuring Device

A Laser-Doppler Velocimeter (LDV) was used for the measurements of velocity in the large towing tank of HSVA. The device allows to measure three velocity components simultaneously. The layout of this LDV-device is shown in Fig. 3. At first the beam from an argon ion laser (Spectra Physics Model 165-08) is split into two beams (one blue and one green) in an optical unit by using a colour separator. The blue beam then is split into two beams and one of these beams is frequency shifted with 38 MHz by means of a Bragg cell. Then these beams are transmitted down in the interior of the fin to the lower end. The green beam is first split into three beams. Then one beam is frequency shifted with 42 MHz and the second one with 38 MHz, both with respect to the unshifted third beam. Then these three beams are also

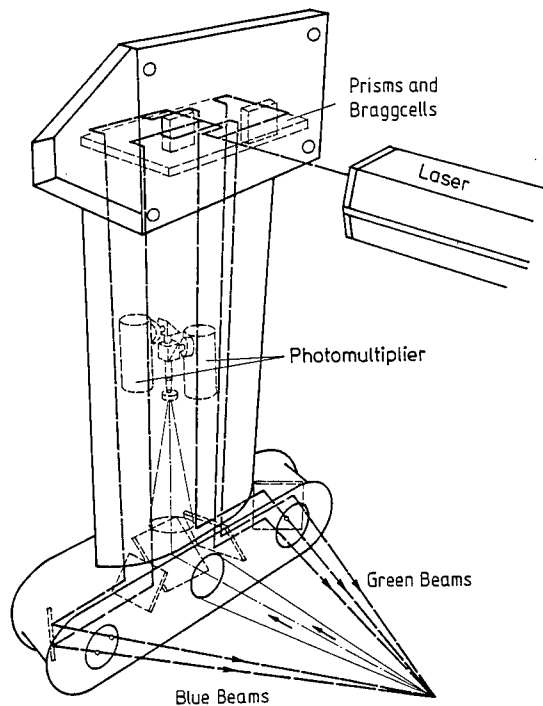


Fig. 3 Optics of Towing Tank LDV-System

transmitted down through the fin. At the bottom of the pod the five beams are deflected by a system of mirrors and leave the pod through two wedge-shaped lenses, which focus the beams. The measuring volume is thus formed by the intersection of five laser beams. All the beams have passed through the same optical path length, so that they have equal diameters at the intersection. This diameter is adjusted to a minimum by means of a beam waist adjuster on the laser head.

The vertical component of velocity is measured by two of the green beams. The transverse and longitudinal components are not measured directly, but are found by calculation from the two horizontal components of velocity, measured by the blue pair and a second pair of green beams. These intersect under an angle of 40 degrees. The relative large angle does not allow to choose the measuring plane very close to the propeller. On the other hand the large angle is necessary in order to get sufficient accuracy for the calculation of thwartship velocity.

The light scattered by particles in the flow is collected by a lens which is focussed onto a pinhole. The distance between the lens and the probe volume is 773 mm.

The lower end of the fin is submerged sideways of the model into the water. The mechanical displacement of the transducer in the vertical and transverse direction is carried out by means of computer controlled motors. The displacement in the longitudinal direction is carried out manually. The range of translation in each direction is 500 mm. The

whole device is mounted on the ship model.

The separation of the information on the velocity components detected by the receiving optics is based on the colour difference (green/blue) and on the frequency shift applied to the pairs of green beams. The signal processing is done by counters (DISA Counter Processor 55190a).

The final evaluation of data (about 65000 per measurement plane) is done by a computer - which is not on the carriage - after the measurement.

For the determination of the model wake field a software package was produced. Thus the measurement can be done fully automatically. A detailed description of the device and principle of method can be found in Laudan (1981).

The relative systematic error is according to the view of errors in Kirschnek, Laudan (1980) about one to two per cent and the mean random error is about three per cent.

### 3.1.2 Results, "Sydney Express", Model

Wake measurements in the HSVA towing tank were carried out at a model speed of 1.97 m/s, which corresponds to a full scale velocity of 20.3 kn ( $F_n = 0.23$ ). Model displacement and trim were adjusted according to the draught values during full scale tests.

The rate of propeller revolution was adjusted to yield a torque coefficient of  $K_Q = 0.031$ . This exceeds the full scale value by 6.4 per cent, compensating for the relatively high friction of the model propeller due to the lower Reynolds number as compared to full scale conditions.

During a first run without LDV-device at the desired model speed, the model trim and immersion was measured. During LDV-measurements the model was fixed to the carriage at the detected trim angle.

Wake measurements by LDV were done in two different planes ahead of the propeller, lying parallel to the propeller plane. One of the planes had a distance of 0.12 propeller diameters from the propeller plane, corresponding to the full scale measurement, Fig. 4. Another wake measurement was done at a distance of 0.2 propeller diameters from the propeller plane, Fig. 5. These values were needed as a supplement for the inner region to the measurement 0.12 D in front of the propeller.

The figures show the isotaches of the axial velocity component and the vectordigram of the transversal components. The values are normalized to the model speed. The wake is quite uniform. The isotaches contours show a significant analogy to the frame outlines. In the region of 120 degree a weak vortex can be imagined.

### 3.1.3 Results, "ST.Michaelis", Model

Wake measurements were carried out at a model speed of 1.46 m/s corresponding to a full scale velocity of 14.3 kn ( $F_n = 0.19$ ). The measurements at full scale through the

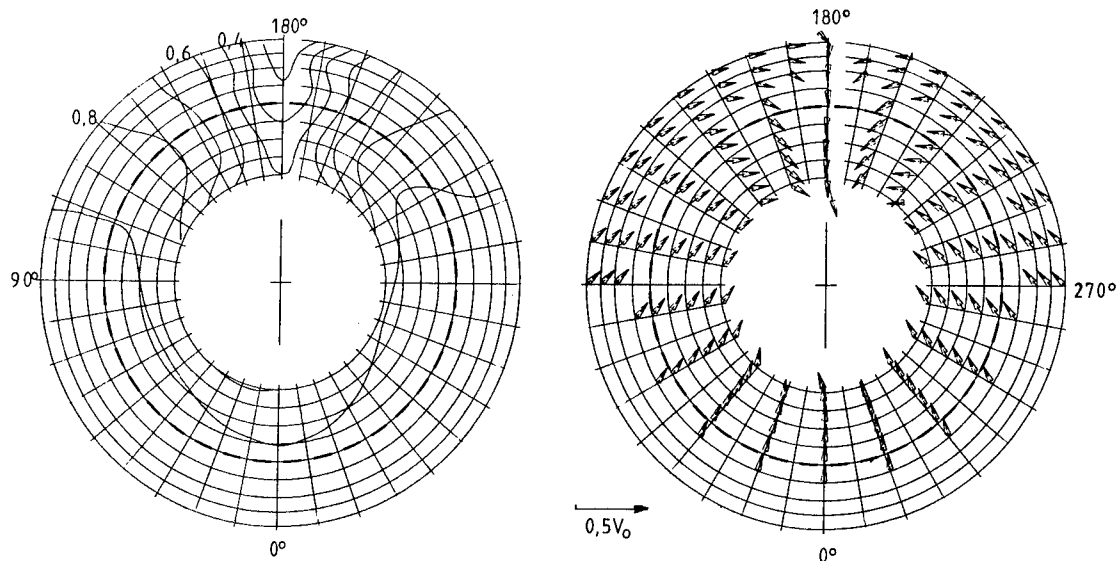


Fig. 4 Velocity Distribution, Wake of "Sydney Express" Model,  
 $0.12 D = 30 \text{ mm}$  in Front of Propeller Plane,  
 $K_T = 0.19$ ,  $K_Q = 0.031$ ,  $V_0 = 1.97 \text{ m/s}$ ,  $F_n = 0.23$ ,  
 Isotaches for Axial Component, Vector Diagram for Transversal Components

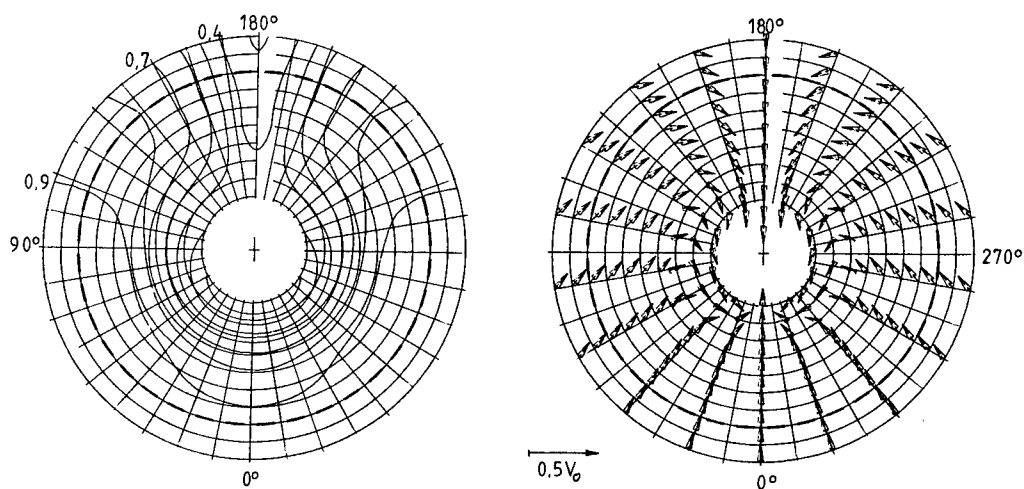


Fig. 5 Velocity Distribution, Wake of "Sydney Express" Model,  
 $0.2 D = 50 \text{ mm}$  in Front of Propeller Plane,  
 $K_T = 0.19$ ,  $K_Q = 0.031$ ,  $V_0 = 1.97 \text{ m/s}$ ,  $F_n = 0.23$ ,  
 Isotaches for Axial Component, Vector Diagram for Transversal Components

starboard window cover a larger area than those measurements at the port side. There is a slight difference between the torque coefficients between these two measurements. However, supplementary measurements have shown that the values normalized to the ship velocity are independent of velocity fluctuations within a certain range. The results were thus based on

the operating conditions valid for the measurements on the starboard side.

Model displacement and trim were adjusted according to the draught values picked up during full scale tests. At a first run without LDV-device at the desired model speed, the model trim and immersion was measured. For LDV-measurements the model was fixed to the

carriage at the detected trim angle.

Wake measurements were supposed to be carried out at a propeller load corresponding to the full scale torque values, with a small correction due to friction effects caused by the difference in Reynolds number. This load was significantly lower at full scale than expected with respect to the conventional model propulsion test. This result was confirmed by the measurements during full scale trials. The desired velocity was reached at a much lower power than expected according to the model test. The inflow to the ship propeller must therefore be quite different from the model propeller inflow. The isotaches from full scale and model tests at corresponding load are significantly different.

Differences regarding the character of flow separation can be responsible for the large deviations between the wake fields of model and full scale tests. Being a stability problem, flow separation is strongly influenced by the propeller load. Therefore, additional wake measurements were carried out at the model under load conditions similar to the propulsion test results ( $K_Q = 0.025$ ). The results of the measurement 0.23 propeller diameters (51 mm) in front of the propeller plane are given in Fig. 6. The distance of 0.23 D corresponds to

formed using the LDV system developed at the IfS since 1976. This system has been used in 6 journeys on 5 different ships and meanwhile funds have been provided for further measurements on two ships, one of these with an asymmetrical stern.

The LDV optics is of the crossed beam (differential Doppler) type and is used in backscattering mode. The incident beams are focused by the front lens onto the measuring point. They are deflected by mirrors out into the flowfield through windows below the water line. The front lenses of the optics compose a zoom lens which allows to displace the measuring point, the intersection point of the incident beams, several meters along the optical axis of the arrangement. This optical axis can be positioned into different directions by appropriate adjustment of the deflecting mirror. Thus a lobe like area in one plane can be scanned out of one window. The plane is chosen parallel to the planes of the ship frames. In principle designed to measure two components of the velocity (at right angles) simultaneously, the system was used as a one component velocimeter for these wake surveys. The backscattered radiation is collected through the same window along the same path over the mirrors by the same front lens.

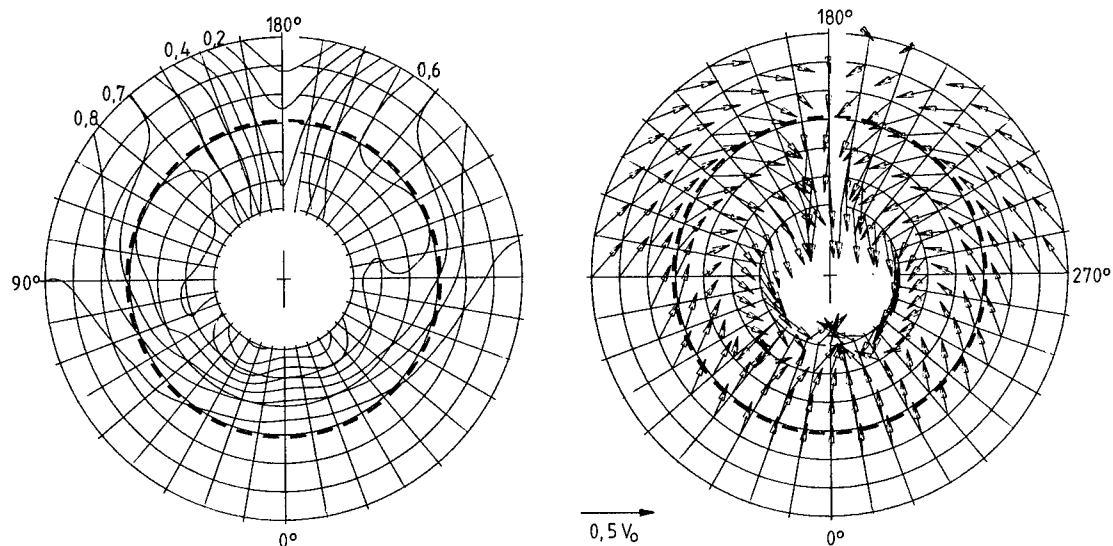


Fig. 6 Velocity Distribution, Wake of "St. Michaelis" Model,  
0.23 D = 51 mm in Front of Propeller Plane,  
 $K_T = 0.21$ ,  $K_Q = 0.025$ ,  $V_0 = 1.46$  m/s,  $F_n = 0.19$ ,  
Isotaches for Axial Component, Vector Diagram for Transversal Components

the distance at full scale measurements. The vector diagram (Fig. 6) obviously shows vortex centres in the regions of 120 and 240 degrees at a radius of  $r = 0.63 R$ .

### 3.2 Full Scale Wake

#### 3.2.1 Description of Measuring Device

The full scale wake measurements were per-

This is the principle of integrated optics, best suited to warrant a good focusing under a high level of vibration. The intersection angle of the incident beams is restricted, of course, and given by focal length and front lens diameter (30 cm). The design of the zoom lens is such, that the beam intersection angle is kept constant independent of the focal length chosen. The principles of the LDV technique will not be reviewed here again and may be

found elsewhere. A special feature of the optics is its modular design allowing for a different geometrical arrangement of the main modules (laser, central optical unit (two clour optics) with detector and beam splitter, zoom) conforming to the restrictions imposed by the space available in the ship. In the case of these two ships, the "Sydney Express" and the "St. Michaelis", an elongated base plate served as support for the optical modules. This plate was lowered in vertical position along rails into the space between two frames (60 cm). Mirrors, as shown on Fig. 7, direct the light

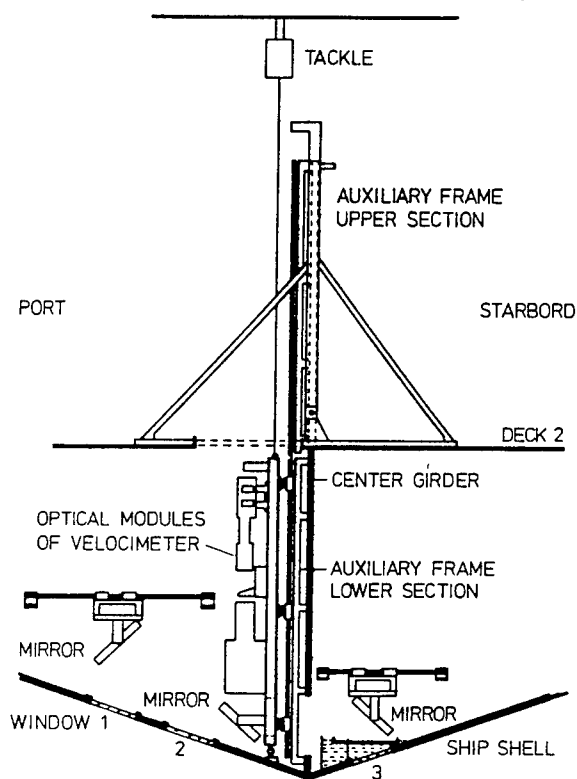


Fig. 7 Typical Arrangement of LDV-Optics in the Ship

to and from the windows which are covered by water-filled boxes as shown, in order to avoid unwanted skew beam deflections.

Signal processing devices used were counter processors and the data is further processed in a computer by a software package with appropriate routines allowing even to draw an isoline plot of the results on board. (More details in (Kux et al., 1982), (Stoehrman, 1983) and (Laudan, 1983)).

Time resolved measurements are possible: In the computer the momentaneous position of the propeller delivered by a shaft encoder is attached to the value given by the signal processor for each measurement. Averaging over a selected angular interval the variation of the velocity component about its mean at the measuring point during a propeller revolution emerges. Of course, the values averaged stem from many propeller revolutions. Averaging over a complete propeller revolution gives the mean

values as presented in the following two sections.

### 3.2.2 Measurements on the "Sydney Express"

Measurements were taken between the 29th of November of 1980 and the 13th of January of 1981 in the Red Sea and the Indian Ocean. Three windows had been installed for this purpose as indicated in Fig. 8, 0.12 propeller diameters

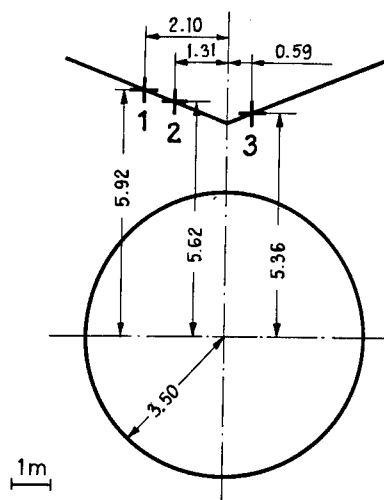


Fig. 8 Relative Location of Windows and Propeller Disc, "Sydney Express"

(0.84 m) in front of the propeller plane. The measurements were taken at several different ship speeds and those measurements were grouped together where speed and torque did not differ too much. From the several groups of values thus obtained only one has been selected for presentation here. It is composed of three subgroups comprising measurements out of each of the three windows and the isotaches of the mean axial velocity component for these are shown in Fig. 9. The degree of matching of the curves in this figure derived from values obtained on different days gives an impression of the reliability of these measurements. Results have been presented on earlier occasions (Kux, Stoehrman, 1982), and details may be found in an IfS report (Kux et al., 1982). In the frame of this paper no results are presented on the time resolved velocity measurements which were obtained along three directions out of window 2 nor on the turbulence detected. Reference is made to the same report for details (Kux et al., 1982).

### 3.2.3 Measurements on the "St. Michaelis"

These measurements were performed between the 18th and 22nd of November of 1981 in the Mediterranean during the first journey of this ship. Two windows had been installed their centers 0.23 propeller diameters (1.31 m) in front of the propeller plane, Fig. 10. The wake was scanned through both, though at slightly different conditions: The ship speed was



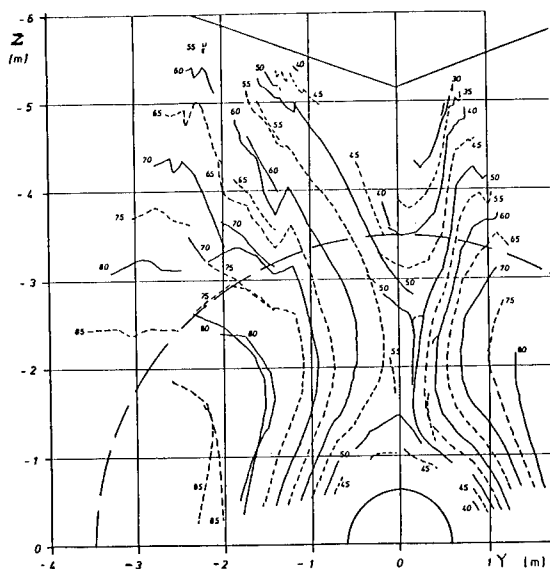


Fig. 9 Isotaches of Axial Velocity Component in the Wake of the "Sydney Express",  $0.12 D = 0.84$  m in Front of Propeller Plane  $K_Q = 0.029$ ,  $V_0 = 20.3$  kn =  $10.4$  m/s,  $F_n = 0.23$ , Labelling of Curves in per Cent of Ship Speed

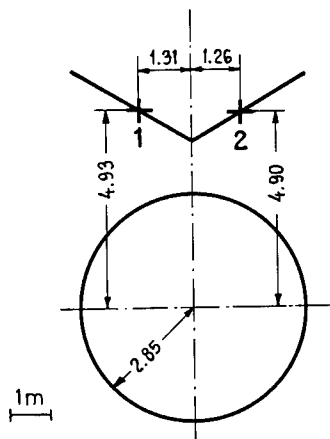


Fig. 10 Relative Location of Windows and Propeller Disc, "St. Michaelis"

$14.3$  kn =  $7.37$  m/s and the torque coefficient  $K_Q = 0.0185$  for the measurements through the starboard window and the corresponding values were  $15.0$  kn =  $7.74$  m/s and  $K_Q = 0.0180$  for the port window while the rate of revolution of the propeller was the same in both cases, i.e.  $2.12$  1/s. Notwithstanding these differences Fig. 11 gives the combined pattern of isotaches (axial component) obtained. Again results have been presented on earlier occasions (Kux, Stoehrmann, 1982), and details may be found in an IfS report (Stoehrmann, 1983) as well as results on some time resolved velocity measurements in the periodically instationary wake field for this ship which are not presented

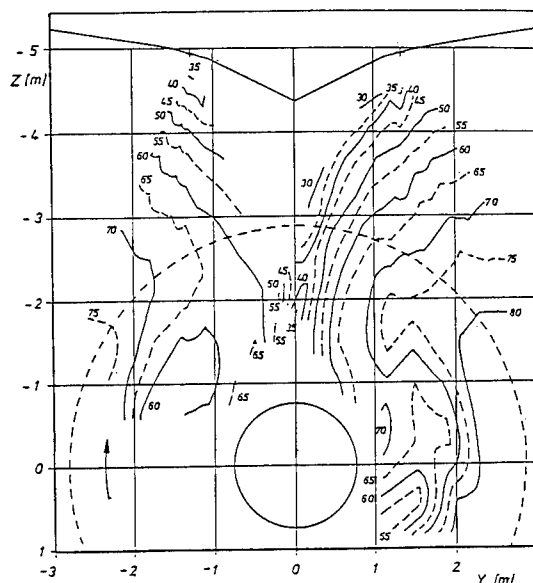


Fig. 11 Isotaches of Axial Velocity Component in the Wake of the "St. Michaelis",  $0.23 D = 1.31$  m in Front of Propeller Plane  $K_Q = 0.018$ ,  $V_0 = 14.8$  kn =  $7.4$  m/s,  $F_n = 0.19$ , Labelling of Curves in per Cent of Ship Speed

here.

In Fig. 12 the isoline patterns of axial

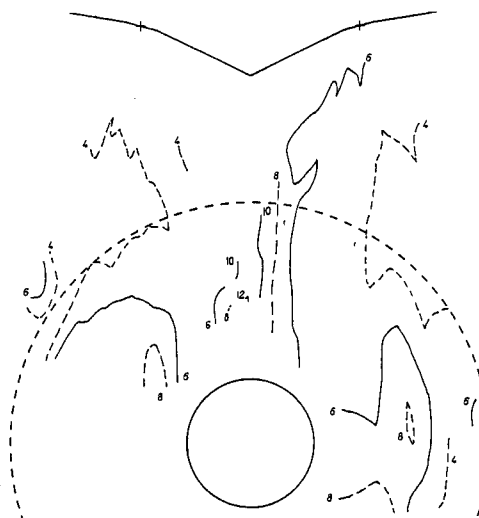


Fig. 12 Isolines of Axial Turbulence Intensity in the Wake of the "St. Michaelis",  $0.23 D = 1.31$  m in Front of Propeller Plane,  $K_Q = 0.018$ ,  $V_0 = 14.8$  kn =  $7.4$  m/s,  $F_n = 0.19$ , Labelling of Curves in per Cent of Ship Speed

turbulence intensity as referred to the ship speed  $V_0$  from both windows have been combined. Though the isolines refer to the total variation of velocity about the mean including the induction by the blades, this latter variation is rather small (a fact confirmed by the time

resolved measurements not shown) since the plane is 1.31 m upstream of the propeller plane. Thus the region of the wake is depicted where the highly turbulent material from the boundary layer has been swept.

#### 4. COMPARISON OF PREDICTED AND FULL SCALE WAKE

##### 4.1 Scale Transformation Methods for the Wake

As the knowledge of the velocity field is fundamental to the treatment of interaction between propeller and hull, a large number of procedures for adapting the model wake field to full scale has been developed. An excellent review of different procedures is given by Dyne (1972). Usually scaling procedures are based on model test results from wake-measurements, resistance- and propulsion tests. Therefore, propulsion and resistance tests were carried out for the described models, and open water tests for the model propellers. The results are given in tables 1 and 2.

According to Helmbold (1931), the wake of a ship can be divided into three components: displacement wake, friction wake and wave wake.

At the Froude numbers of the described measurements (up to 0.23), there is only a small influence of waves on the wake distribution. As model and full scale tests were carried out at the same Froude number, the scale effect is assumed to be negligible.

In an ideal liquid, geometrically similar bodies have the same displacement wake.

As the velocity for model tests is selected to yield the same Froude number as under full scale conditions, the Reynolds numbers of model and full scale tests must be different. The Reynolds number has a strong influence on the thickness of boundary layer and, as a consequence, on the friction part of the wake. The boundary layer thickness under full scale conditions is relatively smaller than at model conditions. The growth of boundary layer also affects the potential flow field. Nevertheless, generally all scaling procedures only consider for the friction wake.

In the following, some of the scaling procedures will be applied to the investigated model wakes.

To scale measured values from a geosim series of Victory ships, van Manen and Lap (1958) assume that the friction wake of a ship behaves like the wake field of a flat plate with the same length. This results in

$$w_S = w_M - (w_{FM} - w_{FS})_{\text{flat plate}}$$

for the ship's wake field.

In order to calculate the volume mean value of the wake, the propeller disc diameter is selected to yield the same length/propeller diameter ratio as on the ship. This mean value amounts to

$$w_f = \frac{4}{\pi} \int_0^1 \frac{V_0 - V}{V} \sqrt{1 - (y/\delta)(\delta/R)} \cdot (\delta/r) d(y/\delta)$$

and is calculated numerically. Following a proposal by Wieghardt (1973), the expression of the boundary layer velocity profile is somewhat different from the formula as in the original reference.

Based on the values derived from tables 1 and 2, wake-ratio full scale model amounts to  $w_S/w_M = 0.79$  for the "Sydney Express" and  $w_S/w_M = 0.67$  for the "St. Michaelis".

The mathematical effort for this solution should not conceal the fact that this procedure is based on assuming the ship boundary layer to behave like the flat plate one, which means over simplifying physical relations.

Following from the momentum equation, the momentum loss in the wake must be proportional to the sum of forces acting on the model. As a first order approach, differences between model and full scale are supposed to depend on friction alone, yielding the following equation for the wake fraction:

$$w_S = w_{dM} + (w_M - w_{dM}) \frac{C_{FS}}{C_{FM}}$$

Dickmann (1939) concludes from the momentum equation that the potential thrust deduction fraction must be proportional to the displacement wake fraction. Sasajima (1966) postulates the friction part of thrust deduction to be negligible. From this, for the ship wake follows

$$w_S = t_M + (w_M - t_M) \frac{C_{FS}}{C_{FM}}$$

From the values of tables 1 and 2  $w_S/w_M$  can be calculated for the "Sydney Express" as  $w_S/w_M = 0.77$ , and for the "St. Michaelis" as  $w_S/w_M = 0.73$ .

For full scale wake fraction, Brard and Aucher (1960) give a formulation similar to Sasajima's, additionally considering the fact that the displacement wake depends on the propeller load. For displacement wake, Dickmann's formulation is applied:

$$w_{dM} = \left[ \frac{t}{2} (1 - w_M) + \sqrt{(1 - w_M)^2 + C_{Th}} \right]$$

where the thrust load coefficient is based on the ship's velocity.

$$C_{Th} = \frac{T}{0.5 \rho V_0 A}$$

Using the values from tables 1 and 2, the result is  $w_S/w_M = 0.79$  for the "Sydney Express" and  $w_S/w_M = 0.70$  for the "St. Michaelis".

For the scaling procedures of different model basin, a summary was published by ITTC 78 (1978). The result was a modification of

Sasajima's formula:

$$w_S = (t+0.04) + (w_M - t - 0.04) \frac{(1+k)C_{FS} + \Delta C_F}{(1+k)C_{FM}}$$

This yields  $w_S/w_M = 0.89$  for the "Sydney Express" and  $w_S/w_M = 0.80$  for the "St. Michaelis".

All the above mentioned formulae, that were developed for prediction of the rate of propeller revolution, result in a constant factor for the complete wake pattern, can be regarded as a homogeneous concentric contraction of the wake field.

Another procedure published by Hoekstra (1975) gives different scaling factors for different regions of the wake field. This procedure does not separate displacement induced from friction induced contributions to the wake field and takes into account both effects.

For a wake field without bilge vortex, Hoekstra distinguishes between three different types of wake patterns, leading to three different types of contraction:

1. For an axisymmetric body the isotaches are circles, and the Fourier component has a value only for the zero order. This wake character gives rise to a contraction in radial direction.
2. Fourier analysis wake field of a vertical plate gives nonvanishing values only for the even-numbered coefficients. The contraction will be directed towards the plate, i.e. towards the centreplane.
3. Differences between velocities at the upper and the lower half of the measuring plane are due to the hull shape above the propellers. These differences cause the odd-numbered orders of harmonic analysis to have non-zero values, and the contraction is directed normal to the hull.

The overall contraction is assumed to behave like the boundary layer contraction of a plate. The resulting contraction factor amounts to

$$c = \frac{C_{FS} + \Delta C_F}{C_{FM}}$$

Friction coefficients are calculated according to ITTC-57-line. This contraction factor is divided into the three above mentioned components with respect to the Fourier analysis.

The peaks of wake at the centre plane are comparatively smaller behind the full scale ship than behind the model. The scale effect covers a range of

$$\Delta d = \sqrt{\frac{x_S}{V_0}} (1 - \lambda^{0.25})$$

The character of contraction leaves the flow velocity unchanged at a distance of  $\Delta d$  from the centre plane and causes the velocity in

the centre plane to be equal to the velocity at  $0.5\Delta d$ , where  $x_S$  is the distance between propeller plane and stern at a radius of  $r/R = 0.7$ .

The calculation of volume mean value yields for the wake ratio  $w_S/w_M = 0.87$  for the "Sydney Express" and  $w_S/w_M = 0.88$  for the "St. Michaelis".

The special treatment of bilge vortex by Hoekstra was not considered here.

Other scaling procedures are based on statistical analysis of results from series of model tests and full scale trials. Naturally, application of formulas obtained in this way is restricted to a special type of ships.

So Sudo (1969) has investigated a series of single screw tankers. He made an factor analysis for full scale and model wake separately and took account of seven parameters. The ratio of the full scale to model scale wake can be described by two parameters with a sufficient accuracy.

$$1 - w_S = (1 - w_M) \cdot (C_{BA}^2 \frac{B}{T})^{0.4/5}$$

For the "St. Michaelis" by this formula  $w_S/w_M$  amounts to 0.67.

Table 3 gives a review of all results.

Isotaches were drawn for the wake patterns obtained by Hoekstra's procedure and the ITTC-proposal (Fig. 13 and 14).

#### 4.2 Wake Predicted by the Hoekstra and ITTC Method

In the following the scaling procedures of Hoekstra and the ITTC on the wakes of the "Sydney Express" and the "St. Michaelis" are treated detailed. These two methods are chosen, because the velocities - calculated according to the other methods - give too large values.

##### 4.2.1 "Sydney Express"

Comparison of the isotaches of the velocity field for full scale (Fig. 9) with model results (Fig. 4 and 5) show a rather good congruence. The outline of the isotaches is quite similar. As expected, the isolines get closer to the centre plane at the full scale ship than at the model due to the comparatively smaller extent of boundary layer thickness at full scale.

The flow field converted to full scale according to ITTC-proposal (Fig. 13 right) is quite congruent to the full scale measurements. The same is valid for the flow field converted according to Hoekstra (Fig. 13 left). The somewhat unsymmetric character of the full scale measurement only slightly appears at the model test.

##### 4.2.2 "St. Michaelis"

Comparing the isotaches of the velocity field from model (Fig. 6) and full scale measurements (Fig. 11) shows the significantly

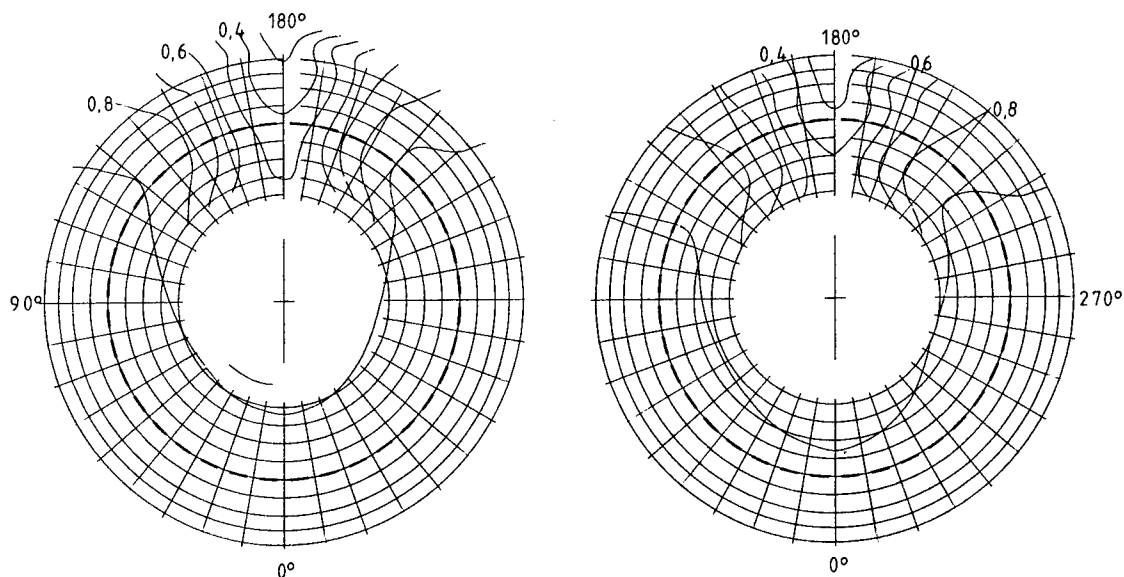


Fig. 13 Isotach Pattern Transformed from Model to Full Scale, "Sydney Express"  
 0.12 D in Front of Propeller Plane,  $K_Q = 0.029$ ,  $F_n = 0.23$ ,  
 Hoekstras Method left, ITTC Method right

larger velocity values of the full scale test. Even the higher load coefficient for the model test caused no essential improvement. Only on the port side of the full scale measurement a faint analogy to the model test results can be imagined.

Scaling of the model velocities at a higher propeller load according to ITTC-proposals gives a better congruence regarding corresponding isotachs (Fig. 14 right). It must be considered that at regions of small velocity gradients even a small change of the velocity value will shift the isoline by a considerable amount. In the upper region, the scaling produces velocity values larger than the values from full scale measurements. The vortex centers indicated by relative minima of the axial velocity are placed closer to the centre plane at full scale than at model scale.

Scaling according to Hoekstra (Fig. 14 left) yields a rather good congruence compared with the full scale results in the upper region (between 140 and 190 degrees). However, the isolines in the lower region as well as the vortex centres are lifted too much, obviously because of a too large amount of contraction normal to the hull surface. The different velocity values in the upper and lower half of the measuring plane are not only due to the hull above the propeller but also caused by the stern bulge of the "St. Michaelis".

## 5. ANALYSIS OF VELOCITY FIELDS

### 5.1. General Considerations

The velocity field in the wake of a ship hull is an example of an extremely complicated three-dimensional vector field. In order to be able to describe and understand it any concept clarifying the complex topology and reducing it to simpler terms should be examined and might proportionate guidance in the search for tools for this purpose. Well known aids are vector lines and sheets, here streamlines and stream surfaces, but for a complex flow even drawing these, be it in a perspective view or as projection to an appropriate plane, in a way that really elucidates the characteristic features of the field is generally a problem. A few possibilities to gain some insight into the structure of the field are reviewed at continuation.

Popular are also "sectional" streamlines, the vector lines of the (two-dimensional) field of velocities measured on points of one plane and projected to that plane. These streamlines of projected velocities are in general different from the projections of the streamlines of the (three-dimensional) velocity field to that plane.

Calculation procedures for flows of this complexity are not available. Since it is possible to calculate the field of potential-theoretic velocity it is of interest to compare such calculations with the real field as measured (see section 5.2).

Important features of the field are found

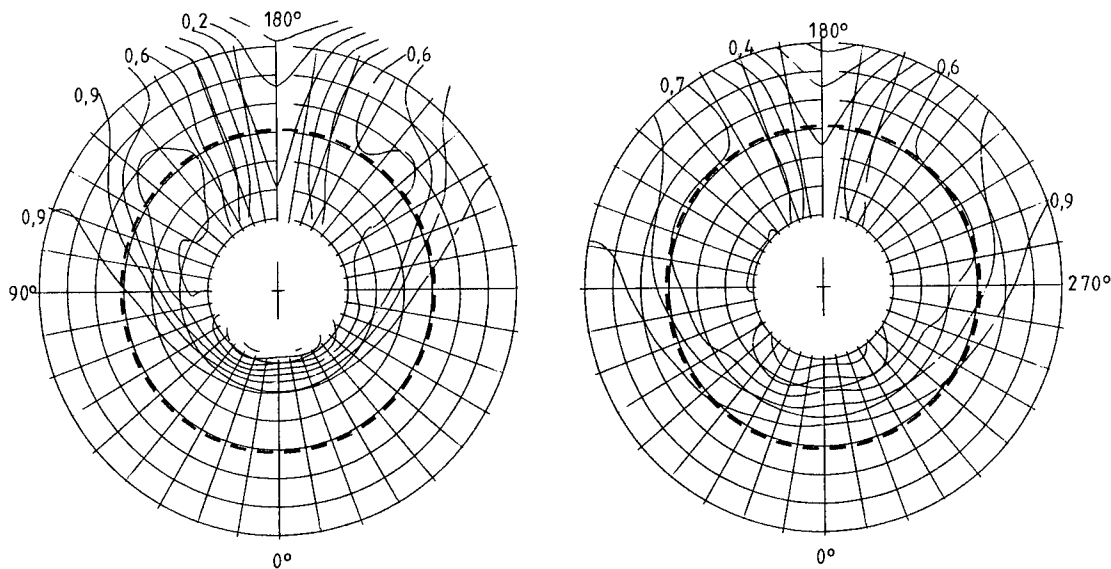


Fig. 14 Isotach Pattern Transformed from Model to Full Scale, "St. Michaelis", Plane  $x = 0.23 D$  in Front of Propeller Plane,  $K_Q = 0.025$ ,  $F_n = 0.19$ , Hoekstras Method left, ITTC Method right

in free space as well as on the bounding wall surfaces. Typical for the latter are separation lines and foci as foot points of vortices. In the free field vortices and bifurcation lines (intersection lines of stream surfaces) are the corresponding features with determined character of singularity. Expanding the velocity field in a Taylor series around a critical point gives locally insight into the structure of the field (Hornung and Perry, 1984).

Vector fields are classified according to the properties of the second rank tensor  $V = \text{grad } \vec{v}$ , the tensor whose components are the spatial derivatives  $v_{i,j} = \partial v_i / \partial x_j$  of the components  $v_i$  ( $i = 1, 2, 3$ ) of  $\vec{v}$  (Ericksen, 1960) with respect to the three coordinates  $x_i$  ( $x_1 = x$ ,  $x_2 = y$ ,  $x_3 = z$ ).

Now the acceleration  $\vec{a} = (\vec{v} \cdot \text{grad}) \vec{v}$  in stationary flow (and we restrict our discussion to this class of flows), the left hand side of the basic equations of motion (once they have been divided by the density  $\rho$ ), may be interpreted as  $V \vec{v}$ , the action of the transformation  $V$  onto the velocity vector  $\vec{v}$ . It follows at once that  $\vec{v}$  will keep its direction (i.e. that  $\vec{v}$  will remain parallel to itself) if it is an eigendirection of  $V$ , being merely lengthened or shortened as prescribed by the pertinent eigenvalue

$$V \vec{v} = \lambda \vec{v}$$

It is seen, that the solution of the eigenvalue problem for  $V$  in a suitable mesh of space

points proportionates a means to locate such specific features within the field.

We realize, that since the axis of a vortex needs not to be a straight line, this approach does not give us generally at once the location of the axis of a vortex in three-dimensional fields.

A method has been proposed (Vollmers et al., 1983) to introduce a transformation to a frame of reference where the velocity vector  $\vec{v}$  aligns with one of the coordinate directions of this new frame, and features of the flow field are found from the differential-geometric characteristics (derived from  $V$ ) of a hypothetical surface everywhere perpendicular to the local velocity direction.

Since insight may be found from an analysis of  $V$ , both the decomposition of  $V$  and the reduction to lower rank magnitudes, to vectorial if not to scalar descriptors are paths offering some success. Scalar quantities related to a second rank tensor are e.g. its principal invariants (three in three dimensions, the first one being its trace, the third its determinant) or its eigenvalues. Decompositions may be thought of as additive decompositions and as factorial decompositions.

A factorial decomposition of  $V$  may be achieved in several ways. We recall that an arbitrary matrix may be represented in infinitely many ways as the product of two symmetric matrices, one of which is nonsingular (Ericksen, 1960). Much more interesting is the following theorem: Any nonsingular matrix may be written as the product of an orthogonal and a symmetric positive definite matrix (Ericksen,

1960), (Zurmuehl, 1950). This special kind of decomposition is known as polar decomposition. The orthogonal factor may be interpreted as a rotation ( $\pm \text{curl } \vec{V}$ ) of the vector  $\vec{V}$  (as long as its determinant is  $> 0$ ) and the other factor describes the stretching of  $\vec{V}$  in three mutually perpendicular directions. The rotation factor determines a rotation axis in space (the eigen-direction to its only real eigenvalue) which is not identical with the direction of  $\text{curl } \vec{V}$  at that location,  $\text{curl } \vec{V}$  being the mean of rotation obtained as average over all possible positions of the rotated vector (Truesdell, 1954).

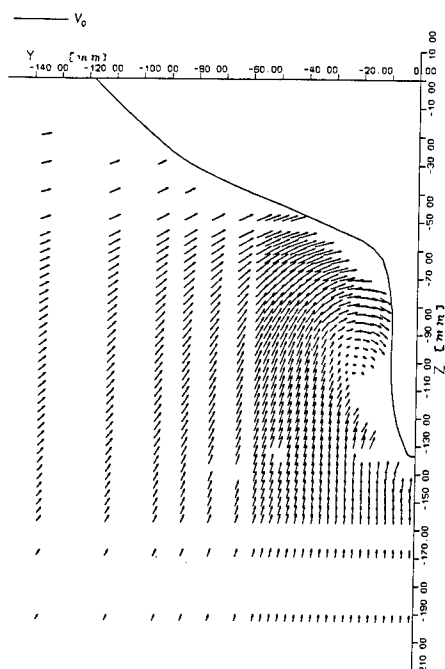


Fig. 15 Velocity Field in the Wake of a Double Model in the Wind Tunnel (HSVA Tanker), Measured Transversal Components in the Plane  $x = 47$  mm in Front of Propeller Plane,  $V_0 = 27$  m/s

The polar decomposition is popular in elasticity theory where it is applied to the displacement gradient tensor (Zander, 1970), (Becker, Buerger, 1975).

In this paper only the additive decomposition of  $V$  will be pursued (section 5.3). We will use a combined symbolic and tensor notation. If the quantity is referred to in general terms a single letter is chosen. Vectors are characterized as those by an arrow while upper case symbols are used for second rank tensors without further characterization. Formulae giving the law of construction of the components or relations between them are written in the manner of tensor calculus with indices according to the rank of the quantity. We adhere to the Einstein summation convention: If in a term an index appears twice this term is understood as a sum of terms over the range of these indices (here 1 to 3) in the sense of a scalar product. We do not differentiate be-

tween covariant and contravariant (nor mixed) components in this contribution. The partial derivative with respect to the coordinate  $x_i$  is denoted using  $,$  as e.g.  $v_{i,j}$ . So  $V = (v_{i,j})$ .

## 5.2 Decomposition of the Velocity Field into Potential and Non-potential Flow

Since the velocity field for potential flow may nowadays be computed using singularity (panel) methods on the computer without too much effort, it is easy to do so for those flow fields, where experimental results are available. It is then interesting to subtract from the real field the computed potential field.

Fig. 15 to 17 show the procedure as applied to wind tunnel data (Wieghardt, Kux 1980), (Wieghardt, 1982) from pressure probe measurements in a transverse plane in the stern region of a double model of a hull (the HSVA Tanker) thoroughly investigated at the IfS. (Notice the different scales for the arrow lengths!) The procedure is demonstrated using this data set since more values in the plane lead to a more detailed picture of the vortical flow. Fig. 15 shows the measured values, Fig. 16 the computed potential velocity field

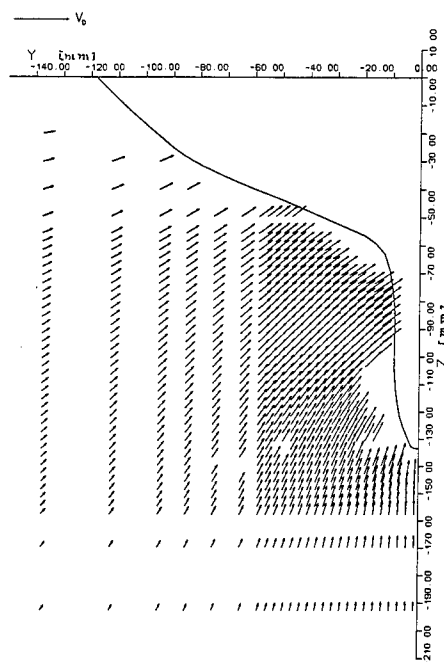


Fig. 16 Velocity Field in the Wake of a Double Model in the Wind Tunnel (HSVA Tanker), Potential Theory, Computed Transversal Components (Same Points as in Fig. 15)

at the same locations and Fig. 17 finally the remaining velocity field after subtraction. It is seen that in the outer region the arrows have been practically reduced to zero, the arrow heads showing random orientations. The potential flow there describes well reality while in the neighbourhood of the frame the longitudinal vortex with the superimposed displacement flow induced by the boundary layer

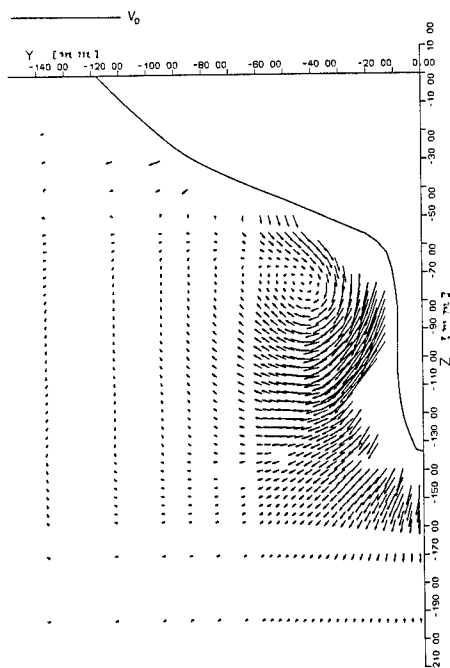


Fig. 17 Remaining Velocity Field in the Wake of Double Model (HSVA Tanker) when Potential Theoretical Field (Fig. 16) is Subtracted from Measured Field (Fig. 15)

becomes evident. The vortex does not appear at the location suggested by Fig. 15. Since the displacement velocity of boundary layer has not been subtracted, even Fig. 17 does not show the real location. Pinpointing vortices may be helpful for the application of scaling procedures as that forwarded by Hoekstra (1975).

### 5.3 Additive Decomposition of the Tensor $\text{grad } \vec{v}$ , Vorticity and Deformation

#### 5.3.1 Theory

In the usual additive decomposition the tensor ( $V$  in our case) is split into its symmetric part ( $S = (d_{ij})$ ,  $d_{ij} = \frac{1}{2}(v_{i,j} + v_{j,i})$ ) and its antisymmetric part ( $\Omega = (\omega_{ij})$ ,  $\omega_{ij} = \frac{1}{2}(v_{i,j} - v_{j,i})$ ). Following Ericksen (1960)  $S$  may again be split into a spherical tensor (given by  $\text{tr}(S)\delta_{ij} = \text{tr}(V)\delta_{ij}$ ) and a remaining traceless symmetric tensor. Since  $V$  is the gradient tensor of the velocity field, we see that for the incompressible case (and we restrict our discussion to this case) this spherical tensor vanishes in theory:  $\text{tr}(V) = \text{div } \vec{v} = 0$ . Dealing with experimental data this is never exactly fulfilled due to errors in measurement and numerical processing.

It is not too easy, to obtain a vivid impression of the components thus obtained.

For  $\Omega$  as an antisymmetric second rank tensor we have no more than three components of different absolute value in three dimensional space. We know that it has become usual to take them as the components of a vector (the vector of that second rank tensor), the vorticity

vector  $\vec{\omega} = \text{curl } \vec{v}$ , since they transform as vector components (but for a change in sign under reflections). The connection between  $\Omega$  and  $\vec{\omega}$  is given by

$$\omega_i = \epsilon_{ijk} \omega_{jk} \quad \vec{\omega} = \begin{pmatrix} \omega_1 \\ \omega_2 \\ \omega_3 \end{pmatrix}, \quad \Omega = \frac{1}{2} \begin{pmatrix} 0 & -\omega_3 & \omega_2 \\ \omega_3 & 0 & -\omega_1 \\ -\omega_2 & \omega_1 & 0 \end{pmatrix},$$

$$\omega_{jk} = -\frac{1}{2} \epsilon_{jkl} \omega_l$$

where  $\epsilon_{ijk}$  is the totally antisymmetric (third rank) tensor

$$\epsilon_{ijk} = \begin{cases} 1 & \text{for } ijk = 123, 312, 231 \\ -1 & \text{for } ijk = 321, 213, 132 \\ 0 & \text{else} \end{cases}$$

With  $\omega = |\vec{\omega}|$  it follows  $\omega^2 = 2 \omega_{jk} \omega_{jk}$ .

The vector  $\vec{\omega}$  is suited to be represented graphically as any vector field: As arrow diagram by projecting onto a suitable plane (Wieghardt, 1983), as isolines of the component normal to such a plane drawn on that same plane or as isolines of modulus (or other components) drawn similarly. Projection onto a bounding wall surface also is popular.

The symmetrical part  $S$  is much less suited to a graphical representation. To free ourselves from the arbitrariness introduced by the coordinate system (generally chosen a priori without relation to the velocity field) we may look for the eigenvalues and the eigendirections (better known as eigenvectors) of  $S$  and choose a graphical representation for these. The eigenvalues of  $S$  give the deformation rate in three directions, precisely the eigendirections of  $S$ . We may also derive scalars from the components  $d_{ij}$  of  $S$  by appropriate algebraic manipulation. Specifically the scalar  $d$  defined by

$$d^2 = 2 d_{ij} d_{ij}$$

interpreted as deformation rate has found broad acceptance. We find

$$d^2 = 2(v_{1,1}^2 + v_{2,2}^2 + v_{3,3}^2) + (v_{3,2} + v_{2,3})^2 + (v_{1,3} + v_{3,1})^2 + (v_{2,1} + v_{1,2})^2$$

$$\text{and } d^2 = \omega^2 + 2 \text{div } \vec{a} \quad (\text{Appendix})$$

with  $\omega = |\vec{\omega}|$  and  $\vec{a}$  as acceleration ( $\vec{a} = (\vec{v} \cdot \text{grad}) \vec{v}$ ,  $a_i = v_j v_{i,j}$ , in the case of stationary flow). Again isolines of  $d$  may be plotted showing the distribution of deformation rate.

With  $\omega$  and  $d$  the kinematical vorticity number  $W_k$  introduced by Truesdell (1953), (1954) now follows quite naturally as

$$W_k = \frac{\omega}{d} = \sqrt{\frac{\omega_{ij} \omega_{ij}}{d_{kl} d_{kl}}} = \left(1 + \frac{2 \text{div } \vec{a}}{\omega^2}\right)^{-1/2}$$

and is seen to be the ratio between scalars characterizing vorticity (or the antisymmetric part) and deformation (or the symmetric part). Emerging solely out of  $V$ ,  $d$  is a rate most appropriate to nondimensionalize the vorticity.

### 5.3.2 Application to Experimental Data

Out of a much larger amount of available data obtained as described in section 3, some graphical representations regarding model and full scale measurements are shown. Since the experiments do not yield  $\text{div } \vec{v} = 0$  exactly, it is evident that the results are somewhat in error. No attempt has been made to manipulate the data to achieve a better fulfillment of continuity equation.

Fig. 18 to 22 show the vorticity distri-

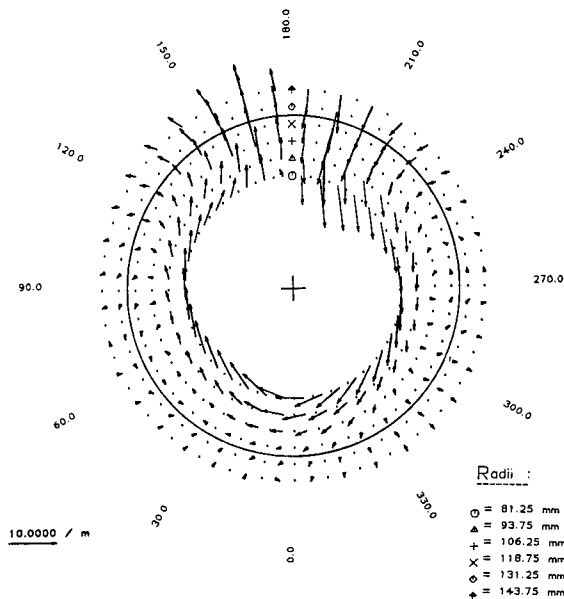


Fig. 18 Vorticity of the Model Wake, "Sydney Express", Transversal Components,  $0.16 D = 40 \text{ mm}$  in Front of Propeller Plane  $K_T = 0.19$ ,  $K_Q = 0.031$ ,  $V_0 = 1.97 \text{ m/s}$ ,  $F_n = 0.23$

bution in the wake of the "Sydney Express" and "St. Michaelis".

Fig. 18 and Fig. 20 show transversal components of the vorticity distribution in the model wakes in planes intermediate between the two measuring planes closest to the propeller plane. The axial derivatives of the velocity components were computed taking the differences of corresponding velocity components in the mentioned two planes. These derivatives were assigned to the intermediate plane and all circumferential and radial derivatives obtained in the measuring planes were interpolated onto the intermediate plane. Though the measuring planes closest to the propeller in the model wake correspond to the measuring plane at full scale, vorticity, deformation, etc. is computed for a plane that has a location somewhat upstream as is seen from the x coordinates given in the figure captions. Fig. 18 and Fig. 21 give the transversal components of the vorticity for the full scale case derived from the axial velocity component (solely) measured. The assumption was made that the derivatives in

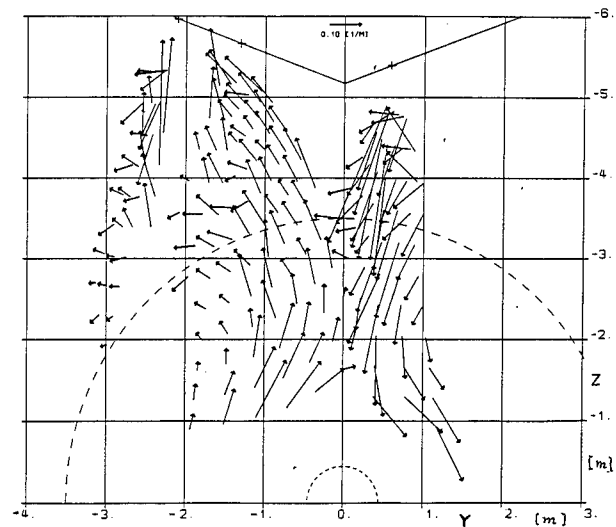


Fig. 19 Vorticity in the Wake of the "Sydney Express", Transversal Components,  $0.12 D = 0.84 \text{ m}$  in Front of Propeller Plane  $K_Q = 0.029$ ,  $V_0 = 20.3 \text{ kn} = 10.4 \text{ m/s}$ ,  $F_n = 0.23$

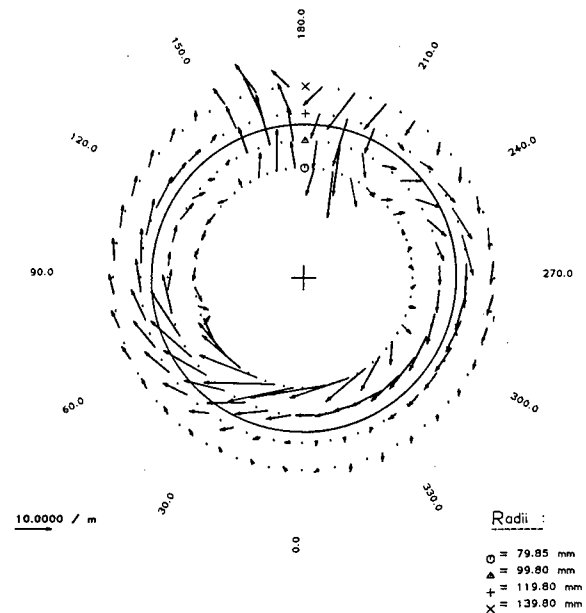


Fig. 20 Vorticity of the Model Wake, "St. Michaelis", Transversal Components,  $0.28 D = 63 \text{ mm}$  in Front of Propeller Plane  $K_T = 0.21$ ,  $K_Q = 0.025$ ,  $V_0 = 1.46 \text{ m/s}$ ,  $F_n = 0.19$

direction of the x axis are negligible anyhow (i.e.  $\omega_2 = v_{1,3}$ ,  $\omega_3 = -v_{1,2}$ ).

Fig. 22 gives an example of the distribution of



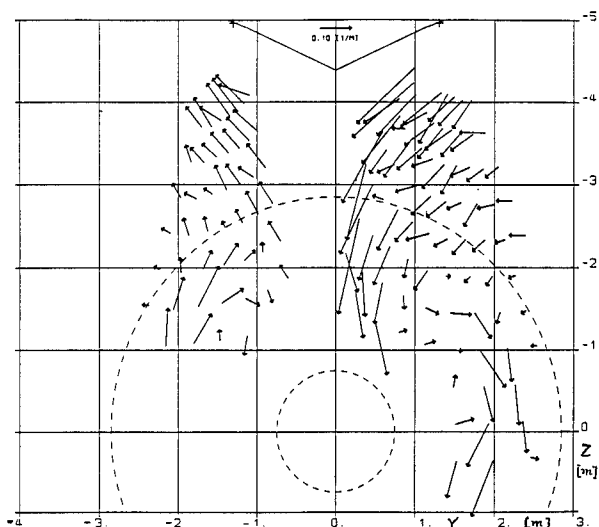


Fig. 21 Vorticity in the Wake of the "St. Michaelis", Transversal Components,  $0.28 D = 1.31$  m in Front of Propeller Plane  $K_Q = 0.018$ ,  $V_0 = 14.3$  kn  $= 7.4$  m/s,  $F_n = 0.19$

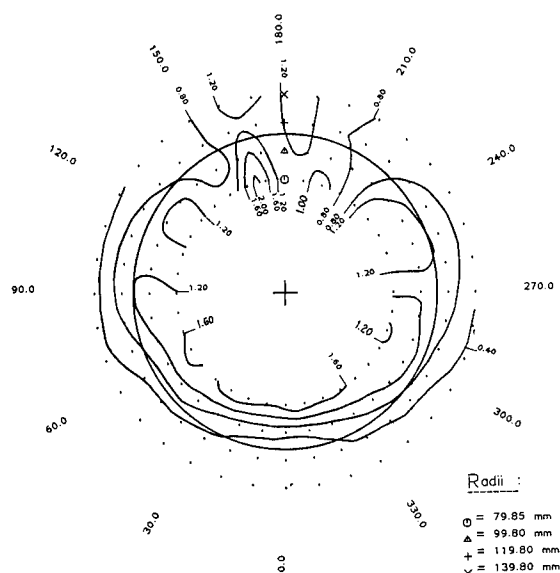


Fig. 23 Isolines of Deformation Rate in the Model Wake, "St. Michaelis"  $0.28 D = 63$  mm in Front of Propeller Plane,  $K_T = 0.21$ ,  $K_Q = 0.025$ ,  $V_0 = 1.26$  m/s,  $F_n = 0.19$  Labelling of Curves is in 10/m

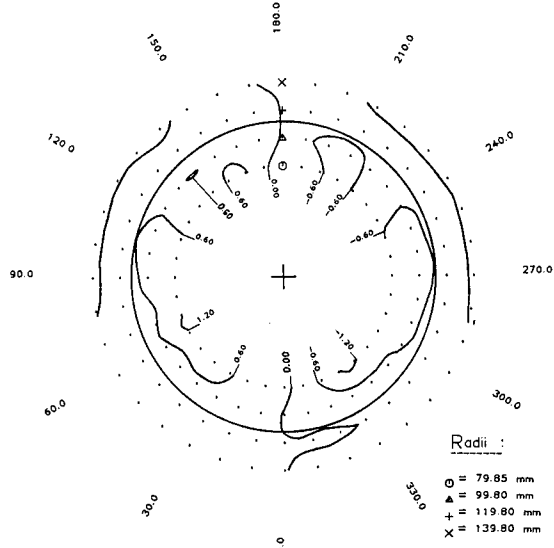


Fig. 22 Isolines of Axial Component of Vorticity-Field in the Model Wake, "St. Michaelis"  $0.28 D = 63$  mm in Front of Propeller Plane,  $K_T = 0.21$ ,  $K_Q = 0.025$ ,  $V_0 = 1.26$  m/s,  $F_n = 0.19$  Labelling of Curves is in 10/m

the axial vorticity component in a model wake as isoline plot. Fig. 18 and 19 correspond to the "Sydney Express", Fig. 20 to 22 to the "St. Michaelis". The deformation rate  $d$  for the model wake of this latter ship on the described intermediate plane is shown in Fig. 23 and the kinematic vorticity number  $W_k$  (same plane, same model) in Fig. 24, both as isoline plots.

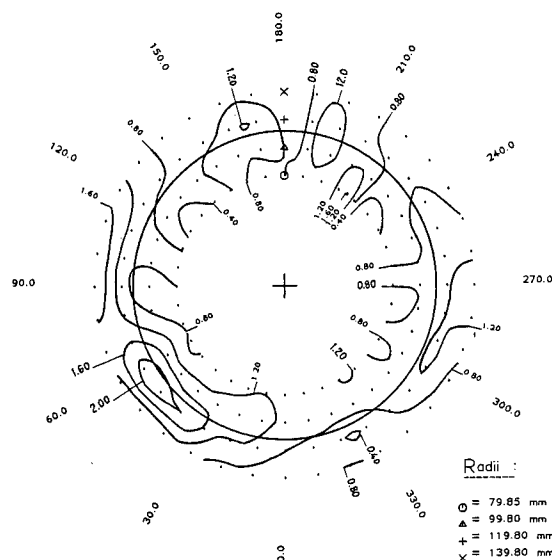


Fig. 24 Isolines of Kinematic Vorticity Number in the Model Wake "St. Michaelis",  $0.28 D = 63$  mm in Front of Propeller Plane,  $K_T = 0.21$ ,  $K_Q = 0.025$ ,  $V_0 = 1.26$  m/s,  $F_n = 0.19$

#### 5.4 The Acceleration Field as Derived from the Velocity Measured in the Model Wake

Since for stationary flow  $\vec{a} = (\vec{v} \text{ grad}) \vec{v} = V \vec{\nabla} V$ , it is easy to compute  $\vec{a}$  once  $V$  has been determined by differentiation of measured components of  $\vec{v}$ . The characteristics of the acceleration field  $\vec{a}$  may also be studied by

the computation of  $\text{div } \vec{a}$ . From the basic equation of motion for incompressible flow it follows that

$$\text{div } \vec{a} = -\frac{1}{\rho} \Delta p, \quad a_{i,i} = -\frac{1}{\rho} p_{,ii}$$

Now it is easily derived (Appendix, (Truesdell, 1954)) that for incompressible flow

$$\text{div } \vec{a} = -2 \text{II} = \frac{1}{2} (a^2 - \omega^2)$$

(where II is the second principal invariant of V) and may therefore be deduced directly from the components of V, that is from first derivatives of the velocity, eliminating risks implied in the computation of second derivatives starting from experimental data.

By calculating the acceleration for a certain value of  $K_T$  and for  $K_Q = 0$  and subtracting the net acceleration action of the propeller may be visualized.

Fig. 25 and Fig. 26 give examples of the

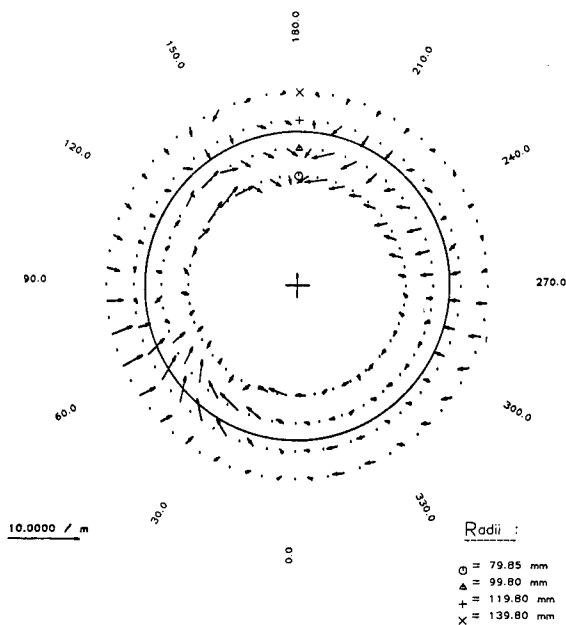


Fig. 25 Vector Diagram of the Transversal Components of Acceleration, Model Wake, "St. Michaelis", 0.28 D = 63 mm in Front of Propeller Plane  $K_T = 0.21$ ,  $K_Q = 0.025$ ,  $V_0 = 1.46$  m/s,  $F_n = 0.19$

acceleration field in one plane of the model wake of the "St. Michaelis" and Fig. 27 shows the corresponding isoline pattern for  $\text{div } \vec{a}$ .

#### 5.5 Boundary Layer Characteristics of the Detaching Flow

Though the LDV is a versatile tool, extensive measurements in a ship model boundary layer have not been presented. The data set selected as test cases for the 1980 workshop on ship boundary layers in Gothenburg (Larsson, 1980) was obtained by hot wire anemometry (Larsson, 1974) or by pressure probes (Hoffmann, 1976).

In the IfS a thorough investigation of the wake of the mentioned double model (Wieghardt, Kux, 1980) has been undertaken in the wind

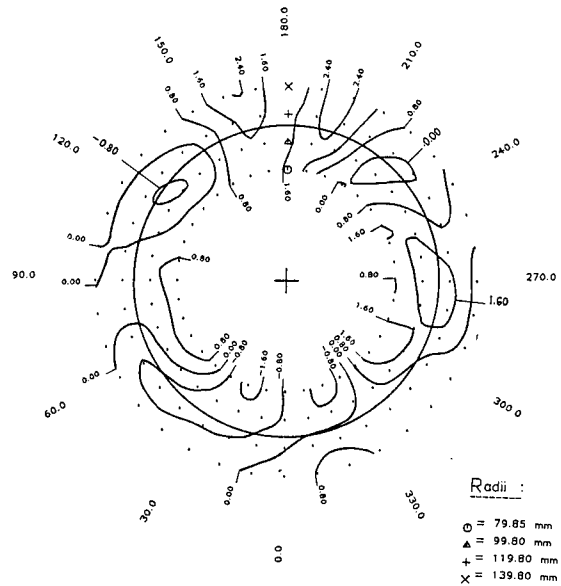


Fig. 26 Isolines of Axial Component of Acceleration, Model Wake, "St. Michaelis", 0.28 D = 63 mm in Front of Propeller Plane,  $K_T = 0.21$ ,  $K_Q = 0.025$ ,  $V_0 = 1.26$  m/s,  $F_n = 0.19$

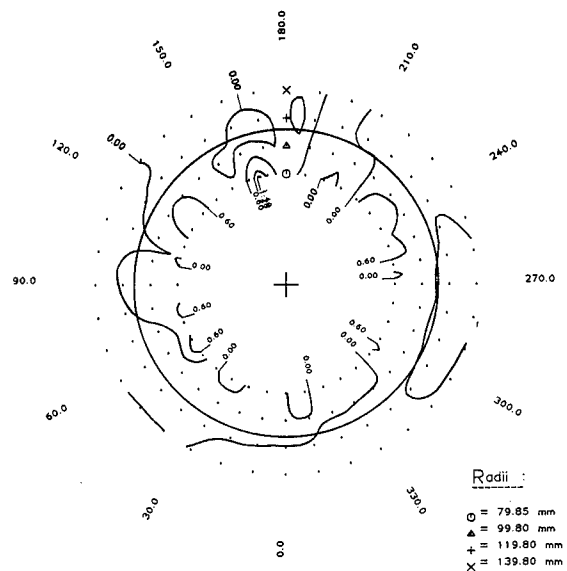


Fig. 27 Isolines of the Divergence of Acceleration, Model Wake, "St. Michaelis", 0.28 D = 63 mm in Front of Propeller Plane,  $K_T = 0.21$ ,  $K_Q = 0.025$ ,  $V_0 = 1.26$  m/s,  $F_n = 0.19$  Labelling of Curves is in 0.1/m

tunnel and the completion of this data set is still under way. Though the measuring points do not approach the wall very closely and are arranged in planes transverse to the model axis (as seems adequate for description of the

wake), it is possible to transform the results locally to a wall oriented coordinate system as

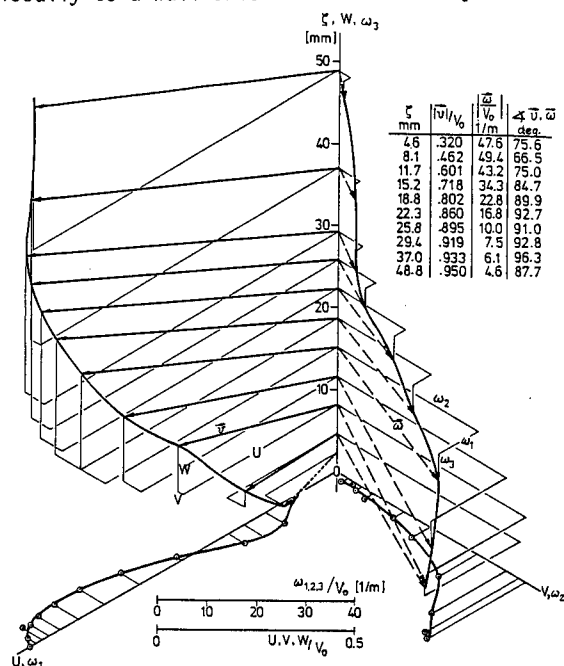


Fig. 28 Boundary Layer in the Region of Detachment, Double Model (HSVA Tanker) in the Wind Tunnel, showing Normal Component and Cross Flow and Vorticity Vector,  $V_0 = 27$  m/s,  $R_n = 5 \cdot 10^6$ , 101 mm in Front of Propeller Plane at the Wall

used in boundary layer description. If one does so (Wieghardt, Kux, 1984, unpublished) a velocity profile emerges as shown in Fig. 28.

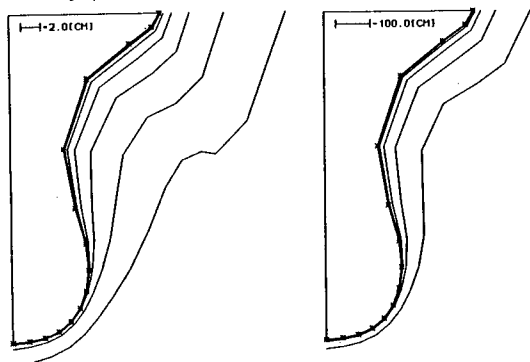


Fig. 30 Isolines (labelled 0.9, 0.8,... beginning with outer line, fraction of speed) of Longitudinal Velocity Component in Boundary Layer from Calculation (Integral Method for Three-Dimensional Boundary Layers with Energy Equation) for "Sydney Express" 1.03 D in Front of Propeller Plane, Model Left,  $R_n = 1.3 \cdot 10^7$ , Full Scale Right,  $R_n = 1.8 \cdot 10^9$

Notice the large component normal to the wall, considerably larger than the maximum value in

the cross flow profile which shows one crossover. The high value of the normal velocity component may be an argument in favour of those boundary layer calculation methods which include this component (Nagamatsu, 1980), (Soejima, 1978). The vorticity vector has also been drawn in Fig. 28 and it is seen that vorticity reaches rather high values. The behaviour of the normal velocity component ( $W$ ) is plotted as function of wall distance ( $\zeta$ ) in Fig. 29 at different positions along the girth as shown in the inset.

It is nowadays not yet possible to determine the details of wake from computed boundary layer separation. With an integral three-dimensional boundary layer calculation method using the energy equation, power law profiles in outer flow direction and Mager profiles for the cross flow some boundary layer calculations have been performed for the hull of the "Sydney Express" at both model scale and full scale. The method developed at the IfS (Achner, Kux, IfS report, to appear) does not consider a normal velocity component nor does it take into account curvature effects. The results of such a calculation are shown as isolines for the longitudinal velocity component in Fig. 30. Typical is the extremely thin boundary layer at the keel which correlates

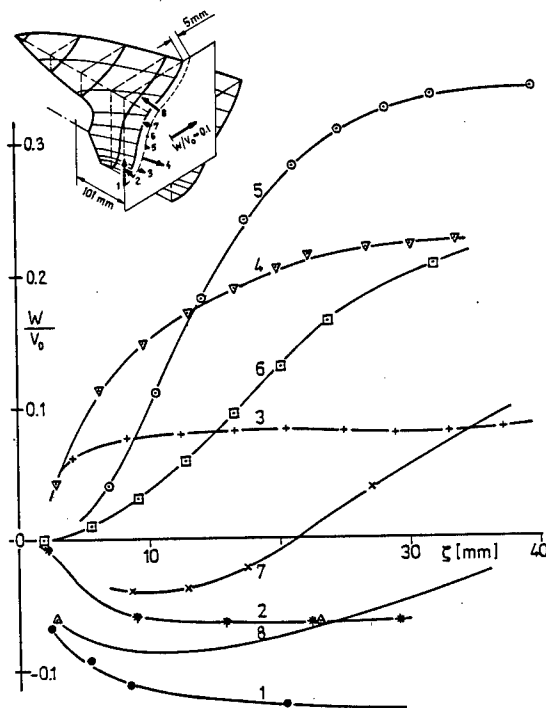


Fig. 29 Normal Component of Separating Boundary Layer Versus Wall Distance, Double Model (HSVA Tanker) in the Wind Tunnel, for Different Locations Along Frame (as Shown in Inset) 101 mm in Front of Propeller Plane

well with the concentrated transverse vorticity

found in the model wakes (Figs. 18 and 20) As stated, such a method does not in principle provide information on the normal component. It is probably also inadequate to describe the cross flow realistically, the Mager profiles being unable to reproduce cross flow profiles as the one shown in Fig. 28 (for a different hull!).

#### ACKNOWLEDGEMENTS

Many people contributed to these investigations, our thanks to all of them. We acknowledge the willingness of the shipping companies HAPAG-Lloyd and Hamburg-Sued to allow the measurements on their ships and of the German federal ministry of technology BMFT to raise the funds needed for this investigation. The LDV system for the full scale measurements was developed with funds from the German ministry of defense and the towing tank LDV system with aid of funds by the German research council Deutsche Forschungsgemeinschaft. Special thanks go to Mr. Stoehrman who developed hardware and software components for the full scale LDV system and organized the measurements. The contributions of Mr. Niemeier, Mr. Jaeger and Mr. Koop to the measurements in the planning phase and on the ships and the contribution of Mr. Lammers to both, these measurements and the towing tank tests are acknowledged as well as the multiple contributions of the staffs of HSVA and IfS. Considerable work done by Prof. Wieghardt is included in this paper and is gratefully acknowledged. Thanks go to Mr. Pose and Mr. Achner which performed a lot of programming and computer work needed.

#### REFERENCES

- Becker, E., Buerger, W. (1975): *Kontinuumsmechanik*. B.G. Teubner, Stuttgart
- Brard, R., and Aucher, M. (1969): The Prediction of Ship Performances in Calm Water. Proc. of 12th ITTC, Rome, pp.223-225
- Dickmann, H.E. (1939): Wechselwirkung zwischen Propeller und Schiff unter Beruecksichtigung des Welleneinflusses. Jahrb. STG Vol. 40, pp. 234-282
- Dyne, G. (1972): On the Scale Effect on Wake and Thrust Deduction. Proc. of 13th ITTC, Berlin/Hamburg, pp. 336-361
- Ericksen, J.L. (1960): Tensor Fields, Encyclopedia of Physics, S. Fluegge, editor Vol. III/1, pp. 794-858, Springer Verlag, Berlin, Goettingen, Heidelberg
- Helmbold, H.B. (1931): Beitrag zur Theorie der Nachstromschrauben. Ingenieur-Archiv Vol. 2
- ITTC (1978): Report of the Performance Committee. Proc. of 15th ITTC, the Hague, pp. 338-404
- Hoekstra, M. (1975): Prediction of Full Scale Wake Characteristics Based on Model Wake Survey. International Shipbuilding Progress Vol. 22, No. 250, pp. 204-219
- Hoffmann, H.-P. (1976): Untersuchung der 3-dimensionalen, turbulenten Grenzschicht an einem Schiffsdoppelmodell im Windkanal, IfS-Report Nr. 343
- Hornung, H., Perry, E. (1984): Some Aspects of Three-Dimensional Separation. Zeitschrift fuer Flugwissenschaften und Weltraumforschung Vol. 8, pp. 77-87
- Kirschneck, E. and Laudan, J. (1980): Laseraufmessungen des Nachstromfeldes am Modell ohne und mit Propeller. Jahrb. STG Vol. 74, pp. 269-294
- Kux, J., Niemeier, Th. and Stoehrman, H. (1982): LDV-Nachstrommessungen auf der "Sydney Express". IfS-Report No. 424
- Kux, J., Stoehrman, H. (1982): Measuring Full-Scale Ship Wakes by Laser Doppler Velocimetry. International Symposium on Applications of Laser Doppler Anemometry to Fluid Mechanics, Lisbon, Proceedings 12.4
- Kux, J., Stoehrman, H. (1982): Wake Measurements by Laser Doppler Velocimetry on Full Scale Ships, 5th International Conference on Photon Correlation Techniques in Fluid Mechanics, Damp 2000, Kiel, Proc., Schulz-DuBois, E.O., editor, Springer Verlag, Berlin, Heidelberg, New York, pp. 153-158
- Larsson, L. (1974): Boundary Layers of Ships, Part III: An Experimental Investigation of the Turbulent Boundary Layer on a Ship Model. SSPA Report No. 46
- Larsson, L. (editor) (1980): SSPA-ITTC workshop on "Ship Boundary Layers 1980", Proceedings, ISBN 91-38-06443-X, Liber Distribution, S-162, Vaellingby, Sweden
- Laudan, J. (1981): The Influence of the Propeller on the Wake Distribution as Established in a Model test. Proceedings of Propellers '81, Virginia Beach, Virginia
- Laudan, J. (1983): Korrelation von Nachstromaufmessungen an Modell und Grossausfuehrung. HSVA Report No. 1529
- v. Manen, J.D. and Lap, A.J.W. (1958): Scale-Effect Experiments on Victory Ships and Models. Part II, International Shipbuilding Progress Vol. 5, No. 47, pp. 301-308
- Nagamatsu, T. (1980): Calculation of Viscous Pressure Resistance of Ships Based on a Higher Order Boundary Layer Theory, Journal of the Society of Naval Architects of Japan, Vol. 147, pp. 21-35
- Stoehrman, H. (1983): LDV-Nachstrommessungen auf der "St. Michaelis". IfS Report No. 433
- Sasajima, H. and Tanaka, I. (1966): On the Estimation of Wakes of Ships. Proc. of 11th ITTC, Tokyo, pp. 140-143
- Soejima, S., Yamazaki, R. (1978): Calculation of Three-Dimensional Boundary Layers on Ship Hull Forms, Transactions of the West-Japan Society of Naval Architects, Vol. 55, pp. 43-59
- Sudo, S. (1969): An Analysis of Model-Ship Correlation on Wake Fraction of Large Tankers. Proc. of 12th ITTC, Rome, pp. 243-245
- Truesdell, K. (1953): Two Measures of Vorticity. J. Rational Mech. Anal. 2, pp. 173-217
- Truesdell, K. (1954): The Kinematics of Vorticity. Indiana University Press, Bloomington
- Vollmers, H., Kreplin, H.-P., Meier, H.U.,

(1983): Separation and Vortical-Type Flow around a Prolate Spheroid-Evaluation of Relevant Parameters. AGARD - FDP "Aerodynamics of Vortical Type Flow in Three Dimensions" Conference Proceedings 342.

- Wieghardt, K. (1973): Ueber den Reibungswiderstand der Platte. IfS Report No. 291
- Wieghardt, K. (1980): Bemerkungen zu den LDA-Messungen in der Propelleranströmung eines HSVA-Modells (unpublished)
- Wieghardt, K., Kux, J. (1980): Nomineller Nachstrom auf Grund von Windkanalversuchen. Jahrb. STG Vol. 74, pp. 303-318
- Wieghardt, K. (1982): Kinematics of Ship Wake Flow. The Seventh David Taylor (Memorial) Lecture DTNSRDC Report 81/093
- Wieghardt, K. (1982): Transition of Rotational Flow into outer Irrotational Flow. in Recent Contribution to Fluid Mechanics, Haase, W., (editor), Springer Verlag, Berlin, Heidelberg, New York, pp. 303-311
- Wieghardt, K. (1983): Zur Kinematik einer Nachlaufströmung, 26. Ludwig-Prandtl-Gedächtnisvorlesung, Hamburg, Zeitschrift fuer Flugwissenschaft und Weltraumforschung, Vol. 7, No. 3, pp. 149-159
- Wieghardt, K., Kux, J. (1984): Ergebnisse von Untersuchungen am Institut fuer Schiffbau, Beitrag zur AGARD Round Table Discussion on 3D Boundary Layers, in Three-dimensional boundary layers, a report on work in Germany, Hornung, H., unpublished
- Zander, W. (1970): Sätze und Formeln der Mechanik und Elektrotechnik in "Mathematische Hilfsmittel des Ingenieurs", Sauer, R., Szabo, I., editors, Vol. IV, Springer Verlag, Berlin, Heidelberg, New York
- Zurmuehl, R. (1950): Matrizen. Springer Verlag, Berlin, Goettingen, Heidelberg

#### APPENDIX

With  $\text{div } \vec{v} = 0$ ,  $v_{i,j} = 0$  we write for  $\text{div } \vec{a} = \text{div } (\vec{v} \text{ grad}) \vec{v}$

$$\begin{aligned} (v_{i,j} v_j)_{,i} &= v_{i,j} v_{j,i} \\ &= (d_{ij} + \omega_{ij})(d_{ji} + \omega_{ji}) \\ &= (d_{ij} + \omega_{ij})(d_{ji} - \omega_{ij}) \\ &= d_{ij} d_{ji} - \omega_{ij} \omega_{ji} \\ &= 1/2 (d^2 - \omega^2) \end{aligned}$$

We derive

$$\begin{aligned} II &= 1/2 \epsilon_{ijk} \epsilon_{lmn} \delta_{il} v_{j,m} v_{k,n} \\ &= 1/2 (\delta_{jm} \delta_{kn} - \delta_{jn} \delta_{km}) v_{j,m} v_{k,n} \\ &= 1/2 (v_{j,j} v_{k,k} - v_{j,k} v_{k,j}) \\ &= -1/2 v_{j,k} v_{k,j} \\ &= -1/2 a_{i,i} \end{aligned}$$

Hence

$$\text{div } \vec{a} = -2 II = 1/2 (d^2 - \omega^2)$$

#### TABLES

Table 1 Principal Characteristics "Sydney Express"

Length between perpendiculars	210.0 m
Length, overall submerged	218.4 m
Draught	10.2 m
Breadth	30.5 m
Block coefficient	0.61
Surface, wetted	7681 m
Propeller diameter	7.00 m
Pitch ratio	0.94
Expanded area ratio	0.78
Number of blades	5
Model scale ratio	28
Froude number	0.23
Torque coefficient, ship	10KQ 0.29
Torque coefficient, model	10KQ 0.31
Thrust coefficient, model	K <sub>T</sub> 0.20
Thrust loading coefficient	C <sub>Th</sub> 1.76
Thrust deduction fraction	t 0.18
Wake fraction	w <sub>T</sub> 0.33
Formfactor	k 0.138
Direction of propeller rotation	right

Table 2 Principal Characteristics "St. Michaelis"

Length between perpendiculars	174.0 m
Length, overall submerged	182.6 m
Draught	11.6 m
Breadth	32.2 m
Block coefficient	0.80
Block coefficient of afterbody	0.75
Surface, wetted	8293 m
Propeller diameter	5.70 m
Pitch ratio	0.68
Expanded area ratio	0.62
Number of blades	4
Model scale ratio	25.5
Froude number	0.19
Torque coefficient, ship	10KQ 0.18
Torque coefficient, model	10KQ 0.25
Thrust coefficient, model	K <sub>T</sub> 0.21
Thrust loading coefficient	C <sub>Th</sub> 1.17
Thrust deduction fraction	t 0.21
Wake fraction	w <sub>T</sub> 0.45
Formfactor	k 0.141
Direction of propeller rotation	right

Table 3 Comparison of Wake Ratio Computed by Different Scaling Procedures

Procedure	"Sydney Express"	"St. Michaelis"
Sasajima	0.77	0.73
Brard, Aucher	0.79	0.70
ITTC	0.89	0.80
v. Manen	0.79	0.67
Sudo	-	0.74
Hoekstra	0.87	0.88

## DISCUSSION

E. BABA and T. NAGAMATSU,  
Mitsubishi Heavy Industries, Ltd.  
Nagasaki, Japan:

The authors should be commended for their long term efforts in developing measuring system of ship wake distributions by means of Laser Doppler Velocimetry. In the present paper, by use of the conventional scale transformation methods the wake distributions measured at the plane in the vicinity (0.23D) of a working propeller for ship models were transformed into the full-scale condition, and they were compared with those measured for full-scale ships. Though the authors state the conventional scaling procedures only consider the frictional wake, these procedures were applied to the prediction of ship wake distribution from model's velocity field which includes propeller effects. The discussor is afraid of overestimation of the scale effect, i.e. the potential velocity field induced by a working propeller for a ship model is scaled together with viscous wake field based on the friction law. The discussor's view is that the conventional scaling procedures should be applied to the viscous wake distribution which is determined from measured total velocity field by subtracting potential velocity field induced by a propeller and a hull. The authors' comment on this matter will be appreciated.

Prof. KAZU-HIRO MORI,  
Hiroshima University,  
Higashi-Hiroshima, Japan:

The paper is quite interesting and covers a wide range. But my comment is quite brief on the vorticity distributions which the authors showed us. I would like to draw our attention to the importance of vorticity.

When the vorticity distribution is discussed, only the axial component is so often exaggerated. This is mainly because the measurement is easy. The transverse component is no less important. The boundary layer flow produces the tangential component dominantly. The authors showed us both.

Though, like velocity potential, the vorticity does not provide velocity fields or pressure fields, it has important physical aspects as pointed out in the paper.

I have been involved for several years in the computations of near-wake flow by making use of the vorticity transport equation. First, it does not contain the pressure term. And, as shown in Figs. A1 and A2, which are the calculated vorticity distribution and the corresponding velocity, the non-zero vorticity region is much less than the non-zero perturbed velocity region. This means the computing domain is less.

The viscous resistance can be expressed in terms of the vorticity. For the scale-up problem of the nominal wake, the vorticity distribu-

tion can be used. This is because the induced velocity by vorticity gives the viscous component.

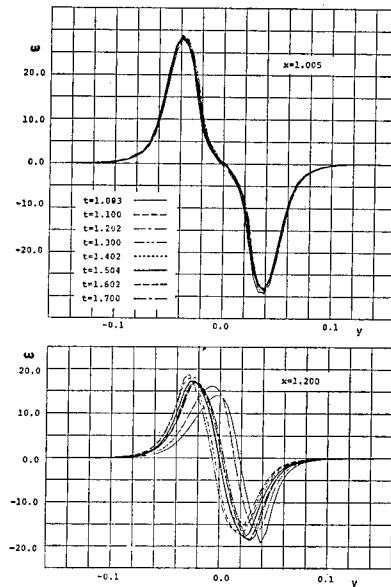


Fig. A1: Vorticity Distribution (EM-125)

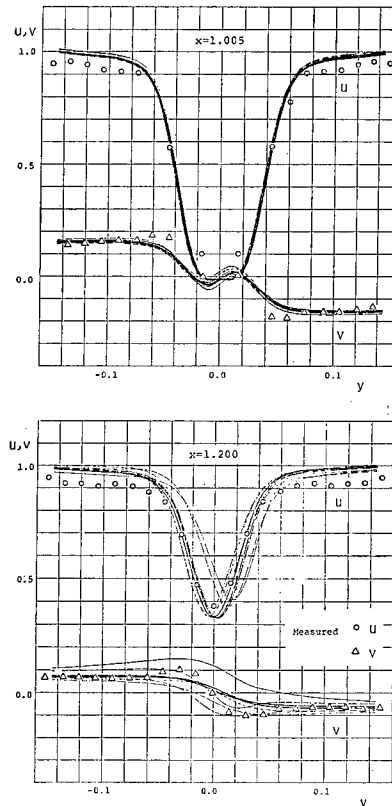


Fig. A2: Velocity Distribution (EM-125)

Dr. DAVID FRY,  
David Taylor Naval Ship R&D Center,  
Bethesda, MD, USA:

I want to thank the authors for a very interesting and comprehensive paper. With some experimental experience, I can imagine a part of the people and dedicated efforts behind each of the model and especially full-scale data figures. And even with all the obstacles to overcome that I can imagine, there must have actually been many times more.

I feel a certain frustration in flipping between pages and figures. For all the information presented on model and full scale measurements, there is no way to illustrate, with a comprehensive graphic, the differences between the measured flow fields. This frustration is familiar to me from my own work of measuring 3-D velocity fields and comparing them to other measurements or numerical model results. Even putting one result beside or on top of the other is not totally satisfactory. And paragraphs of words qualitatively describing the authors' impressions of the differences seem anti-climactic when compared to the volume and quality of the measurements. The detail and space devoted in section 5 to various alternative methods of analysis and/or display of velocity field data may indicate similar feelings by the authors.

The flow field decomposition of the tanker wake (section 5.2) into potential and non-potential flow suggests a good route to generally follow when comparing velocity fields (either measured-to-measured or measured-to-calculated results). Plots containing either isotachs of velocity component differences or displays of velocity vector differences would seem to be effective. In addition, the displayed velocity difference magnitudes could be non-dimensionalized by expected error magnitudes. This could have beneficial effects including: 1) forcing an experimenter to give adequate thought to the limitations of his measurements; 2) yield a display from which the observer/reader could readily see where important differences were; 3) whether the differences were consistent in the velocity field; 4) whether the differences were significant (with respect to error estimates). This could help clarify where/whether efforts should be made to improve scaling laws or numerical models to get better velocity field matches.

Dr. THOMAS T. HUANG,  
David Taylor Naval Ship R&D Center,  
Bethesda, MD, USA:

The experimental data of the velocity in the wake of two ships of two different block coefficients at full scale and at model scale are extremely valuable in our profession.

Could the authors indicate to us the accuracy of determining full-scale ship speed and propeller thrust, and the effects of ship motion and current on the velocities measured at full scale? Could the authors provide the best estimates of the ratio of the Taylor wake frac-

tion measured from the propulsion experiments and the ratio of the measured volume-mean wake at full scale and at model scale? These measured ratios together with the predicted wake ratios listed in Table 3 will provide us with a clue for selecting a more reliable empirical wake scaling procedure from the six procedures listed in Table 3.

Dr. ERNST-AUGUST WEITENDORF,  
Hamburg Ship Model Basin,  
Hamburg, Germany:

The authors have to be congratulated on their interesting work from which I learned a lot regarding effects involved in model cavitation tests (1). I would like to discuss two points:

The first one is related to the "St. Michaelis." In connection with this ship it may be interesting to mention that the full scale trial speed was about 1 knot higher than predicted from tank tests. Moreover, the full-scale cavitation observation showed a rather different behaviour compared with that from model tests performed with grids for the nominal hull wake. The reason for the differences in cavitation and trial speed behaviour may be found in the occurrence of separations in model scale, which, in full scale, may take place less frequently or not at all. The question here is whether the research work on vorticity mentioned by Dr. Kux can help tackle the problem of model separation.

The second point is related to the measuring distance from the full scale windows (Fig. 7+8 of the paper). In order to determine the effective wake field we need measurements over the whole propeller disc. Is there any intention to extend the measuring range of the full-scale test set-up shown in Fig. 7 of the paper?

Reference:

- (1) Weitendorf, E.-A. (1983): Influence of Unsteady Cavitation on Hull Pressure Fluctuations. Report No. 1531, Hamburg Ship Model Basin (HSVA), Hamburg, FRG.

## AUTHORS' REPLY

We would like to thank all discussers for their kind remarks and comments.

We agree with the point of view of Dr. Baba and Dr. Nagamatsu regarding the use of conventional scale transformation. The potential velocity field induced by the propeller may be calculated to a certain degree and in fact this has been done for the model cases. In the full scale case we had the problem that since it had not been possible to scan the total area of the propeller disc, we did not have a complete data set for the wake. To determine the propeller-induced velocity field would have had required an intuitive completion of the velocity distribution over the region not scanned, certainly a dubious extrapolation in view of the size of its area. So the total wake has been scaled.

As to the remarks by Dr. Fry we would like to say that it is precisely this feeling of dismay he points out, why we are searching for means and suitable descriptors to characterize 3-D velocity fields. It seems that there are several ways which could lead to a comprehensive method and we stressed some. As potential flow may easily be computed, it is in fact worth remarking that plots of the non-potential velocity field have not yet become common practice. Measured to calculated, this subtraction is of course easy to perform while, measured against measured, some problems will arise with the location of the measuring points (which could possibly not coincide) requiring interpolation, with all those consequences implied by the method applied and the error margins in the values of velocity components and coordinates. With this in mind, we also see such "beneficial effects" in the suggested difference plots as listed.

In reply to Prof. Mori we want to stress that no directly measured vorticity has been shown in the paper. We are not convinced that the direct determination of vorticity by appropriate probes might prove more reliable than the method of obtaining the vorticity from the spatial derivatives of velocity data as long as figures are available on a net of points in space of adequate density. We agree that the transverse components of the vorticity vector are no less important than the axial component. The beautiful vorticity data presented by Prof. Mori are acknowledged.

As to the contribution by Dr. Huang we have to admit that the precise determination of full-scale ship speed is one of our problems. The same is valid for the thrust which in fact should be measured and generally is not, most of the ships not even allowing for an appropriate measuring device to be installed. We have to accept that torque is all we may measure. The effects of ship motions (and of currents as well) have not been considered and ship motions were not registered at all in our experiments. Fig. 9 is all we can offer to de-

monstrate the influence this neglect may cause. There the results of measurements out of the same window taken under different conditions on different days have been plotted together and show the degree to which the values may be reproduced. As to the wake fraction ratios it is again the lack of reliable wake figures for the full-scale case due to the fact, as already exposed, that it would be necessary to extrapolate the measured velocity values to those regions of the measuring plane not scanned in our experiments, a procedure considered to be dubious in view of the large fraction of the propeller disc area not scanned. We have not attempted to determine wake fraction figures for the full scale case and consequently no ratios of measured and predicted values are included. Measured wake fraction figures (based on thrust identity) for the model cases are included in Table 1 and Table 2.

Replying to Dr. Weitendorf we would like to state that projects are underway to elucidate separation (specifically line separation of three dimensional boundary layers on ship hulls). Whether the vorticity concepts will play an important role in this respect can not be answered at our present status of understanding of the relevant phenomena. As to the range of the measuring device, we are fully aware of the limitations of the actual system. There are several ideas to improve the optics of the device including the possibility to discard the appealing method of the integrated optics in favor of distributed optical components at different windows (with all the shortcomings this would imply in view of the high vibration level) which would eventually lead to a more complete scanning of the interesting area. We can not expect to cover the whole area of interest, a fraction around 6 o'clock position always remaining covered as long as we keep our devices inside the hull. In addition there are - at the moment - no funds we might obtain to design, manufacture and test a new device.



# THEORETICAL PREDICTION OF UNSTEADY PROPELLER CHARACTERISTICS IN THE NON-UNIFORM WAKE FIELD

HAJIME MARUO, MITSUHISA IKEHATA AND MASAHIRO ANDO

## ABSTRACT

Making use of the vortex lattice method, characteristics of a propeller working in the circumferentially non-uniform wake field are computed, in order to analyse the fluctuating thrust and torque, transverse forces on the propeller shaft and the effect of non-uniform intake velocities on the propeller efficiency.

We have employed wake models which have sinusoidal variations in the circumferential direction such as  $V_x(\theta) = V_{x0} + V_{xj} \cos j\theta$  ( $j = 1 \sim 8$ ). The non-linear vortex model with roll up trailing vortices is employed for the slip stream behind the propeller. Propeller blades are replaced by the vortex-source system, and the boundary value problem is solved by means of the discrete function method. The thrust and torque computed by exact unsteady calculations are computed with results by quasi-steady calculations. Differences are observed in the fluctuation amplitude and phase between both computation methods. Load distributions of blades are also computed by these methods.

Experiments are conducted on a propeller model working behind screen meshes which generate the wake distribution corresponding to the condition of the computation. The comparison shows a plausible agreement in the phase relationship of the unsteady propeller forces.

As to the effect of the non-uniformity of wake upon the propeller efficiency, the time average of the propeller characteristics is computed. It has been proved that the relative rotative efficiency different from unity is due to the circumferential non-uniformity of the inflow velocity in the propeller disc.

## 1. INTRODUCTION

A remarkable progress in the application of lifting surface theory to marine propellers has been achieved in recent years. It has enabled the theoretical assessment of the open characteristics of propellers in uniform flow with high accuracy, and the theoretical computation has now become a practical method in the propeller design practice, thanks to the recent progress of high speed computers. However marine propellers are fitted at the ship stern in

general and operate in the non-uniform wake field. Therefore the steady calculation of open characteristics is not enough to assess various important factors, such as the cavitation inception, vibratory forces and the relative rotative efficiency.

The unsteady theory for propellers operating in non-uniform flow has been discussed by several researchers such as Yamazaki(1966) and Tsakonas(1968), but a complete lifting surface theory for unsteady propellers, which is feasible to practical computation, has been established by Hanaoka(1969). Extending Hanaoka's formulation, Koyama(1975) has developed a practical computation method for unsteady characteristics of marine propellers operating in non-uniform flow field. This method is based on the potential theory, by which the velocity field is obtained by integration of the acceleration potential along the trajectory of blade element and the slip stream of the propeller is represented by doublets distributed on helicoidal surfaces which correspond the trailing vortex sheets. Therefore it is originally formulated as the linearized theory for lightly loaded propellers. For moderately loaded propellers, the non-linear effect is taken into account by means of the correction of pitch of the trailing vortex helix according to the induced velocity there. However there exist other types of non-linear effects for heavily loaded propellers, such as the contraction of the slip stream and roll up of trailing vortex sheets. The potential theory is not able to take account of these phenomena. The vortex lattice method is on the other hand, suitable to deal with the above effects, because the configuration of the trailing vortices can be chosen arbitrarily. Kerwin(1978) has proposed a roll up model for trailing vortices, taking account of various non-linear effects. In his approach, the configuration of trailing vortices are assumed a priori from the experimental point of view. It takes account of the contraction of slip stream, roll up of vortex sheets and the separation at the edge of the blade. As to the computation technique, Koyama's method employs the mode function expansion for the circulation distribution over the blade, but the singular behavior of the kernel function in the integral equa-

Dept. of Nav. Arch. & Ocean Eng., Yokohama National University, 156 Tokiwadai, Hodogaya-ku, Yokohama 240  
Masahiro Ando, Hitachi Shipbuilding Co. Ltd., 1-3-22 Sakurajima, Konohana-ku, Osaka 554

tion necessitates some mathematical technique. The discrete function approach, which is conveniently applied to the vortex lattice method, is free from the difficulty of singular behavior of the solution and seems to be suitable to computational work by high speed computers.

The aim of the present work is to provide numerical data for unsteady characteristics of wide bladed marine propellers operating in the non-uniform wake field with circumferential variation of inflow velocities, including thrust and torque fluctuations, vibrating forces and moments on the propeller shaft and vibratory moments on each blade. The computation employs Kerwin's deformed vortex model, which takes account of the roll up of trailing vortices and the separation at the blade tip, but the numerical method is slightly different from that of Kerwin's computation. The circumferential distribution of inflow velocities is decomposed into harmonic elements and the response of propeller blades to each element is examined, like van Oossanen's analysis (1977), which employed lifting line theory. Computations by means of Koyama's method, as well as the quasi-steady approximation, are also carried out for comparison. Then experiments are conducted in the towing tank with respect to propeller models operating behind mesh screens, which simulate the harmonic wake field. Non-linear response, such as the time independent term, which determines the relative rotative efficiency, is also examined. Sample calculations for wake distributions, which simulate the measured wake of ship models, are presented too.

## 2. VORTEX MODEL

We employ Kerwin's deformed wake model in the present calculation, because some of non-linear effects such as contraction and roll up of trailing vortex sheets can be taken into account. The configuration of the vortex wake is illustrated in Fig. 1. It is assumed that each

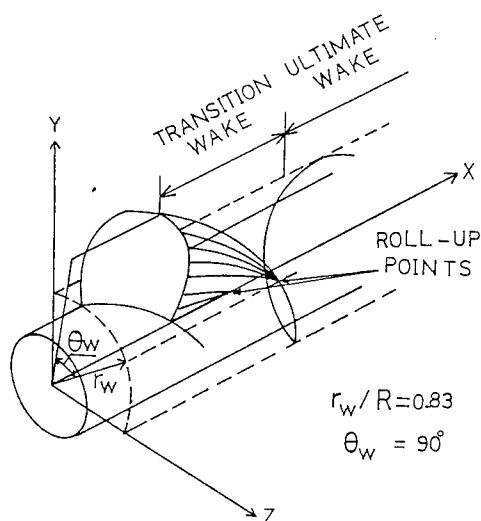


Fig. 1 - Deformed wake model

trailing vortex sheet converges in the transition wake up to the roll up point, and hereafter it is reduced to a helical vortex line constituting the ultimate wake. The blade surface is replaced by the distribution of bound vortices and sources. The latter represents the thickness of the blade. The vortices on the blade surface and in the transition wake are discretized by vortex lattice for the sake of computation. In case of steady condition, the trailing vortices are chordwise only, but in the unsteady case, spanwise vortices are shed behind according to the change of circulation of bound vortices. Because of these shed vortices, the vortex lattice in the transition wake is composed of square vortex rings. The bound vortices and sources on the blade surface discretized by square elements as shown in Fig. 2. The spanwise

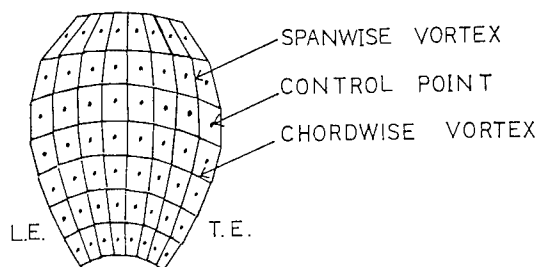


Fig. 2 - Discrete singularity elements

vortex and source are placed at 1/4 chord length from the leading edge of each element on the mean camber surface, and the boundary condition on the blade surface is satisfied at the control point at 3/4 chord length in the mid-span of the element. We have investigated the necessary number of division of the blade element,  $M \times N$  where  $M$  is spanwise and  $N$  is chordwise, to keep enough accuracy in the computation. It is desirable to choose it as small as possible for the sake of short computer time. As the consequence we have decided  $M \times N = 7 \times 8$ . The configuration of trailing vortices is defined by following parameters.

- The diameter of the trailing vortex helix in the ultimate wake  $r_w$ .
- The azimuthal angle between blade tip and the roll up point  $\theta_w$ .
- The pitch angle of the helical vortex in transition wake at the tip  $\beta_T$ .
- The pitch angle of the ultimate wake vortex  $\beta_w$ .

Kerwin studied the influence of above parameters, and according to his result, we choose  $r_w/R = 0.83$  and  $\theta_w = 90^\circ$ , where  $R$  is the screw diameter. Kerwin proposed the pitch angle of tip vortex  $\beta_T$  to be taken as the mean of undisturbed inflow angle  $\beta(\text{tip})$  and the hydrodynamic pitch angle  $\beta_g$  determined by the lifting line theory, but the latter may not be seriously different from the geometrical pitch angle at the tip  $\phi_g(\text{tip})$ . After some trial computations, we assume

$$\beta_T = 0.4[\beta(\text{tip}) + \phi_g(\text{tip})] \quad (1)$$

The exact configuration of the ultimate wake is hardly determined, because the velocity distribution there is different from that at the propeller disc and the trailing vortex is not a helix of constant pitch. After some study on the effect of pitch in the ultimate wake and inspection of experimental data, we employ an assumption that the pitch angle of tip vortices is approximated by the geometrical pitch angle at the blade tip  $\phi_g$ . It can be said that a slight variation of pitch in far wake does not have much influence to the induced velocity at the propeller blade. This approximation simplifies the computation program to a great extent. The transition wake is composed of  $N_t$  segments connecting the points which have cylindrical coordinates

$$\begin{aligned} x_n &= x_t + (n - 3/4)\delta x \\ r_n &= r_t + (n - 3/4)\delta r \\ \theta_n &= \theta_t + (n - 3/4)\delta\theta \quad n = 1, 2, \dots, N_t \end{aligned} \quad (2)$$

where  $x_t, r_t, \theta_t$  are coordinates of points on the trailing edge and  $\delta x, \delta r, \delta\theta$  are increments of each coordinate. Writing coordinates of the trailing edge at the tip by  $x_t(\text{tip}), r_t(\text{tip}), \theta_t(\text{tip})$ , the coordinates of the roll up point is given by  $x_t(\text{tip}) + (\theta_w/2)(R + r_w)\tan\beta_T, r_w, \theta_t(\text{tip}) + \theta_w$ .

In case of steady propeller, the transition wake is constituted by trailing vortices which are extension of chordwise vortices, while shed vortices which are parallel to spanwise direction exist in case of unsteady propeller. Therefore the slip stream is also expressed by lattice of discrete lines.

The computation is carried out in each step of time interval  $\delta t$  or angular interval  $\delta\theta = \delta\theta(\text{tip}) = \omega\delta t$ , where  $\omega$  is the angular velocity of propeller rotation. The number of step  $N_t$  is an important factor with respect to the accuracy of computation. We have chosen the time step in such a way that the angular interval  $\delta\theta = 6^\circ$ , so that we have  $N_t = 15$ .

As one of the non-linear effects, we take account of the separation at the tip of blade approximately. The configuration of model for separated vortices is illustrated in Fig.3.

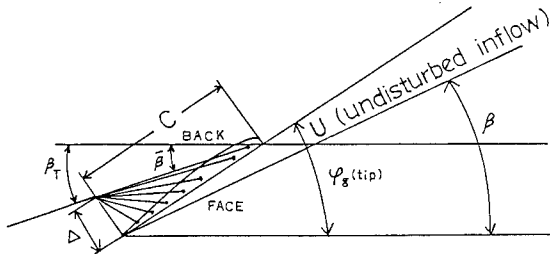


Fig. 3 - Tip vortex separation

The pitch angle of the separated tip vortex is approximated by

$$\bar{\beta} = \frac{1}{2}[\beta(\text{tip}) + \beta_T] \quad (3)$$

and its maximum deviation is

$$\Delta = c(\text{tip}) \tan[\phi_g(\text{tip}) - \bar{\beta}] \quad (4)$$

where  $c(\text{tip})$  is the chord length at the tip.

### 3. DETERMINATION OF CIRCULATION IN THE STEADY CONDITION OF UNIFORM FLOW

In the first place, let us consider a propeller operating in a uniform flow, for the purpose of comparison between the computation by the present method and that by other methods. The steady state calculation by the vortex lattice method was carried out by Yuasa(1980) for the case of ducted propellers. The method of computation in the present work follows along the same line as his.

The vortex lattice configuration in the steady state is shown in Fig.4. We designate

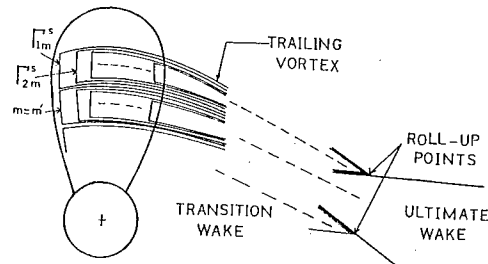


Fig. 4 - Steady vortex lattice scheme

the circulation of the  $(n,m)$ th element of spanwise vortex by  $\Gamma_{nm}^s$ , where  $n = 1, 2, 3, \dots, N$ , and  $m = 1, 2, 3, \dots, M$ , and let the number of blades be  $K$ . Let  $U_{i,nm}(k)$  be the component of induced velocity normal to the mean camber surface at the  $i$ -th control point due to the spanwise vortex of unit circulation on the  $k$ -th blade at the  $(n,m)$ th element, which accompanies chordwise and trailing vortices starting therefrom. The induced velocities are determined by the Biot-Savart law, and the normal component of the induced velocity due to the total vortex system can be written as

$$d_i = \sum_{k=1}^K \sum_{m=1}^M \sum_{n=1}^N U_{i,nm}(k) \Gamma_{nm}^s \quad (5)$$

The flow model on the blade surface is constituted by the lattice of vortices and sources as stated before. The strength of sources is determined by the slope of the blade thickness, and we write the velocity vector induced by the source distribution at the  $i$ -th control point as  $V_i^q$ . The boundary value problem is solved on the key blade for which we put  $k = 1$ . The boundary condition at the  $i$ -th control point is expressed by

$$d_i = -n_i \cdot (V_i + V_i^q) \quad (6)$$

where  $n_i$  is the unit normal vector at the  $i$ -th control point and  $V_i$  is the vector of relative velocity in the uniform inflow. The latter is given by

$$V_i = (V_a, -2\pi n r_i \sin \theta_i, 2\pi n r_i \cos \theta_i) \quad (7)$$

where  $V_a$  is the inflow velocity,  $n$  is the number of revolution and  $r_i, \theta_i$  are the coordinates of the  $i$ -th control point. The right hand side of (6) is determined from the blade configuration and the equation implies  $M \times N$  simultaneous linear equations which determine the circulation  $\Gamma_{nm}^s$  at each point. Because of the model of roll up vortex, the trailing vortices in the transition wake are reduced to a single vortex line behind the roll up point, and only the circulation of the mid-span element ( $m=m'$ ) contributes the vortex strength to the ultimate wake.

#### 4. DETERMINATION OF CIRCULATION IN THE UNSTEADY CONDITION IN THE NON-UNIFORM WAKE

Here we assume the wake field with velocity parallel to the screw shaft and non-uniformity over the disc plane. The circumferential variation of the inflow velocity is decomposed by the harmonic elements such as

$$V_a = V_{x0} + V_{xj} \cos j\theta \quad (j = 1, 2, 3, \dots) \quad (8)$$

The angle between the  $k$ -th blade and the key blade is

$$\delta_k = 2\pi(k-1)/K \quad (K = 1, 2, 3, \dots, K) \quad (9)$$

Now let us introduce the index of time step denoted by  $t_s (= \dots, -2, -1, 0, 1, 2, \dots)$  with the interval  $\delta t$ . In case of the unsteady motion we have to take account of shed vortices, whose strength is determined by the time variation of bound vortices. The induced velocity of the total vortex system at the  $i$ -th control point on the key blade is expressed by the form like

$$d_i = \sum_{k=1}^K \left[ \sum_{n=1}^N \left( \sum_{m=1}^M U_{inm}^s \Gamma_{nm}^s + \sum_{m=1}^{N_w} U_{inm}^w \Gamma_{nm}^w \right) + \sum_{n=1}^K \left( \sum_{m=1}^N U_{inm}^c \Gamma_{nm}^c + \sum_{m=1}^{N_w} U_{inm}^t \Gamma_{nm}^t \right) \right] \quad (10)$$

The superscripts  $s$  and  $c$  relate to spanwise and chordwise vortices respectively, and subscripts  $w$  and  $t$  relate to shed and trailing vortices respectively.  $N_w$  is the number of shed vortices considered in the computation. According to Lord Kelvin's theorem, we have the relation

$$\Gamma_{1m}^w = - \left( \sum_{n=1}^N \Gamma_{nm}^s + \sum_{n=N_w+1}^{N_w+N} \Gamma_{nm}^w \right) \quad (11)$$

Therefore we can write the induced velocity at time  $t = t_s \delta t$  in the form like

$$\begin{aligned} & \sum_{k=1}^K \left[ \sum_{n=1}^N \left\{ U_{inm}^s + \sum_{l=1}^N (U_{iln,m+1}^c - U_{iln,m}^c) - U_{iln}^w \right\} \Gamma_{nm}^s(k) \right. \\ & \left. + \sum_{n=N_w+1}^{N_w+N} (U_{inw-1,m}^w + U_{inw-1,m+1}^w - U_{inw-1,m}^t - U_{inw}^w) \right. \\ & \left. \times T_m^{(t_s-n_w+1)}(k) \right] \end{aligned} \quad (12)$$

where  $T_m^{(t_s)}(k)$  is the strength of vortex ring in the wake, such as

$$T_m^{(t_s)}(k) = \sum_{n=1}^N \Gamma_{nm}^s(k) \quad (13)$$

The configuration of the vortex system is shown in Fig.5.

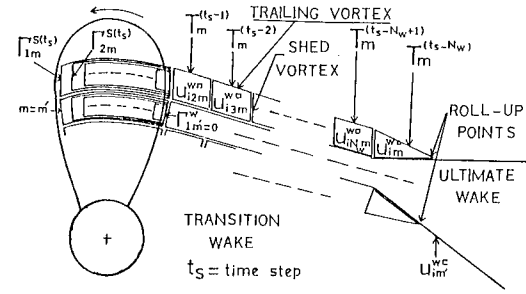


Fig. 5 - Unsteady vortex lattice scheme

One can express the spanwise vortex,  $\Gamma_{nm}^s$ , by the sum of steady and unsteady parts like

$$\text{steady part: } \bar{\Gamma}_{nm}^s = g_{0nm} \quad (14)$$

$$\begin{aligned} \text{unsteady part: } \tilde{\Gamma}_{nm}^s = & g_{1nm} \cos \{j(\theta_{nm} + \delta_k - t_s \delta \theta) \\ & + g_{2nm} \sin \{j(\theta_{nm} + \delta_k - t_s \delta \theta) \end{aligned} \quad (15)$$

and write the vortex ring  $T_m^{(t_s)}(k)$  in the similar way,

$$\text{steady part: } \bar{T}_m = \sum_{n=1}^N g_{0nm} \quad (16)$$

$$\begin{aligned} \text{unsteady part: } \tilde{T}_m = & \sum_{n=1}^N [g_{1nm} \cos \{j(\theta_{nm} + \delta_k - t_s \delta \theta) \\ & + g_{2nm} \sin \{j(\theta_{nm} + \delta_k - t_s \delta \theta) \}] \end{aligned} \quad (17)$$

Next we define the normal component of induced velocity of a unit vortex ring on the  $k$ -th blade in the transition wake as follows.

$$\begin{aligned} U_{inm}^a(k) = & \{U_{inm}^s(k) - U_{inm}^w(k)\} \\ & + \sum_{l=1}^N \{U_{iln,m+1}^c(k) - U_{iln,m}^c(k)\} : \text{on blade} \\ & \dots \dots \dots \end{aligned} \quad (18)$$

$$\begin{aligned} U_{inm}^w(k) = & U_{in-1,m}^w(k) + U_{in-1,m+1}^t(k) - U_{in-1,m}^t(k) \\ & - U_{inm}^w : \text{in transition wake} \end{aligned} \quad (19)$$

where  $U_{inm}^s(k)$ ,  $U_{inm}^c(k)$ ,  $U_{inm}^w(k)$  and  $U_{inm}^t(k)$  are defined as the normal component of induced velocity of spanwise (index  $s$ ), chordwise (index  $c$ ) shed (index  $w$ ) and trailing (index  $t$ ) vortex segment on the  $(n,m)$ th element respectively, with unit circulation at the  $i$ -th control point on the key blade. Further we define  $U_{inm}^w(k)$  for the normal component of the induced velocity of the last vortex ring, which is of triangular shape and given by putting  $n = N_w$  and  $U_{inm}^w = 0$  in eq.(19), and  $U_{inm}^t$  for that of horseshoe trailing vortex given by

$$\begin{aligned} U_{inm}^t = & U_{inm}^w(k) + \sum_{n=N_w+1}^{N_w+N} \{U_{inw-1,m+1}^t(k) \\ & - U_{inw-1,m}^t(k)\} \end{aligned} \quad (20)$$

Then one can write

$$\begin{aligned} & \sum_{k=1}^K \left[ \sum_{n=1}^N \sum_{m=1}^M U_{inm}^a(k) \Gamma_{nm}^s(k) \right. \\ & \left. + \sum_{m=1}^{N_w} \left\{ \sum_{n=N_w+1}^{N_w+N} U_{inm}^w(k) T_m^{(t_s-n_w+1)}(k) \right\} \right] \end{aligned}$$

$$+ U_{im}^w(k) T_m^{(t_s - N_w)}(k) \} + U_{im}^w(k) \sum_{n=1}^N \Gamma_{nm}^s(k) \} = d_i \quad (21)$$

Equating  $d_i$  to the right hand side of (6), we obtain the system of simultaneous linear equations, which determines the circulation of spanwise vortices. In case of the harmonic wake expressed by eq.(8), the above equation provides the system of algebraic equations which determines the coefficients  $g_{0nm}$ ,  $g_{1nm}$  and  $g_{2nm}$  in eqs.(14)(15)(16) and (17). Kerwin employed the Kutta condition at the trailing edge in his calculation, whereas we have not used it because the condition of smooth out flow at the trailing edge is satisfied by the relation (21) at the control point on the last element close to the trailing edge.

The quasi-steady calculation is often used to predict the unsteady characteristics of propellers. In the present paper, the unsteady calculation programs will be simplified by the quasi-steady condition. In this case, the circulation of all vortex rings in the transition wake with respect to the  $m$ -th spanwise blade element is constant, so that

$$T_m^{(t_s - n_w + 1)}(k) = T_m^{(t_s)}(k), \quad n = 2, 3, \dots, N_w + 1 \quad (22)$$

This results the vortex arrangement which is identical with that in the steady case. Since the non-uniformity of the wake field is taken in full in the boundary condition, the present computation program provides the quasi-steady calculation of high accuracy.

## 5. HYDRODYNAMIC FORCES

The hydrodynamic force acting on a blade is composed of four component forces as follows.

a) The Lagally force on sources representing the blade thickness effect:

Putting

$\rho$  = the density of fluid,  
 $\Delta \ell_{nm}$  = the length of spanwise segment of the  $(nm)$ th element,  
 $Q_{nm}$  = the density of source distribution along the line  $\Delta \ell_{nm}$ ,  
 $V_{nm}$  = the resultant velocity vector at the mid point of  $\Delta \ell_{nm}$ ,  
 we have the Lagally force acting on the line source along  $\Delta \ell_{nm}$  given by

$$F_{nm}^{(L)} = -\rho \Delta \ell_{nm} \cdot Q_{nm} \cdot V_{nm} \quad (23)$$

b) The Kutta-Joukowski force on the bound vortex:

The Kutta-Joukowski force appears on spanwise bound vortices only and its amount for the segment  $\Delta \ell_{nm}$  is given by

$$F_{nm}^{(K)} = \rho \Delta \ell_{nm} \cdot V_{nm} \times \Gamma_{nm} \quad (24)$$

where  $\Gamma_{nm}$  is the vector representation of the circulation of the bound vortex on  $\Delta \ell_{nm}$ .

c) The frictional drag:

The frictional drag on the surface element  $\Delta A_{nm}$  is given by

$$F_{nm}^{(F)} = \frac{1}{2} \rho C_f \Delta A_{nm} |V_{nm}| V_{nm} \quad (25)$$

In the present calculation, we employ the Prandtl-Schlichting formula with blade thickness correction, such as

$$C_f = (1 + t_h/c) \{0.455 / (\log_{10} Re)^{2.58}\} \quad (26)$$

as the frictional drag coefficient, where  $t_h$  is the maximum thickness,  $c$  is the chord length and  $Re$  is the Reynolds number of the blade element. We assume that the effect of the unsteadiness is small and substitute the resultant velocity  $V_{nm}$  by its mean value  $\bar{V}_{nm}$ .

d) The force which comes from the time derivative term:

There is a term of partial derivative with respect to time in the momentum equation, which yields a component of force on the blade element. Let us take the length  $s$  along the chord from the leading edge of a blade element. The acceleration of the fluid along  $s$  is expressed by  $\partial u / \partial t + u \partial u / \partial s$ , where  $u$  is the tangential velocity along  $s$ , and the pressure gradient is  $\partial p / \partial s$ . Since  $u$  is different on upper and lower sides of  $s$ , the time derivative term in the acceleration yields the pressure difference. If we write  $u^+$  and  $u^-$  for the tangential velocities on upper and lower sides respectively, the force acting on the element  $\delta A$  of the blade is given by

$$\delta F = \rho n \frac{\partial}{\partial t} \int_0^s (u^+ - u^-) ds \cdot \delta A \quad (27)$$

Since we have the relation

$$\int_0^s (u^+ - u^-) ds = \int_0^s \gamma ds = \sum \Gamma_{nm} \quad (28)$$

the equation (27) can be rewritten in the discrete form like

$$F_{nm}^{(T)} = \rho n_{nm} \frac{\partial}{\partial t} \left[ \sum_{\ell=1}^N \Gamma_{\ell m}^s \right] \Delta r_{nm} / \cos \delta \cdot \delta s \quad (29)$$

where  $\Delta r_{nm}$  is the radial length of the  $m$ -th spanwise segment,  $\delta$  is the rake angle of the segment and  $\delta s$  is the chord length of  $\delta A$  ( $= \delta s \cdot \delta r_{nm} / \cos \delta$ ). Because of the expression (15) for the unsteady portion of circulation, one can write the time derivative of circulation in the form like

$$\frac{\partial}{\partial t} \left( \sum_{\ell=1}^N \Gamma_{\ell m}^s \right) = \omega j \sum_{\ell=1}^N [g_{1\ell m} \sin \{j(\theta_{\ell m} - t_s \delta \theta)\} - g_{2\ell m} \cos \{j(\theta_{\ell m} - t_s \delta \theta)\}] \quad (30)$$

for computation purposes.

## 6. THRUST, TORQUE, SIDE FORCE AND BENDING MOMENT

Fig.6 gives the coordinate system for various components of forces and moments, namely thrust  $T$ , torque  $Q$ , side force  $F_y$ ,  $F_z$ , and bending moment  $M_y$ ,  $M_z$ . The force  $F_z = (F_{nm}^x, F_{nm}^y, F_{nm}^z)$  is the sum of various components given in the preceding section and is regarded as acting at the middle point of each segment. The coordinate axes are fixed at the propeller position, with  $Y$  axis in vertical direction and

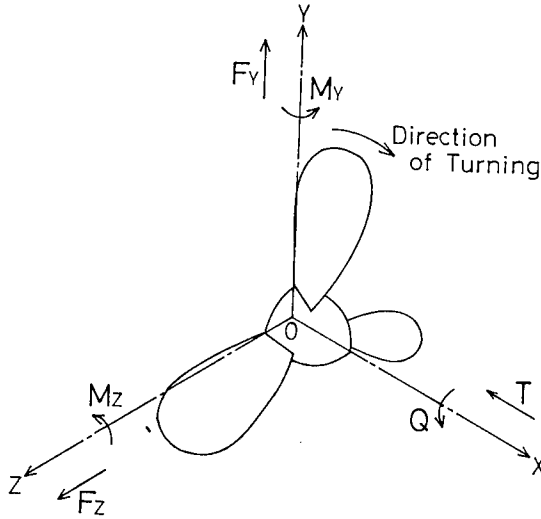


Fig. 6 - Coordinate system of forces and moments

Z axis in horizontal direction. The angular position of propeller blades is defined by the angle of generator line of the key blade  $\theta'$ , and it is expressed at each time step by

$$\theta'(t_s) = -\theta(t_s) = t_s \delta \theta \quad (31)$$

Expressions for various forces and moments are as follows.

a) Thrust per one blade:

Since angle  $\beta(r)$  of the steady component of undisturbed inflow is given by

$$\beta(r) = \tan^{-1}(V_{x0}/2\pi nr) \quad (32)$$

the viscous drag of the blade element becomes

$$dD_f = \rho C_f C (V_{x0} \sin \beta + 2\pi nr \cos \beta)^2 / dr \quad (33)$$

Then the thrust per one blade is given by

$$T_1 = - \sum_{n,m}^{N,M} F_{nmz} - \int_{R_h}^R (dD_f \sin \beta) \quad (34)$$

where  $R$  and  $R_h$  are radii of propeller and hub respectively, and  $F_{nmz}$  means the z component.

b) The torque per one blade:

$$Q_1 = \sum_{n,m}^{N,M} r_{nm} (-F_{nmy} \sin \theta_{nm} + F_{nmz} \cos \theta_{nm}) + \int_{R_h}^R (r dD_f \cos \beta) \quad (35)$$

where  $r$  and  $\theta$  are radius and angle of (nm) element, and  $F_{nmy}$  and  $F_{nmz}$  are y component and z component of the force.

c) The upward force per one blade:

The coordinate of a point on the mid-chord line is expressed by

$$(x_{mc1}, r_{mc1}, \theta_{mc1} - t_s \delta \theta),$$

so that the upward force per one blade is given by

$$F_{Y1} = \sum_{n,m}^{N,M} \{F_{nmz} \sin(t_s \delta \theta) + F_{nmy} \cos(t_s \delta \theta)\}$$

$$- \int_{R_h}^R \{dD_f \cos \beta \sin(\theta_{mc1} - t_s \delta \theta)\} \quad (36)$$

d) The horizontal force per one blade:

$$F_{Z1} = \sum_{n,m}^{N,M} \{F_{nmz} \cos(t_s \delta \theta) - F_{nmy} \sin(t_s \delta \theta)\} + \int_{R_h}^R \{dD_f \cos \beta \cos(\theta_{mc1} - t_s \delta \theta)\} \quad (37)$$

e) The horizontal bending moment per one blade:

$$M_{Y1} = \sum_{n,m}^{N,M} [F_{nmz} r_{nm} \sin(\theta_{nm} - t_s \delta \theta) - \{F_{nmz} \cos(t_s \delta \theta) - F_{nmy} \sin(t_s \delta \theta)\} x_{nm}] + \int_{R_h}^R [dD_f \sin \beta r_{mc1} \sin(\theta_{mc1} - t_s \delta \theta) - \{dD_f \cos \beta \cos(\theta_{mc1} - t_s \delta \theta)\} x_{mc1}] \quad (38)$$

f) The vertical bending moment per one blade:

$$M_{Z1} = \sum_{n,m}^{N,M} [-F_{nmz} r_{nm} \cos(\theta_{nm} - t_s \delta \theta) + \{F_{nmz} \sin(t_s \delta \theta) + F_{nmy} \cos(t_s \delta \theta)\} x_{nm}] + \int_{R_h}^R [-dD_f \sin \beta r_{mc1} \cos(\theta_{mc1} - t_s \delta \theta) - \{dD_f \cos \beta \sin(\theta_{mc1} - t_s \delta \theta)\} x_{mc1}] \quad (39)$$

The bearing force at the propeller shaft is obtained from the sum of forces and moments of all blades, taking account of the phase difference  $\delta_k$  between each blade, in such a manner as

$$F = F_1(\theta') + \sum_{k=2}^K F_1(\theta' + \delta_k) \quad (40)$$

g) The distribution of bending moment along the span:

The radial distribution of lift of each element is expressed by

$$dL/dr = (\sum_{n,m}^{N,M} n_s \cdot F_{nm}^S) / \Delta r_m \quad (41)$$

Then the hydrodynamic moment of a blade element at radius  $r_B$  is given by

$$M_B = \int_{r_B}^R (dL/dr) \cos\{\phi_g(r_B) - \beta(r)\} (r - r_B) dr \quad (42)$$

## 7. NUMERICAL RESULTS AND SOME CONSIDERATIONS

We have chosen a marine screw propeller model, AU5-50, with five blades, whose expanded area ratio is 0.50 and pitch ratio is 1.0, for the comparative computation by means of present method, Koyama's method and quasi-steady method. Principal particulars of the above model are given in the first column of Table 1, which is shown in the next page. We use the abbreviation such as P.M. for the present vortex lattice method and K.M. for Koyama's method.

### 7.1 Steady Characteristics in a Uniform Flow

The steady characteristics of the model propeller AU5-50 has been calculated in the condition of advance in open water. The advance constant  $J = Va/nD$ , where  $Va$  is the advance

Table 1 - Principal Particulars of Model Propellers

Type of Propeller	AU5-50	TB3-50	AU4-55	MAU5-66
Diameter (m)	0.250	0.1732	0.1667	0.175
Boss ratio	0.180	0.167	0.180	0.180
Pitch ratio (const)	1.00	0.800	0.710	0.7143
Exp. area ratio	0.500	0.500	0.550	0.6649
Max blade width ratio	0.226	0.3698	0.311	0.3008
Blade thickness ratio	0.050	0.050	0.050	0.050
Angle of rake	10°0'	14°50'	10°0'	10°0'
Number of blades	5	3	4	5
Blade section	AU-type	Troost-type	AU-type	MAU-type
Direction of turning	right-handed	right-handed	right-handed	right-handed
Notes	Calculation of the characteristics by P.M. & K.M.			
	Comparison between calculation results and experimental data			

speed,  $n$  is the number of revolutions and  $D$  is the diameter, is taken 0.3, 0.5, 0.7, 0.9. The diagrams of thrust and torque constants and propeller efficiency, are shown in Fig. 7. The experimental result is taken from Yazaki's paper(1961). The results of P.M. and K.M. coincide very well with each other and are very close to experimental curves.

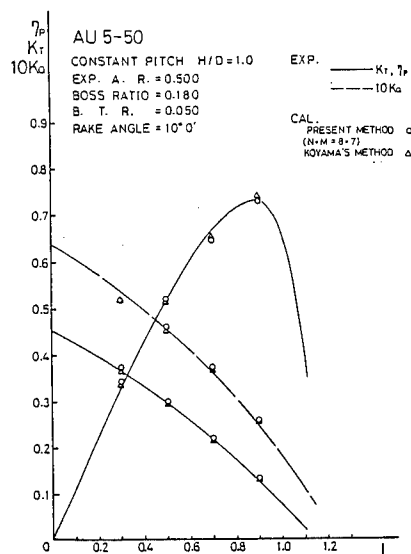


Fig. 7 - Open Water Characteristics of AU5-50 Propeller

So the number of elements on a blade,  $N \times M = 8 \times 7$ , is proved enough to assure the accuracy of calculation by these numerical results.

However, there are some differences in the circulation distribution along the chord near the tip between P.M. and K.M. as seen in the upper of Fig. 8. At the 0.918R section, the density of circulation by P.M. is smaller in the vicinity of the leading edge and higher in most mid-chord part compared to K.M. But, at a section,  $r \leq 0.809R$ , P.M. gives the almost same distribution of the circulation density as that of K.M., as seen in the lower of Fig. 8. Such difference at the tip may be brought by the consideration of separation of the trailing vortex at the blade tip in P.M. This is the same tendency as the tip correction for Koyama's results(1979).

Spanwise distributions of the total

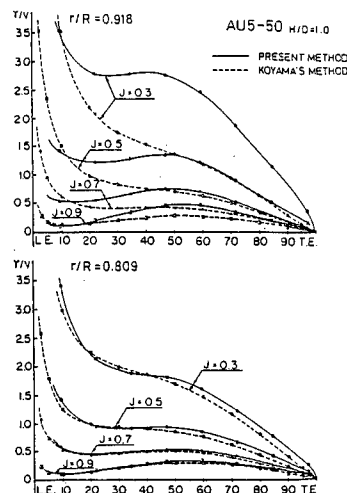


Fig. 8 - Circulation Density Distribution along Chord

circulation of a blade section integrated along the chord are shown in Fig. 9. There are seen not much differences between P.M. and K.M. near the tip as in the chordwise distributions. This is the reason why almost the same open characteristics are obtained by P.M. and K.M.

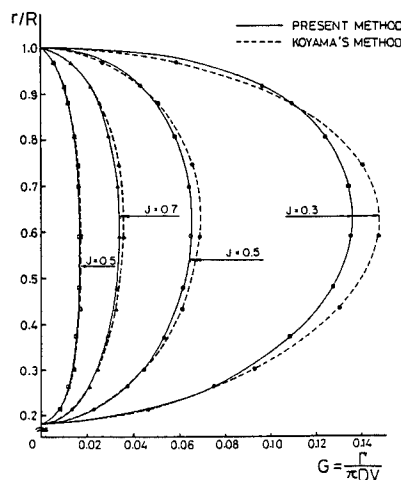


Fig. 9 - Spanwise Distribution of Total Circulation

## 7.2 Thrust and Torque of One Blade (Key Blade) in Harmonic Wake

Let us set the conditions for calculation as follows:

The advance speed of propeller:

$$V_A = 2.5 \text{ m/s.}$$

The number of revolutions of propeller:

$$n = 10 \text{ r.p.s.}$$

The harmonic wake:  $w_x = 0.3 + 0.3 \cos j\theta$ .

So the mean advance constant  $J = 0.7$ .

The thrust and the torque of one blade (key blade) are calculable using aforementioned equations. Examples of calculated results of the thrust are shown in Figs. 10, 11 & 12 and of the torque in Figs. 13, 14 & 15. They are

variations of thrust and torque constants,  $K_T = T_1 / \rho n^2 D^4$ ,  $K_Q = Q_1 / \rho n^2 D^5$ , in the harmonic wake of  $\cos 2\theta$ ,  $\cos 4\theta$  and  $\cos 5\theta$ .

It is found that phase advance appears in unsteady calculations, while there is phase lag in the result of quasi-steady calculations, and further more in the calculations excluding time-derivative terms. These facts are seen in common in all calculated results of thrust and torque for the harmonic wake of  $\cos \theta - \cos 8\theta$ . The phase lag of the quasi-steady calculation seems to be attributed to the effect of interactions between blades and that of the trailing vortices. Though the existence of shed vortices brings more phase lag to the calculation without time-derivative term ultimately. One can conclude that the effect of time-derivative term is the main source of the phase advance of the thrust and torque fluctuations. Such a phase shift has been observed in calculations by Yamazaki(1966), Koyama(1975) and Hatao et. al.(1975), but the reason has never been elucidated. One can explain the decrease of forward shift of phase in higher harmonic modes due to the increased reduced frequency.

Let us compare the amplitudes of oscillations of  $K_T$ , and  $K_Q$  in Figs. 10 -15. The highest amplitude is obtained normally by the quasi-steady calculation, the next is the unsteady one and the least is by the calculations without time-derivative terms in most cases. However, we find the unsteady calculation in case of  $\cos 4\theta$  in Figs. 11 and 14 exceeds the quasi-steady one. Such amplification of the unsteady calculation of P.M. seems to be the effect of time-derivative

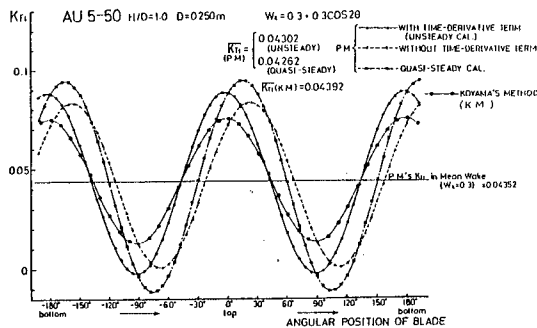


Fig. 10 - Thrust of One Blade in  $\cos 2\theta$  Wake

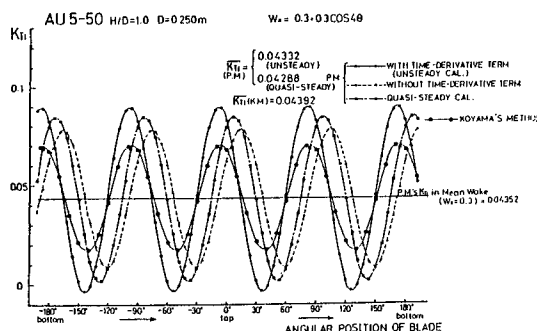


Fig. 11 - Thrust of One Blade in  $\cos 4\theta$  Wake

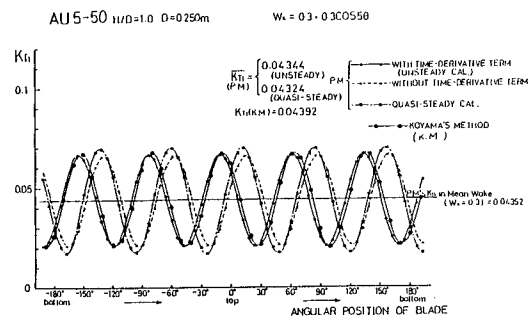


Fig. 12 - Thrust of One Blade in  $\cos 5\theta$  Wake

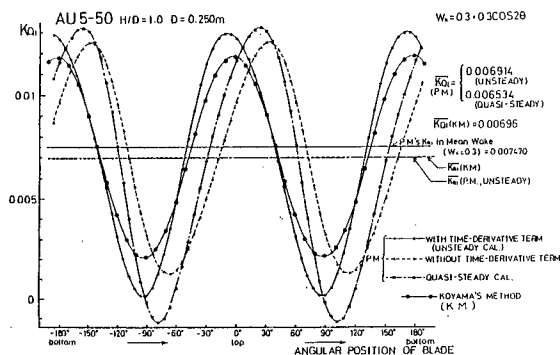


Fig. 13 - Torque of One Blade in  $\cos 2\theta$  Wake

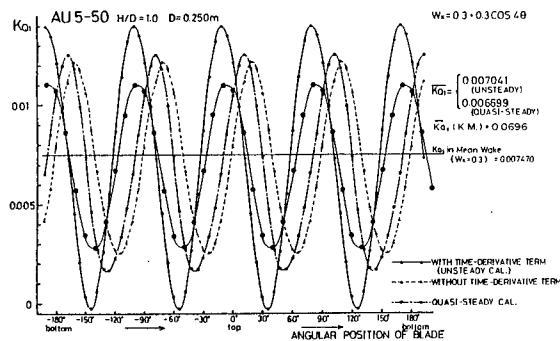


Fig. 14 - Torque of One Blade in  $\cos 4\theta$  Wake

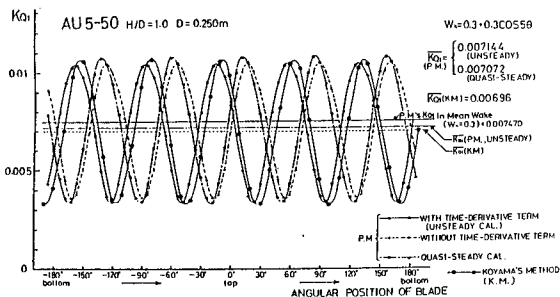


Fig. 15 - Torque of One Blade in  $\cos 5\theta$  Wake

terms, because the amplitude of thrust or torque fluctuations is reduced below that of the quasi-steady condition even for  $\cos 4\theta$  as seen in Figs. 11 and 14, if the time-derivative term is omitted.



Thus, it can be understood that the time-derivative term of the blade forces has the remarkable influence of amplitude increase and phase shift forward. This effect attains to maximum nearly in case of  $\cos 4\theta$ . We see that the unsteady calculation gets close to the calculation without time-derivative terms in case of  $\cos 5\theta$  as shown in Figs. 12 and 13. This is convinced by the fact that the increment of the reduced frequency weakens the effect of the time-derivative term.

Figs. 16 and 17 show the amplitude and phase of harmonic components of the same modes as those of the wake and components of doubled mode which mean the non-linear contribution to the unsteady thrust and torque calculated by the present method. The maximum magnification

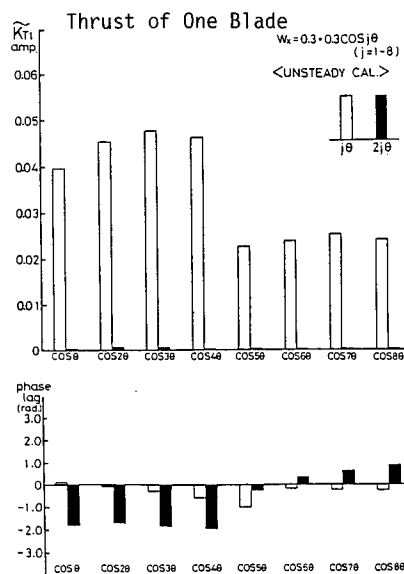


Fig. 16 - j-th & 2j-th Modes in Thrust

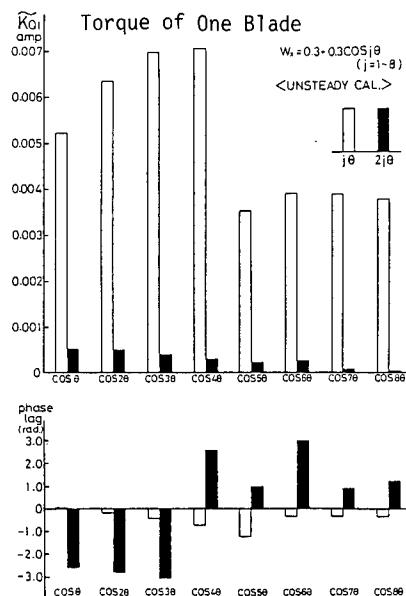


Fig. 17 - j-th & 2j-th Modes in Torque

of the same harmonic mode as that of the wake is observed more clearly in case of  $\cos 3\theta$  for the thrust and in case of  $\cos 4\theta$  for the torque by the unsteady calculation of P.M. in the comparison of the amplitudes for various harmonic wakes shown in Figs. 16 and 17. The double harmonic mode will be mentioned in the next section.

Let us introduce the complex transfer function of lift like the Sears function of two dimensional problems of oscillating blades.

If the transfer function  $Sp(\omega_r)$  is defined by

$$Sp(\omega_r) = \frac{dL/dr}{\pi \rho c W v_n e^{ij\omega t}} \quad (43)$$

at the blade section of radius  $r$ , where  $W$  is the steady undisturbed inflow velocity,  $v_n$  is the amplitude of the harmonic wake velocity normal to  $W$ . Fig. 18 shows the vector diagram of the lift transfer function obtained by the unsteady calculation of P.M. The diagrams are given with respect to four sections of a blade. The Sears function for the same case is also shown in the same figure. One can find that  $Sp(\omega_r)$  of the unsteady calculation exists almost in the space of the first quadrant in Fig. 18. The amplification is dominant near the 45 degrees diagonal at 1.0 - 2.0 of  $\omega_r$  in Fig. 18. There are no 3-dimensional lift transfer functions at any section similar to the 2-dimensional Sears function in the calculations of P.M.

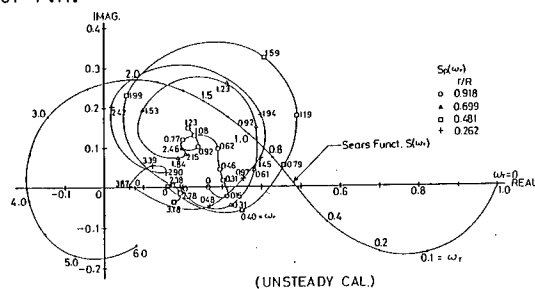


Fig. 18 - Lift Transfer Function by P.M.

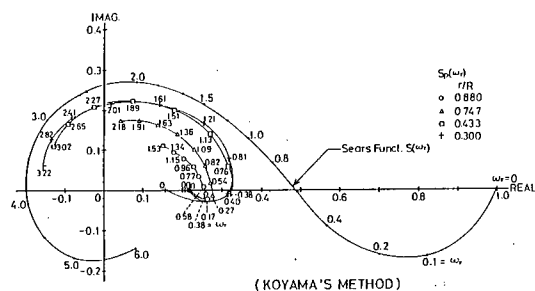


Fig. 19 - Lift Transfer Function by K.M.

Here the authors wish to mention the results of Koyama's method (K.M.). Their time histories are shown in Figs. 10 - 15. They show the coincidence in the phase of oscillation with the results of the unsteady calculation of P.M. but amplitudes are smaller than those of unsteady P.M. for lower harmonic modes of wake,

$\cos 2\theta - \cos 4\theta$ . The amplitude calculated by K.M. attains as much as half of the prediction by the unsteady P.M. for  $\cos 4\theta$ . This is an important problem in the practical prediction for the propeller design by K.M. Characteristics of the response of the blade force in K.M. can be demonstrated more explicitly in the vector diagram of the lift transfer function  $Sp(\omega_r)$ . Fig. 19, shows those of K.M. with respect to four blade sections. Comparing Fig. 19 with Fig. 18, one can see that most parts of  $Sp(\omega_r)$  of K.M. are located in the space of the first quadrant that is common to the unsteady P.M. but some parts extend within the second quadrant when  $\omega_r$  is high. So a more advanced phase may be predicted by K.M. than by P.M. when  $\omega_r$  is high, that corresponds to a high harmonic mode wake such as  $\cos 6\theta$ ,  $\cos 7\theta$  and so on. The feature of diagrams of K.M. looks a pretty like that of the Sears function except for the zone of smaller  $\omega_r$ .

### 7.3 Constant Term and Double Harmonic Mode of Blade Forces due to Non-Linear Effect of Non-Uniformity of Wake

The Kutta-Joukowski force is given by eq. (24), i.e. the product of the resultant velocity and the circulation of the spanwise vortex. They are both given by the summation of the steady constant term and the  $j$ -th mode in the harmonic wake of  $w_x = 0.3 + 0.3\cos j\theta$ . Therefore, the product of ( $j$ -th harmonic mode of the resultant velocity) and ( $j$ -th harmonic mode of the circulation) generates the constant term and the double harmonic mode, namely the term of the  $2j$ -th harmonic mode. This is the characteristic non-linear effect of Kutta-Joukowski force. The constant term results a deviation of the mean value of the blade forces.

The mean values of the unsteady and the quasi-steady calculations of P.M.,  $K_T$  or  $K_Q$ , are described in Figs. 10 - 15, and the steady result of  $K_T$  or  $K_Q$  in the uniform mean wake is exhibited by the constant straight line with its value. The difference of unsteady one or quasi-steady one from steady one is little in the thrust coefficient as seen in Figs. 10 - 12 but not little in the torque constant as seen in Figs. 13 - 15. One finds the deviation on the negative side, so that one can guess it brings about a higher efficiency of the propeller in a non-uniform wake than in open water, that means the high relative rotative efficiency above unity.

Ikehata(1977) verified that the difference of relative rotative efficiency from unity was caused by such constant term due to non-linear effect of non-uniformity of wake using a simple quasi-steady theory.

The relative rotative efficiency analyzed from these calculated results is shown in Fig. 20 for the unsteady and the quasi-steady calculations in various harmonic wakes of  $\cos\theta - \cos 8\theta$ . Both of them based on the concept of the thrust identity in reference to the open water characteristics. Some interesting aspects are found in Fig. 20. All plotted points fall

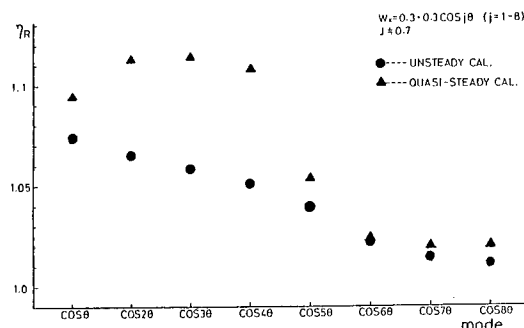


Fig. 20 - Relative Rotative Efficiency

above unity. The unsteady calculations show the tendency that the deviation from unity is maximum in case of  $\cos\theta$  and decreases gradually toward unity as the order of harmonic mode increases, while the quasi-steady calculations show values of  $\eta_R$  higher than 1.1 in cases of  $\cos 2\theta$ ,  $\cos 3\theta$  and  $\cos 4\theta$  and suddenly drops to the value of unsteady calculation in case of  $\cos 5\theta$  or higher modes. Therefore the quasi-steady calculation may predict too high  $\eta_R$  on account of such excessive non-linear effect of the non-uniformity of the wake distribution. Since Koyama's method is a linear theory, the mean value of the thrust or the torque becomes same as the steady value in the mean wake which is independent of the mode of the harmonic wake. Moreover, since the frictional drag is left out of consideration in Koyama's method, mean values of K.M. given in Figs. 10 - 15, are all different from those of P.M. The difference is noticeable especially in the torque.

Another non-linear effect of the non-uniformity of the wake distribution is the existence of the double harmonic mode, shown in Figs. 16 and 17. As seen in Fig. 16, the double harmonic mode of the thrust can be regarded as negligible in comparison with the single harmonic mode, and that of the torque attains to several percents of the primary mode at maximum 10 percents in  $\cos\theta$  as shown in Fig. 17.

This effect appears prominent in a lower harmonic mode of wake but reduces in higher modes. The phase of component of the double harmonic mode is different by more than one radian in most harmonic wakes from that of the primary mode.

This double harmonic mode affects to make the curve of the variation of the torque or the thrust deviate from simple harmonic. However the deviation is not remarkable as seen in Figs. 5 - 10, even for torque variations. One can know such magnitude of the double harmonic mode gives no significant effect to the configuration of fluctuation.

The existence of the double mode component in the blade force should be emphasized because it generates other excitations in the vibration of a propeller.

### 7.4 Circulation and Load Distributions of Blade Section

In Fig. 21 are shown the non-dimensional

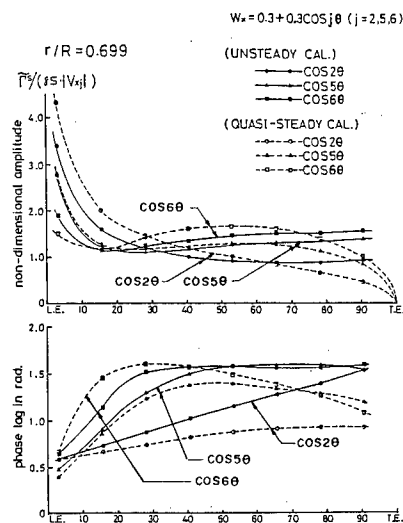


Fig. 21 - Unsteady Spanwise Vortex Distribution along Chord

amplitudes and phase lag of the circulation of the spanwise vortices at the 0.699R blade section in the harmonic wake,  $\cos 2\theta$  and  $\cos 5\theta$  and  $\cos 6\theta$ . The circulation at the trailing edge obtained by the unsteady calculation does not become zero but continues to the value of the shed vortex in any mode of the harmonic wake. So there are a great deal of difference near the trailing edge both in the amplitude and the phase between unsteady and quasi-steady calculations.

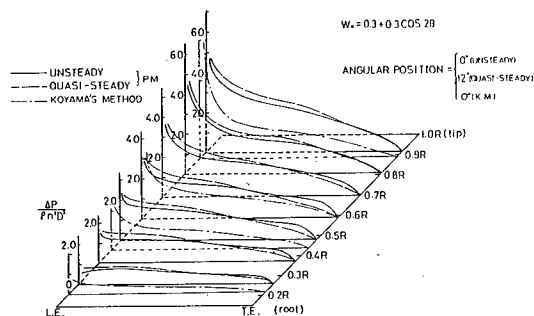


Fig. 22 - Load Distribution along Chord in  $\cos 2\theta$  Wake

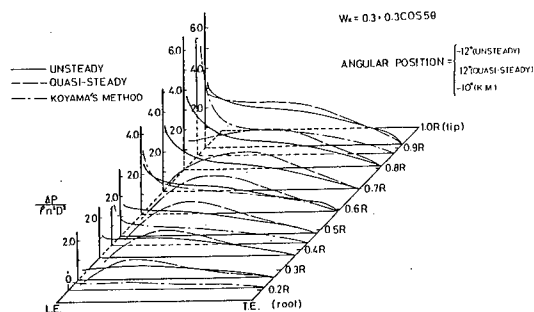


Fig. 23 - Load Distribution along Chord in  $\cos 5\theta$  Wake

It will be found from these surveys that the time-derivative term has a great influence on the load distribution near the leading edge and the shed vortex does in the after part near the trailing edge.

Figs. 22 and 23 show examples of load distributions along the chord of the blade section calculated by P.M., that is the difference of pressure on back and face. They have been computed at the angular position of the maximum total load, which is different between the unsteady and the quasi-steady conditions because of their phase differences, in the wake of  $\cos 2\theta$  and  $\cos 5\theta$  respectively. The uniformly decreasing tendency from the leading edge toward the trailing edge is seen in the unsteady calculation commonly for  $\cos 2\theta$  and  $\cos 5\theta$ . This feature seems to be quite natural. The same tendency is kept in the quasi-steady calculation for  $\cos 2\theta$ , but not for  $\cos 5\theta$ . The peculiar load distribution of the quasi-steady calculation for  $\cos 5\theta$ , decreasing near the leading edge and maximum in the midpart, may be attributed to the inadequacy of the quasi-steady method. The load distribution by Koyama's method is found quite similar to that of P.M. in  $\cos 5\theta$  but lower in  $\cos 2\theta$  excluding the steep rise at the leading edge.

## 7.5 Bearing Forces and Moments of One Blade

The bearing forces and moments, vertical and horizontal vibratory forces and vertical and horizontal bending moments, have been calculated for the propeller AU5-50 in the harmonic wake of the type  $W_x = 0.3 + 0.3\cos j\theta$ .

The vertical force,  $F_{Y1}$ , and the vertical bending moment of one blade about the shaft centre,  $M_{Z1}$ , in the harmonic wake  $\cos 4\theta$  are shown non-dimensionally in Fig. 24.

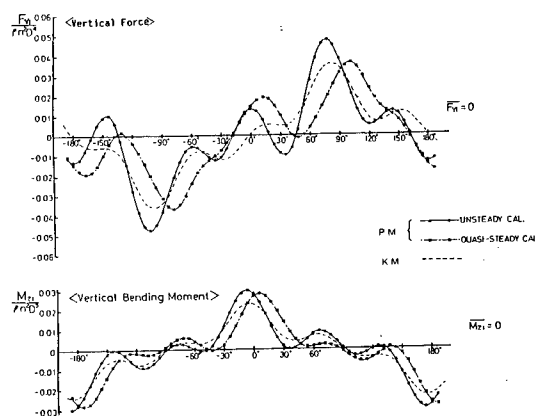


Fig. 24 - Bearing Force and Moment of One Blade in  $\cos 4\theta$  Wake

Those by P.M. consist of the harmonic components of the order,  $(j\pm 1)$  and  $(2j\pm 1)$ , i.e. 3, 5 and 7, 9, when  $j = 4$ . The components of  $(2j\pm 1)$  derive from the non-linear effect of the non-uniformity of the wake similarly as the double mode component of the thrust or torque fluctuation. They have not much effect as to deform the variation curve.

thoroughly.

The unsteady calculation by P.M. gives the highest peak amongst three methods in Fig. 24. It is 1.3 times as high as the peak of K.M. for both  $F_{Y1}$  and  $M_{Z1}$ . Attention should be paid to this fact in connection with the practical design of a propeller by the linear method like Koyama's. The angular position of the peak is nearly same in the results of P.M. and K.M.

The quasi-steady calculation gives the peak lower than the unsteady result by P.M. and higher than K.M. in case of the harmonic wake of  $\cos 4\theta$ . The most significant defect of the quasi-steady method is the considerable phase lag at the peak, by about 20 degrees in  $F_{Y1}$  and 10 degrees in  $M_{Z1}$ .

The difference between P.M. and K.M. is the most in case of  $\cos 4\theta$  shown in Fig. 24 because of the maximum amplification effect at  $\cos 4\theta$  mentioned in the section 7.2, and the least in case of  $\cos 5\theta$ .

The radial distribution of blade bending moment acting on a blade section is the most important data for the choice of the blade thickness in design problems. The bending moment at the position of maximum total load of a blade and of its minimum total load is calculated by P.M. and by K.M. The results are shown in Fig. 25. The peak-to-peak value at the

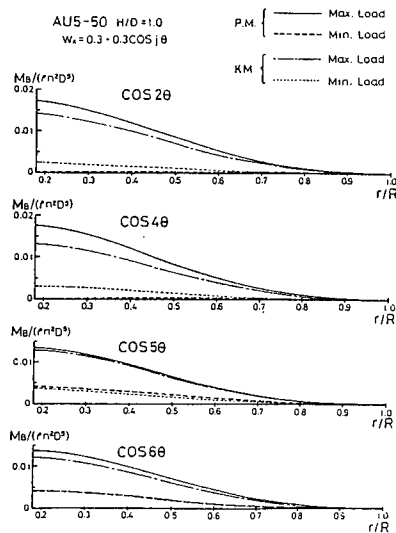


Fig. 25 - Blade Bending Moment Distribution

root of the blade calculated by P.M. attains to 1.75 times as much as that of K.M. in case of  $\cos 4\theta$  and the ratio of the maximum value by P.M. and that of K.M. is 1.3 similar to that of  $F_{Y1}$  or  $M_{Z1}$  in Fig. 24.

This is one of the most important results, because the level of the cyclic load or the cyclic stress will be likely to be underestimated if linear theories such as K.M. are employed. There are more or less same problems in a harmonic wake except for  $\cos 5\theta$  in the case of the propeller AU5-50.

Therefore it is recommended that the non-linear theory like P.M. has to be employed for the prediction of unsteady characteristics of

propellers.

## 7.6 Unsteady Characteristics of a Propeller in Harmonic Wake

On summing up all blade forces for calculating unsteady thrust, torque and bearing forces and moments of a propeller, we find that the non-zero sum is resulted only if the mode of the harmonic wake has the well-known relation of Lewis(1963) with respect to the number of blades of a propeller. According to that relation, only the harmonic mode of the wake which satisfies the following relations has a contribution to the vibratory forces and moments.

$j = nK$ , for thrust and torque,

$j = nK \pm 1$ , for bearing force and moment,

where  $n$  is an integer and  $K$  is the number of blades. Since the vibratory forces acting on a propeller consists of harmonic modes of not only those of the wake distribution which satisfy the above relations, but also the harmonic mode resulted by the non-linear effect.

The latter is specified by the following relations.

$2j = nK$ , for thrust and torque,

$2j = nK \pm 1$ , for bearing force and moment.

In case of five bladed propellers such as AU-5-50, the above-mentioned components become  $j = 5$ , for thrust and torque,  $j = 2, 3, 4, 6, 7, 8$ , for bearing force and moment, for  $j$  less than 8.

Then, the total thrust or torque acting on all blades is that of one blade multiplied by the blade number. It includes the component of double mode, i.e.  $10\theta$ .

As for bearing forces and moments, the above-mentioned modes of  $j = 2, 3, 4, 6$  yield a component of phase  $5\theta$ , and those of  $j = 7$  and 8 yield a component of  $15\theta$ . There exists no component other than these two for 5 bladed propellers in the harmonic wake of the type  $\cos \theta - \cos 8\theta$ . Three examples of the bearing force and moment calculated for the case of  $j = 6, 4$  and 2 are shown in Figs. 26, 27 and 28 respectively. Comparing Fig. 27 with Fig. 24 for one blade, we see the value at the peak is in the same level in both cases but the  $3\theta$ -component completely disappears. Bearing forces and moments which are derived from the double harmonic mode are shown in Fig. 28. This result is not derived by K.M. The height of the

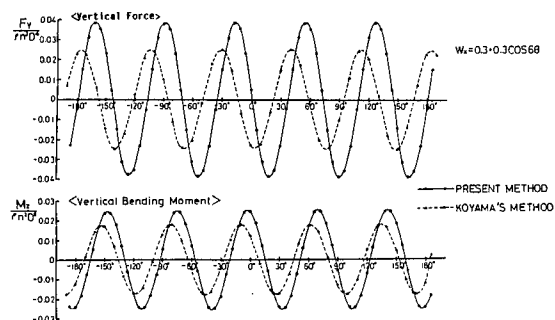


Fig. 26 - Bearing Force and Moment of Propeller in  $\cos 6$  Wake

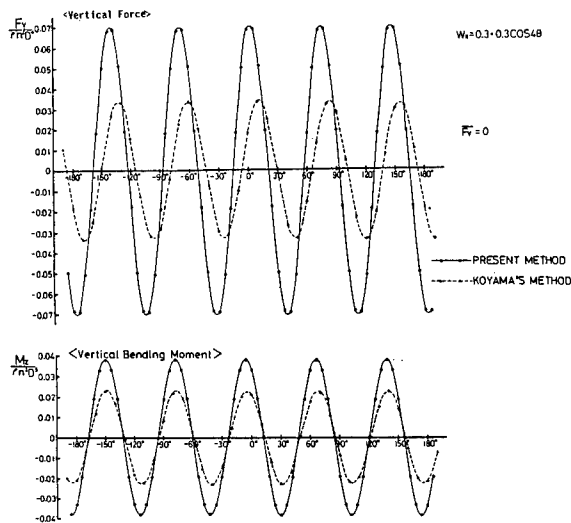


Fig. 27 - Bearing Force and Moment of Propeller in  $\cos 4\theta$  Wake

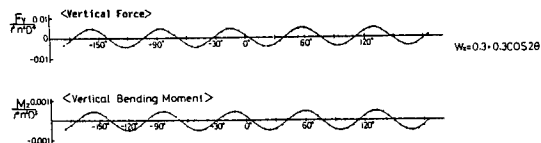


Fig. 28 - Double Harmonic Bearing Force and Moment in  $\cos 2\theta$  Wake

peak is much less significant than the total vibratory force. However, this is important because linearized theories are not able to predict it.

### 7.7 Unsteady Characteristics of a Propeller in Ship's Wake

The ship's wake distribution can be decomposed into several harmonic components. As aforementioned, the circulation of each vortex of the lifting surface may be also decomposed into same harmonic components. The strength of circulation in each harmonic component can be determined from respective boundary conditions.

For instance, the torque of one blade calculated by P.M. in the ship's wake is shown in Fig. 29. 5-bladed MAU5-66 propeller model is employed. Principal particulars are shown in the last column of Table 1. The wake distribution which is determined by model tests and given in Fig. 29, has dominant components of 2nd and 4th harmonics, and other harmonics are smaller. The amplitude of torque fluctuation calculated by P.M. is greater than twice as much as that by K.M. This must be amplification effect of P.M. for the 2nd and 4th harmonics and in addition their double harmonic modes. The non-trivial difference between the time averages of torque predicted by P.M. and that by K.M. indicates the existence of a considerable non-linear effect. Thus, the linear theory like K.M. is likely to underestimate the fluctuation of the torque and

other propeller vibratory forces in the ship's wake than in the simple harmonic wake. The phase characteristics are quite similar in two calculation methods of P.M. and K.M.

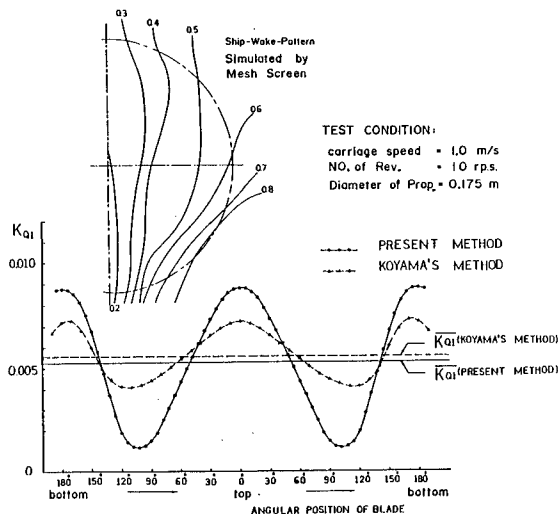


Fig. 29 - Torque of One Blade of MAU 5-66 Propeller in Ship's Wake

### 8. COMPARISON WITH EXPERIMENT

The experiments of propeller characteristics have been carried out in the harmonic wake simulated by the mesh screen. Thrust and torque of a model propeller have been measured by the propeller dynamometer of the strain gauge type. As mentioned before, we know that thrust and torque have the harmonic components of the blade frequency and thier multiples. Three model propellers of 3, 4, and 5 blades have been tested in respective types of harmonic wake such as  $\cos 3\theta$ ,  $\cos 4\theta$  and  $\cos 5\theta$ . The principal particulars of propeller models are shown in Table 1.

Test conditions are so chosen as 1.0 m/sec for the advance speed and as 8 r.p.s. for the number of revolution.

The iso-wake contours measured in the section 190mm behind the mesh screen are shown in Fig. 30. The wake distributions are fitted by following equations.

$$\cos 3\theta : W_x = 0.36 + 0.35\cos 3\theta \quad (44)$$

$$\cos 4\theta : W_x = 0.35 + 0.30\cos 4\theta \quad (45)$$

$$\cos 5\theta : W_x = 0.34 + 0.25\cos 5\theta \quad (46)$$

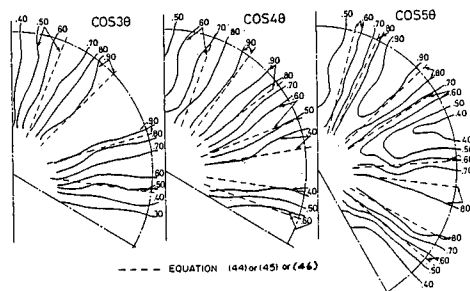


Fig. 30 - Harmonic Wake Simulated by Mesh Screen,  $1 - W_x$

Measured thrust and torque are Fourier analysed and principal modes for respective types of wakes superimposed to the time average are shown in Figs. 31, 32 and 33. The results of computations by P.M. are given in the same figures for comparison.

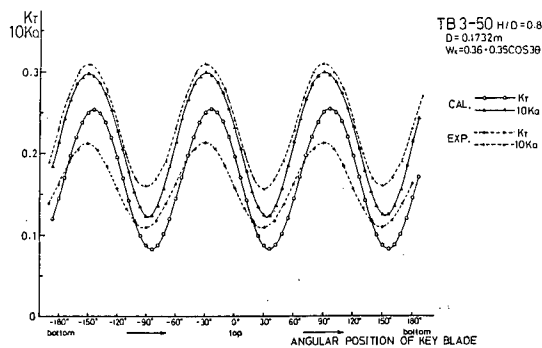


Fig. 31 - Thrust and Torque of 3 blades Propeller in  $\cos 3\theta$  Wake

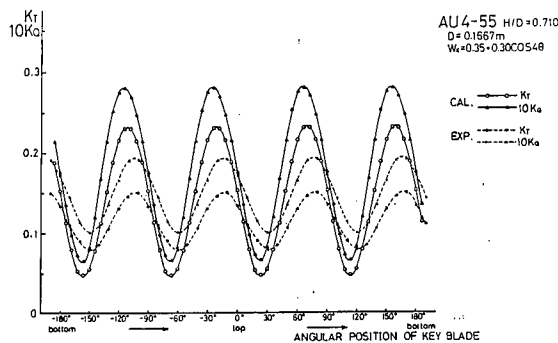


Fig. 32 - Thrust and Torque of 4 blades Propeller in  $\cos 4\theta$  Wake

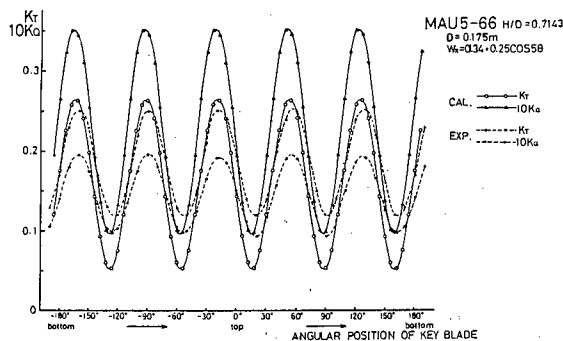


Fig. 33 - Thrust and Torque of 5 blades Propeller in  $\cos 5\theta$  Wake

It is found in the case of 3 bladed propeller in the wake of the type  $\cos 3\theta$  shown in Fig. 31 that computed torque curves are similar to measured results, but there is some difference in the amplitude between computed and measured thrust. In cases of 4 and 5 blades, greater differences are observed both in thrust and torque. The poor agreement in higher frequency may be attributed to the defect in

the response of the dynamometer. The fluctuation amplitudes of thrust and torque of the 5 bladed propeller are greater than those of 4 bladed propeller, in spite of greater variation of the wake of type 4. This tendency is common in the computation and the measurement.

The phases of computed thrust and torque are nearly equal to measured ones in all cases. Therefore the phase relationship is rightly predicted by the present computation method.

## 9. CONCLUSIONS

Following are conclusions of the present work.

- (1) The unsteady thrust, torque, bearing forces and moments, of a propeller and the bending moment of blades calculated by the present method are generally greater than those predicted by the linear theory like Koyama's method.
- (2) The phase relationship by the present method is verified to agree with the experimental result, and also is nearly similar to that by Koyama's method.
- (3) Non-linear effects of Kutta-Joukowski force due to the non-uniformity of the wake, which have been clearly demonstrated by the numerical results by the unsteady lifting surface theory, appear in two aspects. One is the deviation of the relative rotative efficiency from unity and the other is the existence of double harmonic modes in the fluctuation of the thrust, torque and all bearing forces and moments of a propeller.
- (4) The time-derivative term in the pressure equation is the origin of the forward shift of phase in the force and moment fluctuation.
- (5) The comparison between unsteady and quasi-steady calculations has revealed the lift reduction and phase lag due to shed vortices.
- (6) The quasi-steady calculation by the present method provides a good approximation for the unsteady propeller characteristics in case of the wake distribution of type  $\cos\theta$ , but unrealistic phase lag appears in case of higher modes. In case of the wake of  $\cos 2\theta$  to  $\cos 4\theta$ , quasi-steady calculation shows excessive amplitude.

## REFERENCES

- Breslin, J.P., Van Houten, R.J., Kerwin, J.E and Johnsson, C.-A. (1982) : Theoretical and Experimental Propeller - Induced Hull Pressures Arising from Intermittent Blade Cavitation, Loading, and Thickness, Transactions of the Society of Naval Architects and Marine Engineers, Vol. 90.
- Hanaoka, T. (1968) : Fundamental Theory of a Screw Propeller ( Especially on Munk's Theorem and Lifting Line Theory), Report of Ship Research Institute, Vol. 5, No. 6.
- Hanaoka, T. (1969) : Numerical Lifting-Surface

- Theory of a Screw Propeller in Non-Uniform Flow ( Part I Fundamental Theory ), Report of Ship Research Institute, Vol. 6, No. 5.
- Hanaoka, T. (1977) : Fundamental Theory of a Screw Propeller - III ( Two Numerical Methods for Solving Propeller Lifting - Surface Problems by the Use of Discrete Loading Functions ), Report of Ship Research Institute, Vol. 14, No. 6.
- Hatano, S., Minakata, J. and Yamasaki, S. (1975) : The Estimation of the Performance Characteristics of the Propeller by the Lifting Line and Lifting Surface Theory, Transactions of the West-Japan Society of Naval Architects, No. 49.
- Ikehata, M. and Yuasa, H. (1971) : Turbulence in the Wake of Model Ship and Its Influence on a Propeller, Journal of the Society of Naval Architects of Japan, Vol. 130.
- Ikehata, M. (1977) : Study on the Relationship between Propulsion Factors and Velocity Field of Flow in the Propeller Disk behind the Hull, International Shipbuilding Progress, Vol. 24, No.273.
- Ikehata, M., Maruo, H., Ando, M. and Itoh, M. (1981) : The Effects of Non-Uniformity and Tubulence on Hydrodynamic Characteristics of Propeller, Journal of the Society of Naval Architects of Japan, Vol. 150.
- Ikehata, M., Ando, M. and Maruo, H. (1983) : The Analysis of Unsteady Characteristics of Marine Propeller in Harmonic Wake by Vortex Lattice Lifting-Surface Model, Journal of the Society of Naval Architects of Japan, Vol. 153.
- Ishida, S. and Koyama, K. (1979) : Prediction of Propeller Vibratory Forces, Text of Symposium on Theory of Resistance and Propulsion for Hull Design, the Society of Naval Architects of Japan.
- Kerwin, J. E. and Lee, C.-S. (1978) : Prediction of Steady and Unsteady Marine Propeller Performance by Numerical Lifting -Surface Theory, Transactions of the Society of Naval Architects and Marine Engineers, Vol. 86.
- Koyama, K. (1972) : A Numerical Analysis for the Lifting Surface Theory of a Marine Propeller, Journal of the Society of Naval Architects of Japan, Vol. 132.
- Koyama, K. (1975) : A Numerical Method for Propeller Lifting Surface in Non-Uniform Flow and Its Application, Journal of the Society of Naval Architects of Japan, Vol. 137.
- Koyama, K. (1979) : A Method for Treating the Singularity at the Blade Tip of Marine Propellers, Journal of the Society of Naval Architects of Japan, Vol. 145.
- Kumai, T. (1967) : On Propeller Vibratory Forces, Symposium on Marine Propellers of Zosen Kiokai.
- Lewis, F. M. (1963) : Propeller-Vibration Forces, Transactions of the Society of Naval Architects and Marine Engineers, Vol. 71.
- Sears, W. R. (1941) : Some Aspects of Non-Stationary Airfoil Theory and Its Practical Application, Journal of the Aeronautical Science, Vol. 18, No. 3.
- Sugai, K. (1970) : A Method for Calculating the Hydrodynamic Characteristics of Marine Propellers, Journal of the Society of Naval Architects of Japan, Vol. 128.
- Tsakonas, S. and Jacobs, W. R. (1965) : Unsteady Lifting Surface Theory for a Marine Propeller of Low Pitch Angle with Chordwise Distribution, Journal of Ship Research, Vol. 9, No. 2.
- Tsakonas, S., Jacobs, W. R. and Rank, P. (1968) : Unsteady Propeller Lifting Surface Theory with Finite Number of Chordwise Modes, Journal of Ship Research, Vol. 12, No. 1.
- Van Oossanen, P. (1977) : Theoretical Prediction of Cavitation on Propellers, Marine Technology, Vol. 14, No. 4.
- Van Oossanen, P. (1977) : The Choice of Propeller Design Parameters with Respect to Cavitation Control, Proceeding of Symposium on Hydrodynamics of Ship and Offshore Propulsion Systems, Oslo, March.
- Yamazaki, R. (1966) : On the Theory of Screw Propellers in Non-Uniform Flows, Memoir of the Faculty of Engineering, Kyushu University, Vol. 25.
- Yazaki, A. (1961) : The Design of AU-Type Ship Screw Propellers, Monthly Report of Transportation Technical Research Institute , Vol. 11, No. 7.
- Yuasa, H. (1980) : Application of Numerical Lifting-Surface Theory on Steady Performance of Propeller/Duct System, Journal of the Society of Naval Architects of Japan, Vol. 147.
- Yuasa, H., Ishii, N. and Kamiirisa, H. (1981) : Numerical Analysis on Propeller/Duct Loading, Cavitation and Excitation Forces, Mitsui Zosen Tecnical Review, No. 109.

## DISCUSSION

Prof. JOHN C. BRESLIN,  
Stevens Institute of Technology,  
Hoboken, NJ, USA:

This contribution by Prof. Maruo and his strong team to extend the literature on steady and unsteady propeller forces is most interesting in that it includes several non-linear effects. As many know we at Davidson Laboratory have labored in this area for many years.

It is not clear to me, without additional study of the paper, how this treatment differs from Kerwin et al.

A significant set of comparisons with Kerwin's model with vortex wake contraction and wrap-up was made by Jacobs and Tsakonas some four years ago, at the SNAME annual meeting. This showed that the DL program gave results which were as good or better than Kerwin's results as judged against measured mean thrust and torque. The effects of contraction and wrap-up were seen to be compensating.

Kerwin has not shown any significant effects of these non-linear aspects on blade-frequency forces.

I do not understand how the unsteady force module can be greater than the quasi-steady. It would be very effective if Prof. Maruo and colleagues would exercise their procedure against the S-propeller series data produced by DTNSRDC which has been used by Kerwin and Tsakonas and others to compare their results. In that way a common norm could be had for examining these disparate procedures.

STUART JESSUP,  
David Taylor Naval Ship R&D Center,  
Bethesda, MD, USA:

I would like to congratulate the authors on their investigation of unsteady propeller forces. As you have stated your procedure is very similar to that of Kerwin and Lee (1978). Could you explain exactly what the differences in the two procedures are? Also it would be interesting to compare calculations of the same propeller and wake, perhaps as performed by Kerwin and Lee in their paper. This might point to possible numerical errors in either procedure.

Your discovery of the offset in mean torque and the double harmonic mode produced by wake non-uniformity is very interesting. We would be interested in checking these effects with Kerwin and Lee procedure. If they are attributed to nonlinear effects then possibly more refinements of the spatially varying downstream wake structure should be incorporated. Unfortunately, the double harmonic mode is difficult to verify because of the difficulty in generating pure single harmonic wakes.

Finally, I am concerned with the possible influence of the unsteady propeller loading on the nonuniformity of the wake - a so called spatially varying effective wake. In the case

of pure harmonic wakes the propeller action may reduce the wake harmonic amplitude. Could you please comment on this?

Prof. HELMUT SCHWANECKE,  
Berlin Ship Model Basin (VWS),  
Berlin, Germany:

This is an excellent paper. The newly developed method for predicting unsteady propeller characteristics is very promising. For practical design purposes it is very important to know how, and if so, to what extent the operational point of the propeller differs from that considered in conventional design procedures. A couple of years ago I made some investigations regarding an "unsteady wake adaption" resulting in a correction for the pitch due to the higher efficiency of the propeller in an inhomogeneous flow. I should like to learn whether the authors have made investigations considering this phenomenon and if they got any results. Referring to Fig. 20 of the paper (relative rotative efficiency) I can confirm the tendency obtained by Koyama's method, because this is mainly caused by the ratio of the wavelength of the harmonic modes and the chord lengths of the blades, and is therefore dependent on the blade area ratio of the propeller.

## AUTHORS' REPLY

Thank you for your kind comments and discussion, Prof. Breslin. The first question of yours is the same as that of Dr. S. Jessup. We would like to give the same answer to it and hope you will refer to that answer. The amplification effect of the non-linearity on blade forces has been revealed in the present paper. This is a significant result of the paper. This is brought about by the remarkable effect of the time derivative term in the blade force. I hope you will see Fig. 14 again. I appreciate your suggestion of further exercises of the present procedure.

Thank you also for your interesting discussion, Prof. Schwanecke. In our present work, we have investigated the influence of the circumferential non-uniform flow on the unsteady characteristics of a propeller. But we have never researched the application of the present method to the wake adaption. We think that it is a future problem. It may be mentioned that the circumferential non-uniformity of flow has a favorable effect to make a higher efficiency of a propeller like in the presented example. Koyama's method is based on the linearized theory which has no consideration of the variational distribution of inflow velocity along the chord. So, it always predicts the constant relative rotative efficiency of unity in any non-uniform flow. Of course it is not dependent on the blade area ratio of the propeller.

We thank also Dr. Jessup for his interesting discussion. There are three points of the present procedure different from that of Kerwin



and Lee. The first one is the modification of the discretization of blade elements so as to avoid the Kutta condition at the trailing edge. The second one is the choice of parameters of tip vortex and numbers of elements on a blade to optimize the accuracy of computation and time consumption. The third one is the introduction of expressions of equations (14) to (17) which are given in the form of Fourier series of the particular harmonic of the wake. By these expressions, we can obtain the solution of circulations of spanwise vortices in terms of three coefficients  $g_{0nm}$ ,  $g_{1nm}$ ,  $g_{2nm}$ , while the circulations have been determined at each instantaneous position of a blade step by step in time in the procedure of Kerwin and Lee.

The propeller for application has been chosen from a practical point of view. We have had available data in hand. We are also interested in your suggestion of calculations of the same propeller and wake as Kerwin and Lee. If there were a chance, we would try the calculations. The offset in mean torque and the double harmonic mode fluctuation of forces are mainly owing to the non-linear effect of Kutta - Joukowski force in non-uniform wake. We appreciate your interesting remarks on the refinement of the downstream wake and the difficulty of verification of the double harmonic mode.

We have investigated the influence of the non-uniform flow field on the propeller action in the present paper. We think the reverse problem suggested by Dr. Jessup, namely the influence of the propeller action on the velocity field, is an important future problem.

# CALCULATION OF THE TURBULENT FLOW AROUND THE STERN AND IN THE WAKE OF A BODY OF REVOLUTION WITH THE PROPELLER IN OPERATION

LIAN-DI ZHOU AND JIA-LE YUAN

## ABSTRACT

This paper is the continuation of "A Streamline-Iteration Method for Calculating Turbulent Flow around the Stern of a Body of Revolution and Its Wake" (Zhou, 1982), which was presented at the 14th ONR symposium. The present paper further generalizes the streamline-iteration method to the calculation of turbulent flow around the stern and in the wake of a body of revolution with the propeller in operation. Two-equation ( $K-\epsilon$ ) model is still employed as turbulence model. The propeller is modelled as lifting line-sink disk with radial distribution of the strength. The pressure field, the velocity field and the distributions of the turbulent properties around the stern and in the wake of a body of revolution with the propeller in operation may be calculated by using the present method. The pressure defect component of the thrust deduction can be obtained from the computed surface pressure distributions over the stern of a body of revolution with and without propeller in operation. By subtracting the propeller induced velocity distributions from computed velocity distributions at the propeller plane with the propeller in operation, the effective velocity distributions at the propeller plane may be obtained. Agreements between measured and computed values of axial velocity profile immediately upstream of the propeller and of the surface pressure distributions over the stern of the body with and without the propeller in operation which proved the effectiveness of the present method.

Outstanding features of the present method are: (1) the thrust deduction and the effective wake distribution may be computed in the same iteration cycle of the interaction analysis; (2) the flow downstream of the propeller plane may be predicted. It can be generalized and extended to the interaction calculation between a body of revolution and a ducted propeller, the contrarotating propeller or the tandem propeller

## 1. INTRODUCTION

In order for a propulsor to produce a

required thrust to propel a ship with minimum power, minimum cavitation, minimum vibration excitation and noise at a prescribed propulsor rotational speed, the effective inflow velocity distribution and the thrust deduction are both necessary in the design of a wake-adapted propeller. Until quite recently, however, in the design of wake-adapted propeller, the radial distribution of effective inflow velocity is replaced by the nominal velocity profile (the velocity profile at the location of the propulsion device in the absence of a propeller) due to lack of knowledge of effective inflow velocity or is estimated by ratioing the nominal velocity profile can be significantly different from the nominal velocity profile. The constant-factor empirical approach for obtaining effective inflow velocity distribution is not based on a rational hydrodynamic theory either. Put then it is very difficult to measure the velocity profile at the location of the propeller with the propeller in operation, though the most advanced Laser Doppler Velocimeter (LDV) is used. It is therefore essential to develop a reliable and sound theoretical method to predict the effective velocity profile. As for the determination of thrust deduction, the conventional approach is to conduct model-scale propulsion tests using a stock propeller with similar principal dimensions. However, the experiments are generally time consuming and costly. Particularly, in order to investigate the effects of different afterbody forms, propeller locations, blade geometry and loading characteristics, it is impracticable to determine these effects by making a large number of experiments. But on the other hand, the data of both effective inflow velocity distribution and thrust deduction used in the design of a wake-adapted propeller must be accurate enough to meet the ever increasing demand for energy saving and reduction in vibration excitation and noise. However, these knowledges depend on the mutual interaction between the propeller and ship's afterbody. Thus, recently naval architects pay great attention to the investigation on the theoretical calculation of interaction.

Up to now it is very difficult to predict

Zhou Lian-di and Yuan Jia-le, China Ship Scientific Research Centre, P.O. Box 116, Wuxi, Jiangsu, The People's Republic of China

the nominal velocity profile even for the conventional ship, not to say the effective velocity profile based on the complex interaction between a propeller and the ship's afterbody. In order to focus on the physical nature of the complex interaction, axisymmetric bodies were chosen in all the existing investigations of the interaction. The representative works on the interaction between an axisymmetric body and the propeller at the moment are the investigations in DTNSRDC (see Huang et al. 1976, Huang and Cox, 1977, Cox and Hansen, 1977, Huang and Groves, 1980). On the part of experiment, the Laser Doppler Velociometer (LDV) was successfully used by Huang et al. (1976) to measure velocity profiles very close to the propeller and the theoretical method of calculating interaction between an axisymmetric body and the propeller was verified by using the measured differences between the velocity profiles, stern pressure distributions and stern shear stress distributions with and without the propeller in operation. On the part of theory, the effective velocity profile and thrust deduction can be predicted by using the inviscid approximation computer programs developed in DTNSRDC. The agreements between the predicted and measured total axial velocities in front of the operating propeller and stern pressure defect distribution are very good. Though the analytical prediction method of thrust deduction of DTNSRDC (Huang and Cox, 1977, Cox and Hansen, 1977) will be potentially viable to be generalized and extended to the calculations of interaction between an axisymmetric body and a ducted propeller, the contrarotating propeller or the tandem propeller, their numerical prediction method of effective velocity profile (Huang et al. 1976, Huang and Groves, 1980) is only applicable to the upstream of propeller as a result of making approximate assumptions. The development of theoretical research between the thrust deduction and the effective velocity profile is uneven. Thus, the complete interaction analysis between an axisymmetric body and above propeller configurations-ducted, contrarotating and tandem propeller can not be carried out. Subsequent detailed measurements of the velocity profiles with and without a propeller operating in two axisymmetric wake were made by Nagamatsu and Tokunaga (1978), who used a five-hole pitot probe of NPL type to measure it. The theoretical prediction of effective velocity profile was made by means of streamline tracing under the same assumptions as Huang et al. employed. The method of Nagamatsu and Tokunaga is only applicable to the upstream of propeller too.

In this paper, the assumptions used by Huang et al. (1976 and 1980) are exempted. Based on the basic equations of the turbulent flow, the propeller influence is added to the basic equations of the turbulent flow suited the streamline iteration calculation, which were derived in our previous paper (Zhou, 1982). The turbulence model still uses a two-equation (K- $\epsilon$ ) model and the coordinate transformations technique presented in Zhou's paper is also used. In the streamline iteration method of turbomachine, the influence of rotator row was

neglected in general. In the present case, however, the unstream influence of propeller will be the research object. Addition of propeller induced velocity field (unstream and downstream) to the computed velocity field of the turbulent flow around the stern and in the wake of a body of revolution without the propeller (Zhou, 1982) and corresponding contracted streamlines are the assumptions of the initial locations of streamlines and of the initial velocity distribution. Thus, not only the influence of propeller to the un-stream is added to the streamline iteration calculation, but also the streamline iteration calculation is accelerated as a result of the reasonable assumptions of the initial locations of streamlines and of initial velocity distribution.

## 2. BASIC EQUATIONS

In calculating the three-dimensional incompressible, steady turbulent flow by two equation (K- $\epsilon$ ) model, the general forms of basic equation are as follows.

### Continuity Equation

$$\nabla \cdot \bar{V} = 0 \quad (1)$$

### Momentum Equation

$$(\bar{V} \cdot \nabla) \bar{V} = -1/\rho \nabla p + 1/\rho \nabla \cdot [\tau] \quad (2)$$

where the stress tensor  $\tau$  is represented by the effective viscosity as

$$[\tau] = \mu_{eff} (\nabla \bar{V} + \nabla \bar{V}^T) \quad (3)$$

$\mu_{eff}$  is the effective viscosity and defined by

$$\mu_{eff} = \mu_l + \mu_t = \mu_l + C_D \cdot \rho K^2 / \epsilon \quad (4)$$

where  $\mu_l$  and  $\mu_t$  are the laminar and turbulent viscosity respectively, and  $K$  and  $\epsilon$  are the turbulent kinetic and its dissipation rate, respectively. The governing equations for  $K$  and  $\epsilon$  are:

### K-Equation

$$\nabla \cdot (PK \bar{V}) = \nabla \cdot \left( \frac{\mu_{eff}}{\sigma_{eff,K}} \nabla K \right) + GE - P\epsilon \quad (5)$$

### $\epsilon$ -Equation

$$\nabla \cdot (P\epsilon \bar{V}) = \nabla \cdot \left( \frac{\mu_{eff}}{\sigma_{eff,\epsilon}} \nabla \epsilon \right) + C_1 GE - \frac{\epsilon}{K} - C_2 \rho \frac{\epsilon^2}{K} \quad (6)$$

where

$$GE = \mu_t (\nabla \bar{V} + \nabla \bar{V}^T) : \nabla \bar{V} \quad (7)$$

In these equations,  $\mu_{eff,K}$  and  $\mu_{eff,\epsilon}$  Prandtl/Schmidt Numbers;  $C_1$ ,  $C_2$  and  $C_D$  are proportionality constants. The values of  $C_1$ ,  $C_2$ ,  $C_D$ ,  $\sigma_{eff,K}$  and  $\sigma_{eff,\epsilon}$  are given in Table 1.

Table 1

$C_1$	$C_2$	$C_D$	$\sigma_{eff,K}$	$\sigma_{eff,\epsilon}$
1.44	1.92	0.09	1	1.23

For the general axisymmetric flow, the above basic equations can be transformed into convenient forms suited the streamline iteration calculation forms suited the streamline iteration calculation, which were derived in Zhou's paper (1982). But it can not be applied mechanically in the streamline iteration calculation with the propeller in operation. The propeller influence must be added to the general axisymmetric equations suited the streamline iteration calculation. The propeller may be treated with same method as in the streamline iteration method of turbomachine. That is, the propeller is neglected in form, but two effects due to the propeller are retained. (1) The fluid in the wake of propeller possesses the rotational flow (the assumption that the influence of propeller on the upstream fluid of propeller is inviscid is used, otherwise the upstream fluid of propeller will also possess the rotational component); (2) The fluid is acted on by the blade force as the fluid passes through the propeller, thereby the energy transference between the propeller and the fluid is carried out. Thus, the flow field can be considered as that the propeller is "not present", and the calculation can be carried out in a static absolute coordinate system. Now the spatial static cylindrical polar coordinate system  $(r, \theta, z)$  is used, and  $u, v, w$  are axial, radial and circumferential velocity components of velocity  $V$  respectively. As the above mentioned two propeller effects which must be retained do not relate with the number of a propeller, the flow may be considered as an axisymmetric flow, i.e., the partial derivatives of all flow variables with respect to  $\theta$  must be equal to zero. But this axisymmetric flow differs from the axisymmetric flow without the propeller in our previous paper (Zhou, 1982). At present case,  $w$  is not equal to zero. With the above treatment and assumption, the governing equations suited the streamline iteration calculation for the turbulent flow around the stern and in the wake of a body of revolution with the propeller in operation can be derived in the way similar to that in Zhou's paper (1982).

Continuity Equation We employ the same integral form as in above mentioned reference

$$2\pi\rho \int_{r_0(z)}^{r_1(z)} r dr = Q_0 = \text{const} \quad (8)$$

where  $r_0(z)$  and  $r_1(z)$  are the locations of the lower and the upper boundary of the channel in the meridian plane.

Energy Equation

$$\begin{aligned} \frac{dp_0}{dz} \Big|_{\text{along streamline}} &= \mu_{\text{eff}} \left[ \left( \frac{\partial^2 u}{\partial r^2} + \frac{\partial^2 u}{\partial z^2} + \frac{1}{r} \frac{\partial u}{\partial r} \right) + \frac{v}{u} \left( \frac{\partial^2 v}{\partial r^2} + \frac{\partial^2 v}{\partial z^2} + \frac{1}{r} \frac{\partial v}{\partial r} - \frac{v}{r^2} \right) \right. \\ &\quad \left. + \frac{w}{u} \left( \frac{\partial^2 w}{\partial r^2} + \frac{\partial^2 w}{\partial z^2} + \frac{1}{r} \frac{\partial w}{\partial r} - \frac{w}{r^2} \right) \right] \\ &\quad + \left[ \frac{\partial \mu_{\text{eff}}}{\partial z} \left( 2 \frac{\partial u}{\partial z} \right) + \frac{\partial \mu_{\text{eff}}}{\partial r} \left( \frac{\partial u}{\partial r} + \frac{\partial v}{\partial z} \right) + \frac{v}{u} \left[ \frac{\partial \mu_{\text{eff}}}{\partial z} \left( \frac{\partial u}{\partial r} + \frac{\partial v}{\partial z} \right) \right] \right] \end{aligned}$$

$$+ \frac{\partial \mu_{\text{eff}}}{\partial r} \left( 2 \frac{\partial v}{\partial r} \right) + \frac{w}{u} \left[ \frac{\partial \mu_{\text{eff}}}{\partial z} \frac{\partial w}{\partial z} + \frac{\partial \mu_{\text{eff}}}{\partial r} \left( \frac{\partial w}{\partial r} - \frac{w}{r} \right) \right] \quad (9)$$

This equation denotes the change in total pressure  $p_0$  along the streamline due to the turbulent flow of the fluid (when the fluid is inviscid, the total pressure remains constant along the streamline). Owing to the presence of the operating propeller, while the fluid passes through the propeller, the work done by the propeller also results in the change of total pressure. The magnitude of this change is  $\rho \Omega \Delta(rw)$ , where  $\Omega$  is the propeller angular velocity,  $\Delta(rw)$  is the difference of  $rw$  at aft and fore plane of the propeller disc. Thus, when equation (9) is used, the total pressure  $p_0$  is replaced by new total pressure  $p_0 + \rho \Omega(rw)$  while the fluid passes through the propeller disc.

Radial Pressure Gradient Equation

$$\begin{aligned} \frac{dp}{dr} &= -\rho \left( u \frac{dv}{dz} \Big|_{\text{along streamline}} - \frac{w^2}{r} \right) \\ &\quad + \mu_{\text{eff}} \left( \frac{\partial^2 v}{\partial r^2} + \frac{\partial^2 v}{\partial z^2} + \frac{1}{r} \frac{\partial v}{\partial r} - \frac{v}{r^2} \right) \\ &\quad + \frac{\partial \mu_{\text{eff}}}{\partial z} \left( \frac{\partial u}{\partial r} + \frac{\partial v}{\partial z} \right) + \frac{\partial \mu_{\text{eff}}}{\partial r} \left( 2 \frac{\partial v}{\partial r} \right) \end{aligned} \quad (10)$$

K-Equation

$$\begin{aligned} \frac{dK}{dz} \Big|_{\text{along streamline}} &= \frac{1}{\rho u} \left[ \frac{1}{r} \frac{\partial}{\partial r} \left( r \frac{\mu_{\text{eff}}}{\sigma_{\text{eff},K}} \frac{\partial K}{\partial r} \right) + \frac{\partial}{\partial z} \left( \frac{\mu_{\text{eff}}}{\sigma_{\text{eff},K}} \frac{\partial K}{\partial z} \right) \right. \\ &\quad \left. + GE - P\xi \right] \end{aligned} \quad (11)$$

$\xi$ -Equation

$$\begin{aligned} \frac{d\xi}{dz} \Big|_{\text{along streamline}} &= \frac{1}{\rho u} \left[ \frac{1}{r} \frac{\partial}{\partial r} \left( r \frac{\mu_{\text{eff}}}{\sigma_{\text{eff},\xi}} \frac{\partial \xi}{\partial r} \right) + \frac{\partial}{\partial z} \left( \frac{\mu_{\text{eff}}}{\sigma_{\text{eff},\xi}} \frac{\partial \xi}{\partial z} \right) \right. \\ &\quad \left. + C_1 GE \frac{\xi}{K} - C_2 P \frac{\xi^2}{K} \right] \end{aligned} \quad (12)$$

The forms of above K and  $\xi$  equations are entirely same as in the case without the propeller (Zhou, 1982), but GE in these equations are different. At present case, GE is given as

$$\begin{aligned} GE &= \mu_x \left\{ 2 \left[ \left( \frac{v}{r} \right)^2 + \left( \frac{\partial v}{\partial r} \right)^2 + \left( \frac{\partial u}{\partial z} \right)^2 \right] \right. \\ &\quad \left. + \left( \frac{\partial u}{\partial r} + \frac{\partial v}{\partial z} \right)^2 + \left( \frac{\partial w}{\partial r} - \frac{w}{r} \right)^2 + \left( \frac{\partial w}{\partial z} \right)^2 \right\} \end{aligned} \quad (13)$$

Finally, the rotational flow in the wake of the propeller which is induced by the operating propeller must be considered. If the flow is an axisymmetric without the operating propeller,  $w$  in equations (9), (10) and (13) must be equal to zero. Owing to the presence of the operating propeller, the fluid in the wake of the propeller possesses the flow in  $\theta$  direction

(circumferential) as it passes through the propeller, i.e.  $w \neq 0$ . Because the radial distribution of  $w$  at the aft plane of propeller disc is known (since circulation distribution  $\Gamma = rw$  is known, it can be obtained by an iterative procedure which is made up of combining the present method with the existing performance prediction or design procedure. There is no harm in assuming that the radial distribution of circulation  $\Gamma$  is known,)  $w$  which must be retained in the wake of the propeller is obtained by using circumferential momentum equation. The  $w$ -equation can be derived from circumferential momentum equation by using  $\partial p / \partial \theta = 0$ .

w-Equation

$$\left. \frac{d(rw)}{dz} \right|_{\text{along streamline}} = \frac{r}{\rho u} \left[ \mu_{eff} \left( \frac{\partial^2 w}{\partial r^2} + \frac{\partial^2 w}{\partial z^2} \right) + \frac{1}{r} \frac{\partial w}{\partial r} - \frac{w}{r^2} \right] + \frac{\partial \mu_{eff}}{\partial z} \frac{\partial w}{\partial z} + \frac{\partial \mu_{eff}}{\partial r} \left( \frac{\partial w}{\partial r} - \frac{w}{r} \right) \quad (14)$$

Thus, six unknown variables  $u$ ,  $w$ ,  $p_0$ ,  $p$ ,  $k$  and  $\xi$  can be solved with six equations, equations (8) through (12) and equation (14). So these equations are closure and can be used to evaluate these six unknown variables numerically. The radial velocity component  $v$  can be calculated from the obtained  $u$ ,  $w$ ,  $p_0$  and  $p$ .

Owing to the fact that the physical flow region of the turbulent flow around the stern and in the wake of a body of revolution with propeller in operation extends to infinity both in the radial and the axial direction, the coordinate transformations

$$\left. \begin{aligned} \eta &= 1 - e^{-\frac{r}{C_r}} \\ \xi &= \frac{z}{\pi} \arctg\left(\frac{z}{C_z}\right) \end{aligned} \right\} \quad (15)$$

used in our previous paper (Zhou, 1982) is still employed in this paper. Thus, the physical infinite flow region can be transformed into a finite region. Then the streamline-iteration method can be used in this finite region. The partial derivatives of flow variables with respect to  $r$  and  $z$  and the direction derivatives appeared in equations (9) through (14) can be evaluated by using the method as in above mentioned paper.

The boundary conditions are defined as is Zhou's paper (1982). But in the present case, the propeller conditions must be added, i.e. the number of propeller blades, rate of revolution of propeller and the radial distributions of circulation  $\Gamma$  and hydrodynamic pitch angle  $\text{tg}\beta_i$  are required (the radial distributions of  $\Gamma$  and  $\text{tg}\beta_i$  can be obtained by an iterative procedure which is made up of combining the present method with the existing propeller performance prediction or design procedure. So there is no harm in assuming that these distributions are known). Thus the problem is solvable.

### 3. CALCULATION PROCEDURE

The calculation is performed in the transformed flow region which is in the  $(\xi-\eta)$  plane after the calculation results of turbulent flow around the stern and in the wake of a body of revolution without the propeller (Zhou, 1982) have been obtained. The sequence of calculation is as follows:

- (1) Assumptions of the initial locations of the streamlines and of the initial distributions for  $u$ ,  $v$ ,  $w$ ,  $p$ ,  $p_0$ ,  $k$  and  $\xi$ .

After the calculation in Zhou's paper has been carried out, the locations of the streamlines around the stern and in the wake of a body of revolution without propeller and the values of  $u$ ,  $v$ ,  $p$ ,  $p_0$ ,  $k$  and  $\xi$  at these streamline locations can be obtained. Based on these calculation results, the initial locations of the streamlines and the initial distributions for  $u$ ,  $v$ ,  $w$ ,  $p$ ,  $p_0$ ,  $k$  and  $\xi$  in the streamline iteration calculation of the turbulent flow around the stern and in the wake of a body of revolution with the propeller in operation can be assumed.

- (a) Assumptions of the initial locations of the streamlines and of the initial distributions for  $u$  and  $v$

Owing to the fact that the number of propeller blades, the angular velocity and the radial distributions of  $\Gamma$  and of  $\text{tg}\beta_i$  are assumed to be known in this paper, the circumferential-average propeller-induced axial and radial velocity (denoted by  $u_a$  and  $u_r$  respectively) at the streamline locations around the stern and in the wake of a body of revolution without the propeller can be calculated by using the lifting line-sink disk model (Dong, 1977). Let  $u_p = u + u_a$ ,  $v_p = v + u_r$ . Substituting the distribution of  $u_p$  into equation (8) the radial distribution of the massflow at each station-line can be calculated. Within a given stream annulus with or without an operating propeller the massflow is constant. Thus, according to the calculated distributions of the massflow with and without the operating propeller, the new locations of the streamlines on station-line,  $r_p$ , can be obtained by inverse interpolation of the massflow (see Fig.1). The initial locations of the streamlines in the streamline iteration calculation with the propeller in operation are taken as this distribution of  $r_p$ . Then these initial locations of the streamlines are transformed into the  $(\xi, \eta)$  plane by using coordinate transformations (15). By using the values of  $u_p$  and  $v_p$  at the original locations of the streamlines without the propeller as the values of  $u$  and  $v$  at this initial locations of the streamlines with the propeller in operation, the initial distributions of  $u$  and  $v$  can be obtained.

- (b) Determinations of the initial distributions for  $p_0$ ,  $k$  and  $\xi$

By using the values of  $p_0$ ,  $k$  and  $\xi$  at the original locations of the streamlines without the propeller as the values of  $p_0$ ,  $k$  and  $\xi$  at the new initial locations of the streamlines with the propeller in operation, the initial distributions for  $p_0$ ,  $k$  and  $\xi$  can be obtained.

(c) Determination of the initial distribution for  $w$

According to the assumption that the influence of the propeller on the fluid is inviscid, then  $w=0$  at upstream of propeller; for each streamline, according to the  $d(rw)/dz$  along streamline  $=0$ , i.e. according to the  $rw$  const along the streamline in inviscid flow, the values of  $w$  downstream of propeller at the new initial locations of the streamline can be obtained. Then the initial distribution of  $w$  is determined.

(e) Determination of the initial distribution for  $p$ .

According to the determined values of  $u$ ,  $v$ ,  $w$  and  $p_0$  at the new initial locations of the streamlines, the values of  $p$  at these locations can be calculated from following formula

$$p = p_0 - \frac{\rho}{2} (u^2 + v^2 + w^2) \quad (16)$$

Then the initial distribution of  $p$  is obtained.

(2) Calculations of the meridian flow angle and of the new distribution for  $v$

By using the same formula and method as in the Zhou's paper (1982),  $tg \beta$  and the distribution for  $v$  can be calculated from the coordinates  $(\xi, \eta)$  of grid points of the streamlines and the distribution for  $u$ .

(3) Calculation of new distribution for  $w$ .

Solve equation (14) for each streamline (except on the wall and the centreline of wake, at these places  $w=0$ ). Because  $w=0$  upstream of propeller (assuming that the influence of the propeller on the fluid upstream of propeller is inviscid), so the equation (14) is solved only for the downstream of propeller. The  $w$  appeared in the right-hand of equation (14) is given the values of the previous iteration. Taking the known values of  $w$  at the aft plane of propeller disc as the integral constants ( $w$  can be calculated with formula  $w = \Gamma/r$  from the known radial distribution of circulation  $\Gamma$ ), this equation can be solved by ordinary numerical integration. Then the new distribution of  $w$  can be obtained.

(4) Calculations of the new distributions for  $K$  and  $\epsilon$

Solve equations (11) and (12) simultaneously by using the same method as in Zhou's paper (1982) to obtain the new distributions for  $K$  and  $\epsilon$

(5) Calculation of the new distribution for static pressure  $p$

Solve equation (10) by using the same method as in Zhou's paper to obtain the new distribution for  $p$ .

(6) Calculation of the new distribution for total pressure  $p_0$

In the present case, each streamline must be divided into two sections. Then, for each section the energy equation (9) may be solved in the same way as in Zhou's paper (1982). That is, for the first section taking the value of  $p_0$  at the inlet station on the relevant streamline ( $p_0$  being calculated by expression  $p_0 = p + 1/2 \rho v^2$  using the given boundary conditions for  $u$ ,  $v$  and  $p$  at the inlet station) as the integral constant, equation (9) can be solved by ordinary numerical integration along this streamline from the inlet station to the fore plane of propeller

disc. Equation (9) can be solved along the second section of this streamline by ordinary numerical integration too. But the interval of integration is from the aft plane of propeller disc to the exit station and the integral constant is taken as the total pressure  $p_0$  at the aft plane of propeller disc. This total pressure  $p_0$  is equal to the total pressure value at the fore plane of propeller disc on the corresponding streamline plus  $\rho \Omega \Delta(rw)$ , where  $\Omega$  is known propeller angular velocity,  $\Delta(rw)$  is equal to the value of  $rw$  at the aft plane of propeller disc on the corresponding streamline at present case.

(7) Calculation of the new distribution for  $u$

$p_0$ ,  $p$ ,  $tg \beta$  and  $w$  being solved,  $V_m$  and  $u$  can be calculated as follows

$$\left. \begin{aligned} V_m &= \sqrt{2(p_0 - p)/\rho - w^2} \\ u &= \frac{V_m}{1 + tg^2 \beta} \end{aligned} \right\} \quad (17)$$

(8) Calculation of the new locations of the streamlines

By substituting the obtained new distribution for  $u$  into the formula (8), the radial distribution of the massflow along each station-line can be calculated. According to the prescribed distribution principle of the massflow along the station-line, the new locations of the streamlines on station-line,  $\eta_{cal}$ , can be obtained by inverse interpolation of the massflow (the same principle as shown in Fig.1). Using a relaxation factor  $s$  which is less than 1, the assumed new locations of the streamline, new, can be obtained as follows,

$$\eta_{new} = \eta_{old} + s(\eta_{cal} - \eta_{old}) \quad (18)$$

Repeat step (2) through (8) until the maximum deviation between the locations of the streamlines in two successive iteration calculations is within prescribed accuracy. Then, these distributions for  $u$ ,  $v$ ,  $w$ ,  $p$ ,  $p_0$ ,  $K$  and  $\epsilon$  and the locations of the streamlines are the final results for problem.

#### 4. NUMERICAL RESULTS

In order to prove the effectiveness of the present method, numerical calculations are carried out for the flow field of a model of axisymmetric body (Model 1) fitted with a propeller (Propeller T) and the calculated results are compared with the experiments by Huang et al. (1980). All the cases of the numerical calculations are shown in Table 2, they are different in loadings.

Table 2. cases of the numerical calculations

Model of a body of revolution	$J_V$	$C_{TS}$	Propeller
Model 1	1.25	0.370	T
	1.07	0.654	

where  $J_V = V_\infty / nD$  is ship-speed advance coefficient,  $C_{TS} = T / (P/2 V_\infty^2 \pi R_p^2)$  is thrust loading coefficient based on ship speed,  $V_\infty$  is ship speed,  $n$  is rate of revolution,  $D$  and  $R_p$  are propeller diameter and radius respectively and  $T$  is propeller thrust. The radial distributions of non-dimensional circulation,  $G = \Gamma / 2\pi R_p V_\infty$ , and hydrodynamics pitch angle,  $\tan \beta_i = (u_e + u_a) / (\omega r - u_\theta)$  used in the calculations are the values given in the paper of Huang et al. (1980), where  $u_e$  is the effective velocity at lifting-line,  $u_a$  and  $u_\theta$  are the axial and tangential propeller induced velocities (circumferential average) at lifting-line, respectively. The results of calculations are shown in Fig. 2 to Fig 7.

Fig 2 shows the calculated streamline of the flow fields around the stern and in the wake of body of revolution with and without the propeller in operation. From this figure streamline contraction due to the operation of the propeller can be seen. The comparison between the computed and measured axial velocity profiles immediately upstream of propeller ( $x/R_p = -0.277$ , i.e.  $Z/L = 0.9771$ ) with and without the propeller in operation is shown in Fig.3. The comparison between the computed and measured distributions of the surface pressure defect over the stern of body of revolution with and without the propeller in operation is shown in Fig 4. The agreement between the calculated and measured result and within the accuracy required in engineering. As for the calculated streamlines shown in Fig 2, so far we have no experimental results at hand, so no comparison was made. But they seem to be quite reasonable.

After the effectiveness of the present method has been confirmed through the comparisons between the calculated and measured results shown in Fig 3 and Fig 4, the predicted nominal ( $u_x/V_\infty$ ), total ( $u_p/V_\infty$ ) and effective axial velocity profiles ( $u_e/V_\infty$ ,  $u_e/V_\infty = u_p/V_\infty - u_a/V_\infty$ ) at the propeller plane ( $Z/L = 0.9831$ ) by using present method are shown in Fig 5. From this figure, it is obvious that the difference between the effective and nominal velocity profile is greater at the region near the hub and gradually vanishes forward the propeller tip. This conclusion is same as that obtained by Huang et al. (1980).

As mentioned in section 1, the flow field in propeller wake can be calculated by using present method. Thus, results obtained will be useful for the design of the rudder situated in the propeller wake and the interaction analysis between a body of revolution and the contrarotating propeller or the tandem propeller can be carried out by means of present method. Fig 6 and Fig 7 show the calculated nominal, total and effective axial velocity profiles at two stations ( $Z/L = 1.057$  and  $Z/L = 1.182$ ) in the pro-

peller wake, respectively. But, so far no experimental data in the propeller wake for a body of revolution and propeller combination are available, no comparisons were made with experimental data for these figures.

Finally, from Fig 3 to Fig 7, one can perceive the effect of propeller loading upon the magnitude of interaction. The trend seems to be reasonable and self-evident.

## 5. CONCLUDING REMARKS

From the calculated examples in the previous section, it may be concluded that:

(1) The flow field (including the streamlines, the distributions of velocity and pressure) around the stern and in the wake of a body of revolution can be predicted by using the present method. The agreements between the numerical prediction and measured results are satisfactory within the accuracy required for engineering purpose. If the present method is incorporated into the existing propeller design or performance prediction computer program, the complete interaction analysis between a body of revolution and the propeller can be carried out by an iterative procedure. That is, the wake-adapted propeller design or the performance calculation in the wake behind the ship can be really carried out. The thrust deduction and the effective wake distribution may be computed in the same iteration cycle of the interaction analysis.

(2) Owing to the fact that the flow state downstream of the propeller plane may be predicted, it is potentially viable to be generalized and extended to the calculations of the thrust deduction, the effective wake distribution and the interaction analysis between a body of revolution and a ducted propeller, contrarotating propeller or the tandem propeller.

(3) At the present paper, the lifting line-sink disk model of the propeller and the assumption that the influence of the propeller on the upstream fluid is inviscid were used. In order to improve the accuracy of the calculation, the lifting-surface model of the propeller instead of the lifting line-sink disk model can be employed, or even the viscosity of the fluid is taken into account in calculating the induced velocity field of the propeller. But the lifting surface model requires a great deal of calculating work. It is unwise to adopt the lifting surface model from the beginning to the end in the calculation of the interaction analysis. So we propose that the lifting line model is used in the preliminary design calculations and the lifting surface correction or calculation is introduced at final stage of design or calculation. As to the induced velocity field of the propeller in turbulent flow, till now it is very difficult to treat in purely theoretical way.

## REFERENCES

- Cox, B.D., and Hansen, A. G. (1977): A Method for Predicting Thrust Deduction Using Propeller Lifting Surface Theory. DTNSRDC Report 77-0087.

- Dong shi-tang (1977): Ducted Propeller Design Method Based on Vortex Theory. China Ship Scientific Research Centre Report.
- Huang, T. T., and Cox, P. D. (1977): Interaction of Afterbody Boundary Layer and propeller. Symposium on Hydrodynamics of Ship and Offshore Propulsion Systems, Hovix Outside Oslo.
- Huang, T. T., and Groves, M. C. (1980): Effective Wake: Theory and Experiment. Thirteenth Symposium on Naval Hydrodynamics, Tokyo.
- Huang, T. T., Wang, H. T., Santelli M., and Groves, M. C. (1976): Propeller/Stern Boundary Layer Interaction on Axisymmetric Bodies Theory and Experiment. DTNSPDC Report 76-0113.
- Nagamatsu, T., and Iokunaga, K. (1978): Prediction of Effective Wake Distribution for a Body of Revolution. Journal of Society of Naval Architects of Japan, Vol. 143.
- Zhou Lian-di (1982): A Streamline-Iteration Method for Calculating Turbulent Flow around the Stern of a Body of Revolution and Its wake. Fourteenth Symposium on Naval Hydrodynamics, Michigan

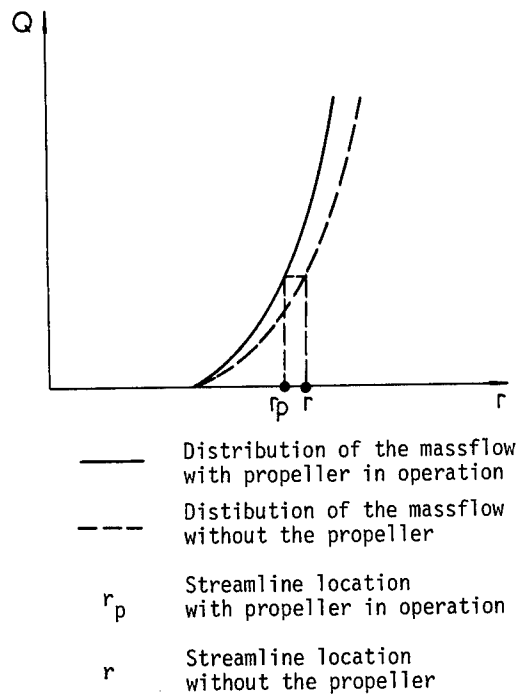


Fig. 1:  
Sketch for Obtaining Streamline Location  
by Inverse Interpolation of the Massflow

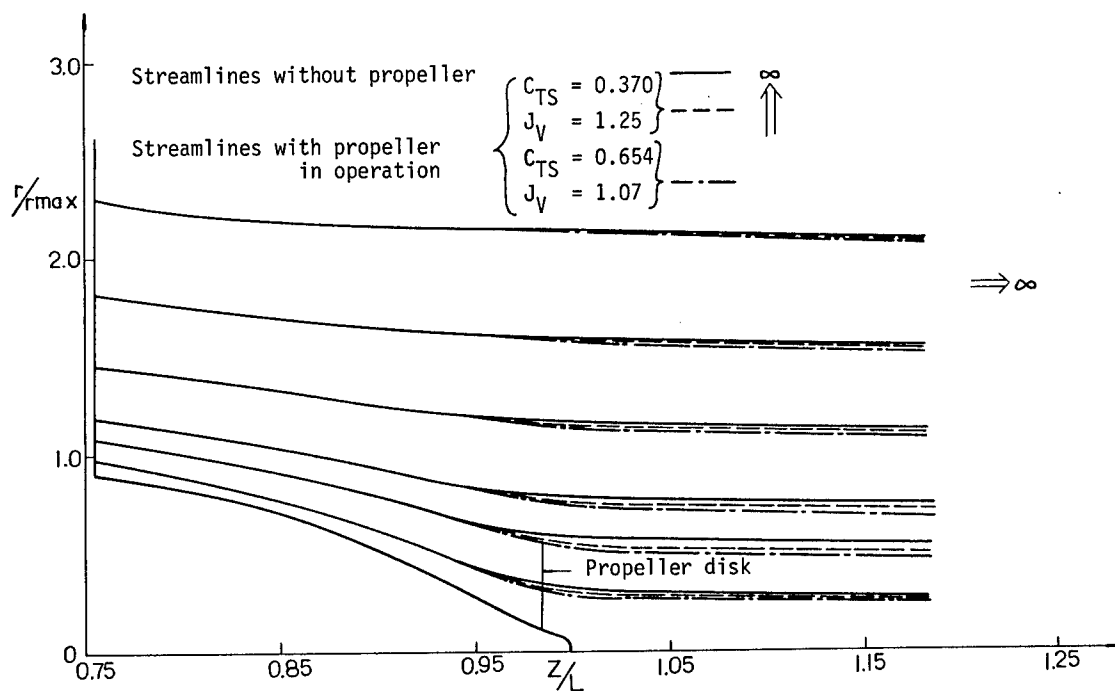


Fig. 2: Computed Streamlines for Afterbody 1  
with and without Propeller in Operation



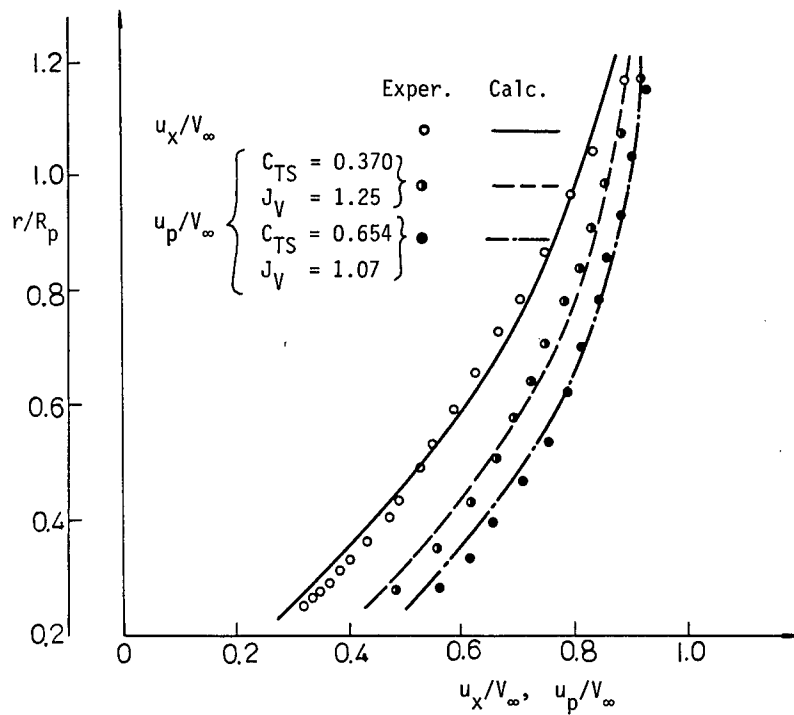


Fig. 3: Measured and Computed Axial Velocity Profiles Immediately Upstream of Propeller ( $Z/L = 0.9771$ ) with and without Propeller in Operation

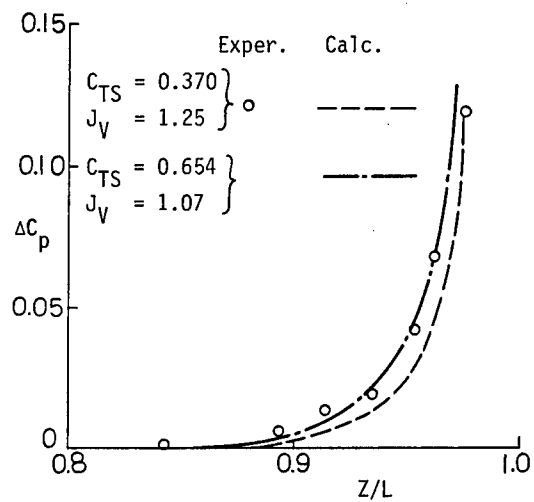


Fig. 4: Measured and Computed Distribution of Surface Pressure Defect over the Stern of Afterbody 1 with and without Propeller in Operation

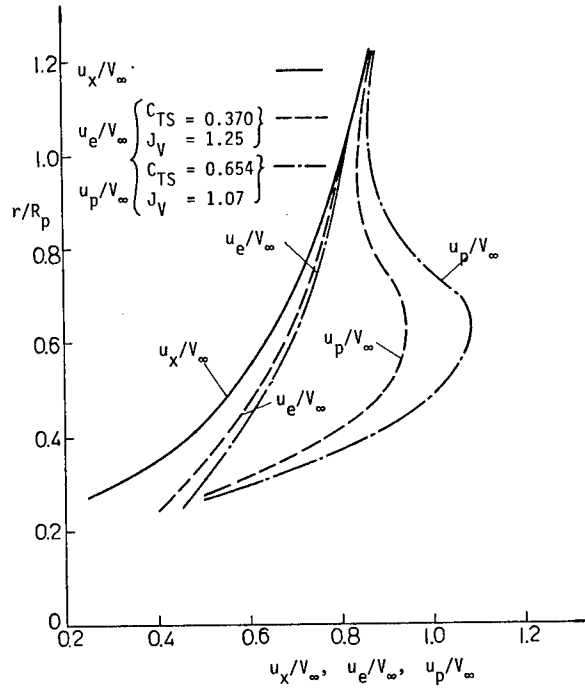


Fig. 5: Computed Nominal, Total and Effective Axial Velocity Profiles at the Propeller Plane ( $Z/L = 0.9831$ )

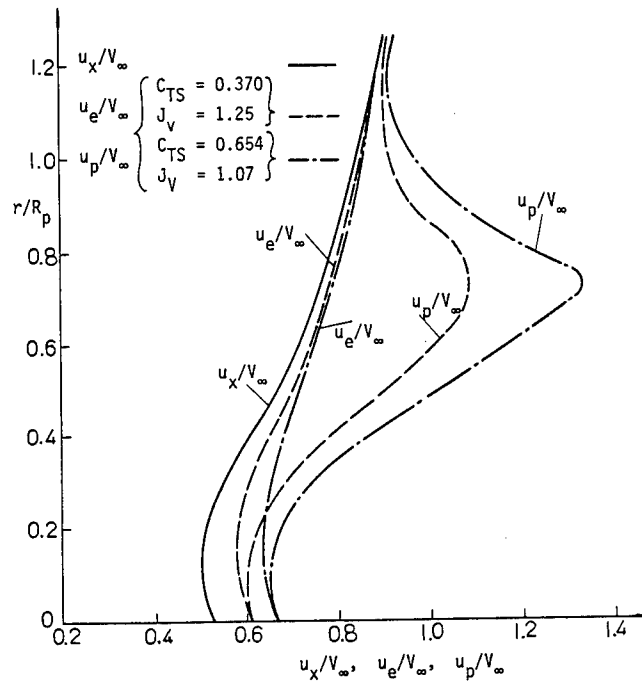


Fig. 6: Computed Nominal, Total and Effective Axial Velocity Profiles at the Station ( $Z/L = 1.057$ ) in the Propeller Wake

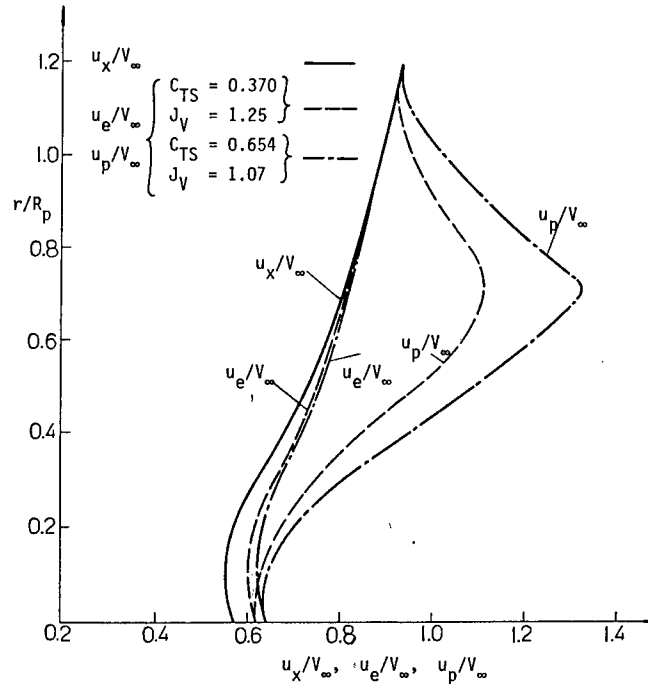


Fig. 7: Computed Nominal, Total and Effective Axial Velocity Profiles at the Station ( $Z/L = 1.182$ ) in the Propeller Wake

## DISCUSSION

Dr. MING S. CHANG and Dr. THOMAS T. HUANG,  
David Taylor Naval Ship R&D Center,  
Bethesda, MD, USA:

The authors have developed a streamline-iteration numerical procedure for computing propeller/hull interaction. The thrust deduction, the effective wake distribution, the flow downstream of the propeller plane, together with turbulence quantities, are computed by this method. The good agreement between their computed results and our experimental data demonstrates the general validity of the authors' numerical approach. The authors are to be congratulated on their achievement.

The effective wake distribution computed by this method is in good agreement with the inviscid interaction theory of Huang. Furthermore, our method has been extended to treat the inviscid interaction of ducted propulsors. The extension is straightforward and accurately predicts the mass flow through the ducted propulsor. Since the authors mentioned the ducted propulsor in this paper, we would like the authors to state their approach in computing the streamline on the duct and hence the mass flow through the duct.

In the design of tandem and contrarotating propellers, the actual location of the trailing propeller wake is extremely important. The lifting line-sink disk model used by the authors may not be very appropriate. The wake and the induced velocities generated by the forward propeller at the location of the downstream propeller are known to be poorly predicted by the lifting line-sink disk model. This limitation is more serious for the tandem propeller design, since the effective wake must be accurately defined at the lifting surface of the downstream propeller.

Figures 6 and 7 show that the location of the maximum velocity downstream of the propeller moves away from the propeller/body axis in comparison with that at propeller plane (Fig. 5). The contraction of the slipstream and high induced velocities downstream of the propeller usually cause the location of the maximum velocity downstream of the propeller to move toward the propeller/body axis. This discrepancy may be caused by the approximation of the induced velocities downstream of the propeller computed by the lifting line-sink disk model, since the propeller trailing vortices are assumed at constant radii for this model.

Again, we congratulate the important achievement of the authors.

Prof. MICHAEL SCHMIECHEN,  
Berlin Ship Model Basin (VWS),  
Berlin, Germany:

The authors are to be congratulated on their success in extending the procedure of Zhou to include the propeller in operation. Quite apparently they have already reached many goals of the program outlined in my paper on optimal ducted propellers for bodies of revolution presented at the International Symposium on Ship Hydrodynamics and Energy Saving at El Pardo 1983.

I hope that in the near future we can cooperate in doing what I consider the necessary final steps. These include in particular the determination of the initial conditions in an optimal fashion which is possible without explicit reference to hull-duct-propeller interaction. As far as I have seen, the authors have not addressed this problem in their paper. I wonder whether they might care to comment on this subject at this stage, where verification of the computational procedure is of course the primary concern.

Neither in the 1982 paper nor in the present paper do the authors refer to the work of Dyne, whose streamline iteration procedure appears to be very similar to their own. The same holds for the work of Chen and Patel, which will be presented in the last Session of this Symposium. The latter procedure even includes the transformation to a finite domain. Maybe the authors could elaborate on the differences between the procedures quoted.

Prof. LARS LARSSON,  
SSPA Maritime Consulting AB,  
Gothenburg, Sweden:

My students and I have for some years been developing a three dimensional version of the streamline curvature method. The first paper on this development was presented at the previous ONR Symposium and further work was reported at the Symposium on Numerical and Experimental Methods in Aerodynamic Flows in 1983. Presently we are improving the pressure calculation by a more exact procedure for the pressure variation across the viscous region and a better scheme for the interaction with the potential flow. We are also considering the inclusion of the propeller effect.

I have found Dr. Zhou's papers extremely interesting and there are several ideas we would like to borrow for our own method. I think one of the key problems is the integration of the pressure inwards from some outer surface (infinity in the present method). Very minute errors in the radial velocity component will create pressure fluctuations which can be severe on the body. In the discussion on his first paper Dr. Zhou mentioned that such problems had indeed been encountered. My question to Dr. Zhou is now: Haven't these problems become much more severe after the introduction of the propeller? At the propeller plane the total pressure and the tangential velocity are given a stepwise change, which must yield stepwise changes in

the other variables, for instance the static pressure. This in turn would imply uneven streamlines and I would expect large stability problems. However, in Fig. 2 the streamlines seem very smooth also close to the propeller disk. Has the problem been overcome by taking large steps at this position or has some other smoothing technique been applied? As far as I can see, the grid spacing is not given in the paper.

I also have a question related to Fig. 5. The body radius at the propeller plane is  $0.2 R_{\max}$  and the nominal wake velocity seems to go to zero there, but this is not the case for the effective wake velocity. Has the no-slip condition been violated when introducing the propeller? If not, the gradient close to the surface has increased very much due to the propeller action, which must imply that there is a large frictional component of the thrust deduction.

Dr. GILBERT DYNE,  
SSPA Maritime Consulting AB,  
Gothenburg, Sweden:

Some years ago when I was working on my streamline curvature method (1) I tested the turbulence model used by the authors. I found, however, that this model was unable in my case to treat the boundary layer when it left the body and was transformed into a wake flow. To get reliable results I had to use a simpler model. It would be interesting to hear if the authors have had the same experience and if so - how they solved the problem. I can mention that in the calculations I used many more streamlines than the authors - about 35 between the body and the edge of the boundary layer and wake. The distance between the inner streamlines was extremely small to permit detailed calculations also of the inner parts of the boundary layer and wake.

I have also tried to use my streamline curvature method for the propeller-hull interaction problem, although I gave it up in favour of a less complicated method (2). One of my experiences from this work was, however, that it was not possible to use a circulation distribution with zero circulation at the hub. If I did that the energy addition to the low energy flow in the inner streamlines when it passed the propeller disk was too small to avoid flow separation in the high static pressure region immediately behind the propeller. The calculations broke down. The solution was to have a finite circulation of a certain magnitude at the hub. Since I can see from the figures that the authors have used zero hub circulation my second question is: How did you avoid the separation? Is not the speed at your innermost streamline just ahead of the propeller low?

My third question refers to the total velocity profiles in Figs. 6 and 7. Can you explain why these velocity profiles are so peaky at  $r/R_p \approx 0.7$ ? I would be interested in getting the calculated values of tangential velocity and static pressure in these figures. The static pressure distribution along the body and

in the wake would also be of interest.

Finally I would like to congratulate the authors on a very fine paper. Their streamline-iteration method has shown itself to be very useful.

#### References:

- (1) Dyne, G. (1978): A Streamline Curvature Method for Calculating the Viscous Flow around Bodies of Revolution. Int. Symposium on Ship Viscous Resistance, SSPA, Göteborg, Sweden, Paper No. 6.
- (2) Dyne, G. (1983): On Optimal Wake Vorticity Adapted Propellers. 2nd Int. Symposium on Practical Design in Shipbuilding, Tokyo, Japan, pp. 77-84.

### AUTHORS' REPLY

Thank you, Dr. Huang, for your kind discussion on our work. We agree with your point of view that the lifting line-sink disk model poorly predicts the induced velocities downstream of the propeller. So if we want to generalize our method to the design of tandem and contra-rotating propellers, we must employ a more refined propeller model instead of the lifting line-sink disk model, but the method is still applicable.

Thank you, Prof. Schmiechen, for your kind discussion on our work. This method is a basic procedure for calculating the interaction between a body of revolution and a propeller. If the present method is incorporated into the existing propeller design or performance prediction computer programs, it is not difficult to complete the final propeller design by an iterative procedure.

The works of Dr. Dyne in 1978 and of mine (Zhou) in 1982 were developed independently. Though these two papers appear to be similar in some points, there were some essentially different points. For example, we employed K- $\epsilon$  two-equation turbulence model and the flow field within and outside boundary layer can be solved by using a uniform equation system in my paper. Of course, the coordinate transformation used in my paper is also a feature. As for Dyne's paper presented in 1983, I am sorry to say that I have not studied it yet. So I cannot answer on it. Finally, I also hope that in the near future we can cooperate on the interesting problems before us.

Thank you, Prof. Larsson, for your kind remarks. With regard to your first question, I (Zhou) had made a written reply in the discussion of my last paper (1982) read at the 14th ONR Symposium. To accurately integrate radially the pressure gradient is indeed difficult. However, adopting our coordinate transformation can partly improve the calculation accuracy. Another way is to apply a method of relaxation, in which both stability and accuracy of calculation may be improved, but at the expense of increasing the number of iterations. As to the present case, i.e., body-with-propeller, the initial value used was the final result of calculation of body without propeller, then

the induced velocity field by the propeller is superimposed. Thus the initial values of the streamline iteration method are rather reasonable, hence increased speed of convergence, and iterations are few.

The second point: The programming for computing stream tube convergence depends on propeller loading. We did not employ extra smoothing techniques. The grids near the propeller are  $Z/L = 0.9771, 0.9881, 0.996, 1.057, 1.181, \dots$

The third question: For the velocity profile with propeller added (Fig. 5), we forced a nonslip condition at the wall, i.e. the velocity at wall = 0. Frictional force was not carefully computed in our method, because our emphasis is on flow field calculation. The thrust deduction computed is also the pressure component only. We agree that the lack of detailed consideration of frictional force is an area needing further improvement.

We thank Dr. Dyne also for his written discussion. The first question of Dr. Dyne had been replied to previously in discussions of Zhou (1982). We shall repeat it here. Owing to the thin laminar sublayer, it is difficult to apply the K- $\epsilon$  two-equation model in this region. Therefore we applied a technique something like using a wall function in the laminar sublayer, and avoided the computation in this region. The second point: We did not meet the problem in our computation. Maybe because our radial grids are rather coarse; the nearest gridline to the axis is at about  $0.35 R$ . The third question: The peak value depends on the induced velocity. If this seems not rational, maybe that is because of what Dr. Huang has pointed out, i.e. the lifting line-sink disk model is not good for accurate prediction of induced velocities behind the propeller. We did not bring along the computed tangential velocities and static pressures, so we shall communicate with Dr. Dyne later.

SESSION V  
NONLINEAR FREE-SURFACE INTERACTIONS

# SPLASHLESS BOW FLOWS IN TWO DIMENSIONS?

E.O. TUCK AND J.M. VANDEN-BROECK

## ABSTRACT

In two-dimensional bow-like flows past a semi-infinite body, one must in general expect a free-surface discontinuity, in the form of a splash or spray jet. Similarly, if one reverses the flow direction, so generating a stern-like flow, one must expect a train of waves at infinity. For example, we have shown in previous work that there is no stern-like flow without waves for a flat-bottomed body with a single corner. However, this is not necessarily the case for polygonal bodies with two or more corners, or for smooth bodies. The question of the existence of smooth, continuous solutions, having neither splashes nor waves is considered in this paper. Conclusive numerical evidence is given of the existence of such solutions.

## 1. INTRODUCTION

The experimental work of Baba (1976) and Miyata (1980) indicate that a bulbous bow can eliminate or at least reduce the splash at the extreme bow of a ship.

In the present paper we examine the flow at the bow of a ship within the framework of the steady two-dimensional potential flow theory. This problem was considered before by Vanden-Broeck and Tuck (1977), and Vanden-Broeck, Schwartz and Tuck (1978). These authors attempted to construct models for near stern flows and near bow flows. Although their scheme worked very well for stern flows, they did not succeed in finding continuous solutions without waves. On the other hand their work suggested the existence of waveless solutions with splashes.

It should be emphasized that elimination of waves from a stern flow is equivalent to elimination of splashes from a bow flow. That is if we have been able in one way or another to construct a waveless stern flow, there is no radiation condition for that flow, which can be reversed in direction to yield a splashless bow flow.

Vanden-Broeck et. al.'s analysis was restricted to bow shapes consisting of a plane lower surface and an oblique plane front.

Although their work rules out splashless and waveless solutions, the possibility still exists that by considering different families of bow shapes one could identify a special shape for which splashless and waveless flow exists. This possibility is strongly suggested by the recent work of Schmidt (1981) and Vanden-Broeck and Tuck (1984).

One of the main results of this paper is the numerical demonstration of the existence of such shapes. The corresponding solutions model bow flows in which the splash drag component has been completely eliminated. The bow shapes for which this elimination is possible are bulbous.

In Section 2 we discuss some properties of bow flows with splashes. In Section 3 we derive a numerical scheme which enables us to compute splashless bow flows.

## 2. FLOWS WITH SPLASHES

What is a splash? In the present two-dimensional context, a flow meeting a body contains a splash if a portion of the incident stream is deflected upward and backward in the form of a jet, which then falls freely for ever in an approximately parabolic trajectory. Figure 1 shows a sketch of one possible flow.

Such a flow is obviously an idealization of what might occur in practice near the bow of a ship. The most glaring non-physical feature is that Figure 1 has the jet and the incident stream apparently passing across each other without interference. The mathematical artifice that allows this to happen is that these two pieces of the flow do not occupy the same space, but lie on quite distinct "Riemann sheets".

In practice, unless some action is taken to avoid it, the falling jet must actually fall upon and hence interfere with the incident stream. The avoiding action could involve diverting the jet, catching it in a bucket, etc. Whether or not such action is taken there are interesting "St. Venant's principle" type of questions to be answered; that is, does action taken or interference caused at a point relatively far removed from

E.O. Tuck, Applied Mathematics Dept., The University of Adelaide S.A. 5000, Australia  
J.-M. Vanden-Broeck, Dept. of Mathematics, The University of Wisconsin-Madison, Madison WI 53705

the main domain of interest affect the flow significantly in that domain? The answer is clearly "No", providing the jet is sufficiently thin, but that observation merely shifts the nature of the question to one concerning whether or not the jet is indeed thin.

One form of "diverting action" for the jet is to re-introduce the third dimension. That is, the flow near a bluff but not quite plane bow could be expected to be close to two-dimensional. However, the ballistic trajectory of the jet will not in general quite lie in planes parallel to the incident stream, and hence the interference will be interference to another (further downstream) plane of nearly two-dimensional flow. Thus, paradoxically, one might expect to be able to see flows like those sketched in Figure 1 more easily in actual three-dimensional bow flows than in artificially-constructed two-dimensional experiments.

infinity beneath the free surface. All streamlines originating from above **F** will be diverted into the jet, while all below **F** will pass under the body. In the most general case, we must expect that **F** lies at a distance below the free surface that is comparable with the draft of the body, and hence the jet's thickness is likewise of the order of the draft.

Such a very thick jet is unlikely to be observed. So either circumstances must be such as to produce a thin jet (perhaps no jet at all!) or else the flow model of Figure 1 is not even qualitatively accurate. Indeed Hanji (1976) has demonstrated experimentally some two dimensional bow flows with a "forward wake", consisting of a closed region of high vorticity, lying above an essentially-irrotational flow field, as sketched in Figure 2. It is not implausible that such a rotating bubble is a final manifestation of a thick jet that has so thoroughly (and non-

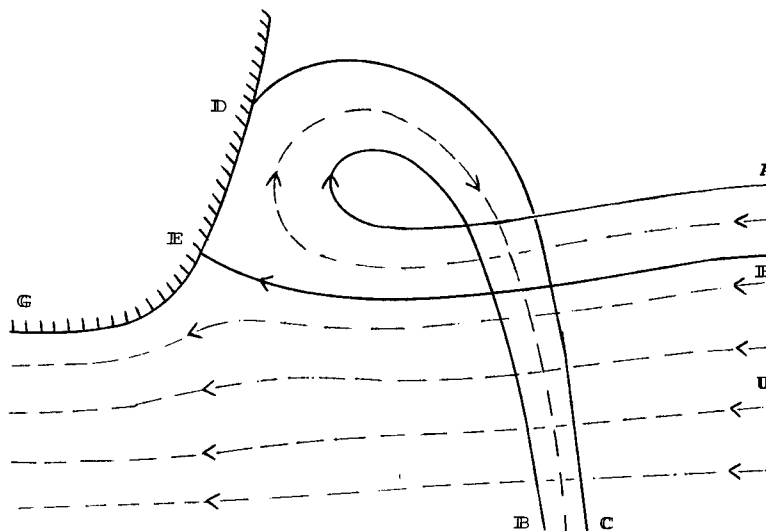


Figure 1: Sketch of a bow flow with splash.

Indeed, this does appear to be the case. Even for not-so-bluff bows, with V-shaped bows of small angle, a pronounced splash sheet often seems to be present, and furthermore appears to be thin. At first sight, one would not expect that a two dimensional flow model would have any validity for a fine three-dimensional bow flow, but there may exist a suitable set of planes such that the flow varies slowly with respect to a co-ordinate normal to these planes. This concept is being explored by one of us (E.O.T.) in on-going research.

If we return now to truly two-dimensional flow, there is no reason to believe that the jet is thin in general. There will be a submerged stagnation point **E** on the body, with an attached stagnation streamline **EF** extending to **E** from a point **F** at upstream

conservatively) interfered with the incident stream as to destroy irrotationality, and has converted itself into a distributed vortex.

Nevertheless, we are entitled to try to compute irrotational flows like those of Figure 1, and efforts are being made by both of the present authors to do so. In view of the above discussion, such efforts are worthwhile only if the jet that is produced is in some sense thin. One approach is to exploit existing thin-jet theories, e.g. as in Keller and Geer (1973) or Tuck (1976).

To indicate the type of mathematical considerations involved, whether or not the jet is thin, let us note that all falling jets will become thin eventually, and their asymptotic form will be a parabolic arc with a ballistic velocity distribution, i.e. with a



speed of fall proportional to the square root of distance fallen, and a constant horizontal velocity. This is consistent with an asymptotic form

Providing we choose the constant  $a$  as

$$a = \left(\frac{9}{8g}\right)^{1/3}, \quad (8)$$

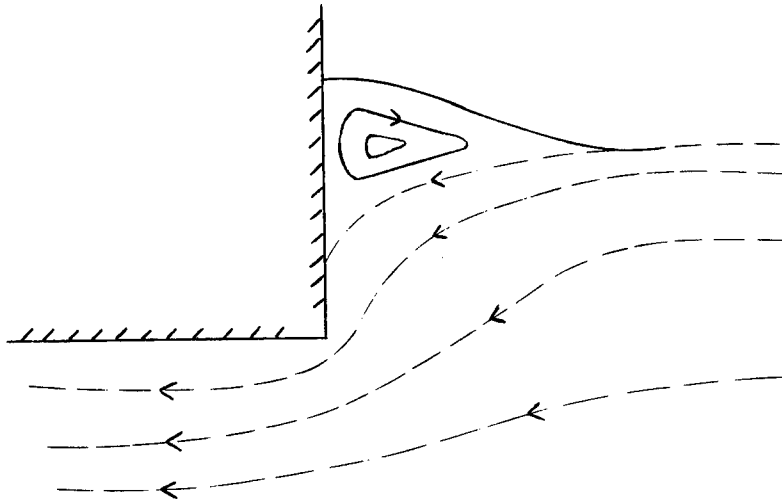


Figure 2: Sketch of a bow flow with a "forward wake".

$$z(f) = -iaf^{2/3} + bf^{1/3} + O(1), \quad \phi \rightarrow +\infty, \quad (1)$$

for the relationship between complex potential  $f = \phi + i\psi$  and co-ordinate  $z = x + iy$ , where  $a$  and  $b$  are real positive constants. For example, on the streamline  $\psi = 0$  to leading order as  $\phi \rightarrow +\infty$ ,

$$x = b\phi^{1/3} \quad (2)$$

and

$$y = -a\phi^{2/3} = -a(x/b)^2. \quad (3)$$

The corresponding velocity components are

$$u = \frac{3b}{4a^2} = \text{constant} \quad (4)$$

and

$$v = -\frac{3}{2a}\phi^{1/3} = -\frac{3}{2a}(-y/a)^{1/2}, \quad (5)$$

as for a free ballistic projectile.

The pressure is given by Bernoulli's equation as

$$\frac{p}{\rho} = \frac{1}{2}U^2 - \frac{1}{2}(u^2 + v^2) - gy \quad (6)$$

$$= \left(ga - \frac{9}{8a^2}\right)\phi^{2/3} + O(1). \quad (7)$$

the pressure remains bounded throughout the jet as  $\phi \rightarrow \infty$ . In fact, we require  $p = 0$  on both of its free boundaries, but we can only distinguish between different finite values of  $\psi$  as  $\phi \rightarrow +\infty$  by including more terms in the asymptotic representation (1). The usefulness of (1) is that any attempt to solve for a general flow of the type sketched in Figure 1 must build in an analytic character like (1) near the jet asymptote  $BC$ , with  $a$  given by (8) and  $b$  to be determined.

Although numerical solution of such problems seems somewhat distant, the following simple explicit example is of illustrative value. Suppose we concentrate attention on the portion of Figure 1 lying above the dividing streamline  $EF$ . Then the curve  $DEF$  can be replaced by a given boundary. That is, this part of the flow will look like that for a stream in water of finite non-uniform depth, in a channel that terminates with a barrier.

Suppose we normalise the stream velocity at  $AF$  to unity, i.e.

$$z \rightarrow -f + \text{constant}, \quad \text{as } \phi \rightarrow -\infty. \quad (9)$$

We also normalise the length scale so that  $g = 9/8$ ; hence  $a = 1$ . Then one function satisfying both (1) and (9) is

$$z(f) = \frac{-if^{2/3} + f^{1/3} + 1.69i}{1 - 1.3ie^{-2f}} + \frac{-f + 0.85i}{1 + ie^{2f}} + i \quad (10)$$

### 3.1 Formulation

We consider the steady two-dimensional potential flow of an inviscid incompressible fluid past a semi-infinite body whose lower surface  $y^* = -H$ ,  $x^* < 0$  is plane (see Figure 4). As  $x^* \rightarrow -\infty$ , the velocity is assumed to approach a constant  $U$ . The

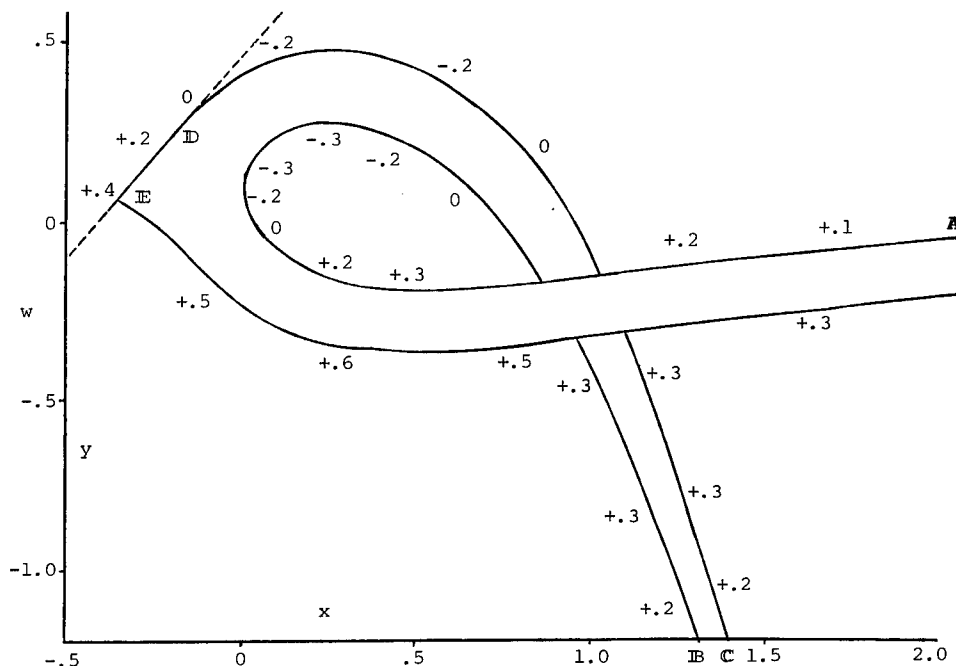


Figure 3: Computed bow flow with splash.

level  $y^* = 0$  corresponds to the level of the free surface at which the velocity is equal to  $U$ . We assume that the flow rises up the rear face of the body up to a stagnation point  $S$  at which separation occurs. Other flow configurations in which the flow separates tangentially from the body are also possible (Vanden-Broeck (1980)). However they will not be considered in this paper.

In previous work Vanden-Broeck and Tuck (1977) and Vanden-Broeck, Schwartz and Tuck (1978) solved numerically the problem sketched in Figure 4 with a plane oblique rear face. All their solutions contain a train of waves on the free surface. Therefore they can not serve as models for bow flows.

In this paper we generalize Vanden-Broeck et al.'s approach for bodies of arbitrary shape. For most shapes, waves are present on the free surface. However we shall see that there exists particular shapes for which the waves are absent.

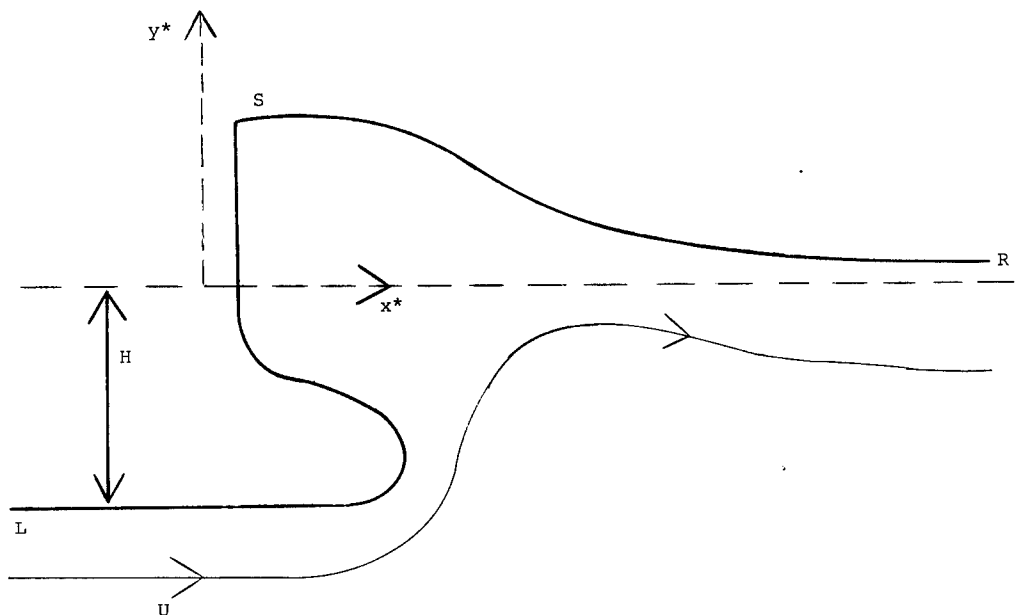


Figure 4. Sketch of a flow past of a semi-infinite body.

We denote the potential function by  $\phi^*$  and the stream function by  $\psi^*$ . We choose  $\phi^* = 0$  at the stagnation point and  $\psi^* = 0$  on the free surface and on the surface of the body (see Figure 4). We denote by  $-K$  the value of  $\phi^*$  at  $x^* = 0$ ,  $y^* = -H$ . We shall seek the complex velocity  $u^* - iv^*$  as an analytic function of the complex potential  $f^* = \phi^* + i\psi^*$ . We make the variables dimensionless by referring them to the velocity scale  $U$  and the length scale  $\frac{K}{U}$ . Thus we introduce the new dimensionless variables

$$x + iy = \frac{U}{K} (x^* + iy^*) \quad (11)$$

$$u - iv = \frac{1}{U} (u^* - iv^*) \quad (12)$$

$$f = \phi + i\psi = \frac{1}{K} f^* = \frac{1}{K} (\phi^* + i\psi^*) \quad (13)$$

Bernoulli's equation and the condition of constant pressure on the free surface yield

$$y + \varepsilon(u^2 + v^2) = \varepsilon, \quad \psi = 0, \quad \phi > 0. \quad (14)$$

Here  $\varepsilon$  is defined by

$$\varepsilon = \frac{U^3}{2gK} \quad (15)$$

We find it convenient to define the new function  $\tau - i\theta$  by the relation

$$u - iv = e^{\tau - i\theta} \quad (16)$$

Relation (14) can now be rewritten as

$$\int_0^\phi e^{-\tau} \sin \theta d\phi + \varepsilon e^{2\tau} = 0, \quad \psi = 0, \quad \phi > 0 \quad (17)$$

The function  $\tau - i\theta$  is an analytic function of  $f = \phi + i\psi$  in the half plane  $\psi < 0$ . On  $\psi = 0$ , its real part is the Hilbert transform of its imaginary part, thus we have

$$\tau(\phi) = \frac{1}{\pi} \int_{-\infty}^{+\infty} \frac{\theta(\phi)}{\phi - \phi'} d\phi' \quad (18)$$

Here  $\tau(\phi)$  and  $\theta(\phi)$  denote respectively  $\tau(\phi, 0_-)$  and  $\theta(\phi, 0_-)$ . The integral in (18) is to be interpreted in the Cauchy principal value sense. The kinematic condition on the body yields

$$\theta = 0, \quad \psi = 0, \quad \phi < -1 \quad (19)$$

$$\theta = g(\phi), \quad \psi = 0, \quad -1 < \phi < -b \quad (20)$$

$$\theta = \frac{\pi}{2}, \quad \psi = 0, \quad -b < \phi < 0 \quad (21)$$

Here the constant  $b$  and the function  $g(\phi)$  define the shape of the body. Relation (21) implies that the body is vertical for  $-b < \phi < 0$ . Our aim is to identify particular values of  $b$  and  $\varepsilon$  and a particular function  $g(\phi)$  for which no waves are present of the free surface. We shall restrict our attention to bodies with continuous slope. Therefore we impose the conditions

$$g(-1) = 0 \quad (22)$$

$$g(-b) = \frac{\pi}{2} \quad (23)$$

Substituting (19)-(21) into (18) we get

$$\tau(\phi) = \frac{1}{2} \ln \left| \frac{\phi}{b + \phi} \right| + \frac{1}{\pi} \int_{-1}^{-b} \frac{g(\phi)}{\phi - \phi} d\phi + \frac{1}{\pi} \int_0^{\infty} \frac{\theta(\phi)}{\phi - \phi} d\phi \quad (24)$$

For given  $\varepsilon$ ,  $b$  and  $g(\phi)$  the problem reduces to finding a function  $\tau(\phi) - i\theta(\phi)$  satisfying the nonlinear integro-differential equation defined by (17) and (24). A numerical scheme to solve this equation is described in the next subsection.

### 3.2 Numerical Results

We choose

$$g(\phi) = \frac{\pi}{2} \frac{(\phi + \lambda)^2 - (\lambda - 1)^2}{(\lambda - b)^2 - (\lambda - 1)^2} \quad (25)$$

This function satisfies the condition (22) and (23). The parameter  $\lambda$  in (25) will be adjusted to remove the waves on the free surface.

We introduce the  $N$  mesh points  $\phi_I$  given by

$$\phi_I = -1 + (I - 1)E, \quad I = 1, \dots, N$$

Here  $E$  is the interval of discretization. We also introduce the  $N$  corresponding unknowns

$$\theta_I = \theta(\phi_I), \quad I = 1, \dots, N$$

We find it convenient to define  $E$  as

$$E = 1/M$$

where  $M$  is an integer. With this particular choice

$$\phi_{M+1} = 0$$

We shall also use the  $N - 1$  intermediate mesh points

$$\phi_{I+1/2} = \frac{1}{2} (\phi_I + \phi_{I+1}), \quad I = 1, \dots, N - 1$$

From (19)-(21) we see that  $\theta$  has a jump discontinuity at  $\phi = 0$  with  $\theta(0_-) = \frac{\pi}{2}$  and  $\theta(0_+) = 0$ . Therefore the values of  $\theta$  at  $\phi = \phi_{M+1} = 0$  are known. In addition  $\theta_1 = 0$ , so only  $N - 2$  of the  $\theta_I$  are unknown. From (20)-(21) we obtain  $M - 1$  equations for

$$\theta_I = \theta(\phi_I), \quad I = 2, \dots, M \quad (26)$$

We now compute

$$\tau_{I+1/2} = \tau(\phi_{I+1/2})$$

in terms of  $\theta_I$  and  $b$  by applying the trapezoidal rule to the integral in (24) with the mesh points  $\phi_I$ . The symmetry of the discretization enables us to compute the Cauchy principal value as if it were on

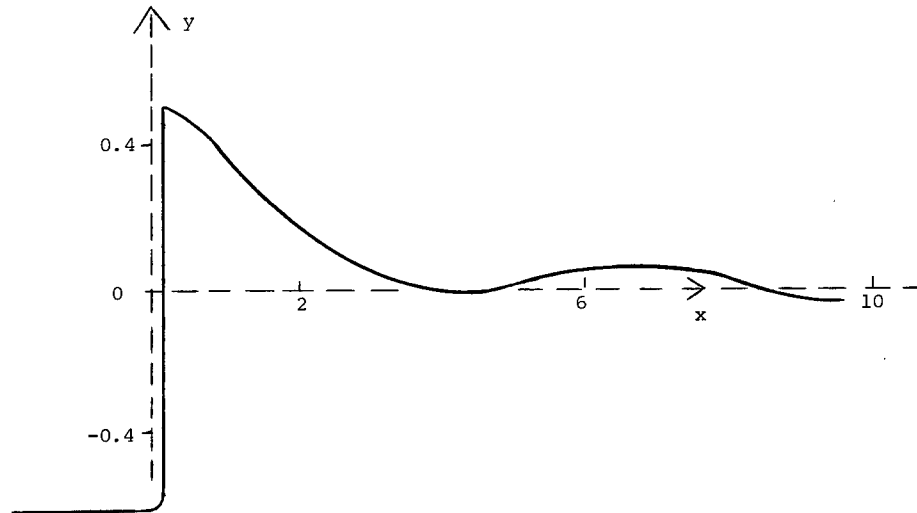


Figure 5: Computed body profile and free surface profile for  $\lambda = 0.3$  and  $\varepsilon = 0.5$ .

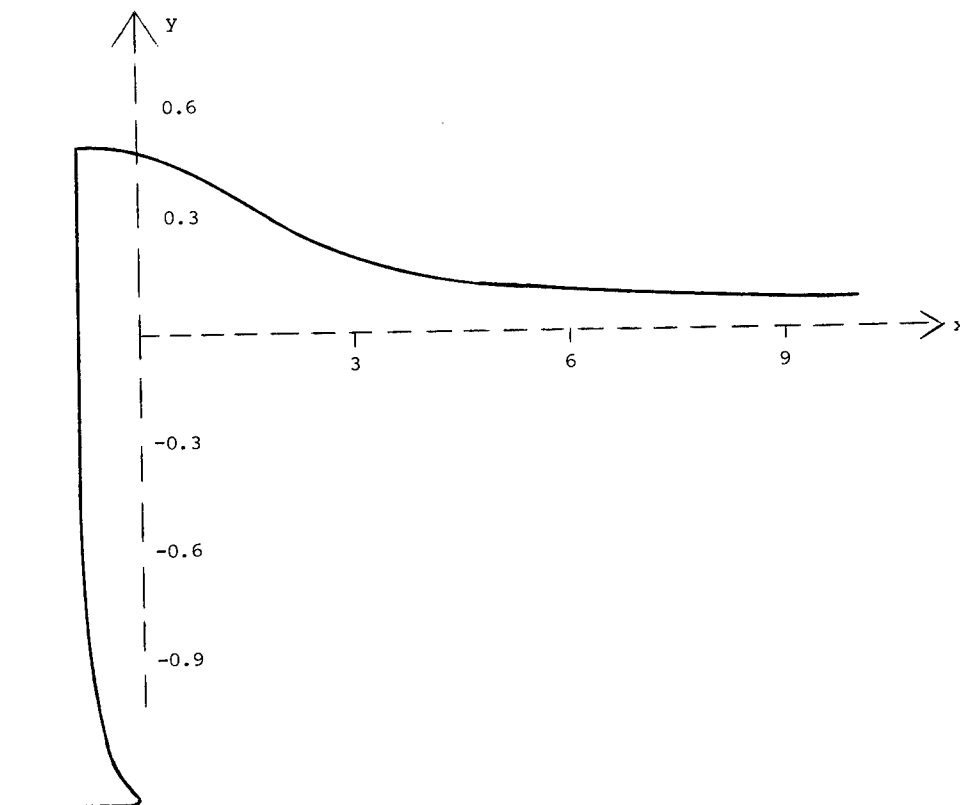


Figure 6: Computed body profile and free-surface profile for  $\lambda = 0.53$  and  $\epsilon = 0.5$ .

ordinary integral. The error inherent in approximating the integral by an integral over a finite interval was found to be negligible for  $N$  large enough. We now use the values of  $\tau_{I+1/2}$  and  $\theta_I$  to satisfy (17) at the mesh points  $\phi_{I+1/2}$ ,  $I = M + 2, \dots, N - 1$ .

The integral in (17) was computed by the trapezoidal rule. Thus we obtain  $N - M - 2$  equations for the  $N - 2$  unknowns  $\theta_I$ ,

$I = 2, \dots, N$ . Relation (26) provides  $M - 1$  extra equations. Therefore we have  $N - 3$  equations for the  $N - 2$  unknowns  $\theta_I$ .

The last equation is obtained by expressing  $\theta_{M+4}$  in terms of  $\theta_{M+1} = 0$ ,  $\theta_{M+2}$  and  $\theta_{M+3}$  by an extrapolation

formula. This equation is motivated by the work of Vanden-Broeck and Tuck (1977) and Vanden-Broeck, Schwartz and Tuck (1978). These authors showed that special care had to be taken near the stagnation point to insure convergence of the numerical scheme.

For given values of  $\epsilon$ ,  $b$  and  $\lambda$ , the  $N - 2$  equations are solved by Newton method with the initial guess

$$\theta_I = g(\phi_I), \quad I = 2, \dots, M$$

$$\theta_I = 0, \quad I > M + 2$$

Once a solution was obtained the profiles of the bow and of the free surface were obtained by numerically integrating the identities

$$\frac{\partial x}{\partial \phi} = e^{-\tau} \cos \theta \quad (27)$$

$$\frac{\partial y}{\partial \phi} = e^{-\tau} \sin \theta \quad (28)$$

For most values of  $\epsilon$ ,  $b$  and  $\lambda$ , waves are present on the free surface. Moreover many values of  $\epsilon$ ,  $b$  and  $\lambda$  lead to unacceptable body profiles which cross themselves. This is due to the fact that the profile of the body is obtained in the parametric form  $x(\phi)$ ,  $y(\phi)$   $-1 < \phi < -b$ . Therefore the mathematical formulation does not prevent unacceptable crossing of the profile.

By running the scheme for many different values of  $\epsilon$ ,  $\lambda$  and  $b$  we were able to identify particular values of these parameters for which waveless solutions with no crossing in the profile of the bow exist.

Typical profiles for  $\epsilon = 0.5$  and  $b = 0.2$  are shown in Figures 5 and 6. These solutions were computed with  $E = 0.1$  and  $N = 100$ . To check the accuracy of our results we ran the scheme with  $E = 0.05$  and  $N = 200$ . The results were found to be

indistinguishable within graphical accuracy from those presented in Figure 5 and 6.

The profile in Figure 5 corresponds to  $\lambda = 0.3$ . A train of waves is present on the free surface. This profile is qualitatively similar to the solutions obtained by Vanden-Broeck and Tuck (1977) and Vanden-Broeck, Schwartz and Tuck (1978). The main difference is that the corner has now been rounded.

The profile in Figure 6 corresponds to  $\lambda = 0.53$ . The free surface is completely waveless. Therefore this solution (when reversed in direction) demonstrates numerically the existence of splashless bow flows in two dimensions. It is interesting to note that the profile of the bow has a definite bulbous character.

Other splashless bow flows could be obtained by using different functions  $g(\phi)$  in (20). By analogy with the work of Vanden-Broeck and Tuck (1984) we expect that all the corresponding bow shapes are bulbous.

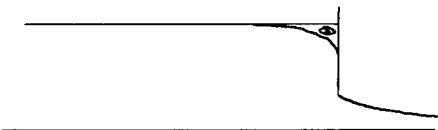
#### Acknowledgement

The work of the first author was supported during a visit to Stanford University in January-May 1984 by a contract to Prof. Keller under the ONR Fluid Mechanics Program. The work of the second author was sponsored by the United States Army under contract No. DAAG 29-80-C-0041 and the National Science Foundation under Grant No. MCS-8001960.

#### DISCUSSION

Prof. CHIA-SHUN YIH,  
University of Michigan,  
Ann Arbor, MI, USA:

In every hydraulic laboratory one can find a flume with a sluice gate. In a typical experiment the gate is partially open, with a free streamline downstream as well as upstream of the sluice gate. For the purpose of this discussion the downstream free streamline can be replaced by a solid boundary, and the sluice gate can be identified with the bow.



If the Froude number based on the upstream conditions is well below 1, one does not notice any splash at the sluice gate, nor any waves upstream from it. There is, however, a corner eddy at the region where the top surface (free streamline) meets the gate. I am glad that Dr. Vanden-Broeck did find solutions which give a free streamline tangent to the bow, so that the conclusions of the authors do not really contradict the common phenomenon observed in hydraulic laboratories. Nevertheless, I do not believe their search for solutions of their problem giving a stagnation point at the intersection of the free streamline with the bow

#### REFERENCES

- Baba, E. (1976): Proc. Int. Seminar on Wave Resistance, Tokyo, Soc. Nav. Arch. Japan.
- Honji, H. (1976): Journal of the Physical Society of Japan, 40, No. 5.
- Keller, J. B. and J. Geer (1973): J. Fluid Mech. 59, 417.
- Miyata, H. (1980): 13th Symp. Naval Hydro, Office of Naval Research, Washington, DC.
- Schmidt, G. H. (1981): J. Ship Res. 25, 236.
- Tuck, E. O. (1976): J. Fluid Mech. 76, 625.
- Vanden-Broeck, J.-M. (1980): J. Fluid Mech. 96, 603.
- Vanden-Broeck, J.-M. and E. O. Tuck (1977): Proc. 2nd Int. Conf. Num. Ship Hydrodynamics, Berkeley.
- Vanden-Broeck, J.-M. and E. O. Tuck (1984): J. Ship Res. (submitted).
- Vanden-Broeck, J.-M., L. W. Schwartz, and E. O. Tuck (1978): Proc. Roy. Soc. Lond. A 361, 207.

can be exhaustive, especially since the locations of their points  $\phi = -1$  and  $\phi = -b$  and the curves connecting these two points cannot be assigned a priori in the physical plane. One is not yet convinced that solutions to their problem giving a stagnation at the bow surface exist only for the case (of a bulbous bow) they presented.

Prof. ROBERT F. HALLIDAY,  
University of Sydney,  
Sydney, Australia:

This remark relates to a question raised after the presentation of the paper and not to the paper itself. The question referred to lack of "splash" on the upstream face of a sluice gate. In a flume it is very difficult to obtain truly uniform flow. Also there will be a boundary layer on the face of the sluice gate. Our experience with these two effects is that it is often not possible to demonstrate inviscid flow predictions.

A full-width two-dimensional model is a possibility in a small ship model tank. The forces would be very large and a massive structure would be needed. However, the attempt may be worth the effort since, unlike the stern flow case, interference from boundary layers will be much less.

Prof. SOM D. SHARMA,  
Institut für Schiffbau,  
Hamburg, FR Germany:

My congratulations to the authors on an absolutely fascinating paper. Unfortunately, in my opinion, an unseparated two-dimensional flow around a bow of the shape sketched in Fig. 6 is altogether impossible. On the basis of experimental evidence I can assure them that a real flow would separate twice, once in front of the bow just below the free surface to form a bow vortex and then again at the toe to form a deadwater regime. So their potential flow model is rather academic as far as 2D flow is concerned. In 3D flow, of course, an essentially unseparated flow is possible around a bulbous bow of reasonable shape.

#### AUTHORS' REPLY

We thank Professor Yih for his kind comments on our work and its possible application to the flow under a sluice gate.

The numerical work of section 3 demonstrates the existence of splashless bow flows in two dimensions. A typical solution is shown in Fig. 6. Other splashless bow flows could be obtained by using different functions  $g(\phi)$  and other values of the parameters  $b$ ,  $\lambda$  and  $\epsilon$ .

We thank Professor Halliday for his interest in our calculations. In future work we intend to compute accurate solutions for the flow under a sluice gate.

For most bow shapes (but not that of our Fig. 6) we agree with Prof. Sharma's statement that unseparated 2D bow flows are impossible. In the paper we speculate about how this separation would occur via the unphysical splash converting itself into a vortex.

However, Professor Sharma's comment refers more particularly to our Fig. 6, which is the special splashless case. Here there is potential for disagreement between us, although the particular example computed in Fig. 6 may not be typical of splashless shapes that could be computed.

In essence, we are asserting that, among families of idealized bow shapes, there is a subfamily that is splashless. The flows in this sub-family are expected to be closer to reality, and may have a reduced tendency to forward-wake generation. More daringly, we suggest that they may contain members that are in some sense "good" choices for bows.

# NECKLACE VORTEX AND BOW WAVE AROUND BLUNT BODIES

KAZU-HIRO MORI

## ABSTRACT

The bow wave phenomena are studied experimentally and theoretically to make clear the mechanism of the wave-breaking. A stress is made on the flow before the so-called breakdown takes place. It can be divided into several phenomena; the development of the free-surface shear layer, the formation of the necklace vortex, and the production of unsteady turbulent surface-flow.

Flow observations and measurements of wave profiles, mean velocity and turbulent characteristics are carried out for two 2-D vortical cylinders. The free-surface boundary layer theory, the vorticity-stretching theory and the instability analysis are invoked to explain experimental results.

The free-surface curvature is concluded as one of the sources for the shear flow beneath the free-surface. It is also concluded that the deceleration of the approaching velocity in the proximity of the bow is responsible for the formation of the upstream necklace vortex.

Prior to the occurrence of the breakdown, the free-surface becomes unsteady; the turbulent quantities become intense on the free-surface. The stability analysis draws a conclusion that the approaching velocity, its defect, if any, and its decelerating rate are important factors for the inception of the free-surface instability.

Controlling undesirable velocity defects and surface curvatures by a special bow-bulb, the sub-breaking waves, which appear prior to the breakdown, can be successfully oppressed.

## 1. INTRODUCTION

The scene where a ship advances making white waves around its bow is dynamic and picturesque; it sometimes enchants us. From the view point of ship resistance, however, they are absolutely not desirable.

Baba (1969) and Taneda et al.(1969) independently pointed out their importance. The former called them "bow breaking-waves", while the latter a "necklace vortex" because they

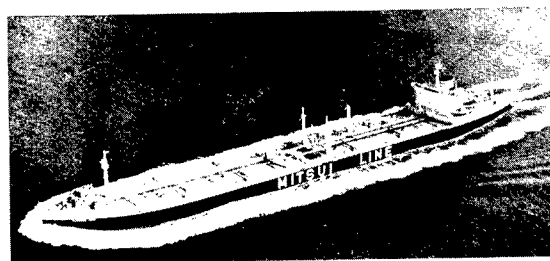


Fig.1 Breaking-Waves around Ship; Taneda et al.(1969)

look like a necklace of pearls surrounding ship (Fig. 1).

Since then many have studied on the bow wave-breaking both experimentally and theoretically; Dagan et al. (1972), Suzuki (1975), Inui et al. (1979), Doi et al. (1981), Kayo et al. (1981) and recently Matsui et al. (1983). Two-dimensional waves by submerged bodies or varying bottoms are also studied which are essentially the same phenomena as the bow wave-breaking; Peregrine et al.(1978), Battjes et al.(1981), Duncan (1983) and so on.

The so-called breaking waves are not so simple as expressed in a word. The term of the bow wave-breaking was literally used for the white waves as shown in Fig. 1 (Baba). It implied a plunging type breaking defined in Peregrine which breaks down vortically at the bow. It was related either to a hydraulic jump(Taneda et al.) or to a bow-returning jet (Dagan et al.). The breakdown is the last state of breakings. Prior to it, there are several important aspects which can be hardly covered by a simple word of breaking.

Dagan et al. suggested an existence of a Taylor instability on the free-surface over a certain Froude number. Suzuki supported this experimentally. Kayo et al.'s demonstration, where the region of breaking expanded by an artificial free-surface shear flow, is related to this kind of unstable surface.

† Hiroshima University, Saijo Higashi-Hiroshima 724 Japan.



On the other hand, several flow visualizations show that an upstream vortex, surrounding the bow and adhering to it, exists even at a low Froude number where no significant breakings apparently occur (Kishimoto et al. 1976, Kayo et al.).

Both the free-surface instability and the upstream vortex have different dynamical mechanisms from the so-called breakdown waves. The author is reluctant to call them breakings simply. We use here the term of the "breaking" narrowly for such waves as white waves (Fig. 1) or plunging-type breaking waves where a breakdown or a collapse occurs. And the instability of the free-surface is called "sub-breaking" in distinction from the breakdown. This is because the unstable surface develops into the breakdown finally. The upstream vortex is referred to as a "necklace vortex" to which a different explanation is given from the original definition by Taneda.

Once the breakdown takes place, the phenomena change catastrophically (Battjes et al., Duncan). We confine here ourselves mainly to the phenomena prior to the breakdown, for our purpose is to make clear how the bow wave-breakings take place.

Two vertical cylinders with a circular section (diameter: 0.42 m) and an elliptic section (length: 1 m, beam: 0.3 m) were used; they are designated as CM-42 and EM-300 respectively. Observations of wave patterns and profiles around bows, and measurements of wave height and velocity including turbulent characteristics have been carried out. Their drafts are both 0.5 m for the free-surface flow to be free from the end effects; §2.

Theoretical explanations of experimental results have been proposed in §3. The free-surface shear flow, the formation of the necklace vortex and the instability of the bow-wave flow are discussed.

Finally in §4 an attempt has been made to prevent the breaking of bow-waves by an SP-bulb. The free-surface flow, the incident flow velocity, the turbulence intensity are compared with those without the bulb, and its effectiveness is discussed.

## 2. EXPERIMENTAL FINDINGS

We shall use the cartesian coordinate shown in Fig. 2; the origine is at the bow of fixed bodies and on the still water. The

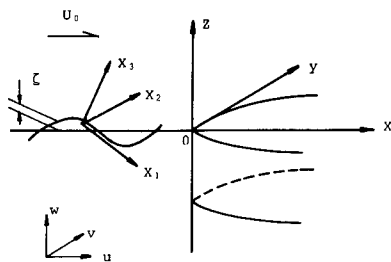


Fig.2 Coordinate Systems

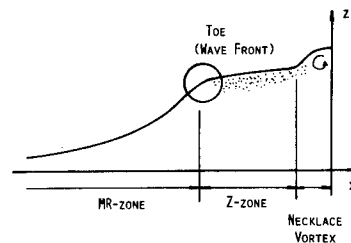


Fig.3 Flow Model of Bow-Wave

incident flow is in the positive x-direction with velocity  $U_0$ .  $u$ ,  $v$ , and  $w$  are velocity components in the x-, y- and z-directions respectively. Here absolute values are used for the velocity of the incident flow. This is because it has not been made clear whether the draft or the bow radius can be a reference length scale (Matsui et al.).

Summarizing all the experiments, which will be shown in the following sections, a flow model is introduced as shown in Fig. 3; the bow-wave is assumed to consist of the three regions with significantly different flow-characteristics.

The "MR-zone" is the part ahead of the obstacle where the free-surface is stable and rising monotonically with a concave curvature. Through a sharp change of curvature, the flow enters the horseshoe-like "Z-zone" where it may not be stable. In the immediate vicinity of the bow, there develops a necklace vortex and the flow is reverse at the free-surface. The "toe" is the border between the MR-zone and the Z-zone; it can be called alternatively the "wave-front".

### 2.1 Wave Patterns and Profiles

Wave patterns were photographed at the two speeds for both models. Fig. 4 shows those of CM-42 at  $U_0 = 1.0$  m/sec and 1.2 m/sec. The wave-front is clearly observed surrounding the bow with capillary waves ahead of it. Inside the wave-front the Z-zone develops where the surface becomes rather unsteady or turbulent at  $U_0 = 1.2$  m/sec compared with that at  $U_0 = 1.0$  m/sec. Very close to the body, the necklace vortex is observed.

Fig. 5 shows photographs of EM-300 at  $U_0 = 0.85$  m/sec and 1.0 m/sec. A significant difference in surface disturbances of the Z-zone is observed between the two speeds; at  $U_0 = 1.0$  m/sec many wrinkles are observed, while the surface appears smooth at  $U_0 = 0.85$  m/sec.

The wrinkles of CM-42 are less intense than those of EM-300 at the same speed of  $U_0 = 1.0$  m/sec. On the other hand, the necklace vortex of CM-42 seems larger and more intense than that of EM-300.

Fig. 6 shows the wave profiles ahead of the bow of EM-300. Photographs, taken horizontally, show the wave profiles on a symmetry plane ( $y = 0$ ). The plateau-like elevation, which corresponds to the Z-zone with wrinkles,

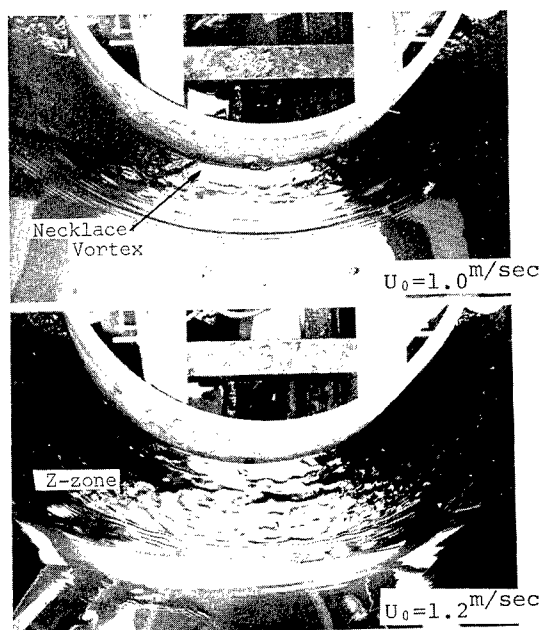


Fig.4 Bow-Wave Patterns of CM-42



Fig.5 Bow-Wave Patterns of EM-300

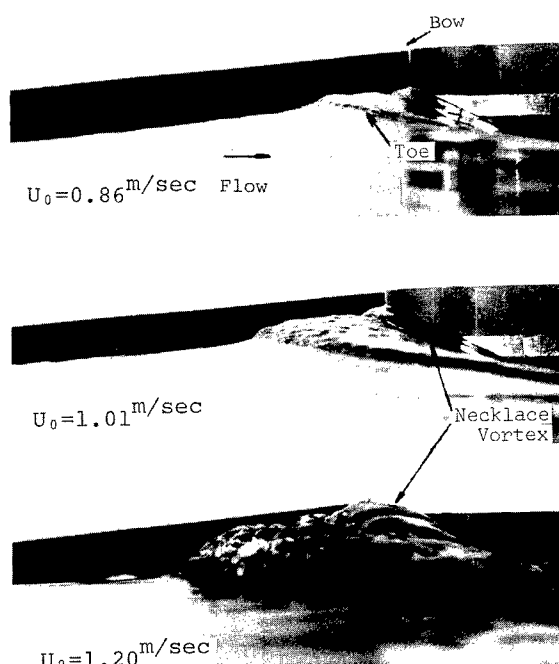


Fig.6 Bow-Wave Profiles of EM-300

becomes larger as the velocity of the incident flow increases and the necklace vortex becomes more prominent.

The free-surface in the Z-zone seems to become turbulent or unsteady beyond a certain speed. The turbulence of the free-surface is other than the breaking; there is neither reverse nor plunging flow. The turbulent flow, however, develops into breakings at higher speeds merging with the reverse flow of the necklace vortex.

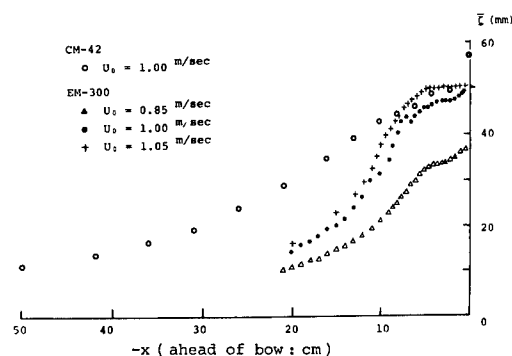


Fig.7 Bow-Wave Heights of CM-42 and EM-300

Upstream, the free-surface is observed to rise monotonically without any instabilities. It can be clearly distinguished from the Z-zone flow. The gradients and the curvatures of the surface seem to increase as the incident flow velocity increases. There is a sharp change in the curvature at the toe.

The above situation can be quantitatively understood by Fig. 7 showing measured wave profiles. It is noteworthy that the free-surface of CM-42 has less curvature than that of EM-300.

The plateaus of CM-42, and EM-300 at  $U_0 = 0.85$  m/sec are less horizontal than those of EM-300 at  $U_0 = 1.0$  m/sec and  $1.05$  m/sec. We should remind that the wrinkles of the formers are much less than those of the latters; the flatness of the plateau, i.e.,  $w/u$  is suspected to be related to the

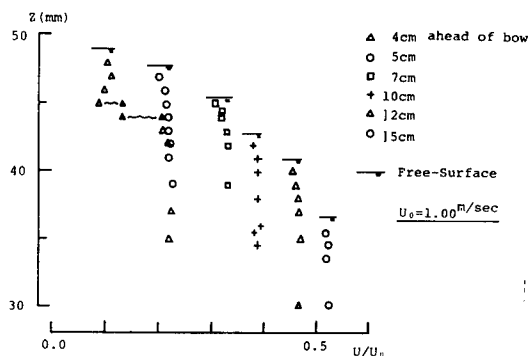


Fig.8 Mean Velocity of CM-42

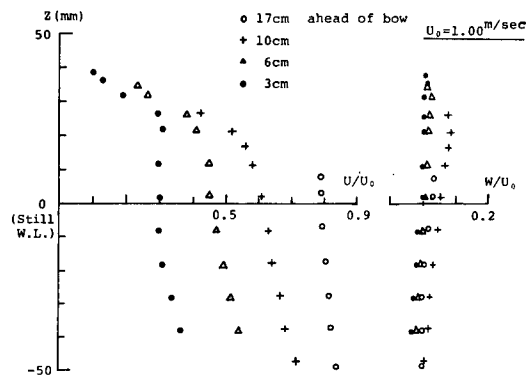


Fig.9 Mean Velocity of EM-300

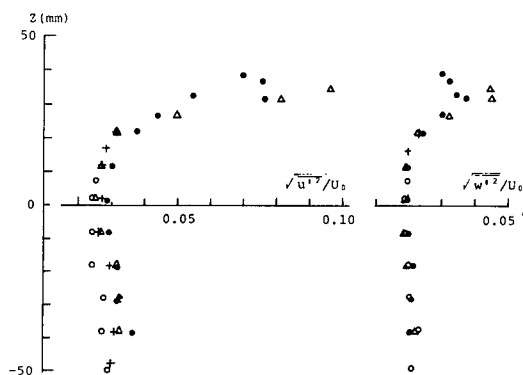


Fig.10 Turbulence Intensity of EM-300  
(for symbols see Fig.9)

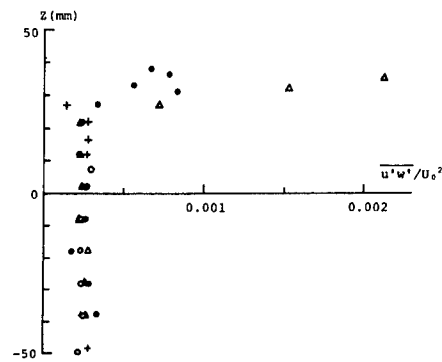


Fig.11 Reynolds Stress of EM-300 (for  
symbols see Fig.9)

occurrence of the wrinkles, the instability of the free-surface flow.

## 2.2 Mean Velocity and Turbulence

Mean velocity and turbulent quantities were measured in the plane of symmetry ( $y = 0$ ), assuming the flow is symmetric; i.e.  $v = 0$ . Measurements for CM-42 were carried out by a total-pressure tube with 1.0 mm diameter at the towing tank of Hiroshima University, while for EM-300 by a X-type hot-film anemometer at a circulating water channel. The supports of probes were set carefully as to avoid possible disturbances. The speed of measurement was 1.0 m/sec for both models. The measuring position is designated as  $X_3$  etc. when it is 3 cm ahead of the bow.

Fig. 8 shows the mean velocity profiles of CM-42. Only the x-component was measured. Although it is quite modest, some velocity defects can be seen beneath the free-surface. A free-surface shear layer is suspected to develop there.

This is shown more clearly by the results for EM-300 given in Fig. 9. Measurements were

carried out at four positions;  $X_{10}$  and  $X_{17}$  are in the MR-zone, while  $X_6$  approximately at the toe and  $X_3$  in the Z-zone. Significant velocity defects are observed at  $X_3$ ,  $X_6$  and  $X_{10}$ , but none at  $X_{17}$ . The velocity profile at  $X_{10}$  suggests that the velocity defect exists even in the MR-zone where nothing particular seems to happen such as unsteady flows in the Z-zone. No reverse flows are observed in the Z-zone.

We should remember here that the curvature of the free-surface profile of CM-42 is quite small while that of EM-300 has relatively appreciable concave curvatures. Some analytical relations between the velocity defect and the curvature of the free-surface will be derived in the following section. The thin layer where the velocity defect exists can be referred to as the free-surface shear layer.

The vertical component  $w$  is almost zero at  $X_3$  and  $X_6$  which are both in the Z-zone. This should be borne in mind in the forthcoming discussion in §3-3.

Figs. 10, 11 and 12 show the results of the turbulence measurements for EM-300. These were carried out in the circulating water channel where the mainstream turbulence intensity is less than 1% but locally about

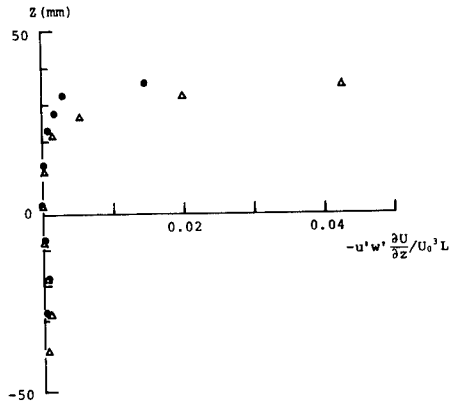


Fig.12 Turbulence Production of EM-300  
(for symbols see Fig.9)

2 ~ 3% in the vicinity of the free-surface, while the Reynolds stress is zero except near the free-surface.

The turbulence intensities, shown in Fig. 10, are considerable in the free-surface shear layer at  $X_3$  and  $X_6$ , while those at  $X_{10}$  and  $X_{17}$  are effectively zero. Since  $X_3$  and  $X_6$  are in the Z-zone, the wrinkles of the free-surface observed in Fig. 5 appear to be due to turbulent fluctuations of the free-surface. Thus it can be concluded that the Z-zone is that where the free-surface flow can be turbulent while, in the MR-zone, that is impossible. The turbulent surface-flow may be called a sub-breaking wave to distinct from the breaking-wave. This is because the turbulent surface-flow has neither reverse nor plunging flow but develops into breaking waves.

Figs. 11 and 12 show the Reynolds stress and the turbulence production respectively. It is interesting to note that both the Reynolds stress and the production are much greater at  $X_6$  than at  $X_3$ . Because  $X_6$  is just inside the toe, the turbulent flow may be supposed to be generated at the toe; in other words, the toe plays the role of a trigger for the turbulence transition when some required conditions for turbulence are present.

Summarizing the experimental results, the following tentative conclusions may be drawn.

- 1) The bow wave consists of three regions. One is where the free-surface rises monotonically (MR-zone); the second is a plateau-like elevated region where the surface-flow becomes turbulent beyond a certain velocity (Z-zone); and the last is the necklace vortex.
- 2) The free-surface curvature, the surface wrinkles (turbulence) and the velocity defect of CM-42 are all less than those of EM-300, while the necklace vortex is much more intense than that of EM-300.
- 3) Turbulence transition takes place around the wave-front where a sharp change of the free-surface curvature exists.
- 4) In the plateau-like region, the vertical

velocity component is almost zero when the sub-breaking wave exists.

- 5) A thin shear layer exists below the free-surface where the velocity component in the main stream direction has a defect.

### 3. THEORETICAL DISCUSSION ON BOW-WAVE PHENOMENA

In this section, possible theoretical explanations of the experimental results are proposed.

#### 3.1 Free-Surface Shear Layer

The theoretical background for the free-surface shear layer is given in the textbook of Batchelor (1970). The governing equation for it is derived in the integral form in Mori (1983).

In a curvilinear coordinate system ( $0-x_1 x_2 x_3$ ), shown in Fig. 2, the zero-shearing stress condition on the free-surface is given as follows;

$$\mu \left( \frac{\partial u_1}{\partial x_3} - \frac{u_1}{h_1 h_3} \frac{\partial h_1}{\partial x_3} \right) = 0, \quad (1)$$

$$\mu \left( \frac{\partial u_2}{\partial x_3} - \frac{u_2}{h_2 h_3} \frac{\partial h_2}{\partial x_3} \right) = 0, \quad \text{on } x_3 = 0,$$

where  $u_i$  is the velocity component in the  $x_i$ -direction and  $\mu$  is the viscosity coefficient;

$$h_i = \sqrt{\left( \frac{\partial x}{\partial x_i} \right)^2 + \left( \frac{\partial y}{\partial x_i} \right)^2 + \left( \frac{\partial z}{\partial x_i} \right)^2}. \quad (2)$$

(1) is automatically satisfied if  $\mu = 0$ , otherwise,

$$\frac{\partial u_1}{\partial x_3} - \frac{u_1}{h_1 h_3} \frac{\partial h_1}{\partial x_3} = 0, \quad (3)$$

$$\frac{\partial u_2}{\partial x_3} - \frac{u_2}{h_2 h_3} \frac{\partial h_2}{\partial x_3} = 0, \quad \text{on } x_3 = 0.$$

On the other hand, the  $x_1$ - and  $x_2$ -components of vorticity on the free-surface are

$$\omega_1 = - \frac{\partial u_2}{\partial x_3} - \frac{u_2}{h_2 h_3} \frac{\partial h_2}{\partial x_3}, \quad (4)$$

$$\omega_2 = \frac{\partial u_1}{\partial x_3} + \frac{u_1}{h_1 h_3} \frac{\partial h_1}{\partial x_3}, \quad \text{on } x_3 = 0.$$

Then, from (3) and (4), we have

$$\omega_1 = -2 \frac{u_2 \partial h_2}{h_2 h_3 \partial x_3} = -2\kappa_1 u_2, \quad (5)$$

$$\omega_2 = 2 \frac{u_1 \partial h_1}{h_1 h_3 \partial x_3} = 2\kappa_2 u_1,$$

where  $\kappa_1$  and  $\kappa_2$  are curvatures of the free-surface given by

$$\left\{ \begin{matrix} \kappa_1 \\ \kappa_2 \end{matrix} \right\} = - \left\{ \frac{\partial^2 \xi / \partial y^2}{\partial^2 \xi / \partial x^2} \right\} \cdot \left[ 1 + \left( \frac{\partial \xi}{\partial x} \right)^2 + \left( \frac{\partial \xi}{\partial y} \right)^2 \right]^{-\frac{3}{2}}, \quad (6)$$

$\zeta(x, y)$  is the wave elevation.

$\omega_1$  and  $\omega_2$  are obviously not zero if non-zero free-surface curvatures exist; and eventually nonzero velocity gradients exist on the free-surface. If the curvature is negative as in the MR-zone, a shear layer may be present underneath the free-surface.

Now we can offer an explanation for the fact that the velocity defect of CM-42 is more modest than that of EM-300. We need only to recall that the free-surface curvature of the former is less than that of the latter. The toe, at which the sign of the free-surface curvature changes, is likely to play the role as a trigger for the inception of the turbulence; a sharp change of the curvature must be followed by a rapid change of vorticity which is hardly attained.

As stated in §3.3, the velocity defect in the Z-zone becomes more intense by the headloss due to the turbulence production.

### 3.2 Formation of Necklace Vortex

We assume that the vorticity generated in the free-surface shear layer is one of the sources of vortex motion of the necklace vortex. As the drift theory, Lighthill (1956), suggests, even a slight vorticity can form an intense vortex because of the stretching of vortex tubes.

In an inviscid fluid, the circulation remains constant while a vortex tube moves with fluid particles (Helmholtz's theorem);

$$|\omega \cdot \Delta s| = \text{const.}, \quad (7)$$

where  $\omega$  is the vorticity vector and  $\Delta s$  is the sectional area of the vortex tube. Invoking the continuity condition

$$\Delta s \cdot l = \text{const.}, \quad (8)$$

we have

$$\left| \frac{\omega(t+\Delta t)}{\omega(t)} \right| = \left| \frac{l(t+\Delta t)}{l(t)} \right|, \quad (9)$$

where  $l$  represents the length of a material line element which was initially chosen to be parallel to the local vorticity;  $t$  is the time and  $\Delta t$  is a small time increment.

Solving (9) is equivalent to solving the vorticity transport equation with the viscous diffusion term neglected. Here it is solved numerically by the Lagrangian approach.

Fig. 13 shows the stretching of the vortex tube of CM-42 and EM-300, obtained by the double-model flow calculation. The particles, consisting of a material element of vortex tubes, change their relative positions (initially on the straight line at  $2x/L = -2.0$  and  $-1.46$  for CM-42 and EM-300 respectively;  $L$ : length of model) as they move downstream. In the case of CM-42, the vortex tube is stretched more than ten-times around the stagnation point, but somewhat less in the case of EM-300. Since this ratio is equal to the vorticity intensification, the vorticity of CM-42 is much more amplified than that of EM-300. This supports the experimental findings that the necklace vortex of CM-42 is more intense than that of EM-300.

Fig. 14 shows the equi-vorticity contours of CM-42. The results show how the intensity of the vorticity, initially assumed to be unity, increases in strength as the particles flow downstream. Both the  $x$ - and  $y$ -components,  $\omega_x$  and  $\omega_y$  say respectively, are seen to grow as much as five- or seven-times. The accumulated vorticity around the bow can be

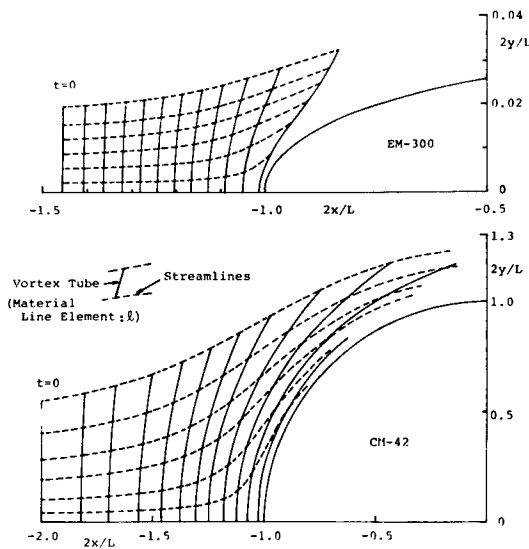


Fig.13 Stretching of Vortex Tube of CM-42 and EM-300

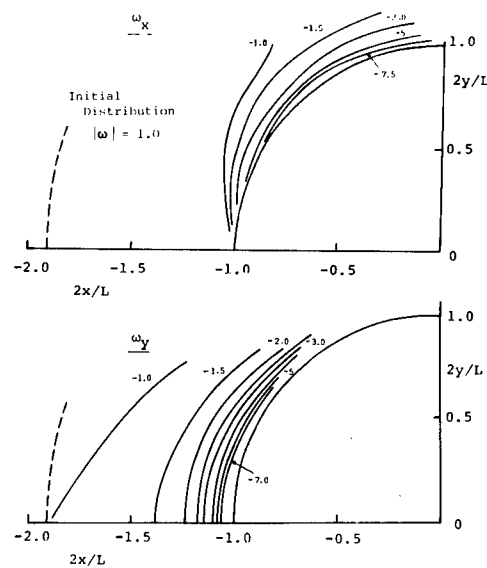


Fig.14 Equi-Vorticity Contour of CM-42

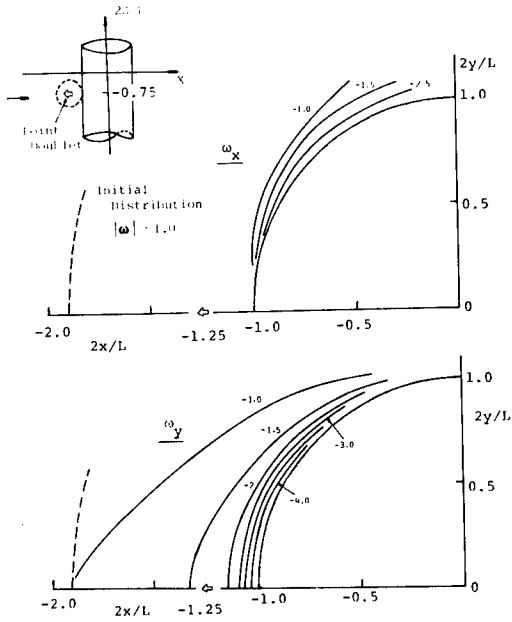


Fig.15 Equi-Vorticity Contour of CM-42 with a Point Doublet at Bow

observed as a necklace vortex.

It can be concluded that the basic flow is one of the important factors for forming the necklace vortex. This suggests that it may be possible to prevent the formation of the necklace vortex by modifying the basic flow on the free-surface.

Fig. 15 shows the equi-vorticity contours of CM-42 with a point doublet, whose moment is  $0.015U_0L^3$ , in front of the bow. In this accelerated flow by it, the vorticity intensification is seen to be greatly reduced. Since a point doublet approximately simulates a large bow-bulb, the present results may explain in the effectiveness of bulbs attached to full low-speed ships.

### 3.3 Discussion of Momentum Balance

We discuss the stability of the bow-wave flow by means of the small disturbance analysis. Though any turbulent flow cannot be 2-dimensional, we confine ourselves to a 2-D flow, which is expected to be applicable to the bow-wave flow on the symmetric plane,  $y=0$ , discussed in the previous section.

The momentum equations are

$$\frac{\partial u}{\partial t} + u \frac{\partial u}{\partial x} + w \frac{\partial u}{\partial z} = -\frac{1}{\rho} \frac{\partial p}{\partial x} + \nu \nabla^2 u, \quad (10)$$

$$\frac{\partial w}{\partial t} + u \frac{\partial w}{\partial x} + w \frac{\partial w}{\partial z} = -\frac{1}{\rho} \frac{\partial p}{\partial z} - g + \nu \nabla^2 w, \quad (11)$$

where  $p$ : pressure,  $g$ : gravity acceleration,  $\rho$ : density,  $\nu$ : kinematic viscosity coefficient and  $\nabla^2 = \partial^2/\partial x^2 + \partial^2/\partial z^2$ .

Invoking the boundary layer assumptions, (11) becomes

$$-\frac{1}{\rho} \frac{\partial p}{\partial z} - g = 0. \quad (12)$$

Substitution of (12) into (10) yields

$$\frac{\partial u}{\partial t} + u \frac{\partial u}{\partial x} + w \frac{\partial u}{\partial z} = -g \frac{\partial \xi}{\partial x} + \nu \nabla^2 u, \quad (13)$$

where  $\xi$  is the free-surface elevation.

The kinematic condition on the free-surface is given by

$$\frac{\partial \xi}{\partial t} + u \frac{\partial \xi}{\partial x} - w = 0, \quad \text{on } z = \xi. \quad (14)$$

Eliminating  $\partial \xi / \partial x$  from (13) and (14), we obtain

$$u \frac{\partial u}{\partial t} + u^2 \frac{\partial u}{\partial x} + uw \frac{\partial u}{\partial z} + wg = g \frac{\partial \xi}{\partial t} + \nu u \nabla^2 u, \quad \text{on } z = \xi. \quad (15)$$

Now we write the velocity and the wave height in the forms of

$$u = U + u', \quad w = W + w', \quad \xi = \bar{\xi} + \xi', \quad (16)$$

where  $U$ ,  $W$  and  $\bar{\xi}$  are the time-averaged components, while  $u'$ ,  $w'$  and  $\xi'$  are the disturbances.

Substituting (16) into (15) and taking a time-average, we get

$$\begin{aligned} & \overline{u' \frac{\partial u'}{\partial t}} + U^2 \frac{\partial U}{\partial x} + (2Uu' + u'^2) \frac{\partial U}{\partial x} + \overline{u'^2} \frac{\partial U}{\partial x} \\ & + UW \frac{\partial U}{\partial z} + (Uw' + Wu' + u'w') \frac{\partial U}{\partial z} + \overline{u'w'} \frac{\partial U}{\partial z} \\ & = -gW + \nu(U \nabla^2 U + \overline{u' \nabla^2 u'}), \end{aligned} \quad (17)$$

where  $\overline{\quad}$  denotes the time-average.

(17) is a time-averaged equation through which we can discuss momentum or energy balances of the fluid motion. The last term on the lhs can be assumed the most important term among those related to the disturbance quantities, and the viscous term is assumed small compared with the convection terms. Then (17) can be simplified into

$$U^2 \frac{\partial U}{\partial x} + UW \frac{\partial U}{\partial z} + gW + \overline{u'w'} \frac{\partial U}{\partial z} = 0, \quad z = \bar{\xi}. \quad (18)$$

On the other hand if there exists a flow with velocity components  $u_0$ ,  $w_0$  with neither velocity defects nor disturbances, the free-surface flow, assumed to be irrotational, satisfies

$$u_0^2 \frac{\partial u_0}{\partial x} + u_0 w_0 \frac{\partial w_0}{\partial x} + g w_0 = 0, \quad z = \xi_0. \quad (19)$$

Let  $\xi_0$  be the associated free-surface elevation. Such a flow which satisfies (19) on the free-surface may be supposed to be related to

an outer flow to the shear layer.

Under the approximation of

$$W = w_0 \text{ and } \bar{\xi} = \xi_0, \quad (20)$$

the subtraction of (19) from (18) yields

$$\frac{1}{2} (U \frac{\partial U^2}{\partial x} - u_0 \frac{\partial u_0^2}{\partial x}) = W (u_0 \frac{\partial W}{\partial x} - U_0 \frac{\partial U}{\partial z}) - \overline{u'w'} \frac{\partial U}{\partial z}, \quad z = \xi_0. \quad (21)$$

In order to interpret (21) qualitatively, we write approximately,

$$U(x, \xi_0) = u_0(x, \xi_0)(1 - \epsilon), \quad (22)$$

where  $\epsilon$  is the velocity-defect fraction. If  $\epsilon$  is assumed small, we have

$$-\frac{3}{2} \epsilon u_0 \frac{\partial u_0^2}{\partial x} = -u_0 W \omega_y - \overline{u'w'} \frac{\partial U}{\partial z}. \quad (23)$$

(23) suggests that the changes in the energy transport caused by the velocity defect (lhs, E say) is balanced by the vorticity transport (the first term on the rhs, V say) and the turbulence production (the second on the rhs, T say). In the decelerating region, E is positive and both V and T are also positive.

According to the experimental results, W is appreciable in the MR-zone and hence V is also but T is not. Therefore we have  $E \neq V$ . On the other hand, in the Z-zone, where the free-surface is like a plateau and W is almost zero, V is negligible there, T becomes large, as shown in Fig. 12, and we have  $E \neq T$ . In other words, the production on the turbulence compensates for the surplus momentum due to the velocity defect. (23) also implies a possibility that the turbulence production may amplify the velocity defect still more; it can be resumed as the head loss.

The above discussion implies that the velocity defect is the most important factor for generation of unsteady free-surface flow, because, if there is no velocity defects, i.e., if  $E = 0$ , nothing can happen. Of course the present discussion does not explain the occurrence of the turbulence and nature of the flow in the Z-zone.

### 3.4 Discussion of Instability of Disturbance

For the discussion of the instability of disturbance, we substitute (16) into (13), (14) and the continuity equation. Then the disturbance components satisfy

$$\frac{\partial u'}{\partial t} + U \frac{\partial u'}{\partial x} + u' \frac{\partial U}{\partial x} + w' \frac{\partial U}{\partial z} + W \frac{\partial u'}{\partial z} = -g \frac{\partial \xi'}{\partial x} + \nu \nabla^2 u', \quad (24)$$

$$\frac{\partial \xi'}{\partial t} + U \frac{\partial \xi'}{\partial x} + u' \frac{d\bar{\xi}}{dx} - w' = 0, \quad (25)$$

and

$$\frac{\partial u'}{\partial x} + \frac{\partial w'}{\partial z} = 0. \quad (26)$$

Because all the disturbant variables appear in linear forms in (24), (25) and (26), they can be written in the form

$$\begin{Bmatrix} u' \\ w' \\ \xi' \end{Bmatrix} = \begin{Bmatrix} \hat{u}(z) \\ \hat{w}(z) \\ \hat{\xi} \end{Bmatrix} e^{i\alpha(x-ct)}, \quad (27)$$

where  $\hat{u}$ ,  $\hat{w}$  and  $\hat{\xi}$  are real while  $\alpha$  and  $c$  are complex variables;  $i = \sqrt{-1}$ .

By making use of (27); (24), (25) and (26) may be written as follows:

$$-i\alpha c \hat{u} + i\alpha U \hat{u} + \hat{u} \frac{\partial U}{\partial x} + \hat{w} \frac{\partial U}{\partial z} + W \frac{d\hat{u}}{dz} = -i\alpha g \hat{\xi} + \nu (-\alpha^2 \hat{u} + \frac{d^2 \hat{u}}{dz^2}), \quad (28)$$

$$-i\alpha c \hat{\xi} + i\alpha U \hat{\xi} + \hat{u} \frac{d\bar{\xi}}{dx} - \hat{w} = 0, \quad (29)$$

and

$$i\alpha \hat{u} + \frac{d\hat{w}}{dz} = 0. \quad (30)$$

Eliminating  $\hat{u}$  and  $\hat{\xi}$  from (28), (29) and (30), we obtain

$$i\alpha \left( \frac{\partial U}{\partial z} + \frac{g}{U^*} \right) \hat{w} - (i\alpha U^* + \frac{\partial U}{\partial x} - \frac{g}{U^*} \frac{d\bar{\xi}}{dx}) \frac{d\hat{w}}{dz} - W \frac{d^2 \hat{w}}{dz^2} + \nu (-\alpha^2 \frac{d\hat{w}}{dz} + \frac{d^3 \hat{w}}{dz^3}) = 0, \quad (31)$$

where  $U^* = U - c$ .

If  $\nu$  can be assumed small enough, we obtain

$$\alpha \left( \frac{\partial U}{\partial z} + \frac{g}{U^*} \right) \hat{w} + i \left( i\alpha U^* + \frac{\partial U}{\partial x} - \frac{g}{U^*} \frac{d\bar{\xi}}{dx} \right) \frac{d\hat{w}}{dz} + iW \frac{d^2 \hat{w}}{dz^2} = 0, \quad z = \bar{\xi} \quad (32)$$

(32) may be referred to the inviscid Orr-Sommerfeld equation for the 2-D free-surface flow where  $\hat{w}$  is the unknown.

We assume that (32) has a solution in the form

$$\hat{w} \propto e^{\kappa z}, \quad (33)$$

In order for the disturbance to vanish as  $z \rightarrow -\infty$ , the real part of  $\kappa$  must be positive.

The substitution of (33) into (32) yields a characteristic equation for  $\kappa$ ;

$$\alpha \left( U_z + \frac{g}{U^*} \right) + (-\alpha U^* + iU_x - i\frac{g}{U^*} \bar{\xi}_x) \kappa + i\kappa^2 W = 0, \quad (34)$$

where the subscripts denote the differentiations with the referred variables. (34) is written in a nondimensional form by  $U_0$  and  $\alpha$ ,

$$W\kappa^2 + (U_X - \frac{1}{F^2} \frac{\bar{\xi}_X}{U^*} + iU^*)\kappa - i(U_Z + \frac{1}{F^2} \frac{1}{U^*}) = 0, \quad (35)$$

where all the variables are used with the same notations and  $F^2 = U_0^2 \alpha / g$ .

Here we discuss the temporal growth, and  $\alpha$  is supposed to be real. Putting  $C = C_r + iC_i$ , the exponential part of (27) is nondimensionally written as

$$e^{-i(x - C_r t) + C_i t}, \quad (36)$$

where  $C_r$  and  $C_i$  are real. If  $C_i$  is negative, the disturbance may vanish temporally; the flow can be steady and no sub-breaking waves ensue.

As suggested by (35), the analysis depends on whether  $W = 0$  or not. We therefore discuss each case separately. Recall that  $W \neq 0$  in the Z-zone while  $W \approx 0$  in the MR-zone.

i)  $W = 0$

For this case,  $\bar{\xi}_X$  can be assumed zero; (35) becomes

$$(U_X + iU^*)\kappa - i(U_Z + \frac{1}{F^2} \frac{1}{U^*}) = 0, \quad (37)$$

and the real part of  $\kappa$ ,  $\kappa_r$  say, is given by

$$\kappa_r = \frac{1}{(U_X + C_i)^2 + U_r^{*2}} \left\{ -\frac{U_X + C_i}{U_r^{*2} + C_i^2} \cdot \frac{C_i}{F^2} + U_r^* \left( U_Z + \frac{U_r^*}{U_r^{*2} + C_i^2} \cdot \frac{1}{F^2} \right) \right\}. \quad (38)$$

The solution of (38) with  $\kappa_r > 0$  and  $C_i < 0$  provides a stability criterion for every wave number. We discuss here only an extreme case where  $\kappa_r \rightarrow 0$ ; this may give the sufficient conditions for the convergence.

Then (38) is

$$C_i^2 (U_r^* U_Z F^2 - 1) - U_X C_i + U_r^{*2} (1 + U_r^* U_Z F^2) = 0. \quad (39)$$

In order for  $C_i$  to be real and negative, the following two inequalities are required:

$$U_X^2 - 4U_r^{*2} (U_r^{*2} U_Z^2 F^4 - 1) > 0, \quad (40)$$

$$(U_r^* U_Z F^2 - 1) \{ U_X \pm \sqrt{U_X^2 - 4U_r^{*2} (U_r^{*2} U_Z^2 F^4 - 1)} \} < 0. \quad (41)$$

It suffices that (41) be satisfied by either sign. For the decelerating flow, where  $U_X < 0$ , the inequality (41) can be satisfied by choosing the plus sign for  $U_r^* U_Z F^2 < 1$  and the minus for  $U_r^* U_Z F^2 > 1$ .

Then the inequalities of (40) is the only condition for the stability. It yields

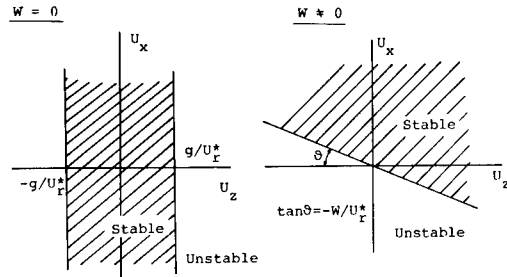


Fig.16 Stability Zone for Free-Surface Disturbance

$$-\frac{g}{U_r^*} \sqrt{1 + \frac{1}{4} \left( \frac{U_X}{\alpha U_r^*} \right)^2} < U_Z < \frac{g}{U_r^*} \sqrt{1 + \frac{1}{4} \left( \frac{U_X}{\alpha U_r^*} \right)^2}. \quad (42)$$

The variables in (42) are all dimensional. As the experimental data suggest that the wave number of the disturbance, if any, is quite large, we may assume  $1/\alpha \ll 1$ . Then (42) may be simply written as

$$-\frac{g}{U_r^*} < U_Z < \frac{g}{U_r^*}. \quad (43)$$

In the similar way, (43) is obtained for  $U_X > 0$  also.

(43) implies that, if the velocity defect is not greater than  $g/U_r^*$ , as seen in Fig. 16, the free-surface can be stable; namely, no sub-breaking waves can exist. In the vicinity of a body, where  $U_r^*$  becomes smaller, the sub-breaking waves may be less possible, because the stability band for  $U_Z$  becomes wider. This finding is supported by the experimental results that the turbulent intensity at  $X_3$  is less than that at  $X_6$ .

ii)  $W \approx 0$

Since  $\alpha$  is supposed large enough, i.e.,  $1/F^2 \ll 1$ , we drop the terms carrying  $1/F^2$ ; then (35) is simplified as

$$W\kappa^2 + (U_X + iU^*)\kappa - iU_Z = 0. \quad (44)$$

Then the real part of the solution is given by

$$\kappa_r = \frac{1}{2W} [-(U_X + C_i) \pm \text{Re} \{ \sqrt{D} \}], \quad (45)$$

where

$$D = (U_X + C_i)^2 - U_r^{*2} + 2i \{ (U_X + C_i) U_r^* + 2W U_Z \}, \quad (46)$$

and  $\text{Re} \{ \}$  means to have the real part of  $\{ \}$ .

We search for a criterion in the same manner as the previous case by setting  $\kappa_r \rightarrow 0$ ; (45) becomes



$$(U_x + C_i)^2 = [\text{Re} \{\sqrt{D}\}]^2, \quad (47)$$

where

$$[\text{Re} \{\sqrt{D}\}]^2 = \frac{1}{2}[(U_x + C_i)^2 - U_r^{*2} + \sqrt{\{(U_x + C_i)^2 + U_r^{*2}\}^2 + 16WU_z\{(U_x + C_i)U_r^{*2} + WU_z\}}]. \quad (48)$$

(47) is reduced to

$$U_z \{(U_x + C_i)U_r^{*2} + WU_z\} = 0. \quad (49)$$

If  $U_z \neq 0$ , the stability condition,  $C_i < 0$ , yields an inequality of

$$U_r^{*2}(WU_z + U_r^{*2}U_x) > 0 \quad (50)$$

(50) is illustrated in Fig. 16 for the positive  $U_r^{*2}$ . It is made clear by (50) that  $U_x$ ,  $U_z$  and  $U_r^{*2}$  are the key variables for the stability as suspected experimentally. The negative values of  $U_x$  and  $U_z$  possibly lead to the instability. For the negative  $U_x$ , only the positive  $U_z$  can conditionally provide a stable flow. On the other hand, for the negative  $U_z$ , only the positive  $U_x$  can attain it; a smaller value of  $W/U_r^{*2}$  widens the stability band.

It can be safely concluded that there is a certain criterion for a stable bow-flow and that  $U_x$ ,  $U_z$  and  $U$  on the free-surface are its key variables.

#### 4. CONTROL OF WAVE-BREAKING BY SP-BULB

According to the previous discussion, the control of wave-breakings is possible by preventing the inception of a turbulent flow; the sub-breaking wave. Because the velocity defect,  $U_z$ , and the deceleration rate,  $U_x$ , are concluded as important factors for the instability, as well as  $U$ , it may be effective to minimize the surface curvature and to accelerate the surface flow. To moderate the change of curvatures at the toe and to maximize the vertical velocity-component in the Z-zone are also favorable.

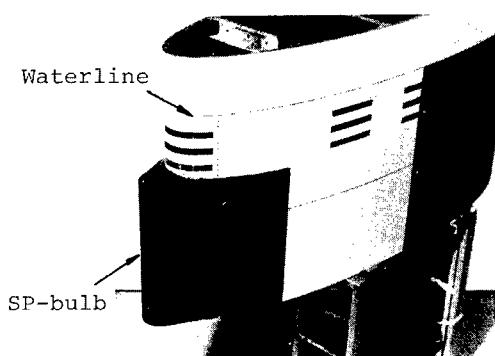


Fig.17 EM-300 with SP-Bulb

For this sake, an SP-bulb is attached to EM-300 which has rather a wide upper area and is cylindrical as shown in Fig. 17. Fig. 18 shows the measured wave profiles; the attachment of the bulb makes the free-surface curvature less. The smaller curvature is expected to decrease the velocity defect and eventually the turbulence.

Fig. 19 shows the comparison of the velocity at  $X_6$  between with and without the SP-bulb. Though the  $W$  component stays unchanged, the velocity defect,  $U_z$ , is remarkably diminished. Differences in the turbulence quantities are still more significant; Fig. 20 shows the comparison of the turbulence intensity. Both the Reynolds stress and the turbulence production, shown in Figs. 21 and 22, are strikingly oppressed by the bulb.

The above changes bring forth improvements in wave making phenomena. Fig. 23 is the wave profile at  $U_0 = 1.01$  m/sec with the SP-bulb. Compared with that shown in Fig. 6, the free-surface curvature is less and the Z-zone is not distinguished any more. Fig. 24 is the top-view picture of the bow-wave; compared with Fig. 5, the wrinkles in the Z-zone have all faded away. It is surprising that a slight change in the wave profile, which is attained by the attachment of a bulb here, yields such big changes in the velocity field and in the free-surface flow.

The practical application of the SP-bulb to a high speed fishing boat is attempted (Tamashima et al. 1984) where it is reported that the SP-bulb prevents the occurrence of the sub-breaking waves and that the breaking-waves are eventually reduced strikingly.

Through the present study, the effectiveness of the SP-bulb is made clear. Although the configuration of the bulb is determined intuitively here, it can be done theoretically for the key factors such as  $U$ ,  $U_x$  and  $U_z$  to be favorable. Thus the control of the wave

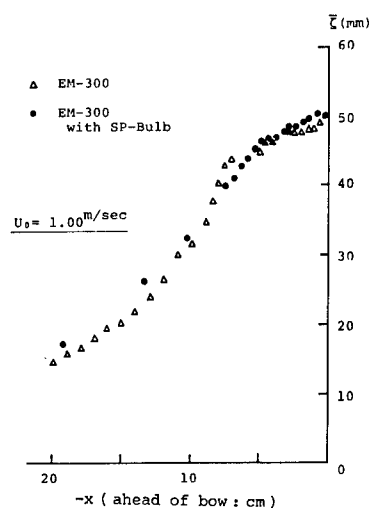


Fig.18 Comparison of Bow-Wave Heights of EM-300 with and without SP-Bulb

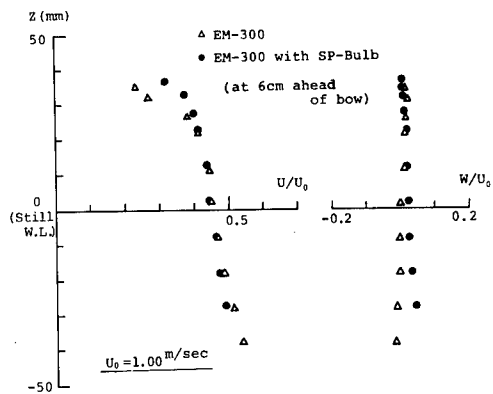


Fig.19 Comparison of Mean Velocity of EM-300 with and without SP-Bulb

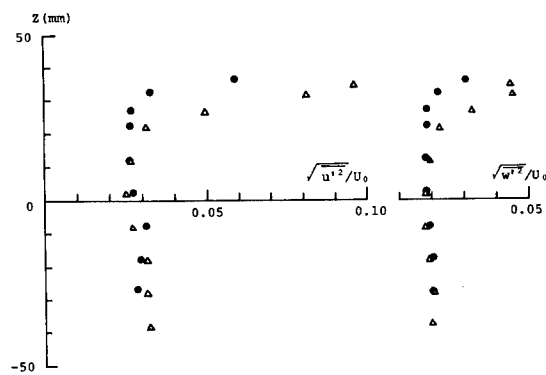


Fig.20 Comparison of Turbulence Intensities of EM-300 with and without SP-Bulb (for symbols see Fig.19)

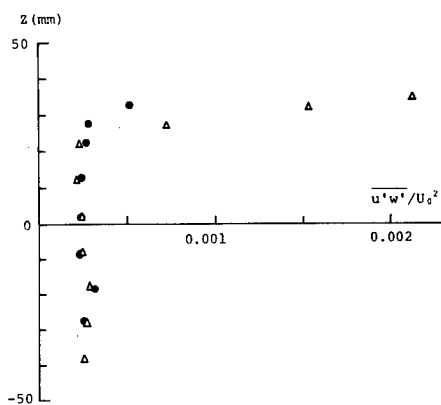


Fig.21 Comparison of Reynolds Stress of EM-300 with and without SP-Bulb (for symbols see Fig.19)

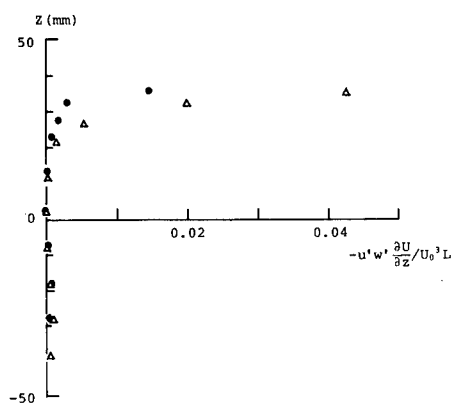


Fig.22 Comparison of Turbulence Productions of EM-300 with and without SP-Bulb (for symbols see Fig.19)

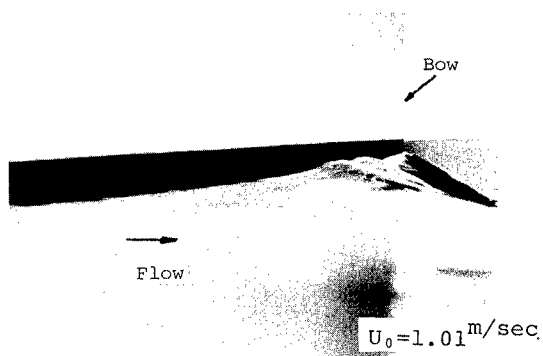


Fig.23 Bow-Wave Profile of EM-300 with SP-Bulb

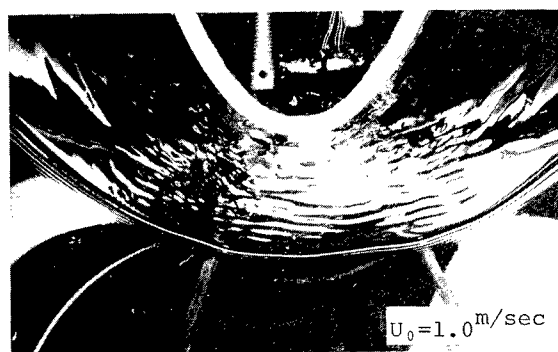


Fig.24 Bow-Wave Pattern of EM-300 with SP-Bulb

breaking is expected to be done by an off-design procedure.

## 5. CONCLUSIONS

Bow waves around a circular cylinder and an elliptic cylinder are studied being stressed on breakings.

Prior to the breakdown, turbulent flow becomes visible on the free-surface. There is a monotonically-rising-surface ahead of the turbulent zone, and a necklace vortex is at the bow. The formation of the necklace vortex is explained by the stretching theory of vorticity. A shear layer exists beneath the free-surface for which the surface curvature is responsible.

The turbulent surface is referred to as a sub-breaking wave which provides neither a reverse flow nor a plunging flow, but it develops into breaking-waves beyond a certain speed. The turbulent intensity of the sub-breaking wave is much related to the free-surface curvature, the velocity defect in the free-surface shear layer and the decelerating rate. Their relation is derived in a time-averaged momentum rate equation.

An instability analysis is made to conclude that there are certain criteria for the appearance of the sub-breaking wave.

Through the present study on the sub-breaking wave, an SP-bulb is suggested to suppress the wave-breaking. It is confirmed experimentally that a slight change in the bow flow to increase the surface flow velocity and to decrease the surface curvature makes the sub-breaking waves significantly less.

## ACKNOWLEDGEMENT

The present study is initiated while the author was staying at the Institute of Hydraulic Research, The University of Iowa. He expresses his cordial thanks to Prof. L. Landweber at The Univ. of Iowa. The use of the drift theory is suggested by him.

The General Hydrodynamics Research program of the Naval Sea Systems Command, David W. Taylor Naval Ship Research and Development Center is appreciated for the partial support of the present study under the contract No. N00014-82-K0016.

The author wishes to extend his thanks to Prof. S. Hatano at Hiroshima University for his encouragements and discussion.

## REFERENCES

- Baba, E. (1969): A New Component of Viscous Resistance of Ships. *Jour. of The Soc. of Naval Arch. of Japan*, Vol. 125, pp. 23-34.
- Batchelor, G.K. (1970): *An Introduction to Fluid Dynamics*, Cambridge University Press, pp. 364.
- Battjes, J.B. and Sakai, T. (1981): Velocity Field in a Steady Breaker. *Jour. of Fluid Mech.*, Vol. 111, pp. 421-437.
- Dagan, G. and Tulin, M.P. (1972): Two-Dimensional Free-Surface Gravity Flow Past Blunt Bodies. *Jour. of Fluid Mech.*, Vol. 51, No. 3, pp. 529-543.
- Doi, Y., Kajitani, H., Miyata, H. and Kuzumi, S. (1981): Characteristics of Stern Waves Generated by Ships of Simple Hull Form. *Jour. of The Soc. of Naval Arch. of Japan*, Vol. 150, pp. 30-39.
- Duncan, J.H. (1983): The Breaking and Non-Breaking Wave Resistance of a Two-Dimensional Hydrofoil. *Jour. of Fluid Mech.*, Vol. 126, pp. 507-520.
- Inui, T., Kajitani, H., Miyata, H., Tsuruoka, M., Suzuki, A. and Ushio T. (1979): Non-Linear Properties of Wave Making Resistance of Wide-Beam Ships. *Jour. of The Soc. of Naval Arch. of Japan*, Vol. 146, pp. 18-26.
- Kayo, Y. and Takekuma, K. (1981): On the Free Surface Shear Flow related to Bow Wave Breaking of Full Models. *Jour. of Soc. of Naval Arch. of Japan*, Vol. 149, pp. 11-20.
- Kishimoto, O., Kusaka, Y., Tamura, M. and Miike, T. (1976): On the Observation of Flow Pattern in Front of Ship's Bow. 4th Symposium on Flow Visualization ISAS Univ. of Tokyo, pp. 53-56 (in Japanese).
- Lighthill, M.J. (1956): Drift. *Jour. of Fluid Mech.*, Vol. 1, pp. 31-53.
- Matsui, M., Kitazawa, T. and Nagahama, M. (1983): Observation of Nonlinear Waves around Ship Bow Models. *Jour. of The Kansai Soc. of Naval Arch.*, Japan, No. 190, pp. 63-71 (in Japanese).
- Mori, K. (1983): Free Surface Boundary Layer and Necklace Vortex Formation. Iowa Institute of Hydraulic Research Report, No. 262.
- Peregrine, D.H. and Svendsen, I.A. (1978): Spilling Breakers, Bores and Hydraulic Jumps. *Proc. of 16th Conf. Coastal Eng.*, pp. 540-550.
- Suzuki, K. (1975): On the Drag of Two-Dimensional Bluff Bodies Semi-Submerged in a Surface Flow. *Jour. of Soc. of Naval Arch. of Japan*, Vol. 137, pp. 22-35 (in Japanese).
- Tamashima, M., Nishimoto, H., Ogura, R. and Mori, K. (1984): Experimental Studies on Bow-Flow of Full High-Speed Ships under Calm Condition, to appear in *Trans. of The West-Japan Soc. of Naval Arch.*, No. 68 (in Japanese).
- Taneda, S. and Amamoto, H. (1969): Necklace Vortex of the Ship. *Bulletin of Research Institute for Applied Mechanics*, Vol. 31, pp. 17-28 (in Japanese).

## DISCUSSION

MITSUHIRO ABE,  
Mitsui Eng. & Shipbuilding Co., Akishima Lab.,  
Tokyo, Japan:

I congratulate Prof. Mori who analysed the bow wave mechanism. The SP-bulb will be effective, while there is a difficulty to apply at full scale. At the stage of designing ships, we have already taken into account the principle which the author presented. In my experience, when a SP-like bulb was applied, the free wave pattern resistance once tended to be worse than on the original hull, and the effect of it depended on the draft condition of the ship. Thus my point is that the design complex will be necessary to forward the development of SP-bulb.

Prof. SERGE BINDEL,  
Ecole Nationale Supérieure de Techniques Avancées,  
Paris, France:

I was very interested in the paper by Prof. Mori which gives a very good analysis of the phenomenon involved in bow wave-breaking. Nevertheless, the main question for the naval architect seems to me not so much to know how wave breaking can occur, and how it can be suppressed - we have known that for some years - but what is its true effect on the resistance of the ship. When wave breaking occurs energy is of course dissipated inside the fluid, but when it is suppressed there may exist some compensation, the part of the wave energy which is radiated being increased.

Therefore, I would like to ask Prof. Mori whether he believes that bow wave-breaking is so "catastrophic", and whether he can give us some information on the energy balance and on the experiments attempted on a high speed fishing boat.

Dr.-Ing. ALFRED KRACHT,  
Berlin Ship Model Basin (VWS),  
Berlin, Germany:

I would like to congratulate Mr. Mori on his interesting paper. The detailed results presented are a valuable contribution to the theory of bulbous bows. It is a pleasure to read this paper.

The bulb body influences the total velocity field ahead of a blunt body and acts like a straightener due to its additional displacement. The SP-bulb acts in the same way. Its slight change of the wave profile is a small part of its action only.

But some questions remain, which the author may care to comment on. What is the meaning of "SP-bulb"? What is the influence of a hydrofoil or foil grid on the flow field ahead of a blunt body? What is the geometrical configuration of the SP-bulb, which is attached to a high speed fishing boat? The sea-going qualities of a sharp edged bulb body are very unfavourable.

Prof. VIRENDRA C. PATEL,  
Iowa Institute of Hydraulic Research,  
Iowa City, IA, USA:

(This discussion addresses also the paper of K. Takekuma and K. Eggers.)

The authors are to be congratulated for presenting additional experimental evidence on the complexity of the flow over the bow. In both papers it is also shown that bow vortices can be explained on the basis of the amplification of vorticity in the free-surface shear layer through vortex stretching, as the flow wraps around the bow. However, such a theory is purely kinematical and hides the viscous origin of the vortex since a vortex is also present in two-dimensional flow (as sketched in Fig. 2 of Tuck and van den Broeck). In an ongoing experimental and theoretical study of this phenomenon, we have been able to show that the vortex arises as a result of a stagnation (separation) point on the free surface ahead of the body and that its location depends upon the slope of the free surface, viscosity and surface tension, i.e. on the Froude, Reynolds and Weber numbers. A consistent set of equations for the free-surface boundary layer, alluded to in the two papers presented here, has been derived and an attempt is being made to solve them to predict the vorticity distribution. Some experiments are also being carried out ahead of a horizontal cylinder in our towing tank to support the theory. We hope to report this work in a forthcoming paper (Ref.1).

### Reference:

- (1) V.C. Patel, L. Landweber and C.J. Tang, "Free-Surface Boundary Layer and the Origin of Bow Vortices", to be presented at the Second International Symposium on Ship Viscous Resistance, SSPA, Göteborg, Sweden, March 1985.

Dr. EIICHI BABA,  
MHI Nagasaki Technical Institute,  
Nagasaki, Japan:

From experimental and theoretical studies Prof. Mori showed clearly that the bow wave breaking phenomenon is very sensitive to the flow conditions around the bow. Most of the experimental work was conducted in the circulating water channel. The discussor would like to ask a few questions on the experiment:

- (1) How was the uniformity of vertical velocity distribution in the circulating water channel, especially near the free surface?
- (2) Are pictures shown in Fig. 4 for a circular cylinder taken in the circulating water channel?
- (3) If so, is there any difference of free-surface phenomena around a circular cylinder between the towing tank (Fig. 8 is the result in the towing tank) and the circulating water channel?

Prof. HIDEAKI MIYATA,  
The University of Tokyo, Tokyo, Japan:

(See Discussion following the paper of K. Takekuma and K. Eggers.)

# AUTHOR'S REPLY

To Mr. Abe:

The discussion on the applicability of the SP-type bulb is out of the scope of the present paper. However, the practical application has been made in Tamashima et al. (1984). We got the same conclusion as mentioned by the discussor; the depth of the bulb immersion is very important. The wave pattern pictures may be found in my discussion to the paper by Mr. Takekuma and Prof. Eggers.

To Prof. Bindel:

In the present paper, the flow field phenomena are exclusively studied, the effects of the breaking or the sub-breaking on the resistance are not discussed here. Guessing from the results of the elliptic cylinder with a bow bulb, the total resistance may be reduced, for the sub-breaking waves are remarkably suppressed by fitting a bow bulb while the wave height itself remains almost the same. I am not sure whether it can be said "catastrophic" or not, but my point is that the sub-breaking waves can take place when a certain criterion, which is carrying  $U_x$ ,  $U_y$  and  $U_z$ , is satisfied. Some experimental results as to the high-speed fishing boat will be found in Tamashima et al. (1984), though it is only a progress report.

To Dr. Kracht:

The "SP" is the abbreviation of the "snow-plow" which works as if plowing snow (wave in reality). Recently Mr. Ogiwara has succeeded in reducing the breaking wave by fitting a small wing at the bow. The geometrical configuration of the SP-bulb and its sea-going qualities are discussed in Tamashima et al. (1984) referred to in the present paper.

To Prof. Patel:

The present study was started by the present author together with the third author of Patel et al. (1985) during his stay at the discussor's affiliation, the University of Iowa. The boundary layer equation for the free surface flow is derived in the integral form in Mori (1983). However, it has not been successfully solved there. In this connection, the present author is delighted to know that the sowed seed has been successfully developed by the discussor. And he is quite anxious about knowing the mentioned results. It is true that the vorticity stretching theory hides the viscous origin, but the present analysis is attempted to elucidate one of the aspects of the necklace vortex in the framework of the inviscid double-model flow. So if the boundary layer equation is solved exactly, as reported in the discussion, the vorticity stretching effects, no need to say, are included. The author has never concluded that the stretching theory can explain all the aspects of the necklace vortex, but concluded that the basic flow is the important factor for the necklace vortex formation.

To Dr. Baba:

Our circulating water channel has a surface accelerator by which we can expect a vertically uniform flow. We adjusted it to get a uniform flow at least near the free-surface.

Fig. A-1 shows the comparison of the measured velocity with the calculated double-model velocity. Due to the free-surface effects they cannot be the same but the results at 17 cm upstream agree rather well with those calculated.

Fig. A-2 shows the velocity profiles at 17 cm and 10 cm ahead of the assumed bow; those measured at the same positions but without the cylinder. Though slight velocity defects are still observed, they are much less than those shown in Fig. 9 in the text.

When we started the present research, we could not manage the hot-film anemometer in the towing tank. But now we get used to managing it in the towing tank. It is scheduled to carry out the same measurements in the towing tank in the near future.

The pictures shown in Fig. 4 were taken in the towing tank (all the experiments of CM-42 were carried out in the towing tank). The free-surface flow around the bow is delicately affected by the surface flow; the bow wave phenomena differ significantly depending on the free-surface acceleration.

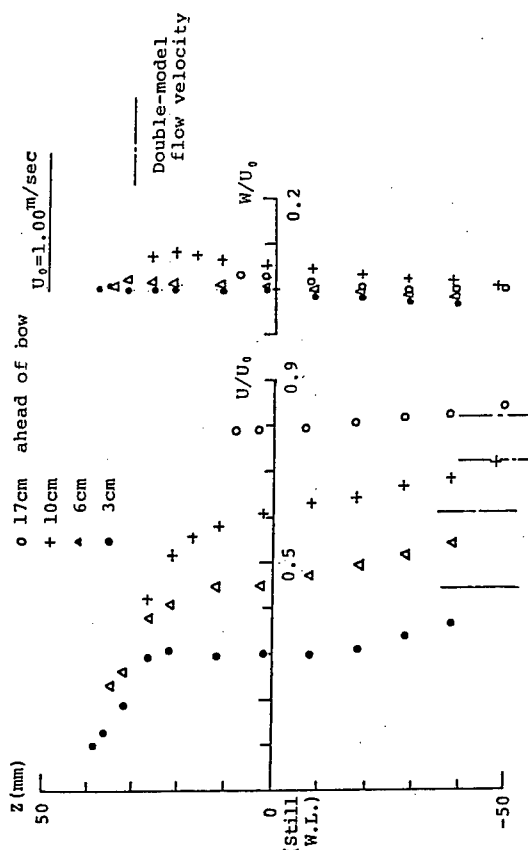
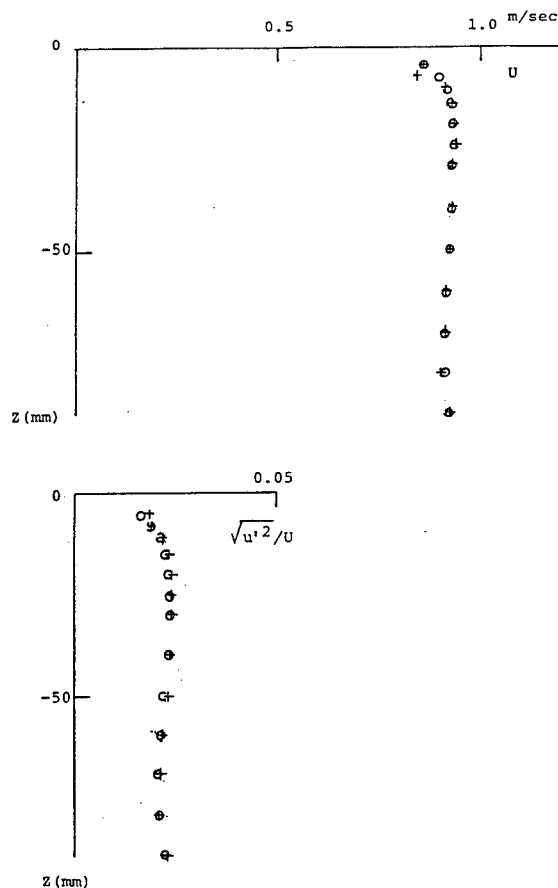


Fig. A-1: Velocity Profiles



+ 17 cm ahead of Assumed Bow  
 o 10 cm

Fig. A-2: Mean Velocity and  
 Turbulent Intensity of  
 Circulating Water Channel

can develop into the breaking waves at higher speeds, but are different from the breaking wave as is pointed out by Prof. Miyata, they are called sub-breakings here in distinction from the breaking.

With no overturning flows, the velocity defect is attributed to the turbulence production which is more or less related to the viscosity. This statement does not mean that the wave breaking cannot occur without viscosity. Again let me say that the present paper is dealing with the sub-breaking waves defined above which take place prior to the so-called breaking.

Prof. Miyata's numerical results must be highly appreciated. It is hoped, however, that they are compared with the corresponding experimental results quantitatively. The wave ridge (where an overturning is in his computation) never moved so far upstream as shown in Fig. 2 by our experiments by making use of a 50 cm square box with 10 cm draft at 1.2 m/sec; it remains almost at the same position. I wonder if his numerically simulated sub-breaking waves at lower speed have been actually observed in model experiments.

Prof. Miyata's comments that the overturning motion generates vortical flows and that breaking phenomena are the consequence of the steep unstable waves may be true for welldeveloped breakings.

The waves, however, dealt with in the present paper are related to the phenomena prior to them. The phenomena, for example shown in Fig. 5, are completely different from those Prof. Miyata imagines. Neither reverse flows, nor steepness enough for breakings, nor spillings, much less air-entrainments, nor plungings are observed at all. There are observed only wrinkles, which are confirmed turbulent flows, shear flows and vortical flows in contact with the bow. Because they

# BOW FLOW FIELD OF SURFACE SHIPS

DAVID J. FRY AND YOON HO KIM

## ABSTRACT

The details of the bow flow field of two surface ship forms were experimentally measured and numerically modeled. The shipforms included a Series 60, Block 60 ship model and a high speed surface ship with a bulbous bow configuration.

A three component laser doppler velocimeter was used to establish the velocity field in the bow region. A dense grid of pressure taps in the ship bow supplemented the direct velocity measurements. Surface elevation measurements were made with non-intrusive probes.

Detailed comparisons are made between the numerical model and the experimental results. Predictions of the computation method of Dawson for solving the ship wave problem are compared to the measured bow flow velocities and wave profiles.

The results are presented in a series of flow field and pressure field maps. These maps are discussed in terms of indicated stagnation points and attachment lines.

## 1. INTRODUCTION

The prediction of total resistance and flow around a ship depends on an ability to compute accurately the potential flow and boundary layer flow around the entire ship. The calculation of the potential flow not only provides the wave resistance and wave profiles, but also provides the "outer" flow for the boundary layer computation. In order to properly initialize the boundary layer computation detail flow characteristics near the bow region must be determined.

The flow and the wave profiles near the bow undergo rapid change without being significantly affected by the displacement of the boundary layer and wake. Therefore, accurate measurements of the flow and the waves near the bow will provide the numerical ship hydrodynamicists with the necessary data to verify their computation methods.

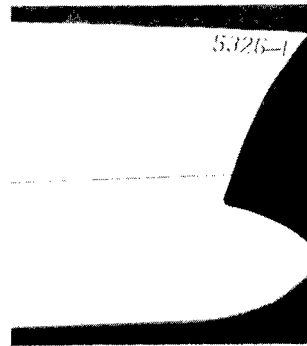
Both Michell's thin-ship theory<sup>1</sup> and slender-ship theory (Tuck<sup>2</sup> or modified by Ogilvie<sup>3</sup> for the bow region) provide analytical expressions for the wave resistance and wave

profiles of a ship moving in a calm, inviscid fluid. Because the theories fail to satisfy exactly the ship body boundary condition, neither theory is expected to model accurately the flow in the bow region. In fact, thin-ship theory and slender ship theory are known to overpredict the amplitude and phase shift of the oscillation (humps and hollows) of measured ship wave resistance curves<sup>2</sup>. Recent developments in numerical ship hydrodynamics have produced many quasi-analytic methods capable of computing the wave resistance, wave profiles, and flow field around a ship (e.g. Survey by Chapman<sup>4</sup>). Most of the methods use analytical linearized free-surface conditions and satisfy the ship body boundary conditions exactly. The Havelock or Rankine-Source Green functions are used to solve the numerical boundary integral equations. The computed wave resistances have been compared with measured residual resistance and wave resistance derived from wave pattern measurements. Promising comparisons of quasi-analytic methods and wave resistance data appear in the Proceedings of the First through the Third International Conference on Numerical Ship Hydrodynamics (20-22 October 1975 at the National Bureau of Standards, Gaithersburg, MD; 19-21 September 1977 at the University of California, Berkeley, CA; and 16-19 June 1981 at Palais des Congres, Paris) and the Proceedings of the First, the continued, and the Second Workshop on Ship Wave-Resistance Computations (13-14 November 1979 at DTNSRDC, 10-12 October 1980 at Izu Shuzenji, Japan, and 16-17 November 1983 at DTNSRDC). Dawson's<sup>5</sup> practical computer method for solving the ship wave problem, which is representative of the quasi-analytic methods, is compared in detail to the measured bow flow velocities and wave profiles of this paper.

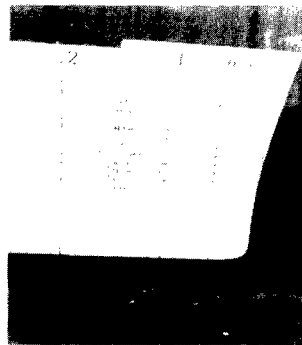
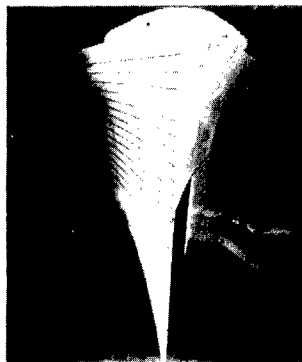
This paper presents details of the bow flow field of two surface ship forms which were experimentally measured and numerically modeled. This paper first discusses experimental techniques used for velocity, surface elevation, and bow pressure field measurements. The paper next discusses the underlying equations of the potential flow numerical model and some details of their application to the experimental conditions. Finally, experimental and numerical results are displayed and compared.

David W. Taylor Naval Ship Research and Development Center, Bethesda, Maryland 20084, USA

## MEDIUM-SPEED SHIP MODEL



### SERIES 60, BLOCK 60



## A HIGH-SPEED SHIP MODEL

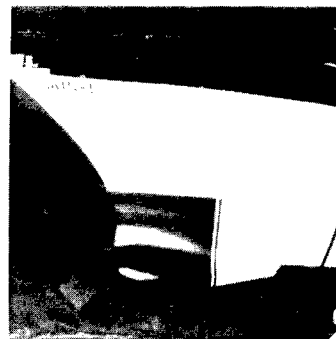
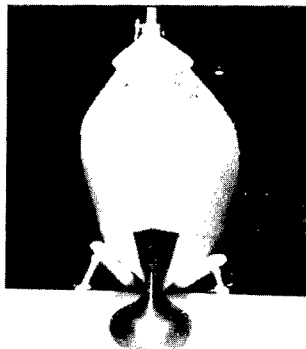


Figure 1 Photographs of Model Bows

### 2. SCOPE OF EXPERIMENTS

Experiments were conducted to determine the three dimensional velocity field and the free surface perturbation in the bow region of two model surface ships. The pressure fields on the ship hulls were also measured.

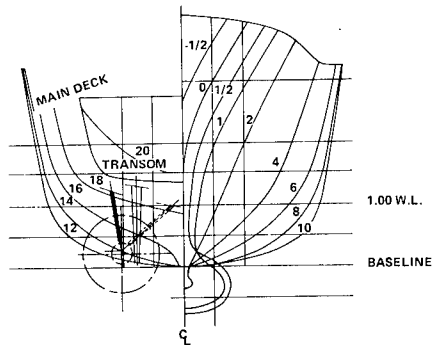
The models chosen for investigation were a Series 60, Block 60 surface ship (with a fine bow entrance angle and no bulb) and a "high speed" surface ship (with a bulb below the keel line). Photographs of the two model bows appear in Figure 1 and line drawings in Figure 2. A limited number of bow region velocity measure-

ments were made also on a "medium speed" ship model with a bulbous bow of a different shape above the keel line (Figures 1 and 2).

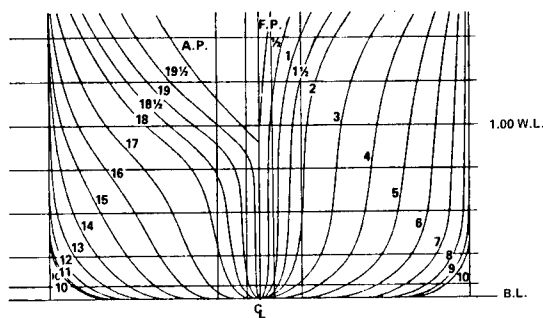
Table 1 displays relevant data on the ship model dimensions and towing conditions. Both the Series 60, Block 60 (S60-B60) model and the "high speed" (H.S.) model employed roughness elements to trip a turbulent boundary layer. The S60-B60 model used a 0.8 mm diameter wire stapled to the model bow (located at station 1.00 on the water line and at station 1.13 on the keel). The HS model employed studs (cylinders of 3 mm diameter and 3 mm height) located along a line from the water line (at



## BODY PLAN FOR HIGH-SPEED SHIP



## BODY PLAN FOR SERIES 60, BLOCK 60



## BODY PLAN FOR MEDIUM-SPEED SHIP

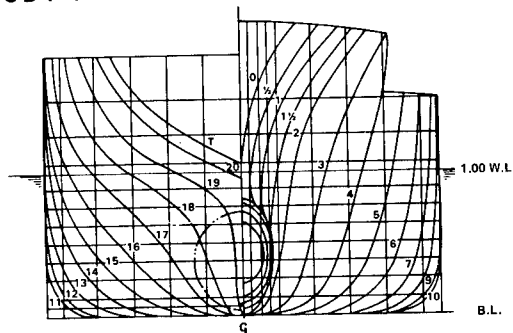


Figure 2 Body Plans of Ship Models

station 0.17) around the under the bulbous bow (station 0.3). These studs were spaced on 25 mm centers. The "medium speed" (M.S.) model had no added roughness for tripping a turbulent boundary layer. The roughness elements are marginally visible in the photographs of Figure 1.

A non-dimensional, rectangular coordinate system (fixed to the model) was chosen to define measurement locations and ship hull boundaries. All coordinate locations are in ship station units (i.e., non-dimensionalized by 1/20 of the ship model length). The origin of the coordinate system is at the intersection of the undisturbed free surface, the ship forward per-

pendicular, and the vertical plane running down the ship centerline. The "X" or streamwise axis is directed aft (positive direction) from the origin in the model centerline plane. The "Y" or transverse axis is directed to starboard from origin. The "Z" or vertical axis is directed upward to complete the orthogonal, right-handed, coordinate system (Figure 3).

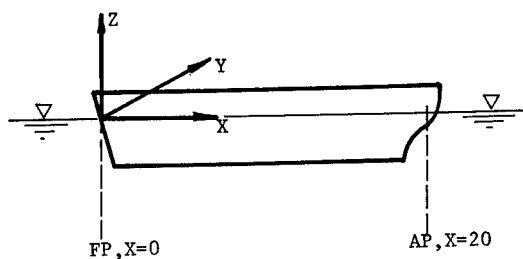


Figure 3 Model Coordinate System

Table 1 - Model Parameters and Measurements

Model NSRDC No.	High Speed 5415-1	S60-B60 4287	Med. Speed 5326-1
Length*	5.72 m	6.10 m	6.53 m
Beam	.76 m	.81 m	1.04 m
Draft	.25 m	.33 m	.39 m
Block Coef	.506	.600	.597
Tow Speed	3.09 m/s	2.06 m/s	2.50 m/s
Froude No.	.41	.28	.32
Measurements:			
Velocity	X	X	X
Surface El.	X	--	X
Pressure	X	X	--

\*Length between forward and aft perpendiculars

## 3. EXPERIMENTAL MEASUREMENTS

### 3.1 Velocity Measurements

Three component mean velocity measurements were taken using a Laser Doppler Velocimetry (LDV) system developed jointly by DTNSRDC and TSI Inc. of St. Paul, Minnesota (Figure 4). Basically, the system collects velocity information from the light scattered by small particles carried by the water through the intersection point of five laser beams.

Within the intersection or measurement

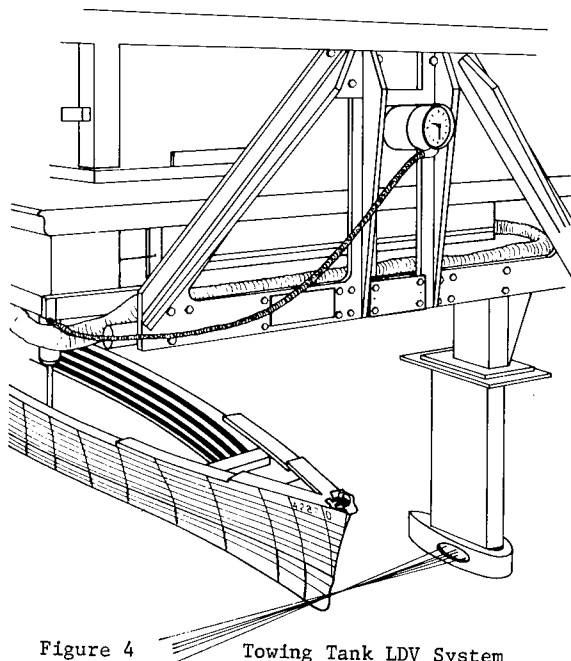


Figure 4 Towing Tank LDV System

"point" are fringes (alternating light and dark planes) created by the focused, polarized, coherent laser beams. The scattered light signal can be understood as an "on - off - on..." flashing as a particle passes from light to dark to light fringes... This flashing is observed through an optics train ending in a photomultiplier whose output is timed electronically. In a properly aligned LDV system the fringe spacing is uniform across the measurement point and a function of only the beam crossing angle and the light wavelength. Fringe spacing and "flashing" frequency information allows calculation of the particle and fluid speed.

The optics and signal processing of the towing tank LDV are similar to the standard system described in Reference 6. Table 2 lists the five laser beams and their characteristics. Table 3 lists the dimensions and fringe spacings of the three velocity component measurement volumes.

The accuracy of the LDV velocity measurements depends on many factors. It is worthwhile

Table 2 - Laser Beam Descriptions

#	Color	Water Wavelength (μm)	Freq. Shift (MHz)	Angle to Lens Axis (Degrees)	Velocity Component
1	Blue	.366	0	+2.39	Vertical
2	Green	.386	+40	+6.65	Streamwise Transverse
3	Blue	.366	+40	-2.39	Vertical
4	Green	.386	-60	-6.65	Streamwise Transverse
5	Green	.386	0	0.0	Transverse

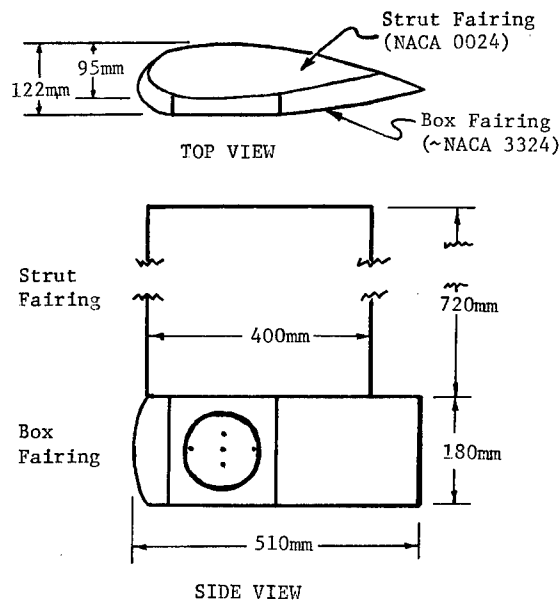
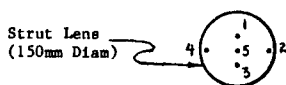


Figure 5 Strut Dimensions Drawing

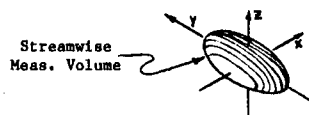
to discuss the important factors to give the reader a better feeling for the reliability of the displayed velocity data.

The DTNSRDC towing basins did not have sufficient particles naturally in the water to use in the measurements. The water was therefore "seeded" between towing runs. The seed chosen had to be large enough to scatter sufficient light plus small and "light" enough to follow the flow. Silver coated glass spheres were chosen after an extensive search (Reference 7). Ninety percent of the spheres had diameters between 2μm and 8μm. Their specific gravity was 2.6.

LDV system design required a hollow strut to conduct the laser beams (and scattered light signal) through the water surface before sending them out to the measurement point (displaced 600 mm from the front lens). This strut can disturb the flow and affect velocity measurements. Strut dimensions and fairings were chosen carefully to allow measurements with negligible disturbance. The strut is pictured in Figure 4. Its outside dimensions appear in Figure 5. Tests were conducted with pitot tubes (both 2-hole and 5-hole types) taking measurements with the LDV strut present and with it removed. In the free stream

Table 3 - LDV Measurement Volume Characteristics

Component	Beams (#)	Meas. Volume Dimensions X x Y x Z (mm)	Fringe Spacing (μm)
Streamwise	2,4	.08 x .71 x .08	1.67
Vertical	1,3	.08 x 1.87 x .08	4.41
Transverse	2,4,5	.08 x .71 x .08	28.7



(with no ship model) measured disturbances at the LDV measurement point were uniformly less than 1% of the tow speed. The same test done for measurements in the propeller plane of the A0 model was in agreement except for an isolated region where the disturbance approached 3% of the tow speed.

Mean velocities were calculated from 256 samples of each velocity component. The samples were collected over a period of usually 8 - 15 seconds (no less than 5 seconds). Ideally, far fewer velocity samples would be needed in the steady flow around the bow. This was the case for the vertical and streamwise components. However, the inherent difficulty in obtaining the transverse velocity component is reflected in a non-biasing noise that broadens the range

of component magnitudes measured in even a steady flow field (Figure 6). The 256 samples were needed to average out this noise (and real flow fluctuations when present). Repeatability of measurements (on different carriage runs) is shown for each component in Figure 7.

An accurate determination of the fringe spacing is needed to convert the "flashing" frequencies measured to fluid velocities. The critical inputs were beam crossing angles. Calculated fringe spacings and hence fluid velocity measurements were in error  $< 1.5\%$  for the vertical ("Z") or transverse ("Y") components

Figure 6:

**LDV VELOCITY COMPONENT HISTOGRAMS  
BOW FLOW STUDY; 6.0 KNOTS; 4 APR 84**

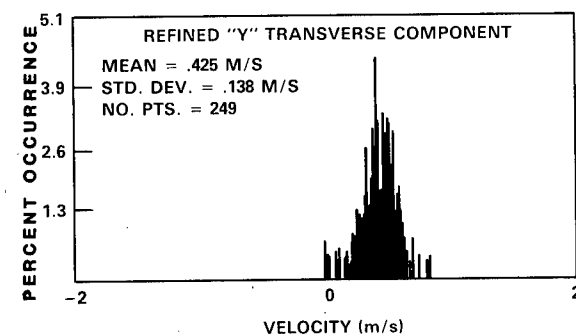
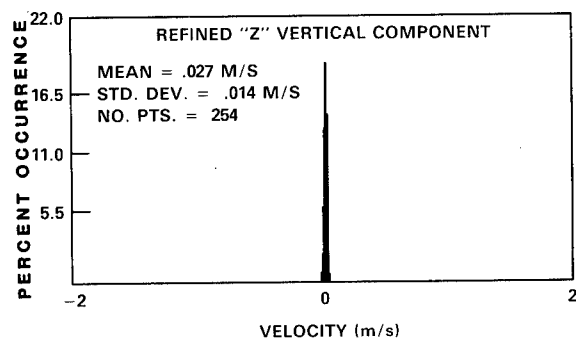
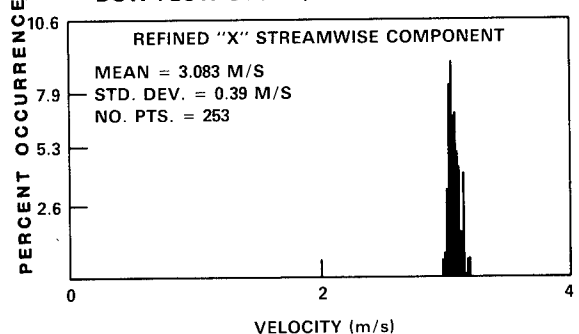
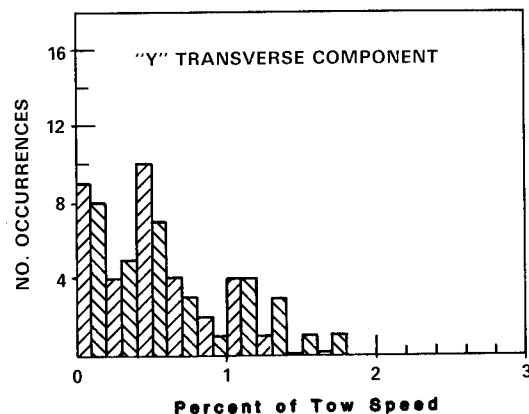
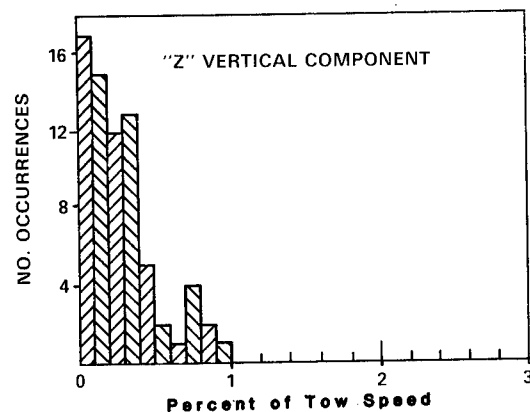
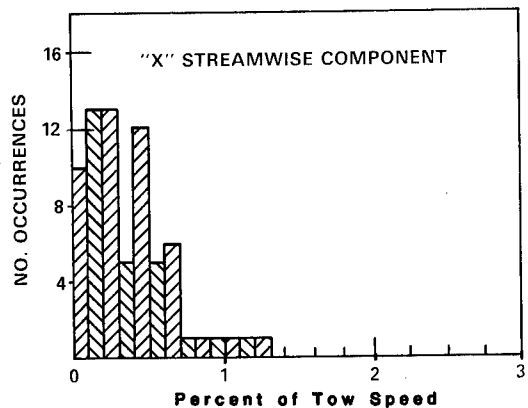


Figure 7:

**DIFFERENCES IN REPEATED LDV DATA POINTS**



and  $< 0.5\%$  for the streamwise ("X") component. These are percentages of the component magnitude not the towing speed.

Ideally the three velocity components measured fall exactly on the orthogonal directions of the coordinate system described earlier. While it was possible to align the streamwise and vertical measurements to within a  $1/2$  degree, the transverse component was inherently very sensitive to alignment. Although in the future tools will be available to do much better, in this test the "transverse" component could actually be turned by as much as  $\pm 10$  degrees toward the streamwise direction. This angle was determined by making LDV measurements with no model and assuming any measured transverse velocity was due to the non-orthogonality of the "transverse" and streamwise components.

LDV support structure bending changed as a function of traverse position. This movement of the whole system relative to the model did not appear on the traverse axis encoders and was the main source of positioning error. By using carefully measured correction factors a positioning accuracy of  $< 0.8$  mm was attained over the entire traverse range (0.5m. x 1.0m. x 0.5m.). Relative translations over short distances ( $< 100$  mm) had a better positioning accuracy ( $< 0.2$ mm.). The 0.8 mm accuracy was comparable to the amount the model was observed to move when brought up to speed by the towing carriage.

Most biases, attributed to LDV mean velocity measurements, occur only when velocity fluctuations at a measurement location are significant relative to the mean magnitude. These bias effects are not important to this data set because almost all measurements were in the steady flow around the bow.

### 3.2 Surface Elevation Measurement

To complement the velocity data, elevation measurements of the water surface around the H.S. model (Froude No. = .41) and the S60-B60 model were taken. Measurements were not only made in the bow region of the H.S. model, but the entire wave field in a 6m. x 15m. area was defined. All measurements were done without the interference of the LDV strut which was removed. Two non-disturbing techniques were used to collect the data.

The bulk of the elevation measurements used an array of five ultrasonic probes. Each probe was located 250-450 mm above the water surface. Electronics timed the delay between the emission of a sound pulse and the reception of its echo. Knowing the speed of sound allowed conversion of the time delay into a distance from the probe to the surface. These probes were zeroed before each towing pass in calm water and carefully calibrated by use of the LDV traverse system to which they were attached. Mean elevations represent averages of 5 to 10 seconds worth of measurements.

The diameter of the sound pulse striking the water surface was about 20 mm. In the distance range used, the instrument manufacturer specifies an accuracy of  $\pm 2$  mm. However,

this instrumentation had two limitations. It could not measure extreme water surface slopes which did not reflect enough of the sound pulse back to the probe ( $\sim 5\%$  of locations). It also needed to look directly down on the point being measured and therefore could not be used very close to the model hull.

A second technique was used to get a limited number of elevation measurements near the model hulls. This was simply a pointed rod extending down from the LDV traverse. The traverse was positioned up and down manually until an observer felt that the point was just at the water surface for a particular X-Y location. LDV traverse encoder readings were then recorded. The unsteadiness of the surface caused errors in some locations on the order of several millimeters. By angling the rod, measurements could be made right up to the ship hull.

### 3.3 Hull Pressure Measurements

Pressure taps were located on the bulbous bow of the H.S. model and the S60-B60 hull. Only pressure measurements on the H.S. model (at Froude numbers of 0.41 and 0.28) were made. Measurements on the S60-B60 model had previously been taken by Huang and von Kerczek (Reference 8).

Sixty pressure taps were flush mounted on mostly the starboard side of the H.S. model bulbous bow. A Datametrics pressure transducer was used in the measurements. Figure 8 shows the distribution of the pressure taps on this model.

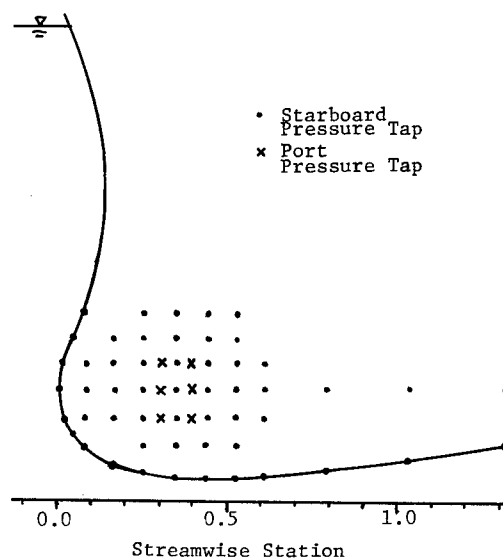


Figure 8 Bulbous Bow Pressure Taps (H.S. Model)

#### 4. STATEMENT OF COMPUTATION APPROACH

We assume that the fluid is inviscid and incompressible and the flow is irrotational. Furthermore we neglect surface tension. Then a steady state flow can be described by a velocity potential function  $\phi$  and the velocity vector field can be represented by the gradient of  $\phi$ . The velocity potential  $\phi$  must satisfy the Laplace equation

$$\nabla^2 \phi = 0. \quad (1)$$

On the free surface,  $z = \zeta(x, y)$ , we have dynamic and kinematic boundary conditions.

$$2g\zeta + |\nabla\phi|^2 = U_0^2 \quad (2)$$

$$\phi_x \zeta_x + \phi_y \zeta_y - \phi_z = 0 \quad (3)$$

where  $g$  is the gravitational acceleration constant. Combining both dynamic and kinematic conditions (2) and (3) yields

$$g\phi_z + \nabla\phi \cdot \nabla(1/2 |\nabla\phi|^2) = 0 \quad (4)$$

The boundary condition on the ship hull surface  $S_0$  is

$$\phi_n = 0, \text{ on } S_0, z < \zeta(x, y) \quad (5)$$

where  $\vec{n}$  is the unit normal vector directed outward from the fluid. The bottom condition for infinite depth water is

$$\phi_z = 0, \text{ as } z \rightarrow -\infty \quad (6)$$

The radiation condition is

$$\begin{aligned} \phi &= U_0 x + o(1/r), \quad x < 0 \\ \phi &= U_0 x + O(1/r), \quad x > 0 \end{aligned} \quad (7)$$

$$\text{as } r = \sqrt{x^2 + y^2} \rightarrow \infty$$

It is exceedingly difficult to solve this exact formulation because the free surface condition is nonlinear and the location of the free surface is not known a priori. It is convenient to express the total velocity potential  $\phi$  as the sum of two potential functions

$$\phi = \phi_d + \phi \quad (8)$$

Here  $\phi_d$  is the double-body potential which satisfies the following equations:

$$\nabla^2 \phi_d = 0 \quad \text{in the fluid}$$

$$\frac{\partial}{\partial n} \phi_d = 0 \quad \text{on } z = 0$$

$$\frac{\partial}{\partial n} \phi_d = 0 \quad \text{on } S_0, z < 0 \quad (9)$$

$$\phi_d = U_0 x \quad \text{as } \sqrt{x^2 + y^2 + z^2} \rightarrow \infty$$

Once  $\phi_d$  is defined, then a systematic linearization procedure may be applied to the exact nonlinear free surface condition. It is usual to expand the perturbation potential  $\phi$  in a

Taylor series in terms of the free surface elevation  $\zeta(x, y)$  which is assumed to be small. Then the linearized free surface condition for a perturbation potential  $\phi$  can be expressed in terms of double-body potential  $\phi_d$ . When the linearized free-surface condition is used, the exact ship hull boundary condition is only satisfied at the hull surface below the undisturbed free surface,  $z = 0$ . This is the well known Neumann-Kelvin problem.

There are at least two approaches to the solution of this boundary-value problem. One approach is to distribute Havelock sources at the body surface. A second approach<sup>5</sup> is to distribute simple Rankine sources at both the body surface and the free surface. A successful computation method of Dawson<sup>5</sup>, representing the second approach, was used to produce the numerical results reported herein. In Dawson's method, the hull surface as well as free surface was replaced by a faceted form. Each facet or element is a quadrilateral and is treated as a source patch; that is, a surface distribution of source of constant strength was distributed over each element. This results in a set of simultaneous linear equations to be solved for the source strength on each panel. The hull boundary condition is satisfied exactly below the undisturbed free surface and the linearized free surface condition is satisfied along the streamline of double-body potential.

#### 5. NUMERICAL TEST

Accurate prediction is the ultimate goal of all hydrodynamicists. As a first step toward this ultimate goal, it is desirable to use a set of reliable experimental measurements to compare against the results of an existing computational tool. The outcome of such comparisons may guide us either to develop a new mathematical model or to improve the existing tool.

The numerical model was applied to all three hulls used in the experiment. Table 4 shows the number of panels used to represent the ship hull and the truncated free surface. Some features of the panel arrangement were the same for all three models: eight rows of panels were

Table 4 Computation Details

	High Speed Ship Model	Series 60 Block 60	Med. Speed Ship Model
Number of Panels and Computing Time			
Main Hull	192	192	192
Bulbous Bow	96	0	32
Free Surface	320	320	320
After Transom	48	0	0
Total	656	512	544
CPU (sec)	38	24	28
Extent of Free Surface/Ship Length			
Ahead	0.50	0.50	0.50
Athwartships	0.41	0.42	0.44
Astern	0.56	0.55	0.50
Off-Body Points			
Number	2000	936	27
CPU (sec)	66	27	5

used to represent the hull from the keel line to the free surface, the free surface extended to about 3/8 of a ship length in the athwartship direction and was represented by eight rows of panels. The panels were smaller near the bow and stern and near the hull and free surface intersection. More details of panel arrangement are discussed in Reference 5. After obtaining the source strength of each panel, velocity computations at arbitrary points in the flow field are straight-forward. A CRAY Computer was used for computations. The computation time required for each ship is tabulated in Table 4.

## 6. PRESENTATION OF RESULTS

Velocities and surface elevations were plotted for H.S. model experimental data ( $Fr = .41$ ) and numerical results. Appendix 1 contains two types of plots for various transverse - vertical planes. One type shows the magnitude and direction of the crossflow velocity (vertical and transverse components) in the plane. The other type uses contour lines to show the distribution of the streamwise velocity magnitude (divided by the tow speed). Note that these contours are constructed from discrete values at the arrow locations in the other plot. The surface elevations appear as solid dots. The line drawn between the dots is simply a spline fit to the data (or numerical results). Both plots show the ship hull (if present) as a cross-hatched area.

Figure 9 presents the general features of the bow wave for the H.S. model ( $Fr = .41$ ). It may be of help in understanding the surface elevation measurements presented in Appendix 1.

Velocity and surface elevation data for each of the models appear on plots (Appendix 2) of the streamwise - vertical plane where  $Y = 0$ . The velocity components in that plane (streamwise and vertical) are displayed as arrows showing velocity magnitude and direction.

The experimental pressure tap measurements are partially presented in two plots (Figure 10) showing the pressure variation on the hull keel line ( $Y = 0$ ) below the bulbous bow tip and on the bulbous bow center axis ( $Z = -1.03$ ).

## 7. DISCUSSION OF RESULTS

Initial overall comparisons between the H.S. model measurements and calculations show an excellent agreement. Three features in the data

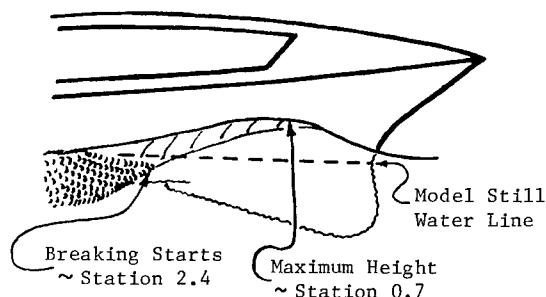


Figure 9. High Speed Model Bow Wave Form

however, cannot be predicted by the numerical model.

Surface elevation values very close to the hull, relating to the breaking wave (see planes  $X = .50, .93, 1.41$ ) are not computed by the numerical model. However not too far from the hull the surface elevation calculations agree well with the experimental data. The near-surface velocity measurements and calculations are also comparable.

Secondly the LDV velocity measurements started picking up a boundary layer underneath the bulbous bow at station  $X = .50$ . Measurement locations 2 mm from the hull boundary were made. Because of scattered light noise and the probe volume shape, velocity measurements on the model's side could not be made closer than 5 - 8 mm. Boundary layers on these surfaces were not found until the plane  $X = 1.41$ . The potential flow numerical model by itself cannot predict the boundary layer or its growth.

Finally at stations aft of the bulbous bow it is apparent that a pair of vortices is formed under the model centerline (see plane  $X = 2.8$ ). At the stations near the bow, the pair seem to only have a very local effect in this instance.

Comparing the streamwise and vertical velocity data for the three models, a simple stagnation point for each of the bulbous bow models (H.S. and M.S. in Appendix 2) is apparent. Velocity measurements were taken as close as 2 mm forward of the stem line in all three cases.

Along the stem lines of the S60-B60, the

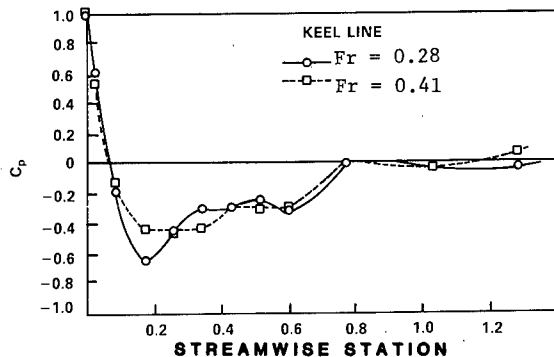
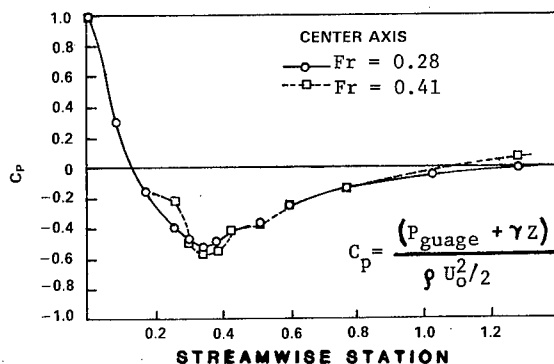


FIGURE 10. PRESSURE MEASUREMENT OF HIGH-SPEED SHIP MODEL

H.S., and the M.S. models (above the stagnation points), velocity components normal to the stem profile are zero. However, the tangential velocity component is not zero. These flow patterns are similar to the attachment line of a three dimensional flow <sup>10&11</sup>.

## 8. CONCLUSIONS

The detailed comparisons of experimental data and numerical results given in this paper show good correlation of both the general flow field and specific velocity directions and magnitudes.

The formulation of the numerical model precludes it from predicting the boundary layers, the breaking bow wave, and the vortex formation observed in the experiment. To the extent that these features are important, the potential flow model should be extended or combined with other three dimensional flow models to include boundary layer and non linear free-surface effects.

## ACKNOWLEDGEMENTS

This work was funded by ONR under NR number 062-751(075-012X), Research Project RR014-11-08, Program Element 61153N.

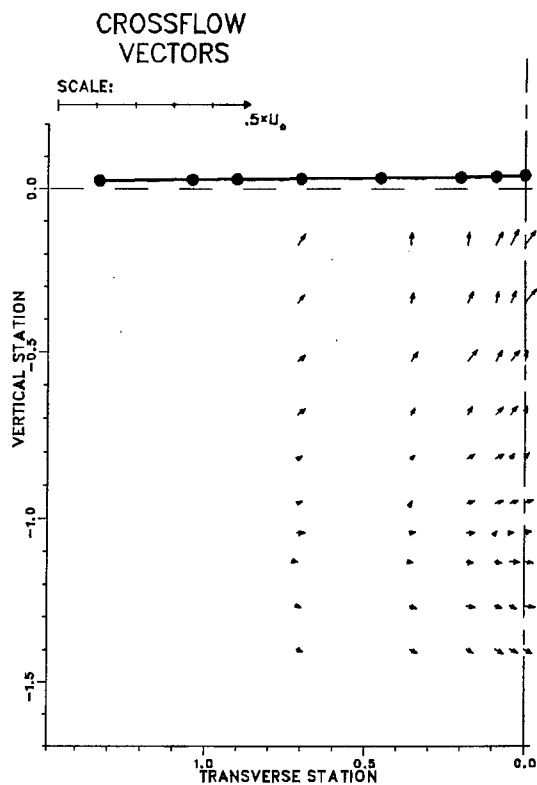
The authors want to express their appreciation of the support and technical guidance given by Dr. Thomas T. Huang. Technical discussions about the numerical model with Dr. M.S. Chang were very useful and greatly appreciated. The authors are especially grateful for the technical skills and long enthusiastic hours offered by Mr. Steve McGuigan as well as for many staff and support personnel that also contributed to the success of the experimental work. The support of the Computation, Mathematics and Logistics Department regarding the numerical method is also gratefully acknowledged. Finally the authors wish to acknowledge Ms. Lauri Jeantheau for the timely and accurate typing of this paper. The LDV development was funded by Ship and Submarine Technology Program Element 62543N, Ship Performance Subproject SF 43421.

## REFERENCES

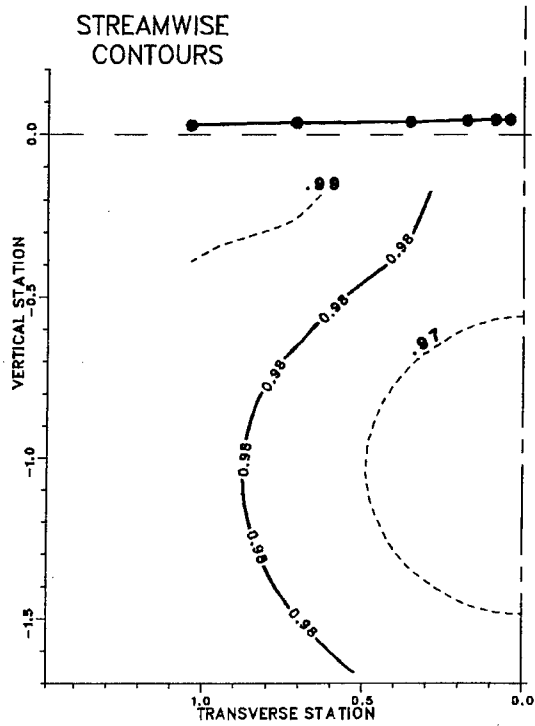
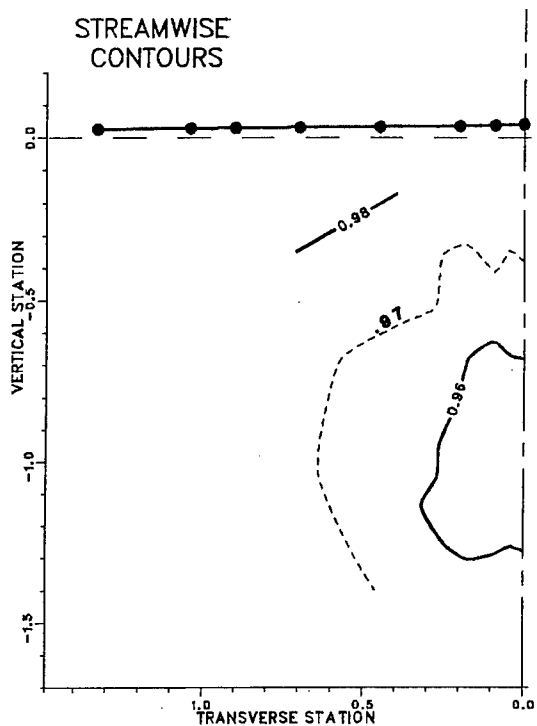
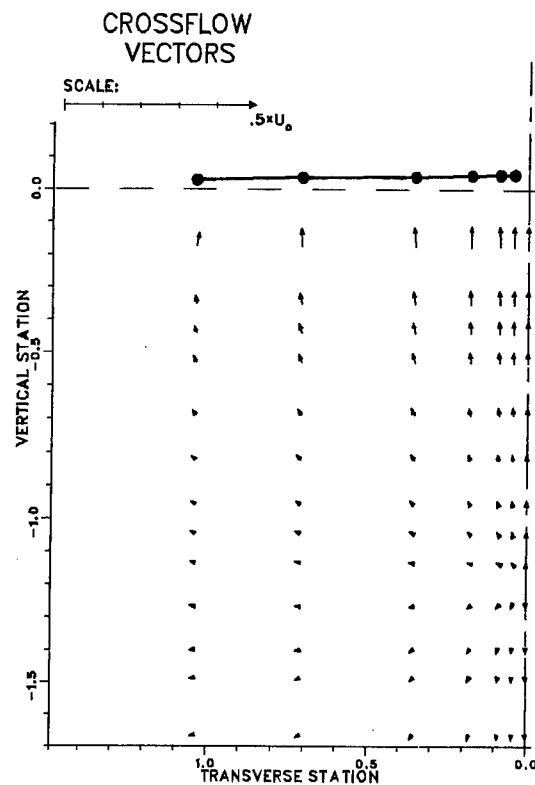
1. Michell, J.H., "The Wave Resistance of a Ship," Phil. Mag., 5, 45, pp. 106-123 (1898).
2. Tuck, E.O., "A Systematic Asymptotic Expansion Procedure of Slender Ships," Journal of Ship Research, No. 8, Vol. 1, pp. 15-23 (1964).
3. Ogilvie, T.F., "The Wave Generated By A Fine Ship Bow," Proceedings, 9th Symposium On Naval Hydrodynamics, U.S Government Printing Office ACR-203, pp. 1483-1525 (1972).
4. Chapman, R.B., "Survey of Numerical Solutions For Ship Free-Surface Problems," Proceedings, 2nd International Conference on Numerical Ship Hydrodynamics, University Extension Publications, University of California, Berkeley, pp. 5-16 (16-19 June 1981).
5. Dawson, C.W., "A Practical Computer Method for Solving Ship Wave Problems," Proceedings of the Second International Conference on Numerical Ship Hydrodynamics, University Extension Publications, University of California, Berkeley, pp. 30-38, (19-21 September 1977).
6. System 9100-10: 5 Beam, 3 Component LDV Instruction Manual, TSI, Inc., St. Paul, Minn, May 1982.
7. Chlebeczek, R., Personal Communication on "An evaluation of Seed Materials for Use in LDV Water Applications", TSI, Inc, St. Paul, Minn. January 1984.
8. Huang, T.T., von Kerczek, C., "Shear Stress and Pressure Distribution on a Surface Ship Model: Theory and Experiment", Ninth Symposium on Naval Hydrodynamics, Office of Naval Research, pp. 1963-2010.
9. Chang, M.S., "Computations of Three Dimensional Ship-Motions with Forward Speed", Proceedings of the Second International Conference on Numerical Ship Hydrodynamics, University Extension Publications, University of California, Berkeley, (19-21 September 1977).
10. Cumpsty, N.A., and Head, M.R., "The Calculation of Three-Dimensional Turbulent Boundary Layers, Part II: Attachment-Line Flow on An Infinite Swept Wing", The Aeronautical Quarterly, Vol. XVIII, pp. 150-164, May 1967.
11. Cebeci, T. and Bradshaw, P., Momentum Transfer in Boundary Layers, McGraw-Hill Book Co., New York, pp. 324-330, 1977.

## APPENDIX 1: Velocity Field for Transverse Plane $X=-0.890$

Measured



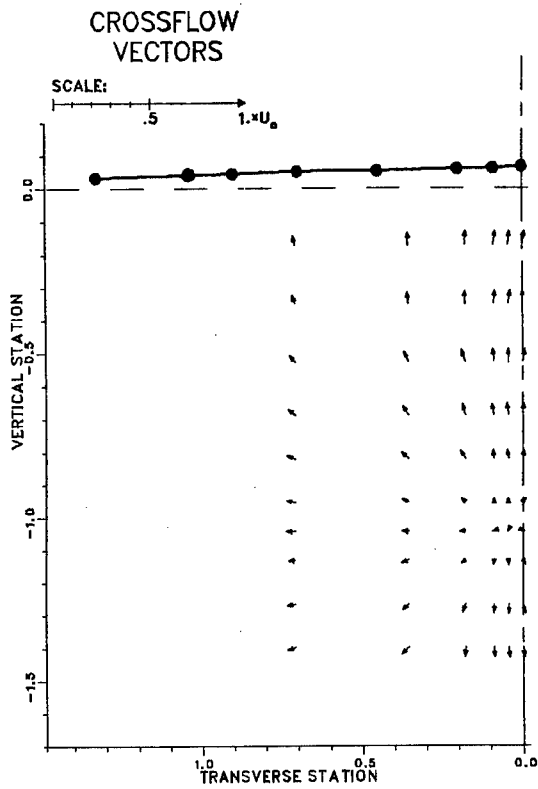
Calculated



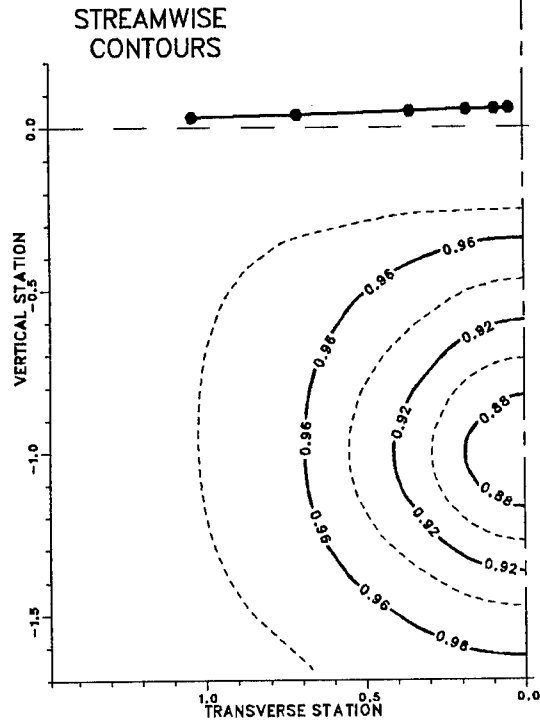
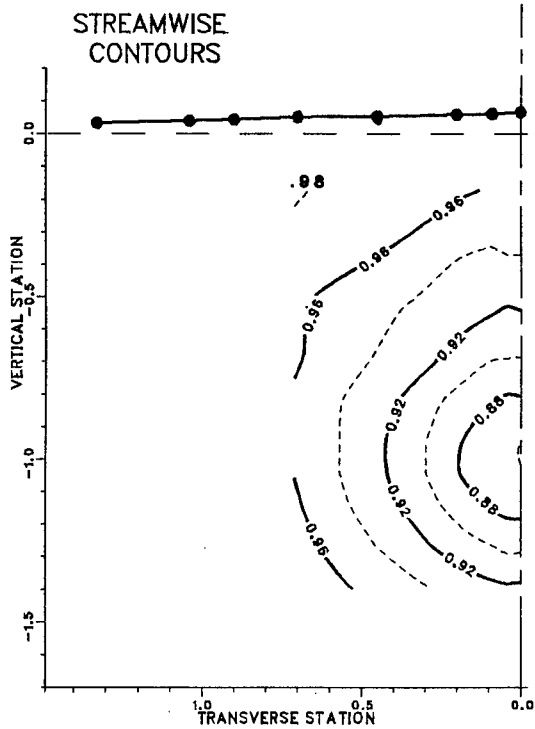
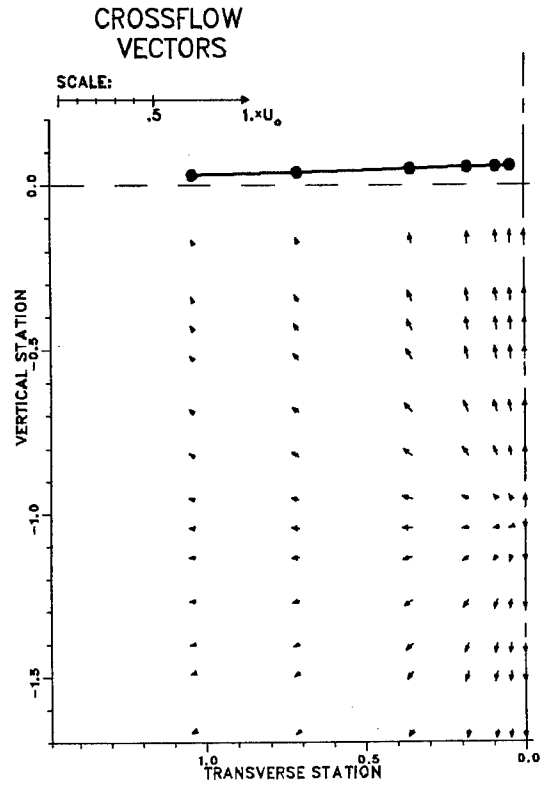


## APPENDIX 1: Velocity Field for Transverse Plane $X = -0.376$

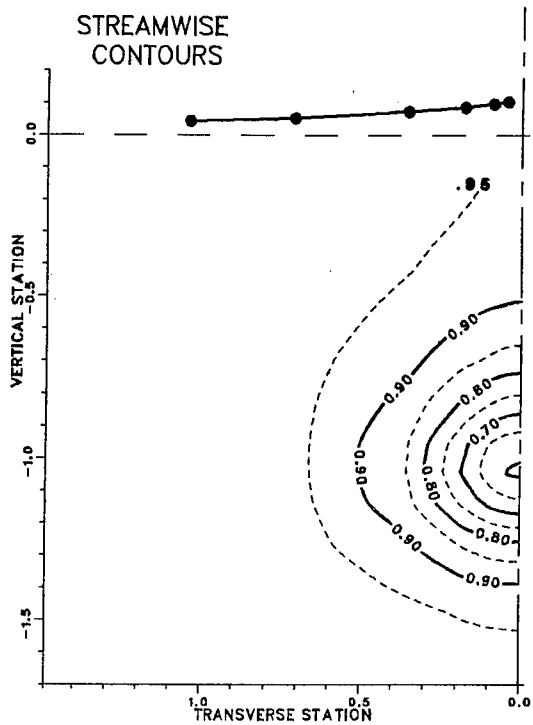
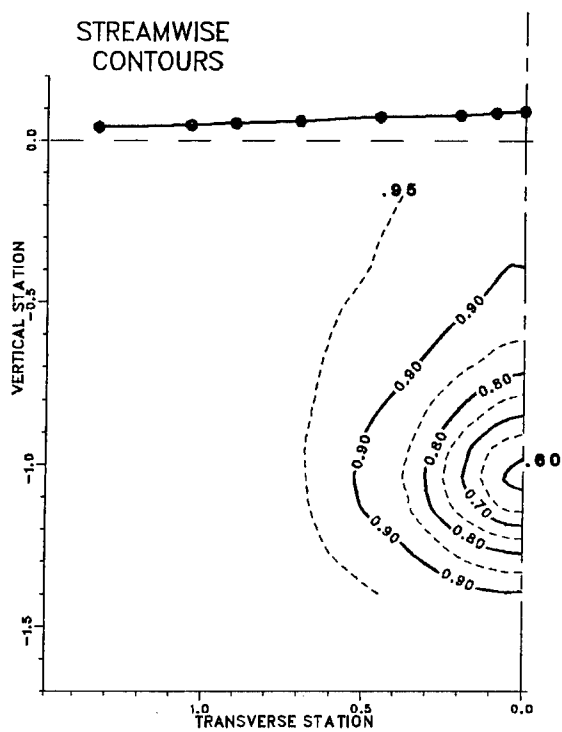
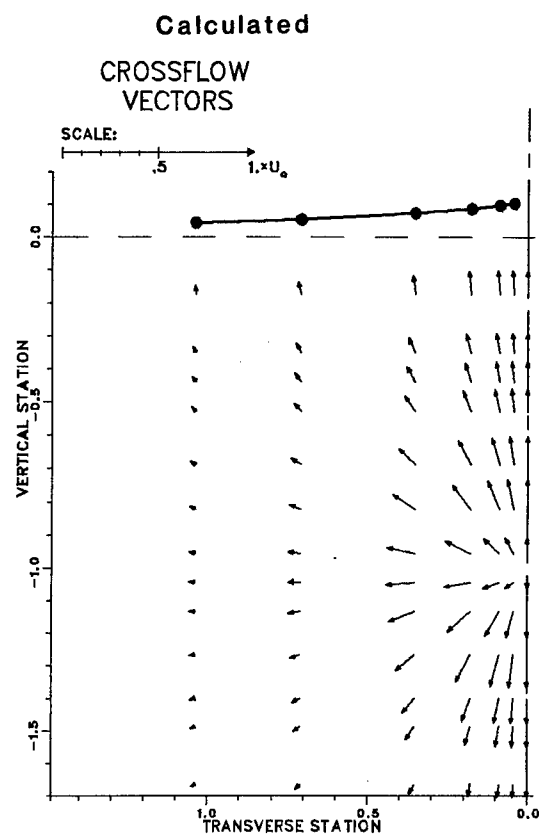
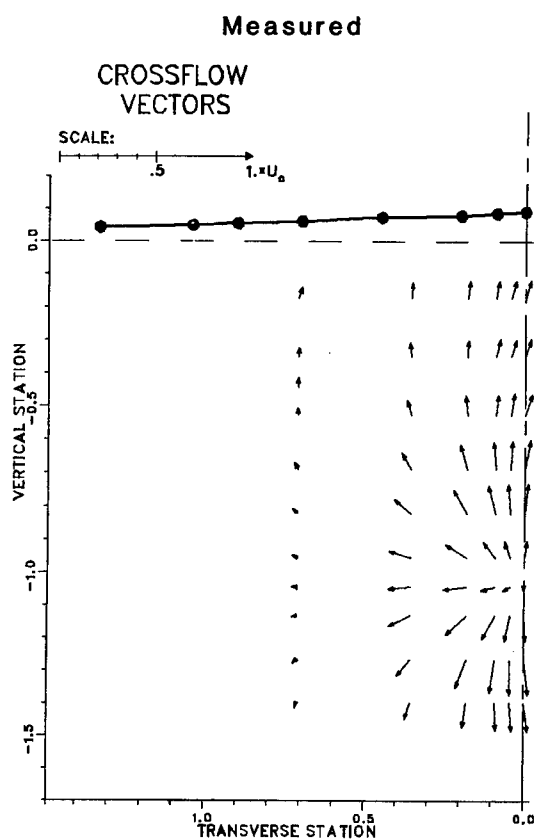
Measured



Calculated



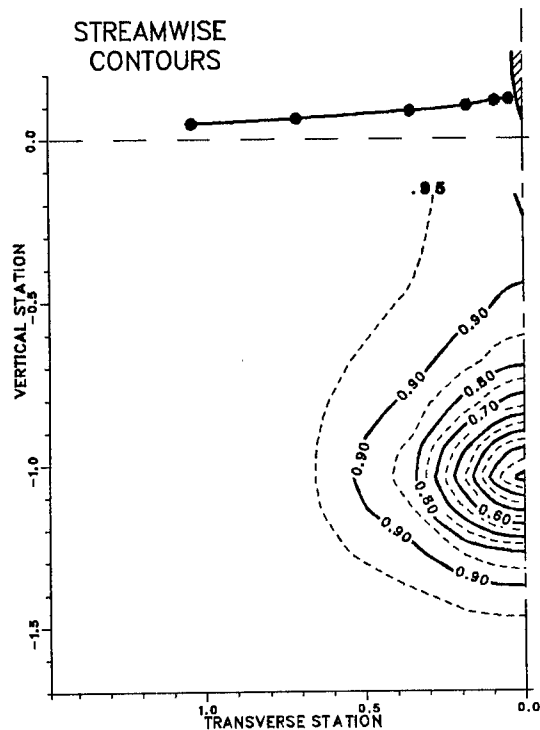
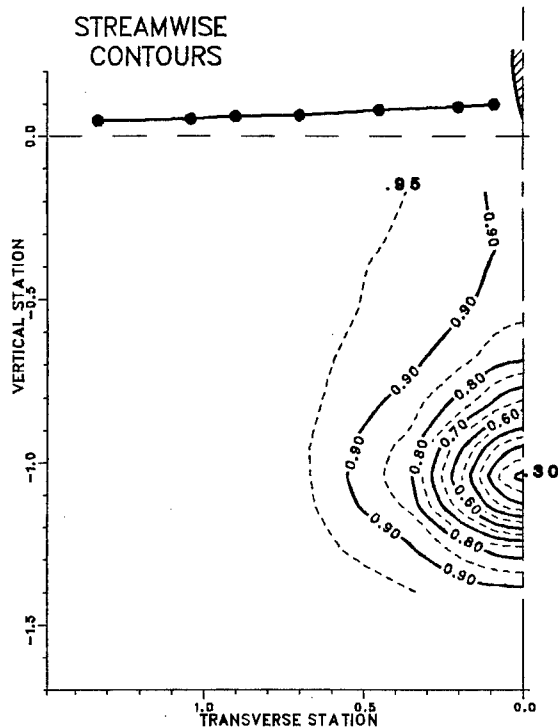
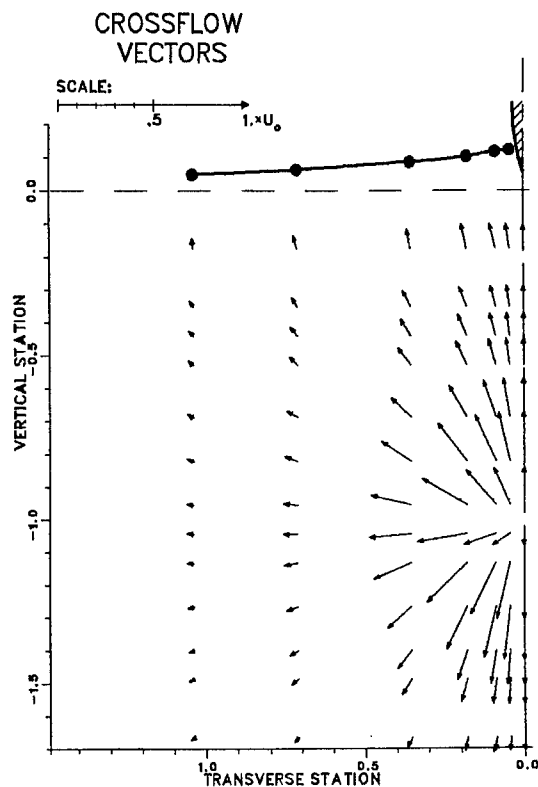
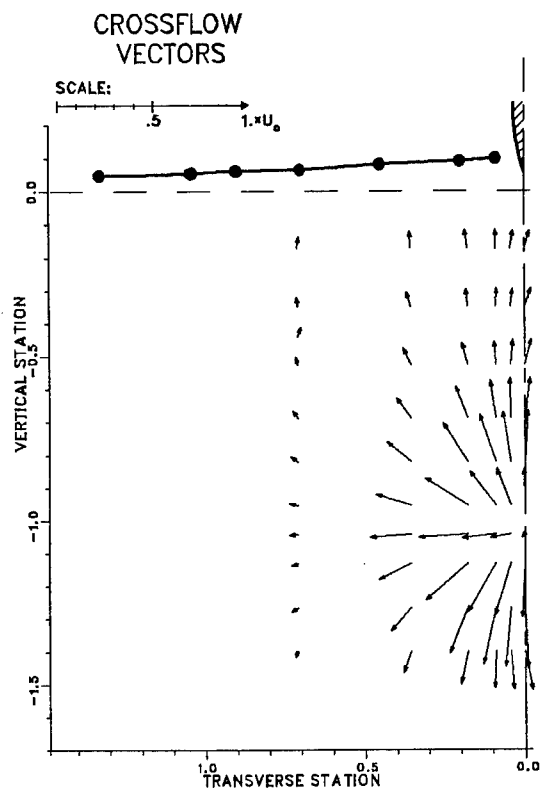
## APPENDIX 1: Velocity Field for Transverse Plane $X=-0.127$



# APPENDIX 1: Velocity Field for Transverse Plane $X = -0.043$

Measured

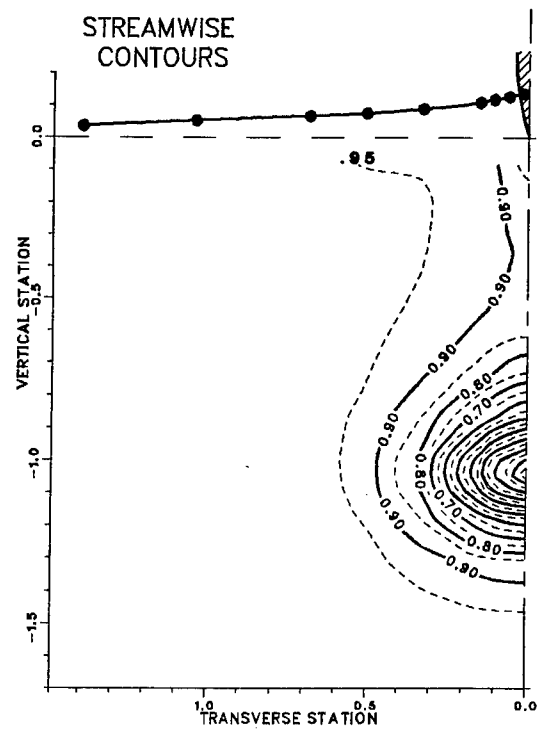
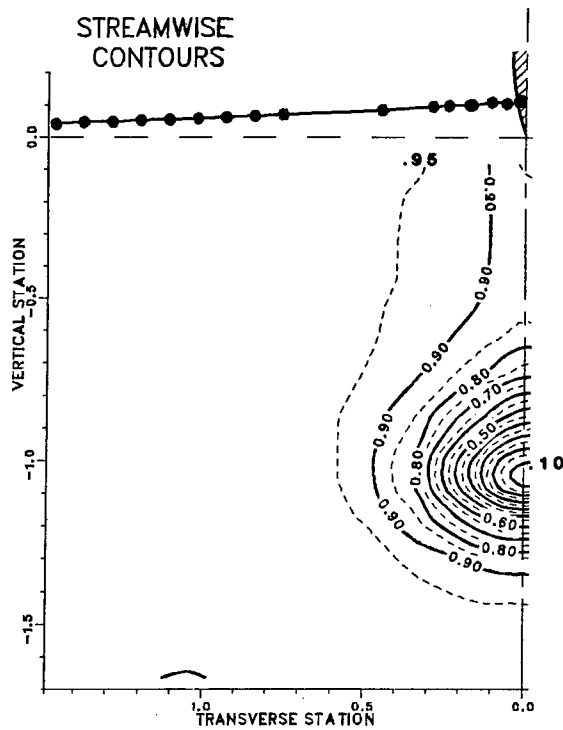
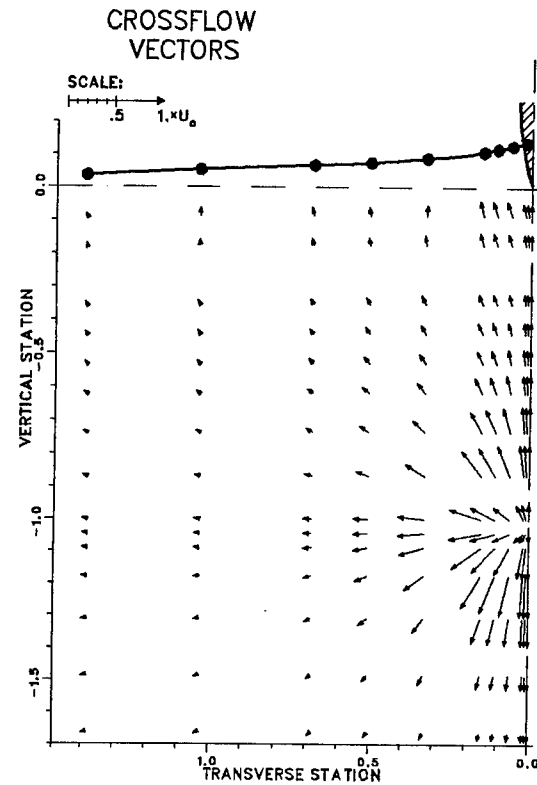
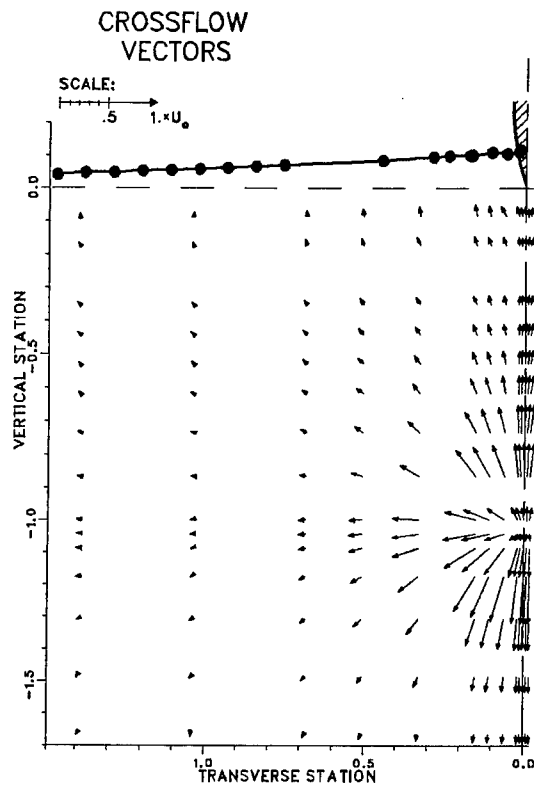
Calculated



# APPENDIX 1: Velocity Field for Transverse Plane $X = -0.009$

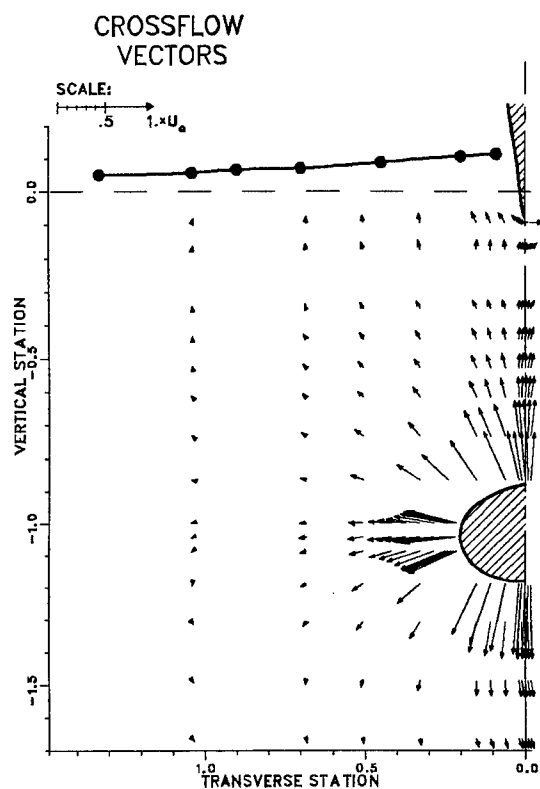
Measured

Calculated

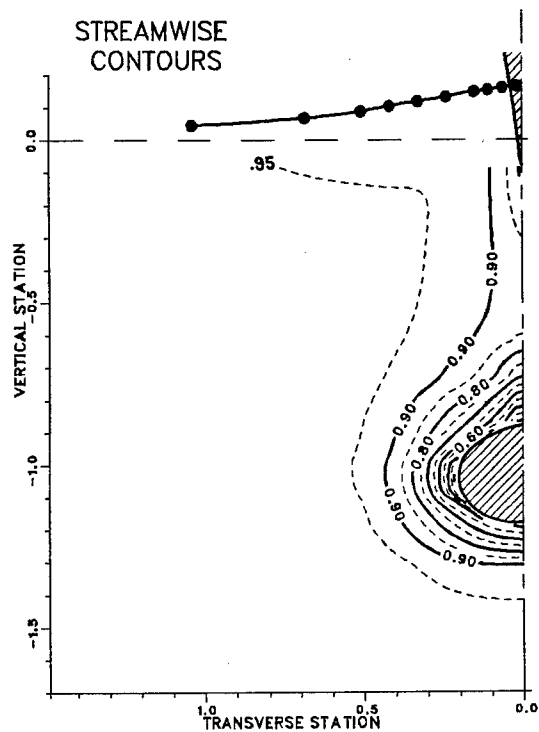
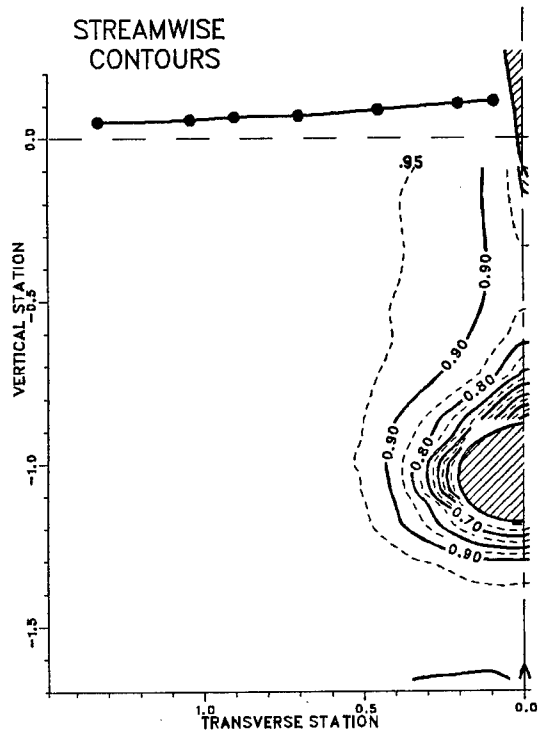
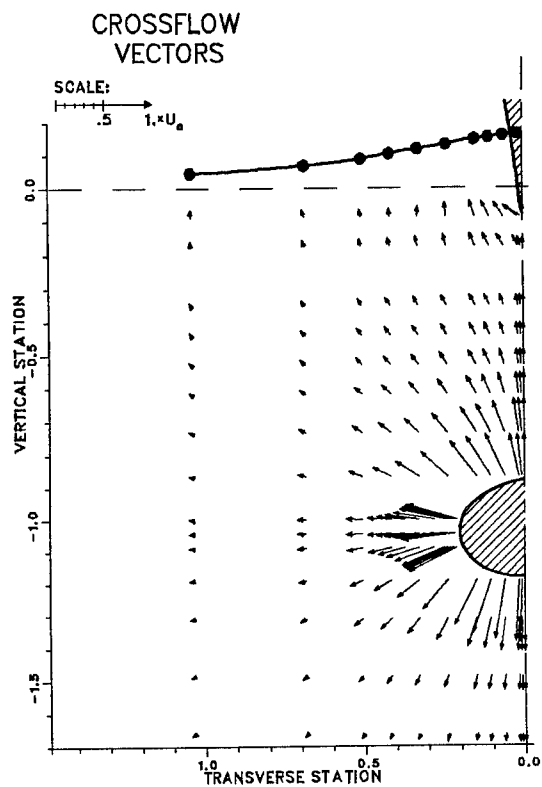


## APPENDIX 1: Velocity Field for Transverse Plane $X = 0.040$

Measured



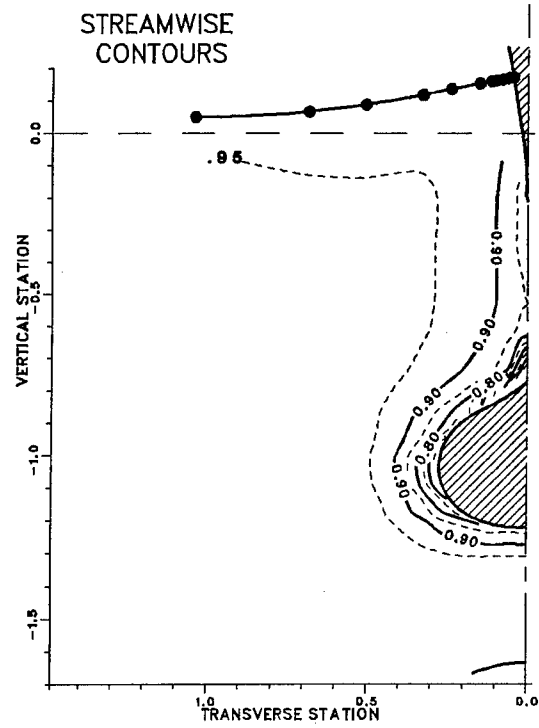
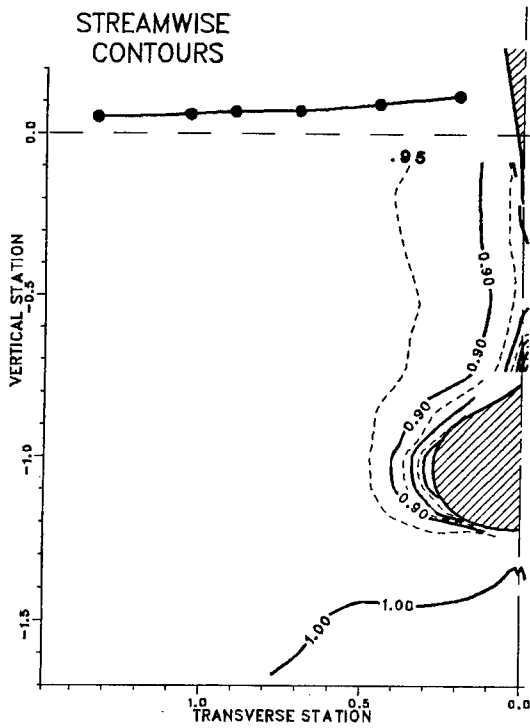
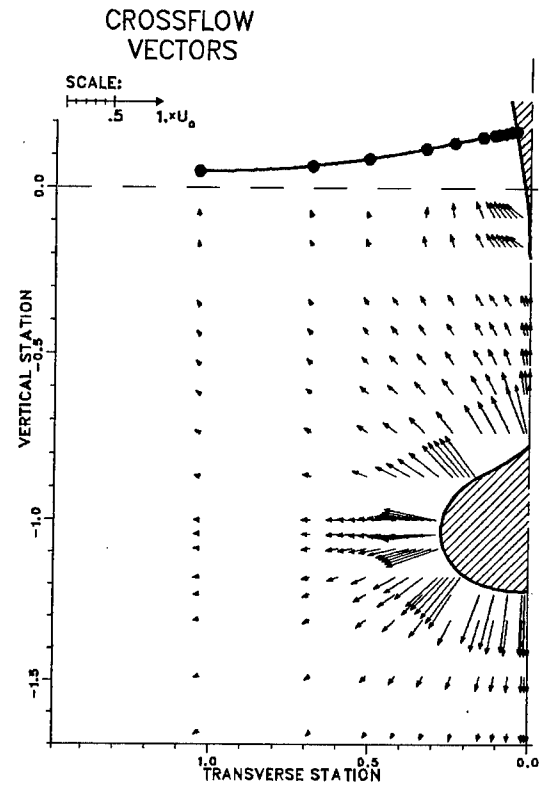
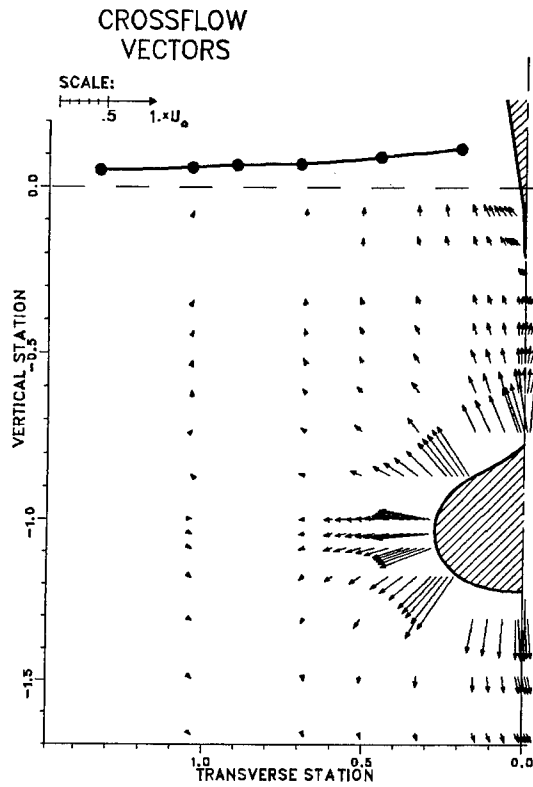
Calculated



# APPENDIX 1: Velocity Field for Transverse Plane X = 0.082

Measured

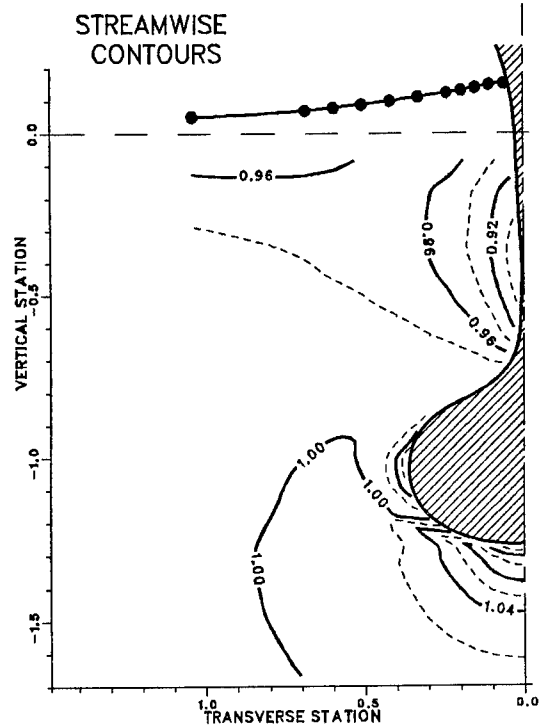
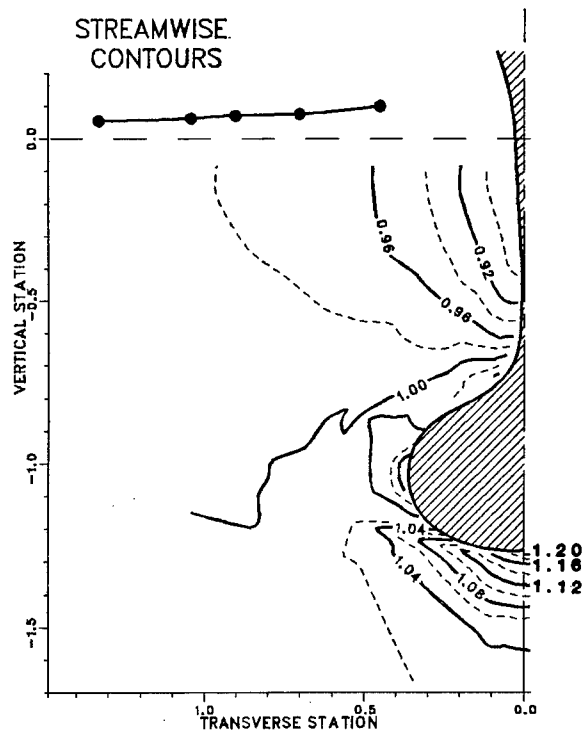
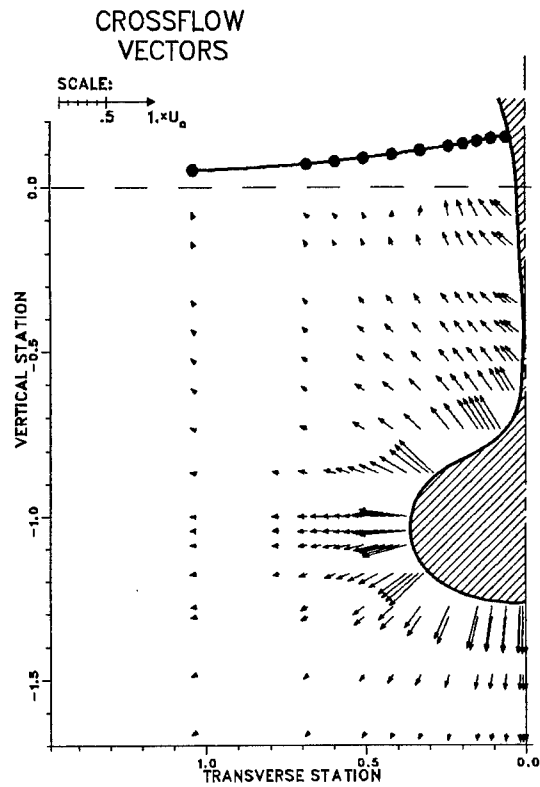
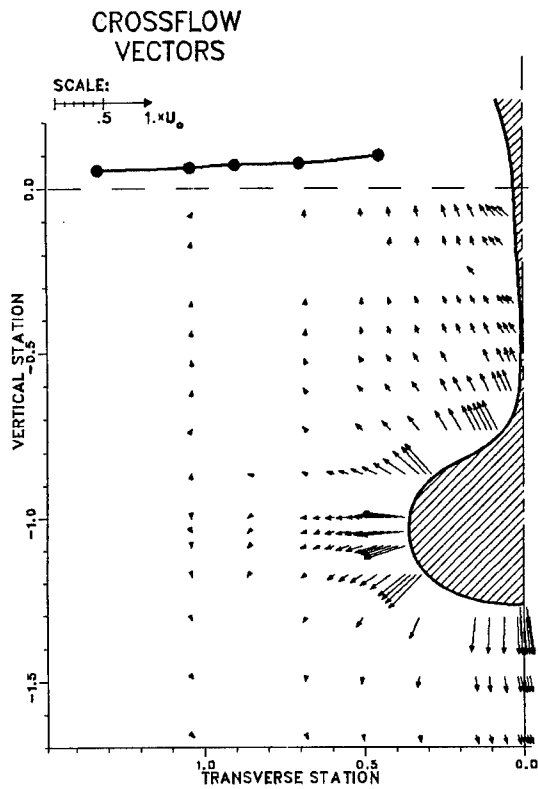
Calculated



# APPENDIX 1: Velocity Field for Transverse Plane X = 0.165

Measured

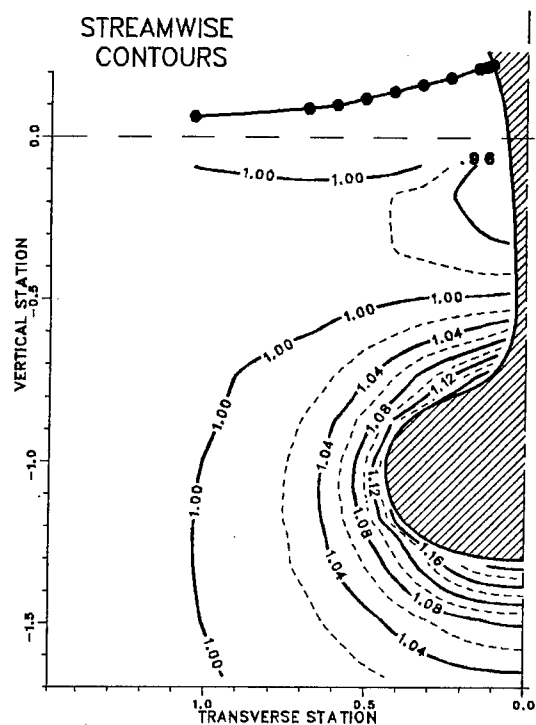
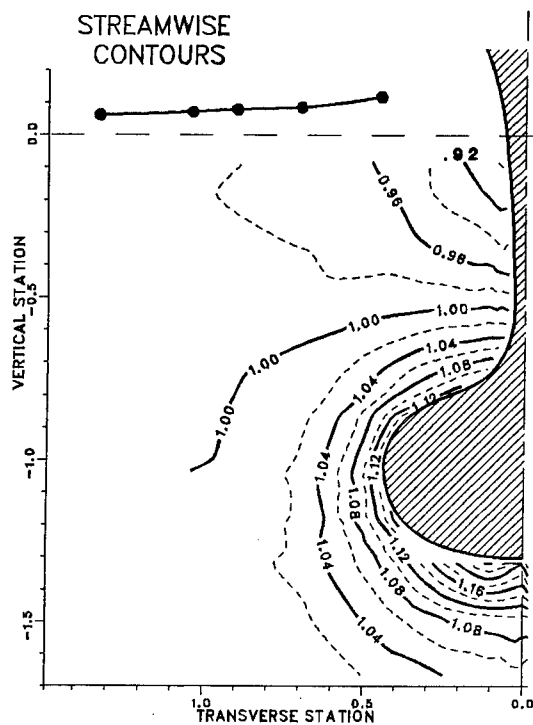
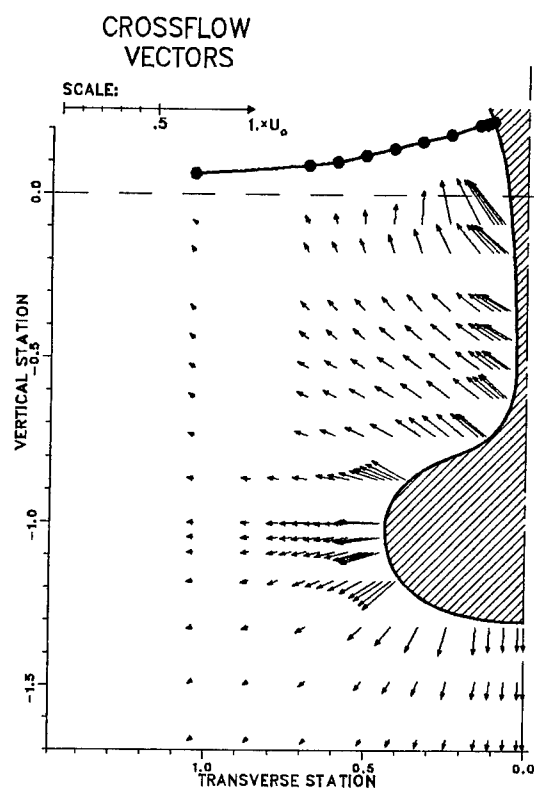
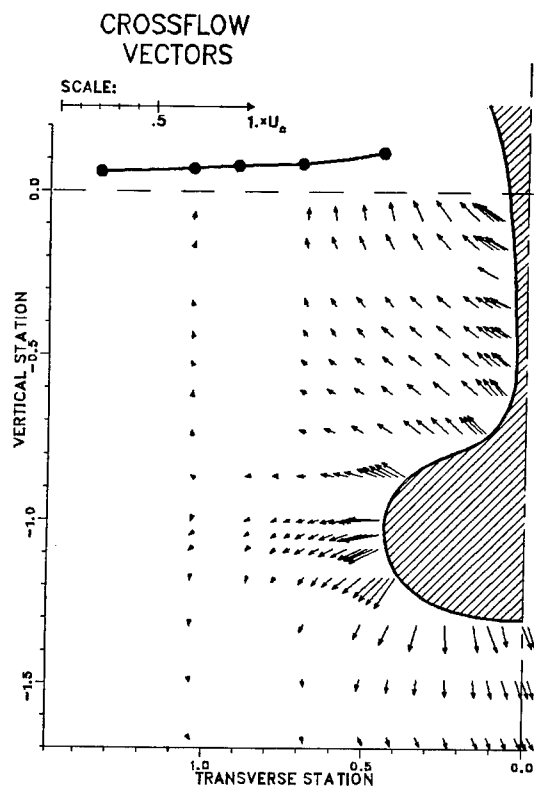
Calculated



# APPENDIX 1: Velocity Field for Transverse Plane X = 0.333

Measured

Calculated

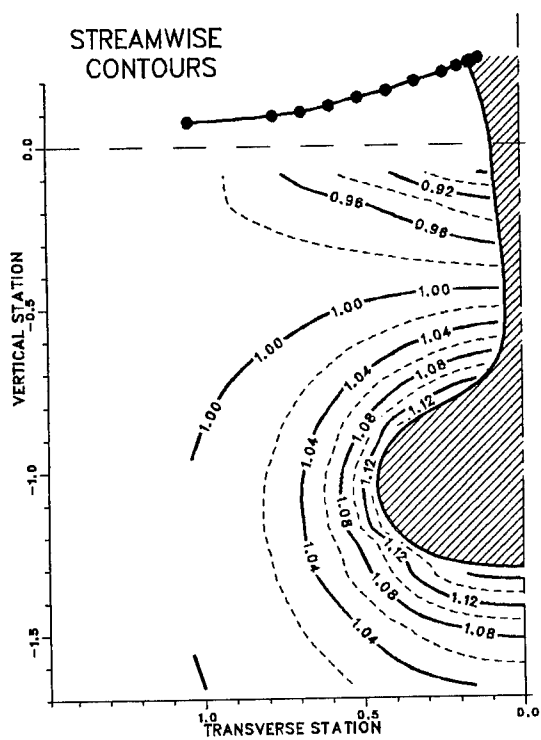
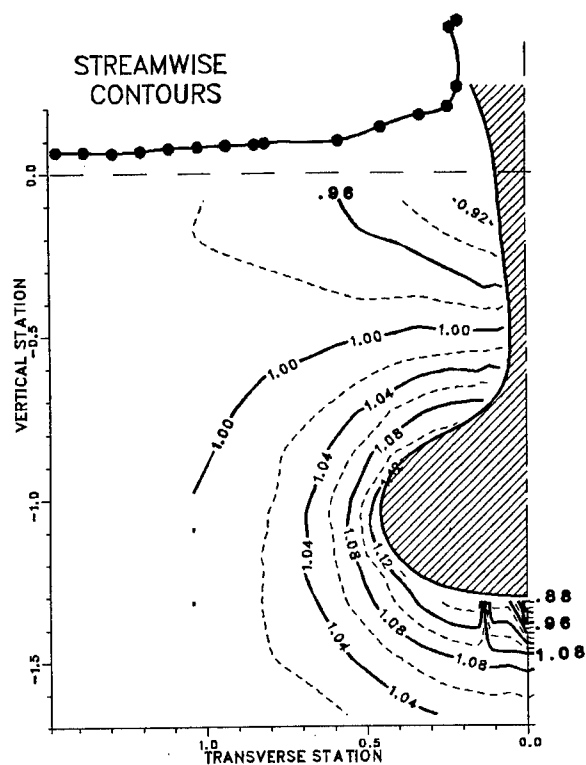
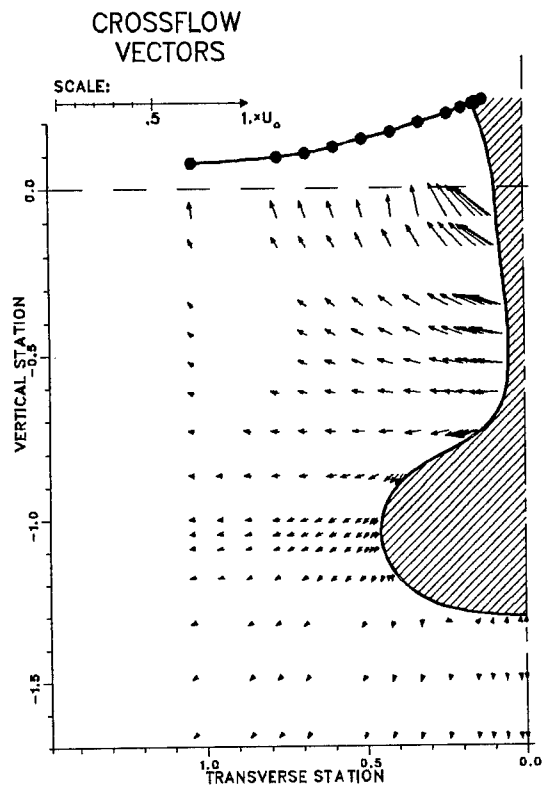
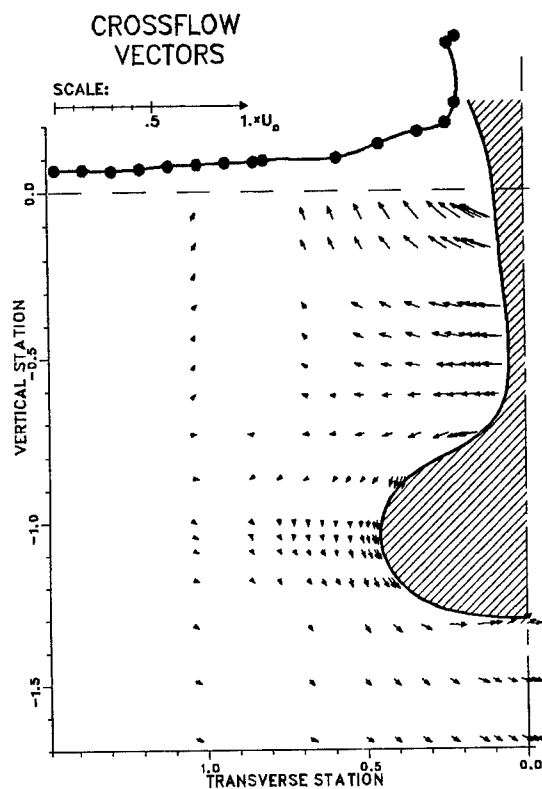




# APPENDIX 1: Velocity Field for Transverse Plane X = 0.504

Measured

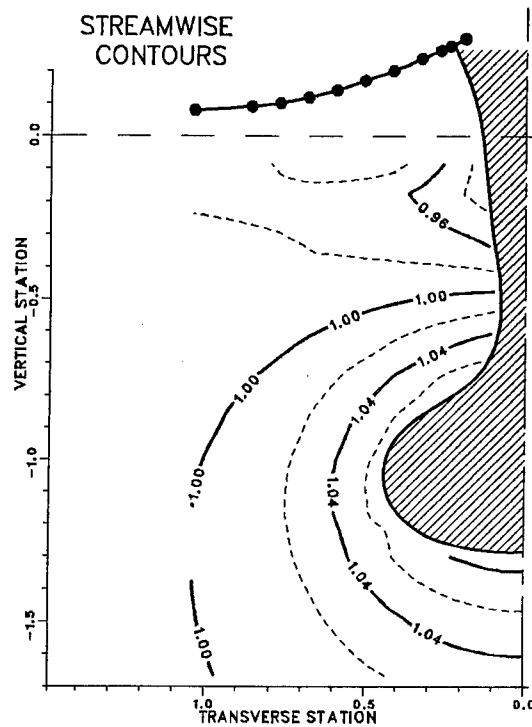
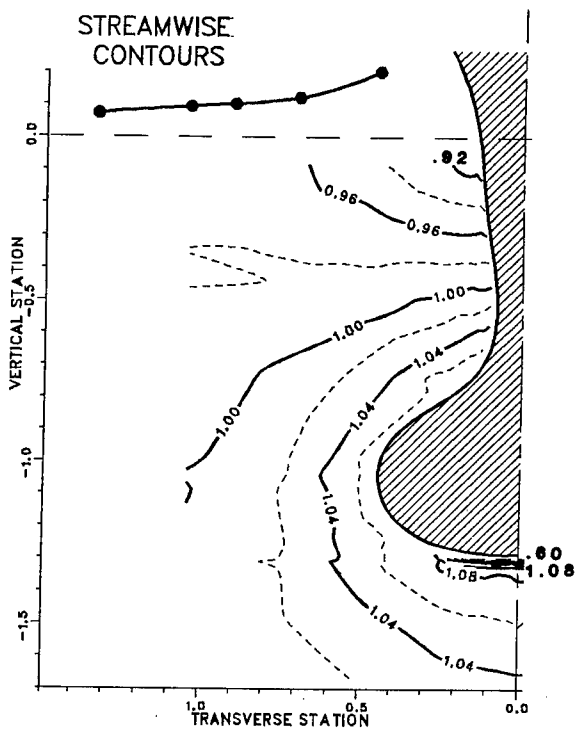
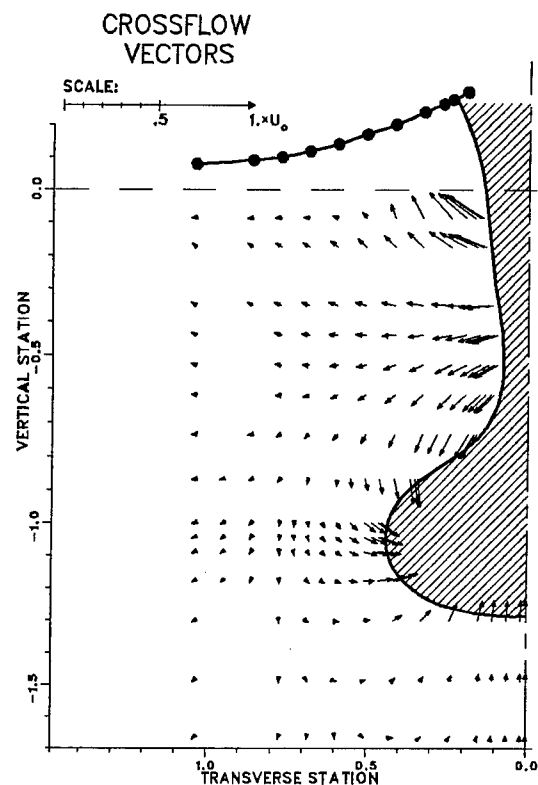
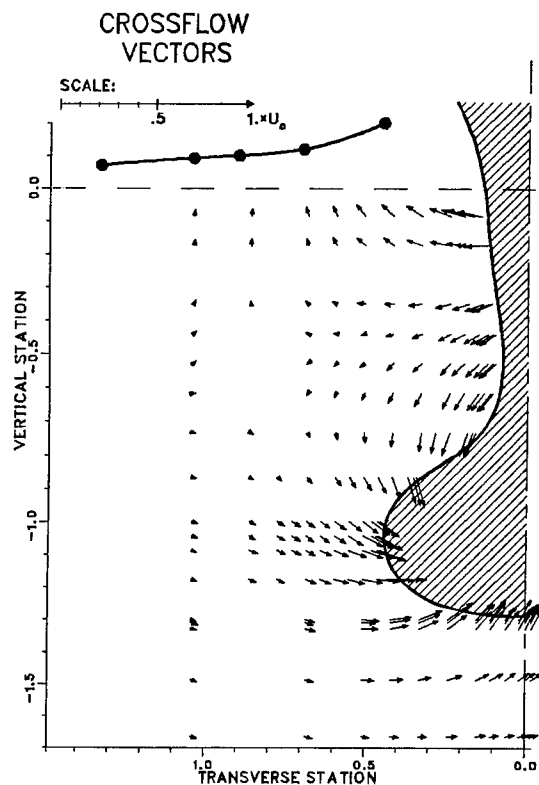
Calculated



# APPENDIX 1: Velocity Field for Transverse Plane X=0.727

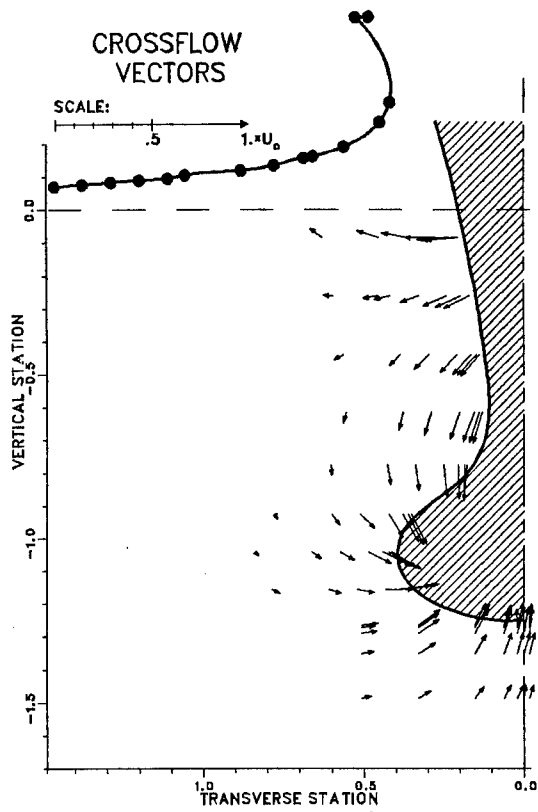
Measured

Calculated

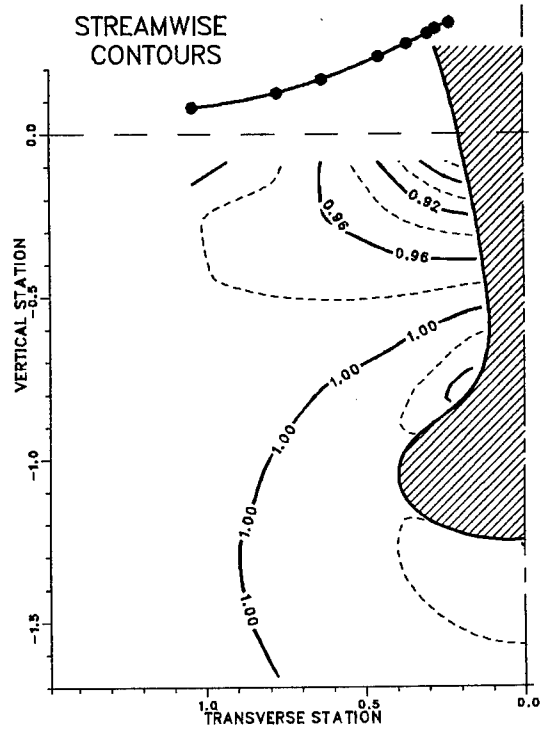
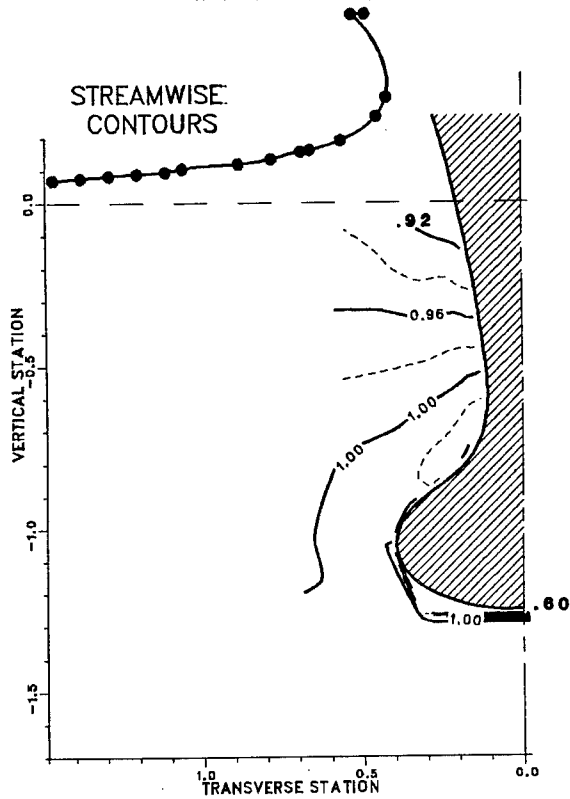
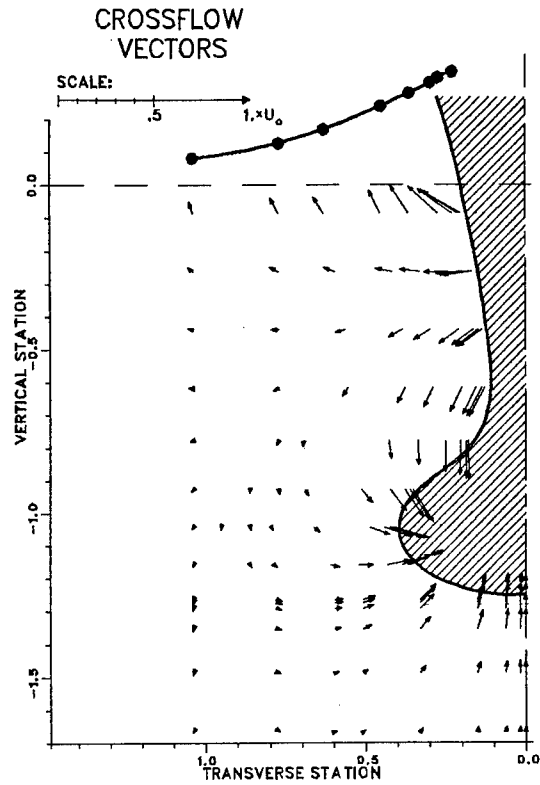


# APPENDIX 1: Velocity Field for Transverse Plane X = 0.930

Measured

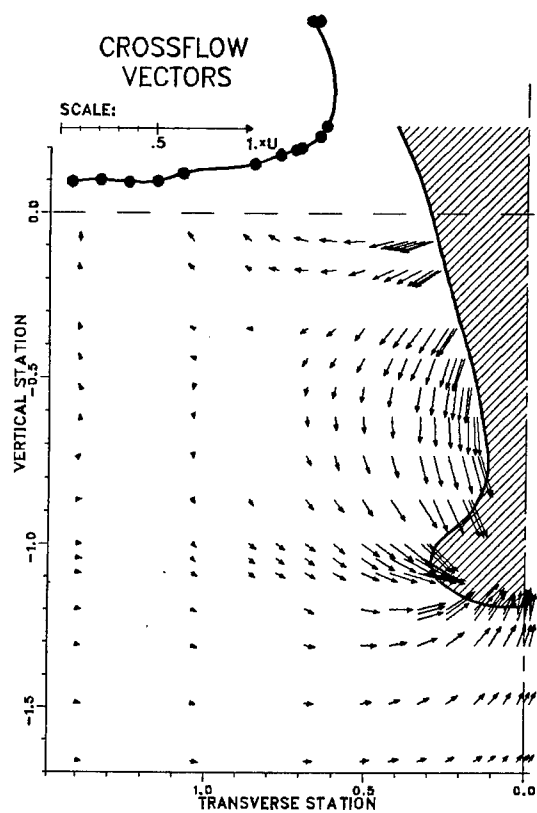


Calculated

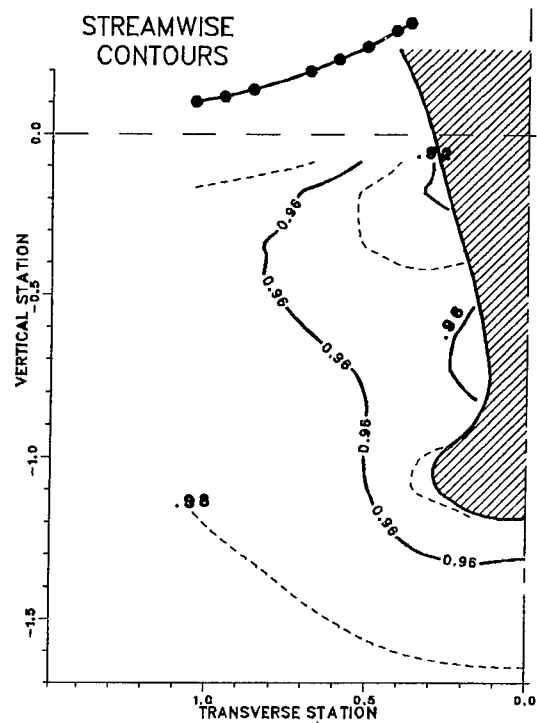
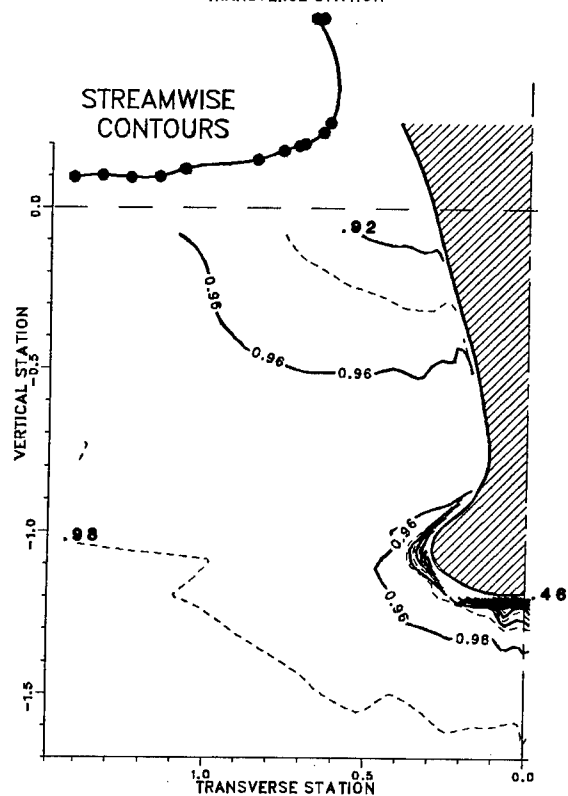
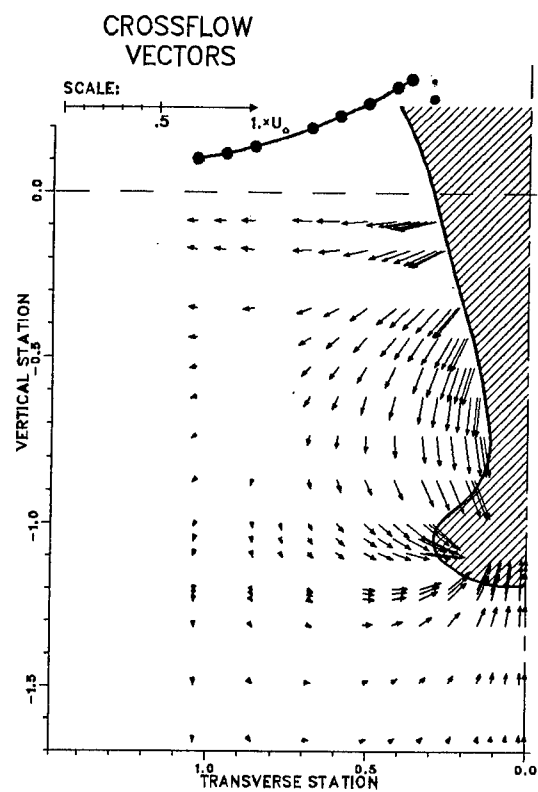


# APPENDIX 1: Velocity Field for Transverse Plane X=1.414

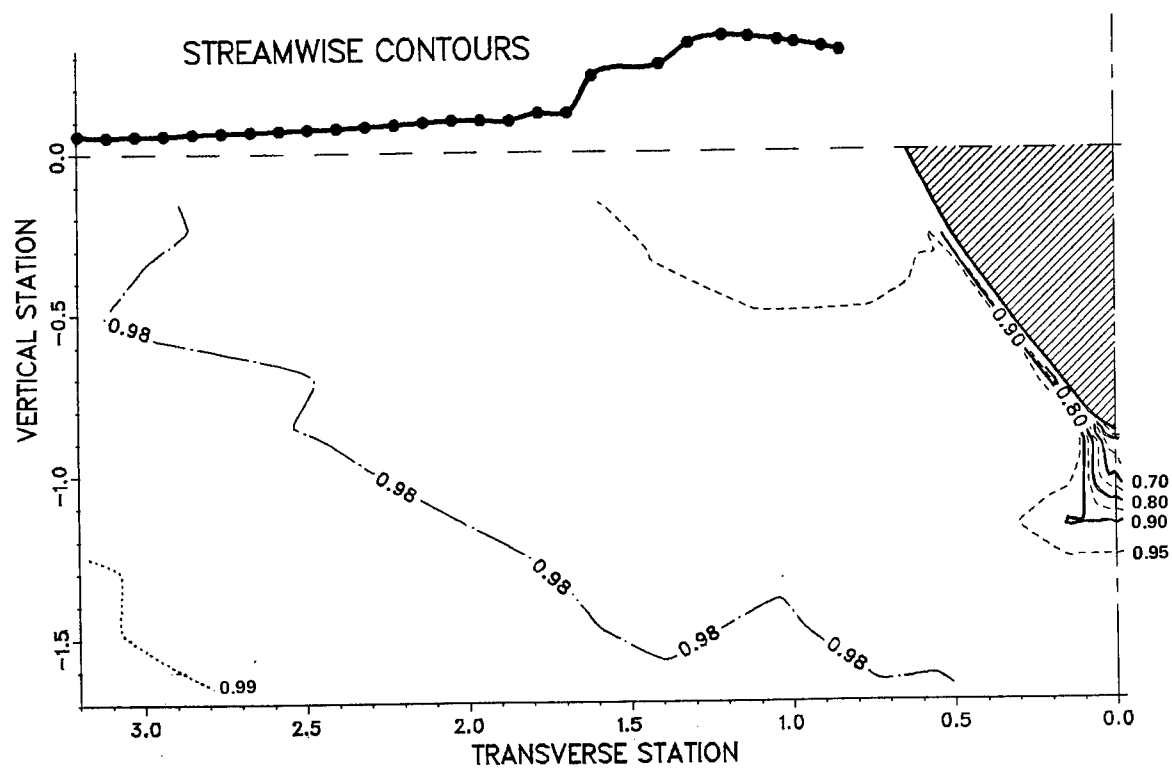
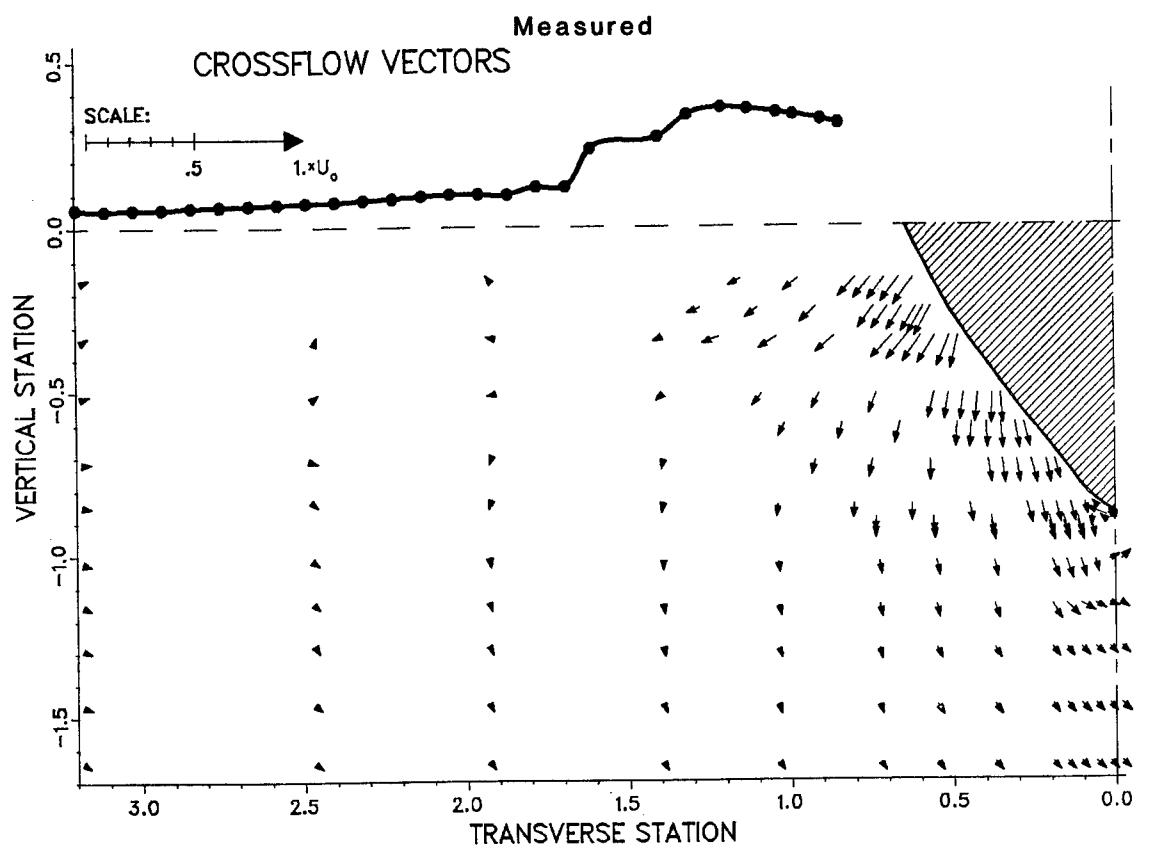
Measured



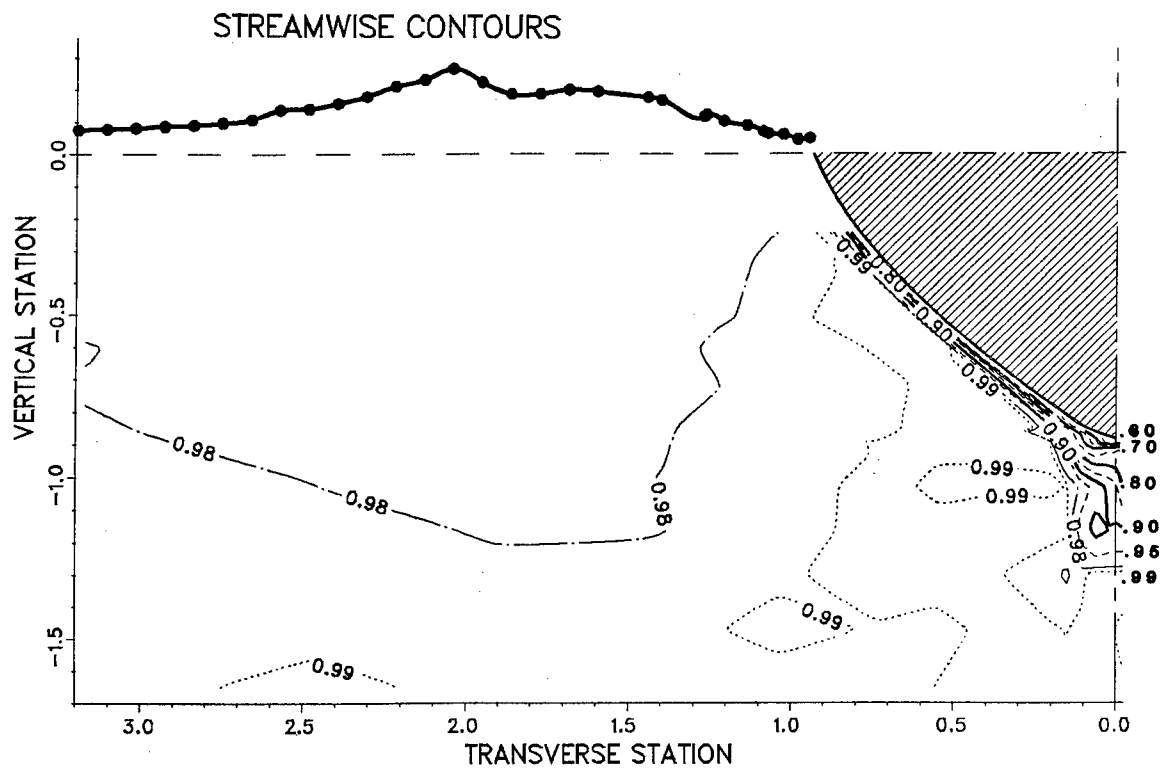
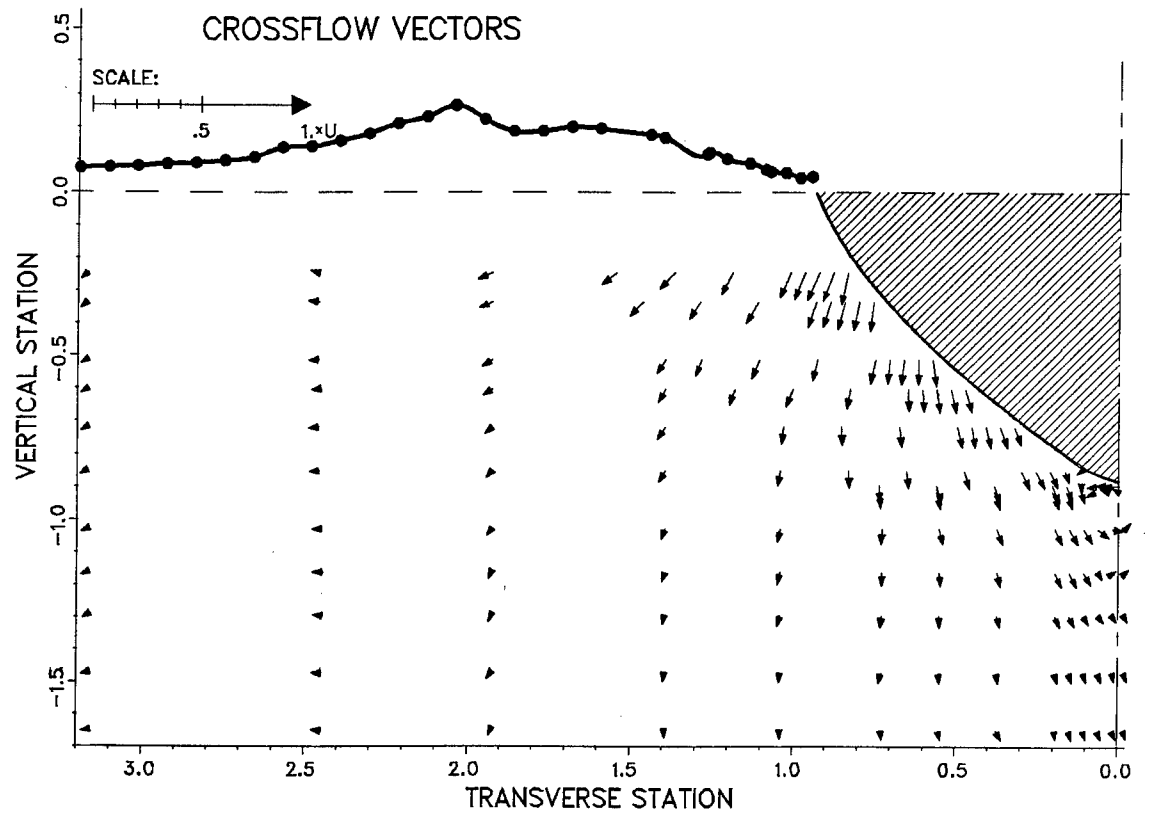
Calculated



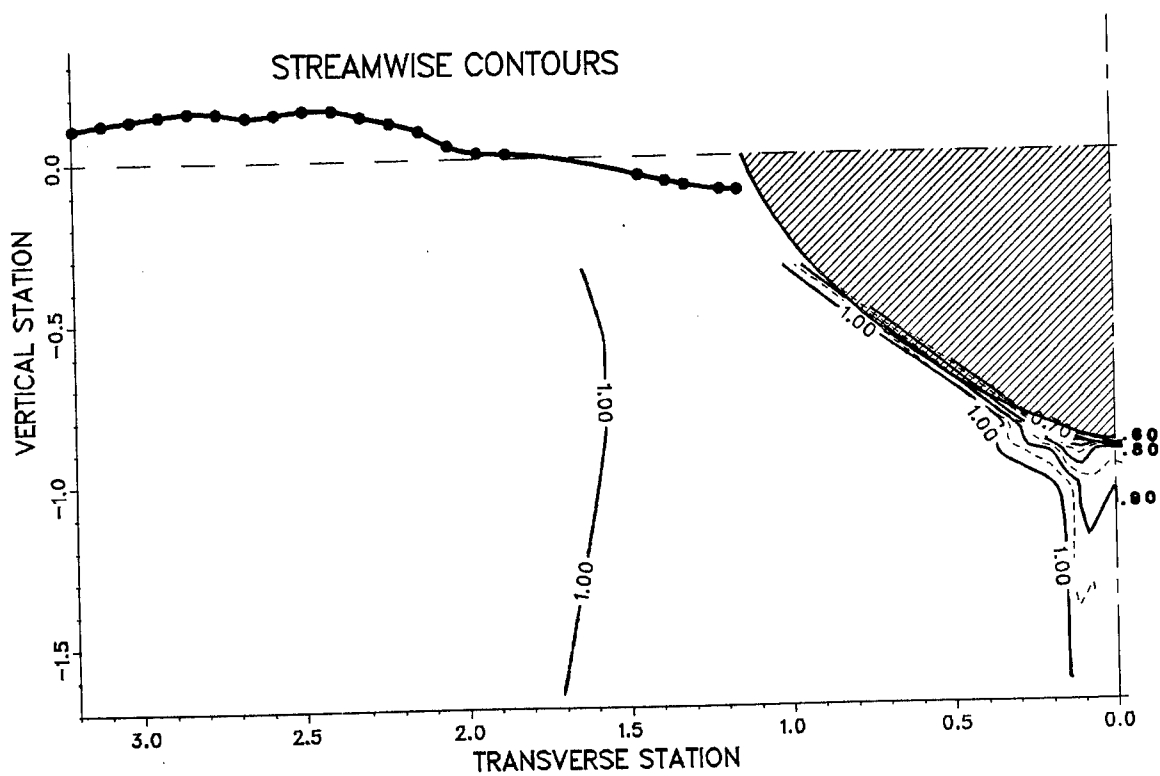
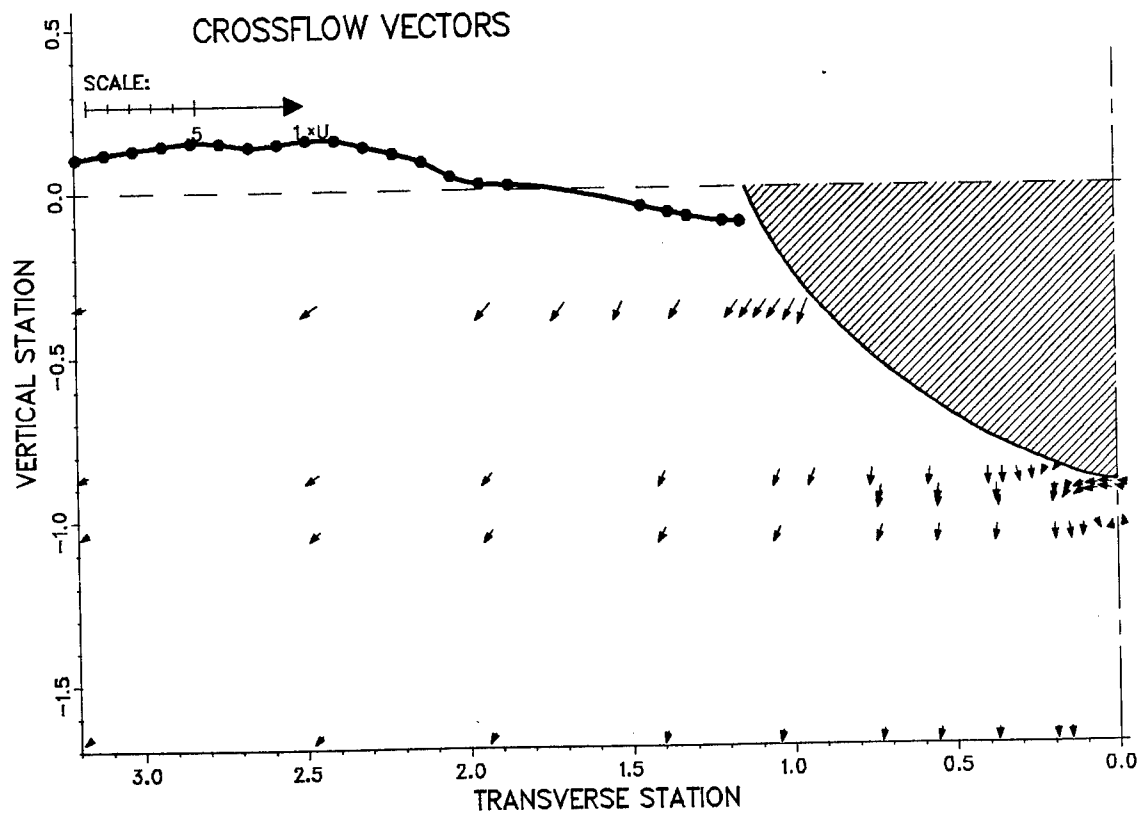
# APPENDIX 1: Velocity Field for Transverse Plane X=2.80



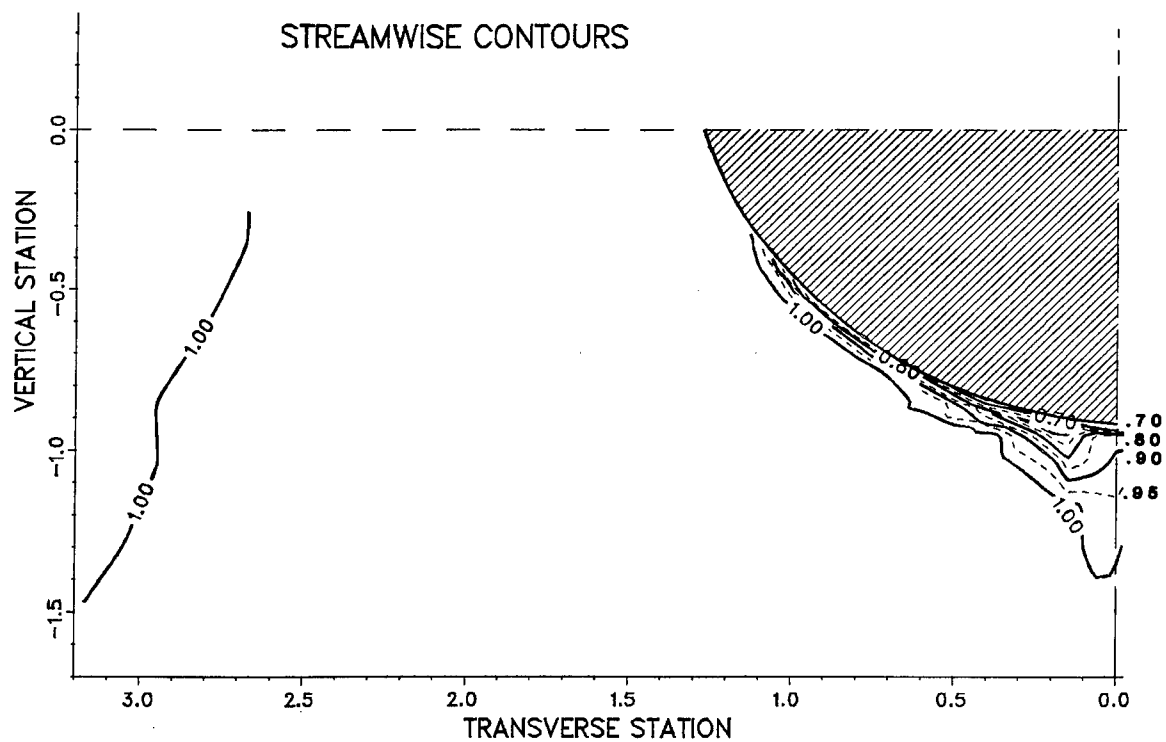
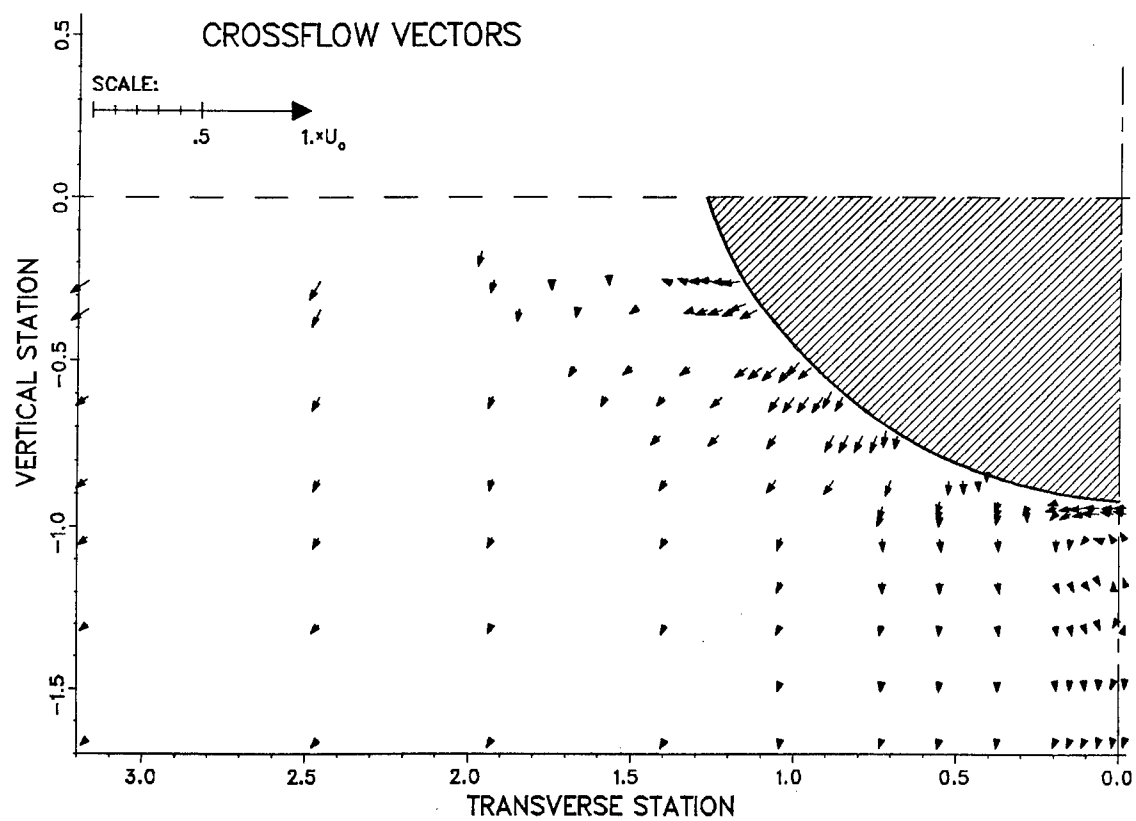
# APPENDIX 1: Velocity Field for Transverse Plane X=4.20



# APPENDIX 1: Velocity Field for Transverse Plane X=5.60

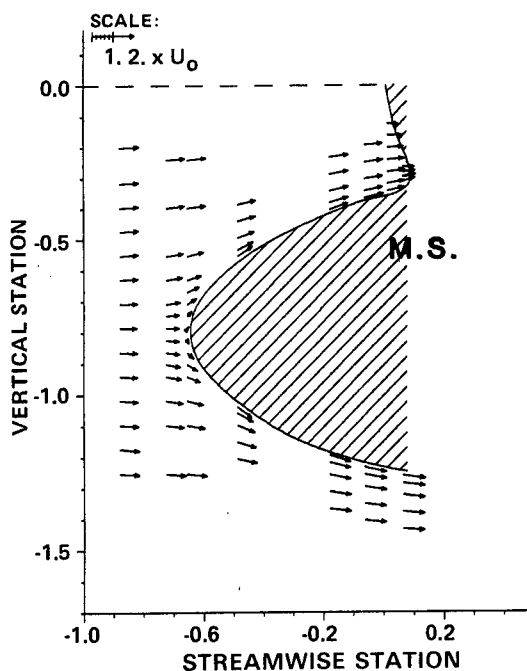
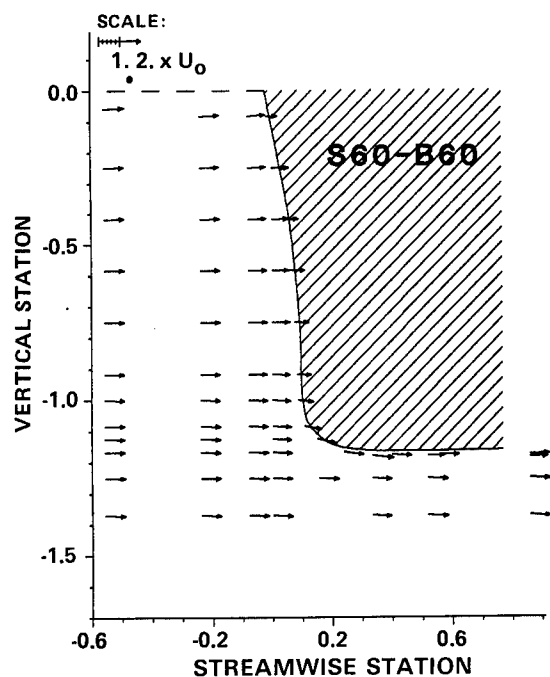
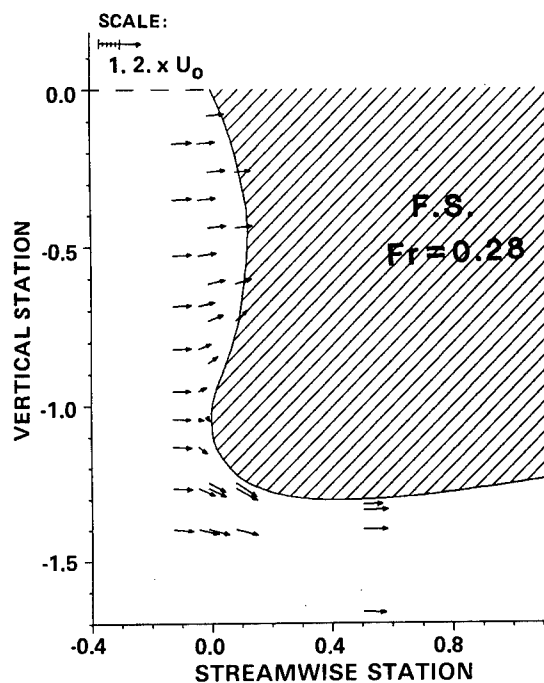
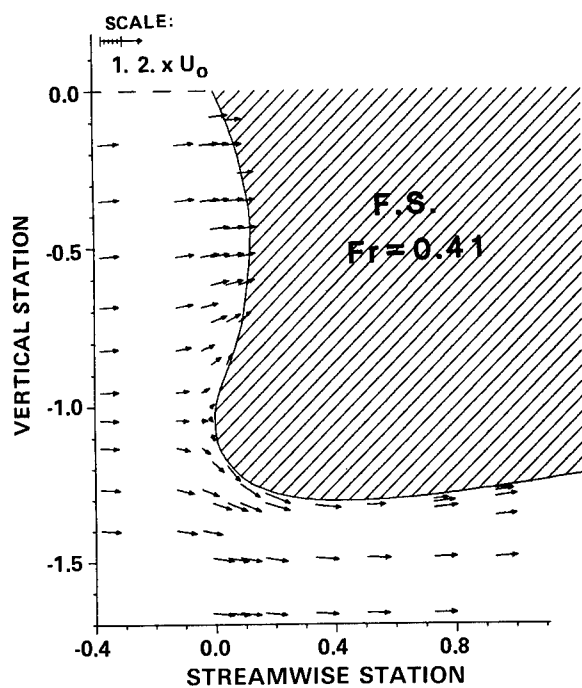


# APPENDIX 1: Velocity Field for Transverse Plane X=6.99





## APPENDIX 2: Velocity Field for Longitudinal Plane $Y = 0.00$



## DISCUSSION

Dr. ANTONY J. MUSKER,  
Admiralty Research Establishment,  
Haslar, England:

I appreciate that this paper represents an initial study but I would be glad to receive any comments from the authors on the comparison between Dawson's method and experimental data near the stern region and when we might expect a further report.

Concerning the ultrasonic probes, I note that the manufacturer's specified accuracy is  $\pm 2$  mm but that the authors claimed  $\pm 1\%$  during the presentation. Also the calibration was performed in calm water without the effect of wave slope and its consequent effect on the reflected beam. I should have thought that even a small wave slope would give rise to errors in wave elevation greater than that quoted.

Prof. Dr.-Ing. SOM D. SHARMA,  
Institut für Schiffbau,  
Hamburg, FR Germany:

The authors are to be congratulated on a very fine piece of work. We at Hamburg have also been trying to measure the bow flow-field by various techniques including LDV and can therefore well appreciate the great difficulties the authors have obviously mastered. Now I have one important question to the authors. One of the most interesting features we have observed in the flow field of bulbous forms is the existence of a pair of necklace vortices, one just below the free surface and another just above the stagnation point on the bulb. As these vortices are of opposite sense of rotation, by proper design and dimensioning of the bulb they can be made to cancel each other. This mechanism provides yet another explanation of the beneficial effect of a bow bulb in decreasing resistance and smoothing the flow. Apparently there are no bulb vortices in the flow fields reported by the authors. Have they observed this phenomenon in other experiments not shown in their paper?

Of course, we realize that their hull form was much finer than ours and so the missing vortex would not necessarily be a contradiction of our observation.

## AUTHORS' REPLY

The authors wish to thank Dr. Musker for his discussion. We do have plans to put out an internal DTNSRDC report within 6 months covering more completely the data set developed during our 3/84 - 5/84 experiments. In that report will be a limited amount of velocity and surface elevation data taken in the stern region of the "High Speed" model ( $Fr = 0.41$ ).

The inconsistency noted by Dr. Musker was a result of the authors reporting an accuracy in "millimeters" in the paper and in "ship stations" during the presentation. The authors apologize for any confusion created by this change.

The authors will investigate the degree to which "wave slope" affects ultrasonic probe accuracy. In the future, we will revise our accuracy estimate and/or data values accordingly. We wish to emphasize that all the steepest wave slopes (close to the model boundary) were obtained with the pointed rod technique ( $\sim 40\%$  of reported elevations).

The authors agree with Prof. Sharma that the reason we did not observe necklace vortices was because our bulbous bow hull forms were so fine. Experiments to date have been only on the three hull forms shown in Figure 1 and Figure 2. The necklace vortices, if present, should have appeared in the velocity data displays of Appendix II.

The authors wish to thank Prof. Sharma for his kind remarks and for his indirect suggestion of an interesting area for future experiments.

## SHIP-GENERATED SOLITONS

R.C. ERTEKIN, W.C. WEBSTER AND J.V. WEHAUSEN

### ABSTRACT

When a ship moves at a constant velocity in a rectangular channel of breadth  $b$  and depth  $h_0$ , it has been observed to generate a sequence of solitons, one after another, provided that the depth Froude number,  $F_h$ , is less than about 1.2. A series of experiments to investigate this phenomenon systematically has been conducted at U. C. Berkeley. It has been found that the dominant parameter governing soliton generation is the blockage coefficient,  $A_x/bh_0$ , where  $A_x$  is the midships section area. Numerical calculations of the flow created by moving two-dimensional disturbances are also carried out using both the fluid sheet equations of Green and Naghdi, as well as the Boussinesq equations, in the form derived by T. Y. Wu.

### 1. INTRODUCTION

This paper may be considered as a sequel to several earlier ones [T. Y. Wu (1982,1983), D.-M. Wu and T. Y. Wu (1982), Huang et al. (1982a,b)], and perhaps also as a kind of status report on investigations of the generation of solitons in shallow water by ships, pressure distributions and bottom bumps. As far as we are aware, the papers above provide almost a complete list of the systematic studies of the phenomenon. However, reports by Thews and Landweber (1935,1936) describe it quite clearly and appear to be the first published mention of it. In addition, there have long been reports of the difficulty of achieving steady-state results in towing-tank tests of models of river boats in shallow water, and indeed there have appeared observations and analyses of hydraulic jumps and of single solitary waves associated with such tests. We make no attempt here to summarize or reference these [see, however, Wu (1983)]. On a larger scale, single solitary waves have been observed preceding ships on the Suez Canal and one must suppose that the phenomenon we shall describe has often been observed in other canals. (The solitary wave described by J. S. Russell does not seem to fit into the same category). More recently, the staff members of the Bulgarian Ship Hydrodynamics Centre in Varna have reported it oral-

ly, and Mr. M.-G. Sun of the Zhongshan University in Guangzhou, People's Republic of China has sent photographs of what is clearly the same phenomenon.

Finally, we call attention to the monograph by Favre (1935, especially Chap. VIII). Favre generated waves in a rectangular channel by discharging water at a constant rate into one end of the channel. The waves that developed at the beginning of the discharge quite evidently have much in common with those generated by the motion of a ship or pressure distribution. Still another paper relevant to the observed phenomenon is that of Benjamin (1970). Although Benjamin does not specifically discuss soliton generation by moving disturbances, he does describe certain important aspects of the behavior ahead of the disturbance, aspects confirmed experimentally by Salvesen and von Kerczek (1978).

In order to clarify what is being discussed, consider Figure 1. This shows a model of a Series 60,  $C_B = 0.80$  hull being towed in the Ship Towing Tank of the University of California, Berkeley. The depth Froude number  $F_h = U/\sqrt{gh_0}$  is 0.90, where  $U$  is the velocity of the model,  $g$  the acceleration of gravity and  $h_0$  is the undisturbed water depth. Preceding the ship model and moving at speed,  $c$ , which is supercritical ( $c/\sqrt{gh_0} > 1$ ), are waves of substantial amplitude. Figure 2 shows the same phenomenon for  $F_h = 1.1$ . As the Froude number increases the solitons become more steep, and at a Froude number of about 1.2 the solitons begin to break. For  $F_h = 1.3$  and above, a hydraulic jump is formed ahead of the model. If one decreases  $F_h$  below 0.9, the waves preceding the model are no longer so visible, but have been observed for model Froude numbers  $F_h$  as low as 0.2; they are always supercritical and appear perfectly two-dimensional, spanning the tank from wall to wall. These waves are not the Cauchy-Poisson waves associated with the starting of the model that were treated in Sibul et al. (1979). Nonlinear shallow-water equations are needed to calculate them and they are essentially the solitons that appear in solutions of the Korteweg-de Vries equation for the motion following an initial hump of water. We shall call them solitons here also.

† Dept. of Naval Architecture & Offshore Engineering, University of Calif., Berkeley, CA 94720.

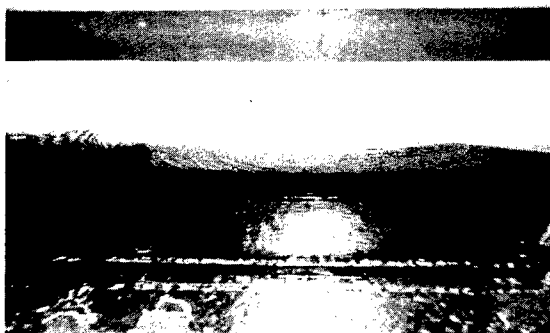
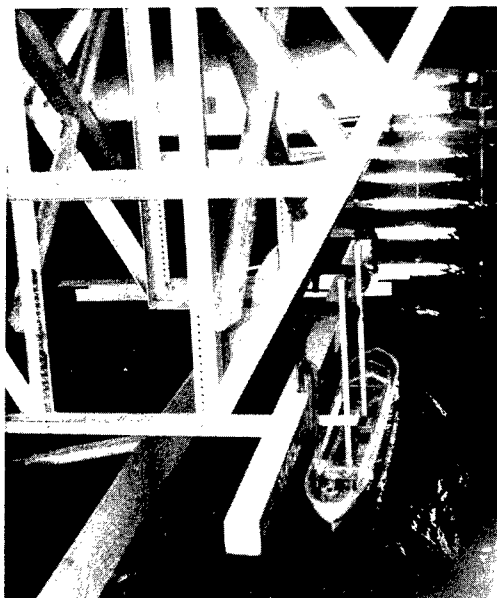


Figure 1.  $F_h = 0.90$ ,  $h_o = 12.5$  cm,  $d = 7.5$  cm,  $b = 122$  cm. Back view (above) and side view (below).

Figure 2. The same as Figure 1, except for the Froude number. Here  $F_h = 1.1$ .

## 2. EXPERIMENTS

Let us now turn to the experiments designed to investigate systematically this phenomenon. For all the experiments to be described, a model of a Series 60,  $C_B = 0.80$  hull was used. Its length was 152.4 cm, its beam 23.4 cm. Four drafts were tested:  $d = 2.5$  cm, 5.0 cm, 7.5 cm and 10.0 cm. Three water depths were used:  $h_o = 10.0$  cm, 12.5 cm and 15.0 cm. The bottom of the towing tank has an unevenness of  $\pm 0.7$  cm and, as a result, we did not test in water depths less than 10 cm. We also desired to have an average of at least 2.5 cm clearance under the keel of the model and, thus, not all drafts could be used with all water depths. The width of the tank was also varied. The normal tank width is  $b = 244$  cm. A false wall gave a reduced width of  $b = 122$  cm. By towing a half-model along one wall we effectively doubled the normal width to  $b = 488$  cm. Figure 3 shows the

combinations for which experiments were made and the blockage which is associated with each combination. Finally, the model was always fixed to the carriage. Although this may not seem to conform to standard practice or to model "reality", it avoided an added complication in an already complex situation.

The most important measurements were wave measurements. Two sorts of measurements were made. In one, the wave gauges were fixed at various locations in the tank as shown in Figure 4a. In the other, the gauges were fixed to the towing carriage ahead of, and to the side of, the model. Their location is shown in Figure 4b. The wave records were recorded on a strip chart for visual inspection and simultaneously recorded digitally every 0.04 - 0.05 sec. The wave resistance was also recorded in the experiments where the wave gauges were fixed to the carriage (except for the half-model experiments). Tests were carried out for

d = 2.5				d = 5.0			
b \ h <sub>0</sub>	122.0	244.0	488.0	b \ h <sub>0</sub>	122.0	244.0	488.0
10.0	4.6339	2.3170	1.1585	10.0	9.4085	4.7043	2.3521
12.5	3.7071	1.8536	0.9268	12.5	7.5268	3.7634	1.8817
15.0	—	—	—	15.0	6.2723	3.1362	1.5681

d = 7.5				d = 10.0			
b \ h <sub>0</sub>	122.0	244.0	488.0	b \ h <sub>0</sub>	122.0	244.0	488.0
10.0	14.1831	7.0916	3.5458	10.0	—	—	—
12.5	11.3464	5.6732	2.8366	12.5	—	—	—
15.0	9.4554	4.7277	2.3639	15.0	12.6384	6.3192	3.1596

Figure 3. Combinations of the experimental parameters and the blockage coefficient,  $S = A_x/bh_0$  (in percent).  $h_0$ ,  $d$  and  $b$  are in centimeters.

depth Froude numbers from about 0.6 to 1.2 in increments of 0.1 (except in the neighborhood of  $F_h = 1.0$ , where the increments were 0.05). However, runs at both higher and lower values were occasionally made, and sometimes we did not go as far as 1.2.

It is evident that we have a plethora of data, much more than we can reproduce here. However, it is instructive to look at some samples of the wave records. Figure 5 shows the wave records taken at the four gauges fixed in the tank for  $F_h = 0.8$ ,  $h_0 = 12.5$  cm,  $d = 7.5$  cm and  $b = 122$  cm, 244 cm and 488 cm. Figures 6 and 7 show wave records taken under the same circumstances, except that now  $F_h = 1.0$  and 1.1, respectively. There are typical differences between the three records. For  $F_h = 0.8$  one sees an oscillation of gradually decreasing amplitude about a mean line situated above the still-water level. This is typical of what we observed for subcritical speeds. One might conjecture that the amplitudes of oscillation approach zero, and indeed, calculations to be introduced later on seem to confirm this. By contrast, for  $F_h = 1.0$  and 1.1 the oscillations appear to be of nearly constant amplitude but also about a mean line well above the still-water level.

Figure 8 shows wave records taken at three Froude numbers with gauges fixed to the towing carriage as shown in Figure 4b. The generated waves are now stretched out since the record is taken in a moving coordinate system. However, one still sees for  $F_h = 0.95$  a noticeable decrease in amplitude of successive solitons, although the decrease is not as marked as for  $F_h = 0.8$  in Figure 5. For  $F_h = 1.0$  and greater, no general pattern appears. We shall not show any more wave records but instead the results of analysis of the records.

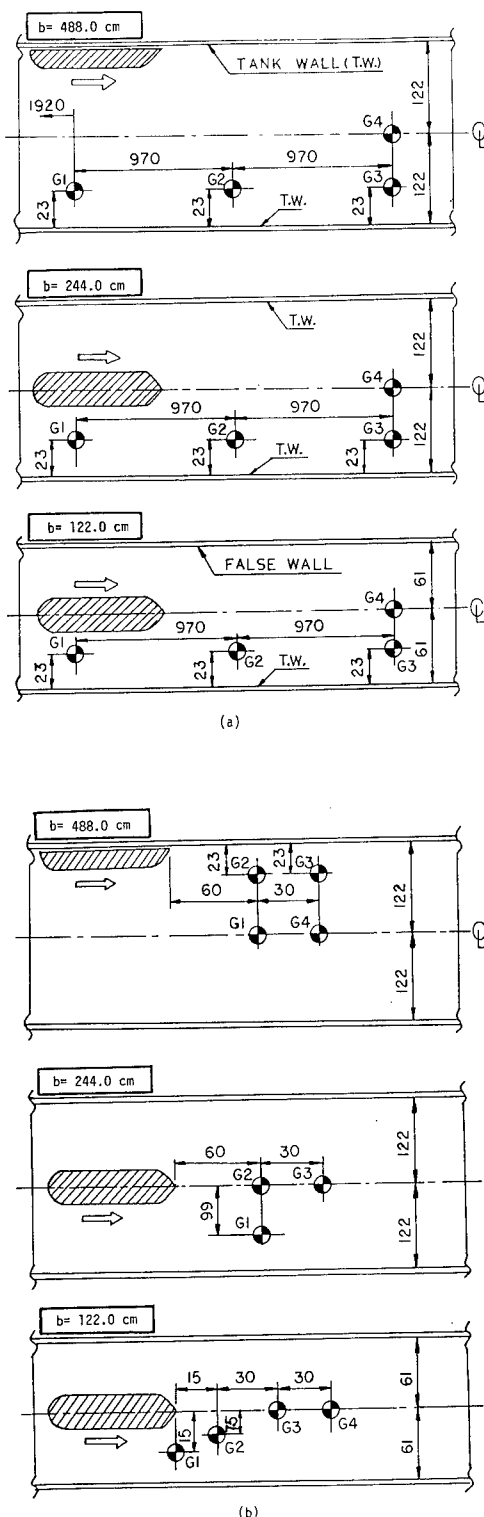


Figure 4. Locations of the wave gauges used in: (a) the fixed-gauge experiments, and (b) the moving-gauge experiments. Distances are in centimeters.

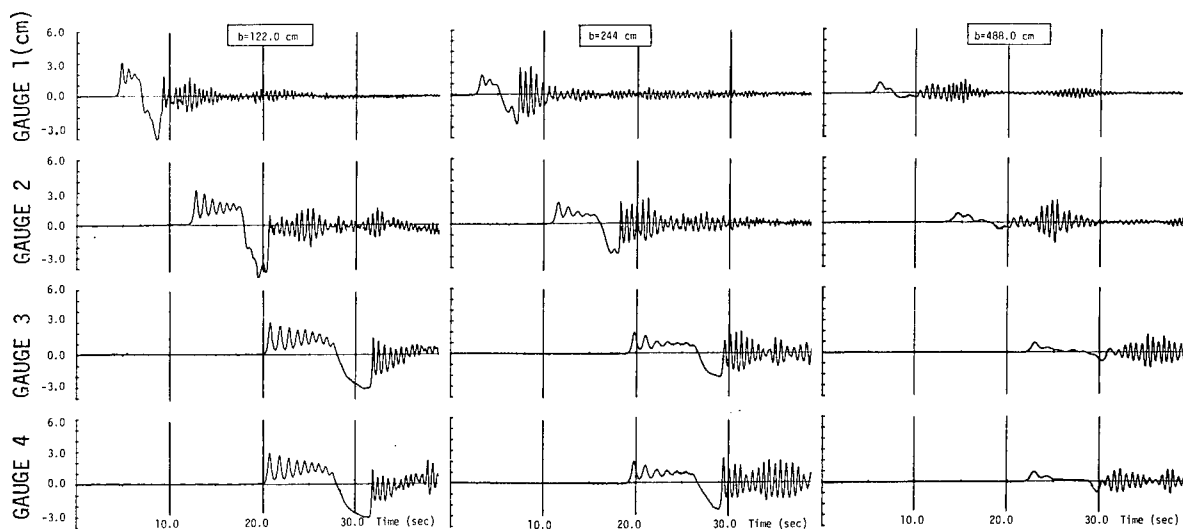


Figure 5. Wave records from fixed gauges for  $F_h = 0.8$ ,  $h_o = 12.5$  cm,  $d = 7.5$  cm.

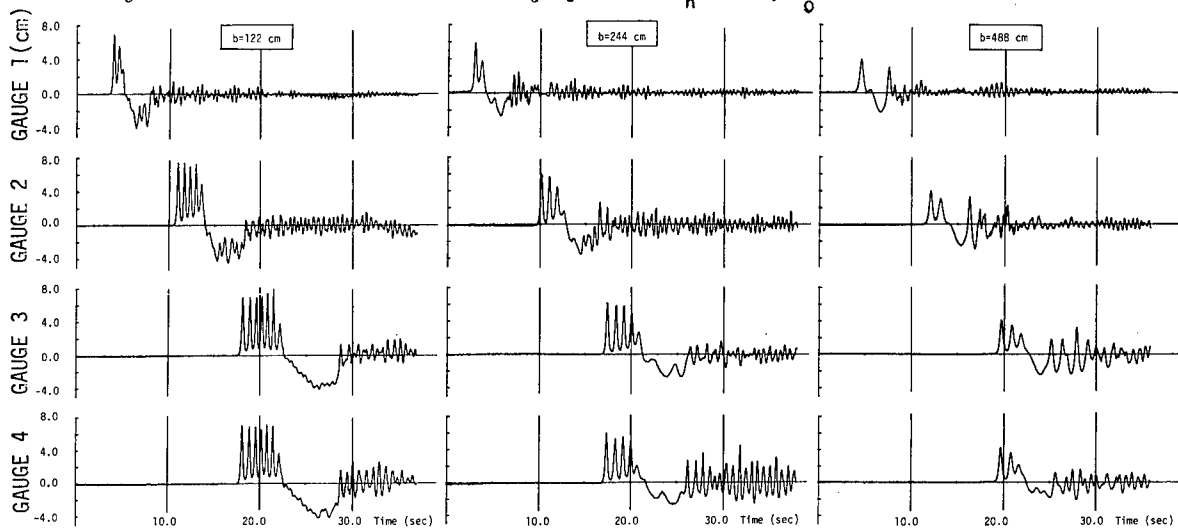


Figure 6. Wave records from fixed gauges for  $F_h = 1.0$ ,  $h_o = 12.5$  cm,  $d = 7.5$  cm.

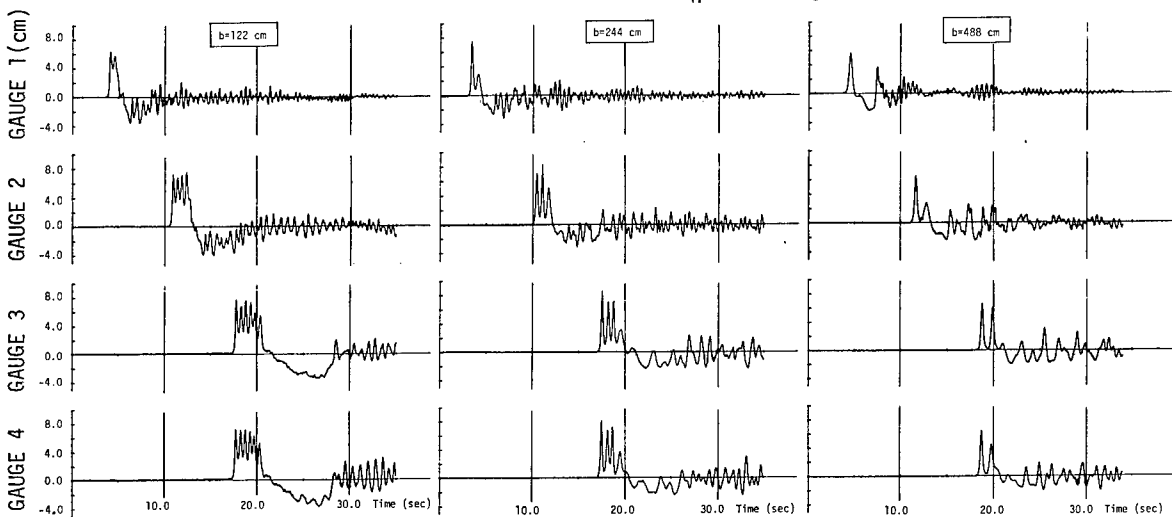


Figure 7. Wave records from fixed gauges for  $F_h = 1.1$ ,  $h_o = 12.5$  cm,  $d = 7.5$  cm.

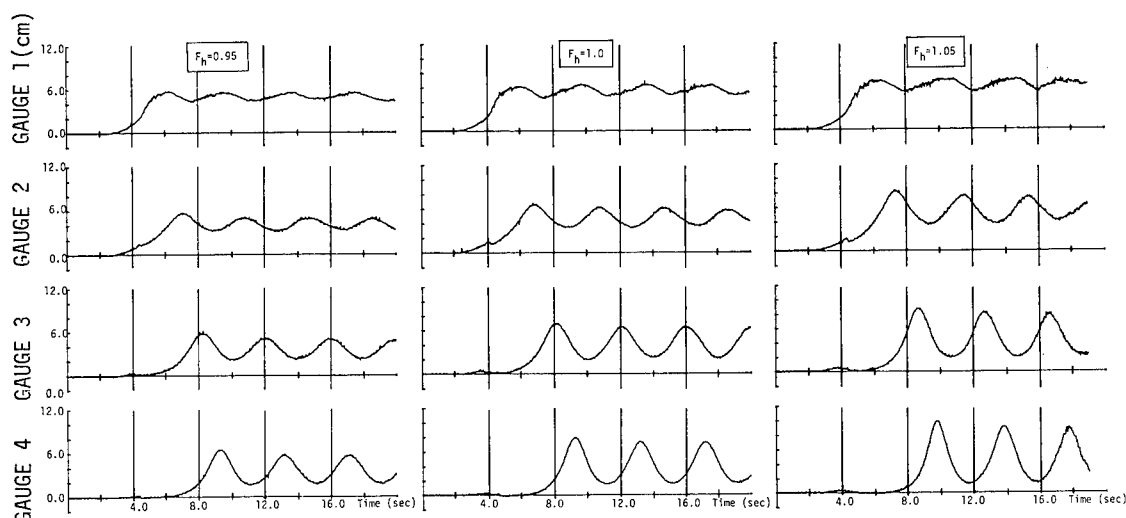


Figure 8. Wave records from gauges fixed to the towing carriage. Here  $h_0 = 15$  cm,  $d = 7.5$  cm and  $b = 122$  cm.

An observer of the generation of solitons by a moving model is immediately struck by the two-dimensionality of the solitons, in spite of the three-dimensionality of the generator, i.e. the model. This happens very quickly. By the time the wave leaves the bow of the model it is already essentially two-dimensional, stretching across the tank from wall to wall with almost constant amplitude. Having observed this, one then asks, "What happens if the tank is very wide, or unbounded?". If solitons of the same amplitude were shed with the same frequency, the model would be transferring increasing amounts of energy to the water as the width increases, which is contrary to experience.

The effect of tank width upon the amplitude of the first soliton is shown in Figure 9 for two water depths,  $h = 10$  cm and  $15$  cm and  $d = 5$  cm and  $7.5$  cm, respectively. It is evident that the amplitude decreases as the tank width increases except at the highest Froude numbers. The turning down of  $A/h_0$  between  $F_h = 1.1$  and  $1.2$  is typical of almost all combinations of  $h_0$  and  $d$ , although it does not happen here for the greatest width. This is usually associated with the onset of breaking and the formation of a bore. The two examples in Figure 9 were chosen to have approximately the same blockage coefficient,  $S = A_x/bh_0$ . It is evident that the behavior of the corresponding curves is very similar. In fact, when superposed they agree quite well. Figure 10 shows  $A/h_0$  as a function of  $S$  with  $F_h$  as a parameter. The data collapse fairly well into single curves for each Froude number.

There remains the effect of tank width upon the period  $T$  of generation of solitons. If this increases with increasing tank width, then the average rate at which the model transfers energy to the water will decrease as long as the soliton amplitude does not increase, and we have just seen that it usually does not. It is possible to determine  $T$  either from the gauges fixed to the carriage or from those fixed in the tank. If  $T_m$  is the period of

generation observed in coordinates moving with velocity  $U$ ,  $T_f$  the period between solitons observed in fixed coordinates, and  $c$ , the average wave celerity (since the celerity is not quite constant), then to a good degree of approximation

$$T_m = [c/(c-U)] T_f. \quad (1)$$

Here we shall use  $T_m$  to present our data. Figure 11 is a counterpart to Figure 9. It shows  $UT_m/h_0$  plotted against  $F_h$  for the three widths used in the experiments, with all other parameters being the same. As anticipated,  $T_m$  increases as the width does. As was the case for the amplitudes, plotting the dimensionless period of generation against the blockage coefficient tends to collapse the data. This is shown in Figure 12.

Let  $z = \zeta(x, t)$  be the free surface measured from the still-water level, and for a solitary wave, a single soliton, let

$$E = \int_{-\infty}^{\infty} \zeta^2 dx. \quad (2)$$

$\rho g E$  is then the energy per unit width carried by the soliton. If  $A$  is the amplitude of the soliton, it is well known [see Miles (1980), p. 15] that

$$E = \{4Ah_0/3\}^{3/2}. \quad (3)$$

It is pointed out in Huang et al. (1982b) that if this same relation may be applied to the individual solitons successively generated by the ship model, then the average rate at which the model is transferring energy to the water through soliton generation is

$$\begin{aligned} \rho g E b / T_m &= \rho g b \{4Ah_0/3\}^{3/2} / T_m \\ &= \{8\sqrt{3} \rho g h_0^3 U b (A/h_0)^{3/2} \\ &\quad (UT_m/h_0)^{-1} / 9h_0. \end{aligned} \quad (4)$$

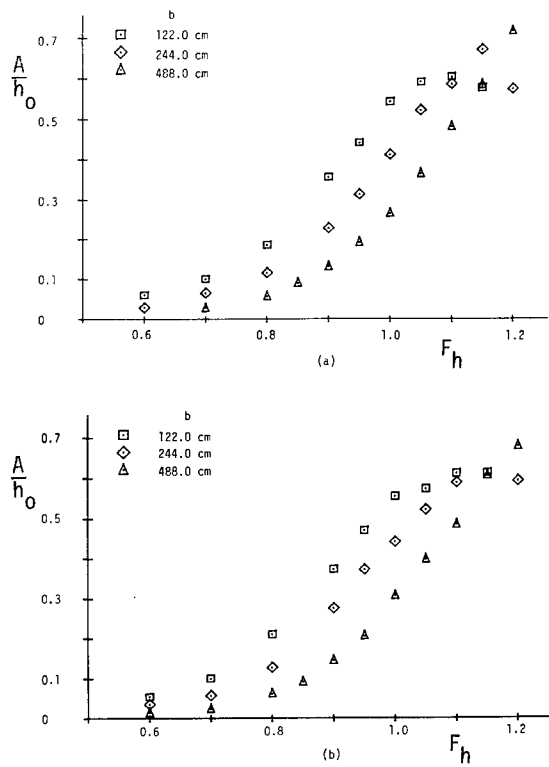


Figure 9.  $A/h_0$  as a function of  $F_h$  for  $b = 122$  cm, 244 cm and 488 cm. (a)  $h_0 = 10$  cm and  $d = 5$  cm, (b)  $h_0 = 15$  cm and  $d = 7.5$  cm.

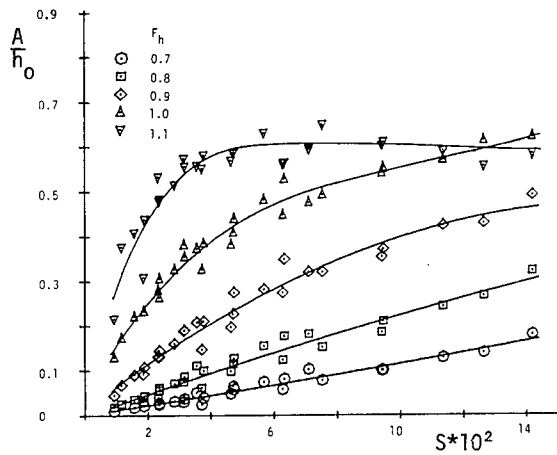


Figure 10.  $A/h_0$  for all data (obtained from the gauges fixed to the tank) plotted against the blockage coefficient,  $S$ , for Froude numbers 0.7, 0.8, 0.9, 1.0 and 1.1.

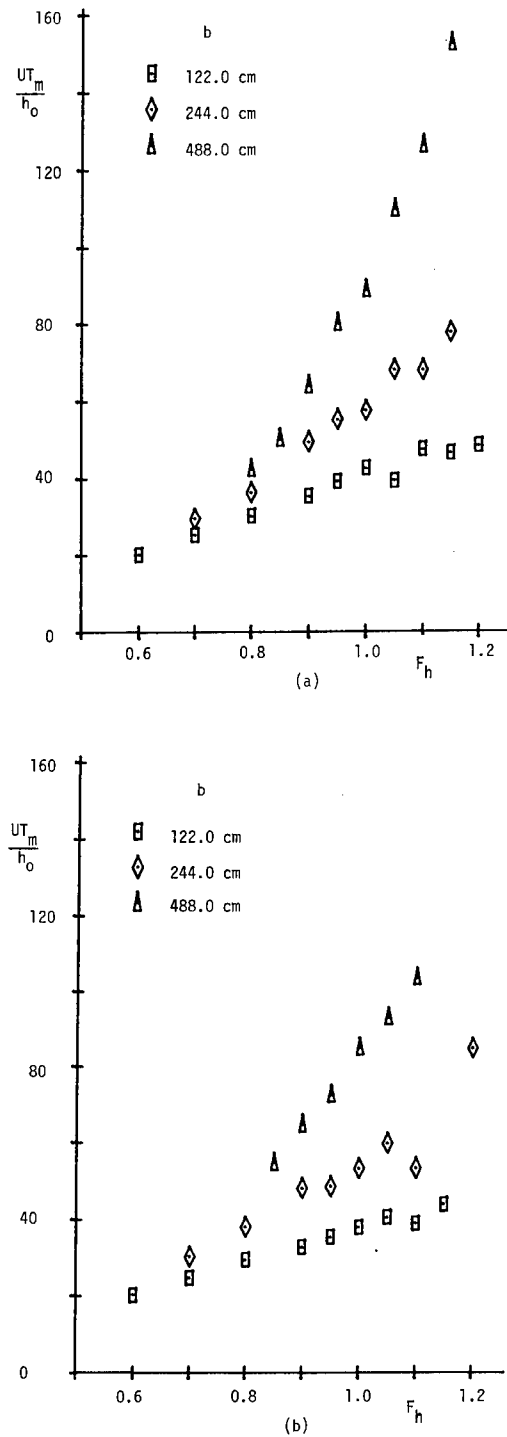


Figure 11. Dimensionless period of generation,  $UT_m/h_0$ , of solitons as a function of  $F_h$  for  $b = 122$  cm, 244 cm and 488 cm. (a)  $h_0 = 10$  cm and  $d = 5$  cm, (b)  $h_0 = 15$  cm and  $d = 7.5$  cm.



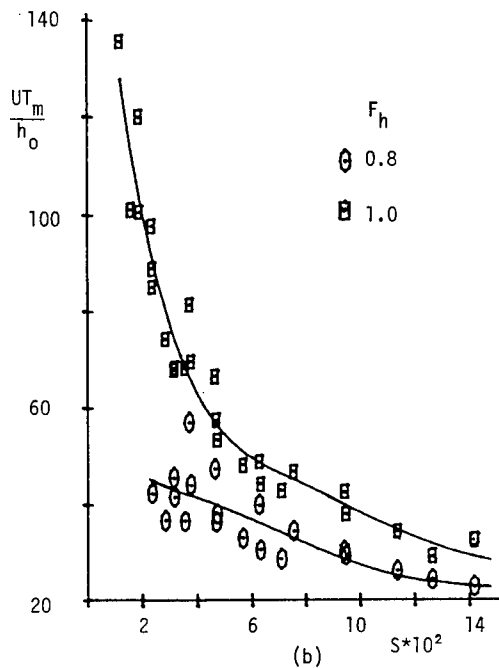
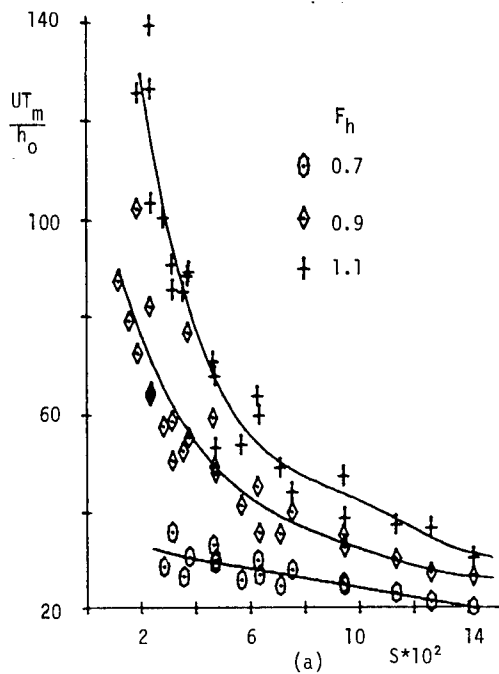


Figure 12.  $UT_m/h_o$  plotted against the blockage coefficient  $S$  for: (a)  $F_h = 0.7, 0.9$  and  $1.1$ , (b)  $F_h = 0.8$  and  $1.0$ .

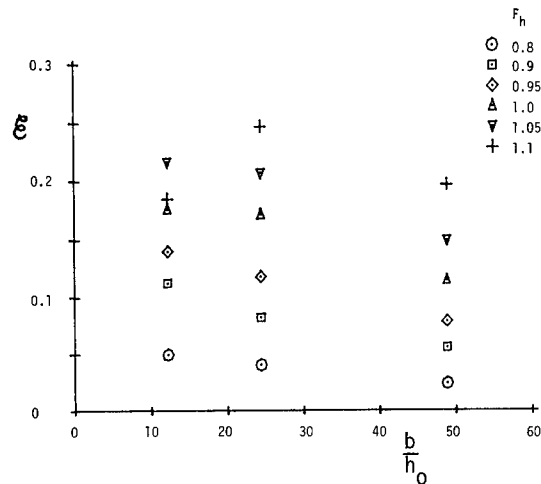


Figure 13. Dimensionless rate of work done in soliton generation by the model.  $h_o = 10$  cm and  $d = 5$  cm.

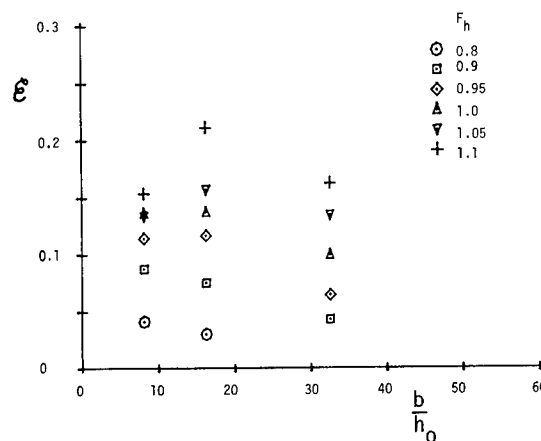


Figure 14. Dimensionless rate of work done in soliton generation by the model.  $h_o = 15$  cm and  $d = 7.5$  cm.

Figures 13 and 14 show  $E = \rho g E_b / \rho g h_o^3 U T_m$  plotted against  $b/h_o$  for the same values of  $h_o$  and  $d$  as in Figures 9 and 11, respectively.

One of the important properties of solitons is that their speed is supercritical. Figure 15 shows  $c/\sqrt{gh_o}$  plotted against the Froude number  $U/\sqrt{gh_o}$  for  $h_o = 12.5$  cm and  $d = 5.0$  cm. With the exception of the two lowest values of  $F_h$ , all values of  $c/\sqrt{gh_o}$  are  $> 1$  and are necessarily greater than the associated  $F_h$ . The apparently slightly subcritical values are not a result of measurement error of  $c$  but can possibly be explained by bottom unevenness of the towing tank. This was as much as  $\pm 0.7$  cm in some places and is sufficient to explain values of  $c/\sqrt{gh_o}$  apparently less than 1. The effect of unevenness of the bottom shows up in other variables also. Every dimensionless variable containing water depth uses the nominal

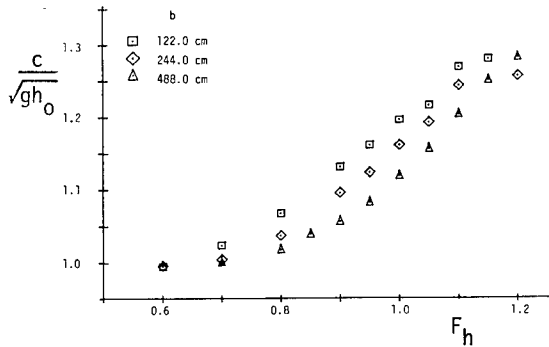


Figure 15. Dimensionless speed of the first soliton as a function of  $F_h$  for  $h_0 = 12.5$  cm,  $d = 5.0$  cm and  $b$  as indicated.

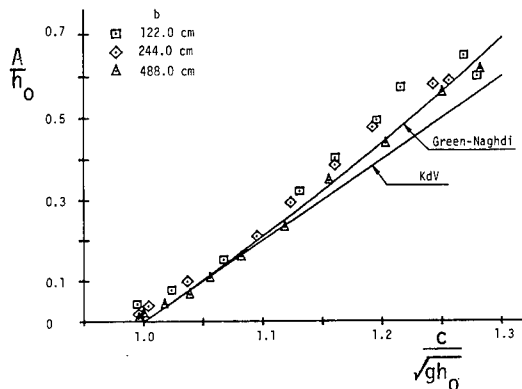


Figure 16.  $A/h_0$  plotted against  $c/\sqrt{gh_0}$  for  $h_0 = 12.5$  cm,  $d = 5.0$  cm and  $b$  as indicated.

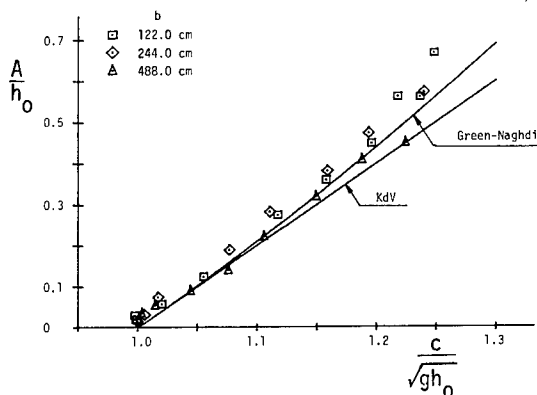


Figure 17.  $A/h_0$  plotted against  $c/\sqrt{gh_0}$  for  $h_0 = 15.0$  cm,  $d = 5.0$  cm and  $b$  as indicated.

value  $h_0$ , which represents the average value of the water depth throughout the tank.

The curves of  $c/\sqrt{gh_0}$  against  $F_h$  show a sudden downturn near  $F_h = 1.2$ , especially for  $b = 244$  cm. This downturn was also observed in the curves for other parameter values.

Another important property of solitons is that there is a relationship between amplitude and speed, unlike linearized dispersive waves. Two estimates are available, one resulting from the Korteweg-DeVries equation and the other resulting from Green-Naghdi theory [Green and Naghdi (1977)] which, incidentally, is identical with that of Boussinesq [Lamb (1932, § 252)]. Figure 16 shows  $A/h_0$  plotted against  $c/\sqrt{gh_0}$  for  $h_0 = 12.5$  cm,  $d = 5.0$  cm and  $b = 122$  cm, 244 cm and 488 cm. The data points match the Green-Naghdi prediction very well throughout the range of amplitudes tested, but differ significantly from the Korteweg-deVries prediction at the higher wave amplitudes and celerities. The values of  $c/\sqrt{gh_0} < 1$  have been discussed earlier. Figure 17 shows a similar plot, but now for  $h_0 = 15$  cm and the draft and three widths, as before.

Many more experimental data are available than have been shown in this paper. We believe, however, that what has been shown is representative of our observations. These appear to show that the waves preceding the model are indeed solitons and furthermore that no steady state is approached in the entire domain if  $F_h$  is less than about 1.2, no matter how long the motion continues. For subcritical model velocities the amplitude of the successive solitons appears to decrease, resulting eventually in just a shelf of water moving ahead of the model. On the other hand, for supercritical velocities successive solitons appear to maintain their amplitudes. Such conclusions would be more certain if they could be confirmed by calculation with appropriate fluid-dynamical equations. We turn to this problem next.

### 3. CALCULATIONS

In making our calculations we shall choose two out of several alternative sets of equations for wave motion in shallow water, those derived by T. Y. Wu (1981) and those derived by A. E. Green and P. M. Naghdi (1976a). For both sets of equations it is assumed that the water is inviscid, incompressible and homogeneous. Both have been presented at earlier Symposia, those of Wu in a paper by D.-M. Wu and T. Y. Wu (1982) at the 14th Symposium and the Green-Naghdi equations in a paper by Naghdi (1978) at the 12th. Before stating the equations, in their 2-dimensional forms, for we are not prepared to tackle the 3-dimensional problems, it is appropriate to discuss the nature of the approximation in each, even though we do not carry through the derivations.

Wu's derivation is in the spirit of Boussinesq. He begins with the complete 3-dimensional equations for an inviscid, incompressible fluid of constant density, bounded below by a possibly deformable bottom,  $z = -h(x, y, t)$ , and above by a free surface,  $z = \zeta(x, y, t)$ , upon which a possibly moving pressure distribution

is acting. His first step is to find equations for the variables averaged over the depth. For example, if  $u(x,y,z,t)$  is the x-component of the fluid velocity, he defines

$$\bar{u}(x,y,t) = \frac{1}{\zeta + h_0} \int_{-h}^{\zeta} u(x,y,z,t) dz. \quad (5)$$

and similarly for  $v$ ,  $w$  and  $\nabla p$ . Equations corresponding to conservation of mass, horizontal and vertical momentum and energy are found. So far there is no approximation, but, of course, the description of the flow is somewhat crude. Wu now assumes that the unaveraged motion is irrotational, and introduces the usual stretched variables, using a representative wave length  $\lambda$  in the horizontal direction and a representative depth  $h_0$  in the vertical. In addition, with a representative wave amplitude  $A$ , he introduces the parameters  $\epsilon = h_0/\lambda$  and  $\alpha = A/h_0$ . After expanding the velocity potential  $\Phi$  (that now exists) in powers of  $\epsilon$  and making use of both the averaged and the original equations, he finally arrives at a set of three equations for  $\zeta$ ,  $\bar{u}$  and  $\bar{v}$ . The conservation-of-mass equation is exact, the conservation-of-momentum equations have an error term  $O(\alpha\epsilon^4, \alpha^2\epsilon^2)$ . The solution  $\bar{u}, \bar{v}$  will no longer be irrotational in the  $(x,y)$  plane if  $\nabla h \neq 0$ , but Wu shows how to find equations valid to the same order whose solution is irrotational. The solution is, of course, for  $\nabla\bar{\Phi}$  rather than  $\nabla\Phi$ , but it is shown that  $|\nabla\bar{\Phi} - \bar{u}| = O(\alpha\epsilon^2)$ . These equations reduce to the Boussinesq equations if  $h = \text{const.}$  and the motion is 2-dimensional. We omit further details but note that the equations are to be used in circumstances where the Ursell number  $\alpha/\epsilon^2 = O(1)$ , so that not only  $\alpha \ll 1$  but also  $\epsilon \ll 1$ . We summarize by saying that Wu's derivation starts with the exact 3-dimensional equations for irrotational flow of an inviscid fluid and arrives at approximate equations that should be valid for "small"  $\epsilon$  and  $\alpha/\epsilon^2 = O(1)$ . We emphasize this, for the Green-Naghdi equations present a different sort of approximation.

The derivation of the Green-Naghdi equations should properly start with a discussion of Cosserat surfaces and the special set of conservation laws associated with them. This would, however, be too great a digression and may be avoided here, for Green and Naghdi (1976b) have shown how the equations necessary for our particular case may also be derived starting with the usual 3-dimensional equations (really the conservation laws and invariance requirements that lead to them). Although the final equations are written in Eulerian variables, the nature of the approximation is easier to understand in Lagrangian variables. Let  $(x_0, y_0, z_0)$  be reference variables for a particle in a fluid flow; they may be, but need not be the coordinate values at some special instant of time. The flow may then be represented by functions

$$\begin{aligned} x &= \hat{x}(x_0, y_0, z_0, t), \\ y &= \hat{y}(x_0, y_0, z_0, t), \\ z &= \hat{z}(x_0, y_0, z_0, t). \end{aligned} \quad (6)$$

We assume that the Jacobian  $\partial(x,y,z)/\partial(x_0, y_0, z_0) \neq 0$  anywhere in the fluid or on its boundaries, so that we can also solve for  $x_0 = \hat{x}_0(x,y,z,t)$ , etc. Let the bottom beneath the fluid be represented by  $z_0 = r(x_0, y_0)$  and the free surface by  $z_0 = s(x_0, y_0)$ , where it will be convenient to suppose that  $r < 0 < s$ . Evidently, these surfaces have counterparts in  $(x,y,z)$  space. For instance, solving  $\hat{z}_0(x,y,z,t) = r(\hat{x}_0(x,y,z,t), \hat{y}_0(x,y,z,t))$  for  $z$  yields a function  $z = \alpha(x,y,t)$ . Similarly,  $\hat{z}_0 = s(\hat{x}_0, \hat{y}_0)$  yields  $z = \beta(x,y,t)$  and  $\hat{z}_0 = 0$  yields  $z = \psi(x,y,t)$ . This last surface will be called the middle surface and will be used as a reference surface for describing the flow in the following sense. We shall expand the functions  $\hat{x}_j(x_0, y_0, z_0, t)$  in Taylor series about  $z_0 = 0$ , discard terms higher than the first power of  $z_0$ , and furthermore discard even the linear terms for  $x$  and  $y$ . The Lagrangian representation of the flow then takes the following approximate form:

$$\begin{aligned} x &= \hat{x}(x_0, y_0, 0, t), \\ y &= \hat{y}(x_0, y_0, 0, t), \\ z &= \hat{z}(x_0, y_0, 0, t) + z_0 \phi(x_0, y_0, t). \end{aligned} \quad (7)$$

where  $\phi$  is an unknown function, as well as  $\hat{x}, \hat{y}$  and  $\hat{z}$  and also  $\beta$  ( $\alpha$  is prescribed since  $h = h_0 - \alpha$ ). Beyond this no approximations are made. The usual conservation laws and invariance requirements are now imposed in a familiar way to find the equations of motion. There quite evidently is an approximation, perhaps even a bold one, but not one that fits easily into the usual perturbation methods for finding approximate equations. It also obviously requires a fairly thin horizontal sheet of water for it to give a good approximation to the 3-dimensional equations. Presumably the approximation could be improved by retaining more terms in the Taylor series, although it is by no means clear that all such choices will allow satisfying the conservation laws and invariance requirements. On the other hand, there is no parameter appearing that can be used to indicate the expected region of usefulness of the approximation, as there is in Wu's approximation. The equations stand on their own and may be said to present a complete physical theory in the sense that all conservation laws and invariance requirements are satisfied. As we shall see later on, this property has interesting consequences when calculations are made.

We now give the equations, but only for 2-dimensional motion. The undisturbed free surface is taken at  $z = 0$  with  $Oz$  directed oppositely to the force of gravity and  $Ox$  to the right. The free surface is described by  $z = \zeta(x,t)$ , the bottom by  $z = -h(x,t)$ . The x-component of the velocity is denoted by  $u(x,t)$ . Bars over  $u$  are dropped in the Wu equations. The imposed pressure on the free surface is  $p_0(x,t)$ . Surface tension is neglected.

Wu's equations are as follows:

$$\begin{aligned} \zeta_t + [(h+\zeta)u]_x &= -h_t + \frac{\partial}{\partial x} \left\{ \left[ \frac{h}{2} (h_t + (hu)_x) \right. \right. \\ &\quad \left. \left. - \frac{1}{3} h^2 u_x \right] h_x \right\}, \end{aligned} \quad (8)$$

$$u_t + uu_x + g\zeta_x + \frac{1}{\rho} p_{0x} = \frac{1}{2} h_x \frac{\partial}{\partial t} [h_t + (hu)_x] \\ + \frac{1}{2} h \frac{\partial^2}{\partial x \partial t} [h_t + (hu)_x] \\ - \frac{1}{6} h^2 u_{xxt} - \frac{1}{3} h h_x u_{xt}.$$

We note parenthetically that Wu's equations before he altered them to make them irrotational in the horizontal plane are somewhat simpler than those above, namely,

$$\zeta_t + [(h+\zeta)u]_x = -h_t, \\ u_t + uu_x + g\zeta_x + \frac{1}{\rho} p_{0x} = \frac{1}{2} h \frac{\partial^2}{\partial x \partial t} [h_t + (hu)_x] \quad (9) \\ - \frac{1}{6} h^2 u_{xxt}.$$

However, to facilitate numerical comparisons we have used the first set of equations.

The Green-Naghdi equations are the following:

$$\zeta_t + [(h+\zeta)u]_x = -h_t, \\ u_t + uu_x + g\zeta_x + \frac{1}{\rho} p_{0x} = -\frac{1}{6} \{ (4\zeta+h)_x \ddot{\zeta} \\ + (\zeta+h)(2\ddot{\zeta}-\ddot{h}) - (2\zeta-h)_x \ddot{h} \}, \quad (10)$$

where the dot over a variable indicates the material derivative.

It is evident that any one of the sets of equations simplifies considerably on the right-hand side if  $h = \text{const.}$  Setting  $p_0 = \text{const.}$  has much less effect (on the equations, not the solutions). If, in addition to setting  $h$  and  $p_0$  constant, terms of the  $O(\alpha^2)$  are discarded, then the Green-Naghdi equations reduce to the Wu equations. To find the appropriate steady-state equations in a coordinate frame moving with velocity  $U$ , say to the left, we need only replace  $\partial/\partial t$  by  $U\partial/\partial x$ . We refrain from writing down the equations. We shall also not write down the equations in dimensionless form, although all our computations were done with dimensionless equations.

We can avoid describing the details of the numerical methods used to solve the equations, for we followed the lead of Wu and Wu (1982) in using a modified Euler method to derive a set of finite-difference equations. The method is described in their paper. We differ, however, in our method for solving these. Whereas Wu and Wu used an iterative method, we have put our equations into tridiagonal form and solved the resulting set of simultaneous, linear equations by the Thomas algorithm. Our open-boundary condition (a modified Sommerfeld condition) is the same one used by Wu and Wu, and is described in their paper. However, its implementation for the current studies is quite different [see, Ertekin (1984)]. It appears to be very effective in preventing reflection at the down-

stream boundary. All computations for initial-value problems were done in a fixed coordinate frame, even though the results are presented in a moving frame. Here too we follow Wu and Wu.

Various computations have been made, generally with the aim of trying to throw light upon the measurements described earlier. One must keep in mind, of course, that the computations are all for 2-dimensional situations, whereas the experiments were 3-dimensional. Hence comparisons must be chiefly qualitative. Two kinds of disturbances were used: one a pressure distribution on the free surface,  $p_0(x+Ut)$ , and the other a bump on the channel bottom, both impulsively started at  $t = 0^+$  with a constant velocity  $U$ . The pressure distribution in the moving frame ( $x' = x + Ut$ ) is described by

$$p_0(x') = \frac{1}{2} p_a [1 - \cos(2\pi x'/L)], \quad 0 \leq x' \leq L, \quad (11) \\ = 0, \quad \text{elsewhere},$$

and the bump by

$$z = -h(x') = -h_0 + \frac{B}{L^3} [4x'(x'-L)], \quad 0 \leq x' \leq L, \quad (12) \\ = -h_0, \quad \text{elsewhere},$$

where  $L$  is the extent of the disturbances. The initial conditions for  $u$  are  $u(x,0) = 0$  for all problems. For pressure disturbances we require that  $\zeta(x,0) = -p_0(x,0)$  and for bottom bump disturbances we require  $\zeta(x,0) = 0$ . The magnitude of the disturbance is specified by the amplitudes  $p_a$  and  $B$ . In the experiments the parameter analogous to  $p_a$  is the draft  $d$ . The ratio  $d/b$  represents roughly the ship model disturbance smeared out over a band of length  $L$  stretching from wall to wall.

First we shall show computations that are analogous to the wave records themselves. We have more flexibility as computers than as experimenters, for we can equally easily show snapshots of the surface at successive instants of time or time records at different positions. Figure 18 shows snapshots of  $\zeta/h_0$  for  $F_h = 0.8$ ,  $L/h_0 = 2$  and  $p_a = 0.1$ , calculated both by the Green-Naghdi and the Wu equations. ( $p_a$  is non-dimensionalized with respect to  $\rho$ ,  $g$ , and  $h_0$ .) There is quite good agreement between the two methods. Furthermore, they reproduce, qualitatively at least, the same phenomenon observed in the experiments (cf. Figure 5). Figure 19 shows  $\zeta/h_0$  for  $F_h = 1.0$ ,  $L/h_0 = 2$  and  $p_a = 0.25$ . It is no longer possible to say that the two results are in agreement. Is it possible to say which one is the more reliable, for both are approximations? Wu's approximation is so formulated that one anticipates its deterioration as  $p_a$  increases whereas the Green-Naghdi approximation has no especially favored (or disfavored) region of  $p_a$  built into it. How then do we assess its accuracy? From the standpoint of the theory of Cosserat surfaces it is an independent theory and must be judged by its predictions. We are not in a position to make comparisons between calculation and measurement. However, in all our computations the two approximations agree well for small  $p_a$  or

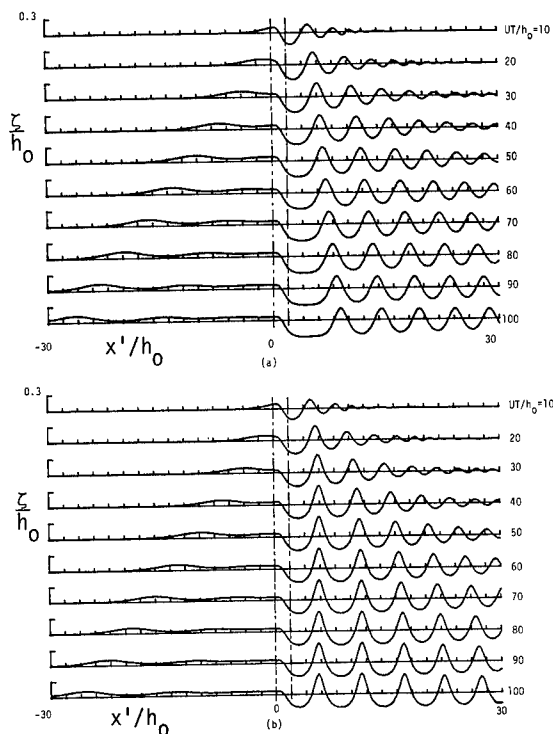


Figure 18. Free-surface profiles at various instants of time calculated according to: (a) the G-N, and (b) the Wu equations. Here  $F_h = 0.8$ ,  $L/h_0 = 2.0$ ,  $p_a = 0.1$ ,  $\Delta x = 0.2$  and  $\Delta t = 0.125$ .

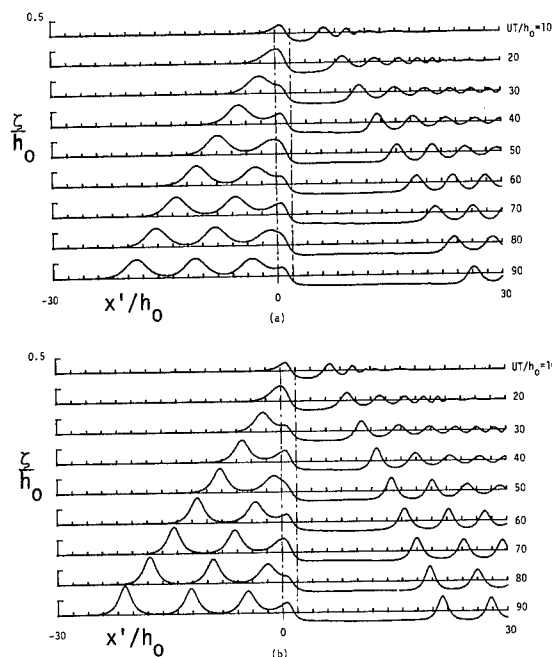


Figure 19. Free-surface profiles at various instants of time calculated according to: (a) the G-N, and (b) the Wu equations. Here  $F_h = 1.0$ ,  $L/h_0 = 2.0$ ,  $p_a = 0.25$  and  $\Delta x = \Delta t = 0.2$ .

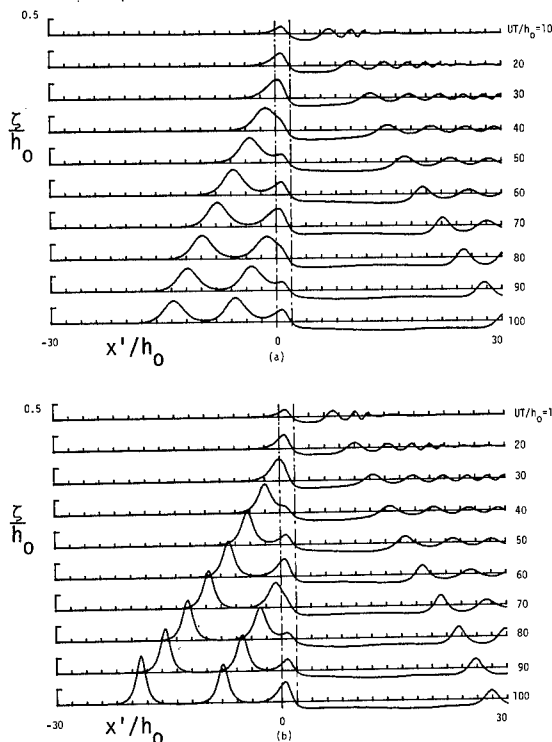


Figure 20. Free-surface profiles at various instants of time calculated according to: (a) the G-N, and (b) the Wu equations. Here  $F_h = 1.1$ ,  $L/h_0 = 2.0$ ,  $p_a = 0.25$ ,  $\Delta x = 0.2$  and  $\Delta t = 0.182$ .

B, and the Green-Naghdi equations continue to give reasonable-appearing results when Wu's equations have clearly begun to lose validity.

Figure 20 shows  $\zeta/h_0$  for essentially the same situation as Figure 19 except that now  $F_h = 1.1$ . We call attention to the fact that in Figure 18 where  $F_h = 0.8$ , the amplitude of the solitons is slowly diminishing as it also did in the experiments (cf. Figure 5) whereas in Figures 19a and 20a they remain essentially constant, as also happened experimentally (cf. Figures 6 and 7). Figure 21 is the computed analog of Figure 8 for  $F_h = 1.0$ . It shows the time record of  $\zeta/h_0$  for two positions of a numerical wave gauge mounted ahead of the pressure distribution and moving with it. Calculations are made with the G-N equations.

All the calculations above can be repeated for a moving bump on the bottom of the channel, although they become somewhat more complicated, as can be appreciated by a glance at the right-hand sides of the equations. However, computer programs have been written for both the Green-Naghdi and the Wu equations (both the nonlinear equations shown above and the linearized version). Figure 22 shows snapshots at different times for  $F_h = 1.0$ ,  $L/h_0 = 2.0$  and  $B/h_0 = 0.3$ . Here again there is a substantial difference between the two predictions, whereas they are indistinguishable for small  $B/h_0$ . We note that in all the computations presented in Figures 18-22, the left and right numerical boundaries were at  $x'/h_0 = -50$  and  $50$ , respectively.

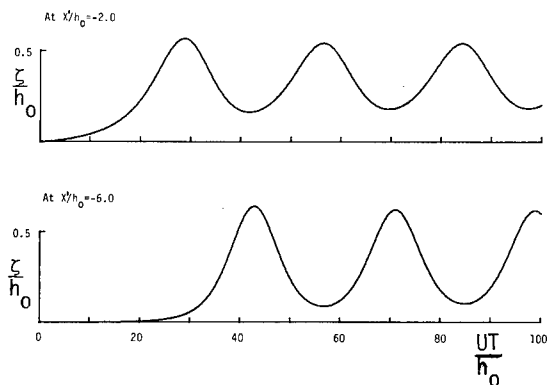


Figure 21. Calculated time record of  $\zeta/h_0$  at two fixed distances ahead of the pressure distribution. Here  $F_h = 1.0$ ,  $L/h_0 = 2.0$ ,  $p_a = 0.25$  and  $\Delta x = \Delta t = 0.2$ .

Since calculation has been able to reproduce the essential features of the experimental wave records, it is clear that all the derived experimental quantities shown in Figures 9 - 17 can also be obtained by calculation as long as parameters strictly associated with the tank width are not involved. We show only a few of these.

Figure 23 shows  $A/h_0$  against  $F_h$  for three values of  $p_a$ . The next Figure 24 shows experimental values of  $A/h_0$  against  $F_h$  for  $h_0 = 15$  cm and three values of  $d$ . One sees that the behavior near  $F_h = 1.1$  is similar. Figure 25 shows  $UT_m/h_0$  plotted against  $F_h$  for the same values of  $p_a$  and Figure 26 shows the corresponding experimental results for the same values of  $d$  as in Figure 24.

Figures 27 and 28 show analogous plots for  $c/\sqrt{gh_0}$  against  $F_h$ , computed for three values of  $p_a$  in Figure 27, measured for three values of  $d$  in Figure 28. Again one sees the qualitative similarity in the two plots.

Figure 29 shows  $A/h_0$  plotted against  $c/\sqrt{gh_0}$  for, again,  $p_a = 0.10, 0.15$  and  $0.20$ . The solid lines are the curves relating  $A/h_0$  and  $c/\sqrt{gh_0}$  for a single solitary wave according to the Korteweg-deVries equation and the Green-Naghdi equations. The individual points are, of course, computed for the unsteady initial-value problem as before.

#### 4. CONCLUDING REMARKS

As has been mentioned earlier, we have many more experimental results than could be shown here. We also have more computed results than we have shown, and with little effort and expense could produce still more, but these are limited to 2-dimensional motion for the present. However, as is mentioned in Huang et al., (1982b), the fact that solitons can be generated by 2-dimensional disturbances tells us that their generation by ship models is not a 3-dimensional effect only. Also, this phenomenon is not associated with viscosity nor with equipment malfunction such as poor speed control. Although we have not discussed resis-

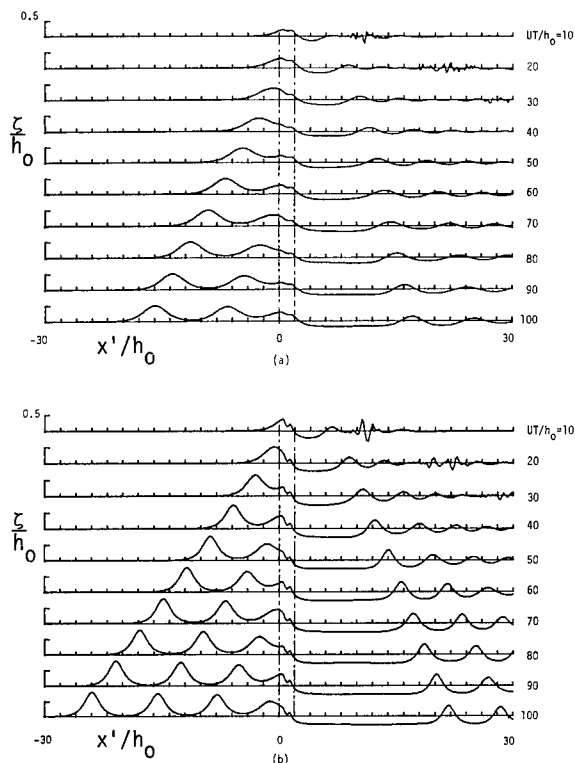


Figure 22. Free-surface profiles at different times for a moving bump on the bottom calculated according to: (a) the G-N, and (b) the Wu equations. Here  $F_h = 1.0$ ,  $L/h_0 = 2.0$ ,  $B/h_0 = 0.3$ ,  $\Delta x = 0.2$  and  $\Delta t = 0.1$ .

tance, it was both measured and computed, and oscillates about a mean value with a period equal to that of soliton generation. Hence the model experimenter need not look to anything but the laws of fluid dynamics when he finds that his resistance measurements seem to oscillate. However, both the experimental and computational evidence seems to indicate that for subcritical speeds the soliton amplitudes gradually diminish to zero. For supercritical speeds below a depth Froude number of about 1.2 a steady state does not seem to be approached.

As was shown by Wu and Wu (1982), it is essential that the full nonlinear equations, either Wu's or Green-Naghdi's, be used. The linearized equations, which are the same for both, cannot predict the generation of solitons.

We have not discussed solutions of the steady-state equations in a coordinate system moving with velocity  $U$ . Since both the experiments and the computations seem to show that a steady state is never reached if  $F_h < 1.2$ , it is not clear that solutions of the steady-state equations correspond to the desired physical problem. For subcritical speeds, at least, the solutions apply more properly to a flow with a rigid top ahead of the disturbance. For such flows small values of  $p_a$  or  $B$  produce a cnoidal-wave pattern behind the pressure distribu-

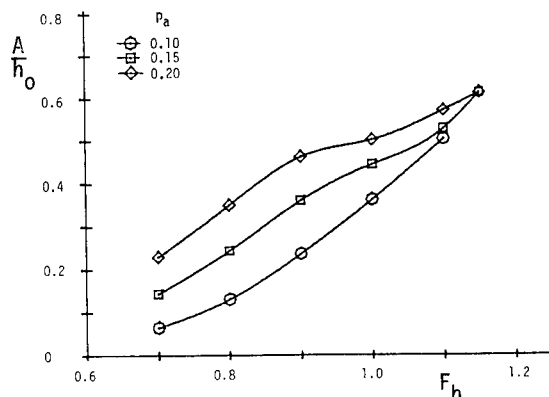


Figure 23. Dimensionless amplitude of the first soliton plotted against  $F_h$  for  $L/h_0 = 2.0$  and  $p_a = 0.10, 0.15$  and  $0.20$ . Computations made with the Green-Naghdi equations.

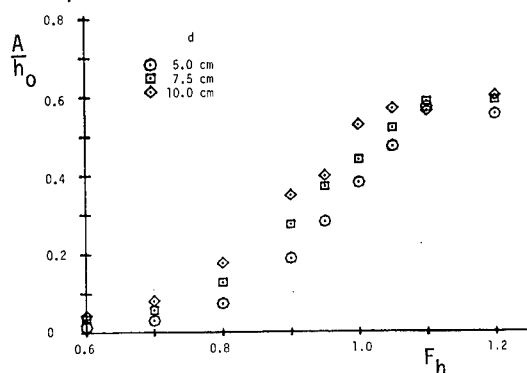


Figure 24. Experimental values of  $A/h_0$  plotted against  $F_h$  for  $h_0 = 15$  cm,  $b = 244$  cm and  $d = 5.0, 7.5$  and  $10.0$  cm.

tions or bottom bumps, large values lead to a hydraulic jump in the downstream region.

It was mentioned in the Introduction that the generated solitons begin to break for  $F_h = 1.2$  and that for  $F_h = 1.3$  they are replaced by a hydraulic jump moving ahead of but together with the model. In the computations of Huang et al. (1982b), it was found that for  $F_h \geq 1.175$ , solitons were no longer generated. This phenomenon was also investigated with the Green-Naghdi equations. We found that the amplitude of the disturbance had a strong effect on this phenomenon. The value of  $F_h$  above which no solitons are generated decreases as the disturbance amplitudes  $p_a$  or  $B$  decrease.

As part of the study, the effect of negative disturbances (negative pressures or indentations on the bottom) were also investigated. Although we do not present these results here, we found that the solutions for these flows are quite similar to those for positive disturbances. However, the time required for the solitons to develop was considerably longer than for the positive disturbances.

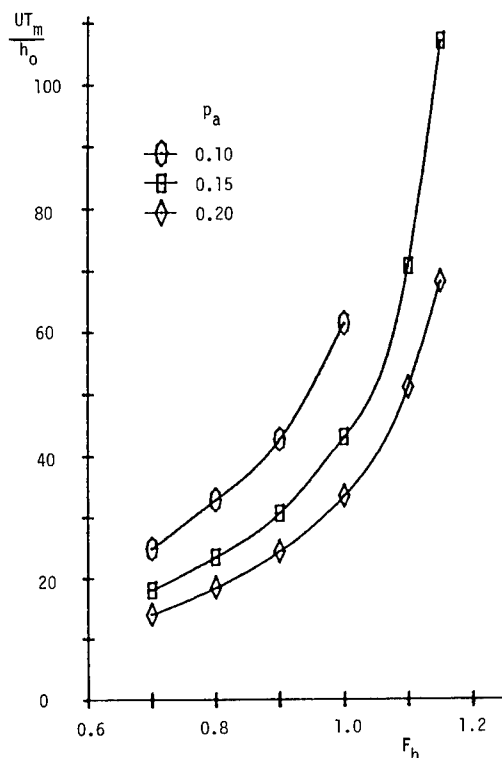


Figure 25.  $UT_m/h_0$  plotted against  $F_h$  for  $L/h_0 = 2.0$ ,  $p_a = 0.10, 0.15$  and  $0.20$ . Computations made with the Green-Naghdi equations.

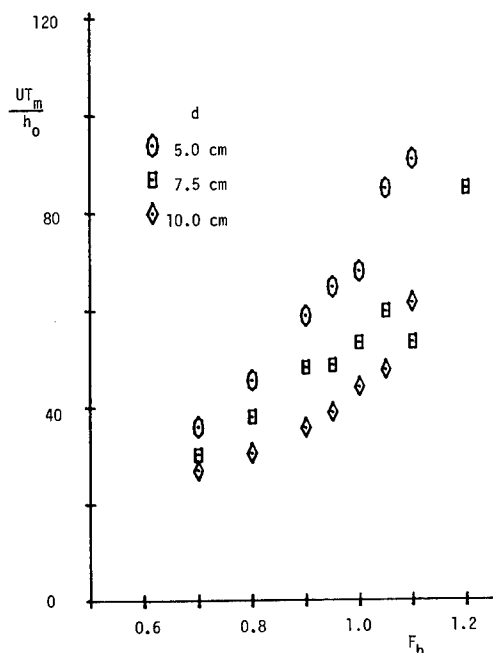


Figure 26. Experimental values of  $UT_m/h_0$  plotted against  $F_h$  for  $h_0 = 15$  cm,  $b = 244$  cm and  $d = 5.0, 7.5$  and  $10.0$  cm.

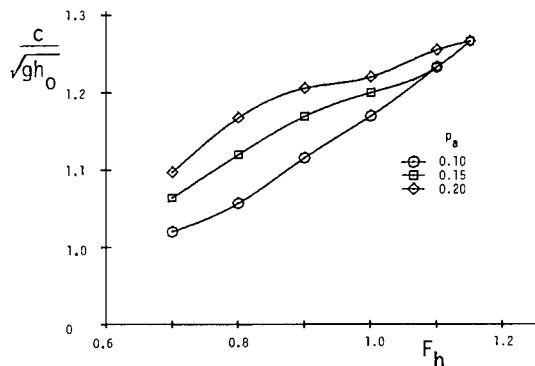


Figure 27. Dimensionless speed of the first soliton plotted against  $F_h$  for  $L/h_0 = 2.0$ ,  $p_a = 0.10, 0.15$  and  $0.20$ . Computations made with the Green-Naghdi equations.

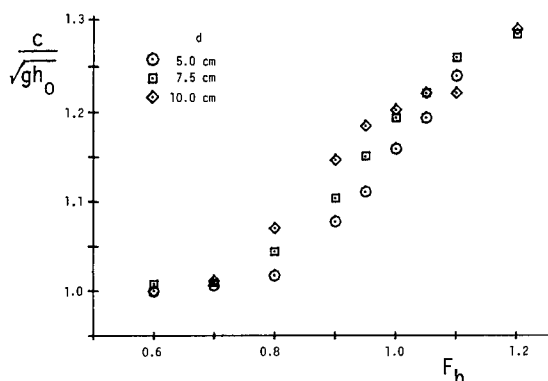


Figure 28. Experimental values of  $c/\sqrt{gh_0}$  plotted against  $F_h$  for  $h_0 = 15$  cm,  $b = 244$  cm and  $d = 5.0, 7.5$  and  $10.0$  cm.

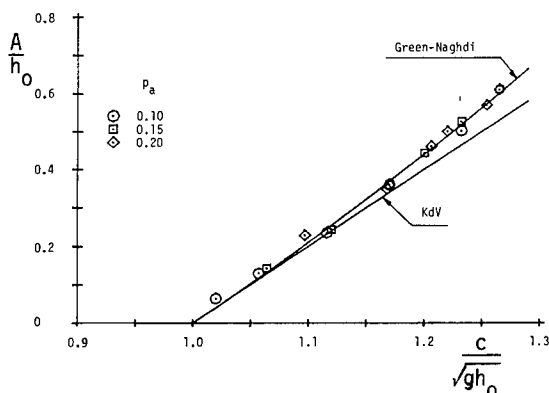


Figure 29. The amplitude  $A/h_0$  plotted against  $c/\sqrt{gh_0}$  for  $L/h_0 = 2.0$ ,  $p_a = 0.10, 0.15$  and  $0.20$ . Computations made with the Green-Naghdi equations.

Although we have given what we hope is a representative sample of our experimental and computational results, those who are interested in more details concerning the theory, numerical techniques or experimental procedures should consult the doctoral thesis of Ertekin (1984).

## 5. ACKNOWLEDGEMENT

We are pleased to acknowledge the support of the Office of Naval Research, Fluid Dynamics Branch under contract N00014-84-K-0026 for much of the work reported here. We are also pleased to acknowledge many helpful conversations with T. Y. Wu and his colleagues, S. J. Lee and G. T. Yates.

## 6. REFERENCES

- Benjamin, T.B. (1970), Upstream Influence, *J. Fluid Mech.*, vol. 40, Part 1, pp.49-79.
- Ertekin, R.C. (1984), Soliton Generation by Moving Disturbances in Shallow Water: Theory, Computation and Experiment. Ph.D. Thesis, University of California, Berkeley.
- Favre, H. (1935), Etude Théorique et Expérimentale des Ondes de Translations dans les Canaux Découverts. Dunod, Paris. 215 pp. + 7 plates + 4 fold-outs.
- Green, A.E. and Naghdi, P.M. (1976a), Directed Fluid Sheets. *Proc. Roy. Soc. London, Ser. A*, Vol. 347, pp. 447-473.
- Green, A.E. and Naghdi, P.M. (1976b), A Derivation of Equations for Wave Propagation in Water of Variable Depth. *J. Fluid Mech.* vol. 78, Part 2, pp.237-246.
- Green, A. E. and Naghdi, P. M. (1977), Water Waves in a Nonhomogeneous Incompressible Fluid, *J. Appl. Mech.*, vol. 44, pp. 523-528.
- Huang, D.-B., Sibul, O.J. and Wehausen, J.V. (1982a), Ships in Very Shallow Water. Festkolloquium, Dedicated to Karl Wieghardt, Institut für Schiffbau der Universität Hamburg.
- Huang, D.-B., Sibul, O.J., Webster, W.C., Wehausen, J.V., Wu, D.-M. and Wu, T.Y. (1982b), Ships Moving in the Transcritical Range. Conference on Behaviour of Ships in Restricted Waters, Varna, Proc. Vol II, pp. 26/1-26/10.
- Miles, J.W. (1980), Solitary Waves. *Ann. Rev. Fluid Mech.*, vol. 12, pp.11-43.
- Naghdi, P.M. (1978), Fluid Jets and Fluid Sheets: A Direct Formulation. 12th Symp. Naval Hydrodynamics, Washington, D.C., 1978, pp. 500-515.
- Salvesen, N. and von Kerczek, C. (1978), Non-linear Aspects of Subcritical Shallow-Water Flow Past Two-Dimensional Obstructions. *J. Ship Res.*, vol. 22, No. 4, pp. 203-211.
- Sibul, O.J., Webster, W.C., and Wehausen, J.V. (1979), A Phenomenon Observed in Transient Testing. *Schiffstechnik*, vol. 26, pp. 179-200.
- Thews, J.G. and Landweber, L. (1935), The Influence of Shallow Water on the Resistance of a Cruiser Model. U.S. Experimental Model Basin, Navy Yard, Washington, D. C.,



Rep. No. 408.

- Thews, J.G. and Landweber, L. (1936), A Thirty-Inch Model of the S. S. Clairton in Shallow Water. U. S. Experimental Model Basin, Navy Yard, Washington, D. C., Rep. No. 414.
- Wu, T.Y. (1981), Long Waves in Ocean and Coastal Waters. J. Eng. Mech. Div., ASCE, Vol. 107, No. EM3, pp. 501-522.
- Wu, T.Y. (1982), Nonlinear Long Waves. Festkolloquium, Dedicated to Karl Wieghardt, Institut für Schiffbau der Universität Hamburg.
- Wu, D.-M. and Wu, T.Y. (1982), Three-Dimensional Nonlinear Long Waves due to Moving Surface Pressure. 14th Symp. Naval Hydrodynamics, Ann Arbor, pp. 103-125, discussion pp. 126-129.
- Wu, T.Y. (1983), Shallow Water Effects - No Steady Disturbances Always Result in Steady Responses? 6th Georg P. Weinblum Lecture, Hamburg, (also, Washington D.C., March 1984).

## DISCUSSION

Dr.-Ing. HIROSHI ISSHIKI,  
Technical Research Institute, Hitachi Zosen Corp.,  
Osaka, Japan:

I would like to express my sincere respect and gratitude to the authors for this very nice paper of fundamental importance. I would like to raise two points:

1. On page 31, you write: "The ratio  $d/b$  represents roughly the ship model disturbance smeared out over a band of length  $L$  stretching from wall to wall". I think it is not correct. Since  $\rho g d B L$  may be a measure of the buoyant force where  $B$  is the breadth of a ship, the external pressure applied on the free surface which corresponds to ship disturbance may be  $\rho g d B L / (\rho L) = \rho g d B / b$ . If we normalize this with hydrostatic pressure  $\rho g h$ , we then have  $\rho g d B / (b \rho g h) = dB / (bh)$ . This is nothing but the blockage coefficient. This may be the reason why the blockage coefficient is so significant in this phenomenon.
2. Wu's equation, I think, is really a very nice equation, since its physical background is very clear and easily understandable. However, your results seem to suggest that some problem is hidden in Wu's equation. According to his equation, the amplitude of soliton increases as it proceeds. I feel some uneasiness about this tendency. I have a feeling that the nonlinearity may be a little bit too strong or the dispersion is a little bit too weak.

The discussor would be very grateful if he could have your reply and/or comment on these problems.

Dr. ANTONY J. MUSKER,  
Admiralty Research Establishment,  
Haslar, England:

Users of towing tanks will no doubt appreciate this extensive study performed by the authors even though it may cast some doubt on their experimental techniques in certain circumstances. To the best of my knowledge the phenomenon reported in the present paper has not been investigated at Haslar - certainly not in recent years. Any difficulties in achieving steady state conditions have invariably been associated (perhaps incorrectly) with structural resonances in the carriage or imperfect speed control. However, the supporting computational work by the authors would seem to rule out these factors for the present investigation.

I think it is important not to lose sight of the fact that at the end of the day what we are invariably interested in, for a simple towing test, is the resistance and I note that this was measured during the experiments and can no doubt be recovered from the computational work. Can the authors therefore provide any quantitative information regarding how the presence of these solitons affects the resistance and, specifically, what is the amplitude of the oscillatory component of resistance as a fraction of the mean value for a typical run?

S.J. LEE, G.T. YATES and T.Y. WU,  
California Institute of Technology,  
Pasadena, CA, USA:

Having shared common interest and collaborated for mutual benefit with the present authors, we appreciate how much effort they must have devoted to this work. They should be commended for this valuable paper which presents extensively some essential features of the newly identified phenomenon of continuous soliton generation. We would like to take this opportunity to offer some of our numerical and preliminary experimental results very recently obtained in order to provide more information for comparison between experiment and theories.

We have investigated experimentally the wave generation by a two-dimensional bottom bump (having a circular arc top of height  $b_0 = 0.8$  cm and flat base of chord  $L = 5$  cm) towed with velocity  $U$  along the floor of a water tank of dimensions 2.5'w X 2'h X 25'l containing a layer of shallow water of depth  $h$ . Figure 1 shows the results for  $B_0 \equiv b_0/h = 0.185$ , the depth Froude number  $F_h \equiv U/\sqrt{gh} = 1$ ,  $EP \equiv \epsilon_1 \equiv h/L = 0.88$ . The top two curves in Figure 1 show the spatial distributions of the wave profile at the dimensionless time (being defined the same as in the paper)  $T = 56.8$  and  $= 113.6$ , respectively, fixed with respect to the bump which is spanning one spatial unit between the two vertical bars. The third and fourth set of curves in Figure 1 present the experimental water surface elevation (shown in dashed curves) measured by a wave gage (No. 1) fixed at 1L ahead, and by another gage (No. 2) held at 5L behind the bump leading edge, respectively;

also shown for comparison are the corresponding theoretical predictions (in solid curves) based on the Wu equation as cited in the paper. The last curve of Figure 1 gives the theoretical variation of the wave resistance with time.

Figure 2 exhibits the water surface elevation measured (shown with dashed curves) by five wave gages held fixed inside the tank at distances of 27.2L, 44.2L, 61.2L, 78L and 95L, respectively, from the starting position; the solid curves show the corresponding theoretical predictions by the Wu equation.

Figure 3 presents results similar to that of Figure 1 except that the disturbance is now stronger, with  $b_0/h = 0.283$ , and the water depth is relatively shallower, with  $h/L = 0.6$ , but the speed is again critical, at  $F_h = 1.0$ . In addition, the wave gage No. 1 is now fixed at 2L and gage No. 2 at 7.4L, both ahead of the bump. We note that the measured surface elevation (shown with dashed curves) becomes smaller in maximum height and greater in its minimum elevation than those of the corresponding numerical results (shown with solid curves) and this trend appears to be gradually magnified as the solitons move farther ahead. This variance between experiment and theory may in part be due to wave breaking (arising from such a high forcing excitation) which was observed in the experiment in this case; it is however unlikely that this can fully explain all the differences and our complete understanding is not yet in hand. With respect to the period of soliton generation, we see that the experimental value is in general slightly shorter than our theoretical prediction; e.g., by the time of  $T = 100$ , wave gage No. 1 (held fixed at 2L ahead of the

BUMP) measured just four solitons having passed it, as versus three and one-half according to the theory.

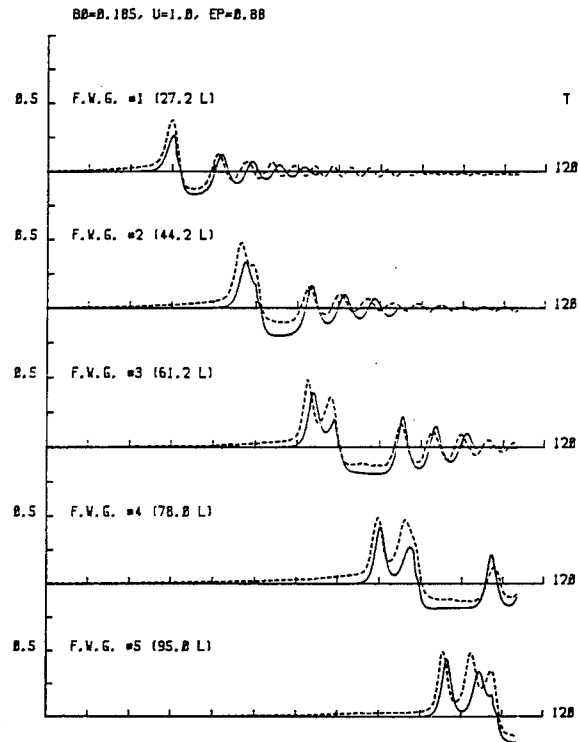


Fig. 2

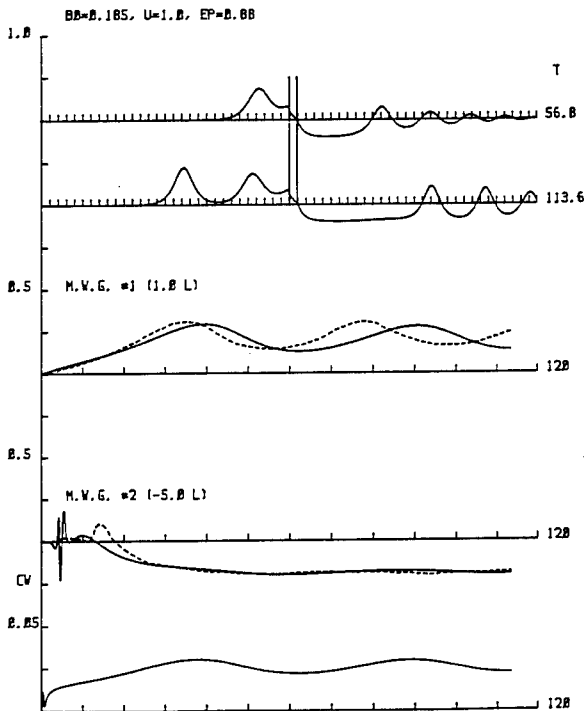


Fig. 1

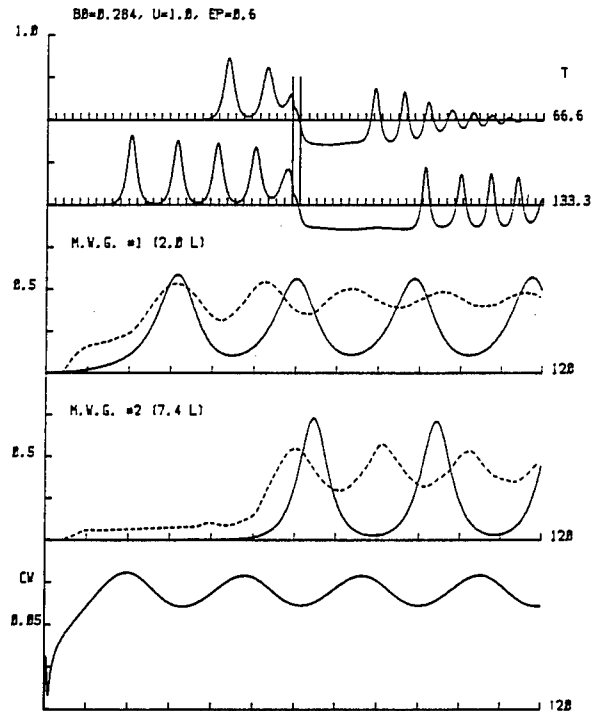


Fig. 3

Somewhat related to this point, we note that the authors have made a separate comparison between the theory of G-N and that of Wu, for a bottom bump of different shape, with the most striking difference being that the G-N equations predict fewer and smaller runaway solitons than Wu's equations.

While the foregoing two cases should not be directly compared for lack of a precise common base, comparisons between our own calculations and experiment have nevertheless indicated quite satisfactory agreement for  $B_0 = b_0/h$  as great as 0.185 at the critical speed of  $F_h = 1$  before the nonlinear effects become more significant such as shown in Figure 3. Such good agreements can be regarded as providing verifications that the assumption of both  $\epsilon = h_0/\lambda$  and  $\alpha = a/h_0$  being small (on which Wu's equations are based) is not necessary for Wu's theory to yield satisfactory results for the forced generation of solitons of somewhat greater amplitudes than originally assumed. If estimated by the results (of comparison) shown in Figures 1 and 2, it would be reasonable to accept for  $\alpha = a/h_0$  the value up to 0.5, and hence the value of up to 0.7 for  $\epsilon = h_0/\lambda$  as the range of validity for the model in question, which happens to coincide with that established for the Korteweg-de Vries equation (Hammack & Segur, 1974, J. Fluid Mech. 65, 289) and for the Boussinesq model (see, e.g., Miles 1980, Ann. Rev. Fluid Mech. 12, 11) in predicting the motion of free solitons. However, we must stress that the range of validity of the new models at hand cannot be fully established without more extensive experimental studies and verifications. In fact, the phenomenon of continuous generation of solitons is so new and so little understood that, we believe, further research will be urgently needed before any reliable conclusions can be safely drawn.

## AUTHORS' REPLY

To Prof. Isshiki:

1) Our statement several lines below equation (12) concerning an interpretation of the ratio  $d/b$  was intended to be only suggestive. The discussor notes that the blockage coefficient is even more closely associated with this "smearing out". It is indeed equally suggestive, more precise, and is borne out by the experimental data.

2) We think both sets of equations, Wu's and G-N's, are "nice" and think that we understand the physical and mathematical assumptions underlying each. For small values of  $\alpha$  and  $\epsilon$  they give nearly identical predictions. One anticipates that Wu's equations must fail for sufficiently large values of  $\alpha$  and  $\epsilon$ . However, the fact that the G-N equations continue to provide reasonable-looking results for large disturbances is no proof that the results are correct. This must be determined by comparison with experimental data or with more precise calculations based on the exact fluid-dynamical equations.

To Dr. Musker:

We did not discuss our measurements of resistance in order not to make the paper too long. Figure D.1 shows the total resistance together with the wave records shown in Figure 8,  $F_h = 1.05$ . We take the opportunity to note that the experimental records of Figure 8 and Figure D.1 start before the towing carriage was put into motion. This was done in order to observe the transient behavior of the resistance. Therefore in these Figures the actual start of the test corresponds to a point on the time axis where the resistance record starts to deviate from zero. The amplitude of the fluctuation of resistance in Figure D.1 is approximately 10 % of the mean total resistance and the fluctuations have approximately the same period as that of the solitons. It has also been observed that measured amplitude of the resistance fluctuation increases with increasing Froude number and blockage coefficient. However, the amplitude seems negligible for values of  $F_h < 0.9$ .

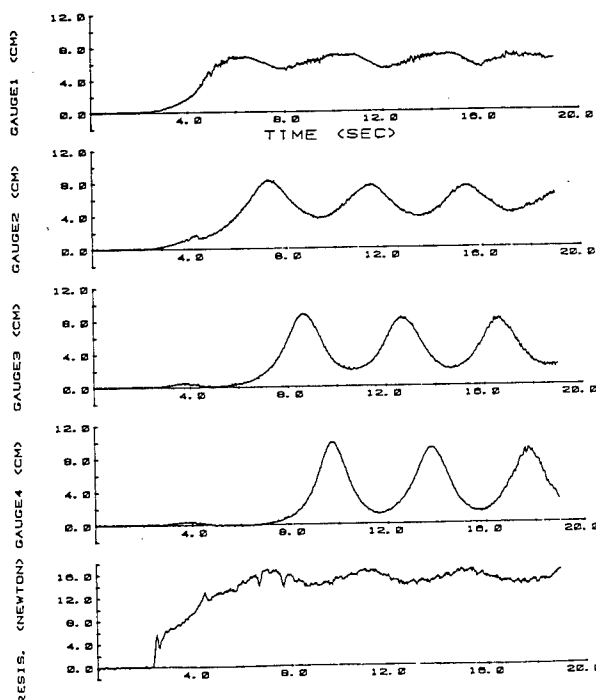


Fig. D.1

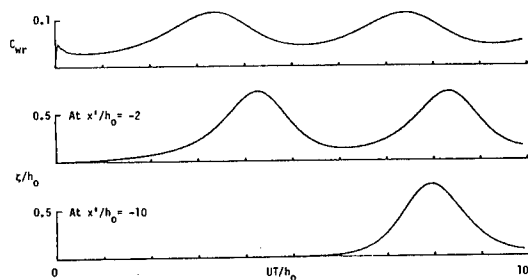


Fig. D.2

In Figure D.2 we show the calculated wave resistance and the wave records (at two moving "numerical" wave gauges ahead of the disturbance) that correspond to Figure 20a ( $C_{Wr} = F_w / \rho g h_0^2$ ). In general, calculated wave-resistance fluctuates with larger amplitudes, as can also be seen in Figures 1 and 3 in the discussion of Lee, Yates and Wu. We should remember, however, that these are two-dimensional calculations and viscosity is ignored.

To Drs. Lee, Yates and Wu:

We are naturally delighted to have these comments from Lee, Yates and Wu, for they complement our paper with additional experimental and computational data as well as with information about the range of validity of Wu's equations, information that seems to be excluded in principle for the G-N equations. The discussers warn, however, against placing too much credence in the suggested range, and we concur in this warning.

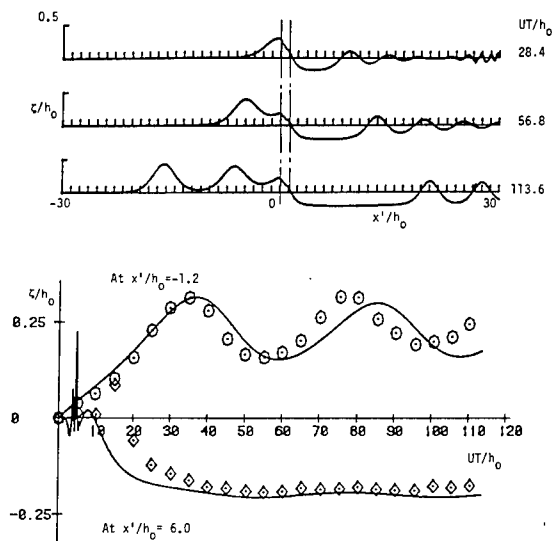


Fig. D.3

Figure D.3 shows wave profiles computed with the G-N equations for a circular-arc bump with  $L/h_0 = 1.2$ ,  $B/h_0 = 0.185$  and  $F_h = 1.0$ ; this corresponds to the discussers' Figure 1. Computations for this bump present some difficulties, since the ends of the circular arc have discontinuities in the derivatives required by either the Wu or the G-N equations. The agreement with the discussers' experimental data (shown by symbols) seems very good, but with seemingly innocent modifications of the treatment of the discontinuities one can produce quite different results. Figure D.4 shows our calculated results with Wu's equations of the curves in the discussers' Figure 1. The differences are notable, probably because of slightly different treatments of the discontinuities at the ends of the arc. In principle, when such discontinuities appear one should employ suitable jump conditions. We plan to do this in the future.

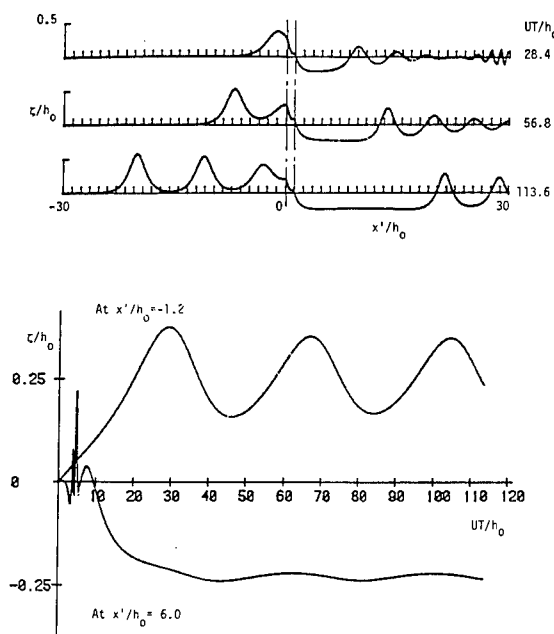


Fig. D.4

In Figure D.5 we show calculations using the G-N equations for a situation corresponding to the discussers' Figure 3:  $L/h_0 = 1.7$ ,  $B/h_0 = 0.284$ ,  $F_h = 1.0$ . We note that the continuous increase of soliton amplitude shown in their Figure 3 does not occur with the G-N equations. (The caveat concerning computations applies here also; however, the G-N equations have not given solitons of increasing amplitude in other situations.)

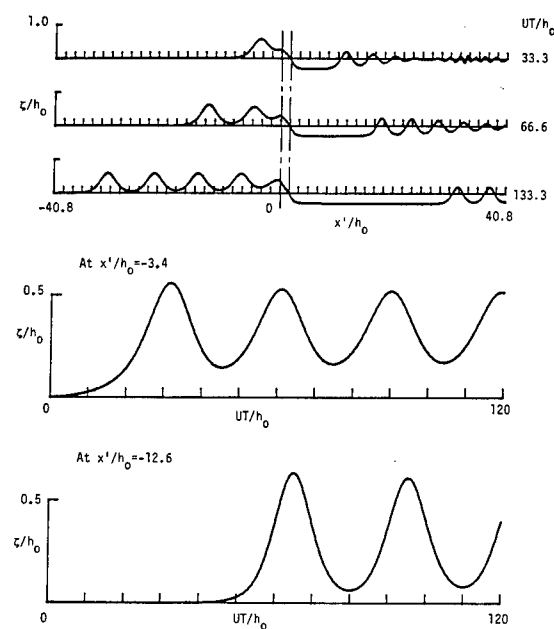


Fig. D.5

SESSION VI  
NONLINEAR FREE-SURFACE INTERACTIONS

# EDGE WAVES CREATED BY A LONGSHORE CURRENT AND A RIDGE IN THE SEA-BED

CHIA-SHUN YIH

## ABSTRACT

A mechanism for creation of edge waves is proposed. It is shown that a longshore current flowing over a ridge in a sloping sea-bed with an angle of inclination  $\gamma$  not greater than  $\pi/4$  produces edge waves in the lee of the ridge. These edge waves have a wave number equal to  $gU^{-2}\sin\gamma$ , where  $g$  is the gravitational acceleration,  $U$  the velocity of the longshore current, and  $\gamma$  the angle of inclination of the sea-bed. The amplitude of the edge waves produced depends on the amplitude and geometry of the ridge as well as on the three variables mentioned above.

## 1. INTRODUCTION

Edge waves, discovered theoretically by Stokes (1846), are waves with amplitude decreasing exponentially toward sea, and exist if the sea-bed is an inclined plane. The question of creation of edge waves in nature, however, has never been studied. Creation by wind is, of course, a possibility, but any creation of edge waves by wind would seem to require that the wind be along the shore, and that its velocity decrease toward sea - a condition not often satisfied.

In this paper a mechanism of creation of edge waves is proposed: by a longshore current flowing over a ridge in a sloping sea-bed. The ridge assumed is either two- or three-dimensional, depending on  $\gamma$ .

It will be shown that the wave number of the edge waves produced is  $gU^{-2}\sin\gamma$ , where  $g$  is the gravitational acceleration,  $U$  the general velocity of the longshore current, apart from perturbations due to the ridge, and  $\gamma$  is the angle of inclination of the sea-bed to the undisturbed sea surface. The amplitude of the edge waves created depends on the amplitude of ridge as well as on  $g$ ,  $U$ , and  $\gamma$ . The attenuation of the amplitude of the ridge toward sea depends, however, on  $\gamma$ , if edge waves are to be produced.

## 2. FORMULATION

Let  $x$ ,  $y$ , and  $z$  be Cartesian coordinates,

with the shoreline as the  $x$ -axis when the sea is at rest, with  $y$  measured horizontally away from the sea, and with  $z$  measured vertically upward (Figure 1). We neglect the effects of viscosity, and consequently can, as usual,

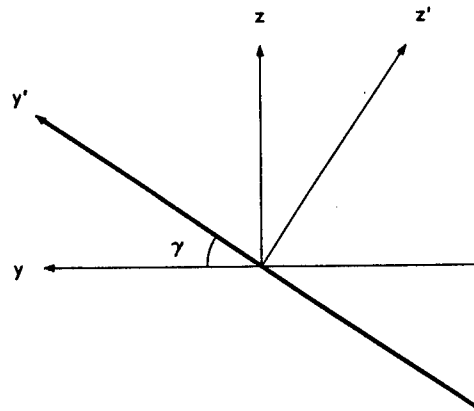


Figure 1. Definition of Coordinates.

assume the motion to be irrotational, so that a velocity potential  $\phi$  exists, in terms of which the velocity components  $u$ ,  $v$ , and  $w$ , in the direction of increasing  $x$ ,  $y$ , and  $z$ , can be expressed:

$$u = \phi_x, \quad v = \phi_y, \quad w = \phi_z,$$

where the subscripts indicate partial differentiation. The equation of continuity then gives

$$\phi_{xx} + \phi_{yy} + \phi_{zz} = 0 \quad (1)$$

which is the equation governing the motion.

At the free surface, where  $z = \zeta$ , the kinematic condition is

$$\left(\phi_x \frac{\partial}{\partial x} + \phi_y \frac{\partial}{\partial y}\right)\zeta = \phi_z, \quad (2)$$

and, since the flow is supposed to be steady,

\*University of Michigan, Ann Arbor, Michigan 48109-2125, U.S.A.

the Bernoulli equation is

$$q^2 + 2gz = \text{constant}, \quad (3)$$

in which

$$q^2 = u^2 + v^2 + w^2 = \phi_x^2 + \phi_y^2 + \phi_z^2. \quad (4)$$

Combining (3) and (4), we have the free-surface condition

$$(\phi_x \frac{\partial}{\partial x} + \phi_y \frac{\partial}{\partial y}) q^2 + 2g\phi_z = 0. \quad (5)$$

At the sea-bed the boundary condition is

$$\frac{\partial \phi}{\partial n} = 0, \quad (6)$$

where  $n$  is measured along the normal to the sea-bed. Very far from the shore the condition is

$$\phi = Ux \quad \text{at} \quad y = -\infty. \quad (7)$$

Equations (1), (5), (6), and (7) constitute the differential system to be solved. The exact shape of the ridge will be specified later.

### 3. ANALYSIS

To solve the problem posed, we introduce another set of Cartesian coordinates  $(x', y', z')$ . The axes of  $y'$  and  $z'$  are shown in Figure 1. The  $y'$ -axis, inclined at angle  $\gamma$  with the  $y$ -axis, is along the line of steepest ascent of the sea bed in the absence of the ridge. Thus

$$y' = y \cos \gamma + z \sin \gamma, \quad z' = -y \sin \gamma + z \cos \gamma. \quad (8)$$

Both sets of Cartesian coordinates are right-handed. In the absence of the ridge, the sea-bed would be given by  $z' = 0$ . Since the amplitude of the ridge is supposed to be small (compared with its width or with the wave length of the edge waves produced), the kinematic condition for the velocity at the sea-bed can be imposed at  $z' = 0$ .

Before considering a ridge, we shall consider a corrugated sea-bed given by  $z' = \zeta'$ , with

$$\zeta' = a \cos kx \exp(ky' \cos 2\gamma), \quad (9)$$

where  $k$  is the wave number in the  $x$ -direction. If  $\gamma = \pi/4$ , the ridge is cylindrical. If  $\gamma < \pi/4$ , the amplitude of the ridge decreases exponentially toward sea. We shall therefore restrict ourselves to values of  $\gamma$  in the range

$$\gamma \leq \pi/4.$$

The explanation for the form of the ridge assumed by (9) will become clear later. In terms of the new coordinates  $(x, y', z')$ , the equations for  $\phi$  is still the Laplace equation

$$\phi_{xx} + \phi_{y'y'} + \phi_{z'z'} = 0. \quad (10)$$

It can be readily verified that, to the first order in  $a$ , the velocity potential that will produce the bottom corrugation specified by (9) is

$$\phi = Ux + \frac{U}{\sin 2\gamma} \sin kx [b \exp ky' + a \exp (ky' \cos 2\gamma - kz' \sin 2\gamma)]. \quad (11)$$

It is evident that (10) is satisfied, and that the term with amplitude  $b$  does not contribute a velocity in the  $z'$ -direction. At  $z' = 0$ ,

$$U \frac{\partial}{\partial x} \zeta' = \phi_{z'},$$

is satisfied by (9) and (11), as a brief calculation will show. Thus the satisfaction of (6) is guaranteed.

On the free surface, the condition (5) reduces to the form

$$(g \sin \gamma - U^2 k) b - (g \sin \gamma + U^2 k) a = 0, \quad (12)$$

or

$$b = \frac{k_e + k}{k_e - k} a = -(1 + \frac{2k_e}{k - k_e}) a, \quad (13)$$

in which

$$k_e = \frac{g \sin \gamma}{U^2}. \quad (14)$$

Equations (11) and (13) give the solution sought.

As to the free-surface displacement  $\zeta$ , it is to be found from

$$U \frac{\partial}{\partial x} \zeta = \phi_z. \quad (15)$$

Noting that (8) gives

$$y' \cos 2\gamma - z' \sin 2\gamma = y \cos \gamma - z \sin \gamma, \quad (16)$$

we obtain from (11), (13), and (15) that

$$\zeta = \frac{a}{\cos \gamma} (1 + \frac{k}{k - k_e}) \cos kx \exp(ky \cos \gamma). \quad (17)$$

Thus edge waves are obtained. These are bound waves, however, with the wavelength exactly equal to the wavelength of the sea-bed corrugation. For  $k = k_e$ , the solution fails, however small  $a$  is, and there is resonance. It will be seen that, when the bottom protrusion is a single ridge, the edge waves produced have exactly the wave number  $k_e$ .

It is appropriate here to note that Stokes' edge waves attenuate seaward as  $\exp(ky \cos \gamma)$ . This attenuation is provided by the term with amplitude  $b$  in (11), and further demands the factor

$$\exp k(y' \cos 2\gamma - z' \sin 2\gamma)$$

in (11), which, as can be seen from (16), gives the required attenuation at  $z = 0$ . Thus the assumption (9) is not arbitrary, but is forced upon us if we want the bottom corrugation to produce pure edge waves. As a consequence, the form of any sea-bed geometry cannot be arbitrary either, if pure edge waves are to be produced.

The results just obtained for a sea-bed corrugation periodic in  $x$  can be generalized by Fourier integration. Consider, for instance, a bottom protrusion given by

$$z' \equiv \zeta' = \frac{A(B - y' \cos 2\gamma)}{(B - y' \cos 2\gamma)^2 + x'^2}, \quad (18)$$

which can be expressed as

$$\zeta' = A \int_0^\infty \frac{e^{-Bk}}{k} \cos kx \exp(ky' \cos 2\gamma) dk, \quad (19)$$

where  $A$  has the dimension of length squared. We shall now, for economy, write (11) as

$$\phi = Ux + Ua\phi_1, \quad (20)$$

where

$$\phi_1 = \frac{\sin kx}{\sin 2\gamma} \left[ \frac{k_e + k}{k_e - k} \exp ky' + \exp(ky' \cos 2\gamma - kz' \sin 2\gamma) \right]. \quad (21)$$

Then on inspection of (9) and (19), the solution for  $\phi$  for the protrusion (18) or (19) is

$$\phi = Ux + UA \int_0^\infty e^{-Bk} \phi_1(k) dk, \quad (22)$$

and the free-surface displacement is given by, on inspection of (9), (19), and (17),

$$\zeta = \frac{A}{\cos \gamma} \int_0^\infty \left(1 + \frac{k_e}{k - k_e}\right) e^{-Bk} \cos kx \cdot \exp(ky \cos \gamma) dk. \quad (23)$$

Equations (22) and (23) give the solution to the problem. But the integrals therein need to be evaluated to exhibit the edge waves created in the lee of the protrusion on the one hand, and the local disturbances, on the other.

#### 4. EVALUATION OF THE INTEGRALS

Let us define the integrals  $I$  and  $J$  by

$$I = \int_0^\infty \frac{1}{k - k_e} \sin kx \exp k(y' - B) dk = \operatorname{Im} \int_0^\infty \frac{1}{k - k_e} \exp k(y' - B + ix) dk, \quad (24)$$

$$J = \int_0^\infty \frac{1}{k - k_e} \cos kx \exp k(y \cos \gamma - B) dk =$$

$$\operatorname{Re} \int_0^\infty \frac{1}{k - k_e} \exp k(y \cos \gamma - B + ix) dk \quad (25)$$

We shall, in calculating  $I$  and  $J$ , which are the two most significant integrals in (22) and (23), first replace  $k$  by  $k_e + i\mu$ , with  $\mu$  positive, and then let  $\mu$  approach zero. This is the well-known and often used device of Rayleigh, to make the gravity waves appear only in the lee of the obstacle. Furthermore, we shall replace the variable  $k$  by the complex variable  $\chi = k + im$ , and use the Cauchy integral theorem in the plane of the complex variable  $\chi$ .

For  $x > 0$ , we shall use the contour shown in Figure 2. Upon letting  $R$  tend to infinity,

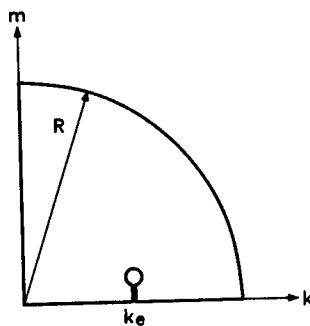


Figure 2. Contour in the  $\chi$ -plane for  $x > 0$ .

we have,

$$I = 2\pi \cos k_e x \exp k_e(y' - B) +$$

$$\operatorname{Im} \int_0^\infty \frac{i}{im - k_e} \exp[-mx + im(y' - B)] dm = 0, \quad (26)$$

or

$$I = 2\pi \cos k_e x \exp k(y' - B) + I_1, \quad (27)$$

where

$$I_1 = \int_0^\infty \frac{1}{m^2 + k_e^2} e^{-mx} [m \sin m(y' - B) - k_e \cos m(y' - B)] dm.$$

For  $x < 0$ , we use the contour shown in Figure 3, and obtain



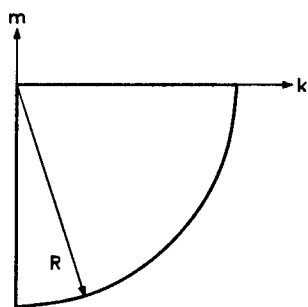


Figure 3. Contour in the  $k$ -plane for  $x < 0$ .

$$I = -\int_0^\infty \frac{1}{m^2 + k_e^2} e^{mx} [m \sin m(y' - B) - k_e \cos m(y' - B)] dm. \quad (28)$$

It can be shown that (27) and (28) give the same value for  $I$  at  $x = 0$ . All we need to do is to evaluate the integral

$$\int \frac{1}{x - k_e} \exp \chi(y' - B + ix) dx$$

along a contour consisting of a section of length  $2R$  of the  $m$ -axis and a large semi-circle to the right of it, with that section as its diameter, use the Cauchy residue theorem, and let  $R$  approach infinity. The center of the semi-circle is the origin.

As to  $J$ , a similar approach gives, for  $x > 0$ ,

$$J = -2\pi \sin k_e x \exp k_e (y \cos \gamma - B) + J_1, \quad (29)$$

where

$$J_1 = \int_0^\infty \frac{1}{m^2 + k_e^2} e^{-mx} [m \cos m(y \cos \gamma - B) + k_e \sin m(y \cos \gamma - B)] dm. \quad (30)$$

For  $x < 0$ , the contour in Figure 3 is used, and we obtain

$$J = \int_0^\infty \frac{1}{m^2 + k_e^2} e^{mx} [m \cos m(y \cos \gamma - B) + k_e \sin m(y \cos \gamma - B)] dm. \quad (31)$$

The other integrals in (22) and (23) are

easy to evaluate. The final results are

$$\phi = Ux + \frac{UA}{\sin 2\gamma} \left[ -2k_e I - \frac{x}{(y' - B)^2 + x^2} + \frac{x}{(y \cos \gamma - z \sin \gamma)^2 + x^2} \right], \quad (32)$$

where  $I$  is given by (26) if  $x > 0$  and by (28) if  $x < 0$ , and

$$\zeta = \frac{A}{\cos \gamma} \left[ k_e J + \frac{B - y \cos \gamma}{(B - y \cos \gamma)^2 + x^2} \right], \quad (33)$$

where  $J$  is given by (29) if  $x > 0$ , and by (31) if  $x < 0$ . It is evident from (32) and (26), and from (33) and (29), that there is a wave component for  $\phi$  and one for  $\zeta$  for  $x > 0$ , but no wave component at all for  $\phi$  and  $\zeta$ , if  $x < 0$ . The other terms in  $\phi$  and  $\zeta$  represent local disturbances. Fig. 4 shows a perspective of  $\zeta$ .

## 5. DISCUSSION

We note first of all that the  $J_1$  given by (30) for  $x > 0$  is exactly equal to the  $J$  given by (31) for  $x < 0$ , for the same absolute value of  $x$ . Thus the  $J_1$  given by (30) and the  $J$  given by (31) represent local disturbances of the free surface due to the bottom protrusion. Furthermore, the last term in (33), which is symmetric with respect to  $x$ , also represents such a disturbance.

The edge waves created are given by the first term on the right-hand side of (29), after it has been multiplied by the factor  $A k_e \sec \gamma$ , as shown in (33). It is interesting that the amplitude of these waves decreases exponentially as  $\exp(-k_e B)$ , as  $B$  increases. That is, the wider (in the  $x$ -direction) the protrusion is, the smaller the amplitude. It should be noted that, for a fixed  $x$ , (18) gives a  $\zeta'$  which decreases asymptotically with  $y'$  as  $A(B - y' \cos 2\gamma)^{-1}$ .

Inspection of (9) and (19) shows that the solution fails if  $\gamma > \pi/4$ , for then  $\zeta'$  would be so large that the linear theory fails. This seems to indicate that pure edge waves cannot be created by a long-shore current if  $\gamma > \pi/4$ . To reassure oneself that this is so one may consider the case  $\gamma = \pi/2$ . The sea-bed is then a vertical sea wall. If there is any seaward protrusion of it, the waves created by it are certainly more like ship waves than edge waves.

The question naturally arises: For  $\gamma \leq \pi/4$ , if the bottom protrusion does not have exactly the  $y'$ -dependence required, what waves will be created? In that case, it seems that, in addition to the edge waves there will be other waves created, which account for the deviation of the  $y'$ -dependence of  $\zeta'$  from the required one. What we have presented in this paper is the solution of pure edge waves created by a longshore current flowing over a sloping sea-bed inclined generally at an angle  $\gamma \leq \pi/4$ , with a protrusion that decreases in some way as  $y'$  decreases toward negative infinity.

nity.

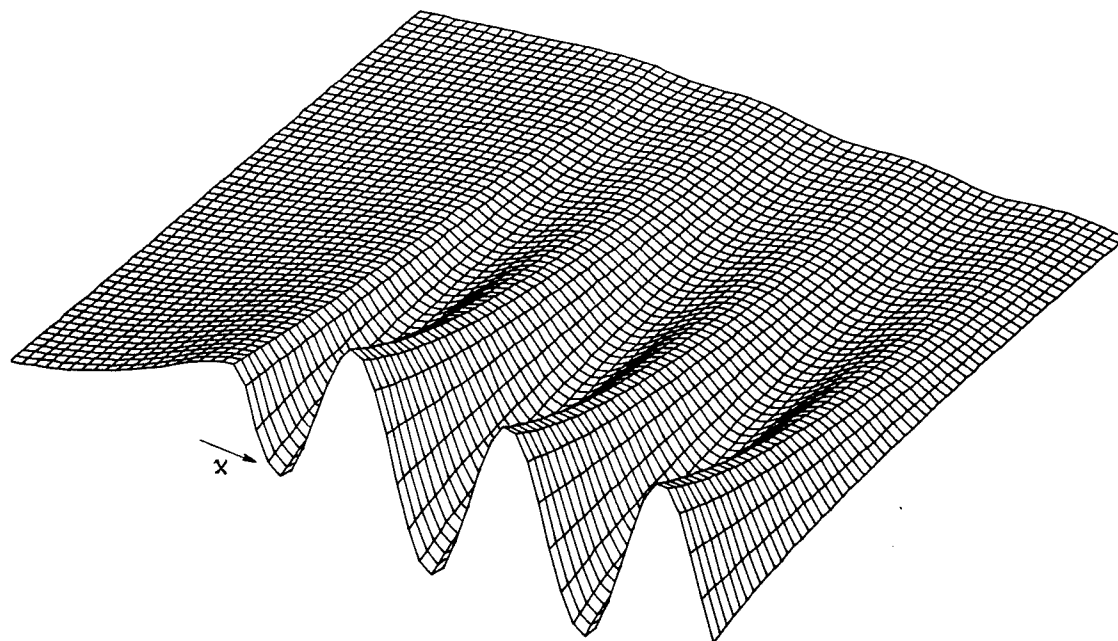


Figure 4. A perspective of the free surface for a bottom protrusion given by (18). With  $\gamma = \pi/4$ ,  $k_e = 5$ , and with  $B$  as the length scale.

#### ACKNOWLEDGEMENT

This work has been sponsored by the Office of Naval Research. Drafting and computation assistance has been rendered by Mr. Marc Ingber. The sponsorship and the assistance are much appreciated.

#### REFERENCE

Stokes, G.G., (1846): Report on recent researches in hydrodynamics, Brit. Assoc. Rept.

# A STUDY OF NONLINEAR WAVE RESISTANCE BY A ZAKHAROV-TYPE INTEGRAL EQUATION

G. DAGAN AND T. MILOH

## ABSTRACT

The nonlinear problem of wave resistance is tackled in this paper by formulating it in the Fourier space and by deriving a nonlinear integral equation of the Zakharov-type for the velocity potential. This procedure is illustrated by computing the wave drag of a submerged cylinder (2D) and a sphere (3D). Special attention is paid to the small Froude number non-uniformity exhibited by the regular perturbation scheme. A uniform generalized expansion which satisfies the new nonlinear integral equation is constructed in this paper and the resulting generalized wave drag is shown to be considerably larger than that predicted by the regular perturbation. Several existing methods, which are based on a quasilinearization of the free-surface boundary conditions, are also discussed and compared against the present nonlinear solution. The promising results thus obtained are believed to open new avenues in exploring the fascinating problem of nonlinear wave resistance.

## 1. INTRODUCTION

The computation of the nonlinear wave resistance of submerged or floating bodies is a subject of intensive research of the last twenty years. Various approximate schemes have been derived in order to tackle this difficult problem (a recent survey has been provided by Tulin, 1978). These approximations are generally based on intuitive arguments and even the elucidation of the main mechanisms of nonlinear wave generation is still a matter of debate.

A rational and consistent approach to free-surface flows and wave resistance is by the regular perturbation expansion of the velocity potential in a deep submergence, thin or slender body approximation (e.g. Wehausen and Laitone, 1960). The first-term of such an expansion satisfies the classical linearized equations which have been investigated for almost a century in the pioneering works of Kelvin, Michell, Havelock, Kochin, Weinblum and

Brard, to mention only a few of the illustrious predecessors of this field. The computation of second-order, nonlinear corrections, to the velocity field and wave resistance, has been made possible only recently by the advent of the electronic computers. This avenue has not been found to be promising so far for at least two reasons: (i) the calculations are quite involved and (ii) and more importantly, the perturbation expansion has been found to be nonuniform. The nonuniformity which occurs at moderate and small Froude numbers is of major concern for the range of speeds experienced by most ships. This state of affairs may explain the flurry of inconsistent, approximate methods, which have been developed as an alternative to the regular perturbation expansion.

In the last few years the problem of weakly nonlinear interaction and stability of trains of gravity waves has been investigated with considerable success by using the Zakharov integral equation (Zakharov, 1968 and for a comprehensive survey see Yuen and Lake, 1982). This success has motivated our interest in applying a similar approach to the problem of wave generation by moving bodies. As we shall show, although the starting point of the studies is similar, the wave resistance problem does not lend itself to the decomposition of the wave field in a slow and rapid components, adopted by Zakharov. For this reason, we prefer to call the basic integral equation which is introduced in this paper, as of "Zakharov type", to distinguish it from the commonly referred to as Zakharov's equation.

The advantage of formulating the nonlinear wave problem as an integral equation in the Fourier transform space is that it permits one to single out in a rational manner and to retain in the first-order approximation of the wave field the most singular terms which are responsible for the strong nonlinear effects. Furthermore, unlike methods which rely heavily on complex variables, and for this reason are restricted only to two-dimensional flows, the present approach is applicable to three-dimensional flows as well.

\* G. Dagan and T. Miloh, Faculty of Engineering, Tel-Aviv University, Ramat-Aviv 69978, Israel

The present study is a first step towards the application of the Zakharov-type equation to free-surface flow past bodies and the general approach is illustrated here for two particular cases only, namely the submerged cylinder and sphere. We hope that the encouraging results presented here will stimulate further investigations of more complex, realistic, problems in the future.

## 2. MATHEMATICAL STATEMENT OF THE PROBLEM

We consider here the steady, irrotational flow of an inviscid and heavy fluid past a submerged body. The variables are made dimensionless with respect to  $U'$  and  $U'^2/g$  as velocity and length scales, respectively,  $U'$  being the unperturbed, constant, velocity at infinity. Let  $x, z$  be cartesian coordinates in the plane of the unperturbed free-surface,  $y$  a vertical coordinate pointing upwards and  $\Phi(x, y, z)$  the perturbation velocity potential, such that the total potential is equal to  $-x + \Phi$ . In the case of two-dimensional flow the  $z$  coordinate has to be deleted.

The exact free-surface conditions

$$\frac{\partial \Phi}{\partial x} - \eta - \frac{1}{2} \nabla \Phi \cdot \nabla \Phi = 0 \quad (y=\eta) \quad (2.1)$$

$$\frac{\partial \Phi}{\partial y} + \frac{\partial \eta}{\partial x} - \frac{\partial \eta}{\partial x} \frac{\partial \Phi}{\partial x} - \frac{\partial \eta}{\partial z} \frac{\partial \Phi}{\partial z} = 0 \quad (y=\eta), \quad (2.2)$$

where  $y=\eta(x, z)$  is the free-surface equation, are now expanded in a Taylor series about  $y=0$ , implying weak nonlinearity. By retaining only quadratic terms and by elimination of  $\eta$  the following equation for the potential is obtained

$$\begin{aligned} & \frac{\partial^2 \Phi}{\partial x^2} + \frac{\partial \Phi}{\partial y} - \frac{\partial}{\partial x} \left[ \frac{3}{2} \left( \frac{\partial \Phi}{\partial x} \right)^2 + \frac{\partial \Phi}{\partial x} \frac{\partial^3 \Phi}{\partial x^3} + \right. \\ & \left. + \frac{1}{2} \left( \frac{\partial^2 \Phi}{\partial x^2} \right)^2 + \left( \frac{\partial \Phi}{\partial z} \right)^2 \right] - \frac{\partial \Phi}{\partial x} \frac{\partial^2 \Phi}{\partial z^2} = 0, \end{aligned} \quad (2.3)$$

whereas  $\eta$  is given to same order by

$$\eta = \frac{\partial \Phi}{\partial x} \left( 1 + \frac{\partial^2 \Phi}{\partial x \partial y} \right) - \frac{1}{2} \nabla \Phi \cdot \nabla \Phi. \quad (2.4)$$

These equations have to be supplemented by a radiation condition requiring wave propagation downstream, to  $x \rightarrow -\infty$ .

To account for the presence of the body we represent the disturbance caused by it in an infinite medium by a singular potential and split  $\Phi$  as follows

$$\Phi = \phi^{(s)} + \phi^{(r)} \quad (2.5)$$

where  $\phi^{(s)}$  is the singular potential, supplemented by appropriate images across  $y=0$ , such that

$$\phi^{(s)}(x, 0, z) = 0, \quad (2.6)$$

whereas  $\phi^{(r)}$  is regular for  $y \leq 0$ . By substituting  $\phi^{(r)}$  into (2.3) we obtain for  $\phi^{(r)}$  the free-surface condition on  $y=0$

$$\begin{aligned} & \frac{\partial^2 \phi^{(r)}}{\partial x^2} + \frac{\partial \phi^{(r)}}{\partial y} - \frac{\partial}{\partial x} \left[ \frac{3}{2} \left( \frac{\partial \phi^{(r)}}{\partial x} \right)^2 + \frac{\partial \phi^{(r)}}{\partial x} \frac{\partial^3 \phi^{(r)}}{\partial x^3} + \right. \\ & \left. + \frac{1}{2} \left( \frac{\partial^2 \phi^{(r)}}{\partial x^2} \right)^2 + \left( \frac{\partial \phi^{(r)}}{\partial z} \right)^2 \right] - \frac{\partial \phi^{(r)}}{\partial x} \frac{\partial^2 \phi^{(r)}}{\partial z^2} = - \frac{\partial \phi^{(s)}}{\partial y}. \end{aligned} \quad (2.7)$$

A solution for  $\phi^{(r)}$  is sought by operating with the Fourier transform on (2.7) and defining

$$\psi(\underline{k}) = (2\pi)^{-m/2} \int_{-\infty}^{\infty} \phi^{(r)}(x, 0, z) e^{i\underline{k} \cdot \underline{x}} d\underline{x}. \quad (2.8)$$

In Eq. (2.8)  $m=1, m=2$  represent two- and three-dimensional flows, respectively. For three-dimensional flows  $\underline{x}$  has the components  $x, z$  and the wave number vector  $\underline{k}$  has the components  $k_x, k_z$  or preferably the polar representation  $k_x = \rho \cos \theta, k_z = \rho \sin \theta$ . In the case of two-dimensional flows,  $\underline{x}$  is replaced by  $x$  and  $\underline{k}$  by  $k$ . The regular potential, satisfying the Laplace equation, is given by

$$\phi^{(r)}(x, y, z) = (2\pi)^{-m/2} \int_{-\infty}^{\infty} \psi(\underline{k}) e^{i\underline{k} \cdot \underline{x} - i k_y y} d\underline{k}. \quad (2.9)$$

In analogy with the problem of wave generation by a moving pressure distribution (investigated in a separate paper) we represent the forcing term in the r.h.s. of Eq. (2.7) with the aid of the function  $\Pi(\underline{k})$  defined as follows

$$\Pi(\underline{k}) = - \frac{i(2\pi)^{-m/2}}{k_x} \int_{-\infty}^{\infty} \frac{\partial \phi^{(s)}}{\partial y} e^{i\underline{k} \cdot \underline{x}} d\underline{x} \quad (y=0). \quad (2.10)$$

Taking now the FT (Fourier transform) of (2.7) yields the following integral equation for  $\psi$

$$\begin{aligned} A(\underline{k}) \psi(\underline{k}) + i k_x \int_{-\infty}^{\infty} B(\underline{k}, \underline{k}_1) \psi(\underline{k}_1) \psi(\underline{k} - \underline{k}_1) d\underline{k}_1 = \\ - i k_x \Pi(\underline{k}). \end{aligned} \quad (2.11)$$

In (2.11)  $A(\underline{k})$  represents the dispersion relationship

$$A(\underline{k}) = |\underline{k}| - k_x^2 + i\mu |\underline{k}|, \quad (2.12)$$

where  $\mu$  is a vanishing and positive fictitious

dissipation coefficient which ensures that in the inversion of  $\psi$  (2.9) the resulting far free-waves propagate downstream.  $A(\underline{k}) = 0$  has the zeros  $k = \pm 1 + i\mu$  in 2D and  $\rho = \sec^2 \theta + i\mu$  in 3D.

The kernel  $B$ , resulting from the application of the Faltung theorem to (2.7) has the following expression:

$$B(\underline{k}, \underline{k}_1) = (2\pi)^{-m/2} \left\{ \frac{1}{2} k_{1x} (k_x - k_{1x}) [-3 + k_{1x} (k_x - k_{1x}) + k_{1x}^2 + (k_x - k_{1x})^2] - k_{1z} (k_z - k_{1z}) - k_{1z} (1 - k_{1x}/k_x) \right\}. \quad (2.13)$$

The nonlinear integral equation for  $\psi$  (2.11), which we shall call of Zakharov-type, is the starting point of the present study. The commonly known Zakharov equation is obtained by applying first the Fourier transform to  $\phi(x, \eta, z)$  and  $\eta$  in the unsteady free-surface conditions, by  $\frac{\partial \phi}{\partial y}$  and  $\frac{\partial \phi}{\partial y}$  in a Taylor series around  $y=0$  and by retaining terms up the third order (See Eqs. 103-104 in Yuen and Lake, 1982). Furthermore, the ensuing equation is simplified considerably by separating the wave amplitude function into a slowly and a rapidly varying component. The essential difference between (2.11) and the corresponding Zakharov-equation is in the presence of the forcing term of a non-wavy character,  $\Pi$ , which is associated with the presence of the body. As for the third-order terms, we have examined their influence in a particular case of a travelling pressure distribution and it has been found to be relatively small. The validity of this conclusion in other cases as well, is a matter of future investigations.

Returning to the Zakharov type equation (2.11) it is convenient to recast it in a slightly different form by defining the amplitude function  $a(\underline{k})$  as follows

$$a(\underline{k}) = \frac{iA(\underline{k}) \psi(\underline{k})}{k_x \Pi(\underline{k})}. \quad (2.14)$$

Substitution in (2.11) yields the equivalent Zakharov-type equation

$$a(\underline{k}) + \int_{-\infty}^{\infty} C(\underline{k}, \underline{k}_1) a(\underline{k}_1) a(\underline{k} - \underline{k}_1) d\underline{k}_1 = 1, \quad (2.15)$$

where the kernel  $C$  is given by

$$C(\underline{k}, \underline{k}_1) = \frac{B(\underline{k}, \underline{k}_1) k_{1x} (k_x - k_{1x}) \Pi(\underline{k}_1) \Pi(\underline{k} - \underline{k}_1)}{A(\underline{k}_1) A(\underline{k} - \underline{k}_1) \Pi(\underline{k})}. \quad (2.16)$$

Once  $a(\underline{k})$  is determined by solving (2.15), the potential  $\phi^{(r)}$  is obtained from (2.9) in terms of  $a(\underline{k})$  as follows

$$\phi^{(r)}(x, 0, z) = -i(2\pi)^{-m/2} \int_{-\infty}^{\infty} \frac{k_x \Pi(\underline{k}) a(\underline{k})}{A(\underline{k})} e^{-i\underline{k} \cdot \underline{x}} d\underline{k} \quad (2.17)$$

and the far free-waves are obtained for  $x \rightarrow -\infty$  in (2.17).

In the two-dimensional case the far free-waves are Stokes wave which have the general expression

$$\eta(x) \rightarrow \eta^{(1)} e^{ix} + \eta^{(1)*} e^{-ix} + \eta^{(2)} e^{2ix} + \eta^{(2)*} e^{-2ix}, \quad (2.18)$$

and the wave resistance, made dimensionless with respect to  $\rho U^4/g$ , is given by

$$D = \eta^{(1)} \eta^{(1)*} = 2\pi a(1) a(-1) \Pi(1) \Pi(-1). \quad (2.19)$$

In the case of three-dimensional flow the wave profile is associated with the residues contribution in (2.17) and is given in terms of the amplitude function  $a(\rho, \theta)$  by

$$\eta(x, z) \rightarrow \frac{i}{2} \int_{-\pi}^{\pi} a(\sec^2 \theta, \theta) e^{-i \sec^2 \theta (x \cos \theta + z \sin \theta)} d\theta \quad (2.20)$$

$$\cdot \Pi(\sec^2 \theta, \theta) \sec^4 \theta d\theta,$$

and the wave drag is given by

$$D = \frac{\pi}{2} \int_{-\pi/2}^{\pi/2} a(\sec^2 \theta, \theta) a^*(\sec^2 \theta, \theta) \cdot \Pi(\sec^2 \theta, \theta) \Pi^*(\sec^2 \theta, \theta) \sec^5 \theta d\theta. \quad (2.21)$$

A regular perturbation solution of the Zakharov type Equation (2.15) can be obtained if it is assumed that  $\Pi = o(1)$ , i.e.  $C = o(1)$ . An asymptotic expansion of  $a(\underline{k})$

$$a(\underline{k}) = a_1(\underline{k}) + a_2(\underline{k}) + \dots \quad (2.22)$$

yields, after substitution in (2.15)

$$a_1(\underline{k}) = 1; \quad a_2(\underline{k}) = - \int_{-\infty}^{\infty} C(\underline{k}, \underline{k}_1) d\underline{k}_1. \quad (2.23)$$

Substitution of  $a_1, a_2, \dots$ , in (2.17) leads to the various approximations  $\phi_1^{(r)}$ ,

$\phi_2^{(r)}$ ... of the potential.  $\phi_1^{(r)}$  is easily recognized as the classical linearized solution, whereas  $\phi_2^{(r)}$  represents the second-order cor-

rection.

At this point we abandon the general discussion and proceed by illustrating the procedure for the particular case of a submerged cylinder or sphere.

### 3. REGULAR PERTURBATION SOLUTION

#### 3.1 Submerged cylinder

We consider here the two-dimensional flow past a submerged cylinder of radius  $a = a'g/U'^2$  at a depth  $h = h'g/U'^2$  beneath the unperturbed free-surface. The first approximation of the singular potential  $\phi_1^{(s)}$  corresponds to a doublet supplemented by its "soft image" across  $y = 0$ , i.e.,

$$\phi_1^{(s)}(x, y) = (\epsilon h)^2 \operatorname{Re} \left[ \frac{1}{x+i(y-h)} - \frac{1}{x+i(y+h)} \right], \quad (3.1)$$

where  $\epsilon = a/h$  is the small parameter of the problem.

By taking the FT of (3.1) and using (2.10) it is found that

$$\Pi(k) = (\epsilon h)^2 (2\pi)^{1/2} e^{-|k|h} \quad (3.2)$$

and subsequent substitution in (2.17) yields for the far free waves in the linearized approximation

$$\eta_1(x) = - \frac{\partial \phi_1}{\partial x} \rightarrow 2\pi i (\epsilon h)^2 e^{-h} (e^{ix} - e^{-ix}) \quad x \rightarrow -\infty. \quad (3.3)$$

Thus, the first order approximation of the wave drag has the well-known expression

$$D_1 = 4\pi^2 (\epsilon h)^4 e^{-2h}; \quad \mathfrak{D}_1 = \frac{D_1}{W} = 4\pi (\epsilon h)^2 e^{-2h}, \quad (3.4)$$

where  $W = \pi a^2 = \pi (\epsilon h)^2$  is the buoyancy and  $\mathfrak{D}_1$  denotes the drag-buoyancy ratio.

The second order approximation  $\phi_2^{(r)}$  involves two terms: the free-surface correction

$\phi_2^{(fs)}$  and the body connection  $\phi_2^{(b)}$ . The first

is found in terms of  $a_2$  (2.23) by substituting  $\Pi_1$  (3.2) in the kernel  $C$  (2.16). It can be shown that the only contribution to the amplitude of the far free-wave  $\eta_2^{(1)}$  (2.18) stems from the principal value integration of  $C$  in (2.23). Thus, the second order wave profile is given by

$$\eta_2 = i(2\pi)^{1/2} a_2(1) \Pi(1) (e^{ix} - e^{-ix}) \quad (3.5)$$

$$a_2(1) = - \int_{-\infty}^{\infty} C(1, k_1) dk_1.$$

The kernel  $C(1, k_1)$  (3.5) has the following simple explicit expressions for the particular form for  $\Pi$  (3.2):

$$C(1, k_1) = -\frac{1}{2} (\epsilon h)^2 \begin{cases} (-2+3k_1-k_1^2) e^{2k_1 h} \\ (2+k_1-k_1^2) \\ -(k_1+k_1^2) e^{-2k_1 h} \end{cases} \begin{cases} k_1 < 0 \\ 0 < k_1 < 1 \\ k_1 > 1 \end{cases} \quad (3.6)$$

Substitution in (3.5) yields after a simple integration the following closed form solution

$$a_2(1) = - \int_{-\infty}^{\infty} C(1, k_1) dk_1 = \quad (3.7)$$

$$= \frac{1}{2} (\epsilon h)^2 \left[ \frac{13}{6} - \frac{2}{h} - \frac{3}{2h^2} - \frac{1}{2h^3} \right]$$

and the final form of the second-order free-surface correction to the drag is

$$\begin{aligned} \mathfrak{D}_2^{(fs)} &= \mathfrak{D}_{21}^{(fs)} + \mathfrak{D}_{22}^{(fs)} = \\ &= \frac{D_2^{(fs)}}{W} = \frac{4\pi a_2(1) \Pi(1) \Pi(-1)}{\pi (\epsilon h)^2} + \\ &+ \frac{2\pi [a_2(1)]^2 \Pi(1) \Pi(-1)}{\pi (\epsilon h)^2} = \end{aligned} \quad (3.8)$$

$$= \epsilon^4 \left[ 4\pi \left( \frac{13}{6} - \frac{2}{h} - \frac{3}{2h^2} - \frac{1}{2h^3} \right) h^4 e^{-2h} \right] +$$

$$+ \epsilon^6 \left[ \pi \left( \frac{13}{6} - \frac{2}{h} - \frac{3}{2h^2} - \frac{1}{2h^3} \right)^2 h^6 e^{-2h} \right]$$

$\mathfrak{D}_{21}^{(fs)}$  represents the contribution of order  $\epsilon^4$  where  $\mathfrak{D}_{22}^{(fs)}$  is of order  $\epsilon^6$  and both

result from  $a_1 + a_2$  in (2.19). Thus, a consistent expansion of the amplitude function yields higher order terms of the wave drag. The advantage of keeping  $\mathfrak{D}_{22}^{(fs)}$  in the second-order approximation is that it renders the drag positive definite.

The second-order correction, stemming from the body boundary condition, has been described by Havelock (1936) and its contribution to the drag is given by

$$\mathcal{D}_2^{(b)} = -\varepsilon^4 \left\{ 8\pi \left[ \frac{h^2}{4} + h^3 - 2h^4 e^{-2h} \text{Ei}(2h) \right] e^{-2h} \right\}. \quad (3.9)$$

The ratios  $\mathcal{D}_1/\varepsilon^2$  (3.4),  $\mathcal{D}_{21}^{(fs)}/\varepsilon^4$ ,  $\mathcal{D}_{22}^{(fs)}/\varepsilon^6$  (3.8) and  $\mathcal{D}_2^{(b)}/\varepsilon^4$  (3.9) which are functions of the depth Froude number  $Fr = h^{-1/2}$  solely, are represented in Fig. 1. Luck (1965) has determined the second-order connection  $\mathcal{D}_{21}^{(fs)}$  numerically for a limited range of Froude numbers and the results of his Fig. 3 and the present analytical solution (3.8) are in good agreement.

We are now in a position to check the uniformity of the regular perturbation expansion. In more precise terms we wish to find out whether for  $\varepsilon = o(1)$  the ratio  $\mathcal{D}_2/\mathcal{D}_1 = o(1)$  for any  $h$ . Starting with the body correction, it is seen from (3.9) and (3.4) that

$$\mathcal{D}_2^{(b)}/\mathcal{D}_1 \rightarrow \frac{1}{2} \varepsilon^2 \quad (Fr \rightarrow 0, \text{ i.e. } h \rightarrow \infty) \quad (3.10)$$

$$\mathcal{D}_2^{(b)}/\mathcal{D}_1 \rightarrow -\frac{1}{2} \varepsilon^2 \quad (Fr \rightarrow \infty, \text{ i.e. } h \rightarrow 0)$$

i.e. the body correction is uniform for any Froude number. The situation is however different for the free-surface nonlinear effect, which by (3.8) and (3.4) gives

$$\mathcal{D}_{21}^{(fs)}/\mathcal{D}_1 \rightarrow \frac{13}{6} (\varepsilon h)^2 + O(\varepsilon^2 h) \quad (Fr \rightarrow 0 \text{ i.e. } h \rightarrow \infty) \quad (3.11)$$

$$\mathcal{D}_{21}^{(fs)}/\mathcal{D}_1 \rightarrow -\frac{1}{2} \frac{\varepsilon^2}{h} + O(\varepsilon^2) \quad (Fr \rightarrow \infty \text{ i.e. } h \rightarrow 0).$$

Thus, the regular perturbation expansion is nonuniform for both low and high Froude numbers and its range of validity is limited by the requirement  $\varepsilon h = \varepsilon/Fr^2 = o(1)$  for small

Froude numbers and by  $\varepsilon^2/h = \varepsilon^2 Fr^2 = o(1)$  for high Froude numbers. The small Froude number range is represented schematically in Fig. 2.

As stated before, our main concern in this study is in the small Froude number non-uniformity. Tracing back of the term of the kernel  $C(1, k_1)$  (3.6) which yields the most singular term in (3.7) shows that it is convenient to separate the kernel  $C(k, k_1)$  into two components

$$C(k, k_1) = C^{(s)}(k, k_1) + C^{(r)}(k, k_1) \quad (3.12)$$

where

$$C^{(s)}(k, k_1) = -\frac{1}{2} (\varepsilon h)^2 \frac{k_1(k-k_1)(3-k^2+kk_1-k_1^2)}{(1-k_1)(1-k+k_1)} \quad (0 < k_1 < k)$$

$$C^{(s)}(k, k_1) = 0 \quad (k_1 < 0; k_1 > k) \quad (3.13)$$

leading to the two components  $a_2^{(s)}(k)$  and

$a_2^{(r)}(k)$  in (2.23).  $a_2^{(s)}(1)$  is equal to  $\frac{13}{12} (\varepsilon h)^2$  whereas  $a_2^{(r)}(1)$  is equal to the remaining terms of (3.7) and  $a_2^{(s)}$  leads to the most singular term of the drag  $\mathcal{D}_2^{(fs)}$  (3.8) for  $Fr \rightarrow 0$ . The origin of this term and the derivation of a uniformly valid solution are investigated in the sequel.

### 3.2 Submerged sphere

We consider next the more interesting case of a three-dimensional flow past a submerged sphere of radius  $a = a'g/U'^2$  at a depth of  $h = h'g/U'^2$  beneath the undisturbed free-surface. According to (2.5), we define the singular part of the velocity potential by adding a "soft-image", to the disturbance potential of a submerged doublet of strength  $\frac{1}{2}(\varepsilon h)^3$  and directed along the negative  $x$  axis

$$\phi^{(s)}(x, y, z) = \frac{1}{2} (\varepsilon h)^3 \left\{ \frac{\partial}{\partial x} [x^2 + (y+h)^2 + z^2]^{-1/2} - \frac{\partial}{\partial x} [x^2 + (y-h)^2 + z^2]^{-1/2} \right\}. \quad (3.14)$$

Taking the FT of (3.14) and using (2.10) we obtain,

$$\Pi(k) = (\varepsilon h)^3 e^{-h|k|}. \quad (3.15)$$

The first-order (linearized) wave drag is readily obtained by substituting  $a = a_1 = 1$  (2.23) and (3.15) in (2.21) which gives

$$D_1 = \pi (\varepsilon h)^6 e^{-h} [K_0(h) + (1 + \frac{1}{2h}) K_1(h)], \quad (3.16)$$

where  $K_0$  and  $K_1$  are the modified Bessel functions of zero and first order respectively. In the small Froude number limit ( $h \rightarrow \infty$ ) the wave drag is given asymptotically by

$$\mathcal{D}_1 = D_1/W = \frac{3\pi}{2} \frac{\varepsilon h^{5/2}}{\sqrt{2\pi}} e^{-2h}, \quad (3.17)$$

where  $W = \frac{4}{3} \pi (\varepsilon h)^3$  denotes the buoyancy.

The second-order approximation for the free-surface correction involves the computation of the second-order amplitude function  $a_2$  (2.23) obtained by using (2.16) and (3.15),

$$a_2(\underline{k}) = -(\varepsilon h)^3 \int_{-\infty}^{\infty} \frac{B(\underline{k}, \underline{k}_1) k_{1x} (k_x - k_{1x})}{A(\underline{k}_1) A(\underline{k} - \underline{k}_1)} e^{-h[|\underline{k}_1| - |\underline{k}| + |\underline{k} - \underline{k}_1|]} d\underline{k}_1. \quad (3.18)$$

The above integral may be also written in terms of polar coordinates, as,

$$a_2(\rho, \theta) = -(\varepsilon h)^3 \int_0^{\infty} \int_{-\pi}^{\pi} B^*(\rho, \theta; \rho_1, \theta_1) e^{-h[\rho_1 - \rho + \delta(\theta_1)]} \rho_1 d\theta_1 d\rho_1 \quad (3.19)$$

where

$$\delta^2(\theta_1) = \rho^2 - 2\rho\rho_1 \cos(\theta - \theta_1) + \rho_1^2.$$

Since our main interest resides in the low-Froude number limit ( $h \rightarrow \infty$ ) we may employ the Laplace method to obtain the asymptotic behaviour of (3.19). Indeed the argument of the exponential in (2.19) has a minimum for  $\theta_1 = \theta$  where the first derivative of the exponential function w.r.t.  $\theta_1$  vanishes and the second derivative is positive, hence,

$$a_2(\rho, \theta) \rightarrow -(\varepsilon h)^3 \int_0^{\infty} \sqrt{\frac{2\pi |\rho - \rho_1|}{h\rho\rho_1}} B^*(\rho, \theta; \rho_1, \theta) e^{-h[\rho_1 - \rho + |\rho - \rho_1|]} \rho_1 d\rho_1. \quad (3.20)$$

It is thus found that in the low Froude number approximation, the range of the integration in (3.20) can be further reduced to  $\rho > \rho_1 > 0$ . In addition, in applying the Laplace method to compute the wave resistance at low Froude numbers from the general expression (2.21), only contributions from the ray  $\theta = 0$  have to be considered. Hence we obtain from (3.18) (3.20) and (2.13),

$$a_2(1, 0) = -\frac{1}{2} \frac{\varepsilon h^{5/2}}{\sqrt{2\pi}} \int_0^1 \rho_1^{1/2} (1 - \rho_1)^{1/2} d\rho_1 \quad (3.21)$$

$$[-3 + \rho_1(1 - \rho_1) + \rho_1^2 + (1 - \rho_1)^2] d\rho_1 = \frac{35\pi}{256} \frac{\varepsilon h^{5/2}}{\sqrt{2\pi}}.$$

The second-order wave drag is then obtained by substituting (3.21) in (2.21) and retaining terms up to  $(\varepsilon h)^9$ . For small Froude number we obtain from (3.17)

$$\begin{aligned} \mathcal{D}_2^{(fs)} / \mathcal{D}_1^{(fs)} &= \mathcal{D}_{21}^{(fs)} / \mathcal{D}_1^{(fs)} + \mathcal{D}_{22}^{(fs)} / \mathcal{D}_1^{(fs)} = 2a_2(1, 0) + a_2^2(1, 0) \\ &= \frac{35\pi}{128} \frac{\varepsilon h^{5/2}}{\sqrt{2\pi}} + \left(\frac{35\pi}{256}\right)^2 \left(\frac{\varepsilon h^{5/2}}{\sqrt{2\pi}}\right)^2. \end{aligned} \quad (3.22)$$

The second order correction to the wave drag, which results from the Neuman boundary conditions applied on the surface of the sphere, has been reported by Havelock (1919), Bessho (1957) and Kim (1969) and is given for any Froude number by,

$$\mathcal{D}_2^{(b)} / \mathcal{D}_1 = -(\varepsilon h)^3 \left\{ \frac{1}{8h^3} - \frac{4}{\pi} \int_0^{\pi/2} [Ei(2h \sec^2 \theta) e^{-2h \sec^2 \theta} \sec^4 \theta - \frac{1}{2h} \sec^2 \theta - \frac{1}{4h^2}] d\theta \right\}, \quad (3.23)$$

where  $Ei$  denotes the exponential integral. For small Froude number (3.23) and (3.22) reduce to

$$\mathcal{D}_2^{(b)} / \mathcal{D}_1 \rightarrow \frac{4-\pi}{8} \varepsilon^3; \quad \mathcal{D}_{21}^{(fs)} / \mathcal{D}_1^{(fs)} = \frac{35\pi}{128} \frac{\varepsilon h^{5/2}}{\sqrt{2\pi}} \quad (3.24)$$

implying a nonuniformity of the type  $\varepsilon^3 / Fr^5$  for

the ratio  $\mathcal{D}_2^{(fs)} / \mathcal{D}_1^{(fs)}$  as  $Fr \rightarrow 0$  and  $\varepsilon = o(1)$ . The small Froude number nonuniformity, which is exhibited by the regular perturbation scheme for a sphere, can be removed by constructing a uniformly valid expansion as demonstrated in the sequel.

### 3.3 Discussion of results

By recasting the nonlinear problem of wave generation by a submerged cylinder or a sphere in the Fourier space, we have been able to show that no matter how small is the submergence parameter  $\varepsilon$ , the perturbation expansion of both the wave amplitude and drag becomes nonuniform for  $Fr \rightarrow 0$  when  $\varepsilon / Fr^2 = 0(1)$  and  $\varepsilon / Fr^{5/3} = 0(1)$  in 2D and 3D flows, respectively. Furthermore, we have been able to single out the free-surface nonlinear terms which cause this nonuniformity.

The small Froude number nonuniformity has been recognized in the past (the topic is reviewed by Tulin, 1978), but it seems that here for the first time its extent and origin have been found in a rigorous manner.

Examination of  $a_2$  (3.7) and  $C$  (3.6) in the two-dimensional case shows that the nonli-



near free-surface effect stems from the interaction of the local terms of the forcing factor represented by  $\Pi$  (3.2) and not from the nonlinear interaction of the far free-waves. The same conclusion is apparently valid for three-dimensional flow as well. In this respect the problem of nonlinear wave generation by a body is fundamentally different from that of nonlinear interaction of progressive waves dealt with by Zakharov's equation. Furthermore, for small  $Fr$  the dominant nonlinear contribution stems from the integration of the product  $\Pi_1(k_1) \Pi_1(k-k_1)$  for  $0 < k_1 < k$  in 2D and for the "transverse" term  $\theta_1 = 0$ ,  $\rho = 0$ ,  $0 < \rho_1 < \rho$  in 3D. Thus, the interaction between the low wave number components of the FT of the forcing term is responsible for the relatively large nonlinear free-surface effect. Although  $\Pi_1$  (3.2),

(3.15) tends to zero like  $e^{-h}$  for  $h \rightarrow \infty$  and

$|k| = 1$ , the product  $\Pi_1(k_1) \Pi_1(k-k_1)$  is seen

to be of the same order, i.e.  $e^{-h}$ , for wave numbers in the above range.

There is a great deal of analogy between the behaviour of the two- and three-dimensional flows for small  $Fr$ , the transverse components for  $\theta = 0$  in the latter case having a two-dimensional character. Still, the nonlinear effect upon the wave drag is somewhat weaker in 3D because of the spread of the far free wave manifold over various  $\theta$  and this should serve as a warning against generalizations of 2D solutions.

The validity of the present results in the case of submerged bodies of more complex shapes or for floating bodies is a matter of further investigations. It is believed that the present approach opens promising avenues for the elucidation of the nonlinear mechanism of wave generation.

#### 4. THE DERIVATION OF A GENERALIZED, UNIFORM SOLUTION

##### 4.1 Derivation of uniform solution

We shall rewrite the basic integral equation (2.15) for the wave amplitude  $a(k)$  as follows

$$a(k) + \int_{-\infty}^{\infty} C^{(s)}(k, k_1) a(k_1) a(k-k_1) dk_1 = 1 - \int_{-\infty}^{\infty} C^{(r)}(k, k_1) a(k_1) a(k-k_1) dk_1 \quad (4.1)$$

We have shown<sup>2,2</sup> that for  $h \rightarrow \infty$  and for  $\epsilon h^{5/2} = 0(1)$  or  $\epsilon h^{3/2} = 0(1)$  in 2D or 3D flows, respectively, the contribution from the second term on the l.h.s. of (4.1) is  $0(1)$ , whereas the last integral contributes terms of  $o(1)$ . Hence, the singular kernel has to be kept in the equation satisfied by the leading order term to avoid the nonuniformity of the naive, regular expansion. We suggest, therefore, the

following generalized expansion:

$$a(k) = a_1^{(g)}(k) + a_2^{(g)}(k) + \dots \quad (4.2)$$

such that  $a_1^{(g)}, a_2^{(g)}, \dots$  satisfy the integral equations

$$a_1^{(g)}(k) + \int_{-\infty}^{\infty} C^{(s)}(k, k_1) a_1^{(g)}(k_1) a_1^{(g)}(k-k_1) dk_1 = 1 \quad (4.3)$$

$$a_2^{(g)}(k) + 2 \int_{-\infty}^{\infty} C^{(s)}(k, k_1) a_1^{(g)}(k_1) a_2^{(g)}(k-k_1) dk_1 = - \int_{-\infty}^{\infty} C^{(r)}(k, k_1) a_1^{(g)}(k_1) a_1^{(g)}(k-k_1) dk_1 \quad (4.4)$$

The sequence  $a_1^{(g)}, a_2^{(g)}$  depends on  $\epsilon$  and  $h$  in a nonlinear fashion and it is asymptotic in the sense that for  $\epsilon h^2 = 0(1)$  (2D) or

$\epsilon h^{5/2} = 0(1)$  (3D) and  $Fr \rightarrow 0$ , the ratio

$a_2^{(g)}/a_1^{(g)}$  is  $0(Fr^2)$ . This ordering is ensured by the diminishing effect of the kernel

$C^{(r)}$  which lowers by  $h^{-1}$  the order of the integrand of the r.h.s. of (4.4).

One of the purposes of the present study is to derive the first-order generalized solution  $a_1^{(g)}$  for the two examples of flow considered here. In this way we extend the range of validity of the perturbation expansion to the range  $Fr = o(1)$ ,  $\epsilon/Fr^2 = 0(1)$  in 2D and  $\epsilon/Fr^{5/2} = 0(1)$  in 3D. The extended range of uniformity is represented schematically in Fig. 2. Further extension for  $\epsilon = o(1)$  and arbitrary Froude number (see Fig. 2) is beyond the scope of the present study and therefore is not considered here.

The generalized wave drag  $D^{(g)}$  is given by Eqs. (2.19) and (2.21) and the ratio  $D_1^{(g)}/D_1$  is seen to be, by (3.4),

$$D_1^{(g)}/D_1 = [a_1^{(g)}(1)]^2 \quad (2D) \quad D_1^{(g)}/D_1 = [a_1^{(g)}(1,0)]^2 \quad (3D) \quad (4.5)$$

To compute  $a_1^{(g)}(k)$  we have to solve the following nonlinear integral equations

$$a_1^{(g)}(k) - \frac{1}{2}(\epsilon h)^2 \int_0^k \frac{k_1(k-k_1)(3-k^2+kk_1-k_1^2)}{(1-k_1)(1-k+k_1)} a_1^{(g)}(k_1) a_1^{(g)}(k-k_1) dk_1 = 1, \quad (4.6)$$

$$a_1^{(g)}(\rho, 0) - \frac{\epsilon h^{5/2}}{2\sqrt{2}\pi} \int_0^{\rho} \frac{\rho_1^{3/2}(\rho-\rho_1)^{3/2}(3-\rho^2+\rho\rho_1-\rho_1^2)}{(1-\rho_1)(1-\rho+\rho_1)} a_1^{(g)}(\rho_1, 0) a_1^{(g)}(\rho-\rho_1, 0) d\rho_1 = 1 \quad (4.7)$$

for the cylinder and sphere, respectively.

It is quite easy to determine  $a_1^{(g)}$  by numerical integration since (4.6) and (4.7) are nonlinear Volterra integral equations. Thus, if (4.6), (4.7) are discretized for

$k_n = n/N$  ( $n = 0, 1, 2, \dots, N$ ),  $a_1^{(g)}(k_n)$  can be determined in terms of  $a_1^{(g)}(k_{n-1})$  by a simple algebraic operation. For  $k = \rho = 1$ ,  $a_1^g$  depends on  $\epsilon^2 h^2$  and  $\epsilon^3 h^{5/2}$  in 2D and 3D flow, respectively.

In Figs. 3 and 4 we have represented the ratio  $\mathcal{D}_1^{(g)}/\mathcal{D}_1$  (4.5) as a function of  $\epsilon^2 h^2$  and  $\epsilon^3 h^{5/2}$ . In the same figures we have also represented the leading order term of the second-order regular perturbation expansion. It is seen that the perturbation solution grossly underestimates the nonlinear drag.

In view of existing approximate approaches in the literature, we have also examined

quasilinear approximations  $a_1^{(ql)}$  of  $a_1^{(g)}$ . This is carried out by substituting  $a_1^{(ql)} = 1 + \delta a_1$  in (4.1) and neglecting the quadratic terms in  $\delta a_1$ . Thus,  $a_1^{(ql)}$  satisfies the following Volterra integral equation

$$a_1^{(ql)}(k) + \int C^s(k, k_1) [a_1^{(ql)}(k_1) + a_1^{(ql)}(k-k_1)] dk_1 = 1 + \int C^s(k, k_1) dk_1 \quad (4.8)$$

It has been found by the same numerical procedure that in the range of Figs. 3 and 4,  $a_1^{(ql)}$  differs from  $a_1^{(g)}$  by less than 0.3% and that the quasi-linearized approximation is extremely accurate in the examples discussed here.

#### 4.2 Discussion

By maintaining the most singular terms in the first approximation of the basic nonlinear integral equation for amplitude function  $a(k)$ , we have been able to derive a generalized solution which is uniform beyond the domain of validity of the regular perturbation expansion for small Froude numbers.

The regular perturbation expansion was seen to be uniform for small  $\epsilon$  and for small  $\epsilon^2 h^2$  or  $\epsilon^3 h^{5/2}$  in the case of cylinder or sphere, respectively. We can replace the radius by the displaced area or volume  $v'$  of the cylinder or sphere respectively. Then, the perturbations expansion is uniform if  $v$  (made dimensionless with the aid of  $U^2/g$  as length scale) is small for the cylinder and if  $v/h^{1/2}$  is small for the sphere.

The generalized solution derived here is assumed to be uniform for small  $\epsilon$ , and for  $v = O(1)$  in the case of the cylinder, i.e. for finite Froude number based on radius. Due

to the weakening of the nonlinear effect in three-dimensions, the generalized solution for the sphere is valid for small  $v$  and for  $v/h^{1/2} = O(1)$ , i.e. for a wider range of  $v$  values.

Examining the behaviour of the generalized drag (Figs. 3,4) shows that it grows approximately exponentially with  $\epsilon^2 h^2$  (2D) or  $\epsilon^3 h^{5/2}$  (3D). Thus, in the case of 2D flow for example we may write

$$\mathcal{D}_1^{(g)} = [a_1^{(g)}(1)]^2 \mathcal{D}_1 - (\epsilon h)^2 \exp(\alpha \epsilon^2 h^2 - 2h) \quad (4.9)$$

where  $\alpha$ , identified from Fig. 3, is approximately equal to 1.1. It is emphasized that for  $h \gg 1$  the drag/buoyancy ratio  $\mathcal{D}_1^{(g)}$  (4.9) still tends to zero since the generalized solution is underlain by the ordering

$$\epsilon^2 h^2 = O(1), \quad \epsilon^2 h = o(1) \quad \text{and} \quad \alpha \epsilon^2 h^2 - 2h = h. \quad (\alpha \epsilon^2 h^2 - 2) \text{ is negative.}$$

It is worthwhile to point out that in a recent work on two-dimensional wave resistance Tulin (1982) has arrived, by a different method, at a similar conclusion. In Tulin's terminology, the wave whose amplitude grows exponentially, as the nonlinear term overtakes the damping effect of the linearized solution, is a "strong wave".

The great accuracy of the quasilinearized solution implies, at least in the cases discussed here, that we could replace Eq. (2.3) by its quasilinearized version

$$\begin{aligned} \frac{\partial^2 \phi}{\partial x^2} + \frac{\partial \phi}{\partial y} - \frac{\partial}{\partial x} \left[ 3 \frac{\partial \phi_1}{\partial x} \frac{\partial \phi}{\partial x} + \frac{\partial \phi_1}{\partial x} \frac{\partial^3 \phi}{\partial x^2} + \right. \\ \left. + \frac{\partial^3 \phi_1}{\partial x^3} \frac{\partial \phi}{\partial x} + \frac{\partial^2 \phi_1}{\partial x^2} \frac{\partial^2 \phi}{\partial x^2} + 2 \frac{\partial \phi_1}{\partial z} \frac{\partial \phi}{\partial z} \right] - \frac{\partial \phi_1}{\partial x} \frac{\partial^2 \phi}{\partial z^2} - \\ - \frac{\partial \phi}{\partial x} \frac{\partial^2 \phi_1}{\partial z^2} = \frac{\partial}{\partial x} \left[ \frac{3}{2} \left( \frac{\partial \phi_1}{\partial x} \right)^2 + \frac{\partial \phi_1}{\partial x} \frac{\partial^3 \phi_1}{\partial x^3} + \right. \\ \left. + \frac{1}{2} \left( \frac{\partial \phi_1}{\partial x} \right)^2 + \left( \frac{\partial \phi_1}{\partial z} \right)^2 \right] - \frac{\partial \phi_1}{\partial x} \frac{\partial^2 \phi_1}{\partial z^2} \quad (4.10) \end{aligned}$$

to achieve essentially the same results. This finding strengthens the belief that at least under the circumstances of the present study, the wave resistance problem is indeed weakly nonlinear.

#### 5. COMPARISON OF GENERALIZED SOLUTION WITH THE "RIGID WALL" APPROXIMATION

The lack of uniformity of the regular perturbation, i.e. of the linearized solution, for small Froude numbers, has been a matter of concern in wave resistance research. A few approximate schemes have been suggested in the past to remedy the situation (see Tulin, 1978, for a complete survey). The first such scheme has been apparently suggest-

ed by Ogilvie (1968) for two-dimensional flows and it has been generalized by Newman (1976) for three-dimensional flows. The basic idea is to split the perturbation velocity potential into a singular potential  $\zeta^{(s)}$  which satisfies the "rigid wall" condition

$$\frac{\partial \zeta^{(s)}}{\partial y} = 0 \quad (y=0) \quad (5.1)$$

and a regular potential  $\zeta^{(r)}$  which has a "wavy" character. By making the assumptions that differentiation of  $\zeta^{(r)}$  increases its order by  $Fr^{-2}$  whereas  $\zeta^{(s)}$  is  $O(1)$  and by subsequent quasilinearization, Newman (1976) arrives at the following free-surface condition, rewritten in our dimensionless variables,

$$\begin{aligned} & (-1 + \frac{\partial \zeta^{(s)}}{\partial x})^2 \frac{\partial^2 \zeta^{(r)}}{\partial x^2} + \frac{\partial \zeta^{(r)}}{\partial y} + 2(-1 + \frac{\partial \zeta^{(s)}}{\partial x}) \\ & \frac{\partial \zeta^{(s)}}{\partial z} \frac{\partial^2 \zeta^{(r)}}{\partial x \partial z} + (\frac{\partial \zeta^{(s)}}{\partial z})^2 \frac{\partial^2 \zeta^{(r)}}{\partial z^2} = \\ & = -(-1 + \frac{\partial \zeta^{(s)}}{\partial x})^2 \frac{\partial^2 \zeta^{(s)}}{\partial x^2} - 2(-1 + \frac{\partial \zeta^{(s)}}{\partial x}) \frac{\partial \zeta^{(s)}}{\partial z} \\ & \frac{\partial \zeta^{(s)}}{\partial z} \frac{\partial^2 \zeta^{(s)}}{\partial x \partial z} - (\frac{\partial \zeta^{(s)}}{\partial z})^2 \frac{\partial^2 \zeta^{(s)}}{\partial z^2} - \eta^{(s)} \frac{\partial^2 \zeta^{(s)}}{\partial y^2} \end{aligned} \quad (5.2)$$

where  $\zeta^{(r)}$  are to be evaluated on  $y=\eta^{(s)}$  and  $\zeta^{(s)}$  on  $y=0$ . The free surface elevation,  $\eta$  is given by

$$\eta^{(s)} = \frac{\partial \zeta^{(s)}}{\partial x} - \frac{1}{2} (\frac{\partial \zeta^{(s)}}{\partial x})^2 - \frac{1}{2} (\frac{\partial \zeta^{(s)}}{\partial z})^2 \quad (5.3)$$

If the dependence on  $z$  is deleted, Ogilvie's (1968) original 2D version of (5.2) is recovered.

This quasilinearized "rigid wall" approximation has been the basis of other related schemes like those forwarded, for example, by Keller (1974) and Inui-Kajitani (1977).

We wish to compare here the wave drag calculated by using the Zakharov-type equation and that based on (5.2) for a submerged cylinder or sphere. Towards this goal we shall carry out an additional Taylor expansion of (5.2) about  $y=0$  and retain only quadratic terms in it, to obtain

$$\begin{aligned} & \frac{\partial^2 \zeta^{(r)}}{\partial x^2} + \frac{\partial \zeta^{(r)}}{\partial y} - 3 \frac{\partial \zeta^{(s)}}{\partial x} \frac{\partial^2 \zeta^{(r)}}{\partial x^2} - \\ & - 2 \frac{\partial \zeta^{(s)}}{\partial z} \frac{\partial^2 \zeta^{(r)}}{\partial x \partial z} + \frac{\partial \zeta^{(s)}}{\partial x} \frac{\partial^3 \zeta^{(r)}}{\partial x^2 \partial y} = \\ & - \frac{\partial \zeta^{(s)}}{\partial x} \frac{\partial^2 \zeta^{(r)}}{\partial z^2} = - \frac{\partial^2 \zeta^{(s)}}{\partial x^2} + 3 \frac{\partial \zeta^{(s)}}{\partial x} \frac{\partial^2 \zeta^{(s)}}{\partial x^2} + \\ & + 2 \frac{\partial \zeta^{(s)}}{\partial z} \frac{\partial^2 \zeta^{(s)}}{\partial x \partial z} + \frac{\partial \zeta^{(s)}}{\partial x} \frac{\partial^2 \zeta^{(s)}}{\partial z^2} \end{aligned} \quad (5.4)$$

This is the version of the "rigid wall" approximation to be compared with the solution of (2.7). It is emphasized that there is a simple relationship between  $\zeta^{(s)}$  (5.1) and  $\phi^{(s)}$  (2.6) and we could as well write from the outset the free-surface condition in terms of  $\zeta^{(s)}$  and  $\zeta^{(r)}$  rather than  $\phi^{(s)}$  and  $\phi^{(r)}$ . The latter decomposition yields, however, a more compact form of the boundary condition. Nevertheless, if  $\phi = \zeta^{(r)} + \zeta^{(s)}$  is substituted in (2.3) the complete free-surface condition, up to quadratic terms, has the following form, written here for simplicity for 2D flow

$$\begin{aligned} & \frac{\partial^2 \zeta^{(r)}}{\partial x^2} + \frac{\partial \zeta^{(r)}}{\partial y} - 3 \frac{\partial \zeta^{(s)}}{\partial x} \frac{\partial^2 \zeta^{(r)}}{\partial x^2} + \\ & + \frac{\partial \zeta^{(s)}}{\partial x} \frac{\partial^3 \zeta^{(r)}}{\partial x^2 \partial y} - 3 \frac{\partial^2 \zeta^{(s)}}{\partial x^2} \frac{\partial \zeta^{(r)}}{\partial x} - \\ & - 3 \frac{\partial \zeta^{(r)}}{\partial x} \frac{\partial^2 \zeta^{(r)}}{\partial x^2} \\ & + \frac{\partial \zeta^{(r)}}{\partial x} \frac{\partial^3 \zeta^{(r)}}{\partial x^2 \partial y} - 2 \frac{\partial \zeta^{(r)}}{\partial y} \frac{\partial^2 \zeta^{(r)}}{\partial x \partial y} \\ & = - \frac{\partial^2 \zeta^{(s)}}{\partial x^2} + 3 \frac{\partial \zeta^{(s)}}{\partial x} \frac{\partial^2 \zeta^{(s)}}{\partial x^2} \end{aligned} \quad (5.5)$$

and it differs from (5.4) by the underlined terms.

If quasilinearization of (5.5) is carried out by neglecting quadratic terms in  $\zeta^{(r)}$  it is seen that the only term neglected in the boundary condition (5.5) based on the Ogilvie-Newman approximation (5.4) is

$-3(\partial \zeta^{(r)} / \partial x)(\partial^2 \zeta^{(s)} / \partial x^2)$ . The latter term has been neglected by them as being of higher order than the remaining ones because  $\zeta^{(r)}$  is differentiated only once in this term.

The solution of  $\zeta^{(r)}$  satisfying (5.4), with  $\zeta^{(s)}$  corresponding to a cylinder or a

sphere, can be obtained easily by the Fourier transform method. Omitting here the details, it can be shown that for the cylinder the most singular term of the amplitude  $a(k)$  satisfies for  $Fr \rightarrow 0$  the following integral equation replacing (4.6)

$$a^{(rw)}(k) + \int_0^k C^{(rw,s)}(k, k_1) a(k_1) dk_1 = 1 + \frac{1}{4} \varepsilon^2 h^2 k^2 \quad (5.6)$$

$$C^{(rw,s)}(k, k_1) = \frac{\varepsilon^2 h^2}{k^2} \frac{(-3+k_1)(k-k_1)k_1^3}{1-k_1} \quad (k > 0).$$

The integral equation (5.6) has been solved numerically and the associated wave drag  $\mathcal{D}^{(rw)}/\mathcal{D}_1$  is represented in Fig. 3 as function of  $(\varepsilon h)^2$ . It is seen that the solution of (5.6) underestimates the generalized solution  $\mathcal{D}_1^{(g)}/\mathcal{D}_1$ , and does not always represent an improvement of the regular perturbation solution, at least in the case of the sphere considered here (see Fig. 4).

If the left-hand side of Eq. (5.6) is supplemented by the missing quasilinearized term  $-3(\partial \zeta^{(r)}/\partial x)(\partial^2 \zeta^{(s)}/\partial x^2)$ , the kernel  $C^{(rw,s)}$  has to be supplemented by the corresponding term  $-3k_1^2(k-k_1)^2/[k^2(1-k_1)]$ . The resulting wave drag which is also represented in Fig. 3 is much closer to the generalized solution, although it is not as accurate as the quasilinearized approximation (4.8).

A similar calculation can be carried out for the sphere, the corresponding integral equation replacing (5.6) is

$$a^{(rw)}(\rho, 0) + \int_0^\rho C^{(rw,s)}(\rho, \rho_1) a^{(rw)}(\rho_1, 0) d\rho_1 = 1 + \frac{9\pi}{256} \frac{\varepsilon^3 h^{5/2}}{\sqrt{2\pi}} \rho^{3/2} \quad (5.7)$$

$$C^{(rw,s)}(\rho, \rho_1) = \frac{\varepsilon^3 h^{5/2}}{\sqrt{2\pi}} \frac{\rho_1^{7/2} (\rho - \rho_1)^{3/2} (-3 + \rho_1)}{\rho^{5/2} (1 - \rho_1)}.$$

The wave drag based on (5.7) and on the quasilinearized version of (5.5), supplemented by the term  $-3(\partial \zeta^{(r)}/\partial x)(\partial^2 \zeta^{(s)}/\partial x^2)$ , are represented in Fig. 4. In this case the "rigid wall" approximation (5.7) grossly underestimates the generalized wave drag, whereas the same equation supplemented by the forementioned term is very close to  $\mathcal{D}_1^{(g)}/\mathcal{D}_1$ .

Concluding, it was shown that the second-order complete free-surface condition (5.5) can be simplified in various ways. The "rigid wall" approximation which is derived from the equations by Ogilvie (1968) and Newman (1976) is a quasilinearized version of

(5.2) in which all underlined terms of (5.5) are neglected. This approximation is shown to underestimate the nonlinear wave drag derived from the generalized solution of (5.5) in the particular cases of a cylinder or a sphere. In contrast, quasilinearization of (5.5) in which only terms quadratic in  $\zeta$  are neglected, yields results close to the generalized solution. It is seen, therefore, that the neglected term  $-3(\partial \zeta^{(r)}/\partial x)(\partial^2 \zeta^{(s)}/\partial x^2)$  plays an important role in generation of nonlinear wave drag. The argument employed in order to discard this term, namely that the regular potential has a "wavy" character and differentiation increases its order, cannot be defended in a rigorous manner. As a matter of fact we have shown that the nonlinear interaction of the local terms is responsible for wave generation at small Froude number and those terms do not change their order by differentiation. It is pointed out that the above neglected term is kept in the quasilinearized free surface condition if the rigid wall velocity  $-1 + (\partial \zeta^{(s)}/\partial x)$  in the first term of the right-hand side of (5.2) is supplemented by  $\partial \zeta^{(r)}/\partial x$  and similarly by supplementing  $\eta^{(s)}$  (5.3) in the last term by  $\partial \zeta^{(r)}/\partial x$ . Hence, our suggested version of the "rigid wall", approximation replacing (5.2) and (5.3) is

$$\begin{aligned} [U^{(rw)}]^2 \frac{\partial^2 \zeta^{(r)}}{\partial x^2} + \frac{\partial \zeta^{(r)}}{\partial y} + 2 U^{(rw)} W^{(w)} \frac{\partial^2 \zeta^{(r)}}{\partial x \partial z} \\ + [W^{(rw)}]^2 \frac{\partial^2 \zeta^{(r)}}{\partial z^2} + \frac{\partial^2 \zeta^{(s)}}{\partial y^2} \frac{\partial \zeta^{(r)}}{\partial x} \\ + \eta^{(s)} \frac{\partial^2 \zeta^{(r)}}{\partial y^2} = -2 U^{(rw)} W^{(rw)} \frac{\partial^2 \zeta^{(s)}}{\partial x \partial z} \\ - [W^{(rw)}]^2 \frac{\partial^2 \zeta^{(s)}}{\partial z^2} - [U^{(rw)}]^2 \frac{\partial^2 \zeta^{(s)}}{\partial x^2} - \\ - U^{(rw)} \frac{\partial^2 \zeta^{(s)}}{\partial y^2} \end{aligned} \quad (5.8)$$

$$\eta^{(s)} = \frac{\partial \zeta^{(s)}}{\partial x} + \frac{\partial \zeta^{(r)}}{\partial x} \quad (5.9)$$

where  $U^{(rw)} = -1 + (\partial \zeta^{(s)}/\partial x)$ ,

$W^{(rw)} = \partial \zeta^{(s)}/\partial z$ .

Finally, the closest result to the generalized drag, is obtained by a complete quasilinearization of (2.5).

## 6. CONCLUSIONS AND OUTLINE OF FUTURE INVESTIGATIONS

In the present study we have demonstrated in two particular cases (cylinder, sphere), that the origin of the nonuniformity of the regular perturbation expansion of the velocity potential at small Froude number can be elucidated by employing the Zakharov-type version of the free-surface condition. On the same basis we have derived a generalized solution of the nonlinear wave problem by retaining the

most singular nonlinear term of the Zakharov-type integral equation in its first-order approximation. The generalized solution is valid in an extended range of Froude numbers as compared with the regular perturbation solution, and the latter grossly underestimates the wave drag.

It was encouraging to find out that a systematic quasilinearization of the free-surface condition yields results very close to the generalized solution. The quasilinearized "rigid wall" version suggested in the literature is shown to underestimate the wave drag as compared to the generalized solution and the additional terms which have to be retained in the "rigid wall" approximation are singled out.

Encouraged by these first results achieved by the use of the Zakharov-type representation of the nonlinear wave problem we plan to investigate in the future the case of three-dimensional ship-like bodies, the influence of nonlinear third-order terms and the problem of nonlinear free-surface effects in ship motion in waves.

#### REFERENCES

- Bessho M. (1957), "On the Wave Resistance Theory of a Submerged Body", Society of Naval Architects, Japan, 60th Anniv. Series, Vol. 2.
- Havelock, T.H. (1919), "Wave Resistance: Some Cases of Three-Dimensional Fluid", Roy. Soc. Proc. Ser. A. Vol. 95.
- Havelock, T.H. (1926), "The Method of Images in Some Problems of Surface Waves", Proc. Roy. Soc. A. Vol. 115.
- Inui, T. and Kajitani H. (1977), "A Study on Local Nonlinear Free Surface Effects in Ship Waves and Waves Resistance", 25th Anniv. Coll. Inst. fur Schiffbau, Hamburg.
- Keller, J.B., (1974), "Wave Patterns of Non-Thin or Full-Bodied Ships", Tenth. Symp. on Naval Hydrodynamics, Cambridge.
- Kim, W.D. (1969), "Nonlinear Free-Surface Effects on a Submerged Sphere", J. of Hydrodynamics, Vol. 30, No. 1.
- Newman, J.N. (1976), "Linearized Wave Resistance Theory", Proc. of the International Seminar on Wave Resistance", Tokyo.
- Ogilvie, T.F. (1968), "Wave Resistance: The Low Speed Limit", Report No. 002, Department of Naval Architecture and Marine Engineering, University of Michigan.
- Tuck, E.O. (1965), "The Effect of Non-Linearity at the Free-Surface on Flow past a Submerged Cylinder", J. Fluid Mechanics, Vol. 22, Pt. 2.
- Tulin, M.P. (1978), "Ship Wave Resistance - a Survey", Proc. 8th U.S. National Congress App. Mechanics, UCLA, Los Angeles.
- Tulin, M.P. (1982), "An Exact Theory of Gravity Wave Generation by Moving Bodies, its Approximation and its Implications", Proc. 14th Symp. on Naval Hydrodynamics, Ann Arbor, Michigan.
- Wehausen, J.V. and Laitone, E.V., (1960), "Surface Waves", Encyclopaedia of Physics, Vol. 9 (ed. S. Flugge), Springer.
- Yuen, H.C., & Lake, B.M. (1982), "Nonlinear Dynamics of Deep-Water Gravity Waves", Advances in App. Mechanics, Vol. 22.
- Zakharov, V.E., (1968), "Stability of Periodic Waves of Finite Amplitude on a Surface of a Deep Fluid", J. App. Mech. Tech. Phys. (English Translation), Vol. 9.

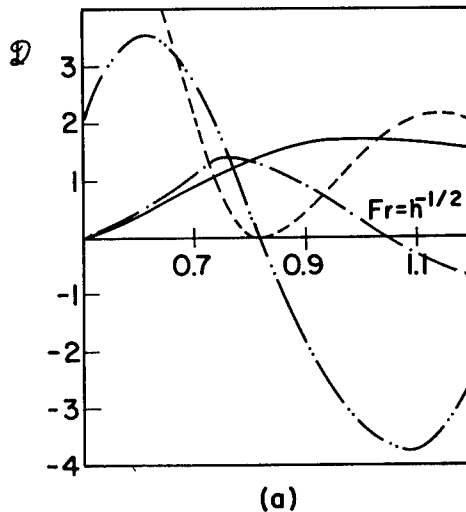


Figure 1:(a) The wave drag components based on the second order regular perturbation for the two-dimensional cylinder:

$$\begin{aligned} \text{---} & D_1/\epsilon^2 \text{ Eq. (3.4);} \\ \text{---} & D_{21}^{(fs)}/\epsilon^4 \text{ Eq. (3.8);} \\ \text{---} & D_{22}^{(fs)}/\epsilon^6 \text{ Eq. (3.8);} \\ \text{---} & D_2^{(b)}/\epsilon^4 \text{ Eq. (3.9).} \end{aligned}$$

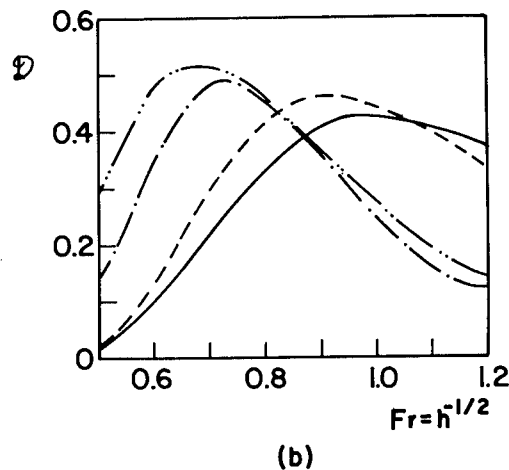


Figure 1:(b) A comparison between the linearized and the second-order wave resistance of a submerged cylinder for  $\epsilon = 0.5$ ;

$$\begin{aligned} \text{---} & D_1; \text{---} D_1 + D_2^{(b)}; \\ \text{---} & D_1 + D_2^{(b)} + D_{21}^{(fs)}; \\ \text{---} & D_1 + D_2^{(b)} + D_{21}^{(fs)} + D_{22}^{(fs)}. \end{aligned}$$

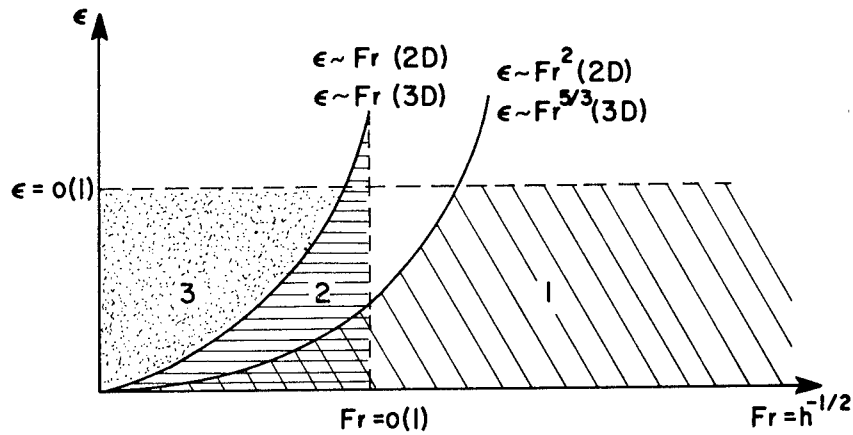


Figure 2 - Schematic representation of domains of uniformity of various nonlinear approximations for small Froude numbers: (1) regular perturbation  $\epsilon = o(1)$ ;  $\epsilon^2/Fr^4 = o(1)$  (2D) and  $\epsilon^3/Fr^5 = o(1)$  (3D), (2) generalized solution  $\epsilon = o(1)$ ,  $Fr = o(1)$ ,  $\epsilon/Fr = o(1)$  and (3)  $\epsilon = o(1)$ , arbitrary Froude number.

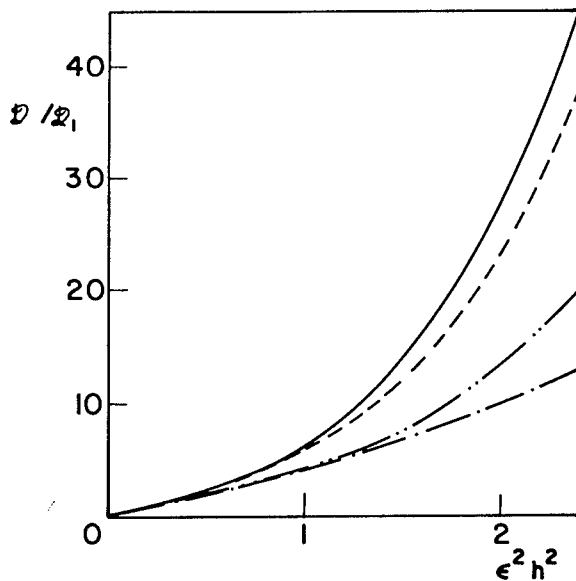


Figure 3 - The ratio between various wave drag nonlinear expressions and the first order wave drag for a two-dimensional flow past submerged cylinder at small Froude number; — second order regular perturbation expansion Eq. (3.7); — Nonlinear generalized solution Eq. (4.6); — Rigid wall solution Eq. (5.6); — Modified rigid wall solution.

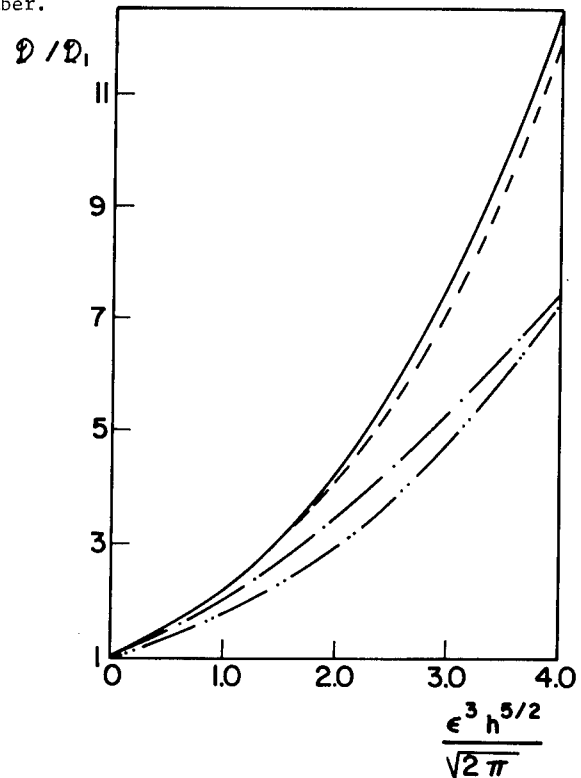


Figure 4 - The ratio between various wave drag nonlinear expressions and the first order wave drag for a three-dimensional flow past submerged sphere at small Froude number; — second order regular perturbation Eq. (3.21); — Nonlinear generalized solution Eq. (4.7); — Rigid wall approximation Eq. (5.7); — Modified rigid wall approximation.

## DISCUSSION

Dipl.-Ing. GERHARD JENSEN,  
Institut für Schiffbau,  
Hamburg, FR Germany:

Trying to follow your interesting method for solving the second order wave resistance problem, I had trouble to understand your basic equation (2.3) for the second order potential. This equation looks quite different from the formula given by Maruo (1) and others for the consistent second order potential. It only reminds me of the equation given in your ONR-paper in Paris (2).

A comparison gives:

Present paper:

$$\phi_{xx} + \phi_y = \frac{\partial}{\partial x} \left( \frac{3}{2} \phi_x^2 + \phi_x \phi_{xxx} + \frac{1}{2} \phi_{xx}^2 + \phi_z^2 \right) = \delta_D$$

From Maruo or Wehausen and Laitone (3) eq. (10.12) one gets:

$$\phi_{xx} + \phi_y = \frac{\partial}{\partial x} (\phi_x^2 + \phi_y^2 + \phi_z^2) - \phi_x \frac{\partial}{\partial y} (\phi_{xx} + \phi_y) = \delta_M$$

The difference between the two right hand sides should vanish, if they are equivalent; or at least be small of third order.

But:

$$\begin{aligned} \delta_D - \delta_M &= \frac{\partial}{\partial x} \left( \frac{1}{2} \phi_x^2 - \phi_y^2 + \phi_x \phi_{xxx} + \frac{1}{2} \phi_{xx}^2 \right) + \phi_x \frac{\partial}{\partial y} (\phi_{xx} + \phi_y) \\ &= \phi_x (\phi_{xx} + \phi_{yy}) + \frac{1}{2} \frac{\partial}{\partial x} (\phi_{xx}^2 - \phi_y^2) + (\phi_{xx} \phi_{xxx} - \phi_y \phi_{yx}) + \\ &\quad (\phi_x \phi_{xxy} + \phi_x \phi_{xxx}) \end{aligned}$$

With the first order free surface condition  $\phi_{xx} = -\phi_y$  (which holds up to second order), and its derivatives with respect to x, one may show that the last three brackets are in fact small of third and higher order. But the remaining first term  $\phi_x (\phi_{xx} + \phi_{yy})$  is only small of second order since the 2-D Laplace equation no longer holds in the 3-D case.

Therefore I need some explanation for this second order difference between your formula and the conventional one.

References:

- (1) Maruo H.: A Note on Higher-Order Theory of Thin Ships, Bulletin of the Faculty of Engineering, Yokohama National University, Vol. 15, March 1966.
- (2) Dagan G.: Nonlinear Ship Wave Theory, Ninth Symposium on Naval Hydrodynamics, Paris, 1972.
- (3) Wehausen J.V. and Laitone E.V.: Surface Waves, in Flüge S.: Handbuch der Physik, Springer Verlag 1960.

Prof. KLAUS EGGERS,  
Institut für Schiffbau,  
Hamburg, FR Germany:

I would like to amplify on Mr. Jensen's discussion. I sympathize with the authors' keen new approach to higher order wave resistance via a multiple convolution series in the Fourier domain, though I think that a consistently truncated

regular expansion as evaluated in section 3 should not differ from the conventional second order approach, provided that  $\phi(s)$  is a consistent first order term. Hence your method is really pioneering only in section 2 where you advocate solving an integral equation (rather than iterative increase of order), as here you take account of some terms of more than second order in spite of truncating the convolution series before the twofold convolution term.

It is here that Mr. Jensen's discussion certainly goes deeper than just pointing at the omission of a leading second order term. Due to the above inconsistency, the alternate expressions he compares lead to different results even after correction. He deserves respect for clarifying this from the formidable analysis at hand! Let me say that I feel by no means orthodox with regard to rules of consistency. Prof. Tuck may recall an exclamation of mine "I hate that word consistency!" when he rightly tried to convince me about some invariance of second order wave resistance as questioned in my 6th ONR paper some 20 years ago. But meanwhile I have learned my lesson!

Still, I am aware of situations where even serious mathematicians may legally take profit from inconsistent procedures in order to eliminate local infinities occurring in a regular approach. But always if you sacrifice consistency, i.e. if you do not discard all contributions of more than second order in our case, you will trade in ambiguity i.e. non-uniqueness. You thus have to invent selective principles for retaining certain, discarding other terms. Even though formally "of higher order", such terms represent numbers with no upper bound prediction at hand in a practical case.

Save omission of all more than simple convolution terms, your selective principle seems to be the elimination of any derivative in the vertical direction at the expense of obtaining rather high derivatives in the lengthwise horizontal direction. I fear that this may seriously affect the convergence of the Fourier integrals considered (though their free-wave part is not changed) in the case of floating ships, where not all integrand terms will display exponential decay.

Still worse, you will be confronted with an ambiguity of defining  $\phi(s)$  inside the volume displaced by the ship, and I wonder if you can find an inner potential with so weakly singular vertical flow induced in the water plane area that a corresponding Fourier integral representation i.e. the r.h.s. of your integral equation exists?

Thus I fear that the promising avenues you envisage may turn out as rather bumpy roads- if not dead ends- and I admire your courage of really intending to embark upon such adventure! Bon voyage!

## AUTHORS' REPLY

We are very grateful to Mr. Jensen for his readiness to check carefully our paper and to point out to us the omission of the term

$$\phi_x (\phi_{xx} + \phi_{yy}) = -\phi_x \phi_{zz} \text{ in Eq. (2.3). It is rather}$$

fortunate that this omission did not affect at all the solution of the two-dimensional problem since this term is identically zero in this case. Furthermore, the same expression does not appear in the leading term of the small Froude number approximation of the three-dimensional solution either.

We have taken advantage of the kindness of the organizers and we have corrected the final version of the paper, which is published herein. Once again we would like to thank Mr. Jensen for his discussion.

Most of the discussion of Prof. Eggers revolves around the missing term analyzed above. Since we have corrected this omission, we shall not dwell in a detailed reply to this part of the discussion. After the correction, our regular perturbation expansion is consistent and complete to second-order.

As for the last part of the comments by Prof. Eggers, we thank him for pointing out to us a few difficulties which may be expected in the extension of our approach to the ship problem. We shall keep in mind his observations, which are based on his rich experience in this field. Nevertheless, as a citizen of his great Hanseatic City, Prof. Eggers is aware of the fact that some audacity is needed by those who chart unknown seas by new approaches. His final wish is, therefore, quite appropriate and most welcome!



# EFFECT OF BOW SHAPE ON FREE-SURFACE SHEAR FLOW

KATSUYOSHI TAKEKUMA AND KLAUS EGGERS

## ABSTRACT

Assuming a priori the existence of free-surface shear flow in front of blunt ship bows, investigations are made on the relationship between the major bow form parameters such as draught, entrance angle and protruding bulb, and the production of the secondary vortices (necklace vortex) around the bow. The analysis showed that the bow forms with fine entrance angle and the protruding bulb are effective in reducing the secondary vortices around the bow. In parallel with these analytical studies, experimental observations were made by means of flow visualization. As a result of image processing of observed data, a qualitative agreement with the analytical studies is obtained.

## 1. INTRODUCTION

Ship wave resistance may roughly be defined as a resistance component connected with the free surface disturbance around the ship's hull apparent through the wave profile along the water line, a domain of wave breaking both around bow and stern, and a wave pattern trailing in the rear. It was realized hardly more than two decades ago that wave breaking in particular may contribute a major part to the total resistance in case of full ship forms. Accordingly, efforts have been made for a deeper understanding of this phenomenon with the aim of improving design methods both for better prediction and reduction of this resistance component. In this paper, we have compiled experimental findings related to this complex physical phenomenon which according to our own observations seems to be intrinsically interrelated with the occurrence of some kind of shear flow and the generation of transverse vortices ahead of the ship's bow, finally deforming to necklace vortices around the bow. It has been suggested by Baba (1981) that there might be a partial analogy of this process with the generation of a horseshoe vortex (i.e. of "secondary vorticity") around a vertical strut piercing a flat plate through distortion of the boundary (-shear-) layer along this plate. We have evaluated an approach by Hawthorne (1954) for the

generation of such secondary vorticity and its distribution around the strut in order to obtain a qualitative model for the relative strength of this disturbance as a possible measure of wave breaking intensity of such struts in the presence of a free surface under uniform flow. In particular, the influence of certain ship form parameters such as draft, bow entrance angle, location of a protruding bulb and waterline shape was considered. Such numerical results were qualitatively compared with corresponding experimental observations. In the last part of this paper, we report on an attempt to measure the velocity components on and beneath the free surface around the bow by some image processing technique, i.e. by particle tracing. It should be mentioned that within our limited work we could not treat the questions connected with modeling. The effect of Froude and Reynolds number on our experiments (quite apart from surface tension, contamination and of stationarity) can not be dealt with.

## 2. REVIEW OF INVESTIGATIONS ON FREE SURFACE SHEAR FLOW

During model tests as well as full scale trials, marked surface disturbance can be observed around bows as shown in Fig.1. On the way of the study on separation of ship resistance components, Baba (1969) could provide quantitative evidence of a resistance component due to wave breaking around the bow through measuring loss of head by wake survey methods; he could even trace this loss on the way from the bow where it is generated to the wake area (Fig.2). For full hull forms, this contributes a significant portion of the total resistance, and attempts have been made to decrease it by ship form improvement. Investigations into hydrodynamic mechanism of the wave breaking around bow have been made by many researchers. Those investigations can be classified into the following three areas.

- (1) Pioneering early experimental studies by means of wake survey and resistance tests on the effect of ship form parameters, by protruding bulb in particular, by Taneda

K. Takekuma, Nagasaki Experimental Tank, Mitsubishi Heavy Industries, Post Box 14 Nagasaki, Japan.  
K. Eggers, Institut für Schiffbau, Lämmersiekh 90, D-2000 Hamburg 60, FR Germany

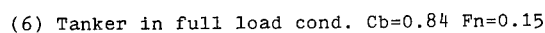
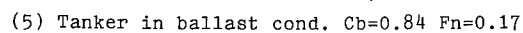
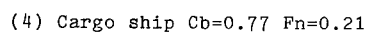
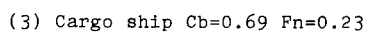
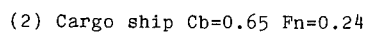
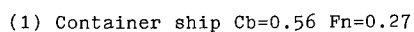


Fig.1 Wave patterns around bow of typical conventional ships

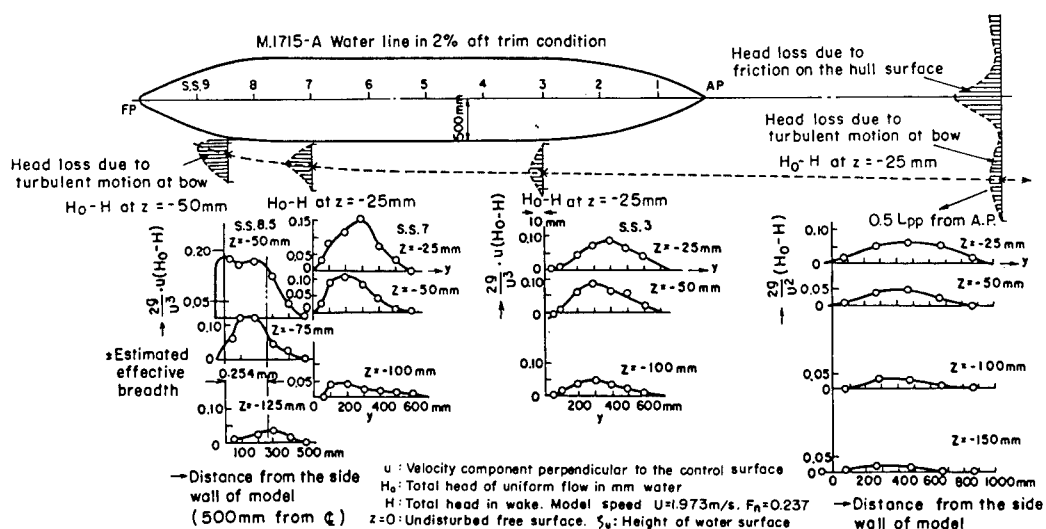


Fig.2 Separation of ship's resistance components (Wake survey)

- (1969), Eckert and Sharma (1970), and Taniguchi et al. (1972).
- (2) Analytical studies on mathematical flow models for the flow around a bow and the associated free surface deformation by Dagan and Tulin (1969), Baba and Takekuma (1975), Inui (1981), Eggers (1981), Maruo and Fukazawa (1981), and Mori (1983).
- (3) Numerical studies in solving the full inviscid flow boundary value problem (i.e. without smallness assumptions for flow components) either for potential flow (Gadd (1976) Rankine source method), (Chan & Chan (1980)), or with models including rotational flow (Miyata (1983)).

After the above primary experimental investigation, mainly performed in his institution, the first author (1972), aiming to provide material for constructing a rational mathematical model to describe this phenomenon as a useful tool for ship design, conducted a series of flow measurements around the bow of a full ship model by use of five-hole pitot tubes. Comparing the results with those calculated by potential theory, it was found that:

- (1) except a thin layer beneath the free surface, velocity components obtained by

the measurement coincide well with those obtained by numerical calculation based on the assumption of double model flow, and

- (2) in this thin layer, velocity components change abruptly in the vertical direction (Fig.3).

These observations suggested the importance of detailed studies on this phenomenon inside the thin layer near the free surface.

More recently, the flow beneath the free surface around some ship models and semisubmerged circular cylinders was visualized by use of metal flakes and water color dye (Kayo et al. 1981, 1982, 1983). A shear layer beneath the free surface corresponding to the abrupt change of velocity profile was visualized as illustrated in Fig.4 and Fig.5. It was observed that the intensity of the shear layer and vortices increased with advance speed. In particular, an artificial increase of the shear layer caused wave breaking already at a much lower speed than without such manipulation as illustrated in Fig.6. Neither the analytical investigations nor the purely numerical ones mentioned under (2) and (3) resulted into models for the shear flow and vortex generation observed.

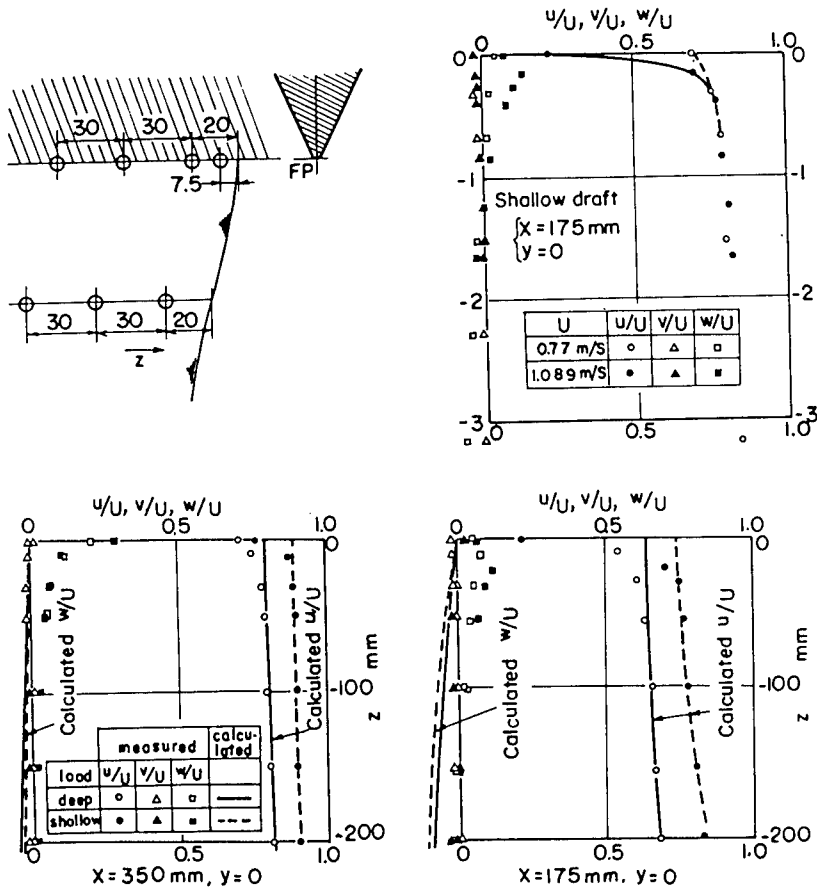


Fig.3 Velocity profile around bow obtained by flow measurement and numerical calculation



$U = 0.05 \text{ m/s}$

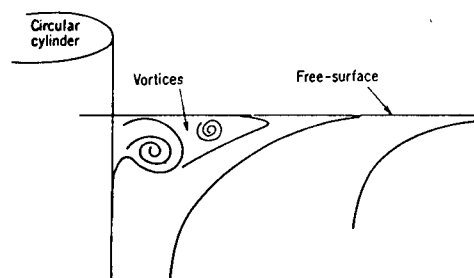
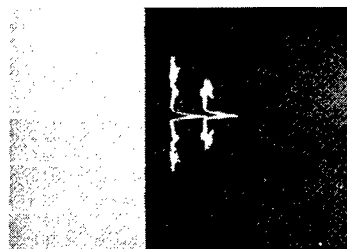
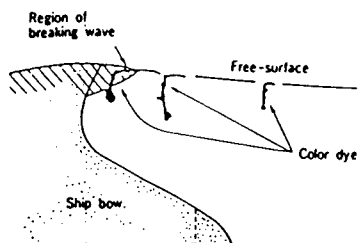


Fig.4 Shear flow and vortices observed by flow visualization



$U = 0.05 \text{ m/s}$



$U = 1.00 \text{ m/s}$

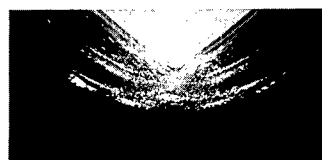


$U = 0.05 \text{ m/s}$

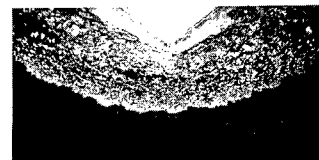
Fig.5 Shear flow and vortices observed by flow visualization



$U = 0.700 \text{ m/s}$   
 $Fn = 0.091$   
without vinyl sheet



$U = 1.089 \text{ m/s}$   
 $Fn = 0.142$   
without vinyl sheet



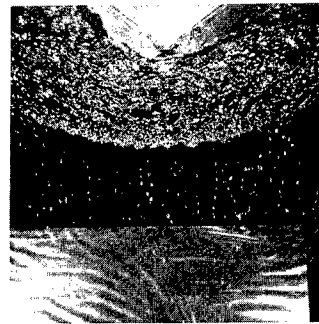
$U = 1.284 \text{ m/s}$   
 $Fn = 0.168$   
without vinyl sheet



$U = 0.700 \text{ m/s}$   
 $Fn = 0.091$   
with vinyl sheet

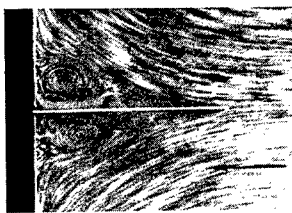


$U = 1.089 \text{ m/s}$   
 $Fn = 0.142$   
with vinyl sheet

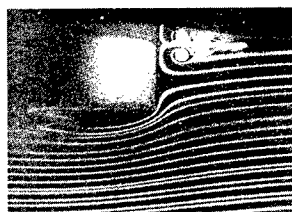


$U = 1.284 \text{ m/s}$   
 $Fn = 0.168$   
with vinyl sheet

Fig.6 Effect of an artificial increase of shear layer



Retarded stagnation flow with separation



Horseshoe vortex

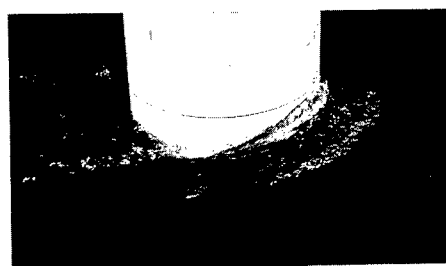
Fig.7 Examples of similar flow patterns

### 3. EFFECT OF BOW SHAPE ON THE FREE SURFACE SHEAR FLOW

In the course of ship form design, it is imperative to make efforts to decrease wave breaking resistance for improvement of propulsive performance. Thus, an attempt was made for explanation of the effect of some typical ship form parameters on the free surface phenomena around bow by the secondary flow theory. It has been recognized that some ship form parameters have remarkable effect on the wave breaking phenomena around bow and accordingly wave breaking resistance. They are fore draft, entrance angle, underwater protruding bulb and waterline curvature around the shoulder part. To start with, the effect of these parameters on the behaviour of a free surface shear layer and on the vorticity distribution was examined. Both flow visualization techniques and calculations of the secondary flow theory as explained in more detail in Appendix A were applied to help to understand the mechanism. In this section, results of the examinations are described together with the knowledge obtained in the previous investigations.

#### 3.1. Effect of Draft

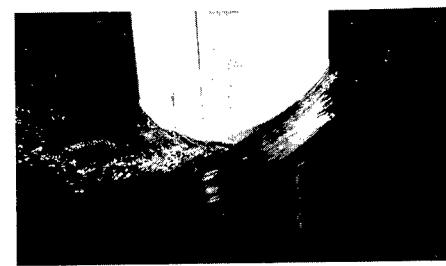
It is well known that the wave breaking phenomena forward of the bow of a full ship are stronger in ballast condition (shallow draft) than in full load condition (deep draft), while those around shoulder parts are more significant in full load condition (deep draft) than in ballast condition (shallow draft). In this section, an attempt was made to examine the effect of draft on breaking bow waves by using a vertical circular cylinder as a simple model of full ships. Calculations of the relative secondary vorticity  $\xi = \epsilon / \frac{dU}{dz}$  and  $\eta = \eta / \frac{dU}{dz}$  were performed along certain streamlines around a vertical circular cylinder taking the double body potential flow as the basic one.  $U$  is the far upstream velocity in horizontal direction;  $\frac{dU}{dz}$ , meant to be its variation in downward direction due to shear,



$d = 1/8 \cdot D$   $U = 1.0$  m/s



$d = 1/4 \cdot D$   $U = 1.0$  m/s



$d = 1/2 \cdot D$   $U = 1.0$  m/s

Fig.8 Effect of draft on wave breaking around bow of a circular cylinder (moving from left to right)

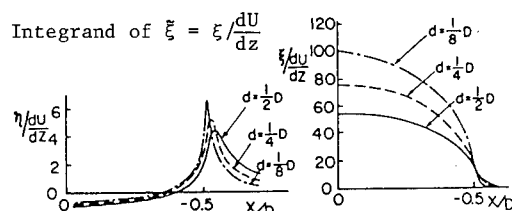
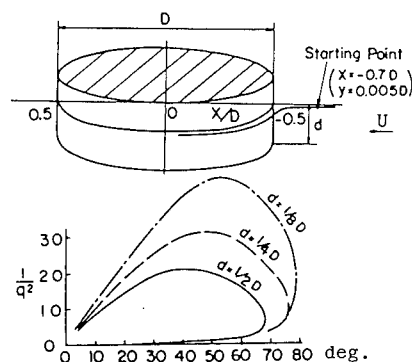
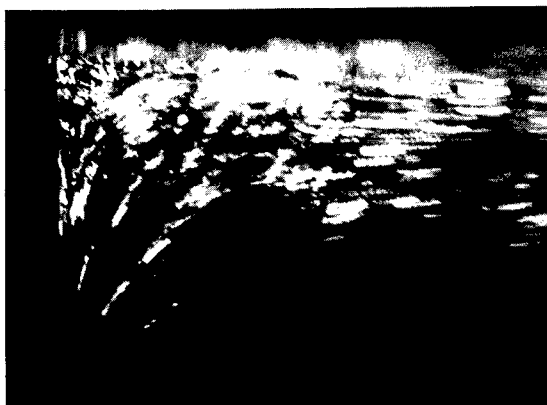


Fig.9 Effect of fore draft on  $\xi$  and  $\eta$  around a full ship bow and a vertical cylinder



$$d = 1/2 \cdot D \quad U = 0.60 \text{ m/s}$$



$$d = 1/8 \cdot D \quad U = 0.60 \text{ m/s}$$

Fig.10 Effect of draft on behaviour of free surface shear layer and vortical motion in it

need not be specified within our quantitative approach. Here  $\xi$  stands for the secondary vorticity component along the streamline of the basic flow whereas the vorticity component of intensity  $\eta$  is oriented horizontally in normal direction to such line. The results shows that:

- (1) around the vertical circular cylinder,  $\xi$  and  $\eta$  are higher in shallow draft than in deep draft,
- (2) almost the same tendency as above is found in the relative secondary vorticity around the bow of full ships, but
- (3) no substantial difference in relative secondary vorticity can be observed around shoulder parts as resulting from the effect of change in draft.

A visualization of the flow beneath the free surface forward of bow of a circular cylinder shows that intensity of the vortical motion is higher in shallow draft than in deep draft (Fig.10). Thus, it can be said that tendency of wave breaking and shear flow, experimentally observed forward of the bow, coincides with

that of magnitude of  $\xi$  and  $\eta$  calculated by the secondary flow theory. However, on the phenomena around the shoulder parts, the secondary flow theory provides little information, in spite of the significant feature of the phenomena observed there.

### 3.2. Effect of Underwater Protruding Bulb

Around 1969, it was realized how resistance of full ship in ballast condition can be decreased by fitting bulbous bow. The decrease of resistance was shown to be caused by decrease of wave breaking phenomena around bow by fitting bulb as illustrated in Fig.11. In the present study, investigation was extended to effect of underwater protruding bulb on the shear flow and vortical motion beneath the free surface by flow visualization and calculation of amplification factor of perturbation vorticity on the basis of the secondary flow theory as follows. Flow beneath the free surface around a vertical circular cylinder with and without underwater protruding bulb was visualized as illustrated in Fig.12 and Fig.13. It is found that the vortical motion beneath the free surface has been eliminated and flow pattern has been remarkably improved by fitting an underwater protruding bulb. The amplification factor of perturbation vorticity  $\xi$  and  $\eta$  around the vertical cylinder with and without bulb was calculated by the secondary flow theory as illustrated in Fig.14. As a result, magnitude of  $\xi$  and  $\eta$  was found to decrease largely by the protrusion to the cylinder.

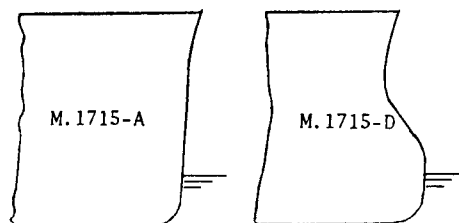
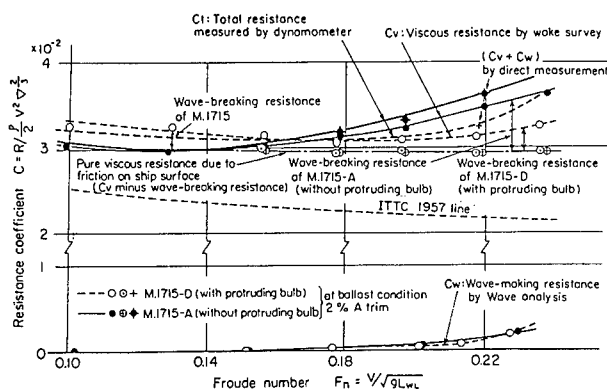
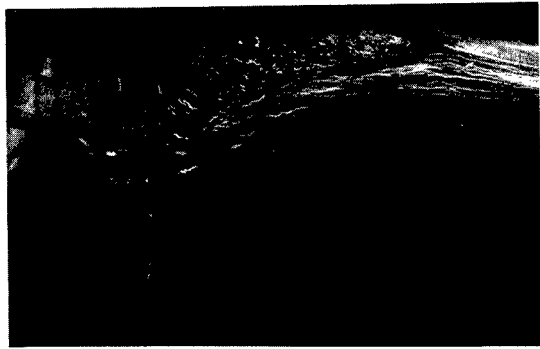


Fig.11 Effect of protruding bulb on decrease of wave breaking resistance.

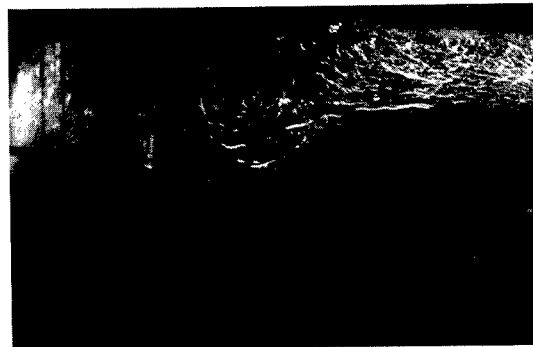


without bulb  $U = 0.80$  m/s



with bulb  $U = 0.80$  m/s

Fig.12 Flow beneath the free surface around a circular cylinder with and without underwater protruding bulb (1)



without bulb  $U = 1.00$  m/s



with bulb  $U = 1.00$  m/s

Fig.13 Flow beneath the free surface around a circular cylinder with and without underwater protruding bulb (2)

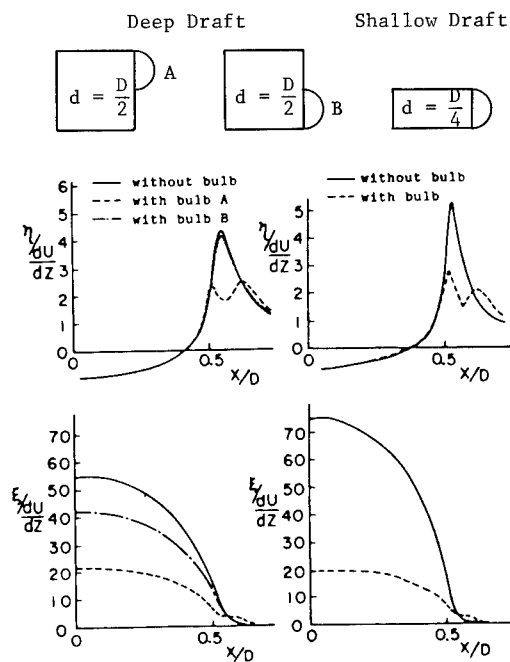


Fig.14 Effect of underwater protruding bulb on perturbation vorticity around a vertical cylinder calculated by the secondary flow theory

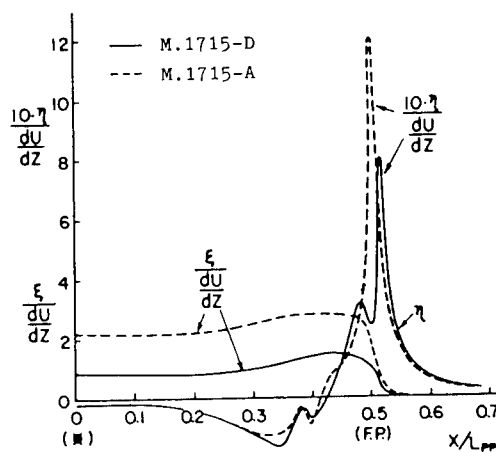


Fig.15 Effect of protruding bulb on perturbation vorticity around bow of a full ship

Further, almost the same tendency as above is also shown in magnitude of  $\xi$  and  $\eta$  calculated around bow of the full ship as shown in Fig.15. Accordingly, it is said that flow beneath the free surface around bow of full ships is much improved by fitting an underwater protruding bulb and the secondary flow theory provides helpful information in the design of bulbous bow.

### 3.3. Effect of Entrance Angle of the Bow

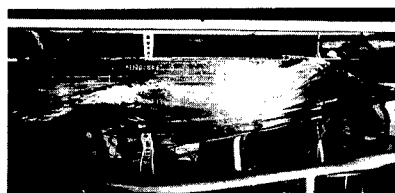
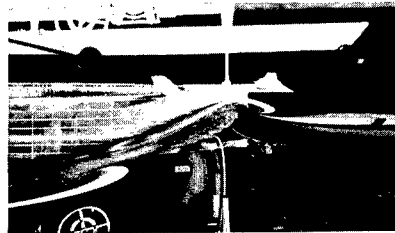
The bow entrance angle also has a significant effect on the flow characteristics. Observation and measurement of wave pattern made on a series of mathematical models with systematically varied entrance angle of bow show that the entrance angle strongly influences the flow geometry as illustrated in Fig.16. For a closer study, the flow around a vertical circular cylinder and a cylinder with wedge front

part examined by flow visualization and the relative secondary vorticity components were calculated along certain streamlines. The results are shown in Fig.17 and Fig.18. The intensity of the observed shear flow and vortical motion beneath the free surface increases with entrance angle of the bow; this tendency is confirmed by the calculations of the secondary vorticity intensity.

Further, the calculation of the perturbation vorticity around bows with systematically varied entrance angle was made as illustrated in Fig.19. Result shows a tendency corresponding to the behaviour of wave pattern observed around the bows (Fig.16). Wave breaking phenomena around bow with relatively small entrance angle such as that of cargo ships are found to be characterized by the wave breaking lines diverging afterward of bow with increase advance speed (Fig.20). But such change in



Entrance angle 25°



Entrance angle 30°

Fig.16 Wave pattern around a series of mathematical models with systematically varied entrance angle of bow

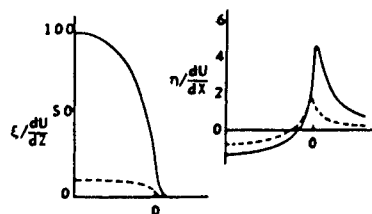
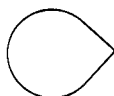
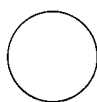


Fig.17 Free surface shear flow and vortical motion forward of a vertical cylinder with and without wedge front part ( $d = D/4$ )

Fig.18 Perturbation vorticity around a vertical cylinder and a biconvex section calculated by the secondary flow theory



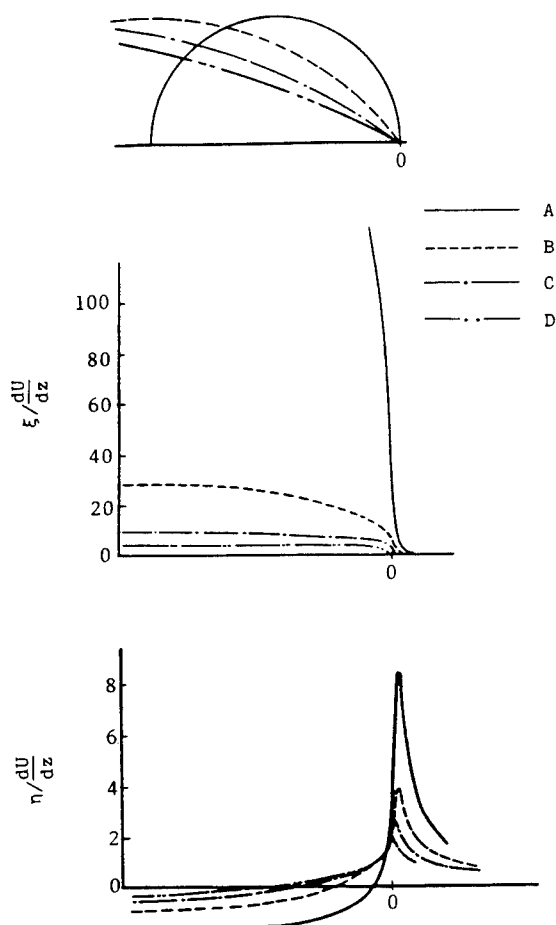


Fig.19 Calculated perturbation vorticity for a series of struts with different entrance angles

flow geometry with advance speed cannot be taken care of by our numerical approach. Further studies are needed to make clear the marked effect of the advance speed on the wave breaking around bow.

### 3.4. Effect of Waterline Shape

It is known that waterline shape has also influence on the wave breaking around bow. This effect is characterized by wave breaking around the shoulder parts. Amplification factor of perturbation vorticity  $\xi$  and  $\eta$  calculated by the secondary flow theory seems to indicate some information on this phenomenon (Fig.21). However, it should be noted that difference of  $\xi$  and  $\eta$  calculated on both water line shapes is not so significant as that of intensity of the free surface phenomena observed around the shoulder parts. It may be assumed that the influence of shoulder curva-

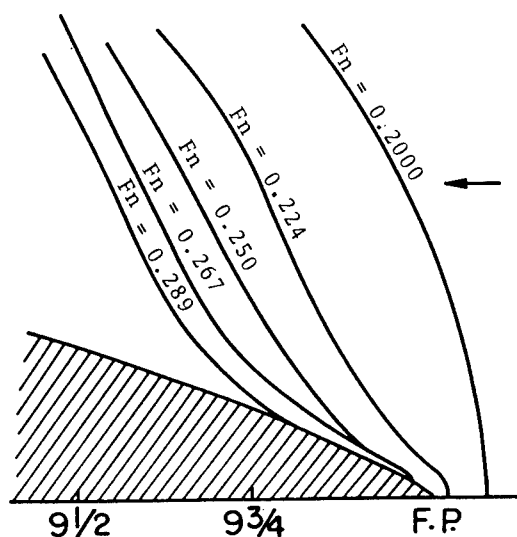


Fig.20 Wave breaking lines around a ship bow with small entrance angle



Model A



Model B

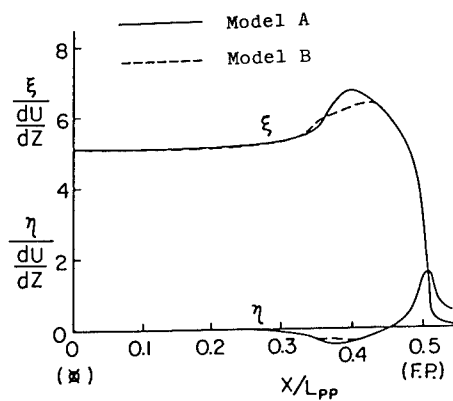


Fig.21 Perturbation vorticity around bow with different water line shape

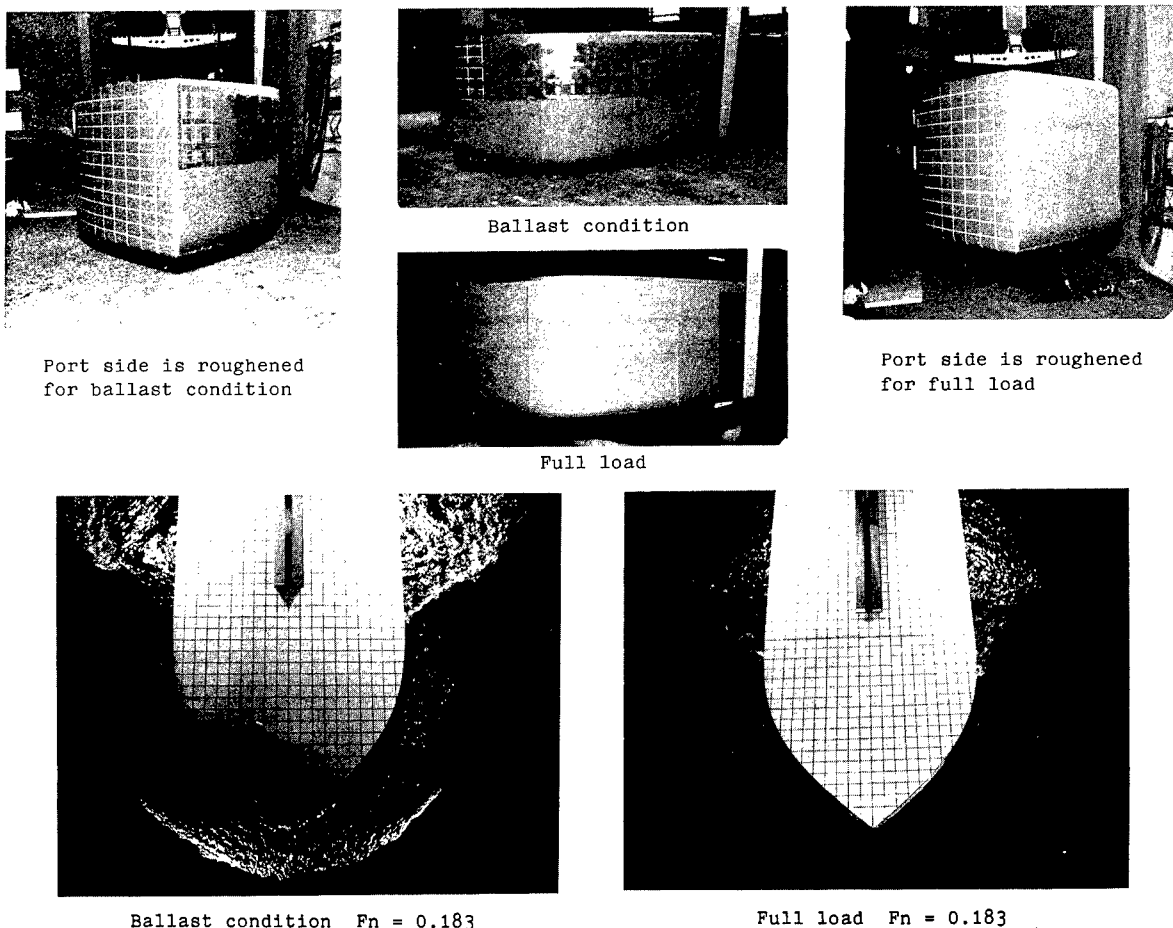


Fig.22 Effect of roughening surface on wave breaking around bow

ture on wave breaking is rather associated with the difference in viscous boundary layer configuration, since Baba (1981) could show that an artificial roughening of the ship surface may drastically change the free surface phenomena around the shoulder part as shown in Fig.22.

As the results of investigations above, it is concluded that;

- (1) the free surface shear flow and vortices in it are closely related to the wave breaking around the bow,
- (2) major parameters of ship form, namely, fore draft, underwater protruding bulb, entrance angle of bow and waterline shape influence largely the free surface shear flow and vortices in it, and
- (3) the secondary flow theory is considered to provide some guidance in the course of ship form design on the basis of understanding of the hydrodynamic mechanism of the free surface shear flow and vortices in it.

#### 4. QUANTITATIVE MEASUREMENT OF FLOW AROUND A SEMI-SUBMERGED CIRCULAR CYLINDER

As described in the previous sections, the character of the free surface phenomena around bow of full ships was made clear to some extent. The next step to be taken will be quantitative measurement of flow beneath the free surface. Thus, an attempt was made to measure the flow around a semi-submerged vertical circular cylinder with and without an underwater protruding bulb. On the basis of the results obtained, property of flow beneath the free surface, namely, velocity components, perturbation vorticity etc. was quantitatively examined.

##### 4.1. Flow Measurement by Image Processing of the Visualized Flow

Since the free surface phenomena are sensitive to instationary effect beneath the free surface, flow measurement should be made without causing any disturbance in flow such as by Laser Doppler Velocimeter. In our preliminary study, an alternative approach was made by application of an image processing technique to video recorded or photographed flow pattern

obtained by flow visualization. They were quantified by tracing particles and plotting at a certain interval as illustrated in Fig.23 (left). The velocity components along stream line close to the center line of the flow field were obtained by measuring the distances the particles moved in that interval as shown in Fig.24 (left).

#### 4.2. Effect of Underwater Protruding Bulb

The chief interest was concentrated on the determination of the free surface configuration, the flow components and the vorticity to be calculated therefrom by differentiation.

The flow field forward of the vertical cylinder with protruding bulb was analyzed by the same procedure as above and illustrated in Fig.23 and Fig.24 (right). It is found that the longitudinal velocity component increases largely beneath the free surface and vortical motion is mostly eliminated, while there may be recognized a small sized vortical motion near the junction of protruding bulb and the circular cylinder as shown in Fig.25.

Thus, it can be concluded that the underwater protruding bulb influences largely the increase of velocity components beneath the free surface and this effect provides improvement of flow and decrease of wave breaking around the bow of full ships.

#### 4.3. Vortex Intensity

Quantitative measurement of flow beneath the free surface around the vertical circular cylinder is expected to provide helpful materials for better understanding of the hydrodynamic mechanism of the free surface phenomena around bow of ships. For this, information should be obtained on velocity components, and horizontal thickness and extent of shear flow and its intensity.

For example, velocity profile at some locations forward of the vertical cylinder and magnitude of circulation which indicates intensity of vortical motion beneath the free surface were analyzed on the basis of the results of flow measurement around the vertical cylinder with and without an underwater protruding bulb (Fig.25). Results show some decrease of the change of the velocity profile and hence of the magnitude of circulation due to vortical motion beneath the free surface by fitting an underwater protruding bulb.

However, the results obtained so far both at IfS in Hamburg and at MHI in Nagasaki cannot be considered conclusive yet, some discrepancies between results from different methods have to be resolved. A research project with the aim of measuring velocity components under use of Laser Doppler Velocimeter was initiated at IfS. Further investigations are necessary for the quantitative evaluation of the free surface disturbance around bows with the aim of providing material for a more rational mathematical model.

## 5. CONCLUSION

For better understanding of the hydrodynamic mechanism of the free surface phenomena around bow of ships, investigations were made into behaviour of the shear flow and vortices induced in the upstream of the bow. In the study, calculation of vorticity on the basis of the secondary flow theory, flow visualization and flow measurement by means of image processing technique on the video records were conducted for evaluation of the effect of the major ship form parameters, such as draft, entrance angle of bow, underwater protruding bulb and waterline shape on the shear flow and vortices in it. The results are summarized as follows.

- (1) The free surface shear flow and vortices in it are closely related to wave breaking around bow.
- (2) Of the major parameters of ship form, fore draft, underwater protruding bulb, entrance angle of bow and waterline shape influence largely the free surface shear flow and vortices in it.
- (3) Underwater protruding bulb gives acceleration of velocity components beneath the free surface and this effect provides improvement of flow, such as remarkable decrease of vortical motion, and decrease of wave breaking around bow of full ships.
- (4) The secondary flow theory is considered to be a useful guidance for explanation of the hydrodynamic mechanism of the free surface shear flow and vortices in it and seems to provide some helpful suggestions on bow shape in the course of design of full ship form.
- (5) Measurement of flow beneath the free surface around a vertical cylinder by image processing of video records gave materials for quantitative evaluation of the free surface shear flow and vortical motion in it. However, the results obtained are still inconclusive.

Free surface phenomena around bow of full ships are characterized by the free surface shear flow, vortices in it and wave breaking phenomena. The hydrodynamic mechanism of these phenomena has been clarified to some extent by investigations made up to the present, but there still remain various aspects to be studied further. Of primary importance is considered to be better understanding of the hydrodynamic mechanism.

## 6. ACKNOWLEDGEMENT

The authors express sincere gratitude to Dr. S.D. Sharma and Dr. J. Kux, Institut für Schiffbau der Universität Hamburg, Dr. E. Baba and Dr. Y. Kayo, Nagasaki Experimental Tank, MHI for their helpful suggestions and discussions. Thanks are due to Mr. K. Tamura, Deputy manager of Nagasaki Technical Institute for his encouragement. Special thanks to the staff of both institutes for their cooperation.

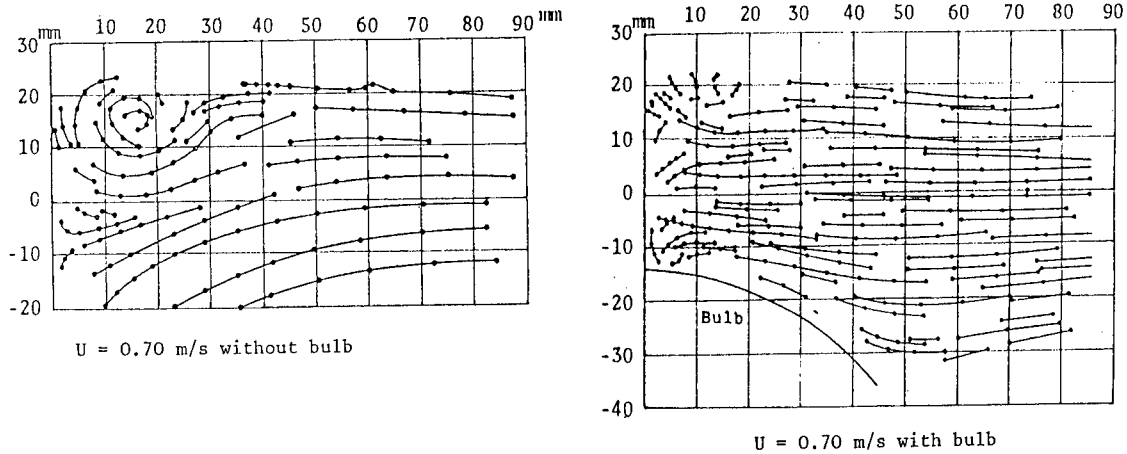


Fig. 23 Flow patterns obtained by tracing particles (Interval : 1/25 s)

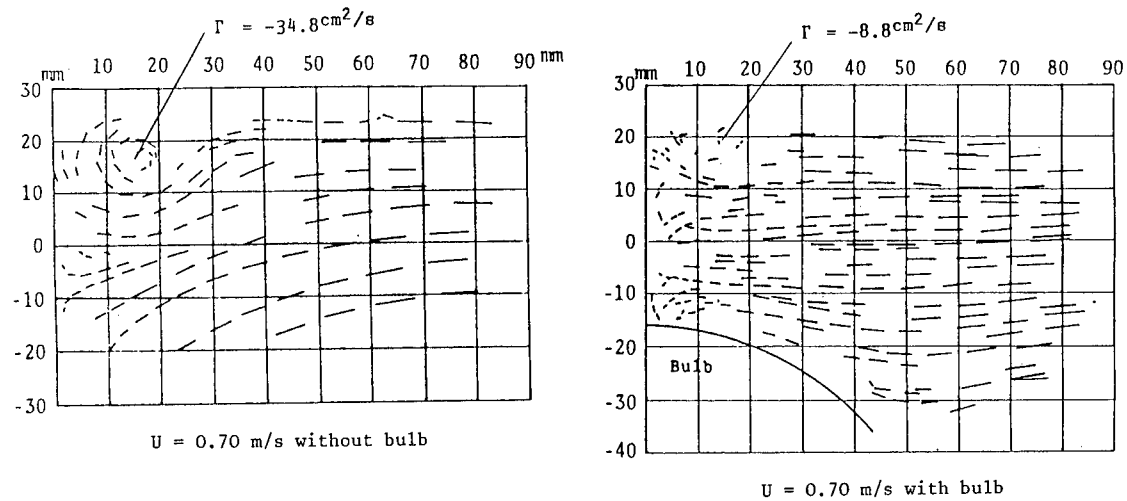


Fig. 24 Velocity vector obtained by image processing

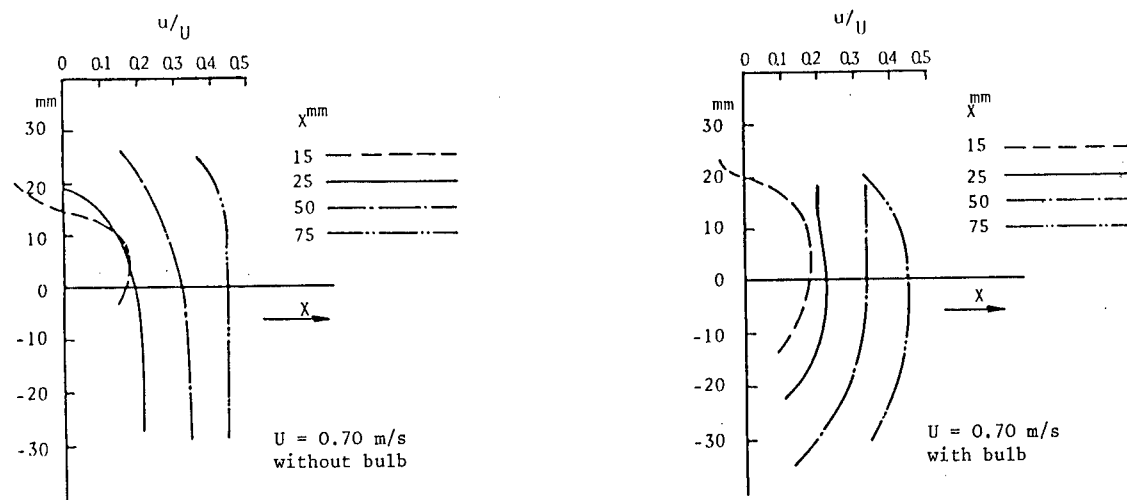


Fig. 25 Variation of horizontal velocity  $u/U$  in the vertical direction

# APPENDIX A SUMMARY OF HAWTHORNE'S THEORY

Hawthorne studied the flow around a strut placed in the approach velocity varying in the depthwise direction (Fig.26). As described in the previous sections, the flow around a blunt bow with forward free surface shear is considered to belong to this type of flow.

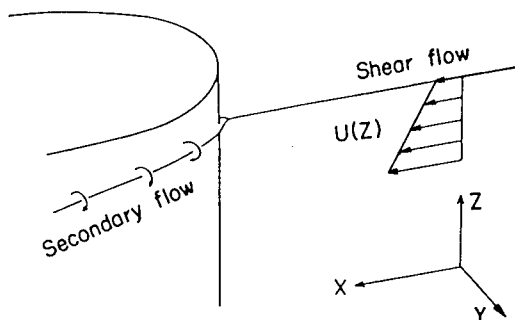


Fig.26 Coordinate system and shear layer encountering surface-piercing body

The disturbance induced by the strut or bow of ship may be understood as due to the variation in stagnation pressure at the leading edge, which causes an upward velocity and thus horseshoe vortex. For analytical expression of such a flow field, Hawthorne supposed that the flow can be expressed as a sum of the two-dimensional flow with varying approaching velocity and the three-dimensional disturbance, namely, according to the notation shown in Fig.26, the velocity field is approximated by

$$U(z) \cdot \vec{V}(x, y) + \vec{v}(x, y, z) \quad (A.1)$$

$$\xi(x, y, z) = 2q \frac{dU}{dz} \frac{d\theta}{q^2} \quad (A.2)$$

$$\eta(x, y, z) = \frac{1 - q^2}{q} \frac{dU}{dz} \quad (A.3)$$

$$\zeta(x, y, z) = 0 \quad (A.4)$$

where  $\xi$ ,  $\eta$ ,  $\zeta$  are the perturbation vorticity components in the direction of the streamline  $\vec{V}(x, y)$ , normal to it in the horizontal plane and upwards;  $q$  is  $|\vec{V}|$  as mentioned above and  $\theta$  is the angle of this streamline against the x-axis. One should observe that  $\theta$  will increase along the streamline along which it has to be integrated from zero far ahead to a maximum aside of the bow and then decrease to zero again. Hence the integrands for the  $\xi$  integrals as displayed in Fig.9 are multivalued and  $\xi$  is related to the area enclosed by these curves. Whereas far ahead of the bow we have  $q = 1$ ,  $\theta = 0$  (i.e. parallel flow),  $q$  must vanish at the stagnation point, leading to infinite values of  $\eta$  there and a divergent integral for  $\xi$  along the bow waterline. Hawthorne excluded this domain when formulating his theory. By choosing streamlines passing the stagnation point closely enough, we may obtain secondary

vorticity of whatever magnitude. Thus the absolute value of the secondary vorticity is not representative for the magnitude of the global disturbance created. Hence for evaluating the merits of different bow geometries, the comparison was based on relative secondary vorticity components  $\tilde{\xi} = \xi \frac{dU}{dz}$  and  $\tilde{\eta} = \eta \frac{dU}{dz}$  along two stream lines with the same origin far ahead of the different bows.

## APPENDIX B RELATION BETWEEN SURFACE CURVATURE AND SHEAR FLOW AT A FREE SURFACE

Hawthorne's theory was derived for the case of a uniform linear vertical shear profile, with the shear layer along a horizontal plane wall of unlimited extent ahead of the bow. In such case, there is no need to impose a dynamical boundary condition along this wall.

A shear layer generated by a ship bow can have only finite extent; moreover, the dynamic boundary condition on the free surface can not be disregarded. Hence there is the need for an improved analysis.

Consider a point  $P_0$  at a stationary free surface  $S_f$  and local cartesian x-y-z coordinate system adjusted to this point such that the z-axis is directed normal to  $S_f$  in the coordinate origin  $P_0$  and the x-axis coincides with the direction of the flow in  $P_0$  which then must be tangential to  $S_f$ . Let  $S_f$  be described by  $z = Z(x, y)$  in the vicinity of  $P_0$  (such that  $Z(0, 0)$  then is zero) and let  $u, v, w$  stand for the velocity components in x-, y-, and z-direction (thus we have  $v = w = 0$  in  $P_0$ ). Then the requirement that there should be no viscous force component acting across  $S_f$  in  $P_0$  can only be satisfied under the three conditions.

$$u_z + w_x = 0, v_z + w_y = 0, w_z = 0 \quad (B.1)$$

in  $P_0$ . If we even had  $v_y = 0$  at  $P_0$  (i.e. if the flow were essentially two-dimensional there), the continuity equation would require  $u_x = 0$ , that means that the flow variation with  $x, y$  and  $z$  would be purely rotational like that of a fluid mass under angular velocity  $\omega = (u_z - w_x)/2 = u_z = -w_x = \eta/2$ , where  $\eta$  is the vorticity component along the y-axis which is the axis of rotation. Hence under dynamic equilibrium at  $S_f$  there can not be shear in the z-direction only.

The kinematic boundary condition on  $S_f$  may be expressed as

$$G(x, y, z) = 0 \quad (B.2)$$

with

$$G(x, y, z) = (u\delta/\delta x + v\delta/\delta y + w\delta/\delta z)(z - Z(x, y)) \quad (B.3)$$

Observing that through our conventions we have  $Z = Z_x = Z_y = 0$  and  $v = w = 0$  in  $P_0$ , through differentiation along a line  $y = \text{const}$  on  $S_f$  we obtain

$$\frac{dG}{dx} = G_x + G_z \cdot Z_x = w_x - u \cdot Z_{xx} \quad \text{at } P_0 \quad (B.4)$$

i.e.  $\eta/2 = -w_x = -u \cdot Z_{xx} = -uk$ , where  $k$  is the curvature of  $S_f$  at  $P_0$  in a cut with the x-z

plane (As  $Z_x$  is zero at  $P_0$ ,  $Z_{xx}$  equals  $k!$ ) Batchelor (1970) proved this relation using tools of differential geometry, i.e. with a general curvilinear coordinate system adjusted to  $S_f$  and the flow direction within this surface. Note that the only assumption needed is stationarity of the flow and the free surface in an appropriate system of reference. Note that there is no influence of any viscosity coefficient on this relation, though positive viscosity (however small) is assumed. One may observe that the sense of vorticity corresponds to that of orbital motion in case of an infinitesimal irrotational wave progressing with speed  $u$  in the crest, opposite sense in the trough.

According to above analysis, no stationary free surface shear flow can exist where the free surface does not display curvature. Expressed otherwise: On a plane free surface the vertical derivatives of all flow components must be zero. Thus Hawthorne's secondary flow model is not appropriate for quantitative predictions, apart from being unable to take account of the influence of advance speed on flow geometry. The above more refined conditions are taken care of in a recent study by Prosperetti (1982) together with a genuine influence of gravity, though for time dependent flow only so far.

#### REFERENCES

- Baba, E., A New Component of Viscous Resistance of Ships, *Journal of the Society of Naval Architects of Japan*, Vol.125 (1969), pp.23-34.
- Baba, E. and Takekuma, K., A Study on Free Surface Flow around Bow of Slowly Moving Full Forms, *Journal of the Society of Naval Architects of Japan*, Vol.137 (1975).
- Baba, E., Some Free Surface Phenomena around Ships to be Challenged by Numerical Analysis, *Third International Conference on Numerical Ship Hydrodynamics*, Paris (1981).
- Batchelor, G.K., *Introduction to Fluid Dynamics*, Cambridge Univ. Press (1970).
- Chan, R.K.-C. and Chan, F.W.-K., Numerical Solution of Transient and Steady Free Surface Flows about a Ship of General Hull Shape, *Proc. 13th Symp. Naval Hydrodynamics*, Tokyo (1980), 257-280.
- Dagan, G. and Tulin, M.P., Bow waves before blunt ships, *Hydrodynamics, Inc., Technical Report 117-14* (1969).
- Eckert, E. and Sharma, S.D., Bugwülste für langsame, völlige Schiffe, *Jahrb. Schiffbau-tech. Ges.* 64 (1970), pp.129-171.
- Eggers, K., Non-Kelvin Dispersive Waves around Non-Slender Ships, *Schiffstechnik* Vol.28 (1981), 223-250.
- Gadd, G.E., A method of computing the flow and surface wave pattern around full form. *Trans. Roy. Inst. Naval Arch.* 188 (1976). 207-219.
- Hawthorne, W.R., Secondary Flow about Struts and Airfoils, *J. Aeronautical Soc.*, Vol.21, (1954), 588-608.
- Inui, T., From Bulbous Bow to Free Surface Shock Wave-Trends of 20 Years' Research on Ship Waves at the Tokyo University Tank, *J. Ship Res.* 25 (1981), 147-180.
- Kayo, Y. and Takekuma, K., On the Free Surface Shear Flow Related Bow Wave-Breaking of Full Ship Models, *Journal of the Society of Naval Architects of Japan*, Vol.149 (1981), 11-20.
- Kayo, Y., Takekuma, K., Eggers, K. and Sharma, S.D., Observation of Free Surface Shear Flow and its Relation to Bow Wave-Breaking on Full Forms, *Inst. Schiffbau, Univ. Hamburg, Rept.* 420 (1982).
- Kayo, Y. and Takekuma, K., Shear Layer and Secondary Vortical Flow Beneath Free Surface around Bow of Full-Form Ship Model, *Trans. West Japan Soc. Nav. Arch.*, No.65, (1983), 17-25.
- Maruo, H. and Fukazawa, M., On the Free Surface Flow around a Two-Dimensional Body Fixed in a Uniform Stream, *Proceedings of the 29th Japan National Congress for Applied Mechanics*, 1979, University Tokyo Press (1981).
- Maruo, H., On the breaking of waves at the bow, *Symposium on New Developments of Naval Architecture and Ocean Engineering*, Shanghai (1983).
- Miyata, H. et al., Numerical and Experimental Analysis of Nonlinear Bow and Stern Waves of a Two-Dimensional Body, *J. Soc. Nav. Arch. Japan*, Vol.154, 1983.
- Mori, K., A. Calculation of Wave Resistance and Sinkage by Rankine-Source Method, B. Prediction of 2-D Near Wake Flow by Making Use of Time Dependent Vorticity Transport Equation, C. Free Surface Boundary Layer and Necklace Vortex Formation, *IIHR Report No.262*, (1983).
- Prosperetti, A. et al., Small-Amplitude Waves Produced by a Submerged Vorticity Distribution on the Free Surface of a Viscous Liquid, *Phys. of Fluids* 25(12), Dec. (1982), pp.2188-2192.
- Takekuma, K., Study on the non-linear free surface problem around bow. *J. Soc. Naval Arch. Japan*, Vol.132 (1972), 1-9.
- Taneda, S. and Amamoto, H., On the necklace vortex, *Bulletin of Res. Inst. Appl. Mech.*, Kyushu Univ., No.31, Japanese, (1969).
- Taniguchi, K., Tamura, K. and Baba, E., Reduction of Wave-Breaking Resistance 'MHI-Bow', *Mitsubishi Juko Giho* Vol.8, No.1, (1971), pp.146-152, Japanese, or *Mitsubishi Technical Review*, Vol.9, No.1, (1972), pp.62-69, English.

## DISCUSSION

Prof. HIDEAKI MIYATA,  
The University of Tokyo,  
Tokyo, Japan:

This discussion is also partly addressed to the paper by Prof. K. Mori (Session V).

These experimental works seem to be very useful for a sound understanding of the nonlinear flow mechanism around a ship. However, despite the fact that these works have been continued by increasing number of researchers, the most important aspects of the mechanism seem to me still left vague. It may be because they have not investigated into the nonlinear wave making and breaking mechanism. The characteristics of nonlinear waves are most substantial for the understanding of wave breaking, which is a dissipative process of nonlinear waves. The systematic variation of wave geometry that Mr. Takekuma and Prof. Eggers showed is one of the important characteristics of nonlinear waves in the nearfield of a ship, which I called free-surface shock wave. Breaking phenomena are natural consequences of the generation of steep unstable waves in the water wave problems.

It must be noted that there are many types of wave breaking, spilling and plunging breakers and others depending on the circumstances. Prof. Mori seems to concentrate his attention on rather gentle spilling breakers. However, other types of breaker also have potential to occur, such as plunging breaker with air entrainment at a higher Froude number.

It is clear that wave breaking is a natural result of steep wave generation. However, it is not clear how wave breaking and vortex generation are related. The variety of vortex generation seems to confuse the discussion. Prof. Mori points out the role of viscosity on the free-surface that produces a shear layer.

Can this shear layer develop to a scale significant to bow wave motion without the presence of wave breaking phenomenon? Can it be still important at the Reynolds number of a full-scale ship? Takekuma and Eggers do not show how the shear layer is generated.

To the discussor's knowledge at least two types of significant vortex generation can take place in the vicinity of a bow. One type is generated by wave breaking at the wave front. It is not difficult to understand that overturning or spilling motions generate vortical motion. The other is generated by the interaction of a stagnant flow with a shear flow in the vicinity of a stagnant point. The former was called necklace vortex by Taneda and the latter horseshoe vortex. The generation is quite different between the two.

A result of numerical simulation by the TUMMAC-Vot method based on Navier-Stokes equations is cited here to show some aspects of vortex generation in front of an advancing 2D floating body in deep water. The rectangular body is advancing to the left at the Froude number based on draft 1.25. The bow wave moves forward with the breaking wave front. The overturning motion generates vortical flows and the successive occurrence of breaking produces a vortical layer with steep velocity gradient near the free-surface. And then, a vortical motion near the floating body develops. The role of the vortical layer or shear layer, which is a consequence of wave breaking, in this horseshoe vortex generation may be acceptable. In the experiment of flow visualization the gentler vortex, namely the horseshoe vortex, can be easily observed, whereas the necklace vortex is very hard to be visualized, because the fluid motion is very violent with intense turbulence on the free-surface and sometimes with air entrainment. This kind of numerical simulation that shows averaged motions is sometimes more useful than experiment for clear understanding of complicated fluid motions.

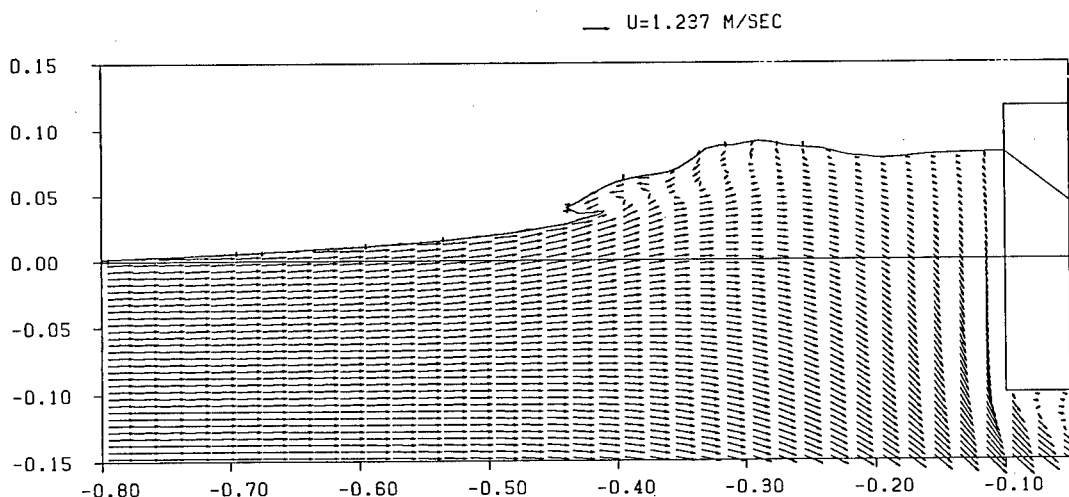


Fig. 1 Velocity vector field in front of an advancing floating body at  $T = 2.004$  sec.

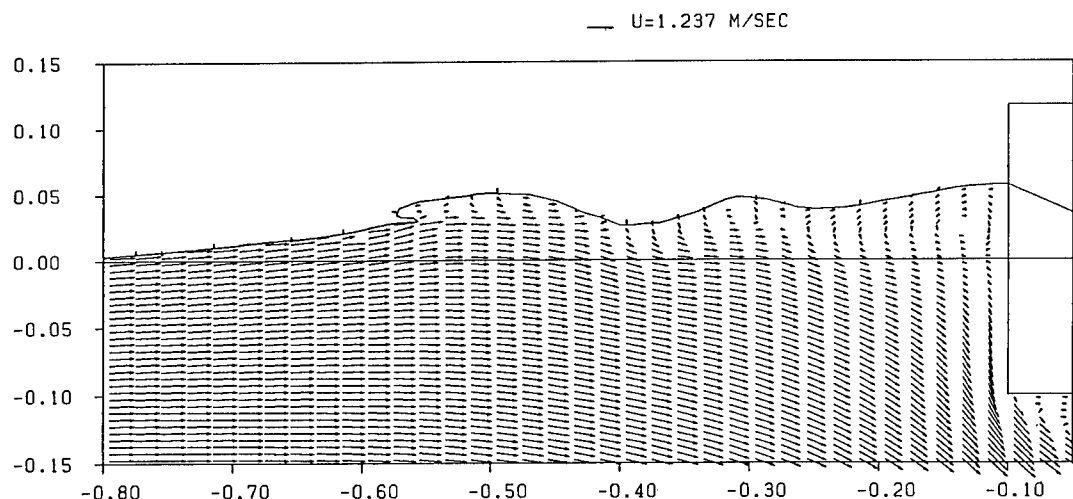


Fig. 2 same as Fig. 1, at  $T = 2.586$  sec.

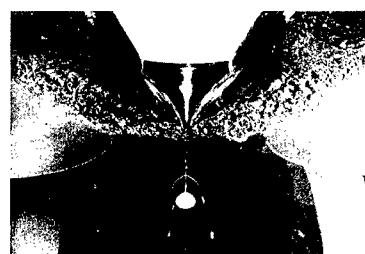
Prof. KAZU-HIRO MORI,  
Hiroshima University,  
Higashi-Hiroshima, Japan:

In the present paper waves shown in Fig. 1(3) and in Fig. 6 are called "wave breaking" altogether. I think they are different not only in their phenomena but in their mechanism; the former is a plunging type breaking coupled with an overturning of the bow necklace vortex, while the latter is a turbulent free-surface flow. I am afraid it may cause an unnecessary confusion to call both by the same term. In my paper the latter is called "sub-breaking waves" in distinction from the former. The breaking lines shown in Fig. 2 are also misleading in this sense. The phenomena are suspected to be different between those at  $Fn=0.200$  and at other speeds.

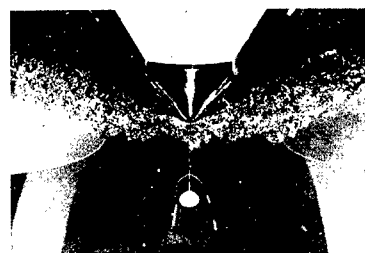
Does "vortices in the free-surface shear layer" mean the "necklace vortex" mentioned in the abstract? If so, it had better be called necklace vortex simply.

The effectiveness of a protruding bulb on the bow sub-breaking and breaking waves is confirmed through our experiments also.\* Fig. A1 shows bow wave profiles of a highspeed fishing boat. It is seen the bow wave breakings are strikingly reduced by a large protruding bulb. It is measured that the velocity is accelerated by the bulb as pointed out by the authors.

\* Tamashima, M., Nishimoto, H., Ogura, M. and Mori, K.: Experimental Studies on Bow-Flow of Full High-Speed Ships under Calm Condition, Trans. of The West-Japan Soc. of Naval Arch., No. 68, 1984.



$Fn = 0.26$



$Fn = 0.28$



$Fn = 0.26$



$Fn = 0.28$

Fig. A1



Dr.-Ing. ALFRED M. KRACHT,  
Berlin Model Basin (VWS),  
Berlin, Germany:

The interference effect of the bulbous bow is well known but it is not sufficient to explain the resistance reduction on slow full ships where the wave making resistance is negligibly small but the wave breaking resistance is a substantial part of total resistance. In the paper presented here the authors give an additional plausible physical interpretation of the wave breaking phenomenon, which depends not only on the steepness of the waves but also on the free surface shear flow.

The detailed statements of the authors provide an interpretation for the fact that a bulb is not always advantageous. In the case of good hull forms on which the hull's perturbation vorticity is lower than that of the bulb the latter is unfavourable. Therefore, in optimizing ship and bulb the interactions of both, the waves and the perturbation vorticities have to be taken into account. Both contributions to the total resistance depend on the ship's speed and block coefficient in a different way.

The influence of most of the main hull parameters on resistance is known to naval architects but in this paper the physical reasons of the influences are given, e.g. the influence of the waterline entrance angle.

From the paper it is not quite clear what the purpose of the surface roughening was and in what way wave breaking is changed. In model tests the surfaces have to be smooth except for the small turbulence stimulating area.

Another question concerns the relationship of the present work to that of Mr. Kazu-Hiro Mori presented in Session V.

Prof. Dr.-Ing. CLAUD PETER THOMSEN,  
Fachhochschule Hamburg,  
Hamburg, FR Germany:

On the vortex flow component at the bow and hull I should like to support our views by some photos. They were taken last year in way of flow experimentation of some new type.

Applied was an erodable material of poly-wax. Under the action of water flow the material is washed off the body leaving the body in continuously changing new relative forms. The starting form had been box shaped  $60 \times 15 \times 15$  cm at 3 cm freeboard. Froude number was 0.21. The body was towed over a total distance of 3000 metres through the tank of Hamburg Ship Model Basin HSVA. I show you three forms as photographed intermittently.

Fig. 1: The flow feature of interest is the strong vortex engirdling the body in the free surface. Its trace is carved into the material at constant depth and cross-section along hull's constant middle part. The bow shape has the strong action of the vortex in it- and so has the transom.

Fig. 2: All forms take on more distinct profiles. The longer one has the flow oper-

ating on the deformable body. Look at the bulb that developed here. Look at the stern. The vortex has sawed into it deeply and in characteristic form.

Fig. 3: There are more features of vortex flow to look at. However, the photos I could reproduce here are too poor in quality. So I better restrict myself now.

Thank you.

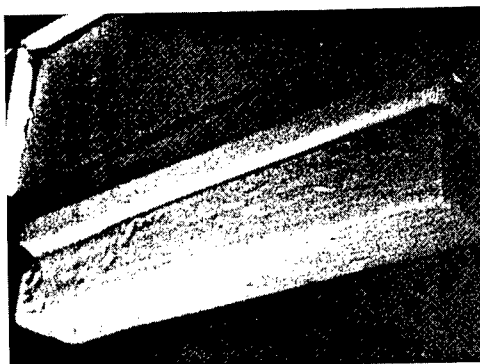


Fig. 1a: Model after 900 m through water at  $Fn = .206$  (form to cast the wax, in upper part of display)

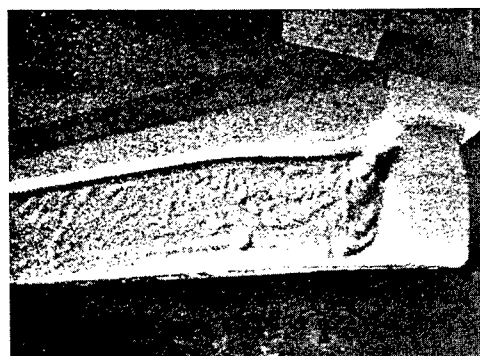


Fig. 1b: Model after 900 m through water, another close-up

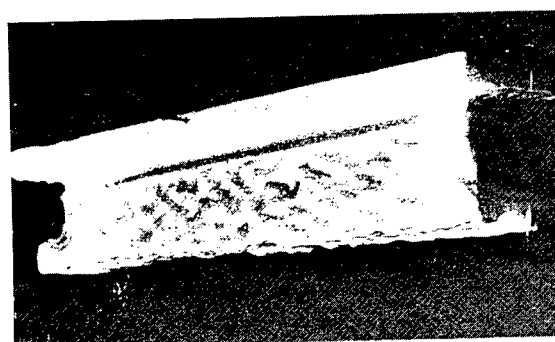


Fig. 2: Model after 3000 m through water at  $Fn = .206$



Fig. 3: Afterbody form after 3000 m through water

Prof. VIRENDRA C. PATEL,  
The University of Iowa,  
Iowa City, IA, USA:

(See discussion following the paper of K. Mori, Session V.)

Drs. S. OGIWARA and A. MASUKO,  
Ishikawajima-Harima Heavy Industries Co. Ltd.,  
Yokohama, Japan:

The authors related the wave breaking inception with the secondary vorticity proposed by Hawthorne, and explained that the relative strength of the vorticity in shear flow corresponded to the measure of wave breaking intensity.

In order to investigate the mechanism of wave breaking phenomenon around the bow of full ships, the present discussers recently carried out the measurement of wave profiles around a blunt bow form having elliptic waterline shape (1). Length, breadth and draft of the model are 6.0 m, 1.0 m and 0.4 m respectively.

Fig. 1 shows the wave profiles in front of the bow along the center line. The development of free surface elevation can be characterized as follows:

- (1) At the lower speed of  $U = 1.0$  m/s, a streak can be observed in front of the bow (point B in Fig. 1). The free surface disturbance in the region bounded by this streak is comparatively gentle.
- (2) At the speed of  $U = 1.1$  m/s, the free surface flow in the region between the bow and the point B is disturbed and there exists the reverse flow region close to the bow that corresponds to the phenomenon shown in Figs. 12, 13 of the authors' paper. The point A indicates the front line of the reverse flow region. At the higher speed of  $U = 1.2$  m/s, a new swell arises in front of the point B; this swell seems to be caused by gravitational effect.
- (3) At the speed of  $U = 1.3$  m/s, wave breaking takes place at the front of this swell and the front line of breaking (point C) moves forward as the speed increases.

The wave breaking that is related to the vorticity in free surface shear layer corresponds to the phenomenon in the reverse flow region between the bow and the point A. However, the wave breaking which is usually observed around full ships advancing on the sea corresponds to the breaking of the gravity wave at the point C. The idea of free surface shear flow seems to have difficulty in explaining the wave breaking mechanism at the point C.

The authors discussed the influence of ship form parameters, such as draft, bow entrance angle, protruding bulb and waterline shape, on free surface shear flow.

Besides the change of the bow shape, there are some additional devices to control wave breaking intensity. Recently, reduction of bow wave breaking was attempted by attachment of a bow wing or a bow fin (1), (2). The present discussers would like to show an example of reduction of breaking wave by using a horizontal bow wing.

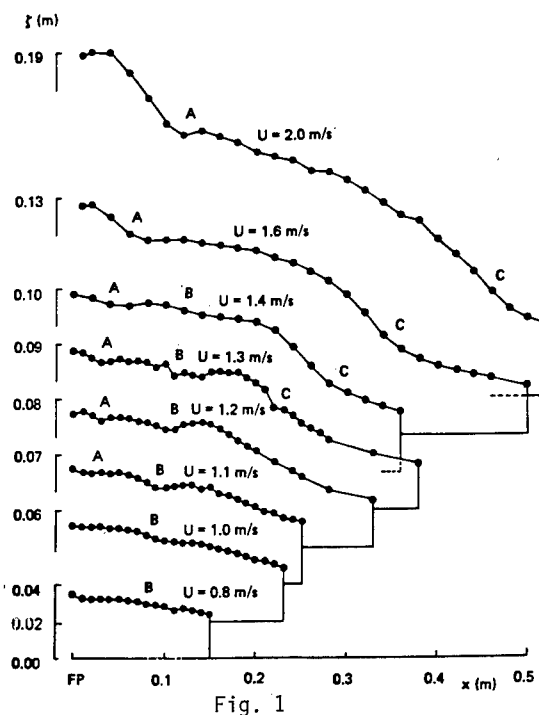


Fig. 1

Fig. 2 shows a comparison of wave pattern around bow without wing (above) and with wing (below). A ship form with a sharp bow ( $L = 6.0$  m,  $B = 1.0$  m,  $d = 0.4$  m) was used and the waterline shape of the bow is represented by a parabola. The horizontal wing (chord length on center line =  $0.12$  m, span =  $0.48$  m) was attached to the bow. The position of leading edge is  $0.075$  m before F.P. and the position of wing in vertical direction is  $0.06$  m above still water level. In this case, leading edge coincides with the breaking front and the wing is submerged beneath the free surface when ship is running at  $U = 2.0$  m/s. By attachment of the bow wing, the turbulence of free surface is remarkably suppressed and the angle between wave front and center line of ship is decreased.

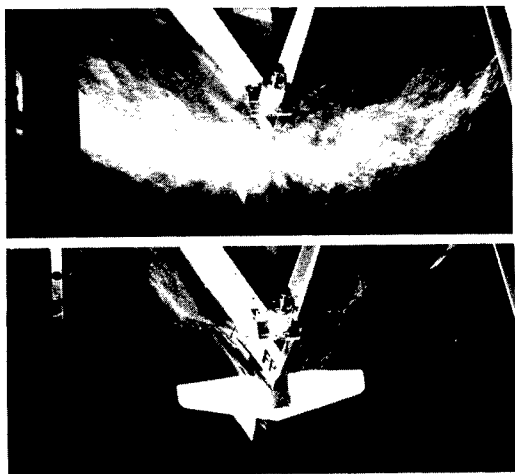


Fig. 2

Fig. 3 shows the results of flow field measurement near the bow. When the bow wing is attached, flow above the wing is accelerated and wave height is reduced. Velocity defect near the free surface has also disappeared. According to Mori's instability criterion (3), the bow wing may have an effect to stabilize the free surface disturbance.

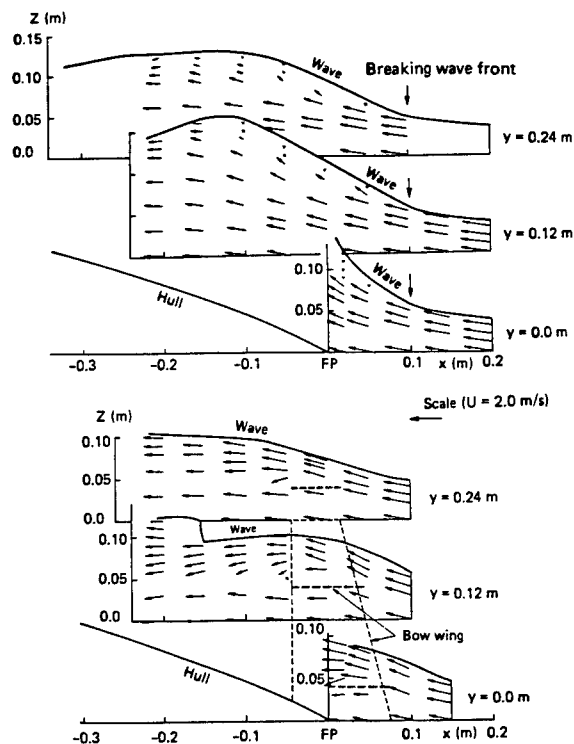


Fig. 3

- (1) Ogiwara, S., Masuko, A., Sato, R. and Tsutsumi, T.: Experimental Investigation on Free Surface Flow Related to Bow Wave Breaking, J.Kansai Soc.Nav.Arch.Japan (1984).
- (2) Miyata, H. et al.: Resistance Reduction by a Horizontal-Bow-Fin and a Movable Bulb, J.Kansai Soc.Nav.Arch.Japan, No. 191 (1983).

- (3) Mori, K.: Necklace Vortex and Bow Wave around Blunt Bodies, 15th Symposium on Naval Hydrodynamics, Hamburg (1984).

## AUTHORS' REPLY

The authors feel gratified with the vivid response to their paper. We could hardly expect such resonance, since we have mainly displayed some experimental material together with calculations based on a crude theoretical model. As explicitly stated, we do not make any claims about the generating mechanism for shear layers, vortices and wave-breaking. Accordingly, we feel unable to comment on problems of scaling as well as on effects of surface tension, in-stationarity or contamination. In this situation, the substantial additional information from the discussers' related experiments is certainly appreciated. We hope that the material compiled may provide a base for future studies, if not for a coordinated joint international research program. The pioneering experimental series at the Hamburg IFS tank in collaboration with Dr. Y. Kayo of the MHI Nagasaki Technical Institute may have set some standards for such ventures.

It is a demanding task to evaluate the relevance of Prof. Miyata's broad discussion to our work presented. In any case, it appears notable that his approach, maybe less efficient for modeling a free surface shear layer, does display some amount of backflow i.e. circulatory motion. This is then complementary to the spiraling flow derived from a true potential flow approach in the earlier lecture of Tuck and Vandenbroek, referred to in the discussion of Prof. Patel, who undoubtedly is right in calling our attention to the viscous component of vortex generation. (Note that a free surface shear layer needs only an infinitesimal amount of viscosity for its incipience.)

We feel grateful for the experimental results contributed by Drs. Ogiwara and Masuko and their careful observations of bow wave profiles. They are surely right when discriminating between wave breakers at their points A and C respectively. In fact, it is evident already from the first discussion that prior to any constructive dialogue we have to agree on an unambiguous terminology. In this respect, the endeavor of Prof. Mori in his preceding paper and in his present comment deserves attention; his recommendation regarding a necklace vortex in the region close to the bow is accepted.

Dr. Kracht asked for the motivation to roughen one ship side for the experiments shown in Fig. 22. According to Dr. Baba, such roughness may create a local region of low speed which may affect the inception of wave-breaking.

Prof. Thomsen's interesting experiments concerning flow erosion effects on a block of wax under continual towing deserve attention. They provide additional evidence for the existence of a persistent necklace vortex around a blunt bow.

# WAVE-TRAPPING DUE TO A POROUS PLATE

ALLEN T. CHWANG AND ZENGNAI DONG

## ABSTRACT

The reflection and transmission of small-amplitude surface waves by a vertical porous plate fixed in an infinitely long channel of constant depth and the wave-trapping by a thin porous plate fixed near the end of a semi-infinitely long open channel of constant depth are investigated. Analytical solutions in closed forms are obtained for the surface wave profile and the net hydrodynamic force acting on the porous plate. A dimensionless porous-effect parameter and a Reynolds number associated with the flow passing through the porous plate are introduced. It is found that, when the distance between the porous plate and the channel end-wall is equal to a quarter-wavelength plus a multiple of half-wavelength of the incident wave, the reflected wave amplitude reduces to a minimum. Thus, the porous plate together with the fluid region between it and the channel end-wall acts as a wave absorber or eliminator. The effect of nonlinear porous flow, governed by the square law of resistance, on the resulting surface waves is also studied. It is found that higher harmonic waves are generated due to this nonlinear porous flow.

## 1. INTRODUCTION

The reflection and transmission of small-amplitude surface waves by a thin vertical barrier were first studied by Dean (1945). In Dean's analysis, the semi-infinitely long vertical barrier was submerged in infinitely deep water with its top edge being at a distance below the free surface. In a similar manner, Ursell (1947) analyzed the reflection of surface waves by a surface-piercing barrier of finite length in infinitely deep water. Mei and Black (1969) extended the analyses of Dean (1945) and Ursell (1947) to consider the scattering of infinitesimal surface waves normally incident

on a rectangular surface obstacle or a bottom obstacle in a channel of finite depth.

The linearized problem of transmission of surface waves through a gap or a small aperture in a vertical barrier in water of infinite depth was analyzed by Tuck (1971) and Porter (1972). The corresponding problem for a finite water depth was studied by Guiney et al. (1972) and Packham and Williams (1972).

Lewin (1963) investigated the effect of many gaps in a vertical barrier on the propagation of surface waves. He analyzed the motion of small-amplitude surface waves in the presence of  $N$  vertical barriers separated by prescribed distances in water of infinite depth. These barriers may vibrate in a prescribed manner. Mei (1966) also solved the problem of radiation and scattering of surface waves by an arbitrary number of vertical plates in an infinitely deep ocean. Instead of monochromatic waves, Mei (1966) considered a set of general initial data on the free surface and a set of general boundary values on the plates. Using the method of singular integral equations, Porter (1974) analyzed the radiation and scattering of surface waves by thin barriers lying in a vertical plane in infinitely deep water. Each barrier was allowed to make small rolling or swaying oscillations of the same frequency as that of the incident wave. Reference was also made by Porter (1974) to the calculation of forces and moments on the barriers.

Adopting the method of matched asymptotic expansions, Tuck (1975) considered many problems involving flows through small holes, including the problem of transmission of water waves through holes in a thin barrier placed vertically in water of infinite depth. Macaskill (1979), following Tuck's (1975) formulation, studied the reflection of water waves by a thin barrier of arbitrary permeability in water of finite depth. The general problem was reduced to a

+Allen T. Chwang, Department of Mechanical Engineering, Institute of Hydraulic Research, The University of Iowa, Iowa City, Iowa 52242, USA  
++Zengnai Dong, Department of Hydraulic Engineering, Tsinghua University, Beijing, People's Republic of China

set of integral equations using standard techniques. These equations were then solved numerically using a special decomposition of the finite-depth source potential. Numerical results were presented by Macaskill (1979) for a single surface-piercing barrier and a single submerged barrier reaching partway to the surface in water of finite depth, and for a two-gap barrier in water of infinite depth.

Recently, Chwang (1983) investigated free-surface gravity waves produced by the horizontal oscillation of a uniformly porous plate. In his linearized analysis, the thin vertical porous plate (wavemaker) was placed in the middle of an infinitely long channel of finite depth. In comparison with the classical impermeable-wavemaker theory developed by Havelock (1929), Biesel and Suquet (1951), and Ursell et al. (1960), Chwang (1983) found that the porous effect reduces not only the wave amplitude but also the hydrodynamic pressure force acting on the wavemaker. The velocity of the flow passing through the porous plate was assumed by Chwang (1983) to be linearly proportional to the pressure jump across it. In other words, the porous flow is governed by Darcy's law. Chwang and Li (1983) applied the linearized porous-wavemaker theory developed by Chwang (1983) to analyze the small-amplitude surface waves produced by a piston-type porous wavemaker near the end of a semi-infinitely long channel of constant depth. They discovered that, when the distance between the wavemaker and the channel end-plate is a multiple of the half-wavelength of propagating surface waves, no propagating wave would radiate out at infinity. They called this new phenomenon "wave-trapping".

In the present paper, we shall further explore the wave-trapping phenomenon by a thin vertical porous plate. The problem of reflection and transmission of small-amplitude surface waves by a vertical porous plate fixed in the middle of an infinitely long channel of constant depth is analyzed in section 2. A dimensionless porous-effect parameter and a Reynolds number associated with the flow passing through the porous plate are also introduced. The complete or partial trapping of an incident surface wave by a porous plate fixed near the end of a semi-infinitely long channel of constant depth is discussed in section 3. Finally, the effect of nonlinear porous flow on reflection and transmission of surface waves is introduced in section 4.

## 2. INFINITELY LONG CHANNEL

We shall first consider the problem of reflection and transmission of an incident sinusoidal wave by a vertical porous plate in water of finite depth. The vertical porous plate is fixed at the  $x = 0$  plane (see Fig. 1a). The  $y$  axis points vertically upwards with the plane  $y = 0$  being the horizontal bottom of the channel. An incident wave represented by

$$\eta_0 = a \sin(\omega t + k_0 x) \quad (1)$$

propagates in the negative  $x$  direction toward the porous plate, where  $\eta_0$  is measured from the undisturbed mean free surface at  $y = h$ . In equation (1),  $k_0$  is the wave number,  $\omega$  is the circular frequency, and  $a$  is the maximum wave amplitude which is assumed to be very small in comparison with the undisturbed fluid depth  $h$ .

We shall assume the fluid in the channel to be inviscid and incompressible, and its motion irrotational. Therefore, the velocity potentials satisfy the two-dimensional Laplace equation

$$\nabla^2 \phi_i = 0 \quad (i = 1, 2), \quad (2)$$

where the subscript 1 refers to the fluid region  $x > 0$  and 2 refers to the fluid region  $x < 0$ . The linearized free-surface conditions for the velocity potentials  $\phi_i$  are

$$\frac{\partial^2 \phi_i}{\partial t^2} + g \frac{\partial \phi_i}{\partial y} = 0 \quad \text{at } y = h \quad (i = 1, 2), \quad (3)$$

where  $g$  is the gravitational constant. The normal velocity of the fluid must vanish at the bottom of the channel. Hence

$$\frac{\partial \phi_i}{\partial y} = 0 \quad \text{at } y = 0 \quad (i = 1, 2). \quad (4)$$

Let the normal velocity of the fluid passing through the porous plate from region 1 to region 2 be  $W(y, t)$ . Therefore, the boundary conditions on both sides of the thin porous plate are

$$\frac{\partial \phi_i}{\partial x} = -W \quad \text{at } x = 0 \quad (i = 1, 2). \quad (5)$$

We assume the flow inside the porous plate obeys Darcy's law. Hence, the porous flow velocity  $W$  is linearly proportional to the pressure difference between the two sides of the porous plate (Taylor, 1956; Chwang, 1983)

$$W(y, t) = \frac{b}{\mu} (P_1 - P_2) \quad \text{at } x = 0, \quad (6)$$

where  $\mu$  is the constant coefficient of dynamic viscosity and  $b$  is a material constant having the dimension of a length. The hydrodynamic pressures  $P_i(x, y, t)$  ( $i = 1, 2$ ) are related to the velocity potentials through the linearized Bernoulli equation

$$P_i = -\rho \frac{\partial \phi_i}{\partial t} \quad (i = 1, 2), \quad (7)$$

where  $\rho$  is the constant density of the fluid.

Since the incident wave is a sinusoidal wave, we assume, based on the linearity of the equation and of the boundary conditions,

that the velocity potentials, the hydrodynamic pressures, and the porous flow  $W$  all have a time factor  $\exp(i\omega t)$ ,

$$\begin{aligned}\phi_j &= \phi_j(x, y) e^{i\omega t}, \quad W = w(y) e^{i\omega t}, \\ p_j &= p_j(x, y) e^{i\omega t} \quad (j = 1, 2).\end{aligned}\quad (8)$$

Only the real parts should be taken to represent physical quantities.

The solutions of equation (2), satisfying boundary conditions (3) and (4), are given by

$$\phi_1 = \phi_0 + A_0 \cosh k_0 y e^{-ik_0 x}, \quad (9a)$$

$$\phi_2 = B_0 \cosh k_0 y e^{ik_0 x}, \quad (9b)$$

where

$$\phi_0 = A \cosh k_0 y e^{ik_0 x} \quad (9c)$$

corresponds to the incident wave, and  $k_0$  satisfies the dispersion relation

$$\omega^2 = gk_0 \tanh k_0 h. \quad (10a)$$

Equation (10a) can also be written as

$$1 - C k_0 h \tanh k_0 h = 0, \quad (10b)$$

where  $C$  is a dimensionless wave-effect parameter given by (Chwang, 1981)

$$C = \frac{g}{\omega^2 h}. \quad (10c)$$

Through the linearized dynamic boundary conditions at the free surface,

$$\frac{\partial \phi_i}{\partial t} + g\eta_i = 0 \quad \text{at } y=h \quad (i=0,1,2), \quad (11)$$

and equation (1), the constant  $A$  in equation (9c) is related to the maximum amplitude of the incident wave,  $a$ , by

$$A = \frac{ag}{\omega \cosh k_0 h}. \quad (9d)$$

In equation (11),  $\phi_0 = \phi_0 \exp(i\omega t)$  represents the velocity potential of the incident sinusoidal wave.

By equation (7) to (9), and the relations (5) and (6), we have

$$A_0 = \frac{A}{1+2G_0}, \quad B_0 = \frac{2G_0 A}{1+2G_0}, \quad (12a)$$

$$w(y) = -\frac{2ik_0 G_0 A}{1+2G_0} \cosh k_0 y, \quad (12b)$$

where  $A$  is given by (9d) and  $G_0$  is a dimensionless porous-effect parameter (Chwang and Li, 1983),

$$G_0 = \frac{\rho \omega b}{\mu k_0}. \quad (12c)$$

Substituting equations (8), (9), (10) and (12) into (11) and taking the real parts only, we obtain the surface wave profile in both regions

$$\eta_1 = \eta_0 + \frac{a}{1+2G_0} \sin(\omega t - k_0 x), \quad (13a)$$

$$\eta_2 = \frac{2aG_0}{1+2G_0} \sin(\omega t + k_0 x), \quad (13b)$$

where the incident wave  $\eta_0$  is given by equation (1). The second term on the right-hand side of equation (13a) represents the reflected wave which propagates in the positive  $x$  direction, whereas equation (13b) represents the transmitted wave which propagates in the negative  $x$  direction.

If we define the coefficient of reflection  $C_R$  as the square of the amplitude ratio of reflected wave to incident wave, then by (13), we have

$$C_R = \frac{1}{(1+2G_0)^2}. \quad (14a)$$

Similarly, we define the coefficient of transmission  $C_T$  by

$$C_T = \frac{4G_0^2}{(1+2G_0)^2}. \quad (14b)$$

Since the wave energy is proportional to the amplitude square, the coefficient of reflection may be interpreted as an energy ratio of the reflected wave to the incident wave. Similarly, the coefficient of transmission represents an energy ratio of the transmitted wave to the incident wave.

The coefficient of reflection  $C_R$  and the coefficient of transmission  $C_T$  are plotted in Fig. 2 versus the porous-effect parameter  $G_0$ . We note from Fig. 2 that, if  $G_0$  vanishes, the thin vertical plate becomes impermeable, all incident wave energy will be reflected. Therefore  $C_R = 1$  and  $C_T = 0$  at  $G_0 = 0$ . On the other hand, as  $G_0$  approaches infinity, the thin porous plate becomes completely permeable or transparent to fluid, all incident wave energy will be transmitted. Hence  $C_T$  tends to one and  $C_R$  tends to zero as  $G_0$  approaches infinity. For finite values of  $G_0$ , both  $C_R$  and  $C_T$  lie between zero and one. The sum  $C_R + C_T$  is less than one for finite values of  $G_0$ , which indicates some of the incident wave energy is dissipated in passing through the porous plate. At  $G_0 = 0.5$ , the energy dissipation reaches a maximum, only 50% of the incident wave energy remains in the reflected and transmitted waves, each of which carries 25% of the incident wave energy.

The porous-effect parameter  $G_0$  defined by (12c) depends on the fluid properties ( $\rho$  and  $\mu$ ), the property of the porous plate

(b), and the given incident wave ( $\omega$  and  $k_0$ ). By equations (10a) and (12c), we can rewrite  $G_0$  as

$$G_0 = R(\tanh k_0 h / k_0 h)^{1/2}, \quad (15a)$$

where

$$R = \frac{\rho b \sqrt{gh}}{\mu} \quad (15b)$$

is a dimensionless Reynolds number for flow inside the porous plate, which is independent of the incident wave.

By means of (14) and (15), the coefficient of reflection  $C_R$  and the coefficient of transmission  $C_T$  are plotted in Fig. 3 and Fig. 4 versus  $k_0 h$  for  $R = 1$  and  $R = 5$  respectively. Since the wave number  $k_0$  is related to the wavelength  $\lambda$  of incident wave by

$$k_0 = 2\pi / \lambda, \quad (16)$$

we note from Fig. 3 and Fig. 4 that, as the wavelength increases, the reflection coefficient  $C_R$  decreases whereas the transmission coefficient  $C_T$  increases. For fixed values of  $k_0 h$ , the energy dissipation by the porous plate increases, that is  $C_R + C_T$  decreases, as the Reynolds number  $R$  decreases.

### 3. SEMI-INFINITELY LONG CHANNEL

For a porous plate fixed near the end of a semi-infinitely long channel (see Fig 1b), we have an additional boundary condition on the end plate for region 2,

$$\frac{\partial \phi_2}{\partial x} = 0 \text{ at } x = -L. \quad (17)$$

The solutions of equation (2), satisfying boundary conditions (3), (4) and (17), are

$$\phi_1 = \phi_0 + A_0 \cosh k_0 y e^{-ik_0 x}, \quad (18a)$$

$$\phi_2 = B_0 \cosh k_0 y \cos k_0(x + L), \quad (18b)$$

where  $\phi_0$  is given by (9c), and  $k_0$  satisfies the dispersion relation (10).

Substituting equations (7), (8) and (18) into boundary conditions (5) and (6), we obtain, without much difficulty,

$$A_0 = \frac{G_0^2 + T_0^2 (1 - G_0^2) - 2iT_0 G_0^2}{G_0^2 + T_0^2 (1 + G_0^2)} A, \quad (19a)$$

$$B_0 \cos k_0 L = \frac{2G_0^2 - 2iG_0 T_0 (1 + G_0)}{G_0^2 + T_0^2 (1 + G_0^2)} A, \quad (19b)$$

where

$$T_0 = \tan k_0 L, \quad (19c)$$

$G_0$  and  $A$  are given by equations (12c) and (9d) respectively.

Substituting the known solutions  $\phi_1$  and  $\phi_2$  into equation (11), we have the surface wave profile in both regions

$$\begin{aligned} \frac{\eta_1}{a} &= \frac{\eta_0}{a} + E_0 \sin(\omega t - k_0 x) \\ &\quad - F_0 \cos(\omega t - k_0 x), \end{aligned} \quad (20a)$$

$$\begin{aligned} \frac{\eta_2}{a} &= (H_0 \cos \omega t + I_0 \sin \omega t) \\ &\quad \cos k_0(x + L), \end{aligned} \quad (20b)$$

where

$$E_0 = \frac{G_0^2 + T_0^2 (1 - G_0^2)}{G_0^2 + T_0^2 (1 + G_0^2)}, \quad (20c)$$

$$F_0 = \frac{2T_0 G_0^2}{G_0^2 + T_0^2 (1 + G_0^2)}, \quad (20d)$$

$$H_0 \cos k_0 L = -\frac{2T_0 G_0 (1 + G_0)}{G_0^2 + T_0^2 (1 + G_0^2)}, \quad (20e)$$

$$I_0 \cos k_0 L = \frac{2G_0^2}{G_0^2 + T_0^2 (1 + G_0^2)}, \quad (20f)$$

and the incident wave  $\eta_0$  is given by equation (1). The last two terms on the right-hand side of equation (20a) represent the reflected wave propagating away from the porous plate along the positive  $x$  direction.  $\eta_2$  given by (20b) represents the transmitted waves passing through the porous plate. These transmitted waves propagate in both positive and negative  $x$  directions inside the finite region bounded by the porous plate and the channel end-plate.

The reflected wave amplitude normalized with respect to the incident wave amplitude  $a$ ,  $(E_0 + F_0)^{1/2}$ , is plotted versus  $L/\lambda$  in Fig. 5 for several fixed values of  $G_0$ . The wavelength  $\lambda$  is related to the wave number  $k_0$  by  $\lambda = 2\pi/k_0$ . We note from Fig. 5 that, when  $L$  is equal to a quarter-wavelength plus a multiple of half-wavelength of the incident wave, the reflected wave amplitude reduces to a minimum. This minimum value is plotted versus the porous-effect parameter  $G_0$  in Fig. 6 at  $L/\lambda = 0.25$ . At  $G_0 = 0$ , the porous plate becomes impermeable, the reflected wave has the same amplitude as that of the incident wave. As  $G_0$  increases from zero, the reflected wave amplitude decreases until  $G_0 = 1$ , where it reduces to zero. Then the reflected wave amplitude increases with a further increase in  $G_0$ . As  $G_0$  approaches infinity, the porous plate becomes completely transparent to fluid. The incident wave then reflects from the end-plate of the semi-infinitely long channel, the reflected wave amplitude again tends to that of the incident

wave. Thus, the porous plate together with the fluid region between it and the channel end-plate acts as an efficient wave absorber or eliminator for incident surface waves whose wavelength is

$$\lambda = \frac{4L}{1+2m} \quad (m = 0, 1, 2, \dots) \quad (21)$$

When the condition (21) is met, the magnitude of  $T_0$  defined by (19c) tends to infinity.

In order to separate the material properties from the given incident wave, we plot in Fig. 7 the reflected wave amplitude  $(E^2 + F^2)^{1/2}$  versus  $k_0 h$  for several fixed values of the Reynolds number  $R$  (defined in (15b)) at  $L/\lambda = 0.25$ . It can be seen from Fig. 7 that, at  $k_0 h = 0$ , it is desirable to make  $R$  equal to one in order to eliminate the reflected wave completely.

As a passing interest, we may obtain the net hydrodynamic pressure distribution on the porous plate by equations (7), (8), (9d), (10), (18), and (19) (taking the real part only) as

$$\frac{P_2(0, y, t) - P_1(0, y, t)}{-\rho a h \omega^2} = C_p \cos(\omega t - \theta_p), \quad (22a)$$

where the dimensionless pressure coefficient  $C_p$  is

$$C_p = \frac{2T_0 \cosh k_0 y}{k_0 h [G_0^2 + T_0^2 (1 + G_0)^2]^{1/2} \sinh k_0 h} \quad (22b)$$

and the phase angle  $\theta_p$  is

$$\theta_p = \tan^{-1} [T_0 (1 + G_0^{-1})], \quad (22c)$$

$G_0$  and  $T_0$  being given by equations (12c) and (19c) respectively. The dimensionless force coefficient  $C_f$  is obtained by integrating equation (22b) with respect to  $y$ ,

$$C_f = \frac{1}{h} \int_0^h C_p dy = \frac{2T_0}{k_0^2 h^2 [G_0^2 + T_0^2 (1 + G_0)^2]^{1/2}}. \quad (23)$$

#### 4. EFFECT OF NONLINEAR POROUS FLOW

Equation (6) governing the flow inside the porous plate is valid only for low flow velocities at which the Reynolds number based on the flow velocity and the "average grain diameter" of the porous medium is less than unity (Muskat, 1946). This condition is equivalent to the assumption that the fluid inertia is very small in comparison with the viscous force such that the fluid resistance is governed by the Stokes law (De Wiest, 1969). At high flow velocities, as in the case when the porous plate is made of wire gauze or perforated sheets, Darcy's law is no longer valid and equation (6) has to be replaced.

As described and discussed by Muskat (1946) and Scheidegger (1960), many

investigators have attempted to modify Darcy's law for high velocities. A majority of these investigators proposed a relation in which the pressure gradient is proportional to the  $n^{\text{th}}$  power of the porous flow velocity, where  $n$  is intermediate between 1 and 2. As reported by Muskat (1946), experimental results indicate that  $n$  has a value in the neighborhood of 2. From studies of the flow of water through columns of shot of uniform size, Lindquist (1933) found  $n$  to be exactly 2. Taylor (1956) also used the square law of resistance ( $n=2$ ) to analyze the fluid flow in regions bounded by porous surfaces made of wire gauze and perforated sheets. His theoretical results agree with the experimental results within one percent. We shall adopt the square law of resistance in the form of

$$W^2 = \frac{2}{\rho C_s} (P_1 - P_2) \quad \text{at } x=0, \quad (24)$$

which  $C_s$  is a dimensionless constant depending only on the material properties of the porous plate.

To illustrate the effect of nonlinear porous flow, governed by the square law of resistance (24), on the resulting surface waves, we shall analyze the reflection and transmission of small-amplitude surface waves by a thin porous plate fixed in the middle of an infinitely long channel of constant depth (see Fig. 1a).

The velocity potential corresponding to the incident wave given by (1) is

$$\phi_0 = A \cosh k_0 y e^{i(\omega t + k_0 x)}, \quad (25a)$$

where  $A$  is determined by equation (9d).

We shall assume the velocity potential for region 1 ( $x > 0$ ), the velocity potential for region 2 ( $x < 0$ ), and the porous flow velocity be of the form

$$\phi_1 = \phi_0 + \sum_{m=1}^{\infty} \phi_{1m}(x, y) e^{im\omega t}, \quad (25b)$$

$$\phi_2 = \sum_{m=1}^{\infty} \phi_{2m}(x, y) e^{im\omega t}, \quad (25c)$$

$$W = \sum_{m=1}^{\infty} w_m(y) e^{im\omega t}. \quad (25d)$$

From equation (25d), we have

$$W^2 = \sum_{m=2}^{\infty} v_m(y) e^{im\omega t}, \quad (26a)$$

where

$$v_m(y) = \sum_{s=1}^{m-1} w_s(y) w_{m-s}(y). \quad (26b)$$



Substituting equation (25) into the governing equation (2) and applying the boundary conditions (3) and (4), we have

$$\phi_{1m} = A_{m0} \cosh k_{m0} y e^{-ik_{m0} x} + \sum_{n=1}^{\infty} A_{mn} \cos k_{mn} y e^{-k_{mn} x}, \quad (27a)$$

$$\phi_{2m} = B_{m0} \cosh k_{m0} y e^{ik_{m0} x} + \sum_{n=1}^{\infty} B_{mn} \cos k_{mn} y e^{k_{mn} x}, \quad (27b)$$

where  $A_{m0}$ 's,  $B_{m0}$ 's,  $A_{mn}$ 's and  $B_{mn}$ 's ( $m=1,2,3, \dots; n=1,2,3, \dots$ ) are constant coefficients yet to be determined,  $k_{m0}$  and  $k_{mn}$  ( $m=1,2,3, \dots; n=1,2,3, \dots$ ) satisfy the relations

$$m^2 - Ck_{m0}h \tanh k_{m0}h = 0 \quad (27c)$$

and

$$m^2 + Ck_{mn}h \tan k_{mn}h = 0, \quad (27d)$$

and the wave-effect parameter  $C$  is defined in equation (10c). Equation (27c) reduces to (10b) when  $m=1$ . Therefore

$$k_{10} = k_0 \quad (27e)$$

which is the wave number of the incident wave.

We note that, for any fixed integer values of  $m$ ,  $\cosh k_{m0}y$  and  $\cos k_{mn}y$  ( $n=1, 2, 3, \dots$ ) form a complete set of orthogonal eigenfunctions over the interval from  $y=0$  to  $y=h$ . Substituting equations (7), (25), (26) and (27) into boundary conditions (5) and the square resistance law (24), and equating the coefficients of terms having the same time-factor  $\exp(im\omega t)$ , we obtain

$$A_{10} = 0, B_{10} = A, \quad (28a)$$

$$A_{1n} = B_{1n} = 0 \quad (n=1,2,3, \dots), \quad (28b)$$

$$B_{20} = -A_{20} = \frac{iC_s k_0^2 A^2 E_{20}}{\omega(4+CP_{20}^2)}, \quad (28c)$$

$$B_{2n} = -A_{2n} = \frac{iC_s k_0^2 A^2 E_{2n}}{\omega(4-CP_{2n}^2)}, \quad (28d)$$

and so on. In equation (28),  $C$ ,  $A$  and  $C_s$  are given by (10c), (9d) and (24) respectively, and

$$E_{20} = \frac{P_{20}}{2k_{20}h} + \frac{4k_0^P 10^Q 10^Q 20^{-k_{20}P_{20}(1+2P_{10}^2)}}{2h(4k_0^2 + k_{20}^2)} \quad (29a)$$

$$E_{2n} = \frac{P_{2n}}{2k_{2n}h} + \frac{4k_0^P 10^Q 10^Q 2n + k_{2n}P_{2n}(1+2P_{10}^2)}{2h(4k_0^2 + k_{2n}^2)} \quad (29b)$$

$$P_{m0} = \sinh k_{m0}h \quad (m=1, 2, 3, \dots), \quad (29c)$$

$$P_{mn} = \sin k_{mn}h \quad (n=1, 2, 3, \dots), \quad (29d)$$

$$Q_{m0} = \cosh k_{m0}h, \quad (29e)$$

$$Q_{mn} = \cos k_{mn}h. \quad (29f)$$

We note that the coefficients  $A_{30}$ ,  $B_{30}$ ,  $A_{3n}$  and  $B_{3n}$  ( $n=1, 2, 3, \dots$ ) are proportional to  $A^3$  etc.  $A$  is linearly related to the maximum amplitude of the incident wave,  $a$ , through equation (9d). Since  $a$  is assumed to be very small in comparison with the undisturbed fluid depth  $h$ , we do not have to evaluate any more coefficients except those given explicitly in equation (28) if we neglect the terms of the order of  $(a/h)^3$ .

Substituting equations (25), (27), (28) and (29) into equation (11) and neglecting terms of  $O(a/h)^3$ , we have the free-surface elevations in both regions

$$\frac{\eta_1}{a} = \frac{\eta_0}{a} - D_{20} \cos(2\omega t - k_{20}x) - \sum_{n=1}^{\infty} D_{2n} e^{-k_{2n}x} \cos(2\omega t), \quad (30a)$$

$$\frac{\eta_2}{a} = \frac{\eta_0}{a} + D_{20} \cos(2\omega t + k_{20}x) + \sum_{n=1}^{\infty} D_{2n} e^{k_{2n}x} \cos(2\omega t), \quad (30b)$$

where

$$D_{20} = \frac{2CC_s k_0^2 ah Q_{20} E_{20}}{Q_{10}^2 (4 + CP_{20}^2)}, \quad (30c)$$

$$D_{2n} = \frac{2CC_s k_0^2 ah Q_{2n} E_{2n}}{Q_{10}^2 (4 - CP_{2n}^2)}. \quad (30d)$$

The second term on the right-hand side of equation (30a) represents the reflected wave with amplitude  $D_{20}$ , which propagates in the positive  $x$  direction. The last term in (30a) denotes the non-propagating waves due to reflection with exponential-decay amplitudes away from the porous plate. Both the propagating and non-propagating reflected waves are periodic functions in  $t$  with a frequency twice that of the incident wave. The transmitted wave given by (30b) has three components: the original incident wave without any change, a second-harmonic wave with amplitude  $D_{20}$  propagating in the negative  $x$  direction, and non-propagating waves with frequency  $2\omega$  and exponential-decay amplitudes away from the porous plate. Similarly, the third-order terms would contain reflected and transmitted waves with frequency  $3\omega$ , and so on.

The second-order wave amplitude  $D_{20}$  is plotted in Fig. 8 versus  $k_0 h$  at  $a/h = 0.1$  and  $C_s = 1$ . We note from Fig. 8 that  $D_{20}$  increases as  $k_0 h$  increases.  $D_{20}$  is equal to 0.025 at  $k_0 h = 0$ , and it reaches a value of 0.333 at  $k_0 h = 10$ .

## ACKNOWLEDGEMENTS

The authors are grateful to Mr. K.H. Wang for his competent assistance in numerical studies. This work was sponsored by the Office of Naval Research through the Special Focus Research Program in Ship Hydrodynamics under Contract N00014-83-K-0136.

## REFERENCES

- Biesel, F. and Suquet, F. (1951): Les appareils generateurs de houle en laboratoire. *La Houille Blanche*, Vol. 6, pp. 147-165, 475-496, 723-737.
- Chwang, A.T. (1981): Effect of stratification on hydrodynamic pressures on dams. *J. Eng. Math.*, Vol. 15, pp. 49-63.
- Chwang, A.T. (1983): A porous-wavemaker theory. *J. Fluid Mech.*, Vol. 132, pp. 395-406.
- Chwang, A.T. and Li, W. (1983): A piston-type porous wavemaker theory. *J. Eng. Math.*, Vol. 17, pp. 301-313.
- De Wiest, R.J.M. (1969): *Flow through porous media*. Academic Press, New York.
- Dean, W.R. (1945): On the reflexion of surface waves by a submerged plane barrier. *Proc. Camb. Phil. Soc.*, Vol. 41, pp. 231-238.
- Guiney, D.C., Noye, B.J. and Tuck, E.O. (1972): Transmission of water waves through small apertures. *J. Fluid Mech.*, Vol. 55, pp. 149-161.
- Havelock, T.H. (1929): Forced surface-waves on water. *Phil. Mag.*, Vol. 8, pp. 569-576.
- Lewin, M. (1963): The effect of vertical barriers on progressing waves. *J. Math. and Phys.*, Vol. 42, pp. 287-300.
- Linquist, E. (1933): *Premier Congres des Grands Barrages*, Comm. Stockholm, Vol. 5, p. 81.
- Macaskill, C. (1979): Reflexion of water waves by a permeable barrier. *J. Fluid Mech.*, Vol. 95, pp. 141-157.
- Mei, C.C. (1966): Radiation and scattering of transient gravity waves by vertical plates. *Quart. J. Mech. Appl. Math.*, Vol. 19, pp. 417-440.
- Mei, C.C. and Black, J.L. (1969): Scattering of surface waves by rectangular obstacles in waters of finite depth. *J. Fluid Mech.*, Vol. 38, pp. 499-511.
- Muskat, M. (1946): *The flow of homogeneous fluids through porous media*. J.W. Edwards, Publisher, Ann Arbor.
- Packham, B.A. and Williams, W.E. (1972): A note on the transmission of water waves through small apertures. *J. Inst. Maths. Applics.*, Vol. 10, pp. 176-184.
- Porter, D. (1972): The transmission of surface waves through a gap in a vertical barrier. *Proc. Camb. Phil. Soc.*, Vol. 71, pp. 411-421.
- Porter, D. (1974): The radiation and scattering of surface waves by vertical barriers. *J. Fluid Mech.*, Vol. 63, pp. 625-634.
- Scheidegger, A.E. (1960): *The physics of flow through porous media* (Revised edition). MacMillan Co., New York.
- Taylor, G.I. (1956): Fluid flow in regions bounded by porous surfaces. *Proc. Roy. Soc. London*, Vol. A 234, pp. 456-475.
- Tuck, E.O. (1971): Transmission of water waves through small apertures. *J. Fluid Mech.*, Vol. 49, pp. 65-74.
- Tuck, E.O. (1975): Matching problems involving flow through small holes. *Advances in Applied Mech.*, Vol. 15, pp. 89-158.
- Ursell, F. (1947): The effect of a fixed vertical barrier on surface waves in deep water. *Proc. Camb. Phil. Soc.*, Vol. 43, pp. 374-382.
- Ursell, F., Dean, R.G. and Yu, Y.S. (1960): Forced small-amplitude water waves: a comparison of theory and experiment. *J. Fluid Mech.*, Vol. 7, pp. 33-52.

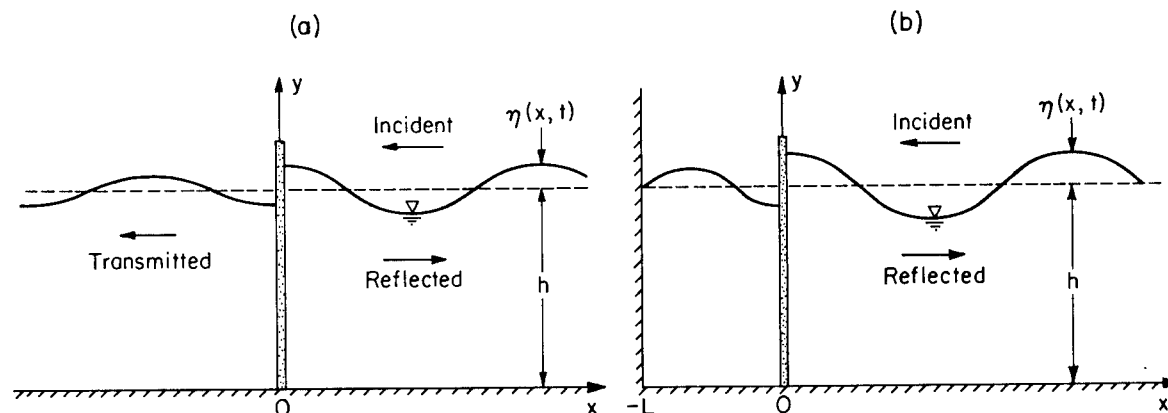


Figure 1. Schematic diagram of a thin porous plate fixed in a channel of constant depth: (a) an infinitely long channel, (b) a semi-infinitely long channel.

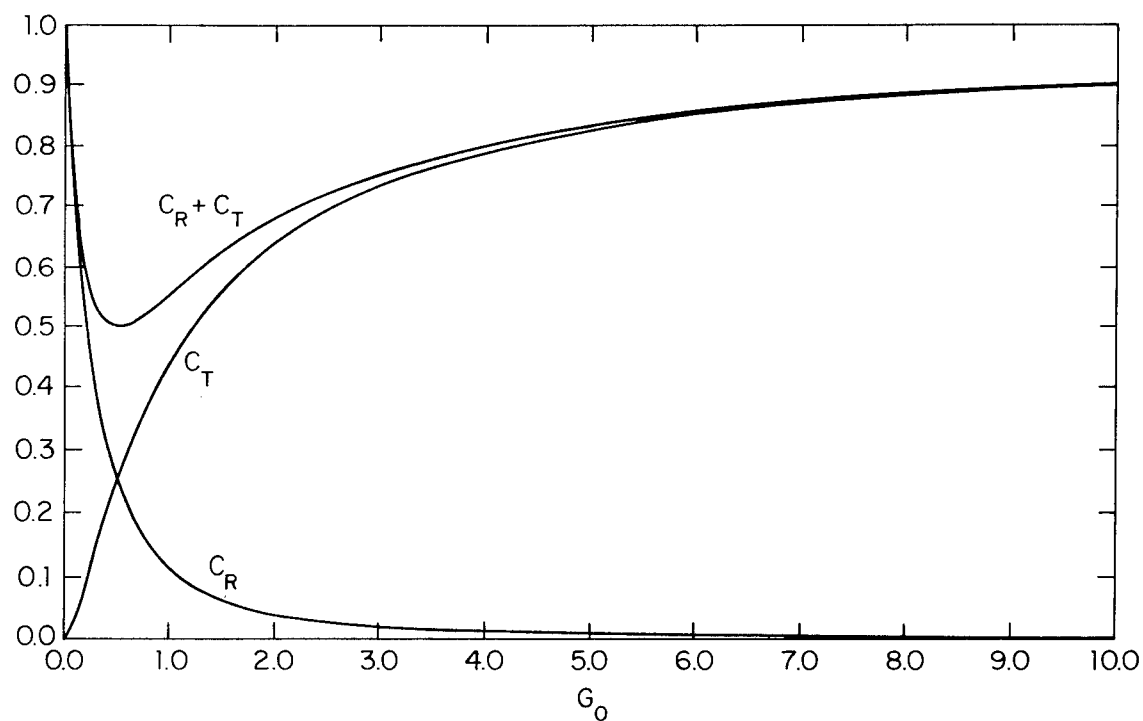


Figure 2. The coefficient of reflection  $C_R$  and the coefficient of transmission  $C_T$  versus the porous-effect parameter  $G_0$ .

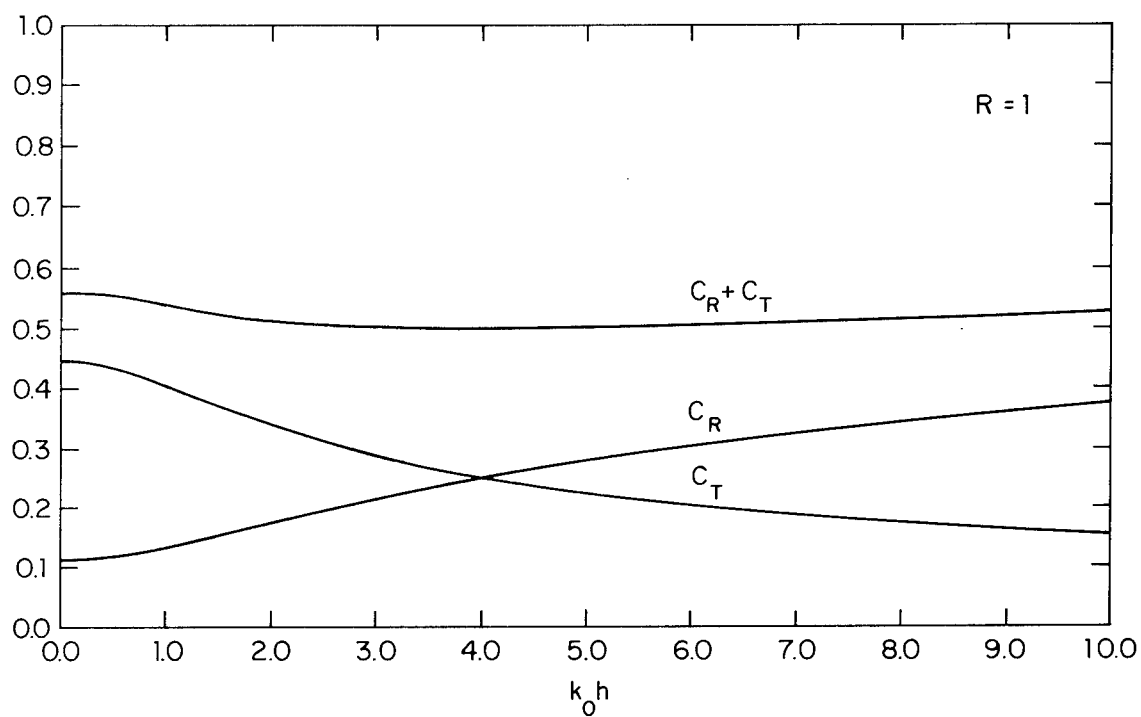


Figure 3. The coefficient of reflection  $C_R$  and the coefficient of transmission  $C_T$  versus  $k_0 h$  at  $R = 1$ .

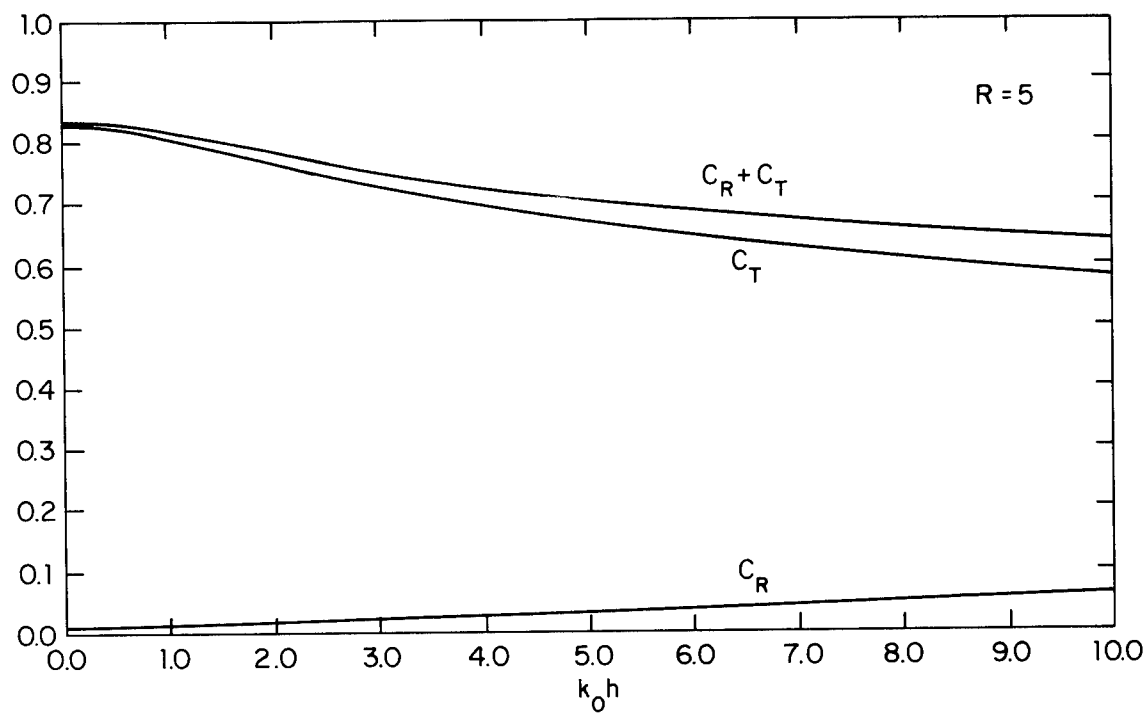


Figure 4. The coefficient of reflection  $C_R$  and the coefficient of transmission  $C_T$  versus  $k_0 h$  at  $R = 5$ .

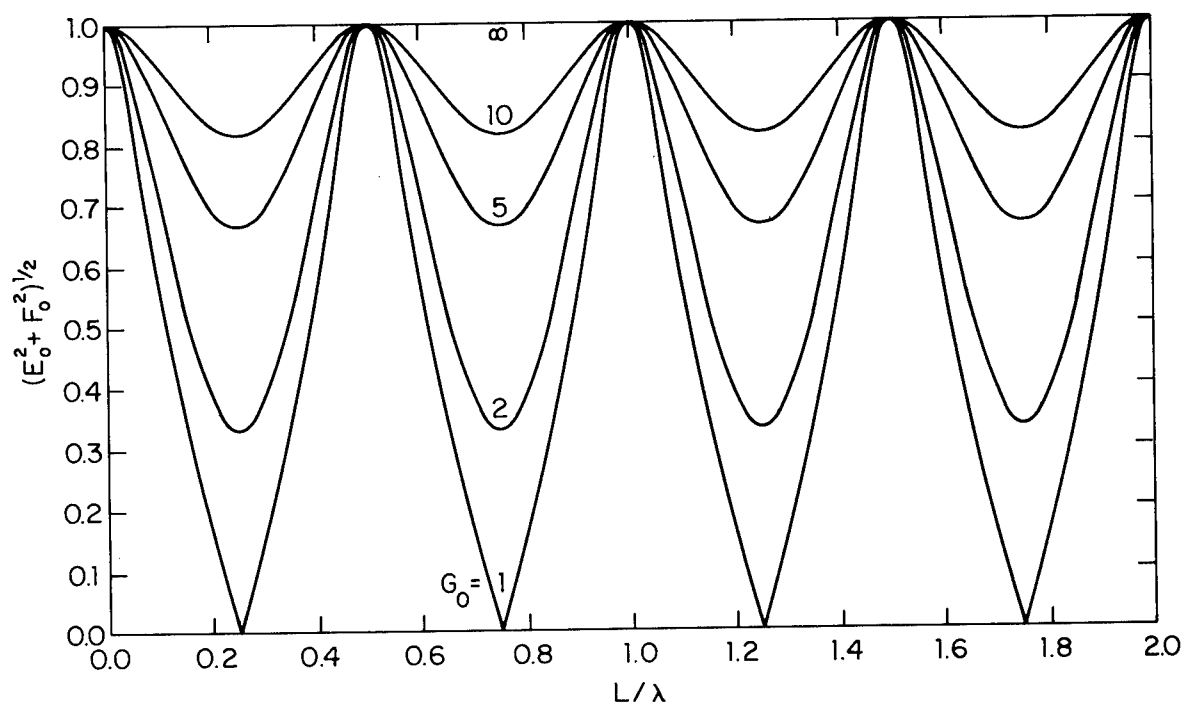


Figure 5. Amplitude of the reflected wave versus the ratio  $L/\lambda$  at fixed values of  $G_0$ .

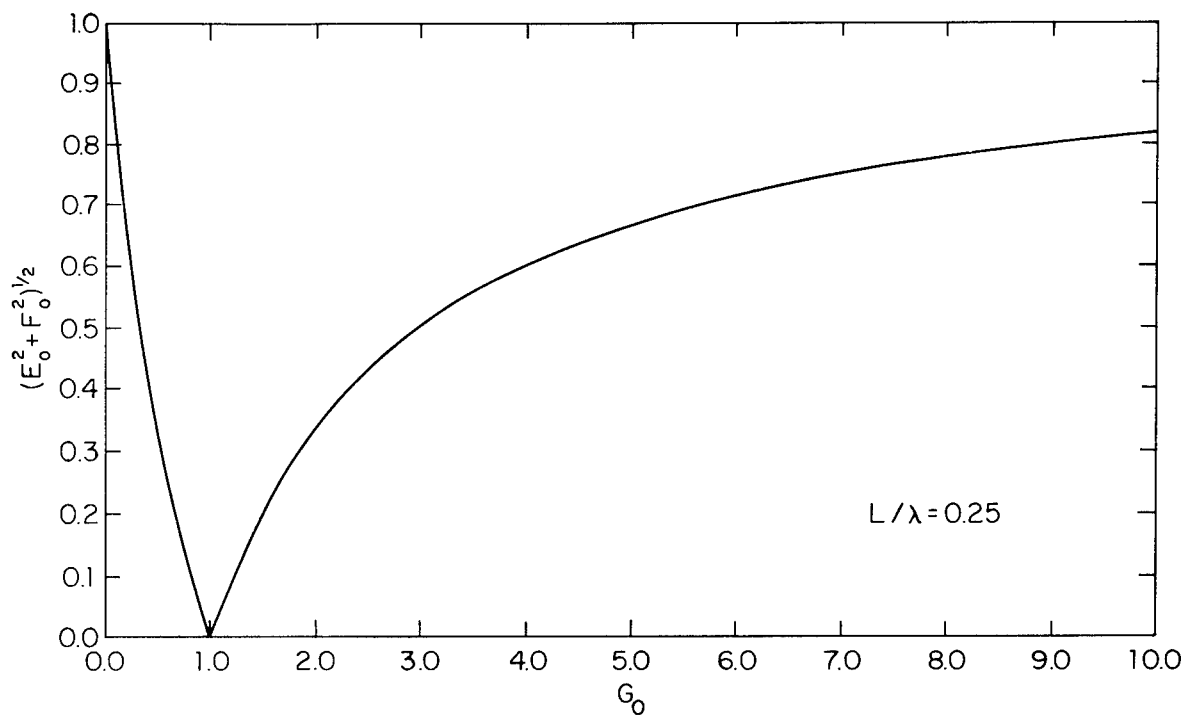


Figure 6. Amplitude of the reflected wave versus the porous-effect parameter  $G_o$  at  $L/\lambda = 0.25$ .

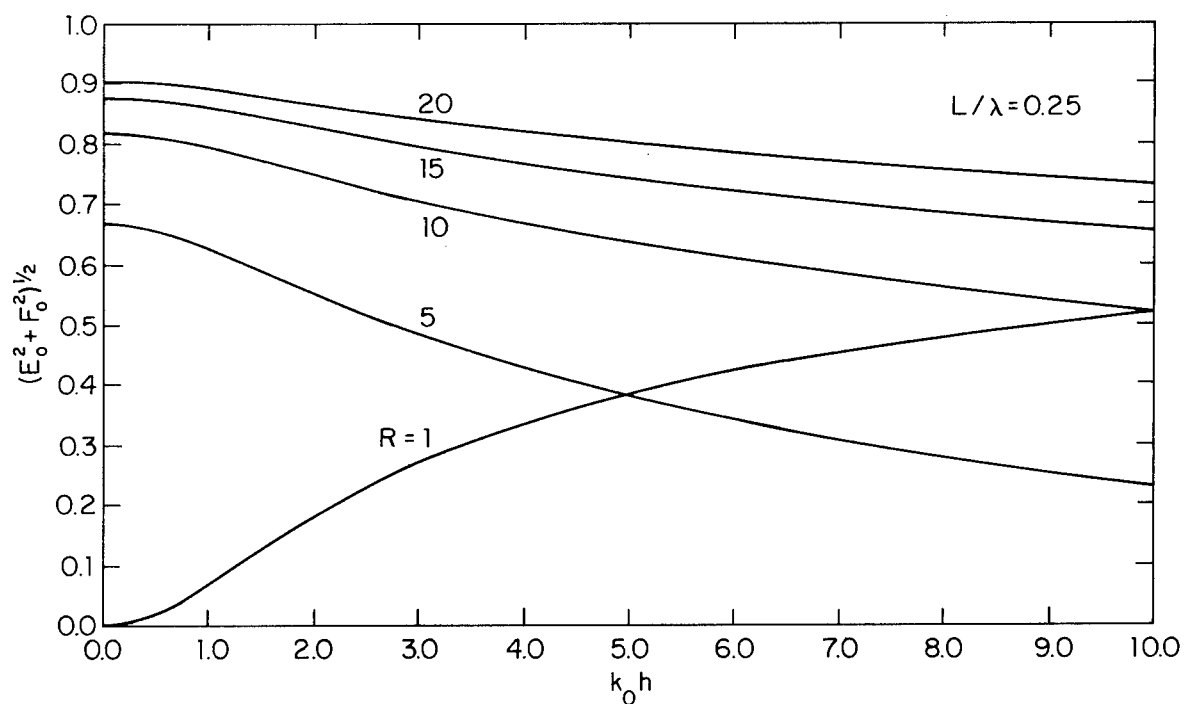


Figure 7. Amplitude of the reflected wave versus  $k_o h$  for several fixed values of  $R$  at  $L/\lambda = 0.25$ .

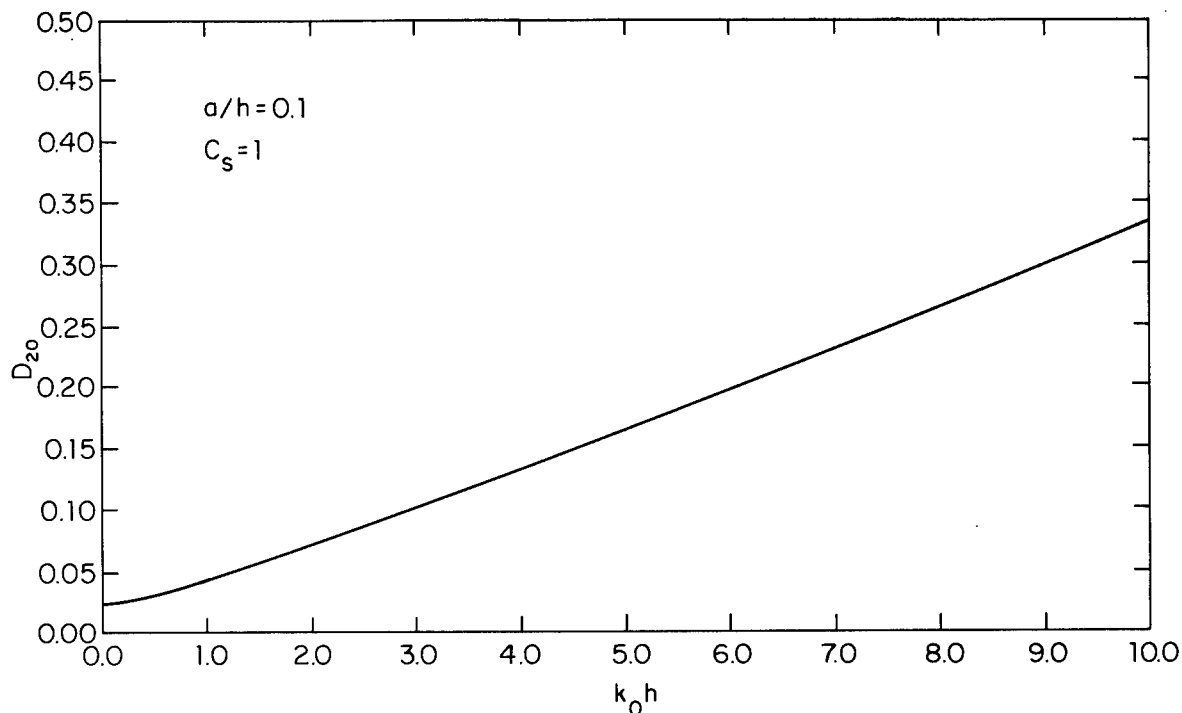


Figure 8. Second-order wave amplitude versus  $k_0h$  at  $a/h = 0.1$  and  $C_s = 1$ .

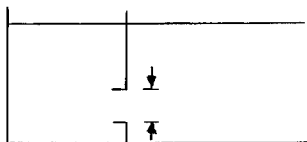
## DISCUSSION

Dr.-Ing. HIROSHI ISSHIKI,  
Technical Research Institute, Hitachi Zosen Corp.,  
Osaka, Japan:

I am very impressed by your interesting and unique ideas, and would like to make one comment and ask one question from an engineering point of view.

My comment is that your theory may find an important application when we try to calculate the effect of a breakwater made of porous materials such as rocks or tetrapods. In this case, the introduction of viscous effects may be essential.

My question is that the viscous effect should be reduced as much as possible if your idea is applied to a wave maker and/or wave absorber. In this case, you should use, for example, a method used in audio speaker systems as shown below.



The discussor believes that the authors' idea should be extended further to develop a wave absorber of high performance so as to eliminate the troublesome effect of reflected waves present in an ordinary wave absorber.

## AUTHORS' REPLY

Thank you very much for your kind comments. Your suggestions of applying our theory to calculate the effect of porous breakwater on wave reflection and extending our ideas to further develop a high-performance wave absorber are very encouraging and stimulating. We shall continue our research on this subject following your suggestions.

# ON THE INFLUENCE OF NONLINEARITY OF BOUNDARY CONDITIONS AT THE HULL AND WATER SURFACE IN THE PROBLEM OF A SHIP'S WAVE RESISTANCE

E.L. AMROMIN, A.N. IVANOV, I.O. MIZIN, AND Y.S. TIMOSHIN

## ABSTRACT

Linear theory of ship waves does not make it possible to predict the value of the wave resistance of the displacement ships with satisfactory accuracy. In connection with the absence of accurate non-linear solutions of the three-dimensional problems concerning ship waves attempts were made to improve the methods of calculation of the wave resistance mainly in two ways - either by specifying the boundary conditions on the surface of a ship, or taking into account the non-linearity of the condition on free surface. Analysis of boundary conditions of free surface is presented here and the method of calculation of the wave resistance of a ship with due regard for the non-linearity of these considerations of the effect of non-linearity of boundary conditions on the ship hull on the wave resistance are presented in this paper.

## NOTATION

- $L, T, \delta, V_\infty$  - length, draft, coefficient of fullness of displacement and ship speed;  
 $\xi_w$  - wave resistance to the product of the wetted surface area and dynamic head of the incident flow;  
 $\xi_z$  - residual resistance to the same value;  
 $\{x, y, z\}$  and  $\{\xi, \eta, \zeta\}$  - systems of Cartesian coordinates connected with intersections of midsection, centerplane and construction waterline of a ship;  
 $g$  - gravity acceleration;  
 $\lambda$  - wave length;  
 $U$  - speeds on free surface;  
 $F_R = V_\infty (g\lambda)^{-0.5}$ ,  $u = U/V_\infty$  - induced velocity;

- $q$  - intensity of the sources distributed over the ship surface;  
 $q_\lambda, u_\lambda, z_\lambda$  - values of the  $q, u, z$  that correspond to linear theory.

## 1. INTRODUCTION

Potentials of the linear theory while calculating the wave resistance of a ship were essentially comprehensively studied by Girs and Sretensky in 1946. They compared the results of the resistance measurement of a series of vertical sided models of great length-beam ratio with waterlines of big angle of declination with calculations according to Mitehell formula. Differences between the theory (curve 1 in Fig.1) and the experiment (dots) proved to be great. A similar comparison for a model of Todd's 60-th series (1953) with coefficient of fullness of displacement  $\delta = 0.6$  is given in Fig.2, and a comparison for a model with a bow bulge carried out by Amromin, Mizin, Pashin and Timoshin (1983) - in Fig.3.

The linearization of boundary conditions on the ship surface and free surface of the fluid is one of the main causes of differences between the calculated and experimental data. Considerations concerning the influence of the boundary conditions on the calculated values of the wave resistance of a ship and a procedure of considering of non-linear conditions on the free surface of the fluid first used by Amromin and Mizin are presented below.

## 2. ON LINEARIZATION OF BOUNDARY CONDITIONS ON FREE SURFACE

A steady flow around the ship hull in the associated system of coordinates where the wave system is stable is discussed. The fluid is believed to be incompressible, perfect and the flow beyond the ship hull - potential.

Krylov Shipbuilding Research Institute, Leningrad 196158 USSR

One of the significant points of the linearized theory of the wave resistance is the linearization of the Bernoulli integral.

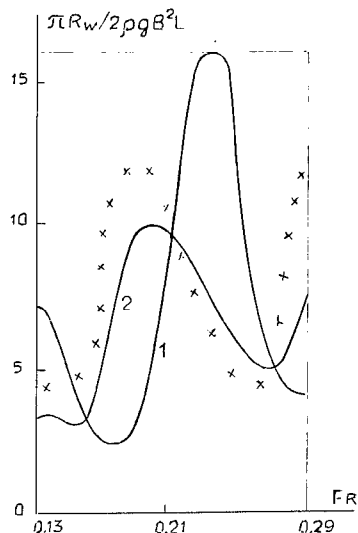


Figure 1 - Relation for the model with vertical sides.

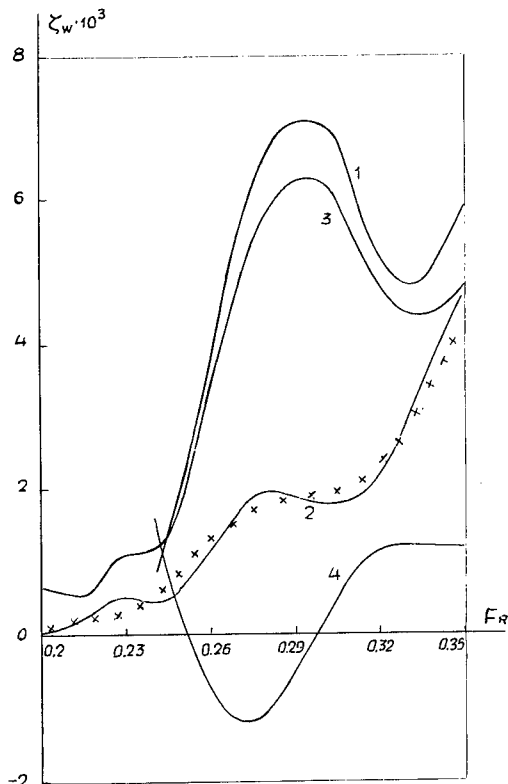


Figure 2 - Relation for the model of Series 60.

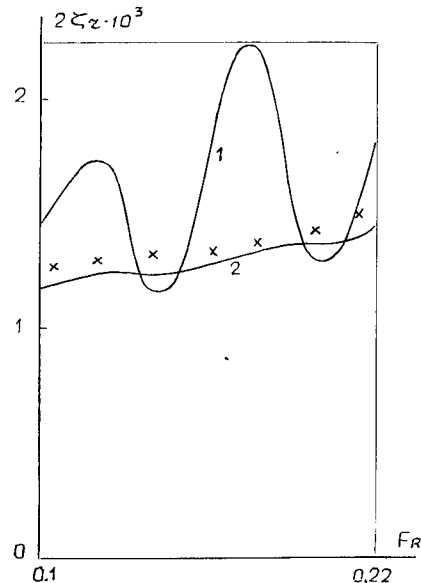


Figure 3 - Relation for the model of large fullness with nose bulb

In this case the original assumption is the smallness of the induced velocities on the ship hull and free surface as compared with the value of undisturbed speed.

Bernoulli integral for the points of the surface of the fluid can be written down as

$$U^2 + 2gz = U_\infty^2 \quad (1)$$

For the further analysis it is convenient to write Eq.(1) as follows

$$\bar{U} = (1 - 2gz U_\infty^{-2})^{-0.5} \quad (2)$$

where

$$\bar{U} = U U_\infty^{-1}$$

assuming that

$$z \ll U_\infty^2 g^{-1} \quad (3)$$

the right part (2) can be expanded in a Taylor series with the terms not higher than the first order of smallness in it. The linearized Bernoulli integral can be written as

$$\bar{U} = 1 - \nu z, \quad \nu = g U_\infty^{-2} \quad (4)$$

Condition (3) is equal to the condition of smallness of the induced velocities in all the points of the free surface of the fluid, strictly speaking, that can take place only for the ships of a great length-beam ratio the waterlines of which in addition have zero angles of declination in the fore and after ends in way of the free surface. The waterline configurations of



real ships considerably differ from the influence of the mentioned fact on the errors in the wave-resistance estimating can be performed using (2) and (4). In doing so it should be borne in mind that a ship wave system and consequently its wave resistance depends on the deformation extent of the free surface in close proximity to the fore and after ends of a ship where waves are generated. Deceleration of the inflow occurs in these zones. The mentioned fact is of special significance for full ships.

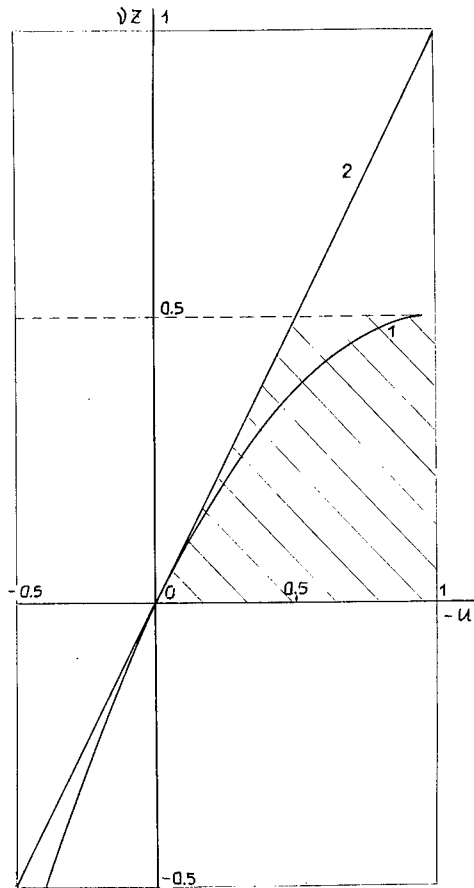


Figure 4 - Relation of wave elevation to the speed.

Dependences (2) and (4) express the relation between the speeds in the points of the free surface mentioned above. The plots illustrating the dependences mentioned earlier are presented in Fig.4. Curve 1 corresponds to the non-linearized Bernoulli integral, curve 2 - to the linearized one. The given data indicate considerable distortion of the disturbance extent of the fluid free surface due to Bernoulli integral linearization.

It follows from (2) and (4) that

there is a possibility to define also qualitative differences in linear and non-linear wave interference. The linearized Bernoulli integral does not place restrictions on the rising of the free surface which results from the condition that the radicand in (2) cannot take negative values.

$$\sqrt{z} \leq 0.5 \quad (5)$$

The limiting values of rising are shown by dotted line in Fig.4. Since the speed of wave propagation  $U_\infty$  remains inviolable equal to ship speed after the interference of the bow and stern wave systems limitation (5) is true for the sum of the non-linear waves. Thus, if the bow and stern wave systems are of the height that is equal to more than half of the limiting one and are close in phase the law of simple geometrical summation of waves is not valid any more and the height of the sum of waves should be less than their arithmetic sum, or resulting height proves to be of limiting value and the process of the resulting wave profile breakage occur due to the necessity of fulfilling condition (5). The above mentioned fact should result in oscillation subduing of the wave resistance coefficient curves representative of the linear theory calculation.

If  $U_\infty^2$  is substituted for the dependence of propagation speed of plane waves of finite amplitude on length

$$U_\infty^2 = \frac{g\lambda}{2\pi} \left[ 1 + \left( \frac{2\pi\alpha_1}{\lambda} \right)^2 \right]$$

there will be obtained a limiting value of the wave amplitude to wave length ratio

$$2\pi\alpha_1 = \lambda \quad (6)$$

which is close to the value obtained by Stokes and the value given in Sretensky monograph (1975). Here  $\alpha_1$  is the value of the first harmonic wave amplitude in a representation of the wave form as a trigonometric series.

It can be seen from the diagrams of Fig.4. that the main errors due to linearization of Bernoulli integral are observed for the values of the total velocities on the free surface less than  $0.5 U_\infty$ . A significant improvement can be achieved if the maximum values of free surface deformation, including wave height values, are restricted by the limiting values indicated in Fig.4 by a dotted line. Thus, the simplified relation between the velocities and deformations will be represented by the lines confining the shaded region. A further improvement, apparently a minor one, is obtained when the broken line in Fig.4 is replaced by curve 1. It is also of im-

portance that the limiting of free surface deformation values partly compensate the negative effect of linearization performed for the boundary condition on the ship's hull.

It is difficult to use the relations of Fig. 4 for practical design purposes directly because there is a need to determine velocities in the points of the disturbed free surface. So, the effect of Bernoulli integral linearization should be considered not only in terms of ship's wave resistance values but also in terms of transferring kinematic boundary condition from the disturbed free surface on to the plane which coincides with the level of undisturbed flow. This effect is difficult to assess in the general case. So, let us consider plane waves of a finite amplitude for this purpose. Such treatment is acceptable because the lines of crests of lateral ship waves are nearly normal to the center line plane.

The estimate is suitably made using the integro-differential equation suggested by Ivanov (1975, 1980) to determine the shape of the finite amplitude waves on the surface of the liquid of the infinite depth. Using symbols assumed here this equation can be written in the following form:

$$\frac{dz}{dx} = \frac{1}{\pi} \int_{-\infty}^{\infty} \frac{\varphi_1(x, \xi) \varphi_2(\xi)}{x - \xi} d\xi \quad (7)$$

where

$$\varphi_1 = \frac{(1 + \xi^2)^{0.5} \left[ 1 + \frac{dz}{dx} (z - \xi) / (x - \xi) \right]}{1 + (z - \xi)^2 / (x - \xi)^2},$$

$\varphi_2 = (1 - 2\sqrt{\xi})^{0.5}$ ,  $\xi = \xi(x)$   
equation of the wave profile.

Substitution into Eq. (7) of the series

$$z = \alpha_1 \cos(kx) + \alpha_2 \cos(2kx) + \dots \quad (8)$$

clearly shows that the well-known expressions of finite amplitude wave theory are obtained for the coefficients contained in the series. The first term of series (8) corresponds to the solution of the problem with the linearized Bernoulli integral and boundary conditions transferred on to the surface of the undisturbed flow, and the other terms are added because of nonlinearities.

Eq. (7) makes it possible to study separately the effect of Bernoulli integral linearization and the effect of boundary conditions transfer on the magnitude of the added terms.

In the first case the function  $\varphi_1$  remains the same as in Eq. (7) while the function  $\varphi_2$  is expressed in the form similar to (4)

$$\varphi_2 = 1 - \sqrt{\xi}$$

because the second summand in the radicand is small compared to a unit. In this case using Eq. (7) the elevation  $z_\lambda$  can be calculated which is related by dependence (4) to the velocity  $U_\lambda$  estimated with the help of the linearized kinematic condition. In the second case it should be assumed that  $\varphi_1 = 1$  and  $\varphi_2$  should be left without changes. Finally, in the third case  $\varphi_1, \varphi_2$  are treated without simplification. Calculations of the coefficients contained in series (7) (up to the third order of smallness in terms of  $\alpha_1/\lambda$ ) reveal that the linearization of kinematic condition on the free surface affects the values of  $z(x)$  to the same extent as the linearization of Bernoulli integral, i.e.

in the second case  $-\sqrt{z_\lambda} = -U_\lambda^2/2 - U_\lambda$  (9)

in the third  $-z - z_\lambda = 0.5(z_\lambda - z)$

This conclusion agrees with the results of Gadd's (1976) calculations for the ship. In these calculations Rankine sources were located on the undisturbed flow surface, and calculated values of  $\xi_w$  obtained were significantly less than measured values. Using (9) relation  $z/z_\lambda$  can be expressed in terms of  $U_\lambda$ .

By means of transforming (9) to the form

$$\sqrt{z} = \frac{\sqrt{z_\lambda}}{2} + \frac{\sqrt{z}}{2} = -\frac{U_\lambda}{2} + \left(-\frac{U_\lambda}{2} - \frac{U_\lambda^2}{4}\right) = -U_\lambda - \frac{U_\lambda^2}{4},$$

and using (4) the following expression is obtained

$$z/z_\lambda = 1 + U_\lambda/4.$$

By means of relating  $U_\lambda$ , using linear theory formulae, to the amplitude induced by the plane feature of the wave intensity  $q$

$$\alpha_\lambda = 2q \exp\{-F_{\tau_z}^2\},$$

the value

$$\chi_2 = \frac{\alpha_2}{2\pi} = \frac{\alpha_\lambda}{2\pi} \left(1 - \frac{\alpha_\lambda}{4}\right) \quad (10)$$

can be expressed in terms of  $q$ .

Fig. 5 compares relation (10) with the solution of the plane nonlinear problem obtained by Salvesen and von Kerczek (1976). The results of the calculations performed by them agree well with formula (10), and apparently formula (10) can be used practically for the whole range of permissible  $\alpha/\lambda$  values.

In conclusion it should be noted that as waves move away from ship's stern their length in transverse direction increases while wave amplitude to length ratio decreases. At a certain distance from the stern the assumptions of the linear theory become valid, and, consequently, the use of

the linear theory methods to determine wave resistance on the basis of wave parameters at a long distance from the ship is justified.

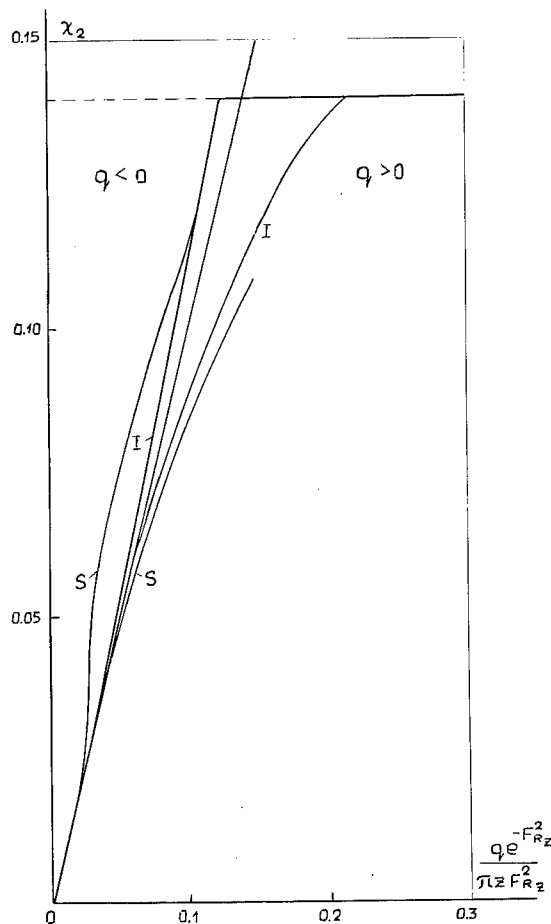


Figure 5 - The main graphic for the determining of corrections. Curve is plotted according to Salvesen and von Kerczek, curve I - according Eq. (10).

### 3. CALCULATION OF WAVE RESISTANCE

One way to account for the non-linear effects on the free surface is to introduce corrections in the linear theory formulae, in particular in Mitchel integral

$$\zeta_w = \frac{\rho v}{\pi} \int_0^\infty F |H(F)|^2 dW$$

where

$$F = (1 + W^2)^{0.5}, \quad k = \sqrt{F^2},$$

$$H(F) = \int_{-L/2}^{L/2} \int_{-T}^0 q(x, z) e^{kz + ikx/F} dx dz \quad (11)$$

Kochin's function,  $H$ , is proportional to wave amplitudes, so expression (11) implicitly reflects the re-

lation between induced velocities and the amplitude of ship's waves because these velocities are proportional to the intensity  $q(x, z)$  of the sources representing the hull. As the wave resistance is determined by the wave amplitude it is natural to correct the amplitude first of all. Amplitude corrections correspond in (11) to source intensity corrections, and  $q(x, z)$  assumes the following form

$$q(x, z) = q_\lambda(x, z) \chi(q_\lambda, F_{R2}) \quad (12)$$

Here  $q_\lambda$  is  $q$  as taken in the linear theory, for example, relation

$$q_\lambda(x, z) = 2 \partial y(x, t) / \partial x \cdot V_\infty$$

used in Mitchel's formula. Comparison of (2) and (4) show that

$$F_{R2} = V_\infty (-gz)^{-0.5}$$

affects  $\chi$ .  $\chi$  is used here in the following form

$$\chi(q_\lambda) = \chi_2(q_2) \ln(1, \exp\{F_{R2}^2 - 1\}) \quad (13)$$

while relation  $\chi_2(q_2)$

is taken from Fig. 5.

It is assumed in the calculations that

$$q_2(x, z) = q_\lambda |z|^{-1} dz$$

where  $dz$  - width of surface element,  $z$  - immersion of surface element centre. (The centre line plane is divided into surface elements bounded by the neighbouring waterlines  $x = \text{const}$  and frame lines  $z = \text{const}$ .  $q$  is assumed within each surface element and placed outside the integral sign for these elements in (11). After this the integral is calculated in terms of elementary functions as in Timoshin's calculations (1975)). Values of  $\zeta_w$  obtained this way are shown in Fig. 1, 2, 3, 6 by curves 2. The latter one shows the results for the model with the ordinates

$$y = 0.1(1 - x^2)(1 - 64z^2),$$

where

$$-1 \leq x \leq 1, \quad -0.125 \leq z \leq 0$$

It can be seen that major discrepancies between the theory and experiment are removed by means of these corrections. The presence of yet considerable oscillations of the calculated curve can be attributed to the approximate relation for  $\chi$  used here. However, the presence of similar oscillations in the experiment cannot be excluded either. The absence of the

oscillations in the measured results at low Froude numbers can be explained by the fact that it is difficult to determine  $\zeta_w$  precisely basing on the towing test results. The corrections used here have the advantage of clear physical interpretation and allow gradual refinement.

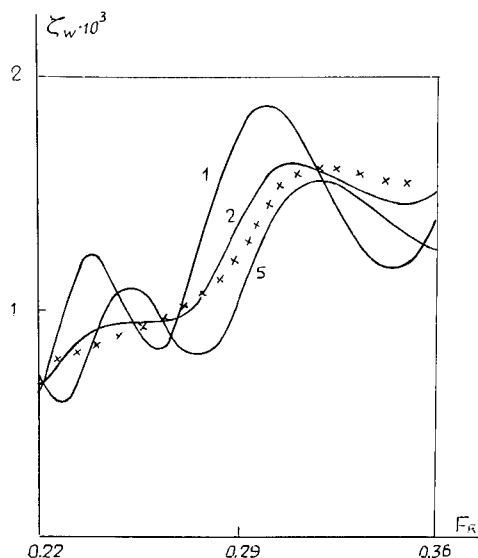


Figure 6 - Relation for the model of Gadd.

As to the effect of the linearization of ship's hull boundary conditions on  $\zeta_w$  the authors give the results of calculations by formula (11), values  $q$  being obtained from the integral equation for the double surface in the unbounded flow (curve 3 in Fig. 2 - Smorodin's results (1975), curve 5 in Fig. 6 - Gadd's results (1970) ) and the results of Young Hong's calculations in the second approximation (curve 4 in Fig. 2) where the value inverse to ship's length-beam ratio was used as small parameter. Boundary conditions were used in the simplified form in these three cases of calculations. These results need no comments.

#### REFERENCES

- Amromin, E.L., Mizin, I.O., Pachin, V.M.  
Timoshin, Y.S. (1983): Minimum Resistance Hull Form Problem and Methods of Improving Real Ship's Lines. International symposium on ship hydrodynamics and energy saving. El Pardo., Pap. No 11-2.  
Gadd, G.E. (1970): Methods for Calculating the Flow over Ship Hulls. TRINA, v 112, No 3.  
Gadd, G.E. (1976): Wave Theory Applied to Practical Hull Forms. International symposium on wave Resistance, Japan.  
Girs, I.V., Sretenskiy, L.N. (1946): The Effect of the Change of Ship's Main Dimensions on Ship's Wave Resistance. PMM, v.10, vyp. I (In Russian).  
Ivanov, A.N. (1975): Das nichtlineare Problem stationärer Wellen an einer freien Flüssigkeitsoberfläche. Schiffbau Forschung, Sonderheft.  
Ivanov, A.N. (1980): Hydrodynamics of Fully-Cavitating Flows. L., Izd. Sudostroenie.  
Salvesen, N. and von Kerczek, C. (1976): Comparison of Numerical and Perturbation Solution of Two-Dimensional Nonlinear Water-Wave Problems. J. of Ship Res., v. 20, No 3.  
Smorodin, A.I. (1975): Development of the Methods of the Wave Resistance Theory and their Practical Application to the Problems of Ship Hydromechanics. In: Problems of the Applied Ship Hydromechanics. L., Izd. Sudostroenie. (In Russian).  
Sretenskiy, L.M. (1975): The Theory of fluid wave motion, M., Izd. Nauka.  
Timoshin, Y.S. (1975): Possibilities of Employing Numerical Methods for Optimization of Ship lines. In: Problems of the Applied Ship Hydrodynamics. L., Izd. Sudostroenie.  
Todd, F.N. (1953): Some Further Experiments on Simple-Screw Merchant Ship Forms-Series 60. The Soc. of Natural Architects and Marine Eng. Transactions, v. 61.  
Young S. Hong (1977): Numerical Calculation of Second Order Wave Resistance. J. of Ship Res., v. 21, No 2.

## DISCUSSION

Dr. EIICHI BABA,  
Mitsubishi Heavy Industries Ltd.,  
Nagasaki, Japan:

In the present paper and the authors' previous paper presented at the International Symposium on Ship Hydrodynamics and Energy Saving in El Pardo (Reference 1), the non-linear free-surface effect is ingeniously incorporated into the linearized Michell theory to obtain better predictions of wave-making resistance of ships. Based on the discussor's study, the non-linear effects of free-surface condition appear in such a way that the transverse wave system is reduced very much. As a result, humps and hollows in wave resistance coefficient curve are reduced as shown in Figs. 12 and 13 of the discussor's paper "Numerical Evaluation of a Wave Resistance Theory for Slow Ships" presented at the 2nd International Conference on Numerical Ship Hydrodynamics, Berkeley, 1977. It would be very much appreciated, if the authors could show us a comparison of the integrand  $F|H(F)|^2$  of the expression (11) for two cases: One is the conventional Michell theory corresponding to their notation 1 in Figs. 1, 2, 3 and 6 and the other is the corrected value based on the authors' method corresponding to the notation 2 in the same figures. If there is a large reduction of the integrand near  $w = 0$  in the authors' notation (near  $\theta = 0$  in discussor's paper), it would be very interesting to see the consistency of the non-linear effect between different approaches.

Mr. ROBERT F. HALLIDAY,  
University of Sydney,  
Sydney, Australia:

I feel a good deal of sympathy for the authors when they propose a fairly simple procedure for overcoming the failure of Michell's linear theory to match experiment. Many elaborate procedures fail to achieve a better result and I am far from satisfied that the possibilities of simple modifications of Michell's integral have been exhausted. However the model shown in Figure 6 is similar to a Wigley form. We use such a model for a class exercise. It has length 42 inches, beam 3.5 inches and draught 9 inches and should be a fair approximation to Michell's thin ship. However, the agreement between Michell's integral and experiment is no better. Very good agreement can be obtained by introducing an attenuation factor based on the parameter (boundary layer displacement thickness)/(wavelength). In support of a viscous correction, it has been observed that roughening the model reduces the wave resistance and markedly reduces the oscillation of wave resistance as a function of Froude number. I would therefore suggest that procedures for improving the usefulness of Michell's integral should take account of both the free surface and hull boundary conditions and also viscous effects.

Michell's integral is given in most text books in terms of infinitesimal panels on the median plane. This leads to computational difficulties. It is a simple matter to transform Michell's integral to apply to small but finite elements. For a Froude Number of, say,  $F$ , then  $1/F^2$  elements in the  $X$  direction and perhaps half as many in the  $Y$  direction will be sufficient for a Wigley or similar arbitrary form. I wonder how widely this simple point has been appreciated.

Dr. ANTONY J. MUSKER,  
Admiralty Research Establishment,  
Haslar, England:

The authors appear to have brought about a dramatic improvement to the predictions according to Michell's theory by an apparently simple correction. This is indeed impressive but I should like to express my dismay at the relatively poor performance of Gadd's method. Referring to Fig. 6, there is considerable discrepancy between the observed and predicted wave elevations notwithstanding the fact that an exact body kinematic boundary condition and non-linear forms of the free-surface conditions are satisfied using Gadd's procedure. I suspect that Gadd's method has not yet been fully exploited in the sense of using a finely discretised hull and free surface and that much better agreement might therefore be expected if it were implemented on a large computer. The present technique (albeit aesthetically appealing) might then have some competition.

## AUTHORS' REPLY

To Dr. E. Baba

Thank you for your interest in our paper. In our turn it is with great interest that we are studying your work in the field of wave and wave-breaking resistance.

Enclosed are the figures comparing  $F|H(\omega)|^2$  for Wigley form according to Michell theory and that of ours. The computations for our method are shown with an interrupted line.

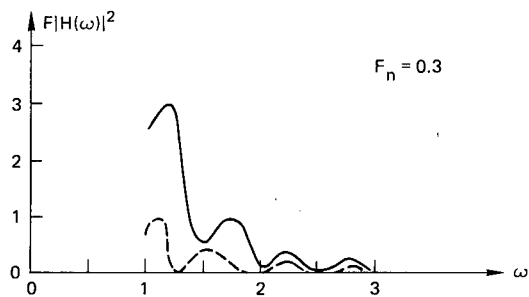
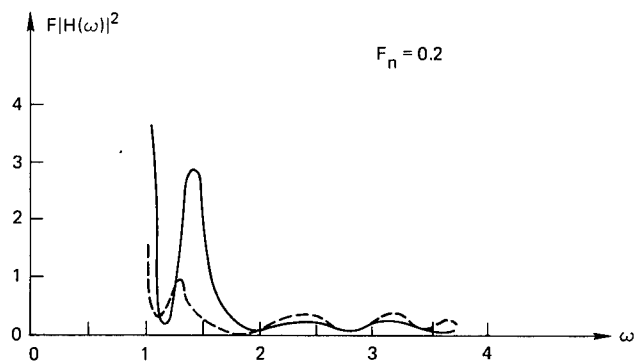
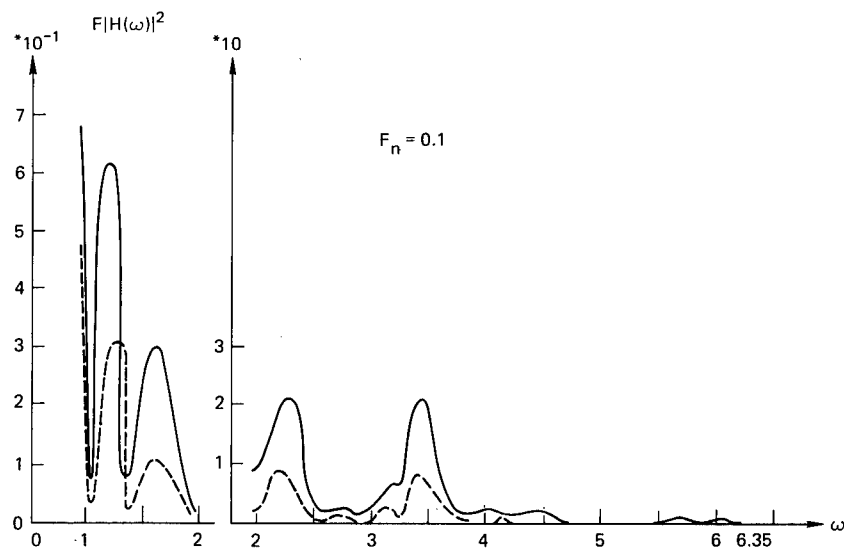
We hope to learn about your further advances in developing research in this direction.

To Dr. A.J. Musker

We, same as you, hope that the remarkable Gadd's procedure will find further development.

To Mr. R.F. Halliday

We agree that the viscosity has a certain effect in the relation of the wave-making resistance to the Froude number and we consider that in future it would be desirable to take viscosity into account.



Relationship of the function  $F|H(\omega)|^2$  for the Wigley model in linear (continuous line) and suggested (interrupted line) approach.

SESSION VII  
PROPELLER-HULL INTERACTIONS

# A DIFFERENTIAL PREDICTION METHOD FOR THREE-DIMENSIONAL LAMINAR AND TURBULENT BOUNDARY LAYERS OF ROTATING PROPELLER BLADES

NANCY C. GROVES AND MING S. CHANG

## ABSTRACT

A general formulation is given for the three-dimensional boundary-layer flow on a rotating propeller blade. The basic equations are presented in a nonorthogonal coordinate system which rotates with the blade. Finite difference methods are used to develop a computer code for solving the laminar and turbulent boundary-layer equations. The Reynolds stress tensor is modeled by an algebraic eddy-viscosity formulation. In general, the equations are solved numerically using the standard Keller box method. However, regions of flow reversal across the boundary-layer are computed by the characteristic box method. A companion geometry computer code, developed to model propeller geometry characteristics, and an existing inviscid flow code for computing propeller blade pressures are combined with the boundary-layer computer code to form an efficient computation scheme. For a given potential-flow solution, a typical boundary-layer solution of 690 grid points requires 64 seconds CPU time on a CYBER 176 computer.

Computed results are presented for several blade geometries. The rotating segment solution compares well with analytical and experimental data. Predictions for a model propeller also compare favorably with experimental data and illustrate that two-dimensional theory may provide adequate predictions for applications where crossflow effects are not important. Geometry effects of warp and skew are shown to be small for the boundary-layer predictions on three model propellers.

## 1. INTRODUCTION

The ability to predict local flow properties on propeller blades will aid in the basic understanding of propulsor performance and cavitation. Knowledge of propeller viscous phenomena at model scale, such as laminar and turbulent separation, prior to testing, will lead to selection of test conditions appropriate to simulate prototype performance. Determination of the flow-field velocity distributions near the tip will improve the

basic understanding of propeller tip vortex cavitation and provide information for defining the position of the shed vortex sheet in the inviscid propeller model.

This paper describes a general method for calculating the three-dimensional boundary layer around propeller blades. The solution is divided into three calculations (1) potential flow, (2) geometric parameters, and (3) boundary layer flow. The potential flow computer code adopted is the Brockett (1981) code for use at design conditions. The geometry and boundary layer codes are modifications of the codes developed by Cebeci, et al. (1978) for calculating three-dimensional laminar and turbulent boundary layers on ship hulls. The significant modifications to the Cebeci, et al. (1978) formulation, for propeller blade boundary-layer applications, include the addition of the Coriolis and centrifugal forces due to rotation, the use of a coordinate system appropriately describing propeller surfaces, and the specification of appropriate initial conditions.

The present boundary-layer formulation predicts both laminar and turbulent flow using the differential solution method. The earlier calculation methods of both Groves (1981), for propeller blades, and Arakawa, et al. (1983), for axial flow pump blades, compute only turbulent flow using a momentum integral solution method. There is much discussion regarding the merits of each of the solution methods. The momentum integral method requires considerably less computation time. The differential method is generally considered to give a more accurate and complete prediction of the flow characteristics. However, the major advantage of the present solution procedure is its capability of predicting laminar flow. This region is particularly important for model propeller applications where a large region of the flow over the blades is laminar. Additionally, laminar flow predictions are necessary for instability.

A similar differential calculation scheme has been developed by Itoh, et al. (1984) for predicting the three-dimensional laminar and turbulent boundary-layer flow on the rotating blades of axial flow pumps. The present calcu-

David W. Taylor Naval Ship Research and Development Center, Bethesda, Maryland, USA



lation procedure varies from their method in two major respects. First, Itoh, et al. (1984) use an orthogonal coordinate system to represent an axial flow pump blade. While this system simplifies the governing flow equations, it encounters difficulties in grid generation for blades which deviate from a fan shape. A more general surface coordinate system defined in terms of  $x_c$ , fraction of chord measured from the leading edge, and  $x_R$ , fraction of tip radius, is chosen for the present study. The use of this coordinate system alleviates any problems associated with the calculation grid. The second variation from the work of Itoh, et al. (1984) is the specification of the initial conditions at the leading edge and the hub. Itoh, et al. (1984) applied the usual leading edge and hub conditions for three-dimensional boundaries to compute the growth for a rotating blade. Their computation diverged. In order to obtain meaningful results, they applied an averaging process to both the leading edge and the hub and developed an iterative procedure to obtain these average values within a certain accuracy. In the present study, the leading edge and hub conditions are handled differently. The methods proposed in this paper do not require an iterative procedure and the solution converges quickly for all grid points. The details of the procedures are discussed in Section 5.

The boundary-layer equations are solved numerically using the Keller (1970) two-point finite-difference method and the characteristic box procedure (see Bradshaw, et al. (1981)) for computing regions of reverse crossflow. A turbulence model is required for closure of the turbulent boundary-layer equations. The zero-order eddy-viscosity model with gradual transition, given by Cebeci and Smith (1974), is adopted here.

Even though the present analysis allows computation of the three-dimensional laminar and turbulent boundary-layer on the complex propeller blade geometry, two desirable flow predictions are beyond the scope of this study. These are the complex hub interaction and the flow transition calculation. No hub interaction is considered and the location of transition is an input parameter to the computer code determined by the user. It should be noted that the restriction of computing at design conditions only is a limitation of the Brockett (1981) formulation and not of the boundary-layer formulation. The boundary layer may be computed with any potential flow and associated blade offsets. Finally, there is no distinction in the boundary-layer solution procedure between the pressure and suction blade surfaces. The differences between the surfaces are accounted for in the potential flow and geometry calculations.

Results of the propeller blade boundary-layer calculation are presented for several geometries. The first blade studied is the large chordlength segment investigated experimentally and analytically by Lakshminarayana, et al. (1972). The laminar predictions for the blade are in agreement with the computed results of both Banks and Gadd (1962) for a

rotating sector and Morris (1981) for a rotating helical blade. Overall, the turbulent predictions agree well with both the experimental data of Lakshminarayana, et al. (1972) and the analytical values of Cham and Head (1969) for the limiting case of a rotating disk. Discrepancies occur in the limiting streamline angle  $\beta$  which is consistently over-predicted by the present method. The second blade evaluated is a model propeller designed at DTNSRDC by Denny (1968) and tested in the DTNSRDC 12-in. water tunnel by Jessup, et al. (1984). Both two- and three-dimensional calculations were made for this blade. The results show that two-dimensional theory can adequately predict the measured data as well as three-dimensional theory with the exception of the crossflow. The final geometries investigated are an unwarped, a warped, and a skewed model propeller, examined earlier by Groves (1981), with no experimental boundary-layer data available. The current predictions show little variation in the predicted local skin friction coefficient for the three blades.

## 2. COORDINATE SYSTEMS

Figure 1 depicts a typical propeller blade and hub configuration. In practice, there are  $N$  symmetrically-spaced identical blades attached to the hub, but, for clarity, only one is shown in Figure 1. The propeller rotates with the constant angular velocity  $\Omega$  about the  $x$ -axis. The Cartesian  $x, y, z$ , coordinate system is fixed in space and does not rotate with the blade. In this system,  $x$  is the axis of rotation, with positive displacement measured aft;  $z$  is taken as upward positive; and  $y$  forms a right-handed orthogonal system as shown in Figure 1. In the present calculation scheme, the blade geometry and potential velocities are initially specified in the Cartesian system by the Brockett (1981) lifting surface computer code.

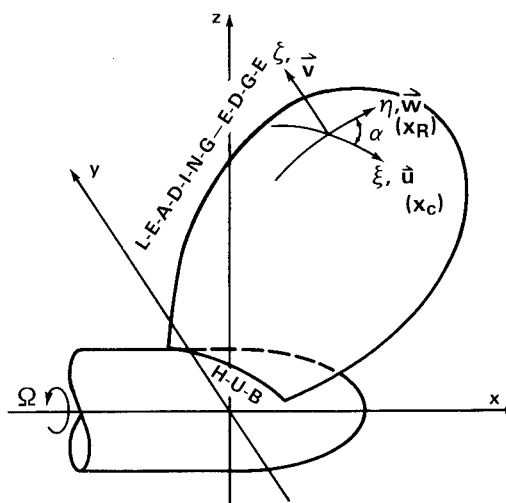


Fig. 1 - Schematic of Blade Coordinate Systems

Although the Cartesian coordinate system could be used for the boundary-layer solution procedure, a system fixed to the blade surface and rotating with the blade is chosen for its convenient representation of the complex geometry. The surface coordinates  $\xi$ ,  $\eta$ , and  $\zeta$  are defined with  $\xi$  equal to the nondimensional fraction of chord measured from the leading edge;  $\eta$  equal to the nondimensional radius as a fraction of the tip radius; and  $\zeta$  equal to the outward normal to the blade surface. These coordinates are also illustrated in Figure 1, where  $\alpha$  is shown as the angle between the  $\xi$  and  $\eta$  surface coordinates. The velocity components  $u$ ,  $v$ , and  $w$  are defined in the  $\xi$ ,  $\zeta$ , and  $\eta$  directions, respectively.

The  $\xi$  and  $\eta$  coordinates, the Cartesian offsets on the blade reference surface (i.e., no blade thickness), and the velocity components in a helical reference frame are standard quantities produced by the Brockett lifting surface (1981) computer code. In preparation for its use in the present computation system, the Brockett code (1981) has been modified to calculate the Cartesian offsets on the actual blade surfaces and the velocities in the Cartesian reference frame. The surface offsets are needed to define certain derivative quantities i.e., the metric coefficients, geodesic curvatures, etc., used in the boundary-layer solution. Metric coefficients, denoted by  $h_1$ ,  $h_2$ , and  $h_3$  for the  $\xi$ ,  $\eta$ , and  $\zeta$  coordinates, respectively, correlate surface distances between the Cartesian and surface coordinate systems. As is typical practice in boundary-layer formulations, the boundary layer thickness is assumed to be small and the  $\zeta$  coordinate is assumed to measure distance along the surface normal. Therefore, the metric  $h_3$  is set to unity with no loss of generality. The remaining metric coefficients are defined as

$$h_1 = \left[ \left( \frac{\partial x}{\partial \xi} \right)^2 + \left( \frac{\partial y}{\partial \xi} \right)^2 + \left( \frac{\partial z}{\partial \xi} \right)^2 \right]^{1/2}$$

$$h_2 = \left[ \left( \frac{\partial x}{\partial \eta} \right)^2 + \left( \frac{\partial y}{\partial \eta} \right)^2 + \left( \frac{\partial z}{\partial \eta} \right)^2 \right]^{1/2}$$

### 3. BOUNDARY LAYER EQUATIONS

The steady, incompressible boundary layer equations for rotational flow in a non-orthogonal coordinate system are given by Yamazaki (1981). The equations are identical to those presented by Cebeci, et al. (1978), with the addition of two terms in the momentum equations representing the centrifugal and Coriolis forces. The governing equations, using the surface coordinates  $\xi$ ,  $\eta$ , and  $\zeta$ , are:

Continuity:

$$\frac{\partial}{\partial \xi} (u h_2 \sin \alpha) + \frac{\partial}{\partial \eta} (v h_1 \sin \alpha) + \frac{\partial}{\partial \zeta} (w h_1 h_2 \sin \alpha) = 0 \quad (1)$$

$\xi$ -Momentum:

$$\begin{aligned} & \frac{u}{h_1} \frac{\partial u}{\partial \xi} + \frac{w}{h_2} \frac{\partial u}{\partial \eta} + \frac{v \partial u}{\partial \zeta} - K_1 u^2 \cot \alpha + K_2 w^2 \csc \alpha \\ & + K_{12} u w + 2\Omega(w + u \cos \alpha) \eta_1 \csc \alpha + \Omega^2 (\eta_2 \eta \cot \alpha \csc \alpha) \quad (2) \\ & = - \frac{\csc^2 \alpha}{h_1} \frac{\partial}{\partial \xi} \left( \frac{p}{\rho} \right) + \frac{\cot \alpha \csc \alpha}{h_2} \frac{\partial}{\partial \eta} \left( \frac{p}{\rho} \right) + \frac{\partial \tau_1}{\partial \zeta} \end{aligned}$$

$\eta$ -Momentum:

$$\begin{aligned} & \frac{u}{h_1} \frac{\partial w}{\partial \xi} + \frac{w}{h_2} \frac{\partial w}{\partial \eta} + \frac{v \partial w}{\partial \zeta} - K_2 w^2 \cot \alpha + K_1 u^2 \csc \alpha \\ & + K_{21} u w - 2\Omega(u + w \cos \alpha) \eta_1 \csc \alpha - \Omega^2 \eta_2 \eta \csc^2 \alpha \quad (3) \\ & = - \frac{\csc^2 \alpha}{h_2} \frac{\partial}{\partial \eta} \left( \frac{p}{\rho} \right) + \frac{\cot \alpha \csc \alpha}{h_1} \frac{\partial}{\partial \xi} \left( \frac{p}{\rho} \right) + \frac{\partial \tau_2}{\partial \zeta} \end{aligned}$$

In these equations,  $u$ ,  $v$ , and  $w$  represent the velocity components in the  $\xi$ ,  $\zeta$ , and  $\eta$  directions, respectively,  $\alpha$  is the angle between the surface coordinates  $\xi$  and  $\eta$ , and  $\Omega$  is the constant angular velocity. The metric coefficients  $h_1$  and  $h_2$  were defined in the previous section. The quantities  $K_1$  and  $K_2$  are the geodesic curvatures of the curves  $\eta = \text{constant}$  and  $\xi = \text{constant}$ , respectively, and are defined by

$$K_1 = \frac{1}{h_1 h_2 \sin \alpha} \left[ \frac{\partial (h_2 \cos \alpha)}{\partial \xi} - \frac{\partial h_1}{\partial \eta} \right] \quad (4a)$$

$$K_2 = \frac{1}{h_1 h_2 \sin \alpha} \left[ \frac{\partial (h_1 \cos \alpha)}{\partial \eta} - \frac{\partial h_2}{\partial \xi} \right] \quad (4b)$$

The parameters  $K_{12}$  and  $K_{21}$  are defined in terms of the geometry as

$$\begin{aligned} K_{12} = \frac{1}{\sin \alpha} \left[ - \left( K_1 + \frac{1}{h_1} \frac{\partial \alpha}{\partial \xi} \right) \right. \\ \left. + \cos \alpha \left( K_2 + \frac{1}{h_2} \frac{\partial \alpha}{\partial \eta} \right) \right] \quad (5a) \end{aligned}$$

$$\begin{aligned} K_{21} = \frac{1}{\sin \alpha} \left[ - \left( K_2 + \frac{1}{h_2} \frac{\partial \alpha}{\partial \eta} \right) \right. \\ \left. + \cos \alpha \left( K_1 + \frac{1}{h_1} \frac{\partial \alpha}{\partial \xi} \right) \right] \quad (5b) \end{aligned}$$

The remaining parameters in the boundary layer equations are:

$$\begin{aligned} p &= \text{static pressure in the fluid} \\ \rho &= \text{fluid density} \\ \tau_1 &= \text{shear stress in the } \xi\text{-direction,} \\ \tau_1 &= \nu \frac{\partial u}{\partial \zeta} - u'v' \end{aligned}$$

$\tau_2$  = shear stress in the  $\eta$ -direction, (6)

$$\tau_2 = \nu \frac{\partial w}{\partial \zeta} - \overline{v'w'}$$

$\nu$  = kinematic viscosity of the fluid

$\overline{u'v'}$ ,  $\overline{v'w'}$  = Reynolds stresses

$\Omega$  = constant angular velocity of propeller

$\eta_1, \eta_2, \eta_3$  = directional cosines between the systems (x, y, z) and ( $\xi, \eta, \zeta$ )

The boundary layer thickness is denoted by  $\delta$  and the boundary layer is defined in the region  $0 < \zeta < \delta$ . The boundary conditions are:

$$\begin{aligned} \zeta=0, u=v=w=0 \\ \zeta=\delta, u=u_e(\xi, \eta), w=w_e(\xi, \eta) \end{aligned} \quad (7)$$

The pressure gradients are determined from the momentum equations at the edge of the boundary layer. The edge equations are

$\xi$ -momentum:

$$\begin{aligned} \frac{u_e}{h_1} \frac{\partial u_e}{\partial \xi} + \frac{w_e}{h_2} \frac{\partial u_e}{\partial \eta} - K_1 u_e^2 \cot \alpha + K_2 w_e^2 \csc \alpha \\ + K_{12} u_e w_e + 2\Omega(w_e + u_e \cos \alpha) \eta_1 \csc \alpha \\ + \Omega^2 \eta_2 \eta_3 \cos \alpha \csc^2 \alpha = -\frac{\csc^2 \alpha}{h_1} \frac{\partial}{\partial \xi} \left( \frac{p_e}{\rho} \right) \\ + \frac{\cot \alpha \csc \alpha}{h_2} \frac{\partial}{\partial \eta} \left( \frac{p_e}{\rho} \right) \end{aligned} \quad (8)$$

$\eta$ -momentum:

$$\begin{aligned} \frac{u_e}{h_1} \frac{\partial w_e}{\partial \xi} + \frac{w_e}{h_2} \frac{\partial w_e}{\partial \eta} - K_2 w_e^2 \cot \alpha + K_1 u_e^2 \csc \alpha \\ + K_{21} u_e w_e - 2\Omega(u_e + w_e \cos \alpha) \eta_1 \csc \alpha \\ - \Omega^2 \eta_2 \eta_3 \csc^2 \alpha = -\frac{\csc^2 \alpha}{h_2} \frac{\partial}{\partial \eta} \left( \frac{p_e}{\rho} \right) + \frac{\cot \alpha \csc \alpha}{h_1} \frac{\partial}{\partial \xi} \left( \frac{p_e}{\rho} \right) \end{aligned} \quad (9)$$

Transformed variables are defined as

$$\xi = \xi, \quad \eta = \eta, \quad d\sigma = \left( \frac{u_e}{\nu s_1} \right)^{1/2} d\zeta, \quad s_1 = \int_0^\xi h_1 d\xi \quad (10)$$

A two component vector potential is introduced with

$$u h_2 \sin \alpha = \frac{\partial \psi}{\partial \zeta} \quad (11)$$

$$w h_1 \sin \alpha = \frac{\partial \phi}{\partial \zeta}$$

$$v h_1 h_2 \sin \alpha = - \left( \frac{\partial \psi}{\partial \xi} + \frac{\partial \phi}{\partial \eta} \right)$$

where  $\psi$  and  $\phi$  are defined as

$$\psi = (\nu s_1 u_e)^{1/2} h_2 \sin \alpha f(\xi, \eta, \sigma) \quad (12)$$

$$\phi = (\nu s_1 u_e)^{1/2} \frac{u_{ref}}{u_e} h_1 \sin \alpha g(\xi, \eta, \sigma)$$

and  $u_{ref}$  is a reference velocity.

The potential velocities  $u, v,$  and  $w$  are rewritten using the vector potentials  $\psi$  and  $\phi$ , the Reynolds stresses are rewritten in terms of the eddy viscosity factor  $\epsilon_m$ , and the boundary-layer edge conditions are applied to eliminate the pressure terms. The transformed  $\epsilon$ - and  $\eta$ -equations are

$$\begin{aligned} \epsilon\text{-momentum: } (bf'')' + m_1 f f'' - m_2 (f')^2 - m_5 f' g' \\ + m_6 f' g' - m_8 (g')^2 + m_{11} - m_{13} f' - m_{14} g' + m_{15} \\ = m_{10} \left( f' \frac{\partial f'}{\partial \xi} - f'' \frac{\partial f}{\partial \xi} \right) + m_7 \left( g' \frac{\partial f'}{\partial \eta} - f'' \frac{\partial g}{\partial \eta} \right) \end{aligned} \quad (13)$$

$\eta$ -momentum:

$$\begin{aligned} (bg'')' + m_1 f g'' - m_4 f' g' - m_3 (g')^2 + m_6 g g'' \\ - m_9 (f')^2 + m_{12} + m_{16} f' + m_{13} g' - m_{17} \\ = m_{10} \left( f' \frac{\partial g'}{\partial \xi} - g'' \frac{\partial f}{\partial \xi} \right) + m_7 \left( g' \frac{\partial g'}{\partial \eta} - g'' \frac{\partial g}{\partial \eta} \right) \end{aligned} \quad (14)$$

In these equations, primes denote differentiation with respect to  $\sigma$  and

$$f' = \frac{u}{u_e}, \quad g' = \frac{w}{u_{ref}}, \quad b = 1 + \frac{\epsilon_m}{\nu} \quad (15)$$

The coefficient terms  $m_1$  through  $m_{12}$ , identical to those given by Cebeci, et al. (1978), are

$$m_1 = \frac{1}{2} \left( 1 + \frac{s_1}{h_1 u_e} \frac{\partial u_e}{\partial \xi} \right) + \frac{s_1}{h_1 h_2 \sin \alpha} \frac{\partial}{\partial \xi} (h_2 \sin \alpha)$$

$$m_2 = \frac{s_1}{h_1 u_e} \frac{\partial u_e}{\partial \xi} - s_1 K_1 \cot \alpha$$

$$m_3 = -s_1 K_2 \frac{u_{ref}}{u_e} \cot \alpha$$

$$m_4 = s_1 K_{21}$$

$$m_5 = \frac{s_1}{h_2} \frac{u_{ref}}{u_e^2} \frac{\partial u_e}{\partial \eta} + s_1 K_{12} \frac{u_{ref}}{u_e}$$

$$m_6 = \frac{s_1}{h_1 h_2 \sin \alpha} \frac{1}{\sqrt{u_e s_1}} \frac{\partial}{\partial \eta} \left( \sqrt{u_e s_1} h_1 \sin \alpha \frac{u_{ref}}{u_e} \right)$$

$$m_7 = \frac{s_1}{h_2} \frac{u_{ref}}{u_e} \quad (16)$$

$$m_8 = s_1 K_2 \left( \frac{u_{ref}}{u_e} \right)^2 \csc \alpha$$

$$m_9 = s_1 K_1 \csc \alpha \frac{u_e}{u_{ref}}$$

$$m_{10} = \frac{s_1}{h_1}$$

$$m_{11} = m_2 + m_5 \frac{w_e}{u_{ref}} + m_8 \left( \frac{w_e}{u_{ref}} \right)^2$$

$$m_{12} = m_4 \frac{w_e}{u_{ref}} + m_3 \left( \frac{w_e}{u_{ref}} \right)^2 + m_9 + \frac{m_{10}}{u_{ref}} \frac{\partial w_e}{\partial \xi} + \frac{m_7 w_e}{u_{ref}^2} \frac{\partial w_e}{\partial \eta}$$

The new terms  $m_{13}$  through  $m_{17}$  account for the blade rotation and are defined as

$$m_{13} = \frac{2\Omega s_1}{u_e} \eta_1 \cos \alpha \csc \alpha$$

$$m_{14} = 2\Omega s_1 \eta_1 \csc \alpha \frac{u_{ref}}{u_e}$$

$$m_{15} = m_{13} + m_{14} \frac{w_e}{u_{ref}} \quad (17)$$

$$m_{16} = \left( \frac{u_e}{u_{ref}} \right)^2 m_{14}$$

$$m_{17} = m_{16} + m_{13} \frac{w_e}{u_{ref}}$$

The boundary conditions for the transformed equations are

$$f = f' = g = g' = 0 \text{ at } \sigma = 0$$

$$f' = 1, g' = w_e/u_{ref} \text{ at } \sigma = \sigma_\infty$$

#### 4. INITIAL CONDITIONS

The propeller boundary-layer solution is obtained by marching in the radial direction for chordwise locations increasing from the leading edge to the trailing edge. In this manner, the computation covers the entire blade surface. The solution procedure requires initial velocity profiles along two intersecting planes. These planes are chosen to be the propeller leading edge and hub. Although the marching begins at the radial location termed the hub, the actual flow at hub/blade intersection is too complex to be represented by the boundary-layer analysis. For this paper, the term hub defines a small radial distance outboard of the actual hub/blade intersection where the boundary-layer equations apply. Since the initial conditions are not, in general, known quantities for a given blade geometry, assumptions become necessary to begin the computation. The remainder of this section describes the initial conditions adopted in the present propeller boundary-layer calculation.

For the rotating helical blade, Banks and Gadd (1962) theoretically show that the leading-edge similarity function for the streamwise velocity  $u$  satisfies the Blasius equation. This analysis can be extended for application to the propeller blade leading-edge using the equations for the similarity solution of wedge flow. The leading-edge solution of this paper is similar to that adopted by Itoh, et al. (1984) in which the Karman-Pohlhausen profile is used. However, the current method computes the crossflow velocity component  $w$  at the leading edge from the  $\eta$ -momentum equation. Itoh, et al. (1984) set these profiles to zero. With the present analysis, the governing equations at the leading edge are

$$\xi\text{-momentum: } (bf'')' + m_1 f f'' - m_2 (f')^2 + m_{11} = 0$$

$$\eta\text{-momentum: } (bg'')' + m_1 f g'' + m_{12} = 0$$

with the same coefficient terms  $b, m_1, m_2, m_{11}$  and  $m_{12}$  defined in equations 15 through 17. These equations compute two-dimensional stagnation flow, wedge flow, or flat plate flow at zero incidence depending upon the specified external potential flow velocities at the leading edge. This solution has proven to be both stable and smooth in the boundary-layer calculation at the leading edge and does not require averaging or iterating.

For nonrotating three-dimensional calculations, the second initial condition is specified at locations where the crossflow velocity  $w$  equals zero everywhere inside the boundary layer. For the ship hull (Cebeci, et al. (1978)) and the arbitrary wing (Cebeci et al. (1977)), the locations of zero crossflow are the ship keel and the wing root, respectively. For these regions, the  $\eta$ -momentum equation is identically equal to zero and the unknown variables become  $u, v$ , and  $\frac{\partial w}{\partial \eta}$ . That

is, for  $w=0$ , Equation 14 becomes  $0=0$ . To obtain a solution, a new equation is derived by differentiating the singular  $\eta$ -momentum equation with respect to  $\eta$ . This equation is called the attachment line equation.

For a propeller blade, the solution  $w=0$  everywhere inside the boundary layer is valid only for the blade radius equal to zero and, therefore, should not be used to begin the computation for arbitrary nonzero radii. Itoh, et al. (1984) apply the attachment line solution to the hub of the axial flow pump blade but find it necessary to use an iterative method to obtain a reasonable solution at the hub. In this paper, the method of a similarity solution is adopted at the hub as well as at the leading edge. The similarity relations used at the present time are:

$$\frac{u}{u_e} = F(\xi, \sigma); \quad \frac{\partial}{\partial \eta} \frac{u}{u_e} = 0$$

$$\frac{w}{u_{ref}} = \frac{u_e}{u_{ref}} \frac{w}{u_e} = \frac{u_e}{u_{ref}} G(\xi, \sigma) + \frac{u}{u_{ref}} \frac{w_e}{u_e}$$

$$\frac{\partial \frac{w}{u_{ref}}}{\partial \eta} = \frac{\partial \frac{u_e}{u_{ref}}}{\partial \eta} G(\xi, \sigma) + \frac{u}{u_{ref}} \frac{\partial w_e}{u_e \partial \eta} \quad (19)$$

For the special case of  $w_e = 0$ , as in the rotating disk solution reduces the similarity relations reduce to

$$\frac{u}{u_e} = F(\xi, \sigma)$$

$$\frac{w}{u_{ref}} = \frac{u_e}{u_{ref}} G(\xi, \sigma) \quad (20)$$

$$\frac{\partial \frac{w}{u_{ref}}}{\partial \eta} = \frac{\partial u_e}{\partial \eta} \frac{1}{u_{ref}} G(\xi, \sigma)$$

This hub similarity condition is exact for the cases of laminar flow on a rotating segment and a two-dimensional swept wing.

By substituting the general similarity formulations in Equation 19 into the momentum Equations 13 and 14, the derivative quantities  $\partial w / \partial \eta$  are eliminated and marching can proceed in the  $\xi$ -direction. Details of the numerical procedure used in the computer code at the hub are given in Section 6 in the numerical analysis. The procedure is self-starting and stable.

## 5. TURBULENCE MODEL

The governing flow equations presented in Section 4 contain more unknown quantities than equations. A standard procedure in boundary-layer solutions is the introduction of a turbulence model to approximate the Reynolds stress terms  $-u'v'$  and  $-v'w'$ . Various techniques have been developed to handle turbulence modeling, all involving some degree of correlation with experimental data. The zero-equation model is the simplest approach and does not require the solution of any additional differential equations. This method assumes the algebraic specification of both length scale and turbulence energy as explained and used by Cebeci and Smith (1974). The one-equation model solves an equation for the turbulence energy but uses an algebraic specification for the length scale. Although this formulation has been used by Bradshaw, et al. (1976) for thin shear-layers with considerable success, its usage is not wide-spread. Two equation turbulence models, particularly the K- $\epsilon$  model, are experiencing increased popularity. These models are general, but require the solution of two differential equations.

For the present work, the simple zero-equation model of Cebeci and Smith (1974) has been adopted. An eddy-viscosity factor  $\epsilon_m$  is defined to relate the Reynolds stresses to the mean velocity profiles by

$$-\overline{u'v'} = \epsilon_m \frac{\partial u}{\partial \xi} \quad \text{and} \quad -\overline{v'w'} = \epsilon_m \frac{\partial w}{\partial \xi} \quad (21)$$

The theoretical boundary layer is divided into an inner region and an outer region with a separate equation defining  $\epsilon_m$  in each region. The inner-region formulation is applied from the wall surface to the location in the boundary layer where both inner and outer equations predict the same eddy viscosity. From this location to the edge of the boundary layer, the outer wall formulation is applied.

Eddy viscosity in the inner region is defined as

$$(\epsilon_m)_i = L^2 \left[ \left( \frac{\partial u}{\partial \xi} \right)^2 + \left( \frac{\partial w}{\partial \xi} \right)^2 + 2 \cos \alpha \left( \frac{\partial u}{\partial \xi} \frac{\partial w}{\partial \xi} \right) \right]^{1/2} \quad (22)$$

where  $L$  is a mixing length approximation equal to  $0.4\zeta [1 - \exp(-1 - \zeta/A)]$ ,  $A$  is a damping factor

equal to  $26\nu(\tau_{tw}/\rho)^{1/2}$ , and  $\tau_{tw}$  is the turbulent

wall shear stress equal to  $\mu \left[ \left( \frac{\partial u}{\partial \xi} \right)_w^2 + \left( \frac{\partial w}{\partial \xi} \right)_w^2 \right]$

$+ 2 \cos \alpha \left( \frac{\partial u}{\partial \xi} \right)_w \left( \frac{\partial w}{\partial \xi} \right)_w \right]^{1/2}$ . In the outer region, the

eddy viscosity becomes

$$(\epsilon_m)_o = 0.0168 \left| \int_0^\infty (u_{te} - u_t) d\zeta \right| \gamma_{tr} \quad (23)$$

where  $u_{te}$  equals  $(u_e^2 + w_e^2 + 2u_e w_e \cos \alpha)^{1/2}$ ,  $u_t$  equals  $(u^2 + w^2 + 2uw \cos \alpha)^{1/2}$  and  $\gamma_{tr}$  is an intermittency factor to account for the transition region between viscous and turbulent flow.

## 6. NUMERICAL ANALYSIS

The governing three-dimensional boundary-layer equations for propeller blades are solved numerically using the Keller (1970) box method. This solution technique may be divided into four steps. Initially, the governing equations are written as a system of first order equations by the introduction of transformed variables. The first order equations are then written in finite difference form using central differences. Newton's method is applied to linearize the difference equations and, finally, the linear system is solved by the block triangular elimination method. New variables  $u$ ,  $v$ ,  $w$ ,  $t$ , and  $\theta$ , defined as

$$\begin{aligned} u' &= v = f'' \\ w' &= t = g'' \\ \theta' &= m_1 u + m_6 w + m_{10} \frac{\partial u}{\partial \xi} + m_7 \frac{\partial w}{\partial \eta} \end{aligned} \quad (24)$$

are introduced to reduce the  $\xi$ - and  $\eta$ -momentum equations to first order. The new system is

$$\begin{aligned} u' &= v \\ w' &= t \\ (bv)' &= m_2 u^2 + m_5 u w + m_8 w^2 + m_{11} \end{aligned}$$

$$\begin{aligned} & (bt)' - m_{4u}w - m_{3w}^2 - m_{9u}^2 + m_{12} \\ & + m_{16}u + m_{13}w - m_{17} + \theta t \\ & = m_{10}u \frac{\partial w}{\partial \xi} + m_{7w} \frac{\partial w}{\partial \eta} \\ & \theta' = m_{1u} + m_{6w} + m_{10} \frac{\partial u}{\partial \xi} + m_{7} \frac{\partial w}{\partial \eta} \end{aligned}$$

$$u = w = \theta = 0 \text{ at } \sigma = 0 \quad (26)$$

$$u = 1, \quad w = \frac{w_e}{u_{ref}} \text{ at } \sigma = \sigma_\infty$$

The calculation of the blade boundary-layer proceeds as follows. Solution marching begins at the hub/leading-edge intersection and moves outward along increasing radii to the tip. Calculations continue in this manner for successively increasing chordwise stations until, finally, the blade trailing edge is reached. Calculations are made over the entire blade surface.

leading edge begin as laminar at the node denoted (A) in Figure 2 and march radially outward. After completing the leading edge, the solution is obtained at the location of the next chord and first outward radius from the hub, node (B) in Figure 2, using a modified characteristic box method (Bradshaw, et al. (1981)). The characteristic box, which estimates a solution based on the results at the previous chordwise position lying along the same streamline, is traditionally applied only in regions of reverse crossflow. However, this method has been found to be extremely beneficial for propeller blade application near the hub in that it eliminates a complex solution of hub initial conditions.

$$\begin{aligned} (f')_H &= (f')_B \\ (g')_H &= \left( \frac{u_e}{u_{ref}} \right)_H \left( g' \frac{u_{ref}}{u_e} - \frac{f' w_e}{u_e} \right) + (f)_B (g')_H \end{aligned}$$

A transition computation is not incorporated in the present boundary-layer scheme and the location of transition to turbulent flow is an input parameter supplied by the user. The location of transition may be estimated by experimental results, such as flow



visualization techniques, or by assuming transition empirically. One empirical formulation which may be used is the flat-plate critical Reynolds number,  $R_x = \Omega r^2 \theta / \nu = 3 \times 10^5$ . The input transition location is overridden if laminar separation, identified as a negative streamwise skin friction coefficient, occurs. Once transition occurs, each succeeding node is computed as turbulent. Presently, the calculations stop once turbulent separation is encountered.

## 7. COMPUTATIONAL RESULTS AND DISCUSSION

A variety of geometries were considered during the verification stage of the three-dimensional boundary-layer computation scheme. These geometries include a flat plate, a rotating disk, rotation above the ground, a skewed and an unskewed rotating segment, an upwarped model propeller, and three model propellers, one with warp, one with skew, and one with neither warp nor skew. Overall agreement with exact solutions and test results is quite good. The largest discrepancy with experimental data occurs for the limiting streamline angle  $\beta$  in turbulent flows.

Computational results are presented for the following geometries. A single, nonlifting blade of large chord length is examined initially. Predictions in the initial laminar flow region are compared with the results of Banks and Gadd (1962) on a rotating sector and with Morris's (1981) predictions on a helical blade. The boundary layer on this blade is computed a second time with a small laminar flow region to simulate the test conditions of Lakshminarayana, et al. (1972). At large chord length, this blade approximates a rotating disk and comparisons are shown with turbulent flow solutions for a disk. To investigate the laminar flow region more extensively, the flow about a three-bladed model propeller is examined. Transition for this blade is set at 43 percent of the chord length to simulate the test data of Jessup, et al. (1984). Comparisons are made with the suction surface measurements of Jessup, et al. at the fraction of radius  $x_r = 0.7$ . Finally, the effects on the boundary layer of the geometry parameters warp and skew are examined using three model propellers. No experimental results exist for these blades.

### 7.1 Rotating Segment

The large chord length rotating segment examined is the blade generated for investigation of turbulent flow by Lakshminarayana, et al. (1972). The blade, shown in Figure 3, is a single nonlifting rotating sector of 92.6 cm (36.6 in.) diameter with a 300 degree included angle. The hub radius is 22.86 cm (0.75 ft.). The pitch/diameter ratio of 0.273 for this blade is small enough to approximate the blade by a flat circular disk with a leading and trailing edge 300 degrees apart. Present calculations are performed using the surface coordinates  $\xi$  (or  $x_c$ , fraction of chord),  $\eta$  (or  $x_r$ , fraction of

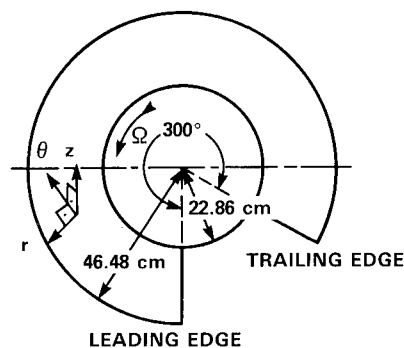


Fig. 3 - Geometry and Coordinates of Rotating Helical Segment

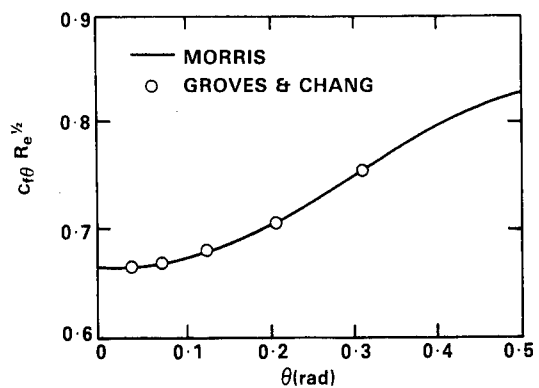
radius), and  $\zeta$  (surface normal). For comparisons with measured data, the cylindrical coordinates ( $r$ ,  $\theta$ , and  $z$ ) are used where  $r$  is the dimensional radius varying in the radial direction,  $\theta = 300\pi\xi/180$  radians varying in the chordwise direction, and  $z$  varies along the surface normal as  $z = \zeta$ .

Lakshminarayana, et al. (1972) tested the blade in a housing with a 0.20 cm (0.08 in.) clearance between the blade tip and the wall. The free-stream onset flow was zero and the rotational speed of the blade, denoted  $\Omega$ , remained constant at 47 rad/sec (450 rev/min). The kinematic viscosity  $\nu$  equaled  $1.49 \times 10^{-5} \text{ m}^2/\text{s}$  ( $160 \times 10^{-6} \text{ ft}^2/\text{sec}$ ) which corresponds to air at 20°C (68°F). These conditions, which yield a Reynolds number based on tip radius and tip rotational speed of  $7 \times 10^5$ , are used in the evaluation of the present method. In addition, present calculations begin at the blade surface location  $\theta = 0.016$  radians and  $x_r = r/R = 0.492$ .

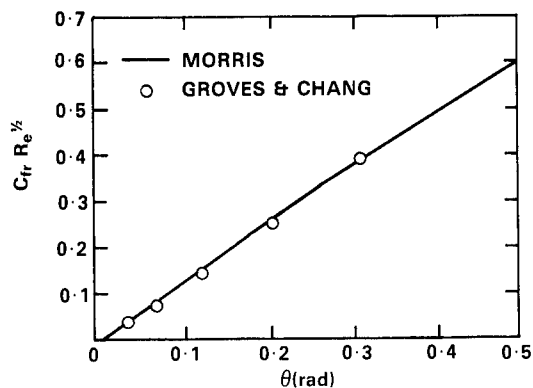
Initially, a boundary-layer calculation of the rotating blade was made with transition set to 1.0 radian to allow a comparison with the laminar flow predictions of Banks and Gadd (1962) on a flat sector and of Morris (1981) on a helical blade. The comparisons with the predictions of Morris (1981) are valid at large radii; the twisted blade used by Morris has not yet been evaluated with the present method. Nonetheless, the large radii comparison is important for validating the radial skin friction coefficient. Figures 4 a through c show comparisons with Morris's (1981) calculations at  $r/R = 0.95$ . Figures 4a and 4b compare the streamwise and radial skin friction coefficients

$$C_{f\theta} = \frac{\tau_c}{\frac{1}{2}\rho u_{ref}^2} ; C_{fr} = \frac{\tau_r}{\frac{1}{2}\rho u_{ref}^2}$$

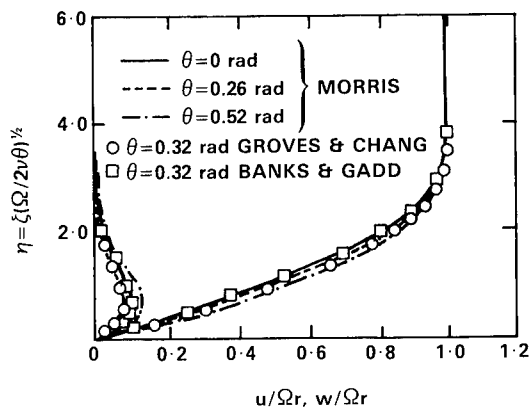
In these definitions,  $\tau_c$  and  $\tau_r$  are the shear stresses in the chordwise and radial directions, respectively,  $\rho$  is the fluid density, and  $u_{ref}$  is the reference velocity. The solid lines in Figures 4a and 4b denote the Morris computation and the circles denote the present calculations. The agreement between the two prediction methods is excellent.



(a) STREAMWISE SKIN FRICTION COEFFICIENT



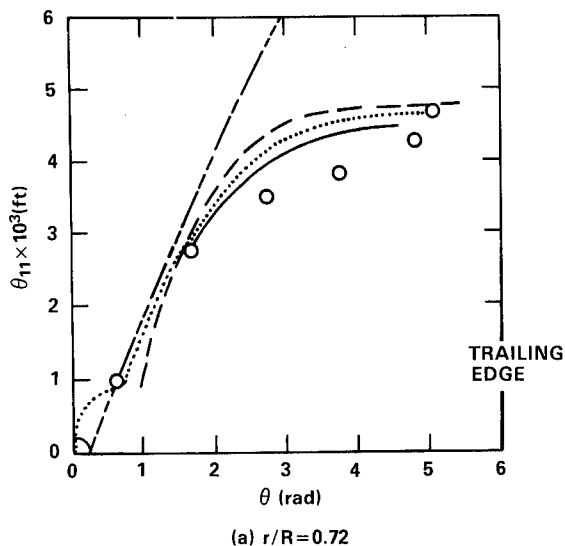
(b) RADIAL SKIN FRICTION COEFFICIENT



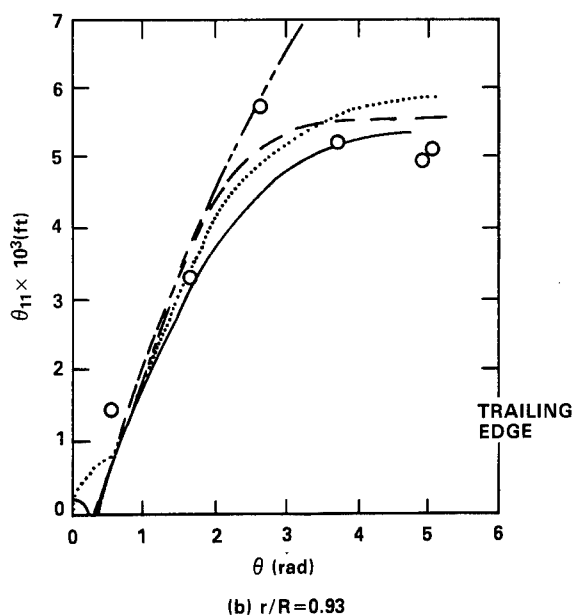
(c) VELOCITY PROFILES

Fig. 4 - Laminar Flow Comparisons for Rotating Helical Segment at  $r/R=0.95$

Crosswise and radial velocity profiles are compared in Figure 4c. Morris's profiles are shown at chordwise locations of 0, 0.26, and 0.52 radians. The present predictions are shown at  $\theta = 0.32$  radians as the circle. The square symbols denote the radial and crosswise velocity of Banks and Gadd (1962) at  $\theta = 0.32$  radians. This figure shows that the laminar crosswise velocity profile is predicted quite well and the radial velocity profile is just slightly underpredicted by the present method.



(a)  $r/R=0.72$



(b)  $r/R=0.93$

MEASURED  
(LAKSHMINARAYANA ET AL.)

COMPUTED {  
FLAT PLATE  
LAKSHMINARAYANA ET AL.  
INTEGRAL  
DIFFERENTIAL

Fig. 5 - Variation of Momentum Thickness  $\theta_{11}$  on Rotating Helical Blade

A second calculation was made with transition set to  $\theta = 0.32$  radians. This location is forward of the experimentally determined transition location of  $\theta = 0.73$  radians. However, with the gradual transition model used in the current computer code, this forward transition location gives good agreement with



the flow parameters calculated by Lakshminarayana, et al. (1972).

Figures 5a and 5b show the momentum thickness as a function of chordwise position for fraction of radius,  $x_R$ , values of 0.72 and 0.93, respectively. The streamwise momentum thickness is defined as

$$\theta_{11} = \int_0^{\infty} \left(1 - \frac{u}{u_e}\right) \frac{u}{u_e} d\zeta$$

The dotted lines denoting the present calculation and the dashed lines denoting the calculation of Lakshminarayana, et al. are in close agreement. The experimental data are denoted by the circular symbols. At the radial location  $r/R = 0.72$  shown in Figure 5a, all calculation methods overpredict the measured values of  $\theta_{11}$  for 2 radians  $< \theta < 5$  radians. However, agreement between experiment and theory is quite good for the early stages of turbulence,  $\theta < 2$  radians, and for the blade trailing edge,  $\theta > 5$  radians. The experimental data shown in Figure 5b at the radius  $r/R = 0.93$  are more scattered. Agreement between experiment and theory at this radius is reasonable only for  $\theta < 2$  radians.

The tangent of the limiting streamline angle  $\beta$ ,  $\beta = \tan^{-1} \left( \frac{C_{fr}}{C_{f\theta}} \right)$ , is shown in Figure 6.

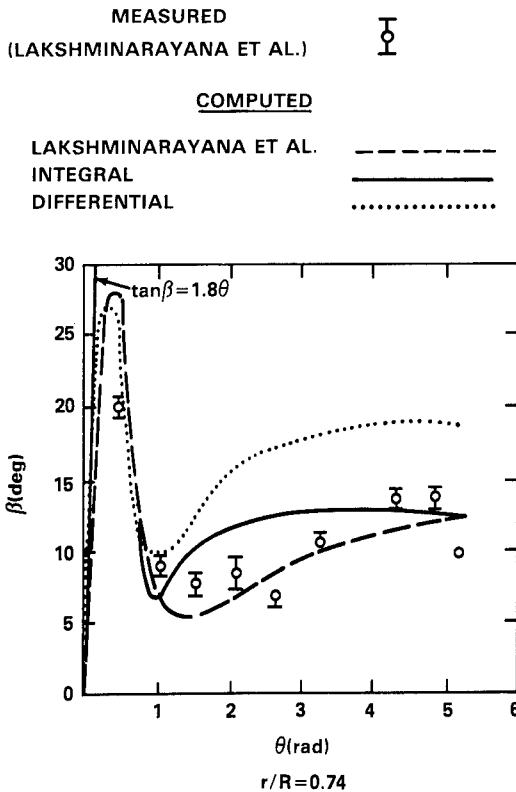


Fig. 6 - Variation of Limiting Streamline Angle  $\beta$  on Rotating Helical Segment

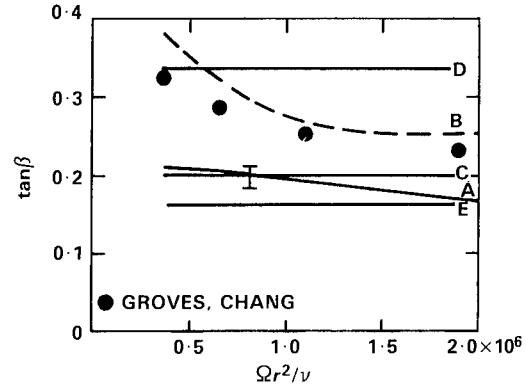


Fig. 7 - Angles of Surface Streamlines on a Rotating Disk; I, experiment; A, Cham and Head calculation using the entrainment method; B, calculation with isotropic eddy viscosity; C, Banks & Gadd (1962); D, Goldstein (1935); E, von Kármán (1921).

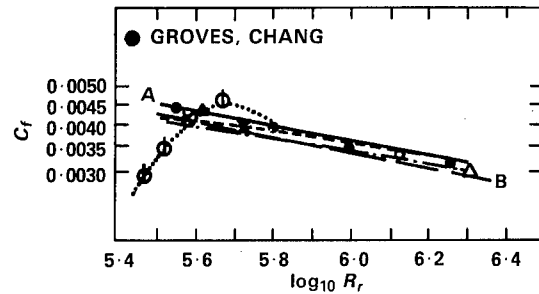


Fig. 8 - Development of the Streamwise Skin-Friction Component. — A, Cham and Head calculation using the entrainment method; — B, von Kármán (1921); --- C, Goldstein (1935); -.- D, calculation, with isotropic eddy viscosity; . . . E, Theodorsen & Regier (1944). Results taken from Clauser plots of the present measurements: X, 515 rev/min; O, 1000 rev/min; Δ, 1550 rev/min.

The momentum integral methods of both Lakshminarayana, et al. (1972) and Groves (1981) show closer agreement to the measured values of  $\tan \beta$  than does the present method. Figure 7, from the Cham and Head (1969) study of the turbulent boundary-layer flow on a disk, shows the discrepancy in various calculation methods of the parameter  $\tan \beta$ . As shown by the dotted line labeled B and the circular symbols denoting the present calculation method, the eddy viscosity model predicts a larger value of the limiting streamline than do the other turbulence models. Referring to Figure 6 again, the solid line labeled  $\tan \beta = 1.8\theta$  shows the exact analysis result of Banks and Gadd (1962) for laminar flow on a rotating segment. The present calculation agrees well with this line. One further factor to note is that the momentum integral method of Groves (1981) included a modification to reduce the entrainment function from the flat plate value to include the rotational effect. The viscosity coefficient in the differential method has not been modified. The current  $\tan \beta$  prediction may be reduced if a more precise eddy viscosity model were used.

The final comparison shows the skin friction coefficient for a rotating disk. Figure

8, taken from Cham and Head (1969), shows comparisons of experimental data with several calculation methods. The circled asterisks denoting the present predictions are in good agreement with both previous theories and measured data.

In summary, the present differential method solution procedure has been shown to accurately predict both laminar and turbulent boundary-layer characteristics on a simple three-dimensional blade. The previous momentum integral methods of Groves (1981) and Arakawa, et al. (1983) could not predict laminar flow, a region important in model propeller and instability applications. The limiting streamline angle for turbulent flow is overpredicted, perhaps indicating that a change in the eddy viscosity model is needed to account for the rotation.

## 7.2 Propeller 4119

DTNSRDC Model Propeller 4119 (see Denny (1968) for the complete model geometry) was evaluated experimentally on the suction surface by Jessup, et al. (1984) in the DTNSRDC 24-in water tunnel. The three-bladed unskewed, propeller model has a 0.30 m (1 ft) diameter with a hub radius of 0.03 m (0.1 ft). The design advance coefficient  $J_V$  of the model is 0.833 where  $J_V = V/(nD)$  and  $V$  equals the onset speed,  $n$  is the constant rotational speed in revolutions per unit time, and  $D$  is the rotor diameter. The flow conditions set for Jessup's (1984) experiments are the kinematic viscosity of 68° fresh water  $\nu = 1.00 \times 10^{-6} \text{ m}^2/\text{s}$  ( $1.08 \times 10^{-5} \text{ ft}^2/\text{sec}$ ), the onset velocity  $V = 1.83 \text{ m/s}$  (6.0 ft/sec) and the rotational speed  $\Omega = 44 \text{ rad/s}$  (7 rev/sec). These conditions yield a 0.7-radius Reynolds number of  $R_n = 7.3 \times 10^5$  where

$$R_n = \frac{(c)_{0.7} V \sqrt{1 + \left(\frac{0.7\pi}{J_V}\right)^2}}{\nu} \quad (27)$$

and  $(c)_{0.7} = 0.14 \text{ m}$  (0.46 ft) is the blade chord at 0.7 radius.

The 0.7 radius was chosen for comparison with Jessup's (1984) experiments since the measured data are most complete at this radius. Flow visualization techniques predict fully turbulent flow begins in the region between fraction of chord values  $x_c$  of 0.5 to 0.6. The present theoretical eddy viscosity model incorporates an intermittency region of gradual transition from laminar to turbulent flow. The use of an intermittency region requires an early specification of the transition location to the computational scheme. It has been determined by trial and error that an input transition location to the computational procedure of  $x_c = 0.43$  yields fully turbulent flow at the chord values  $x_c$  of 0.5 to 0.6.

The boundary-layer characteristics compared with experimental data are the streamwise displacement thickness

$$\delta^* = \int_0^\infty \left(1 - \frac{u}{u_e}\right) d\zeta, \text{ the shape factor } H = \delta^*/\theta,$$

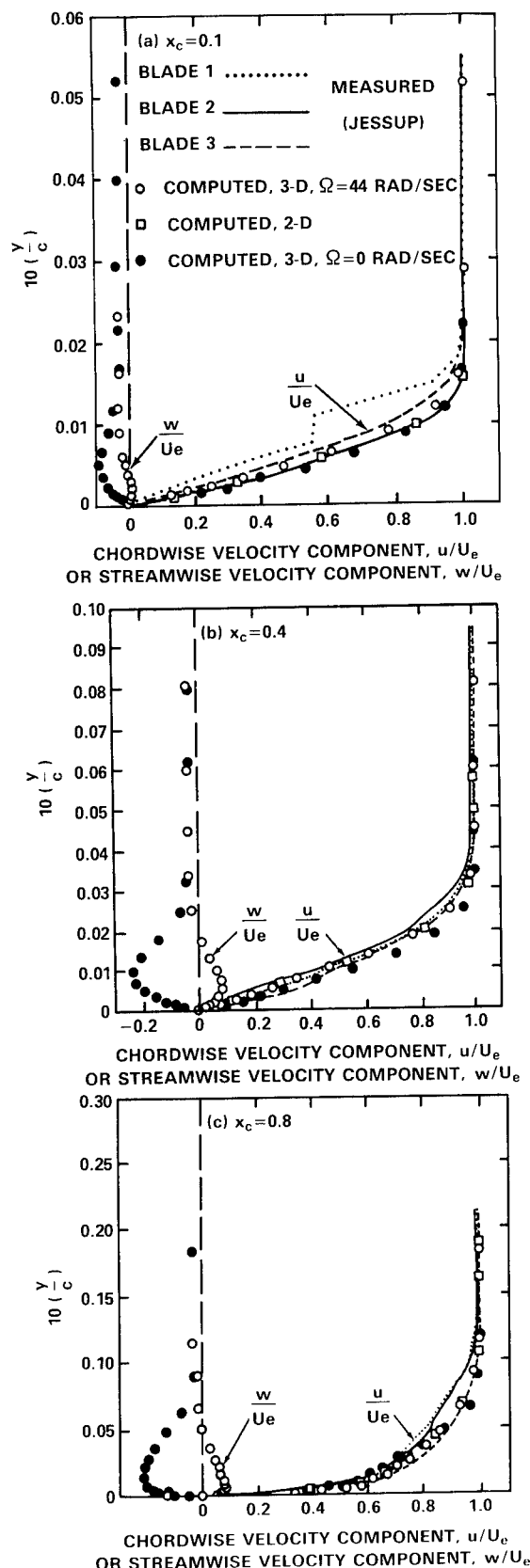


Fig. 9 - Velocity Profile Comparison on Model Propeller 4119

and the chordwise velocity  $u$ . In addition, the momentum thickness  $\theta_{11}$  and skin friction coefficient  $C_f$  are compared with two-dimensional predictions from a computer code developed by Cebeci (1978). The radial velocity  $w$  and the limiting streamline angle  $\beta$  are the two parameters shown which are unique to three-dimensional flow. No measurement has been made of these quantities as yet. A second calculation was made using the present method. This calculation is performed with the rotational effects included in the potential-flow velocities but not in the boundary-layer computation. These results, which approximate the rotating flow above a solid ground, are also presented.

Figures 9 through 14 show the boundary-layer comparisons for Model 4119. The series of dashed and dotted lines in Figures 9a through 9c represent Jessup's (1984) measured chordwise velocity profiles for the three blades at three chordwise locations,  $x_c = 0.1, 0.4, 0.8$ , respectively. The boundary layer is shown to thicken considerably as the blade trailing edge is approached. The open circles and squares, denoting the fully-rotational three-dimensional calculation and the two-dimensional calculation, respectively, are both shown to approximate the measured chordwise profiles equally as well. However, the calculation without the rotation in the boundary layer overpredicts the velocity. It is further seen from Figure 9 that disregarding the rotational effects in the boundary-layer computation leads to the prediction of an inward rather than an outward radial flow. An inward flow contradicts the flow visualization results of Jessup (1984).

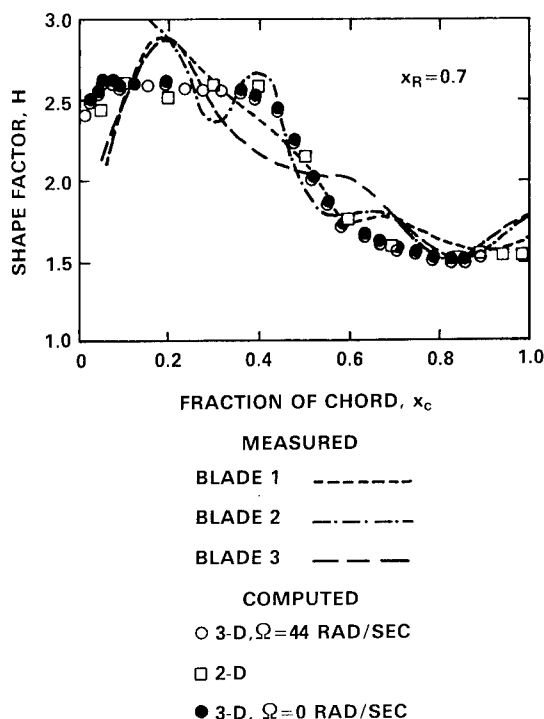


Fig. 10 - Variation of Shape Factor on Model 4119

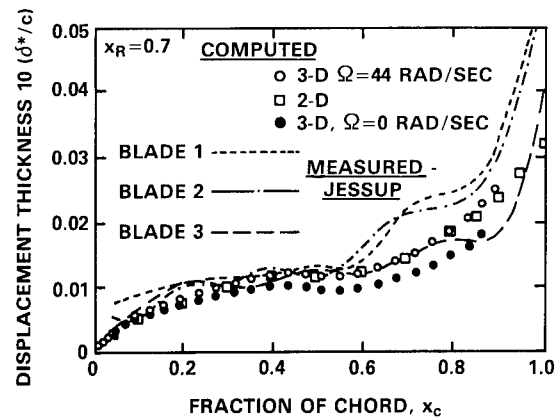


Fig. 11 - Variation of Displacement Thickness on Model 4119

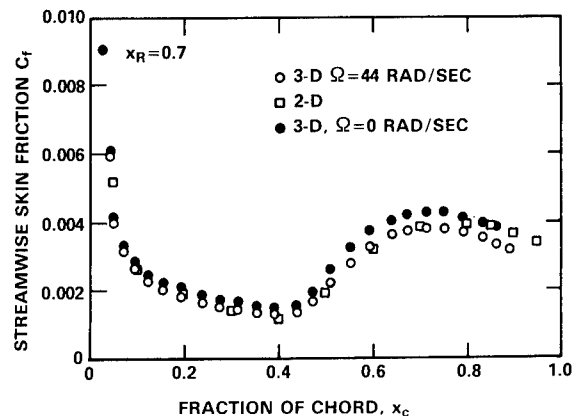


Fig. 12 - Variation of Streamwise Skin Friction Coefficient on Model 4119

Considerable scatter is noted in Figure 10 for the measured shape factor parameter  $H$ . Nevertheless, the overall character of the variable is reasonably well-predicted by the various theoretical methods, including the three-dimensional boundary layer without rotation. The displacement thickness, shown in Figure 11 is again well-predicted by two-dimensional flow theory and three-dimensional flow theory with rotation. Without the rotational effects, three-dimensional flow is shown to underpredict the displacement thickness.

Jessup (1984) does not present measurements for either the streamwise skin friction coefficient  $C_f$  or the momentum thickness  $\theta_{11}$ . Comparisons of the calculated values of  $C_f$  and  $\theta_{11}$  are given in Figures 12 and 13. Again, two-dimensional theory agrees well with three-dimensional predictions with rotation and both disagree somewhat with three-dimensional predictions with no rotation.

Finally, the tangent of the limiting streamline angle  $\beta$  is compared in Figure 14 for the three-dimensional calculations with and without rotation. Unsurprisingly, this para-

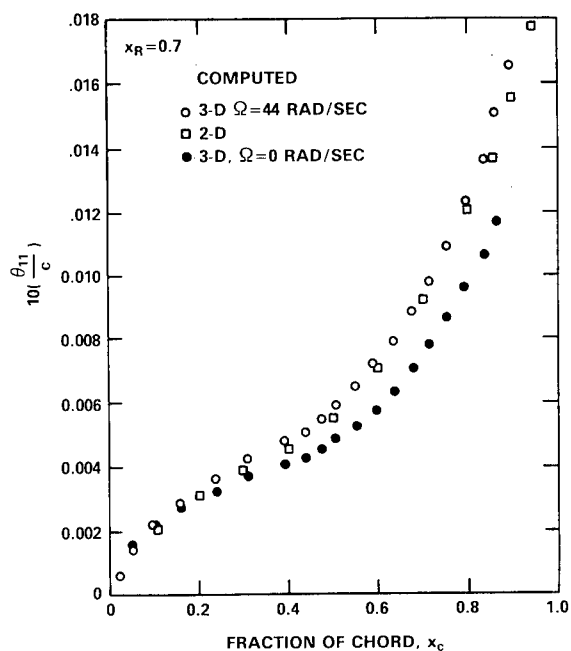


Fig. 13 - Variation of Streamwise Momentum Thickness on Model 4119

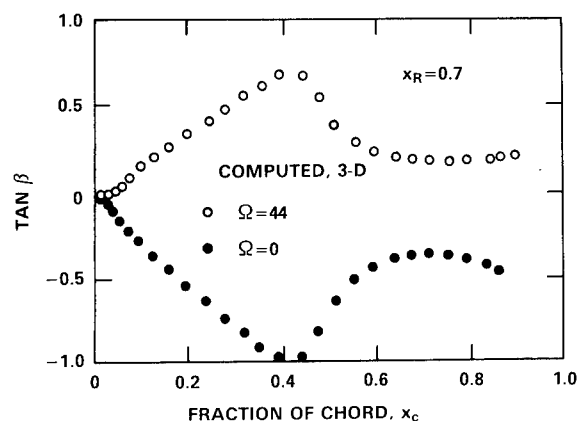


Fig. 14 - Variation of Limiting Streamline Angle on Model 4119

meter is positive for flow with rotation and negative for flow with no rotation, as predicted for the radial velocity distribution.

To summarize, the boundary layer characteristics of a propeller blade can be computed with reasonable accuracy. Two dimensional theory gives excellent predictions of the flow for applications where crossflow is not important. Applications where the crossflow is important, including model propeller studies where large regions of laminar flow exist and in the study of instability, require use of the full three-dimensional equations. The use of three-dimensional theory without including rotation in the boundary-layer solution should be avoided.

### 7.3 Skewed and Warped Propellers

In this section, results are presented for the computed boundary-layer characteristics of three analytically-defined propeller blades. These three 0.30 m (1 ft) diameter model propellers were chosen to investigate the effects of varying geometry on boundary-layer flow. The propellers, denoted as Model 4381, an unwarped blade; Model 4498, a 72-degree warped blade; and Model 4383, a 72-degree skewed blade, are depicted in Figure 15. The complete geometry of these model propellers is given in Groves (1981) and is not repeated here.

Since no experimental data exist for these particular models, the transition location must be estimated. Unpublished experimental results at DTNSRDC on a similar geometry indicate that the flow over the blades is fully turbulent at a 0.7-radius Reynolds number of  $4 \times 10^6$ . This Reynolds number corresponds to tripping the boundary layer at the fraction of

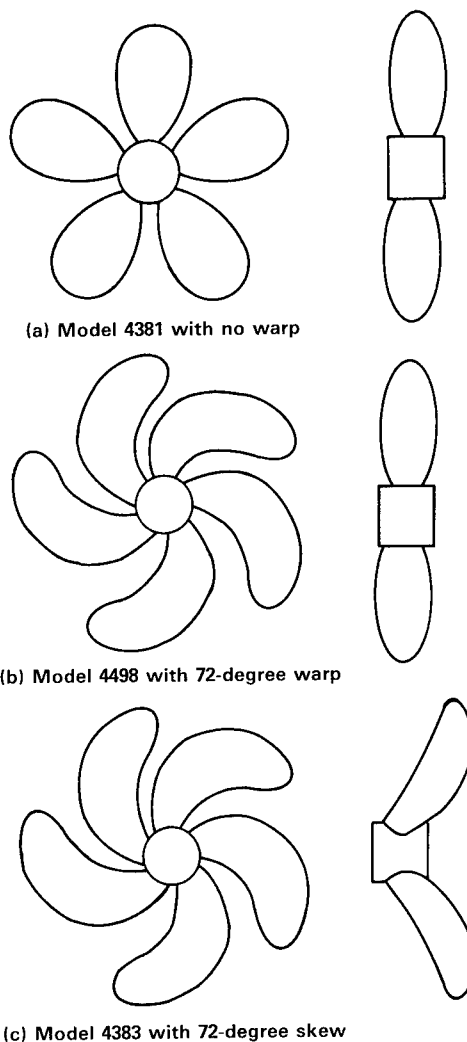


Fig. 15 - Geometry of Three Model Propellers

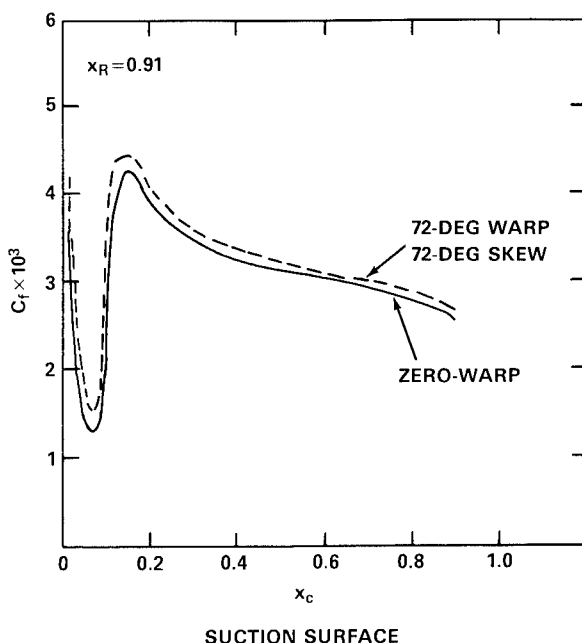


Fig. 16 - Variation of Streamwise Skin Friction Coefficient on Three Model Propellers

chord value  $x_c = 0.18$ . The design advance coefficient  $J_y$  of all three models is 0.889 and the flow conditions are  $v = 1.191 \times 10^{-6} \text{ m}^2/\text{s}$  ( $1.28 \times 10^{-5} \text{ ft}^2/\text{sec}$ ),  $V = 16.9 \text{ m/s}$  ( $55.3 \text{ ft/sec}$ ), and  $\Omega = 391.5 \text{ rad/sec}$ .

Figure 16 shows the predicted skin friction coefficient on the suction surface for the three model propellers at the fraction of radius value  $x_r = 0.91$ . This location corresponds to streamline 14 used for comparisons in the earlier work of Groves (1981) where the turbulent boundary layer is computed using momentum integral methods. The present results predict only a slight increase in the skin friction coefficient for the warped and skewed blades. This contradicts the results obtained by the integral method of Groves (1981) where the skin friction coefficient was predicted to increase by nearly 30 percent for the zero warp blade. An investigation into the momentum integral coding has identified an error in the specification of certain geometry parameters for these blades and thus leads to the different and erroneous earlier conclusion of Groves.

## 8. CONCLUSIONS

This paper presents analysis and results for computing three-dimensional laminar and turbulent boundary layers on the surface of a propeller blade using the differential method. The solution procedure is a modification of the Cebeci, et al. (1978) scheme for boundary-layer calculations on three-dimensional ship hulls. The major changes to the scheme result from the propeller blade rotation, the complex propeller

geometry, and the specification of initial conditions in order to begin the calculation procedure. Typical boundary layer computations use a grid of 30 chordwise and 23 radial points thereby covering the entire blade surface. For this grid size, 64 seconds CPU time on a CYBER 176 computer are required for a complete calculation.

Overall, the predicted boundary-layer parameters are shown to give reasonable agreement with experimental data for both simple (rotating disk and rotating helical segment) bodies and a model propeller. The largest discrepancies between the current predictions and experimental data and previous theories occur for the limiting streamline angle  $\beta$  which is overpredicted in the turbulent region. For the rotating segment, this parameter is shown to be correctly computed by the differential method in the laminar region. For turbulent flows, momentum integral methods, which include a modified entrainment function to account for rotational effects, have been shown (see Banks and Gadd (1962) and Groves (1981)) to improve the prediction of  $\tan\beta$ . The viscosity coefficient in the present differential method has not been modified. The value of  $\tan\beta$  may be reduced if the eddy viscosity were modeled more precisely.

The analysis of model Propeller 4119 has provided insight into the boundary-layer calculation on propeller blades. First, the large extent of laminar flow on the model blade necessitates the capability of a laminar calculation procedure and an instability prediction method to determine the transition location. Figures 9 through 13 show that two-dimensional theory can be used for the prediction of boundary-layer parameters such as chordwise velocity profiles, shape factor, and chordwise skin friction. However, applications involving crossflow, such as the instability calculation or tip vortex investigations, require the full three-dimensional computation. Figures 9 and 14 show the dangers of using a partially rotating three-dimensional calculation. Incorrect values of the crossflow velocities and  $\tan\beta$  are predicted when rotation is included in the potential-flow solution and not included in the boundary-layer solution.

Calculations of the three-dimensional boundary-layer characteristics of three model propellers of varying geometry indicate only slight differences in the skin friction parameters; see Figure 16. This result, contrary to the earlier momentum integral result of Groves (1981), led to the discovery of a geometry error in the earlier computer code.

The results in this paper are encouraging. Although computed with the present preliminary version of the code, comparisons with measured data are quite good. Further code modifications are anticipated to allow the calculation to proceed past the location of turbulent separation and to improve the eddy viscosity model. Additional comparisons will be made with the experimental data of Itoh, et al. (1984) for a rotating axial flow pump blade.

## ACKNOWLEDGEMENTS

This work was funded under the DTNSRDC General Hydrodynamics Research Program, Work Unit 1542-103, Task Area ZR0230101, Program Element 61152N.

The authors would like to thank Dr. Thomas T. Huang for his continuous support and technical guidance. Special appreciation is extended to Dr. Yu-Tai Lee and to Dr. Tuncer Cebeci of the University of California, Long Beach for their technical discussion in the difference scheme used in this paper. The authors also wish to acknowledge Ms. Lauri Jeantheau for her patient and accurate typing of the paper.

## REFERENCES

- Arakawa, C., T. Tagori, and M. Shirakura (1983): Analysis of Three-Dimensional Turbulent Boundary Layer on the Rotating Blade of Axial Flow Pump. *Trans. JSME*, 49-437(B).
- Banks, W.H.H. and G.E. Gadd (1962): A Preliminary Report on Boundary Layers on Screw Propellers and Simpler Rotating Bodies. *Nat. Physics Lab. Report SHR27*.
- Bradshaw, P., T. Cebeci and J.H. Whitelaw (1981): *Engineering Calculation Methods for Turbulent Flow*. Academic Press, New York.
- Bradshaw, P., D.H. Ferriss, and N.P. Atwell (1967): Calculation of Boundary-Layer Development Using the Turbulent Energy Equation. *J. Fluid Mech.*, Vol. 28.
- Brockett, T. (1981): *Lifting Surface Hydrodynamics for Design of Rotating Blades. PROPELLERS '81*, Virginia Beach, Va; Published by The Society of Naval Architects and Marine Engineers, New York.
- Cebeci, T. and P. Bradshaw (1977). *Momentum Transfer in Boundary Layers*. Hemisphere-McGraw Hill, Washington.
- Cebeci, T. and A.M.O. Smith (1974): *Analysis of Turbulent Boundary Layers. Applied Mathematics Mechanics*, Vol. 15, Academic Press, New York.
- Cebeci, T., K.C. Chang, and K. Kaups (1978): A General Method for Calculating Three-Dimensional Laminar and Turbulent Boundary Layers on Ship Hulls. *MDC J7998*.
- Cebeci, T., K. Kaups, and J.A. Ramsey (1977): A General Method for Calculating Three-Dimensional Compressible Laminar and Turbulent Boundary Layers on Arbitrary Wings. *NASA CR-2777*.
- Cham, T.S. and M.R. Head (1969): The Turbulent Boundary-Layer Flow on a Rotating Disk. *J. Fluid Mech.*, Vol. 37, part 1, pp. 129-147.
- Denny, S.B. (1968): *Cavitation and Open-Water Performance Tests of a Series of Propellers Designed by Lifting Surface Methods*. DTNSRDC Report 2878.
- Groves, N.C. (1981): *An Integral Prediction Method for Three-Dimensional Turbulent Boundary Layers on Rotating Blades. PROPELLERS '81*, Virginia Beach, Va; Published by The Society of Naval Architects and Marine Engineers, New York.
- Itoh, S., C. Arakawa, and T. Tagori (1984): Differential Method of 3-D Boundary Layer on the Rotating Blade of Axial Flow Pump. *Journal of Japan*, Vol. 50, No. 454B; Published by Association for Mechanical Engineers.
- Jessup, S.D., C. Shott, M. Jeffers, and S. Kobayashi (1984): *Local Propeller Blade Flows in Uniform and Sheared Onset Streams Using LDV Techniques. Fifteenth ONR Symposium on Naval Hydrodynamics*, Hamburg.
- Keller, H.B. (1970): A New Difference Scheme for Parabolic Problems. *Numerical Solution of Partial-Differential Equations*, J. Bramble (ed.), Vol. 2, Academic Press, New York.
- Lakshminarayana, B., A. Jabbari, and H. Yamaoka (1972): Turbulent Boundary Layer on Rotating Helical Blade. *J. Fluid Mech.*, Vol. 51, Part 3, pp. 545-569.
- Morris, P.J. (1981): The Three-Dimensional Boundary Layer on a Rotating Helical Blade. *J. Fluid Mech.*, Vol. 112, pp. 283-296.
- Yamazaki, R. (1981): *On the Theory of Marine Propellers in Non-Uniform Flow*. Reprinted from the *Memoirs of the Faculty of Engineering, Kyushu University*, Vol. 41, No. 3.

## DISCUSSION

Prof. JOHN P. BRESLIN,  
Stevens Institute of Technology,  
Hoboken, NJ, USA:

Ms. Groves has given us a very clear exposition of a very complicated problem.

My conception of the viscous flow over propeller blades is largely intuitive. I think that it should be necessary to start the calculation at the single stagnation point which must be on the pressure side of the blade. The boundary layer flow must migrate away from this point. It would be instructive if the authors could explain why the calculation is initiated at the root of the blade rather than at the stagnation point.

## AUTHORS' REPLY

The authors wish to thank Professor Breslin for his compliments and question.

Professor Breslin asks for an explanation of our beginning the propeller boundary-layer calculation at the blade root instead of at the stagnation point. The nature of the governing differential equations used for the flow calculations dictates that the computation initiates at both the blade root and the leading edge. At the leading edge, the present initial condition is the wedge flow solution. This condition implies that the leading edge is locally a two-dimensional stagnation line. We believe that this approximation to the leading edge initial condition is in agreement with Professor Breslin's intuition.

# A PERFORMANCE PREDICTION THEORY FOR PARTIALLY SUBMERGED VENTILATED PROPELLERS

OKITSUGU FURUYA

## ABSTRACT

A partially submerged propeller theory was developed by employing a singularity distribution method. Unsteady pressure doublets and pressure sources represented the blade camber and blade-and-cavity thickness, respectively. The induced velocities were derived by reducing the formula to a lifting line configuration. The free surface effect was considered by the image method. The induced velocities contained the singular integrals of fifth-order, which are usually numerically unstable. Effort was made to derive numerically stable formulae from these singular equations by applying a method similar to the induction factor method of Morgan and Wrench (1965) and Lerbs (1952) used for steady-state fully wetted propeller problems. These new formulae are not only applicable to the present partially submerged ventilated propeller problem but also to general unsteady subcavitating and cavitating propeller problems such as propeller starting-up and non-periodic loading problems. By combining the two-dimensional water entry-and-exit theory of Wang (1979), the thrust and torque coefficients were calculated for representative partially submerged propellers and favorably compared with the experimental data.

## NOMENCLATURE

- |  |  |
|--|--|
| <p>A, B = the coefficients for Tulin-Bukart two-term camber</p> <p><math>C_{Df}</math> = friction drag coefficient (<math>D_f / \frac{1}{2} \rho U_e^2 \cdot c</math>)</p> <p><math>C_L, C_D</math> = lift and drag coefficients (<math>L / \frac{1}{2} \rho U_e^2 \cdot c, D / \frac{1}{2} \rho U_e^2 \cdot c</math>)</p> <p><math>C_{LD}</math> = design lift coefficient used for the two-term camber</p> <p><math>\bar{C}_p, \tilde{C}_p</math> = instantaneous and time-averaged power coefficients (<math>= P / \frac{1}{2} \rho U^3 \pi R^2</math>)</p> <p><math>\bar{C}_T, \tilde{C}_T</math> = instantaneous and time-averaged thrust coefficients (<math>= T / \frac{1}{2} \rho U^2 R^2</math>)</p> <p>c = propeller blade chord</p> | <p>D = pressure drag</p> <p><math>D_f</math> = friction drag</p> <p>d = distance between the propeller shaft center and free surface</p> <p>h = the width of water layer used for two-dimensional water entry and exit analysis</p> <p>J = advance speed (<math>= U / 2\pi nR</math>)</p> <p>K = number of propeller blades</p> <p><math>\bar{K}_T, \tilde{K}_T</math> = instantaneous and time-averaged thrust coefficients (<math>\bar{K}_T = T / 16 \rho n^2 R^4</math>)</p> <p><math>\bar{K}_Q, \tilde{K}_Q</math> = instantaneous and time-averaged torque coefficients (<math>\bar{K}_Q = P / 32 \rho n^2 R^5</math>)</p> <p><math>\underline{n}_0</math> = outward normal unit vector for the propeller blade surface and wake plane</p> <p>P = propeller power and also used as loading function</p> <p><math>\hat{p}</math> = static pressure</p> <p>R = propeller radius</p> <p>r = radial coordinate</p> <p><math>r_f(\theta)</math> = distance between the propeller shaft center and the point of free surface</p> <p>S = propeller blade surface area</p> <p><math>S_b, S_c</math> = areas corresponding to the propeller blade and cavity, respectively</p> <p>T = propeller thrust</p> <p>t = time</p> <p>U = ship speed</p> |
|--|--|

Dr. O. Furuya, Tetra Tech, Inc., 630 North Rosemead Boulevard, Pasadena, California 91107, USA



$U_e$  = local effective flow velocity  
 $(=[(\omega r - w_t)^2 + (U + w_a)^2]^{1/2})$   
 $u_x^*, u_r^*, u_{\theta 0}^*$  = perturbed velocity components in  
 $x, r, \theta$  directions  
 $u$  = vector representation for  
 $(u_x^*, u_r^*, u_{\theta 0}^*)$   
 $v_x, v_r, v_{\theta 0}$  = velocity components in the  $x, r,$   
 $\theta$  directions  
 $V_a$  = incoming flow velocity to the  
propeller ( $V_a = U(1-w)$  where  $w$  is  
a ship wake factor)  
 $w_a, w_t$  = induced flow velocities in the  
axial and tangential directions  
(i.e.,  $x$ - and  $\theta$ -directions),  
respectively  
 $x_B, y_B$  = orthogonal coordinates fixed on  
the blade  
 $x$  = the coordinate in the axial  
direction, also used as nor-  
malized blade radial location  
 $(= r/R)$   
 $\alpha, \alpha_e$  = geometric and effective flow  
incidence angles  
 $\beta_g$  = geometric blade setting angles  
measured with respect to the line  
connecting the trailing edge of  
blades  
 $\beta_i$  = blade angle  $\beta_g$  corrected with the  
induced flow velocities  
 $\delta$  = Dirac delta function  
 $\bar{\eta}$  = time averaged propeller effi-  
ciency  $(= \bar{C}_T/\bar{C}_p)$   
 $\theta$  = tangential coordinates  
 $\theta_L, \theta_T$  = tangential coordinates corre-  
sponding to the blade leading  
and trailing points  
 $\tilde{\theta} = -\omega t - (\bar{v} - \bar{x}^*)/\lambda - \theta_0^*$   
 $\lambda$  = advance coefficient  $(= U(r)/\omega R)$   
 $\rho$  = fluid density  
 $\phi$  = velocity potential  
 $\omega$  = angular velocity of propeller

#### Symbols attached to variables

$\bar{\phantom{x}}$  = one bar under the variables  
refers to the quantities related  
to the image singularities

$\bar{\phantom{x}}$  = bar above the variables indicates  
that they are normalized quan-  
tities

#### Subscripts

$o$  = refers to the coordinates based  
on the inertial system

#### Superscripts

$*$  = refers to the coordinates for  
which the induced velocities are  
to be calculated

### 1.0 INTRODUCTION

In recent years partially submerged air-  
ventilated propellers have attracted growing  
attention as efficient thrusting devices used  
for high speed sea crafts. This type of pro-  
peller potentially provides a better perfor-  
mance than fully submerged supercavitating  
propellers. This seems attributable to the  
following two major factors:

- i) reduction of the hydrodynamic  
resistance for the appendages such  
as shafts, struts, etc., which would  
support the propeller in water, and
- ii) reduction of the adverse cascade  
effect by providing the free surface  
for air-ventilation.

The origin of the partially submerged pro-  
peller goes back to the late 19th Century, and  
many such propellers have been tested with dif-  
ferent types of actual boats since then.  
(Hadler and Hecker (1968) summarized its  
history in their report.) Most of the develop-  
ment conducted for the propeller was, however,  
on a trial-and-error basis and until recently  
no theoretical foundation existed for improve-  
ment of the partially submerged propeller per-  
formance. The pioneer work in this subject was  
provided by Yim (1969, 1971, 1974) who devel-  
oped the theory for the hydrodynamic entry-  
and-exit characteristics of the thin foil and  
symmetric wedge with ventilation. The method  
applied there assumed the two-dimensional flow  
field by unfolding the cylindrical plane which  
is the rotational path of a blade at a certain  
radius. The problem to be solved was therefore  
that of an unsteady blade motion going in  
(entry) and out (exit) of this water layer.  
Using a similar two-dimensional assumption,  
Wang (1977, 1979) recently solved a rather  
complete water entry-and-exit problem including  
such features as general nonsymmetric blade  
profile, ventilation and oblique entry-and-  
exit. This facilitated a convenient and power-  
ful tool for determining the two-dimensional  
sectional loading for practical blade profiles  
at various entry and exit angles.

All the theoretical works conducted so far  
were based on the two-dimensional assumptions  
and, to the best of our knowledge, we are not  
aware of any three-dimensional theory for par-  
tially submerged propellers with ventilation.  
The preliminary work of this title problem was  
conducted by the author who incorporated various  
three-dimensional effects such as propeller  
configurations and presence of a free surface.  
The unsteady propeller theory developed there

used a linearized approximation for velocities and thus could solve a linearized equation of motion for a potential function  $\phi$ . This function  $\phi$  was then determined by distributing the pressure doublets and pressure sources which represented the blade camber and blade-and-cavity thickness, respectively. The induced velocities were then derived by taking the derivatives of  $\phi$ . Up to this point the theory was developed as a lifting surface theory. However, for simplicity, this lifting surface expression was reduced to that of lifting line by shrinking the propeller chord to a single line with the total amount of loading left remaining the same. In order to represent the free surface effect for propeller performance, the image method was applied. For the image of pressure doublet, that of the same strength and sign was distributed whereas for the image of pressure source, that of the same strength but with negative sign is distributed, both on the location of the mirror image with respect to a free surface.

The induced velocities obtained there included the integrals of the fifth-order singularities. A singular integral method of Hadamard (see the report by Mangler (1951) for its detailed treatment) was employed to avoid the numerical instabilities, but resulted in only partial success. As the numerical control points along the span direction increased, first the results showed a trend of convergence but then started diverging as the number of points further increased. Although the solutions of intermediate convergence were presented and compared with the experimental data of Hadler and Hecker, the accuracy of the solutions was uncertain.

The objective of the present work was, therefore, to improve the accuracy of the theory by resolving the numerical instabilities encountered in the previous work. In order to avoid the numerical instabilities, instead of finding other numerical integral methods, better mathematical formulae for calculating the induced velocities were sought. It means that effort has been made on converting the integrals having the fifth-order singularities into those of the third-order singularities. This type of conversion is typical in the steady-state lifting-line theory but had not been done for the unsteady problem. The conversion has been successfully done here and the numerical stability and accuracy are then guaranteed by using the concept of induction factors similar to that of Lerbs (1952) and Morgan and Wrench (1965).

In the following the mathematical formulation, solution method and numerical analysis will be described in detail, followed by some representative results of computations obtained with the present theory. Although many experiments were conducted to date regarding the partially submerged propeller, they are limited for distribution. We have thus chosen the experimental data of Hadler and Hecker (1968) for comparison which existed in the open literature.

## 2.0 MATHEMATICAL FORMULATION

### 2.1 Basic Equations

Fig. 1 shows a schematic diagram of a partially submerged propeller blade rotating around the x-axis in the uniform flow of velocity  $U$  approaching from the negative infinity of  $x$ . This type of flow model is similar to that used by Cox (1968) who developed the theory for supercavitating propellers. The propeller shaft line represented by the x-axis is placed in the air domain, being apart from the free surface boundary, distance of  $d$ . The cylindrical coordinate system  $(x, r, \theta)$  will be used throughout the present analysis with no subscripts for the coordinate  $\theta$  fixed on the blade and with subscripts  $0$  for the inertial coordinate  $\theta$ . The time is measured when the center line component of the blade helical plane is located at  $\theta_0 = 0$  so that the time corresponding to that of Fig. 1 is interpreted as of negative value. It means that the event of propeller rotation started at some negative time. In order to identify the quantities related to the blade singularities from those of interest we will use superscripts  $*$  for the latter.

In the present analysis an unsteady linearized theory with inviscid and no-gravity assumptions is employed. The velocity components in the  $x, r, \theta_0$  directions are written as  $(U + u_x^*, u_r^*, u_{\theta}^*)$ . Defining the perturbed velocity quantities  $^0(u_x^*, u_r^*, u_{\theta}^*)$  by  $u$ , one can write linearized equation of motion

$$\frac{\partial u}{\partial t} + U \frac{\partial u}{\partial x} = - \nabla \frac{\hat{p}}{\rho},$$

which can be expressed in terms of velocity potential  $\phi$

$$\frac{\partial \phi}{\partial t} + U \frac{\partial \phi}{\partial x} = - \frac{\hat{p}}{\rho} \quad (1)$$

where

$$u = \nabla^* \phi. \quad (2)$$

and  $\hat{p}$  is the static pressure of the fluid.

Solution of Equation (1) for  $\phi$  is given

$$\phi(x^*, r^*, \theta_0^*; t) = - \frac{1}{U} \int_{-\infty}^{x^*-x} \frac{\hat{p}}{\rho} \left( v+x, r^*, \theta_0^*, t - \frac{x^* - (v+x)}{U} \right) dv \quad (3)$$

where the boundary condition  $p = 0$  at  $x^* = -\infty$  has been used. Applying the continuity equation  $\text{Div} \cdot u = 0$  to Equations (1) and (2), we obtain the Laplace equation for  $\hat{p}$ ,

$$\nabla^{*2} \hat{p} = 0.$$

Green's theorem will be used for  $\hat{p}$  which satisfies the above Laplace equation so that the solution for  $\hat{p}$  can be expressed

$$\hat{p}(x^*, r^*, \theta_0^*; t) = p + \bar{p} \quad (4)$$

where

$p(x^*, r^*, \theta_o^*; t)$  = Pressure due to the real blade (pressure doublet term) and cavity (pressure source term)

$$= -\frac{1}{4\pi} \sum_k \left\{ \iint_{S_b} \Delta p(x, r, \theta; t) \frac{\partial}{\partial n_o} \left( \frac{1}{R_{\psi_o}} \right) dS - \iint_{S_b + S_c} \frac{1}{R_{\psi_o}} \Delta \left\{ \frac{\partial}{\partial n_o} [p(x, r, \theta; t)] \right\} dS \right\}, \quad (5)$$

$p(x^*, r^*, \theta_o^*; t)$  = Pressure due to the image blade and cavity

$$= -\frac{1}{4\pi} \sum_k \left\{ \iint_{S_b} \Delta p(x, r, \theta; t) \frac{\partial}{\partial n_o} \left( \frac{1}{R_{\psi_o}} \right) dS + \iint_{S_b + S_c} \frac{1}{R_{\psi_o}} \Delta \left\{ \frac{\partial}{\partial n_o} [p(x, r, \theta; t)] \right\} dS \right\}, \quad (6)$$

$$\Delta p = p^+ - p^-$$

$$\Delta \left\{ \frac{\partial}{\partial n} p \right\} = \left( \frac{\partial p}{\partial n} \right)^+ - \left( \frac{\partial p}{\partial n} \right)^-$$

$n$  = normal to linearized surface, positive from pressure side to suction side

$$R_{\psi_o} = [(x^* - x)^2 + r^2 + r^{*2} - 2rr^* \cos \psi_o]^{1/2}$$

$$\psi_o = \theta_o - \theta_o^* + \sigma_k$$

$$\theta_o = \theta - \omega t$$

$$\sigma_k = \frac{2\pi}{K} (k - 1)$$

$K$  = number of blades

$S$  = moving surface consisting of propeller blade surface  $S_b$  and cavity surface  $S_c$

$S_b, S_c$  = propeller blade and cavity surfaces, respectively, where the zero pressure condition on the free surface, the image part  $p$ , has been added in Equation (4) with the pressure doublet term of the same sign and the pressure source of the opposite sign. Detailed derivations of the image part will be treated separately later.

The detailed description for the image part will be provided later.

The moving blade surface  $S$  is considered to be composed of helical lines of varying pitch in the  $r$ -direction;

$$S: x - \theta R \lambda(r) = 0 \\ \lambda = U(r)/\omega R$$

where  $\lambda$  denotes advance coefficient as a function of  $r$ . It must be mentioned here that the theory developed will be applied to the wake-adapted flow field by varying  $\lambda$  as a function of  $r$  as is seen above. By using the gradient components of this helical plane one can write the directional derivative  $\partial/\partial n_o$  as follows,

$$\frac{\partial}{\partial n_o} = - \frac{r \frac{\partial}{\partial x} - r(\theta_o + \omega t) R \lambda_r \frac{\partial}{\partial r} - \frac{R \lambda}{r} \frac{\partial}{\partial \theta_o}}{[r^2 + (R \lambda)^2 + (r(\theta_o + \omega t) R \lambda_r)^2]^{1/2}} \quad (7)$$

where  $\lambda_r = d\lambda/dr$ . Thus,

$$\frac{\partial}{\partial n_o} \left( \frac{1}{R_{\psi_o}} \right) = - \frac{r(x^* - x) + R \lambda r^* \sin \psi_o - r(\theta_o + \omega t) R \lambda_r (r - r^* \cos \psi_o)}{[r^2 + (R \lambda)^2 + \{r(\theta_o + \omega t) R \lambda_r\}^2]^{1/2} R_{\psi_o}^3}, \quad (8)$$

and

$$dS = [r^2 + (R \lambda)^2 + \{r(\theta_o + \omega t) R \lambda_r\}^2]^{1/2} d\theta dr. \quad (9)$$

In order to derive a simplified first-cut method of partially submerged propeller theory, we take only the doublet effects for the present analysis, neglecting the source effects, i.e., the cavity thickness effects on the induced flow velocities. Therefore, application of (8) and (9) into (5) yields

$$p(v+x, r^*, \theta_o^*; \tau) = \frac{1}{4\pi} \sum_k \int_{r_f(\tau)}^{R} \int_{\theta_L}^{\theta_T} \Delta p(r, \theta, \tau) \frac{N_v}{R_v^3} dr d\theta \quad (10)$$

$$\text{where } \tau = t - \frac{x^* - (v+x)}{U} \quad (11)$$

$$\psi_v = \theta - \omega \tau - \theta_o^* + \sigma_k \quad (12)$$

$$N_v = rv + R \lambda r^* \sin \psi_v - r(\theta_o + \omega \tau) R \lambda_r (r - r^* \cos \psi_v) \quad (13)$$

$$R_v = [v^2 + r^2 + r^{*2} - 2rr^* \cos \psi_v]^{1/2} \quad (14)$$

$\theta_L, \theta_T$  = angular coordinates of the blade leading and trailing edges, respectively

$r_f, R$  = radial coordinates defining the radial distances at the free surface and tip measured from the center of shaft, respectively

Substituting (10) into (3), one obtains

$$\phi(x^*, r^*, \theta_o^*; t) =$$

$$- \frac{1}{4\pi U} \sum_k \int_{-\infty}^{x^* - x} \int_{r_f(\tau(v))}^R dv \int_{\theta_L}^{\theta_T} dr \int_{\theta_L}^{\theta_T} \Delta P(r, \theta, \tau(v)) \frac{N_v}{R_v^3} d\theta. \quad (15)$$

A further simplification of the problem is made by representing each of the submerged blades as a lifting line so that one can define the dipole-like singularity

$$\int_{\theta_L}^{\theta_T} \frac{1}{\rho} \Delta P(r, \theta, \tau) d\theta = \frac{P(r, \tau)}{\rho} \delta(\theta) \quad (16)$$

$\delta(\theta)$  = Dirac delta function.

The velocity potential  $\phi$  in Equation (15) is now written under the linearized lifting line assumptions

$$\phi(x^*, r^*, \theta_o^*; t) = - \frac{1}{4\pi U} \sum_k \int_{-\infty}^{x^* - x} \int_{r_f(\tau(v))}^R dv \int_{\theta_L}^{\theta_T} \frac{P(r, \tau)}{\rho} \frac{N_v}{R_v^3} dr. \quad (17)$$

Before calculating the induced velocities from  $\phi$ , all variable numbers will be nondimensionalized and expressed by the straight bar above each character

$$\bar{\phi}(\bar{x}^*, \bar{r}^*, \bar{\theta}_o^*; t) = - \frac{1}{2} \sum_k \int_{-\infty}^{\bar{x}^*} d\bar{v} \int_{\bar{r}_f(\tau(\bar{v}))}^1 \bar{P}(r, \tau) \frac{\bar{N}_v}{\bar{R}_v^3} d\bar{r} \quad (18)$$

where the normalization has been made as follows;

$$(\bar{x}^*, \bar{r}^*, \bar{\theta}_o^*, \bar{v}) \equiv (x^*, r^*, \theta_o^*, v)/R$$

$$\bar{\phi} = \phi/RU$$

$$\bar{P} = P/2\pi\rho U^2$$

$$\bar{N}_v = N_v/R^2 =$$

$$\bar{r} \bar{v} + \lambda \bar{r}^* \sin \bar{\psi}_v + (\bar{x}^* - \bar{v}) \frac{\bar{\lambda}_r \bar{r}}{\lambda} (\bar{r} - \bar{r}^* \cos \bar{\psi}_v) \quad (19)$$

$$\bar{R}_v = R_v/R = \left[ \bar{v}^2 + \bar{r}^2 + \bar{r}^{*2} - 2\bar{r} \bar{r}^* \cos \bar{\psi}_v \right]^{1/2} \quad (20)$$

$$\bar{\psi}_v = -\omega t + \frac{\bar{x}^* - \bar{v}}{\lambda} - \theta_o^* + \sigma_k \quad (21)$$

$$\bar{\lambda}_r = \lambda_r \cdot R.$$

Since the lifting line approach is used,  $x$  and  $\theta$  in Equation (17) have been set to zero. Thus  $\tau$  in (11) becomes

$$\tau = t - (\bar{x}^* - \bar{v}) / \lambda \omega. \quad (22)$$

The top bars used to identify the non-dimensional quantities will be dropped hereafter, but the reader should be reminded that all quantities from now on are nondimensionalized. The induced velocities due to a series of the vortex sheets are then calculated

$$\begin{aligned} u_{x^*}(x^*, r^*, \theta_o^*; t) &= \frac{\partial \phi}{\partial x^*} \\ &= - \frac{1}{2} \sum_k \left\{ \int_{\bar{r}_f(t)}^1 \left[ P(r, \tau(v)) \frac{N_v}{R_v^3} \right] \right\}_{v=x^*} \\ &\quad + \int_{-\infty}^{x^*} P(r, \tau(v)) \cdot \frac{N_v}{R_v^3} \left| \left( -\frac{\partial r_f}{\partial x^*} \right) dv \right. \\ &\quad \left. + \int_d^1 dr \int_{-\infty}^{x^*} \frac{\partial}{\partial x^*} \left[ P(r, \tau(v)) \frac{N_v}{R_v^3} \right] dv \right\} \quad (23) \end{aligned}$$

where  $d$  is the distance of the free surface measured from the center of the shaft. It should be noted that the order of integration between  $r$  and  $v$  has been changed. This change has been made carefully with the change of the integration limits, particularly for  $r$ ; in order to cover the maximum blade wetted length, the lower limit now should be " $d$ " (the distance of the free surface measured from the center of shaft). This does not mean that the induced velocities are independent upon the time-varying blade-wetted length. The effect of the time-varying blade-wetted length is now taken care of by the integration in the  $v$ -direction; during the  $v$ -integration, the arc length of integration at each fixed  $r$  varies depending upon  $r$  since the blade wetted length changes. Since  $P(r, \tau(v))$  becomes zero at the free surface, the second term disappears and thus

$$\begin{aligned} u_{x^*} &= - \frac{1}{2} \sum_k \left\{ \int_{\bar{r}_f(t)}^1 \left[ P(r, \tau(v)) \frac{N_v}{R_v^3} \right] \right\}_{v=x^*} \\ &\quad + \int_d^1 dr \int_{-\infty}^{x^*} \frac{\partial P(r, \tau(v))}{\partial x^*} \frac{N_v}{R_v^3} dv \\ &\quad + \int_d^1 dr \int_{-\infty}^{x^*} P(r, \tau(v)) \frac{\partial}{\partial x^*} \left[ \frac{N_v}{R_v^3} \right] dv \right\} \quad (24) \end{aligned}$$

Furthermore, with the following identity

$$\frac{\partial}{\partial x^*} \left[ \frac{N_v}{R_v^3} \right] = \left( \frac{r}{R_v^3} - \frac{3vN_v}{R_v^5} \right) - \frac{\partial}{\partial v} \left[ \frac{N_v}{R_v^3} \right],$$

Equation (24) becomes

$$\begin{aligned} u_{x^*} &= - \frac{1}{2} \sum_k \left\{ \int_{\bar{r}_f(t)}^1 P(r, \tau(v)) \frac{N_v}{R_v^3} dr \right\}_{v=x^*} \\ &\quad + \int_d^1 dr \int_{-\infty}^{x^*} \frac{\partial P(r, \tau(v))}{\partial x^*} \frac{N_v}{R_v^3} dv \end{aligned}$$

$$\int_d^1 dr \int_{-\infty}^{x^*} P(r, \tau(v)) \left\{ \frac{r}{R_v^3} - \frac{3vN_v}{R_v^5} - \frac{\partial}{\partial v} \left[ \frac{N_v}{R_v^3} \right] \right\} dv \quad (25)$$

Integration by parts for the last integral I in Equation (25) will yield

$$I \equiv \int_d^1 dr \int_{-\infty}^{x^*} P(r, \tau(v)) \left[ \frac{r}{R_v^3} - \frac{3vN_v}{R_v^5} \right] dv + \int_d^1 dr \left\{ \left[ -P(r, \tau(v)) \frac{N_v}{R_v^3} \right] \right|_{-\infty}^{x^*} + \int_{-\infty}^{x^*} \frac{\partial P(r, \tau(v))}{\partial v} \frac{N_v}{R_v^3} dv \right\}$$

Since  $N_v/R_v^3$  becomes zero as  $v \rightarrow \infty$  and  $\partial P/\partial v = -\partial P/\partial x^*$  by using Equation (22), Equation (25) can finally be written

$$u_{x^*} = -\frac{1}{2} \sum_k \int_d^1 dr \int_{-\infty}^{x^*} P(r, \tau(v)) \left( \frac{r}{R_v^3} - \frac{3vN_v}{R_v^5} \right) dv. \quad (26)$$

This form is similar to the induced velocity in the x-direction obtained by Cox (1968) except that  $P(r, \tau(v))$  here is a function of both  $r$  and time so that this term is now inside the integral for  $v$ . It must be mentioned here that one would not immediately see if the loading term  $P$  in Cox's expression for the steady case could be moved into the  $v$ -integral without the detailed derivation like the one made above.

The induced velocity in the tangential direction is obtained in the similar manner,

$$u_{\theta_0^*}(x^*, r^*, \theta_0^*; t) = \frac{1}{r^*} \frac{\partial \phi}{\partial \theta_0^*} = -\frac{1}{2} \sum_k \int_d^1 dr \int_{-\infty}^{x^*} \frac{1}{r^*} \frac{\partial}{\partial \theta_0^*} \left[ P(r, \tau(v)) \frac{N_v}{R_v^3} \right] dv \quad (27)$$

Since  $P(r, \tau(v))$  is independent of  $\theta_0^*$ ,

$$u_{\theta_0^*}(x^*, r^*, \theta_0^*; t) = -\frac{1}{2} \sum_k \int_d^1 dr \int_{-\infty}^{x^*} P(r, \tau(v)) \left( \frac{-\lambda \cos \psi_v + \frac{r}{\lambda} (v - x^*) \lambda_r \sin \psi_v}{R_v^3} + \frac{3N_v r \sin \psi_v}{R_v^5} \right) dv \quad (28)$$

A numerical integral method of Hadamard (see the report of Mangler (1951) for detailed treatment) for handling the singularities of fifth order in  $u_{x^*}$  and  $u_{\theta_0^*}$  was used for Equations (26) and (28). It was discovered, however, that there existed a numerical instability; the numerical results first converged as the mesh size of numerical control points decreased, but started diverging as the mesh size was further reduced. The Hadamard integral method which was successfully used for

the air foil integral, did not work properly due to the fifth-order singularities existing in the propeller integrals (instead of the third-order singularities in the air foil integrals). The present work was therefore devoted to fixing this numerically unstable problem by entirely changing the forms for  $u_{x^*}$  and  $u_{\theta_0^*}$ .

## 2.2 Induction Factors for Unsteady Wakes

The philosophy adopted here for avoiding the numerical instability is that similar to Moriya (1942), Lerbs (1952) and the work later elaborated on by Morgan and Wrench (1965). Since the propeller problem treated by these researchers was the steady flow one and thus had uniform wakes, they were able to introduce the ideas of the induction factors. All integrals for obtaining the induction factors were reduced to those involving only the third-order singularities where the loading part was expressed in terms of the derivative with respect to  $r$ . By virtue of the steady flow assumption, they were finally converted into the series of Bessel's functions. The real challenge for the present unsteady case will, therefore, be (i) to analytically derive the integral forms similar to those in the steady problem mentioned above, and then (ii) to numerically assure the accuracy of calculating these integrals by having lower-order singularities.

First, the integral dummy variables  $v$  in Equations (26) and (28) are changed to new angular variables  $\tilde{\theta}$  with the following relationship

$$\tilde{\theta} = -\omega t - \frac{v - x^*}{\lambda} - \theta_0^*. \quad (29)$$

By rewriting the lifting-line induced velocities in the  $x$ - and  $\theta$ -direction by a more conventional expression, i.e.,  $w_a$  and  $w_t$ , respectively, we can write

$$w_a \equiv u_{x^*}(x^*, r^*, \theta_0^*; t) = -\frac{1}{2} \sum_k \int_d^1 dr \int_0^\infty \lambda P(r, \tau(\tilde{\theta})) \left( \frac{r}{R_{\tilde{\theta}}^3} - \frac{3(-\lambda \tilde{\theta} + x^*) N_{\tilde{\theta}}}{R_{\tilde{\theta}}^5} \right) d\tilde{\theta} \quad (30)$$

$$w_t \equiv u_{\theta_0^*}(x^*, r^*, \theta_0^*; t) = -\frac{1}{2} \sum_k \int_d^1 dr \int_0^\infty \lambda P(r, \tau(\tilde{\theta})) \left( \frac{-\lambda \cos \psi_{\tilde{\theta}} - \lambda_r r \tilde{\theta} \sin \psi_{\tilde{\theta}}}{R_{\tilde{\theta}}^3} + \frac{3N_{\tilde{\theta}} r \sin \psi_{\tilde{\theta}}}{R_{\tilde{\theta}}^5} \right) d\tilde{\theta} \quad (31)$$

where

$$R_{\tilde{\theta}}^2 = [(-\lambda \tilde{\theta} + x^*)^2 + r^2 + r^{*2} - 2rr^* \cos \psi_{\tilde{\theta}}]^{1/2}$$

$$N_{\tilde{\theta}} = r(-\lambda \tilde{\theta} + x^*) + \lambda r^* \sin \psi_{\tilde{\theta}} + \lambda_r r \tilde{\theta} (r - r^* \cos \psi_{\tilde{\theta}})$$

$$\psi_{\tilde{\theta}} = \tilde{\theta} + \tilde{\theta}_0^* + \sigma_k$$

$\hat{\theta}_0^* = -\omega t - \theta_0^*$  (this value will be zero for the induced velocity calculation on the lifting line itself since  $\theta_0^* = -\omega t$ )

$$\lambda = U(r)/\omega R$$

$\lambda_r = d\lambda/dr \cdot R$  (since this is in nondimensional expression).

With the fact kept in mind that  $P$  is a function of both  $r$  and  $\tilde{\theta}$ , the following identities have successfully been derived after lengthy algebraic computations,

$$\frac{r}{R_0^3} - \frac{3(-\lambda\tilde{\theta} + x^*)N_{\tilde{\theta}}}{R_0^5} = -\frac{\partial}{\partial r} \left[ \frac{r(r-r^* \cos \psi_{\tilde{\theta}})}{R_0^3} \right] - \frac{\partial}{\partial \tilde{\theta}} \left[ \frac{r^* \sin \psi_{\tilde{\theta}}}{R_0^3} \right] \quad (32)$$

$$\begin{aligned} & \frac{-\lambda \cos \psi_{\tilde{\theta}} - \lambda_r r \tilde{\theta} \sin \psi_{\tilde{\theta}}}{R_0^3} + \frac{3N_{\tilde{\theta}} r \sin \psi_{\tilde{\theta}}}{R_0^5} \\ &= -\frac{\partial}{\partial r} \left[ \frac{\lambda(r^*-r \cos \psi_{\tilde{\theta}}) + (-\lambda\tilde{\theta} + x^*)r \sin \psi_{\tilde{\theta}}}{R_0^3} \right] + \\ & \quad \frac{\partial}{\partial \tilde{\theta}} \left[ \frac{(-\lambda\tilde{\theta} + x^*) \cos \psi_{\tilde{\theta}} + \lambda_r \tilde{\theta} (r^*-r \cos \psi_{\tilde{\theta}})}{R_0^3} \right] \quad (33) \end{aligned}$$

By using these identities, the kernel function of the integrals for  $w_a$  and  $w_t$  in Equations (30) and (31) will be converted into the radial and tangential derivative forms with only the third order singularities. Performing the integration by parts in terms of  $r$  and  $\tilde{\theta}$ , we will obtain

$$\begin{aligned} w_a(x^*, r^*, \theta_0^*; t) = & -\frac{1}{2} \sum_k \int_0^\infty d\tilde{\theta} \int_{r_f(\tau(\tilde{\theta}))}^1 \frac{\partial}{\partial r} \left[ \lambda P(r, \tau(\tilde{\theta})) \right] \cdot \frac{r(r-r^* \cos \psi_{\tilde{\theta}})}{R_0^3} dr \\ & -\frac{1}{2} \sum_k \int_d^1 dr \int_0^\infty \lambda \frac{\partial P(r, \tau(\tilde{\theta}))}{\partial \tilde{\theta}} \cdot \frac{r^* \sin \psi_{\tilde{\theta}}}{R_0^3} d\tilde{\theta} \quad (34) \end{aligned}$$

and

$$\begin{aligned} w_t(x^*, r^*, \theta_0^*; t) = & -\frac{1}{2} \sum_k \int_0^\infty d\tilde{\theta} \int_{r_f(\tau(\tilde{\theta}))}^1 \frac{\partial}{\partial r} \left[ \lambda P(r, \tau(\tilde{\theta})) \right] \cdot \\ & \frac{\lambda(r^*-r \cos \psi_{\tilde{\theta}}) + (-\lambda\tilde{\theta} + x^*)r \sin \psi_{\tilde{\theta}}}{R_0^3} dr \\ & + \frac{1}{2} \sum_k \int_d^1 dr \int_0^\infty \lambda \frac{\partial P(r, \tau(\tilde{\theta}))}{\partial \tilde{\theta}} \cdot x \end{aligned}$$

$$\frac{-(-\lambda\tilde{\theta} + x^*) \cos \psi_{\tilde{\theta}} + \lambda_r \tilde{\theta} (r^*-r \cos \psi_{\tilde{\theta}})}{R_0^3} d\tilde{\theta} \quad (35)$$

It is clearly seen from these results that the induced velocities obtained here consist of the two parts, i.e., the steady part relating to  $\partial(\lambda P)/\partial r$  and the unsteady part relating to  $\partial P/\partial \tilde{\theta}$ .

For the case of the steady propeller flow problem,  $\partial P/\partial \tilde{\theta}$  becomes zero and  $\partial P/\partial r$  becomes independent of  $\tilde{\theta}$ .  $w_a$  and  $w_t$  in Equations (34) and (35) will be reduced to the forms exactly identical to those of the steady flow case in Cox (1968). It is considered that the present results will be extremely useful, not limited to the current partially submerged propeller problems, but also in analyzing any general unsteady propeller flows.

$w_a$  and  $w_t$  in Equations (34) and (35) are further modified for securing numerical stability, i.e.,

$$w_a = -\frac{1}{2} \int_d^1 \frac{I_{ar}(r, r^*)}{r-r^*} dr - \frac{1}{2} \int_d^1 \frac{I_{a\tilde{\theta}}(r, r^*)}{r-r^*} dr \quad (36)$$

$$w_t = -\frac{1}{2} \int_d^1 \frac{I_{tr}(r, r^*)}{r-r^*} dr + \frac{1}{2} \int_d^1 \frac{I_{t\tilde{\theta}}(r, r^*)}{r-r^*} dr \quad (37)$$

where

$$I_{ar}(r, r^*) = \sum_k \int_0^\infty \left\{ \frac{\partial}{\partial r} \left[ \lambda P(r, \tau(\tilde{\theta})) \right] \right\} \cdot \frac{(r-r^*) \cdot r \cdot (r-r^* \cos \psi_{\tilde{\theta}})}{R_0^3} d\tilde{\theta}, \quad (38)$$

$$I_{a\tilde{\theta}}(r, r^*) = \sum_k \int_0^\infty \lambda \frac{\partial P(r, \tau(\tilde{\theta}))}{\partial \tilde{\theta}} \cdot \frac{r(r-r^*)r^* \sin \psi_{\tilde{\theta}}}{R_0^3} d\tilde{\theta}, \quad (39)$$

$$\begin{aligned} I_{tr}(r, r^*) = & \sum_k \int_0^\infty \left\{ \frac{\partial}{\partial r} \left[ \lambda P(r, \tau(\tilde{\theta})) \right] \right\} \cdot \\ & \frac{(r-r^*) \left\{ \lambda(r^*-r \cos \psi_{\tilde{\theta}}) + (-\lambda\tilde{\theta} + x^*)r \sin \psi_{\tilde{\theta}} \right\}}{R_0^3} d\tilde{\theta}, \quad (40) \end{aligned}$$

$$\begin{aligned} I_{t\tilde{\theta}}(r, r^*) = & \sum_k \int_0^\infty \lambda \frac{\partial P(r, \tau(\tilde{\theta}))}{\partial \tilde{\theta}} \cdot \\ & \frac{r(r-r^*) \left\{ -(-\lambda\tilde{\theta} + x^*) \cos \psi_{\tilde{\theta}} + \lambda_r \tilde{\theta} (r^*-r \cos \psi_{\tilde{\theta}}) \right\}}{R_0^3} d\tilde{\theta} \quad (41) \end{aligned}$$

and the order of integration between  $r$  and  $\tilde{\theta}$  has been changed with the same justification as that for Equation (23).

$I_{ar}$ ,  $I_{a\tilde{\theta}}$ ,  $I_{tr}$ ,  $I_{t\tilde{\theta}}$  in Equations (38) to (41) are similar to the induction factors introduced by Lerbs (1952) who developed the

steady-state propeller lifting-line theory. As a matter of fact, in the steady-state problem  $\partial/\partial r[\lambda P(r, \tau(\tilde{\theta}))]$  is independent of  $\tilde{\theta}$  so that this term can be taken out of the  $\tilde{\theta}$ -integrals. Without the terms of  $\partial/\partial r[\lambda P(r, \tau(\tilde{\theta}))]$ ,  $I_{ar}$  and  $I_{tr}$  should be identical to the induction factors of Lerbs who calculated them in a totally different way, as mentioned above. In order to test the accuracy of the numerical integral method to be employed for the present analysis,  $I_{ar}$  and  $I_{tr}$  in Equations (38) and (40) were numerically calculated with  $\partial(\lambda P)/\partial r = 1$ ,  $x_0^* = 0$  and  $\theta_0^* = -\omega t$  for various  $r/r^*$  ratios and  $\beta_{i0}$ 's (flow pitch angles) by applying Simpson's rule. It was found that for large  $\beta_{i0}$ 's such as  $60^\circ$  and  $r/r^*$  ratios larger than 0.6,  $I_{ar}$  and  $I_{tr}$  matched with those of Lerbs within 0.1% accuracy if 10 turns of wakes were used, whereas for smaller  $\beta_{i0}$ 's such as  $15^\circ$  and  $r/r^*$  less than 0.6, the errors were about 3%. However, the accuracy greatly improved if 20 turns of wakes were taken for the numerical calculations, with the accuracy less than 1% for all combinations of  $\beta_{i0}$  and  $r/r^*$ . Furthermore, the errors were observed at only small  $r/r^*$ 's so that they would play a negligibly small role in the overall integral with respect to  $r$  for the final values of  $w_a$  and  $w_t$  (a sample case showed an error less than 0.1%). Also,  $I_{ar}$  and  $I_{tr}$  values calculated with the present method showed smooth transition near  $r/r^* = 1$  (taken to be unity). Finally, it must be mentioned that reducing the integral intervals both in  $\tilde{\theta}$  and  $r$  made the calculated values of the integrals converge to the single numbers.

It has now been determined that by applying the integral method mentioned above to  $I_{ar}$ ,  $I_{a\tilde{\theta}}$ ,  $I_{tr}$  and  $I_{t\tilde{\theta}}$  with  $P$  varying as a function of  $\tilde{\theta}$  due to the flow unsteadiness, we will be able to obtain the accurate and numerically stable induced velocities for the present partially submerged propeller problem.

The method for obtaining the image induced velocities is rather simple; instead of constructing the image wake system in the air domain, we will first obtain the mirror image for the point of interest on the lifting line and then obtain the induced velocities due to the real wake systems. In this flow configuration, the relative geometry between the point of interest and wake system is identical to the one considered above except that the direction of wake helical windings is opposite. It means that the induced velocity in the  $x$ -direction will be added to the real part whereas that in the tangential direction will have to be subtracted from the counterpart.

The only work to be done for implementing the above method is to obtain the new coordinates for the point of the lifting line in the water, i.e.,  $(x^*, r^*, \theta_0^*)$ . Defining the image point by  $(x^{**}, r^{**}, \theta_0^{**})$ , one will readily find the following relationships (see Figure 2).

$$\begin{aligned} x^{**} &= x^* = 0 \\ r^{**} \cos \theta_0^{**} &= r^* \cos \theta_0^* \\ r^{**} \sin \theta_0^{**} + r^{**} \sin \theta_0^{**} &= 2d. \end{aligned} \quad (42)$$

It is straightforward to obtain  $(x^{**}, r^{**}, \theta_0^{**})$  from Equation (42) once  $(x^*, r^*, \theta_0^*)$  are given. These new coordinate points will be substituted into Equations (36) and (37) to obtain the induced velocities,  $w_a$  and  $w_t$ , due to the image wakes, i.e.,

$$w_a = w_a(0, r^{**}, \theta_0^{**}(t); t) \text{ in Equation (36)} \quad (43)$$

$$w_t = w_t(0, r^{**}, \theta_0^{**}(t); t) \text{ in Equation (37)}. \quad (44)$$

The total induced velocities are finally obtained

$$\Sigma w_a = w_a(0, r^*, -\omega t; t) + w_a(0, r^{**}, \theta_0^{**}(t); t) \quad (45)$$

$$\Sigma w_t = w_t(0, r^*, -\omega t; t) + w_t(0, r^{**}, \theta_0^{**}(t); t). \quad (46)$$

### 3.0 SOLUTION METHOD

The off-design propeller problem to be solved here is to satisfy the velocity vector relationship shown in Figure 3, i.e.,

$$\tan \beta_i = \frac{U + \Sigma w_a}{\omega r - \Sigma w_t} \quad (47)$$

or

$$\begin{aligned} \tan \left\{ \beta_g(r^*) - \alpha_e(r^*) \right\} &= \left[ \frac{\pi r^*}{J} - \Sigma w_a(P(r^*, \alpha_e(r^*), t)) \right] \\ - \left[ 1 + \Sigma w_t(P(r^*, \alpha_e(r^*), t)) \right] &= 0 \text{ for all } r^* \end{aligned} \quad (48)$$

where  $\beta_g$  is a propeller geometric parameter, see Figure 3. In Equation (48),  $P$ -function should be determined as functions of  $r^*$  and time (or the relative position of blade in reference to the free surface).

The relationship between the lifting forces and the  $P$  function will be given as follows:

$$\lambda P = \frac{1}{4\pi} \frac{U_e}{U} C_L \left( \frac{c}{R} \right) \quad (49)$$

where

$c$  = chord

$U_e$  = effective relative velocity

$$= \left[ (U + w_a)^2 + (\omega r + w_t)^2 \right]^{1/2}$$

$C_L$  = lift coefficient

$U = V_a$  if no wake reduction factor is considered

It must be pointed out that in order to account for the induced flow effects on the location of the vortex sheets, use of  $\lambda_i(r)$  instead of  $\lambda(r)$  is recommended where

$$\lambda_i(r) = x \tan \beta_i = \frac{U + \Sigma w_a(r)}{\omega r - \Sigma w_t(r)} \frac{r}{R}. \quad (50)$$

Unlike Prandtl-type of steady-state, three-dimensional wing problem, the  $P$ -function cannot conveniently be expressed in terms of Fourier series for two reasons. The first is

that  $P$  is an intermittent function of time, increasing from zero to the maximum value and decreasing back to zero when the blade is out of water and staying zero until the next entry of the blade to water. The second reason is that the span length of blade continuously changes as blades move and  $P$ -function does not have similarity even for the normalized span scale.

A proposed method for solution will employ a numerical iterative method as in Furuya (1980). First, we use the geometric incidence angle at each blade spanwise position to calculate the lifting force as function of blade location or time. D.P. Wang's (1979) blade entry and exit theory will be used to evaluate this loading function  $P$  through Equation (48) by assuming  $\Sigma w_a = \Sigma w_t = 0$ . Once the initial distribution of  $P$  is given as functions of  $r^*$  and  $t$ , the induced flow velocities  $\Sigma w_a$  and  $\Sigma w_t$  will be calculated from the formula obtained in the previous section. These induced velocities now change the local effective flow incidence angles  $\alpha_e$ . With a new set of  $\alpha_e$ , a new loading function  $P$  is recalculated again with the two-dimensional water entry-exit method. This iterative procedure will be repeated until a convergent solution is obtained.

#### 4.0 CALCULATIONS OF TWO-DIMENSIONAL SECTIONAL LOADINGS WITH D.P. WANG'S PROGRAM

In order to determine the strength of circulation at various blade radial stations in the propeller lifting-line theory, the two-dimensional lifting force must be provided as functions of blade geometry, angle of incidence, submergence depth and angle of entry or exit. D.P. Wang (1979) recently developed the theory for solving the problem of oblique water entry and exit for a fully ventilated foil. The theory employed a linearized initial value problem approach for the mixed-type boundary condition. However, the computer program developed there is only applicable for foils having straight line and circular arc camber profiles. Practically used ventilating propellers under the partially submerged condition are usually designed to have a somewhat different type of foil profile shape. One of the most frequently used blade profiles for this type of propeller is that of Tulin-Bukart (1955) two-term camber, which is expressed in the following equation

$$y_B = \frac{A}{2} \left( x_B + \frac{8}{3} x_B^{3/2} - 4 x_B^2 \right) + B x_B \quad (51)$$

where the first group of terms in the brackets is the two-term camber part and  $B x_B$  is merely a rotation of  $(x-y)$  coordinates. It is readily understood that the terms related to  $x_B$  and  $x_B^{3/2}$  represent the straight line and circular arc profiles, respectively, whereas a term proportional to  $x_B^2$  is the specific term in the two-term camber profile. Incidentally, the partially submerged propellers, Models 3767 and 4002, tested by Hadler and Hecker (1968) had the two-term camber expressed by Equation (51). Table 1 presents the values of coefficients  $A$

and  $B$  at various radial stations. More generally, supercavitating or fully ventilated blade profiles can be written

$$y_B = \sum_{n=0}^m a_n x_B^{n/2} \quad (52)$$

In order to handle these general blade profile cases, Wang's computer code needed modification. It was not simply a replacement of a few cards in the computer code, but involved the detailed understanding of the program due to the various variable transformation and singularity removal techniques used in the program. After this modification was made, the program has become much easier for users to incorporate any type of blade profile shape such as that expressed in Equation (51) or (52); the only change of the computer code to be made for different types of profile now is that of a subroutine specifying the profile shape.

With this modified computer code we made computations for lift and drag forces for the Tulin-Bukart two-term camber at various water depths and angles of blade entry and exit, some results being shown in Figures 4 and 5 (see the report of Furuya (1979) for the cases of  $h/\pi = 0.5$  and  $1.5$ ). Use will be made of these graphs in the following manner. Assuming that the two-term camber is given by Equation (51) with  $h/\pi$  and  $\lambda$ , the force coefficients for the two-term camber and straight line can be read from each graph. The total  $C_L$  and  $C_D$  will then be calculated

$$\begin{pmatrix} C_L \\ C_D \end{pmatrix} = \frac{A}{A_d} \begin{pmatrix} C_{L(2-T)} \\ C_{D(2-T)} \end{pmatrix} - 10(B-\alpha_e) \begin{pmatrix} C_{L(Flat)} \\ C_{D(Flat)} \end{pmatrix} \quad (53)$$

where  $A_d = .10186$  has been used in the present calculation, which corresponds to  $C_{Ld} = 0.2$  and  $\alpha_e$  denotes the flow incidence angle. This calculation should be made for all  $h/\pi$ 's and  $\lambda$ 's since the specified  $h/\pi$  and  $\lambda$  for which  $C_L$  and  $C_D$  to be calculated are usually different from those for which the present computation was made. Then an interpolation method is necessary in  $h/\pi$  and  $\lambda$  planes to finally determine  $C_L$  and  $C_D$  for the specified values of  $h/\pi$  and  $\lambda$ . The computer code developed for the propeller calculation uses one such interpolation scheme. Incidentally, the accuracy of the modified Wang computer code was checked in the following way. By increasing  $h/\pi$  values to 5, 10, etc., for the two term camber, it was observed that calculated  $C_L$  values asymptotically approached 0.2. Since  $A_d$  used here corresponds to the lift coefficient of  $C_{Ld} = 0.2$ , it was considered that the accuracy of the computer code, as well as the theory, has been proved.

It must be mentioned that one of the most interesting features regarding the two-term camber used for the partially submerged propeller appears in the results of the calculations for the present two-dimensional sectional characteristics. For a short time period immediately after a blade leading edge entry into the water, the lifting forces for the two-term



camber show negative values. As the blade proceeds and has a larger submergence, these negative values turn around and rapidly change to positive values. This means that the blade tip material experiences the oscillatory force from a negative to a positive value at each cycle of rotation. The reason for this phenomena can readily be understood if one closely investigates the profile shape of the two-term camber, particularly near the leading edge where negative slope exists (see Figure 6). When only the blade tip is plunged into water, the lifting force is naturally negative. However, as a larger portion of the blade is submerged into the water, the positive camber starts taking effect and thus the direction of force changes.

It must be further pointed out that these lift and drag forces during such a critical period were calculated based upon an assumption that the face portion of the blade is wetted and the back portion has ventilation. This assumption may be erroneous; the flow configuration to be used for such a case is that the face part must have ventilation whereas the back part must be fully wetted. As the blade proceeds, the water starts filling in the face part, maybe trapping the air near the leading edge while the back part cannot sustain the negative pressure so that either cavitation and/or ventilation may suddenly take place. Therefore, the change of forces near the leading edge may be even more drastic than is shown in Figures 4 and 5; it could even be of impulse type.

In any case, this type of repeated oscillatory force will easily lead to material failure due to fatigue phenomena. According to private communications with D.P. Wang and other documents, the partially submerged propeller can survive only for a few hours of operation, ending with material breakdown. As a matter of fact, most of the partially submerged propellers designed to date employed the two-term or similar camber profiles (see Table 1). The findings mentioned here suggest that the use of the two-term or higher order cambers, known to be superior in the area of fully submerged supercavitating propellers, is not necessarily suitable for the environment encountered by the partially submerged propeller. Since material failure is the most critical problem in this type of propeller design, the selection of the propeller blade profile needs a specific consideration for material integrity as well as for avoidance of oscillatory forces at the time of entry. One of the possible candidates for the leading edge profile used for the partially submerged propeller may be that of smooth straight line or wedge type or even finite thickness with rounded leading edge followed by an appropriate camber profile.

## 5. THRUST AND POWER COEFFICIENTS

The time-averaged thrust and power coefficients,  $\bar{C}_T$  and  $\bar{C}_P$ , can be calculated as follows. The thrust and power forces for the k-th blade at an instantaneous time t or equivalently at a rotational angle  $\theta$  are given

$$T(\theta + \sigma_k) = \int_{r_h}^R \left\{ C_L \cdot \frac{1}{2} \rho U_e^2 \cdot C \cos \beta_i - (D + D_f) \sin \beta_i \right\} dr \quad (54)$$

$$P(\theta + \sigma_k) = \int_{r_h}^R \left\{ C_L \cdot \frac{1}{2} \rho U_e^2 \cdot C \sin \beta_i + (D + D_f) \cos \beta_i \right\} dr \quad (55)$$

where

$D$  = form drag on the blade,  $D(r, \theta)$

$D_f$  = friction drag,  $D_f(r, \theta)$

$U_e = \left[ (\omega r - w_t)^2 + (U + w_a)^2 \right]^{1/2}$ , (see Fig. 3)

$\beta_i = \tan^{-1} [(U + w_a) / (\omega r - w_t)]$ , (see Fig. 3).

First  $T$  and  $P$  are normalized;

$$\bar{C}_T(\theta + \sigma_k) = \frac{T(\theta + \sigma_k)}{\frac{1}{2} \rho U^2 \pi R^2} = 4 \int_{\bar{r}_h}^1 \left\{ \frac{U_e}{U} \cdot \lambda P \cos \beta_i - \frac{1}{4\pi} (C_D + C_{Df}) \cdot \bar{c} \cdot \left( \frac{U_e}{U} \right)^2 \sin \beta_i \right\} d\bar{r}$$

$$\bar{C}_P(\theta + \sigma_k) = \frac{P(\theta + \sigma_k)}{\frac{1}{2} \rho U^3 \pi R^2} = 4 \int_{\bar{r}_h}^1 \left\{ \frac{U_e}{U} \cdot \lambda P \sin \beta_i + \frac{1}{4\pi} (C_D + C_{Df}) \cdot \bar{c} \cdot \left( \frac{U_e}{U} \right)^2 \cos \beta_i \right\} d\bar{r}$$

where

$$\lambda P = \frac{1}{4\pi} \frac{U_e}{U} \bar{c} \cdot C_L$$

$$C_L = \frac{L}{\frac{1}{2} \rho U_e^2 \cdot \bar{c}}$$

$$C_D = \frac{D}{\frac{1}{2} \rho U_e^2 \cdot \bar{c}}$$

$$C_{Df} = \frac{D_f}{\frac{1}{2} \rho U_e^2 \cdot \bar{c}}$$

$$\bar{c} = \text{normalized chord} (= c/R).$$

In order to obtain the averaged thrust and power coefficients  $\bar{C}_T$  and  $\bar{C}_P$ ,  $T_k$  and  $P_k$  must be integrated over one rotation of propeller and then be divided by  $2\pi$ .

$$\bar{C}_T = \frac{1}{2\pi} \int_0^{2\pi} \left\{ \sum_{k=1}^K \bar{C}_T(\theta + \sigma_k) \right\} d\theta \quad (56)$$

$$\tilde{C}_P = \frac{1}{2\pi} \int_0^{2\pi} \left\{ \sum_{k=1}^K \tilde{C}_P (\theta + \sigma_k) \right\} d\theta. \quad (57)$$

The conversion of  $\tilde{C}_T$  and  $\tilde{C}_P$  into more conventional thrust and torque coefficients  $\bar{K}_T$  and  $\bar{K}_Q$  is a simple matter, i.e.,

$$\bar{K}_T = \frac{\pi J^2}{8} \tilde{C}_T \quad (58)$$

$$\bar{K}_Q = \frac{J^3}{16} \tilde{C}_P \quad (59)$$

where the definition of  $\bar{K}_T$  and  $\bar{K}_Q$  is given by

$$\bar{K}_T(\theta + \sigma_k) = \frac{T(\theta + \sigma_k)}{16\rho n^2 R^4} \quad (60)$$

$$\bar{K}_Q = \frac{P(\theta + \sigma_k)}{32\rho n^2 R^5}. \quad (61)$$

The averaged efficiency of the propeller is thus provided

$$\bar{\eta} = \frac{\tilde{C}_T}{\tilde{C}_P} = \frac{\bar{K}_T}{\bar{K}_Q} \frac{J}{2\pi}. \quad (62)$$

## 6.0 RESULTS

The computer program was developed on the basis of the new theory and was applied for calculating the off-design performance of two different types of partially submerged propellers, i.e., NSRDC Propeller Model 3768 and 4002. The geometric characteristics of these propellers were provided in the report of Hadler and Hecker (1968) who conducted water tunnel tests for these propellers with submerged depth of 40% and 33.3%, respectively (the submergence depth was defined based on the propeller diameter). Some of the important features used for the present computations are summarized in Tables 2 and 3.

The calculated results for the time-averaged thrust and torque coefficients  $\bar{K}_T$  and  $\bar{K}_Q$  of Equations (58) and (59) are shown in Figures 7 and 8 and compared with the experimental data of Hadler and Hecker (1968). The experimental data used in this comparison for Propeller Model 3768 are those of the incoming tunnel flow speeds of  $U = 10.3$  fps and  $20.7$  fps. For  $U = 10.3$  fps, much more data than are shown here (particularly beyond  $J = .6$ ) are available in their report. However, they indicated that the transition from the leading-edge ventilation to the base-ventilated condition took place at around  $J = .5$ . Since the base-ventilated flow configuration is not of current interest, the data beyond  $J = .5$  were omitted from the present comparison. On the other hand, for the data taken at  $U = 20.7$  fps, there was no indication of such flow transition in the report. It is assumed that the flow configuration matches with that of the current theory and all available data are presented. For the Propeller Model 4002, Hadler and Hecker conducted the experiments with variable incoming speeds and did not indicate the transition point in their data presentation. All experimental data for 4002 are presented for comparison.

In any case the thrust coefficients obtained with the present theory compare favorably with the experimental data over a wide range of  $J$ 's, whereas there exists some discrepancy for the torque coefficients. Various reasons for the discrepancy are considered and they will be summarized in the following.

- i) The two-dimensional loadings used in the present calculations are those obtained with Wang's (1979) program which was based on the linearized theory. According to the recent investigation of D.P. Wang\*, the effect of nonlinearity during the phase of blade entry sometimes accounts for 20 to 30% of the forces by the linearized theory. This difference may be caused by the fact that the linearized theory is unable to determine the accurate wetted area of the blade during the entry phase.
- ii) In the present computations only the pressure doublet terms were considered in the evaluation of the induced velocities and the pressure source terms were neglected. It was reported in many documents that the thickness effect of blade or cavity played an important role in the propeller performance prediction theory (see, e.g., Kerwin and Leopold (1963) and Furuya (1980)).
- iii) There exists some uncertainty in interpreting the experimental data, particularly for the case of 4002 as mentioned above. As is seen in Figure 8, both  $\bar{K}_T$  and  $\bar{K}_Q$  of the experiments suddenly increase around  $J = .3 \sim .4$ . There is a suspicion that this behavior represents the transition from the fully ventilated flow to the base-ventilated flow. If that is the case, the flow configurations of the theory and experiments are not comparable and thus the comparison beyond  $J$  of larger than say .4, may not be appropriate.
- iv) There exists a limitation of the present lifting-line theory, particularly in the range of small  $J$ 's where the induced velocities become substantial.

Figures 9 to 12 present the detailed calculated data for 3768 at  $J = 1.0$ . Figure 9 shows the time-dependent  $K_T$  and  $K_Q$  as a function of blade rotation. Angle " $\theta$ " of the horizontal axis in this figure is measured from the point when a blade is located at the shaft centerline level. Since the propeller 3768 has three blades, the shaft forces are periodic over every 120 degrees of rotation, as is seen from Figure 9. The broken lines show  $K_T$  and  $K_Q$  at each blade, indicating that the water entry point of the blade is about 12 degrees of rotation after the blade passing the shaft centerline.

\* Private communication

Figure 10 shows the calculated results of the variation in local lifting forces on the blade at various spanwise points as a function of blade location. Figures 11 and 12 show their corresponding effective flow incidence angles, and the induced velocities,  $w_a/U$  and  $(-w_t/U)$ , respectively. With the information provided in Figures 10 to 12, together with the geometric data shown in Table 2, one will readily construct the flow diagram at any location of the Propeller Model 3768 for  $J = 1.0$ .

The numerical aspects regarding the present unsteady propeller problems with the new formula obtained will be discussed in detail in a separate literature in the near future.

## 7.0 CONCLUSIONS

The purpose of the present work was to develop a mathematical model for solving the time-dependent partially submerged propeller problems and computer program with suitable numerical methods. In the previous work of the author the direct integral forms were derived for calculating the induced velocities together with the Hadamard integral method applied. Unfortunately, this effort resulted in numerical instabilities. Based on the experience encountered there, the new mathematical formulae have been successfully developed by converting the fifth-order singularities into the third-order singularities. The formulae are similar to those shown by Morgan and Wrench (1965) by utilizing the concept of the induction factors (see also the work by Lerbs (1952)). These new formulae are not only applicable to the present partially submerged ventilated propeller problem but also useful for analyzing and designing any unsteady sub-cavitating and cavitating propeller problems, the loading of which does not necessarily have to be periodic.

With the new development of the unsteady propeller lifting-line theory here, the singular integrals in determining the induced velocities have become numerically stable. By combining the two-dimensional water entry-and-exit theory of Wang (1979), the numerical results have been obtained and compared with the existing experimental data of Hadler and Hecker (1968). It has been found that the overall comparison for  $K_T$  is excellent, and that  $K_Q$  is moderate, presumably due to the various power losses such as those of entry-and-exit, not accounted for in the present method.

## 8.0 ACKNOWLEDGMENT

The work was supported by the DWTNSRDC of the U.S. Navy, under Contract No. N000167-80-C-0044. The author thanks Dr. W. Morgan, Messrs. D. Cieslowski and V. Monacella of NSRDC and Dr. D.P. Wang for various support.

## 9.0 REFERENCES

Cox, G.G. (1968): Supercavitating Propeller Theory--The Deviations of Induced Velocity, 7th Symposium of Naval Hydrodynamics, Rome.

- Furuya, O. (1980): Off-design Performance Predictive Method for Supercavitating Propellers. Thirteenth Symposium of Naval Hydrodynamics, Tokyo, Japan, II-2-1 ~ II-2-24.
- Hadler, J.B., and R. Hecker (1968): Performance of Partially Submerged Propellers. Seventh Symposium of Naval Hydrodynamics, Rome, Italy, 1449-1496.
- Kerwin, J.E., and R. Leopold (1963): Propeller-incidence Correction Due to Blade Thickness. Journal of Ship Research, Vol. 7, No. 2, 1-6.
- Lerbs, H.W. (1952): Modulated Loaded Propellers with a Finite Number of Blades and an Arbitrary Distribution of Circulation. SNAME, Transactions 60, 73-123.
- Mangler, K.W. (1951): Improper Integrals in Theoretical Aerodynamics. Royal Aircraft Establishment, Farnborough, Report No. Aero 2424.
- Monacella, V.J. (1967): On Ignoring the Singularity in the Numerical Evaluation of Cauchy Principal Value Integrals. U.S. Navy, NSRDC. Research and Development Report No. 23-56.
- Morgan, W.B., and J.W. Wrench, Jr. (1965): Method of Computational Physics. Vol. 4, Some Computational Aspects of Propeller Design, 301-331, Academic Press.
- Wang, D.P. (1977): Water Entry and Exit of a Fully Ventilated Foil. Journal of Ship Research, Vol. 21, No. 1, 44-68.
- Wang, D.P. (1979): Oblique Water Entry and Exit of a Fully Ventilated Foil. Journal of Ship Research, Vol. 23, No. 1, 43-54.
- Yim, B.Y. (1969): Application of Linearized Theory to Water Entry and Water Exit Problems (Part 2) with Ventilation. NSRDC Report 3171.
- Yim, B.Y. (1971): Investigation of Gravity and Ventilation Effects in Water Entry of Thin Foils. IUTAM Symposium, Leningrad, U.S.S.R.
- Yim, B.Y. (1974): Linear Theory on Water Entry and Exit Problems of a Ventilating Thin Wedge. Journal of Ship Research, Vol. 18, No. 1, 1-11.

Table 1

Two-term camber profiles for NSRDC propeller Model 3768 and 4002 (see Hadler and Hecker (1968)) defined by Eqn. (51)

$$y_B = \frac{A}{2} (x_B + \frac{8}{3} x_B^{3/2} - 4 x_B^2) + Bx_B,$$

Equation (51)

r/R	Propeller 3768		Propeller 4002	
	A	B	A	B
.2	.01718	.00286	0	0
.3	.08446	.01408	.05833	.00972
.4	.11974	.01996	.08333	.01389
.5	.13748	.02291	.09552	.01592
.6	.14516	.02419	.09583	.01597
.7	.14514	.02419	.08729	.01455
.8	.13606	.02268	.07982	.01330
.9	.12734	.02122	.08855	.01476

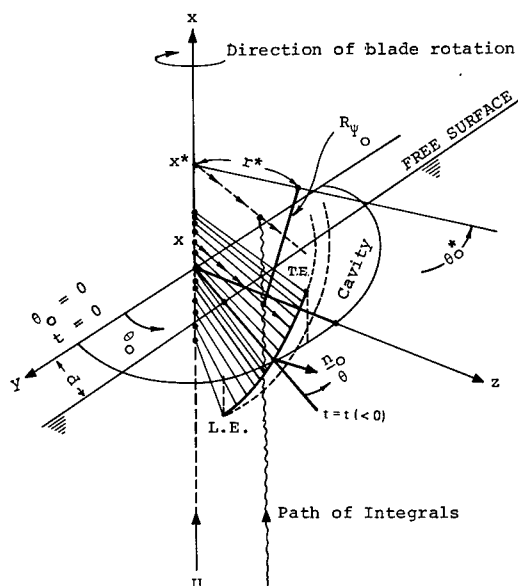


FIGURE 1 A schematic diagram for propeller flow configuration in which the propeller rotates at a fixed position while the flow approaches with the uniform velocity  $U$

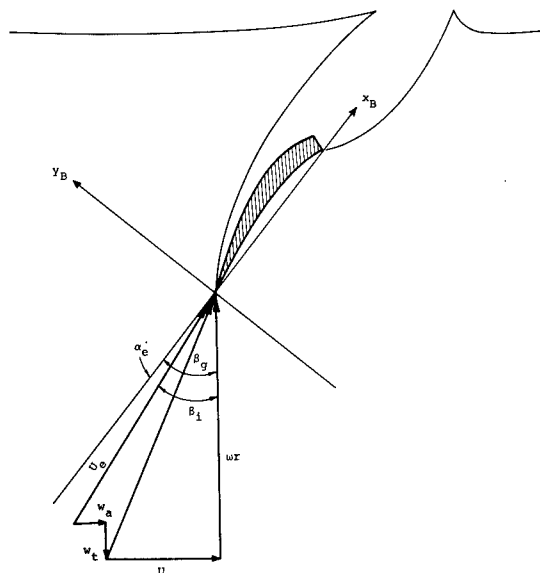


FIGURE 3 Local flow configuration in the two-dimensional plane

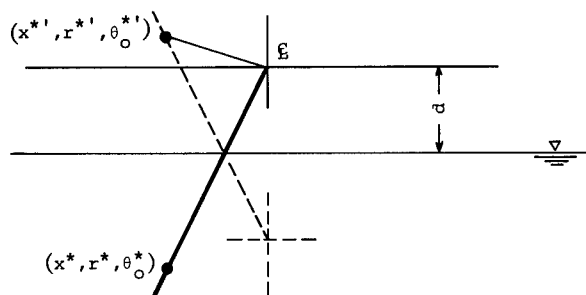


FIGURE 2 Mirror image point used for calculating the induced velocity effect due to the image wakes

Table 2

Propeller Characteristics of NSRDC Propeller Model 3768 and 4002

	Propeller Model 3768	Propeller Model 4002
Diameter	10"	12"
Number of Blades	3	2
Camber	2-Term Camber (see Table 1)	2-Term Camber (see Table 1)
P/D at $x=0.7$	1.180	1.319

Table 3

Detailed Blade Characteristics of Propeller Models 3768 and 4002

Radial Station/R	Propeller Model 3768		Propeller Model 4002	
	Chord/R	Geometric Blade Angle $\beta_g$ (Degrees)	Chord/R	Geometric Blade Angle $\beta_g$ (Degrees)
0.2	.7640	61.966	.6876	64.118
0.3	.7640	51.385	.6876	54.049
0.4	.7640	43.199	.6876	46.033
0.5	.7620	36.914	.6858	39.767
0.6	.7460	32.047	.6714	34.850
0.7	.7020	28.217	.6318	30.949
0.8	.6120	25.150	.5508	27.816
0.9	.4600	22.653	.4140	25.250

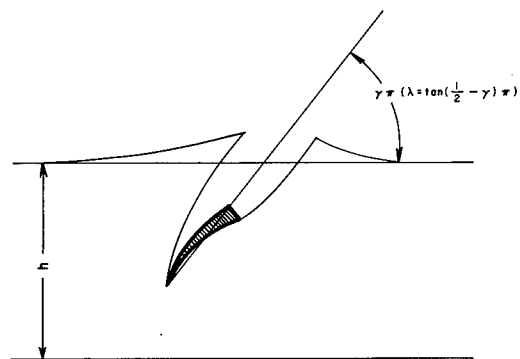
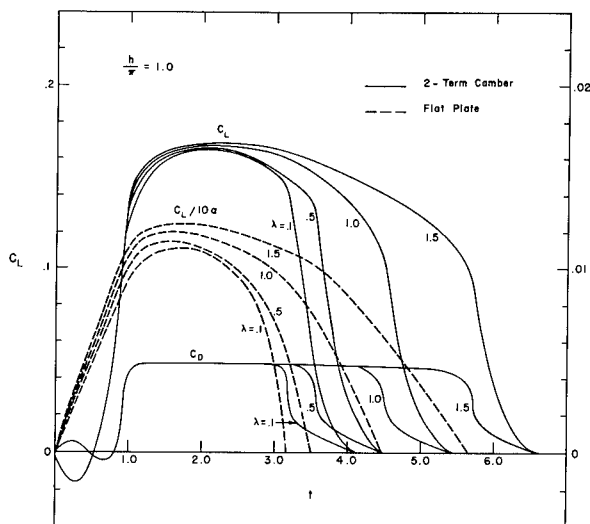


FIGURE 4 Two-dimensional lift and drag coefficients for Tulin-Bukart two-terms camber and flat plate calculated with Wang's theory (1979) where  $A_d = .10186$  (i.e.,  $C_{LD} = .20$ ) in Equation (51) has been used and  $h/\pi = 1.0$

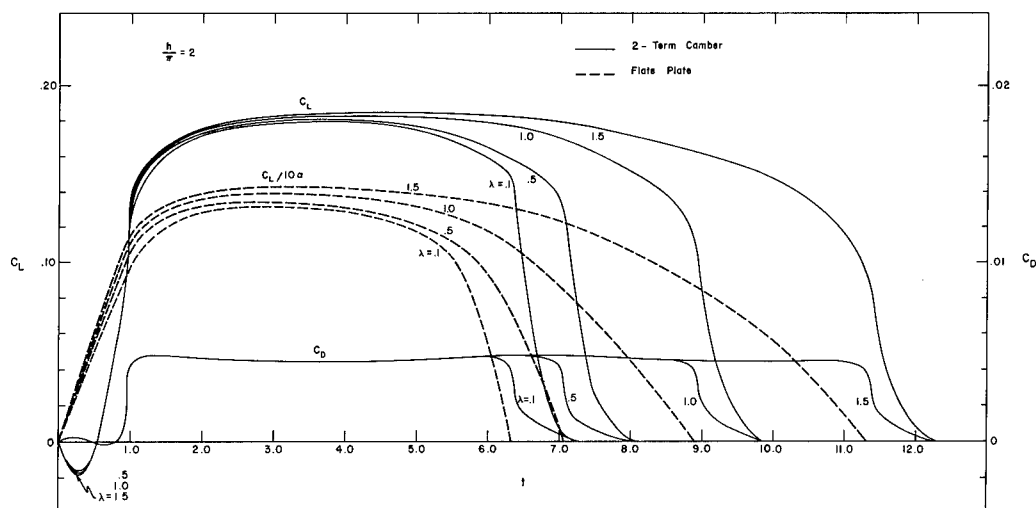


FIGURE 5 The same as Figure 4 except that  $h/\pi = 2.0$

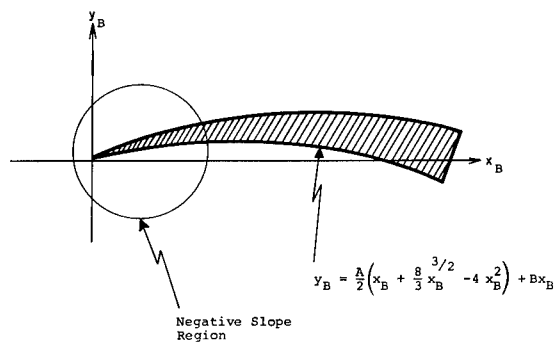


FIGURE 6 Schematic diagram for Tulin-Bukart two-term camber

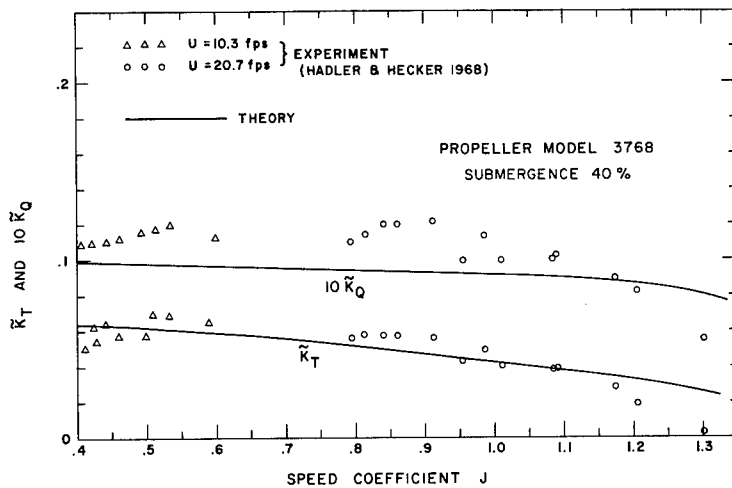


FIGURE 7 Comparison between the present theory and experimental data of Hadler and Hecker (1968) for  $K_T$  and  $K_Q$  of propeller Model 3768 at submergence 40%

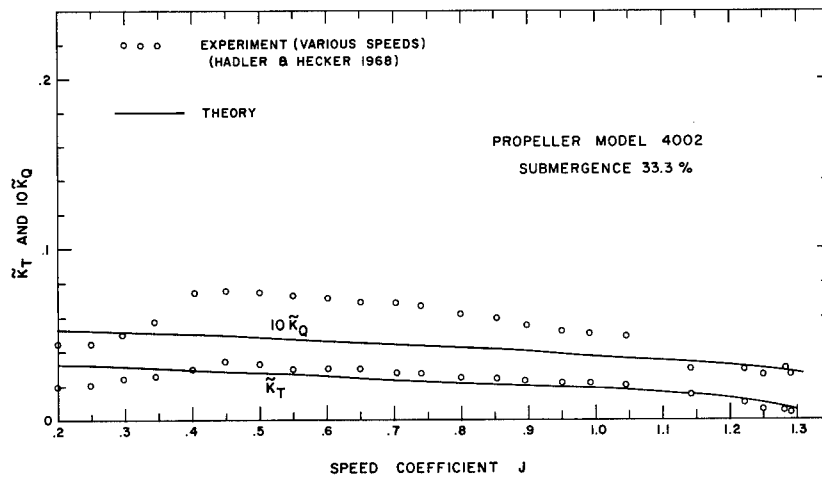


FIGURE 8 Comparison between the present theory and experimental data of Hadler and Hecker (1968) for  $K_T$  and  $K_Q$  of propeller Model 4002 at submergence 33.3%

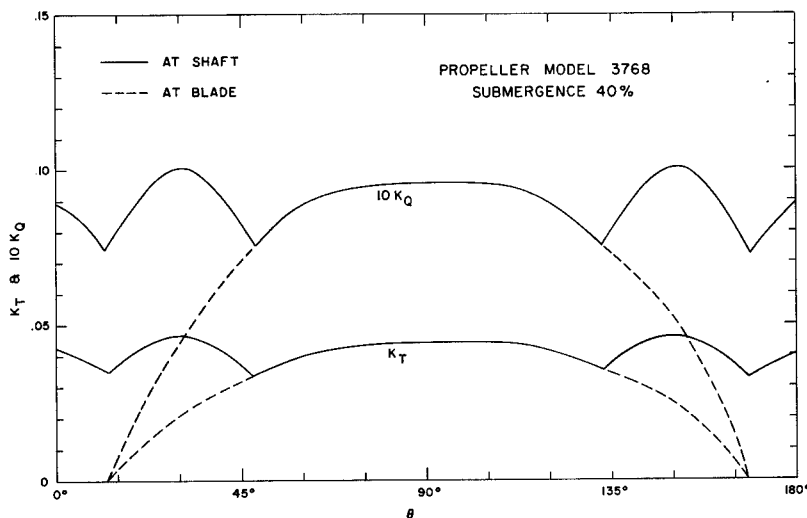


FIGURE 9 Change of thrust and torque coefficients as function of rotational angle both for the propeller shaft and individual blade of 3768 at submergence of 40% and  $J = 1.0$

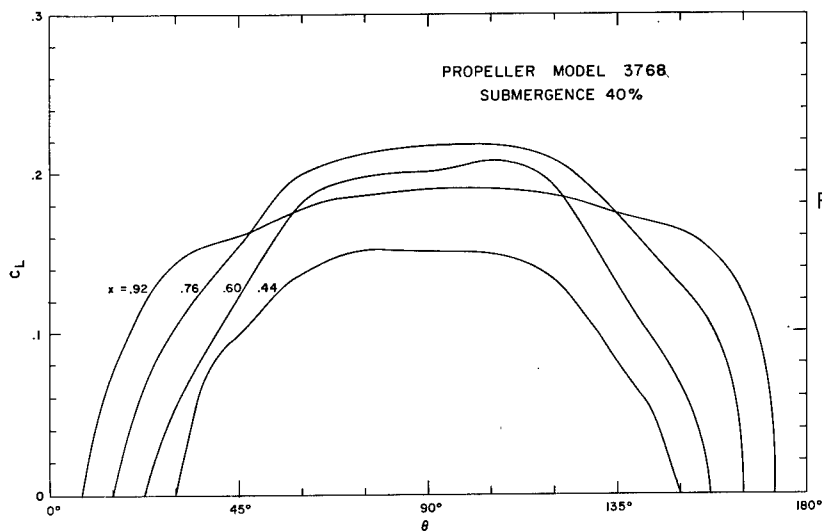


FIGURE 10 Variation of  $C_L$  as function of rotational angle at various blade radial locations for 3768 at  $J = 1.0$

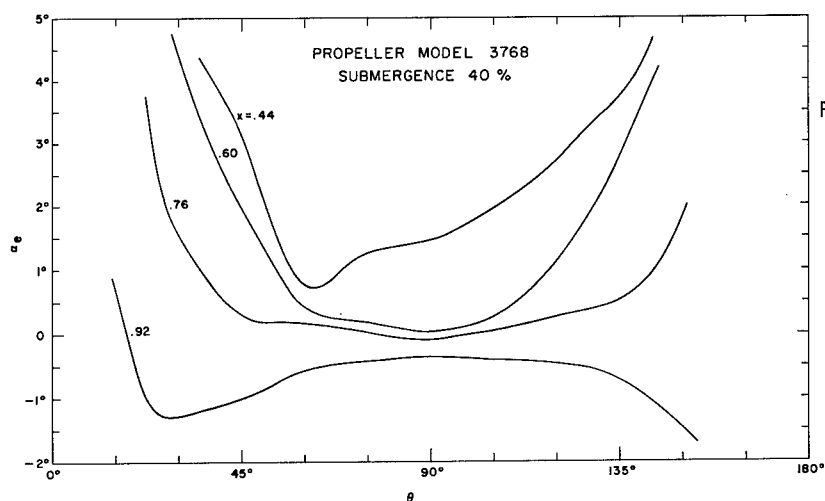


FIGURE 11 Variation of  $\alpha_e$  as function of rotational angle at various blade radial locations for 3768 at  $J = 1.0$

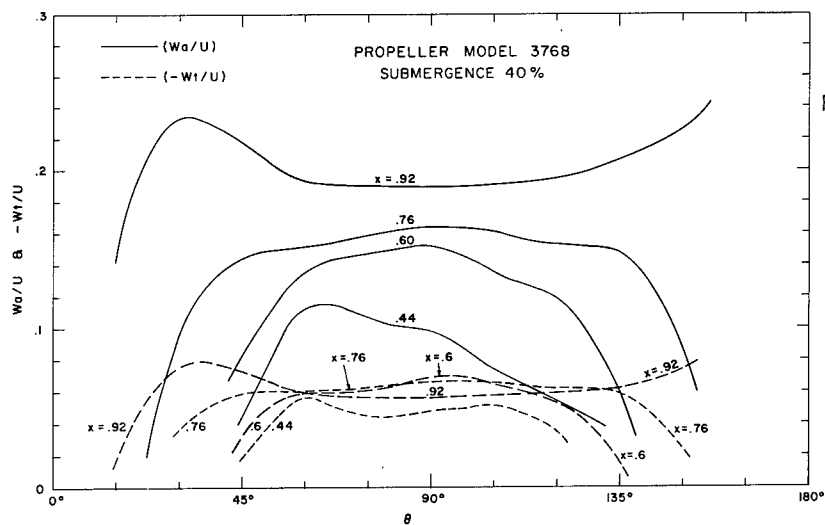


FIGURE 12 Variation of  $(W_a/U)$  and  $(W_t/U)$  as function of rotational angle at various blade radial locations for 3768 at  $J = 1.0$

## DISCUSSION

WILLIAM B. MORGAN,  
David Taylor Naval Ship R&D Center,  
Bethesda, MD, USA:

This paper is a most welcome addition to the literature on partially submerged propellers. It represents a significant advance in understanding these high-speed propellers. I have a question concerning the prediction of performance. It appears from Figures 7 and 8 that the differences between theory and experiment, especially for the torque coefficient, might be due to an underestimation of the section drag, both viscous and cavity drag. Would the author care to comment on the drag prediction?

Dr.-Ing. ERNST-AUGUST WEITENDORF,  
Hamburg Ship Model Basin (HSVA),  
Hamburg, FR Germany:

In addition to the interesting paper of the author I would like to remind you of the investigations on ventilated propellers performed by Brandt (1) and Kruppa (2) in the free-surface cavitation tunnel of the Technische Universität Berlin. His results were not quite consistent, in spite of the fact that they are sensible in a qualitative manner. The inconsistency of Brandt's results was explained - according to the memory of the discussor - by the airflow on the propeller blades when submerging under the water surface. For these flow behaviors laws of similitude could not be formulated. Can the work of the author give some assistance regarding the law of similitude when performing model tests with partially submerged ventilated propellers?

### References:

- (1) Brandt, H.: Modellversuche mit Schiffspropellern an der Wasseroberfläche. Schiff und Hafen, Heft 5, 1973.
- (2) Kruppa, C.: Testing of partially submerged propellers. Appendix V, Cavitation Committee Report, 13th ITTC, Berlin/Hamburg, 1972.

## AUTHOR'S REPLY

The author appreciates the comments of Drs. Morgan and Weitendorf. He fully agrees with Dr. Morgan in the inaccuracy of the drag prediction method used for the present theory. As pointed out in the text, the method is based on a two-dimensional linearized approach so that it does not take into account any nonlinear effects including splashes. Difficulties exist, however, as to how such nonlinear effects can accurately be incorporated. Dr. D.P. Wang used a nonlinear method to evaluate the nonlinear drag only at water entry (due to the complexity) discovering 20 - 30 % drag increase in comparison to the linearized theory. If accurate sectional forces become

available in the future, it is believed that the torque prediction of the present theory will also become much more accurate.

With regard to the similitude law for the title problem, asked by Dr. Weitendorf, the present method did not consider any aspect of it. As shown in Figures 10 and 11, the experimental results show some transition regions at which the thrust and torque coefficients suddenly change. According to Hadler and Hecker (1968), they observed flow pattern change there, from the base ventilation flow to the leading-edge ventilation flow. Despite the fact that the partially submerged propellers tested and used for comparison in the paper have sharp leading edges, this flow separation problem still exists. Therefore, if the partially submerged propeller is designed so as to be used always at the design point, or in its neighboring range, neglect of real fluid similitude law may not cause a severe problem. However, if the propeller is designed for hybrid use as designed by Dr. Kruppa and his colleagues with section profile having rounded leading edges, or to be used over a wide range of speed coefficient, a rigorous real flow separation theory should be introduced.



# FREE-SURFACE EFFECT ON THE HULL-PROPELLER INTERACTION

R. YAMAZAKI AND K. NAKATAKE

## ABSTRACT

By using the model ship hull N-S.1 ( $L=2.55$  m) which is geometrically similar to Nowacki-Sharma's mathematical model ( $L=4.5$  m), several experiments are carried out in order to grasp the effect of the free surface on the propulsive performance of a ship.

On the other hand, we attempt to elucidate the mechanism of the free surface effect on the hull-propeller interactions by using the source-represented hull and the simple sink propeller model. This model is different from the actuator disk model, because the strength of the sink is determined by the boundary condition on the propeller plane. Calculations are performed for the combination of the model hull and the model propeller used in the experiments. Experimental results are qualitatively explained by theoretical ones.

## 1. INTRODUCTION

The effect of the free surface on the propulsive performance of a slow or moderate-speed ship is considered to be small in the full load condition. But the situation seems to be different in the ballast load condition. Because of the shallow immersion of the propeller, the waves generated by the hull affect the wake distribution at the propeller plane and the propeller itself makes waves. Under these free surface effects, the hull resistance balances with the propeller thrust, and therefore the interaction phenomena are fairly complicated. The phenomena will be more complicated in the presence of the rudder piercing the free surface.

The thrust and torque diminutions of the propeller operating near the free surface were studied experimentally from old times (Kempf 1933). Dickmann (1938) explained the phenomena by making use of the sink propeller model and showed that the wave resistance of the propeller is only a small part of the thrust diminution. In recent years, Nowacki-Sharma (1971) calculated the thrust diminutions by using the program of the lifting line theory for the propeller, but did not seem to give the clear clarification for the mechanism

of the propeller-free surface interaction. By utilizing the generalized sink propeller model which Yamazaki (1968) derived, Nakatake (1976) showed that the thrust diminution is due to the wave resistance and the wave wake of the propeller itself and the former is a minor part of the diminution. This propeller model can take the boundary condition on the propeller plane into consideration.

The interaction problems between the ship hull and the sink propeller have been studied by Nakatake (1967), Nowacki-Sharma (1971), Adachi et al. (1978) and Miyata et al. (1980~1981) and it became clear that the free surface effect on the propulsive performance of a ship is not small in the case of the high speed ship or in the ballast load condition of the moderate speed ship. Especially SR-138 (1975) reported that the wave pattern resistance of the self-propelled ship increases by more than 50% compared with that of the towed ship in the ballast load condition. Tanaka et al. (1975) made a study of the wavemaking phenomena of the propeller by calculations and experiments and showed that the sink propeller can explain the wavemaking phenomena of the propeller on the whole.

In spite of much efforts described above, a clear theoretical explanation seems to be lacking as to the mechanism of the free surface effect on the propulsive performance. We intend to clarify the mechanism of the hull-propeller interaction under the free surface effect by experiments and theoretical calculations in which we use the generalized sink propeller model and the mathematical hull form.

Nowacki and Sharma treated this problem in 1971. According to their results, the thrust deduction fraction changes violently with change of Froude number. In order to reexamine those results, we adopt the similar model to the mathematical hull which they used. The model propeller is different, but the ratio of the diameter to the draft is same.

Experiments performed are the hull resistance test, the propeller open test, the self-propulsion test, the measurements of nominal wake distribution, the wake analysis and the wave analysis. The wave analyses are performed in both cases of towed and self-propelled con-

† Kyushu University, Hakozaki 6-10-1, Higashiku, Fukuoka 812

ditions.

Then we try to elucidate the free surface effect by the theoretical calculations developed so far and show that experimental results are qualitatively explained by theoretical ones.

## 2. EXPERIMENT

Experiments were performed in the towing tank (Length×Width×Depth=118m×2.67m×3~5m) of Kyushu University for three years from 1981 to 1983. They are the hull resistance test, the propeller open test, the self-propulsion test, measurement of the nominal wake distribution in the propeller plane, the wake analysis in the towed condition and the wave analysis in the towed and self-propelled conditions. In addition, the hull resistance and the propeller open test, the self-propulsion test and the wave analysis were performed for the same models at the Ship Research Institute (S.R.I), Ministry of Transport, Japan, in order to get the more reliable results.

### 2.1 Model Ship Hull and Model Propeller

In order to reexamine the results which Nowacki-Sharma (1971) obtained for the mathematical model ship (length  $L=4.5\text{m}$ ), we also adopt the geometrically similar hull N-S.1 ( $L=2.55\text{m}$ ). The hull form is expressed by the parabolic equation and symmetrical with respect to midship. Table 1 shows the principal particulars of N-S.1 and Fig. 1 shows the body plan.

Table 1 Principal particulars of model hull N-S.1

LENGTH	L	2.55 m
BREADTH	B	0.255 m
DRAFT	d	0.1697 m
WETTED SURFACE AREA	S	1.12267 m <sup>2</sup>
VOLUME OF DISPLACEMENT		0.070662 m <sup>3</sup>
BLOCK COEFFICIENT	$C_b$	0.640
HEIGHT OF SHAFT CENTER LINE		0.0850 m
DISTANCE BETWEEN CENTER OF PROPELLER AND A.P.		0.0255 m

In case of the wake analysis, we use the smaller model hull N-S.2 ( $L=1.0\text{m}$ ).

The model propeller used is not similar, but the ratio of the propeller diameter to the draft of the hull is same as Nowacki-Sharma's. We name the substitutive propeller MP-1 whose principal particulars are shown in Table 2. The

Table 2 Principal particulars of model propeller MP-1

DIAMETER	D	0.11314 m
PITCH RATIO		1.0068
EXPANDED AREA RATIO		0.6935
BOSS RATIO		0.1848
BLADE THICKNESS RATIO		0.053
ANGLE OF RAKE		9°58'
NUMBER OF BLADES		5

center of the propeller is positioned at 0.01L aft from A.P. and 0.5d under the still water surface. This arrangement is same as Nowacki-

Sharma's experiments.

### 2.2 Hull Resistance Test

The piano wire of 1 mm  $\phi$  is wound round the hull at 9.5 S.S. as the turbulence stimulator. The resistance tests of the model ship hull N-S.1 are carried out in the range of Froude number  $F_n$  from 0.1 to 0.35. The form factor  $K$  is obtained as 0.026 by using Prohaska's method (1960) and ITTC 1957 friction line following Nowacki-Sharma who got 0.025. Fig. 2 shows the total resistance coefficient  $C_t$ , the frictional resistance coefficient  $C_f$  and the viscous resistance coefficient  $C_v$  which are divided by  $\rho S V^2 / 2$ , where  $\rho$  is density of water,  $S$  the wetted surface area and  $V$

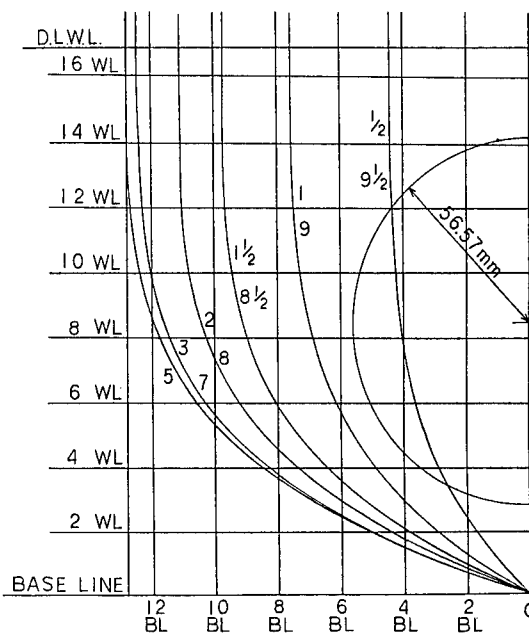


Fig. 1 Body plan of N-S.1

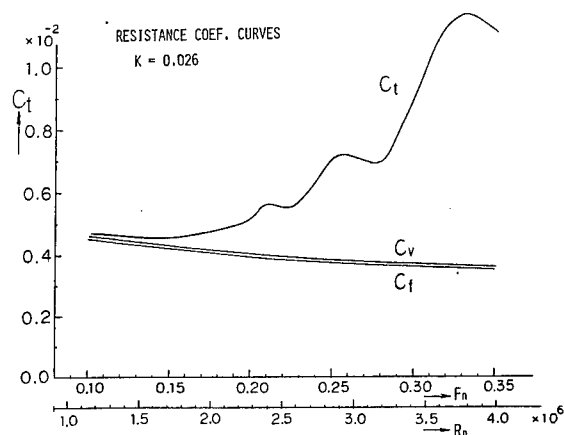


Fig. 2 Resistance coefficient curves

is speed of the model ship. Humps and hollows appear clearly on  $C_t$  curve as experienced by mathematical hull forms. In Fig. 3, we show a comparison between the obtained wave resistance coefficient  $C_w$  and Nowacki-Sharma's one.

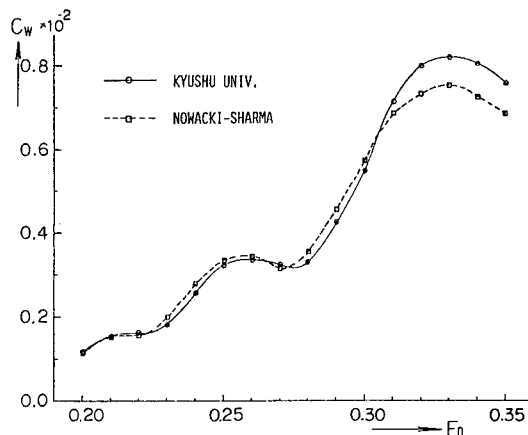


Fig. 3 Comparison of wave resistance

The agreement is good on the whole, but some difference is seen in the high  $F_n$  ( $>0.31$ ). The reason for it is not clear. Our experimental results agree well with those obtained at Ship Research Institute within experimental error.

### 2.3 Propeller Open Test

The open test of the propeller MP-1 are performed at the fixed rate of revolution  $n=14$  rps at the two different immersions: one is deep immersion ( $I=D$ ,  $D$ :diameter) which seems to have no free surface effect on the propeller characteristics, and the other is shallow immersion ( $I=0.75D$ ) which corresponds to the immersion fitted to the model ship N-S.1. The Reynolds number defined by Kempf is  $1.573 \times 10^6$  and is lower than the critical one ( $4.5 \times 10^6$ ). But it does not seem to have effects on the self-propulsion factors. Fig. 4 shows the obtained thrust coefficient  $K_T$ , torque coefficient  $K_Q$  and propeller efficiency  $\eta_p$ . In

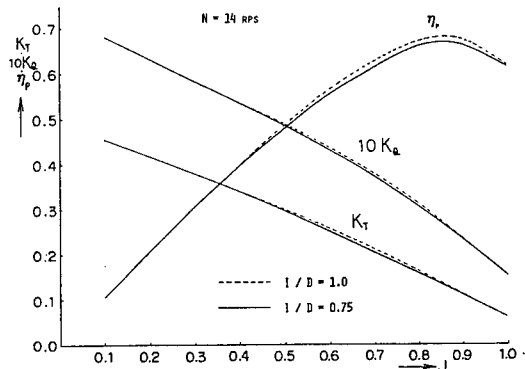


Fig. 4 Comparison of propeller characteristics ( $n=14$ rps)

the case  $I=0.75D$ ,  $K_T$ ,  $K_Q$  and  $\eta_p$  decrease a little in the range of  $J>0.4$ , where  $J$  is advance coefficient. Nowacki-Sharma stated the propeller characteristics are unchanged at the immersion deeper than  $0.75D$ . But it seems to be reasonable that these values change a little, since the propeller makes wave to some extent.

### 2.4 Self-Propulsion Test

At first, we tried to attain the self-propelled state by adjusting the rate of revolutions of the propeller as usual but we found that this method was very difficult, because the speed range was high, and humps and hollows of the resistance curve were outstanding. Therefore we adopt the Propeller Load Varying Test Method (Adachi 1983), which measures the thrust, the torque and the hull resistance while the rate of revolutions of the propeller is fixed. Though Nowacki-Sharma analyzed the self-propulsion test at the ship point (scale ratio 80), we do it at the model point, because the scale effect of the thrust deduction fraction is little as accepted commonly. Based on the thrust-identity method the analyzed self-propulsion factors, i.e. the thrust deduction fraction  $t$ , the effective wake fraction  $w_e$ , the hull efficiency  $\eta_H$ , the propeller efficiency  $\eta_p$ , the relative rotative efficiency  $\eta_R$  and the propulsive efficiency  $e_p$  are shown in Fig. 5.

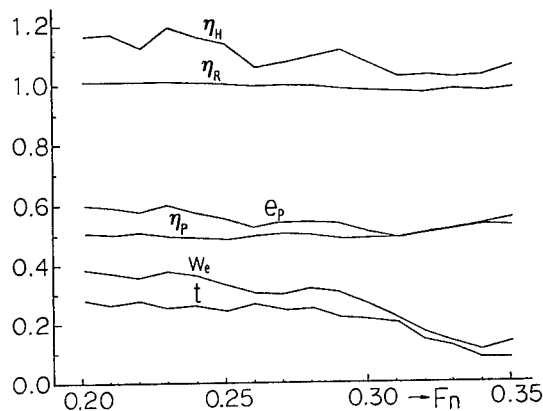


Fig. 5 Change of propulsion factors

We can see the undulations which are unusual in the low speed range. This seems to be caused by the wave-making and separation at the stern. Comparisons of the effective wake fraction  $w_e$  and the thrust deduction fraction  $t$  are shown in Fig. 6 and Fig. 7, respectively.  $w_e$  decreases rapidly undulating considerably with increase of  $F_n$ , and this tendency is same among results obtained by Nowacki-Sharma, Ship Research Ins. and Kyushu Univ., though there are some discrepancies among those values. As to  $t$ , the undulation is not so clear but rapid decrease is same as  $w_e$ . In Fig. 7, we plot the values obtained by Lammeren's experimental equation,

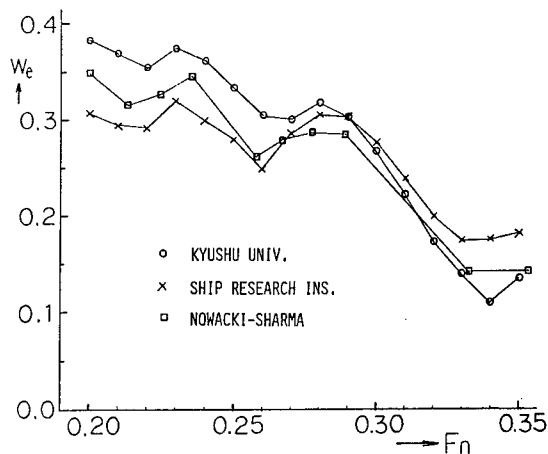


Fig. 6 Comparison of effective wake fractions

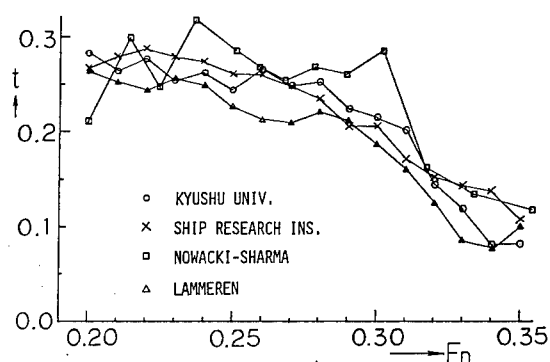


Fig. 7 Comparison of thrust deduction fractions

$$t = w_e / 1.5 + 0.01$$

This equation seems to express the approximate relation between  $w_e$  and  $t$ . Nowacki-Sharma's results change violently in the range  $Fn < 0.31$  and they seemed to be confident of their results. We would like to, however, conclude from the results of Ship Research Ins. and Kyushu Univ. that the thrust deduction fraction does not change so violently as their results. The differences of values of  $w_e$  and  $t$  obtained at three laboratories are, we guess, due to experimental difficulties such as differences of facilities or instruments, though there exist some scale effects on  $w_e$  and  $t$ .

## 2.5 Measurement of Wake Distribution in the Propeller Plane

We know that the effective wake fraction undulates considerably. Then in order to check the behavior of the above phenomena, we measure the nominal wake distribution in the propeller plane by using the propeller type velocimeter of 3 mm  $\phi$ . Fig. 8 shows the mesh division in the propeller plane. The velocimeter is traversed at each constant depth and the wake data on each depth is recorded at one run. Two examples of wake distribution are

MP-1 (14cm mesh) WAKE TEST DIAGRAM

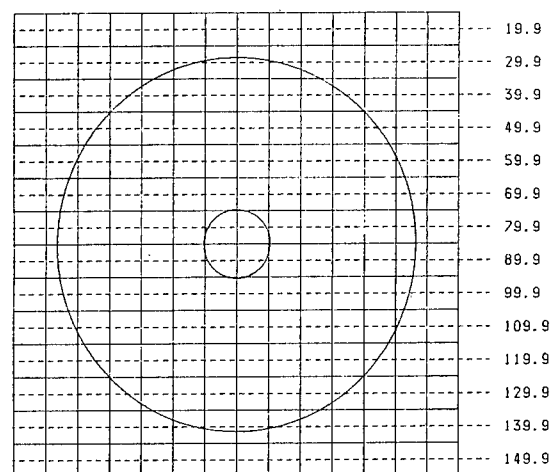


Fig. 8 Mesh division of propeller plane

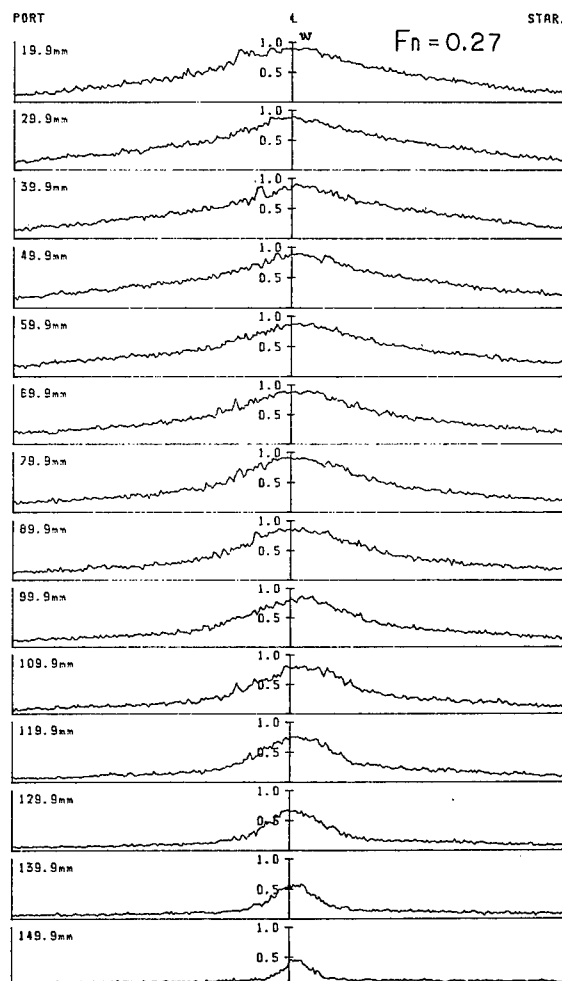


Fig. 9a Measured wake distributions

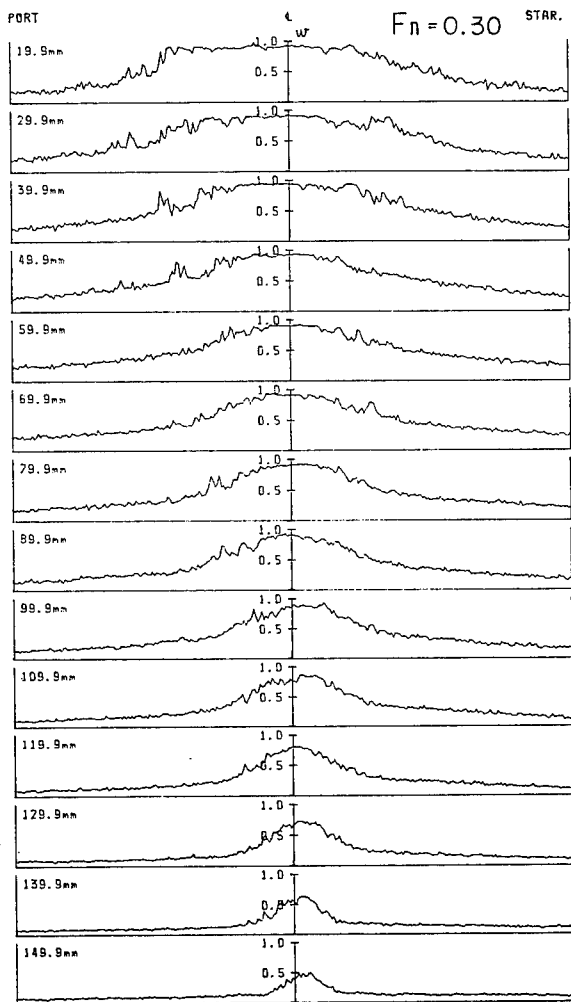


Fig. 9b Measured wake distributions

shown in the form of wake fraction  $w$  in Fig. 9a ( $F_n=0.27$ ) and Fig. 9b ( $F_n=0.30$ ). The distribution in the case  $F_n=0.27$  is a usually expected one which has a peak around the center line, while the one of Fig. 9b shows a different type which has a wide high wake zone near the free surface. This difference of two types seems to depend on the difference of starting points of stern waves with change of  $F_n$  (DOI 1982). By data processing on a micro-computer, the wake contour curves are drawn in Fig. 10a ( $F_n=0.27$ ) and Fig. 10b ( $F_n=0.30$ ). The difference of two types appears as the difference of extension of wake contours in the upper part of the propeller plane. And the type of larger extension ( $F_n=0.30$ ) gives larger nominal wake fraction  $w_n$ . The comparison between  $w_e$  and  $w_n$  is shown in Fig. 11. It is interesting to note that these two curves are quite similar, though the value of  $w_n$  is fairly larger than  $w_e$ . Nowacki-Sharma obtained the nominal wake fraction by using wheel type velocimeter. Their values seem to be small even if the scale effect on the wake is taken into consideration.

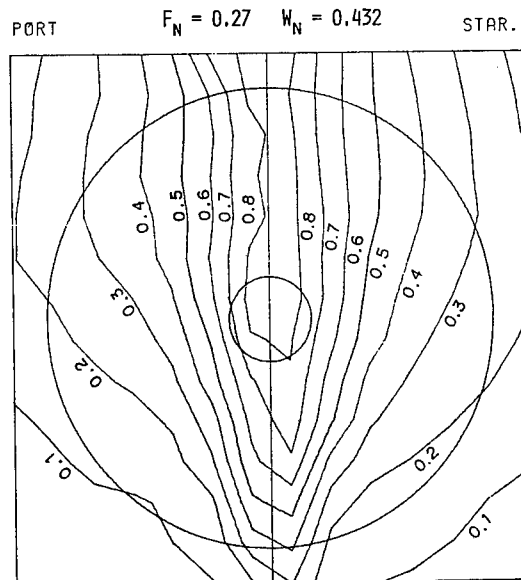


Fig. 10a Wake contours

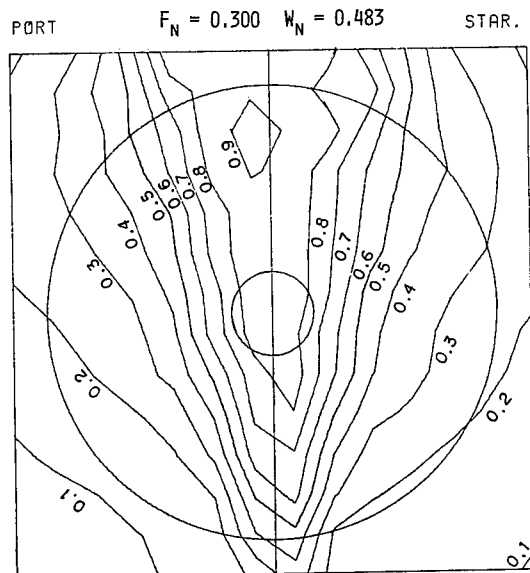


Fig. 10b Wake contours

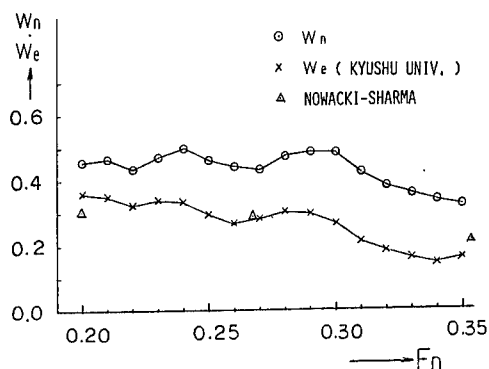


Fig. 11 Comparison of wake fractions

## 2.6 Wake Analysis

At the transverse section half ship length aft from A.P., we measure the wake distribution at each depth by means of the same propeller type velocimeter as before, and the wave height above the velocimeter by the servo-type waterlevel meter, in order to obtain the wake resistance. The model ship used is N-S.2 having length of 1.0 m. Fig. 12 shows the examples of wake distributions  $w$  at the depths  $\bar{z}=18$  mm and 25 mm in case  $Fn=0.225$ .

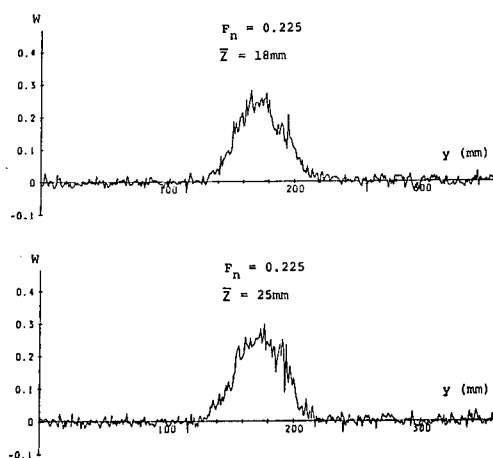


Fig. 12 Examples of measured wake fractions

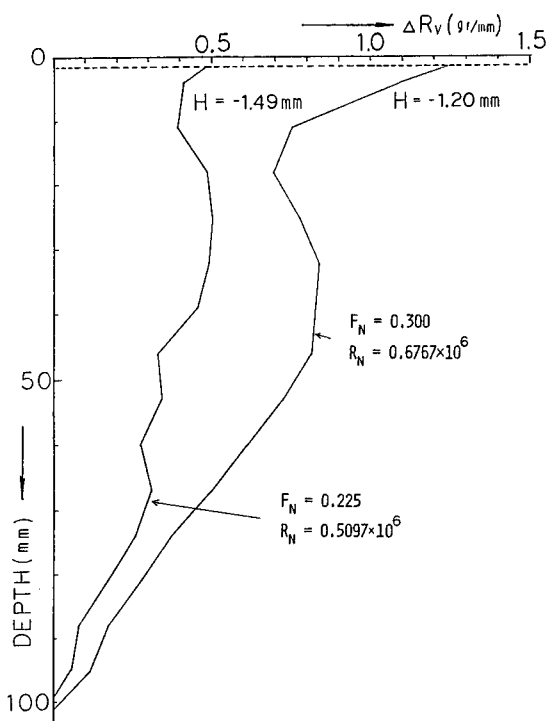


Fig. 13 Depthwise distributions of wake resistance

We define the  $y$ -axis in the transverse direction and the  $\bar{z}$ -axis in the depth-wise direction of the towing tank, and then the wake resistance  $\Delta R_v$  at each depth is obtained by

$$\Delta R_v = \rho V^2 \int_{-\infty}^{\infty} w(1-w) dy$$

Denoting the mean waterlevel by  $H$ , the wake resistance of the hull is given as

$$R_v(\text{wake}) = \int_{-\infty}^H \Delta R_v d\bar{z}$$

Fig. 13 shows the depthwise distributions of  $\Delta R_v$  in cases  $Fn=0.225$  and  $0.30$ , and by integrating  $\Delta R_v$  in the  $\bar{z}$ -direction we get  $R_v(\text{wake})$  which is compared in Fig. 14 with the viscous resistance derived from the resistance test and the ITTC 1957 friction line. The wake resistance is larger than the viscous resistance and undulates with increase of  $Fn$ .

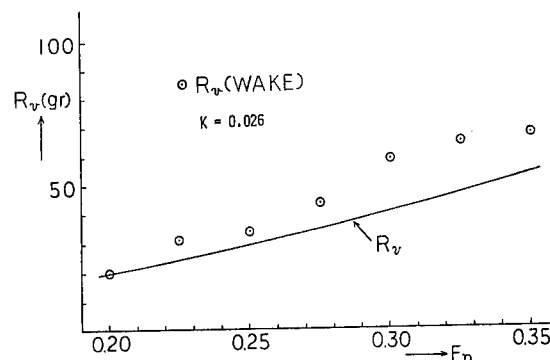


Fig. 14 Comparison between viscous resistance and wake resistance

## 2.7 Wave Analysis

By the capacity-type wave probe set on the tank wall 1.331m apart from the ship center line, we measure the wave profiles in both towed and self-propelled conditions. Fig. 15 shows the examples of measured wave profiles of both conditions in cases  $Fn=0.25$  and  $0.30$ . In both cases, the wave of self-propelled condition has larger amplitude and its phase lags a little. The analyzed amplitude functions  $PQ$  are shown in Fig. 16. Fig. 17 shows the wave pattern resistance coefficient  $\bar{C}_w$  obtained by integrating the curves in Fig. 16. In Fig. 17 the results of Ship Research Ins. are also plotted for comparison. Though the record length of wave profiles is not long enough in the high speed range  $Fn > 0.31$ , the wave pattern resistance curve of the towed condition expresses well the shape of the wave resistance curve, but the values themselves are nearly the half of the wave resistance. The wave pattern resistance of the self-propelled condition has a tendency to increase at the speeds where the humps and hollows occur. From Fig. 16 we understand that the wave pattern resistance increases in case  $Fn=0.25$  and remains unchanged in case  $Fn=0.30$ .

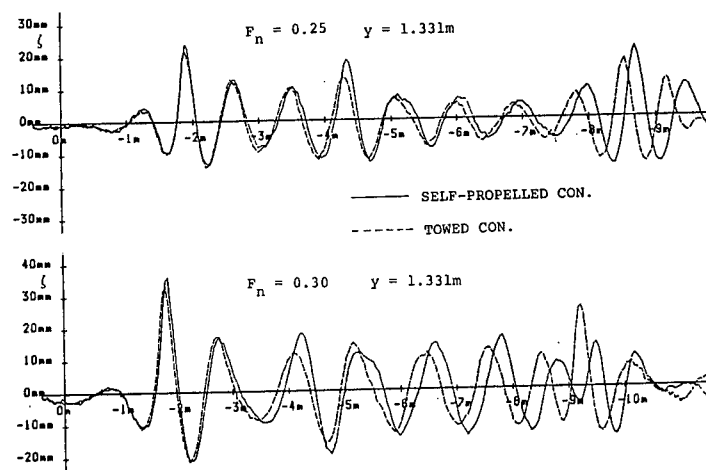


Fig. 15 Comparison of wave profiles

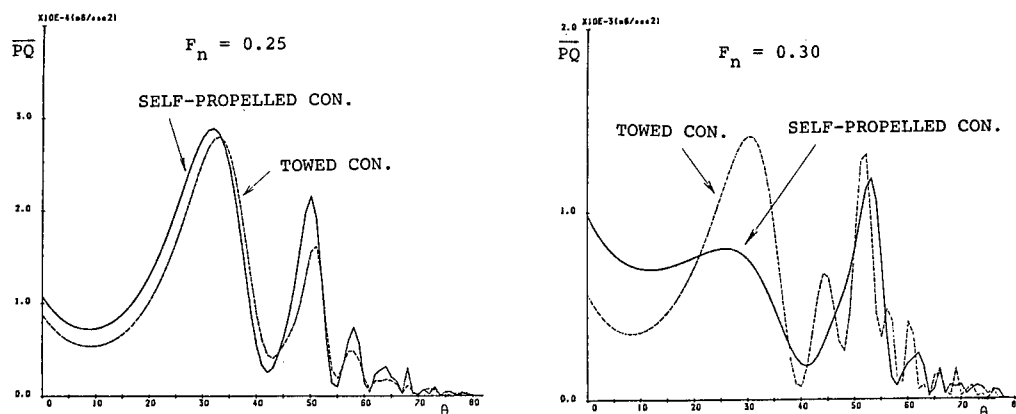


Fig. 16 Comparison of amplitude functions

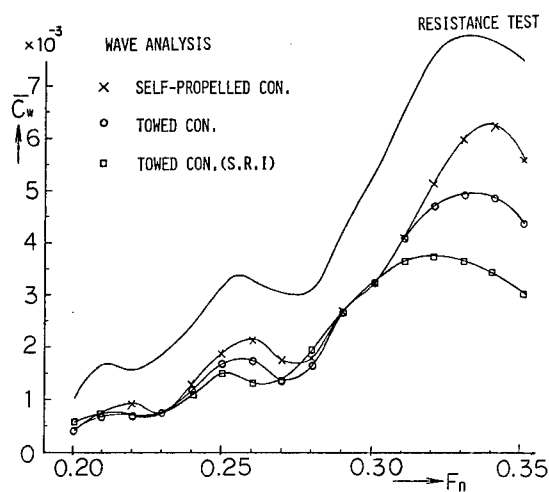


Fig. 17 Comparison of wave pattern resistance coef.

### 3. CALCULATION

#### 3.1 Basic Equation

When a ship with only a propeller is being advanced straight on still water with a constant velocity  $V$ , the propulsive performance of the ship is same as that of the ship fixed in the free stream of speed  $V$ . We define a rectangular coordinate system  $O$ - $xyz$  fixed at the midship, with the  $z$ -axis vertically upwards, the  $xy$ -plane on the undisturbed water surface and the  $x$ -axis in the direction of the free stream (vide Fig.18). The one side of the hull form N-S.1 is expressed as

$$y_0(x, z) = \frac{B}{2} \left\{ 1 - \left( \frac{x}{l} \right)^4 \right\} \left\{ 1 - \left( \frac{z}{a} \right)^4 \right\}, \quad (1)$$

where  $-d \leq z \leq 0$ ,  $-1 \leq x \leq 1$ ,  $l = L/2$ .

And we designate the diameter, the radius, the effective pitch of the given propeller MP-1 by  $D$ ,  $r_0$ ,  $2\pi a$ , respectively and assume that the center of the propeller is located at the

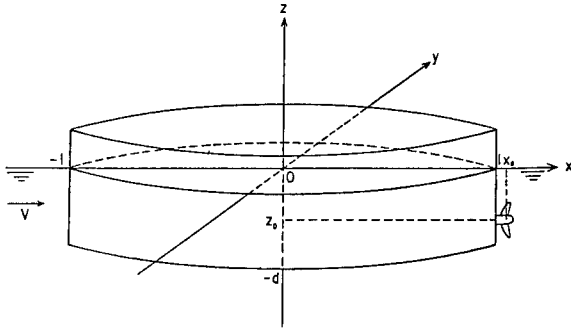


Fig. 18 Coordinate system

point  $(x_0, 0, z_0)$  and the propeller disk is in the plane  $x=x_0$ .

The thin ship hull is represented by the center plane source distribution of the density  $V \cdot m(x, z)$ . Then the disturbed velocity potential  $\phi_H$  due to the hull becomes

$$\phi_H = \frac{V}{4\pi} \int_{-l}^l dx' \int_{-d}^0 m(x', z') \cdot G(x, y, z; x', 0, z') dz' \quad (2)$$

where  $G(x, y, z; x', y', z')$  is the Green function of the source under the free surface and is expressed as

$$G(x, y, z; x', y', z') = - \frac{1}{\sqrt{(x-x')^2 + (y-y')^2 + (z-z')^2}} - \frac{1}{\sqrt{(x-x')^2 + (y-y')^2 + (z+z')^2}} + \frac{1}{\pi} \lim_{\mu \rightarrow 0} \int_{-\pi}^{\pi} d\theta \int_0^{\infty} \frac{e^{k(z+z') + i[(x-x')\cos\theta + (y-y')\sin\theta]}}{k - k_0 \sec^2\theta - i\mu \sec\theta} k dk \quad (3)$$

and  $g$  is acceleration of gravity and  $k_0 = g/V^2$ . Then the propeller is represented by the generalized sink propeller model (Yamazaki 1968) when the pitch of the propeller is very small. And the disturbed velocity potential  $\phi_P$  due to the propeller becomes

$$\phi_P = - \frac{1}{4\pi} \iint_A \sigma(y, z') G(x, y, z; x_0, y', z') dA \quad (4)$$

where  $\sigma(y, z)$  is the density of the sink distribution over the disk plane whose effective area is  $A (= \pi r_e^2)$ , where  $r_e$  is an effective radius.

Next we divide the disturbed velocity into three components, that is, the double body component, the local wave component and the free wave component which are distinguished by the suffixes 0, L, F, respectively. Then the x-directional velocities  $u_H$  and  $u_P$  are expressed as

$$u_H = \frac{\partial \phi_H}{\partial x} = u_{H0} + u_{HL} + u_{HF}, \quad (5)$$

$$u_P = \frac{\partial \phi_P}{\partial x} = u_{P0} + u_{PL} + u_{PF} \quad (6)$$

The source distribution  $m(x, z)$  of the hull is approximated by Michell's distribution. Denote the x-directional viscous wake fraction by  $w_v(y, z)$  and the angular velocity of the propeller by  $\Omega (= 2\pi n)$ , the boundary condition on the propeller plane becomes approximately

$$(u_H + u_P)_{x=x_0} + \sigma(y, z)/2 = \Omega a - V \{1 - w_v(y, z)\} \quad (7)$$

Next, we consider the hull resistance  $R_H$  and the thrust  $T$  and the torque  $Q$  of the propeller.  $R_H$  is divided into the pressure resistance  $R_P$  and the viscous resistance  $R_V$  which is calculated by using the ITTC 1957 line and the form factor. By applying the Lagally's theorem,  $R_P$  is obtained by

$$R_P = -\rho V \int_{-l}^l dx \int_{-d}^0 m(x, z) \cdot (u_{HF} + u_{P0} + u_{PL})_{y=0} dz = R_{HW} + R_{H1} + R_{H2} \quad (8)$$

where  $\rho$  is density of the fluid. In Eq.(8)  $R_{HW}$  is the wave resistance of the hull only and  $R_{H1}$  expresses the interactive pressure resistance without free surface effect and  $R_{H2}$  expresses the interactive pressure resistance between the hull and the local wave component of the propeller. Therefore, neglecting the changes of  $m(x, z)$  and  $R_V$  due to the action of the propeller, the increment of the hull resistance is expressed only as  $R_{H1} + R_{H2}$ . On the other hand, the propeller thrust  $T$  is given as

$$T = \rho \Omega h \iint_A \sigma(y, z) dA, \quad (9)$$

where  $2\pi h$  is the pitch of the propeller free vortex which is determined later so as to agree with the thrust coefficient in the open water condition. Moreover, by introducing the correction term  $\Delta k_a$  which expresses the torque increment due to viscosity and so on, the torque  $Q$  is approximated as

$$Q = k \cdot T + \rho n^2 D^5 \Delta k_a \quad (10)$$

The condition of the self-propelled state of the ship becomes

$$T = R_P + R_V \quad (11)$$

Here, in order to simplify the calculation and to make easy understanding of the mecha-



nism of the hull-propeller interactions, the sink distribution is replaced by the point sink of strength  $V \cdot M_P$  located at  $(x_0, 0, z_0)$ . Then, from Eq. (4)  $\phi_P$  becomes

$$\phi_P = -\frac{V}{4\pi} M_P \cdot G(x, y, z; x_0, 0, z_0). \quad (12)$$

We use the volume mean value  $\bar{w}_v$  over the propeller disk instead of  $w_v(y, z)$  and the mean value  $\bar{\sigma}$  ( $=VM_P/A$ ) instead of  $\sigma(y, z)$ , then Eqs. (7) and (9) become

$$(u_H + u_P)_{x=x_0, y=0, z=z_0} + \bar{\sigma}/2 = \Omega a - V(1 - \bar{w}_v) \quad (13)$$

$$T = \rho A \bar{\sigma} \Omega h \quad (14)$$

### 3.2 Characteristics of a Propeller in Open Water

Let us approximate the given characteristics ( $K_T, K_Q, \eta_p \sim J$ ) of a propeller by using the generalized sink propeller. Denoting the source density in this case by  $\bar{\sigma}$ , and the propeller thrust by  $T$ , these are given from Eqs. (13) and (14) as

$$\bar{\sigma}_0 = 2(\Omega a - V), \quad (15)$$

$$T_0 = \rho A \bar{\sigma}_0 \Omega h.$$

Here we determine the value of  $a$  so as that the relation  $K_T = T_0 / \rho n^2 D^4$  holds. That is,

$$h = K_T n^2 D^4 / (A \bar{\sigma}_0 \Omega).$$

By curve fitting of the value of  $h$  for every  $J$  ( $=V/nD$ ) value, we obtain the curve of second degree  $h(J)$ . As to the torque, we obtain as

$$\Delta K_Q = K_Q - h(J) \cdot T_0 / \rho n^2 D^5$$

Similarly the curve of  $\Delta K_Q$  is expressed by the curve of second degree  $\Delta K_Q(J)$ . Then, by making use of Eq. (15),  $h(J)$  and  $\Delta K_Q(J)$ , we can obtain the characteristics of the given propeller in open water at an arbitrary  $J$  value.

### 3.3 Propeller Operating Near the Free Surface

Let us consider the characteristics of the propeller operating at the depth  $I$  ( $=-z_0$ ) under the free surface. Denoting the value in this case by  $\bar{\sigma}_F$ , the thrust by  $T_F$ , then  $\bar{\sigma}_F$  and  $T_F$  are given as

$$\bar{\sigma}_F = \bar{\sigma}_0 / (1 + F_0), \quad (16)$$

$$T_F = \rho A \bar{\sigma}_F \Omega h(J_F).$$

where

$$F_0 = \frac{2k_0^2 A}{\pi} \int_0^{\pi/2} \exp(-2 \sec^2 \theta / F^2) \sec^3 \theta d\theta,$$

$$k_0 = g/V^2, \quad F = V/\sqrt{gI},$$

$$J_F = V(1 - w_F)/(nD), \quad w_F = -F_0 \bar{\sigma}_F / (2V)$$

The torque  $Q_F$  is obtained from  $T_F$  and Eq. (10). From Eq. (16), we understand that the thrust decreases under the free surface and this is caused by the decrease of sink strength which is due to wave wake since  $F_0 > 0$ . And when the propeller operates near the free surface, we note that the characteristics of the propeller depend on not only  $J$  value but also  $F$  value.

### 3.4 Self-Propulsive Performance and Wave Pattern Resistance

In case of the self-propelled state, the propeller operates in the wake of the ship hull and affects the flow field around the hull. The sink density  $\bar{\sigma}$  of this case is expressed from Eq. (13) as

$$\bar{\sigma} = \sigma_B / (1 + F_0), \quad (17)$$

$$T = \rho A \bar{\sigma} \Omega h(J_s),$$

where

$$\sigma_B = 2\{\Omega a - V(1 - w_n)\},$$

$$w_n = \bar{w}_v - w_H,$$

$$w_H = \frac{1}{V} (u_{H0} + u_{HL} + u_{HF})_{\substack{x=x_0, z=z_0 \\ y=0}},$$

$$J_s = V(1 - w_e)/(nD),$$

$$w_e = w_n - F_0 \bar{\sigma} / (2V).$$

The torque  $Q$  is obtained from  $T$  and Eq. (10). Since the nominal potential wake fraction  $w_H$  of the hull is usually negative, we see that the nominal hull wake increases the thrust and the propeller wake decreases the thrust.

Now the self-propelled state of the ship is attained by determining the sink density  $\bar{\sigma}$  so as to coincide the hull resistance  $R_H$  with the thrust  $T$  iteratively. By making use of the propeller characteristics under the same condition, i.e.  $F$  value, as the self-propelled state, thrust deduction fraction  $t$ , effective wake fraction  $w_e$ , propeller efficiency  $\eta_p$ , hull efficiency  $\eta_H$ , propulsive efficiency  $e_p$ , effective horse power EHP and delivered horse power DHP are defined by the thrust-identity method as

$$t = (R_{H1} + R_{H2})/T, \quad w_e = 1 - nDJ/V$$

$$\eta_p = J K_T / (2\pi K_A), \quad e_p = \eta_H \eta_P, \quad (18)$$

$$EHP = R_t \cdot V, \quad DHP = EHP / e_p.$$

Next let us consider about the change of wave pattern resistance in both towed and self-propelled conditions. When the wave elevation  $\zeta$  far apart from the ship is expressed as

$$\zeta = \int_{-\pi/2}^{\pi/2} \left\{ S(\theta) \sin(k_0 p \sec^2 \theta) + C(\theta) \cos(k_0 p \sec^2 \theta) \right\} d\theta \quad (19)$$

$$p = x \cos \theta + y \sin \theta$$

by using the amplitude functions  $S(\theta)$  and  $C(\theta)$  of the wave, the wave pattern resistance  $\bar{R}_w$  corresponding to this wave elevation is given as (Maruo 1965)

$$\bar{R}_w = \frac{\rho \pi V^2}{2} \int_{-\pi/2}^{\pi/2} \bar{P}Q(\theta) d\theta, \quad (20)$$

where

$$\bar{P}Q(\theta) = \left[ \{S(\theta)\}^2 + \{C(\theta)\}^2 \right] \cos^3 \theta.$$

Now, making use of equations from (2) to (6), the wave elevation  $\zeta_{HP}$  far apart from the self-propelled ship becomes

$$\begin{aligned} \zeta_{HP} &= -\frac{V}{g} (u_{HF} + u_{PF})_{z=0} \\ &= \frac{k_0}{\pi} \int_{-\pi/2}^{\pi/2} \left\{ \zeta_{HP}(\theta) \sin(k_0 p \sec^2 \theta) + C_{HP}(\theta) \cos(k_0 p \sec^2 \theta) \right\} \sec^3 \theta d\theta, \quad (21) \end{aligned}$$

where

$$\zeta_{HP}(\theta) = S_H(\theta) + S_P(\theta),$$

$$C_{HP}(\theta) = C_H(\theta) + C_P(\theta),$$

$$\begin{aligned} \left. \begin{aligned} S_H(\theta) \\ C_H(\theta) \end{aligned} \right\} &= \int_{-l}^l \int_{-d}^0 m(x, z) e^{k_0 \sec^2 \theta \cdot z} \cdot \left\{ \begin{aligned} \sin(k_0 x \sec \theta) \\ \cos \end{aligned} \right\} dx dz, \end{aligned}$$

$$\left. \begin{aligned} S_P(\theta) \\ C_P(\theta) \end{aligned} \right\} = \frac{\bar{\sigma} A}{V} e^{k_0 \sec^2 \theta \cdot z_0} \left\{ \begin{aligned} \sin(k_0 x_0 \sec \theta) \\ \cos \end{aligned} \right\}.$$

The corresponding wave pattern resistance  $\bar{R}_{WHP}$  is given from Eqs. (19), (20) and (21) as

$$\begin{aligned} \bar{R}_{WHP} &= \frac{\rho V^2 k_0^2}{\pi} \int_0^{\pi/2} \left[ \{S_H(\theta)\}^2 + \{C_H(\theta)\}^2 \right. \\ &\quad \left. + 2\{S_H(\theta)S_P(\theta) + C_H(\theta)C_P(\theta)\} \right. \\ &\quad \left. + \{S_P(\theta)\}^2 + \{C_P(\theta)\}^2 \right] \sec^3 \theta d\theta \quad (22) \\ &= \bar{R}_{HW} + \rho A \bar{\sigma} (u_{HF})_{\substack{x=x_0, \\ y=0, \\ z=z_0}} + \bar{R}_{PW}, \end{aligned}$$

where  $\bar{R}_{HW}$  and  $\bar{R}_{PW}$  express the wave pattern resistance of the hull in the towed condition and the one of the propeller itself, respectively and the second term expresses the interaction term between the hull and the propeller. The sum of last two terms becomes the change of wave pattern resistance in the self-propelled condition and can have plus or minus value according to the second term. But usually it becomes the increase of the wave pattern resistance. Under the free surface effect, the sink strength, the thrust and the torque surely decrease as seen from Eq. (17). As to how these decreased values are connected with the change of the wave pattern resistance, we would like to leave for further theoretical investigation. Anyhow, we understand that the increase of wave pattern resistance of the self-propelled ship is caused by the consumption of a part of engine horse power for wavemaking of the propeller and is not due to the increase of the hull resistance and there exists almost no relation between the thrust deduction fraction and the change of wave pattern resistance.

### 3.5 Calculated Results

Above-described calculation method is applied to the model hull N-S.1 and the model propeller MP-1 used in the experiments. When the open characteristics of the propeller MP-1 is known, we approximate the characteristics by setting

$$A = \pi(0.57344r_0)^2, \quad \alpha = 1.10/(2\pi).$$

Then we determine the values of  $h$  and  $\Delta K_A$  as

$$h = 0.01507(J=0.1) \sim 0.01827(J=1.0)$$

$$\Delta K_A = 0.00896(J=0.1) \sim 0.00607(J=1.0)$$

so as to agree with the given  $K_T$  and  $K_A$  by using the procedure described in 3.2. And  $h(J)$  and  $\Delta K_A(J)$  are expressed by the curves of second degree of  $J$ . Fig. 19 shows the  $K_T$ ,  $K_A$ ,  $\eta_P$  curves of the propeller immersed at  $I=0.75D$  and  $I=D$ , rotating at the rate of revolutions  $n=14$ rps. These curves resemble with those in Fig. 4 obtained in the experiments. In the self-propulsion test, the speed of the model ship is kept constant, and therefore we need

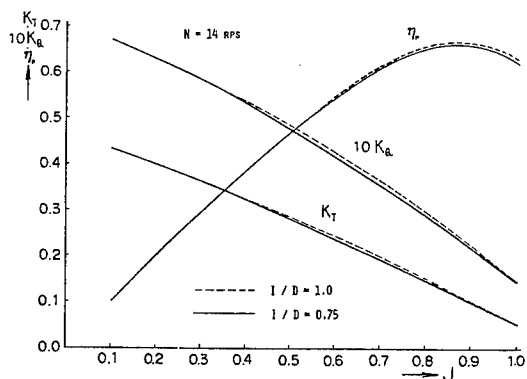


Fig. 19 Comparison of propeller characteristics ( $n=14\text{rps}$ )

the characteristics of MP-1 at the speed of the model ship. Fig. 20 shows an example of the characteristic curves calculated at  $V=1.4\text{ m/sec}$  ( $F_n=0.28$ ). These values, however, are found to be little altered in the range  $F_n=0.2\sim 0.35$ . In the calculation, we assume  $\bar{w}_w=0.125$ . Fig. 21 shows the curves of

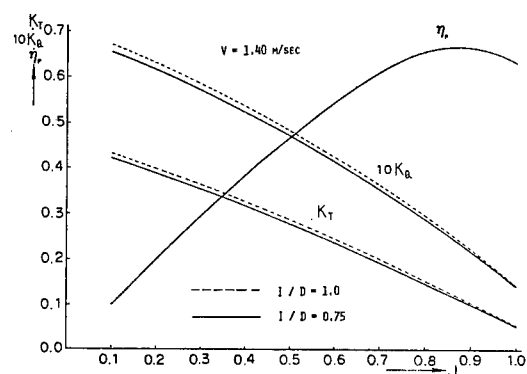


Fig. 20 Comparison of propeller characteristics ( $V=1.4\text{m/sec}$ )

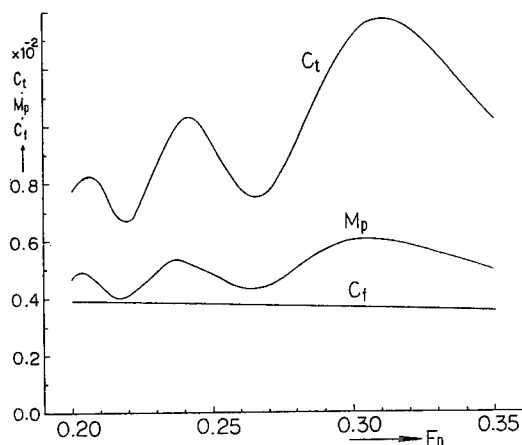


Fig. 21 Total hull-resistance coef. and strength of propeller sink

the total hull resistance coefficient  $C_t$  ( $=2R_t/\rho S V^2$ ) and the strength of the propeller sink  $M_p$  ( $=\bar{w}A/V$ ) in the self-propelled state. The variation of  $M_p$  corresponds to that of  $C_t$ . In Fig. 22 we show the self-propulsion factors analyzed by means of the thrust-identity method based on the characteristic curves of MP-1 obtained at each constant speed. Compared with the experimental results in Fig. 5, we find that the tendencies of the factors are

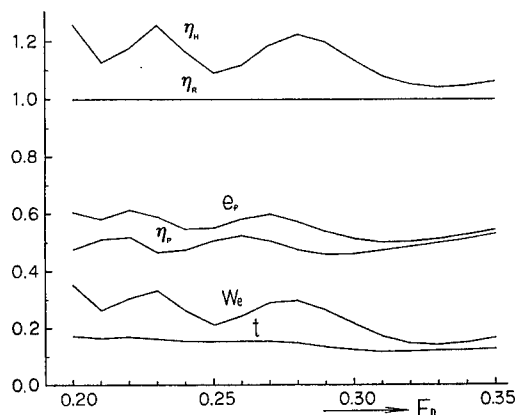


Fig. 22 Change of propulsion factors

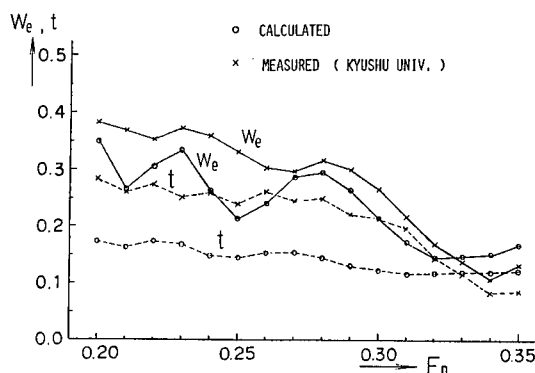


Fig. 23 Comparison of effective wake and thrust deduction fractions

similar to each other, though the values themselves are a little different. Fig. 23 shows comparisons between measured and calculated values of the effective wake fraction  $w_e$  and thrust deduction fraction  $t$ . There appear the similar undulations in both experimental and calculated curves of  $w_e$  and  $t$ , and the speeds at which the humps and hollows occur are near to each other. The experimental value of  $t$  changes drastically in the high speed range ( $F_n>0.31$ ). The reason for is not clear to us.

Since the undulation of  $w_e$  curve seems to be caused by the wake distribution in the propeller plane, we calculate the potential wake distributions at the speeds of humps and hollows and show them in the forms of wake contours and the mean wake fraction  $w_{wm}$  in Fig. 24. The case  $F_n=0.01$  represents the

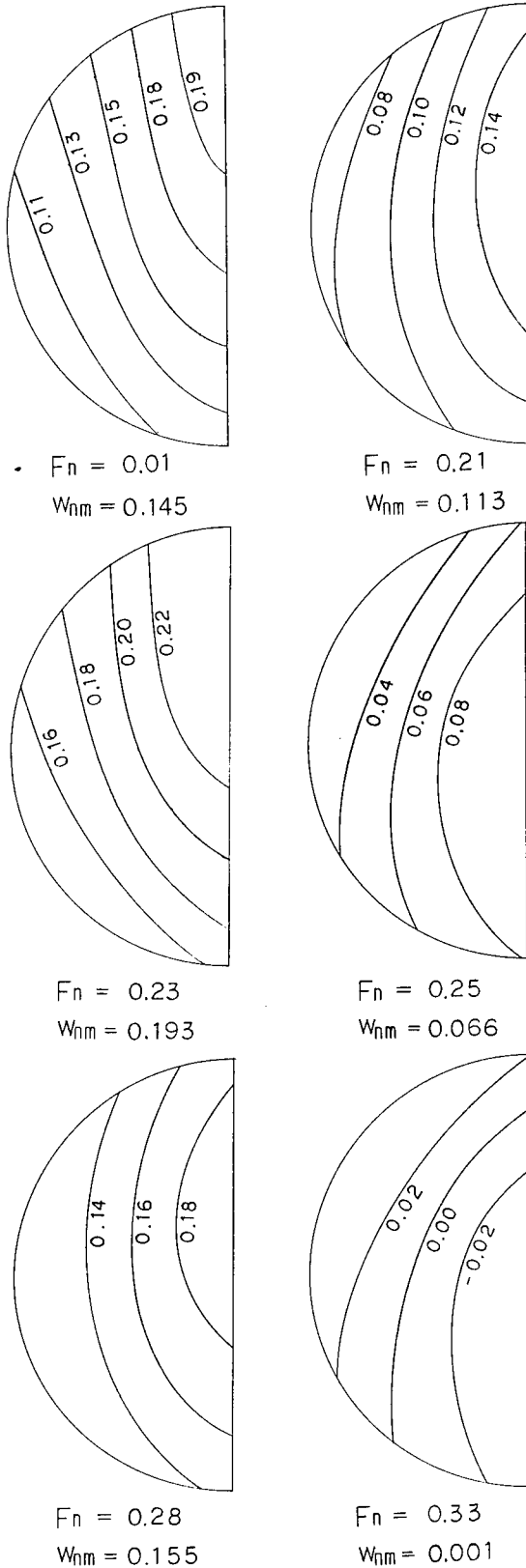


Fig. 24 Potential wake contours

wake contour of the double body flow, and the cases  $F_n=0.21, 0.25, 0.33$  do the ones at the hollow speeds, and the rests at hump speeds. As seen from Fig. 24, the wake contours bend outwards in the upper part of the propeller plane at the hump speeds, while the ones do inwards at the hollow speeds. And these tendencies seem to correspond to the experimental contours in Fig. 10. In Fig. 25, we show the wave profiles around the propeller position corresponding to the above wake distributions. It is interesting that the wave elevations at the propeller position correspond to the values of  $w_{nm}$ . Fig. 26 shows the changes of the nominal wake fractions. We see that the potential mean wake fraction corresponds to the potential wake fraction at the propeller center where the point sink propeller is located.

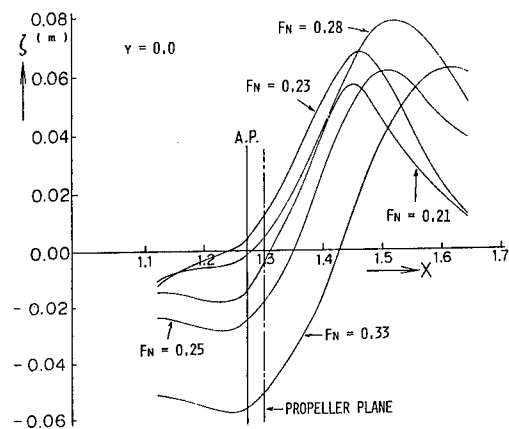


Fig. 25 Wave profiles around propeller

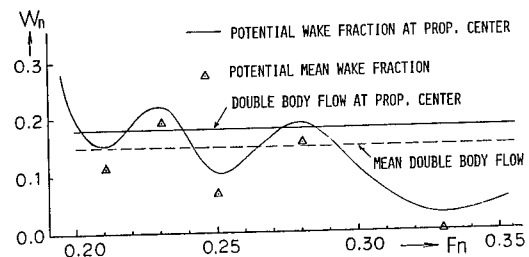


Fig. 26 Change of potential wake fractions

Lastly, we calculate the wave profiles by Eq. (21) at the constant transverse section ( $y=0.3L$ ) and perform the wave analysis by using the wave profiles in both towed and self-propelled conditions according to the procedures in 3.4. The wave profiles are calculated approximately by the 100 point sources in the ship center plane. Fig. 27 shows the wave profiles in the towed and self-propelled conditions and the propeller waves at  $F_n=0.280$  and  $0.320$ . In both cases, the amplitudes of the self-propelled conditions increase and the phases of the former lag a little. In Fig. 28 we show a comparison of amplitude functions of these waves obtained by means of Newman-Sharma's wave analysis method

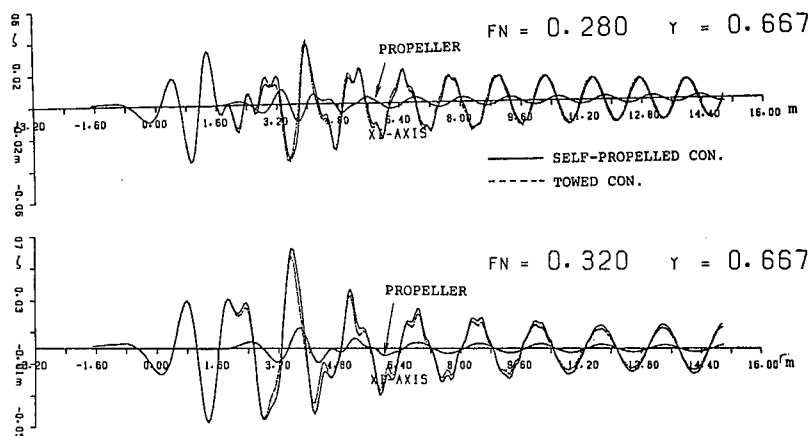


Fig. 27 Comparison of wave profiles

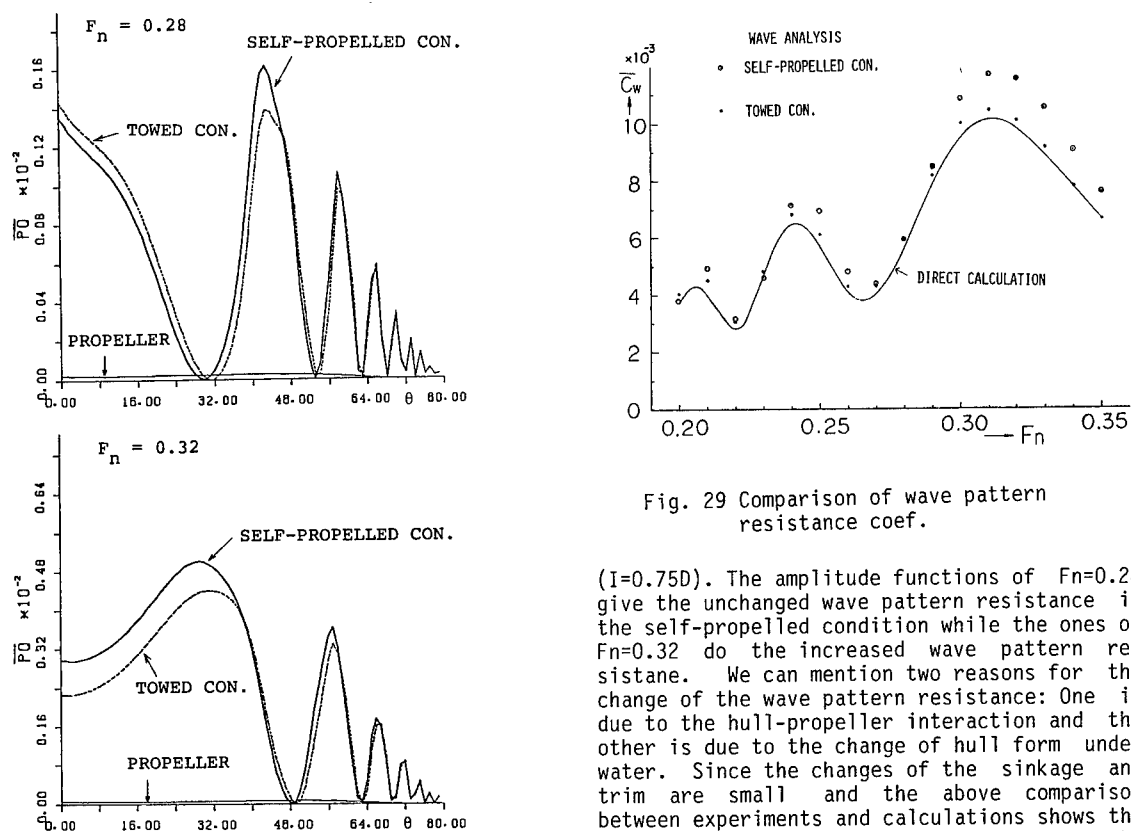


Fig. 28 Comparison of amplitude functions

Fig. 29 Comparison of wave pattern resistance coef.

( $I=0.750$ ). The amplitude functions of  $Fn=0.28$  give the unchanged wave pattern resistance in the self-propelled condition while the ones of  $Fn=0.32$  do the increased wave pattern resistance. We can mention two reasons for the change of the wave pattern resistance: One is due to the hull-propeller interaction and the other is due to the change of hull form under water. Since the changes of the sinkage and trim are small and the above comparison between experiments and calculations shows the similar tendency, we dare to say that the former reason is the main one.

As to the free surface effects on the hull-propeller interactions, we can summarize as follows. As the immersion of the propeller becomes small, the thrust  $T$  and the torque  $Q$  decrease due to wavemaking of the propeller. Therefore we should increase the rate of revolutions  $n$  so as to hold the self-propelled state. This increases  $\Omega (=2\pi n)$  and the horse power  $P_p (= \Omega Q / 75)$  delivered to the propeller. Accordingly  $e_p$  becomes worse with shallow immersion of the propeller and this effect appears mainly as decreases of  $\eta_p$  and  $\eta_H$ . The decrease of  $\eta_H$  is due to decrease of  $w_e$ , and

(Newman 1963, Sharma 1963). Fig. 29 shows a comparison of wave pattern resistance coefficients  $\bar{C}_w (=2R_w/\rho S V^2)$  obtained by the wave analysis and the direct calculation. The wave pattern resistance in the towed condition is a little larger than the wave resistance calculated directly, because the wave pattern resistance has some numerical approximations. As seen in the experimental results in Fig.17, the wave pattern resistance has a tendency to increase considerably in the self-propelled condition even at the non-shallow immersion

the increase of wave pattern resistance does not affect the thrust deduction fraction. The difference of  $P_D$  between the shallow and deep submergence of the propeller is considered to consist of the increase of wave pattern resistance and the horse power consumed for the decrease of the thrust due to hull-propeller interactions. Therefore, with increase of wave pattern resistance, it is expected that  $e_p$  becomes worse. Another results calculated by assuming no propeller waves tell  $e_p$  becomes worse by about 5% at the immersion of  $I=0.75D$ .

#### 4. CONCLUSION

From the experimental and calculated results for the model ship hull N-S.1 and the propeller MP-1, following conclusions may be drawn.

- 1) The wake fraction and the thrust deduction fraction generally undulate under the free surface effect.
- 2) It is confirmed experimentally that the nominal and effective wake fractions have close relation even under the free surface effect. Their undulations are caused by the wavemaking of the hull.
- 3) The wave pattern resistance in the self-propelled condition has a tendency to increase at the hump and hollow speeds, and is related little to the thrust deduction fraction.
- 4) The simple theoretical models of the hull and the propeller can predict qualitatively the mutual interactions of the hull and the propeller under the effect of the free surface.
- 5) In order to clarify wholly the mechanism of the hull-propeller interactions under the free surface effect, we should adopt the more accurate propeller model.

#### ACKNOWLEDGEMENTS

We wish to express our heartfelt gratitude to Dr. H. Adachi, late Mr. F. Moriyama and staffs of Ship Research Institute, Japan for their kind executions of the model tests. We are also very grateful to Mr. K. Oda, Mr. K. Ueda and Mr. A. Nishida for their experimental works, and to Miss K. Matsuki, Mr. T. Sato and Mr. K. Kataoka for their making the manuscript. We wish to sincerely thank the persons who engaged in the numerical and experimental works as the student theses from 1981 to 1983. Further we are deeply indebted to the staffs of the Large-Sized Computer Center of Kyushu University for their help in the computer work using FACOM M-382. This research is partly supported by the Grant-in-Aid for Research of the Ministry of Education, Science and Culture.

#### REFERENCES

- Adachi, H. and Sugai, N. (Dec. 1978): On the Thrust Deduction Coefficient, Journal of the Kansai Society of Naval Architects, Japan, No.171 (in Japanese).
- Adachi, H. (Dec. 1983): On the Teoretical Bases and Appication Methods of the Propeller Load Varying Test Method, Journal of the Society of Naval Architect of Japan, No.154 (in Japanese).
- Dickmann, H.E. (1938): Schiffskörpersog, Wellenwiderstand eines Propellers und Wechselwirkung mit Schiffswellen, Ingenieur-Archiv, Band 9.
- Doi, Y., Takeuchi, S., Hong, S., Kajitani, H. and Miyata, H. (Jul. 1982): Characteristics of Stern Waves Generated by Ships of Simple Hull Form (Second Report), Journal of Society of Naval Architects of Japan No.151.
- Kempf, G. (1933 1934): Immersion of Propeller, Transactions of the North-East Coast Institutions of Engineers and Shipbuilders
- van Lammeren, W.P.A.: The Design and Calculation of Cavitation-Free Wake Propeller, Netherland Experiment Tank, Wageningen.
- Maruo, H. (Jun. 1965): An Outline of Wave making Resistance Theory, Text of Symposium on Wavemaking Resistance (in Japanese).
- Miyata, H. et al (1980 1981): On the Optimization of the Aft-Part of Fine Hull Forms, Journal of the Kansai Society of Naval Architects, Japan, No. 180
- Nakatake, K. (Jul. 1967): On the Interaction between the Ship Hull and the Screw Propeller, Journal of Seibu Zosenkai, No.34 (in Japanese).
- Nakatake, K. (Feb. 1976): Free Surface Effect on Propeller Thrust, ISWR.
- Newman, J.N. (1963): The Determination of Wave Resistance from Wave Measurements along a parallel Cut, International Seminar on Theoretical Wave Resistance, Ann Arbor, Michigan.
- Nowacki, H. and Sharm, S.D. (Sept. 1971): Free Surface Effects in Hull Propeller Interaction, Report of the University of Michigan, No. 112.
- Prohaska, C.W. (1960): A Simple Method for the Evaluation of the Form Factor and the Low Speed Wave Resistance, Proceedings ITTC 11.
- Sharma, S.D. (1963): A Comparison of the Calculated and Measured Free-Wave Spectrum of an Inuid in Steady Motion, International Seminar on Theoretical Wave Resistance, Ann Arbor, Michigan.
- SR-138 (1975): Report of the Shipbuilding Research Association of Japan, the 138 Research Committee No.220 (in Japanese).
- Tanaka, H. et al. (Sept. 1975): On Waves Generated by Propellers, Journal of the Kansai Society of Naval Architects, Japan, No.158 (in Japanese).
- Yamazaki, R. (1968): On the Propulsion Theory of Ships on Still Water—Introduction—, the Memoirs of the Faculty of Engineering, Kyushu University, Vol. XXVII, No.4.

## DISCUSSION

Dipl.-Ing. JÖRG BLAUROCK,  
Hamburg Ship Model Basin (HSVA),  
Hamburg, FR Germany:

First I want to congratulate the authors on their paper. There are two remarks I want to make on it:

1. Fig. 4 gives a difference in  $K_T$ - and  $K_Q$ -values at  $J$ -values higher than 0.4 which is explained by you as a consequence of the difference in propeller immersion. My impression is that this small difference could also be caused by uncertainty in measurement. On the other hand I would expect as a consequence of immersion more difference in  $K_T$ - and  $K_Q$ -values at low  $J$ -values than at higher  $J$ -values.

2. We normally at our institute correct the open water test result using the "method of equivalent profile" before using it for analysing the propulsion test results. In this we assume fully turbulent flow in the behind ship condition. As different from this we can expect laminar flow on a larger extent on the propeller blades in open water tests, especially when the tests will be carried out at such extremely low Reynolds number as in your case. Did you apply any corrections like this? I think this will not influence the results of your investigation in general, but some of the analysed data, for example the wake fraction, might be different when applying such correction procedures.

Prof. HORST NOWACKI,  
Technical University of Berlin,  
Berlin, Germany, and  
Prof. SOM D. SHARMA,  
Institut für Schiffbau,  
Hamburg, FR Germany:

The Authors have revisited a classical area of ship hydrodynamics, that of hull-propeller interaction, in which several fundamental questions remain open despite so many efforts for more than half a century. In fact, they have repeated with much care our set of experiments performed in 1971. The independent verification of such a test series is very rare, and particularly valuable in this case.

Their experiments were carried out under very similar test conditions as ours, but it is important to note the few differences that did exist: There were, in particular, differences with respect to model size, propeller rake, test evaluation at model versus ship self-propulsion point, and most notably in the fact that the model was apparently free to move in their tests whereas it was constrained in sinkage and trim in ours. This may account for certain differences in the results, especially at higher Froude numbers.

Concentrating now on the important results for the interaction quantities we note, first, that the measured values of effective wake fraction were found to be in close agreement at three independent test sites and are showing a

significant decrease toward high Froude numbers as well as certain oscillations at lower speeds. These types of free-surface effects are well understood.

As for the thrust deduction, its mean trend shows the same type and degree of Froude number dependence as the effective wake in both sets of tests. Regarding the magnitude of the Froude number dependent oscillations we do not want to overstretch the validity of data derived from such sensitive experiments. But we do maintain that one should be prepared to expect oscillations in the thrust deduction of the same magnitude as in the effective wake fraction. Otherwise the close agreement in the large drop of the two quantities at high Froude numbers would be difficult to explain.

Finally, the biggest remaining open question pertains to the large discrepancy between measured and calculated thrust deduction. The authors' views on the cause of this would be of much interest. Among other possibilities we feel that one must improve the accuracy of both the propeller model (with respect to its finite extent, rake etc.) and of the hull representation (with regard to displacement effects neglected in centerplane source distributions).

Our compliments again for a very valuable paper!

Dr. EIICHI BABA,  
Mitsubishi Heavy Industries Ltd.,  
Nagasaki, Japan:

The authors' long term efforts in developing theories of ship propulsion have inspired those researchers who study the interaction of hull, propeller and rudder. In the present paper, the authors have studied the free-surface effect on the hull-propeller interaction and compared calculated results with experiments in various aspects. The discussor would like to ask a question on one point. In Fig. 15 of the present text, phase difference is observed for measured wave systems with and without an operating propeller. On the other hand, in the calculation (Fig. 27) such difference is not observed. Is this difference between measurement and calculation suggesting inadequacy of physical modeling of flow by use of a sink disc representing a working propeller? The present discussor measured a wave system of a towed ship model when the direction of propeller rotation is reversed and compared it with the wave system for normal direction of propeller rotation, i.e. for the condition producing thrust. As shown in Fig. 30 the direction of phase shift of wave system changed toward ship stern. In addition to this, a remarkable reduction of wave heights is observed. This experiment suggests a clear interference between ship wave system and propeller wave system. The discussor suspects that the flow around a working propeller may affect in shifting the starting point of stern wave system of a ship. Thus phase difference between wave systems with and without a working propeller has occurred. There might be a difference of flow characteristics between a sink disc and an actual propeller. The flow

field corresponding to propeller slipstream is apparently different for both cases. The authors' comment would be appreciated on this matter.

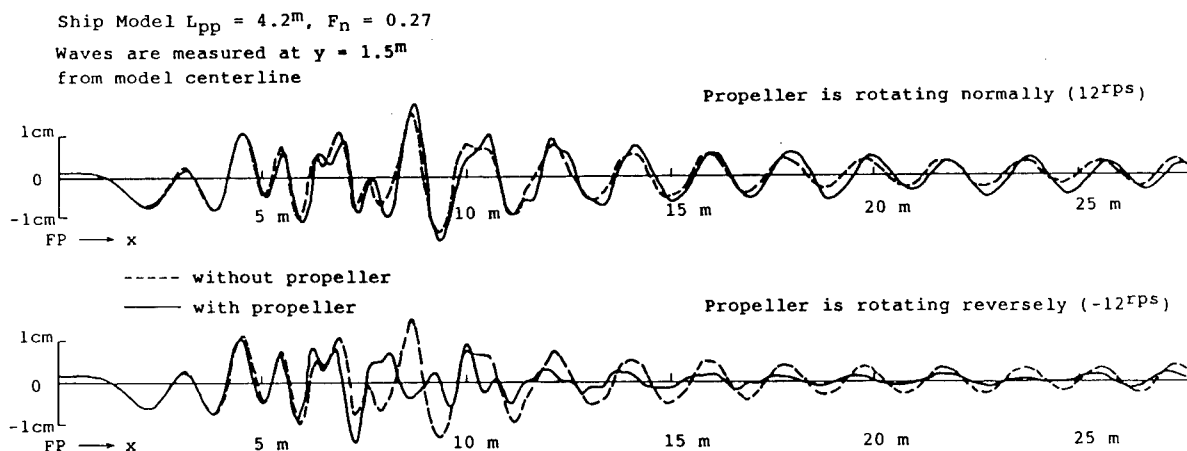


Fig. 30 Comparison of wave systems with and without a working propeller

Prof. MICHAEL SCHMIECHEN,  
Berlin Model Basin (VWS),  
Berlin, Germany:

The authors deserve our thanks for the wealth of data they have produced. It will certainly take much time before we fully understand the implications. My remarks can therefore only be of a more qualitative nature and relate to the observation that the values of the wake and thrust deduction fractions drastically drop in the speed range above  $F_n = 0.3$ ; Figs. 5, 7, 23.

Looking at the wave profiles at the location of the propeller provided by the authors, Fig. 25, the reason for the phenomenon in question is immediately clear. Obviously the deceleration of the flow around the afterbody is suppressed by the waves, i.e. the potential or rather the displacement wake is decreasing with increasing speed. This argument is confirmed by the computations of the authors; Fig. 26.

From fundamental theory of hull-propeller interaction we know now that the thrust deduction fraction is directly related to the relative potential wake fraction or the displacement influence ratio, as I prefer to call it in my paper to be presented right after this discussion.

Although the data having been derived by the authors in the traditional way from hull resistance, propeller open water, and propulsion tests do not exactly correspond to my definitions I have used them to determine values of

the displacement influence ratio. While up to the speed  $F_n = 0.3$  the values slowly decrease without any detectable undulation, they exhibit a dramatic drop in the speed range from  $F_n = 0.31$  to  $0.34$  as expected.

What disturbs me in the paper is that the authors, although computing decreasing values of the potential wake fraction, Fig. 26, do not come up with corresponding changes in the values of the thrust deduction fraction, Fig. 23, for increasing values of the speed. Maybe they can comment on this apparent inconsistency in their computed results.

## AUTHORS' REPLY

To Mr. Blaurock:

Thank you very much for your discussion from the experimental side. The first remark is related to Fig. 4. We admit there are some experimental scatters in the obtained values. In case of more shallow immersion, say  $I/D = 0.5$ , there exists clear free-surface effect on  $K_T$  and  $K_Q$  values, as you may admit. We think the immersion  $I/D = 0.75$  is, maybe, near to the border region of the existence of the free-surface effect. Then one may treat such a small difference as an experimental scatter, if one does not know the free surface effect. Since the  $J (=V/nD)$  value decreases, the speed of propeller and the wave formation decreases. Then we think that the free surface effect appears reasonably in the intermediate  $J$  value range.



The next one is related to the analysis method of the propulsion factors. We did not make any correction for the open water propeller characteristics concerning the low Reynolds number. If we use such a corrected diagram, we will obtain a little different values of wake fractions. But we think that the general trends of the propulsion factors will not be affected.

To Profs. Nowacki and Sharma:

Thank you very much for your detailed and encouraging discussion. The discussers mentioned four differences of the test conditions between present work and theirs. Among them, we also think that the constraint of the model is the main reason for the differences of wave resistance coefficient and others. We agree with discussers' opinion that the thrust deduction fraction undulates fairly in the high speed range in case of the mathematical hull form. Since the conventional hull form is well designed so as not to make large waves, the undulation will become generally small. As to the analytical results we would like to say, at first, that we intended to explain the qualitative behaviors of the hull-propeller interaction under the effect of free surface. The smallness of the mean value of the thrust deduction fraction will be much improved by using the double-body sources instead of Michell's sources as pointed out by the discussers. We add the fact that Michell's sources correspond to the fairly fine hull form. We wish to treat the hull-propeller-rudder interaction problem including the free surface effects by using a more realistic propeller model.

To Dr. Baba:

Thank you very much for the discussion on the propeller model and for showing us very interesting wave profiles. In our theory, the wave due to the propeller rotating in the normal direction can be expressed approximately as the wave due to the equivalent sink, and is not concerned with the slip stream, i.e., the non-potential flow behind it. The thrust and torque of the propeller have no direct relation with the action of the sink. Further we suppose that the wave due to the propeller, i.e., the propeller wave, can be superposed linearly with the hull wave. Then the wave number  $k_0$  due to the propeller agrees with that due to the hull.

The calculated wave profiles in Fig. 27 show phase difference between the hull wave and the propeller wave though they are small. Fig. 31 indicates the three kinds of wave profiles obtained from Fig. 30. One is due to the hull only and the others are due to the propellers in the two conditions. Figs. 27 and 31 show that the phase difference between the hull wave and the normally rotating propeller wave is small theoretically and experimentally, and the phase difference between the waves due to the propellers in the two working conditions is about  $180^\circ$  experimentally. Thus, though the calculated results in the phase contain some errors, we may say roughly that the propeller rotating in the normal direction makes the wave due to the sink, and the propeller rotating in the reverse direction makes the wave due to the source in a sense. That is, we can not say that the sink disk propeller is an inadequate model in treating the hull-propeller interaction approximately. Furthermore, the sink disk propeller is, of course, the most simplified model obtained by approximating the exact theory as derived in Reference of Yamazaki (1968). We wish to calculate numerically by using a more realistic propeller model in the future.

To Prof. Schmiedchen:

Thank you very much for the discussion on the behaviors of the wake and the thrust deduction fractions. We expected that the thrust deduction fraction would change clearly according to the change of the wake fraction in the range  $F_n > 0.31$ . Though we do not know the true reasons, we can say the following:

1. The calculated thrust deduction fraction is generally insensitive to the change of the wake fraction as seen from Nowacki-Sharma's calculated results (1971).
2. In Fig. 23, the calculated wake fraction  $w_e$  shows a little different behavior from the experimental wake fraction in the range  $F_n > 0.31$ . Though we assumed  $w_v = 0.125$  for all Froude numbers, this value is expected to decrease in the high speed range, say  $F_n > 0.3$ , since the thickness of the boundary layer decreases. Taking such decrease into account, we may improve the inconsistency to some extent.

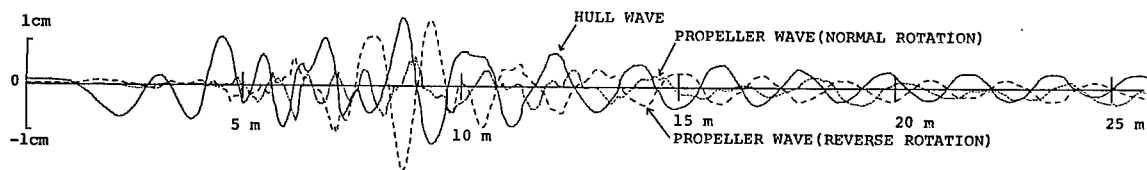


Fig. 31 Comparison of hull wave and two kinds of propeller wave profiles

# ON WAKE AND THRUST DEDUCTION FROM PROPULSION TESTS ALONE A RATIONAL THEORY OF SHIP HULL-PROPELLER INTERACTION

MICHAEL SCHMIECHEN

## ABSTRACT

In view of the inconsistencies and the deficiencies of the traditional evaluation of the propulsive performance of ships a method of evaluation based on propulsion tests, i. e. service conditions alone, applicable at model and full scale in the same way has been proposed. In accordance with modern methodology the conceptual solution of the problem is formulated as an axiomatic theory together with the corresponding interpretation and scaling theories. The formal presentation of the whole system of theories provides a sound and common basis not only for the discussion and evaluation of former and current research, but for future experimental and theoretical work as well.

The basic concepts are the traditional ones with the addition of the mass, momentum, and energy flows to the propeller. In total there are fifteen basic concepts, of which only ten may be measured, at least in principle. The remaining five are coherently defined in terms of five axioms, i. e. a mathematical model implying the concept of an equivalent propeller outside the displacement influence of the ship. In terms of derived concepts, factors of merit independent of the displacement wake in particular, some important implications of the axioms may be derived.

The theoretical concepts of the axiomatic theory may be interpreted in terms of the measured or computed inflow to the propeller. With the adoption of hypotheses on the invariance of the resistance and the propeller advance speed in overload tests at constant speed an interpretation in terms of results of thrust and power measurements in propulsion tests has been derived based on the concept of the equivalent state of vanishing thrust. In view of full scale tests, where no towing forces can be applied under service conditions, and in view of the signal-to-noise ratio a technique using quasisteady oscillations around the conditions to be investigated is being developed.

Further some results of hydrodynamic theory on hull-propeller interaction are analysed in terms of the axiomatic theory. And finally

the impact of the new theory on the design of propellers for optimum propulsion of ships is discussed. For given resistance and given circumferentially uniform wake a procedure is outlined for the design of optimal wake vorticity adapted ducted propellers, taking hull-propeller-duct interaction properly into account.

## NOMENCLATURE

Note: The symbols introduced in the sections indicated are as close as possible to the ITTC Standard Symbols (1976), but may have a slightly different meaning, which may not be concluded from the names stated, but only from the formal context and the operational interpretation developed in the paper.

Symbol Section Name

### Quantities

A	2.2	propeller disc area
$c_x$	2.3	loading factors
D	3.2	propeller diameter
e	7.5	volume specific energy
$e_x$	4.2	errors
E	2.2	energy flux
f	3.4	differential force function
f	7.5	mass specific external force field
F	2.2	towing force
$F_S$	5.5	sink force
$F_n$	6.2	Froude number
g	3.1	mass specific gravity
g	3.5	differential power function
$J_x$	3.2	advance ratios
$J_{ij}$	4.3	matrix of powers of advance ratios
$k_x$	3.2	load functions
$K_x$	3.2	load ratios
m	4.2	number of measurements, sample size
$m_l$	5.2	mass, longitudinal inertia
M	2.2	momentum flux
n	4.2	order of approximation
N	3.2	frequency of propeller revolutions
$O_{pq}$	4.3	orthogonalized matrix

Prof.Dr.-Ing. Michael Schmiechen  
Versuchsanstalt fuer Wasserbau und Schiffbau

Mueller-Breslau-Strasse (Schleuseninsel)  
D-1000 Berlin 12, FR Germany

p	3.1	pressures
p <sub>0</sub>	2.2	surface pressure level
p <sub>p</sub>	2.2	propeller pressure
P <sub>x</sub>	2.2	powers
P <sub>p</sub>	2.3	propeller power
q	7.5	flow rate, stream function
Q	2.2	volume flux
Q <sub>s</sub>	5.5	volume flux of suction
Q <sub>x</sub>	3.2	torques
r	7.5	radial coordinate
R	2.2	ship resistance
s	7.5	streamline coordinate
s <sub>x</sub>	4.2	standard deviations
S	4.2	standard deviation function
t	2.3	thrust deduction fraction
T	2.2	propeller thrust
T <sub>pq</sub>	4.3	triangular transformation matrix
v <sub>l</sub>	3.1	velocity vector
V	2.2	ship speed
V <sub>H</sub>	3.2	hull speed
V <sub>p</sub>	2.2	propeller speed
V <sub>x</sub>	2.3	velocities
w <sub>x</sub>	2.3	wake fractions
W	2.2	ship weight
x	7.5	axial coordinate
z	3.1	vertical coordinate
η <sub>xy</sub>	2.3	efficiencies, factors of merit
θ	3.1	time, period
ρ	2.2	water density
τ <sub>x</sub>	2.3	velocity increase ratios
X	2.3	displacement influence ratio

#### Indices

E	2.3	energy
E	7.5	inlet
F	3.2	force
H	3.2	hull
J	2.3	jet
J	7.5	outlet
K	4.5	load
L	3.3	loss
M	2.3	momentum
M	6.2	model
O	2.2	surface
O	2.4	outlet
PX	3.2	powers
QX	3.2	torques
R	2.3	resistance
S	3.2	service
S	5.5	suction
S	6.2	ship
T	2.3	thrust
T	3.3	towing
W	2.3	weight
X,Y,Z	2.3	variable
i,j,k		operational
l,m,n		operational
p,q		operational

#### Operators

(j)	3.2	differentiation
∂ <sub>i</sub>	7.5	partial differentiation: ∂/∂ <sub>i</sub>
ε()	2.3	element of set
—	3.2	averages
°	6.2	scale factors

## 1. INTRODUCTION

### 1.1 Problem

The traditional evaluation of the propulsive performance of ship models is based on the results of towing tests with the hulls and of open-water tests with the propellers. If the flows around the hulls in the resistance and propulsion tests are "very different" and the inflow to the propellers in the propulsion tests is "far from uniform" the traditional procedure is not particularly satisfactory. Furthermore, hull towing and propeller open-water tests cannot be performed routinely with full scale ships, although a performance analysis, preferably on-line under service conditions, would be of extreme value for ship operation and research.

In view of these inconsistencies and deficiencies of the traditional evaluation of the propulsion factors of ships a method of evaluation based on propulsion tests, i. e. service conditions alone, applicable at model and full scale in the same way has been proposed (Schmiechen, Schiffstechnik and STG, 1980). This work is closely related to earlier studies on performance criteria for jet propellers and propulsors in general (Schmiechen, 1968, 1970).

In accordance with modern methodology the conceptual solution has been formulated as an abstract axiomatic theory together with a corresponding interpretation theory. While the axiomatic theory proved to serve its purpose as it was first proposed, further studies have shown that the solution of the interpretation problem could be greatly improved to meet all theoretical and practical requirements (Schmiechen, 1984).

Another problem having been studied in the meantime is that of propeller design in the context of the present theory (Schmiechen, 1983). The rather speculative outline suffered from the drawback that some fundamental work on ideal propellers (Schmiechen, 1978, Sparenberg, 1979) and the whole conceptual background had not been published in English so far, except for oral presentations of the latter to colleagues at many institutes all over the world (Schmiechen, 1980/1984).

It is consequently felt that a complete survey of the state of the current research, which is a systematic continuation of Horn's school on hull-propeller interaction (Weinblum, 1972), is more than due.

### 1.2 Model

The theoretical overall model underlying the following exposition is the dual structure of rational theories as already mentioned and shown in Figure 1.

Accordingly the distinction is being made between the abstract axiomatic theory of hull propeller interactions and the theory of its interpretation, i. e. of the correspondence between measured and theoretical quantities. As the measurements are mostly performed on model scale an additional theory of scaling, i. e. of model-ship correlation is necessary.

The axiomatic theory is a formal language, or a representation space, adequate for the statement of the problems at hand and the design of possible solutions. This language will, after appropriate extensions, in particular be used for the formulation of the theories of interpretation and scaling. The theoretical overall model itself is evidently the adequate formal structure for the whole exposition.

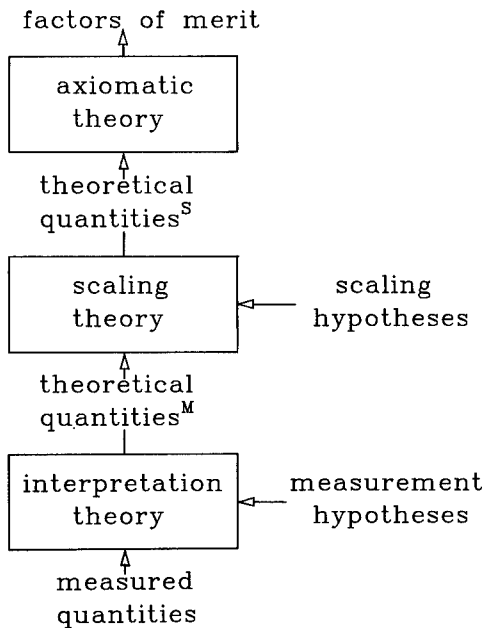


Figure 1: Theoretical overall model: structure of rational theories

The theoretical overall model, i. e. the theory of theories is well understood today (Leinfellner, 1980). After the development of many axiomatic theories from Euclid's Elements on, it is now possible to construct such theories ad hoc according to the pattern, which is considered the ideal of mature theories. A well known more recent example is the axiomatic theory of probability together with its statistical interpretation.

### 1.3 Goal

The goal of this paper is a coherent and self-contained exposition of the whole hierarchy of theories for ready reference in their further development and application. References to the basic philosophy and intermediate steps and discussions in the development so far shall be limited to the bare minimum in order not to obscure the essential issues, although the whole work as it stands would have been completely impossible without permanent reference to the theory of ethics (Lorenzen, Schwemmer, 1975), rational resolution of conflicts in particular, to the theory of knowledge (e.g. Leinfellner, 1980) and to hydromechanic theory and experience, and without continual discussions with many colleagues.

The goal of the present paper is to develop the conceptual framework by way of a paradigmatic, maybe somewhat speculative reconstruction of the very fundamentals of the theory of propulsion. The goal is not to discuss solutions of the many problems identified, maybe by more or less well established procedures directly or after appropriate adaptation.

The purpose of the exercise is to establish a solid foundation for common reference in qualitative arguments as well as quantitative evaluations, and to put some unresolved problems into a new perspective, maybe showing that some of them are no problems any longer.

### 1.4 Plan

In the present scope this goal can only be reached if the presentation is rigorously structured and formalized as far as possible. The basis for this will be the theoretical overall model and axiomatic theories where applicable.

Consequently the development will proceed in a top-down approach from the axiomatic theory of hull-propeller interaction to the axiomatic theory of its interpretation and the statistical theory of measurements, and further to the theories of testing and scaling.

In addition the relation of the present theory to hydromechanic theories of hull-propeller interaction and its impact on propeller design will be elaborated on. The paper shall conclude with a review of the results obtained so far and an outlook on problem areas identified.

In terms of the underlying philosophy the goal of the paper is to put forward basic propositions, which are generally acceptable as basis for the rational resolution of "conflicts" between shipowners, shipbuilders, ship-designers, and ship-researchers. As the traditional procedure the procedure proposed is a conventional one. Many discussions have expressly been conducted to reach this acceptance of the axioms.

## 2. THEORY OF INTERACTIONS

### 2.1 Introduction

According to the plan the problem of this chapter is the development of an abstract formal language for the description of ship hull-

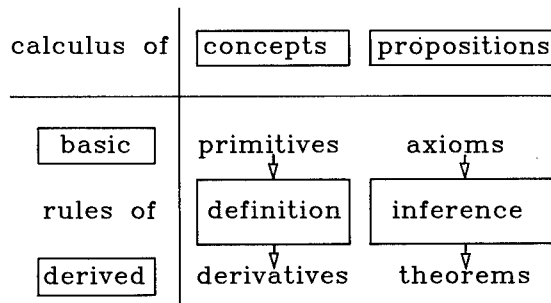


Figure 2: Structure of axiomatic theories: grammar of formal languages

propeller interactions, time averaged, without reference to its interpretation.

The structure or grammar of such languages is shown in Figure 2.

Any such language consists of two separate calculi: the calculus of concepts and the calculus of propositions. The structure itself is a calculus of concepts defining the terms "primitives", "axioms", etc. at least in the present context.

The goal is consequently to develop these two calculi as far as necessary. In order to take advantage of past experience and in view of a wide acceptance and application the conceptual framework shall be as close as possible to the traditional one.

According to the structure indicated the development will proceed from the primitives to the derived concepts and from the axioms to the theorems. The rules of definition and inference will not be touched upon, as the necessary rules for the transformation of equations are well known.

## 2.2 Basic Concepts

As basic concepts at first the usual ones are introduced, as already mentioned without reference to any operational interpretation despite the use of the traditional names:

$\rho$  : the water density,  
 $P_0$  : the free surface pressure,  
 $A$  : the propeller (disc) area,  
 $W$  : the ship weight,  
 $V$  : the ship speed,  
 $T$  : the propeller thrust,  
 $P_p$  : the propeller power,  
 $F$  : the towing force,  
 $V_p$  : the propeller (advance) speed,  
 $R$  : the ship (not hull!) resistance.

Of these ten quantities the first eight are considered in principle measurable more or less directly.

In addition to these concepts conventionally used in ship performance analysis the following concepts related to propeller, i. e. pump performance are introduced:

$Q$  : the volume flux,  
 $E$  : the energy flux, and  
 $M$  : the momentum flux into the propeller at  
 $p_p$  : the propeller pressure level, and  
 $P_j$  : the jet power.

Of these additional five quantities the first two are considered in principle measurable.

## 2.3 Derived Concepts

As derived concepts

$P_W \equiv WV$  : the reactive weight power,  
 $P_R \equiv (R-F)V$  : the net resistance power,  
 $P_T \equiv TV_p$  : the thrust power

may be introduced and subsequently the power ratios, so-called efficiencies, factors of merit, etc.

$\eta_{XY} \equiv P_X/P_Y$  :  $X, Y, Z \in (W, R, T, J, P)$ ,  
 for which the rules

$\eta_{XY} \eta_{YZ} = \eta_{XZ}$

and

$$\eta_{YX} = \eta_{XY}^{-1}$$

hold.

The choice of the power ratios to be used depends on the purpose, i. e. the aspects to be evaluated. Of more general interest are the factors of merit

$\eta_{WR} \equiv P_W/P_R$  : of the hull,  
 $\eta_{RJ} \equiv P_R/P_J$  : of the hull-propeller configuration, and

$\eta_{JP} \equiv P_J/P_p$  : of the propeller,  
 while conventionally the efficiencies  
 $\eta_{RT} \equiv P_R/P_T$  : of the hull and  
 $\eta_{TP} \equiv P_T/P_p$  : of the propeller  
 are still preferred.

Further the derived concepts

$V_M \equiv M/\rho Q$  : the momentum velocity,  
 $V_E \equiv (2E/\rho Q)^{1/2}$  : the energy velocity,  
 $V_J \equiv (2(E+P_J)/\rho Q)^{1/2}$  : the jet velocity

may be introduced and subsequently the velocity ratios or wake fractions

$w_X \equiv 1 - V_X/V$  :  $X \in (P, M, E, J)$

and the ratios of increase

$\tau_M \equiv T/M$  : of the momentum velocity,

$\tau_E \equiv V_J/V_E - 1$  : of the energy velocity  
 and the corresponding loading factors or coefficients

$c_X \equiv \tau_X(\tau_X + 2)$  :  $X \in (M, E)$ .

For short the notation

$w \equiv w_p$  : for the effective wake fraction,  
 $\tau \equiv \tau_M$  : for the momentum velocity increase ratio,  
 $c_p \equiv P_J/E$  : for the energy loading factor

will be used.

Finally

$X \equiv V_E/V_p - 1$  : the displacement influence ratio and  
 $t \equiv 1 - (R-F)/T$  : the thrust deduction fraction

are introduced as derived concepts.

## 2.4 Basic Propositions

In total fifteen basic concepts have been introduced, of which only ten are in principle directly measurable. The remaining five are implicitly or coherently defined in terms of five basic propositions, axioms, or principles, i. e. an explicit mathematical model of hull-propeller interaction. Independent operational interpretations are in general inadequate from the point of view of methodology and physics, as will be shown in the theory of interpretation in Chapter 3.

For more or less conventional afterbody-propeller configurations the following five axioms are introduced

$V_p = V_M$  : for the propeller speed,  
 $R = \rho Q(V_J - V_E) + F$  : for the resistance,  
 $M = \rho Q^2/A - T/2$  : for the momentum flux,  
 $p_p = P_0 + \rho(V_E^2 - V_p^2)/2$  : for the pressure level, and

$P_j = TQ/A$  : for the jet power.

The axioms, which are arbitrary within certain limits are chosen in such a way, that they are at least plausible for the ideal model of ideal propellers in uniform wakes. The resistance axiom is the condition of selfpropul-

sion in this model, but not in general. The axioms imply the model of an equivalent propeller outside the displacement influence of the hull which has been introduced by Fresenius (1921) and used e. g. extensively by Horn (1935, 1956). This model may, contrary to past conceptions, be introduced as an artifice with no physical reality, and certainly independent of any additional assumptions on the flow.

The argument that the axioms are nothing else but further definitions, as in the calculus of concepts, does not hold for the simple reason that they "only" state equalities and not identities. E. g. Newton's law states that the value of the rate of change of the momentum and the value of the net force are equal, although the concepts are by no means identical, but have totally different meanings, i. e. intensions. For the same reason it would at least be highly artificial if not wrong, if any of the concepts coherently defined by the axiomatic system would be introduced as derived concepts by formal definitions.

The five axioms proposed have been proved in a simple minded direct approach to be non-contradictory (Schmiechen, Schiffstechnik, 1980), the minimum requirement an axiomatic system has to fulfill in order to be useful, i. e. to permit the derivation of true theorems and not of any.

If instead of the propeller disc area,

$A_0$ : the outlet area

of a duct or nozzle is a more adequate parameter, the axioms may be changed as follows:

$M = \rho Q^2/A_0 - T$ : for the momentum flow and

$P_j = TQ/A_0 - T^2/(2\rho Q)$ : for the jet power.

The problem is that the thrust in this case includes the thrust of the duct. As has been shown earlier (Schmiechen, 1968) and will be done in the outline of a propeller design procedure in Chapter 7, it may be of advantage to avoid the concept of thrust as a propulsive force under these circumstances altogether. In order to avoid confusion this line of thought will not be followed any further in this context.

## 2.5 Derived Propositions

Based on the axioms there may be derived any number of propositions, so-called theorems, for any particular purpose. Only some of more general interest will be stated here without derivation.

For the factors of merit introduced the following relations are obtained:

$$\eta_{WR} = W/(\rho Q(V_J - V_E)),$$

$$\eta_{RJ} = 2V/(V_J + V_E),$$

$$\eta_{JP} = \rho Q(V_J^2 - V_E^2)/(2P_p).$$

Obviously they are all independent of the displacement wake and the thrust deduction and equal for energetically equivalent propellers. Consequently they are particularly useful for the evaluation and comparison of configurations as has been stated earlier (Schmiechen, 1968, 1970, 1980). Another advantage of these factors of merit is that their values remain meaningful even at extreme conditions, e.g. at 100 % wake, where the values of the usual efficiencies degenerate.

The propeller factor of merit at vanishing propeller speed

$$\eta_{JP} = (\rho A/2)^{1/2} T^{3/2}/P_p$$

may be considered as an example. While the propeller efficiency vanishes at vanishing propeller speed the factor of merit assumes values in the range

$$\eta_{JP} = 0.45 \dots 0.68$$

for the Wageningen B-Series.

Thrust deduction, displacement wake, and propeller loading are in the present theory connected by the theorem

$$t = (1 + \chi + \tau - ((1 + \chi + \tau)^2 - 2\chi\tau)^{1/2})/\tau.$$

Under the condition

$$2\chi\tau \ll (1 + \chi + \tau)^2,$$

which practically always holds, the above theorem reduces to the approximate relationship

$$t \approx \chi/(1 + \chi + \tau),$$

shown in Figure 3, for all values of the ratio

$$\tau = (c_M + 1)^{1/2} - 1.$$

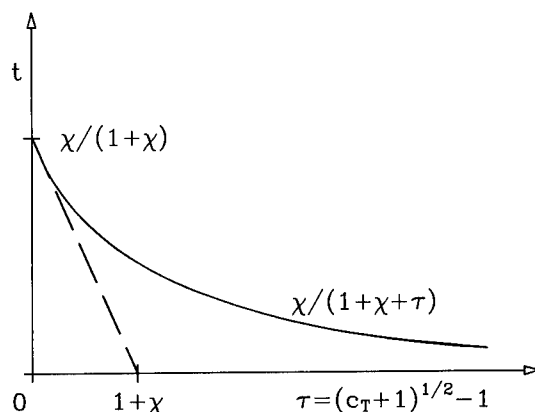


Fig.3: Thrust deduction as function of propeller loading and displacement influence

Further the theorems

$$c_T \equiv 2T/\rho V_p^2 A = c_M: \text{ for the thrust loading factor and}$$

$$\eta_{TJ} = 1/(1 + \tau/2) = 2/(1 + (1 + c_T)^{1/2}): \text{ for the jet efficiency}$$

may be derived. If the outlet area of a duct would have been chosen as reference the theorem

$$\eta_{TJ} = 4/(3 + (1 + 2c_{T0})^{1/2})$$

is implied by the modified axioms stated before.

All the theorems are obviously not statements about physical relationships but formal consequences of the axioms chosen for convenience.

## 2.6 Conclusion

The axiomatic system developed for the description of hull-propeller interaction uses the well-known conceptual frameworks for the evaluation of propulsive and pump performance, so far without reference to any interpretation. Contrary to the usual conceptual framework the present theory is a complete language containing not only words but sentences as well. The theory includes a fully developed calculus of propositions, which was heretofore lacking.

In the present theory, which is an attempt to rationalize the traditional description of the hull-propeller interaction the problem of thrust deduction is a formal one. The solution derived already earlier (Schmiechen, 1968) shows that the usual way to deal with the problem will not lead to success unless the displacement influence is explicitly taken into account.

Instead of the usual breakdown of the propulsive efficiency into hull and propeller efficiencies the theory shows that the frequently suggested breakdown into configuration and propeller factors of merit appears to be much more adequate, independent of the interpretation of the abstract theory to be developed in the next chapter.

### 3. THEORY OF INTERPRETATION

#### 3.1 Introduction

While the water density, the surface pressure, the propeller area, the ship weight and speed, the propeller thrust and power, and the towing force may in principle be measured rather directly, though not always easily, the same does not hold for the volume or mass and the energy fluxes. Even in future there will be no chance to measure them directly in routine tests, model or full scale.

For that purpose velocity and pressure distributions  $v_1$  and  $p$ , respectively, would have to be measured over a typical period  $\theta$  on a relatively arbitrary control surface  $A_c$  with the vectorial elements  $dA_1$  in front of the propeller provided its boundary could be agreed upon. From these distributions integrals

$$Q = \frac{1}{\theta} \int_0^\theta d\theta \int_{A_c} dA_1 v_1$$

and

$$E = \frac{1}{\theta} \int_0^\theta d\theta \int_{A_c} dA_1 v_1 (\rho v^2/2 + p - p_0 + \rho g(z - z_0))$$

with the vertical coordinate  $z$  and the mass specific gravity  $g$ , alias gravitational acceleration, would have to be determined with sufficient precision. Even with computer controlled Laser-Doppler velocimeters this problem can obviously not be solved, as they do not provide the essential information concerning the energy of the flow.

Consequently integral measurements of propeller thrust and torque or power in overload tests have already been proposed by Horn (1935) for the solution of the interpretation problem. In terms of the theoretical overall model shown in Figure 1, the interpretation theory to be developed has to establish a correspondence between the measured values and the theoretical concepts introduced before in Chapter 2.

The structure of the interpretation theory, as shown in Figure 4, suggests the distinction between an axiomatic theory of interpretation and a statistical theory of measurements to be developed in Chapter 4.

The present solution of the interpretation problem greatly improves the first solution

proposed (Schmiechen, STG, 1980), which was based on too many ad hoc and inadequate hypotheses, with implications lacking the transparency necessary for general acceptance and application.

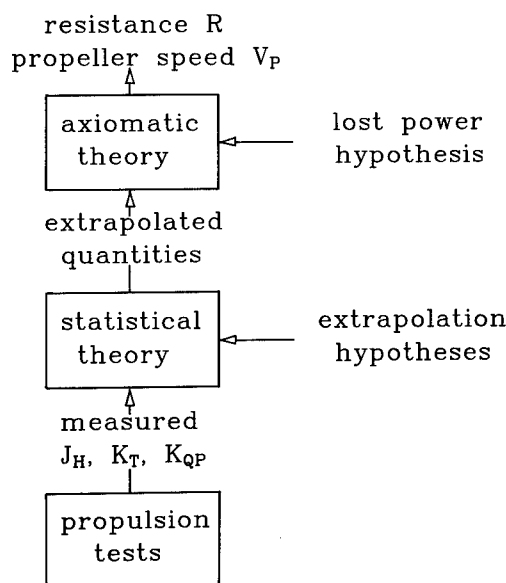


Fig.4: Structure of the interpretation theory

#### 3.2 Statements

Assumed a ship or its model moves at constant speed and the frequency of revolutions of the propeller is changed stepwise, then the force, the thrust, and the power at equilibrium change as well.

In view of the following this statement may be expressed in terms of the derived concepts:

$$\begin{aligned} J_H &\equiv V_H/DN && \text{the hull advance ratio,} \\ K_F &\equiv F/(\rho D^4 N^2) && \text{the force ratio,} \\ K_T &\equiv T/(\rho D^4 N^2) && \text{the thrust ratio,} \\ K_{PP} &\equiv P_P/(\rho D^5 N^3) && \text{the power ratio.} \end{aligned}$$

The additional basic concepts

$$\begin{aligned} V_H &: \text{the hull speed,} \\ D &: \text{the propeller diameter, and} \\ N &: \text{the frequency of revolution} \end{aligned}$$

are linked with those previously introduced by the following axiom and theorem

$$\begin{aligned} V_H &= V, \\ D &= (4A/\pi)^{1/2}. \end{aligned}$$

The introductory statement may therefore be phrased: the force, thrust, and power ratios are functions of the hull advance ratio, i. e.

$$K_X = k_{XH}(J_H) \quad : X \in (F, T, PP).$$

For convenience the functions may be expressed in terms of series

$$K_X = k_{XH}(J_H) = \sum_{j=0}^n K_{XjH} k_{jH}(J_H),$$

e. g. as Taylor series

$$K_X = k_{XH}(J_H) = \sum_{j=0}^n K_{XHS}^{(j)} / j! (J_H - J_{HS})^j,$$

developed at the point of service condition S, practically always with a finite number of terms.

The universal functions of the advance ratio may be chosen so as to suit the problem best, i. e. they need not be the powers of the hull advance ratio. The constants are additional basic concepts, which in the present context are considered as directly measurable.

Instead of the power ratio usually  $K_{QP} \equiv Q_P / (\rho D^5 N^2)$  : the torque ratio is being used, where the basic concept

$Q_P$  : the propeller torque  
is related to the propeller power by the axiom  $Q_P = P_P / (2\pi N)$ ,  
so that the relation  $K_{QP} = K_{PP} / (2\pi)$   
holds.

Quite obviously the torque axiom or convention can be proved to be "wrong", if the angular velocity and the torque of the propeller oscillate as they always do. But it is an acceptable approximation in view of the relative magnitude of the systematic errors possible and the random errors encountered in actual measurements.

### 3.3 Basic Propositions

In addition to the foregoing statements the following basic propositions may be introduced.

Firstly it is assumed that the functions  $k_{XH}$  observed in a limited range of the hull advance ratio can be extrapolated to the state of vanishing thrust

$T_T = 0$ ,  
i. e. to the advance ratio defined by the equation

$$K_{TT} = k_{TH}(J_{HT}) = 0.$$

The details of the extrapolation procedure are dealt with in the next chapter. In principle the procedure has to be agreed upon, as also the axioms.

At the state of vanishing thrust the following "initial" conditions hold:

$$(\partial F / \partial T)_T = -1 / (1 + \chi) : \text{for the force and} \\ (\partial P_J / \partial T)_T = (P_J / T)_T \text{ or} \\ (\partial \ln P_J / \partial \ln T)_T = +1 : \text{for the jet power.}$$

The first condition implies vanishing thrust deduction at vanishing thrust, while the second implies the jet power vanishing with vanishing thrust.

Secondly for

$P_L \equiv P_P - P_J$  : the "lost" power  
or rather  $Q_L = P_T / (2\pi N)$  : the "lost" moment  
the condition

$$(Q_L / V_H^2)_T = \text{const}$$

is assumed to hold. In terms of

$K_{PL} \equiv P_L / (\rho D^5 N^3)$  : the loss ratio  
or the corresponding torque ratio

$$K_{QL} = K_{PL} / (2\pi)$$

the condition reads

$$(K_{PL} / J_H^2)_T = \text{const}$$

or

$$(K_{QL} / J_H^2)_T = \text{const.}$$

This crucial condition is at least plausible and, more important, is supported by experimen-

tal evidence, as will be shown in Section 3.5.

### 3.4 Resistance

At the state of vanishing thrust

$$T_T = 0$$

the force equals the resistance

$$R = F_T.$$

It should be kept in mind that  $F_T$  is the extrapolated force

$$F_T = (K_F \rho D^4 N^2)_T$$

and not a real towing force.

For

$$C_R \equiv 2R / (\rho A V_H^2)$$

: the resistance coefficient

the relation

$$C_R = 8 / \pi (K_T / J_H^2)_T$$

holds.

The resistance and consequently the thrust deduction fraction may in principle be determined from the extrapolated differential force function

$$f(T) \equiv 1 + \partial F / \partial T$$

with the initial value

$$f(T)_T = \chi / (1 + \chi) \equiv c$$

Integration results in

$$T + F - F_T = \int_0^T f(T) dT,$$

i. e. the resistance

$$R = F_T$$

appears as integration constant and the thrust deduction fraction

$$t = 1/T \int_0^T f(T) dT = 1 + \overline{\partial F / \partial T}$$

as average over the differential force function introduced.

From the last statement it may be concluded that random errors in the extrapolation of the differential force function will in general have little influence on the result.

Formally introducing the function

$$f(T) = aT^b + c$$

results in the thrust deduction fraction

$$t = aT^b / (1 + b) + c$$

or, expressed in terms of derivatives

$$t = (1 - c + \partial F / \partial T)^2 / (1 - c + \partial F / \partial T + T \partial^2 F / \partial T^2) + c.$$

This result shows again that simplified solutions of the problem, e. g.

$$t \approx 1 + \partial F / \partial T,$$

as proposed by Holtrop (1978) and Keil (1983), will in general not be satisfactory.

The fact, that the resistance of a ship under service conditions can in general only be determined by extrapolation is due to the nature of the flow around the afterbody, which changes with propeller loading. The value of the resistance determined in this way will in general be different from the force necessary to tow the ship with propeller at vanishing thrust or the bare hull.

### 3.5 Propeller Speed

At the state of vanishing thrust

$$T_T = 0$$

the jet efficiency of a propeller equals unity

$$(\eta_{TJ})_T \equiv (TV_P / P_J)_T = 1,$$

i. e. the propeller velocity is



$$V_p = (P_J/T)_T = (\partial P_J/\partial T)_T \cdot$$

The propeller velocity and hence the wake fraction may in principle be determined from the extrapolated differential power function

$$Tg(T) \equiv 1 - \partial \ln P_J / \partial \ln T$$

with the initial value

$$(Tg(T))_T = 0.$$

Integration results in

$$\ln T - \ln P_J + \ln (P_J/T)_T = \int_0^T g(T) dT,$$

i. e. the propeller velocity

$$V_p = (P_J/T)_T = ((P_p - P_L)/T)_T$$

appears as integration constant as did the resistance before, while for the jet efficiency the expression

$$\eta_{JP} = \exp\left(\int_0^T g(T) dT\right) = \exp(Tg(T))$$

is obtained. Consequently the same remarks apply as before concerning the thrust deduction fraction and a similar relation may be derived in terms of derivatives.

The problem in this case is, that an interpretation along this line would require the knowledge of the lost power over the whole range from the condition of vanishing thrust to the service condition, while the original interpretation, which may be phrased

$$J_{PT} = (K_{PPHT} - K_{PLHT})/K_{THT},$$

requires only the knowledge of the first derivative of the lost power at the state of vanishing thrust. After the propeller advance ratio at this state has been determined the wake fraction is obtained according to the rule

$$w = 1 - J_{PT}/J_{HT}$$

and the values of all other quantities may be determined.

The derivative in question is obtained from the basic proposition

$$(K_{PL}/J_H^2)_T = \text{const}$$

for the lost power, which results in

$$(1) \quad K_{PLHT} = (2K_{PP}/J_H)_T,$$

if the equality of total and lost propeller power at vanishing thrust

$$K_{PLT} = K_{PPT}$$

is taken into account.

The determination of the propeller advance ratio at zero thrust may consequently be described in terms of the following simple graphical procedure shown in Figure 5:

1. extrapolation of the functions

$$K_T = k_{TH}(J_H)$$

$$K_{PP} = k_{PPH}(J_H)$$

2. determination of the zero crossing point from the equation

$$K_{TT} = k_{TH}(J_{HT}) = 0$$

3. construction of the tangents touching the extrapolated functions at that point

4. determination of the intersections p and q of the tangents with the axis

$$J_H = J_{HT}/2$$

5. determination of the propeller advance ratio

$$J_{PT} = q/p$$

and consequently the wake fraction

$$w = 1 - J_{PT}/J_{HT}.$$

If, as usual, instead of the power ratio ten times the torque ratio is plotted the rule is obviously

$$J_{PT} = 2\pi/10 \cdot q/p.$$

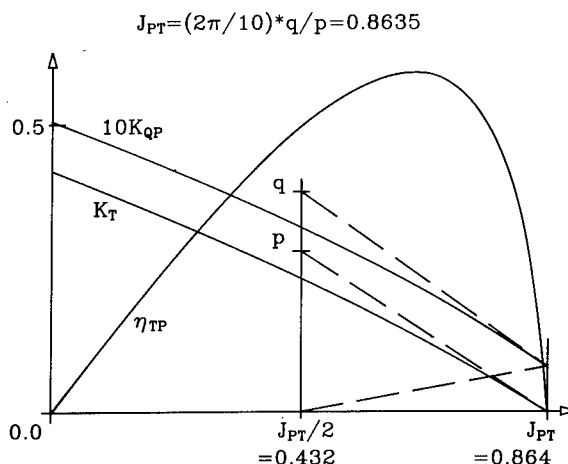


Figure 5: Verification of the interpretation rule using open water tests, e. g. VWS Propeller No. 1349

The procedure has been tested on a great number of randomly chosen propeller open-water charts, Figure 5 being only one example. In all cases the agreement of the actual and the derived propeller advance ratios at zero thrust was very good, independent of the number of blades, the pitch ratio, and the blade area ratio.

It has to be noted however, that in the test cases of propellers in the open-water condition no extrapolations were applied, but the observed physical functions have been used. In general this is not possible, due to the same reason mentioned before, i. e. the nature of the flow around the afterbody being dependent on propeller loading. Consequently the wake determined from extrapolation and from the actual condition of zero thrust must in general be different.

Any reference to open-water tests, which is usually necessary in comparable procedures based on overload tests, e. g. that proposed by Horn (1935) and improved by Dickmann (1936), more recently e. g. by Adachi et al. (1983), would have been inadequate for the performance analysis under service conditions aimed at.

Horn's proposal, trying to avoid the ill defined wakes based either on thrust or on torque identity, replacing the latter by the condition

$$\partial \ln K_{QP} / \partial \ln J_p = 2 - \partial \ln Q_p / \partial \ln N,$$

was recommended by the 3rd ITTC 1935 in Paris for testing by member organisations. Results of such tests were reported at the 4th ITTC in Berlin (Horn, 1937). Without reference to his earlier solution Horn (1964) proposed another solution of the wake problem based on the principle of virtual power, apparently without any resonance.

### 3.6 Conclusion

The proposed interpretation of the concepts of resistance and propeller speed based on extrapolations of the results of integral or macroscopic measurements in load varying tests uses the customary format of the thrust and power or torque ratios as functions of the apparent or hull advance ratio.

So far the axiomatic part of the theory has been developed. The introduction of the resistance and the propeller speed as integration constants may be surprising, but is totally in line with other macroscopic theories. So e. g. in hydromechanics the group velocity of vortex streets (Schmiechen, 1960/62) and in thermodynamics the temperature (Schmidt, 1958) may be introduced as integrating factors.

The actual interpretation of the resistance and propeller speed, or thrust deduction and wake fractions, respectively, along the lines proposed requires the "reliable" extrapolation of the thrust, force, and power functions. As has already been stated, the problem is not to predict the physical behaviour at vanishing thrust, but rather to construct a physically meaningful extension of the behaviour of the flow around afterbody and propeller under service conditions. The extrapolation rules to be adopted have themselves the character of conventions or axioms to be agreed upon, preferably before the measurements.

The idea underlying the extrapolation is to continue the "laws" of the functions observed in a limited range around the service condition, practically about

$0.6 J_{HT} \leq J_H \leq 0.8 J_{HT}$ ,  
to the condition of zero thrust, not to predict what happens there, but only to construct resistance and propeller speed in the narrow range of observation. The state of zero thrust considered is therefore an artifice and may be called the equivalent state of zero thrust in direct analogy to Fresenius' concept of the equivalent propeller underlying the axioms of hull-propeller interaction in Chapter 2.

The concept of the equivalent state of zero thrust is not a substitute for missing information, but is the only way to exclude irrelevant information outside the range of interest, e. g. a change from turbulent to laminar flow, a change in flow separation, etc.

## 4. THEORY OF MEASUREMENTS

### 4.1 Introduction

In view of the finite number of measurements and random disturbances of these measurements the force, thrust, and power functions can only be determined within certain confidence ranges. The goal of this chapter is consequently to develop an adequate statistical theory of extrapolation including the necessary numerical procedures and to test them.

For convenience and lack of any other more adequate proposition optimum polynomials will be assumed for the functions in question. Implicit, non-linear techniques of extrapolation in terms of autoregressive models (Schmiechen,

Lang, 1983) would have been another choice.

Prerequisite for the application of the following procedure is of course that all relevant quantities have been measured without systematic errors. Without sufficient information on the behaviour of the system it is obviously impossible to derive statements on its properties and evaluate its performance. But the problems of data acquisition cannot be solved by confusing them with the present issue.

### 4.2 Optimum Polynomials

The determination of the optimum polynomials may be considered as a non-linear optimization problem, which can be solved in two consecutive steps.

The basis is a number of "measured" quadruples of values

$$J_{Hi}, K_{Fi}, K_{Ti}, K_{Ppi}; i = 1, \dots, m.$$

For stepwise increasing order the derivatives are now in each case determined in such a fashion, that the estimate of the variance will be minimal.

The optimal polynomial order may subsequently be determined from the required condition of minimum confidence range. For assumed confidence range and given confidence level a condition for the minimum sample size may be derived; see e. g. Zurmühl (1963).

### 4.3 Numerical Procedure

Basic requirement for the application of the procedure described are reliable optimum solutions of the systems of linear equations

$$J_{ij} x_{Xj} = K_{Xi} + e_{Xi}$$

with

$$J_{ij} = (J_{Hi} - J_{HS})^j / j!$$

and

$$(j)$$

$$x_{Xj} = K_{XHS}$$

providing that the condition

$$e_{Xi} e_{Xi} = \min$$

is observed.

Gauss' transformation, i. e. multiplication with the transposed matrix  $J_{ik}$  leads to the normal equation

$$J_{ik} J_{ij} x_{Xj} = J_{ik} K_{Xi},$$

which due to rounding errors may lead to erroneous results. If only interpolation is intended these may cause no problems, but in view of the extrapolation and differentiation they are quite unacceptable.

In order to avoid such problems it is in general advisable to perform an orthonormalization

$$-1$$

$$J_{ip} T_{qp} T_{qj} x_{Xj} = K_{Xi}$$

before the application of Gauss' transformation. The triangular transformation matrix  $T_{qp}$  is built up recursively in a Gram-Schmidt procedure (Zurmühl, 1963) so that the columns of the matrix

$$O_{iq} = J_{ip} T_{pq}$$

are orthonormal to each other.

Consequently Gauss' transformation of the orthonormalized equation leads to a degenerate normal equation with the solution

$$x_{Xj} = T_{jk} O_{ik} K_{Xi}$$

and the errors

$$e_{Xi} = K_{Xi} - O_{ik} k_{Xk}$$

with the generalized Fourier coefficients

$$K_{XK} = O_{ik} K_{Xi}$$

This recursive procedure of data analysis is perfectly reliable if applied to extremely ill conditioned or even singular systems of equations. It has the advantage that it may be applied to very large systems, due to the fact that for all operations necessary only single columns of the matrices have to be available in core, while the rest may be stored on external storage media.

The procedure developed for purposes of systems identification (Schmiechen, 1969, 1973) had been proposed as a standard to the 12th ITTC in Rome (Schmiechen, 1969), but the written contribution was not published in the Proceedings.

#### 4.4 Statistical Confidence

The optimal polynomials having been determined, the values of all other quantities may be obtained. Due to the random disturbances of the measurements the resistance and propeller speed determined are themselves random variables, the probability distributions of which have to be known in order to establish the confidence in the results.

The simplest and most direct way to determine the probability distributions in question is to perform the evaluation of the two quantities repeatedly based on samples randomly drawn from the total set of measured values. This procedure can be done routinely without any additional assumptions as necessary for explicit error estimations, which are limited to linear problems anyway.

The same procedure may be used even if only a limited number of measurements has been performed. In this case the samples are constructed by repeated random selection of single values from the total set of measurements, i. e. the samples are not subsets of the total set. This so-called bootstrap (in German: Münchhausen) procedure (Diaconis, Efron, 1983) does provide reliable estimates of the probability distribution, but can apparently not improve the confidence level of the values estimated.

#### 4.5 Numerical Example

The whole procedure has been tested using as an example a fictitious propeller in a wake of 25 %. For simplicity the quadratic thrust and loss functions

$$K_T = 0.50 - 0.30(J_H/1.7) - 0.20(J_H/1.7)^2$$

and

$10K_{QL} = 0.40 - 0.80(J_H/1.7) + 0.45(J_H/1.7)^2$ , respectively, have been assumed, closely resembling a Wageningen B-Series propeller.

From "measured" triples

$J_{Hi}, K_{Ti}, K_{pi} : i = 1, \dots, 36$ , uniformly distributed over the range

$$1.0 \leq J_H \leq 1.35,$$

the wake could be reconstructed without problems, when the computation was performed in double precision, fourth order polynomials having been assumed. Figure 6 shows the service chart of the fictitious propeller derived from

the simulated results of overload tests in the range quoted.

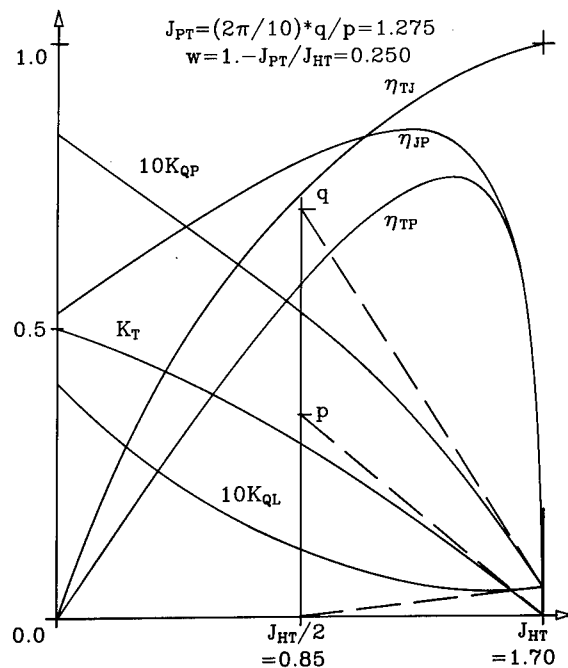


Figure 6: Service chart of a fictitious propeller derived from the simulated results of overload tests

In order to simulate measurement noise normally distributed pseudo-random values were added to the "measured" values, at first with the standard deviation

$$s_K = 10^{-4}$$

Depending on the order of the polynomials assumed the following averages and standard deviations were obtained

n	$\bar{w}$	$s_w$
2	0.306	0.003
3	0.244	0.032
4	0.221	0.233

Due to the non-linearity of the problem the estimated wake is not unbiased, and increasing the order of the polynomial does, as expected, not improve the confidence in the result.

Reduction of the noise by an order of magnitude to

$$s_K = 10^{-5}$$

resulted in the estimated wake

$$w = 0.249$$

with a standard deviation of

$$s_w = 0.003$$

for third order polynomials. Consequently in order to avoid systematic errors and achieve acceptable tolerances large samples are necessary.

Assuming a standard deviation of the individual measurements of

$$s_K = 10^{-3}$$

requires apparently  $10^4$  repetitions of each of

the thirty-six measurements or a total of  $0.36 \cdot 10^6$  measurements. This is the price to be paid for the information wanted.

#### 4.6 Conclusion

The exposition has shown that apart from the axiomatic theory of interpretation a fully developed statistical theory of measurements and extrapolation is necessary. The first numerical tests show that the requirements concerning data acquisition and reduction are much higher as compared with the traditional procedure, but the latter has the disadvantage that it may not be applicable at all, certainly not at full scale.

The sensitivity of the procedure does not come as a surprise, but is a well known fact from comparable procedures of systems identification. An application of systems identification techniques to the analysis of the propulsive performance at full scale has been reported by Abkowitz (1980), the conceptual framework being the traditional one.

Error sensitivity was already the problem of Horn's (1935) method, still depending on propeller open-water tests. Dickmann (1936) stated that at least five measurements over a wide range of load conditions would be necessary to ensure reasonably correct results.

Although the present procedure permits to derive a complete service chart for a propeller, only the part in the range of measurements may be considered as physically meaningful. In order to reduce the error sensitivity of the procedure it appears possible to introduce further conventions.

### 5. THEORY OF TESTING

#### 5.1 Introduction

In principle the propulsive performance of a ship can only be determined from measurements performed at the ship itself under service conditions. Consequently testing of full scale ships will be the first subject to be dealt with before the corresponding model test techniques are considered.

In principle the procedure outlined for the first time permits the experimental determination of the scale effects to be discussed in the next chapter. Horn (1935) already claimed this advantage for his procedure, although it still depended on propeller open-water tests.

#### 5.2 Selfpropelled Ships

If the method of performance analysis described is to be applied to a full scale ship the various load conditions necessary can under service conditions not routinely be realized by application of external forces nor can steady states be achieved. In this case the external force can be replaced by the inertial force due to quasisteady changes of the velocity as a consequence of quasisteady changes of the frequency of propeller revolutions.

At quasisteady changes of the frequency of revolutions the values

$N_i, V_i, T_i, Q_{pi} : i = 1, \dots, m$   
of the frequency, speed, thrust, and torque, respectively, have to be measured as primitives. From these the values of the force

$$F_i = -m_i \partial V_i / \partial \theta$$

and the power

$$P_{pi} = 2\pi N_i Q_{pi}$$

and subsequently the values

$$J_{Hi}, K_{Fi}, K_{Ti}, K_{Ppi}$$

of the advance, force, thrust, and power ratios, respectively, may be derived.

In order to determine the force, not only the acceleration, but also the longitudinal inertia including hydrodynamic components have to be known. The latter may in principle be determined from special experiments, particularly on model scale. Much more "realistic" are in general and for practical purposes theoretical estimates and agreements or, if possible, general conventions.

More difficult is the determination of the acceleration which requires advanced filtering techniques. If the frequency of revolutions is changed periodically differentiation and filtering can be performed in the frequency domain. The same technique has been used successfully in an approximate way in case of non-periodic load changes. A similar technique has been developed for application in case of transient changes (Schmiechen, Lang, 1983).

#### 5.3 Selfpropelled Models

The test technique described for selfpropelled ships may be applied in model testing without change. The proposal to develop a test procedure utilizing the information that becomes available during the initial unsteady phases of traditional steady state propulsion tests has found favourable response and will after all lead to a sponsored research project at VWS, the Berlin Model Basin.

$$J_{PT} = (2\pi/10) \cdot q/p = 1.123$$

$$w = 1 - J_{PT}/J_{HT} = 0.413$$

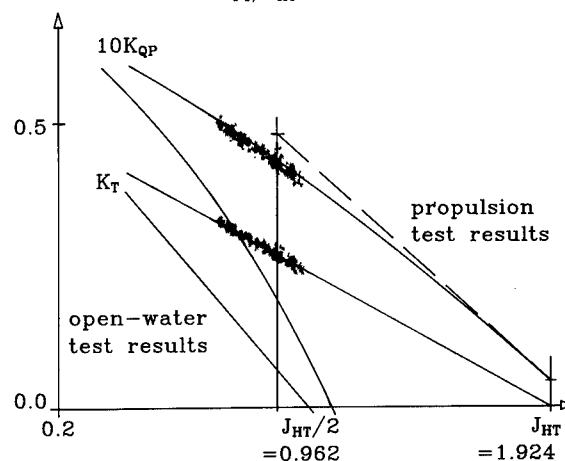


Figure 7: Determination of the wake from quasi-steady propulsion tests.

In order to show the feasibility of the procedure preliminary tests have been performed and analysed. VWS Model No. 2005, 6 m long, fitted with Propeller No. 1195, 0.211 m in diameter, was run at the Froude number 0.180 in the VWS shallow water tank at 1 m water depth. The frequency of revolutions was changed manually, certainly not always quasisteady. Data were acquired at a rate of 10 per second.

Based on the data in the range  $0.75 \leq J_H \leq 1.05$ , about 250 values, optimum linear and quadratic extrapolations have been used for the thrust and torque functions, respectively. Figure 7 shows the results including the open-water test results. In view of the very large scatter, partly due to a very poor resolution of the velocity, and the extreme range of extrapolation the resulting wake of 41 % must be considered as a reasonably successful estimate as compared with the wake of about 30 to 36 % determined in the usual way.

#### 5.4 Boundary Layer Suction

The problem with model testing is that the flows around the ship and the model are only partially similar. The traditional way to account for this dissimilarity in model propulsion tests is the application of a towing force  $F_D$  balancing the excessive drag of the model.

In view of the hull-propeller interaction under consideration this very simple and convenient procedure is not particularly satisfactory. All the essential factors of merit are dependent on energy velocities, and the theorem on thrust deduction

$$t = \chi / (1 + \chi + \tau)$$

shows explicitly the rôle of the displacement influence ratio

$$\chi \equiv V_E / V_p - 1.$$

This important parameter is different on model and full scale and remains unaffected by the towing force.

The only way to affect this ratio is to modify the boundary layer of the model, either by additional propulsors, i. e. boundary layer "acceleration", or by boundary layer suction. The difficulty with both techniques is that they may introduce disturbances into the flow, which may easily upset the purpose of the whole exercise.

Boundary layer suction, as far as possible uniformly distributed over the hull surface, is being tested in a preliminary research project at the Berlin Model Basin. Application in propulsion testing is certainly far from routine and may in fact never become routine, if the correct simulation of the ship wake is to be achieved.

One of the big problems apart of the experimental set-up and the time necessary for adjustment is that the full scale wake to be simulated cannot be computed so far, but may only be determined more or less crudely by some rule from the model wake (Sasajima, Tanaka, 1966; Tanaka et al., 1984). As has been shown experimentally by Huse (1977) the boundary layer thickness does affect the bilge vortices quite differently than the remainder of the wake.

#### 5.5 Suction Rule

In view of the afore-mentioned problems it has been suggested that suction according to some simple rules may serve the same purpose. As already stated the suction should be as uniformly distributed over the model surface as possible in order to avoid major disturbances of the flow and the wave pattern.

The main parameter of the suction is the total volumetric flow rate  $Q_S$ , which corresponds to a net force

$$F_S = \rho Q_S V.$$

As simple suction rule

$$F_S = F_D,$$

may be suggested, i. e. the suction force should compensate the excessive model drag, resulting in the required suction rate

$$Q_S = F_D / (\rho V).$$

In practical application it is necessary that no other forces are acting on the model. According to a proposal by R. Snay of the Berlin Model Basin this can be achieved, if the model is fitted with a well from which a pump, mounted on the accompanying carriage, can suck the water without transmitting net forces to the model. Preliminary tests have shown the feasibility of this set-up (Schmiechen, 1984).

#### 5.6 Conclusion

The present chapter does rather state problems and point out directions in which developments are necessary and have been started. Results of on-going research and development projects will be published in due course.

### 6. THEORY OF SCALING

#### 6.1 Introduction

Due to the lack of similarity between the flows around a ship and its geometrically similar models in traditional model testing the problem of scaling of dynamical quantities arises. In terms of the overall model, shown in Figure 1, the scaling theory has to establish a correspondence between ship and model quantities, the ratios of which are called scaling factors.

The goal of this chapter is to show the impact of the axiomatic theory of hull-propeller interaction on the theory of scaling. The exposition will proceed from the scaling factors to the scaling theorems, to the necessary scaling hypotheses, and finally to the scaling rules.

#### 6.2 Scaling Factors

As in the previous expositions of this subject (Schmiechen, 1980) the ship itself operating in a fluid of reduced density and increased viscosity, but at the same mass specific gravity, the same displacement, and the same velocity will be considered as its own model. The advantage of this artifice is that it reduces the problem to the essentials, namely the so-called scale effects.

If, as usual, smaller models are tested at

the same Froude number

$$F_n = V/(g L)^{1/2}$$

additional, well-known scaling factors have to be applied, in order to obtain the model quantities used in the following.

If ship and model quantities are denoted by upper indices S and M, respectively, the scaling factors may be uniformly and conveniently introduced as shown by the example

$$\eta_{XY}^0 \equiv \eta_{XY}^S / \eta_{XY}^M$$

Scaling factors of value 1 indicate, that there are no net (!) scale effects.

### 6.3 Scaling Theorems

Due to the fact that the axioms and the theorems apply to the ship and its model in the same way a large number of scaling theorems, i.e. relations between scaling factors may be derived.

In the first place the whole calculus of concepts may be rephrased in terms of scaling factors, e. g.

$$\eta_{XY}^0 \equiv P_X^0 / P_Y^0$$

The same holds for the calculus of propositions although most of the relations cannot be put into a simple format.

As an example it is assumed that the condition

$$T^0 = 1$$

is observed, i. e. propeller loading and jet efficiency are the same at model and full scale. Consequently the condition

$$\rho^0 Q^{02} / T^0 = 1$$

holds and the scaling factor for the power

$$P_P^0 = \rho^0 / \eta_{WP}^0 = T^0 Q^0 / \eta_{JP}^0$$

may be expressed in the form

$$P_P^0 = T^{03/2} / (\eta_{JP}^0 \rho^{01/2})$$

### 6.4 Scaling Hypotheses

In order to provide an operational interpretation of the abstract scaling theory some of the scaling factors, exactly ten, have to be known. If, as usual the values for the ship are not known, but to be determined, experiences with similar ships and hypotheses based on hydrodynamic theory have to be introduced.

So far no attempt has been made to outline the problems and possible strategies for their solution in the context of the present theory. It is felt that any solution will have to rely heavily on the vast experience accumulated using the traditional procedure.

### 6.5 Scaling Rules

Given the values of the scaling factors  $\rho^0$  and  $p_0^0$  and

$$A^0 = W^0 / \rho^0 = V^0 = 1$$

the values of five more scaling factors have to be known or five conditions have to be satisfied to permit the complete determination of all the ship data from the model data.

Assuming that the scaling factor of the resistance is known and that the selfpropulsion condition of the ship, i. e.

$$F_S = 0$$

is of interest, traditionally the condition

$$F_M = F_D = R^M (1 - R^0 / \rho^0)$$

for the towing force of the model is satisfied.

The above condition implies the condition

$$Q^0 (V_J - V_E)^0 = 1$$

and consequently

$$\eta_{WR}^0 = 1$$

i. e. no net scale effect in the hull factor of merit. Without three further hypotheses the scale factors for neither the other two factors of merit nor anything else may be determined.

The usual assumption, that there is no scale effect in the thrust deduction fraction,

$$t^0 = 1$$

e. g. Holtrop (1978), implies a scale effect in the propeller loading factor as may be seen from the thrust deduction theorem.

So far no general agreement on hypotheses to be adopted has been reached by the Performance Committee of the ITTC; see e. g. Lindgren et al. (1978) and later Reports of that Committee. The present theory does not suggest any specific solution, but it permits to clearly state the problem and discuss the physical essentials and not formal matters taken care of by the calculi of concepts and propositions.

In view of the problems of detailed scaling pragmatic procedures reduced to the bare essentials of predicting full scale power and frequency of revolutions, as e. g. proposed by Holtrop (1978), have very definite and practical merits. The method quoted claims, as the present one, not to require resistance and open-water tests, but it requires tests at vanishing thrust and the scale factor of the wake without explicitly stating how the wake concept is to be interpreted in terms of measurements.

Further the approximation

$$t \approx 1 + \partial F / \partial T$$

is implied for the thrust deduction fraction and it is assumed that the flow does not change its character at "extreme" conditions necessary for Prohaska's physical extrapolation. If only model-ship correlation is of interest these assumptions may be as sufficient as any others, "errors" cancelling each other to a certain extent.

### 6.6 Conclusion

The theory of scaling has only been sketched. Its crucial dependence on hypotheses concerning a number of scaling factors has been stated, but nothing has been said about these hypotheses in the present limited scope. The essential statement is rather that the axiomatic theory of hull-propeller interaction permits a large number of explicit formal relations between scaling factors to be derived, while in the traditional conceptual framework these relationships are, in the absence of a calculus of propositions, of experimental character.

## 7. HYDROMECHANIC THEORY

### 7.1 Introduction

So far hydromechanic theory has only been mentioned in connection with the scaling hypotheses. The problem to be discussed in this chapter, at least in outline, is the relation

of hydromechanic theory in general to the present theory.

As has been shown so far the propulsive performance of a ship can only be evaluated in terms of criteria derived in the framework of an abstract set of conventions and interpreted in terms of quantities measured on the ship itself. If the interpretation takes place in terms of quantities measured on physical scale models and/or computed for abstract hydromechanic models the evaluation is indirect.

## 7.2 Ideal Models

Ideal models may be constructed under the assumptions that the momentum and energy wakes are uniform and that the energy wake is the same for equivalent propellers inside and outside the displacement wake.

A special ideal model is obtained if an ideal propeller is assumed, not necessarily an actuator disc as usual (Schmiechen, Sparenberg, 1978/79). For this model the axioms do in fact conform to elementary hydromechanic theory of propulsion. The resistance axiom is in this case, as stated, the condition of selfpropulsion, i. e. zero momentum flux across a control surface around the ship, i. e. hull and propeller.

Consequently the theorem on thrust deduction and its approximate form

$$t = \chi / (1 + \chi + \tau)$$

are implied by elementary hydromechanic theory. Taking into account the pressure ratio

$$c_p \equiv 2(p_p - p_0) / (\rho V_p^2),$$

for which the relation

$$c_p = \chi^2 + 2\chi$$

holds, it becomes evident that the thrust deduction is directly related to that pressure ratio as already stated by Akimov (1935) and Horn (1956).

For small pressure ratios

$$c_p \ll 1$$

the theorem on thrust deduction may be written in the form

$$t = c_p / (4 + c_p + 2\tau).$$

Qualitatively this is directly evident from the fact that for all equivalent propellers the volume flux and the energy, i. e. the "pressure" jump

$$\Delta e = T/A$$

are the same. Consequently the propellers at the higher pressure levels have to be larger and have proportionally larger thrusts to account for the retarded inflows.

If the position of a given propeller in a given wake field is changed the pressure ratio is changed and consequently the thrust deduction fraction. More important is the fact that the same propeller at the lower pressure ratio represents a larger equivalent propeller with a correspondingly higher jet efficiency.

## 7.3 Thrust Deduction Laws

Similar "laws" on thrust deduction have been derived in many ways based on different assumptions, not always easy to follow. Not only the implications of the hydromechanic models have to be considered, but also implica-

tions of additional assumptions, which have usually to be made in order to make the problems amenable to analytical and/or numerical analysis.

Therefore most of the solutions differ from each other. A solution which is most easily compared with the theorem derived from the axioms is that for the potential thrust deduction arrived at by Nowacki and Sharma (1972, Eqn. B69)

$$t = \chi / (1 + \tau/2).$$

This solution is based on the model of equivalent sink strength with the approximation

$$Q_S / (A V_p) \approx \tau$$

due to Dickmann (1939).

If instead of the above approximation the exact relation

$$Q_S / (A V_p) = \tau(1 + \tau/2) / (1 + \tau)$$

(Horn, 1956; Schmiechen, 1978) is introduced the theoretical solution becomes

$$t \approx \chi / (1 + \tau),$$

i. e. almost the same as that derived from the axioms. The remaining difference may be due to necessary linearisations in the theoretical solution.

Horn (1936) has derived a solution for potential wake only from integral principles much in the same way as the present theorem has been derived from the axioms and identical with it for that special case. Horn could explain the difference between his solution and that of Fresenius (1921) along the lines indicated in the foregoing Section 7.2, and expected that the difference between his and Dickmann's (1939) solutions were due to the approximation mentioned before.

The important result of the foregoing analysis is that the general axiomatic solution is in line with the theoretical solutions for particular hydromechanic models. The only possible reason for this situation is, that the resistance and wake concepts underlying the hydrodynamical investigations are implicitly the same as the ones explicitly stated in the axioms. This fact may further support the plausibility of the latter but clearly does not prove them.

Due to the axiomatic approach the thrust deduction theorem cannot be proved by physical evidence. The reason for this situation is the fact that there are no independent interpretations of mass and energy fluxes to the propellers, at least not those without duct.

Horn (1935) already stated that independent interpretations would lead to incoherent results and discarded them for that reason, while Vollheim (1972) expects that only such measurements will eventually lead to the true efficiencies and factors of merit; cf. Section 7.4. Without reference to the existing solutions the law for the thrust deduction has e. g. been re-derived by Stierman (1984) and used for scaling purposes.

## 7.4 Hydromechanic Computations

The essential feature of the hydromechanic theory in the present context is of course not that it suggests concepts and relationships between them nor to show the plausibility of theorems, which may be formally derived, but rather

er its capability to provide, hopefully some day with the necessary reliability, extrapolation and scaling hypotheses and values for the quantities in question which the axiomatic theory by its very nature cannot.

The situation is similar to that of the theory of probability, which based on axioms can derive relationships between probabilities whatever their interpretation, objective or subjective, but cannot provide any values for the basic probabilities. Another example is thermodynamics, the concepts of which have to be interpreted either in terms of macroscopic measurements or quantummechanic theory.

As has been mentioned, measurements of the velocity and pressure distributions may not be performed routinely, certainly not on full scale ships under service conditions. But the distributions in question are or will become routinely available in numerical computations and may be integrated easily.

Provided the border line of the control surface is defined or agreed upon, hydromechanic computations will consequently result in volume and energy fluxes instead of resistance and propeller speed resulting from hydromechanic measurements. In order to ensure coherent and comparable results computations should preferably simulate overload tests and their evaluation should be performed in the same way as has been described.

#### 7.5 Propeller Design

Up to now apparently all propeller design procedures, including those for ducted propellers and pumpjets, are based on the naive conception of a propeller as a thruster.

An inherent difficulty of this approach is that the thrust to be designed for depends on hull-duct-propeller interaction. As a matter of fact rather detailed assumptions about the distribution of the wake and thrust deduction fractions are necessary as design input.

This very disturbing problem can be avoided if a propeller is conceived as a pump supplying energy to the flow around the vehicle so that the condition of selfpropulsion is satisfied.

This concept has been worked out in a recent paper on optimum ducted propellers for bodies of revolution (Schmiechen, 1983), closely related to the work of Dyne (1983) on optimum wake vorticity adapted propellers.

Differences in the expositions are partly due to the fact that the use of existing propeller design programs may require a different wake concept, certainly not the Taylor wake concept based on thrust identity. On the other hand the resistance concept appears to be exactly the one proposed here.

The basic model underlying the investigation is shown in Figure 8.

The flow past the vehicle moving in the negative x-direction with speed  $V$  in an incompressible fluid of density  $\rho$  and at rest at infinity is assumed to be circumferentially uniform in the average, i. e. only depending on the longitudinal position  $x$  and the radial position  $r$  in body-fixed coordinates.

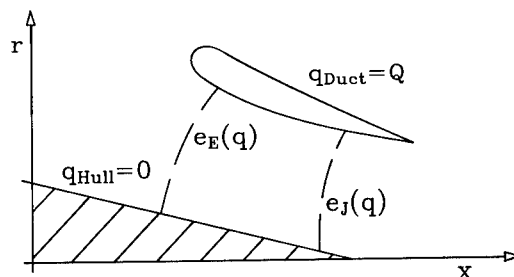


Figure 8: Basic propeller model

Accordingly the flow field may be described by a stream function

$$q = q(x, r),$$

specifically the flow rate, and an energy function

$$e = e(x, r),$$

specifically the volume-specific energy

$$e = \rho v^2/2 + p - p_0 + \rho g(z - z_0)$$

the sum of the local kinetic and potential energy.

In accordance with the assumption of circumferential uniformity the propeller is represented by a circumferentially uniform external force field  $f$ . The fluid is assumed to be Newtonian and the flow to be turbulent and fluctuating.

With the specific energy distributions

$$e_E = e_E(q)$$

and

$$e_J = e_J(q)$$

at the inlet and outlet surfaces, respectively, and the hydraulic efficiency distribution

$$\eta_{JP} = \eta_{JP}(q),$$

the power absorbed is

$$P_p = \int (e_J - e_E) dq / \eta_{JP},$$

and the condition of self-propulsion may be expressed in terms of the resistance axiom

$$R = \rho \int (V_J - V_E) dq.$$

The distributions of the energy velocity at the propeller inlet and of the hydraulic efficiency being given, the optimum distribution of the energy velocity at the propeller outlet has to be determined according to the requirement

$$\int V_J^2 / \eta_{JP} dq = \min$$

under the condition

$$\int V_J dq = \text{const},$$

which leads to the optimum condition

$$V_J / \eta_{JP} = \text{const},$$

which was incorrectly stated in the original paper.

Pertinent in the context of the present paper is the fact that the factor of merit of the configuration determined in this way obviously represents an upper limit under the conditions given and may become an important criterion in performance evaluation.

For the design of ducted propellers, i. e. pump stages meeting the specified optimum requirements, flow fields have to be constructed at least approximately. Computations including turbulence, e. g. by Zhou (1982), are far from being standard practice today, the inclusion of propeller models in such computations has hard-



ly been tried. In order to obtain useful results now the flow model has to be simplified to become tractable routinely in propeller design.

In accordance with the usual practice it is assumed that within a limited region around the propeller, momentum and, consequently, energy and vorticity exchange between stream lines are negligible (Dyne, 1978), i. e. Cauchy's equation reduces to Euler's equation, which may be integrated along stream lines. In this simplified model the specific energy is independent of the coordinate  $s$  along the stream line, outside the propeller region.

The problem, still formidable enough, may be greatly simplified, if it is transformed before the solution is attempted. The transformation is particularly simple, if the consideration is restricted to shock-free entrance into the duct, the stagnation point being located at the forward point of the duct. Even in this simple model there is considerable freedom in design to account for cavitation, noise etc.

For the purposes of numerical computations the flow rate and its radial coordinate may be further transformed as proposed by Zhou (1982) in order to account for the boundary condition at infinite flow rate without extra computations and matching of boundary conditions.

In conclusion of this outline it may be stated that the rigorous conception of a propeller as a pump apparently leads to a coherent design procedure, although in many respects closely resembling the usual procedure, in principle clearly distinct from it.

As in pump design the thrust and its distribution are by-products of the flow field computations and for this reason they did not even have to be mentioned in this outline. This fact may at first appear surprising, but as has been stated earlier (Schmiechen, 1968) is an inherent feature of the basic conception.

It is evident that duct-propeller configurations designed according to the procedure outlined cannot be tested in the open-water condition, not even in the "wrong" model wake. The only meaningful way to establish their performance appears to be the evaluation of overload conditions in propulsion tests, at model or full scale in principle alike, maybe in the same way as described before. All of the procedures outlined by Stierman (1984) are unsatisfactory, resistance tests with the nozzle fitted will certainly result in rather meaningless data.

## 7.6 Conclusion

The whole chapter on hydromechanic theory and its relation to the axiomatic theory is not more than a sketch and had to be limited to some essential ideas, hopefully throwing some new light on some unresolved problems.

Obviously hydromechanic theory cannot replace the axiomatic theory of hull-propeller interaction. But it can support the axioms and the extrapolation to the state of vanishing thrust and it can provide scaling hypotheses and values of the quantities introduced.

## 8. CONCLUSIONS

### 8.1 Review

The proposed conceptual framework is an attempt to rationally reconstruct the traditional procedure for ship performance evaluation presented by R. E. Froude (1883) hundred years ago and followed since by an ever growing community of ship model basins despite its inherent inconsistencies.

The axiomatic theory is the first attempt to explicitly state a formal language including basic propositions, i. e. principles or conventions, which may serve as an adequate general basis for the rational resolution of the problems and conflicting interests and requirements, e. g. of shipowners, shipbuilders, ship-designers, and ship-researchers or of ship operation, ship testing, ship design, ship hydrodynamics, and ship theory.

In order to serve its purpose the formal language has been designed as a macroscopic theory adequately reflecting the structure of the micro-universe of discourse by abstraction from the past hundred years of experience in hydromechanic theory and testing. The concepts introduced are consequently independent of any specific experimental and computational techniques and devices, e. g. towing and open-water tests, sources and sinks, lightly loaded actuator discs, etc. however useful the latter may be in their place. The conceptual model underlying the axiomatic theory is the readily grasped artifice of the equivalent propeller outside the displacement influence of the hull.

According to the dual model of mature theories the abstract axiomatic theory is complemented by an interpretation theory, which itself consists of an axiomatic theory, implying the concept of the equivalent state of vanishing thrust, and a statistical theory of measurements and extrapolation. Provided the necessary data can be acquired, the test procedure outlined can be applied on full and model scale, requiring only load variations around the service conditions, but no reference to towing tests with the hull or open-water tests with the propeller. Like comparable methods of systems identification the procedure is sensitive to measurement noise.

The theories of testing and scaling are rather outlines of necessary developments, the latter providing a series of scaling theorems and once again showing the lack of adequate scaling hypotheses. The reason for this situation is that so far no adequate procedure to determine full scale values experimentally has been available, not even conceptually.

The outline of the relation between the present theory and hydromechanic theory shows that the rôle of latter in hull-propeller interaction research will be different in future.

The whole exposition has been extremely structured, maybe overstressing the point of methodology, in order to avoid the usual confusion of problems caused by the necessity to provide complete procedures, which could be applied immediately to practical problems.

## 8.2 Outlook

The proposed theory of ship performance is a formal language, which has proved to be useful in restating the physical problems to be solved by theoretical and experimental hydrodynamics. To expect solutions now for the many problems, which can be stated only after this exposition, is to underestimate the effort necessary so far and in future.

Specific problems of high priority to be solved have been mentioned in the respective chapters: rigorous foundation of the axiomatic theory, development of practical procedures for measurements on model and full scale, including extrapolation to the equivalent state of vanishing thrust, experimental and theoretical determination of scaling hypotheses, and theoretical flow computations for design purposes.

Most of the problems are not new, but the context in which they have been put. A general task will be to re-analyse past practice and experience from the present point of view in order to rationalize them. This task may only be undertaken by the community concerned, sharing a common language, maybe eventually the one proposed.

## ACKNOWLEDGEMENTS

The author would like to thank his colleagues in Germany for indepth discussions clarifying many aspects of the ideas proposed and documented in "Schiffstechnik" already and the Transactions of the Schiffbautechnische Gesellschaft (1980). In particular the author would like to thank Dr.-Ing. B. Lang and Dipl.-Ing. R. Snay of the Versuchsanstalt für Wasserbau und Schiffbau, the Berlin Model Basin, for their most helpful criticism during the crucial phases in the development of the theory of interpretation.

## REFERENCES

- Abkowitz, M.A. (1980): Measurement of Hydrodynamic Characteristics from Ship Manoeuvring Trials by System Identification. SNAME, Vol. 88, pp. 283-318.
- Adachi, H. and M. Hinatsu (1983): On Effective Wake (Consideration Based on the Propeller Load Varying Test Concept). J. Kansai Soc. N.A. Japan, No. 191, pp. 41-50.
- Diaconis, P. and B. Efron (1983): Statistik per Computer: der Münchhausen-Trick. Spektrum der Wissenschaft No. 7, S. 56-71. From Scientific American, May 1983.
- Dickmann, H. (1936): Auswertung von Schraubenversuchen. Schiffbau, Vol. 37, No. 7, pp. 113-118.
- Dickmann, H. (1939): Wechselwirkungen zwischen Propeller und Schiff unter besonderer Berücksichtigung des Welleneinflusses. Jb. STG, Vol. 40, pp. 234-291.
- Dyne, G. (1978): A Streamline Curvature Method for Calculating the Viscous Flow around Bodies of Revolution. Proc. Int. Symp. on Ship Viscous Resistance, Paper No. 6, pp. 1-22.
- Dyne, G. (1983): On Optimal Wake Vorticity Adapted Propellers. Proc. 2nd Int. Symp. on Practical Ship Design in Shipbuilding, Paper No. 9, pp. 77-84.
- Fresenius, R. (1921): Das grundsätzliche Wesen der Wechselwirkung zwischen Schiffskörper und Propeller. Schiffbau, Vol. 23, No. 10, pp. 257-260 and No. 11, pp. 300-304.
- Froude, R.E. (1883): A Description of a Method of Investigation of Screw Propeller Efficiency. Trans. INA, Vol. 24, pp. 231-255.
- Holtrop, J. (1978): Power Prediction by a Modern Analysis Method without Resistance and Propeller Open-Water Tests. Proc. 15th ITTC, Vol. 2, pp. 174-176.
- Holtrop, J. and G.G.J. Mennen (1982): An Approximate Power Prediction Method. Int. Shipb. Progr., Vol. 29, No. 335, pp. 166-170.
- Horn, F. (1935): Auswertung von Schraubenversuchen. Schiffbau, Vol. 36, No. 18, pp. 303-309, No. 19, pp. 325-330, and No. 20, pp. 335-339.
- Horn, F. (1937): Bestimmung des Mitstroms durch Versuch Modell mit Schraube. Proc. 4th ITTC (Berlin) pp. 54-62. Mitteilungen der Preussischen Versuchsanstalt für Wasserbau und Schiffbau, Berlin, Heft 32, H.O. Weitbrecht Ed.
- Horn, F. (1955): Studie zum Thema "Wechselwirkung zwischen Schiffsrumpf und Propeller". Schiff und Hafen, Vol. 7, No. 10, pp. 601-604.
- Horn, F. (1956): Beziehung zwischen Sog und Mitstrom bei reiner Verdrängungsströmung. Schiff und Hafen, Vol. 8, No. 6, pp. 472-475.
- Horn, F. (1964): Ermittlung des Mittelwerts des Mitstroms aus Propulsions- und Freifahrtversuchen. Schiffstechnik, Vol. 11, No. 59, S. 131-136.
- Huse, E. (1977): Bilge Vortex Scale Effect. Symposium on Hydrodynamics of Ship and Offshore Propulsion Systems. Det Norske Veritas. Paper 6/4 - Session 1.
- International Towing Tank Conference Standard Symbols (1976). Wallsend: British Ship Research Association. BSRA Techn. Memo. No. 500.
- Keil, U. (1982): Prognosegenauigkeit durch neue Versuchstechnik beim Propulsionsversuch. Hansa, Vol. 119, No. 18, pp. 1119-1120.
- Leinfellner, W. (1980): Einführung in die Erkenntnis- und Wissenschaftstheorie. Mannheim, Wien, Zürich: Bibliogr. Institut, 3. Edition.
- Lindgren, H. et al. (1978): Report of the Performance Committee. Proc. 15th ITTC (Den Haag), Vol. 1, pp. 359-404.
- Lorenzen, P. und A. Schwemmer (1975): Konstruktive Logik, Ethik und Wissenschaftstheorie. Mannheim: Bibliogr. Institut.
- Nowacki, H. and S.D. Sharma (1972): Free-Surface Effects in Hull Propeller Interaction. Proc. 9th Symposium on Naval Hydrodynamics, Vol 2, pp. 1845-1861.
- Sasajima, H. and I. Tanaka (1966): On the Estimation of Wake of Ship. Proc. 11th ITTC, pp. 140-143.

- Schmidt, E. (1958): Thermodynamik. Berlin, Göttingen, Heidelberg: Springer-Verlag, 7. Edition.
- Schmiechen, M. (1960/62): Ansätze zu einer allgemeinen Strahltheorie hydrodynamischer Reaktionsantriebe in idealen Flüssigkeiten. Unpublished Manuscript.
- Schmiechen, M. (1968): Performance Criteria for Pulse-Jet Propellers. Proc. 7th Symp. on Naval Hydrodynamics, pp. 1085-1104.
- Schmiechen, M. (1969): Design and Evaluation of Experiments for the Identification of Physical Systems. Cambridge, Mass.: MIT Dept. Nav. Arch. and Mar. Engg., Rep. No. 69-1.
- Schmiechen, M. (1969): Proposed Standard Procedure for the Estimation and Presentation of Regression Functions. Written Contribution to the Session on Presentation at the 12th ITTC (Rome). Unpublished Manuscript.
- Schmiechen, M. (1970): Über die Bewertung hydromechanischer Propulsionssysteme. Schiffstechnik, Vol. 17, No. 89, pp. 91-94.
- Schmiechen, M. (1973): On State Space Models and their Application to Hydromechanic Systems. Tokyo: Tokyo University, Dept. of Nav. Arch., Rep. No. NAUT 5002.
- Schmiechen, M. (1978): Rationale Modelle idealer Propeller endlicher Belastung. Schiffstechnik, Vol. 25, No. 121, pp. 113-120.
- Schmiechen, M. (1980): Eine axiomatische Theorie der Wechselwirkungen zwischen Schiffsrumpf und -propeller. Schiffstechnik, Vol. 27, No. 2, pp. 67-99.
- Schmiechen, M. (1980/84): Wake and Thrust Deduction from Propulsion Tests Alone. Presentations at:
- |                        |               |
|------------------------|---------------|
| Shipb. Inst. Leningrad | 25.04.1980    |
| MARIC Shanghai         | 15.10.1980    |
| CSSRC Wuxi             | 20.10.1980    |
| STG Berlin             | 28.11.1980    |
| UCL London             | 19.01.1981    |
| NSMB Ede               | 20.01.1981    |
| DTNSRDC Washington     | 9./13.01.1984 |
- Schmiechen, M. (1980): Nachstrom und Sog aus Propulsionsversuchen allein. Eine rationale Theorie der Wechselwirkungen zwischen Schiffsrumpf und -propeller. Jb. STG, Vol. 74, pp. 333-351.
- Schmiechen, M. (1982): Über Weiterentwicklung des Vorschlages "Nachstrom und Sog aus Propulsionsversuchen allein". Schiff und Hafen, Vol. 34, No. 1, pp. 91-92.
- Schmiechen, M. (1983): On Optimal Ducted Propellers for Bodies of Revolution. A Speculative Reconstruction. Proc. Int. Symp. on Ship Hydrodynamics and Energy Saving (El Pardo).
- Schmiechen, M. and B. Lang (1983): Estimates of Laplace and Fourier Transforms of Transient Functions from Truncated Records. Berlin: Versuchsanstalt für Wasserbau und Schiffbau, VWS-Bericht No. 972/83. To be published in: Proc. 13th Scientific and Methodological Seminar on Ship Hydrodynamics (Varna).
- Schmiechen, M. (1984): Schiffmodellversuche mit Absaugung der Grenzschicht. Berlin: Versuchsanstalt für Wasserbau und Schiffbau, VWS-Bericht, to be published.
- Spärgen, J.A. and M. Schmiechen (1979): Some Remarks to the Article "Rationale Modelle idealer Propeller endlicher Belastung" of Prof. M. Schmiechen and Author's Reply. Schiffstechnik, Vol. 26, No. 2, pp. 117-121.
- Stiermann, E.J. (1984): Extrapolation Methods for Ships Fitted with a Ducted Propeller. Int. Shipb. Progr., Vol. 31, No. 356, pp. 80-87.
- Tanaka, I. et al. (1984): Investigation of Scale Effects on Wake Distribution Using Geosim Models. J. Kansai Soc. N.A. Japan, No. 192, pp. 103-120.
- Vollheim, R. (1972): Bemerkungen über die Widerstandsanteile, Wirkungsgrade und Gütegrade in der verlustbehafteten Strömung um das propellergetriebene Schiff. Schiffbau-forschung, Vol. 11, No. 1/2, pp. 69-80.
- Weinblum, G. (1972): Contribution to Nowacki, Sharma (1972). Proc. 9th Symp. on Naval Hydrodynamics, pp. 1948-1949.
- Zhou, L. (1982): A Streamline-Iteration Method for Calculating Turbulent Flow around the Stern of a Body of Revolution and its Wake. Proc. 14th Symp. on Naval Hydrodynamics, Prep. Sess's VII and VIII, pp. 35-59.
- Zurmühl, R. (1963): Praktische Mathematik für Ingenieure und Physiker. Berlin, Göttingen, Heidelberg: Springer-Verlag.

## DISCUSSION

Mr. LIAN-DI ZHOU,  
China Ship Scientific Research Center,  
Wuxi, Jiangsu, PR China:

I congratulate Dr. Schmiechen on such an interesting paper. The aim of this paper is to improve the present tradition or concept of propeller-hull interaction, and to regard the flow of the propeller and hull as an inseparable system. As a result the method of testing and design is also different from the traditional.

I am very interested in this design problem, since in my paper the need of knowledge of thrust deduction is also abandoned beforehand, but comes out as a natural outcome of the computation. There are a few questions I would like to ask:

1. Regarding the optimum condition as given on page 495, the condition  $V_j/\eta_{JP} = \text{const.}$ , how is it deduced?

2. How is the distribution of  $\eta_{JP}$  as a function of  $q$  determined or given in a certain design case?

3. Where should the entrance and exit conditions of Fig. 8 be actually placed? If the entrance condition is placed very near to the duct entrance, then how could  $V_E(q)$  be determined beforehand?

Dr. GILBERT DYNE,  
SSPA Maritime Consulting AB,  
Gothenburg, Sweden:

Let me first congratulate the author on a very refreshing paper on an important topic. I really hope that his ideas, when they are made known to a larger audience, will start a discussion on the validity of the propulsion principles. The conventional way of analysing the propulsing by using self propulsion, resistance and open water tests has too long been accepted and used without critical considerations.

The procedure to determine the thrust deduction and the effective wake by comparing the results from self propulsion tests with results from resistance and open water tests respectively has the great advantage of giving relatively consistent results for single screw ships. Drawbacks are, however, that

- o it gives little information on the energy relationships in the propulsion process and that
- o it does not work for more unconventional propulsion systems (how do you, for example, define the thrust deduction and the wake for a water jet system?)

The author has based his theory on energy considerations and regards the propeller as an energy-producing pump. If I have understood him right the energy velocity  $V_E$  at the propeller is related to the frictional wake  $w_F$  as follows:

$$V_E = V(1 - w_F)$$

see Dyne 1983, and the jet velocity

$$V_j = V(1 - w_F + \frac{U_{A00}}{V})$$

where  $w_F$  is the final wake and  $U_{A00}$  is the propeller-induced velocity far behind the propeller. Since the author ignores the slipstream rotation the optimum condition reads

$$\frac{V_j}{\eta_{JP}} = \text{constant}$$

see Fresenius 1921. It would be interesting to hear what the consequences for the theory would be if the slipstream rotation is considered. Certainly some of the basic propositions and maybe also some of the calculation results would be different.

The proposed method to determine the thrust deduction  $t$  and the wake  $w$  has, however, a serious drawback in its present form: It is too sensitive to the choice of polynomial fittings and does not give consistent results. The result from an overload test recently carried out in SSPA towing tank (8 different loadings) may illustrate this: The relationship between  $F$  and  $T$  was found to be nearly linear, giving a thrust deduction of

$$t = 0.11$$

If instead a second order polynomial was used, then

$$t = 0.21 - 0.28$$

i.e. a curvature of the  $F$ - $T$ -curve, which was barely visible doubled the thrust deduction! Also the  $K_T$ - $J$  and  $K_Q$ - $J$  relationships were fairly linear giving a wake fraction of  $w = 0.37$  with the proposed method. Second and third order polynomials did not give any intersection with the  $J$ -axis in the range of interest! Hence no wake could be determined in these cases. My conclusion of this result is therefore: If the thrust deduction and the wake should be determined from self propulsion tests alone with the proposed method only linear relationships must be used to get consistent results. This is probably true also if the number of tests is increased dramatically as suggested by the author.

Personally I believe that the self propulsion test must be combined with some other test to give the information wanted. Would not pressure and velocity measurement around the stern and in the wake be an alternative? The problem with measurements of this kind is, however, that they are not simple enough to be accepted in the daily work of towing tanks.

Mr. MITSUHIRO ABE,  
Mitsui Eng. & Shipbuilding Co, Akishima Lab.,  
Tokyo, Japan:

First I congratulate, as a tankery man, Prof. Schmiechen on his fascinating theory. Really, the now one-hundred year old efforts, namely, self-propulsion tests combined with propeller open-water test, are still valid for conventional and moderately shaped ships.

In recent years, the demand for energy saving has produced unconventional hull-propulsor systems, ducted propellers and flow controlling fins, etc. For such a system the conventional propulsion test may be discour-

aging, as is being discussed at the 17th ITTC.

In this situation, the author's theory will meet our expectation to evaluate the unconventional hull-propulsor systems as well as conventional ships. However, the power prediction requires a consistent and accurate method as good as the present method has been.

My point is how the new method which the author has presented shall become routine at the tank. In so doing, it will be much appreciated if the author will tentatively give us a physical and realistic method in relating the present one, relevant propulsion factors and scaling factors.

Prof. KUNIHARU NAKATAKE,  
Kyushu University,  
Fukuoka, Japan:

I appreciate the author's new proposal concerning the propulsion test and its analysis. Though I can not understand well the theory of theories, the axioms and other terminologies, the author bravely, I think, proposes the method as a substitute for the traditional method. The traditional propulsion test has hydrodynamically two main deficiencies between the model and the full-scale ship. One is the relative difference of the viscous resistance and the other is the relative difference of the wake thickness in the propeller plane. The former is almost compensated for by the skin friction correction, but the latter is not. Then Dr. Schoenherr proposed a new method (JSR 1965) to use a larger model propeller than usual one, which was made by considering the scale effect on the wake. However, since the diameter of the model propeller becomes too large, his method is not used usually though the scale effect on the propulsion factors becomes small. I hope the author's method may improve the traditional one through careful examinations.

At last, I raise one question concerning the presence of the rudder, since the behavior of the rudder drag is complicated but interesting. Is the proposed method applicable to the ship with a rudder?

#### AUTHOR'S REPLY

I would like to thank all who took part in the discussion for their valuable contributions and suggestions. In particular I would like to thank them for their kind support of my attempt to solve a problem which in my view has not received the due attention so far.

Mr. Zhou in his discussion is touching on the design problem, which is covered only cursorily in the paper and has hardly been mentioned in the presentation. The optimum condition stated in the paper is the well-known one due to Fresenius, as Dr. Dyne points out, and may be derived by variational principles. The distribution of the hydraulic efficiency with respect to the flow rate will have to be estimated at the beginning based on past experience and will have to be checked when the propeller

design is completed, maybe necessitating an iteration as mentioned in my paper.

Concerning the actual locations of the inlet and outlet control surface it has to be kept in mind that the description in terms of the energy distributions with respect to the flow rate is practically invariant with regard to those locations. This invariance is due to the fact that within the variations in question the energy exchange between stream tubes is negligible, and is the reason for the adoption of the description and its success.

Dr. Dyne's first question concerns the slipstream rotation, which in the design of optimal propellers, conceived as rotor-stator stages, is not "ignored" but has to be avoided right from the beginning. This optimum condition does, however, not imply, as Dr. Dyne does, that the axiomatic system needs to be changed to account for slipstream rotation, which is present in general. In my view this is taken into account by adequate interpretations of the concepts of jet efficiency and propeller factor of merit, which may be not the ones Dr. Dyne has in mind.

The second point raised by Dr. Dyne concerns the problem of extrapolation, which I have dealt with in great detail in my paper, but hardly outlined in the presentation. As I have stated earlier the problem is essentially the reliable estimation of second derivatives. Consequently the proposal to restrict considerations to linear relationships is not acceptable, as it implies additional inadequate axioms leading to a number of inconsistencies.

In a practical application of the procedure using propulsion tests at only five steady conditions I have avoided the problem of extrapolation by using the physical state of vanishing thrust. As Dr. Dyne already states additional measurements of pressures may be quite unacceptable in routine work, full scale in particular. Although the model had an extremely full form the results turned out to be very close to those obtained by the traditional procedure. In that particular case the goal was to compare the propulsive factors at the model without and with boundary layer suction, as explained in the paper rather too briefly. The results, which will be published in a German research report shortly, agree perfectly well with corresponding geosim tests carried out by the Berlin Model Basin some twenty years ago.

Dr. Abe in his contribution addresses the problem of routine application in power predictions. From my paper and the presentation it is evident that we are still far from such a routine. But it is hoped that future applications, full scale in particular, will help to improve our present state of knowledge on scale effects and help us in providing more adequate power predictions, even for unconventional configurations, which Dr. Abe is referring to and where the traditional procedure is not applicable. The tests with boundary layer suction just mentioned have certainly been an important step towards the final goal of properly simulating full scale conditions on model scale. In my opinion this technique will in fact have to be applied for the investigation of unconventional

configurations. There will be no chance to collect enough data on scale effects for power predictions along the traditional line, even in another hundred years of testing.

Prof. Nakatake refers to the same problem of flow dissimilarity between model and full scale and mentions the idea of Dr. Schoenherr to account for this dissimilarity by changing the propeller geometry. In my view this procedure would require too much knowledge in advance, more maybe than can be gained from the subsequent tests. The same argument applies to the change of hull geometry as proposed by Dr. Björheden in an oral contribution to the discussion of the paper by Professors Yamazaki and Nakatake.

With regard to Prof. Nakatake's question concerning the presence of rudders, it may be inferred from the title of the paper that rudders are always included: There are no ships without rudders. If we want to study the behaviour of the rudder drag in detail special tests will have to be designed. At the present stage I have not yet looked into this problem and may consequently offer no particular procedure.

In an oral contribution Dr. Huang, DTNSRDC, expressed the opinion that in five years time we might compute everything and that the whole theory presented might be not necessary any more. Quite apparently this opinion is based on a misconception of the present undertaking, which aims at solving problems hydrodynamic theory due to its very nature can neither state nor ever solve. As mentioned at the beginning of the presentation the present theory has little or nothing to do with hydrodynamic theory. It is rather an example of hydromechanic systems theory, macroscopic theory of ship propulsion in particular, which may be interpreted by hydrodynamic theory but not replaced. The relationship between both theories is the same as that between thermodynamics and quantum mechanics.

To be more specific: If we want to know the propulsion factors of a given ship there is no way except taking measurements at that ship under service conditions and evaluating them. Clearly the traditional procedure cannot be applied at full scale: Nobody has ever made an open water test with a propeller of 6 or 8 m in diameter. And no hydrodynamicist has so far defined or computed the resistance of a self propelled vehicle. The present paper now for the first time proposes a coherent set of conventions which, if adopted or agreed upon by the community, may help to solve an urgent problem, which can clearly not be solved by hydrodynamic computations.

Although it may sound pretty pretentious I would finally like to quote from the words with which R.E. Froude in reference to the scope of his paper concluded the discussion in 1883:

"... It (the paper) professes to suggest a way which, I think, is the only way of doing it, if it can be done, though I am not as yet certain that it can be done very effectively or successfully. ... I feel that, even if we are baffled ..., this paper has a value, in

that the propositions which I have put forward are a contribution to the science of the subject, and, I think, in virtue of the light thrown on the question by the propositions, we shall be able to do a good deal in analysing and systematising the results which are to be obtained from full-sized trials with ships; and that we can thus make much better use of results obtained from steamship trials than can be made without the light which is thrown on the general question of propulsive efficiency by this investigation."

SESSION VIII  
FRONTIER PROBLEMS

# CALCULATION OF STERN FLOWS BY A TIME-MARCHING SOLUTION OF THE PARTIALLY-PARABOLIC EQUATIONS

H.C. CHEN AND V.C. PATEL

## ABSTRACT

The major features of a general numerical method for the calculation of the flow over the stern and in the wake of a three-dimensional body are described. The method is based on the solution of the partially-parabolic equations for a turbulent flow in curvilinear, nonorthogonal, numerically-generated, body-fitted coordinates using the novel "finite-analytic" numerical scheme. It is shown that the entire zone of viscous-inviscid interaction can be captured, thus avoiding separate viscous-flow and potential-flow calculations and iterative matching, by using a large enough solution domain and coordinate stretching. The generality and flexibility of the method are demonstrated by applications to two-dimensional, axisymmetric and three-dimensional bodies.

## PRIMARY NOMENCLATURE

$A_\phi, B_\phi, D_\phi, E_\phi$	coefficients in equations (11), (14); equations (13a); $\phi \equiv U, V, W, k$ , or $\epsilon$
$a_\phi, b_\phi, c_\phi, d_\phi$	coefficients in equations (13b,c); $\phi \equiv U, V, W, k$ , or $\epsilon$
$b_{ij}^j, g_{ij}^j, g_{ij}^{ij}, J$	geometric quantities from coordinate transformations
$C_{NE}, C_{SW}$ , etc.	finite-analytic coefficients; equations (18)
$f^i$	grid-control functions; equation (1)
$h_i$	metrics in orthogonal coordinates
$k$	turbulent kinetic energy
$p$	pressure
$Re_{eff}$	effective Reynolds number, $(v + v_+)^{-1}$
$S_\phi, s_\phi$	source functions in equations (11,14); equations (13)
$t$	time
$(U, V, W)$	velocity components in $(x, r, \theta)$ coordinates
$(x, r, \theta)$	basic cylindrical coordinates (see Fig. 1)
$\epsilon$	rate of dissipation of turbulent kinetic energy

$\phi$	$\equiv U, V, W, k$ , or $\epsilon$
$v_+^+$	turbulent viscosity
$(\xi, \eta, \zeta)$	general nonorthogonal coordinates

## Subscripts

NE, SW, etc.	nodal points of the numerical element (north-east, south-west, etc.); Fig. 5(a)
e, w, d, u, etc.	nodal points in a staggered grid (east, west, downstream, upstream, etc.); Fig. 5(b)
p	central point in numerical element; Fig. 5
$\phi$	coefficient or value corresponding to $U, V, W, k$ or $\epsilon$
$(\xi, \eta, \zeta)$	derivatives with respect to these space variables

## 1. INTRODUCTION

Experiments and calculations indicate that first-order boundary-layer equations adequately describe the flow over a large part of a ship hull if phenomena associated with the free surface are excluded. The assumptions embodied in boundary-layer theory begin to breakdown gradually over the stern, in a region which may be typically 10 percent of the ship length. Experimental information pertaining to the evolution of the flow over the stern and in the near wake has been reviewed by Patel (1982). Among the features which differentiate the stern flow from that in the boundary-layer over the hull are: (a) a rapid thickening of the viscous layer; (b) variation of pressure across the layer, implying a strong viscous-inviscid interaction; (c) the development of a large longitudinal vorticity component which may lead to a free-vortex type of separation; and (d) a general reduction in the level of turbulence. The wake of the ship evolves gradually from this flow and also shows basically the same features. An important observation that also emerges from the experiments is that there is usually no region

Dept. of Mech. Engineering and Inst. of Hydraulic Res., University of Iowa, Iowa City, Iowa 52242



of flow reversal in the direction of ship motion. The flow features noted above are precisely those which can be addressed by the so-called partially-parabolic or semi-elliptic equations which are obtained from the fully-elliptic Navier-Stokes or Reynolds equations by neglecting terms which represent diffusion in the predominant flow direction. In particular, these equations can be used to describe the flow in the region between the thin boundary layer upstream and the wake far downstream of the hull.

Previous solutions of the partially-parabolic equations in three-dimensional external flows are quite limited. Abdelmeguid et al. (1979) presented the first application to ship hulls and Markatos et al. (1980), Muraoka (1980, 1982), Tzabiras and Loukakis (1983) and Tzabiras (1983) have pursued it further. All of these use essentially the same numerical scheme, based on the work of Patankar and Spalding (1972), and the  $k-\epsilon$  model of turbulence.

This paper is also concerned with the solution of the partially-parabolic Reynolds-averaged equations. However, the present approach differs from the previous work in several important respects. First, in the interest of generality and flexibility for applications to arbitrary ship hulls, the method uses numerically-generated, body-fitted nonorthogonal coordinates which are continuous in all three dimensions. This approach also offers the opportunity to investigate the influence of coordinate choice on the numerical solutions. Secondly, a large solution domain is chosen such that the entire zone of viscous-inviscid interaction is captured. Thus, it is not necessary to perform a potential-flow calculation or match the viscous and inviscid solutions. The results of the method can therefore be used to guide the selection of appropriate matching conditions in conventional viscous-inviscid interaction techniques. Thirdly, the equations are solved using the novel "finite-analytic" numerical scheme of Chen and Chen (1982, 1984) which is quite different from conventional finite-difference and finite-element methods. It uses analytical solutions of the locally-linearized momentum equations for each numerical cell in the computational domain and combines them to obtain the global solution. Fourthly, the pressure field, which is elliptic, is obtained from a modified version of the SIMPLER algorithm of Patankar (1980) which improves the convergence properties of the solution. Finally, the method is formulated for general unsteady three-dimensional flows and can be readily extended to fully-elliptic flows. In the present applications, the steady-state solutions are obtained by a time-marching procedure in which time serves as an iteration parameter.

The various aspects of the method will be described in detail in a forthcoming report (Chen and Patel, 1984). Therefore, it suffices here to describe them briefly.

Although our primary interest lies in the flow over ship sterns, with all the complicating factors noted earlier, we shall also present solutions of some two-dimensional and axisymmetric flows in order to demonstrate the detailed performance of the method.

## 2. OUTLINE OF THE SOLUTION PROCEDURE

### 2.1 Coordinate System

In previous solutions for ship hulls, the Reynolds equations were first written in cylindrical polar coordinates  $(x, r, \theta)$ , with  $x$  in the direction of ship motion (Fig. 1). After neglecting the  $x$ -derivatives of the stresses, these were transformed such that the hull surface became one of the coordinate surfaces. Abdelmeguid et al. and Muraoka employed analytical transformations which led to a nonorthogonal distorted polar coordinate system in the  $(r, \theta)$  plane, while Tzabiras and Loukakis employed conformal-transformation techniques to generate orthogonal coordinates in this plane. In both cases, the coordinate lines in the  $(x, r)$  planes were nonorthogonal. The improved results obtained by the latter authors have been attributed to this difference in the coordinates.

Here we shall follow the increasingly popular method of numerical grid generation, as suggested recently by Cheng and Patel (1983), since it offers the advantages of generality and flexibility and, most importantly, transforms the computation domain into a simple rectangular region with equal grid spacing.

In the numerical grid-generation technique, we seek a coordinate system for the numerical analysis of the flow in the domain  $D$  shown in Fig. 1. This domain is bounded by an arbitrary hull surface  $S$ , the ship centerplane  $C$ , the free surface or water plane  $W$ , the upstream and downstream sections  $A$  and  $B$ , respectively, and the surface  $\Sigma$  in the external flow. Section  $A$  may be located at a hull section where the boundary layer is thin, and  $B$  may be placed at a section in the far wake. The basic idea of a boundary-conforming curvilinear system is to find a transformation such that the curvilinear boundary surfaces of the physical domain  $D$  in cylindrical or in any other basic orthogonal coordinate system, say  $(x^1, x^2, x^3)$ , are transformed into boundaries of a simple rectangular domain in the computational space  $(\xi, \eta, \zeta)$  shown in Fig. 2.

With the values of the curvilinear coordinates specified on the boundaries of  $D$ , it then remains to generate the values of these coordinates in the interior of  $D$ . This is a boundary-value problem in the physical field with the curvilinear coordinates  $(\xi, \eta, \zeta)$  as dependent variables, and the orthogonal coordinates  $(x^1, x^2, x^3)$  as the independent variables, with boundary conditions specified on the curved boundaries. Thus, a system of elliptic partial differential equations can be used to generate the coordinates since the field solu-

tion of such a system is determined entirely by the boundary conditions. However, the elliptic system must be chosen such that it precludes the occurrence of extrema in the interior of the domain and assures a one-to-one mapping between the physical and the transformed planes.

For the general three-dimensional but simply-connected domain of interest here, a set of Poisson equations of the form

$$\begin{aligned} \nabla^2 \xi &= f^1(\xi, \eta, \zeta) & \nabla^2 \eta &= f^2(\xi, \eta, \zeta) \\ \nabla^2 \zeta &= f^3(\xi, \eta, \zeta) \end{aligned} \quad (1)$$

may be taken as the basic coordinate generating system. Here  $\nabla^2$  is the Laplacian operator in orthogonal coordinates ( $x^1, x^2, x^3$ ). The nonhomogeneous source functions  $f^i$  may be assigned appropriate values to yield the desired concentration of coordinate surfaces. The choice of these functions for specific applications are discussed later. Equations (1) are subject to either Dirichlet or Neumann boundary conditions on the boundary surfaces, which are surfaces of constant  $\xi, \eta$  or  $\zeta$ .

Since it is desirable to perform all numerical computations in the transformed ( $\xi, \eta, \zeta$ ) plane with equal grid spacing, i.e.,  $\Delta \xi = \Delta \eta = \Delta \zeta = 1$ , equations (1) are cumbersome to use. It is more convenient to invert them and solve for the orthogonal coordinates. In other words, the dependent and independent variables are interchanged so that the orthogonal coordinates ( $x^1, x^2, x^3$ ) in the physical plane become the dependent variables, with the curvilinear coordinates ( $\xi, \eta, \zeta$ ) as the independent variables. The boundary-value problem in the transformed field then involves generating the values of the orthogonal coordinates  $x^i = x^i(\xi, \eta, \zeta)$  in the interior from the specified boundary values of  $x^i$  on the rectangular boundary surfaces of the transformed field. Since the boundaries in the transformed plane are all rectangular (constant  $\xi, \eta$ , or  $\zeta$  plane), these computations are carried out on a cubic grid regardless of the shape of the physical boundaries.

The inversion of equations (1) yields

$$\begin{aligned} \nabla^2 x^1 &= \frac{1}{h_1 h_2 h_3} \frac{\partial}{\partial \xi} \left( \frac{h_2 h_3}{h_1} \right) \\ \nabla^2 x^2 &= \frac{1}{h_1 h_2 h_3} \frac{\partial}{\partial \eta} \left( \frac{h_1 h_3}{h_2} \right) \\ \nabla^2 x^3 &= \frac{1}{h_1 h_2 h_3} \frac{\partial}{\partial \zeta} \left( \frac{h_1 h_2}{h_3} \right) \end{aligned} \quad (2)$$

where

$$\begin{aligned} \nabla^2 &= g^{11} \frac{\partial^2}{\partial \xi^2} + g^{22} \frac{\partial^2}{\partial \eta^2} + g^{33} \frac{\partial^2}{\partial \zeta^2} \\ &+ 2g^{12} \frac{\partial^2}{\partial \xi \partial \eta} + 2g^{13} \frac{\partial^2}{\partial \xi \partial \zeta} + 2g^{23} \frac{\partial^2}{\partial \eta \partial \zeta} \\ &+ f^1 \frac{\partial}{\partial \xi} + f^2 \frac{\partial}{\partial \eta} + f^3 \frac{\partial}{\partial \zeta} \end{aligned} \quad (3)$$

$h_i$  are the metric coefficients in the chosen orthogonal coordinates  $x^i$ , and  $g^{ij}$  is the conjugate metric tensor. For example, for the cylindrical polar coordinates ( $x, r, \theta$ ), the metrics  $h_i$  are (1, 1,  $r$ ), respectively, and  $g^{ij}$  is given by equations (12b,c).

Equations (2) can be solved numerically in the transformed domain ( $\xi, \eta, \zeta$ ) when proper boundary conditions are specified on all boundary surfaces. If  $f^1 = f^2 = f^3 = 0$ , the transformation is said to be homeomorphic. In general, however, non-zero values are assigned to these functions to exercise control over the grid distribution.

Two examples of the numerical grid are shown in Figs. 3 and 4. The former shows the coordinates for an axisymmetric body. In this case, the constant- $\xi$  stations are chosen to be the constant- $x$  planes (i.e., transverse sections). The first station,  $\xi = 1$ , is located at  $x = 0.6L$  while the last station,  $\xi = 60$ , is located in the far wake at  $x = 5.881L$ , where  $L$  is the body length and  $x$  is axial distance from the nose. In the radial direction, the outer boundary is placed at  $r = 0.4609L$  which corresponds to  $\eta = 23$  in the transformed domain. Under this arrangement, equations (2) reduce to

$$g^{11} r_{\xi\xi} + g^{22} r_{\eta\eta} + 2g^{12} r_{\xi\eta} + f^1 r_{\xi} + f^2 r_{\eta} = \frac{1}{r} \quad (4)$$

$$\text{with } f^1 = -g^{11} \frac{x_{\xi\xi}}{x_{\xi}} \quad (5)$$

for the radial coordinates  $r(\xi, \eta)$ . In order to obtain the desired grid concentration inside the boundary layer, the control function  $f^2$  is prescribed by

$$f^2(\xi, \eta) = \frac{1}{r r_{\eta}} + \begin{cases} F_A(\eta) & \xi < \xi_A \\ F_C(\xi, \eta) & \xi_A < \xi < \xi_B \\ F_B(\eta) & \xi > \xi_B \end{cases} \quad (6)$$

where  $\xi_A = 15$ ,  $\xi_B = 42$ ,  $F_A$  and  $F_B$  are determined by the node distributions at the initial and final stations as

$$\begin{aligned} F_A &= -g^{22} \frac{r_{\eta\eta}}{r_{\eta}} \bigg|_{\xi=1}, \\ F_B &= -g^{22} \frac{r_{\eta\eta}}{r_{\eta}} \bigg|_{\xi=60} \end{aligned}$$

and  $F_C$  is given by

$$F_C = [(\xi_B - \xi) F_A + (\xi - \xi_A) F_B] / (\xi_B - \xi_A)$$

Equation (4) was approximated by finite-difference equations using a central-difference scheme. With the Dirichlet boundary conditions specified at the initial and final stations, the resulting system of algebraic equations was solved by an SOR

algorithm with an over-relaxation factor of 1.8. As seen from Fig. 3, the boundary-fitted coordinates thus obtained evolve smoothly from the body into the wake, and give the desired grid expansion in the thick boundary layer region.

Figure 4 shows the coordinate system for the three-dimensional 3:1 elliptic body of Huang et al. (1983). In this example, the outer boundary is a cylindrical surface of radius  $r = 0.8137L$  which corresponds to  $\eta = 19$  in the transformed plane. For simplicity, the constant- $\xi$  stations are again chosen to be the constant- $x$  planes, with the initial ( $\xi = 1$ ) and final ( $\xi = 66$ ) stations located at  $x = 0.5L$  and  $x = 5.27L$ , respectively. In the circumferential direction, 7 stations are used, with  $\zeta = 2$  and 6 corresponding to  $\theta = 0^\circ$  and  $90^\circ$ , respectively. Under this arrangement, equations (2) become

$$g^{11}r_{\xi\xi} + g^{22}r_{\eta\eta} + g^{33}r_{\zeta\zeta} + 2g^{12}r_{\xi\eta} + 2g^{13}r_{\xi\zeta} + 2g^{23}r_{\eta\zeta} + f^1 r_\xi + f^2 r_\eta + f^3 r_\zeta = \frac{1}{r} \quad (7a)$$

$$g^{11}\theta_{\xi\xi} + g^{22}\theta_{\eta\eta} + g^{33}\theta_{\zeta\zeta} + 2g^{12}\theta_{\xi\eta} + 2g^{13}\theta_{\xi\zeta} + 2g^{23}\theta_{\eta\zeta} + f^1 \theta_\xi + f^2 \theta_\eta + f^3 \theta_\zeta = 0 \quad (7b)$$

The control functions  $f^1$  and  $f^2$  defined in equations (5) and (6) are again employed here, while  $f^3(\zeta)$  is determined by the grid distribution on the outer boundary by

$$f^3 = -g^{33} \frac{\theta_{\zeta\zeta}}{\theta_\zeta} \bigg|_{\eta=19} \quad (8)$$

In order to facilitate the use of wall functions in the turbulence model, Neumann boundary conditions are specified on all boundaries; i.e.,  $\eta = 1, 19$ ;  $\zeta = 2, 6$ ; of the constant- $\xi$  stations to ensure local orthogonality of these coordinates. Equations (7), are then solved by a finite-difference method. Because the central-difference scheme used in the previous example indicated a lack of convergence for large  $f^1$ ,  $f^2$  and/or  $f^3$ , an exponential scheme, based on the one-dimensional analytic solution (see Spalding, 1972, for example) was employed here to formulate the discretization equations. The resulting system of algebraic equations was then solved by the tridiagonal matrix algorithm with an over-relaxation factor of 1.4. The boundary-fitted coordinates thus obtained are nearly orthogonal at each cross-section, and also provide a desired expansion in the thick boundary layer. Fig. 4 shows several views of the coordinates in the stern region.

## 2.2 Governing Equations

Since most of the applications presented in this paper are associated with external flows past axisymmetric and three-dimensional bodies, such as ship forms, it is convenient to choose cylindrical polar coordinates as the basic coordinate system in the physical domain. Formulations starting with other basic coordinate systems can be derived in a similar manner. Limitations of space do not allow us to write out all the equations in full. Consequently, we shall highlight only the overall features.

The exact Reynolds-averaged equations of continuity and momentum are first written in cylindrical coordinates  $(x, r, \theta)$  shown in Fig. 1. The six Reynolds stresses appearing in the momentum equations are related to the corresponding mean rates of strain through an isotropic eddy viscosity  $\nu_t$  which, in turn, is related to the turbulent kinetic energy  $k$  and its rate of dissipation  $\epsilon$  by

$$\nu_t = C_\mu \frac{k^2}{\epsilon} \quad (9)$$

where  $C_\mu$  is a constant and  $k$  and  $\epsilon$  are obtained from two model equations.

Although it is possible to transform the independent variables as well as the dependent variables in these equations from the  $(x, r, \theta)$  coordinates to the  $(\xi, \eta, \zeta)$  coordinates of the previous section, we consider only the transformation of the independent space variables leaving the velocity components  $(U, V, W)$  in the original  $(x, r, \theta)$  coordinates. This approach is similar to that used by some previous investigators and results in some simplifications in the equations without loss of generality. If such a transformation is made, and all quantities are made dimensionless by the characteristic velocity and length scales  $U_0$  and  $L$ , respectively, where  $U_0$  is the stream (or body) velocity and  $L$  is the length of the body, the equation of continuity becomes

$$(b_1^1 U + b_2^1 V + b_3^1 W)_\xi + (b_1^2 U + b_2^2 V + b_3^2 W)_\eta + (b_1^3 U + b_2^3 V + b_3^3 W)_\zeta = 0 \quad (10)$$

and the five transport equations for  $\phi \equiv U, V, W, k, \epsilon$  can be written in the compact form

$$g^{11}\phi_{\xi\xi} + g^{22}\phi_{\eta\eta} + g^{33}\phi_{\zeta\zeta} = 2A_\phi\phi_\zeta + 2B_\phi\phi_\eta + D_\phi\phi_\xi + E_\phi\phi_t + S_\phi \quad (11)$$

where the subscripts  $\xi, \eta$  and  $\zeta$  denote derivatives along those coordinates.

All quantities appearing in equations (10) and (11) are defined in the following set of equations:

$$b_{ij}^j = \frac{r(r_{\xi}\theta_{\xi} - r_{\xi}\theta_{\eta})}{r(r_{\xi}\theta_{\xi} - r_{\xi}\theta_{\eta})} \frac{r(x_{\xi}\theta_{\eta} - x_{\eta}\theta_{\xi})}{r(x_{\xi}\theta_{\eta} - x_{\eta}\theta_{\xi})} \frac{x_{\eta}r_{\xi} - x_{\xi}r_{\eta}}{x_{\eta}r_{\xi} - x_{\xi}r_{\eta}}$$

$$b_{ij}^j = \frac{r(r_{\xi}\theta_{\xi} - r_{\xi}\theta_{\eta})}{r(r_{\xi}\theta_{\xi} - r_{\xi}\theta_{\eta})} \frac{r(x_{\xi}\theta_{\eta} - x_{\eta}\theta_{\xi})}{r(x_{\xi}\theta_{\eta} - x_{\eta}\theta_{\xi})} \frac{x_{\xi}r_{\eta} - x_{\eta}r_{\xi}}{x_{\xi}r_{\eta} - x_{\eta}r_{\xi}}$$

$$r(r_{\xi}\theta_{\eta} - r_{\eta}\theta_{\xi}) \quad r(x_{\eta}\theta_{\xi} - x_{\xi}\theta_{\eta}) \quad x_{\xi}r_{\eta} - x_{\eta}r_{\xi}$$

$$(12a)$$

$$gg^{11} = g_{22} g_{33} - g_{23}^2$$

$$gg^{22} = g_{11} g_{33} - g_{13}^2$$

$$gg^{33} = g_{11} g_{22} - g_{12}^2$$

$$gg^{12} = gg^{21} = g_{13} g_{23} - g_{12} g_{33} \quad (12b)$$

$$gg^{13} = gg^{31} = g_{12} g_{23} - g_{13} g_{22}$$

$$gg^{23} = gg^{32} = g_{12} g_{13} - g_{23} g_{11}$$

$$g_{11} = x_{\xi}^2 + r_{\xi}^2 + r_{\theta_{\xi}}^2$$

$$g_{22} = x_{\eta}^2 + r_{\eta}^2 + r_{\theta_{\eta}}^2$$

$$g_{33} = x_{\zeta}^2 + r_{\zeta}^2 + r_{\theta_{\zeta}}^2 \quad (12c)$$

$$g_{12} = g_{21} = x_{\xi} x_{\eta} + r_{\xi} r_{\eta} + r_{\theta_{\xi}} r_{\theta_{\eta}}$$

$$g_{13} = g_{31} = x_{\xi} x_{\zeta} + r_{\xi} r_{\zeta} + r_{\theta_{\xi}} r_{\theta_{\zeta}}$$

$$g_{23} = g_{32} = x_{\eta} x_{\zeta} + r_{\eta} r_{\zeta} + r_{\theta_{\eta}} r_{\theta_{\zeta}}$$

$$J = \sqrt{g} = \begin{vmatrix} x_{\xi} & x_{\eta} & x_{\zeta} \\ r_{\xi} & r_{\eta} & r_{\zeta} \\ r_{\theta_{\xi}} & r_{\theta_{\eta}} & r_{\theta_{\zeta}} \end{vmatrix} \quad (12d)$$

$$2A_{\phi} = \frac{R_{eff}}{J} (b_{1\alpha}^3 + b_{2\alpha}^2 + b_{3\alpha}^3) - f^3$$

$$2B_{\phi} = \frac{R_{eff}}{J} (b_{1\alpha}^2 + b_{2\alpha}^2 + b_{3\alpha}^3) - f^2$$

$$D_{\phi} = \frac{R_{eff}}{J} (b_{1\alpha}^1 + b_{2\alpha}^2 + b_{3\alpha}^3) - f^1 \quad (13a)$$

$$E_{\phi} = a_{\phi} R_{eff}$$

$$S_{\phi} = s_{\phi} - 2(g^{12}_{\phi\xi\eta} + g^{13}_{\phi\xi\zeta} + g^{23}_{\phi\eta\zeta})$$

$$\alpha_{\phi}^1 = a_{\phi} U - \frac{b_{\phi}}{J} (b_1^1 v_{t,\xi} + b_1^2 v_{t,\eta} + b_1^3 v_{t,\zeta})$$

$$\alpha_{\phi}^2 = a_{\phi} V - \frac{c_{\phi}}{J} (b_2^1 v_{t,\xi} + b_2^2 v_{t,\eta} + b_2^3 v_{t,\zeta})$$

$$\alpha_{\phi}^3 = a_{\phi} W - \frac{d_{\phi}}{J} (b_3^1 v_{t,\xi} + b_3^2 v_{t,\eta} + b_3^3 v_{t,\zeta}) \quad (13b)$$

$$a_U = 1, \quad b_U = 2, \quad c_U = 1, \quad d_U = 1$$

$$a_V = 1, \quad b_V = 1, \quad c_V = 2, \quad d_V = 1$$

$$a_W = 1, \quad b_W = 1, \quad c_W = 1, \quad d_W = 2 \quad (13c)$$

$$a_k = \sigma_k, \quad b_k = 1, \quad c_k = 1, \quad d_k = 1$$

$$a_{\epsilon} = \sigma_{\epsilon}, \quad b_{\epsilon} = 1, \quad c_{\epsilon} = 1, \quad d_{\epsilon} = 1$$

$$s_U = R_{eff} \left[ \frac{1}{J} (b_1^1 p_{\xi} + b_1^2 p_{\eta} + b_1^3 p_{\zeta}) \right.$$

$$+ \frac{2}{3J} (b_1^1 k_{\xi} + b_1^2 k_{\eta} + b_1^3 k_{\zeta})$$

$$- \frac{1}{J^2} (b_2^1 v_{t,\xi} + b_2^2 v_{t,\eta} + b_2^3 v_{t,\zeta})$$

$$(b_1^1 v_{\xi} + b_1^2 v_{\eta} + b_1^3 v_{\zeta})$$

$$- \frac{1}{J^2} (b_3^1 v_{t,\xi} + b_3^2 v_{t,\eta} + b_3^3 v_{t,\zeta})$$

$$(b_1^1 w_{\xi} + b_1^2 w_{\eta} + b_1^3 w_{\zeta}) \left. \right] \quad (13d)$$

$$s_V = R_{eff} \left\{ -\frac{W^2}{r} + \frac{1}{J} (b_2^1 p_{\xi} + b_2^2 p_{\eta} + b_2^3 p_{\zeta}) \right.$$

$$+ \frac{2}{3J} (b_2^1 k_{\xi} + b_2^2 k_{\eta} + b_2^3 k_{\zeta})$$

$$- \frac{1}{J^2} (b_1^1 v_{t,\xi} + b_1^2 v_{t,\eta} + b_1^3 v_{t,\zeta})$$

$$(b_2^1 u_{\xi} + b_2^2 u_{\eta} + b_2^3 u_{\zeta})$$

$$- \frac{1}{J} (b_3^1 v_{t,\xi} + b_3^2 v_{t,\eta} + b_3^3 v_{t,\zeta})$$

$$\left[ \frac{1}{J} (b_2^1 w_{\xi} + b_2^2 w_{\eta} + b_2^3 w_{\zeta}) - \frac{W}{r} \right] \left. \right\}$$

$$+ \frac{2}{rJ} (b_3^1 w_{\xi} + b_3^2 w_{\eta} + b_3^3 w_{\zeta}) + \frac{V}{r^2} \quad (13e)$$

$$s_W = R_{eff} \left\{ \frac{WV}{r} + \frac{1}{J} (b_3^1 p_{\xi} + b_3^2 p_{\eta} + b_3^3 p_{\zeta}) \right.$$

$$+ \frac{2}{3J} (b_3^1 k_{\xi} + b_3^2 k_{\eta} + b_3^3 k_{\zeta})$$

$$- \frac{1}{J^2} (b_1^1 v_{t,\xi} + b_1^2 v_{t,\eta} + b_1^3 v_{t,\zeta})$$

$$(b_3^1 u_{\xi} + b_3^2 u_{\eta} + b_3^3 u_{\zeta})$$

$$- \frac{1}{J} (b_2^1 v_{t,\xi} + b_2^2 v_{t,\eta} + b_2^3 v_{t,\zeta})$$

$$\left[ \frac{1}{J} (b_3^1 v_{\xi} + b_3^2 v_{\eta} + b_3^3 v_{\zeta}) - \frac{W}{r} \right]$$

$$- \frac{2V}{rJ} (b_3^1 v_{t,\xi} + b_3^2 v_{t,\eta} + b_3^3 v_{t,\zeta}) \left. \right\}$$

$$- \frac{2}{rJ} (b_3^1 v_\xi + b_3^2 v_\eta + b_3^3 v_\zeta) + \frac{W}{r^2} \quad (13f)$$

$$s_k = -\sigma_k R_{eff}(G - \epsilon) \quad (13g)$$

$$s_\epsilon = -\sigma_\epsilon R_{eff} \left( C_{\epsilon 1} \frac{\epsilon}{k} G - C_{\epsilon 2} \frac{\epsilon^2}{k} \right) \quad (13h)$$

$$\begin{aligned} G = v_t \{ & \frac{2}{J^2} (b_1^1 u_\xi + b_1^2 u_\eta + b_1^3 u_\zeta)^2 \\ & + \frac{2}{J^2} (b_2^1 v_\xi + b_2^2 v_\eta + b_2^3 v_\zeta)^2 \\ & + 2 \left[ \frac{1}{J} (b_3^1 w_\xi + b_3^2 w_\eta + b_3^3 w_\zeta) + \frac{V}{r} \right]^2 \\ & + \frac{1}{J^2} (b_1^1 v_\xi + b_1^2 v_\eta + b_1^3 v_\zeta + b_2^1 u_\xi + b_2^2 u_\eta + b_2^3 u_\zeta)^2 \\ & + \frac{1}{J^2} (b_1^1 w_\xi + b_1^2 w_\eta + b_1^3 w_\zeta + b_3^1 u_\xi + b_3^2 u_\eta + b_3^3 u_\zeta)^2 \\ & + \left[ \frac{1}{J} (b_2^1 w_\xi + b_2^2 w_\eta + b_2^3 w_\zeta + b_3^1 v_\xi + b_3^2 v_\eta + b_3^3 v_\zeta) \right. \\ & \left. - \frac{W}{r} \right]^2 \} \quad (13i) \end{aligned}$$

All quantities in equations (12) involve only coordinate geometry and can be obtained from the solutions of equations (2). In equations (13),  $p$  is pressure;  $C = 0.09$ ,  $C_{\epsilon 1} = 1.44$ ,  $C_{\epsilon 2} = 1.92$ ,  $\sigma_k = 1.0$ , and  $\sigma_\epsilon = 1.3$  are the standard constants in the turbulence-model equations; and  $R_{eff} = (v + v_t)^{-1}$ , where  $v$  is the molecular viscosity and  $v_t$  the eddy viscosity.

Equations (10) and (11) are still the exact equations insofar as no approximations have been made beyond those inherent in the turbulence model. Formally, equation (11) can be rendered partially parabolic by neglecting the first term which involves the second derivative with respect to  $\xi$ . Physically this is not the same as neglecting  $\phi_{xx}$  nor does it imply that diffusion in either  $x$  or  $\xi$  direction is neglected. In fact, if all diffusive terms in these directions are to be dropped, the equations become much more complicated, especially in the curvilinear nonorthogonal coordinates adopted here. Be that as it may, we shall neglect  $\phi_{\xi\xi}$  in equation (11) and solve the resulting equation, together with the equation of continuity (10), as the partially-parabolic system. This approach has the advantages that the subsequent numerical procedures can be readily extended to solve the fully-elliptic equations or to take into account the neglected terms in an approximate manner. This then offers the opportunity to study the limitations of the partially-parabolic approximations.

### 2.3 Solution Domain and Boundary Conditions

The solution domain for a typical ship stern is shown in Figs. 1 and 2. The up-

stream boundary A is placed at a section where the boundary layer is thin so that the mean velocity components ( $U$ ,  $V$ ,  $W$ ) and the turbulence parameters ( $k$ ,  $\epsilon$ ) can be prescribed readily from a boundary-layer calculation. The location of the downstream boundary B should be "far enough" from the body such that the local flow is parabolic, i.e. no influence propagates upstream from there. The coordinates and the numerical scheme used here enable this boundary to be placed several body-lengths downstream of the stern.

The extent of the solution domain normal to the body can be taken to be of the order of the thickness of the viscous flow but in such a case it would be necessary to perform iterative solutions to account for the influence of the viscous flow on the outer potential flow. In the present approach, such iterations are avoided altogether by placing the external boundary  $\Sigma$  of the solution domain at a sufficiently large distance from the body so that uniform-flow conditions can be imposed. The distance required to capture the zone of viscous-inviscid interaction in this manner depends upon the body geometry.

In the girthwise direction, the solution is bounded by the free surface  $W$  and the ship centerplane  $C$ . Plane-of-symmetry boundary conditions are imposed on these surfaces. The present formulation is therefore restricted to double models. All examples presented in this paper are of this type.

Since the turbulence model employed here does not extend into the sublayer and the transition layer on the hull, the hull boundary conditions are prescribed by a set of "wall functions". At least two of the grid points close to the wall are located in the fully-turbulent layer, and it is assumed that the resultant velocity at these points satisfies the law of the wall (corrected for pressure gradients) and the velocity vector in this region is collateral. The shear velocity  $U_\tau$  is determined iteratively from the velocity at these points and this is used to provide the boundary values of  $k$  and  $\epsilon$  at the first mesh point through the assumption of local equilibrium between turbulent energy production and dissipation.

The boundary conditions which are applied on the various surfaces of the solution domain are summarized below.

Initial condition:  $p = 0$  everywhere

Upstream, A:  $U$ ,  $V$ ,  $W$ ,  $k$ ,  $\epsilon$  prescribed

Downstream, B:  $p_\xi = 0$

External,  $\Sigma$ :  $p=0$ ,  $U=1$ ,  $W = k_\eta = \epsilon_\eta = 0$

Planes of Symmetry,  $C$ ,  $W$ :  $W = 0$ ,  $U_\xi = V_\xi = k_\xi = \epsilon_\xi = 0$

Hull surface  $S$ : wall functions via  $U_\tau$

### 2.4 Numerical Scheme

The partially-parabolic form of the

convective-diffusion equations (11), namely

$$g_{\phi_{nn}}^{22} + g_{\phi_{\zeta\zeta}}^{33} = 2A_{\phi}\phi_{\zeta} + 2B_{\phi}\phi_{\eta} + D_{\phi}\phi_{\zeta} + E_{\phi}\phi_{\eta} + S_{\phi} \quad (14)$$

are solved using the finite-analytic numerical scheme of Chen & Chen (1982, 1984), assuming that the pressure field is known, and the equation of continuity (10) is used to update the pressure field. These procedures are outlined in the following.

In the finite-analytic approach, equations (14) in each rectangular numerical element,  $\Delta\xi = \Delta\eta = \Delta\zeta = 1$ , are locally linearized as

$$g_{\phi_{nn}}^{22} + g_{\phi_{\zeta\zeta}}^{33} = 2(A_{\phi})_p\phi_{\zeta} + 2(B_{\phi})_p\phi_{\eta} + g \quad (15)$$

with

$$g = (D_{\phi})_p(\phi_p - \phi_U) + \frac{(E_{\phi})_p}{\tau}(\phi_p - \phi_p^{n-1}) + (S_{\phi})_p$$

where the subscript  $p$  denotes the center node of the element shown in Fig. 5(a) and  $\tau$  is the time increment. Both the time and  $\xi$ -derivatives are approximated by backward-difference formulae, subscript  $U$  denoting the upstream nodal value, and superscript  $(n-1)$  denoting the nodal value at the previous time step. If we introduce the coordinate-stretching functions

$$\eta^* = \frac{\eta}{\sqrt{g_p^{22}}}, \quad \zeta^* = \frac{\zeta}{\sqrt{g_p^{33}}} \quad (16)$$

equations (15) reduce to the standard two-dimensional convective-transport equations described in Chen & Chen, i.e.,

$$\phi_{\zeta^*\zeta^*} + \phi_{\eta^*\eta^*} = 2A_{\phi}\phi_{\zeta^*} + 2B_{\phi}\phi_{\eta^*} + g \quad (17)$$

with

$$A = \frac{(A_{\phi})_p}{\sqrt{g_p^{33}}}, \quad B = \frac{(B_{\phi})_p}{\sqrt{g_p^{22}}}$$

for a local element with dimensions

$$\Delta\xi = 1$$

$$\Delta\eta^* = k = \frac{1}{\sqrt{g_p^{22}}}$$

$$\Delta\zeta^* = h = \frac{1}{\sqrt{g_p^{33}}}$$

With the boundary conditions properly specified, equation (17) can be solved analytically by the method of separation of variables for each local element. A nine-point finite-analytic algebraic equation is then obtained by evaluating the analytic solution at the center node  $p$  of the local element:

$$\phi_p = C_{NE}\phi_{NE} + C_{NW}\phi_{NW} + C_{SE}\phi_{SE} + C_{SW}\phi_{SW} + C_{EC}\phi_{EC} + C_{WC}\phi_{WC} + C_{NC}\phi_{NC} + C_{SC}\phi_{SC} - C_pg \quad (18)$$

where

$$C_{SC} = \left( \frac{e^{Bk}}{2 \cosh Bk} \right) P_A$$

$$C_{NC} = e^{-2Bk} C_{SC}$$

$$C_{WC} = \left( \frac{e^{Ah}}{2 \cosh Ah} \right) P_B$$

$$C_{EC} = e^{-2Ah} C_{WC}$$

$$C_{SW} = \left( \frac{e^{Ah+Bk}}{4 \cosh Ah \cosh Bk} \right) (1-P_A-P_B)$$

$$C_{SE} = e^{-2Ah} C_{SW}$$

$$C_{NW} = e^{-2Bk} C_{SW}$$

$$C_{NE} = e^{-2Ah-2Bk} C_{SW}$$

$$C_p = \frac{h \tanh Ah}{2A} (1-P_A) = \frac{k \tanh Bk}{2B} (1-P_B)$$

$$P_A = 4E_2 Ah \cosh Ah \cosh Bk \coth Ah$$

$$P_B = 1 + \frac{Bh \coth Bk}{Ak \coth Ah} (P_A - 1)$$

$$E_2 = \sum_{m=1}^{\infty} \frac{-(-1)^m (\lambda_m h)}{[(Ah)^2 + (\lambda_m h)^2]^2 \cosh \sqrt{A^2 + B^2 + \lambda_m^2} k}$$

$$\lambda_m h = \left(m - \frac{1}{2}\right) \pi$$

The above coefficients are simple rearrangements of those given in Chen & Chen, but are more convenient for efficient numerical calculations. Note that

$$C_{NC} + C_{SC} = P_A$$

$$C_{EC} + C_{WC} = P_B$$

$$C_{NE} + C_{NW} + C_{SE} + C_{SW} = 1 - P_A - P_B$$

Since both  $P_A$  and  $P_B$  are positive and  $(P_A + P_B) < 1$ , the finite-analytic coefficients are always positive. Also, the exponents in these coefficients provide a gradual upwind bias as the cell Reynolds numbers  $|2Ah|$  and/or  $|2Bk|$  increase. Thus the behavior of the convective-diffusion equation is properly captured and false numerical diffusion is minimized due to the inclusion of all corner points. For large cell Reynolds numbers, the series summation in  $E_2$  can be avoided by considering the asymptotic expressions of  $P_A$

and  $P_B$  based on the theory of characteristics, i.e.,

$$\begin{aligned} |Ak| > |Bh| : P_A = 0, \quad P_B = 1 - |Bh/Ak| \\ |Ak| < |Bh| : P_B = 0, \quad P_A = 1 - |Ak/Bh| \end{aligned}$$

Since the downstream influence is negligible at large cell Reynolds numbers, no appreciable changes are observed due to the above approximations, but the computing time is greatly reduced.

By substituting the nonhomogenous term  $g$  in equation (17) into equations (18), an eleven-point finite-analytic formula for unsteady, three-dimensional partially-parabolic equations can be obtained:

$$\begin{aligned} \phi_p = \frac{1}{1 + C_p[(D_\phi)_p + \frac{(E_\phi)_p}{\tau}]} \{ C_{NE} \phi_{NE} + C_{NW} \phi_{NW} \\ + C_{SE} \phi_{SE} + C_{SW} \phi_{SW} + C_{EC} \phi_{EC} + C_{WC} \phi_{WC} + C_{NC} \phi_{NC} \\ + C_{SC} \phi_{SC} + (D_\phi)_p C_p \phi_U + \frac{(E_\phi)_p}{\tau} C_p \phi_p^{n-1} - C_p (S_\phi)_p \} \end{aligned} \quad (19)$$

It is seen that  $\phi_p$  depends upon all the eight neighboring nodal values in the cross-sectional ( $\eta\zeta$ ) plane as well as the values at the upstream node  $U$  and the value at the previous time step ( $n-1$ ). Since the finite-analytic coefficients are all positive, the elliptic nature of the flow at each cross-section is represented accurately. Note that  $\phi_p$  is not directly dependent upon the downstream nodal value  $\phi_D$ . This parabolic feature enables us to employ a marching procedure along the  $\xi$ -direction as well as in time. However, the flow is not truly parabolic in the  $\xi$ -direction since the pressure gradient  $P_\xi$ , which appears in the source functions, introduces the downstream influence of the elliptic pressure field. Due to this indirect pressure transmission, several sweeps in  $\xi$ -direction are needed to obtain a fully-converged pressure and velocity field.

If the pressure is known a priori, equations (19) can be employed directly to solve the partially-parabolic convective-diffusion equations (14) for  $U$ ,  $V$ ,  $W$ ,  $k$  and  $\epsilon$ . However, in most practical applications the pressure field is not known and must be determined indirectly through the equation of continuity. The SIMPLER algorithm of Patankar (1980) has been modified and extended to update the pressure field.

In the present algorithm, the pressure field is obtained directly through the definition of pseudovelocities ( $\hat{U}$ ,  $\hat{V}$ ,  $\hat{W}$ ):

$$\begin{aligned} \hat{U}_d &= \hat{U}_d - d_d (P_D - P_p) \\ \hat{V}_n &= \hat{V}_n - d_n (P_{NC} - P_p) \\ \hat{W}_e &= \hat{W}_e - d_e (P_{EC} - P_p) \end{aligned} \quad (20)$$

where

$$\begin{aligned} d_d &= \frac{(R_{eff} b_1^1)_d C_d}{J_d [1 + C_d (D_U + \frac{E_U}{\tau})_d]} \\ d_n &= \frac{(R_{eff} b_2^2)_n C_n}{J_n [1 + C_n (D_V + \frac{E_V}{\tau})_n]} \\ d_e &= \frac{(R_{eff} b_3^3)_e C_e}{J_e [1 + C_e (D_W + \frac{E_W}{\tau})_e]} \end{aligned}$$

and  $C_d$ ,  $C_n$  and  $C_e$  are the finite-analytic coefficients  $C_p$  evaluated at the staggered velocity nodes  $d$ ,  $n$  and  $e$  shown in Fig. 5(b). Note that the pseudovelocities defined here still contain part of the pressure gradient terms if the coordinate system is nonorthogonal in the physical plane. If we require the velocity field to satisfy the discretized equation of continuity of the form of

$$\begin{aligned} (b_1^1 U + b_2^1 V + b_3^1 W)_d - (b_1^1 U + b_2^1 V + b_3^1 W)_u \\ + (b_1^2 U + b_2^2 V + b_3^2 W)_n \\ - (b_1^2 U + b_2^2 V + b_3^2 W)_s \\ + (b_1^3 U + b_2^3 V + b_3^3 W)_e \\ - (b_1^3 U + b_2^3 V + b_3^3 W)_w = 0 \end{aligned} \quad (21)$$

an equation for pressure can be derived in terms of the pseudovelocities. Note that 18 velocity components are involved for each small control volume. However, due to the staggered grid system employed here, only six of these, i.e.  $U_d, U_u, V_n, V_s, W_e$ , and  $W_w$ , can be obtained directly from the governing equations (14). It is therefore necessary to approximate the remaining twelve by interpolation. A linear interpolation is used to obtain these from the values known at the previous iteration, so that the continuity equation becomes:

$$\begin{aligned} (b_1^1 U)_d - (b_1^1 U)_u + (b_2^2 V)_n - (b_2^2 V)_s \\ + (b_3^3 W)_e - (b_3^3 W)_w + D_1 = 0 \end{aligned} \quad (22)$$

where

$$\begin{aligned} D_1 &= (b_2^1 V + b_3^1 W)_d - (b_2^1 V + b_3^1 W)_u \\ &+ (b_1^2 U + b_3^2 W)_n - (b_1^2 U + b_3^2 W)_s \end{aligned}$$

$$+ (b_1^3 u + b_2^3 v)_e - (b_1^3 u + b_2^3 v)_w$$

is the mass source obtained from the velocity field at the previous time step or sweep. If we require the velocity field to satisfy equation (22), an equation for pressure can be derived:

$$a_p p_p = a_d p_D + a_u p_U + a_n p_{NC} + a_s p_{SC} + a_e p_{EC} + a_w p_{WC} - \hat{D} \quad (23)$$

where

$$a_d = (b_1^1)_d d_d, \quad a_u = (b_1^1)_u d_u, \quad a_n = (b_2^2)_n d_n$$

$$a_s = (b_2^2)_s d_s, \quad a_e = (b_3^3)_e d_e, \quad a_w = (b_3^3)_w d_w$$

$$a_p = a_d + a_u + a_e + a_w + a_n + a_s$$

$$\hat{D} = (b_1^1 \hat{U})_d - (b_1^1 \hat{U})_u + (b_2^2 \hat{V})_n$$

$$- (b_2^2 \hat{V})_s + (b_3^3 \hat{W})_e - (b_3^3 \hat{W})_w - D_1 \quad (23a)$$

It should be noted that no additional approximations are made in obtaining this equation and, therefore, if a correct velocity field is employed as the initial guess, it would at once give the correct pressure field. In this fashion, the pressure can be obtained directly from an estimated velocity field, and the slow convergence usually encountered in the SIMPLE algorithm is avoided.

Although the guessed pressure field can be updated directly by equation (23), in practical applications the new pressure field may produce a velocity field which violates the equation of continuity. In order to improve this imperfect velocity field, a pressure-correction equation similar to that used in the SIMPLE algorithm is derived

$$a_p p_p' = a_d p_D' + a_u p_U' + a_n p_{NC}' + a_s p_{SC}' + a_e p_{EC}' + a_w p_{WC}' - D^* \quad (24)$$

with

$$D^* = (b_1^1 U^*)_d - (b_1^1 U^*)_u + (b_2^2 V^*)_n - (b_2^2 V^*)_s + (b_3^3 W^*)_e - (b_3^3 W^*)_w - D_1$$

where  $(U^*, V^*, W^*)$  is the imperfect velocity field obtained from the imperfect pressure field  $p^*$ , and  $p' \equiv p - p^*$  is the pressure correction. The improved velocity field based on this pressure correction is then given by

$$U_d = U_d^* - d_d (p_D' - p_p') \\ V_u = V_u^* - d_u (p_{NC}' - p_p') \quad (25)$$

$$W_e = W_e^* - d_e (p_{EC}' - p_p')$$

where the coefficients  $a_p, a_d, d_d$  etc. are as defined in equations (20) and (23). The overall numerical solution procedure for the case of a steady flow may be summarized as follows:

- 1) Construct the coordinate system for the given body and calculate the geometric coefficients  $b_{ij}^1, g_{ij}^1, g_{ij}^2, J$ , etc. from equations (12).
- 2) Specify the velocity and turbulence profiles at the first station  $\xi = 1$ ; set  $p = 0$  everywhere.
- 3) Calculate the finite-analytic coefficients for pressure, pressure-correction and momentum equations at downstream station.
- 4) Calculate the pseudovelocities  $(\hat{U}, \hat{V}, \hat{W})$  in terms of velocity field at  $(n-1)^{th}$  time step.
- 5) Calculate  $\hat{D}$  from equation (23a) and solve the pressure equation (23) by tridiagonal matrix algorithm. Treat this pressure field as  $p^*$ .
- 6) Solve the momentum equations based on the updated pressure field to obtain the starred velocity field  $(U^*, V^*, W^*)$ . The resulting system of algebraic equations is solved by a tridiagonal matrix algorithm.
- 7) Calculate the mass source  $D^*$ , and solve the pressure-correction equation (24) by tridiagonal matrix algorithm.
- 8) Correct the velocity field using the velocity correction formulae (25), but do not correct the pressure field.
- 9) March to downstream station and repeat steps (3) to (8).
- 10) After reaching the last downstream station, return to step (2) and repeat steps (2) to (9) for several sweeps until both the pressure and the velocity field have converged within a specified tolerance.

### 3. EXAMPLE SOLUTIONS

The method described above has been used to calculate a variety of two-dimensional, axisymmetric and three-dimensional flows and many calculations are still in progress. Here, we shall present a few examples which illustrate the capabilities of the method and indicate areas which require further study.

#### 3.1 The Wake of a Flat Plate

This is by far the simplest example of flows which involve the evolution of a wake from a boundary layer because the viscous-inviscid interaction at the trailing edge is weak, the flow is two dimensional and the equations can be solved in Cartesian coordinates. Nevertheless, it provides a useful test of the numerical method and the turbulence model.

The calculations presented below correspond to the experiments of Ramaprian, Patel and Sastry (1982). If  $x, y$  are coordinates measured along and normal to the plate,  $x = 0$  being the trailing edge,  $L$  is the length of the plate and  $U_0$  is the free-stream velocity, the calculations correspond



to a Reynolds number,  $U_0 L/\nu = 1.6 \times 10^6$ , and the solution domain was chosen as  $-0.4 < x/L < 1.0$ ,  $0 < y/L < 0.05467$ . A nonuniform grid, with 46 points in the  $x$  direction and 10 points in the  $y$  direction was used. Standard flat-plate boundary-layer profiles were specified at the upstream station.

The principal results of the calculations are shown in Figs. 6, 7 and 8. The level of agreement between the calculations and experiments with respect to the mean velocity profiles (Fig. 6) and the increase of the wake centerline velocity (Fig. 7) is comparable with that achieved by Patel and Scheuerer (1982) who solved the boundary-layer equations using the same turbulence model but a different numerical method. Computationally, the two methods differ in the number of grid points required to resolve the large gradients in the near wake. The solutions of Patel and Scheuerer were obtained with 60 points across the wake and some 800 streamwise steps in the region  $0 < x < 610$  mm whereas the present solutions, as noted above, employed  $46 \times 10$  grid nodes over the entire domain. This difference is attributed largely to the use of the finite-analytic scheme in the present method. Physically, the two methods are also different. The use of boundary-layer equations neglects the viscous-inviscid interaction at the trailing edge while the partially-parabolic equations take it into account. Fig. 8 shows that the latter predict a small increase in the wall shear stress on the plate just ahead of the trailing edge and associated with this is a small but sharp reduction in pressure. The pressure recovers rather quickly to near-zero values in the near wake. In fact, the wall shear-stress and pressure variations shown in Fig. 7 are qualitatively similar to those obtained for laminar flow by the present method and by Davis and Werle (1981) and Rubin and Reddy (1983) using other numerical methods.

At large distances from the trailing edge the present calculations agree with those of Patel and Scheuerer with respect to the asymptotic behavior. However, as discussed there, and in Kamaprian, Patel and Sastry (1982), the  $k$ - $\epsilon$  model fails to predict the growth and decay constants for far wakes.

### 3.2 Flow Over the Tail of an Axisymmetric Body

Calculations using the present method have been made for five different axisymmetric bodies for which detailed experimental data are available. We shall, however, present the results for only one case, namely the model with Afterbody 5 tested by Huang, Groves and Belt (1980). This is a particularly interesting case since the stern contains a point of inflexion and leads to quite dramatic changes in the surface pressure distribution.

For an axisymmetric body it is possible to calculate the flow in two ways. The conventional, and easier, way is to solve the axisymmetric-flow equations, with  $\phi = 0$ , along a single generator of the body.

Another is to perform a fully three-dimensional calculation over some circumferential segment of the body, with plane-of-symmetry boundary conditions applied at the sides of the segment. If such calculations are performed using a nonuniform grid distribution in the circumferential direction, comparison of the results with those of a conventional axisymmetric solution would indicate the influence of coordinate geometry. Such tests have been performed with the present method using the coordinates shown in Fig. 3 and, in the case of the three-dimensional solutions, using 4 points in the circumferential direction at  $\theta = 0, 37.5, 67.5$  and  $90^\circ$ . The two sets of results agreed well within the convergence tolerances accepted in the overall iterative solutions.

The axisymmetric calculations were performed with 60 points in the domain  $0.6 < x/L < 5.881$  and 22 points between the body and the external boundary at  $r/L = 0.4609$ . Location of the external boundary beyond about  $0.35L$  produced no appreciable differences in the solution and consequently we conclude that the region of viscous-inviscid interaction in this case extends to about  $0.35L$  or 4 maximum body diameters.

The solutions are started by specifying the grid geometry and the velocity and turbulence-parameter profiles in the boundary layer at the upstream station and assuming that a constant ambient pressure prevails throughout the solution domain. Figure 9 shows the pressure distribution on the body surface and along the wake centerline calculated at different time steps. It is seen that the solution converges monotonically and a "steady-state" or converged solution is obtained after about 80 time steps. The converged solution is in excellent agreement with the experimental data.

Figure 10 shows the variation of pressure in the radial direction across the boundary layer and in the external flow from the body surface,  $r = r_0$ , to the external boundary of the solution domain where  $C_p = 0$ . Here again the agreement with the available experimental data is quite satisfactory, considering the difficulties of measuring pressure in such an environment.

Detailed comparisons between the calculated and experimental profiles of the axial ( $U$ ) and radial ( $V$ ) components of mean velocity and the turbulent kinetic energy ( $k$ ) shown in Fig. 11 at several streamwise stations indicate that the agreement, in general, is good with respect to the boundary-layer thickness, the flow in the relatively thin boundary layer upto  $x/L = 0.87$  and the velocity field away from the wall in the tail region where the boundary layer is thick. The larger values of the mean velocity in the wall region of the thick boundary layer are no doubt related to the over-estimation of the turbulent kinetic energy by the basic  $k$ - $\epsilon$  model and the wall functions used here. The features noted above have also been observed in the

calculations for other bodies and suggest that some modifications are required in the turbulence model or the wall functions, or both. Results similar to those presented here have also been obtained by a variety of other methods, ranging from interacting boundary-layer analyses (Patel and Lee, 1977; Lee, 1978; Huang, Santelli and Belt, 1979; Dietz, 1980; Hoffman, 1980), through partially-parabolic solutions (Muraoka, 1980; Hoffman, 1982; Hogan, 1983), to a fully-elliptic solution (Zhou, 1983). Unfortunately, only Huang et al. and Hogan have presented calculations for the body considered here and in both cases somewhat improved velocity profiles were obtained in the wall region by incorporating an empirical correction in the turbulence model.

A particularly noteworthy feature of these solutions is the behavior of the pressure distribution close to the tail. The present solution, as well as that of Hogan, indicates a region of pressure decrease followed by an increase over the extreme tail and then a monotonic decrease to zero in the wake. In the interacting boundary-layer solutions of Huang et al., on the other hand, the calculated pressure increases continuously at the tail. We believe that the features predicted by the present method are genuine and are associated with the rapid changes in the geometry of this body as well as the upstream influence of the complex pressure interaction in the tail region. Note that such a pressure behavior is also predicted by the present and previous calculations for even the simplest case of the trailing edge of a flat plate (Fig. 8). Fully-elliptic solutions with a much finer grid in this region will shed some light on this phenomenon. Such calculations are in progress.

### 3.3 Flow Over Three-Dimensional Sterns

Huang, Groves and Belt (1983) have reported extensive measurements in the stern boundary layers of two ship-like bodies whose cross-sections are elliptic, with axes ratios 3:1 and 2:1. We shall present some aspects of the calculations performed with the present method for these bodies. Some features of the numerically-generated coordinates for the 3:1 body are shown in Fig. 4. Similar coordinates were also used for the second body. As noted in Section 2.1, the mesh points in the  $(\xi, \eta, \zeta)$  directions are (66, 19, 7), respectively. Although the calculations were continued for 80 time steps, convergence was achieved within about 30 time steps.

Comparisons between calculated and experimental results for a three-dimensional flow are somewhat difficult not only because there is a large body of information which needs to be examined from various perspectives but also because a considerable amount of interpolation is required due to the different coordinates employed in the calculations and experiments. In view of this, we shall present only the results along the

two planes of symmetry, namely  $\theta = 0^\circ$  and  $90^\circ$ .

Figure 12 shows the pressure distributions on the body surface and along the wake centerline. It is seen that the calculations are in agreement with data along both lines and that the pressure recovers to zero quite rapidly in the wake. As in the previous two examples, significant pressure changes are again observed in the tail region. It is interesting to note that the oscillations in the pressure along  $\theta = 90^\circ$  are somewhat larger due to the more rapid changes in the body curvature along that line. The small difference in the calculated pressure at the tail itself is due to the finite numerical control volume surrounding that point.

Figure 13 shows the distributions of the two nonzero components ( $U, V$ ) of mean velocity within the boundary layer and in the wake in the planes of symmetry. This is a close-up view of the viscous region since the solution domain extends well into the external inviscid flow. The calculations are seen to be in good agreement with the measurements, which extend only upto  $x/L = 0.954$ . In fact, the agreement in the wall region is somewhat surprising in view of the discrepancy noted earlier in the axisymmetric flow on Afterbody 5. It is also interesting to observe the evolution of the three dimensionality of the flow over the stern. The boundary-layer thickness is nearly constant around the girth at  $x/L = 0.719$  but the thickness along  $\theta = 90^\circ$  is almost three times that along  $\theta = 0^\circ$  at  $x/L = 0.954$ . Although no data are available in the wake, the calculations indicate that the three-dimensionality of the wake persists for quite large distances. Finally, we note that conventional boundary-layer calculations performed by Huang, Groves and Belt (1983) and Patel, Sarda and Shahshahan (1983) for this body breakdown before  $x/L = 0.93$  due to the thickening of the boundary layer, whereas the present method does not encounter such a difficulty and continues smoothly into the wake.

For the 2:1 axes-ratio body, the calculated pressure distribution is also in good agreement with the corresponding data and shows a behavior very similar to that observed in the other cases. The velocity profiles, which are shown in Fig. 14, also demonstrate excellent agreement with the measurements. The calculated wake again shows three dimensionality for distances as large as five body-lengths downstream of the tail.

### 4. CONCLUDING REMARKS

A new method for the calculation of the flow over the stern and in the wake of ship-like bodies has been outlined and some examples have been presented to demonstrate its capabilities. We note two significant aspects of the method: first, it requires only the body geometry and initial boundary-layer information as inputs and does not involve separate viscous and inviscid solu-

tions and matching between them; and second, all calculations presented here were performed on a Prime 750 minicomputer with computing times of the order of 2 hours for the three-dimensional bodies.

While the overall numerical framework of the method has been established and calculations for practical hull forms are now in progress, there are several basic physical and numerical aspects of the method which require further scrutiny and development. Among these are: (a) the validity of the turbulence model, in general, and the limitations of the wall functions, in particular, in complex three-dimensional flows; (b) the influence of the choice of coordinates on the solutions; and (c) the limitations of the partially-parabolic approximations. The first of these can best be studied by comparisons with detailed experimental data, the second would require the application of rigorous numerical tests in well known laminar and turbulent flows, while the third can be investigated by comparisons with corresponding fully-elliptic solutions. It is planned to subject the present method to such tests. Finally, the generality of the approach adopted here offers encouraging prospects for incorporating propellers and appendages in the solution domain in a more comprehensive manner than has been possible with presently available methods.

#### ACKNOWLEDGEMENTS

This research is supported jointly by the General Hydromechanics Research Program of the Naval Sea Systems Command, technically administered by the David W. Taylor Naval Ship Research and Development Center, under Contract N00014-81-K-0200, and the Office of Naval Research Special Focus Research Program in Ship Hydrodynamics, under Contract N00014-83-K-0136.

#### REFERENCES

- Abdelmeguid, A.M., Markatos, N.C., Muraoka, K. and Spalding, D.B. (1979): A Comparison Between the Parabolic and Partially-Parabolic Solution Procedures for Three-Dimensional Turbulent Flows Around Ship's Hulls. *Appl. Math. Modelling*, Vol. 3, p. 249.
- Chen, C.J. and Chen, H.C. (1982): Development of Finite Analytic Method for Unsteady Three-Dimensional Navier-Stokes Equations. Iowa Inst. Hyd. Research, IIHR Report 232-IV.
- Chen, C.J. and Chen, H.C. (1984): Finite Analytic Numerical Method for Unsteady Two-Dimensional Navier-Stokes Equations. *J. Computational Physics*, Vol. 53, 1984.
- Chen, H.C. and Patel, V.C. (1984): Calculation of Trailing-Edge, Stern and Wake Flows. Iowa Inst. Hyd. Research, IIHR Report in preparation.
- Cheng, W.S. and Patel, V.C. (1983): Numerically-Generated Coordinates Suitable for Ship Stern and Wake Flow Calculations. Iowa Inst. Hyd. Research, IIHR Report 265, p. 33.
- Davis, R.T. and Werle, M. (1981): Progress on Interacting Boundary Layer Calculations at High Reynolds Numbers. *Proc. First Sym. Numerical and Physical Aspects of Aerodynamic Flows*, Long Beach, Springer-Verlag.
- Dietz, M.S. (1980): An Axisymmetric, Strong Interaction Procedure to Include Large, Normal Pressure Gradients. *Applied Research Lab., Penn-State Univ., Tech. Memo. 80-160*.
- Hoffman, G.H. (1980): A Modified Displacement-Body Method for Treating the Axisymmetric Strong Interaction Problem. *J. Ship Res.*, Vol. 24, p. 114.
- Hoffman, G.H. (1982): A Spline Solution of the Incompressible Parabolized Navier-Stokes Equations in a Sheared Coordinate System. *Appl. Research Lab., Penn State Univ., Tech. Memo. 82-S1*.
- Hogan, T.F. (1983): A Calculation of the Parabolized Navier-Stokes Equations for Turbulent Axisymmetric Flows Using Streamline Coordinates and the  $k-\epsilon$  Turbulence Model. DTNSRDC-83/070.
- Huang, T.T., Groves, N.C. and Belt, G.S. (1980): Boundary-Layer Flow on an Axisymmetric Body with an Inflected Stern. DTNSRDC-80/064.
- Huang, T.T., Groves, N.C. and Belt, G.S. (1983): Stern Boundary-Layer Flow on Two Three-Dimensional Bodies Having Elliptic Transverse Cross-Sections. *Proc. 2nd Sym. Numerical and Physical Aspects of Aerodynamic Flows*, Long Beach, CA.
- Huang, T.T., Santelli, N. and Belt, G. (1979): Stern Boundary-Layer Flow on Axisymmetric Bodies. *Proc. 12th Sym. Naval Hydrodynamics*, pp. 127-157.
- Lee, Y.T. (1972): Thick Axisymmetric Turbulent Boundary Layer and Wake of a Low-Drag Body. Ph.D. Thesis, The University of Iowa.
- Markatos, N.C., Malin, M.R. and Tatchell, D.G. (1980): Computer Analysis of Three-Dimensional Turbulent Flows Around Ship's Hulls. *Proc. Inst. Mech. Engineers*, London, Vol. 194.
- Muraoka, K. (1980): Calculation of Thick Boundary Layer and Wake of Ships by a Partially Parabolic Method. *Proc. 13th Sym. Naval Hydrodynamics*, Tokyo, p. 601.
- Muraoka, K. (1982): Calculation of Viscous Flow Around Ships with Parabolic and Partially Parabolic Flow Solution Procedure. *Trans. West-Japan Soc. Naval Arch.*, Vol. 63, p.13.
- Patankar, S.V. (1980): Numerical Heat Transfer and Fluid Flow. Hemisphere Press.
- Patankar, S.V. and Spalding, D.B. (1972): A Calculation Procedure for Heat, Mass and Momentum Transfer in Three-Dimensional Parabolic Flows. *Int. J. Heat and Mass Transfer*, Vol. 15, p. 1787.

- Patel, V.C. (1982): Some Aspects of Thick Three-Dimensional Boundary Layers. Proc. 14th Sym. Naval Hydrodynamics, Ann Arbor, p. 999.
- Patel, V.C. and Lee, Y.T. (1977): Thick Axisymmetric Turbulent Boundary Layer and Near Wake of a Low-Drag Body of Revolution. Iowa. Inst. Hyd. Research, IHR Rept. 210.
- Patel, V.C., Sarda, O.P. and Shahshahan, A. (1983): Calculation of Ship Boundary Layers. Proc. Fourth Sym. Turbulent Shear Flow, Karlsruhe, p. 3.1.
- Patel, V.C. and Scheuerer, G. (1982): Calculation of Two-Dimensional Near and Far Wakes. AIAA Journal, Vol. 20, p.900.
- Ramaprian, B.R., Patel, V.C. and Sastry, M.S. (1982): The Symmetric Turbulent Wake of a Flat Plate. AIAA Journal, Vol. 20, p. 1228.
- Rubin, S.G. and Reddy, D.R. (1983): Global Solution Procedure for Incompressible Laminar Flow with Strong Pressure Interaction and Separation. Proc. 2nd Sym. Numerical and Physical Aspects of Aerodynamic Flows, Long Beach, CA.
- Spalding, D.B. (1972): A Novel Finite Difference Formulation for Differential Equations Involving Both First and Second Derivatives. J. Numerical Methods in Engineering, Vol. 4, p. 551.
- Tzabiras, G.D. (1983): On a Method for the Calculation of Turbulent Flow at the Stern of a Double Model. Proc. 12th SMSSH, Seminar on Ship Hydrodynamics, Varna, Bulgaria, p. 39-1.
- Tzabiras, G.D. and Loukakis, T.A. (1983): A Method for Predicting the Flow Around the Stern of Double Ship Hulls. Nat. Tech. Uni., Athens, Unpublished report.
- Zhou, L-D. (1982): A Streamline-Iteration Method for Calculating Turbulent Flow Around the Stern of a Body of Revolution and its Wake. Proc. 14th Sym. Naval Hydrodynamics, Ann Arbor, p. 1041.

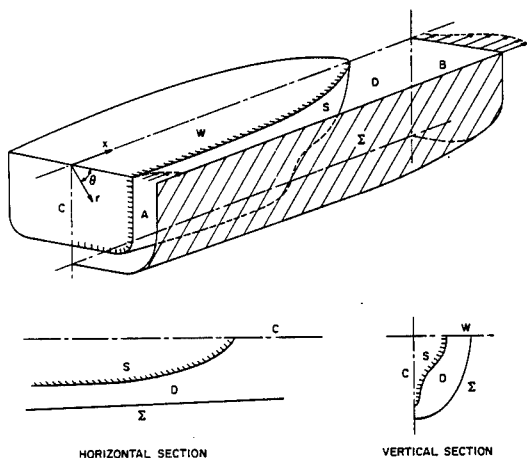


Fig. 1. Physical Solution Domain

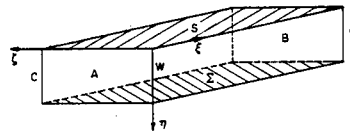


Fig. 2 Transformed Domain

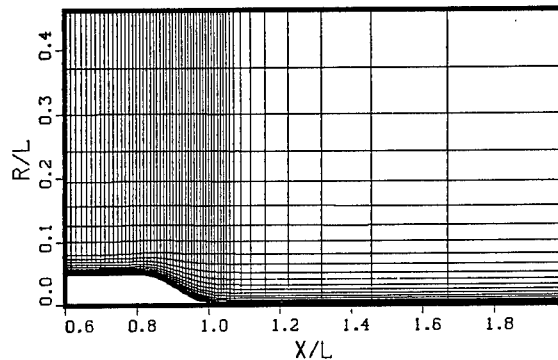


Fig. 3. Numerical Grid for Afterbody 5 (Partial View)

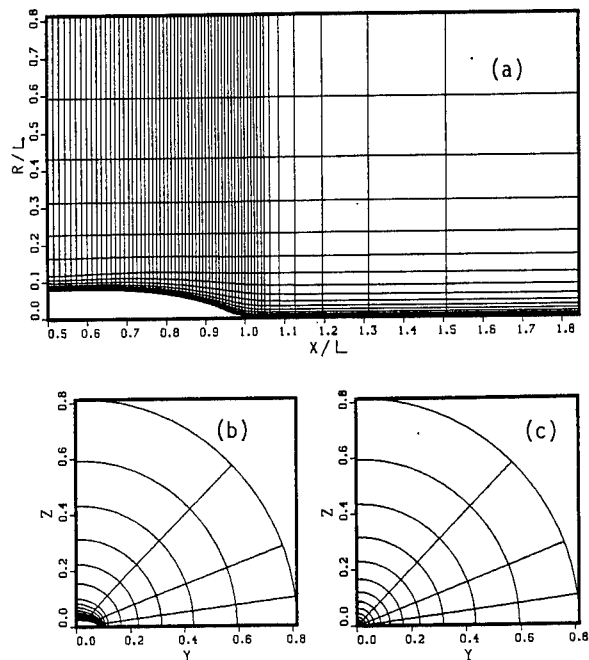
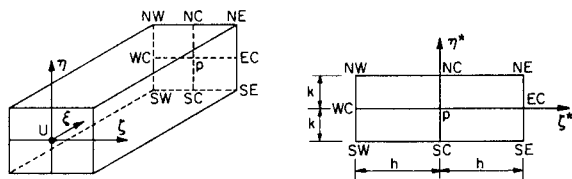
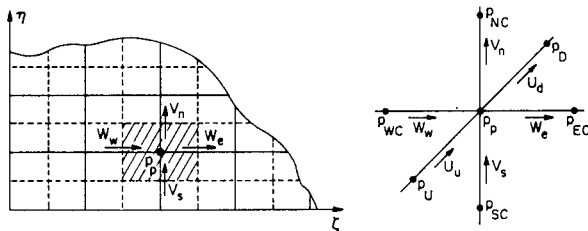


Fig. 4. Numerical Grid for the 3:1 Elliptic Body of Huang et al. (1983), (a) Longitudinal View at  $\theta = 90^\circ$ , (b) Sections at  $x/L = 0.500$  and (c)  $x/L = 1.311$



(a)



(b)

Fig. 5. Numerical Grid and Symbols.  
(a) Local Element (b) Staggered Grid

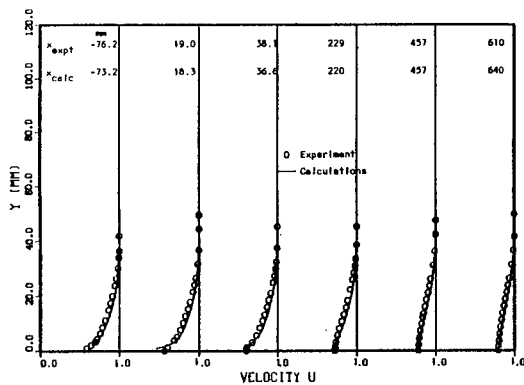


Fig. 6. Velocity Profiles in Boundary Layer ( $x < 0$ ) and Wake ( $x > 0$ ) of a Flat-Plate; Experiments of Ramaprian, Patel and Sastry (1982)

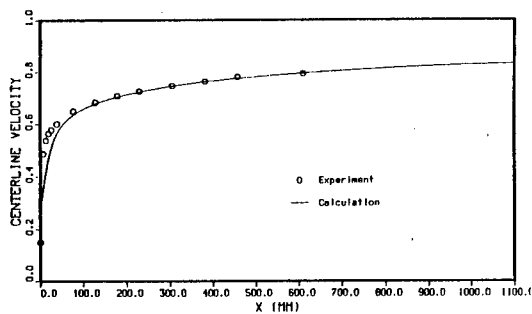


Fig. 7. Velocity along the Wake Centerline

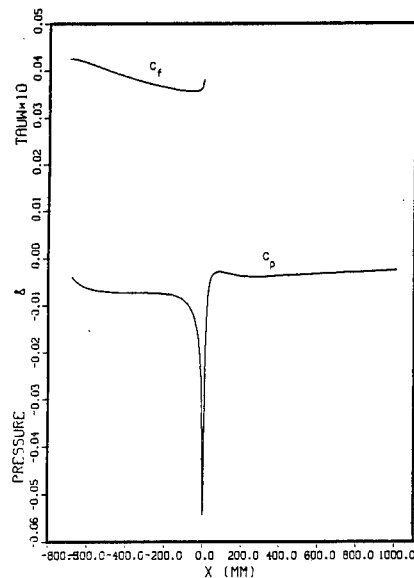


Fig. 8. Wall Shear Stress ( $C_f$ ), and Pressure Distribution ( $C_p$ ) on the Plate and along Wake Centerline

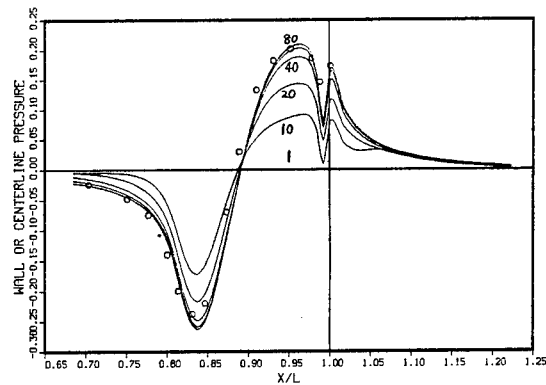


Fig. 9. Convergence of  $C_p$ , Afterbody 5

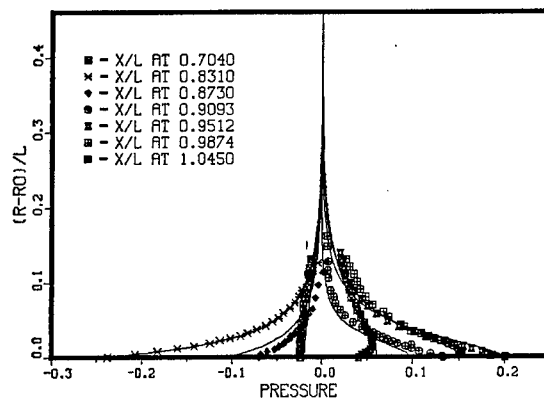


Fig. 10. Pressure Distributions, Afterbody 5

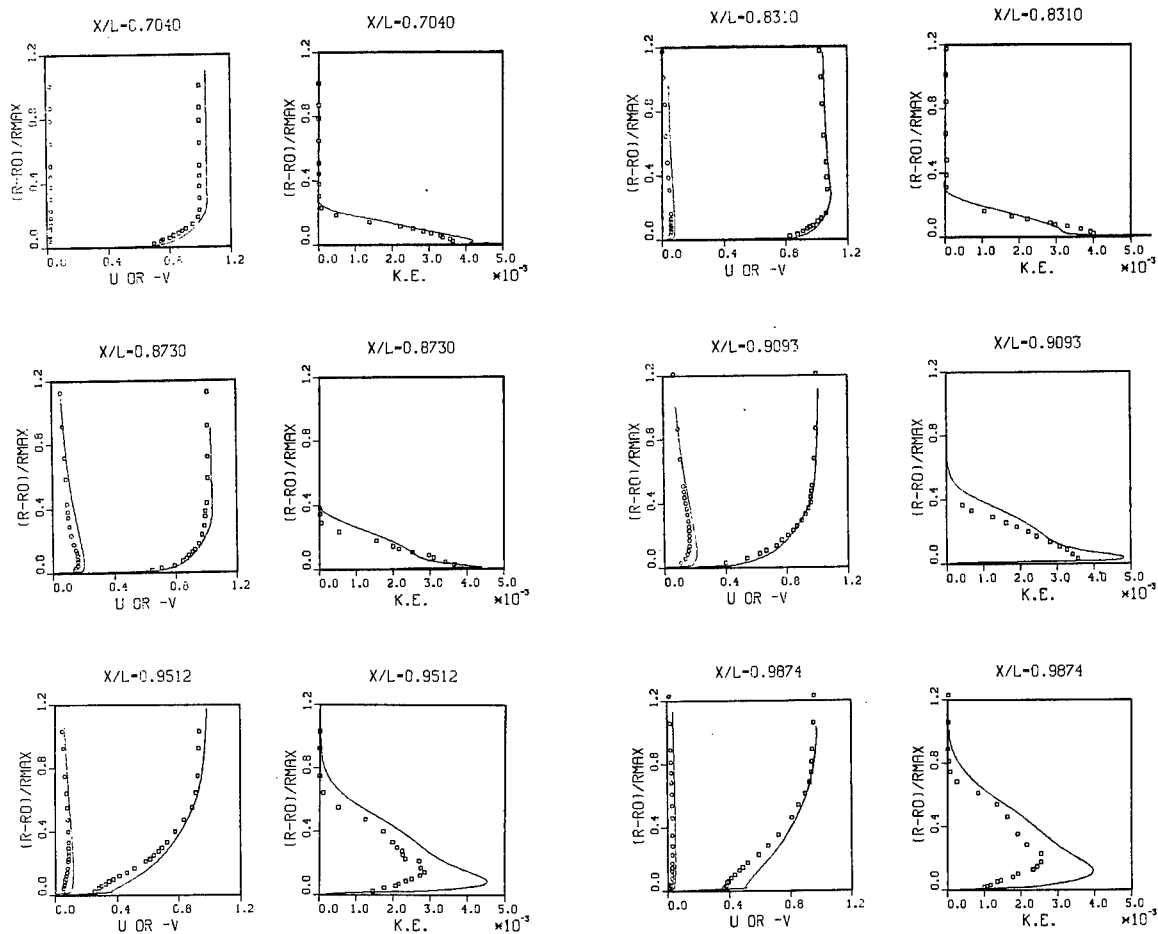


Fig. 11. Mean Velocity Components and Turbulent Kinetic Energy Distributions on Afterbody 5

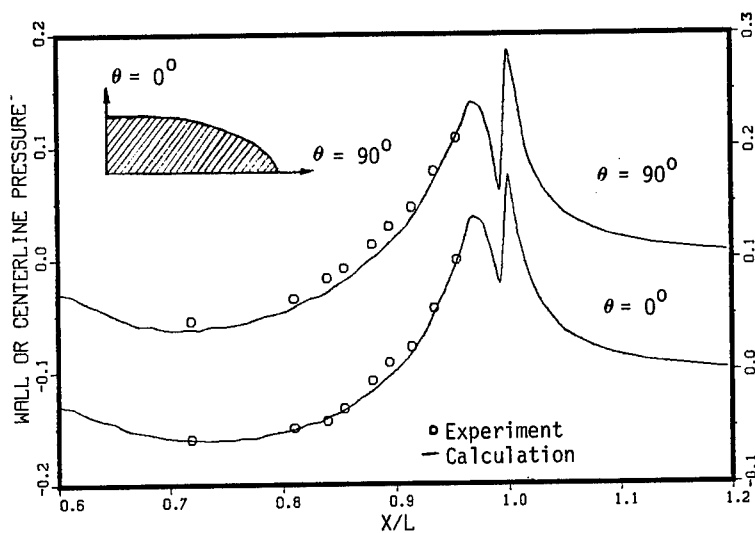


Fig. 12. Pressure Distributions along  $\theta = 0^\circ$  and  $90^\circ$ , 3:1 Elliptic Body

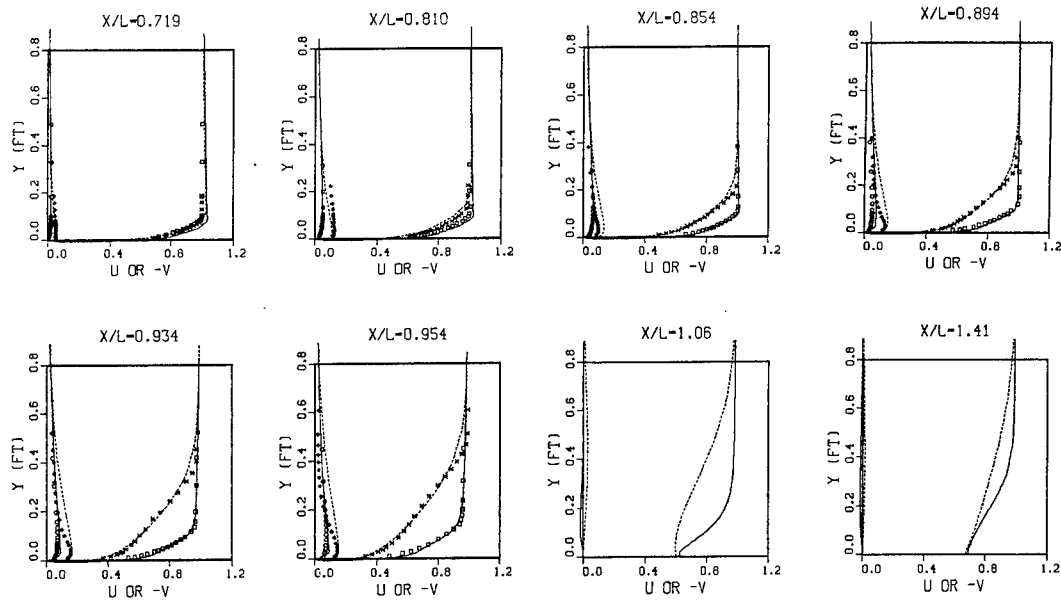


Fig. 13. Mean Axial and Radial Velocity Distributions for 3:1 Elliptic Body  
 —  $\theta = 0^\circ$ ; ----  $\theta = 90^\circ$

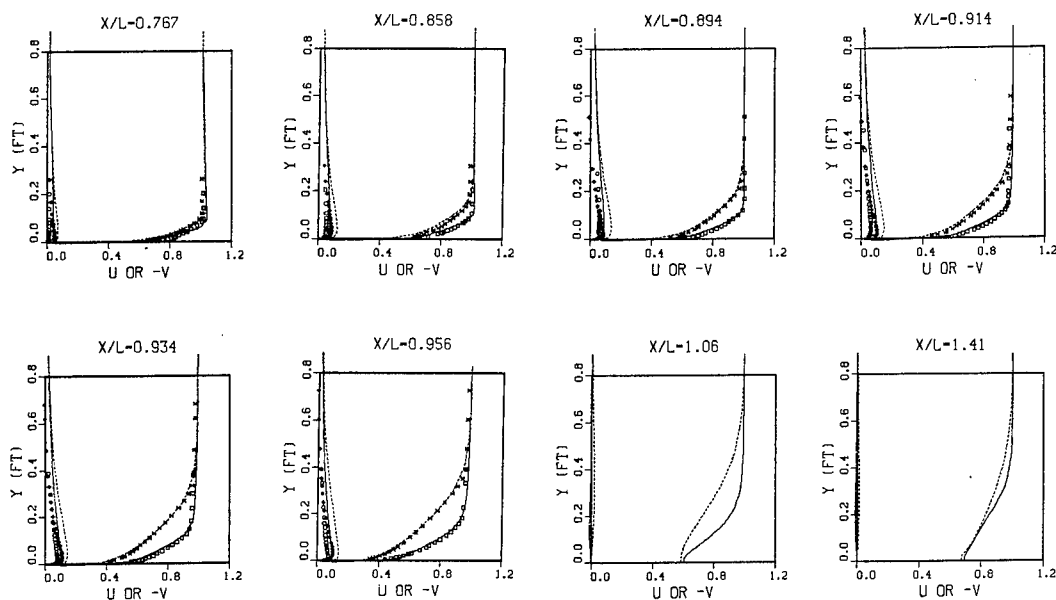


Fig. 14. Mean Axial and Radial Velocity Distributions for 2:1 Elliptic Body  
 —  $\theta = 0^\circ$ ; ----  $\theta = 90^\circ$

## DISCUSSION

YU-TAI LEE and Dr. THOMAS T. HUANG,  
David Taylor Naval Ship R&D Center,  
Bethesda, MD, USA:

The authors have made a very significant advance in the computation of ship stern flows. We sincerely congratulate them. The clarification to the following questions will improve our understanding of this new method.

1. A mild and small streamwise separation region on the plane of  $\theta = 90^\circ$  of the two simple 3-D sterns was measured by the flow visualization. The location was determined to be at  $x/L = 0.91$  for the 2:1 stern and at  $x/L = 0.90$  for the 3:1 stern. This new method predicted a sharp pressure drop over the extreme tail. However, the strong adverse pressure gradient associated with this pressure drop did not cause flow separation. Do you think that this new method predicts flow separation properly? How do the partially-parabolic equations behave near the separation point?

2. The predicted distributions of mean axial velocity and turbulence kinetic energy on afterbody 5 by Hogan (DTNSRDC report) agree with the measured values better than the predicted results obtained from this new method. Do the authors know the reason - turbulence modelling or the numerical procedure?

3. Is the solution procedure for developing body-fitted coordinate system applicable to the wing/body juncture?

Prof. THEODORE LOUKAKIS,  
National Technical University of Athens,  
Athens, Greece:

The authors are to be congratulated on an excellent paper, which certainly improves the state of the art in viscous flow numerical calculations.

The purpose of this discussion is solely to give some information related to comparisons between the partially-parabolic approximation used by the authors and the fully-elliptic solution mentioned in their concluding remarks.

At the National Technical University of Athens we have developed a computer program which can work with either of the aforementioned procedures. Some preliminary results indicate that the pressure and the crosswise velocity profiles are predicted with the same degree of accuracy and that the fully elliptic version gives slightly better results for the longitudinal velocity profiles. Hence, it seems that a serious suspect for the continuity discrepancies between calculated and measured results is the turbulence model, used both by the authors and at N.T.U.A.

Prof. KAZU-HIRO MORI,  
Hiroshima University,  
Higashi-Hiroshima, Japan:

The results computed by Dr. Chen and Prof. Patel are quite impressive. They may be celebrated as the first for the case of a ship-like body by the partially parabolic method where a body-fitted coordinate system is employed.

It is surprising that the present results which were obtained by such small numbers of grid, as shown in Fig. 3 and 4, agree so well with the measured. This may be due to the "finite analytic technique". However, because the results presented in Fig. 13 and 14 are all on the special planes where  $U$ ,  $V$ , and  $W$  are prescribed as boundary conditions, we miss results on other  $\theta$ 's, although I understand the numerical situation.

Usually waterplanes of ships have finite end-bluntness. And the stern flow is more or less asymmetric and unsteady. Although it may be little in the present case where the waterplane-end has an infinitely small radius and  $L/B$  is more than ten, the symmetric and steady flow condition have to be removed when it is applied to blunter bodies. In the course of our computations for 2-D elliptic cylinders, we could not succeed under those conditions. Once they were removed, we could get satisfying results as shown in Fig. A1\*. My question is that the time step which is introduced for iteration in your scheme can serve for the above purpose.

The boundary condition for  $U$  and  $p$  on  $\Sigma$  always bothers us in the method where they must be prescribed. This is because the perturbed velocity and pressure do not diminish so rapidly as expected. For example,  $\Sigma$  seems still not enough in your computations for the 3:1 elliptic body. It is advised that the numbers of grid in the  $r$ -direction may be changed depending on  $x$ .

As far as I understand the definition of  $Y$  in Fig. 13 and 14 is not clear. Is it the normal distance from the hull (from  $x$ -axis in wake), although it differs from that in Fig. 4? If so, both  $U$  on  $\theta = 0^\circ$  and  $90^\circ$  must be the same.

\*Mori, K. and Ito, N.: Wake Calculations around 2-Dimensional Elliptic Cylinders by Time-Dependent Vorticity Transport Equation. J. of Soc. of Nav. Arch. of Japan, Vol. 154, 1983.



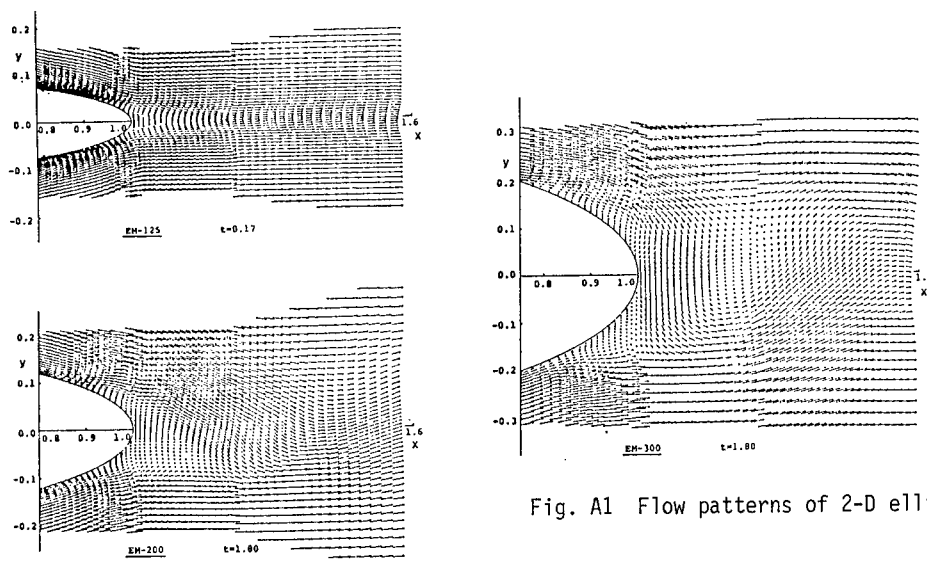


Fig. A1 Flow patterns of 2-D elliptic cylinders

LIAN-DI ZHOU,  
China Ship Scientific Research Center,  
Wuxi, China:

The authors are to be congratulated on their achievement in employing the three-dimensional numerically generated body-fitted coordinates and the novel "finite-analytic" numerical technique. There is a question I would like to ask. In Fig. 4 the numerical grid consists of only five stations. Where do the  $\zeta=1$  and  $\zeta=7$  stations locate and how are the boundary conditions at these places determined? The numbers of circumferential stations are few and the distribution is non-uniform. Maybe this distribution of circumferential stations may be suitable for an elliptic body, but is it suitable for a general ship form?

#### AUTHORS' REPLY

To Drs. Lee and Huang:

1. The detailed boundary-layer data for the 2:1 and 3:1 elliptic bodies do not indicate any streamwise separation. Our calculation also did not show any streamwise flow reversal although small regions of circumferential flow reversal are present at several constant- $x$  crosssectional planes for both bodies. Whether the latter is associated with the separation you mention remains to be verified. The present partially-parabolic formulation neglects longitudinal diffusion and is therefore not suitable for handling longitudinal-flow reversals, although it is fully capable of handling recirculation in the transverse direction. If small streamwise separation exists, one may modify the present formulation by either (a) using the FLARE approximations for the streamwise convective terms or (b) employing a locally elliptic formulation.

2. Hogan included (a) a curvature correction, (b) an intermittency factor, and (c) dif-

ferent wall functions in his turbulence model, while we have used the standard  $k-\epsilon$  model in the present calculations. We believe that these are the main reasons for the differences between Hogan's and our calculations.

3. The numerical grid-generation technique employed in the present calculations can be used for wing/body junctions without major modifications.

To Prof. Loukakis:

We thank Professor Loukakis for showing some of the results of their calculations. We believe that many more detailed comparisons between calculations and experiments for different shapes are required before we can conclusively demonstrate the limitations of the turbulence model. Some of the limitations of the present model are well known but we are not sure how important a role does the turbulence model play in stern flows. Our experience thus far indicates that accurate prediction of the pressure field is much more important than the turbulence model.

To Prof. Mori:

1. Although Figs. 13 and 14 show only the two planes of symmetry, the calculations also show the same qualitative features (e.g., transverse flow reversal and boundary-layer thickness distribution) as those observed in the experiments. However, as mentioned in the paper, detailed comparisons between calculations and experimental data require considerable interpolations. Such comparisons are in progress and will be shown in the IIHR Report of Chen and Patel which is under preparation.

2. Prof. Mori shows some calculations of vortex shedding behind a two-dimensional strut. In order to calculate such a flow it is obviously necessary to use an unsteady formulation, and a fully-elliptic one, to handle the separation from the body. This is not necessary for the examples presented here. Our numerical technique is, however, fully capable of such calculations and is not restricted to two-dimensional or axisymmetric bodies.

3. We apologize for the confusion caused

by the similarity of the notation used in Figs. 4, 13 and 14, which prompted the remaining comments by Professor Mori.

$Y$  in Fig. 4 is the distance from the body axis. This figure clearly shows the computation domain. Note that the external boundary  $\Sigma$  is at  $0.8137L$ . In Figs. 13 and 14, however,  $Y$  refers to the physical distance from the body surface in feet. These figures show only the boundary layer region, which is a very small part of the total computation domain (the outer edge of which is at approximately 8 feet in those coordinates). Thus, the changes in the external inviscid flow are captured totally and the boundary conditions on  $\Sigma$  are simply  $U = 1$ ,  $p = 0$  for all  $\theta$  (or  $\zeta$ ).

To Dr. Zhou:

1. In the generation of body-fitted coordinates for the 2:1 and 3:1 elliptic bodies, seven circumferential stations are used with the symmetry conditions specified as follows:

$$\begin{aligned} r(\xi, \eta, 1) &= r(\xi, \eta, 3) \\ \theta(\xi, \eta, 1) &= -\theta(\xi, \eta, 3) \end{aligned} \text{ at } \theta = 0 (\zeta = 2)$$

and

$$\begin{aligned} r(\xi, \eta, 7) &= r(\xi, \eta, 5) \\ \theta(\xi, \eta, 7) &= \pi - \theta(\xi, \eta, 5) \end{aligned} \text{ at } \theta = 90^\circ (\zeta = 6)$$

The coordinates at  $\theta = 0^\circ$  and  $90^\circ$  are, therefore part of the numerical solution and are not specified directly.

2. For general ship forms, more circumferential stations are certainly needed in order to properly resolve the flow in the constant- $\xi$  planes. Our current applications to the SSPA 720 and the Wigley hulls employ 13 to 18 stations. Whether this is sufficient remains to be determined by comparisons with experiments.

# A CALCULATION METHOD FOR SHIP STERN FLOWS USING AN ANALYTICAL BODY FITTED COORDINATE SYSTEM

LEIF BROBERG AND LARS LARSSON

## ABSTRACT

A new method for calculating ship stern flows is described. The method is based on the thin boundary layer equations cast in an analytic, body-fitted coordinate system. The major part of the paper deals with the definition and generation of this system and the computation of the related metrics and Christoffel symbols. Derivations of the governing flow equations are also made, using tensor algebra, and a short account is given of the numerical solution method. Finally, results from some test calculations are presented.

## NOMENCLATURE

$A_i$  - matrices of coefficients  
 $A_{mn}$  - transformation coefficients  
 $a_2$  - diffusion constant  
 $a_n$  - coefficients in conformal transformation  
 $B_i$  - matrices of coefficients  
 $b_j$  - coefficients of the global stretching polynomial  
 $C_1, C_2$  - three dimensional vectors  
 $c$  - constant  
 $c_f$  - skin friction coefficient  
 $c_i$  - coefficients of the local stretching polynomial  
 $ds$  - line element  
 $e_i$  - Cartesian unit vectors  
 $F$  - vector containing  $u^1, u^2$  and  $q^2$   
 $f$  - global stretching polynomial  
 $g_i, g^i$  - covariant and contravariant base vectors of the curvilinear coordinate system  
 $g_{ij}, g^{ij}$  - covariant and contravariant components of the metric tensor  
 $\sqrt{g}$  - Jacobian  
 $h$  - local stretching polynomial  
 $I$  - number of coefficients  $c_i$   
 $J$  - number of coefficients  $b_j$   
 $L$  - length of ship model  
 $L_p$  - dissipation length  
 $M$  - number of rows in  $A_{mn}$   
 $N$  - number of coefficients  $a_n$ , number of grid points in circumferential direction  
 $p$  - point in space, instantaneous pressure  
 $\bar{p}$  - time averaged pressure  
 $p'$  - turbulent fluctuations of the pressure

$Q_e$  - speed at the edge of the grid  
 $q^2$  - twice the turbulent kinetic energy  
 $q_{\max}$  - maximum turbulent kinetic energy in the outer 75% of the boundary layer  
 $R_{ik}, R^i_k$  - contravariant and mixed components of the Reynolds stress tensor  
 $r$  - radius in transformed plane  
 $\underline{r}$  - position vector of  $P$   
 $t_{ij}, t^{ij}, t^i_j$  - covariant, contravariant and mixed components of a second order tensor  
 $u^i, u_i$  - contravariant and covariant components of the time averaged velocity  
 $u^i$  - contravariant component of the turbulent velocity fluctuations  
 $v_j, v^i$  - covariant and contravariant components of  $\underline{v}$   
 $\bar{v}_i, \bar{v}^i$  - covariant and contravariant components of the vector  $\underline{v}$  in a Cartesian coordinate system  
 $\underline{v}$  - a vector, instantaneous velocity  
 $x^1, x^2, x^3$  - curvilinear coordinates  
 $x^1_P, x^2_P, x^3_P$  - coordinates of point  $P$   
 $y$  - the arc length along the  $x^2$ -axis  
 $\Gamma^i_{jk}$  - Christoffel symbols of the second kind  
 $\delta$  - boundary layer thickness  
 $\delta_{ij}, \delta^i_j$  - covariant and mixed components of Kronecker's delta  
 $n$  - the arc length along the  $x^2$ -axis, dimensionless by  $\delta$   
 $\mu$  - dynamic viscosity  
 $\nu$  - kinematic viscosity  
 $\xi^1, \xi^2, \xi^3$  - global Cartesian coordinates  
 $\rho$  - density  
 $\tau^{ij}, \tau^i_j$  - contravariant and mixed components of the viscous shear stress tensor  
 $\phi^i$  - contravariant component of volume force - a scalar  
 $\partial_i$  - partial derivative with respect to  $x^i$   
 $\partial_t$  - partial derivative with respect to time  
 $\nabla$  - covariant derivative

## 1. INTRODUCTION

In June 1980 a workshop on ship boundary layer calculations was held at the Swedish Maritime Research Centre SSPA, (Larsson, 1981). Com-

Leif Broberg, Division of Mechanics, Chalmers University of Technology, Gothenburg, Sweden  
 Lars Larsson, SSPA and Div. of Ship Hydrod. Chalmers University of Technology, Gothenburg, Sweden

parative calculations were carried out for two different hulls using 17 different calculation methods, developed by universities and commercial organizations within aero- and hydrodynamics. 14 of the methods were based on first order boundary layer theory, while two included extensions of this theory, in order to approximately incorporate some effects of higher order. One method was of a completely different type: the partially parabolic approximation. From the comparative calculations it could be concluded that almost all methods worked reasonably well, except close to the stern. In this region the boundary layer grows thick and the first order theories become too approximate. Better results were obtained by the more exact methods, notably the partially parabolic one.

There seem to be four main reasons why ordinary boundary layer methods fail close to the stern.

1. The curvature of the surface is assumed zero, so the normals are considered parallel to one another, while in reality they may even intersect within the boundary layer. This has a serious effect on the solution since particularly the continuity of the flow is not maintained downstream.

2. The pressure is assumed constant across the boundary layer, which makes the prediction of, for instance, bilge vortices impossible.

3. No interaction between the boundary layer and the potential flow is considered.

4. The only shear stresses taken into account are the ones in the plane of the surface. Momentum diffusion is thus considered only in the normal direction.

In higher order boundary layer theories, attempts are made to incorporate, at least approximately, the features of items 1-3 above, while in the partially parabolic approach also the fourth approximation is improved, by accounting for lateral diffusion.

Since the workshop, large efforts have been made to enable more exact calculations, see the report of the 17th ITTC Resistance Committee for a survey, (1984). In the aircraft industry a number of methods based on either higher order boundary layer theory or the partially parabolic approach have been presented. Most of them are, however, two-dimensional and only a few can be applied to ship flows. More suitable methods in this respect have been developed in hydrodynamics. A higher order integral method was presented by Larsson & Chang (1980), and later the development of a completely different approach, the streamline curvature method, was reported by Larsson & Johansson (1982) and Johansson & Larsson (1983). Other papers of interest are the ones by Odabasi & Davies (1983), Tzabiras (1983) and Cheng & Patel (1983). A promising development of the original partially parabolic method has recently been made by CHAM in England, Spalding (1981). In principle, fully elliptic calculations based on the time averaged Navier-Stokes equations can now be made.

In the present work, which started in 1980 as a cooperation between Chalmers University of Technology and SSPA, the emphasis is placed

on the development of a body-fitted coordinate system for ship flow calculations. The system fits exactly into the space outside the hull and is convenient as a frame for numerical methods. Ultimately a method of the partially parabolic type will be developed based on this system, but in the present approach the flow equations are still based on the boundary layer approximation. Since the most serious one of the above restrictions of such methods has now been removed, reasonably accurate results might be expected even near the stern.

The coordinate system is described in paragraph 2, and in 3 the necessary geometrical quantities, such as metrics and Christoffel symbols, are computed. A derivation of the flow equations is given in paragraph 4 and the results from some test calculations are presented in paragraph 5. For a more detailed description of the project, see Broberg (1984).

## 2. THE COORDINATE SYSTEM

The advantage of using body-fitted coordinate systems for the numerical solution of partial differential equations is that all computations can be done in a fixed square grid in the rectangular transformed region, regardless of the shape of the physical boundaries. In the case of a ship hull one such boundary is the free surface, which in the present work is considered flat, or equivalently, a plane of symmetry. On this and the vertical plane of symmetry one coordinate should be constant. Another coordinate should be constant on the hull and it is convenient to let the remaining coordinate be constant on the hull cross sections.

The location in the physical space of the grid points, defined by constant increments of the coordinates, is of paramount importance for all numerical methods, and this is particularly true in the normal direction, if the viscous sublayer is to be resolved properly.

Several techniques are available for the construction of body-fitted coordinate systems. Examples are differential, algebraic and conformal transformation techniques. Although a conformal transformation is basically a surface-to-surface correspondence, it can be used as one component of a three-dimensional grid generation process, see Ives (1982). This technique is used here to construct a body-fitted coordinate system that satisfies all the requirements above.

The system is based on conformal transformation in each cross section of the hull, where a  $n$ -parameter generalisation of the well known Lewis-transformation is used for representing the hull contour. By making the "constants" of the transformation functions of a coordinate along the hull, its surface may be represented analytically. The hull itself thus corresponds to the unit circle in the transformed plane, and other coordinates surfaces of the same kind are generated by concentric circles with radii greater than one. By letting  $r$  be a function of the coordinates, the distribution of node points in the physical plane can be controlled and all requirements above satisfied.

Let  $(\xi^1, \xi^2, \xi^3)$  be a Cartesian coordinate

system in the physical space with the  $\xi^1$ -axis along the axis of the ship. For later purpose it is convenient to denote coordinates by superscripts.

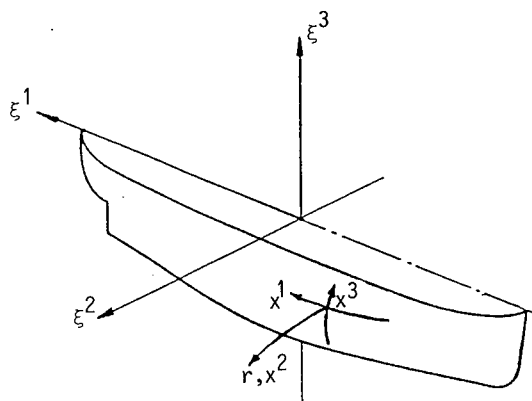


Fig. 1 Coordinate systems

Using the polar coordinates  $r, x^3$  in the transformed plane, the transformation in each plane  $\xi^1 = \text{constant}$  can be written

$$\xi^2 = \sum_{n=1}^N a_n r^{\beta_n} \cos \beta_n x^3$$

$$\xi^3 = \sum_{n=1}^N a_n r^{\beta_n} \sin \beta_n x^3$$

$$\beta_n = 3 - 2n \quad (1)$$

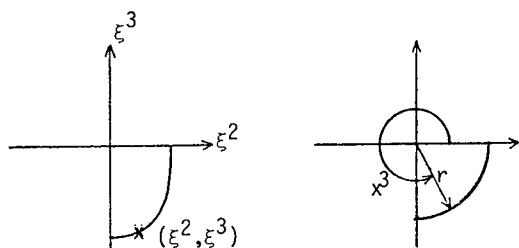


Fig. 2 Conformal transformation (1)

The contour of the ship hull is defined by the line  $r=1$ .

The coefficients  $a_n$  can be determined in the sense of the least-squares, if a set of points is given from the body plan. Thus the set of coefficients  $a_n$  is to be chosen so that the sum of the squares of the distances between the points of the real contour and the generated contour is minimized. Assume that  $P$  points from the body plan are used. Then there are  $P$  corresponding unknown angles for the generated contour. However, it is possible to prescribe these angles a priori, and then calculate the corresponding coefficients  $a_n$ , see Miao (1980). The calculation starts with a first guess on  $a_n$  from the Lewis transformation. The  $a_n$ 's are

then corrected in an iteration process until the error falls within a specified error bound. It is necessary to calculate the optimum fit using successively increasing  $N$ 's to achieve convergence.

The transformation (1) can represent the ship-hull, if the coefficients  $a_n$  are considered functions of  $x^1 = \xi^1$ , see von Kerczek (1982), for instance in the form of polynomials in  $x^1$

$$a_n(x^1) = \sum_{m=1}^M A_{mn} (x^1)^{m-1} \quad (2)$$

Knowing the coefficients  $a_n$  for a number of sections, the coefficients  $A_{mn}$  can be determined in a least squares sense.

The matrix  $A_{mn}$  has been calculated for the SSPA Model 720, in the interval  $0.3 \geq \xi^1/(L/2) \geq 0.95$ . The  $a_n$ 's ( $N=12$ ) were calculated for 11 sections in the interval and the input consisted of 18 data points for each section, taken from the input package of the SSPA - ITTC Workshop on Boundary Layers 1980, Larsson (1981). These sets of  $a_n$ 's were then used to calculate the  $A_{mn}$ 's for  $M=8$ . Fig. 3 shows the approximated hull and the coordinate lines  $r=1$ ,  $x^3 = \text{constant}$  and  $r=1$ ,  $x^1 = \text{constant}$ , respectively. Because of the orthogonality of the conformal transformation the contours must meet the waterline at right angles. From the figure it can be seen that this effect is concentrated very close to the waterline, especially near the stern.

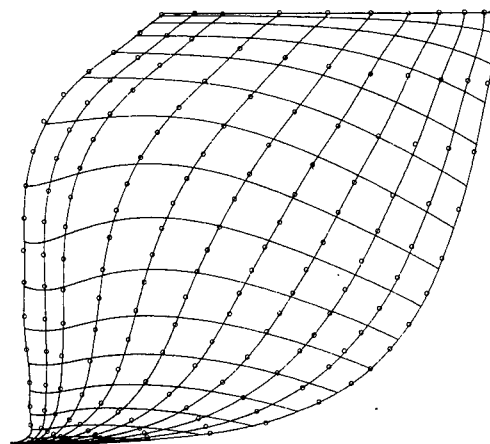


Fig. 3 Hull approximation and lines  $x^1 = \text{constant}$  and  $x^3 = \text{constant}$  resp. on  $r=1$ .

The transformation defines a body fitted coordinate system  $(x^1, r, x^3)$ . Its coordinate surfaces  $x^1 = \text{constant}$  are flat and parallel, normal to the axis of the ship. The surfaces  $x^3 = \text{constant}$  are flat at the symmetry planes but in general they are curved. As mentioned before, the surface  $r=1$  approximates the ship hull and from (1) it can be seen that

$$\begin{aligned}\xi^2 &= a_1 r \cos x^3 + 0(1/r) \\ \xi^3 &= a_1 r \sin x^3 + 0(1/r)\end{aligned}\quad (3)$$

so the lines  $r = \text{constant} \gg 1$  and  $x^1 = \text{constant}$  are circles almost concentric with the unit circle. The coordinate system is in general non-orthogonal but the coordinates in the surface  $x^1 = \text{constant}$  are always orthogonal, because of the conformal transformation, see Fig 4

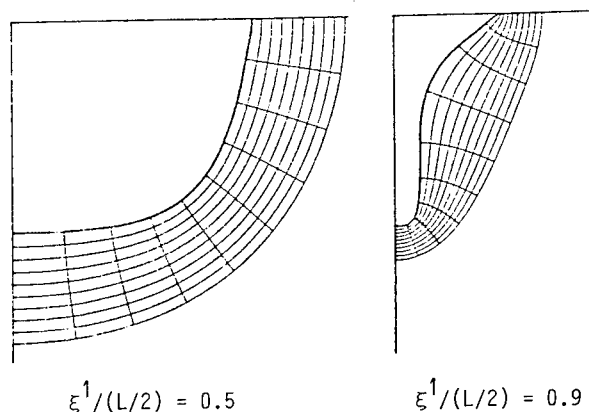


Fig. 4. The grid generated by equation (1),  $r \geq 1$ . Two sections  $\xi^1 = \text{constant}$ .

From Fig 4 it can be seen that the sectional area of the mesh is diminishing considerably downstream. This makes the system inconvenient for calculations of boundary layers, which usually grow thicker in the downstream direction. To cover the boundary layer at the stern a large part of the grid must be outside the boundary layer upstream and to avoid this, the coordinate system has to be stretched. In the following this will be called global stretching.

Many second order finite difference schemes are restricted to constant mesh spacing, that is  $\Delta x^1 = c_1$ ,  $\Delta r = c_2$  and  $\Delta x^3 = c_3$ . If such a method is used to solve a problem with more than one length scale it is the smallest scale that determines the number of grid points. This means that an enormous number of grid points is needed to calculate a boundary layer, even if the turbulence is modelled, because the viscous sublayer must be properly resolved. In Fig. 4,  $\Delta r = 0.044$ ,  $\Delta x^3 = \pi/9$  and it can be seen that the grid points are evenly distributed along a normal. It would be an advantage if the coordinate system could be stretched in the normal direction so that the grid points would be smoothly redistributed and concentrated near the hull. This is in the following called local stretching.

In both types of stretching there is a difficulty involved because the flow field is unknown so it is not evident where the outer edge should be positioned or how to distribute the grid point for the purpose of obtaining higher resolution of the boundary layer. It can be done in connection with flow calculation but there are several difficulties in such a pro-

cedure and it is not applied in this work.

The stretching is performed by letting the coordinate  $r$  be a function of  $x^1$ ,  $x^3$  and a new coordinate  $x^2$ :

$$r = r(x^1, x^2, x^3)$$

If  $x^2$  is defined as zero on the hull, then the following condition must hold if the hull should be left unaffected

$$r(x^1, 0, x^3) = 1$$

and to preserve symmetry, the function must be periodic in  $x^3$  so that

$$r(x^1, x^2, x^3 + \pi) = r(x^1, x^2, x^3) \quad \forall x^3 \in \mathbb{R}$$

In the following, the function  $r$  is assumed to be independent of  $x^3$ , which limits the possibilities of adjusting the grid. Nevertheless the outer edge of the grid essentially follows the variation in boundary layer thickness, except close to the keel, where the boundary layer is extremely thin. More important is the effect on the local stretching. The physical distance between the hull and the innermost grid point is greater in the concave parts of a contour than in the convex parts. This is compensated to some extent by a smaller skin friction in the concave part, which thickens the viscous sublayer. Experience from the SSPA-Model 720 shows that this effect is not large enough to balance the geometrical effect. It is thus the concave region, that must determine the local stretching.

In the present work the function  $r$  is defined as:

$$\begin{aligned}r(x^1, x^2) &= 1 + h(x^2) \cdot f(x^1) \quad \text{where} \\ h(x^2) &= \sum_{i=1}^I c_i (x^2)^{i-1}; \quad h(0) = 0 \\ f(x^1) &= \sum_{j=1}^J b_j (x^1)^{j-1}\end{aligned}\quad (4)$$

The coefficients  $b_j$  in the global stretching function  $f$  can be determined by the least squares method if one  $x^2$ ,  $x^3 = \text{constant}$  line is prescribed. For the SSPA Model 720 the prescribed line was taken as straight and parallel to the  $\xi^1$ -axis in the symmetry plane  $x^3 = 0$ . Note that the outer edge of the grid may be chosen inside this line. The local stretching function  $h(x^2)$  was normalized to one at the line and the value of  $r$ , corresponding to the line was obtained by a method of inverse interpolation for several sections. A polynomial of the 5'th degree was fitted to the calculated  $r$ 's and used as global stretching function  $f$ . The function was calculated for several cases with the prescribed line located at a distance of 1-2 times the boundary layer thickness outside the hull at  $\xi^1/(L/2) = 0.3$ . With the aid of a graphic unit, coordinate surfaces were plotted and it was possible to choose an outer coordinate surface that covered the boundary layer and was suitably curved along the hull.

The local stretching is more difficult to

determine. It demands knowledge of global stretching, number of grid points and skin friction. For the SSPA Model 720 the measured skin friction was used to secure that at least three points were located inside the viscous layer at the most critical part of the model. The choice of a stretching function like (4) makes it easy to change the local stretching without any effects on the global stretching. This is an advantage because if more than one calculation is performed on a model the local stretching can be used for smaller adjustments. Some coordinate surfaces of the final coordinate system are shown in Fig. 5.

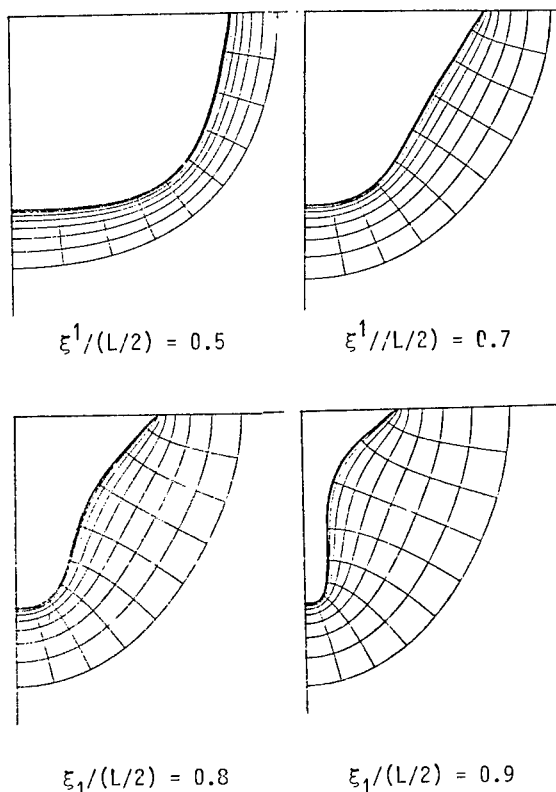


Fig. 5 The stretched grid at some section  $\xi^1 = \text{constant}$

The equations for the coordinate system may finally be summarized as follows (see also Fig. 1)

$$\begin{aligned}\xi^1 &= x^1 \\ \xi^2 &= \sum_{n=1}^N \sum_{m=1}^M A_{mn} (x^1)^{m-1} \cdot r(x^1, x^2)^{\beta_n} \cos(\beta_n x^3) \\ \xi^3 &= \sum_{n=1}^N \sum_{m=1}^M A_{mn} (x^1)^{m-1} \cdot r(x^1, x^2)^{\beta_n} \sin(\beta_n x^3)\end{aligned}\quad (5)$$

where  $\beta_n = 3 - 2n$ ,  $r(x^1, x^2) = 1 + \left( \sum_{i=1}^I c_i (x^2)^{i-1} \right) \cdot \left( \sum_{j=1}^J b_j (x^1)^{j-1} \right)$

### 3. GEOMETRICAL QUANTITIES OF THE COORDINATE SYSTEM

Since tensor formalism is used in the following some general relations from tensor analysis will be given first in this paragraph. Thereafter the computation of metrics and Christoffel symbols will be described.

The coordinate system  $(x^1, x^2, x^3)$  is defined by the transformation (5), which can be written:

$$\xi^i = \xi^i(x^1, x^2, x^3) \quad i = 1, 2, 3 \quad (6)$$

This relation transforms the new coordinates  $(x^1, x^2, x^3)$  to the old ones  $(\xi^1, \xi^2, \xi^3)$  and it can not be inverted explicitly.

Fig. 6 shows a general point P and the three lines formed by the intersection of surfaces of  $x^i = \text{constant}$ .

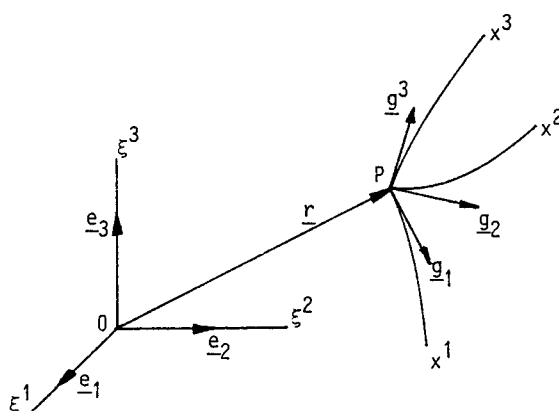


Fig. 6 Curvilinear coordinate system

Let  $\underline{e}_i$  denote the Cartesian unit vectors. The position vector of P is  $\underline{r} = \xi^i(x_p^1, x_p^2, x_p^3) \cdot \underline{e}_i$ . Whenever the same letter appears as a subscript and as a superscript in a product or in a tensor of order two or more the sum is to be taken over this index, unless otherwise stated. The covariant base vectors  $\underline{g}_i$  are defined as

$$\underline{g}_i = \frac{\partial \underline{r}}{\partial x^i} = \frac{\partial \xi^j}{\partial x^i} \cdot \underline{e}_j \quad (7)$$

Replacing the dummy index j by k and multiplying both sides by  $\partial x^i / \partial \xi^j$  gives

$$\underline{e}_j = \frac{\partial x^i}{\partial \xi^j} \underline{g}_i \quad (8)$$

The covariant base vector  $\underline{g}_i$  at P is parallel to the intersection line through the point, on which  $x^i$  varies (while the other two coordinates are constant). Such a line is called coordinate line and the direction of increasing  $x^i$  is called positive. Note that the direction and the magnitude of  $\underline{g}_i$  depend on the position of P. In general the  $\underline{g}_i$  are not unit vectors and they may even have different dimensions.

The contravariant base vectors  $\underline{g}^i$  are defined as

$$\underline{g}^i = \frac{1}{\sqrt{g}} (\underline{g}_j \times \underline{g}_k) = \frac{\partial x^i}{\partial \xi^1} \cdot \underline{e}^1 \quad (9)$$

where  $\sqrt{g}$  is the Jacobian of the transformation. The first part of (9) yields  $\underline{e}^1 = \underline{e}_1$

The inversion of (9) is given by

$$\underline{e}^i = \frac{\partial \xi^i}{\partial x^j} \underline{g}^j \quad (10)$$

The covariant and contravariant metric tensors are defined in terms of base vectors, respectively, as

$$g_{ij} = \underline{g}_i \cdot \underline{g}_j \quad (11)$$

$$g^{ij} = \underline{g}^i \cdot \underline{g}^j = (g_{ij})^{-1} \quad (12)$$

The quantity  $g_{ij}$  is proportional to the cosine of the angle between the coordinate lines  $x^i$  and  $x^j$ . The arc length of the coordinate line  $x^i$  is proportional to  $\sqrt{g_{ii}}$  (unsummed), and for a general line the arc length is given by

$$(ds)^2 = g_{ij} dx^i dx^j \quad (13)$$

Equation (13) can be used to calculate the metric. For a Cartesian coordinate system the metric equals Kronecker's delta  $\delta_{ij}$ , so for a general line element (13) gives

$$\begin{aligned} (ds)^2 &= \delta_{ij} d\xi^i d\xi^j = \delta_{ij} \cdot \frac{\partial \xi^i}{\partial x^k} \cdot \frac{\partial \xi^j}{\partial x^l} \cdot dx^k dx^l = \\ &= g_{kl} \cdot dx^k \cdot dx^l \\ \Rightarrow g_{kl} &= \frac{\partial \xi^1}{\partial x^k} \cdot \frac{\partial \xi^1}{\partial x^l} + \frac{\partial \xi^2}{\partial x^k} \cdot \frac{\partial \xi^2}{\partial x^l} + \frac{\partial \xi^3}{\partial x^k} \cdot \frac{\partial \xi^3}{\partial x^l} \quad (14) \end{aligned}$$

A vector  $\underline{v}$  defined in  $P$ , may be decomposed with respect to the covariant or the contravariant bases. If the components are denoted by  $v^i$  and  $v_i$  respectively, then

$$\underline{v} = v^i \underline{g}_i = v_i \underline{g}^i \quad (15)$$

Multiplying the last equation of (15) by  $\underline{g}_i$ ,  $\underline{g}^j$ , respectively, and making use of the definitions of  $\underline{g}_i$  and  $\underline{g}^i$  yields

$$v_j = g_{ji} v^i \quad (16)$$

$$v^j = g^{ji} v_i \quad (17)$$

An index of a general tensor is raised or lowered by  $g_{ij}$ ,  $g^{ij}$ , for example

$$t^{ik} = g^{kj} t^i_j$$

$$t_{ik} = g_{kj} t^j_i$$

Contravariant components and covariant components are generally different. They are equal only in Cartesian coordinates.

The vector  $\underline{v}$  is easily transformed from the curvilinear to the Cartesian coordinate system. Let  $\bar{v}^i = \bar{v}_i$  denote the components in the

Cartesian system and substitute (7) into the first equation of (15). Then the following can be identified

$$\bar{v}^j = \frac{\partial \xi^j}{\partial x^i} \cdot v^i \quad (18)$$

In a similar manner the natural transformation in the other direction can be obtained. It yields

$$v^j = \frac{\partial x^j}{\partial \xi^i} \bar{v}^i \quad (19)$$

The fundamental difference between contravariant and covariant components is that they are transformed in opposite directions by the transformation matrices  $\partial \xi^i / \partial x^j$  and  $\partial x^i / \partial \xi^j$ , that is

$$\bar{v}_j = \frac{\partial x^i}{\partial \xi^j} v_i \quad (20)$$

$$v_j = \frac{\partial \xi^i}{\partial x^j} \bar{v}_i \quad (21)$$

The process of differentiation involves a comparison of a quantity at points separated in space. In a curvilinear coordinate system the base vectors differ from point to point, so differentiation of a general tensor must take into account the change of the components and the base vectors. Consider a partial derivative of a vector  $\underline{v} = v^i \underline{g}_i$

$$\frac{\partial \underline{v}}{\partial x^j} = \frac{\partial v^i}{\partial x^j} \underline{g}_i + v^i \frac{\partial \underline{g}_i}{\partial x^j}$$

By the use of (7)

$$\frac{\partial \underline{g}_i}{\partial x^j} = \frac{\partial}{\partial x^j} \left( \frac{\partial \xi^k}{\partial x^i} \underline{e}_k \right) = \frac{\partial^2 \xi^k}{\partial x^j \partial x^i} \cdot \frac{\partial x^l}{\partial \xi^k} \underline{g}_l \quad (22)$$

The Christoffel symbols of the second kind are defined as

$$\Gamma^l_{ij} = \frac{\partial^2 \xi^k}{\partial x^i \partial x^j} \cdot \frac{\partial x^l}{\partial \xi^k} \quad (23)$$

From (22) it can be seen that if the  $i$ 'th base vector is differentiated in the  $j$ 'th direction the  $l$ 'th component of the change is  $\Gamma^l_{ij}$ .

It is the values of the geometric quantities at the grid points that are of interest in this work, rather than the functions themselves. Therefore it is convenient to derive analytical expressions for the derivatives

$\partial \xi^i / \partial x^j$  and  $\partial^2 \xi^i / \partial x^j \partial x^k$  from (6) and use their numerical values for calculating the metrics and the Christoffel symbols of the second kind. The components of the covariant metric tensor  $g_{ij}$  can be calculated directly from (14) and the components of the contravariant metric tensor  $g^{ij}$  by inversion of  $g_{ij}$ . The Christoffel symbols can be obtained from (23). The calculations are straightforward and are not presented here.

There are some features of the coordinate system which should be pointed out. The  $g_{ij}$  and  $g^{ij}$  are of course symmetric, as can be seen from (13). The component  $g_{23} = 0$  because of the



orthogonality in the  $x^1 = \text{constant}$  planes and on the symmetry planes  $g_{13} = 0$ . This implies that also  $g^{23} = g^{13} = 0$  on the symmetry planes. Further it can be shown that  $g^{11} = 1$ . From (23) it is seen that  $\Gamma_{jk}^1$  is symmetric in the two lower indices and it can be verified that  $\Gamma_{ij}^1 = 0$ .

The conformal transformation and the polynomial fitting may cause some waviness of the hull approximation and the coordinate system. To give an idea of the waviness due to the conformal transformation, the Christoffel symbol  $\Gamma_{23}^3$  is plotted in Fig. 7 as a function of  $x^3$  at  $\xi^1/(L/2) = 0.9$  and  $x^2 = 0$ . The sharp bend of the hull contour near the water line (Fig. 4) is reflected in the Fig. 7 as a spike. In Fig. 8 the Christoffel symbol  $\Gamma_{11}^2$  is plotted as a function of  $\xi^1/(L/2)$  for  $x^2 = 0$  and  $x^3 = -\pi/6$ , which gives a good indication of the waviness, due to the polynomial fitting. The low frequency of the waviness is remarkable, bearing in mind that the coefficients  $a_n$  are fitted by a polynomial of the 7'th degree.

There are several boundary layer methods which utilize the present transformation for representing the surface of the hull, for instance von Kerczek (1982), Himeno and Tanaka (1981) and Cebeci et al (1981). These methods do not suffer from the minor fluctuation in the hull representation, since the numerical integration of the flow equations smoothens the waviness. For the three-dimensional coordinate system used here there may occur waviness in other coordinate surfaces too. However, as pointed out in paragraph 2, the  $x^3$ -coordinate lines can be considered as perturbed circles with perturbations decreasing as  $1/r$ . The waviness in the transverse and normal directions are proportional to the perturbation terms and are thus reduced outside the hull. It may therefore be concluded that the influence of the waviness in the present method can be at the most of the same magnitude as in the boundary layer methods.

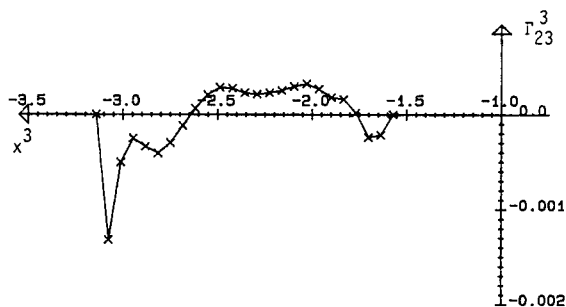


Fig. 7 The distribution of one of the Christoffel symbols around the girth.  
 $\xi^1/(L/2) = 0.9$ ;  $x^2 = 0$

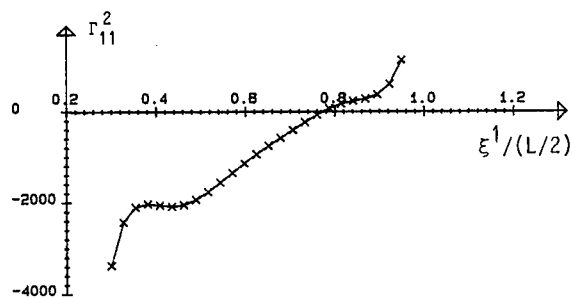


Fig. 8 The distribution of one of the Christoffel symbols around the girth.  
 $x^2 = 0$ ,  $x^3 = -\pi/6$

#### 4. GOVERNING EQUATIONS

As already pointed out, the main reason for the use of body fitted coordinate systems is that expressions for the boundary conditions are simplified. On the other hand, the transformed equations will contain more terms. For orthogonal curvilinear coordinate systems the transformed equations of motion and the derivation of the boundary layer equations can be found in Nash and Patel (1972). The equations transformed to the present body-fitted coordinate system (5) will contain more terms, due to the non-orthogonality. General tensor formalism is used in this paragraph to transform and derive the governing equations. One important advantage of this formalism is that it provides an effective way of handling the huge number of terms in the equations.

In this paragraph a partial derivative will be denoted

$$\partial_i = \frac{\partial}{\partial x^i}$$

and a covariant derivative will be denoted by the symbol  $\nabla_i$ . Let  $\varphi$  be a scalar and  $v^i$ ,  $t_j^i$  components of a first and second order tensor, respectively. With the notation introduced in paragraph 3 the covariant derivatives can be written:

$$\varphi_{;k} = \partial_k \varphi \quad (24)$$

$$v^i_{;j} = \partial_j v^i + \Gamma_{kj}^i v^k \quad (25)$$

$$t^i_{j;k} = \partial_k t^i_j + \Gamma_{kl}^i t^l_j - \Gamma_{ji}^l t^i_l \quad (26)$$

$$v^i_{;jk} = \partial_k \partial_j v^i + \Gamma_{kl}^i \partial_j v^l + \Gamma_{jl}^i \partial_k v^l - \Gamma_{jk}^l \partial_l v^i + v^l \cdot \partial_l \Gamma_{jk}^i \quad (27)$$

An useful definition is

$$v^i_{;k} \equiv g^{kj} v^i_{;j} \quad (28)$$

Let  $\rho$  be the density,  $v^i$  the contravariant velocity components,  $\tau^{ij}$  the contravariant components of the stress tensor and  $\phi^i$  the contravariant components of the volume forces. The equation of continuity and the equations of motion may then be written

$$\partial_t \rho + (\rho v^k)_{;k} = 0 \quad (29)$$

$$\rho \partial_t v^i + \rho v^k v^i_{;k} = \rho \phi^i + \tau^{ik}_{;k} \quad (30)$$

The Newtonian stress tensor components can be written as

$$\tau^i_j = - (P + \frac{2}{3} \mu v^k_{;k}) \delta^i_j + \mu (v^i_{;j} + v^j_{;i}) \quad (31)$$

where  $\mu$  is the viscosity and  $\delta^i_j$  is the Kronecker delta, see Yih (1969).

In the following it is assumed that the flow is incompressible and the volume force zero. It is also assumed that the flow is turbulent but steady in the sense that time mean values of the velocity components are constant. The instantaneous values can then be written as the sum of the time mean values and the turbulent fluctuations:

$$v^i = u^i + u'^i; P = p + p' \quad (32)$$

The equations for the time mean values are obtained by substituting (32) into (29-31) and taking the time average. This yields

$$u^k_{;k} = 0 \quad (33)$$

$$\mu u^k_{;k} = - \frac{1}{\rho} p_{;i} + \mu u^i_{;k}{}_{;k} - R^{ik}_{;k} \quad (34)$$

where  $R^{ik}$  are the contravariant components of the Reynolds stress tensor

$$R^{ik} = \overline{u'^i u'^k} \quad (35)$$

Introducing the expressions (24-28) for the covariant derivatives and substituting the  $g^{ij}$  and  $\Gamma^i_{jk}$  calculated in paragraph 3 the equations can be specialized to the body-fitted coordinate system. However, because of the second derivative in the viscous term, the equations become very lengthy and will not be written out here. In Broberg (1984) the equations are given for the partially parabolic approximation, but in this paper only the boundary layer equations will be considered.

As mentioned in the Introduction, three-dimensional boundary layer methods are based on two types of approximations. One is related to the coordinate system and the other to the equations of motion. In the present method the coordinate system is exact, while the common first order boundary layer approximations are made for the equations (33-35). It is thus assumed that

i. The  $x^2$ -equation can be replaced by  $\partial_2 p = 0$

ii. The only significant viscous terms are  $\nu g^{22} u^i_{;22}$

iii. The only significant Reynolds stress terms are  $g^{22} R^1_{2;2}$

This yields

$$\begin{aligned} & \partial_1 u^1 + \partial_2 u^2 + \partial_3 u^3 + (\Gamma^2_{21} + \Gamma^3_{31}) u^1 + \\ & + (\Gamma^2_{22} + \Gamma^3_{32}) u^2 + (\Gamma^2_{23} + \Gamma^3_{33}) u^3 = 0 \end{aligned} \quad (36)$$

$$\begin{aligned} & u^1 \partial_1 u^1 + u^2 \partial_2 u^1 + u^3 \partial_3 u^1 + \frac{1}{\rho} (\partial_1 p + g^{13} \partial_3 p) - \\ & - \nu g^{22} (\partial_2 \partial_2 u^1 - \Gamma^2_{22} \partial_2 u^1 - \Gamma^3_{22} \partial_3 u^1) + \\ & + g^{22} R^1_{2;2} = 0 \end{aligned} \quad (37)$$

$$\begin{aligned} & u^1 \partial_1 u^3 + u^2 \partial_2 u^3 + u^3 \partial_3 u^3 + \Gamma^3_{11} u^1 u^1 + 2 \Gamma^3_{21} u^2 u^1 + \\ & + 2 \Gamma^3_{31} u^3 u^1 + \Gamma^3_{22} u^2 u^2 + 2 \Gamma^3_{32} u^3 u^2 + \Gamma^3_{33} u^3 u^3 + \\ & + \frac{1}{\rho} (g^{31} \partial_1 p + g^{33} \partial_3 p) - \nu g^{22} (\partial_2 \partial_2 u^3 + 2 \Gamma^3_{21} \partial_2 u^1 + \\ & + 2 \Gamma^3_{22} \partial_2 u^2 + (2 \Gamma^3_{23} - \Gamma^2_{22}) \partial_2 u^3 - \Gamma^3_{22} \partial_3 u^3 + \\ & + \partial_1 \Gamma^3_{22} u^1 + \partial_2 \Gamma^3_{22} u^2 + \partial_3 \Gamma^3_{22} u^3) + g^{22} R^3_{2;2} = 0 \end{aligned} \quad (38)$$

The boundary conditions are

$$x^2 = 0; u^1 = u^2 = u^3 = 0, \quad (39)$$

$$x^2 \rightarrow \delta; u^1_{;2} = u^3_{;2} = 0, \quad (40)$$

and on the symmetry planes

$$u^1_{;3} = 0; u^3 = 0 \quad (41)$$

The Reynolds stress terms are modelled as follows

$$\begin{aligned} R^1_2 &= c \sqrt{q^2} L_D u^1_{;2} \\ R^3_2 &= c \sqrt{q^2} L_D u^3_{;2} \end{aligned} \quad (42)$$

$L_D$  is the dissipation length,  $q^2$  the double kinetic energy of the turbulence and  $c = -0.0225$ .

The model for the dissipation length, including the van Driest damping factor, is

$$\frac{L_D}{\delta} = \frac{7.175}{1 + 4\eta^4 + 5\eta} (1 - e^{-y^+/26}), \quad (43)$$

$y$  is the arc length along  $x^2$ , measured from the surface,  $\delta$  is the boundary layer thickness, and  $\eta = y/\delta$ . If the skin friction coefficient is denoted by  $c_f$ ,  $y^+$  can be written as

$y Q_e \sqrt{c_f/2} / \nu$ .  $Q_e$  is the speed at the outer edge.

The kinetic energy of the turbulence is determined from its transport equation

$$u^1 \partial_1 \overline{q^2}/2 + u^2 \partial_2 \overline{q^2}/2 + u^3 \partial_3 \overline{q^2}/2 + (g_{1j} R^{12} + g_{3j} R^{32}) u^j;_2 + \frac{q_{\max}^2}{Q_e} \frac{1}{\sqrt{g_{22}}} \partial_2 (a_2 \overline{q^2}) + \frac{(\overline{q^2})^{3/2}}{L_D} = 0 \quad (44)$$

where the diffusion and dissipation terms are modelled following Bradshaw (1971).  $q_{\max}^2$  is the maximum of  $\overline{q^2}$  in the outer three-fourths of the boundary layer. The diffusion constant,  $a_2$  is expressed as

$$a_2 = 1.125\eta^2 - 0.375\eta^4 \quad (45)$$

The boundary conditions are

$$x^2 = 0; \quad \overline{q^2} = 0 \quad (46)$$

$$x^2 \rightarrow \delta; \quad \overline{q^2} = 0 \quad (47)$$

and on the symmetry planes

$$\partial_3 \overline{q^2} = 0 \quad (48)$$

A finite difference method of the ADI type has been used to integrate the governing equations. The method has previously been used by Nash and Scuggs (1977), Patel and Choi (1979) and Johansson (1981). The numerical scheme is only briefly described in this paper. A more comprehensive description is given in Broberg (1984).

The equations of motion (37-38) and the transport equation for the turbulent kinetic energy (44) can be written in matrix vector form:

$$A_1 F + A_2 \partial_1 F + A_3 \partial_3 F + A_4 \partial_2 F + A_5 \partial_2 \partial_2 F + A_6 = 0 \quad (49)$$

$F$  is a three-dimensional vector containing  $u^1$ ,  $u^3$  and  $\overline{q^2}$ . The matrices of coefficients  $A_1$  to  $A_5$  are  $3 \times 3$  matrices and  $A_6$  is a three-dimensional vector.

These equations are solved simultaneously in a  $x^1 = \text{constant}$  plane. The equations are non-linear and therefore a local linearization technique is used, involving an iteration procedure which updates the coefficients of the partial differential equations until they are consistent with the converged values of the dependent variables. Within this iteration procedure the velocity components  $u^1$  and  $u^3$  are matched to the potential flow. The  $u^2$  component is calculated from the continuity equation (36) but is not involved in the matching procedure.

Let  $l$ ,  $m$ , and  $n$  denote index for the  $x^1$ ,  $x^2$ - and  $x^3$ - direction, respectively. If the solution in the previous section  $x^1, l-1$  is known, the second order finite difference approximation of (49) can be written:

$$B_1 F_{m+1,n}^1 + B_2 F_{m,n+1}^1 + B_3 F_{m,n}^1 + B_4 F_{m-1,n}^1 + B_5 F_{m,n-1}^1 = B_6 \quad (50)$$

where  $B_1 - B_5$  are square matrices containing linear combinations of the  $A$ 's in (49) and  $B_6$  is a vector, which also contains values of  $F$  and  $\partial_1 F$  at  $l-1$ . The ADI method scans the cross-plane alternatingly in the  $n$ -, and  $m$ -directions. During the scan in the  $n$ -direction  $F_{m,n+1}^1$  are taken from the last solution. Moving the passive terms of equation (50) to the right-hand side it will represent a recursion relationship for  $F$  on the line  $n$ -constant,  $1 \leq m \leq M$

$$B_1 F_{m+1,n}^1 + B_3 F_{m,n}^1 + B_4 F_{m-1,n}^1 = C_1 \quad (51)$$

In the same way,

$$B_2 F_{m,n+1}^1 + B_3 F_{m,n}^1 + B_5 F_{m,n-1}^1 = C_2 \quad (52)$$

will represent a recursion relationship for  $F$  on the line  $m = \text{constant}$ ,  $1 \leq n \leq N$  during the scan in the  $m$ -direction. In both cases the sequence of equations (51-52) leads to a linear system of  $M$  or  $N$  equations. The matrix of the system is tridiagonal, and is solved using a extended Choleski method.

## 5. CALCULATIONS

The input data for the test calculations have been generated by an improved version of the indata program from the SSPA-ITTC Workshop, see Larsson (1981). This program uses algebraic formulae for the velocity and turbulent kinetic energy. Indata are the boundary layer thickness  $\delta$ , the wall cross-flow angle  $\beta_w$  and the friction velocity  $u_\tau$ .

The indata program generates a  $\overline{q^2}$ -profile which is not smooth because different algebraic formulae are used in different regions. If the boundary layer program is started using such a  $\overline{q^2}$ -profile it takes about 1-2 boundary layer thicknesses downstream until the profile is smoothed out. Therefore a smoothing technique, similar to the one used by Johansson (1981) at the SSPA-ITTC Workshop has been applied. The initial profiles from the indata program are taken as a guess of the solution at the first new station, so that the program can calculate a solution at this station. The  $\overline{q^2}$ -profiles of this solution are then taken as initial profiles and the program is restarted. After 2-3 restarts the  $\overline{q^2}$ -profiles are much smoother, and the profiles are more consistent with the turbulence model of the method.

Calculations were first carried out for the boundary layer on a flat plate and along a circular cylinder. Various grids were tested for zero and non-zero pressure gradients and the results were quite good, see Broberg (1984).

The next test case was the SSPA Model 720, also used in the Workshop, see Larsson (1981). In order to obtain indata for the generated grid

the  $x^2$ -axis was considered a normal to the hull in the indata plane. As appears from Fig. 5. This is a good approximation, if this plane is not too close to the stern.

The calculations were started at  $\xi_1/(L/2) = 0.3$  (at 65% of the model length) using 43 grid points in the normal direction and 25 in circumferential direction. There are two reasons to start so "far" from the stern region: the indata program can be used with good results and the distance downstream to the point where the difficulties start is long enough to reduce the sensitivity of the indata. The initial profiles were generated for  $\beta_w = 0$ , a constant value of  $\delta$  and  $u_\tau$ . Interpolated values of  $\delta$  and  $u_\tau$  from measurements were also tried. These gave very small improvements of the results, except at the keel where the results were improved considerably.

The potential flow at any point outside the hull was calculated by the Hess and Smith method (1962). When the  $u^1$ - and  $u^3$ -components were matched to the potential flow at the outermost point, instabilities could occur in the solution outside the boundary layer. More precisely, they occurred if the boundary layer was much thinner than the computational grid (at least 6-10 grid points outside the boundary layer) and if the flow was not strongly divergent. The instabilities can be explained by the small amount of diffusion in this region and by the fact that the artificial viscosity introduced by the difference formulae is too small compared to the relatively big step size in the normal and circumferential directions. Therefore, the velocity components were matched at the point located 3-4 points outside the boundary layer and the solution outside this point was substituted by the potential solution. (The velocity component  $u^2$  is not involved in the matching procedure.)

To achieve good accuracy in the forward marching direction the step size had to be very small at the beginning. Thereafter it was increased to the order of the boundary layer thickness. At the start of the calculation, using indata from the indata program, the iteration process required about 6-8 iterations but after 2 or 3 stations 3-5 were sufficient. Further astern the process again needed more iterations, and in order to achieve faster convergence the step size was reduced by 10% if the required number of iterations exceeded 8. If the iteration process failed the step size was reduced by 30% and if it was larger than a minimum value the program was restarted from the previous station. A frequent reason for slow convergence was that the scans in the two directions found different solutions, which converged slowly towards each other.

The pressure distribution is of great importance near the stern and to study its effects three different distributions were used. The pressure distributions A and B were calculated from the potential flow at surfaces  $x^2$ -constant, the first one fairly close to the hull and the second one very close to the outer edge. The pressure distribution C was interpolated from measurements on the surface, Larsson and Johansson (1982). The three distributions are

plotted in Fig. 9 as functions of  $x^3$  at four stations,  $\xi_1/(L/2) = 0.5, 0.7, 0.8, 0.9$ . Note that  $x^3 = -\pi$  corresponds to the water line and  $x^3 = -\pi/2$  to the keel and that a constant increment  $x^3$  does not correspond to a constant length. The curve is thus stretched at the ends, which means that the changes in the central part look more drastic than they really are. The pressure distribution B is very smooth as could be expected and A is in better correspondence with C, particularly at the stations  $\xi_1/(L/2) = 0.5$  and  $0.7$ .

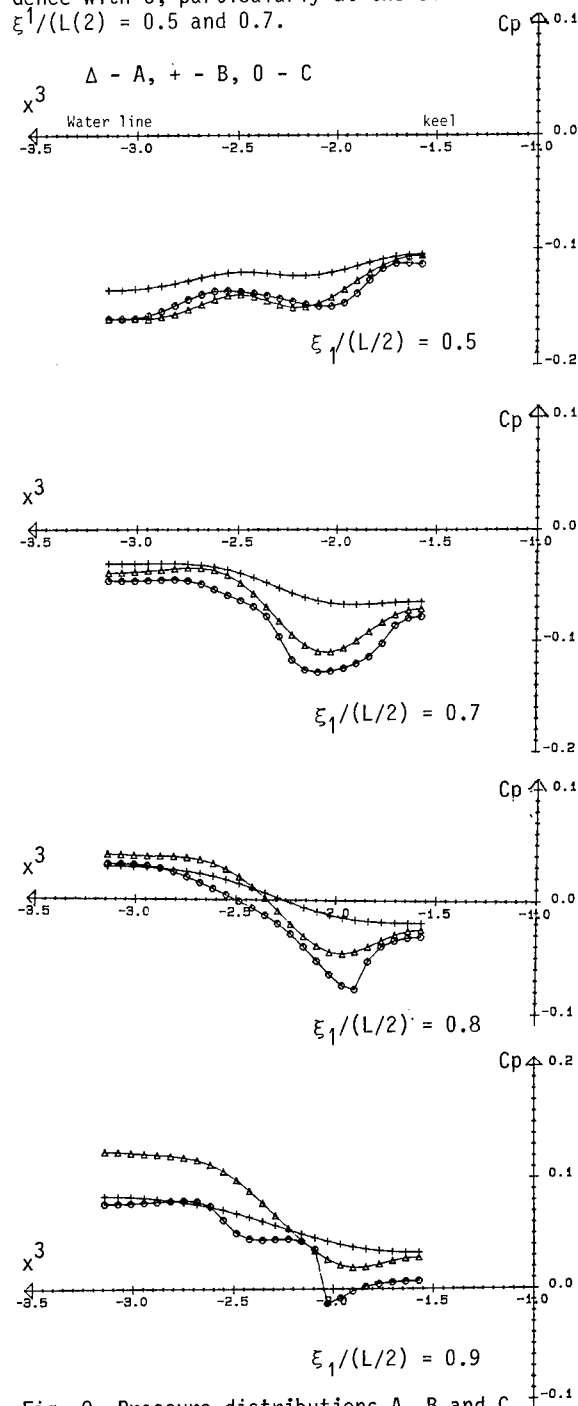
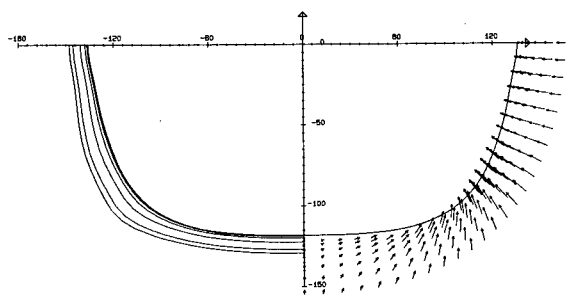
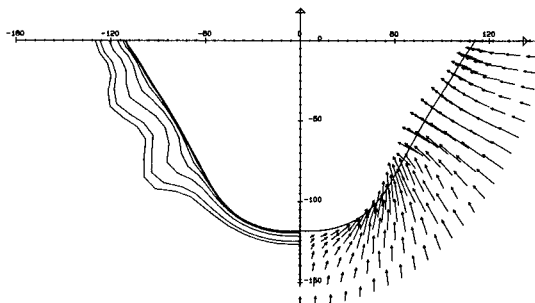


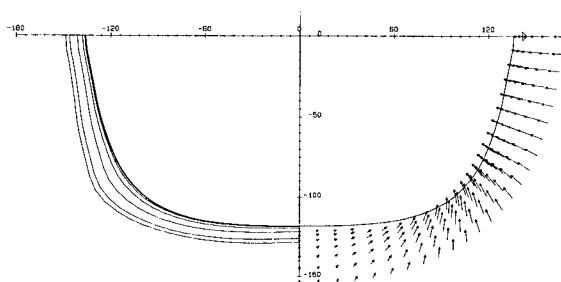
Fig. 9. Pressure distributions A, B and C.



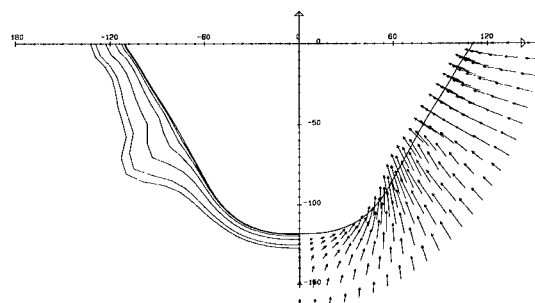
Calculation A.  $Q/Q_{inf} = 0.5, 0.6, 0.7, 0.8, 0.9, 0.95$



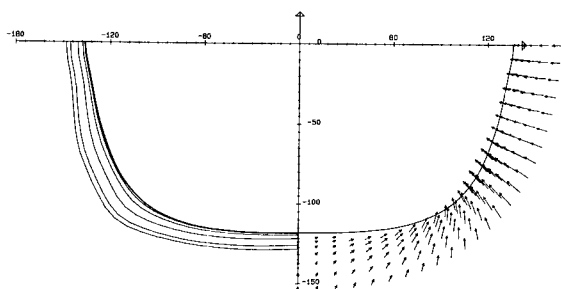
Calculation A.  $Q/Q_{inf} = 0.5, 0.6, 0.7, 0.8, 0.9, 0.95$



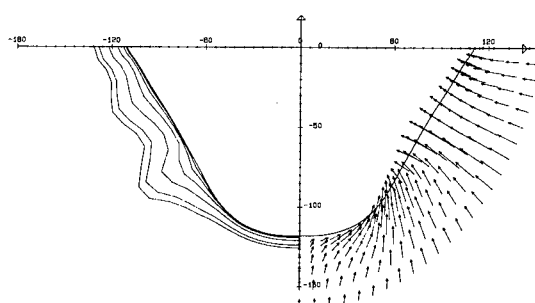
Calculation B.  $Q/Q_{inf} = 0.5, 0.6, 0.7, 0.8, 0.9, 0.95$



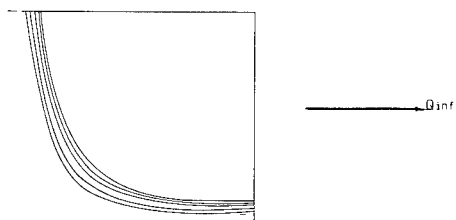
Calculation B.  $Q/Q_{inf} = 0.5, 0.6, 0.7, 0.8, 0.9, 0.95$



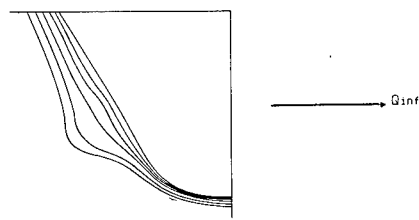
Calculation C.  $Q/Q_{inf} = 0.5, 0.6, 0.7, 0.8, 0.9, 0.95$



Calculation C.  $Q/Q_{inf} = 0.5, 0.6, 0.7, 0.8, 0.9, 0.95$



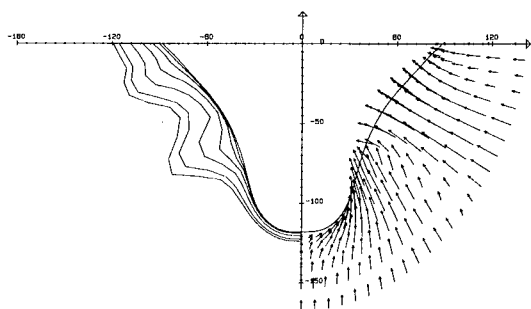
Measurements.  $Q/Q_{inf} = 0.7, 0.8, 0.9, 0.95$



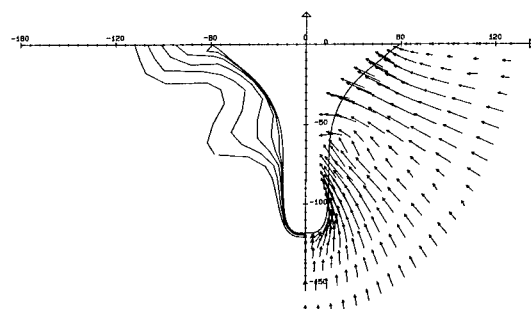
Measurements.  $Q/Q_{inf} = 0.6, 0.7, 0.8, 0.9, 0.95$

Fig 11. Calculations and measurements at  $\xi^1/(L/2) = 0.5$

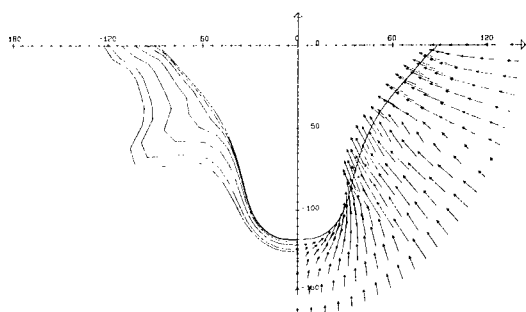
Fig 12. Calculations and measurements at  $\xi^1/(L/2) = 0.7$



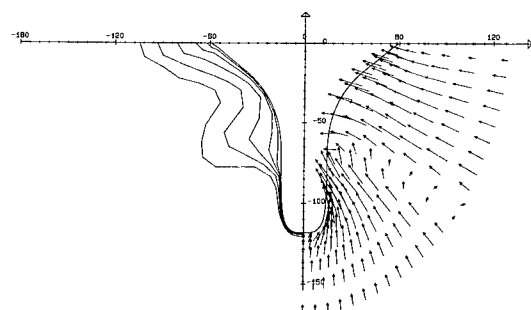
Calculation A.  $Q/Q_{inf} = 0.5, 0.6, 0.7, 0.8, 0.9, 0.95$



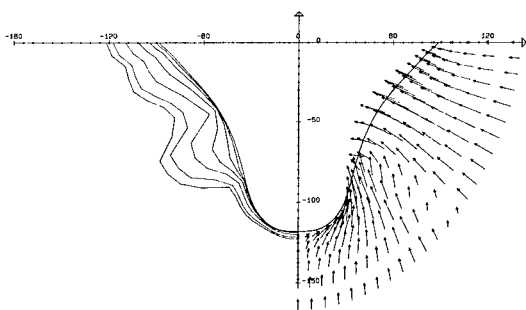
Calculation A.  $Q/Q_{inf} = 0.5, 0.6, 0.7, 0.8, 0.9$



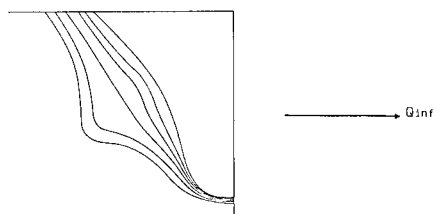
Calculation B.  $Q/Q_{inf} = 0.5, 0.6, 0.7, 0.8, 0.9, 0.95$



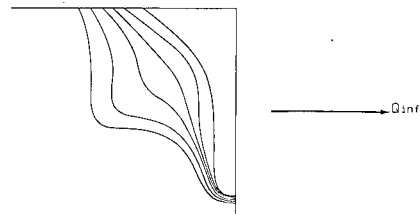
Calculation C.  $Q/Q_{inf} = 0.5, 0.6, 0.7, 0.8, 0.9$



Calculation C.  $Q/Q_{inf} = 0.5, 0.6, 0.7, 0.8, 0.9, 0.95$



Measurements.  $Q/Q_{inf} = 0.6, 0.7, 0.8, 0.9, 0.95$



Measurements.  $Q/Q_{inf} = 0.6, 0.7, 0.8, 0.9, 0.95$

Fig 13. Calculations and measurements at  $\xi^1/(L/2) = 0.8$

Fig 14. Calculations and measurements at  $\xi^1/(L/2) = 0.9$

Since the calculations were carried out using a non-orthogonal curvilinear coordinate system it is difficult to present the solutions in terms of integral parameters. Instead the results are represented by the isowakes based on the speed  $Q = u^1 u_1$  and by the secondary flow (the projection of the velocity on to the plane  $x^1 = \text{constant}$ ). Note that the velocity is made dimensionless by the undisturbed speed  $Q_{inf}$ .

The calculated results are given in Figs 11, 12, 13 and 14, each one showing the isowakes and the secondary flow at one particular cross-section  $\xi^1 = \text{constant}$ . The sections are  $\xi^1/(L/2) = 0.5, 0.7, 0.8$ , and  $0.9$ . For comparison isowakes computed from Larsson's measurements by Larsson and Johansson (1982) are also shown.

At  $\xi^1/(L/2) = 0.5$ , all results are very nearly the same, while at  $0.7$  differences start to occur. The pressure distribution B seems to yield results which correspond better with the measurements than those of A and C. All results are, however, reasonably good.

At  $\xi^1/(L/2) = 0.8$ , calculation B still produces the best results while the A and C results are too irregular. Note that these two cases have the largest cross-wise pressure gradients, which are obviously responsible for the variations. There seems to be no influence of waviness in the coordinate system.

From Fig. 13 it is possible to see that the flow close to the waterline approaches separation in calculation B. This calculation could not be carried further than  $\xi^1/(L/2) = 0.86$ . Results are, however, available to the two other cases up to  $\xi^1/(L/2) = 0.9$ , Fig. 14. At that position both are close to separation at the waterline. Obviously the variations are to large girthwise, but the position of maximum thickness seems to be about right. It might be considered somewhat surprising that the measured pressure distribution on the surface did not produce better results than the theoretical one of case A. A possible explanation for this is the effect of the boundary layer approximation  $\partial^2 p = 0$ , which will be removed in further work.

#### ACKNOWLEDGEMENT

The present project has been carried out in cooperation between the Division of Mechanics Chalmers University of Technology and the SSPA Maritime Research and Consulting AB, and has been partially supported by the Swedish Board for Technical Development, Contract No 81-4313.

The authors are indebted to those members of the staffs of Chalmers and SSPA, who have participated in the project. Special thanks are extended to Professor Bengt Holmberg for many helpful discussions.

#### REFERENCES

Bradshaw, P. (1971): Calculation of Three-Dimensional Turbulent Boundary Layers. *Journal of Fluid Mechanics*, Vol. 46, Part 3.  
 Broberg, L. (1984): Calculation of Ship Stern Flows Using a Body-Fitted Coordinate System. Part I: Development of the Coordinate

System. Stern Flow Calculations Based on the Boundary Layer Approximation, Chalmers University of Technology, Division of Mechanics.  
 Cheng, W.S., Patel, W.C. (1983): Numerically Generated Coordinates Suitable for Ship Stern and Wake Flow Calculations. US-Japan Cooperative Research on Viscous Flow around Ships, Iowa Institute of Hydraulic Research, Report No 265.  
 Cebeci, T., Chang, K.C., Kaups, K. and Bartels, F. (1981): Computed Results for Two Ship Hulls by the C<sup>2</sup>K method, SSPA-ITTC Workshop on Boundary Layers - Proceedings, SSPA-Publication No 90.  
 Hess, J.L. and Smith, A.M.O. (1962): Calculation of Non-Lifting Potential Flow About Arbitrary Three-Dimensional Bodies, Douglas Aircraft Division, Report No. ES. 40622.  
 Himeno, Y. and Tanaka, I. (1981): Calculation Using the Method by Himeno and Tanaka, SSPA-ITTC Workshop on Boundary Layers - Proceedings, SSPA-Publication No 90.  
 Ives, D.C. (1982): Conformal Grid Generation, *Applied Mathematics and Computation*, Vol. 10 and 11, pp. 107-135.  
 Johansson, L.E. (1981): Ship Boundary Layer Calculation using an Alternating Direction Implicit Method, SSPA-ITTC Workshop on Ship Boundary Layers 1980. SSPA-Publication, No 90.  
 Johansson, L.E. and Larsson, L. (1983): Calculations of Thick Boundary Layers Using a Streamline Curvature Method, Proceedings of the Second Symposium on Numerical and Physical Aspects of Aerodynamic Flows, Long Beach.  
 Larsson, L. (1976): An Experimental Investigation of the Three-Dimensional Turbulent Boundary Layer on a Ship Model, Proceedings of the 11th Symposium on Naval Hydrodynamics, London.  
 Larsson, L. (1981): SSPA-ITTC Workshop on Boundary Layers - Proceedings, SSPA-Publication No 90.  
 Larsson, L. and Chang, M-S. (1980): Numerical Viscous and Wave Resistance Calculations Including Interaction, Proceedings of the 13th Symposium on Naval Hydrodynamics, Tokyo.  
 Larsson, L. and Johansson, L.E. (1982): A Streamline Curvature Method for Computing the Flow Near Ship Sterns, Proceedings of the 15th Symposium on Naval Hydrodynamics, Ann Arbor.  
 Miao, G. (1980): On the Computation of Ship Motions in Regular Waves, Chalmers Univ. of Technology, Division of Ship Hydromechanics Report No. 58.  
 Nash, J.F. and Patel, V.C. (1972): Three-Dimensional Turbulent Boundary Layers, SCB Technical Books.  
 Nash, J.F. & Scruggs, P. (1977): An Automated Procedure for Computing the Three-Dimensional Transonic Flow over Wing-Body Combinations, Including Viscous Effects, Vol. III. An Implicit Method for the Calculation of Three-Dimensional Boundary Layers on Finite, Thick Wings, SYBUCON INC.,

- Technical Report AFFDL-TR-77-122, Vol. III.
- Odabasi, A.Y. and Davies, M.E. (1983): Structure of the Turbulent Shear Flow in Ship Boundary Layers, Proceedings of the Second Symposium on Numerical and Physical Aspects of Aerodynamic Flows, Long Beach.
- Patel, V.C. and Choi, D.H. (1979): Calculations of Three-Dimensional Laminar and Turbulent Boundary Layers on Bodies of Revolution at Incidence, Second International Symposium on Turbulent Shear Flows, London.
- Report of the 17th ITTC Resistance Committee, (1984) Göteborg.
- Spalding, D.B. (1981): A General Purpose Computer Program for Multi-Dimensional One- and Two-Phase Flow. Mathematics and Computers in Simulation, North Holland Press. Vol. XXIII.
- Tzabiras, G. and Loukakis, T. (Jan. 1983): A Method for Predicting the Flow around the Stern of Double Ship Hulls. National Technical University of Athens, Department of Naval Architecture and Marine Engineering.
- von Kerczek, C. (1982): A New Generalized Cross-Flow Momentum Integral Method for Three-Dimensional Ship Boundary Layers, Science Applications, Inc., Report No. SAI-463-82-085-LJ.
- Yih, C-S. (1969): Fluid Mechanics. McGraw-Hill Book Company.

## DISCUSSION

Dr. MING S. CHANG,  
David Taylor Naval Ship R&D Center,  
Bethesda, MD, USA:

Your success in the development of an analytical body-fitted coordinate system for ship stern flows is a significant contribution in the stern flow computation. Could the authors clarify the following questions:

1. Equation (40) states that the boundary condition of numerical method is the velocity gradient being zero at the edge of the boundary layer. However, the matching of the potential-flow solutions with the computed boundary layer results was used in the calculation procedure. The velocity gradient computed by the potential-flow solutions at the edge of the boundary layer is not zero.

2. A few streamwise vortices can be identified around the edge of the boundary layer in Fig. 13 and 14. At the edge of boundary layer the boundary-layer solutions were matched to the potential-flow solutions, which should not allow solutions with streamwise vortices.

3. The comparison of the measured and calculated results shows that the measured results are in between the results computed from streamwise pressure distributions of B and C. Why is it so? How do you include the normal pressure distribution across the boundary layer in your computation procedure?

## AUTHORS' REPLY

It should be stressed that the present method is still essentially based on the usual boundary layer approximations. The important improvement as compared with ordinary boundary layer methods is that the coordinate system is now exact. As in other boundary layer methods there is no matching in the normal gradient of the velocity between the potential and boundary layer flows. The treatment of the outer boundary condition is not fully explained in the paper. It is as follows: First the viscous region equations are solved all the way to the outer edge of the grid using the boundary condition given in the paper. Thereafter the boundary layer edge is determined (usually well inside the computational region) and the  $u^1$  and  $u^3$  components of velocity at the edge are computed using potential theory. The corresponding components inside the boundary layer are then multiplied by the ratio of potential flow and actually computed values at the edge. Outside this all  $u^1$  and  $u^3$  components are replaced by the potential flow values. Finally the  $u^2$  component at all points is obtained from an integration of the continuity equation outwards from the surface.

Due to the fact that the pressure is constant across the boundary layer, the  $u^2$  component of velocity sometimes becomes too large, which will also influence this component in the computational region outside the boundary layer.

The pressure distribution B is computed using potential flow theory at a location which should correspond to the outer part of the boundary layer. This distribution might represent the pressure in the entire layer better than the measured pressure on the hull.



## UTILIZATION OF WAVE ENERGY INTO PROPULSION OF SHIPS - WAVE DEVOURING PROPULSION -

HIROSHI ISSHIKI<sup>†</sup>, MITSUNORI MURAKAMI<sup>†</sup> AND YUTAKA TERAOKA<sup>††</sup>

### ABSTRACT

A possibility of utilization of wave energy into propulsion - Wave Devouring Propulsion or WDP - is discussed. To the naval architects, the concept seems to be unfamiliar, since resistance of a ship in waves becomes considerably higher than that in calm water, and the phenomenon is well known to them as resistance increase in waves.

In the present paper, an example of a floating body which moves against waves without any power supply from outside is introduced. In order to clarify the basic aspect of the phenomenon, an oscillatory hydrofoil propulsor which is driven by wave energy and generates thrust is also investigated experimentally. The thrust generation is verified, and the amount of thrust is measured. Some theoretical discussion is also given on the model.

A possibility of easing average and slowly varying components of wave drift force acting on a moored ocean platform through utilization of the above mentioned phenomenon is discussed briefly.

### 1. INTRODUCTION

In general, resistance of a ship in waves becomes considerably higher than that in calm water. The fact is too well known to the naval architects as the phenomenon of resistance increase in waves. Hence, a possibility of utilization of wave energy into propulsion - Wave Devouring Propulsion or WDP - has long been ignored by them. According to the author's survey, some inventions, observations and investigations related to the possibility have been reported as described below.

Surprisingly enough, in 1895, Linden (Ref. 1) filed a British patent. According to the contemporary report, he really built a boat of 13 ft in length named Autonaut, and the boat could move of her own motion due to waves against wind and wave at a speed of three to four knots. Unfortunately, much attention does not seem to have been paid to the invention.

Huse (1977) reports that, for certain platforms and sea states, model tests have shown the towing resistance in head seas to be smaller than in calm water. He explains the phenomenon by introducing viscous drag force.

Longuet-Higgins (1977) gives an example of a submerged body like a sand bar which moves against short and steep waves at a mean speed of 1.2 m/s when wave breaking takes place behind the body. According to him, this phenomenon is qualitatively similar to "the well known behavior of offshore sand-bars". He proposes a theory on the basis of the energy and momentum balance when the wave breaking takes place.

Recently, Jakobsen (1981) published an interesting paper about his experiment. According to his paper, a model ship of 1.03 m in length moved against a wave of wave length 2.25 m and wave height 0.1 m at a speed of about 1 m/s by utilizing wave energy alone. The speed may be surprisingly high.

One of the authors (Terao (1982)) found by chance a floating body which moves against waves at fairly high speed, when he was conducting experiments on a floating breakwater. Some experiments are newly conducted, and the results are discussed in §3.

On the other hand, Wu (1972) first discussed, without knowing Linden's experiments, the problem on utilization of wave energy into propulsion, and he showed theoretically that propulsive efficiency in waves can become more than one or even minus if an oscillatory hydrofoil propulsor is used. The negative propulsive efficiency means that the power put into the propulsor becomes minus and the surplus energy is taken outside. According to Wu, the optimization of foil motions is the most important for the efficient conversion of wave energy. A method to obtain the optimized foil motions is shown in his paper.

Since Wu's idea aims at direct conversion of wave energy into propulsive one through an oscillatory hydrofoil, the hydrofoil should be placed near the free surface. This may suggest that the free surface effect should not be neglected, but the effect is not included in

<sup>†</sup> Technical Research Institute, Hitachi Zosen Corp.; Sakurajima 1-Chome, Konohana-ku, Osaka 554  
<sup>††</sup> Dept. of Naval Architecture, Tokai University; 20-1, Orido 3-Chome, Shimizu, Shizuoka 424

Wu's theory. An approximate treatment of the free surface effect and the results are discussed by Isshiki (1982a,b).

In order to make the above mentioned theoretical and experimental results more clear, some basic experiments were conducted on "a passive-type oscillatory hydrofoil propulsor" as shown in Fig.23 by Isshiki et al (1983). The thrust generation by an oscillatory hydrofoil in waves was verified experimentally, and the amount of thrust was shown. Some of the results are included in §4.1 of the present paper. Since the above mentioned experiments were conducted in a short wave range, some experiments have been added to clarify the performance of the propulsor in a longer wave range, and the results are discussed in §4.2 in comparison with the results in §4.1.

Some theoretical calculations are also conducted for the above mentioned hydrofoil propulsor on the basis of Wu's theory (Wu (1972)). The comparison with experiments shows a rather good correlation in the case cited (§4.3), though the free surface effect is not satisfied.

The theoretical results obtained under an assumption that wave energy is absorbed completely and converted into propulsive energy as much as possible by "a wave devouring propulsor" are discussed in §2. According to the results, the idea of wave energy utilization into propulsion -wave devouring propulsion- seems to be promising, if the assumption is fulfilled.

Recently, Ogilvie (1983) has pointed that thrust generation through utilization of wave energy may be applied to reduce average and slowly varying components of wave drift force acting on a moored ocean platform. So, thrust generation by an oscillatory hydrofoil at bollard condition is also discussed.

## 2. POTENTIAL POSSIBILITY OF AN IDEALIZED WAVE DEVOURING PROPULSION

An "idealized" wave devouring propulsion refers to a wave devouring propulsion which absorbs wave energy completely and converts as much energy as possible into propulsive energy.

Let  $P_W^*$  be wave power per unit breadth of an incoming wave of wave amplitude  $a$  and wave length  $\lambda$ . Then,  $P_W^*$  is given as

$$P_W^* = \frac{1}{2} \rho g a^2 \left( \frac{1}{2} \sqrt{\frac{\lambda g}{2\pi}} + U \right) \quad (1)$$

for a deep water, where  $\rho$ ,  $g$  and  $U$  are density of water, gravitational acceleration and advance speed respectively. If the complete conversion of wave energy into propulsive one is assumed, an ideal thrust per unit breadth  $\bar{T}_i^*$ :

$$\bar{T}_i^* = P_W^* / U = \frac{\rho g}{2} a^2 \left( 1 + \frac{1}{2U} \sqrt{\frac{\lambda g}{2\pi}} \right) \quad (2)$$

may be obtained. This, however, is impossible. In case of complete absorption of wave energy, the wave drift force per unit breadth  $\Delta R^*$ :

$$\Delta R^* = \frac{\rho g}{4} a^2 \quad (3)$$

must be subtracted from  $\bar{T}_i^*$ . Hence, the thrust per unit breadth  $\bar{T}^*$  is obtained as

$$\bar{T}^* = \bar{T}_i^* - \Delta R^* = \frac{\rho g}{4} a^2 \left( 1 + \frac{1}{U} \sqrt{\frac{\lambda g}{2\pi}} \right), \quad (4)$$

and the wave devouring efficiency  $\eta_W^*$  may be written as

$$\eta_W^* = \bar{T}^* U / P_W^* = \frac{1}{2} \left( 1 + \frac{1}{U} \sqrt{\frac{\lambda g}{2\pi}} \right) / \left( 1 + \frac{1}{2U} \sqrt{\frac{\lambda g}{2\pi}} \right). \quad (5)$$

$\eta_W^*$ , therefore, is independent of the incoming wave amplitude  $a$  and has the following nature:

$$\eta_W^* \rightarrow \begin{cases} 1 \\ 1/2 \end{cases} \quad \text{when } U \rightarrow \begin{cases} 0 \\ \infty \end{cases} \quad (6)$$

Figs.1 and 2 show some numerical results of  $\bar{T}^*$  and  $\eta_W^*$ . These results are calculated under an assumption that the wave devouring propulsor is attached to a model ship of about 2 m in length. According to the results, the potential possibility of wave devouring propulsion may not be denied.

## 3. EXPERIMENTS ON H-TYPE WAVE DEVOURING PROPULSOR

In this section, some experimental results of H-type wave devouring propulsor or H-type model are shown. The model was found by chance when one of the authors (Terao (1982)) was conducting experiments on a floating breakwater. The results discussed below were obtained recently by using a more refined model and measuring device.

### 3.1 Model and Experimental Apparatus

The model particulars and shape are shown in Tab.1 and Fig.3. The model consists of an upper hydrofoil, fore and aft lower hydrofoils and two side plates. The upper and lower foil sections are NACA-1410 and NACA-0015 respectively. The model is named "H-type", since the two side plates and upper foil forms a cross section like an alphabetic letter "H".

The model moves against incident waves in head seas in a wide range of wave frequency. In following seas, the model, however, moves in the direction of wave propagation at speed faster than that usually observed as a result of wave drift force.

The experimental apparatus is shown schematically in Fig.4. The size of the tank is 25 m x 1 m x 0.7 m (LxBxD), and a piston-type wave maker is equipped at one end of the tank. A servomechanical carriage is adopted to measure the heave, pitch and surge of the model. The carriage can follow the surge of the model without applying any significant external resistance to the model. The incident and transmitted wave heights are measured with wave probes before and behind the model respectively.

### 3.2 Results of Experiments on H-Type Model

#### 3.2.1 Performance of H-Type Model in Calm Water

The lift, drag and moment which act on the H-type model in calm water are measured in a circulating water tunnel. The results are shown in Fig.5, where  $C_L$ ,  $C_D$  and  $C_M$  refer to the coefficients of lift  $L$ , drag  $D$  and moment  $M$  (about midchord of the upper foil) respectively. The coefficients are non-dimensionalized with the chord  $2\lambda$  and span  $b$  of the upper foil. The lift and moment are positive into vertically upward and nose up directions respectively.

When the draft is decreased and no water flows over the upper surface of the upper foil, the lift and moment are very small. On the other hand, once the model has enough draft to make the water pass over the upper surface, they become very big. It should be noticed that quite a big lift force is generated even when the thickness of water layer above the upper surface is very small. This may suggest that the lift force plays an important role in generating thrust in waves.

#### 3.2.2 Experimental Parameters for Experiments in Waves

Based on the experience in the preceding experiments (Terao (1982), Isshiki et al (1983)), the position and the attack angle of the aft lower foil and the position of the center of gravity are chosen as experimental parameters. They are changed as follows:

- a) Position of the aft lower foil  
... A, B, C (Fig.3)
- b) Attack angle of the aft lower foil  
...  $-5^\circ$ ,  $-8^\circ$ ,  $-11^\circ$ ,  $-14^\circ$  (in the nose up direction)
- c) Center of gravity  
... high and low (Tab.1)

The experimental conditions I~IV are defined in Tab.2. The attack angle of the fore lower foil is  $0^\circ$ , and that of the upper foil is  $4.2^\circ$  in nose up direction.

The model is given an initial bow up trim to cancel the nose down moment which acts on the model when it moves at a constant forward speed. The amount of trim required for the experimental conditions I~IV are  $2.6^\circ$ ,  $8.9^\circ$ ,  $9.5^\circ$  and  $9.6^\circ$  respectively.

#### 3.2.3 Advance Speed

Fig.6 is an example of oscillograph records. The advance speed is obtained by analyzing the surge record, and the results are shown in Figs.7~10.

In these figures,  $\hat{U}$  is a kind of non-dimensional advance speed defined as

$$\hat{U} = U^2 \cdot 2l / (g\alpha^2). \quad (7)$$

This definition corresponds to a ratio of thrust to wave drift force, since the resistance is proportional to  $\rho U^2$  as shown in Fig.5 and the wave drift force is proportional to  $\rho g \alpha^2$  as discussed in §2.

The advance speed is very sensitive to the

position and the attack angle of the aft lower foil as shown in Figs.7~10. Figs.7 and 8 show the effects of the position of the center of gravity, and Figs.8~10 refer to those of the position of the aft lower foil. The maximum of the advance speed is obtained for condition II as shown in Fig.8. In Figs.7 and 8, peaks of the advance speed are present at  $\lambda/2\lambda \approx 2$ . On the other hand, the advance speed is slower for condition III and IV than for condition I and II, and the effect of the wave length on the advance speed becomes less eminent. In Fig.9, the peak position and value are strongly affected by the attack angle of the aft lower foil. The wave length at the peak becomes longer, as the attack angle increases.

#### 3.2.4 Heave and Pitch Motions

The heave and pitch motions are measured at the midchord of the upper foil. The heave amplitude  $Z$  and the pitch amplitude  $\theta$  are shown in Figs.11~13 and Figs.14~16 respectively. Comparing these figures with those for the advance speed, the heave motion has more significant effects on the advance speed than the pitch motion.

The phase lag of pitch from heave is given in Figs.17~19. The phase lag decreases from  $120^\circ$  to  $90^\circ$ , as the wave length increases.

#### 3.2.5 Transmitted Waves

If a reflected wave is assumed to be small, a quantity  $1 - |a_t/a|^2$ , where  $a_t$  is the amplitude of the transmitted wave, may give "a measure" of wave energy absorption. The quantity is shown in Figs.20~22.

From these figures, it is clear that the transmitted wave amplitude increases as the wave length becomes longer. This means that the less wave energy is utilized in longer waves. On the other hand, there exist obvious peaks in Figs.20 and 21. This may correspond to the high advance speed observed in the wave length range of  $\lambda/2\lambda$  between 2 and 4.

An oscillograph record of the transmitted wave is given in Fig.6. The wave pattern is sinusoidal, and the biharmonic frequency component seems to be negligible in the pattern. This suggests that the thrust due to the wave breaking (Longuet-Higgins (1977)) may be small and the unsteady lift force may play an dominant role in generating thrust.

### 4. BASIC EXPERIMENTS AND SOME THEORETICAL CONSIDERATIONS ON A PASSIVE-TYPE OSCILLATORY HYDROFOIL PROPULSOR

In order to clarify the basic aspects of Wave Devouring Propulsion or WDP, an experimental device is made specially. The device consists of a hydrofoil and heave-pitch-motion-mechanism as shown in Figs.23 and 36. Heave and pitch springs are attached to give a restoring force and moment to the heave and pitch motions respectively. The wave energy is absorbed directly by the hydrofoil and converted into the propulsive energy through the same foil. No power is supplied from outside and the foil is

driven by wave force alone. So, the device is called "passive-type".

The purpose of the experiments discussed in this section is to verify the direct conversion of wave energy into propulsive one through an oscillatory hydrofoil and to measure the amount of thrust.

#### 4.1 Experiments in a Short Wave Range ...Model I

At first, experiments in a short wave range (Isshiki et al (1983)) are discussed below. The model used in the experiments is called model I.

The experimental system is shown in Fig.23. Rails of about 7.5 m in length are laid on both sides of a two-dimensional wave making tank of 25 m in length and 1 m in breadth, and a carriage of 1 m in length is set movable on the rails. For measurement of the thrust delivered to the carriage, the carriage is composed of main and sub carriages, and a load cell is set between both carriages. A gravity-type towing device is used to change the velocity of the carriage. A two-dimensional hydrofoil is set under the carriage, and the half chord  $l$  and the span  $b$  are 0.2 m and 0.96 m respectively. The hydrofoil is connected to the heave rods by hinges placed at the position of 0.12 m from the leading edge of the hydrofoil. Heave and pitch spring are used in order to give restoring forces for the heave and pitch motions of the foil. The pitch spring is attached to the foil at the position of 0.175 m from the leading edge. A series of the heave and pitch springs were prepared. Details of the heave and pitch springs are given in Ref.5.

Servomechanical wave height meters are used for measurements of wave heights of incident and transmitted waves. The heave and pitch motions and the displacement of the carriage are measured by using potentiometers. As mentioned above, the thrust can be measured directly by the load cell set between the main and sub carriages. On the other hand, the thrust may be estimated indirectly also by using the results of resistance tests in still water and in waves.

The wave maker used in the experiments discussed in this section is a pneumatic wave maker, and the wave height is controlled by the opening of a valve, but, for simplicity, the experiments are conducted with the valve opened fully. The wave making performance of the tank for the fully opened valve is shown in Fig.24, where  $a$  and  $\lambda$  are the wave amplitude and length. The dispersion equation of a shallow water wave:

$$\frac{1}{g} \left( \frac{2\pi}{T} \right)^2 = \frac{2\pi}{\lambda} \tanh \left( \frac{2\pi h}{\lambda} \right) \quad (8)$$

is used to calculate the wave length  $\lambda$  from the wave period  $T$ , where  $h$  is the depth of water.

Since the length of the tank is only 25 m, effects of reflected waves from the wave absorber may easily appear especially for long waves. Close attention is paid to avoid the effects.

A series of preliminary experiments were conducted to determine a standard condition of the experiments. The draft and attack angle of

the hydrofoil and the combination of the heave and pitch springs as shown in Tab.3 refer to the condition under which the highest advance speed was attained at free running or self-propulsion tests. In the experiments discussed in this section, this condition is adopted as the standard one.

In Fig.25, results of resistance tests of the carriage alone and the carriage with the hydrofoil in still water are shown. The resistance of the hydrofoil is the difference between the resistance of the carriage with the hydrofoil and that of the carriage alone. The foil resistance in waves may be different from that in still water, but the latter is assumed to be equal to the former in the present paper.

In Fig.25, results of resistance tests in a wave are also shown.

In the following, two kinds of definitions of the thrust generated by the hydrofoil are used, that is, the apparent thrust  $\bar{T}_{app}$  and the net thrust  $\bar{T}_{net}$ . The former is the difference between the resistance of the carriage with the foil in still water and that in a wave, and the latter is the difference between the apparent thrust and the foil resistance.

Comparisons between the net thrust  $\bar{T}_{net}$  derived as the time average of the fluctuating thrust measured by a load cell and that estimated from the resistance test results are also shown in Fig.25. A good correlation may be observed between both thrusts, but, as shown in the figure, the thrust measured by the load cell shows a rather big variance. Hence, the thrust estimated from the resistance test is adopted in the following discussions except in case of bollard condition. In case of bollard condition, the thrust is measured by the load cell.

In Figs. 26~30, effects of wave length  $\lambda$  on the advance speed  $U$ , thrusts  $\bar{T}_{net}$ ,  $\bar{T}_{app}$ , foil motions  $Z_c$ ,  $\theta_c$  and wave devouring propulsion (or WDP) efficiencies  $\eta_{Wnet}$ ,  $\eta_{Wapp}$  are shown for free running test.  $Z_c$  and  $\theta_c$  refer to the amplitudes of heave and pitch motions at the rotational axis of the foil. The draft and attack angle of the foil and the combination of the heave and pitch springs are the standard ones as shown in Tab.3. Some correlation may be observed between the advance speed and the foil motion. For example, the heave amplitude  $Z_c$  is maximum at  $\lambda \approx 1.8$  m. On the other hand, the advance speed  $U$  attains its maximum at  $\lambda \approx 1.75$  m.

The net and apparent WDP efficiencies  $\eta_{Wnet}$  and  $\eta_{Wapp}$  in Fig.30 are defined as

$$\left. \begin{aligned} \eta_{Wnet} \\ \eta_{Wapp} \end{aligned} \right\} = \left. \begin{aligned} \bar{T}_{net} \\ \bar{T}_{app} \end{aligned} \right\} U / (P_W^\pm b) \quad (9)$$

where  $P_W^\pm$  is the power of the incident wave per unit breadth of the wave and is given as

$$P_W^\pm = \frac{\rho g a^2}{2} (c_g \pm U) \quad (10)$$

$c_g$  =group velocity of the wave

$$= \frac{1}{2} \left[ 1 + \frac{4\pi h/\lambda}{\sinh(4\pi h/\lambda)} \right] \frac{\lambda}{T} \quad (11)$$

The plus and minus signs in  $P_W^\pm$  refer to head and following seas.

As shown in Fig.30,  $\eta_{\text{net}}$  is only half as big as  $\eta_{\text{wapp}}$ . This means that the resistance of the foil is rather big.

The effects of the attack angle and draft of the foil on the advance speed at free running test are shown in Figs.31 and 32 respectively. According to the results in Fig.31, the attack angle of about  $-8.0^\circ$  seems to give the best results. Fig.32 suggests that the very shallow draft gives good results. Hence, the free surface effect on the performance of a hydrofoil of very shallow draft may be very important problem.

The above-mentioned results are limited to those in head seas. In Figs.33 and 34, some results in following seas are shown. Only the directions of the wave propagation are different in Fig.26 and in Fig.33, and, in this case, much better results are obtained in head seas than in following seas.

The thrust generated by the hydrofoil at bollard condition is shown in Fig.35. As mentioned above, the thrust in this case is the one measured by a load cell. For bollard condition, the thrust is rather big and shows a flat response with respect to wave length. Ogilvie (1983) has pointed that the thrust generation through utilization of wave energy may be applied to reduce average and slowly varying components of wave drift force acting on a moored ocean platform.

#### 4.2 Experiments in a Long Wave Range ...Model II

The experiments mentioned in §4.1 were conducted in a range of rather short waves, since the pneumatic wave maker could not make regular long waves with sufficiently big wave height. So, the wave maker has been replaced by a piston-type one as shown in Fig.36 to make the experiments in a long wave range possible. At the same time, the towing device and the heave-pitch-motion-mechanism etc. are also changed.

Since the resistance of the hydrofoil was quite big in the experiments mentioned in §4.1, the foil support has been changed to make the resistance as small as possible. The rotational hinges placed on the foil surface has been removed as shown in Fig.36. The new model is called model II.

The results of the resistance tests for model II are shown in Fig.37 and compared with those for model I. The draft and attack angle of the foil are 7.7 cm at the midchord and  $7.7^\circ$  in the nose down direction respectively. The foil resistance of model II becomes smaller than that of model I, but the resistance of the carriage is increased since the heave-pitch-motion-mechanism becomes more complex and heavier. These invite a little increase of the total resistance in calm water.

Waves used in the present experiments are shown in Fig.38. Three kinds of wave height are used, that is,  $(2a)_1$ ,  $(2a)_{1/\sqrt{2}}$  and  $(2a)_{1/2}$ . The subscripts refer to the designed values of the wave height ratio between them.

Effects of the wave length and height on free running speed are shown in Fig.39.

The maximum speed of about 0.65 m/s is attained at  $\lambda \approx 3.5$  m. The wave length at the maximum advance speed becomes longer for model II than for model I. This is because softer springs are adapted for model II, referring to the results of preliminary tests.

The apparent and net thrust coefficients are shown in Figs.40 and 41 respectively. The corresponding WDP efficiencies are shown in Figs.42 and 43. The net WDP efficiency is rather small and less than 0.05 for waves of  $\lambda/2l > 10$ . The improvement of the WDP efficiency may be the most important problem.

In Fig.44, the results of the thrust at bollard condition are shown. The thrust coefficients are rather big in the whole range of wave length. In general, the smaller wave heights give the bigger thrust coefficients. The reason is not clear enough, but the non-linear components involved in the long waves with big wave height may be partly responsible for this. Since the water depth is rather small, such waves, strictly speaking, become cnoidal ones.

#### 4.3 Some Theoretical Considerations

In this section, some simple theoretical calculations are conducted on the basis of Wu's theory for an unsteady hydrofoil in waves (Wu (1972)), and the results are compared with the experimental ones for model I discussed in §4.1. Since Wu's theory neglects completely the free surface effects, a good correlation between the theory and experiment was not expected. But, to the authors' surprise, the theory seems to give results better than expected.

In the first place, Wu's result is rewritten as follows. Let a hydrofoil move in a wave of wave length  $\lambda$  and amplitude  $a$  with the advance speed  $U$  as shown in Fig.45 and make the heave and pitch oscillations  $\zeta(t)$  and  $\theta(t)$  with the encounter frequency  $\omega_0$  as

$$\zeta(t) = Z e^{i\omega_0 t} \quad (12)$$

$$\theta(t) = \Theta e^{i\omega_0 t}, \quad (13)$$

where  $\zeta$  and  $\theta$  is defined at the midchord of the foil (Fig.45),  $i$  is the imaginary unit  $\sqrt{-1}$  and  $t$  is the time. Then, the hydrodynamic lift  $L(t)$  and the moment about the midchord  $M(t)$  acting on the foil may be written as (Eqs. (27) and (28) in Ref.3))

$$\begin{aligned} \frac{L(t)}{\pi \rho U^2 l b} = & - \left[ \frac{l}{U^2} \left( 1 + \frac{2}{\sigma_0} \zeta(\sigma_0) \right) \dot{\zeta} + \frac{2}{U} \mathfrak{F}(\sigma_0) \dot{\zeta} \right. \\ & - \frac{l}{U \omega_0} \zeta(\sigma_0) \ddot{\theta} - \frac{l}{U} \left( 1 + \frac{2}{\sigma_0} \zeta(\sigma_0) \right. \\ & \left. + \mathfrak{F}(\sigma_0) \right) \dot{\theta} - 2 \mathfrak{F}(\sigma_0) \theta \left. \right] \\ & + 2 \frac{A_0}{U} \left[ \left( 1 - \frac{\sigma_0}{kl} \right) J_1(kl) - W_1(\sigma_0) \right] \\ & + i W_2(\sigma_0) e^{i\omega_0 t} \end{aligned} \quad (14)$$

$$\begin{aligned} \frac{M(t)}{(\frac{1}{2})\pi\rho U^2 l^2 b} = & - \left[ \frac{2}{U\omega_0} \mathcal{G}(\sigma_0) \dot{\xi} + \frac{2}{U} \mathcal{F}(\sigma_0) \dot{\xi} \right. \\ & + \frac{l^2}{U^2} \left( \frac{1}{4} - \frac{1}{\sigma_0} \mathcal{G}(\sigma_0) \right) \ddot{\theta} \\ & + \frac{l}{U} \left( 1 - \frac{2}{\sigma_0} \mathcal{G}(\sigma_0) - \mathcal{F}(\sigma_0) \right) \ddot{\theta} - 2\mathcal{F}(\sigma_0) \dot{\theta} \left. \right] \\ & + 2\frac{A_0}{U} \left[ -W_1(\sigma_0) + i \left\{ W_2(\sigma_0) \right. \right. \\ & \left. \left. + \left( 1 - \frac{\sigma_0}{kl} \right) J_2(kl) \right\} \right] e^{i\omega_0 t}, \quad (15) \end{aligned}$$

where

$$\begin{aligned} A_0 = & \text{amplitude of wave orbital velocity} \\ & \text{in } z\text{-direction at } z = -h_1 \\ = & \frac{2\pi g a}{\lambda \omega_0} \sinh\left(\frac{2\pi}{\lambda}(h-h_1)\right) / \cosh\left(\frac{2\pi h}{\lambda}\right) \quad (16) \end{aligned}$$

$$\sigma_0 = \text{reduced frequency} = \omega_0 l / U \quad (17)$$

and the definitions of  $\mathcal{F}$ ,  $\mathcal{G}$ ,  $W_1$ ,  $W_2$  and  $J_n$  are found in Ref.3).

The heave  $\zeta_C(t)$  and pitch  $\theta_C(t)$  with respect to the rotational axis of the foil are related with  $\xi(t)$  and  $\theta(t)$  as

$$\xi = \zeta_C - l_C \theta_C, \quad \theta = \theta_C, \quad (18)$$

where  $l_C$  is the distance between the midchord and the rotational axis and positive when the axis locates on the side of the leading edge. Similarly, the hydrodynamic lift  $L_C(t)$  and moment  $M_C(t)$  with respect to the axis have a relation with  $L(t)$  and  $M(t)$  as

$$L_C = L, \quad M_C = M - l_C L. \quad (19)$$

Then, substitution of Eqs. (14), (15) and (18) into Eq. (19) may easily lead to the expressions of  $L_C$  and  $M_C$  written in  $\zeta_C$  and  $\theta_C$ .

Let the mass, moment of inertia about the rotational axis, heave spring constant and pitch spring constant of a vibration system composed of the hydrofoil, heave-pitch-motion-mechanism and heave and pitch springs be  $M'$ ,  $I'$ ,  $k_H$  and  $k_P$  respectively. For simplicity, it is assumed that the rotational axis coincides with the center of gravity of the foil. Then the equation of motion may be written as follows.

For the heave motion

$$\begin{aligned} & \left\{ M' + \pi\rho l^2 b \left( 1 + \frac{2}{\sigma_0} \mathcal{G}(\sigma_0) \right) \right\} \ddot{\zeta}_C + 2\pi\rho U l b \mathcal{F}(\sigma_0) \dot{\zeta}_C \\ & + k_H \zeta_C - \pi\rho l^3 b \left\{ \frac{l_C}{l} + \left( 1 + \frac{2l_C}{l} \right) \frac{\mathcal{G}(\sigma_0)}{\sigma_0} \right\} \ddot{\theta}_C \\ & - \pi\rho U l^2 b \left\{ 1 + \frac{2}{\sigma_0} \mathcal{G}(\sigma_0) + \left( 1 + \frac{2l_C}{l} \right) \mathcal{F}(\sigma_0) \right\} \dot{\theta}_C \\ & - 2\pi\rho U^2 l b \mathcal{F}(\sigma_0) \theta_C \\ = & 2\pi\rho U l b A_0 \left[ \left\{ \left( 1 - \frac{\sigma_0}{kl} \right) J_1(kl) - W_1(\sigma_0) \right\} \right. \\ & \left. + i W_2(\sigma_0) \right] e^{i\omega_0 t} \quad (20) \end{aligned}$$

and for the pitch motion

$$\begin{aligned} & \frac{1}{2} \pi\rho l^3 b \left\{ -\frac{2l_C}{l} + \left( 1 - \frac{2l_C}{l_0} \right) \frac{2\mathcal{G}(\sigma_0)}{\sigma_0} \right\} \ddot{\xi}_C \\ & + \pi\rho U l^2 b \left( 1 - \frac{2l_C}{l} \right) \mathcal{F}(\sigma_0) \dot{\xi}_C \\ & + \left[ l' + \frac{1}{2} \pi\rho l^4 b \left\{ \frac{1}{4} + 2\frac{l_C^2}{l^2} - \left( 1 - 4\frac{l_C^2}{l^2} \right) \frac{\mathcal{G}(\sigma_0)}{\sigma_0} \right\} \right] \ddot{\theta}_C \\ & + \frac{1}{2} \pi\rho U l^3 b \left\{ \left( 1 + \frac{2l_C}{l} \right) - 2 \left( 1 - \frac{2l_C}{l} \right) \frac{\mathcal{G}(\sigma_0)}{\sigma_0} \right. \\ & \left. - \left( 1 - 4\frac{l_C^2}{l^2} \right) \mathcal{F}(\sigma_0) \right\} \dot{\theta}_C \\ & + \left\{ k_P - \pi\rho U^2 l^2 b \mathcal{F}(\sigma_0) \left( 1 - \frac{2l_C}{l} \right) \right\} \theta_C \\ = & \pi\rho U l^2 b A_0 \left[ -\left\{ \frac{2l_C}{l} \left( 1 - \frac{\sigma_0}{kl} \right) J_1(kl) \right. \right. \\ & + \left( 1 - \frac{2l_C}{l} \right) W_1(\sigma_0) \left. \right\} + i \left\{ \left( 1 - \frac{2l_C}{l} \right) W_2(\sigma_0) \right. \\ & \left. \left. + \left( 1 - \frac{\sigma_0}{kl} \right) J_2(kl) \right\} \right] e^{i\omega_0 t}. \quad (21) \end{aligned}$$

If the advance speed  $U$  is assumed, the heave and pitch motions are determined by solving Eqs. (20) and (21). The thrust (apparent thrust  $T_{app}$ ) may then be obtained by using Eq. (13) in Ref.4). The free running speed is now calculated as the speed where the apparent thrust is equal to the resistance of the carriage with the foil in still water.

In Fig.46, a comparison of the apparent thrust between theory and experiment is given, where  $M'$ ,  $I'$ ,  $l_C$ ,  $k_H$  and  $k_P$  are 1.63 kgf·s<sup>2</sup>/m, 0.0241 kgf·s<sup>2</sup>, 0.08 m, 5740 kgf/m and 437 kgf·m/rad. A comparison of free running speed is shown in Fig.47 and that of foil motions in Figs.48 and 49.

In Fig.50, theory and experiment are compared in case of non-oscillatory hydrofoil or linear Wells turbine.

The above-mentioned theory is based on Wu's theory for an unsteady hydrofoil in waves (Wu(1972)) which neglects the free surface effect completely. Hence, it may be questionable to apply the theory when the draft of the foil is very shallow as in the present case. In the above mentioned cases, the theoretical results, nevertheless, seem to show rather reasonable correlation with the experimental results contrary to the authors' anticipation.

## 5. CONCLUSION

The following items are discussed in the present paper.

1) If wave energy is fully utilized into propulsion, potentiality of WDP may not be denied.

2) An example of a floating body which moves against waves is shown. The effects of experimental parameters on the performance are discussed.

3) In order to clarify, the basic aspect of WDP, a passive-type hydrofoil propulsor is investigated experimentally. The model is an oscillatory hydrofoil which is driven by wave force. The thrust generation is verified and the amount of thrust is measured. WDP efficiency is calculated from the experimental results. The efficiency, unfortunately, is not big enough. Its improvement is the most important problem.

4) Some theoretical investigations are also conducted on the passive-type hydrofoil propulsor. The theory is based on Wu's theory (Wu (1972)) for an unsteady hydrofoil in waves. Wu's theory neglects completely the free surface effect which may be important for a hydrofoil of very shallow draft as in the present case. Nevertheless, a rather reasonable correlation is found unexpectedly between theory and experiment.

#### ACKNOWLEDGEMENTS

Professor Emeritus S. Motora of the University of Tokyo and Professor M. Bessho of National Defence Academy of Japan are sincerely acknowledged for their valuable discussions and kind advices. Dr. M. Takagi and Dr. A. Yokogawa of Technical Research Institute of Hitachi Zosen Corporation is also highly appreciated for their kind supports and useful suggestions.

#### REFERENCES

- 1) The Naval Architect (Nov. 1973): Wave Energy for Propelling Craft-Nothing New, pp. 239
- 2) Huse, E. (1977): Wave Induced Mean Force on Platforms in Direction Opposite to Wave Propagation. Norwegian Maritime Research, No. 1, pp. 2-5
- 3) Isshiki, H. (1982a): A theory of Wave Devouring Propulsion (1st Report) -Thrust Generation by a Linear Wells Turbine-. Journal of the Society of Naval Architects of Japan, No. 151, pp. 54-64
- 4) Isshiki, H. (1982b): A theory of Wave Devouring Propulsion (2nd Report) -Optimized Foil Motions for a Passive-Type Wave Devouring Propulsor-. Journal of the Society of Naval Architects of Japan, No. 152, pp. 89-100
- 5) Isshiki, H. and Murakami, M. (1983): A Theory of Wave Devouring Propulsion (3rd Report) - An Experimental Verification of Thrust Generation by a Passive-Type Hydrofoil Propulsor-. Journal of the Society of Naval Architects of Japan, No. 154, pp. 125-135
- 6) Jakobsen, E. (1981): The Foil Propeller, Wave Power for Propulsion. 2nd International Symposium on Wave & Tidal Energy, BHRA Fluid Engineering, pp. 363-368
- 7) Longuet-Higgins, M.S. (1977): The Mean Forces Exerted by Waves on Floating or Submerged Bodies with Applications to Sand Bars and Wave Power Machines. Proceeding of the Royal Society of London, A. 352, pp. 463-480
- 8) Ogilvie, T.F. (Oct. 1983): Second Order Hydrodynamic Effects on Ocean Platforms. International Workshop on Ship and Platform Motions, University of California, Berkeley
- 9) Terao, Y. (1982): A Floating Structure Which Moves Towards the Waves (Possibility of Wave Decouring Propulsion). Journal of the Kansai Society of Naval Architects, Japan, No. 184, pp. 51-54
- 10) Wu, T.Y. (Mar. 1972): Extraction of Flow Energy by a Wing Oscillating in Waves. Journal of Ships Research, pp. 66-78

Tab.1 Principal particulars of H-type model

Lpp	650 mm	
B	924 mm	
d (side plate)	200 mm	
weight of the model	1.70 kg	
	low	high
Center of gravity above B.L.	40 mm	61 mm
from fore edge of side plate	213 mm	
radius of gyration /2l	0.212	0.221

Tab.2 Experimental conditions of H-type model

condition	center of gravity	position of aft foil
I	low	C
II	high	C
III	high	B
IV	high	A

Tab.3 Standard condition of model I

draft of the foil $h_1$	0.06 m
attack angle of the foil $\alpha$	-8.0 deg
spring for heave	H20-2
spring for pitch	P25-2

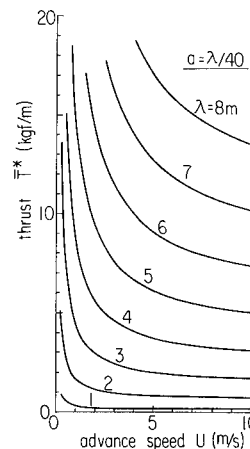


Fig.1 Thrust  $T^*$  generated by an idealized wave devouring propulsor

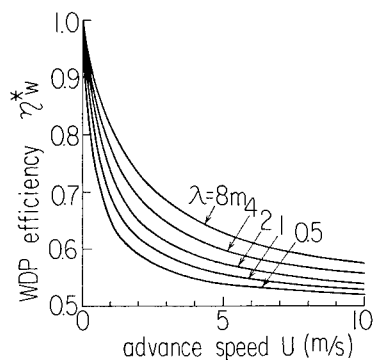


Fig.2 Efficiency  $\eta^*_W$  of an idealized wave devouring propulsor

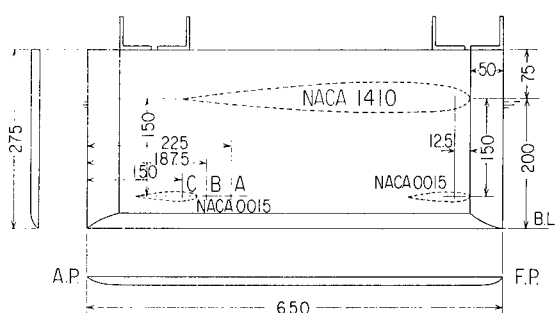


Fig.3a Profile of H-type model

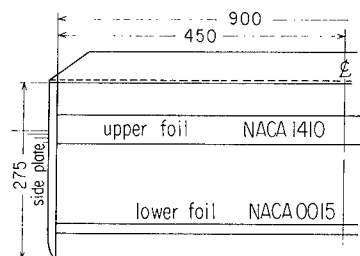


Fig.3b Front view of H-type model

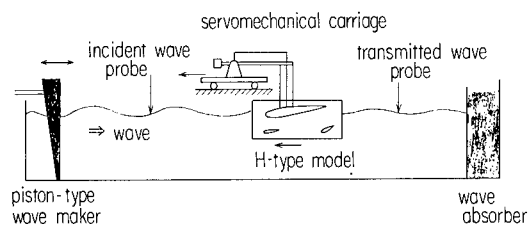


Fig.4 Schematic illustration of test arrangement

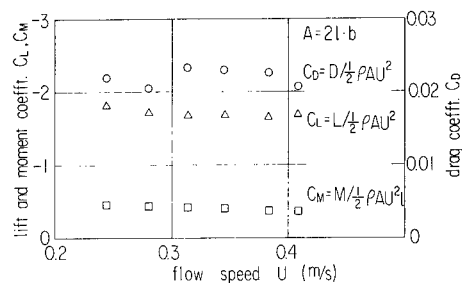


Fig.5 Drag, lift and moment coefficients of H-type model

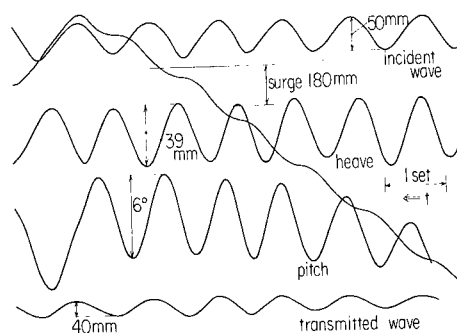


Fig.6 Sample of oscillograph records

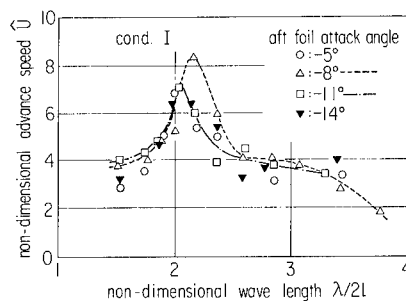


Fig.7 Free running speed of H-type model in head waves. (Cond.I)

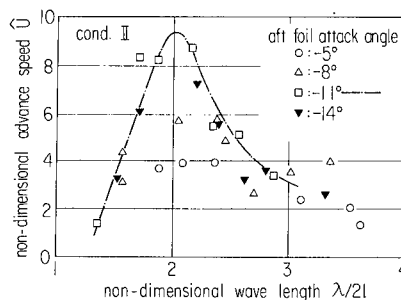


Fig.8 Free running speed of H-type model in head waves. (Cond.II)



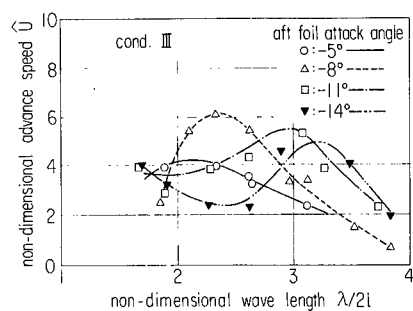


Fig.9 Free running speed of H-type model in head waves. (Cond.III)

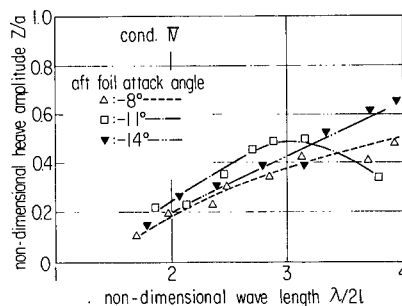


Fig.13 Heave response of H-type model. (Cond.IV)

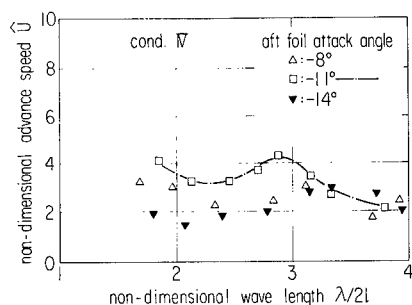


Fig.10 Free running speed of H-type model in head waves. (Cond.IV)

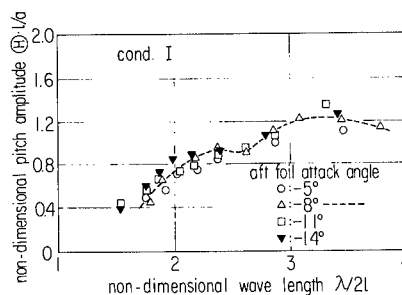


Fig.14 Pitch response of H-type model. (Cond.I)

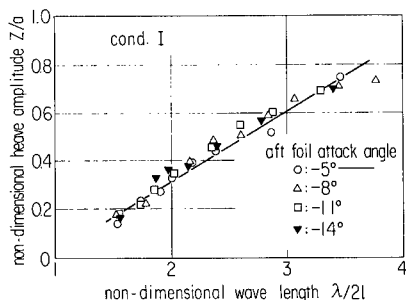


Fig.11 Heave response of H-type model. (Cond.I)

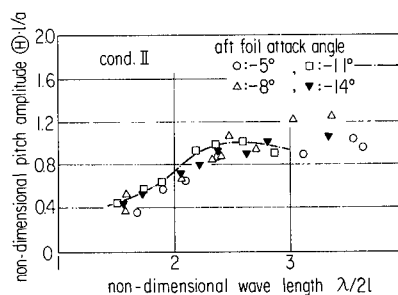


Fig.15 Pitch response of H-type model. (Cond.II)

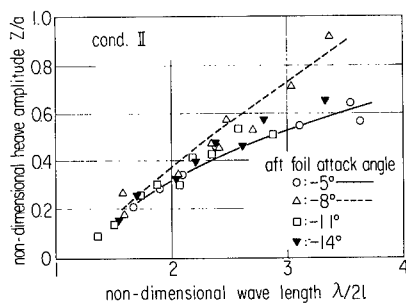


Fig.12 Heave response of H-type model. (Cond.II)

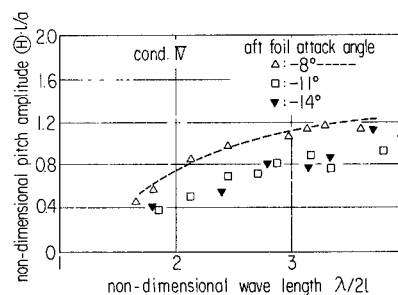


Fig.16 Pitch response of H-type model. (Cond.IV)

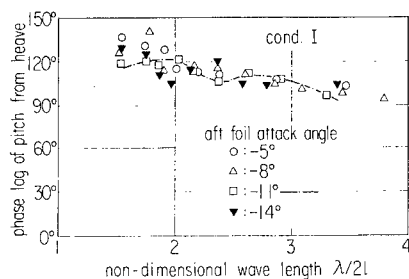


Fig.17 Phase difference between pitch and heave motions. (Cond.I; H-type model)

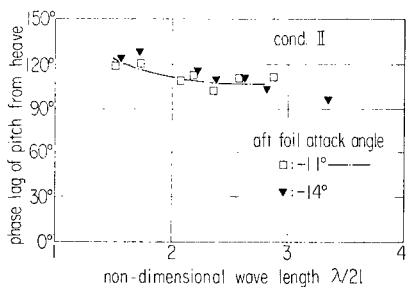


Fig.18 Phase difference between pitch and heave motions. (Cond.II; H-type model)

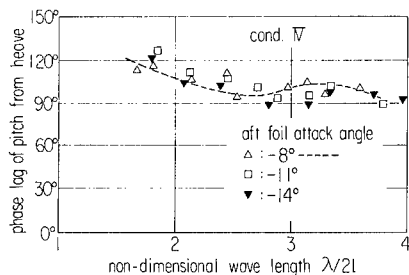


Fig.19 Phase difference between pitch and heave motions. (Cond.IV; H-type model)

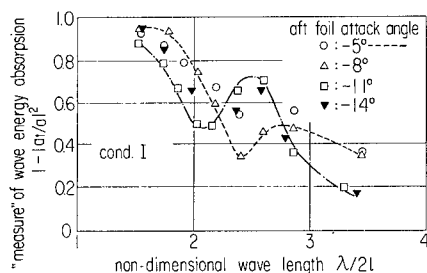


Fig.20 "Measure" of wave energy absorption. (Cond.I; H-type model)

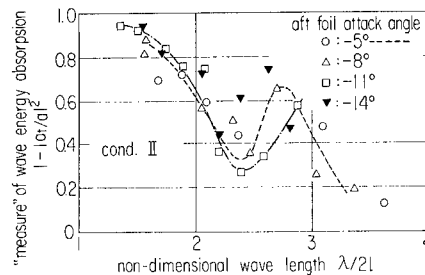


Fig.21 "Measure" of wave energy absorption. (Cond.II; H-type model)

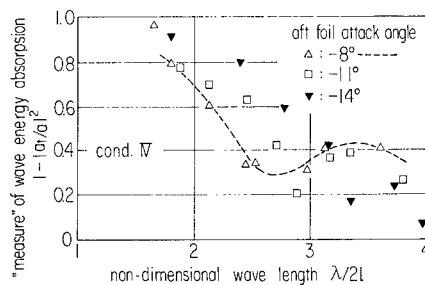


Fig.22 "Measure" of wave energy absorption. (Cond.IV; H-type model)

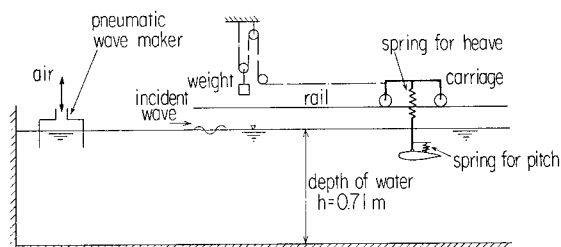


Fig.23 Scheme of a test system of a passive-type hydrofoil propulsor in short waves. (Model I)

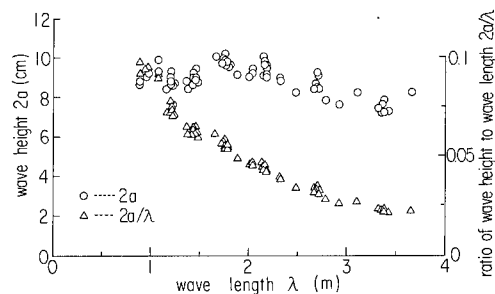


Fig.24 Performance of a pneumatic wave maker when an air valve is fully opened. (Model I)

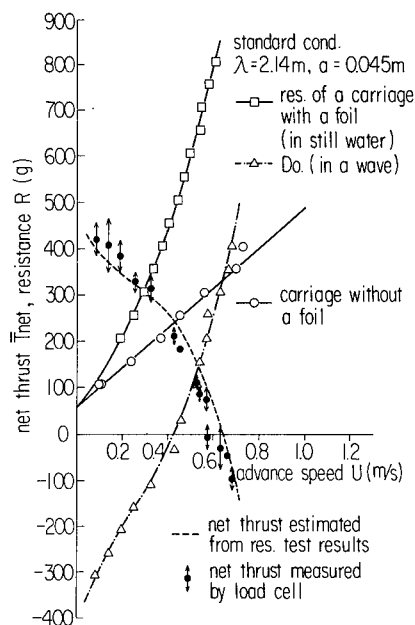


Fig.25 Results of resistance tests of model I

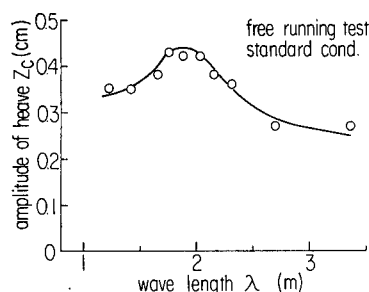


Fig.28 Effect of wave length on heave motion. (Free running test; Model I)

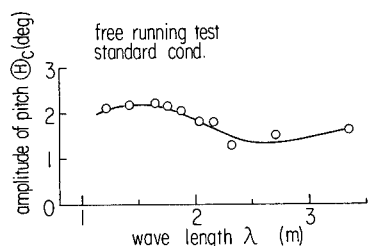


Fig.29 Effect of wave length on pitch motion. (Free running test; Model I)

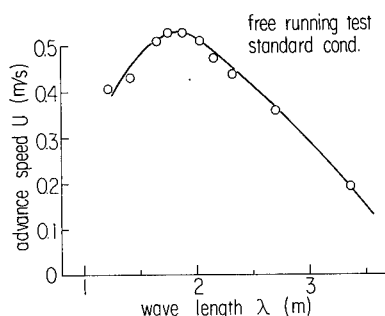


Fig.26 Effect of wave length on free running speed. (Free running test; Model I)

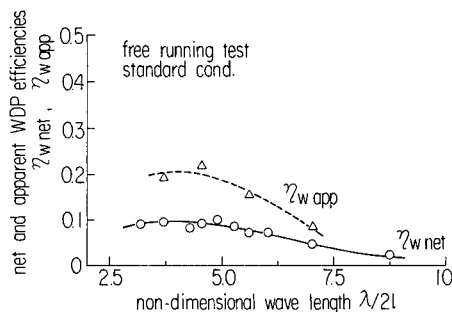


Fig.30 Effect of wave length on net and apparent WDP efficiencies. (Free running test; Model I)

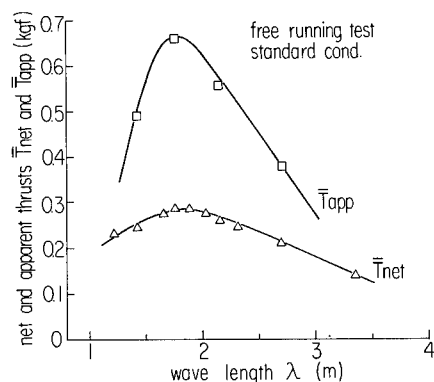


Fig.27 Effect of wave length on net and apparent thrusts. (Free running test; Model I)

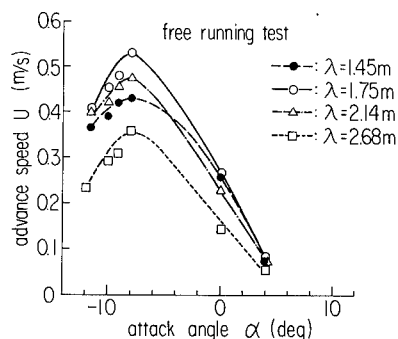


Fig.31 Effect of attack angle on advance speed. (Standard condition except attack angle; Model I)

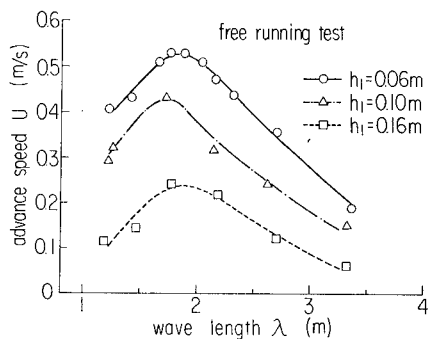


Fig.32 Effect of foil draft on advance speed. (Standard condition except draft; Model I)

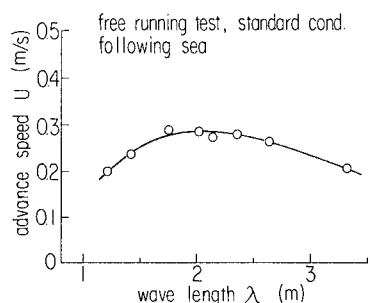


Fig.33 Results of advance speed in following seas. (Model I)

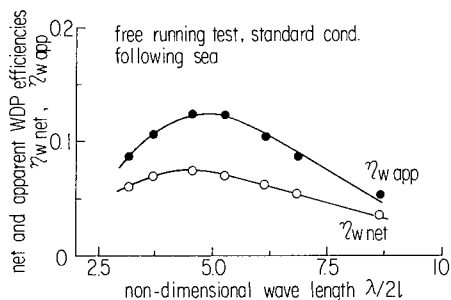


Fig.34 Results of WDP efficiencies in following seas. (Model I)

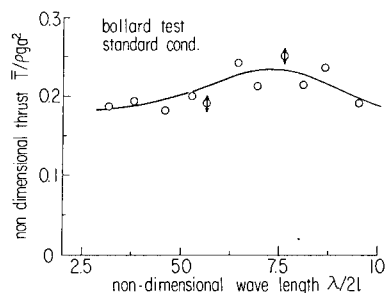


Fig.35 Effect of wave length on thrust. (Bollard condition; Model I)

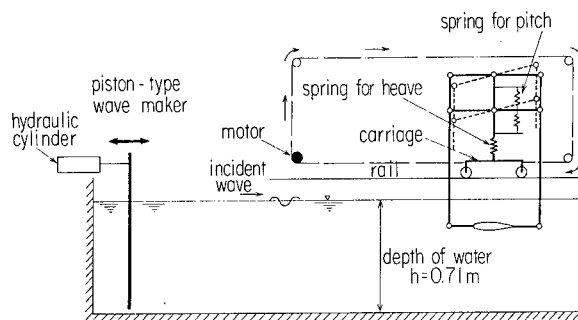


Fig.36 Scheme of a test system of a passive-type hydrofoil propulsor in long waves. (Model II)

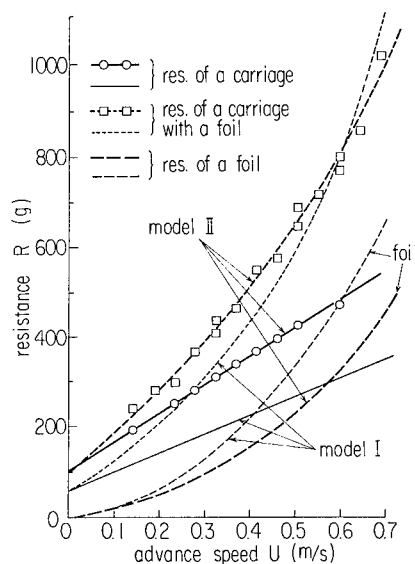


Fig.37 Results of resistance tests of model II

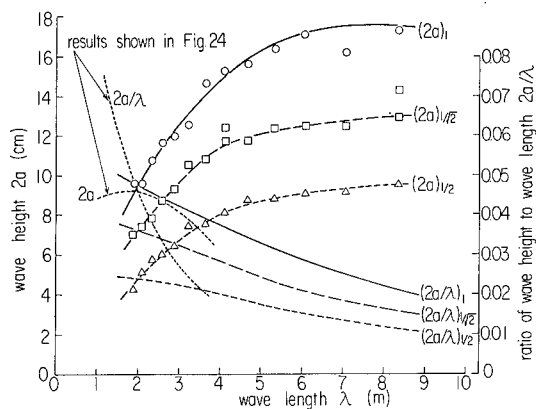


Fig.38 Waves used in experiments of free running tests of model II in long waves

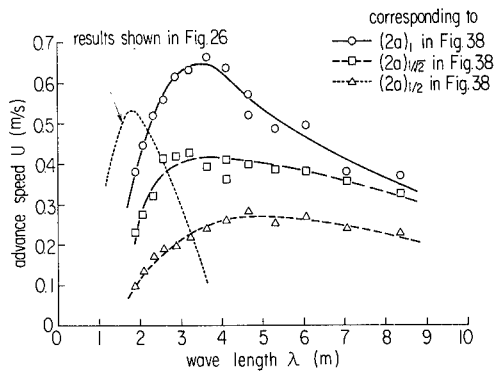


Fig.39 Effect of wave length and height on free running speed of model II

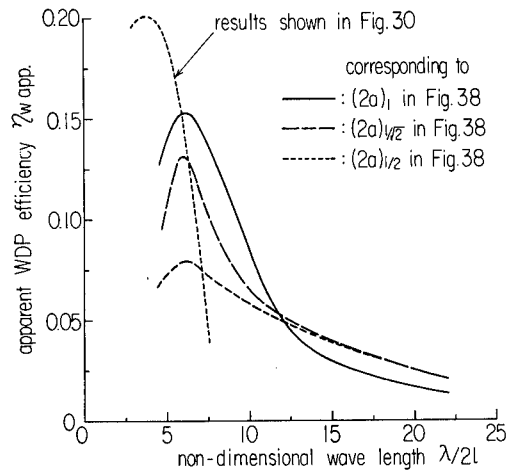


Fig.42 Effect of wave length and height on apparent WDP efficiencies. (Free running test; Model II)

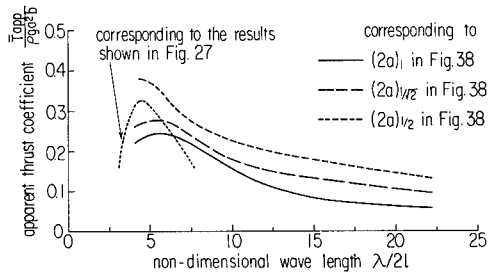


Fig.40 Effect of wave length and height on apparent thrust. (Free running test; Model II)

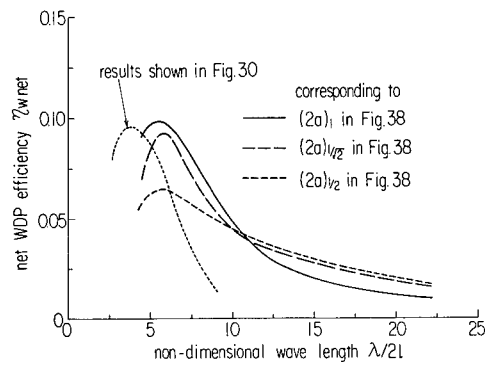


Fig.43 Effect of wave length and height on net WDP efficiencies. (Free running Model II)

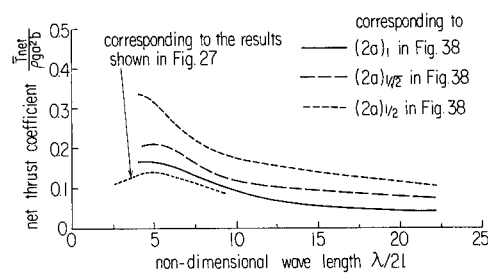


Fig.41 Effect of wave length and height on net thrust. (Free running test; Model II)

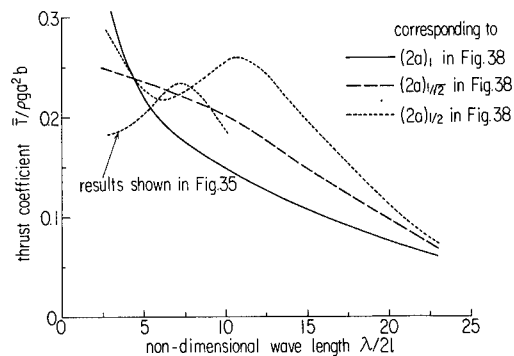


Fig.44 Effect of wave length and height on thrust coefficient. (Bollard condition; Model II)

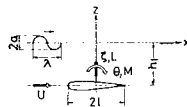


Fig.45 Definition of foil motions  $\zeta$ ,  $\theta$  and hydrodynamic forces  $L$ ,  $M$

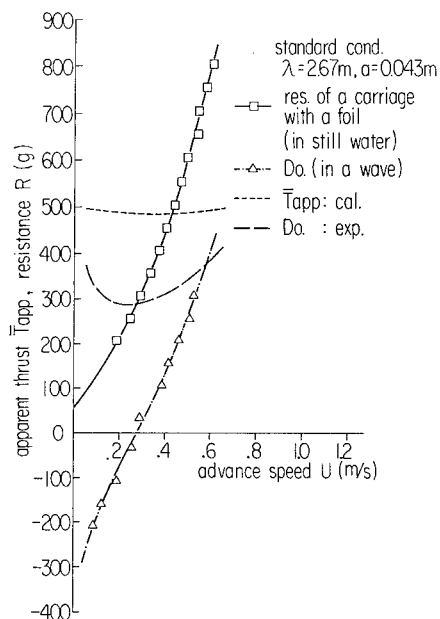


Fig.46 Comparison of apparent thrust between theory and experiment. (Standard condition; Model I)

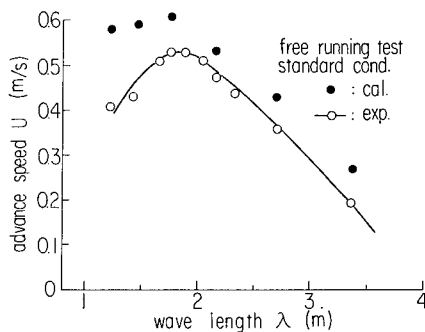


Fig.47 Comparison of free running speed between theory and experiment. (Standard condition; Model I)

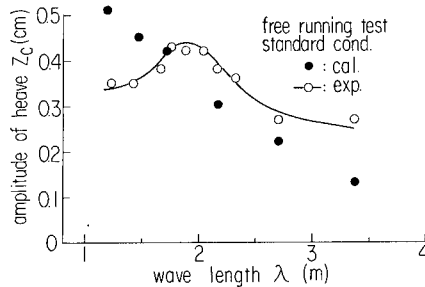


Fig.48 Comparison of heave motion between theory and experiment. (Standard condition; Model I)

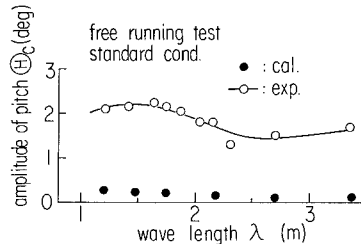


Fig.49 Comparison of pitch motion between theory and experiment. (Standard condition; Model I)

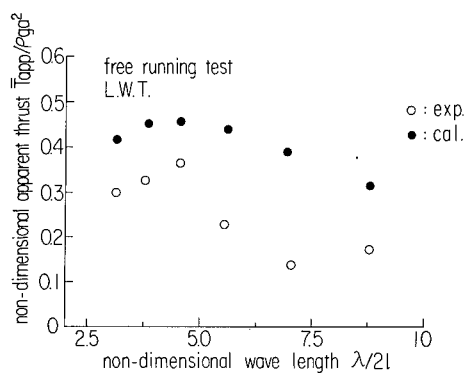


Fig.50 Comparison of apparent thrust between theory and experiment. (Linear Wells turbine,  $h_1 = 0.10$  m,  $\alpha = -8.0$  deg; Model I)

## RESISTANCE INCREASE DUE TO SURFACE ROUGHNESS

M. NAKATO, H. ONOGI, Y. HIMENO, I. TANAKA AND T. SUZUKI

### ABSTRACT

This paper deals with the roughness effects ( $\Delta C_F$ ) on skin friction from a hydrodynamical point of view.

The former part of the paper consists mainly of the experimental reports, that is, the devices of pipe flow experiments, the friction measurements in the roughened pipes and the analyses of their data.

The main results obtained are as follows;

(a) The frictional resistances of variously roughened pipes are obtained. The resistance curves of painted pipes and wavy roughened pipes show clearly different tendencies from those of sand roughened pipes as mentioned by Prof. Sasajima in 1954.

(b) However if the slope of wavy roughness is steeper than about 1/10, its resistance curve becomes a sand roughness type.

(c) The hydrodynamical relationship between the roughness height, measured by the BSRA roughness analyser, and the so-called equivalent sand roughness height, determined by comparing Nikuradse's experimental results, is shown. The relation can be expressed by

$$k_S = 1.47 k_A$$

(d) The roughness functions of various kinds of roughness are analyzed.

The latter part of the paper consists mainly of the theoretical considerations of  $\Delta C_F$  and their applications.

The main results obtained are as follows:

(e) Having a logarithmic type of velocity distribution in the boundary layer, the local  $\Delta C_i$  can be expressed simply by local  $C_i$  and the roughness function  $\Delta U/u_*$  as

$$\Delta C_i \propto C_i^{3/2} (\Delta U/u_*)$$

(f) The procedures used to determine the roughness function  $\Delta U/u_*$  from the

measured resistance data are explained. It can be done without measuring the velocity distribution in the boundary layer.

(g) A new roughness parameter  $h = k \cdot Fn^{2/3} \cdot (g/v^2)^{1/3}$  is proposed, concerning the similarity law for  $\Delta C_F$ . As the parameter can be applied commonly to both the model and the ship, the new parameter may be a powerful tool for estimating  $\Delta C_F$ .

(h) As an application of the above stated considerations, the frictional resistances of a tanker are calculated in the various roughness conditions.

### NOMENCLATURE

C	constant in the Coles' wall wake law
$C_F$	total skin friction coefficient
$\Delta C_F$	augmentation of total frictional resistance due to surface roughness
$C_i$	local skin friction coefficient
$\Delta C_i$	augmentation of local frictional resistance due to surface roughness
$\bar{C}_i$	cross sectional mean of $C_i$
D	pipe diameter
$Fn$	Froude number ( $= U/\sqrt{Lg}$ )
$f$	frictional resistance coefficient of pipe
g	acceleration due to gravity
H	shape factor in boundary layer
$H_w$	wave height of wavy roughened surface
h	new roughness parameter
k	roughness height (in general)
$k_A$	roughness height measured by the BSRA roughness analyser
$k_S$	equivalent sand roughness height
L	length of ship or flat plate
$L_w$	wave length of wavy roughened surface
R	pipe radius ( $= D/2$ )
Re	Reynolds number ( $= UL/\nu$ )
$R_{n0}$	Reynolds number ( $= \bar{U}D/\nu$ )
r	roughness function ( $= \Delta U/u_*$ )
U	velocity at the outer edge of boundary layer or the maximum velocity in pipe
$\Delta U$	velocity defect at the outer edge of boundary layer
u	velocity in the boundary layer or pipe flow

Michio Nakato, Hiroshima University, Dept. of Nav. Arch. & Ocean Eng., Saijo Higashi, Hiroshima 724  
 Hiroshi Onogi, Tsu Res. Lab. of Nippon Kokan KK., 1-Kokan-Cho, Kumozu, Tsu City, Japan  
 Yoji Himeno, University of Osaka Prefecture, Mozu-Umemachi 4-804, Sakai, Osaka 591  
 Ichiro Tanaka, Osaka University, Dept. of Naval Architecture, Yamada-kami, Suita-shi, Osaka 565  
 Toshio Suzuki, Osaka University, Dept. of Naval Architecture, Yamada-kami, Suita-shi, Osaka 565

$\Delta u$	velocity defect in the boundary layer
$\bar{u}$	mean velocity in pipe
$u_*$	friction velocity ( $= \sqrt{\tau_w/\rho}$ )
$y$	distance from the wall
$\alpha$	scale ratio
$\delta$	boundary layer thickness
$\theta$	momentum thickness
$\nu$	kinematic viscosity
$\xi$	roughness Reynolds number ( $= u_* k/\nu$ )
$\pi$	coefficient in the wall-wake law
$\rho$	density of fluid
$\tau_w$	shear stress on the wall

suffix

0	smooth surface
m	model
s	ship

## 1. INTRODUCTION

About twenty years ago, the late Professor Sasajima published a series of papers on roughness research<sup>1),2),3)</sup>. Since that time, research on the problem has not been so active in Japan until the recent publication by Tokunaga and Baba<sup>4),5)</sup>. However, roughness problems have been noted continuously by many researchers around the world.

In the Göteborg symposium in 1978, Lewkowicz<sup>6)</sup>, Musker<sup>7)</sup> and Karlsson<sup>8)</sup> made valuable reports on the roughness effects on skin friction.

The term  $\Delta C_f$  has been used in two ways recently. The first meaning is the augmentation of frictional resistance due to surface roughness and the second one is the model-ship correlation factor in the ship trial analysis. This paper deals with  $\Delta C_f$  as in the first meaning.

As is well known, the essentials of the  $\Delta C_f$  problem are to investigate the roughness functions which are characterized by the kind of roughness.

The main purposes of this report are to find the roughness functions experimentally and with them to discuss the  $\Delta C_f$  problems. The kinds of roughness treated here are; uniform sand roughness, newly painted and regular wavy roughness.

## 2. EXPERIMENTAL EQUIPMENT

The general view of experimental equipment is shown in Fig. 1. The test section is 4 m in length and has about a 50 mm inner-diameter. The inner-diameter of each test pipe was determined by measuring water volume filled in each pipe. The smooth pipe is an ordinary brass pipe and the roughened ones are specially prepared aluminum pipes which are smoothly connected by twenty short pipes as shown in Fig. 1 and in Photo. 1.

To make the sand roughness inside the pipes, the waterproof abrasive papers or abrasive grains are attached by adhesion and to make the paint roughness inside the pipes, they are coated with ordinary marine paint by brushing circumferentially.

The two dimensional wavy roughness inside

the pipes is manufactured by cutting with a numerical controlled lathe, and three dimensional wavy roughness is made by the so-called wire cut method using a strong electric current.

Measuring the inside roughness of pipes is rather difficult, so nearly the same roughness as in the pipes is prepared on flat plates and this roughness is measured instead of the inside pipe roughness.

In the roughness measurements, the BSRA (British Ship Research Association) roughness analyzer (Photo. 2) is mainly used because it is very popular and convenient. However, the recordings of the BSRA roughness analyzer have some ambiguities, as Musker (1980) pointed out<sup>9)</sup>, and another type of roughness meter which is widely used in the field of mechanical engineering, is also used. The static calibration results of these roughness meters and the measured roughness of pipes are listed in Table 1 and 2, and the examples of roughness records are in Fig. 2.

The four static pressure holes (1.0 mm $\phi$ ) are arranged around the circumference at each of the four sections as in Fig. 1 (c) and with these holes the pressure drops between sections. Consequently, friction losses are obtained. In the sand roughened and painted pipes, the region within a radius of about 2.5 mm from each static pressure hole is made smooth for measuring conveniences.

The inlet length for developing the boundary layer is taken as 2 m i.e. about 40 times the pipe diameter.

The velocity distribution inside the pipe is measured by traversing a micro pitot tube. The traverser and the pitot tube are shown in Photo. 3 and in the upper side of Fig. 3 respectively.

## 3. MEASUREMENT OF FRICTIONAL RESISTANCE AND VELOCITY DISTRIBUTION IN PIPES

### 3-1 Smooth Pipe

All the measuring systems are first checked by performing smooth pipe experiments. Velocity distributions at the four sections are compared with each other in Fig. 3 and from the figure it is confirmed that the boundary layer in the pipe is developing sufficiently at the test sections. The symmetry of the velocity distribution along the diameter in section C is also examined (Fig. 3, + marks). The reliability of measured pressure losses between each section is checked by alternating the order of test sections A, B, C and D, and get the same results are gotten in every case.

The frictional resistance of the smooth pipe is obtained by the measured pressure losses and Darcy-Weisbach's formula,

$$f = \frac{\Delta p}{\Delta x} \cdot \frac{2D}{\rho \bar{u}^2}, \quad (1)$$

where  $\Delta p/\Delta x$  is the pressure loss between sections,  $D$  is the pipe diameter,  $\bar{u}$  is the mean velocity, and  $\rho$  is the density of water. In



Fig. 4, the measured results of the frictional resistance of smooth pipes are shown together with Streeter's results (1935)<sup>10)</sup> and Prandtl's formula<sup>11)</sup> and they are in close accord. The frictional resistance is also obtained by measuring the velocity distribution at section D. At Reynolds number  $RnD = 5.5 \times 10^5$ , the frictional resistance coefficient  $f$  is 0.0129 so obtained is very close to the value  $f = 0.0128$  obtained from the pressure drop measurements.

From the above mentioned facts, it is confirmed that the whole experimental system works well.

### 3-2 Sand Roughened Pipes

The frictional resistance of sand roughened pipes obtained by pressure drop measurements is shown in Fig. 5 (Pipe number S1 - S5). As seen in the figure, almost experiments are performed in the all hydrodynamically fully rough region and from the figure, the equivalent sand roughness can be determined by comparing the authors' data to Nikuradse's data, or with the Nikuradse's formula<sup>11)</sup>,

$$f = (2 \log \frac{D}{2k_s} + 1.74)^{-2} \quad (2)$$

The equivalent sand roughness  $k_s$  obtained is listed in Table 3. The relationship between the sand roughness  $k_A$ , measured by the BSRA roughness analyzer, and the hydrodynamical equivalent sand roughness  $k_s$  after Nikuradse is found as seen in Fig. 6 and the relationship can be expressed by

$$k_s = 1.47 k_A \quad (3)$$

The measured velocity distributions of smooth and sand roughened pipes are shown in Fig. 7.

The friction velocities  $u_*$  are computed by the relation,

$$u_* = \sqrt{\tau_w / \rho} = \bar{u} \sqrt{f/8} \quad (4)$$

where the values of  $f$  for sand roughness are taken from Fig. 5.

In Fig. 7, the wall friction law for the smooth pipe,

$$u/u_* = 5.75 \log (u_* y / \nu) + 5.5 \quad (5)$$

and the roughness function for the completely rough regime after Schlichting (1960)<sup>12)</sup>,

$$\Delta u / u_* = 3.0 - 5.75 \log (u_* k_s / \nu) \quad (6)$$

are also drawn.

### 3-3 Painted Pipes and Wavy Roughened Pipes

The frictional resistance of painted pipes is shown in Fig. 5 (pipe number P1, P2 and P3). In the figure, the marks  $\square$ ,  $\square$ ,  $\square$  indicate additional experiments in heated

(about 45°C) water. The resistance curve of painted pipes shows clearly different tendencies from those of sand roughened pipes as pointed out by Sasajima<sup>1)</sup> in 1954. The resistance curves of painted pipes are nearly parallel to that of smooth pipe. It is very interesting to compare the resistance curve of the No.S2 pipe with that of the No.P3 pipe. Both pipes have about the same roughness height in  $k^*$  and in  $k_A$  (Table 2), however, their resistance curves show quite different tendencies.

To investigate the differences in the resistance characteristics between the sand type of roughness and the wavy type of roughness, two series of wavy roughened pipes were tested. In the first series (W1-W5), the wave heights were intended to be kept constant ( $\approx 130 \mu\text{m}$ ), like the No.S2 and the No.P3 pipe, and the wave lengths were varied. In the second series (W4, 6, 7), to the contrary, the wave lengths were intended to be kept constant ( $\approx 4 \text{mm}$ ) and the wave heights were varied. However, to make wavy roughness inside the pipe was not so easy and the wave forms could not be kept exactly in the intended dimensions. The wavy roughened pipes are tabulated in Table 4 and the examples of roughness features are shown in Fig. 8.

The frictional resistance of wavy roughened pipes is shown in Fig. 9. In the figure, the mark attached (I), (II) and mark  $\diamond$  show the additional experimental results obtained by the cooling or heating of water.

All of the frictional resistance curves of wavy roughened pipes except No.W3 are almost parallel to that of the smooth pipe in the range of higher Reynolds number. In the first series (W1-W5) in which the roughness heights are kept constant ( $\approx 130 \mu\text{m}$ ) and their slopes varied, the resistance augmentations from the smooth pipes are in order of roughness slopes. In the second series (W4, 6, 7) in which the roughness length is kept constant ( $\approx 4 \text{mm}$ ) and their heights varied, the resistance augmentations from the smooth pipes are in order of roughness heights. The problem of how the roughness height and the slope contribute to the resistance augmentation will be discussed in the later section on roughness functions.

Comparing the resistance curves of W2 and W3, the curve of W3 shows sand roughness characteristics and that of W2 wavy characteristics, even if both roughness have about the same dimensions of wavy form as seen in Table 4 and Fig. 8. This interesting fact cannot be explained at the present stage. However, the slope of roughness 1/10 seems to be a critical value which separates the resistance characteristics. Sasajima already discussed this in 1954<sup>1)</sup> and showed the critical slope of roughness to be about 1/12.

The roughness of W8 is three dimensional and it is the same roughness as W4 longitudinally and is the same as W1 circumferentially. The resistance curve of W8 is in Fig. 10. As seen in the figure, the resistance curve of W8 is quite similar to that of W4 and P3, however the slope of W8 is a little more gradual.

The measured velocity distributions of painted pipes and two dimensional wavy roughened pipes are shown in Fig. 11 and in Fig. 12 respectively. In these figures, the friction velocities  $u_*$  are computed by equation (4) and the origin of distance  $y$  is taken from the trough of wavy roughness.

The mean lines of universal velocity profiles in these cases are also parallel to that of smooth pipe and the resistance augmentation can be characterized by the roughness function  $\Delta u/u_*$ .

#### 4. ROUGHNESS FUNCTIONS

The augmentation of frictional resistance caused by surface roughness is explained by momentum loss near the wall i.e. the velocity defect in the viscous sub-layer. The velocity defect  $\Delta u$  is transmitted to the outer part of the turbulent boundary layer and the following relation is valid.

$$\frac{u}{u_*} = \frac{u_0}{u_*} - \frac{\Delta u}{u_*} \quad (7)$$

where  $u_*$  is the friction velocity including the roughness effect and  $\Delta u$  can be considered constant except in the sub-layer. The  $u_0$  is the velocity in the turbulent boundary layer for a smooth surface and it is generally represented by an equation of logarithmic form which is a little different from the pipe flow boundary layer or to the flat plate boundary layer.

As equation (7) is valid also at the outer edge of the boundary layer, the velocity  $u$  in the equation can be replaced by the velocity  $U$  of the edge value,

$$\frac{U}{u_*} = \frac{U_0}{u_*} - \frac{\Delta U}{u_*} \quad (8)$$

As for  $U_0/u_*$ , the following equations are available,  
— pipe flow —

$$\frac{U_0}{u_*} = 5.75 \cdot \log\left(\frac{u_* R}{\nu}\right) + 5.5 \quad (9)$$

(Prandtl-Schlichting) ,

— open boundary layer —

$$\frac{U_0}{u_*} = \frac{1}{\kappa} \ln\left(\frac{u_* \delta}{\nu}\right) + C + \frac{2}{\kappa} \Pi \quad (10)$$

(Coles wall-wake law) ,

where  $\kappa = 0.41$ ,  $C = 0.50$  and  $\Pi = 0.55$  for flat plate. The value  $\Pi$  is a coefficient in Coles' wake function and it depends on the pressure gradient.

The roughness function  $\Delta U/u_*$  in eq. (8) is dependent on the roughness form and density of roughness distribution, and as still unknown functions, they have to be investigated. Usually, it is determined experimentally, for

example, Dvorak (1969)<sup>12)</sup> proposed an empirical roughness function which depends on the roughness Reynolds number  $u_* k/\nu$  and density of roughness distribution.

Once the roughness function can be found for a certain kind of roughened surface, then the friction velocity  $u_*$  can be obtained by the iterative computations of eq. (9) or (10).

#### 4.1 Method of Obtaining Roughness Function from Force Measurements Data

As mentioned above, the roughness function  $\Delta U/u_*$  is determined experimentally by measuring the velocity distribution in the boundary layer. However, such experimental data are limited in number and utilizing the force measurement data are considered. This approximate method starts from assuming the velocity distribution in the boundary layer.

For the case of a roughened pipe, the velocity distribution,

$$\frac{u}{u_*} = 5.75 \cdot \log\left(\frac{u_* y}{\nu}\right) + 5.5 - \frac{\Delta u}{u_*} \quad (11)$$

is assumed.

Integrating the equation from very near the wall ( $u > 0$ ) to the center of pipe, the relationship between the mean velocity  $\bar{u}$  and the maximum velocity  $U$  is obtained.

$$\bar{u} = \left(1 - \frac{3}{2\kappa} \cdot \frac{u_*}{U}\right) \cdot U \quad (12)$$

With the definition of the resistance co-efficient of pipe flow,

$$f = 8\tau_w/\rho \bar{u}^2 = 8 \cdot \left(\frac{u_*}{U} \cdot \frac{U}{\bar{u}}\right)^2 \quad (13)$$

together with the above mentioned relationships, the roughness function may be written,

$$\frac{\Delta U}{u_*} = \frac{1}{\kappa} \ln\left(\frac{u_* R_{nD}}{2} \cdot \frac{U}{\bar{u}}\right) + 5.5 - \frac{U}{u_*} \quad (14)$$

where  $R_{nD} = \bar{u} D/\nu$

With the measured  $\tau_w$  and  $\bar{u}$ , one can calculate the roughness function and  $u_* k/\nu$

For the case of roughened flat plate, the velocity distribution,

$$\frac{u}{u_*} = \frac{1}{\kappa} \ln\left(\frac{u_* y}{\nu}\right) + C + \frac{\Pi}{\kappa} \times \left\{1 - \cos\left(\pi \frac{y}{\delta}\right)\right\} - \frac{\Delta u}{u_*} \quad (15)$$

is assumed, where  $\kappa = 0.41$ ,  $C = 5.0$  and  $\Pi = 0.55$ .

Integrating this through the boundary layer, the relationship between momentum thickness  $\theta$  and the boundary layer thickness  $\delta$  is obtained,

$$\frac{R\theta}{R\delta} = \frac{u_*}{U} \left( I_1 - \frac{u_*}{U} I_2 \right), \quad (16)$$

where

$$I_1 = \frac{1}{\kappa} (1 + \pi),$$

$$I_2 = \frac{1}{\kappa^2} (2 + 3.179\pi + 1.5\pi^2),$$

$$R\theta = U \cdot \theta / \nu, \quad R\delta = U \cdot \delta / \nu.$$

with the momentum relations in the flat plate boundary layer,

$$\left. \begin{aligned} C_F &= 2 \cdot \theta / L, \\ C_f &= C_F + Re \cdot dC_F / dRe = 2 \cdot (u_* / U)^2, \\ Re &= UL / \nu, \end{aligned} \right\} \quad (17)$$

the local skin friction  $C_f$  i.e.  $R\theta$  can be obtained by graphical differentiation on the resistance curve of the flat plate. Then  $R\delta$  i.e.  $\delta$  at the trailing edge of plate is obtained in eq. (16) and the roughness function can be calculated in eq. (15) putting  $y = \delta$ . However, the accuracy of the roughness function thus obtained is rather poor because of graphical differentiation.

#### 4.2 Roughness Functions of Sand Roughened Pipe

The roughness functions of sand roughened pipes obtained by friction measurements are shown in Fig. 13. In the figure, the marks are the values obtained by velocity distributions and the results of the two methods are in close agreement. For comparison, the experimental data by Nikuradse and by Streeter<sup>10</sup> are also shown in Fig. 13.

#### 4.3 Roughness Functions of Painted Pipes and Wavy Roughened Pipes

The roughness functions of painted pipes are in the lower side of Fig. 13 together with the painted flat plate data by Sasajima et al. (1965)<sup>21</sup>. In the analysis of flat plate data, the roughness height  $k_a$  is converted to  $k_s$  by eq. (3).

The roughness functions of wavy roughened pipes are in Fig. 14.

From these two figures, it can be understood that paint roughness belongs to wavy roughness from the skin friction's point of view. However, the roughness functions of painted flat plates which are nearly the same as a voyaged ship shell, indicate a little different tendency from those of painted pipes. It is supposed that the reason is the painted roughness of flat plates possibly includes a little higher roughness or steeper slope and also has three dimensional roughness characteristics as the pipe W8 in Fig. 14.

In Fig. 14, the roughness function of three dimensional wavy roughness develops slower than that of the two dimensional, however, it coincides with the two dimensional one in the fully developed roughness Reynolds number.

Roughness functions of wavy roughness are characterized by these regions, hydrodynamically smooth, transition and fully developed regions as illustrated in Fig. 15. The remarkable feature is that they take constant values in the fully developed roughness Reynolds number.

From these experimental results, the empirical formulae are introduced for two dimensional wavy roughness functions as follows.

1) for fully developed region

$$\frac{\Delta U}{u_*} = e^{(A_1 + B_1 z_w / R)} \cdot H_w / R, \quad (18)$$

where  $H_w$  is wavy roughness height,  $z_w$  is wave length,  $R$  is pipe radius and  $A_1, B_1$  are constants ( $A_1 = 8.30, B_1 = -12.11$ ).

2) for transitional region

$$\Delta U / u_* \cdot r = C_0 + C_1 \ln \xi + C_2 \ln^2 \xi + C_3 \ln^3 \xi \quad (19)$$

where  $\xi = u_* k / \nu$ , and the four constants  $C_0 \sim C_3$  can be determined by the following four conditions (c.f. Fig. 15);

$$\left. \begin{aligned} \text{at } \xi = \xi_0, r = 0 \text{ and } dr/d(\ln \xi) &= 0, \\ \text{at } \xi = \xi_1, r \text{ is given by eq. (18),} \\ &dr/d(\ln \xi) = 0. \end{aligned} \right\} \quad (20)$$

The coefficients obtained are listed in Table 5.

3) for the values of  $\xi_0$  and  $\xi_1$  (c.f. Fig. 15)

This case, as seen in Fig. 14, can be regarded as constant and the value  $\xi_0 = 4$ .  $\xi_1$  seems to can be taken be related to the roughness slope as in Fig. 16, and the approximate formula is

$$\ln \xi_1 = A_2 \ln(z_w / H_w) + B_2, \quad (21)$$

where  $A_2 = -1.139, B_2 = 7.322$ . In future, it might be considered better to replace the formula of  $\xi_1$  by the formula of  $\Delta \xi$ .

The roughness functions thus approximated are shown in Fig. 14 in dotted lines and they represent the experimental data fairly well.

#### 5. DISCUSSION ON $\Delta C_F$

In this section some discussion of the local skin friction law of roughened surface, the hydrodynamic similarity law of roughened surface and the augmentation of frictional resistance ( $\Delta C_F$ ) caused by surface roughness are reported.

##### 5.1 Linear Relation between $\Delta U$ and $\Delta C_f$

The following relationships can be written by putting eq. (8) into eq. (9) or (10),

$$\frac{U + \Delta U}{u_*} = 5.75 \log \left( \frac{u_* R}{\nu} \right) + 5.5, \quad (9)'$$

$$\text{or } \frac{U + \Delta U}{u_*} = \frac{1}{\kappa} \ln\left(\frac{u_* \delta}{\nu}\right) + C + \frac{2}{\kappa} \pi \quad (10)'$$

The interpretation of these relationships is that the local skin friction law of roughened surface can be obtained only by substituting  $(U + \Delta U)$  for  $U$  in the local skin friction law of smooth surface. This interpretation seems to call for introducing a new roughness friction law more directly, however, the authors have not yet succeeded in doing it.

Now, the linear relationship between the velocity defect  $\Delta U$  and the augmentation of local skin friction  $\Delta C_f$  will be shown. Separating the friction velocity  $u_*$  as follows;

$$\left. \begin{aligned} u_* &= u_{*0} + \Delta u_* \\ u_{*0} &= \sqrt{C_{f0}/2} \\ \Delta u_* &= \sqrt{\Delta C_f/2} \end{aligned} \right\} \quad (22)$$

put these into eq. (8) and (10), and expand eq. (10) under the condition of  $\Delta C_f/C_{f0} \ll 1$ , the next relation is obtained,

$$\Delta C_f = \frac{\sqrt{2} \kappa}{\kappa + \sqrt{C_{f0}/2}} \cdot C_{f0}^{\frac{3}{2}} \cdot \frac{\Delta U}{u_*} \quad (23)$$

This linear relation is almost strict in the range of  $\Delta U/u_* < 25$ .

## 5.2 Hydrodynamic Similarity Law of Roughened Surface

The roughness effect is confined to only a very narrow region near the wall of the boundary layer, and the roughness function.  $\Delta U/u_*$  may be determined by the roughness Reynolds numbers  $u_* k/\nu$  and some geometrical roughness parameters. The momentum equation is applicable also to the rough walls. Therefore, the flow around a body having a rough surface can be determined completely by the Reynolds number of the body,  $UL/\nu$ , and a certain non-dimensional roughness parameter e.g.  $k/L$  or  $Uk/\nu$ . In other words, the similarity law of boundary layer flow in the case of a roughened body is to be satisfied by adjusting the body Reynolds number and a certain roughness parameter simultaneously. Of course, it is assumed that the roughness of the bodies are geometrically similar.

However, these parameters are inconvenient to use because another similarity law, Froude law, must be taken into consideration. Moreover it is difficult to duplicate the roughness of a real ship on the model ship by reduction or magnification.

Until now, the Prandtl-Schlichting diagram for sand roughened plate had been widely used in the discussion of the similarity law of skin friction between ships and models.

Sasajima and Himeno (1965)<sup>3)</sup> introduced a simple formula based on the Prandtl - Schlichting diagram under the condition of  $Uk/\nu = \text{const.}$ ,

$$\Delta C_{Fs}/\Delta C_{Fm} = \left[ (C_{F0})_s / (C_{F0})_m \right]^2, \quad (24)$$

where  $C_{F0}$  is the frictional resistance coefficient of a smooth flat plate and the suffixes  $s$  and  $m$  indicate a ship and a model respectively.

A numerical example is presented in Table 6. The numerals in the upper column in Table 6 show an example of comparison between a ship and a model, keeping the Froude number and  $Uk/\nu$  constant. On the contrary, the numerals in the lower column in the table show the case of keeping roughness height  $k$  and  $Uk/\nu$  constant, but, the Froude numbers are not equal. This latter case can not be realized by a model ship in a towing tank except for a flat plate because the wave making phenomenon is inevitable at the test speed.

Although  $\Delta C_{Fs}$  can be estimated from the model test with the afore mentioned diagram or simple formula, it is rather inconvenient because of the condition  $Uk/\nu = \text{const.}$

Now, a new and more convenient parameter is introduced. Let the length ratio of the ship and model be  $\alpha = L_s/L_m$ , and let the roughness height  $k$  be common to the ship and to the model, then the following relationships can be described,

$$\left. \begin{aligned} U_s &= \sqrt{\alpha} U_m, \\ Re_s &= U_s L_s / \nu = \alpha^{\frac{3}{2}} Re_m, \\ U_s k / \nu &= \sqrt{\alpha} U_m k / \nu, \\ k / L_s &= \alpha^{-1} k / L_m. \end{aligned} \right\} \quad (25)$$

Eliminating the scale ratio in the equations (25), a new parameter " $h$ " is defined,

$$h = \frac{Uk}{\nu} \left( \frac{UL}{\nu} \right)^{-\frac{1}{3}} \quad (26)$$

This is written also,

$$\left. \begin{aligned} h &= \frac{k}{L} \left( \frac{UL}{\nu} \right)^{\frac{2}{3}}, \\ \text{or } h &= k Fn^{\frac{2}{3}} (g/\nu^2)^{\frac{1}{3}}. \end{aligned} \right\} \quad (27)$$

From the last equation, it is seen  $h$  takes a value common to the ship and to the model because the roughness  $k$  and Froude number  $Fn$  are the same. Accordingly, if a diagram of  $\Delta C_F$  is previously prepared with the parameter  $h$  (as a little later shown in Fig. 17) it will be very useful in estimating  $\Delta C_{Fs}$  practically. If the correction of kinematic viscosity  $\nu$  is necessary, the following equation is available,

$$h_s = (\nu_m/\nu_s)^{\frac{2}{3}} h_m, \quad (28)$$

however, in usual cases, the correction can be neglected.

### 5.3 Augmentation of Frictional Resistance $\Delta C_F$

The  $\Delta C_F$  is calculated assuming a flat plate is covered with uniformly distributed sand roughness; In the calculation, Coles' wall-wake law, Dvorak's roughness function (1969)<sup>12</sup> and Karman's momentum equation of boundary layer are used.

The momentum equation is integrated on the flat plate by Runge-Kutta's method under the condition of  $U=\text{const.}$  and  $k=\text{const.}$  i.e.  $Uk/\nu = \text{const.}$ , and the frictional resistance of roughened flat plate  $C_F$  and  $\Delta C_F (= C_F - C_{F0})$  can be calculated. It is convenient to plot the calculated  $\Delta C_F$  on a logarithmic graph in which the abscissa is  $h$  (eq. (26), (27)) and each curve of  $\Delta C_F$  is drawn according to the Reynolds number  $Re$ . Utilizing this graph as a cross curve, the diagram of Fig. 17 is obtained. It is well understood from the figure that the roughness effects do not appear at the Reynolds number up to  $Re \approx 10^6$ . The dotted line in the figure is the calculated result based on the Prandtl-Schlichting formula and shows fairly high  $\Delta C_F$ , compared with the former results. One of the reasons for this discrepancy is the very small difference in the friction lines of the smooth flat plate. The Prandtl-Schlichting friction line of the smooth plate is deduced from eq. (5) for a pipe flow and it shows a little higher value than the line deduced from Coles wall-wake law. Hence, as mentioned previously eq. (23), the higher the  $C_i$  the higher the  $\Delta C_i$ .

Until now, the case of sand roughness has been discussed. However, the case of painted roughness also can be treated in the same way as Fig. 13 and Fig. 17, and in this case,  $\Delta C_F$  becomes very small.

### 5.4 Increase of Hull Frictional Resistance due to the Roughness

The frictional resistances of a ship having roughened surfaces are calculated by combining Coles-Dvorak's local friction law and the three dimensional boundary layer theory<sup>13</sup>.

In the iterative calculations of  $\delta$ , the following relationships are used, assuming the momentum thickness  $\theta$  and the shape parameter  $H$  are known,

$$\frac{1}{\sigma} = \frac{1}{\kappa} \ln\left(\frac{R_0 H}{I_1}\right) + C + \frac{2}{\kappa} \pi - \frac{\Delta U}{u_*}, \quad (29)$$

$$\theta = \delta (\sigma I_1 - \sigma^2 I_2), \quad (30)$$

$$H = I_1 / (I_1 - \sigma I_2), \quad (31)$$

where  $\sigma = u_* / U = \sqrt{C_i / 2}$ ,  $\kappa = 0.41$ ,  $C = 5.0$ ,

and

$$I_1 = \int_0^1 \left(\frac{U-u}{u_*}\right) d\eta = \frac{1}{\kappa} (1 + \Pi), \quad (32)$$

$$I_2 = \int_0^1 \left(\frac{U-u}{u_*}\right)^2 d\eta = \frac{1}{\kappa^2} \left\{ 2 + \left(1 + \frac{1.852}{\pi}\right) \Pi + \frac{3}{2} \Pi^2 \right\}. \quad (33)$$

The ship used in the calculation is a tanker having particulars  $L \times B \times d \times C_B = 385m \times 70m \times 23.27m \times 0.84$  and her surface is covered with various kinds of roughness of which all the heights are the same,  $130\mu m$ . The Reynolds number and the Froude number of the ship are assumed to be  $Rn = 2.70 \times 10^9$  and  $Fn = 0.13$  respectively. The body plan and the potential stream lines of the tanker are shown in Fig. 18.

The calculated mean local skin frictions for various kinds of roughness are drawn in Fig. 19 and the calculated  $\Delta C_F$  is in Table 7.

From these calculated results it is found that in the condition of the same roughness height;

- \* the  $\Delta C_F$  of painted cases are about a quarter of the sand roughened case,
- \* in the cases of two dimensional regular wavy roughness, the  $\Delta C_F$  are in order of roughness steepness,
- \* the  $\Delta C_F$  of three dimensional wavy roughness shows a little lower value than that of the two dimensional.

Also it can be said that;

- \* Himeno's formula<sup>14</sup> for the roughness function of the painted surface is useful for estimating  $\Delta C_F$ ,
- \* generally, the effect of roughness on skin friction is more remarkable in the front part of a ship, as pointed out by Tokunaga<sup>4</sup>.

### 6. CONCLUDING REMARKS

The main results obtained are as follows;

(a) The frictional resistance of variously roughened pipes are measured (Fig. 5, Fig. 9), and it is found that the resistance curves of painted pipes and wavy roughened pipes show clearly different tendencies from those of sand roughened pipes.

(b) However, if the slope of wavy roughness is steeper than about  $1/10$ , its resistance curve becomes a sand roughness type.

(c) The hydrodynamical relationship between the roughness height measured by the BSRA roughness analyser and the so-called equivalent sand roughness height determined by comparing Nikuradse's experimental results is obtained (Fig. 6).

The relation can be expressed by

$$k_s = 1.47 \cdot k_A.$$

(d) The roughness functions of various kinds of roughness are analyzed (Fig. 13, Fig. 14) and discussed.

(e) Having a logarithmic type of velocity distribution in the boundary layer, the local  $\Delta C_i$  can be expressed simply by local  $C_i$  and the roughness function as

$$\Delta C_i \propto C_{i0}^{3/2} (\Delta U / u_*)$$

(f) The procedures to determine the roughness function from the measured resistance data are explained. It can be done without measuring the velocity distributions in the boundary layer.

(g) A new roughness parameter  $\lambda_z = k \cdot Fn^{2/3} \cdot (g/v^2)^{1/3}$  is proposed, concerning the similarity law of  $\Delta C_F$ . As the parameter can be applied commonly to both the model and the ship, the new parameter may be a powerful tool in estimating  $\Delta C_F$ .

(h) As an application of the above stated considerations, the frictional resistance of a tanker is calculated in the various roughness conditions (Fig. 19).

Lastly, the authors would like to mention future problems to be solved. The important problems are to find the roughness functions of complex roughness and to investigate the density or the distribution effect on the roughness functions. Further, the roughness representation must be examined,

because the  $k_s$  and  $k_A$  are merely conventional and they have a certain limitation for hydrodynamic usage.

## 7. ACKNOWLEDGEMENT

In closing this report, the authors express hearty thanks to Mr. Y. Kasahara (a research fellow of Nippon Kokan Tsu Research Laboratories) for his kind co-operation regarding the boundary layer calculations and also thank to all the experimental staff related to research in the Tsu Research Laboratories.

This research is partially supported by the Grant-in-Aid for Scientific Research of the Ministry of Education, Science and Culture.

## REFERENCES

- 1) Sasajima, H. and Yoshida, E. (1954): Frictional Resistance of Wavy Roughened Surface, Jour. Soc. Nav. Arch. Japan No.95
- 2) Sasajima, H. et al, (1965): Experimental Investigation into Roughness of Hull Surface and Increase of Skin Frictional Resistance, Jour. Soc. Nav. Arch. Japan, No.117.
- 3) Sasajima, H. and Himeno, Y. (1965): Scale Correction for Roughness Effect, Jour. Soc. Nav. Arch. Japan, No.118
- 4) Tokunaga, K. and Baba, E. (1979): A Study on Local Roughness Effect on Ship Resistance, Trans. of The West-Japan Soc. of Nav. Arch. No.59
- 5) Tokunaga, K. and Baba, E. (1982): Approximate Calculation of Ship Frictional Resistance Increase due to Surface Roughness, Jour. Soc. Nav. Arch. Japan, No.152
- 6) Lewkowicz, A. K. and Musker, A. J. (1978): The Surface Roughness and Turbulent Wall Friction on Ship Hulls: Interaction in the Viscous Sublayer., Int. Symp. Ship Visc. Resist., SSPA, Göteborg.
- 7) Musker, A.J. and Lewkowicz, A.K. (1978): The Effect of Ship Hull Roughness on the Development of Turbulent Boundary Layers, ditto
- 8) Karlsson, R.I. (1978): The Effect of Irregular Surface Roughness on the Frictional Resistance of Ships, ditto
- 9) Musker, A.J. and Sarabchi, K. (1980): Wall-Friction and Profilometry Aspects of Coating in Irregularly Rough Surface, I.S.P., Vol. 27, No.306
- 10) Streeter, V. L. (1935): Frictional Resistance in Artificially Roughened Pipes, Proc. Am. Soc. Civil Engr. 61
- 11) Schlichting, H. (1960): Boundary Layer Theory, McGraw-Hill Book Company
- 12) Dvorak, F.A. (1969): Calculation of Turbulent Boundary Layers on Rough Surfaces in Pressure Gradient, A.I.A.A. Journal, Vol.7, No.9
- 13) Okuno, T. (1976): Distribution of Wall Shear Stress and Cross Flow in Three-Dimensional Turbulent Boundary Layer on Ship Hull, Jour. Soc. Nav. Arch. No.139.
- 14) Himeno, Y. (1983): A Study on Frictional Resistance of Painted Rough Surface, Jour. of The Kansai Soc. of Nav. Arch. Japan, No.191

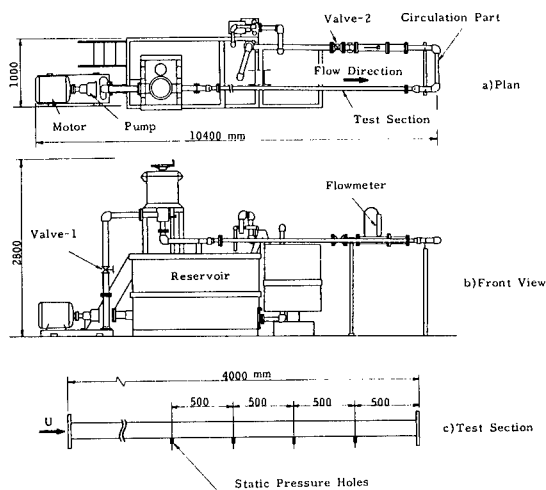


Fig. 1 Experimental equipment

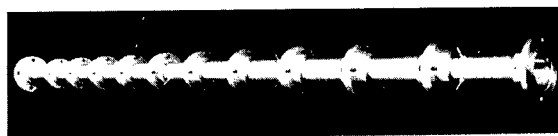


Photo. 1 Example of a roughened pipe

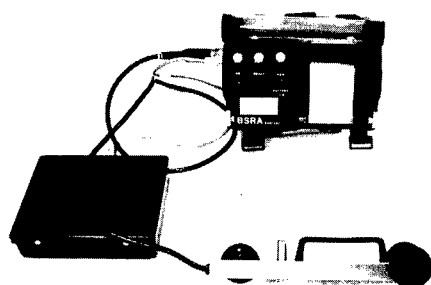


Photo. 2 BSRA hull roughness analyser

Table 1 Calibration of BSRA hull roughness analyser

Calibration Plate	Roughness Analyser		Depth Micrometer ( $\mu\text{m}$ )
	BSRA ( $\mu\text{m}$ )	Kosaka ( $\mu\text{m}$ )	
No. 1	106	105	105
2	489	488	490
3	991	---	987

Table 2 Pipe roughness measurements

Pipe No.	Kind of Roughness	Pipe Diameter (mm)	Grain Size ( $\mu\text{m}$ )	$k^*$ ( $\mu\text{m}$ )	$k_A$ ( $\mu\text{m}$ )
0	Smooth Surface	51.79	---	---	---
S1	Abrasive Paper (#600)	51.65	20	55	64
S2	" (#240)	51.51	70	110	130
S3	" (#100)	51.34	150	240	202
S4	Abrasive Grain (#46)	51.45	350	525	538
S5	" (#24)	51.20	750	---	1137
P1	Painted Surface -1	51.84	---	21	35
P2	" -2	51.70	---	60	78
P3	" -3	51.63	---	123	139

$k^*$  : Peak to valley height in 5-10 mm length

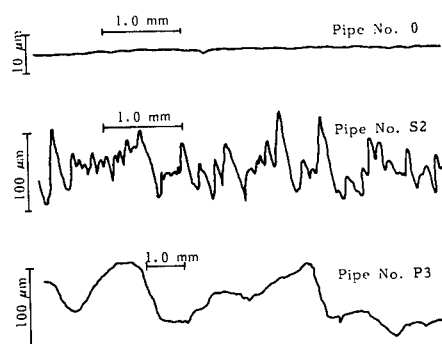


Fig. 2 Roughness records examples

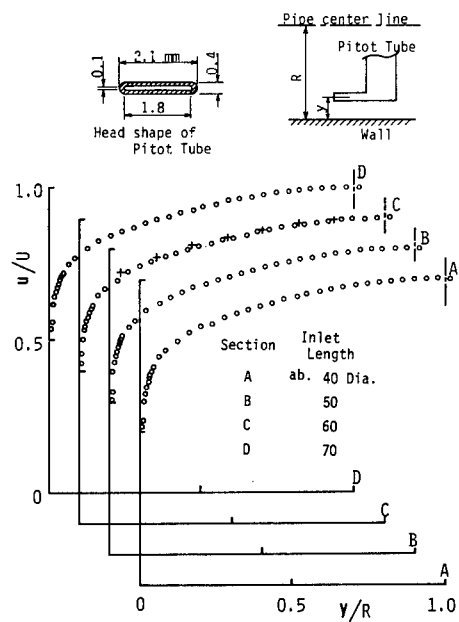


Fig. 3 Velocity profiles in smooth pipe

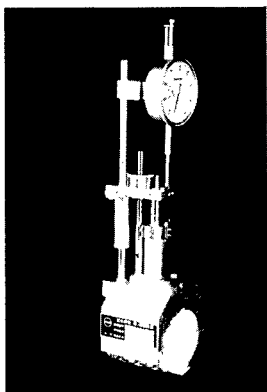


Photo. 3 Pitot tube traverser

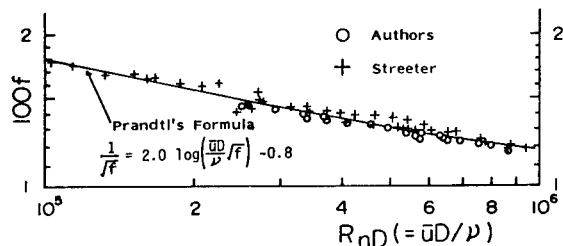


Fig. 4 Frictional resistance in smooth pipe

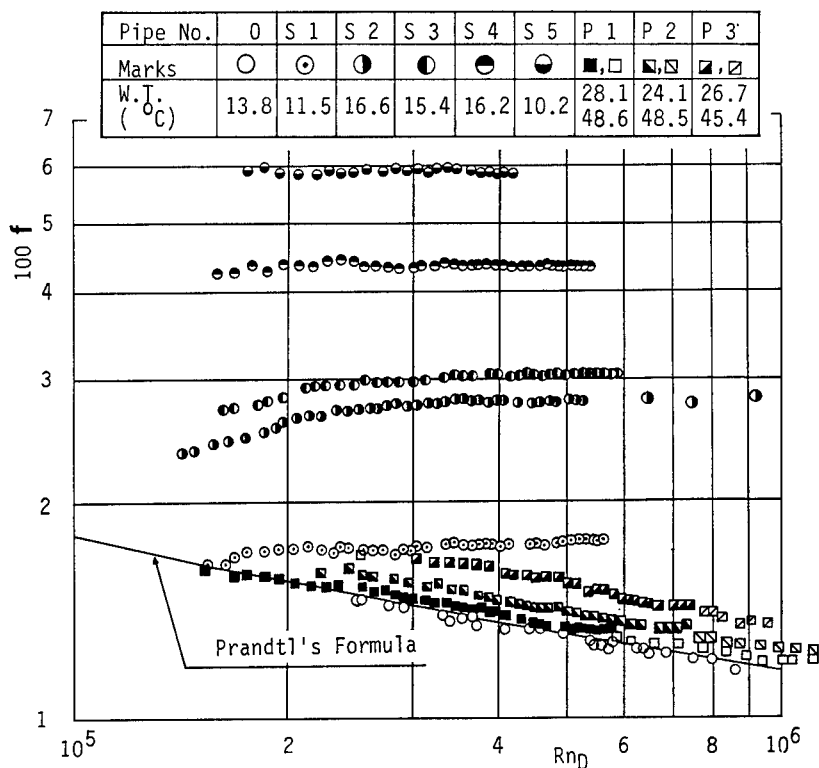


Fig. 5 Frictional resistance in roughened pipes

Table 3 Experimental results of sand roughened pipes

Pipe No.	f	$k_S/D$	$k_S$ (μm)	$k_A$ (μm)	$k_S/k_A$
S1	0.0180	0.00070	36	64	0.49
S2	0.0280	0.00381	196	130	1.51
S3	0.0307	0.00542	266	202	1.32
S4	0.0438	0.0151	778	538	1.45
S5	0.0590	0.0324	1685	1137	1.46

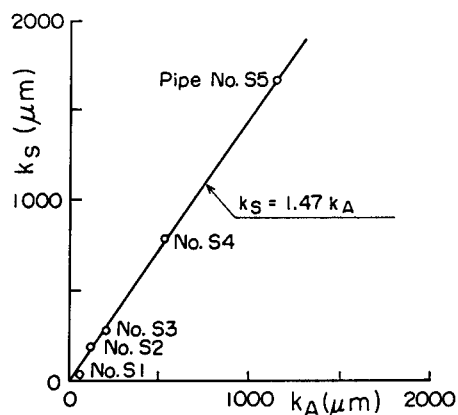


Fig. 6 Relation between  $k_A$  and  $k_S$



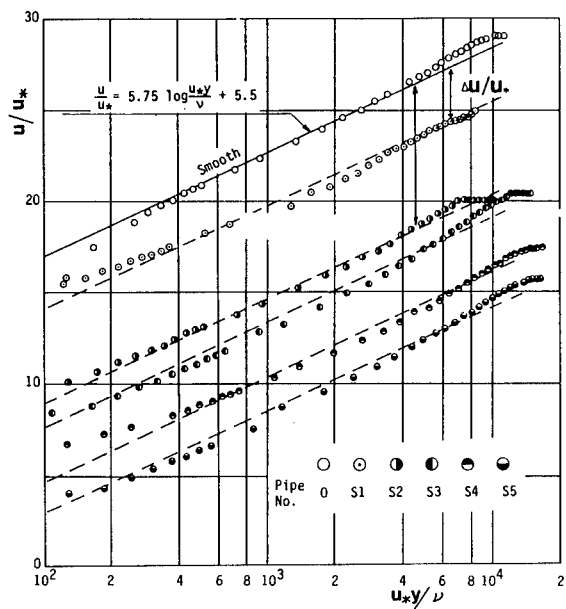


Fig. 7 Universal velocity profiles in smooth and sand roughness pipes

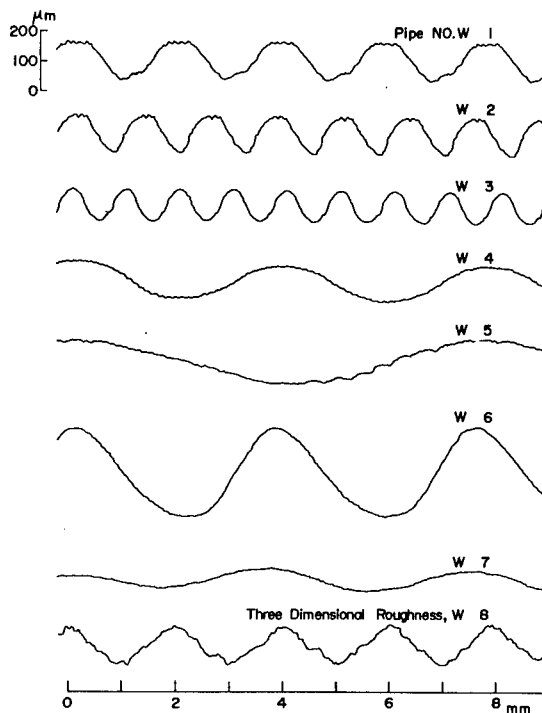


Fig. 8 Roughness records examples of wavy roughened surface

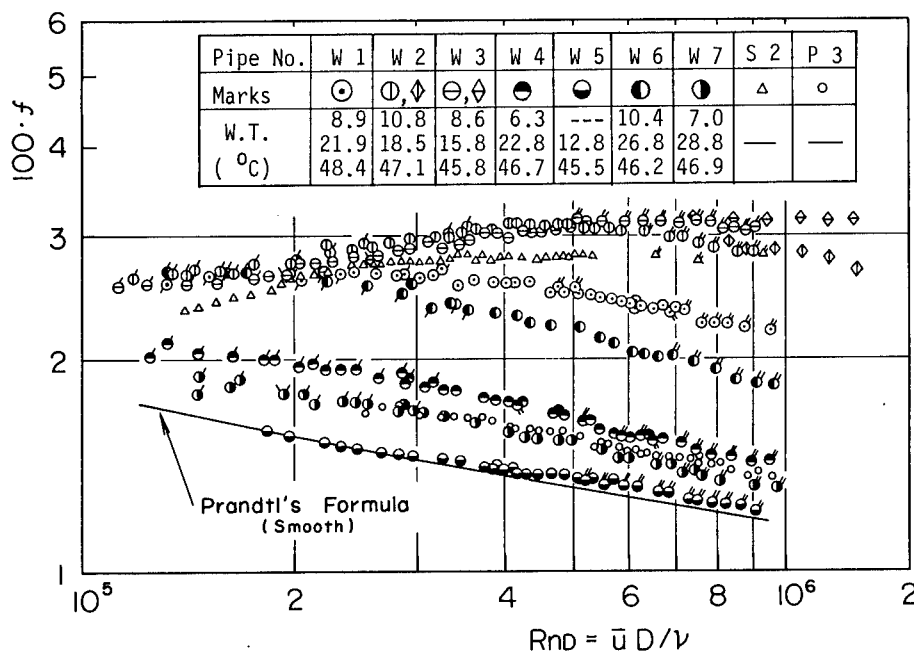


Fig. 9 Frictional resistance in roughened pipes

Table 4 Wavy roughness characteristics

Pipe No.	Wave Shape			$H_w/l_w$	Diameter
	Height	$H_w$	Length $l_w$		
W 1	120	$\mu\text{m}$	2.00 mm	1/16.7	52.00 mm
W 2	122		1.22	1/10.0	52.00
W 3	100		1.00	1/10.0	52.00
W 4	118		3.94	1/33.4	51.90
W 5	140		7.78	1/55.6	51.90
W 6	300		3.81	1/12.7	52.00
W 7	60		3.97	1/66.2	52.00
W 8*)	W 4(Longi.)+W 1(Trans.)			—	52.00

\* Three - Dimensional Wavy Roughness

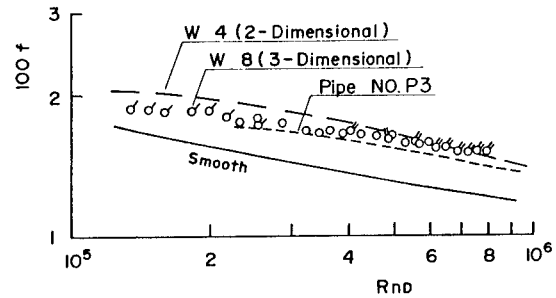
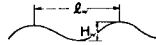


Fig. 10 Frictional resistance in three dimensional wavy roughened pipe

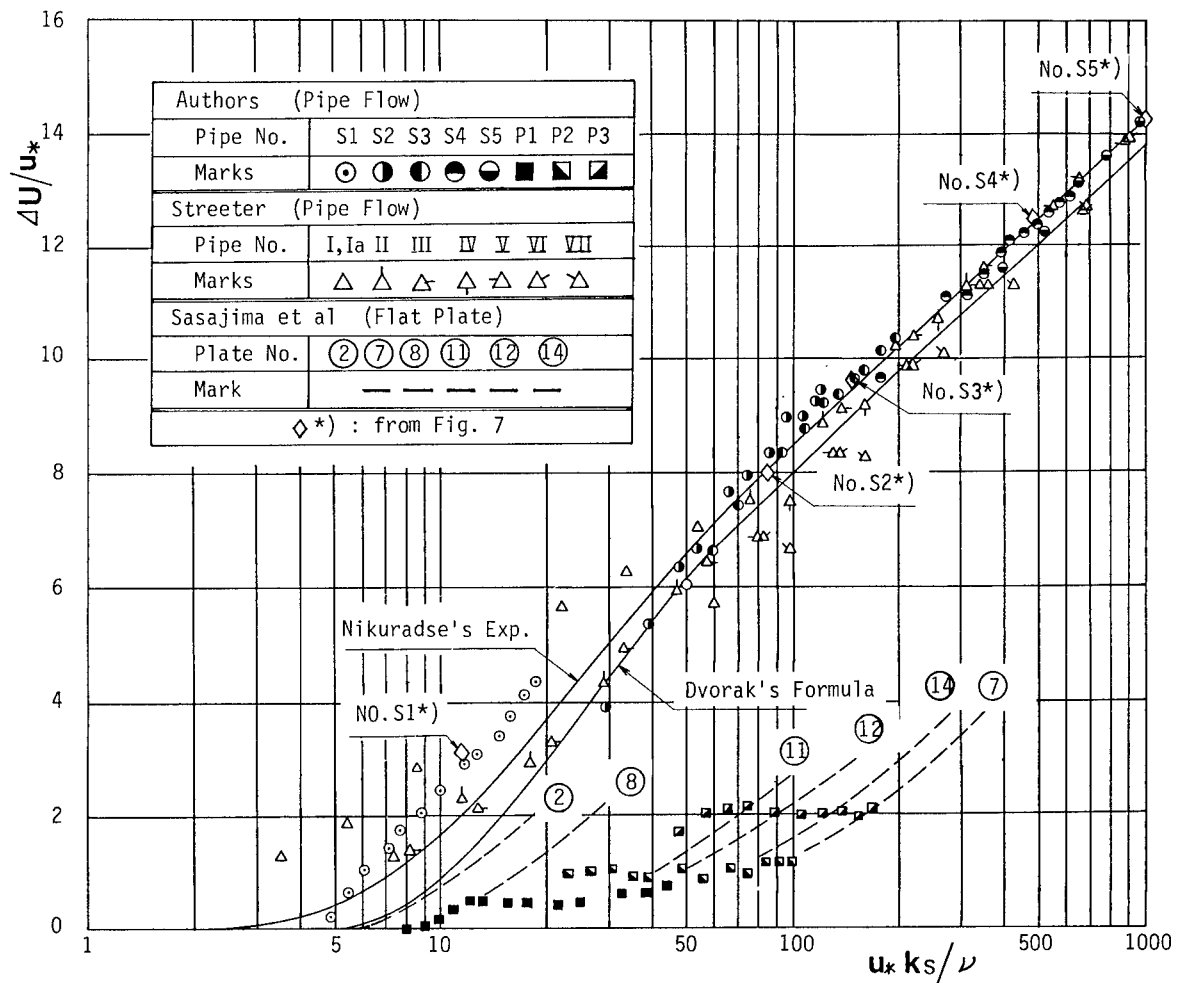


Fig. 13 Roughness function  $\Delta U/u_*$  of sand and painted surface obtained by friction measurements

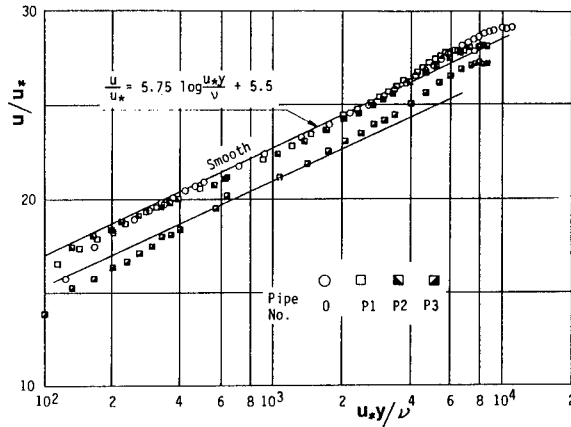


Fig. 11 Universal velocity profiles in smooth and painted roughness pipes

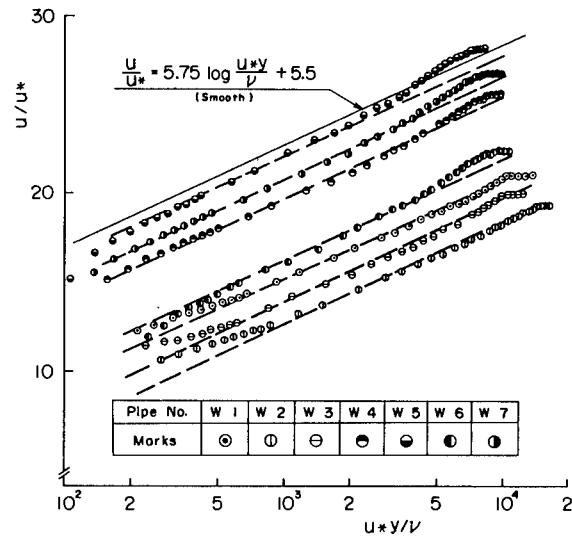


Fig. 12 Universal velocity profiles in two dimensional wavy roughened pipes

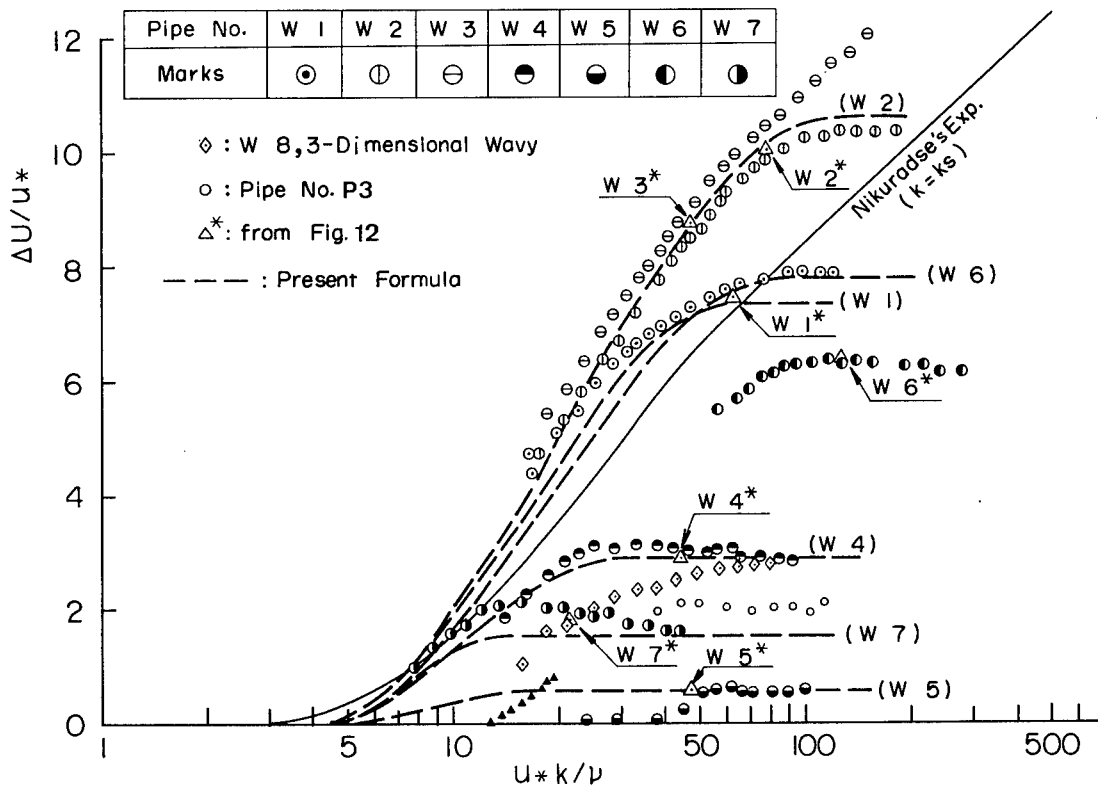


Fig. 14 Roughness function  $\Delta U/u_*$  of wavy roughened surfaces

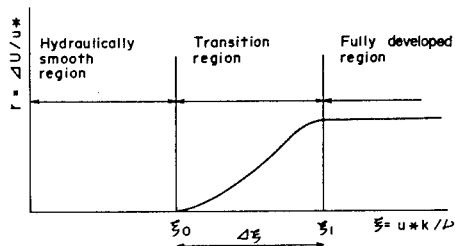


Fig. 15 Three regions of wavy roughness function

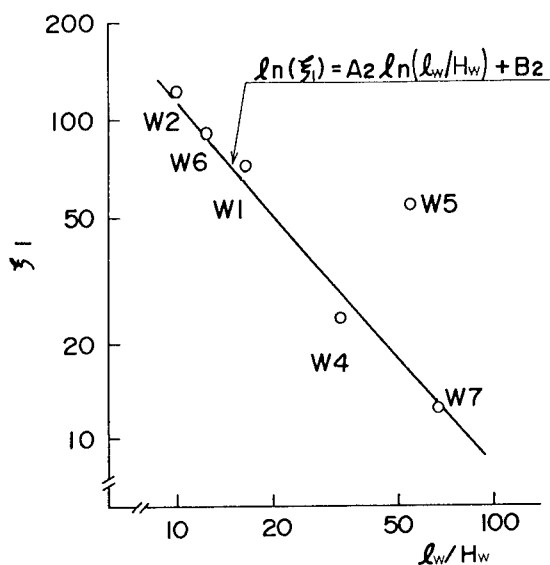


Fig. 16 Boundary values of roughness Reynolds number

Table 5 Coefficients of empirical formula for transition region

Pipe NO.	C0	C1	C2	C3
W 1	7.58	-12.32	5.94	-0.72
W 2	7.18	-11.49	5.36	-0.59
W 3	6.60	-11.06	5.65	-0.80
W 5	3.05	-5.29	2.87	-0.46
W 6	6.41	-10.32	4.89	-0.56
W 7	11.24	-19.82	11.04	-1.87

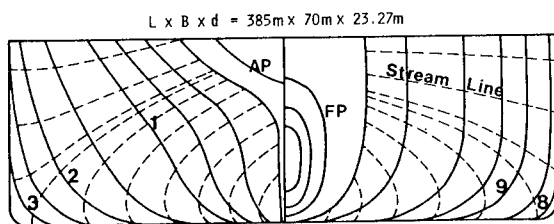


Fig. 18 Body plan and potential streamlines

Table 6 Numerical data used in the calculations

Item	Model	Ship	Note
L (m)	7.0	300	scale=1/15
Fn	0.20	0.20	
U (m/s)	1.657	10.85	$v_m = 1.139 \times 10^{-6}$
Re	$1.018 \times 10^7$	$2.737 \times 10^9$	$v_s = 1.188 \times 10^{-6}$
$C_{F0}$	$2.931 \times 10^{-3}$	$1.352 \times 10^{-3}$	Schoenherr
$Uk/\nu$	300	300	
k (μm)	206	33	
$\Delta C_F$	$0.60 \times 10^{-3}$	$0.128 \times 10^{-3}$	Schlichting
k (μm)	30	30	
U (m/s)	11.4	11.9	$Uk/\nu = 300$
Re	$7.0 \times 10^7$	$3.0 \times 10^9$	
$C_{F0}$	$2.186 \times 10^{-3}$	$1.337 \times 10^{-3}$	Schoenherr
$\Delta C_F$	$0.33 \times 10^{-3}$	$0.12 \times 10^{-3}$	$\Delta C_F \propto (C_{F0})^2$

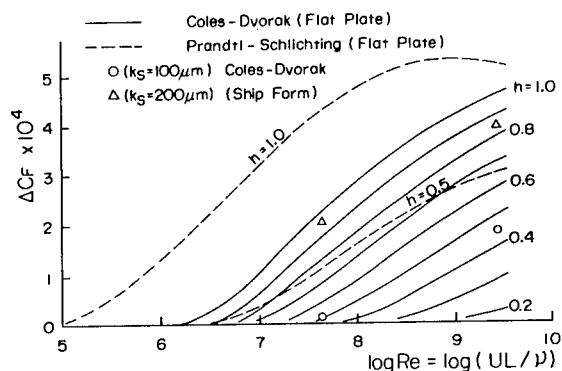


Fig. 17  $\Delta C_F$  expressed by a new roughness parameter "h"

Table 7  $\Delta C_F$  calculated by the three dimensional boundary layer theory

Kind of Surface	Calculated $\Delta C_F$
Authors' Pipe No. P3 ( $K_A = 130 \mu m$ )	$0.86 \times 10^{-4}$
Himeno's Formula ( $K_A = 130 \mu m$ )	$0.60 \times 10^{-4}$
3-Dimensional Wavy ( $H_w = 130 m, \ell_w = 4.0 mm$ )	$1.20 \times 10^{-4}$
2-Dimensional Wavy ( $H_w = 130 m, \ell_w = 4.0 mm$ )	$1.99 \times 10^{-4}$
2-Dimensional Wavy ( $H_w = 130 m, \ell_w = 8.0 mm$ )	$0.36 \times 10^{-4}$
Sand ( $K_S = 130 \mu m$ )	$2.70 \times 10^{-4}$
Calculated $C_{F0}$ of Smooth Surface	$1.243 \times 10^{-3}$

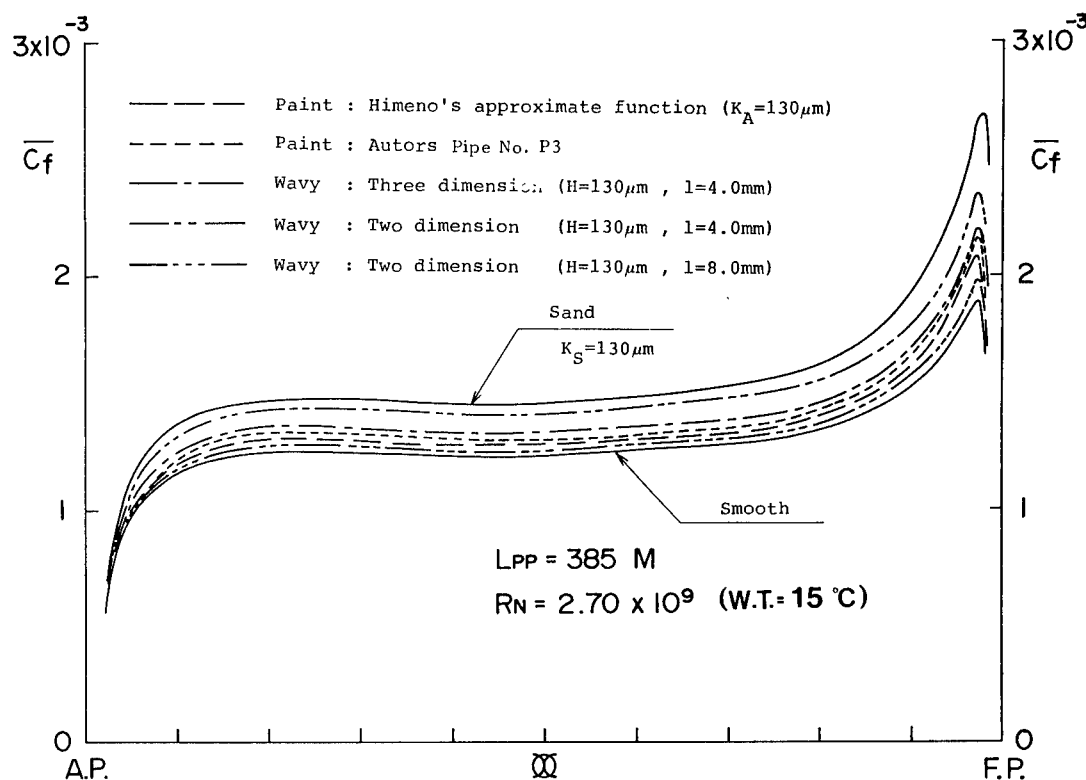


Fig. 19 Longitudinal distribution of cross sectional mean of local skin frictions.

## DISCUSSION

Dr. PAUL S. GRANVILLE,  
David Taylor Naval Ship R&D Center,  
Bethesda, MD, USA:

It should be pointed out to the authors that the determination of the roughness function ( $\Delta U/u_*$ ) or any of its equivalents without measuring the velocity distribution close to the rough wall may be termed the indirect method. Such indirect methods may be said to have been started by Nikuradse for pipe flow in his classic 1932 paper on sand grain roughness wherein the average pipe velocity and the wall shear stress were used. Other indirect methods have been developed for flat plates<sup>a1)</sup> involving the total drag and forward velocity and for rotating disks<sup>a2)</sup> involving the torque and rotary speed.

It should also be pointed out that the roughness function found by Lewkowicz and Musker<sup>6),7)</sup> (also analyzed by Grigson<sup>a3)</sup>) for actual hull roughnesses corresponds mostly to a Colebrook-White engineering roughness which is very unlike that for the painted surface investigated in this paper.

In general, the effect of roughness on ship resistance may be more easily understood by the following: In Reference a4) a nondimen-

sional length  $\Lambda$  is introduced where  $\Lambda = Re/Fn = L^{3/2}\sqrt{g}/v$  for smooth hulls such that

$$C_T = f(Re, Fn)$$

or

$$C_T = f(Re, \Lambda) = f(Re, L^{3/2}\sqrt{g}/v)$$

Here  $C_T$  is the total resistance coefficient. For rough hull

$$C_T = f(Re, Fn, K/L, T)$$

or

$$C_T = f(Re, \Lambda, K/L, T)$$

and eliminating  $L$  with  $L = (\Lambda v / \sqrt{g})^{2/3}$  results in

$$C_T = f(Re, \Lambda, K g^{1/3} / \Lambda^{2/3} v^{2/3}, T)$$

Here  $T$  is the roughness texture representing the geometry of the rough surface.

References:

- a1) Granville, P.S. (1958): The Frictional Resistance and Turbulent Boundary Layer of Rough Surfaces, Journal of Ship Research, Vol. 2, No. 3.
- a2) Granville, P.S. (1982): Drag-Characterization Method for Arbitrarily Rough Surfaces by Means of Rotating Disks, Journal of Fluids Engineering (ASME), Vol. 104, p. 373.

- a3) Grigson, C.W.B. (1981): The Drag Coefficients of a Range of Ship Surfaces, Transactions of the Royal Institution of Naval Architects, Vol. 123.
- a4) Granville, P.S. (1956): The Viscous Resistance of Surface Vessels and the Skin Friction of Flat Plates, Transactions of the Society of Naval Architects and Marine Engineers, Vol. 64.

ANTONY J. MUSKER,  
Admiralty Research Establishment,  
Haslar, England:

I should like to thank the authors for the interesting paper they have presented - it is good to see continued interest in this subject particularly since it has such an immediate application to the economical operation of ships.

There are a number of points I wish to make - most of them are minor. Various sources of possible error appear in the paper. The surface topography measurements have been made on plates whose surfaces are not replicas of the original pipe surface. The surfaces are merely coated in the same manner. I doubt whether adequate quality control can be maintained for this practice but I would appreciate the authors' comments.

The roughness function appears to have been deduced from the cross-stream velocity profile without taking into account the so-called "ε correction", first described by Clauser, which circumvents the problem of not knowing which datum to use for the wall distance. In my experience this parameter, ε, can have a significant effect on the local  $C_f$  (and hence the value  $\Delta U/U_0$ ).

I note that no provision for a wake flow is made in the profile described by equation (9) despite the fact that it is obviously present in the data of Fig. 7.

Finally may I draw the authors' attention to a typographic error in equation (10): I believe C should be 5.0 and not 0.5 as quoted in the text.

## AUTHORS' REPLY

The authors would like to thank Dr. Granville for the comments on the present indirect method which the authors did not know about.

As for the nondimensional length  $\Lambda$  which the discussor mentioned the authors would not always agree that it is more easily understood because  $\Lambda$  takes different values between model scale and ship scale.

The authors would also like to thank Dr. Musker for his comments on several points.

As you pointed out, the rough surfaces on the flat plate are not exactly the same as those in the pipe. However, the authors have confirmed that the peak to valley heights  $k^*$  in both rough surfaces are nearly equal.

We also have other small approximations as you pointed out which should be improved in future work.

The authors also appreciate Dr. Lewkowicz's comments on the importance of the wake component in velocity profile even in the pipe flow, and his advice on the equivalent sand roughness height  $k_s$  and the lack of the Reynolds number range in equation (23).

Finally the authors would like to comment on this problem from a general point of view. The most important problem in hull-surface roughness is a lack of hydrodynamic background for the relationship between the rough-surface configuration and its local friction from a statistical point of view.

As for this point the authors have recently read again the old paper of Prof. van Driest concerning the damping factor in the vicinity of the wall. We assumed unsteady Stokes solution for the turbulence damping near the wall. If we would get back to such a primitive level we might be also able to obtain a new aspect for the statistical hydrodynamics of the surface roughness problem.

REFER TO PAGE 586 FOR ADDENDUM

# NUMERICAL SIMULATION OF FLOW AROUND BLUFF BODIES AT HIGH REYNOLDS NUMBERS

J.J.W. VAN DER VEGT AND R.H.M. HUIJSMANS

## ABSTRACT

The use of vortex models to simulate the flow around bluff bodies has received increasing attention during the last few years. Vortex models possess the elegant feature simulating the actual relevant physical phenomena. Much effort has been devoted to the development of two dimensional numerical models for the simulation of vortical type flows. Many of these numerical methods suffer from bad numerical efficiency. In this paper a modified vortex tracing scheme is presented that correctly models the physical behaviour of the flow and also possesses some very nice numerical advantages over previously developed numerical schemes. In Section 2 a short review of the most commonly used vortex models is discussed. Special attention is paid to the physical modelling of the flow and the numerical efficiency of the described algorithms. In Section 3 a description is given of a new numerical model developed at NSMB, in which a vortex blob representation is used, combined with a variationally optimized grid insensitive vortex tracing technique as developed by Buneman (1974). In Section 4 the results of computations of the flow around a circular cylinder are presented. The numerical results show that the presented model adequately describes the flow for both moderate and high Reynolds numbers at low computational costs.

## NOMENCLATURE

$\sigma$	= source strength
$\sigma_D$	= standard deviation of random walk
$\sigma_L$	= variance of least squares approximation
$\sigma_\mu$	= measure of core radius of vortex $\mu$
$\nu$	= kinematic viscosity
$\gamma_\mu$	= vorticity distribution of vortex $\mu$
$\delta$	= Dirac function
$\delta k_x, \delta k_y$	= wave number spacing in $k_x, k_y$ direction
$\Gamma_\mu$	= circulation of vortex $\mu$
$\nabla$	= gradient operator

$\partial\Omega$	= body contour
$\psi$	= stream function
$\Psi_k$	= Fourier transform of stream function
$\mu$	= index of vortex
$\mu_D$	= doublet strength
$\omega$	= vorticity field
$C$	= body contour
$E_1$	= exponential integral
$\underline{e}_z$	= unit vector perpendicular to 2-D flow field
$J(\psi, x_\mu, y_\mu)$	= action function
$\tilde{J}(\Psi_k, x_\mu, y_\mu)$	= Fourier transform of action function
$\underline{k}$	= wave number vector $[k_x, k_y]^T$
$K_C$	= Keulegan-Carpenter number
$L_x, L_y$	= size of computational space domain in x, y direction
$m$	= number of Fourier harmonics
$M$	= number of grid points
$\underline{n}$	= normal vector on body
$N$	= number of vortices
$P( \underline{k} )$	= filter function, only depending on modules of $\underline{k}$
$R$	= distance between field point p and point q on surface S
$R_n$	= Reynolds number
$S_n$	= body surface
$S^-$	= inner part of surface S
$S^+$	= outer part of surface S
$s$	= distance along body contour, positive clockwise
$S_3$	= standard cubic spline
$U(t)$	= undisturbed onset velocity
$\underline{u}$	= local fluid velocity
$\underline{u}_B$	= fluid velocity due to onset flow or disturbances.
$\underline{u}_w$	= velocity of the body surface
$\underline{t}$	= tangential vector on body
$\underline{x}, \underline{y}$	= Cartesian co-ordinate system
$\underline{x}_\mu$	= position vector of vortex $\mu$
$[x]$	= entier function on x

## 1. INTRODUCTION

The development and exploration of natu-

J.J.W. van der Vegt and R.H.M. Huijsmans, Maritime Research Institute Netherlands (MARIN)  
Haagsteeg 2, P.O. Box 28, 6700 AA Wageningen, The Netherlands

ral resources is increasingly engaged in water depths beyond 500-1000 m. The fatigue and operational limits of production and drilling systems, like riser bundles, is dominated by strong vibrations induced by vortex shedding. The engineering approach to determine the forces on bluff bodies commonly uses the equation of Morison with use of experimentally obtained coefficients. In order to describe the forces on bluff bodies more accurately, it is of importance to take into account the nature of the instationary flow around bluff bodies. This flow is dominated for high Reynolds numbers by vortex shedding. The numerical simulation of high Reynolds number flows can be achieved through the use of discrete vortex models.

There are, however, severe limitations to the application of these methods in engineering practice. This is due to the fact that these discrete vortex models inadequately describe viscous effects in the flow and require large computational efforts.

In this paper an alternative method is presented which solves most of the problems connected with discrete vortex models.

## 2. REVIEW OF EXISTING METHODS

At the moment there exists a vast amount of numerical methods for fluid dynamical problems, each having its own special range of applications. They can be roughly subdivided into three main categories: Eulerian, Lagrangian and Coupled Eulerian-Lagrangian descriptions.

The Eulerian methods can be associated with finite difference methods (FDM) and finite element methods (FEM) using a grid fixed in space. However, despite their wide-spread use, it is still difficult to calculate an unsteady flow around bluff bodies at moderate to high Reynolds numbers using FDM or FEM.

Therefore an interesting alternative is presented by the Lagrangian description of the flow field which is related to vortex models. These methods are based on the fact that the behaviour of high Reynolds number flows with large embedded vortical structures can be described with an inviscid model. However, these Lagrangian descriptions suffer from a poor computational efficiency, which can be improved by using a grid fixed in space, yielding the coupled Eulerian-Lagrangian descriptions such as the Vortex in Cell methods (VIC).

In this paper the discussion is confined to Lagrangian and Coupled Eulerian-Lagrangian descriptions.

### 2.1 Basic Principles of Vortex Methods for Two-Dimensional Flows

In this section the basic principles of vortex methods will be discussed. The oldest and most simple vortex method is the point vortex method in which the vortices are represented by Dirac distributions. Then the vorticity field can be represented by:

$$\omega(\underline{x}, t) = \sum_{\mu=1}^N \Gamma_{\mu} \delta(\underline{x} - \underline{x}_{\mu}(t)) \quad (1)$$

in which  $\underline{x}_{\mu}(t)$  is the instantaneous position of the point vortex with index  $\mu$  and circulation  $\Gamma_{\mu}$  and  $\delta$  is the Dirac distribution.

To satisfy the 2-D inviscid vorticity transport equation:

$$\frac{\partial \omega}{\partial t} + (\underline{u} \cdot \nabla) \omega = 0 \quad (2)$$

the velocity of each vortex has the value of the velocity field at its present location:

$$\frac{d\underline{x}_{\mu}}{dt} = \underline{u}(\underline{x}_{\mu}, t) \quad (3)$$

This local fluid velocity  $\underline{u}(\underline{x}_{\mu}, t)$  is induced by all other vortices, except the vortex itself, plus an additional potential velocity, e.g. due to an onset flow or the disturbance velocity caused by an obstacle. The induced velocity caused by the vortices is given by the Biot-Savart law of interaction:

$$\underline{u}(\underline{x}_{\mu}, t) = -\frac{1}{2\pi} \sum_{\substack{j=1 \\ j \neq \mu}}^N \frac{(\underline{x}_{\mu} - \underline{x}_j) \times \underline{e}_z \Gamma_j}{|\underline{x}_{\mu} - \underline{x}_j|^2} \quad (4)$$

with  $\underline{e}_z$  the unit vector perpendicular to the 2-D flow field.

The local induced velocity is the solution to the Poisson equation:

$$\nabla^2 \underline{u} = -\nabla \times (\omega \underline{e}_z) \quad (5)$$

subject to the boundary condition:

$$\underline{u} \cdot \underline{n} = 0 \quad \text{at } \partial\Omega \quad (6)$$

where  $\underline{n}$  is the unit outward normal at the body contour  $\partial\Omega$ . Inserting equations (1) and (4) into equation (3) finally yields a set of 2N non-linear ordinary differential equations for the position of N point vortices.

$$\frac{d\underline{x}_{\mu}}{dt} = -\frac{1}{2\pi} \sum_{\substack{j=1 \\ j \neq \mu}}^N \frac{(\underline{x}_{\mu} - \underline{x}_j) \times \underline{e}_z \Gamma_j}{|\underline{x}_{\mu} - \underline{x}_j|^2} + \underline{u}_B(\underline{x}_{\mu}, t) \quad (7)$$

in which  $\underline{u}_B$  is an additional velocity due to an onset flow and the disturbance velocity caused by an obstacle. These ordinary differential equations can be solved, e.g. by using an Euler or Runge-Kutta time step integration method.

The described procedure possesses some advantages over FDM or FEM such as:

- The numerical procedure outlined above is gridless, therefore preventing the occurrence of problems related to the generation of a grid or to the numerical viscosity caused by a grid at high Reynolds numbers.
- Since no time-averaging is used the procedure can simulate unsteady flows. Notwith-



standing these advantages, there are some serious problems related to the point vortex method which will be discussed shortly.

### 2.1.1 Chaotic Motions

The velocity induced by a point vortex shows a strong singular behaviour when two vortices come close together. This leads after some time steps to chaotic motions of the vortices. There are two ways of dealing with this singular behaviour:

- Shear Layer approximation;
- Vortex Blob method.

For relatively high Reynolds numbers the vorticity is confined to a very thin shear layer emanating from the body. The velocity induced by these shear layers can be calculated by using panel methods. Applications of first order panel methods are shown by e.g. Faltinsen (1982) while higher order panel methods are used by Hoeijmakers (1984). In order to eliminate the singular behaviour which causes the chaotic motions a rediscritization technique must be applied, Fink and Soh (1974). However, Moore (1981) showed that this process for a circular vortex sheet is not sufficient to eliminate the chaotic behaviour at all times, although most of the time it gives reasonable results.

Another way to avoid the singular behaviour of the point vortex is the spreading of vorticity over some finite core (called a blob) based on the fact that real vortices have finite cores. This method effectively reduces chaotic behaviour and will be discussed in detail somewhat more. In the vortex blob method the vorticity field is represented by a set of smooth functions of compact support.

$$\omega(\underline{x}, t) = \sum_{\mu=1}^N \Gamma_{\mu} \gamma_{\mu}(\underline{x} - \underline{x}_{\mu}(t)) \quad (8)$$

in which  $\gamma_{\mu}$  is the vorticity distribution function normalized by:

$$\int \gamma_{\mu}(\underline{x}') d\underline{x}' = 1 \quad (9)$$

If it is assumed that all vortices have the same circular core shape one may write:

$$\gamma_{\mu}(|\underline{x} - \underline{x}_{\mu}(t)|) = \frac{1}{\sigma_{\mu}^2} f(|\underline{x} - \underline{x}_{\mu}(t)|/\sigma_{\mu}) \quad (10)$$

where the function  $f$  is common to all vortices and  $\sigma_{\mu}$  is a measure for the core radius. A particular choice for  $f(\cdot)$  is a Gaussian distribution.

$$\gamma_{\mu}(|\underline{x} - \underline{x}_{\mu}(t)|) = \frac{1}{\pi \sigma_{\mu}^2} \exp(-|\underline{x} - \underline{x}_{\mu}(t)|^2/\sigma_{\mu}^2) \quad (11)$$

Inserting equation (10) into the Poisson equation written in terms of the stream function  $\psi$  yields the equation for a vortex blob centered in the origin of a Cartesian co-ordinate system.

$$\Delta \psi = - \frac{\Gamma_{\mu}}{\sigma_{\mu}^2} f(|\underline{x}|/\sigma_{\mu}) \quad (12)$$

This equation can be solved analytically for a Gaussian vorticity distribution yielding:

$$\psi(x, y) = - \frac{\Gamma_{\mu}}{4\pi} \left\{ \ln(x^2 + y^2) + E_1\left(\frac{x^2 + y^2}{\sigma_{\mu}^2}\right) \right\} \quad (13)$$

which is a useful result for the investigation of the accuracy of a Fast Elliptic Solver (FES) for a vortex blob method using Gaussian vorticity distribution, as will be discussed later. Once the Poisson equation (12) is solved it is possible to calculate the induced velocities. Only the final result for the induced velocity in the x-direction is presented.

$$u(x, y) = - \frac{\Gamma_{\mu}}{\sigma_{\mu}^2} \frac{y}{x^2 + y^2} \int_0^{\sqrt{x^2 + y^2}} r f(r/\sigma_{\mu}) dr \quad (14)$$

The y-component of the induced velocity  $v(x, y)$  is analogous. Introducing a function  $g(\eta)$  defined as:

$$g(\eta) = \frac{2\pi}{\sigma_{\mu}^2} \int_0^{\eta} z f(z/\sigma_{\mu}) dz \quad (15)$$

the induced velocity of a set of  $N$  vortex blobs becomes:

$$u(\underline{x}_{\mu}, t) = - \frac{1}{2\pi} \sum_{j=1}^N \frac{(\underline{x}_{\mu} - \underline{x}_j) \times \underline{e}_z \Gamma_j g(|\underline{x}_{\mu} - \underline{x}_j|/\sigma_{\mu})}{|\underline{x}_{\mu} - \underline{x}_j|^2} \quad (16)$$

A limiting analysis  $\underline{x}_{\mu} \rightarrow \underline{x}_j$  now shows a regular behaviour of the induced velocity. Equation (16) is nearly the same as the result obtained for the point vortex method equation (4), which showed that the vortex blob with a circular core behaves at all distances similar to a point vortex with an adjusted circulation  $\Gamma_{\mu} g(\cdot)$ .

Actually the vortex blob method is an approximation to the exact solution of the inviscid transport equation. Therefore its accuracy was investigated intensively, showing that special forms of vorticity distributions are superior. Leonard (1980) showed that when using a Gaussian vorticity distribution this would yield a second order accurate method.

### 2.1.2 Computational Efficiency

The point vortex method and related methods, the vortex blob and panel method, all have a computational efficiency which is very poor. The most time consuming part in the algorithm is the calculation of the induced velocities of the vortices which has an operation count proportional to  $N^2$  where  $N$  is the number of vortices. The Vortex in Cell method, using FES, has an operation count proportional

to  $N + M \log_2 M$ , where  $M$  is the number of grid points used for the solution of the Poisson equation for the induced velocities or the streamfunction. In this method the induced velocities are calculated by solving the Poisson equation (5) on a grid fixed in space using FDM after distributing the vorticity to the grid points through linear interpolation. Then the vortices are advanced using a Lagrangian scheme.

An application of this method to the solution of the flow around a circular cylinder can be found in Stansby and Dixon (1983).

Despite its improved efficiency the method is not very useful because improved computational efficiency is gained at the cost of reduced accuracy. When two vortices come close together the resolution of the grid becomes too small leading to incorrect vortex-vortex interactions and anisotropy.

### 2.1.3 Viscous Effects

The point vortex method and related methods are inviscid in nature, which causes problems with the creation of vorticity at the wall or the reduction of circulation in the wake. There are a number of ways to cope with the problem based on empirical or semi-empirical approaches, e.g. Sarpkaya (1979). The Kutta condition is very useful when dealing with a fixed separation point at some sharp edge, but if separation occurs on a smooth surface, knowledge about the location of the separation point is necessary. This must be obtained through experiments which are rather difficult in unsteady flow. Deffenbaugh and Marshall (1976) report that the results of 2-D unsteady boundary layer calculations are not very promising. Chorin (1973) proposed a more ambitious algorithm based on operator splitting of the Navier-Stokes equations. This will be elucidated in the next section.

## 3. NUMERICAL SIMULATION OF FLOW AROUND BLUFF BODIES USING AN EFFICIENT VORTEX BLOB METHOD

### 3.1 Discussion of the Chorin Scheme

All the methods discussed in Section 2 either suffer from a poor computational efficiency or problems associated with viscous effects such as the introduction of vorticity in the fluid. A way to get around these problems is using the scheme proposed by Chorin (1973) and combining this with a vortex blob method and a very accurate and efficient FES.

The Chorin scheme is based on operator splitting, a general review of which has been given by Sod (1980). Consider the Navier-Stokes equations for an incompressible flow written in vorticity transport form:

$$\frac{\partial \omega}{\partial t} + (\underline{u} \cdot \nabla) \omega = \nu \Delta \omega \quad (17)$$

and continuity equation:

$$\text{div}(\underline{u}) = 0 \quad (18)$$

with boundary conditions at the body

$$\underline{u} = \underline{u}_w \text{ at } \partial\Omega \quad (19)$$

and at infinity:

$$\underline{u} = \underline{U}(t) \quad (20)$$

Then operator splitting is used to separate this set of equations into two parts:

- the Euler equations

$$\frac{\partial \omega^E}{\partial t} + (\underline{u} \cdot \nabla) \omega^E = 0 \quad (21)$$

with continuity equation

$$\text{div} \underline{u}^E = 0 \quad (22)$$

subject to boundary conditions at the body

$$\underline{u}^E \cdot \underline{n} = \underline{u}_w \text{ at } \partial\Omega \quad (23)$$

and at infinity

$$\underline{u}^E = \underline{U}(t) \quad (24)$$

and the diffusion equation

$$\frac{\partial \omega^D}{\partial t} = \nu \Delta \omega^D \quad (25)$$

The coupling between these two sets of equations is established through the no-slip condition in order to remove the non-zero tangential velocity at the boundary which still exists after the solution of the inviscid Euler equations. The effect of viscosity results in the creation of vortices at the boundary of the body with strength:

$$\omega^D(s) = \underline{u}^E(s) \cdot \underline{t}(s) \quad \forall s \in \partial\Omega \quad (26)$$

These vortices and the vortices already present in the fluid from previous time steps are diffused according to equation (25). In this way a solution is achieved through the subsequent application of an Euler and a diffusion step.

In general the concept of operator splitting should be considered carefully because convergence to the Navier-Stokes solution is not guaranteed. However, Chorin et al. (1978) showed that the method converged if each sub-step was convergent. Beale et al. (1981) gave expressions for the error introduced by this splitted algorithm showing that the method was second order accurate in time, if a modified algorithm was used. The method consisted of applying a diffusion step with time step  $\Delta t/2$ , followed by an Euler time step  $\Delta t$  and finally one more diffusion step with  $\Delta t/2$ . In this way an interesting grid-free solution method becomes available which is especially suited for moderate and high Reynolds number flows, be-

cause the error in the splitting scheme decreases with increasing Reynolds number.

### 3.2 Solution of the Diffusion Equation

The solution of the diffusion equation presents no special problems. A grid free solution technique of the diffusion equation is the random walk concept in which the vortices are diffused using a random walk with a Gaussian probability distribution and zero mean and standard deviation.

$$\sigma_D = \sqrt{2\Delta t \nu} \quad (27)$$

### 3.3 Variationally Optimized Grid Insensitive Vortex Tracing Method

An accurate and numerically efficient grid free solution technique for the Euler equations presents more problems as discussed in Section 2.

A method which solves most of the problems is introduced by Buneman (1974) for point vortices. It presents a more fundamental approach to the construction of fast elliptic solvers originally given by Lewis (1970). He derived a general three dimensional variational principle for plasmas in the Vlasov limit based on an exact Lagrangian description. In the Vlasov approximation it is possible to represent particles by time-dependent distribution functions, one for each particle. The same approximation is made in vortex blob methods. It is possible to show that a plasma in the Vlasov limit and an inviscid vortical fluid are mathematically equivalent, Wang (1977). Buneman extended the method of Lewis and applied it to two-dimensional time dependent flows with point vortices. He used a variational formulation for point vortices and obtained through filtering in Fourier space vortices with finite cores. However, this filtering in Fourier space was performed without a direct relation with physics. Therefore, the variational formulation is extended for the vortex blob method.

The action function for the inviscid motion of a set of vortex blobs in an unbounded fluid, which is energy and momentum conservative, is given by:

$$\begin{aligned} J(\psi, x_\mu, y_\mu) = & \iiint 0.5 |\nabla \psi|^2 dx dy dt + \\ & - \sum_\mu \Gamma_\mu \{ \iiint \gamma(|\underline{x} - \underline{x}_\mu|) \psi(x, y) dx dy dt + \\ & + 0.5 \int (x_\mu dy_\mu - y_\mu dx_\mu) \} \end{aligned} \quad (28)$$

in which  $\mu$  is the vortex index,  $\psi$  the stream-function and  $(x_\mu, y_\mu)$  the vortex position in a Cartesian co-ordinate system. Variation of  $\psi$ ,  $x_\mu$  and  $y_\mu$  now yields:

$$\Delta \psi = - \sum_\mu \gamma(|\underline{x} - \underline{x}_\mu|) \quad (29)$$

$$\frac{dy_\mu}{dt} = - \iint \gamma(|\underline{x} - \underline{x}_\mu|) \frac{\partial \psi(x, y)}{\partial x} dx dy \quad (30)$$

$$\frac{dx_\mu}{dt} = \iint \gamma(|\underline{x} - \underline{x}_\mu|) \frac{\partial \psi(x, y)}{\partial y} dx dy \quad (31)$$

The paths of the vortex blobs now can be found by solving the Poisson equation (29) and advancing the vortices according to the equations (30) and (31) which is in accordance with the theorems of Kelvin and Helmholtz. These equations, however, can be solved more easily in Fourier space. Applying a two-dimensional discrete Fourier transform with period  $L_x$  and  $L_y$  in x- and y-direction yields the transformed action function:

$$\begin{aligned} J(\psi_k, x_\mu, y_\mu) = & L_x L_y \int 0.5 \sum_k |k|^2 |\psi_k|^2 dt + \\ & - \sum_\mu \Gamma_\mu \{ \sum_k P(|k|) \psi_k e^{ik \cdot \underline{x}_\mu} dt + \\ & + 0.5 \int (x_\mu dy_\mu - y_\mu dx_\mu) \} \end{aligned} \quad (32)$$

in which

$$\delta k_x = 2\pi n/L_x, \delta k_y = 2\pi m/L_y \\ (n, m = 0, \pm 1, \pm 2, \dots)$$

and the filterfunction  $P(|k|)$  is defined as:

$$P(|k|) = \int \gamma(|\underline{x} - \underline{x}_\mu|) e^{-ik \cdot \underline{x}_\mu} d\underline{x} \quad (33)$$

Variation of  $\psi_k$ ,  $x_\mu$  and  $y_\mu$  yields:

$$L_x L_y |k|^2 \psi_k = P(|k|) \sum_\mu \Gamma_\mu e^{-ik \cdot \underline{x}_\mu} \quad (34)$$

$$\frac{dy_\mu}{dt} = - \sum_k ik_x P(|k|) \psi_k e^{ik \cdot \underline{x}_\mu} \quad (35)$$

$$= - \frac{\partial}{\partial x_\mu} \sum_k P(|k|) \psi_k e^{ik \cdot \underline{x}_\mu} \quad (36)$$

$$\frac{dx_\mu}{dt} = \sum_k ik_y P(|k|) \psi_k e^{ik \cdot \underline{x}_\mu} \quad (37)$$

$$= \frac{\partial}{\partial y_\mu} \sum_k P(|k|) \psi_k e^{ik \cdot \underline{x}_\mu} \quad (38)$$

However, the solution of these equations is as expensive as the direct method using the Biot-Savart equation, because it requires at each time step the evaluation of twice as many trigonometric functions as there are vortices. This problem can be circumvented using cubic spline interpolation to trigonometric functions which has the additional benefit of creating the possibility of using Fast Fourier Transforms (FFT). This cubic spline approximation procedure then leads to an operational count of order  $N + m \log m$ , in which  $m$  is the number of Fourier components. The cubic spline

approximation can be performed in several ways, but the method using a least squares approximation turned out to be the most appropriate. The main reason for this is the fact, that standard cubic spline approximations force agreement between function and approximant at the knot points  $x=n$ , ( $n=1,2,\dots$ ), but since the function to be approximated is known throughout the whole interval a more accurate approximation can be obtained.

The mean square error over the interval can be minimized by a proper choice of the coefficient  $S(k)$  in the approximation of  $e^{ikx}$  with unit intervals:

$$e^{ikx} = S(k) \sum_{j=[x]-1}^{[x]+2} e^{ikj} S_3(x-j) = S(k) I(x) \quad (39)$$

in which  $S_3$  is the standard cubic spline. Since the approximation is independent of the chosen interval the function  $S(k)$  is determined with a least squares approximation in the interval  $[0,1]$ .

$$S(k) = \int_0^1 I(x) e^{-ikx} dx / \int_0^1 I(x)^2 dx \quad (40)$$

yielding:

$$S(k) = \left( \frac{2}{k} \sin\left(\frac{k}{2}\right) \right)^4 / \left[ \left( 1 - \frac{4}{3} \sin^2\left(\frac{k}{2}\right) + \frac{2}{5} \sin^4\left(\frac{k}{2}\right) - \frac{4}{315} \sin^6\left(\frac{k}{2}\right) \right) \right] \quad (41)$$

with mean square error:

$$\sigma_L^2 = 1 - \left( \frac{2}{k} \sin\left(\frac{k}{2}\right) \right)^8 / \left[ \left( 1 - \frac{4}{3} \sin^2\left(\frac{k}{2}\right) + \frac{2}{5} \sin^4\left(\frac{k}{2}\right) - \frac{4}{315} \sin^6\left(\frac{k}{2}\right) \right) \right] \quad (42)$$

In Fig. 1 the square root of the mean square error is given for Nearest Grid Point (NGP), linear, quadratic and cubic spline interpolation, which shows superior behaviour of cubic spline interpolation. For the higher wave numbers near the aliasing frequency, which is  $\pi$  for interpolation with unit intervals, the error increases rapidly. However, the wave numbers in this region are heavily filtered by  $P(k)$ . Inserting the interpolation for the trigonometric functions in equations (34) and (38) yields the final equations for the paths of large numbers of vortex blobs.

$$L_x L_y |k|^2 \Psi_k = S(k_x) S(k_y) P(|k|) \cdot \sum_j \sum_l e^{-i(k_x j + k_y l)} \cdot \sum_\mu r_\mu S_3(x_\mu - j) S_3(y_\mu - l) \quad (43)$$

$$\frac{dy_\mu}{dt} = - \frac{\partial}{\partial x_\mu} \sum_{j=[x_\mu]-1}^{[x_\mu]+2} \sum_{l=[y_\mu]-1}^{[y_\mu]+2} \cdot \left\{ \sum_k S(k_x) S(k_y) P(|k|) \Psi_k e^{i(k_x j + k_y l)} \right\} \cdot S_3(x_\mu - j) S_3(y_\mu - l) \quad (44)$$

$$\frac{dx_\mu}{dt} = \frac{\partial}{\partial y_\mu} \sum_{j=[x_\mu]-1}^{[x_\mu]+2} \sum_{l=[y_\mu]-1}^{[y_\mu]+2} \cdot \left\{ \sum_k S(k_x) S(k_y) P(|k|) \Psi_k e^{i(k_x j + k_y l)} \right\} \cdot S_3(x_\mu - j) S_3(y_\mu - l) \quad (45)$$

in which  $j$  and  $l$  run through the entire range of data points in equation (43). Using the symmetry for  $S(k)$  and  $P(|k|)$ , the summations can be transformed into the standard form for application of FFT algorithms. In this way an enormous improvement in computational efficiency is achieved. Equations (35) to (38) show that the induced velocity can be determined in two different ways. Either through multiplication with  $k_x$  and  $k_y$ , (35) and (37), or differentiation of the cubic spline, (36) and (38). Both methods were tested; the differentiation of the cubic spline gave slightly better results. The main reason is that after multiplication with  $k_x$  and  $k_y$  the streamfunction is nearly zero at low wave numbers thus reducing the accuracy of the FFT. An additional advantage of differentiating the spline function is that only one FFT is needed for the calculation of the induced velocities, equation (44) and (45). Therefore all subsequent calculations are performed using differentiation of the cubic splines.

The filter function still has to be determined. The most convenient choice is a Gaussian filter because:

- real vortices frequently have Gaussian cores, Tung et al. (1967)
- vortex blobs with Gaussian cores are second order accurate
- Gaussian vorticity distributions yield a Gaussian filter in Fourier space, eliminating side band effects and reducing aliasing
- a Gaussian filter effectively reduces the errors in the interpolation of the exponentials at aliasing frequency

- vorticity distributions with Gaussian cores satisfy the diffusion equation. Two filter functions were tested: A Gaussian probability function truncated at  $k_{\max} = \pi$

$$P_1^2(k) = \exp(-6 k^2/\pi^2) \quad (46)$$

and a spline approximation of  $P^2(k)$  cubical, tending to zero at  $k_{\max} = \pi$

$$P_2^2(k) = 1 - \frac{6}{\pi} k^2(1 - |k|/\pi) \quad |k| < \frac{\pi}{2} \quad (47)$$

$$= 2(1 - |k|/\pi)^3 \quad \frac{\pi}{2} < |k| < \pi \quad (48)$$

The filters gave slightly different results in the close vicinity of the vortex, Figs. 2 through 4, in which the results of the velocity for different filters and numbers of Fourier harmonics are plotted.

In the vortex tracing method derived in this section it is assumed that the streamfunction  $\psi$  is periodic in  $x$ - and  $y$ -direction. In practice one is mostly interested in solutions in a domain extending to infinity. There are several ways to transform the problem to an infinite domain. One way is to transform the problem into an internal Dirichlet problem using an asymptotic expansion of the exact solution of the streamfunction, Ting (1983). This method is rather expensive because the streamfunction of each vortex has to be calculated at many boundary points thus increasing the operation count to  $O(N^2)$ . An alternative method is discussed in a paper by Hockney (1970); he showed that, by using only one quarter of the computation domain and if in the remaining domain no vortices are present, it is possible to simulate an infinite domain with a periodic FFT. This method has the disadvantage that the computing time for the FFT is four times that for a periodic domain. However, the most time consuming part in the calculations is the calculation of the spline weights; therefore at the moment some overhead in the FFT is considered to be not so serious.

### 3.4 Introduction of a Body in the Vortex Tracing Method

The vortex tracing method discussed in Section 3.3 described the behaviour of a set of vortex blobs in an unbounded fluid without a body. A body can be represented with a boundary integral method using a surface source and vorticity distribution. Stansby et al. (1983) showed that it is advantageous to use a vorticity distribution. Then the strength of the vortices, which must be shed from the body in order to satisfy the no-slip condition, equation (26), is immediately known. Stansby only used a vortex layer but it can be shown that an additional source layer is necessary when the exterior flow is non-uniform, e.g. with the influence of vortices in the exterior flow, Hunt (1980A). In order to obtain a more manageable integral equation viz. a Fredholm integral equation of the second kind, it is

necessary to transform the external Neumann condition, equation (23), into an internal Dirichlet condition using Green's theorem. Consider an unbounded fluid with unperturbed potential  $\phi_\infty$ , viz. the potential of the uniform onflow with vortices present in the fluid, in which a body with surface  $S$  is introduced. The potential  $\phi_p$  inside  $S$  becomes:

$$\phi_p = \phi_\infty - \frac{1}{4\pi} \iint_S \mu_D(q) (\underline{n}_q \cdot \nabla_q \left(\frac{1}{R}\right)) ds + \iint_S \sigma(q) \left(\frac{1}{R}\right) ds \quad (49)$$

in which  $\sigma$  and  $\mu_D$  are the unknown source and doublet strength,  $\underline{n}$  the unit normal vector pointing in the exterior fluid domain and  $R$  the distance between the field point  $P$  and the point  $q$  on the surface  $S$ . Suppose that the internal velocity  $\nabla\phi_p$  is required to be equal to the undisturbed velocity  $\nabla\phi_\infty$  then the source strength  $\sigma$  must be equal to:

$$\sigma(q) = (\underline{n}_q \cdot \nabla\phi_\infty q) \quad (50)$$

because otherwise there exists a finite mass flux through the body. Introducing equation (50) into (49) and differentiating equation (49) along  $S^-$  the inner side of surface  $S$ , results in an integral equation for the vorticity strength  $\gamma$ , using some well known identities to transform a doublet distribution into a vorticity distribution, e.g. Hunt (1980B).

$$\underline{n}_p \times \frac{1}{4\pi} \iint_S (\underline{\gamma}_q \times \frac{\underline{R}}{R^3}) ds = \underline{n}_p \times \frac{1}{4\pi} \iint_S (\underline{n}_q \cdot \nabla\phi_\infty q) \nabla_p \left(\frac{1}{R}\right) ds \quad (51)$$

The integral equation can be simplified by confining the problem to two dimensions ( $\underline{\gamma}_q = \gamma_q \underline{e}_z$ ) yielding:

$$\begin{aligned} \frac{\gamma_p}{2} + \frac{1}{2\pi} \oint_C \left\{ [-(y_p - y_q) \frac{dx_p}{ds} + (x_p - x_q) \frac{dy_p}{ds}] \right. \\ \left. [(x_p - x_q)^2 + (y_p - y_q)^2] \right\} \gamma_q ds_q = \\ = -\frac{1}{2\pi} \oint_C \left\{ [(x_p - x_q) \frac{dx_p}{ds} + (y_p - y_q) \frac{dy_p}{ds}] \right. \\ \left. [(x_p - x_q)^2 + (y_p - y_q)^2] \right\} (\underline{n}_q \cdot \nabla\phi_\infty q) ds_q \end{aligned} \quad \forall p \in S \quad (52)$$

where the distance  $s$  is positive measured clockwise and  $C$  is the body contour ( $\oint$  denotes the principle value of integral). This integral equation can be discretised using a panel method with straight line segments and constant vorticity distribution on it, which presents no special problems. However, the resulting matrix is nearly singular which is caused by the non-uniqueness of the surface vorticity formulation. This can be solved by requiring the additional condition:

$$\oint_C \gamma(s) ds = 0 \quad (53)$$

expressing the fact that the only way to introduce vorticity in the fluid and thereby changing the circulation is through satisfaction of the no-slip condition, equation (26). It is now very easy to calculate the tangential velocity at the exterior surface  $S^+$  of the body. Approaching the surface from the exterior and interior part of the body and subtracting the exterior and interior tangential velocity using the fact that the internal velocity is equal to  $\nabla\phi_\infty \cdot \underline{t}_p$ , one easily finds:

$$u_p \cdot \underline{t}_p = \nabla\phi_\infty \cdot \underline{t}_p + \gamma_p \quad \forall p \in S^+ \quad (54)$$

where  $\underline{t}_p$  is the unit tangential vector, positive clockwise. Then the strength of the vortices which must be shed from the body to satisfy the no-slip condition (equation (26)) is immediately known.

The paths of the vortices now can be determined by integration in time of the induced velocities of the vortices, equations (44) and (45), the uniform onflow velocity, equation (24) and the induced velocity of the vortex and source layer.

### 3.5 Time integration

The set of ordinary first order differential equations for the paths of the vortices equation (7) can be solved in several ways. The methods of Euler, Heun and Adams-Bashforth-Moulton were all tested. The Euler method showed to be the most useful time integration method with regard to computing time and memory requirements. Many authors use a constant time step in their vortex tracing method. However, large variations in induced velocities can occur due to the appearance of large vortical structures for which reason the time step was continuously adjusted to ensure a constant global error during the simulation. The global error can be estimated rather accurately using step doubling, as discussed by e.g. Stoer and Bulirsch (1980). Each basic step  $\Delta t$  is done twice; once as two steps  $\Delta t/2$  and once as one step  $\Delta t$ . In this way the optimum time step can be determined for a certain level of accuracy.

### 3.6 Final algorithm for flow simulation using a Chorin scheme

The Chorin scheme as discussed in Section 3.1 can now be constructed using the methods discussed in the previous sections. The variant of Beale and Majda (1981) was used, because of its improved accuracy. This splitting algorithm gives an error proportional to  $\sqrt{\nu \Delta t^2}$  when using an exact solution of the Euler and diffusion equations with time step  $\Delta t$ . In this way the following steps can be discerned:

1. At time  $t=0$  the fluid is impulsively set into motion.

2. The vortex and source strengths are calculated to satisfy the condition of zero normal velocity at the body surface.
3. Vortices with strength  $\gamma$  are created at the body surface to satisfy the no-slip condition. Due to the fact that one half of the vortices disappears in the body as a consequence of the random walk approach twice as many vortices are created to satisfy the no-slip condition in the average.
4. The vortices at the body surface are diffused using the random walk method with time step  $\Delta t/2$ . The vortices which diffuse into the body in the time step after their creation are removed; vortices from previous time steps which diffuse into the body are replaced at the surface.
5. The vortices are transported using the vortex tracing method with time step  $\Delta t$ .
6. A second diffusion step is applied with time step  $\Delta t/2$  and the induced velocities are updated.
7. New vortices are created at the body surface to satisfy the no-slip condition and the process continues at point 4.

## 4. DISCUSSION OF RESULTS

A computer program was written for the numerical method discussed in Section 3. The computations are performed on a CRAY 1S super computer and tests were carried out for the following problems:

- The influence of various filter functions, number of Fourier harmonics and direction on the velocity field of a single vortex.
- The velocity field of one vortex at various locations to study inaccuracies caused by the cubic spline approximation of the exponentials.
- Paths of two vortices in a fluid which is at rest at infinity.
- A circular cylinder in a steady onflow at  $R_N = 10^4$ .

The computations for the circular cylinder were performed using  $128 \times 128$  Fourier harmonics, average time step  $\Delta t = 0.2/U$ , 44 panels at the body surface and a cylinder diameter of 10 grid spacings.

The results of the two filter functions differ slightly, Fig. 2-3, showing that the cubic spline approximation of the Gaussian vorticity distribution was slightly better than the truncated Gaussian distribution when compared with the exact solution, eq. (13). Fig. 4 demonstrates that the influence of polar angle on the tangential velocity is small. The influence of increasing the number of Fourier harmonics disappears above  $64 \times 64$  Fourier harmonics, Fig. 2-3. Then the errors caused by the interpolation of the exponentials and by aliasing prohibit further improvements of the results. For a further improvement of the accuracy a smaller interpolation interval is necessary. It is, however, possible, to correct for numerical errors caused by the interpolation process by adjusting the filter function because the results are nearly independent of position.

The tangential velocity of a vortex blob is shown in Fig. 3 if a filterfunction  $e^{-0.5|k|^2}$  is applied.

In Fig. 5 a vector plot of the induced velocity of a vortex located in an arbitrary position somewhere between the interpolation points (co-ordinates (7.3;9.8)) is shown. There is no visible distortion of the streamlines through inaccuracies in the interpolation of the exponentials. The absolute value of the largest differences in the induced velocities at various locations is about 5% compared with a value of about 50% in the vortex-in-cell method, Eastwood and Hockney (1974).

Another means to study the accuracy is calculating the paths of two vortices. In Section 2.1 it was shown that vortex blobs with circular cores behave like point vortices with an adjusted strength. Therefore the paths of two vortex blobs in a fluid at rest at infinity are concentric circles both having a diameter equal to the distance between the vortices. In Fig. 6 the paths of the two vortices are presented, showing an almost perfect circular shape. When the two vortices have covered the circle twice the deviation from the circle was about 1%. The positions of the grid points used in the interpolation process are marked with + signs.

In Fig. 7-16 vector plots at various time steps of an impulsively started flow around a circular cylinder at  $Re = 10^4$  are shown. It is interesting to compare them with the pictures obtained by Prandtl (e.g. Batchelor (1980), plate 10 and 11) showing perfect agreement. The flow field starts with a potential flow, Fig. 7, which lasts for quite a long time. Next an almost triangular area develops at the trailing end of the cylinder with low fluid velocities, Fig. 8. In this area two small vortices develop which are symmetric and become larger with time. The wake behind the body is closed and the exterior flow resembles a potential flow around an adjusted body, viz. cylinder and wake, Fig. 9. The vortices grow and remain symmetric until their diameter is about two third of the cylinder diameter. In the meantime the separation points move rapidly to an angle of about 110 degrees measured from the forward stagnation point and a considerable back flow occurs at the base of the cylinder toward the separation points, Fig. 10. Suddenly the vortices become asymmetric, Fig. 11, without an external instability being introduced. The wake grows but remains closed, Fig. 12, until the upper vortex is shed from the body, Fig. 13. Then it is no longer possible to discern a closed wake and the well known Von Karman vortex trail can subsequently be seen to develop, Fig. 14-15. Compared with the relative slow changes when the wake was closed now the variations are large and the separation points are no longer fixed in location. A limiting streamline between the wake and the exterior flow is no longer visible.

One of the most important and powerful properties of the numerical method is its

ability to introduce vorticity into the fluid without requiring any knowledge about the location of the separation points. The vortex layer at the body surface represents an infinitely thin boundary layer, which is broken up into small vortices and diffused using the random walk method. The effects of viscosity are most important when the vortices are created and diffused into the fluid. Due to the small variance of the random walk an accurate representation of the body surface is necessary at the points where the vortices are created. It is interesting to see that the thin boundary layer at the front end of the cylinder is not disturbed despite the large core radius of the individual vortex blobs. At the end of the simulations more than 13000 vortex blobs were present in the fluid. In this way the large vortical structures in the wake consist of thousands of individual vortex blobs. In that case the diffusion is much better simulated using the random walk method than by diffusing some large individual vortices. It must be remarked that in the simulation process no vortices are clustered or removed to reduce computing time or chaotic behaviour. The vortex tracing method showed no chaotic behaviour as observed for instance by Baker (1979) with his vortex-in-cell method. The vector plots proved to be a powerful tool in examining both the accuracy of the numerical method and the physical modelling, as opposed to the widely used plots of the positions of vortices, e.g. Stansby (1983).

The computer program is fully vectorized for a CRAY-1S computer and tests were run on a CRAY-1S as well as a CYBER 175-855 computer. The program was ten times faster on the CRAY, but when calculating paths of vortices without a body in the fluid domain the code was 100 times faster on the CRAY due to the fact that the FFT is very efficient on this machine. The numerical method is suited to vectorization because it consists of a large amount of matrix-vector multiplications and Fast Fourier Transforms. However, as in all particle codes, it is rather difficult to solve the problems of indirect addressing which occur in equations (43) to (45). This can be solved by sorting the vortices as discussed by Hockney et al. (1974). In Fig. 16 the CPU time is given as a function of the number of vortices, showing that the calculation of the induced velocities of the panels is by far the most time consuming part. The computing time for the induced velocities of the panels is linear in the number of vortices instead of quadratic as in other methods, e.g. Faltinsen et al. (1982). As an illustration of the CPU-timing for a panel method (Faltinsen) the CPU-time for a new time step for 900 shear layer elements amounts to about two minutes on a CRAY-1S computer.

## 5. CONCLUDING REMARKS

- The vortex tracing method is able to simulate unsteady two-dimensional flow around bluff bodies at moderate Reynolds numbers.
- The method is accurate compared with the

Vortex-in-Cell Method and does not suffer from noticeable grid effects and chaotic behaviour.

- The method requires no knowledge about the separation points and the vortices are created in a physically correct manner.
- The method has a very good computational efficiency and is able to simulate the behaviour of large numbers of vortices at low costs.
- The vector plots of the computation of the flow around a circular cylinder show a remarkable agreement with flow visualization experiments.

#### REFERENCES

- Baker, G.R. (1979): The "Cloud in Cell" Technique Applied to the Roll Up of Vortex Sheets, *Journal of Comput. Phys.*, Vol. 31, pp. 76-95.
- Batchelor, G.K. (1980): *An Introduction to Fluid Dynamics*, Cambridge University Press.
- Beale, J.T. and Majda, A. (1981): Rates of Convergence for Viscous Splitting of the Navier-Stokes Equations, *Math. of Comput.*, Vol. 37, 156, pp 243-259.
- Buneman, O. (1974): Variationally Optimized Grid-Insensitive Vortex Tracing. *Lecture Note in Physics*, Vol. 35, pp 111-116.
- Chorin, A.J. (1973): Numerical Study of Slightly Viscous Flow. *J. of Fluid Mech.* Vol. 57, 4, pp 785-796.
- Chorin, A.J. et.al. (1978): Product Formulas and Numerical Algorithms. *Comm. on Pure and Appl. Math.*, Vol. 31, pp 205-256.
- Deffenbaugh, F.D. and Marshall, F.J (1976): Time Development of the Flow About an Impulsively Started Cylinder. *A.I.A.A. Journal*, Vol. 14, Part 7, pp. 908-913.
- Eastwood, J.W. and Hockney, R.W. (1974): Shaping the Force Law in Two-Dimensional Particle-Mesh Models, *Journal of Comput. Phys.*, Vol 16, pp. 342-359.
- Faltinsen, O.M. and Pettersen, B. (1982): Vortex Shedding Around Two-Dimensional Bodies at High Reynolds Numbers. 15th Symp. on Naval Hydrodynamics ANN ARBOR, pp 1171-1213.
- Fink, P.T. and Soh, W.K. (1974): Calculation of Vortex Sheets in Unsteady Flow and Application in Ship Hydrodynamics. 10-th Naval Hydr. Symp. Cambridge (MASS), pp 463-487.
- Hoeijmakers, H.W.M. (1984): Numerical Computation of Vortical Flows About Wings. Von Karman Lecture Series 1984-04.
- Hockney, R.W. (1970): The Potential Calculation and Some Applications. *Methods of Comput. Phys.*, Vol. 9, pp 136-211.
- Hockney, R.W., Goel, S.P. and Eastwood, J.W. (1974): Quiet High-Resolution Computer Models of a Plasma, *Journal of Comput. Phys.*, Vol. 14, pp. 148-158.
- Hunt, B. (1980A): *Numerical Methods in Applied Fluid Dynamics*. Academic Press London.
- Hunt, B. (1980B): Recent and Anticipated Advances in the Panel Method: The Key to Generalized Field Calculations?, Von Karman Lecture Series 1980-05.
- Leonard, A. (1980): Vortex Methods for Flow Simulation. *J. of Comput. Phys.*, Vol. 37, pp 289-335.
- Lewis, H.R. (1970): Application of Hamilton's Principle to the Numerical Analysis of Vlasov Plasmas. *Methods of Comput. Phys.*, Vol. 9, pp 307-338.
- Moore, D.W. (1981): On the Point Vortex Method. *Siam J. Sci. Stat. Comput.*, Vol. 2, 1, pp 65-84.
- Sarpkaya, T. and Shoaff, R.L. (1979): A Discrete-Vortex Analysis of Flow About Stationary and Transversely Oscillating Circular Cylinders. NPS-69 SL79011, Naval Postgraduate School, Monterey (Cal.).
- Sod, G.A. (1980): *Computational Fluid Dynamics with Stochastic Techniques*. Von Karman Lecture Series 1980-05.
- Stansby, P.K. and Dixon, A.G. (1983): Simulation of Flows Around Cylinders by a Lagrangian Vortex Scheme. *Appl. Ocean. Res.*, Vol. 5, 3, pp 167-178.
- Stoer, J. and Bulirsch, R. (1980): *Introduction to Numerical Analysis*, Springer-Verlag, New York.
- Ting, L. (1983): On the Application of Integral Invariants and Decay Laws of Vorticity Distributions. *J. of Fluid Mech.*, Vol. 127, pp 497-506.
- Tung, C. and Ting, L. (1967): Motion and Decay of a Vortex Ring. *Physics of Fluids*, Vol. 10, pp 900-910.
- Wang, S.S. (1977): Grid-Insensitive Computer Simulation of the Kelvin Helmholtz Instability and Shear Flow Turbulence. Inst. for Plasma Research, Su-IPR Rep. No. 710, Stanford University (Cal.).



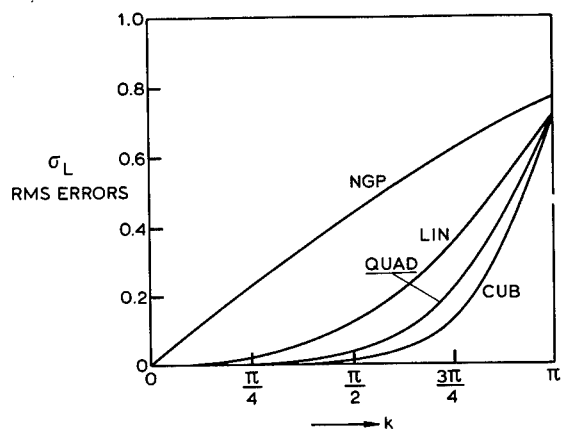


Figure 1 - Square Root of Mean Square Error vs.  $k$  for Nearest Grid Point, Linear, Quadratic and Cubic Spline Interpolation of a Pure Harmonic

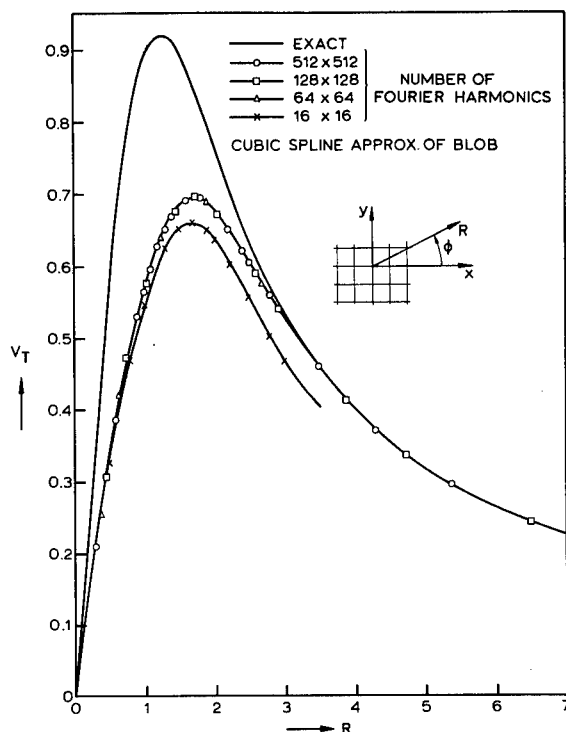


Figure 2 - Tangential Velocity Induced by a Vortex With Strength 10, Using a Cubic Spline Approximation of the Vorticity in the Blob

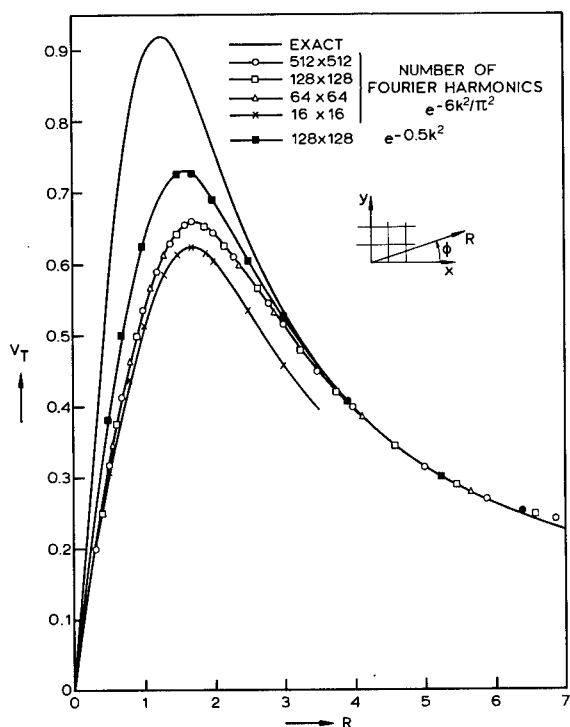


Figure 3 - Tangential Velocity Induced by a Vortex with Strength 10, Using a Truncated Gaussian Vorticity Distribution in the Blob

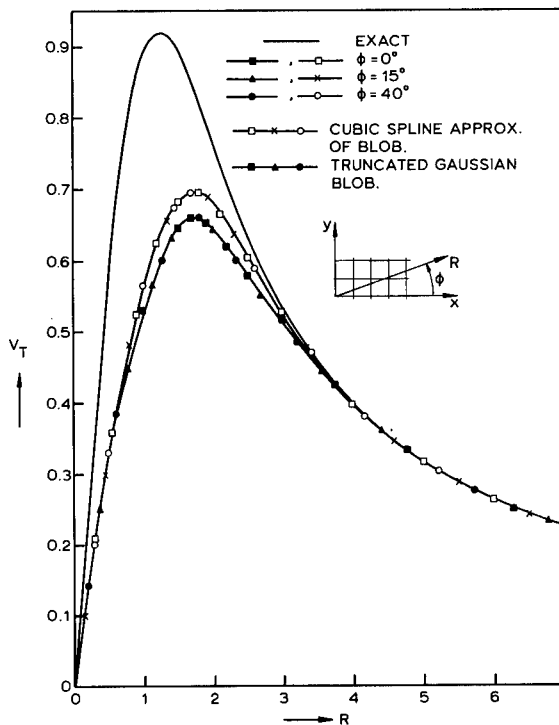


Figure 4 - Tangential Velocity Induced by a Vortex With Strength 10 for Various Polar Angles  $\phi$

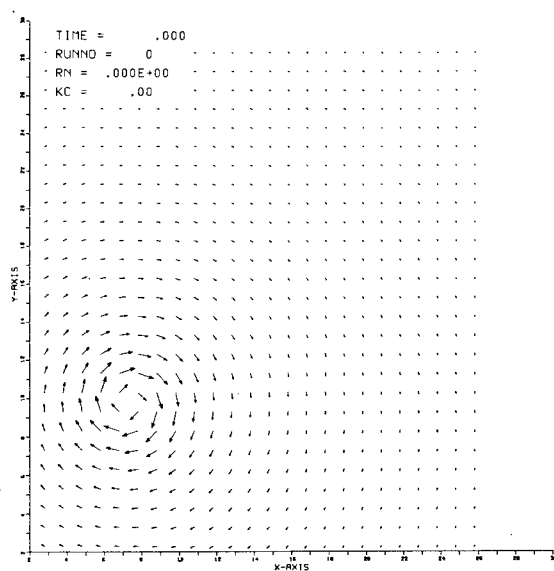


Figure 5 - Vector Plot of the Induced Velocity of a Vortex Located at (7.3;9.8)

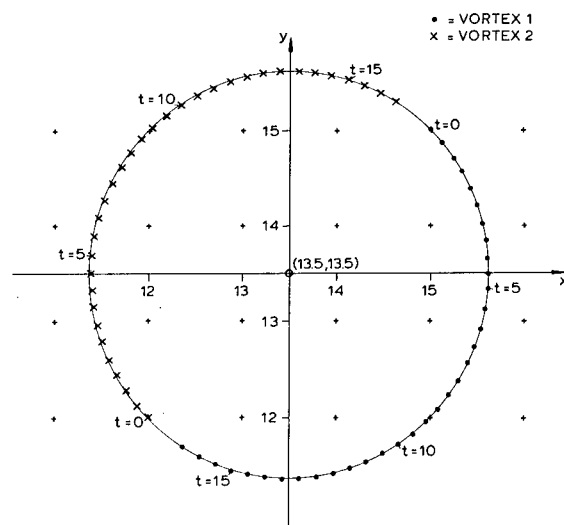


Figure 6 - Paths of Two Vortices in a Fluid at Rest at Infinity

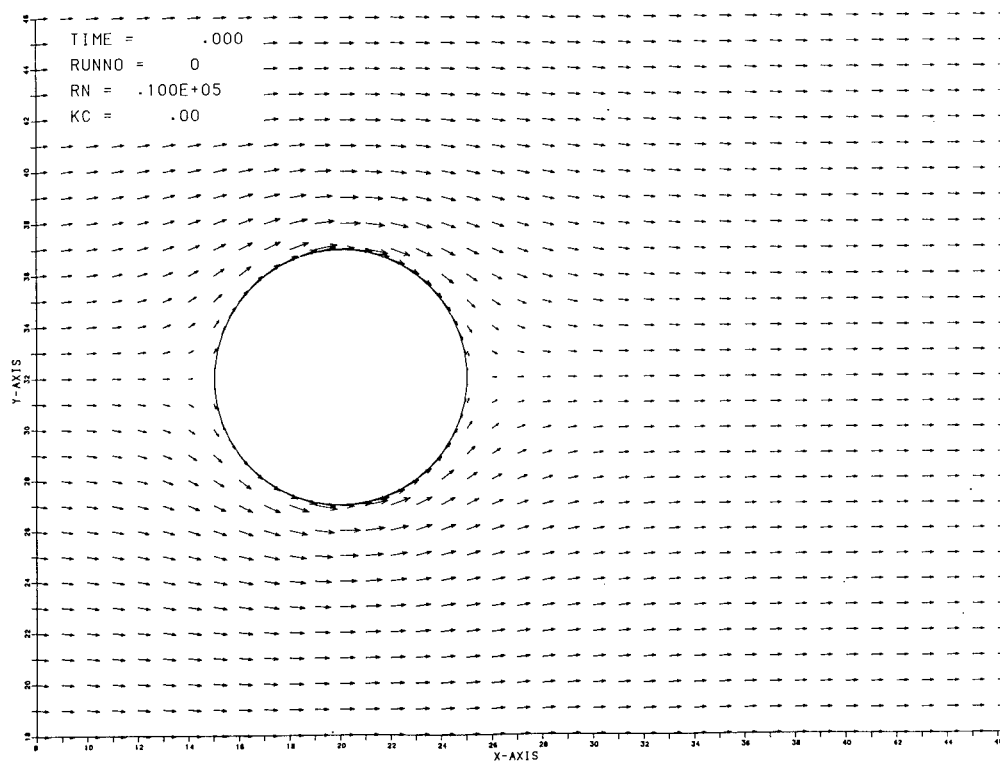


Figure 7 - Evolution of Flow Around A Circular Cylinder in a Steady Onflow

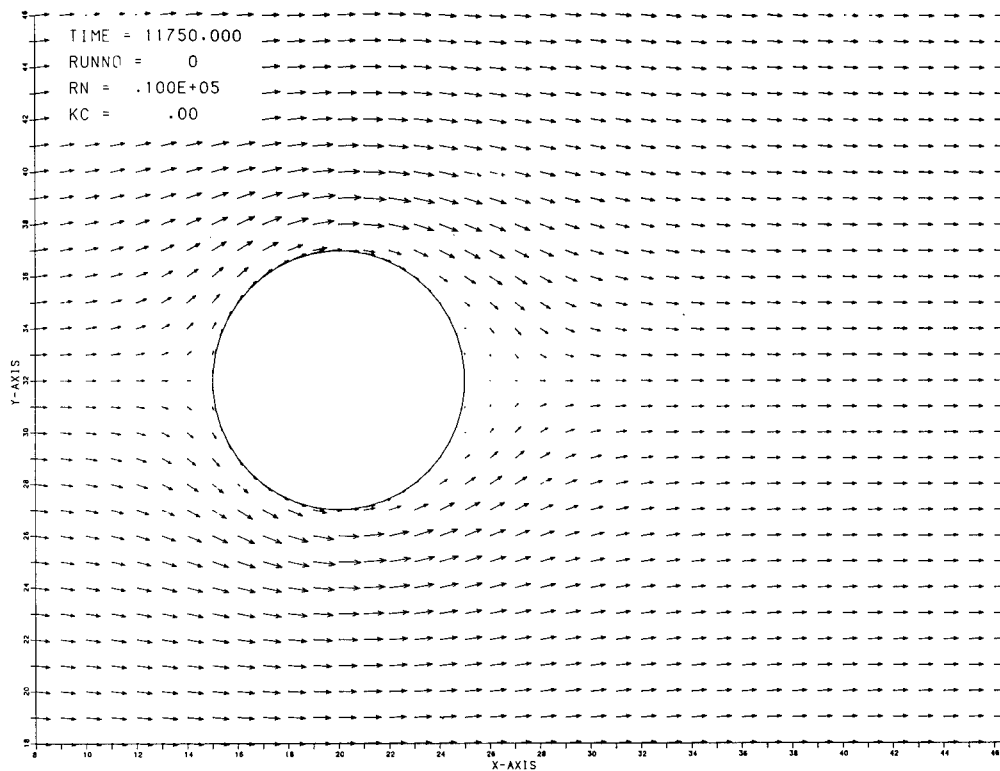


Figure 8 - Evolution of Flow Around a Circular Cylinder in a Steady Onflow

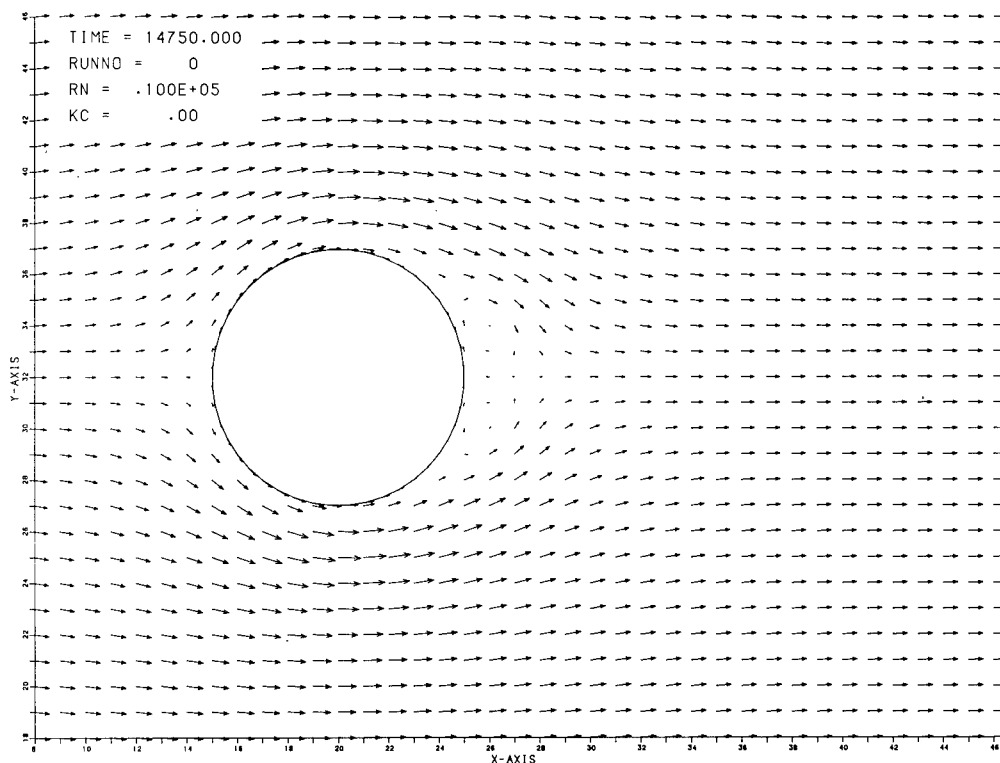


Figure 9 - Evolution of Flow Around a Circular Cylinder in a Steady Onflow

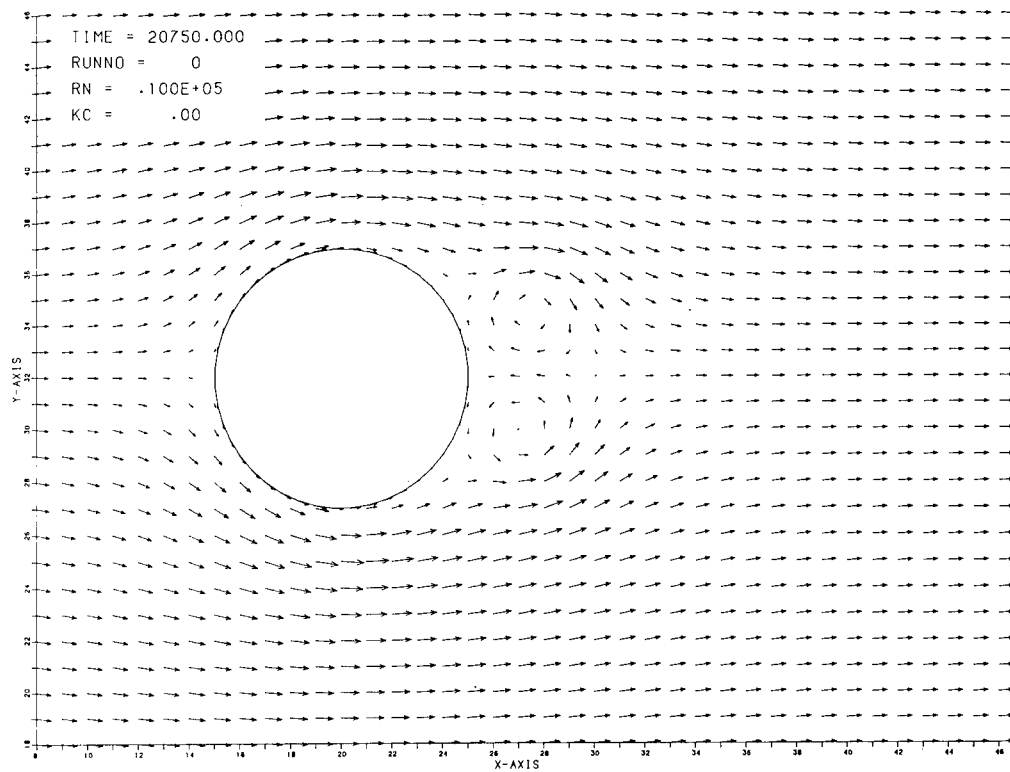


Figure 10 - Evolution of Flow Around a Circular Cylinder in a Steady Onflow

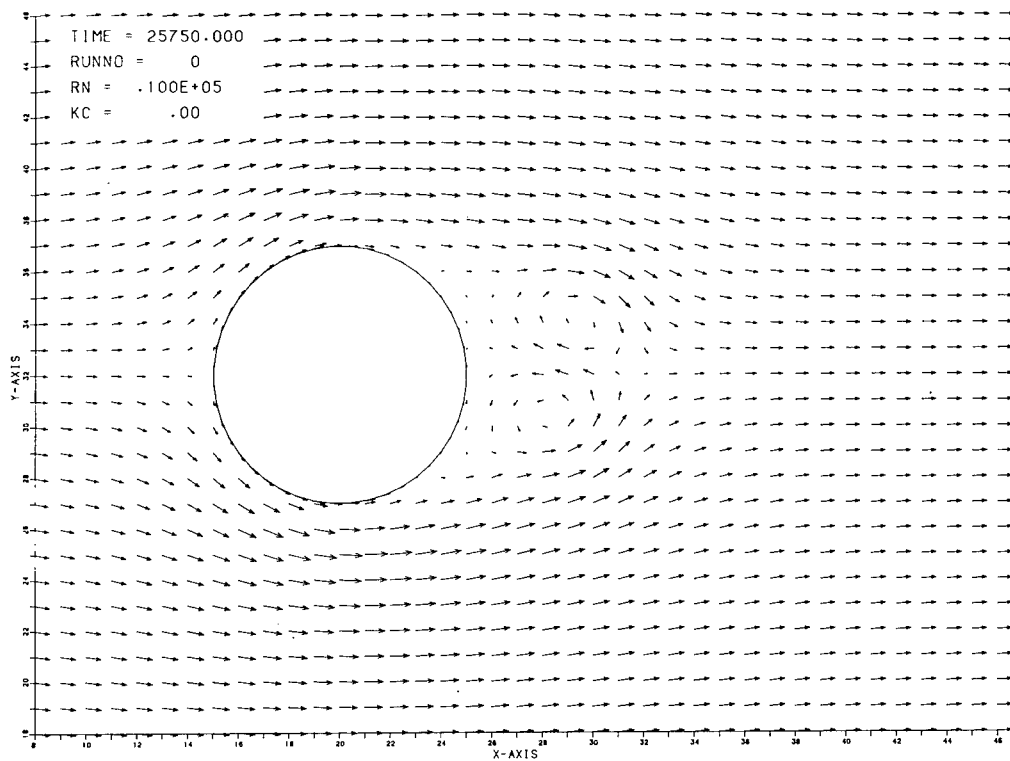


Figure 11 - Evolution of Flow Around a Circular Cylinder in a Steady Onflow

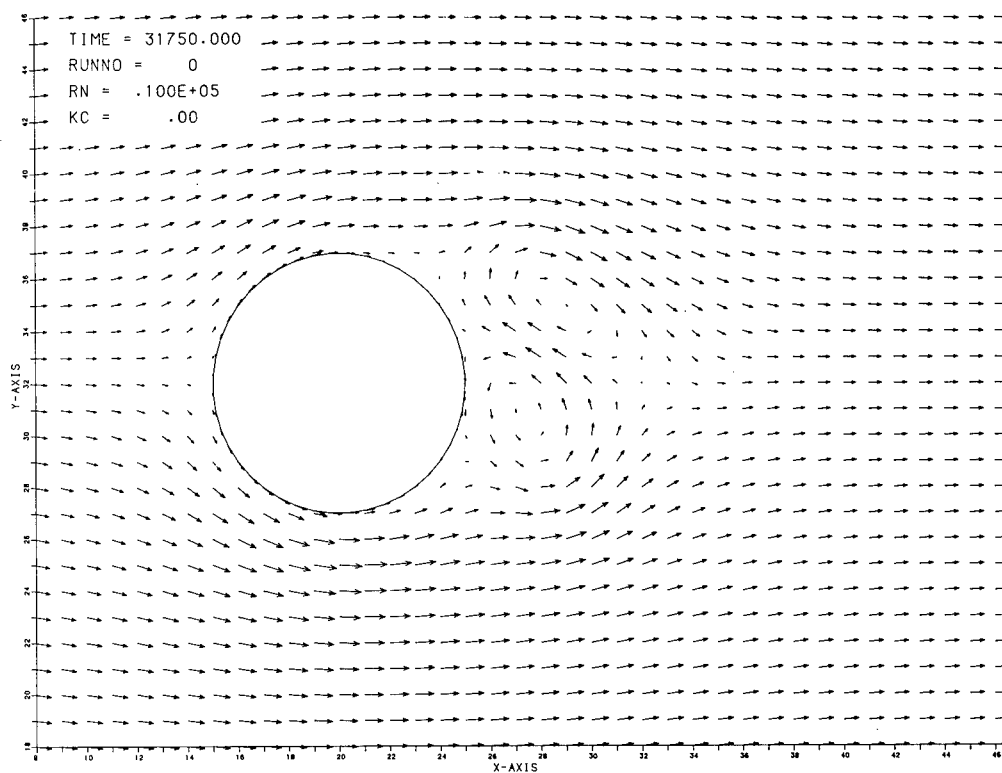


Figure 12 - Evolution of Flow Around a Circular Cylinder in a Steady Onflow

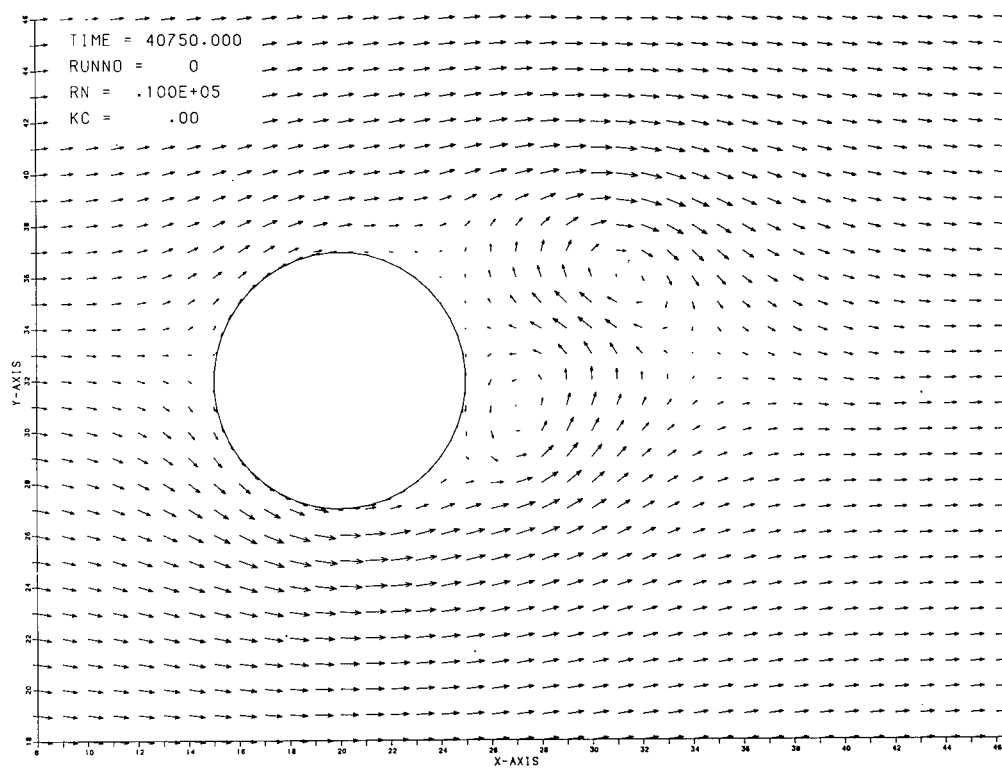


Figure 13 - Evolution of Flow Around a Circular Cylinder in a Steady Onflow

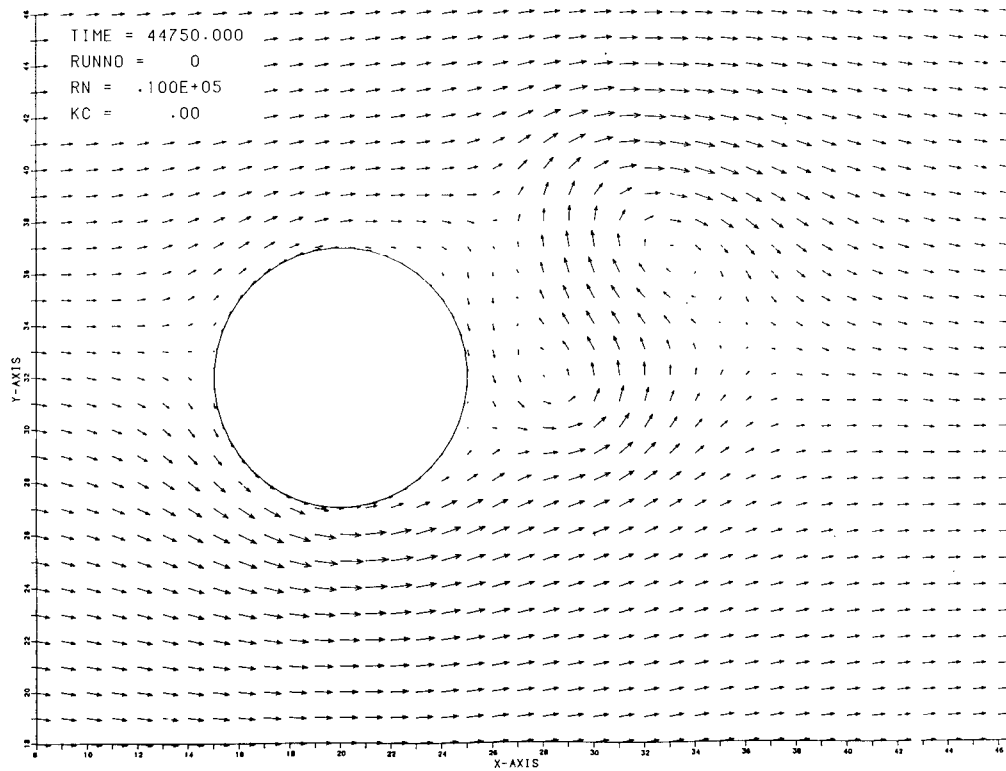


Figure 14 - Evolution of Flow Around a Circular Cylinder in a Steady Onflow

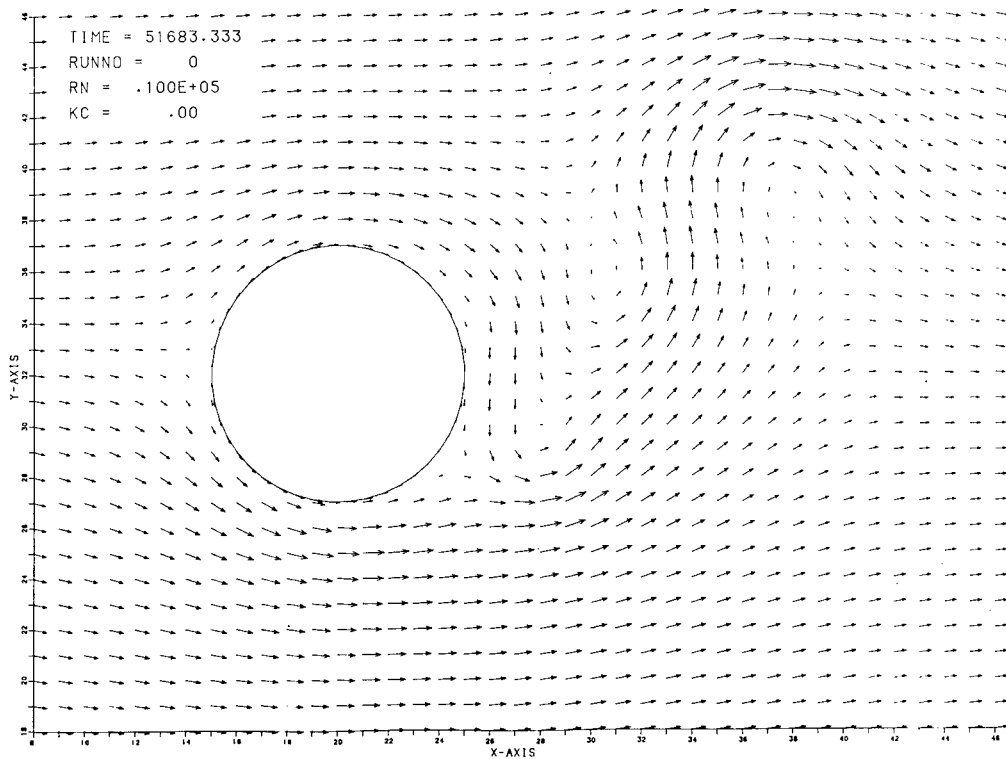


Figure 15 - Evolution of Flow Around a Circular Cylinder in a Steady Onflow

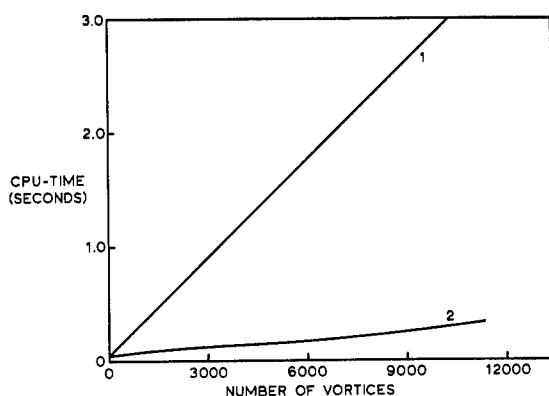


Figure 16 - Timing on CRAY-1S for Calculation of One Time Step:  
 1. Total CPU-Time  
 2. CPU-Time for the Calculation of the Induced Velocities of the Vortices

## DISCUSSION

Dr. BJØRNAR PETTERSEN,  
 The Norwegian Institute of Technology,  
 Trondheim, Norway:

What is the time (dimensionless f.ex  $t^* = Ut/R$ ) in Fig. 15, and how far have you gone with your simulation?

The time when the vortices become asymmetric, is it the same in every run? Is it sensitive to other parameters?

Can the authors give more details about the motion of the separation points?

In some situations when the vortices are close to the cylinder we have large velocities on the back of the cylinder. Secondary separation occurs. Has this been discovered in your model?

I am not sure about the CPU-time for the panel method mentioned in the last part of the paper because we have not used a CRAY 1. We are using a Cyber 205 and in our calculations we use at most 500 elements in the 2D case. The number of elements in the wake varies, it increases with time.

Prof. Dr. AAD J. HERMANS,  
 Technische Hogeschool Delft,  
 Delft, Netherlands:

First I would like to congratulate the authors on their fine paper on the interesting topic of vortex simulation. I am impressed by the fact that the authors are able to combine and improve a classical method of integral equations with a modern method of operator splitting, together with a fast Fourier solver for the overall field equations. To my knowledge it is the first time that these methods have been combined successfully.

I would like to ask the following two questions:

The first one is a purely mathematical one: It is shown in the literature that the operator splitting method of Chorin converges to the exact solution if the time step  $\Delta t$  tends to zero. This time step  $\Delta t$  is the period over which the Euler step and thereafter the diffusion step is carried out exactly. The authors carry out the Euler step and diffusion step approximately. I wonder whether they can give some more information now or in the future about the convergence of their method.

My second question concerns the stability of the method. One of my students worked out the method of Graham for vortex shedding at sharp edges in an oscillatory flow. The vortex pattern looked quite realistic except in the area where the distance between the vortices becomes too small. A recombination of vortices has to be carried out. Similar phenomena turn up if you use Faltinsen's method. Do the authors expect that their method does not show a similar chaotic behavior if they carry out their computations over a large period of time?

## AUTHORS' REPLY

We would like to thank the discussers for their interesting and valuable comments on our paper.

To answer the questions of Dr. Pettersen we must acknowledge that the uniform flow velocity has been dropped from the text in the paper, the uniform onflow velocity amounts to  $1.15 \text{ E-3 m/s}$  so the dimensionless time in Fig. 15 amounts to approximately 11.9. The time where the vortices start to grow asymmetrically is solely dependent in this case on the realisation of the random walk. It can be seen from Fig. 8 that the separation point moves from the aft stagnation point up to  $110^\circ$ , measured from the forward stagnation point, as explained in the text. From thereon the separation point starts to oscillate. More detailed results will be presented in the near future.

The mechanism for secondary separation is not due to the large velocities at the back of the cylinder near the surface. The effect of using the vortex blob model is, that when the vortices come close to the wall of the cylinder (with other vortices) the induced velocities remain finite; however, still secondary separation occurs as can be seen in Fig. 10 and 11 at the back of the cylinder.

The question about the timing of a panel method, e.g. as has been developed by Faltinsen and Pettersen, relates to the calculation of the induced velocities which is done following the Biot-Savart law of interaction. In this case the calculation of the induced velocities at the vortex location is by far the most time-consuming part of the code. As has been explained in the text the computation effort is quadratic with the number of vortices which increases in time.

The question raised by Prof. Hermans about the convergence of the Chorin scheme can be answered by considering that the accuracy of the variant of the Chorin scheme as used by the authors is second order accurate in time. However, the proof given by Beale and Madja (1981) is valid for a flow without the presence of a body. The vortex shedding process still has to be incorporated in the proof.

As far as the question of Prof. Hermans about the chaotic motion is concerned, we believe that the vortex blob method is capable of suppressing randomization of the paths of vortices at all times even if two vortices are very close to each other. A final test of the stability of the Chorin scheme would be the simulation of the growth of a vortex sheet over a large period of time. However, this has still to be performed.

Additional Reference:

Beale J.T. and Madja (1981): Rates of convergence for viscous splitting of the Navier-Stokes equation. *Math. of Comp.*, Vol. 37, 156, pp. 243-259.

ADDENDUM PAGE REFER TO PAGE 568  
FOR AUTHOR'S REPLY

From Dr. A.K. Lewkowicz, The  
University of Liverpool, England

The authors of "Resistance Increase Due to Surface Roughness" have presented a very interesting and useful contribution to the topic which ought to be noticed by many who work in the field. However, to widen the discussion, I should like to raise a few points of argument instigated by the paper. These are:

1. An instrumental concept evolved in the paper is that presented in Sec. 5.2 where the authors propose a new scaling factor for the height of the hull roughness. It is meant to be helpful in interpreting hydrodynamic results, obtained on a hull model, in the light of the flow conditions prevailing on the full size ship. In deriving the thereto pertaining Eq. (28), they seem to have applied the wrong 'roughness Reynolds number':  $U_k/\nu$ . It would have been more appropriate to employ here not the free stream velocity  $U$  but the wall friction velocity  $u_*$ . Should the latter velocity be engaged in this context, a somewhat different Eq. (28) would emerge giving the scaling factor a more realistic meaning.
2. In Sec. 4 the authors show how the roughness function  $\Delta U/u_*$  could be formulated. Coles' law of the wall is being employed in this procedure with the recommendation that  $\Pi$  (strength of

the wake component) be given the value there is ample evidence now that the surface roughness (including modest waviness) can change this value substantially. This is naturally caused by the fact that non-smooth surfaces can interfere with the turbulence diffusivity in a boundary layer which in turn affects the large eddies in the outer region whence the effect on  $\Pi$ . There is not much prospect in finding a substitute value for turbulent boundary layers on rough plates as such a 'universal' value probably does not exist and each roughness generates its own flat plate  $\Pi$ . The only safe way would be to determine  $\Pi$  experimentally in a fully developed turbulent pipe flow for each type of hull roughness in question.

3. Presumably the authors would agree that their formula for 'augmentation of local friction resistance due to surface roughness'

$\Delta C_f = C_{f0}^{3/2} (\Delta U/u_*)$  is Reynolds number ( $Re = UL/\nu$ ) dependent and it is so mainly through  $C_{f0}$ . Such a dependence could profitably be untangled in Eq. (23) in order to render it immediately applicable to large ship hulls.

4. Most likely unintentionally, the authors seem to have overemphasized the relationship between  $k_s$  and  $k_a$ . Someone less knowledgeable in the field than the authors might jump into the conclusion that there always is an equivalent sand grain size (in the Nikuradse sense) for every kind of marine roughness. Of course, this is false since in no way Nikuradse's sand grain roughness could simulate structurally (not only as regards the wall eddy shedding and thereto related local form drag on excrescences) that of a typically irregular marine nature, even though both can be matched on the classic Nikuradse friction factor plot.



## LIST OF PARTICIPANTS

### AUSTRALIA

Goh, Mark  
University of Adelaide  
Halliday, Robert F.  
University of Sydney  
Tuck, Ernst O., Prof.  
University of Adelaide

### AUSTRIA

Strasser, Gerhard, Dr.-Ing.  
Schiffbautechnische Versuchsanstalt, Wien

### BELGIUM

Ferdinande, Valere, Prof.  
State University of Gent

### BULGARIA

Bogdanov, Peter, Dr.  
Bulgarian Ship Hydrodynamics Centre, Varna  
Yosifov, Kostadin, Dr.  
Bulgarian Ship Hydrodynamics Centre, Varna

### CANADA

Calisal, Sander, Prof.  
University of British Columbia, Vancouver  
Ellis, Walter E.  
Defense Research Establishment Atlantic,  
Dartmouth  
Hsiung, Chi-Chao, Prof.  
Technical University of Nova Scotia, Halifax  
Pawlowski, Jacek Stanislaw, Dr.  
National Research Council Canada, Ottawa

### CHINA

Gu, Maoxiang, Prof.  
China Ship Scientific Research Center,  
Beijing  
He, You-Sheng, Prof.  
Shanghai Jiao Tong University, Shanghai  
Yang, Yian-sheng  
Harbin Shipbuilding Engineering Institute,  
Harbin  
Zhao, Lian-en  
Harbin Shipbuilding Engineering Institute,  
Harbin  
Zhou, Lian-di  
China Ship Scientific Research Center, Wuxi,  
Jiangsu

### DENMARK

Jensen, Peter  
The Technical University of Denmark, Lyngby

### FEDERAL REPUBLIC OF GERMANY

Albrecht, Klaus, Dipl.-Ing.  
Fraunhofer-Institut f. Hydroakustik,  
Ottobrunn  
Alwardt, Peter, Dr.rer.nat.  
AEG Schiffbau, Wedel  
Bartels, Fritz, Dr.  
Fraunhofer-Institut f. Hydroakustik,  
Ottobrunn

Chao, Kuo-Yih, Dr.  
Hamburg Ship Model Basin, Hamburg  
Collatz, Günter, Dr.-Ing.  
Hamburg Ship Model Basin, Hamburg  
Eggers, Klaus, Prof. Dr.  
Institut für Schiffbau, Hamburg  
Friesch, J., Dipl.-Ing.  
Hamburg Ship Model Basin, Hamburg  
Hampel, Bernd, Dipl.-Ing.  
Institut für Schiffbau, Hamburg  
Heuser, Hans H., Prof. Dr.  
Versuchsanstalt für Binnenschiffbau,  
Duisburg  
Jensen, Gerhard, Dipl.-Ing.  
Institut für Schiffbau, Hamburg  
Keil, Harald, Prof. Dr.-Ing.  
Technische Universität Hamburg-Harburg  
Kokkinowrachos, K., Prof. Dr.  
Technische Universität Hamburg-Harburg  
Kracht, Alfred M., Dr.-Ing.  
Versuchsanstalt für Wasserbau und Schiffbau,  
Berlin  
Krappinger, Odo, Prof. Dr.-Ing.  
Hamburg Ship Model Basin, Hamburg  
Kux, Jürgen, Dr.  
Institut für Schiffbau, Hamburg  
Lang, Bernt, Dr.-Ing.  
Versuchsanstalt für Wasserbau und Schiffbau,  
Berlin  
Laudan, Jochen, Dipl.-Ing.  
Hamburg Ship Model Basin, Hamburg  
Luthra, Gurdip, Dipl.-Ing.  
Versuchsanstalt für Binnenschiffbau, Duisburg  
Müller, Ernst, Dr.-Ing.  
Versuchsanstalt für Binnenschiffbau, Duisburg  
Nowacki, Horst, Prof. Dr.-Ing.  
Technische Universität Berlin, Berlin  
Østergaard, Carsten, Dr.-Ing.  
Germanischer Lloyd, Hamburg  
Oltmann, Peter, Dr.-Ing.  
Hamburg Ship Model Basin, Hamburg  
Osawa, Yoshihiko  
Institut für Schiffbau, Hamburg  
Payer, Hans G., Dr.  
Germanischer Lloyd, Hamburg  
Pereira, Ricardo  
Institut für Schiffbau  
Rader, Herbert Paul  
formerly Hamburg Ship Model Basin, Hamburg  
Remmers, Bernd, Dipl.-Ing.  
Kempf & Remmers GmbH, Hamburg  
Scheel, Hans W., Baudirektor  
Bundesministerium der Verteidigung, Bonn  
Schmiechen, Michael, Prof. Dr.-Ing.  
Versuchsanstalt für Wasserbau und Schiffbau,  
Berlin  
Schwanecke, H., Prof. Dr.-Ing.  
Versuchsanstalt für Wasserbau und Schiffbau,  
Berlin  
Sharma, Som D., Prof. Dr.-Ing.  
Institut für Schiffbau, Hamburg  
Söding, Heinrich, Prof. Dr.-Ing.  
Institut für Schiffbau, Hamburg  
Thomsen, Claus Peter, Prof. Dr.-Ing.  
Fachhochschule Hamburg

Weitendorf, Ernst-August, Dr.-Ing.  
Hamburg Ship Model Basin, Hamburg  
Wieghardt, Karl Prof. Dr.  
Institut für Schiffbau, Hamburg

#### FINLAND

Matusiak, Jerzy  
Technical Research Centre of Finland,  
Espoo

#### FRANCE

Bindel, Serge, Prof.  
Ecole Nationale Supérieure de Techniques  
Avancées, Paris  
Bovis, Alain, Dr.-Ing.  
Bassin d'Essais des Carènes, Paris  
Coirier, Jean, Prof.  
ENSM, Poitiers  
Dern, Jean-Claude  
Bassin d'Essais des Carènes, Paris  
Euvrard, Daniel, Prof.  
ENSTA/University Paris, Palaiseau  
Fernandes, Gilles, Dr.  
Bassin d'Essais des Carènes, Paris  
Genoux, Philippe F.  
Ministère de la Défense Armement, Paris  
Germain, Jean Pierre, Prof.  
Institut de Mécanique de Grenoble,  
St. Martin d'Hères  
Giovachini, Jean-Luc  
Bassin d'Essais des Carènes, Paris  
le Goff, Jean-Pierre  
D.R.E.T., Paris  
Guilbaud, Michel  
ENSM, University de Poitiers  
Jami, Adrien  
CNRS/ENSTA, Palaiseau  
Julienne  
ONERA Chatillon  
Licht, Christian  
Institut de Recherche de la Construction  
Navale, Paris  
Martin, Daniel  
Institut National des Sciences Appliquées,  
Rennes  
Molin, Bernard, Dr.  
Institut Français du Pétrole, Reuil-Malmaison  
Piquet, Prof.  
E.N.S.M., Nantes  
Richer, Jean-Philippe  
Institut de Recherche de la Construction  
Navale, Paris

#### GERMAN DEMOCRATIC REPUBLIC

Puls, Dieter, Prof.  
University of Rostock, Rostock

#### GREECE

Loukakis, Theodore, Prof.  
National Technical University, Athens

#### INDIA

Nagarajan, Sambamurti, Dr.  
Aeronautical Development Establishment,  
Bangalore

#### ISRAEL

Auslaender, Jakob  
CEMA, Haifa  
Dagan, Gideon, Prof.  
Tel Aviv University, Tel Aviv  
Miloh, Touvia, Prof.  
Tel Aviv University, Tel Aviv

#### ITALY

Boccardo, Guido  
University of Napoli, Napoli  
Chilo, Bruno  
CETENA S.p.A., Genova  
Fasano, Ernesto  
University of Napoli, Napoli  
Nabergoj, Radoslav  
Institute of Naval Architecture Trieste

#### JAPAN

Abe, Mitsuhiro  
Mitsui Eng. & Shipbuilding Co, Akishima Lab.,  
Tokyo  
Arai, Makoto, Dr.-Ing.  
Ishikawajima-Harima Heavy Industries Co.Ltd.  
Yokohama Research Institute, Yokohama  
Baba, Eiichi, Dr.  
Mitsubishi Heavy Industries Ltd., Nagasaki  
Bessho, Masatoshi, Prof.  
National Defense Academy, Yokosuka  
Fukasawa, Toichi, Dr.  
University of Tokyo  
Himeno, Yoichi, Prof.  
University of Osaka Prefecture, Osaka  
Ikehata, Mitsuhiro, Dr.  
Yokohama National University, Yokohama  
Inui, Takao, Prof. Dr.-Ing.  
University of Tokyo  
Isshiki, Hiroshi, Dr.-Ing.  
Technical Research Institute, Hitachi Zosen  
Corp. Osaka  
Maeda, Hisaaki, Prof.  
University of Tokyo  
Maruo, Hajime, Prof. Dr.  
Yokohama National University, Yokohama  
Mori, Kazu-Hiro, Prof.  
Hiroshima University, Higashi-Hiroshima  
Matora, Seizo, Prof.  
Japan Foundation for Shipbuilding Advancement,  
Tokyo  
Nakamura, Shoichi, Prof. Dr.-Ing.  
Osaka University, Osaka  
Nakatake, Kuniharu, Prof.  
Kyushu University, Fukuoka  
Ohkusu, Makoto, Prof.  
Kyushu University, Kasuga  
Onogi, Hiroshi  
Nippon Kokan K.K., Tsu-City  
Takahashi, Hajime, Dr.  
Ship Research Institute, Tokyo  
Takezawa, Seiji, Prof.  
Yokohama National University, Yokohama  
Tasaki, Ryo, Dr.-Ing.  
Ishikawajima-Harima Heavy Industries Co.Ltd.,  
Research Institute, Yokohama  
Terao, Yutaka, Dr.  
Tokai University, Shizuoka

Yamanouchi, Yasufumi, Dr.  
Akishima Laboratory Mitsui Engineering,  
Tokyo  
Yamazaki, Ryusuke, Prof.  
Kyushu University, Fukuoka

#### KOREA

Lee, Chang-Sup, Dr.  
Ship Research Station, KIMM, Chungnam  
Lee, Hong-Gi  
Hyundai Maritime Research Institute, Ulsan  
Yu, Byung-Kun  
Hyundai Heavy Industries Co., Ulsan

#### THE NETHERLANDS

Aalbers, Albert  
MARIN, Wageningen  
Brandsma, Frans, Dr.  
Technische Hogeschool Delft  
den Held, W.J.  
Gusto Engineering B.V., Schiedam  
Hermans, Aad J., Prof. Dr.  
Technische Hogeschool Delft  
Huijsmans, René  
MARIN, Wageningen  
Janse, S.A.W.  
Gusto Engineering B.V., Schiedam  
Muntjewerf, Jacob J., Dr.  
MARIN, Wageningen  
Omta, Roelof, Dr.  
Technological University Twente, Enschede  
van Oortmerssen, Gerard, Dr.  
MARIN, Wageningen  
Potze, Willem  
University Groningen  
Sparenberg, J.A., Dr.  
University Groningen  
Urbach, H.P.  
University Groningen  
van der Vegt, Jaap  
MARIN, Wageningen  
de Vries, Jacob  
University Groningen

#### NORWAY

Børresen, Rolf  
Norwegian Hydrodynamic Laboratories,  
Trondheim  
Faltinsen, O., Prof.  
Norwegian Institute of Technology, Trondheim  
Grue, John  
University of Oslo  
Lian, Walter  
Norwegian Institute of Technology, Trondheim  
Marthinsen, Tom, Dr.  
A/S Veritas Research, Høvik  
McHenry, George  
A/S Veritas Research, Høvik  
Palm, Enok, Prof.  
University of Oslo  
Pettersen, Bjørnar  
Norwegian Institute of Technology, Trondheim  
Skogvang, Arnljot  
SAGA Petroleum, Høvik  
Sogstad, Bjoern  
A/S Veritec, Høvik  
Tellsgard, Finn  
A/S Veritec, Høvik

Vada, Torgeir  
University of Oslo  
Vinje, Tor, Dr.-Ing.  
A/S Veritas Research, Høvik

#### POLAND

Krezelewski, Mieczyslaw, Prof.  
Technical University Gdańsk  
Pawlowski, Maciej, Dr.  
Technical University Gdańsk

#### SWEDEN

van Berlekom, Willem  
Swedish Maritime Research Centre, Göteborg  
Broberg, Leif  
Chalmers University of Technology,  
Gothenburg  
Larsson, Lars, Prof.  
SSPA Maritime Consulting AB, Gothenburg

#### SPAIN

Alaez, Jose A., Prof.  
Canal de Experiencias Hidrodinamicas,  
El Pardo  
Perez-Sobrinio, Mariano  
Canal de Experiencias Hidrodinamicas,  
El Pardo

#### UNITED KINGDOM

Baar, Job, J.M., Dr.  
Mechanical Engineering Dept.,  
Brunel University, Uxbridge, Middlesex  
Ball, Wendy Eve  
Admiralty Research Establishment, Haslar  
Clayton, Brian, Dr.  
University College London  
Dawkins, Robert A., Dr.  
Lloyd's Register of Shipping, London  
Eatock-Taylor, Rodney, Dr.  
University College London  
Evans, David V., Dr.  
University of Bristol  
Fitzsimmons, Patrick  
British Ship Research Association,  
Newcastle upon Tyne  
Glover, Edward J., Dr.  
University of Newcastle, Newcastle upon Tyne  
Hulme, Andrew, Dr.  
University of Manchester  
Lewkowicz, Alexander, Dr.  
University of Liverpool  
Martin, John, Dr.  
University of Edinburgh  
Martin, Paul Andrew, Dr.  
University of Manchester  
McGregor, Robert Dr.  
University of Glasgow  
McIver, Philip, Dr.  
University of Bristol  
Mikelis, Nicos, Dr.  
Lloyd's Register of Shipping, London  
Muskier, Antony, Dr.  
Admiralty Research Establishment, Haslar  
Simon, Michael, Dr.  
The University of Manchester  
Ursell, Fritz, Prof.  
University of Manchester  
Wu, June-Young  
University of Glasgow

UNITED STATES OF AMERICA

Ankudinov, Vladimir  
Tracor Hydronautics, Laurel

Beck, Robert, Prof.  
University of Michigan, Ann Arbor

Breslin, John, Prof.  
Stevens Institute of Technology, Hoboken, NJ

Chwang, Allen, Prof.  
The University of Iowa, Iowa City

Cooper, Ralph, Dr.  
National Academy of Sciences, Washington

Couch, Richard, Prof.  
University of Michigan, Ann Arbor

Forbes, Lawrence K., Prof.  
Kansas State University, Manhattan, Kansas

Fry, David  
DTNSRDC, Bethesda

Furuya, Okitsugu  
Tetra Techn. Inc., Pasadena, CA

Groves, Nancy  
DTNSRDC, Bethesda

Huang, Thomas  
DTNSRDC, Bethesda

Jan, Hsien Yun, Dr.  
American Bureau of Shipping, New York

Jessup, Stuart  
DTNSRDC, Bethesda

Jöns, Otto, Dipl.-Ing.  
Advanced Marine Enterprises Inc.,  
Potomac/MD

Lee, Choung M., Dr.  
Office of Naval Research, Arlington

Lin, Wen-Chin  
DTNSRDC, Bethesda

Lin, Woei-Min  
Massachusetts Institute of Technology,  
Cambridge

McCarthy, Justin H.  
DTNSRDC, Bethesda

Mei, Chiang C., Prof.  
Massachusetts Institute of Technology,  
Cambridge

Mendenhall, Michael  
Nielsen Engineering & Research,  
Mountain View

Morgan, William, Dr.  
DTNSRDC, Bethesda

Newman, John N., Prof.  
Massachusetts Institute of Technology,  
Cambridge

O'Dea, John  
DTNSRDC, Bethesda

Parkin, Blaine, Prof.  
State College Pennsylvania

Patel, Virendra C., Prof.  
Iowa Institute of Hydraulic Research,  
The University of Iowa, Iowa City

Powell, Alan  
DTNSRDC, Bethesda

Schlappi, Herman C.  
Ingalls Shipbuilding, Pascagoula

Schreiber, Herbert  
Lockheed Advanced Marine Systems,  
Santa Clara, CA

Sclavounos, Paul, Prof.  
Massachusetts Institute of Technology,  
Cambridge

St. Denis, Manley, Dr.  
University of Hawaii in Honolulu

Tulin, P., Prof.  
University of California, Santa Barbara

Vanden Broeck, Jean-Marc, Prof.  
University of Wisconsin, Madison

Victoria, Keith J., Dr.  
Acience Applications, Inc., La Jolla, CA

Webster, William C., Prof.  
University of California, Kensington, CA

Wehausen, John V., Prof.  
University of California, Berkely, CA

Wu, Theodore Y., Prof.  
California Institute of Technology,  
Pasadena

Yeung, Ronald W., Prof.  
University of California, Berkeley

Yih, Chia-Shun, Prof. Dr.  
The University of Michigan, Ann Arbor

Yue, Dick, Prof.  
Massachusetts Institute of Technology,  
Cambridge

## INDEX OF CONTRIBUTORS

- Aalbers, A., 69  
 Abe, M., 315, 499  
 Amromin, E.L., 419  
 Ando, M., 261, 276  
 Ankudinov, V., 106  
 Baba, E., 258, 315, 425, 477  
 Ball, W.E., 236  
 Bessho, M., 109, 118  
 Bindel, S., 148, 175, 315  
 Blaurock, J., 236, 477  
 Børresen, R., 51  
 Breslin, J., 276, 444  
 Broberg, L., 525, 538  
 Chang, M.S., 288, 429, 444, 538  
 Chen, H.C., 505, 522  
 Chwang, A., 48, 407, 417  
 Dagan, G., 373, 385  
 Dong, Z., 407, 417  
 Dyne, G., 289, 499  
 Eggers, K., 385, 387, 405  
 Ertekin, R.C., 347, 363  
 Faltinsen, O., 51  
 Fry, D., 259, 319, 346  
 Furuya, O., 445, 461  
 Fukusawa, T., 174  
 Gent, W. van, 69  
 Granville, P., 567  
 Groves, N., 429, 444  
 Halliday, R.F., 300, 425  
 Hermans, A.J., 585  
 Himeno, Y., 553, 568  
 Huang, T., 259, 288, 521  
 Huijsmans, R., 569, 585  
 Ikehata, M., 261, 276  
 Isshiki, H., 117, 361, 417, 539  
 Ivanov, A.N., 419  
 Jeffers, M., 221, 236  
 Jensen, G., 385  
 Jessup, S., 221, 236, 276  
 Kaklis, P.D., 213  
 Kim, S.H., 195, 216  
 Kim, Y.H., 319, 346  
 Kobayashi, S., 221, 236  
 Kracht, A.M., 315, 403  
 Krappinger, O., 3  
 Kux, J., 239, 259  
 Kyojuka, Y., 109, 118  
 Larsson, L., 289, 525, 538  
 Laudan, J., 239, 259  
 Lee, S.J., 361  
 Lee, Y.T., 521  
 Lin, W.M., 33, 48  
 Lo, E., 149  
 Loukakis, T., 174, 521  
 Martin, P.A., 119  
 Maruo, H., 261, 276  
 Masuko, A., 404  
 Matusiak, J., 106  
 McGregor, R., 117, 175  
 Mei, C.C., 149  
 Miloh, T., 373, 385  
 Miyata, H., 315, 401  
 Mizin, I.O., 419  
 Morgan, W.B., 461  
 Mori, K.H., 258, 303, 316, 402, 521  
 Murakami, M., 549  
 Musker, A.J., 346, 361, 425, 568  
 Nagamatsu, T., 258  
 Nakatake, K., 463, 478, 510  
 Nakato, M., 553, 568  
 Newman, J.N., 33, 48  
 Nowacki, H., 477  
 O'Dea, J., 163, 175  
 Ogiwara, S., 404  
 Ohkusu, M., 135, 148  
 Oltmann, P., 83, 108  
 Onogi, H., 553, 568  
 Patel, V.C., 315, 404, 505, 522  
 Pawelczyk, A., 3  
 Pawlowski, J.S., 193, 215  
 Pettersen, B., 585  
 Pfarr, H.M., 4  
 Press, F., 5  
 Sclavounos, P., 177, 193  
 Sharma, S.D., 83, 108, 301, 346, 477  
 Schmiechen, M., 289, 478, 481, 500  
 Schott, C., 221, 236  
 Schwanecke, H., 276  
 Suzuki, T., 553, 568  
 Takekuma, K., 387, 405  
 Tanaka, I., 553, 568  
 Terao, Y., 539  
 Thomsen, C.P., 403  
 Timoshin, Y.S., 419  
 Tuck, E.O., 48, 293, 301  
 Tulin, M.P., 9  
 Vanden-Brock, J.M., 293, 301  
 van der Vegt, J., 569, 585  
 Walden, D.A., 163, 175  
 Webster, W.C., 174, 347, 363  
 Wehausen, J.V., 347, 363  
 Weitendorf, E.A., 259, 461  
 Wu, T.Y., 361  
 Yamazaki, R., 463, 478  
 Yates, G.T., 361  
 Yeung, R.W., 48, 195, 216  
 Yih, C.S., 300, 367  
 Yuan, J., 279, 290  
 Yue, D., 33, 48  
 Zhou, L., 279, 290, 499, 522